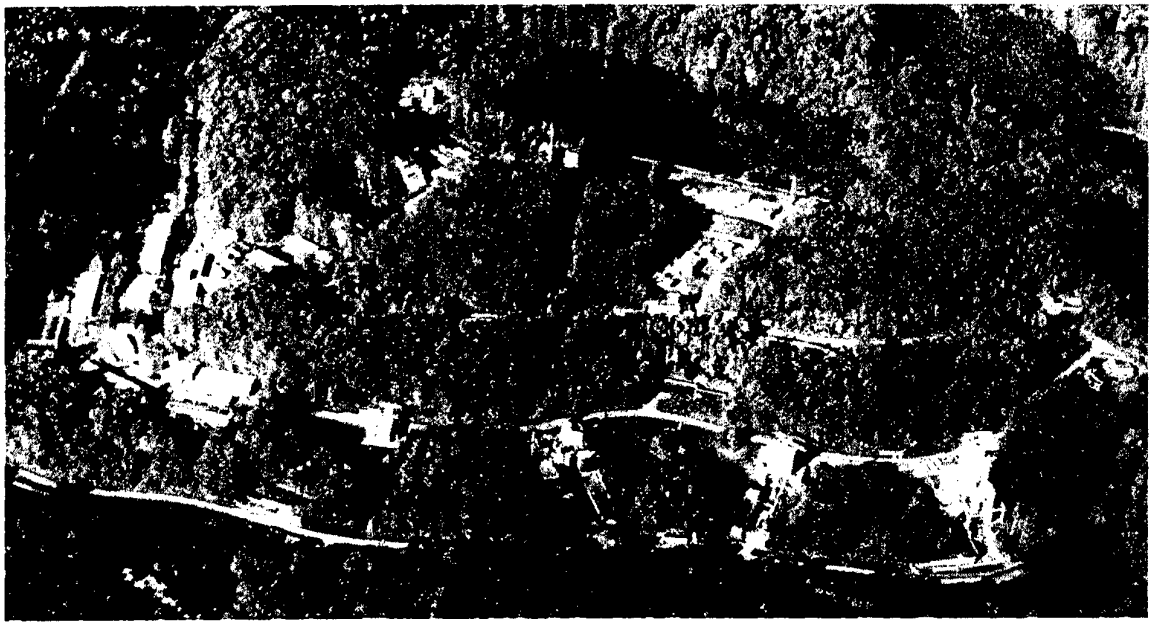
Fourth International Symposium on Liquid Space Propulsion

Scientific Progress in the Service of Space Access at the Beginning of the Third Millennium



DLR - Lampoldshausen, Germany
March 12 - 15, 2000

20010806 094

Sponsored by:

DaimlerChrysler Aerospace (Dasa),
Deutsches Zentrum für Luft- und Raumfahrt e.V. (DLR),
European Office of Aerospace Research and Development (AFOSR),
Office Nationale d' Etudes et de Recherches Aérospaciales (ONERA)

AQ F01-11-2198

REPORT DOCUMENTATION PAGE

Form Approved OMB No. 0704-0188

Public reporting burden for this collection of information is estimated to average 1 hour per response, including the time for reviewing instructions, searching existing data sources, gathering and maintaining the data needed, and completing and reviewing the collection of information. Send comments regarding this burden estimate or any other aspect of this collection of information, including suggestions for reducing this burden to Washington Headquarters Services, Directorate for Information Operations and Reports, 1215 Jefferson Davis Highway, Suite 1204, Arlington, VA 22202-4302, and to the Office of Management and Budget, Paperwork Reduction Project (0704-0188), Washington, DC 20503.

1. AGENCY USE ONLY (Leave blank)	2. REPORT DATE	3. REPORT TYPE AND DATES COVERED
	24 August 2000	Conference Proceedings

4. TITLE AND SUBTITLE

4th International Symposium on Liquid Space Propulsion, Scientific Progress in the Service of Space Access at the Beginning of the Third Millenium

5. FUNDING NUMBERS

F61775-00-WF025

6. AUTHOR(S)

Conference Committee

7. PERFORMING ORGANIZATION NAME(S) AND ADDRESS(ES)

German Aerospace Center
Langer Grund
Lampoldshausen 74239
Germany

8. PERFORMING ORGANIZATION REPORT NUMBER

N/A

9. SPONSORING/MONITORING AGENCY NAME(S) AND ADDRESS(ES)

EOARD
PSC 802 BOX 14
FPO 09499-0200

10. SPONSORING/MONITORING AGENCY REPORT NUMBER

CSP 00-5025

11. SUPPLEMENTARY NOTES

12a. DISTRIBUTION/AVAILABILITY STATEMENT

Approved for public release; distribution is unlimited.

12b. DISTRIBUTION CODE

A

13. ABSTRACT (Maximum 200 words)

The Final Proceedings for 4. International Symposium on Liquid Space Propulsion, Scientific Progress in the Service of Space Access at the Beginning of the Third Millenium, 13 March 2000 - 15 March 2000

The symposium is focused on Liquid Space Propulsion including all aspects of analysis, modeling, and design. Besides an introductory topical session on future programs given by representatives from agencies and industries, prospective authors are invited to contribute to the symposium by presenting papers in the following main categories which are chosen to provide a well-bounded balance.

· Advanced Cycles (SSTO, FFC, RBCC, TBCC, LACE, PDE)
· Advanced Materials for Thrust Chamber Technologies
· Heat-Flux Management and Cooling Techniques
· Transient Flow Phenomena during Start-up and Shut-Down (Ignition and Re-Ignition)
· Nozzle Flow Separation and Side Loads
· Combustion Instability
· High Pressure Combustion Phenomena and Related Diagnostic and Modeling Issues
· Progress in CFD for Rocket Engine Flow and Heat Transfer Analyses
· Propellant Management and Acquisition in Propulsion Systems
· Health Monitoring and Life Extension
· Plume Contamination
· Low Cost Technologies

14. SUBJECT TERMS

EOARD, Chemical Propulsion, Rocket Engines

15. NUMBER OF PAGES

550

16. PRICE CODE

N/A

17. SECURITY CLASSIFICATION OF REPORT	18. SECURITY CLASSIFICATION OF THIS PAGE	19. SECURITY CLASSIFICATION OF ABSTRACT	20. LIMITATION OF ABSTRACT
UNCLASSIFIED	UNCLASSIFIED	UNCLASSIFIED	UL

Fourth International Symposium on Liquid Space Propulsion:

Scientific Progress in the Service of Space Access at the Beginning of the Third Millennium

Final Program

Monday, March 13

Session 1: Boost and Upper Stage Propulsion **Chairs: W. Koschel, P. Kuentzmann**

08.00 - 08.40 "*Critical Boost Propulsion Initiatives and Issues for the First Decade of the Third Millennium*," by R.J. Jensen, R. Edelman, J. Fang, and S. Farhangi, Rocketdyne, U.S.A.

08.40 - 09.20 "*Challenges in Future Liquid Rocket Engine Technologies*", by M. Pons, P. Vuillermoz, Centre National d'Etudes Spatial (CNES), Evry, France, D. Preclik, G. Hagemann, H. Immich, DaimlerChrysler Aerospace (Dasa), Ottobrunn, Germany, V. Duthoit, and J.L. Thomas, SNECMA, Vernon, France

09.20 - 10.00 "*Next-Generation Chemical Propulsion for Spacecraft Attitude Control and Orbital Maneuvering*," by P.-K. Wu, R.P. Fuller, C.R. Stechman, and A.S. Nejad, Kaiser Marquardt, U.S.A.

10.00 - 10.40 "*Peroxide Propulsion at the Turn of the Century*," by W. Anderson, C. McNeal, NASA Marshall Space Flight Center, D. Crockett, T. Lewis, Orbital Sciences Corporation, and K. Butler, Rocketdyne, Propulsion and Power, The Boeing Company, U.S.A.

10.40 - 11.00 Coffee Break

Session 2: Current Space Transportation Systems Developments **Chairs: R. Jensen, M. Pons**

11.00 - 11.40 "*Future Developments of ARIANE 5*", by J. Ackermann, European Space Agency (ESA), Paris, France

11.40 - 12.20 "*Reliability Overview of First-&-Second-Stage Liquid Propellant Rocket Engines of China Long March Launch Vehicle Family,*" by J. Zhang, The 11th Research Institute of China Aerospace Science & Technology Corporation, China

12.20 - 13.00 "*Liquid Space Propulsion at ESTEC*", by F. Felici, H. Schoeyer et al., ESA/ESTEC, Nordwijk, Netherlands

13.05 - 14.05 Lunch

Session 3: Advanced Propulsion Concepts **Chairs: X. Hao, J. Ackermann**

14.05 - 14.45 "*Pulse Detonation Rocket Engines,*" by C. Merkle, University of Tennessee, U.S.A.

14.45 - 15.25 "*In Flight LOX Collection: System Aspects and Experimental Results*", by P. Hendrick et al., Royal Academy, Brussels, Belgium

15.25 - 16.05 "*Current Status of Propellant Injection in a SCRAMJET Engine within the French/German JAPHAR Project*", by D. Gaffié, P. Novelli, ONERA, Chatillon, France U. Brummund, DLR Lampoldshausen and G. Weppler, RWTH Aachen, Germany

16.05 - 16.20 Coffee Break

Session 4: Combustion Stability **Chairs: M. Birkan, G. Langel**

16.20 - 17.00 "*A Study of Combustion Stability of Hypergolic Bipropellant Liquid Rocket Engines,*" by X. Hong and Z. Zhang, Shanghai Academy of Spaceflight Technology, China

17.00 - 17.40 "*Experimental Method of Effectiveness Estimation of Different Damped Measures for Oscillations in LRE Combustion Chambers and Gas Generators*", by D. Lebedinsky and S. Mossolov, Keldysh Research Center, Moscow, Russia

17.40 - 18.20 "*On the Nature of Noise-to-self-oscillation Transition involved in Liquid Rocket Engine Combustion Process*", by K. Denisov , V.N. Ivanov, V.P. and Pikalov, NIICHIMMASH, Moscow, Russia

Tuesday, March 14

7.55 - 8.00 Introductory Remarks

Session 5: Thrust Nozzles Flow and Design **Chairs: F. Felici, V. Smirnov**

08.00 - 08.40 *"Nozzle Flow Separation and Side Loads,"* by G. Hagemann, Dasa, Ottobrunn, Germany, M. Frey, DLR Lampoldshausen, Germany, M. Onofri, University of Rome, Rome, Italy, J. Oestlund, Volvo Aero Corporation, Trollhättan, Sveden, and P. Rejasse, ONERA, Chatillon, France

08.40 - 09.20 *"Thrust Nozzle Profiling"*, by G. Dumnov, N. Ponomariov, Keldysh Research Center, Russia, and M. Terhardt, Dasa, Ottobrunn, Germany

09.20 - 10.00 *"Causes of Thrust Performance Loss on a Clustered Linear Aerospike Nozzle"*, by T. Tomita, H. Sakamoto, M. Takahashi, M. Sasaki, T. Onodera, and H. Tamura, National Aerospace Laboratory (NAL), Kakuda Research Center, Japan

10.00 - 10.40 *"High Accuracy Experimental Investigations of Different Nozzle Characteristics on Nozzle Differential Facility"*, by G. Dumnov and G. Nikulin, Keldysh Research Center, Moscow, Russia

10.40 - 11.00 Coffee Break

Session 6: Spray Combustion **Chairs: K. Denisov, V. Yang**

11.00 - 11.40 "Numerical *Approaches to Spray Combustion"*, by E. Gutheil, and D. Schlotz, Interdisziplinäres Zentrum für Wissenschaftliches Rechnen, Universität Heidelberg, Heidelberg, Germany, F.X. Demoulin and R. Borghi, IRPHE, Marseille, France

11.40 - 12.20 *"Cryogenic Combustion: Effects of Pressure and LOX Injector Recess"*, by A. Tripathi, M. Juniper, P. Scouflaire, C. Rolon, and S. Candel, EM2C-Laboratory, Ecole Central Paris, and L. Vingert, ONERA, Palaiseau, France

12.20 - 13.00 *"Theoretical and Practical Issues of CARS Application to Cryogenic Spray Combustion"*, by V. Smirnov, General Physics Institute, Moscow, Russia, F. Grisch, ONERA, Palaiseau, France, M. Oschwald, and W. Clauß, DLR, Lampoldshausen, Germany

13.05 - 14.05 Lunch

Session 7: Combustion Chamber Design Issues **Chairs: M. Habiballah, J. Wang**

14.05 - 14.45 *"Advanced Materials for Thrust Chamber Technologies"*, by O. Haidn and E. Serbest, DLR Lampoldshausen, H. Hald, G. Korger, and P. Winkelmann, DLR Stuttgart, Germany

14.45 - 15.25 *"Application of Thermomechanical Tools to Cryogenic Liquid Rocket Engine Design"*, by D. Kuhl, Ruhr-Universität, Essen, Germany, J. Riccius, A.Woschnak, and O.J. Haidn, DLR Lampoldshausen, Germany

15.25 - 16.05 *"Performance Investigation of the Pre-Burner Used in Oxygen Hydrogen Rocket Engine,"* by J. Wang, S.Q. Cheng, and P.X. Hu, China Academy of Launch Vehicle Technology, Z.G. Wang, J. Zhou, and W.D. Liu, University of National Defense Technology, China.

16.05 - 16.20 Coffee Break

Session 8: Progress in CFD and Health Monitoring **G. Dumnov, H. Immich**

16.20 - 17.00 *"Heat Flux Management and Cooling Techniques in Rocket Thrust Chambers,"* by D. Preclik, D. Haeseler, and G. Hagemann, Dasa, Ottobrunn, Germany, V. Rubinski and V. Orlow, Chemical Automatics Design Bureau, Voronezh, Russia

17.00 - 17.40 *"Impact of Intentional and Un-Intentional Combustion Chamber Porosity on Rocket Engine Characteristics"*, by J. Görgen, D. Haeseler, and O. Knab, Dasa, Ottobrunn, Germany, and D. Wennerberg, Tecosim, Rüsselsheim, Germany

17.40 - 18.20 *"Engine Health Monitoring with Exhaust Plume Emission Spectroscopy,"* by F. Zavelevich, U. Golovin, U. Matzizkiy, K. Moshkin, and A. Romanovskiy, Keldysh Research Center, Moscow, Russia

Wednesday, March 15.

07.55 - 08.00 Introductory Remarks

Session 9: Primary and Secondary Atomization **Chairs: W. Anderson, H. Tamura**

08.00 - 08.40 *"On the Physics of Droplet Formation"*, by J. Eggers, Universität Essen , Germany

08.40 - 09.20 *"Injection of Cryogenic Jets into Subcritical and Supercritical Environments,"* by B. Chehroudi, ERC Inc., R.K. Cohn, and D.G. Talley, Air Force Research Laboratory, U.S.A.

09.20 - 10.20 *"Hot-Fire Studies of LOX Primary Atomization from Rocket Engine Coaxial Injectors"*, by Y.P. Boniface, A.B. Reeb, R.D. Woodward, S. Pal, W. Mayer, and R.J. Santoro, Pennsylvania State University, State College, U.S.A.

10.20 - 11.00 *"On a New Model for Secondary Breakup Model and its Application"*, by I. Gökalp, B. Vielle, S. Derhay, R. Cousty, C. Chauveau, and I. Fedioun, LCSR-CNRS Orleans, France, D. Saucerau, and S. Zurbach, SNECMA, Vernon, France

10.40 - 11.00 Coffee Break

Session 10: Injector Design Issues **Chairs: O. Haidn, D. Lebedisky**

11.00 - 11.40 *"Impinging Injector Atomization Research and Application,"* by M. Zhang and A. Li, The 11th Research Institute of China Aerospace Science & Technology Corporation, China.

11.40 - 12.20 *"The Effects of LOX Post Biasing on SSME Injector Wall Compatibility,"* by P.A. Strakey, D.G. Talley, Air Force Research Laboratory, L.R. Tseng and K.I. Miner, Rocketdyne Propulsion and Power, The Boeing Company, U.S.A.

12.25 - 13.25 Lunch

13.25 - 14.05 *"Effects of Oxidizer Swirling on Combustion Characteristics of Coaxial Injectors"*, by H. Tamura, NAL, T. Inamura, Hirosaki University, S. Yuasu, Tokio Metropolitan Institute of Technology, H. Sakamoto, NAL, and K. Miyata, Hirosaki University, Japan

14.05 - 14.45 *"A Global Optimization Methodology for GO2/GH2 Single Element Injector Design"*, by P.K. Tucker, NASA Marshall Space Flight Center, W. Shyy and R. Vaidyanatha, University of Florida, U.S.A.

14.45 Closing Remarks

Critical Boost Propulsion Initiatives and Issues for the First Decade of the Third Millennium

R. Jensen, R. Edelman, J. Fang and
S. Farhangi
The Boeing Company
Rocketdyne

3M Boost Propulsion Questions

- Has potential for improved performance and reduced weight been exhausted with traditional propellants/engine cycles?
- What can we do to improve boosters faster, better, and cheaper (FBC)?
  - Better reliability and safety
- How many development initiatives should the industry support?

Answers

- Improvements likely but benefits hard to quantify as yet
  - Hot fire/flight demonstration(s) needed
- Successful FBC will require a better blend of improved analysis and acquiring more data per test
- Both high speed air breathing and advanced rocket cycles should be pursued because of lower life cycle cost potential and risk, and better reliability

Three Examples of Boost Technology

- Advanced combustor design tool
  - HyCAD code
- Recent boost technology demonstrations
  - Single Element Oxidizer-Rich LOX/RP-1 Preburner Technology
  - Full Flow Staged Combustion subscale test program

Support goals of improved F/W and FBC

Proven HyCAD Code has Become More Versatile

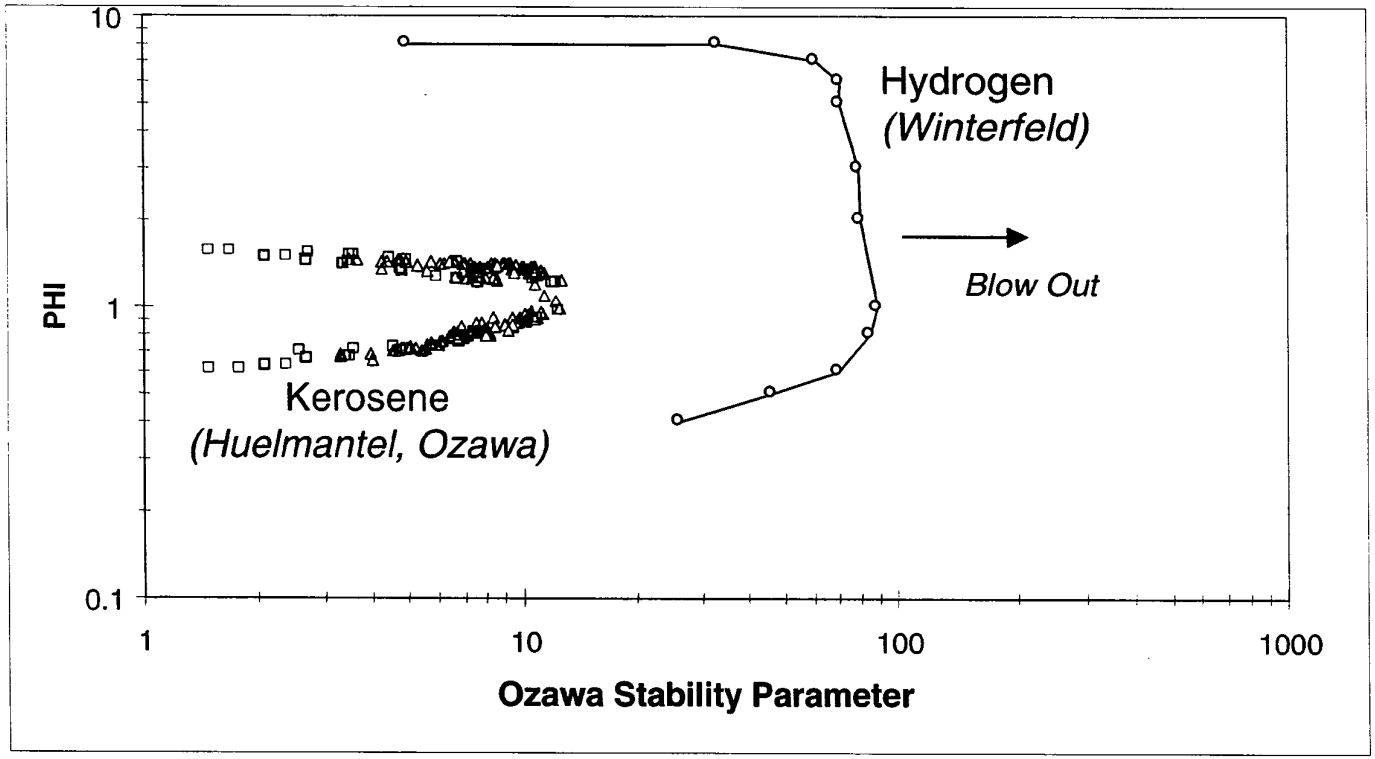
- Developed under NASP program to design combustors and reduce performance data
  - Multi-stream quasi-1D marching code
  - Flameholder, stirred reactor, skin friction, heat transfer, empirical mixing and advanced kinetics
- HC Kinetics package added to support both airbreathing and rocket preburner applications

Flame Stabilization Issues

Pre-Mixed Fuel/Air Combustion

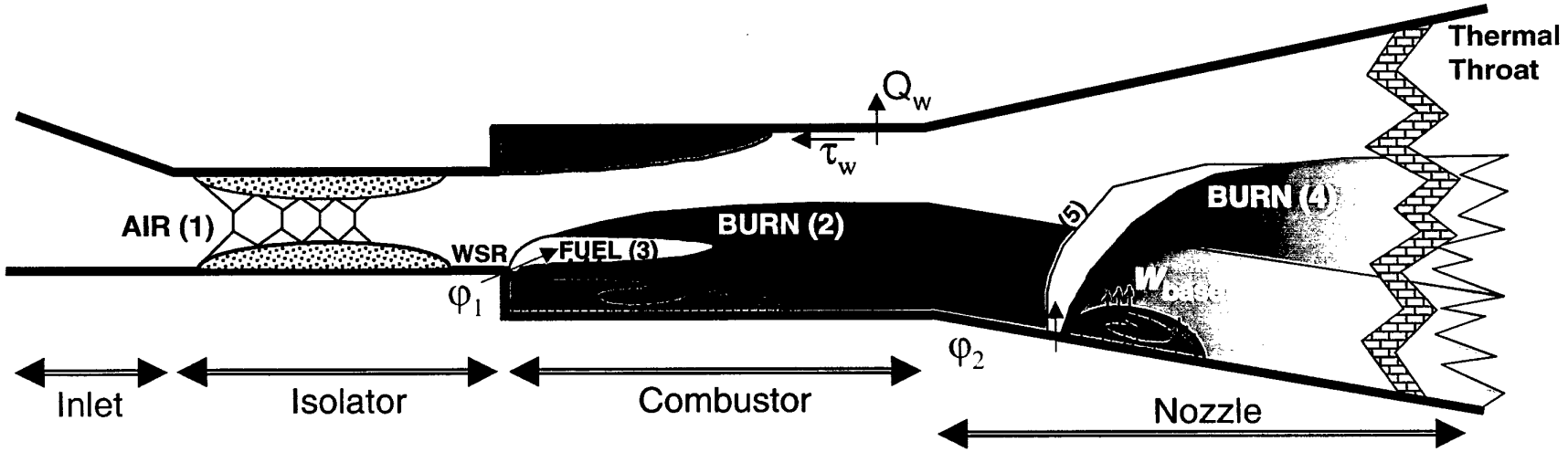
Hydrocarbons:

- **Order of magnitude decrease in flameholding limits**
- **Narrow stability loop requires precise control of equivalence ratio, penetration and mixing**



Multi-Stream HYCAD Model Features

HYpersonic Combustor Analysis and Design Code

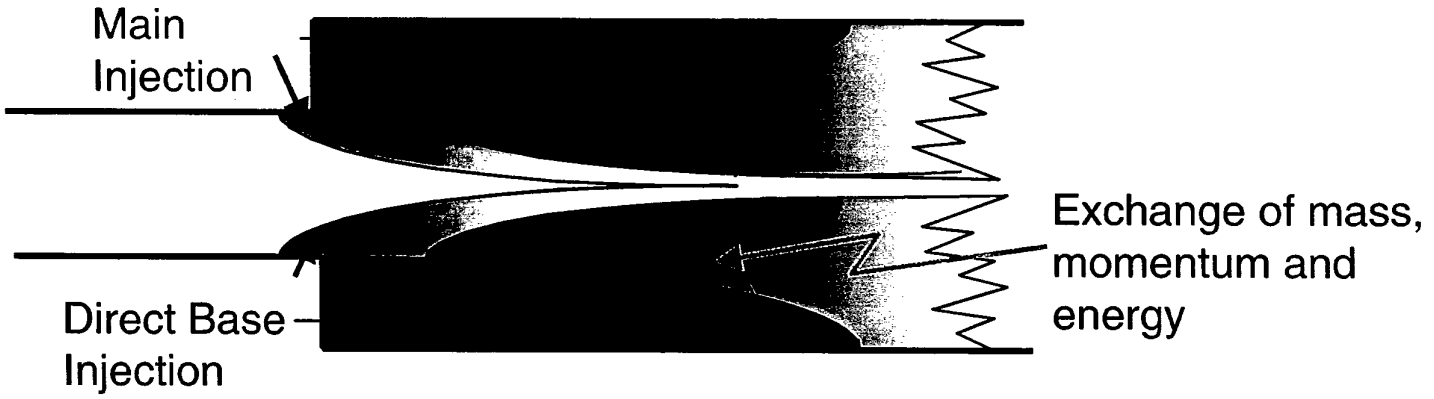


INLET	ISOLATOR	COMBUSTOR	DIFFUSER	SECONDARY INJECTION	NOZZLE
• Supersonic compression	• B.L. Separation • Distortion • Length • Pressure Recovery	• Penetration/Spreading • Mixing • Distortion • j Level • Kinetics **IGNITION & STABILIZATION** • Drag • Propagation • Residence Time • Kinetics • Base Fueling • Mixing	• Separation • Recovery • Kinetics	• Location • j Level • Penetration/Spreading • Flow Distortion • Flameholding • Flame propagation • Thermal Throat • Kinetics	• Distortion • Mixing • Kinetics • Thermal Throat

Flame Holder and Flame Propagation Processes

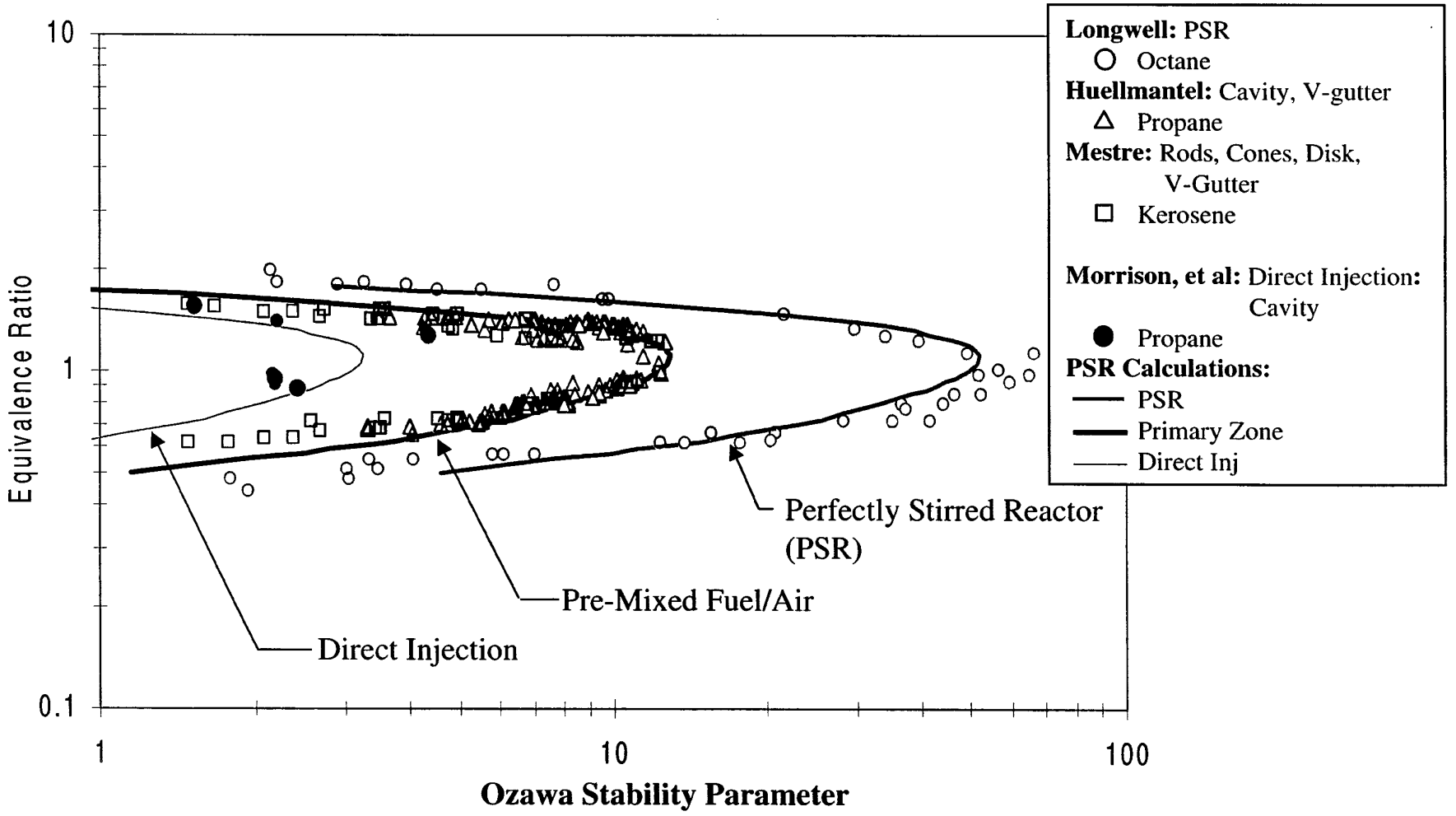
Multi-Stream HYCAD Modeling

- **Recirculation zone (RZ) mass exchange is a fundamental parameter to both flameholding and drag**
  - **Exchange rate determined through empirical relations**
  - **Blow-out and Blow-off limits determined through finite rate kinetics using stirred reactor theory**
  - **Base drag determined by RZ mass exchange**



Recirculation Zone Blowout Limit

Data Compared with HYCAD Blowout Limits

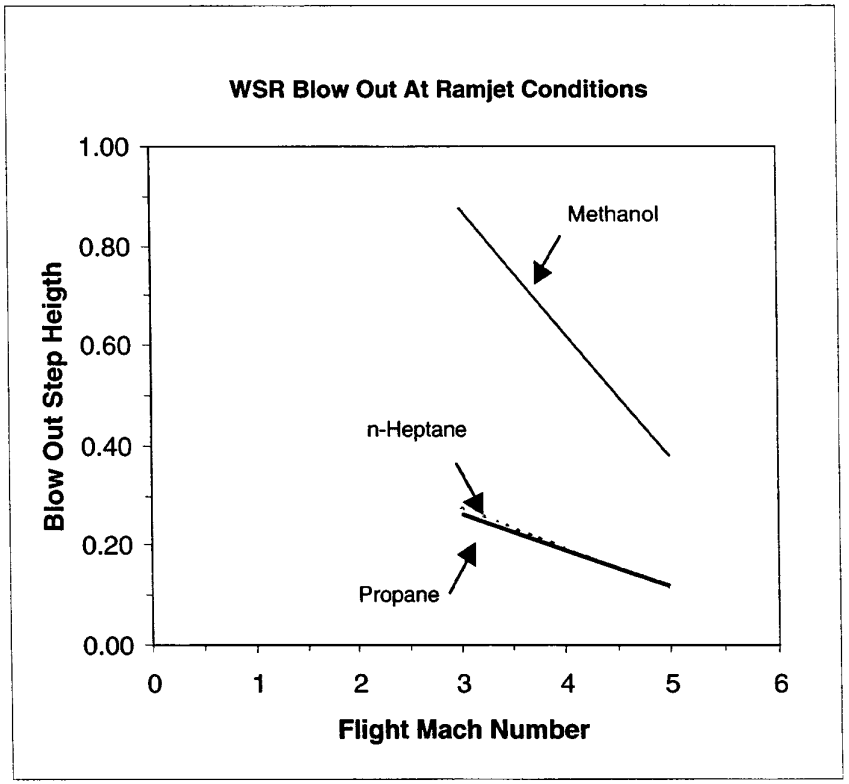


RZ Flame Blow-Out Limit

Minimum Step Height for Direct Fuel Injection



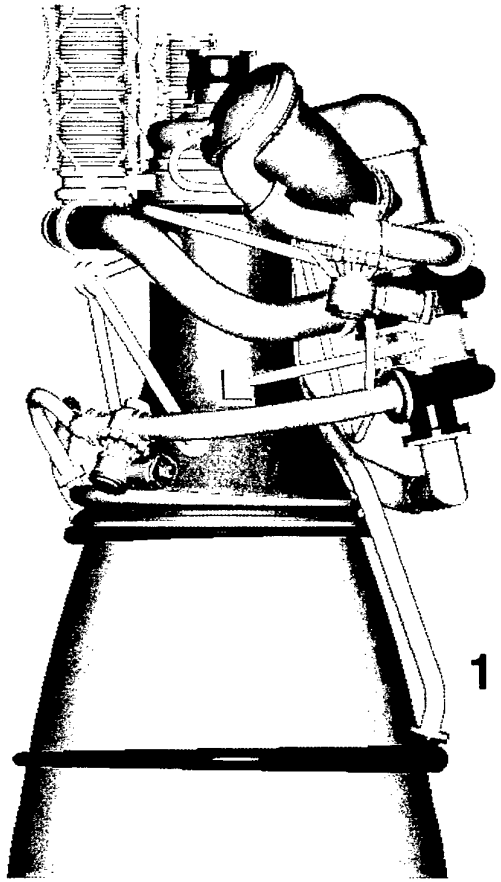


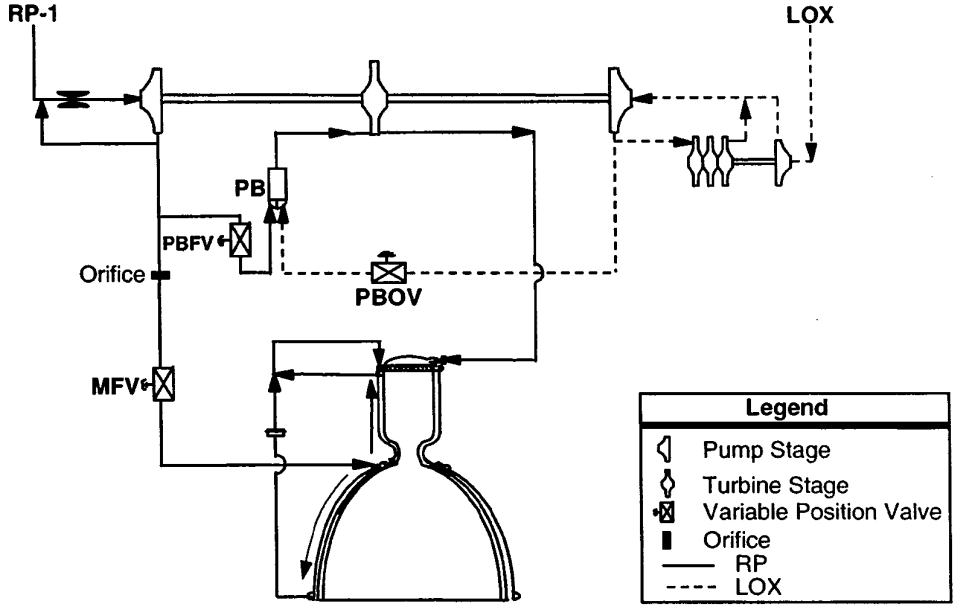


Implications of Code Upgrades

- Good initial definition of combustor flowpath requirements to support advanced HC combustor design limits
  - Ignition, Flameholding, flame stabilization, propellant sensitivity, effects of additives
  - Injector/combustor sizing for minimum weight and improved performance
- Consistent and efficient data analysis tool

RS-76 Boost Engine
A Propulsion System for Low Cost Access to Space





1 million lbf boost engine for LFBB and ELV

- **High Pc, high performance**
- **LOX/RP-1**
- **Oxidizer-rich preburner cycle**
- **Deep throttling**
- **Low cost/high reliability**

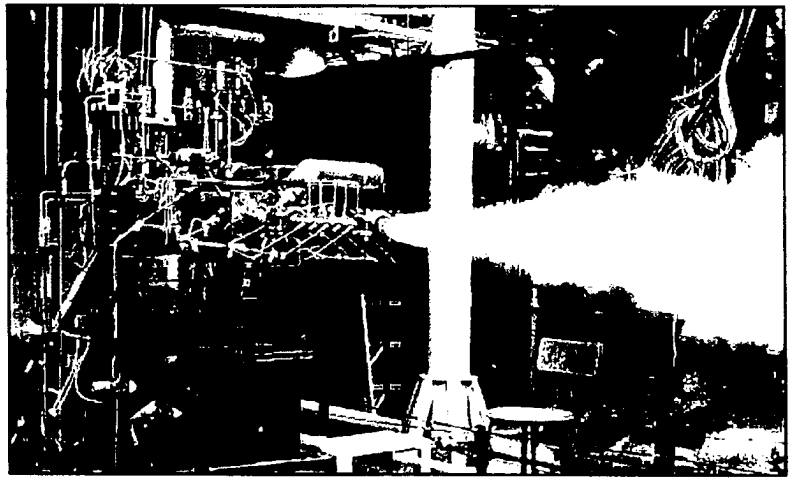
Rocketdyne

BOEING

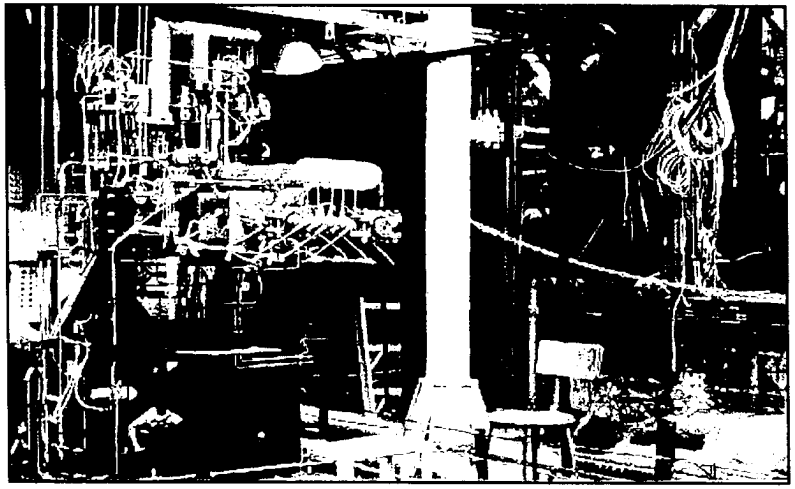
Technical Challenges and Development Approach for LOX/RP-1 ORPB

- Technical Challenges
  - No database available for proven designs
  - Previous domestic research efforts all encountered problems
    - Severe injector and chamber erosions
    - Longitudinal mode combustion instability
  - Development Approach
  - Extensive use of laboratory and sub-scale testing (cold flow/hot fire)
  - Develop and apply advanced engineering analyses
  - Design for minimum risk wherever possible

Single Element Test Facility

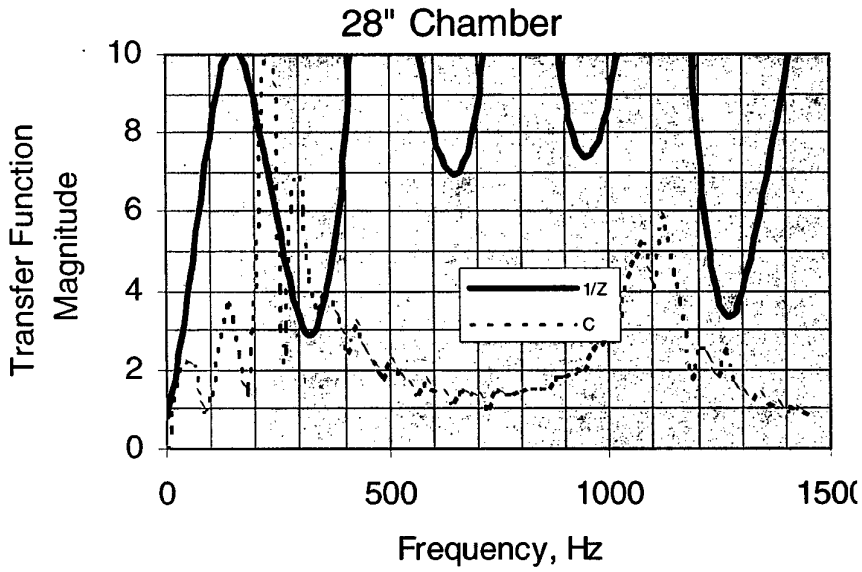


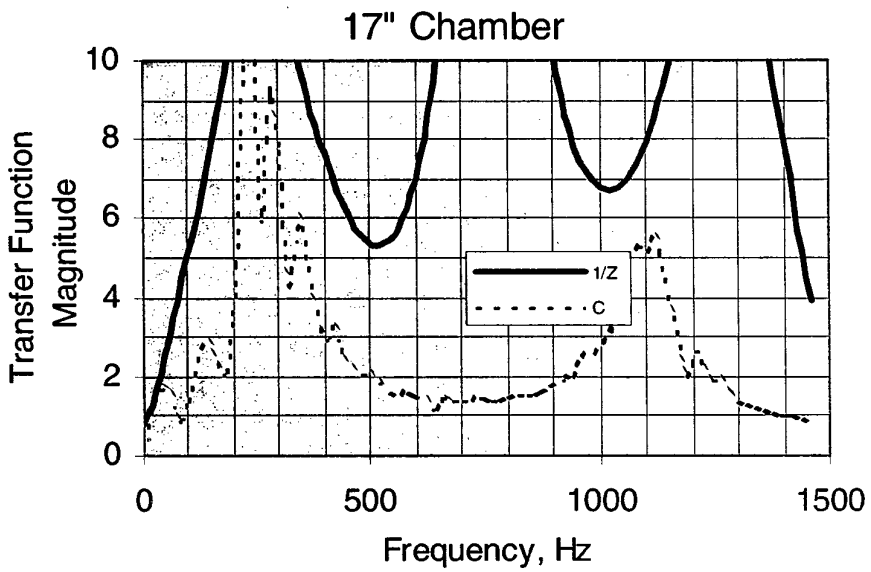
Start Transient



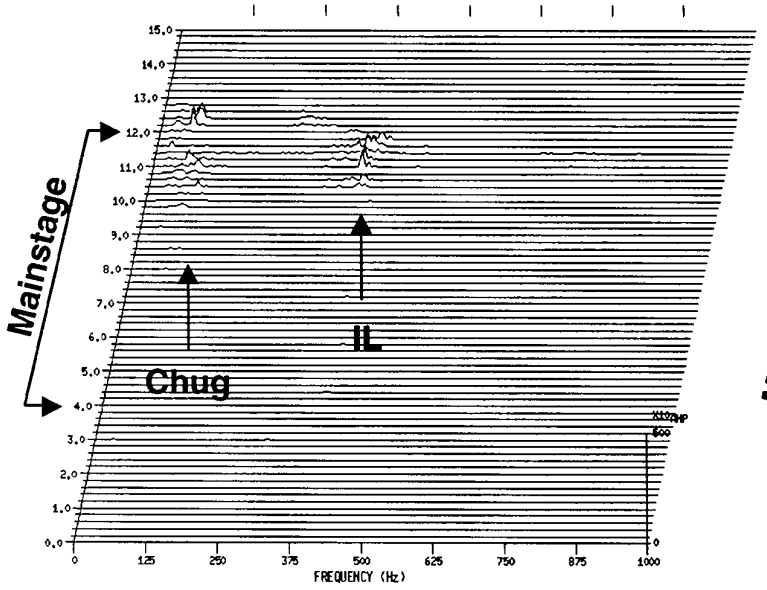
Mainstage

Stability Model Shows Stability Characteristics Can Be Modified by Chamber Length Variation

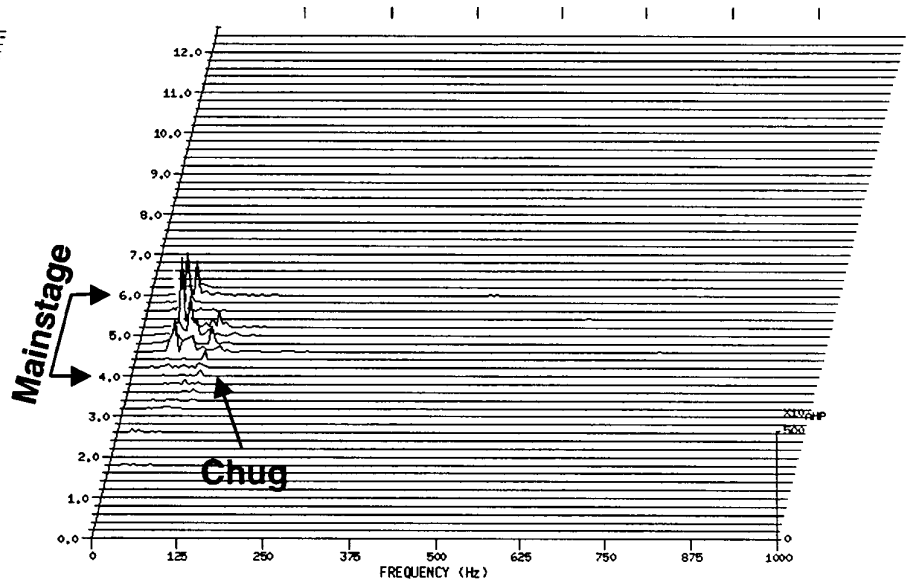




Data Confirmed Capability of Stability Model to Identify Stability Margin

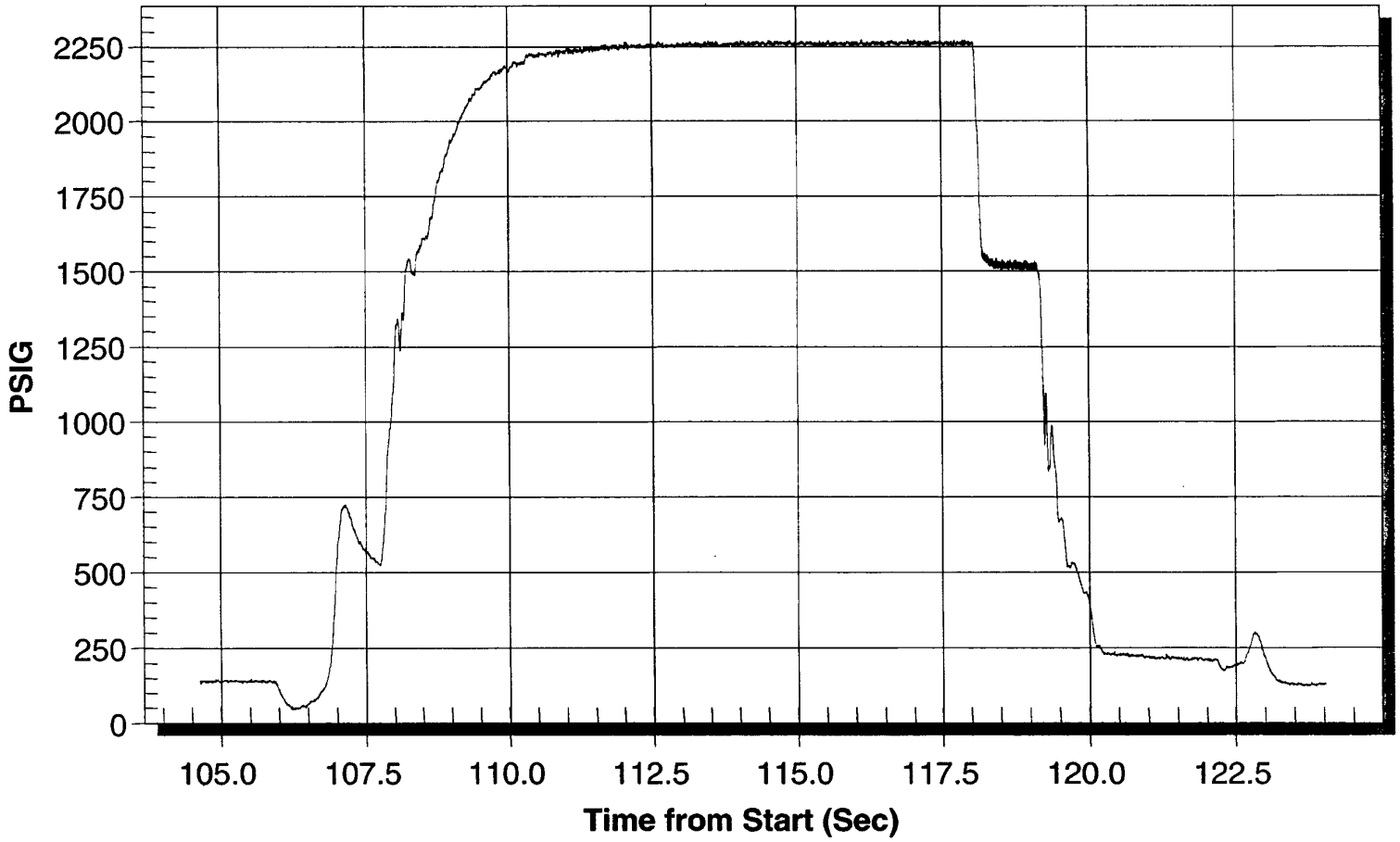


28" Length



17" Length

Optimized Swirl Element Shows Excellent Flame Holding Characteristics



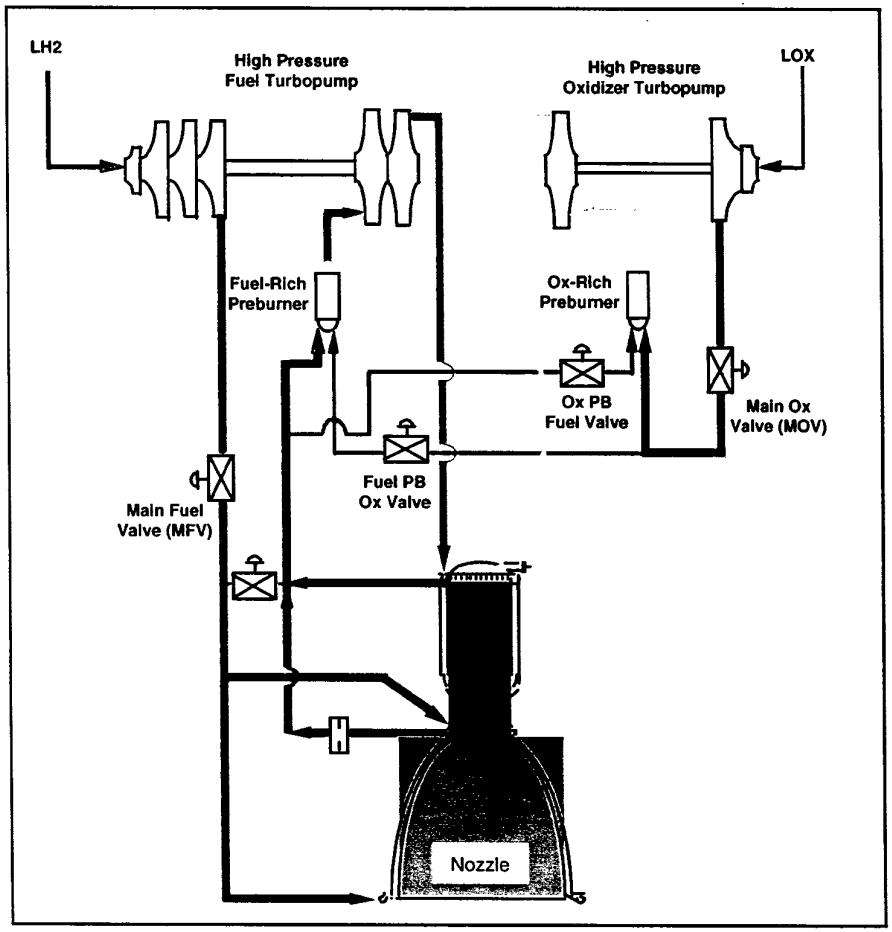
RS-76 LOX/RP-1 ORPB Status

- Oxidizer-rich preburner injector
  - Demonstrated in single element hot fire testing
  - Excellent compatibility and stability characteristics
  - Innovative coaxial swirl design
- The preburner injector posses several favorable design features
  - Low cost/high reliability - Low part count, simple and robust design
  - Lightweight - Short injector length, large flow per element, good atomization
  - System compatibility - Low pressure drop
- Analytical stability tools validated

Full Flow Staged Combustion Approach

- Opportunities for reliability improvement identified
  - Based on previous/present generation of O_2/H_2 booster experience
  - Improvements beyond state of the art needed for Reusable Launch Vehicles (RLV) operability and reduced risk (NASA)
- FFSC "engineers out" many issues on some components but requires validation of unique injectors

FFSC Turbine Drive Flowpaths are Departure from Traditional Configurations



- **Full-Flow, Staged-Combustion (FFSC) uses all propellant flow to power pumps**
  - **Oxidizer-rich gases power the LOX turbopump**
  - **SSME performance at 500 R lower turbine temps**

Rocketdyne

BOEING

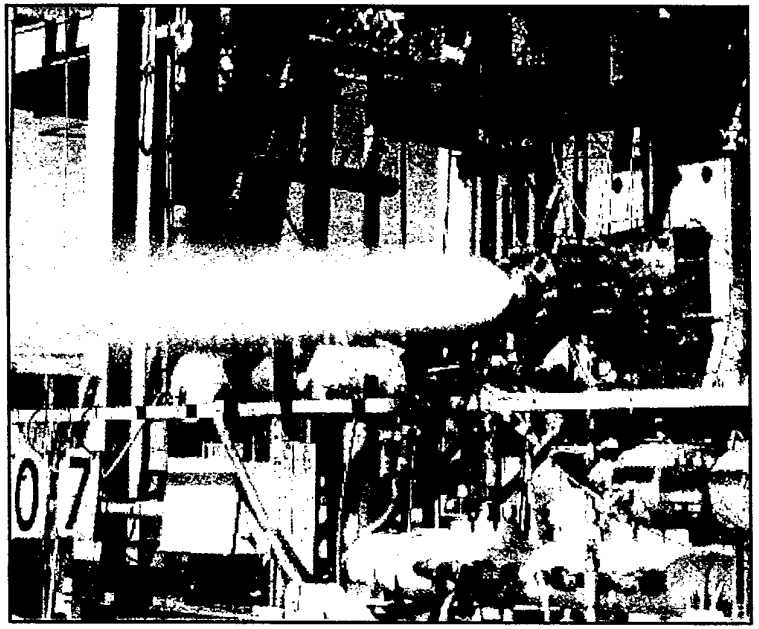
Full-Flow Provides Significant Advantages

- High performance
- Low turbine temperature
  - Long life
- Throttling capability
  - Injector Δp/Pc remains almost constant
    - Margin for chug and acoustic stability
- Simplified turbopump design
  - No inter-propellant seal
  - Lower cost relative to fuel-rich staged cycle
- Enabling Technologies: ORPB and gas-gas main injector
  - Rocketdyne initiated ORPB task in 92 and gas-gas task in 94

Meets Many RLV Requirements

Ox-Rich Preburner Technology Demonstrated

- Ox-rich preburners tested (MSFC, RD)
  - Hot-fire testing showed wide range of ignition and stable operation (100<MR<500 & 2000<pc<3200)
  - Acceptable temperature uniformity



- Ox-rich materials exposure tests performed
  - Promoted combustion tests
  - Long-term exposure tests
  - Particle impact testing

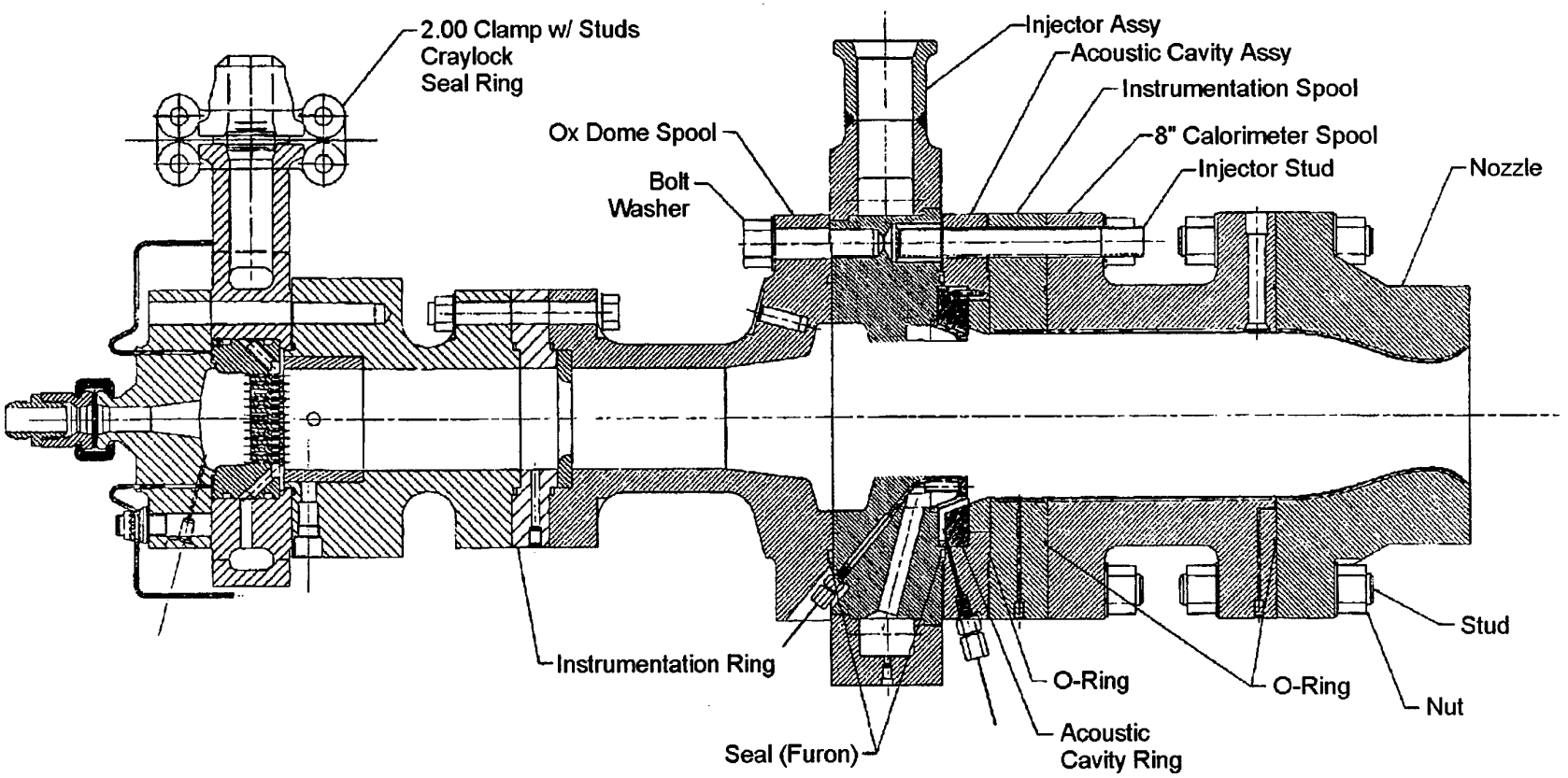
Main Injector Design Considerations

- Classical rocket injector element patterns not satisfactory
  - Fast mixing – thermal/erosion issues
  - Slow mixing – low performance
- A new design was selected with low near face heat flux and high performance
  - Transpiration cooled face
  - Provision for removable cavity
  - Face temperature/heat flux measurement

Main Injector Design Considerations (Cont)

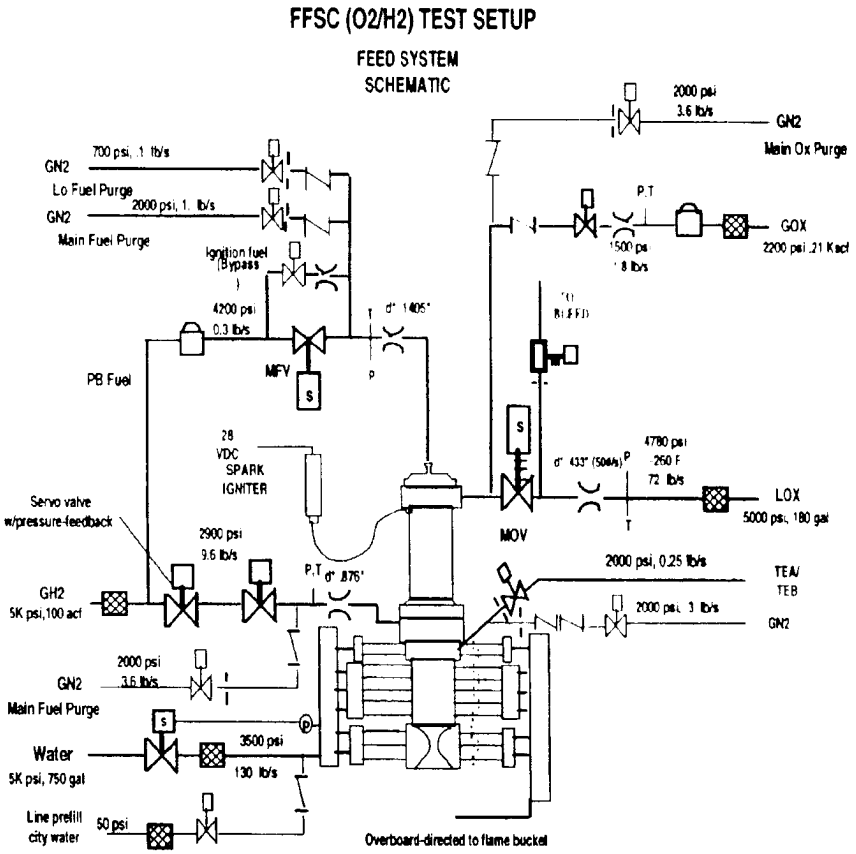
- Design driven by facility/hardware limit conditions
  - Existing 5.67" calorimeter main chamber and 3.5" ox-rich preburner
  - Ox-rich hot gas and ambient H_2
  - Nominal main chamber MR of 6 and chamber pressure of up to 2000 psia

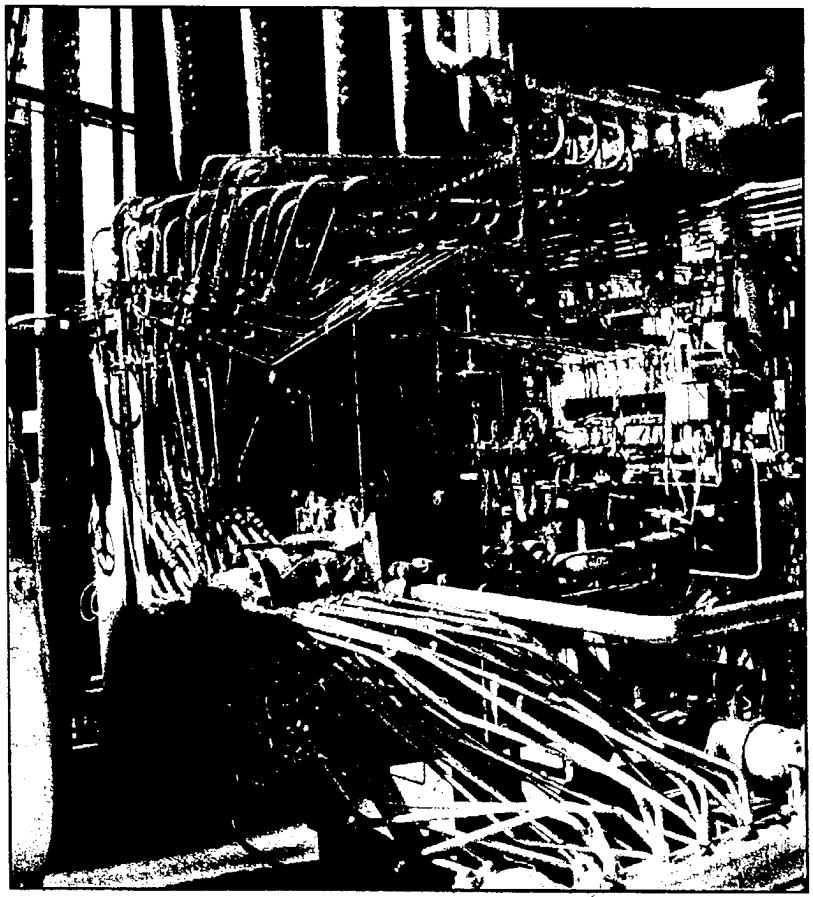
FFSC Test Hardware Layout



Testing Conducted at Rocketdyne APTF

Test program initiated in 1996
TEA/TEB for MCC and Spark plug for ORPB ignition





Rocketdyne

BOEING

Two Series of Tests in 1996-1997

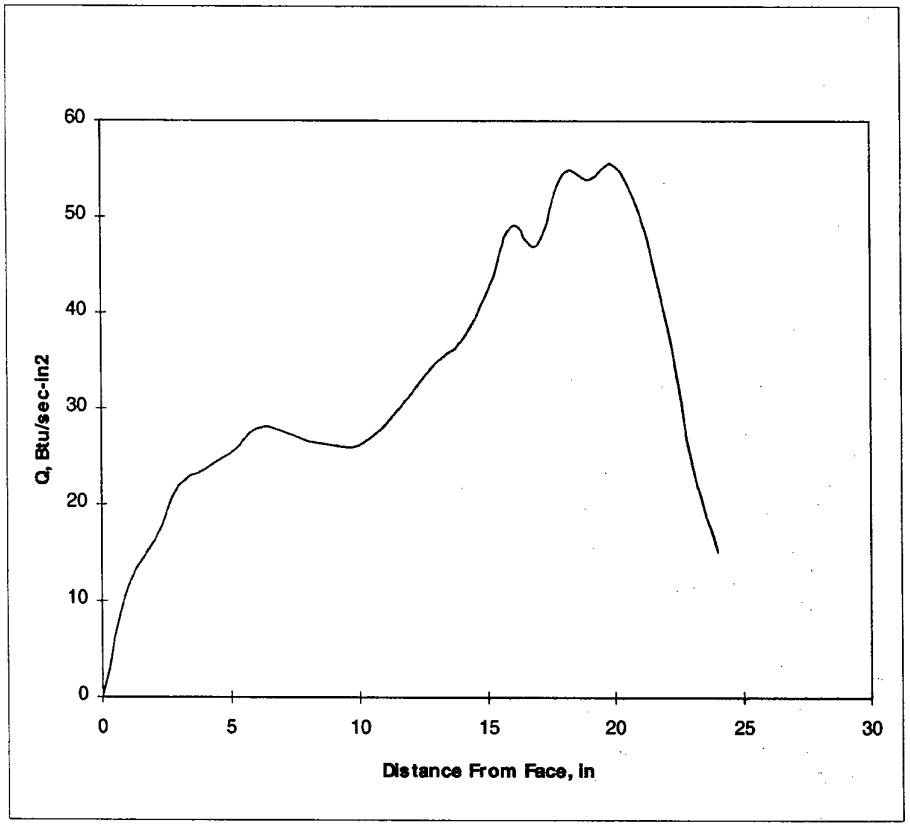
- **Test matrix included ORPB only testing, ignition/sequence check tests and low pressure main stage tests**
- **7 high pressure main stage tests conducted with ambient hydrogen and ORPB product gas**
  - **Thrust level up to ~40 Klbf**
  - **All tests stable—with and without cavity**

Test Number	019	020	021	023	024	025**	028**
PB Pc (psia)	1715	1720	1720	2250	2250	2250	2250
PB Tc (F) average	740	750	750	780	780	780	780
PB MR (o/f)	170	170	170	171	171	171	171
PB LOX (lbm/sec)	51.4	51.4	51.4	65	65	65	65
PB GH2 (lbm/sec)	0.3	0.3	0.3	0.38	0.38	0.38	0.38
MCC Pc (psia)	1385	1380	1380	1775	1775	1775	1775
MCC MR (O/F)	5.1	5.1	5.1	5.7	5.7	5.7	5.7
MCC GH2 (lbm/sec)	9.9	9.9	9.9	11.5	11.5	11.5	11.5
Main-stage Duration (sec)	3.5	3.5	6.0	1.2	3.0	0.2	3.0

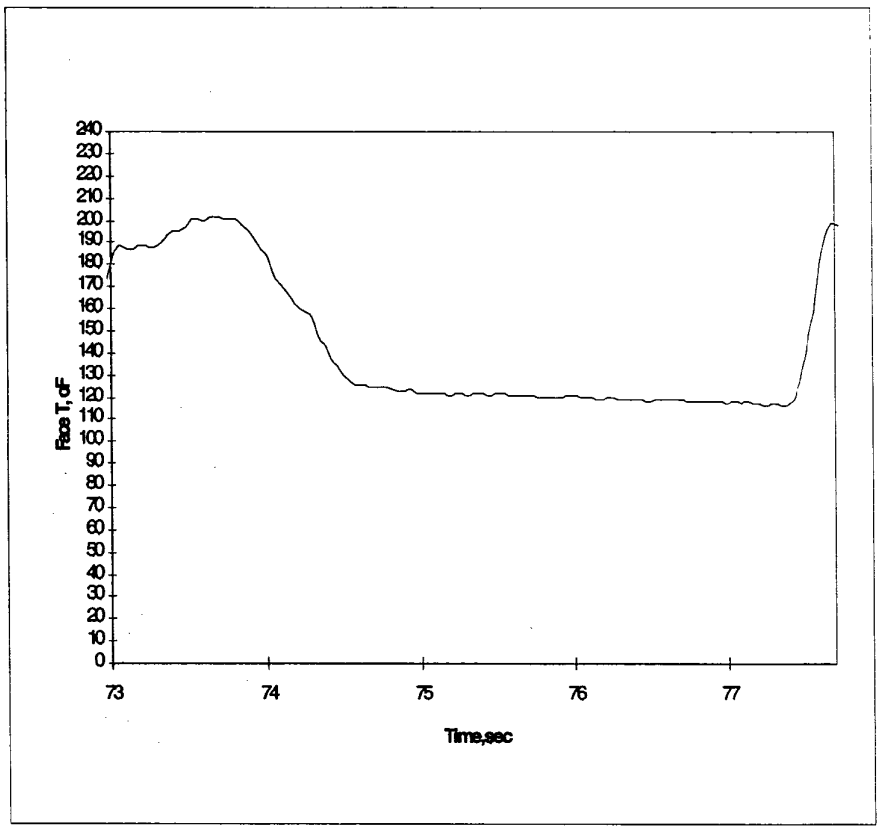
(**) MCC **without** acoustic cavity

Main Chamber Thermal Data, Test 28

Chamber Heat Flux



Injector Face Temperature



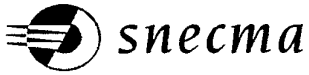
FFSC Technology Effort Status

- Successfully demonstrated high performing,durable and stable gas-gas injector
  - MCC pressures up to 1750 psia and ~40 Klbf thrust level
- Chamber wall and injector face heat flux measured for all tests
  - Heat load acceptable
- Plan for 3000 psia testing with both preburners in formulation
  - Larger scale oxygen rich and fuel rich preburners fabricated
  - A new gas-gas main injector design completed and fabrication in progress
  - Regenerative cooled chamber being fabricated

Conclusions

- Tool and technology development critical to validate new booster concepts
- Opportunities identified and partially quantified for improved F/W
- FBC goals will benefit from strategic technology investments both in analysis and testing







DaimlerChrysler Aerospace
Space Infrastructure

NEW CHALLENGES
in
LIQUID ROCKET PROPULSION

4th Symposium on Liquid Space Propulsion - DLR/Lmp - March 13-15 2000

CNES : M. Pons - N. Girard - P. Vuillermoz
DASA : D. Preclik - G. Hagemann
SNECMA : V. Duthoit - J.L. Thomas

Objectives for the future :

improved access to space

- cheaper
- more versatile
- more reliable
- more performance

two ways :

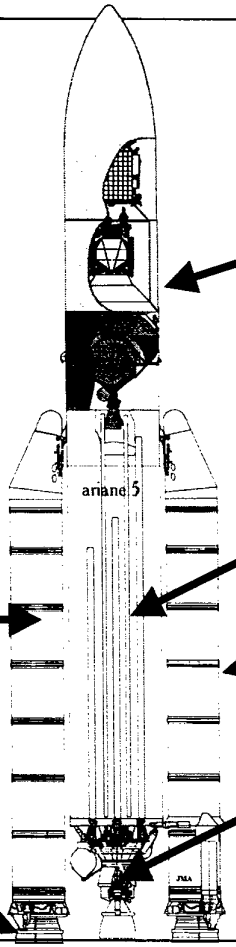
- expendable = A2010, R&T programs = A5 family
- reusable = FLTP, ASTRA => demonstrators

Challenges in future liquid rocket engine technology in Europe

A2010

expendible launchers

- Focus R et T activities
- Initiatives technologieal demonstrators
- Provides for a "catalog" of launcher improvements (cost and/or performance)
- creates a reference for RLV/expendable comparisons



Dynamic load reduction (shocks, acoustics)

Subcooled propellants

. Increased loading
. Low-cost process

Composite SRB structures

Low cost first stage engine :
Low cost components
Flow separation controlled nozzle extension
engine regulation

. Low-cost nozzle
. Low stiffness actuation

What does cheaper mean ?

Less development time and risks

- better scientific knowledge
- improved modelling tools

New technologies

- key technological steps
- reduced manufacturing cost

=> European level coordinated technological demonstrators are proposed

✓ GLOBAL STRATEGY : TECHNOLOGICAL NEEDS

- ➢ VULCAIN family : toward lower costs and incresed performance
- ➢ New upper stage engine VINCI : improvement of expander type cycle + versatility
- ➢ Reusability : improved life duration, health monitoring, high ISP

Equipements

Valves
Pressure regulation
leak-tightness
Instrumentation

Engine system

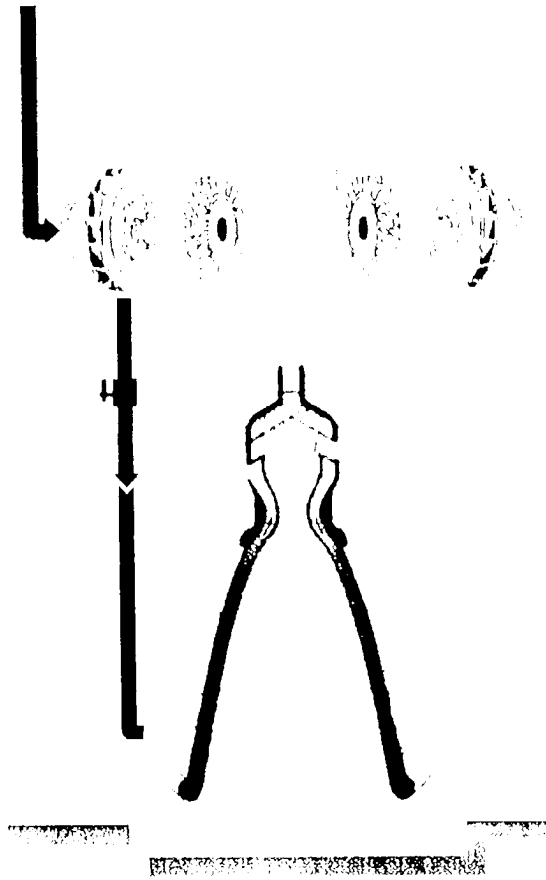
- Propellant management / sloshing
- New Cycles
- « new » propellants
- transient modelization
- engine regulation

Combustion chamber and Nozzle

Combustion
- injection and atomization
- HF Stability
- injector technology

Chamber
- thermal exchanges
- Design optimization

Nozzle
- steady and unsteady aerodynamics phenomena : sides loads, flow separation
- thermal loads
- mechanical behavior



Turbopumps

Pumps
- Mastering steady and unsteady state cavitatio
  - NPSP gains
  - Re ignition
- Mastering pumps transients
- simplify manufacturing (powder metallurgy

Turbines
- design improvement (modellind tools)

Bearings
- improved roller bearings
- Use of Fluid bearings
- rotor dynamics
- tribology

Engine System

⇨Engine system analysis :

- New propellants (LOX / H-C, ...)
- low cost engine use of numerical tools

⇨Engine regulation

- System analysis : performance gain, engine throttling ..
- Valves and regulators
- Software

⇨Propellant management in tanks : COMPERE program

PROPELLANT MANAGEMENT IN LAUNCHER TANKS : COMPERE PROGRAM

Objectives of the program

- Allowing the prediction of the evolution of the characteristics of the fluids in the tanks of the launcher through physical and numerical models :

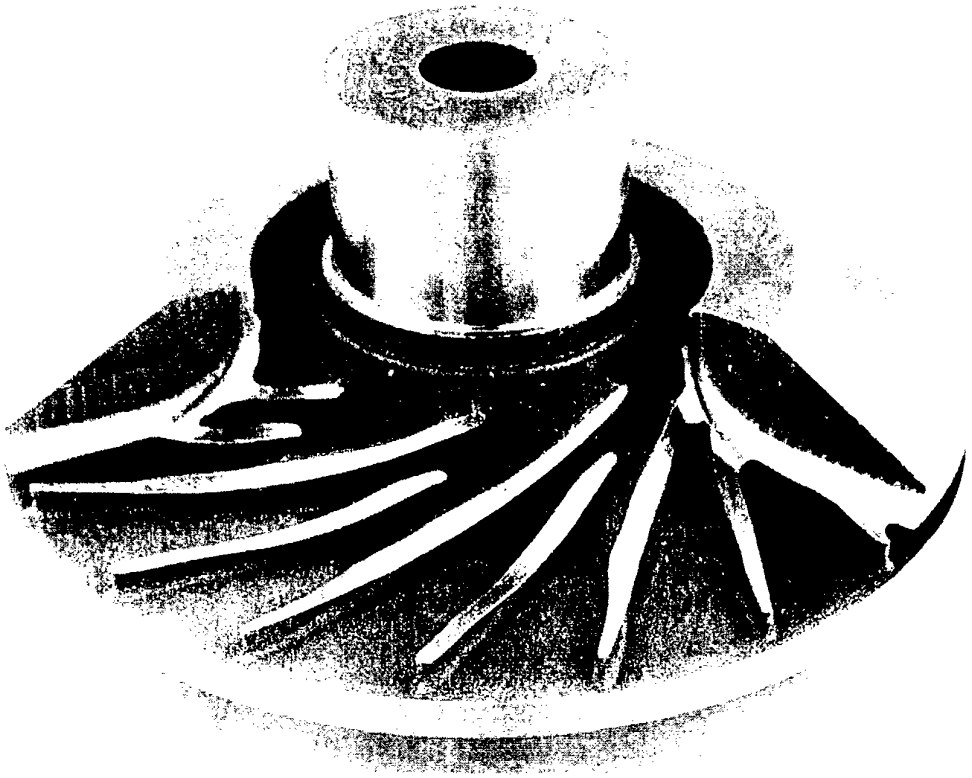
- Fluids submitted to given levels of acceleration and heat fluxes, variable in time, and representative of the different flight phases : propulsion, ballistic, re-ignition.

Turbopumps and equipment :

- Simplify Architecture (mono-shaft concepts, fluid bearings)
- Cavitation process studies

  To master cavitation phenomena in cryogenic fluids :

  - for reducing NPSP (inducers/pumps).
  - For mastering unsteady cavitation loads in pumps.
- Pumps design (Powder metallurgy, unflasqued impeller)
- Turbine design (blisk ..)



snecma

Powder metallurgy impeller

CAVITATION

Objectives

To master cavitation phenomena in cryogenic fluids :

- for reducing NPSP (inducers/pumps).
- For mastering unsteady cavitation loads in pumps.

Research works

- Scientific activities are going on for understanding the physical phenomena and modeling them.
- Today, a pump design CFC code allows taking into account the cavitation pocket in blade profile design.
- About unsteady cavitation problems, technological demonstrators are foreseen in order to demonstrate the avoidance of sub and/or super synchronous frequencies in inducers.

Combustion

COMBUSTION RESEARCH GROUP + GDR

HF COMBUSTION INSTABILITIES RESEACH GROUP

- To improve the knowledge on the basic phenomena which govern the high frequency combustion instabilities.
- To build a modern software allowing HF instabilities prediction.

Nozzle behavior

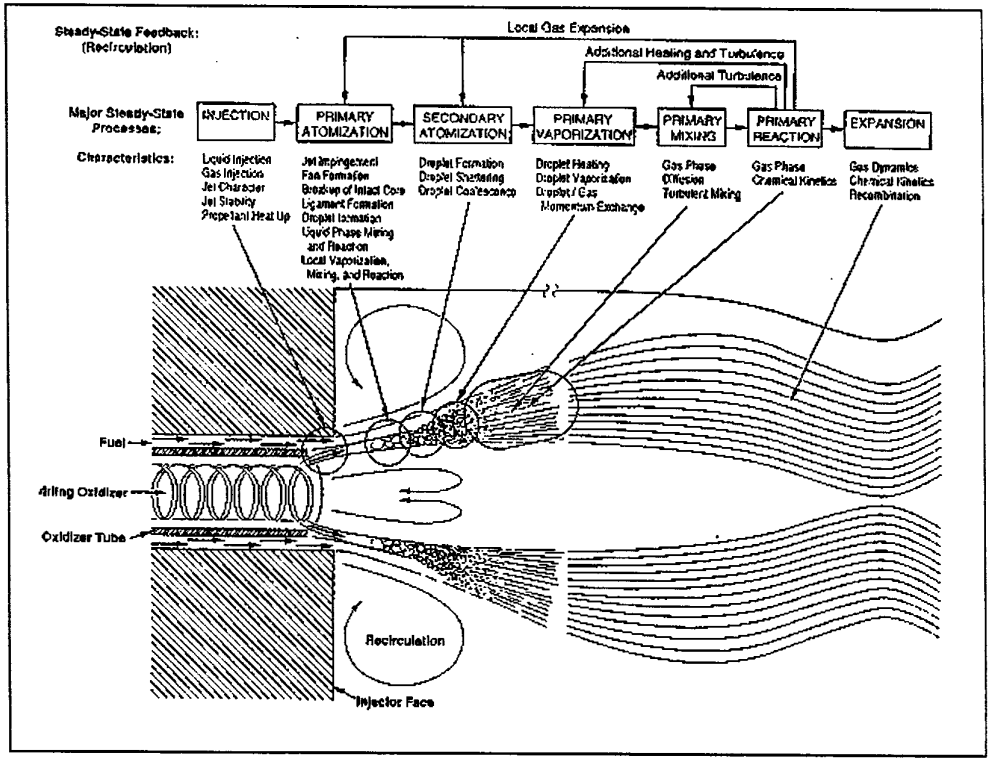
FLOW SEPARATION CONTROL GROUP

To master flow separation phenomena in bell nozzles for :

- Reducing the unsteady side loads.
- Increasing the expansion area ratio.

Extendible nozzle on the plume

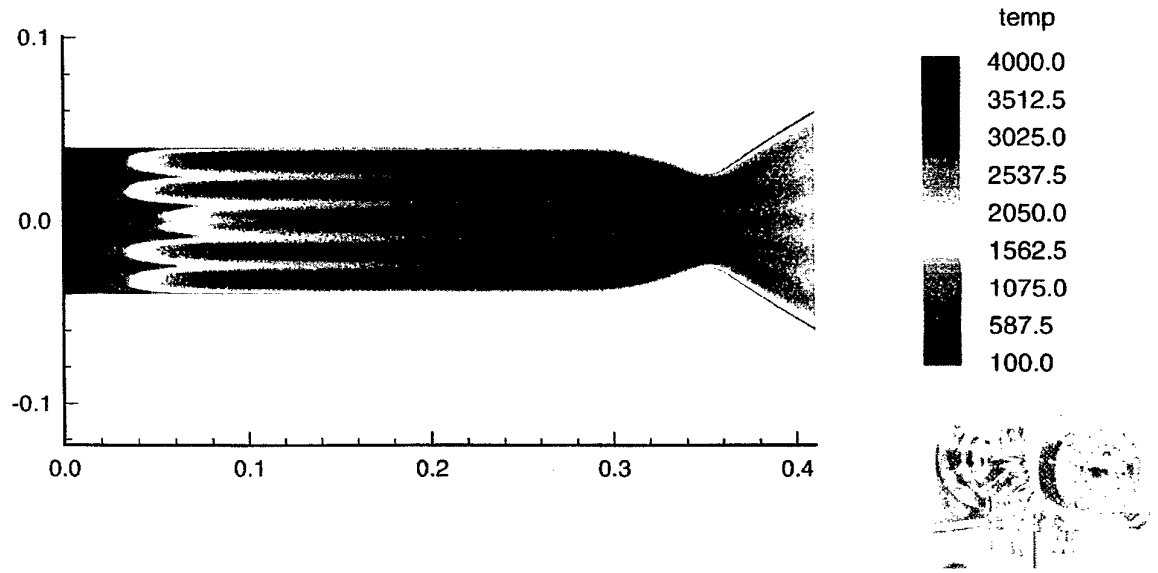
Combustion physical phenomena :



Workshop on Rocket Combustion Modelling
ONERA, Toulouse, March 11-13, 1998

Daimler-Benz Aerospace

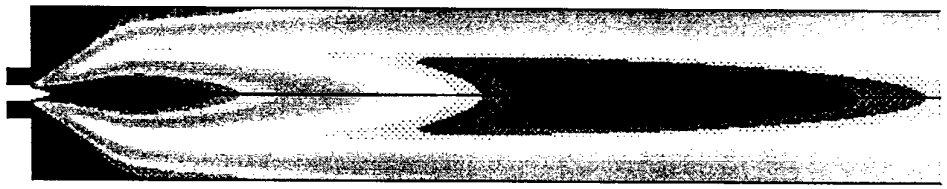
Simulation of Hot Gas Temperature Profile in Calorimeter Combustor



D. Preclik - RIA51
This document is the property of Daimler-Benz Aerospace Dasa and may not be copied or distributed without its written consent
RCM5-5

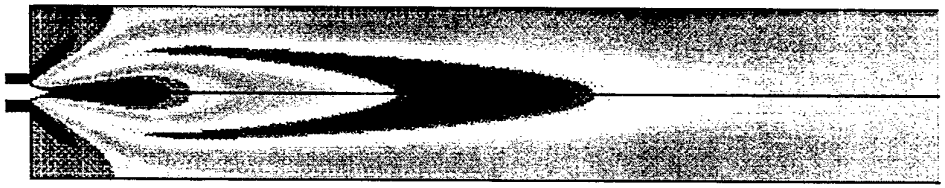
Numerical Simulation of Mascotte 1 bar H2/O2 Flame

(SNECMA computation with THESEE code – RCM Workshop March 1998)



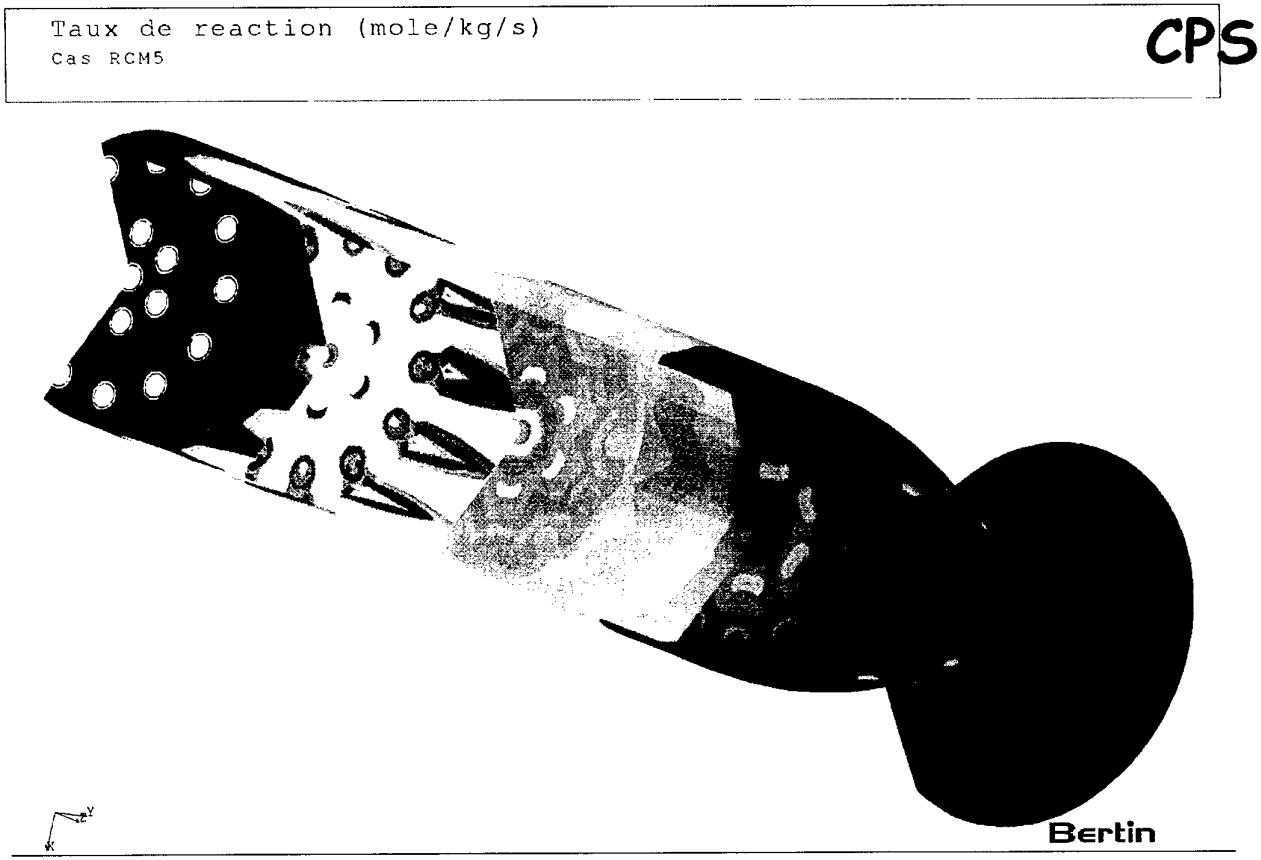
Ch

amps de temérature - Pc = 1 bar



Champs de temérature - Pc = 10 bar

SEP


Taux de reaction (mole/kg/s)
Cas RCM5
CPS
Bertin

COMBUSTION INSTABILITIES

Objectives

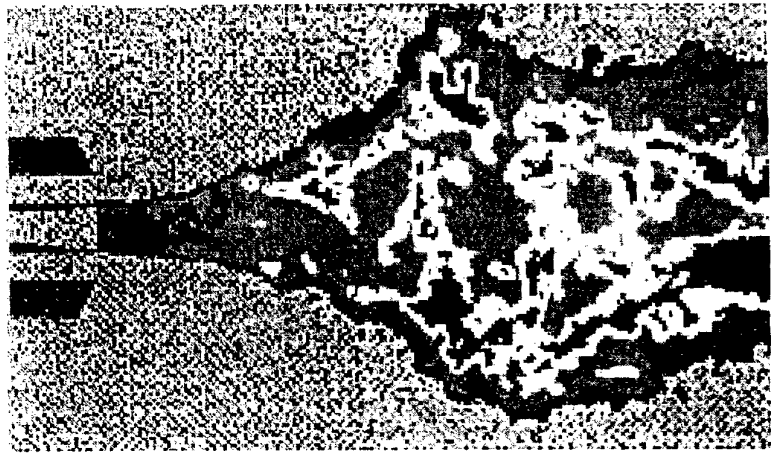
- to improve the knowledge on the basic phenomena which govern the high frequency combustion instabilities.
- To build a modern software allowing HF instabilities prediction.

Applications

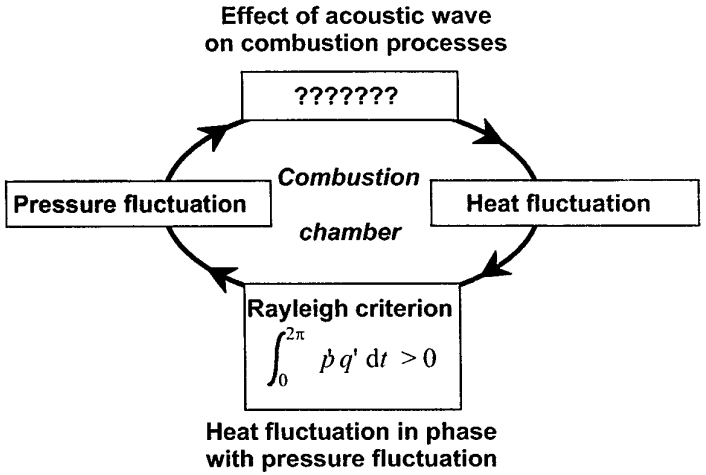
All the modern liquid rocket engine using :

- Storable propellants
- Cryogenic propellants
- Hydrocarbon propellants

Challenges in future liquid rocket engine technology in Europe



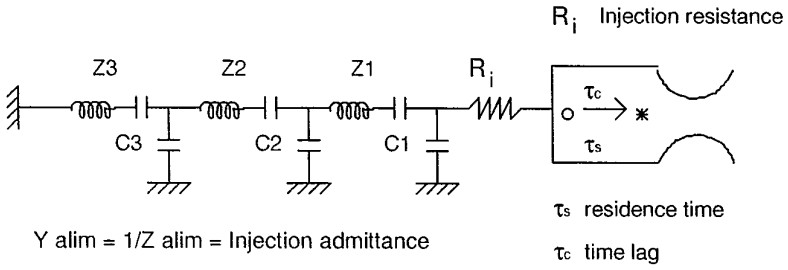
Steady state liquid combustion
Mascotte flame H2/O2



General mechanisms for HF combustion instabilities

➢ DEEP THROTTLING:

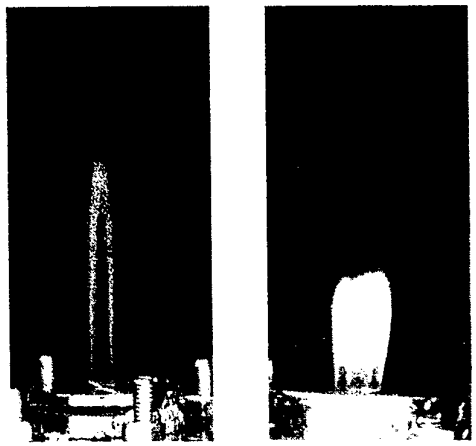
	Vulcain GG	SSME FPB
Nominal Pc	**95 bar**	**350 bar**
High Pc (qualif.)	**115 %**	**109%**
Low Pc (qualif.)	**87%**	**50%**



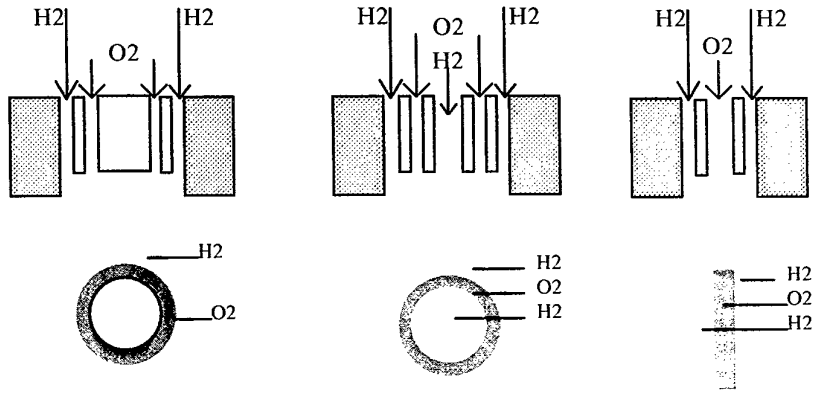
- BEHAVIOR OF THE INJECTOR ON A LARGE OPERATING DOMAIN:
  - ✓ ***Are the classical injection elements adapted to a wide range of operation ?***
  - ✓ *Need for adaptive injection elements ?*
- RELATED ISSUES:
  - ✓ Modelling on system level: linear or non linear
  - ✓ Hydraulic behavior of injection elements (passive or active)
  - ✓ Modelling of combustion side (combustion delays etc...)
  - ✓ Characterization/diagnostics to study combustion in unsteady conditions

➢ LOW COST GAS GENERATORS OR PREBURNERS

- INFLUENCE OF WIDENED TOLERANCES
- HIGH FLOWRATE INJECTOR CONCEPTS



Experimental comparison of the flame behind a coaxial injector and a tricoaxial injector (gaseous oxygen and gaseous hydrogen combustion at atmospheric pressure, same flow ate 0.57 g/s)



Central Body Coaxial Injector | Tricoaxial Injector | Slot injector

Conceptual studies based on the shear principle

➢ NEW INJECTION SCHEMES - NEW PROPELLANTS

- NEW PROPELLANTS (LOX-KERO, LOX METHANE …)
  - ✓ Require specific injectors and injection pattern on the face plate
  - ✓ Require specific organisation of the combustion in the Gas Generator due to very Low Mixture Ratio
  - ✓ Require precise decomposition and kinetic data for various hydrocarbones
  - ✓ Soot production is a problem at very low MR

- HOW TO INJECT FASTER, BETTER, CHEAPER IN 10 YEARS…
  - ✓ Investigation of new concepts (slot, impact, porous...) adapted to very low cost injectors and/or to other propellants



Thrust Chamber Technology Challenges after 2000

Evolution of European VULCAIN Gas-Generator Family:

- Low-cost component technology (new TC structural designs)
- High-area-ratio nozzle extension (flow separation control)
- Alternative liquid/liquid propellant systems (LOX/CH4, LOX/Kerosen, etc.)

Preparation of Staged Combustion Technology:

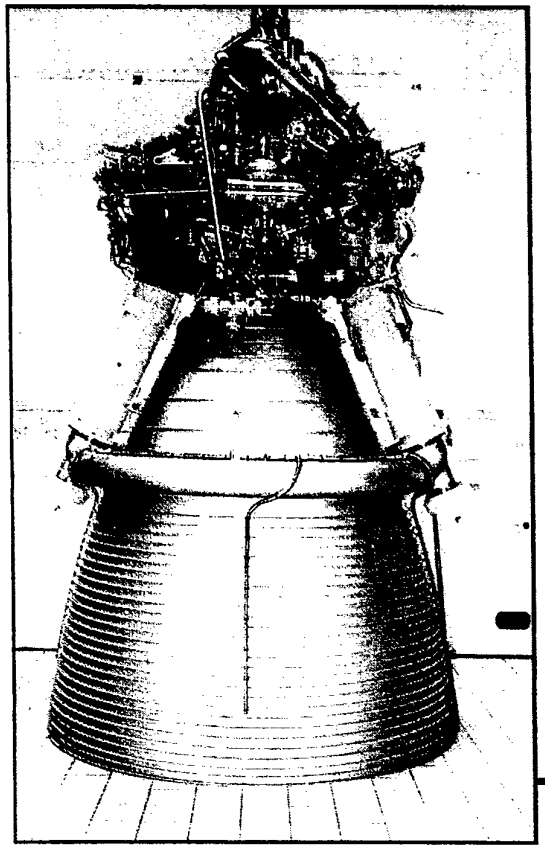
- High injection throttling
- Hot-gas injection and material compatibility (OxRich-PB, FuelRich-PB)
- Elastic structures and new materials (⇒ reusability)

Evolution of Expander-Cycle Technology:

- Advanced heat exchange liner (hot gas fins)

This document is the property of DaimlerChrysler Aerospace and may not be copied or distributed without its written consent!

Evolution of Europe's VULCAIN Gas-Generator Family



Development Goals and Requirements

- Cost ↘ (*without impacting reliability*)
- Performance ↗ (Schub: 1700 kN, P_C= 135 bar)

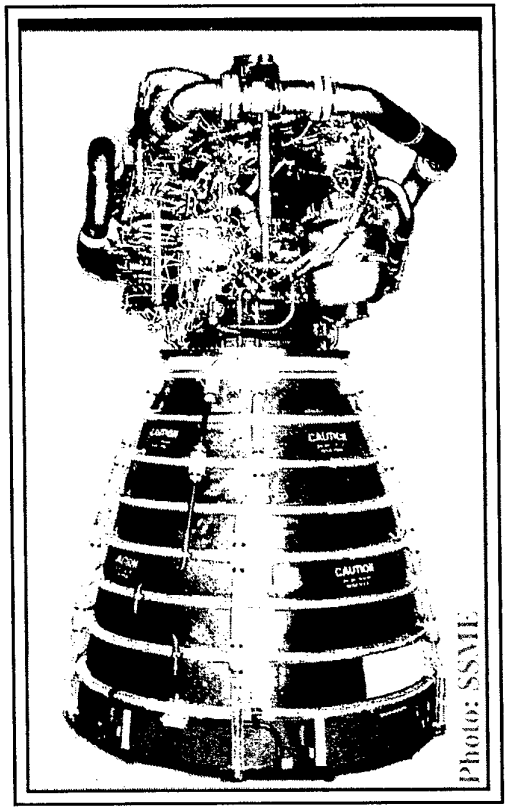
Potential Design Features

- New generation: MCC (simplified structural designs)
- New generation: NE (high area ratio nozzle)
- Alternative liquid/liquid propellant systems (LOX/CH4, LOX/Kerosen, etc.)

Gas Generator Cycle

This document is the property of DaimlerChrysler Aerospace and may not be copied or distributed without its written consent!

Preparation of Europe's Future Advanced Cryogenic Engine (ACE) Technology



Development Goals and Requirements

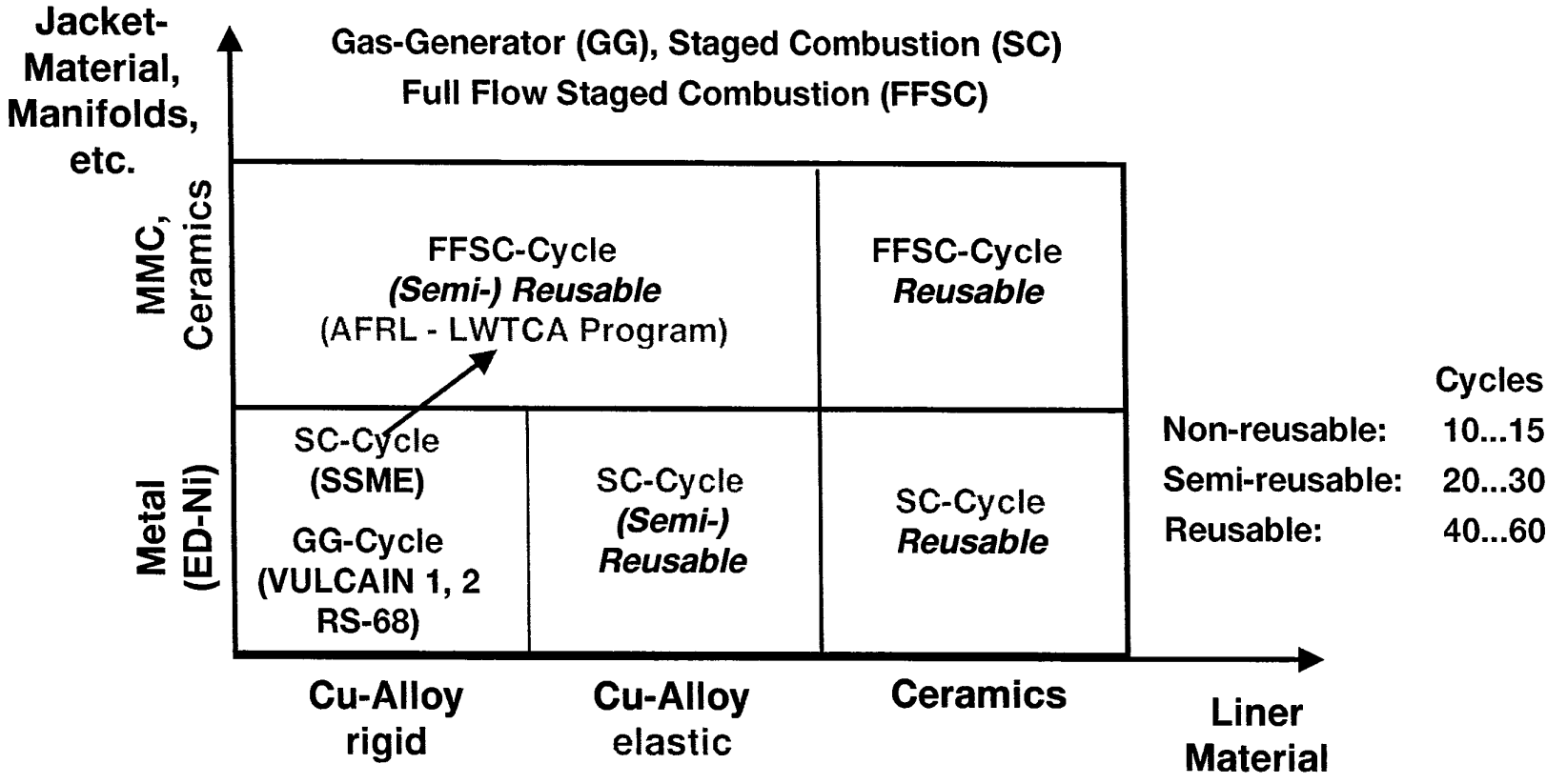
- Reusability (lifetime, cycles↗)
- Performance ↗ (thrust, spec. impuls, system pressure level ↗)
- Operability ↗ (reliability ↗, maintenance effort ↘)
- Cost Effectivity ↗ (cost/performance ↘)

Potential Design Features

- High throttling capability
- Hot gas injection (ox-rich and fu-rich)
- New, elastic liner/jacket-MCC designs
- New materials and manufacturing processes
- Thrust: 2000 kN, P_c: 200 bar, $I_{sp,vac}$: 460 s

This document is the property of DaimlerChrysler Aerospace and may not be copied or distributed without its written consent!

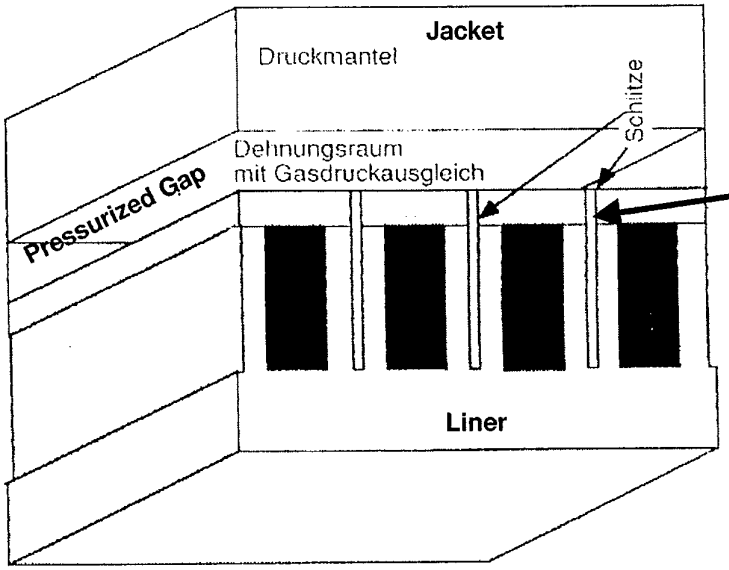
Alternative, Future Thrust Chamber Designs & Materials

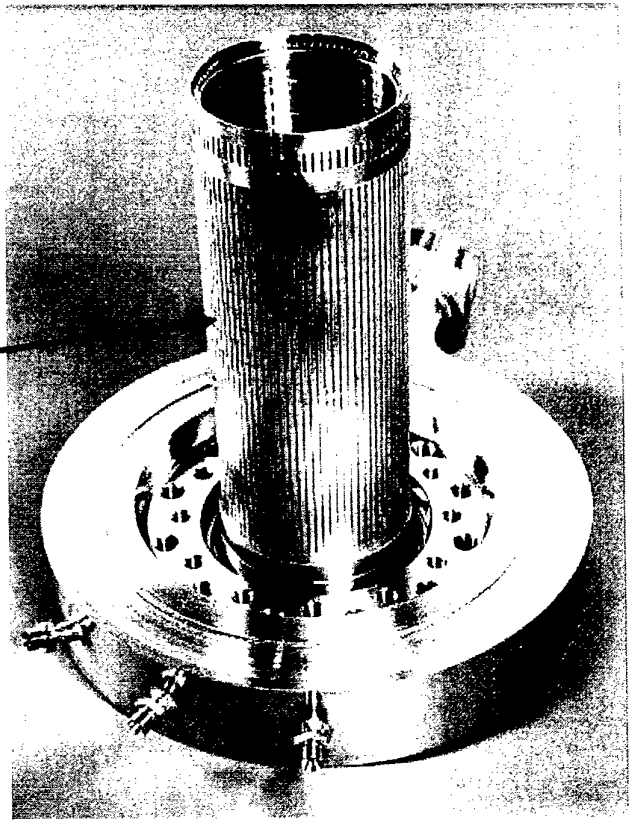


This document is the property of DaimlerChrysler Aerospace and may not be copied or distributed without its written consent!

Elastic Liner Concept Based on Pressurized Liner-Gaps

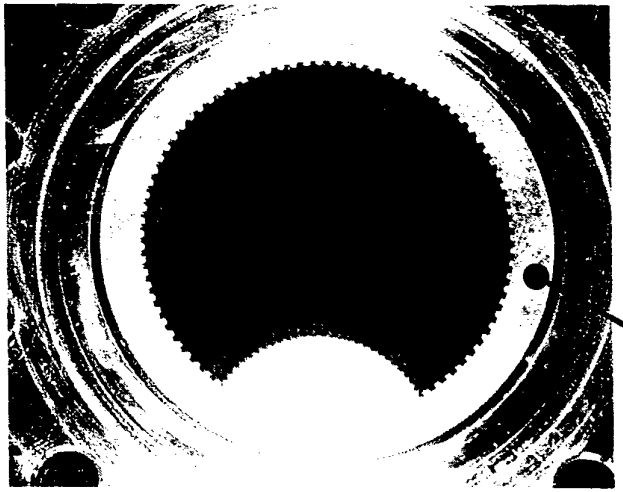
Schematic of Elastic Liner Concept
(investigated within national program TEKAN)





This document is the property of DaimlerChrysler Aerospace and may not be copied or distributed without its written consent!

Advanced Heat Exchange Liner Screening Tests





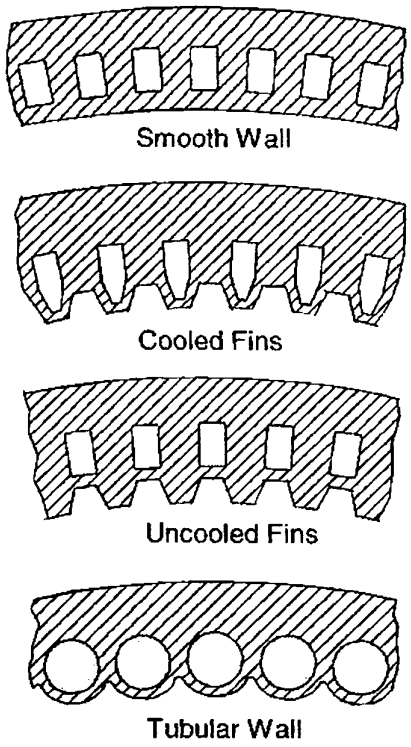
Test Hardware:

Combustor barrel segments employing various heat enhancement designs

Test-Run:

Hot-fire testing to measure integral structural heat transfer efficiencies

(investigated within national techn. program TEKAN)



This document is the property of DaimlerChrysler Aerospace and may not be copied or distributed without its written consent!

FLOW SEPARATION CONTROL GROUP

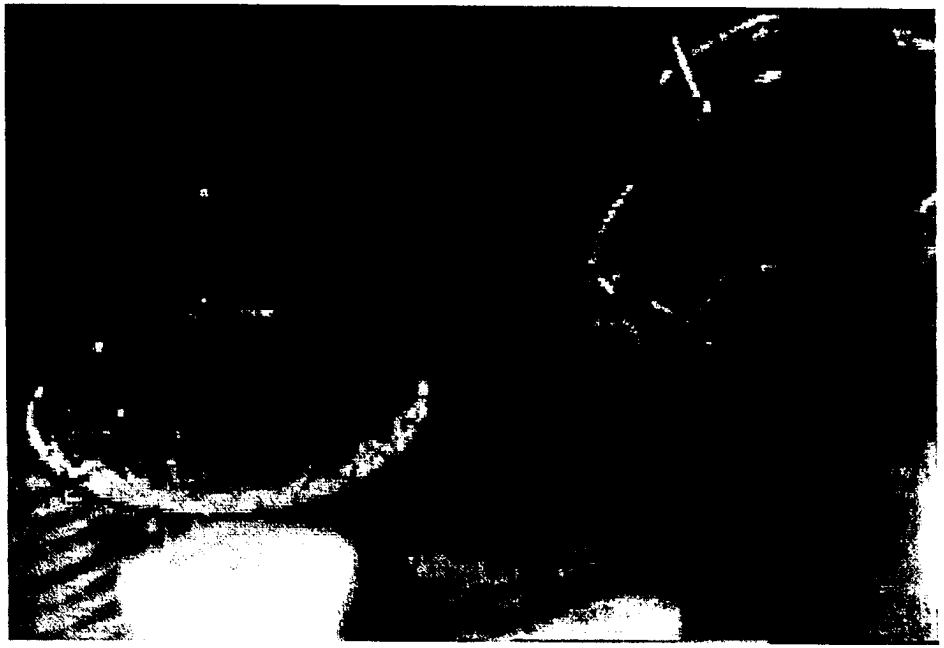
Objectives

To master flow separation phenomena in bell nozzles for :

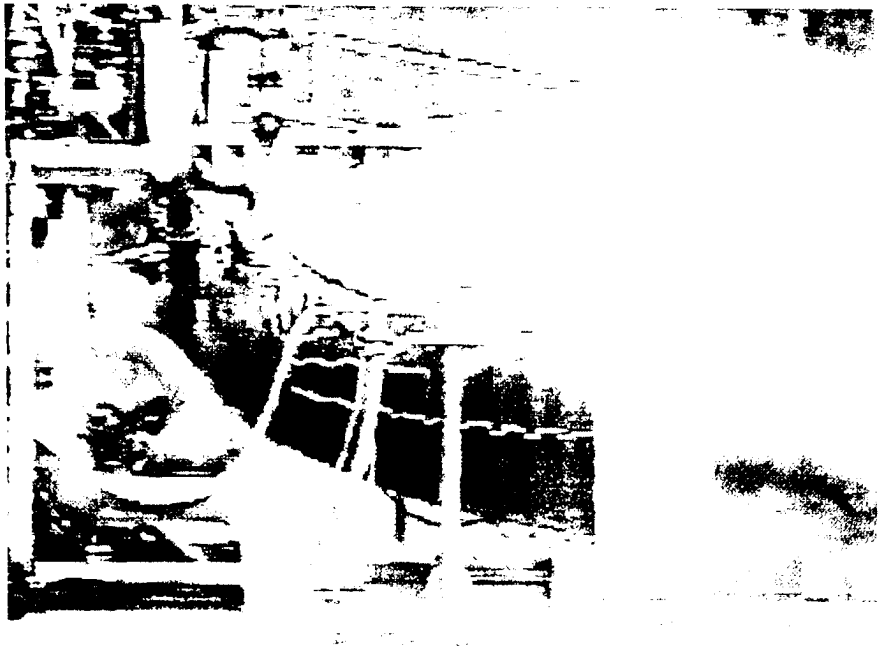
- Reducing the unsteady side loads.
- Increasing the expansion area ratio.

Activities research works

- Different dedicated test facilities are used through Europe in order to understand and model the physical phenomena, mainly for unsteady flows and film re-injection (shocks waves reflection, ...).
- Numerical CDF codes are adapted for modeling these phenomena.
- A technology demonstrator for over expansion aera ratio in real conditions is under evaluation.

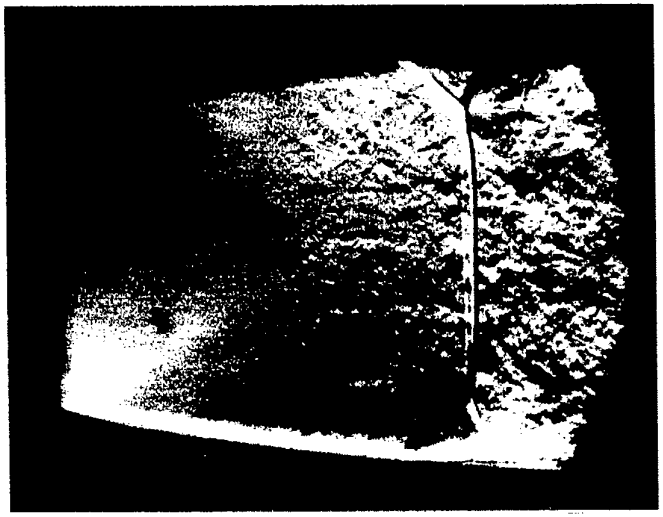


SSME engine at lift-off

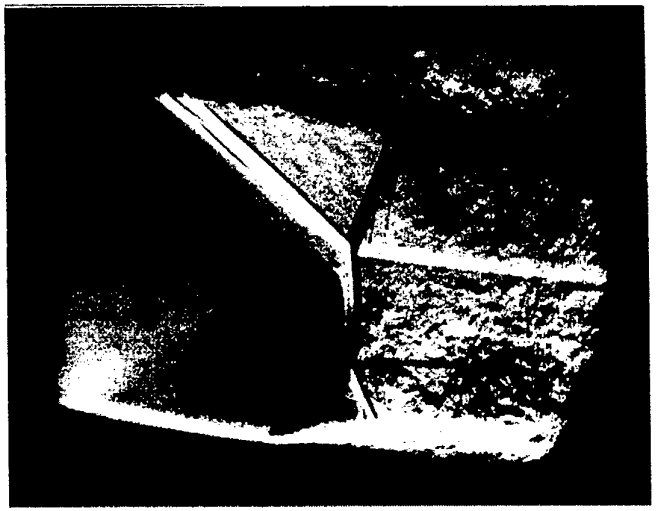


Vulcain engine at start-up

Flow separation



symmetrical



unsymmetrical



Industrial Needs for Advanced Modelling Tools

Advanced engineering tools, e.g. CFD, FEM, etc., are used within the Space Propulsion Industry

- for the design work and the evaluation of new concepts
- to support the daily engineering work, e.g. for the interpretation of test results, trade-offs, and
- to reduce development costs and -times, e.g. by a complementary and efficient support of expensive hardware tests

The use of advanced modelling tools for reliable and cost-effective investigations of critical design aspects will further increase in the near future !

This document is the property of DaimlerChrysler Aerospace and may not be copied or distributed without its written consent!

NEW CHALLENGES IN LIQUID ROCKET PROPULSION

➢ ADVANCED MODELLING TOOLS

• STRONG NEED FOR FASTER, MORE RELIABLE MODELLING TOOLS FOR FUTURE TECHNOLOGY DEMONSTRATION PROGRAMS AND FLIGHT ENGINE DEVELOPMENTS

• NEED FOR MODELLING WILL REMAIN MAJORITARLY DRIVEN BY INDUSTRIAL PROBLEMS

• PURSUE IN THE FUNDAMENTAL UNDERSTANDING AND MODELLING:

- ✓ New atomization schemes (Shear coax and others)
- ✓ Combustion Instability (High and Low Frequency)
- ✓ Combustion/vaporization of propellants in LOX/HC combustion

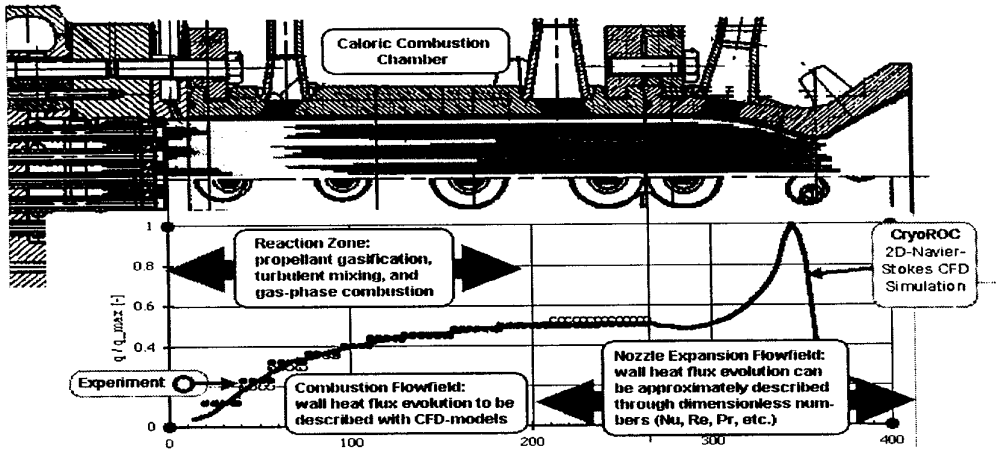


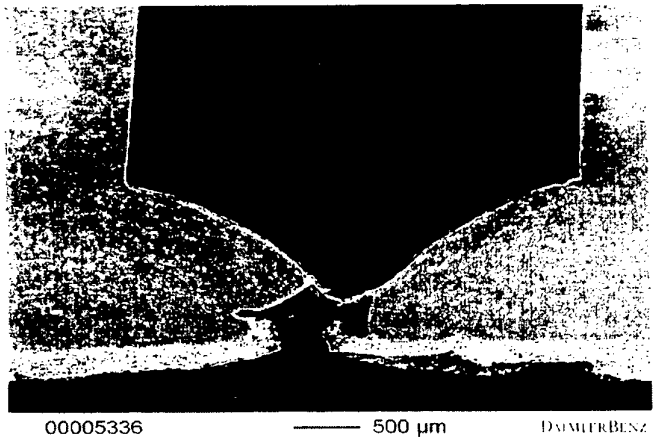
Industrial Needs for Advanced Modelling Tools

Wall heat loading	➟	liquid jet / flame-to-wall interaction
	➟	fully coupled hot gas-to-coolant side approaches employing detailed structural representations
	➟	transpiration cooling
	➟	multi-dimensional hot gas structures
TC reusability, lifetime	➟	full elasto-plastic life-cycle (FEM-) analysis
	➟	advanced material models
Flow separation and side-loads	➟	multi-dimensional turbulent flow modelling
	➟	semi-analytical models for separation pressure ratio, plateau pressure drop, and side-loads
TC performance	➟	multi-dimensional turbulent flow & combustion modelling

This document is the property of DaimlerChrysler Aerospace and may not be copied or distributed without its written consent!

Prospect on Advanced Modelling & Analysis for Liquid Propulsion Rocket Engines





Approach:
Integrated Simulation of Propellant Injection, Mixing, Combustion, Wall Heat Transfer and Flow Expansion



Approach:
Elasto-Plastic Life-Cycle Analysis of MCC-Walls with Material Degradation

Goal: Optimized Cooling Channel Design (Channel Aspect Ratio, ΔP_{CR}, etc. versus Flow Path)

This document is the property of DaimlerChrysler Aerospace and may not be copied or distributed without its written consent!

European partnership

Agencies	Industry	Research Community
CNES	SNECMA	ONERA
DLR	DASA	CNRS
ESA	VAC	DLR
SNSB	TECHSPACE	FFA
...	...	Universities
		...

Working together in cooperative research groups :

- **Combustion** group **HF** group : CNES/SNECMA/DLR/DASA?CNRS/ONERA
- **HF** group : CNES/SNECMA/DLR/DASA?CNRS/ONERA
- **Leak-Tightness** research group : CNES, SNECMA,CNRS, universities
- **FSCD** group : CNES, VAC,DLR,DASA,SNECMA,ONERA,CNRS,ESTEC
- **COMPERE** program : CNES, SNECMA,AL,DLR,DASA,ONERA,Universities

"*Next-Generation Chemical Propulsion for Spacecraft Attitude Control and Orbital Maneuvering*"

by

P.-K. Wu, R.P. Fuller, C.R. Stechman, and
A.S. Nejad, Kaiser Marquardt, U.S.A.

Paper was not available

Peroxide Propulsion at The Turn of the Century

William E. Anderson. NASA MSFC
Kathy Butler, Boeing Rocketdyne Power & Propulsion
Dave Crocket, Orbital Sciences Corp.
Tim Lewis, Orbital Sciences Corporation
Curtis McNeal, NASA MSFC

Introduction

A resurgence of interest in peroxide propulsion has occurred in the last years of the 20th Century. This interest is driven by the need for lower cost propulsion systems and the need for storable reusable propulsion systems to meet future space transportation system architectures. NASA and the Air Force are jointly developing two propulsion systems for flight demonstration early in the 21st Century. One system will be a development of Boeing's AR2-3 engine, which was successfully fielded in the 1960s. The other is a new pressure-fed design by Orbital Sciences Corporation for expendable mission requirements. Concurrently NASA and industry are pursuing the key peroxide technologies needed to design, fabricate, and test advanced peroxide engines to meet the mission needs beyond 2005. This paper will present a description of the AR2-3, report the status of its current test program, and describe its intended flight demonstration. This paper will then describe the Orbital 10K engine, the status of its test program, and describe its planned flight demonstration. Finally the paper will present a plan, or technology roadmap, for the development of an advanced peroxide engine for the 21st Century.

AR2-3 Engine

The AR2-3 rocket engine was developed by Rocketdyne in the 1950's, one of a family of aircraft rocket (AR) engines. The first AR engine was the AR-1, which operated at a fixed thrust of 5750 pounds. The engine was flight proven on the FJ-4 aircraft. The AR2 series of engines consist of the AR-2, AR2-1, AR2-2 and the AR2-3. The AR engine series are shown in Figure 1. All of the AR2 series engines provided a mainstage thrust of 6600 pounds and were variable down to 3300 pounds of thrust. The engines use 90% hydrogen peroxide and kerosene. These engines have been used on the FJ-4, F-86 and NF104A aircraft. The AR series rocket engines are integral, compact, liquid propellant, pump-fed engines designed to provide aircraft thrust augmentation.

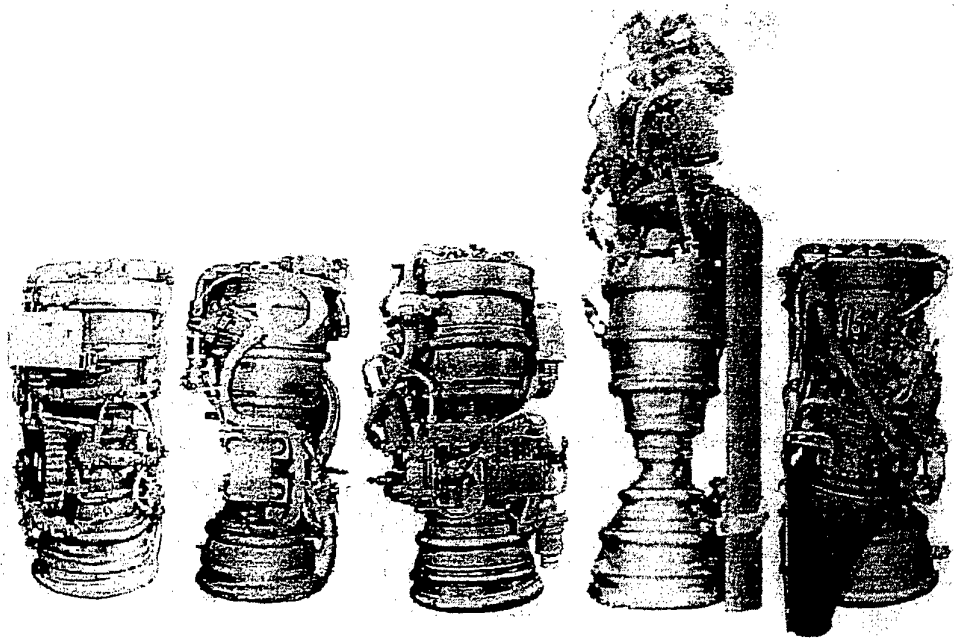


Figure 1. AR-1, AR-2, AR2-1, AR2-2, AR2-3 Rocket Engines.

The AR2-3 rocket engine supplies hydrogen peroxide and kerosene propellants to the thrust chamber by oxidizer and fuel centrifugal pumps, directly driven by a single turbine. Pumps and turbine are mounted on the same shaft. Oxidizer flows from the pump outlet through the pressure-actuated oxidizer valve, through the thrust chamber cooling jacket, and into the main thrust chamber, through the silver-plated catalytic screen pack, where it is decomposed into super-heated steam and oxygen. Fuel flows from the pump outlet through the chamber-pressure-actuated fuel valve, into the concentric annular-ring type fuel injector, and is injected into the hot, oxygen-rich gases, where it combusts and is exhausted through the 12:1 area ratio nozzle. Auto-ignition of the fuel eliminates the necessity for an ignition system. A small oxidizer flow, of about 3% from the oxidizer pump discharge, is delivered and metered through the thrust control valve into a catalytic gas generator, where it is decomposed into super-heated steam and oxygen to drive the turbine. An engine flow schematic is shown in Figure 2. Under emergency situations, the engine may be operated as a mono-propellant engine using the oxidizer. The engine operates at a moderate chamber pressure and provided 6600 pounds thrust at vacuum and 246 sec specific impulse. Additional performance parameters are shown in Figure 3.

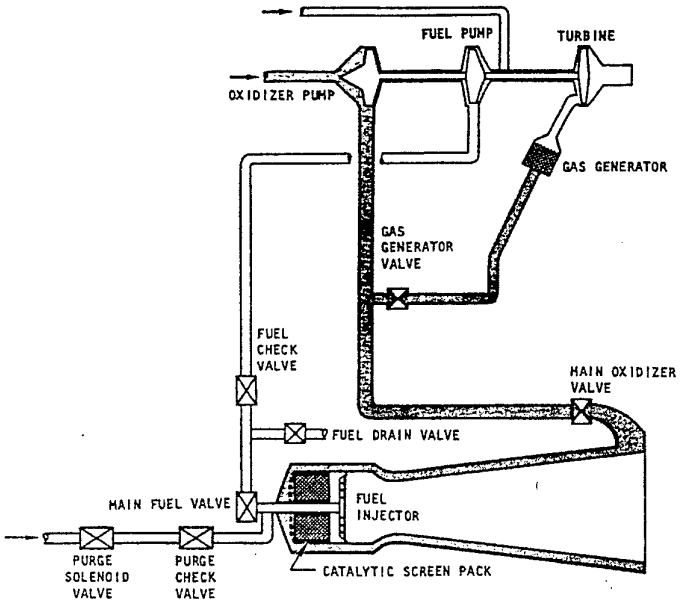
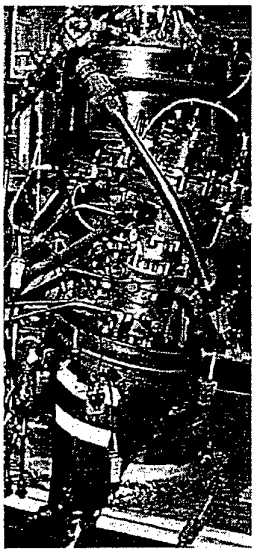


Figure 2. AR2-3 Engine Operating Schematic.



• Propellants	90%H_2O_2/JP
• Thrust, vac (lbf)	6600
• Isp, vac (sec)	246
• Chamber pressure (psia)	560
• Mixture ratio	6.5
• Area ratio	12:1
• Length (in)	32
• Engine diameter (in)	20
• Weight (lbm)	225
• Gimbal angle (degrees)	0
• No. or restarts	multiple
• Engine life	>150 minutes

Figure 3. AR2-3 Engine Performance.

During the development testing, preliminary flight rating testing and qualification testing of the AR engine series, over 2200 tests have been conducted totaling more than 45 hours of engine operation. An AR engine has been operated continuously for up to 15 minutes. Up to 4 hours of operation have been accumulated on one engine. In addition to the long duration tests, many start-stop tests were performed to demonstrate the restart capability of the engine. Figure 4 shows an AR2-3 engine being hot fire tested in Rocketdyne's Santa Susana Test Facility.

The FJ-4 aircraft made 103 flights with a total of 3.5 hours of AR2-3 engine operation. It had a maximum altitude of 68,000 ft with up to 6 starts per flight. The F-86 aircraft made 31 flights with a total of 1.4 hours of AR2-3 engine operation up to an altitude of 72,000 ft. The NF-104A aircraft made 302 flights with a total of 8.6 hours of AR2-3 engine operation with a maximum altitude of over 120,000 ft. This aircraft was used as an astronaut trainer, allowing the trainee to experience a few seconds of weightlessness and permitting this aircraft to operate in the fringes of space. An NF-104F aircraft is shown in Figure 5, with the AR2-3 rocket engine firing over Edwards Air Force Base.

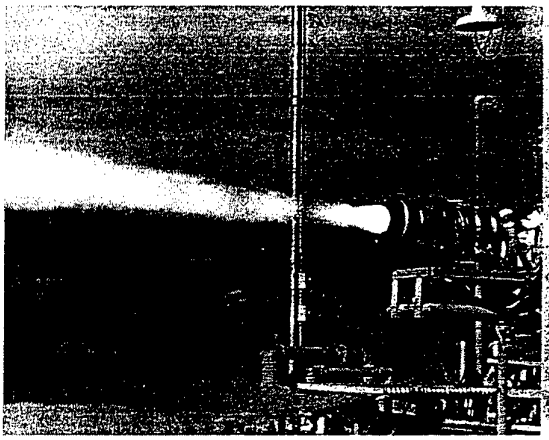


Figure 4. AR2-3 Engine Hot Fire Testing.

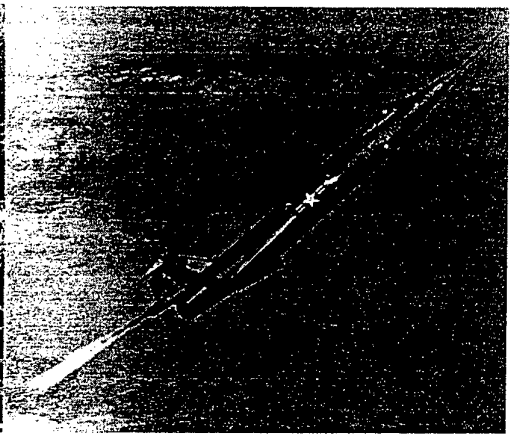


Figure 5. NF-104A Aircraft With AR2-3 Firing

AR2-3 Test Results

AR2-3 engine assets were obtained for a hydrogen peroxide propulsion demonstration. The AR2-3 engine drawings and specifications were pulled from the Rocketdyne vault to guide the refurbishment effort. The engine components were disassembled and inspected for wear and damage. A few had never been hot fired. The individual parts were cleaned and reassembled into the components. The combustion chamber was flow tested with water. The turbopump was balanced and reassembled. The valves were actuated to determine the operating characteristics. The relay box was gutted and rewired. The fuel injector was brought into spec and was water flow tested.

The catalyst packs for the main chamber and the gas generator were disassembled. New screens were obtained and silver plated. The main chamber screens were packed into the main catalyst pack housing ready for engine assembly. Screens for two gas generator catalyst packs were packed, one for the engine and one for gas generator component testing at the Rocketdyne Santa Susanna Test Facility (SSFL). The gas generator testing took place over a period of 5 days. Twenty four tests were conducted with 3,192 seconds of operation and using 230 gallons of 85% hydrogen peroxide. All of the tests were successful and exhibited very stable operation over a range of operating conditions.

The newly refurbished components were assembled into an AR2-3 engine. Instrumentation was installed on many of the components in preparation for hot fire testing. The engine was leak tested and functionally tested before being boxed up and shipped to NASA-SSC for engine hot fire testing.

Engine tests were conducted between September and October of 1999 at NASA-SSC's E-3 facility under a Space Act Agreement with NASA-MSFC. The objectives of the testing included demonstration of both monopropellant and bipropellant startup, shutdown, and main stage performance. The first few tests were planned to be monopropellant operation only. Because the off design performance of the turbopump was unknown, a fuel bypass system was developed so that the pump performance could be fully understood prior to the addition of fuel into the main chamber. Fuel would enter the engine fuel pump and then be bypassed to a catch tank at the facility. This would allow for a more accurate attempt of judging the mixture ratio of the first bipropellant test and it would also allow the pump seals to break in properly. Photos of the engine installed in the test stand are shown in Figure 6.

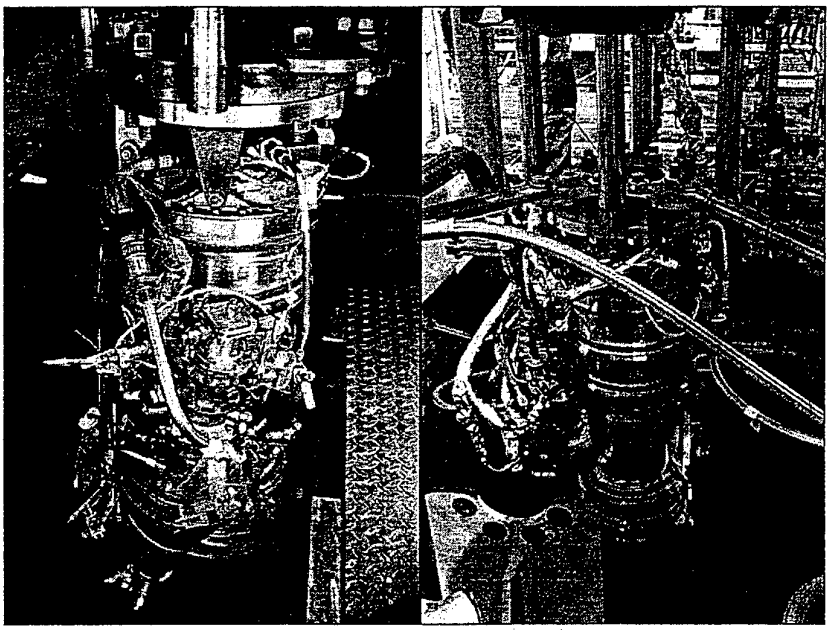


Figure 6. AR2-3 Engine Installed in E-3 Test Stand (2 views).

The objectives of the first few tests were to demonstrate the start and cutoff transient performance. The goal was to open the main oxidizer valve and generate main chamber pressure. The objectives of the later tests were to demonstrate steady state performance and to break-in the catalyst pack for consistent performance. After the first couple of tests, it was determined that residual water in the propellant system left over from water blowdown testing, lowered the hydrogen peroxide concentration to approximately 72%. This caused lower performance than expected and a slower engine start transient.

In many of the tests the engine exhaust was a cloudy vapor of steam and appeared to contain a lot of liquid, especially at startup. In some of the tests the exhaust would clear up and be almost undetectable, as super heated steam. Cloudy exhaust indicated poor hydrogen peroxide decomposition, with low main catalyst pack performance. High turbine exhaust temperatures indicated that the gas generator, on the other hand, performed very well with high efficiency. A comparison of the engine exhaust plumes from tests 5, 6, 8, and 10 can be seen in Figure 7. Tests 5 and 8 had clear plumes showing good hydrogen peroxide decomposition and tests 6 and 10 had cloudy plumes showing poor decomposition.

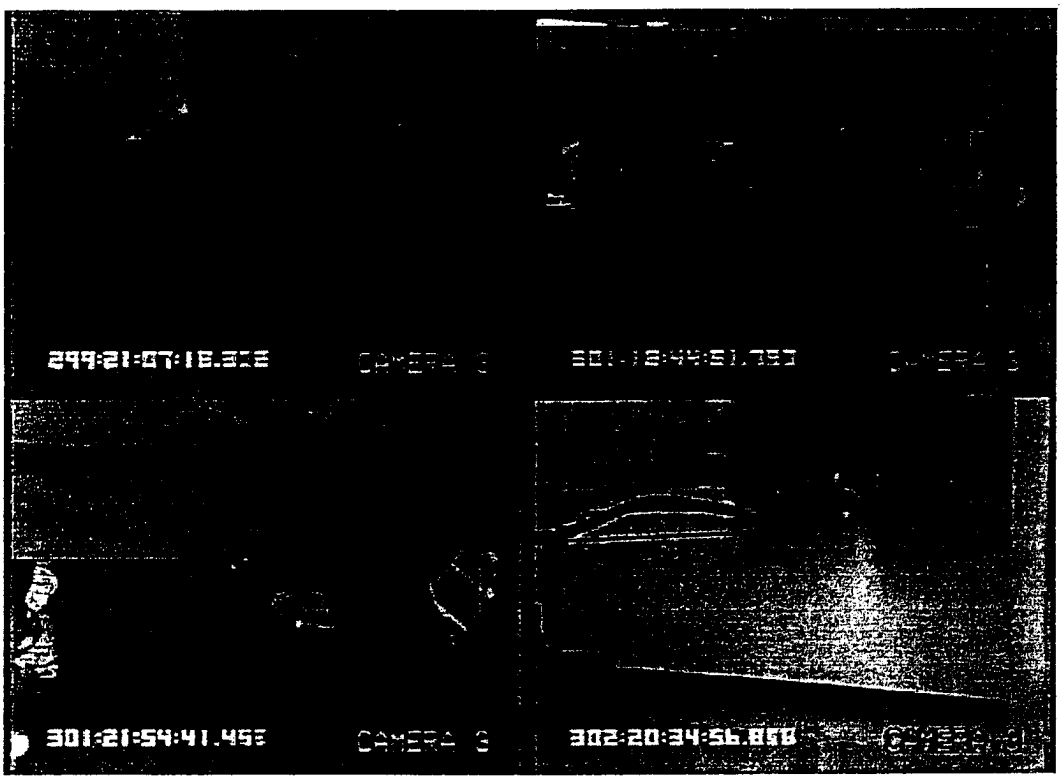


Figure 7. Engine Exhaust Plumes During Tests 5, 6, 8 and 10.

A difference was also noted in the transient and main stage performance between similar tests performed on different days. A faster startup and higher performance was often noted during the second test of the day versus the first test of the day. This was attributed to the difference in main catalyst pack temperature at startup, demonstrating that a warm catalyst pack has a faster startup transient. An example of this was the engine performance increase noted between tests 6, 7, and 8. It was attributed to the increase in temperature of the catalyst pack components with each successive test on the same day. The skin temperatures of chamber jacket head were steadily increasing prior to each test (Figure 8) which in all probability caused the engine performance increase because less energy was required to cause catalysis and thermal decomposition.

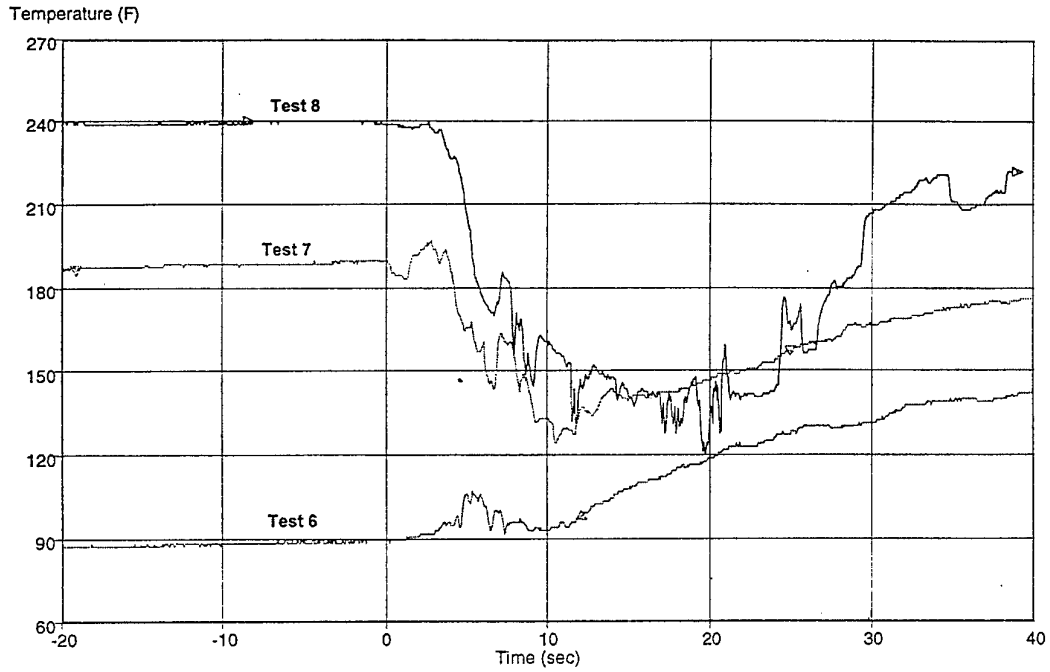
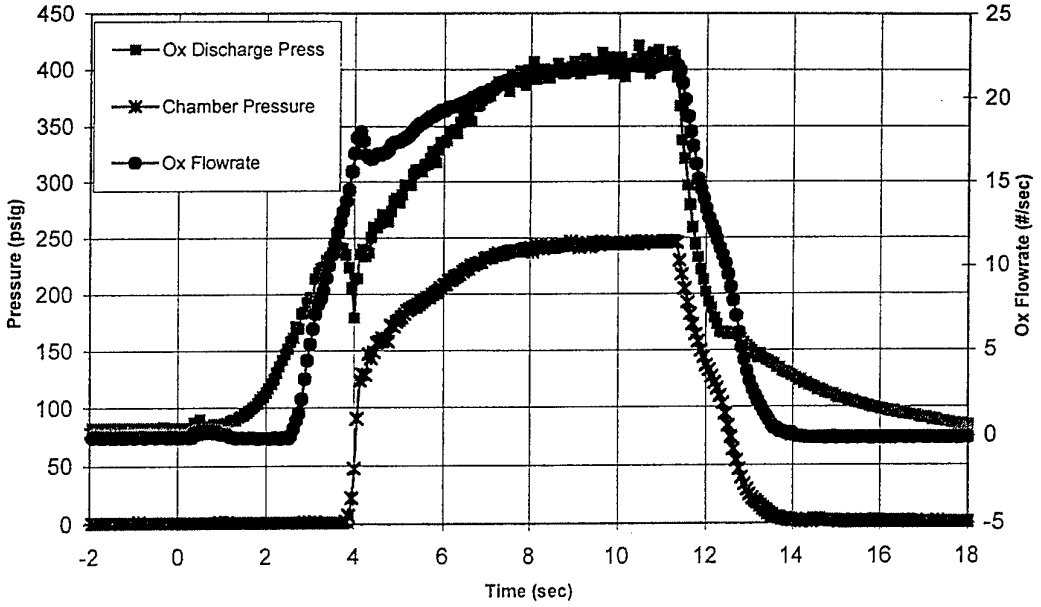


Figure 8. Skin Temperatures of the Head End of the Chamber Jacket for Tests 6, 7 and 8.

From September 30, 1999 to October 29, 1999, a total of 10 monopropellant tests were completed on the refurbished engine for an accumulated test time of 92.4 seconds. 84.3% concentration hydrogen peroxide from Solvay Interox was used with JP-8 as the fuel for the first 8 tests. 89.2% concentration hydrogen peroxide from Degussa was used with JP-8 as the fuel for the last 2 tests, which should have increased the engine performance. Though a performance increase was seen, it was not as great as expected for the higher concentration peroxide. During the last test (test 10), the engine exhaust was dense, opaque atomized hydrogen peroxide and after shutoff liquid was seen dripping out of the nozzle.

Typical transient and steady state performance of the oxidizer system can be seen in the data from test 5 (Figure 9). The pressures and flowrate go up smoothly and level off at steady state. As comparison, the data from test 10 starts much the same way but takes an early dip and levels off at a lower pressure and flowrate, indicating there is a problem (Figure 10). This lower performance coincides with the previously noted cloudy engine exhaust plumes.



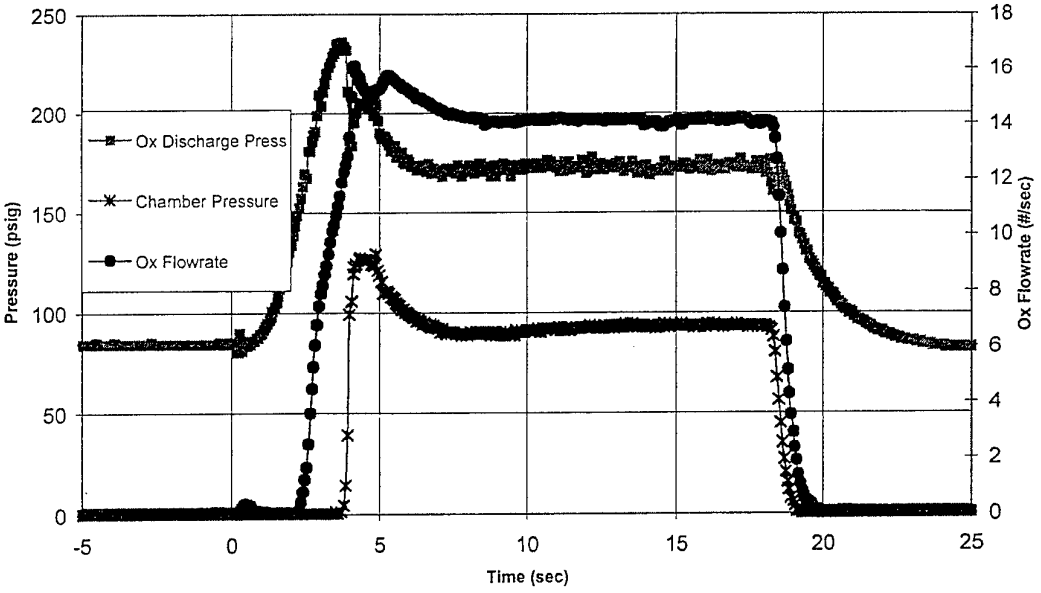


Figure 9. Oxidizer System Data Vs. Time During Test 5.
Figure 10. Oxidizer System Data Vs. Time During Test 10.

The C-star efficiencies of the main catalyst pack varied from test to test causing the main chamber pressure to be below what is required for proper engine bootstrap operation. Figure 11 shows the C-star from test to test as a function of time on the engine. The plot

includes test 2 and tests 4 through 10. Tests 1 and 3 were excluded from the chart because the chamber pressure did not reach a steady state value prior to the test cutoff. A definite improvement can be seen on tests that were completed on the same day with the exception of tests 9 and 10. If a straight line were to be placed across the peaks of tests 2, 5, 8, and 10, a general trendline of decreasing C-star can be seen, which indicates a steady degradation of the main catalyst pack activity and performance. Post test inspections did not indicate any abnormal operation with the remainder of the engine components.

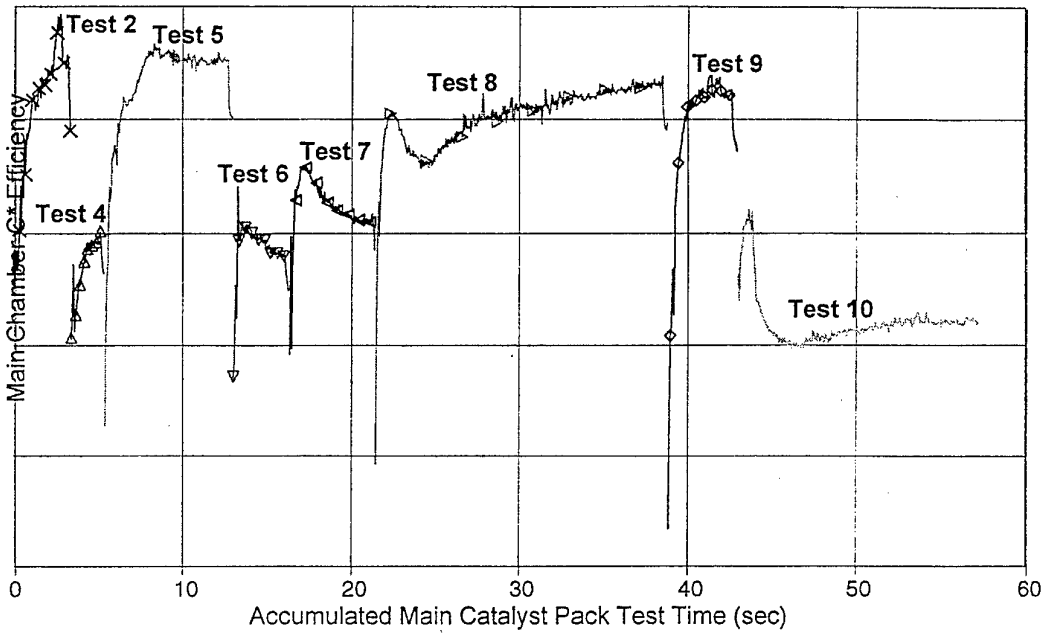


Figure 11. C Efficiency Vs. Engine Hot Fire Time.*

Figure 12 summarizes the test data. A row of the data has been included which indicates the plume condition of the engine exhaust. Initial theories on the performance issues included coring, quenching at startup, inactivation by poisoning, and possible plating and activation process problems. Because of this, a decision was made to remove the engine from the test stand and inspect the main catalyst pack and gas generator catalyst pack. The investigations ultimately found that the catalyst bed was coring, flowing raw undecomposed hydrogen peroxide through the center of the catalyst pack due to insufficient silver along the screen surface. Only the outer _" annulus of screen was active enough to decompose the propellant.

Test No.		1	2	3	4	5	6	7	8	9	10
Date		9/30/99	9/30/99	10/15/99	10/26/99	10/26/99	10/28/99	10/28/99	10/28/99	10/29/99	10/29/99
Test of Day		1	2	1	1	2	1	2	3	1	2
	Unit										
Duration	sec	4	6	3	6	11	6.4	8	20	8	18
Mono/Biprop		Mono	Mono	Mono	Mono	Mono	Mono	Mono	Mono	Mono	Mono
H2O2 Conc.	%	84.3	84.3	84.3	84.3	84.3	84.3	84.3	84.3	89.2	89.2
Operating Parameters											
Oxidizer Flowrate	lbm/sec	9.6	12.9	9.7	17.6	22.0	16.2	16.3	16.9	15.1	14.1
Thrust Chamber Pressure	psig	0.9	137.1	0.9	142.3	246.5	127.7	136.6	180.3	155.8	93.2
Turbine Inlet Temp	Deg F.	479.1	589.7	941.7	1124.6	1148.5	1114.5	1147.5	1144.5	1261.3	1302.2
Clear Exhaust Plume		no	some	no	no	yes	no	some	yes	some	no

Figure 12. Summary Data of Engine Hot Fire Testing.

The X-37 Mission

NASA and Boeing have agreed to work together to build and fly a single X-37 reusable vehicle in orbit. The X-37 is one of several NASA Pathfinder vehicles planned to demonstrate reduced launch costs with advanced technology. The X-37 will be the first X-vehicle to demonstrate this technology in orbital flights.

The X-37 vehicle is 27.5 feet long - about half the length of the Shuttle payload bay – and weighs about 6 tons. Its wingspan is about 15 feet, and it contains an experiment bay 7 feet long and 4 feet in diameter that can accommodate a 500 lb package of experiments and equipment. It is designed to be modular to allow for rapid insertion of technologies and experiments. On-orbit propulsion will be provided by the AR2-3 engine using 90% hydrogen peroxide and JP-8. Hydrogen peroxide was selected over liquid oxygen because it is dense, storable, capable of tolerating months in orbit, and meets safety restrictions for being part of the payload in the Space Shuttle.

The missions will start with the X-37 vehicle traveling up into low earth orbit in the payload bay of the Space Shuttle sometime in late 2002. The different phases of the missions are shown in the series of images in Figure 13. The phases shown are: inside the payload bay of the Space Shuttle, being lifted out of the Shuttle with the remote arm, deployed from the Shuttle, some distance away from the Shuttle prior to main engine start, maneuvering around an orbiting object (2nd flight), reentry into the earth's atmosphere, gliding to the landing site, and landing on a runway. The first mission will last a few days before reentering and landing on earth. The X-37 vehicle will also be demonstrating operability in terms of vehicle turnaround. By using a hydrogen peroxide engine, the propulsion system turnaround is fairly quick. The second mission could last several weeks in orbit, demonstrating maneuvering around an orbiting object and evaluating long-duration mission systems and operations, before reentering and landing again on earth.

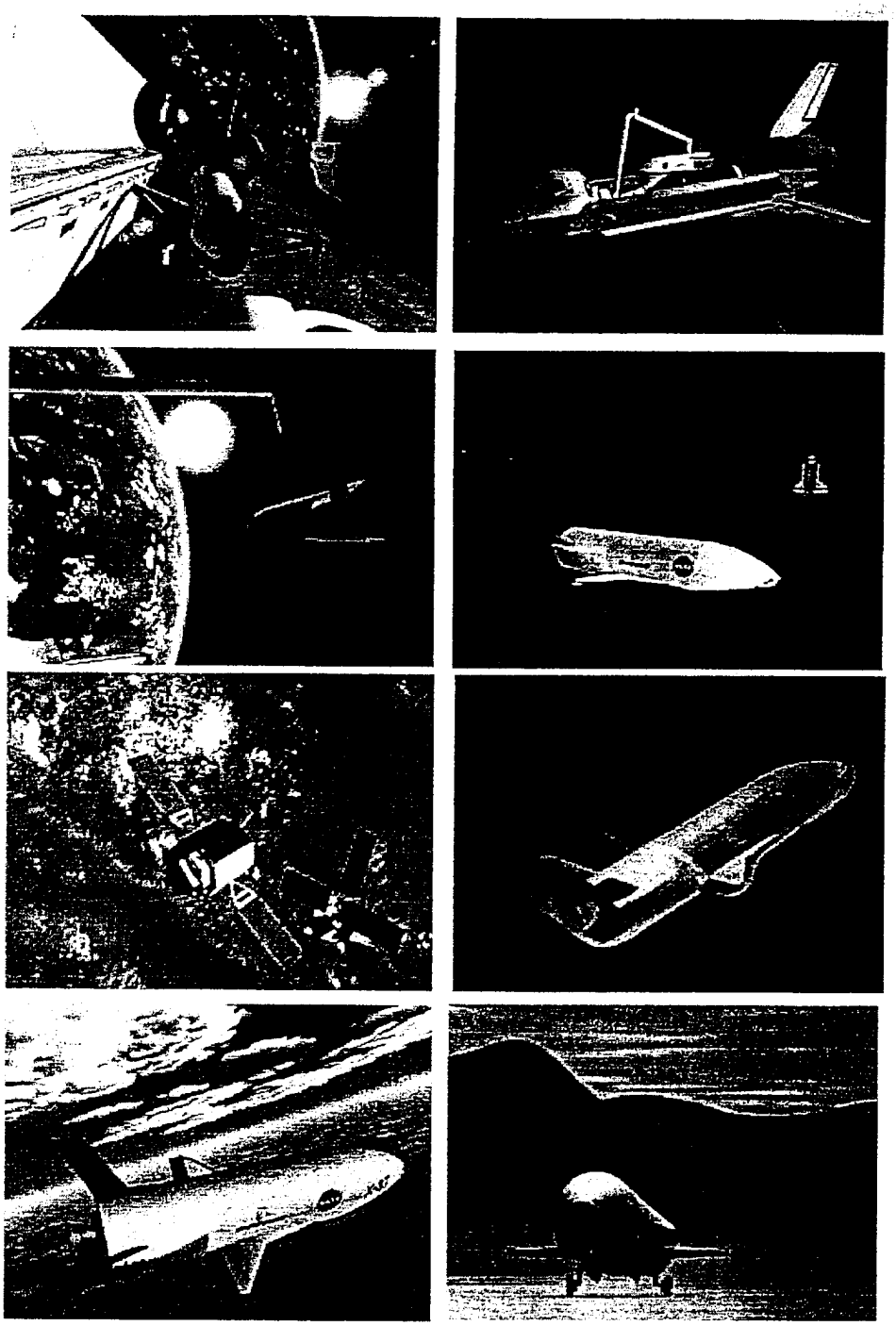


Figure 13. Different Phases of the X-37 Mission

The USFE 10k Engine

The engine consists of pneumatically-actuated ball valves, propellant feed-lines, the oxidizer dome with a mount for gimbal attachments, a catalyst bed to convert the HTP into oxygen and superheated steam, a fuel injector, and an ablative chamber and nozzle. Low material and design costs coupled with robust margins were the guiding philosophy toward selecting a design.

The engine design and operating parameters are provided in Table 1. The engine develops 10,000 lbf of thrust at vacuum conditions with a 40:1 expansion ratio nozzle. Chamber pressure was chosen to be 500 psia, which spans the operating regimes of pressure-fed and pump-fed systems. Based on a component-level-demonstrated C^* efficiency of 0.97 and an estimated nozzle efficiency of 0.98, the delivered vacuum specific impulse is 290 s at a mixture ratio of 6.0.

Parameter	Value
Propellants	90% HTP/JP-8
Vacuum Thrust, lbf	10,000
Chamber Pressure, psia	500
Mixture Ratio	5.75
Nozzle Expansion Ratio	40 (five for ground tests)
Chamber Contraction Ratio	7.1
Delivered Specific Impulse, s	290
Flowrate, lb/s	34.5
Burn Time, s	200
Engine Envelope	60 in. long, 40 in. diameter

Table 1. Design and Operating Parameters of USFE Engine

The catalyst, injector, and ablative chamber designs are based on the results from two sets of subscale tests which used a 50 lbf monopropellant thruster for catalyst bed screening and a subscale bipropellant thrust chamber for injector development tests.[1,2] The subscale configuration captured key design features of the fullscale catalyst bed, the injector and the chamber.

Historical designs were used to size the thrust chamber (TCA, shown in Fig. 14).[3] To ensure autoignition of the fuel, a contraction ratio of about seven was chosen. The resulting chamber inner diameter was ten inches. Maintaining this inner diameter in the catalyst bed led to a bed mass flux, or G, the loading parameter, of about 0.4 lb/s-in^2, which is also within the historical operating range of silver screen-based catalyst beds.

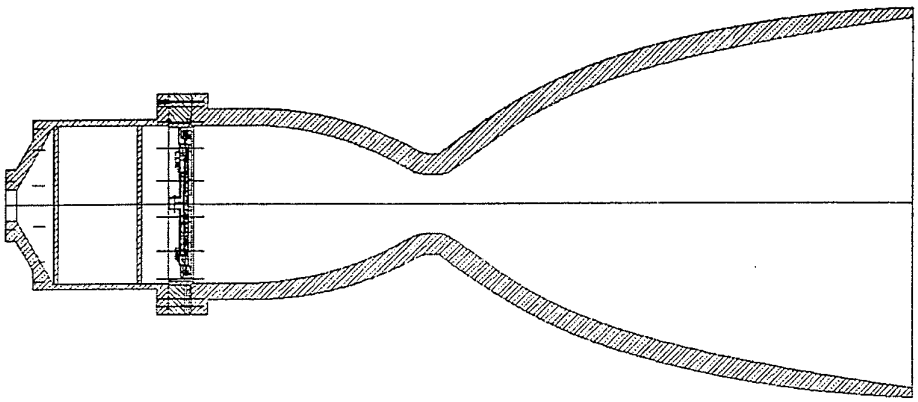


Fig. 14. USFE Thrust Chamber Assembly. TCA consists of oxidizer dome, catalyst bed assembly, fuel injector, and ablative chamber/nozzle. The chamber produces 10,000 lbf of thrust in space at a chamber pressure of 500 psia with an expansion ratio of 40.

USFE 10k Engine Test Results

The full-scale tests consisted of five distinct test series:

- monopropellant tests to verify test operations and the performance of the catalyst bed
- start-up characterization tests to demonstrate reliable starting characteristics
- short duration tests in a copper heat-sink chamber to verify injector performance and to obtain chamber wall heat flux and high frequency combustion stability data
- longer duration tests (~ 30 s) with an ablative chamber to measure the erosion characteristics of the injector/chamber combination
- a long duration test (140 s) that simulates the total burn time of the actual mission to determine life.

Tests to date have used both 85% and 90% concentration (by weight) hydrogen peroxide. Prior to mid-1999, only 85% peroxide was available in bulk quantities for test. When 90% peroxide became available in mid-1999, it was used exclusively. Most of the discussion and data shown below is based on the tests using 85% peroxide. Data from the 90% peroxide tests are being reduced and analyzed at the present time; preliminary analysis has indicated that the results are as would be expected based on the 85% peroxide results.

Over 100 tests have been conducted, with the general objectives being to demonstrate the performance and life of the thrust chamber assembly, including catalyst bed, injector, and ablative chamber, and to demonstrate safe operations with hydrogen peroxide. Component development success criteria were: 95% conversion efficiency in the catalyst bed (as determined from monopropellant C^* measurements); greater than 95% bipropellant C^* efficiency; and throat erosion rates less than 0.001 in/s. All these criteria were exceeded in the full scale tests. All operations were conducted safely. Some of the test highlights are:

- conducted over 125 tests
- accumulated nearly 30 minutes of test time
- accumulated over 300 seconds of bipropellant operation using ablative chambers, including one long-duration test of 140 s
- accumulated over 700 seconds of run time on a single cat bed without performance degradation
- demonstrated throat recession rates of less than 0.001 in/s
- demonstrated C^* efficiencies greater than 0.97 at nominal operating condition
- tested twelve different test article configurations
- tested both 85% and 90% peroxide from two different manufacturers
- demonstrated multiple restarts
- demonstrated throttling to 10% in monopropellant mode and to 20% in bipropellant mode
- maintained perfect safety record

The demonstration test TCA was designed in a bolted-together arrangement to allow for rapid component replacement. The TCA consisted of four distinct subcomponents: a workhorse oxidizer dome with a side inlet which served as a test facility interface; a catalyst bed assembly, including a structural housing and a slip-in catalyst bed to allow different cat bed designs to be tested; a fuel manifold (another test facility interface) and injector; and the chamber/nozzle.

Two basic chamber/nozzle configurations were tested – a copper heat sink chamber and an ablative chamber. The heat sink chamber was well-instrumented for making pressure and temperature measurements. Static pressure measurements were made in four axial locations – between the cat bed exit and the injector, downstream of the injector face, at the entrance to the converging part of the chamber, and in the chamber throat. A water-cooled high-speed pressure transducer was placed one inch downstream of the injector face. Linear array thermocouples were inserted into the chamber to measure heat flux at four different locations. The heat flux measurements in conjunction with the NAT[4] and CMA[5] codes were used to determine the near wall gas temperature. The near wall gas temperature was used to determine the operating O/F that would result in an acceptable amount of throat erosion in the ablative chamber.

The catalyst beds tested were essentially of the silver screen type. Both pure silver and silver-plated nickel screen catalysts were tested. Both uncoated and coated screens were tested. The best configuration tested was made of pure silver screens with a samarium nitrate coating. The bed length was two inches. The nominal bed loading was 0.4 lb/s-in^2, and values up to 0.7 were tested with 85% peroxide. At this high value of G, high decomposition temperatures were measured, but the exhaust plume observed by remote cameras was not transparent like it was for the nominal case.

Catalyst bed performance was determined by comparing pressure and temperature measurements with pressures and decomposition gas temperatures predicted by a chemical equilibrium code. Pressure and temperature were measured at a location

between the cat bed exit and the injector entrance. Whenever the exhaust plume was clear, the measurements indicated essentially 100% decomposition.

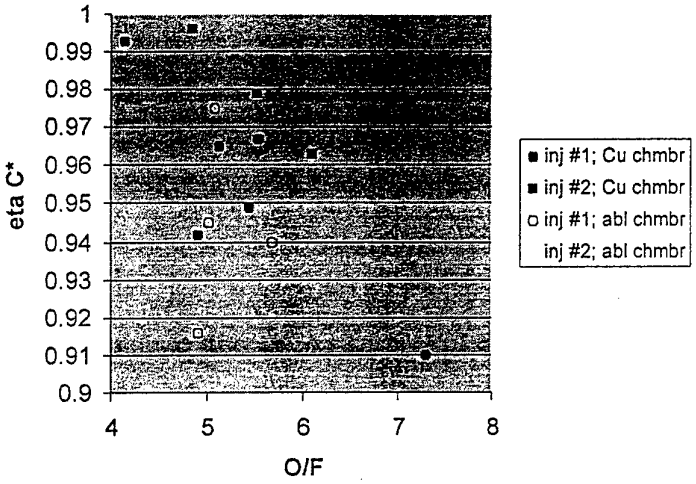


Fig. 15. C^* efficiency as function of O/F in heat sink (Cu) and ablative (abl) chambers. Injector # 1 is "steam port"

Two types of injectors were tested – a "steam port" design, similar to that used in the Gamma engines, and the other a ring-type injector. A third type of steam port injector has been fabricated and tested, with the data reduction ongoing at the present time. The ring injector used O/F biasing to provide a fuel-rich gas around the chamber periphery, and near stoichiometric conditions in the core. This injector has been tested with both 85% and 90% peroxide. Injector performance was determined from chamber pressure measurements and comparison with theoretical C^* values. The pressure loss across the injector was also measured. Both injectors achieved C^* efficiencies greater than 95% at their nominal operating conditions (Fig. 15). A higher operating O/F was possible with the ring injector because the fuel-rich periphery provided for minimal throat erosion.

The ablative chamber/nozzle consists of a silica phenolic liner and an epoxy-glass phenolic overwrap. For sea-level tests, the 40:1 nozzle is cut at a 5:1 ratio, providing a nearly ideal expansion to atmospheric conditions. The ablative chamber was instrumented with thermocouples and strain gages.

The throat erosion was measured after each test with calipers. The rate of erosion was determined to be a function of operating O/F and the injector that was used in the test. The gas temperature and chamber pressure are the primary parameters that determine the erosion rate of the silica phenolic. Silica is non-reactive with the combustion gas, thus there is no thermochemical erosion in this engine configuration. Mechanical (silica melt flow) erosion is the primary mechanism driving the material loss in the throat of the nozzle.

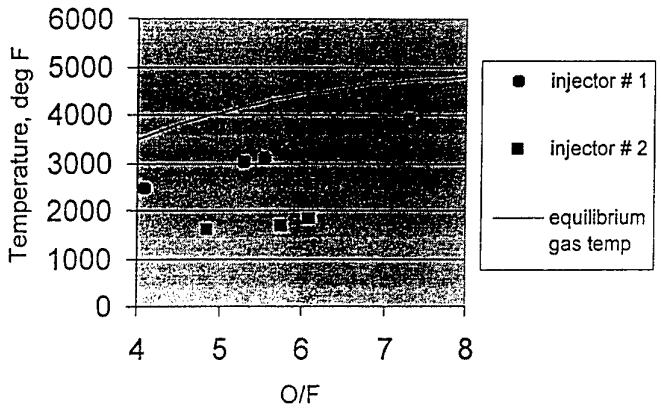


Fig. 16. Effective (near wall) gas temperature as function of O/F for each injector. Equilibrium bulk gas temperature is shown for comparison. Injector # 1 is "steam port" design and injector #2 is ring design.

The heat sink chamber provides an average heat transfer rate in the throat that can be used to infer the effective gas temperature. The effective near wall gas temperature provided by each injector was determined from the thermocouple measurements over a range of O/F conditions as shown in Fig. 16. These results were then used to determine the viable operating conditions for ablation testing with the composite nozzle. The agreement between the measured and predicted erosion rates were excellent. After the long duration (140 s) test, the chamber was cut into sections. A comparison of the measured and predicted char depth in the throat also indicated excellent agreement with less than 5% error. The low near wall gas temperatures indicated in Fig. 6, along with the low throat erosion rate (< 0.001 in/s), prove the efficacy of the O/F biasing method to achieve minimal erosion while maintaining minimal performance loss.

The USFE Mission

The purpose of the Upper Stage Flight Experiment (USFE) is to demonstrate key technologies necessary to the operation of an inherently simple propulsion system with an innovative, state-of-the-art structure. Two key low-cost vehicle elements will be demonstrated – a 10,000 lbf thrust pressure-fed engine and an integrated composite tank structure. These technologies will be demonstrated through numerous development tests culminating in an actual flight.

The Upper Stage Flight Experiment will fly as the third stage aboard an Orbital Suborbital Program (OSP) suborbital launch vehicle. Figure 17 shows an overview of the USFE mission. The USFE/OSP mission will fly out of the Alaska Spaceport on Kodiak Island in November 2001.

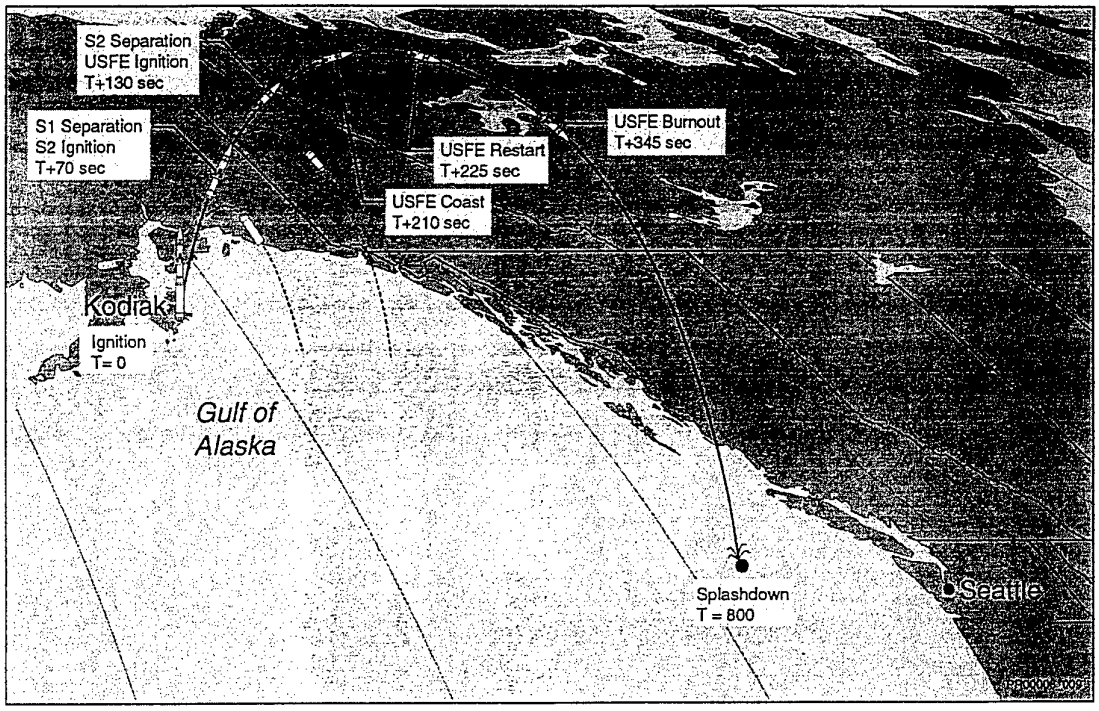


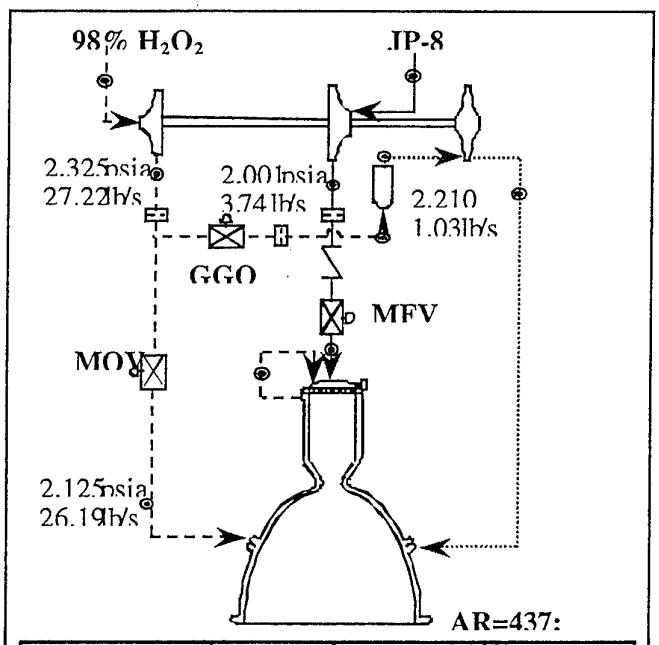
Fig. 17. The Upper Stage Flight Experiment.

Integration of the USFE and the OSP nosecone takes place at Orbital's facility in Arizona. The OSP vehicle avionics are located in the nosecone. After integration and test, including mission simulation testing, the USFE/nosecone assembly is shipped to the Alaska Spaceport for integration with the first and second stage of the OSP launch vehicle. After vehicle integration, checkout, and final mission simulation testing, USFE is loaded with propellants for launch. The propellant loading sequence consists of loading helium, nitrogen (for the attitude control system), JP-8, and hydrogen peroxide. Final checks are done and the count down to launch proceeds.

After stage 1 and 2 burn, USFE is separated from the 2nd stage by an ordnance separation event in the interstage. The vehicle is exo-atmospheric prior to stage 2 burn out. Immediately after Stage 2/USFE separation, USFE goes through its engine startup sequence. After engine start, USFE will burn for 80 seconds, shutdown, coast for 15 seconds, then restart and burn for 120 seconds. After shutdown USFE and the OSP nosecone reenter the atmosphere marking the end of the mission.

An Advanced Peroxide/RP Engine

NASA's interest in peroxide propulsion is fostered by the need to achieve order of magnitude reductions in transportation costs to space. Two stage to orbit (TSTO) systems will need more operable, lower cost, reusable upper-stage propulsion systems than those presently available in the commercial marketplace. Even single stage to orbit (SSTO) systems will need orbital transfer stages with the same operating, cost, and performance characteristics as their TSTO competitors. An early decision by the designers of these advanced upper stages to utilize storable, non-cryogenic, environmental safe propellant systems, like peroxide/RP, can have significant impacts on operations costs for years to come. Storable propellants will enable off-line stage fueling, and storage of fueled stages to respond to short turn-around mission requirements. Non-cryogenic, non-toxic stages will allow off-line installation of payloads and eliminate the need for cryogenic/toxic safety procedures and special equipment. Environmentally safe stages will allow elimination of dangerous and potentially harmful propellant combinations, and their attendant costs, on which today's space transportation systems are dependent. But before tomorrow's advanced stage designers can begin their design they must have an engine system around which to design their airframe and its many subsystems. What might that ideal peroxide/RP engine look like?



Parameter	Engine	Chamber	Gas Gen.
Thrust, LbF	10,000	9,855	145
Isp, sec	323	329.2	140.6
MR	7.3	7.0	---
Pc	---	1500	671

Figure 18: Representative Engine Power Balance

An ideal storable upper stage engine for the 21st Century would have the following characteristics:

1) It would utilize 98% peroxide as the oxidizer, and JP8 as the fuel. 98% peroxide because no advanced stage designer will be willing to carry any amount of water to orbit or the staging altitude. Peroxide/RP systems are only competitive with other traditional propellant systems on a density I_{SP} basis when the water is minimized in the peroxide. It would utilize JP8 because it is the most readily available RP fuel and the lowest cost of the RP propellants.

2) It would include a turbopump. The use of a turbopump allows higher engine pressures, higher I_{SP},

lower stage structural weights, and more flexibility in stage design. The turbopump would be a minimal parts count, low cost, decomposed peroxide gas generator driven design. The turbopump would be robust, but have a recurring price below $100,000. The turbopump would feature composite and ceramic materials, eliminating all metallic parts and their associated weights.

3) It would feature a liquid/liquid injector system. Decomposition of large amounts of peroxide by catalyst prior to JP8 injection is an unnecessary process step when thermal decomposition can be accomplished with proper injector and chamber design.
4) It would utilize an expansion deflection nozzle. Packaging the engine within the stage structure in order to maximize the available booster or advanced stage volume for payload will eliminate the use of today's large bell nozzles.
5) It will feature an integrated fluid/gas control module. Today's snake nest of discrete valves for each function, connecting plumbing, controllers and wiring represent as cost inefficient a design as can be generated.
6) It will be reusable, with a useful life exceeding 100 missions between out-of-airframe maintenance actions. It will be designed for ease of maintenance while installed in the airframe.

The Peroxide Pathway

Developing this advanced peroxide engine will take years of careful development, sometimes stretching new technologies, and sometimes concentrating on integrating them. NASA has begun this development process under the auspices of the Advanced Space Transportation Program at the Marshall Space Flight Center. A technology roadmap (Figure 1) has been developed to guide this development. The development steps are as follows:

Step 1: Secure a reliable source of bulk quantities of high concentration peroxide. NASA, the Air Force, and industry will invest more than $50million in the development of peroxide technology in the next decade in order to realize the potential of peroxide propulsion. That level of investment will be constantly at risk if the supply of 98% peroxide remains the product of a single specialty supplier. One of the proposals selected by NASA in response to the NASA Research Announcement (NRA) 8-21 Cycle 2 in 1999 was a proposal by Orbital Sciences to design, fabricate, and demonstrate a portable peroxide enrichment skid. A portable enrichment skid was selected because of the probable need of high concentration peroxide at multiple locations, including the Stennis Space Center in Mississippi, the Kennedy Space Center in Florida, the Kodiak Launch Center in Alaska, and at several industry facililities in California. Enriching peroxide means reducing the water content of the base product. In this case the enrichment skid is being designed to enrich commercially available 90% concentration material, available from Degussa Huls,

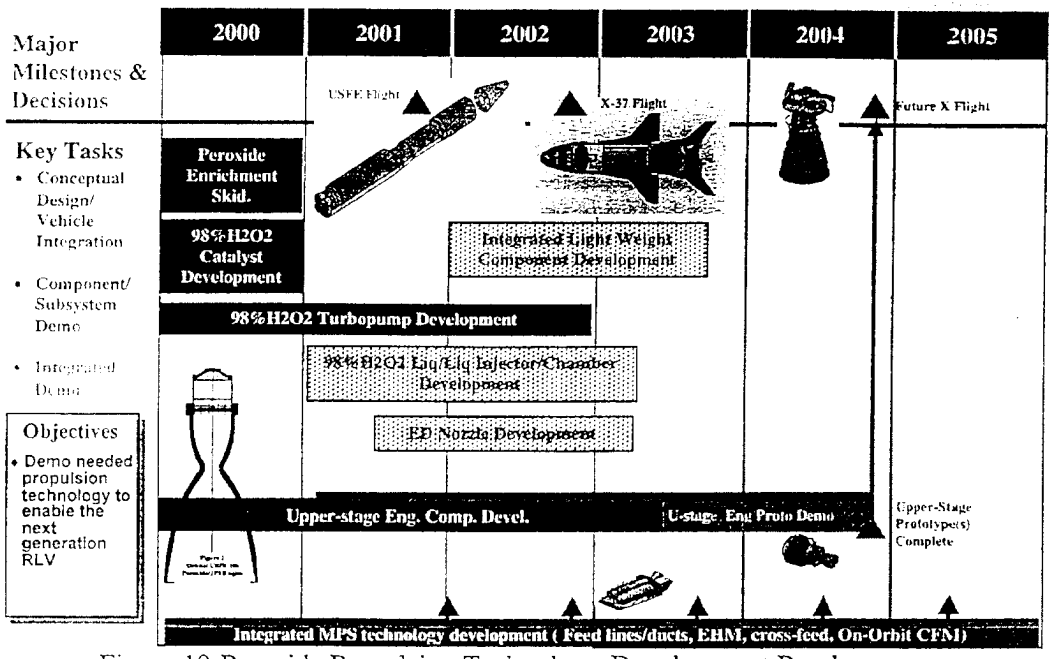


Figure 19-Peroxide Propulsion Technology Development Roadmap

FMC, and X-L Space Systems, to a 98% concentration material at a rate of 1000 pounds per day. The chosen enrichment process is crystall fractilization. The skid design and process controls are being engineered by Orbital's design partner Degussa Huls. The on-site enrichment process allows tighter control of product quality. It also allows concentrated product to be produced only as needed rather than stockpiled, thereby ensuring a safer operation. The enrichment skid also allows shipment of the less reactive 90% concentration product, and avoids exposure of the general public to the shipment of 98% material. The enrichment skid will be completed in 2000.



Figure 20: Monolythic Catalyst Bed

Step 2: Develop catalyst systems compatible with 98% peroxide. Catalyst systems are the key component in the integrated use of peroxide on future advanced upper stages. Catalyst will be used to generate gas to power the turbopump on the engine and to drive turbo generators for electrical power, to provide an ignition gas for thermal decomposition of peroxide in the engine, to decompose 98% peroxide for mono and bi-propellant attitude control thrusters, to generate warm gas heat for some systems, and to generate pressurization gas for tanks. A robust, long life, insensitive catalyst is the key to almost every liquid and gas system onboard future

advanced upper stages. Preliminary work on 98% peroxide catalyst was done in the 50s and 60s, but none of it resulted in definitive fielded systems. Aerojet, Boeing Rocketdyne, TRW, TRW partner General Kinetics, and TRW partner Purdue University were all selected by NASA in response to NRA8-21 cycle 2 to work on advanced catalyst for decomposition of 98% peroxide. In addition, Pratt &Whitney is performing research on 98% concentration catalyst systems on internal company funds. Competition is responsible for more technical innovation in industry than any other factor and this competition in the development of an advanced catalyst all but ensures success. All of the companies offer a different solution. And the costs to explore these potential solutions are moderate. The catalyst development work is planned for completion in 2000.

Step 3: Develop 98% compatible turbopumps. The next development step must be an advanced, low parts count, low recurring price, 98% peroxide compatible, turbopump. This is the longest lead time component in the rocket engine and must be started as early as possible. Once developed it can be used to support pure rocket system development, as well as peroxide/RP Rocket Based Combined Cycle (RBCC) demonstrations and peroxide/hybrid development. Boeing Rocketdyne has teamed with NASA-MSFC to design, fabricate, and demonstrate a state-of-the-art low cost, low parts count, 98% peroxide compatible, gas generator driven turbopump. Boeing recently successfully designed, fabricated, and tested a 60K pound thrust Lox/RP turbopump for the Low Cost Boost Technology project with a projected recurring cost approaching $100,000. And Boeing designed, produced, and fielded a man rated turbopump in the AR2-3 several decades ago. With this success base to draw on, Rocketdyne will still be challenged to produce a modern pump with recurring costs approaching $50,000 to support second generation X-37 and USFE mission plans. But it will still not be the non-metallic, light-weight, low parts count pump that is needed in the 21st Century. That will take an additional design and development cycle. The first peroxide pump iteration is expected to enter tests in 2002.

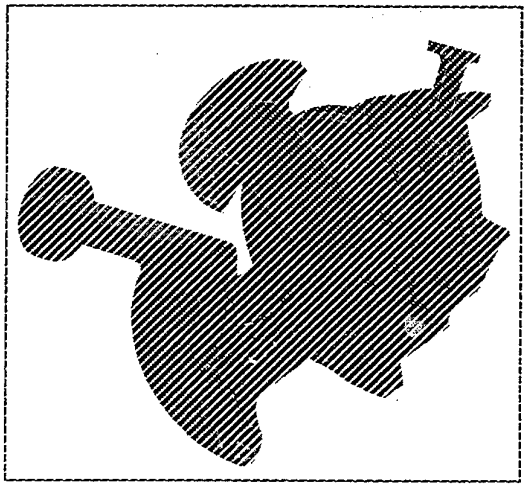


Figure 21 : Peroxide Turbopump

Step 4: Develop lightweight non-metallic reusable liquid/liquid injectors and combustion chambers. Elimination of the large catalyst packs will contribute significantly to lower engine weight and reduced engine maintenance. Liquid/liquid injection will eliminate energy losses occurring in the pre-chamber decomposition of the peroxide. And use of advanced non-metallic materials will substantially lower the weight of the engine. NASA expects to begin this development activity in FY2001.

Step 5: Develop a lightweight non-metallic reusable expansion deflection nozzle. Axial length to cross-sectional diameter ratios in excess of 1:3 will be necessary to meet future engine packaging requirements. Bell nozzles can not hang out the back of re-entering upper stage flight vehicles the way SSMEs do on the Shuttle.

Step 6: Develop a light-weight, non-metallic, fluid/gas control module. NASA and industry took a step in this direction by designing, fabricating, and flight testing a composite hydrogen control valve on the NASA/McDonnell Douglas DC-XA program in 1996. But more than fabrication of individual valves must be done. Consolidation of fluid and gas control functions, elimination of brackets and tubing, and relocation of components for ease of maintenance and test must dominate new designs.

Because safety is of paramount importance in dealing with such an energetic oxidizer, FMC Corporation was selected to perform hazardous materials testing of 98% concentration peroxide. Almost all of the data pertaining to safe handling and storage of 98% peroxide is three or more decades old. More current data will be required to satisfy today safety analyses and review boards. FMC, as a past American supplier of high concentration peroxide, is eminently qualified to perform these tests and establish the required safety data. This work is expected to be completed in 2000.

Conclusion

Five years ago peroxide/RP propulsion figured in no-one's plans. Now at the turn of the century peroxide/RP propulsion is returning to flight status aboard joint Air Force/NASA research vehicles demonstrating it's capability to meet both expendable and reusable mission needs. And development of new peroxide/RP engines has begun to take advantage of the new materials and design processes available today to reach new performance levels. A successful development program will lead to long term commercial application of this technology to 21st century space transportation systems.

Acknowledgements

The authors would like to acknowledge the help of Robert Ross, Doug Peters, Dave Mason, Scott Anderson, Jerry Golden, and Charles Cornelius of Orbital Sciences Corporation; Robert Bruce, Gary Taylor, Don Beckmeyer, Stan Warren and Scott Dracon of NASA Stennis Space Center; Fred Vaughn and Ray Nichols of Lockheed, Jim Guerrero and Dave Perkins of Air Force Phillips Lab; Ray Walsh of Schafer Corporation; Mark Ventura of General Kinetics; Ken and Norm Christensen of American Automated Engineering; and Abdi Nejad, P.-K. Wu, and Phil Morlan of Kaiser-Marquardt.

References

1. "The AR2-3, AR-3 and AR-4 Rocket Engines Technical Information and Program Plan", BC72-29, 1972.
2. "Rocketdyne AR Engines", BC72-21, 1972.

3. "Air Force Evaluation of the F-86F with AR2 Rocket Augmentation", AFFTC-TR-60-39, October 1960.
4. "Final Report for the XLR46-NA-2 Aircraft Superperformance Rocket Engine", R-1726, October 30, 1959.
5. "AR2-3 IR&D Engine Testing At Stennis Space Center", internal Rocketdyne report, unreleased.
6. NASA-MSFC website on Pathfinder vehicles.
"X-37: Taking the X-Planes to Orbit", Aviation Week, August 9, 1999.

References

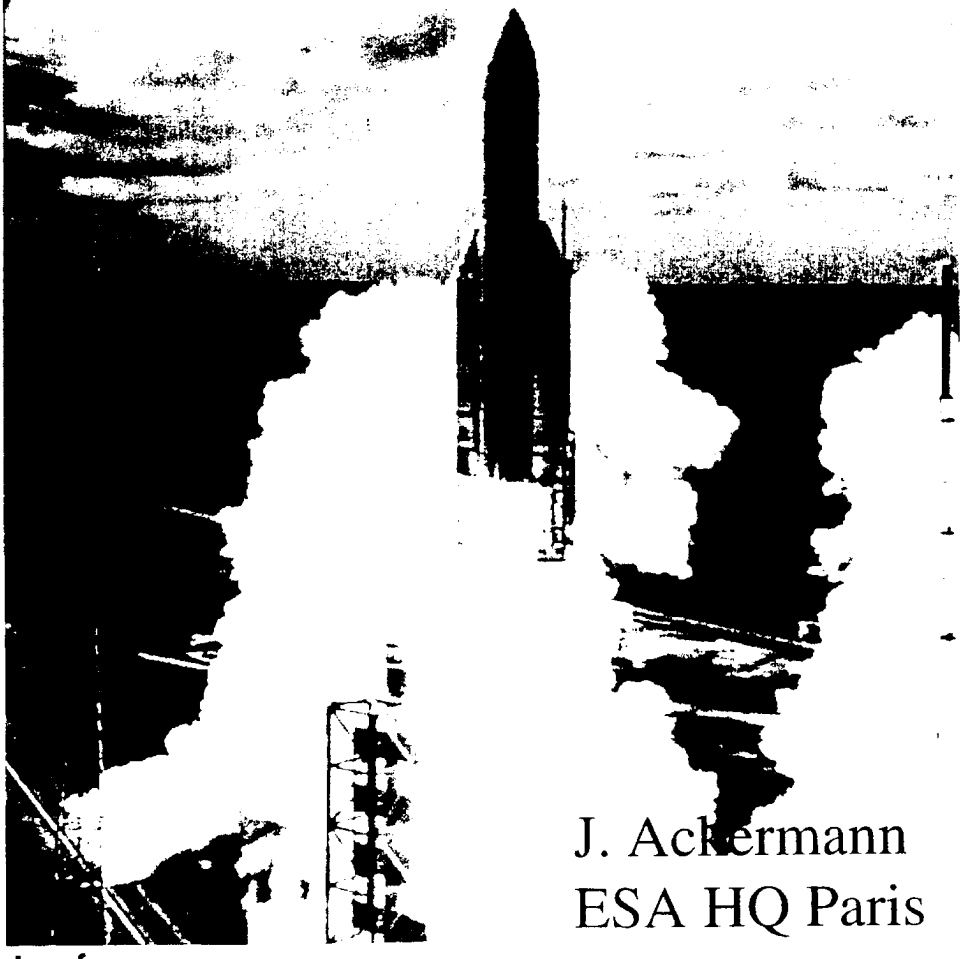
[1]Wu, P.-K., Fuller, R.P., Morlan, P.W., Ruttle, D.W., Nejad, A.S., and Anderson, W.E., "Development of a Pressure-Fed Rocket Engine Using Hydrogen Peroxide and JP-8," AIAA Paper No. 99-2877, Los Angeles, CA, June 20-24, 1999.
[2]Morlan, P., Wu, P., Nejad, A., Ruttle, D., Fuller, R., and Anderson, W.E., "Catalyst Development For Hydrogen Peroxide Rocket Engines," AIAA Paper No. 99-2740, Los Angeles, CA, June 20-24, 1999.
[3]Anderson, W.E., Crockett, D., Hill, S., Lewis, T., Fuller, R., Morlan, P., Ruttle, D., Wu, P.-K., and McNeal, C., "Low Cost Propulsion Using a High-Density, Storable, and Clean Propellant Combination," AIAA Paper No. 98-3679, Cleveland, OH, July 13-15, 1998.
[4]Nozzle Aero Thermochemistry (NAT) Computer Code Version 2.0, February 1994, Aerotherm Corporation, Huntsville Operations, Huntsville, AL.
[5]CMA90S, December 1990, Acurex Corporation, Aerotherm Division, Huntsville Operations, Huntsville, AL.

esa

th International Symposium on uid Space Propulsion

DLR- Lampoldshausen, March 2000

Future Dev. opments of Ariane 5



J. Ackermann
ESA HQ Paris

Directorate of Launchers

Ariane 5 Objectives



- Ariane 5 is today and for the mid-term future **the** European workhorse in space transportation.
- Ariane 5 shall remain tailored to the needs of the commercial customers and for scientific missions, therefore anticipation of the market trends is necessary.
- Ariane 5 shall rely on European know how and technologies to provide access to launch service to world wide customers.
- Ariane 5 shall remain commercially attractive, the marketing and operations being performed by Arianespace.

Ariane 5 Market

The GTO segment will remain the main market of AR5

- The GTO segment will remain the largest one (in turn-over) with an average of 30-35 S/C per year in 1997-2006 (60% of overall turn-over)
- Special GTO launch procedures will appear (GTO+, super-GTO) which require multiple ignition and performance increase
- The average S/C mass will continue to increase
- S/C plat-forms up to 5.5 t are now in project

TELECOM (GTO)

- Few missions (0.5 per year)
- Mass will decrease after SPOT, Hélios and Envisat
- Governmental missions

Earth Observation (SSO)

TELECOM (LEO&MEO)

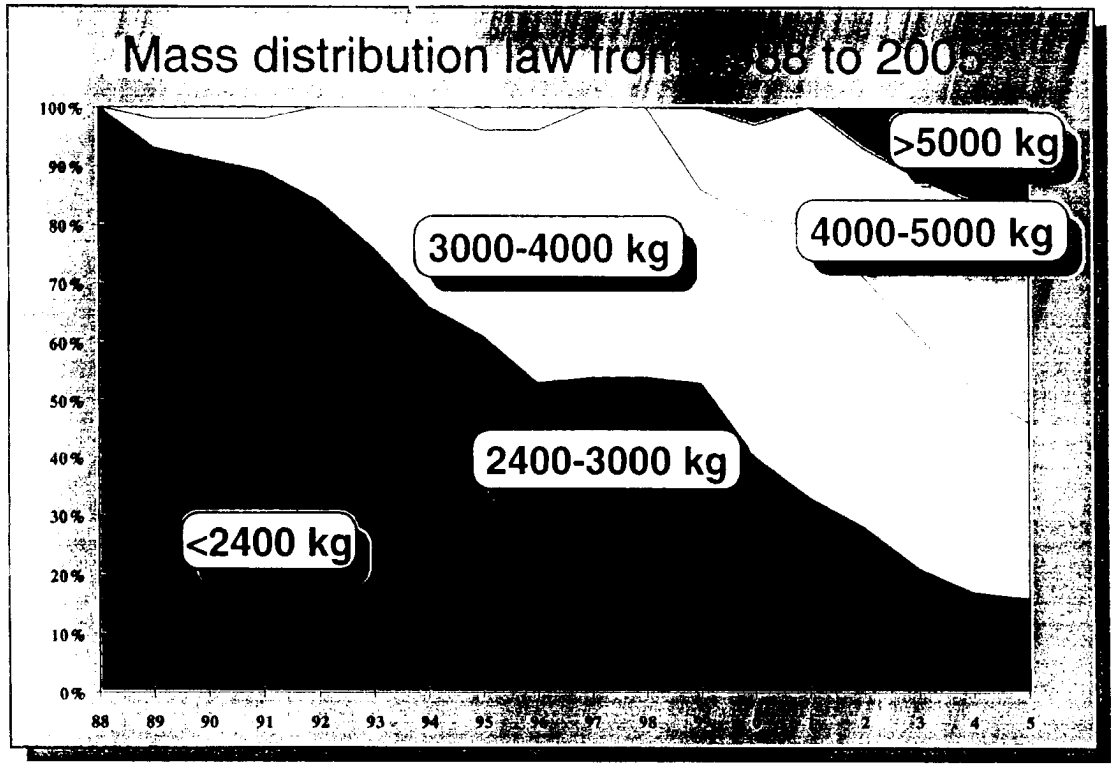
- The constellation segment will be the upcoming segment
- Mass and altitude will increase as more on-board service (data or image transmissions...) number increase

Science (Various)

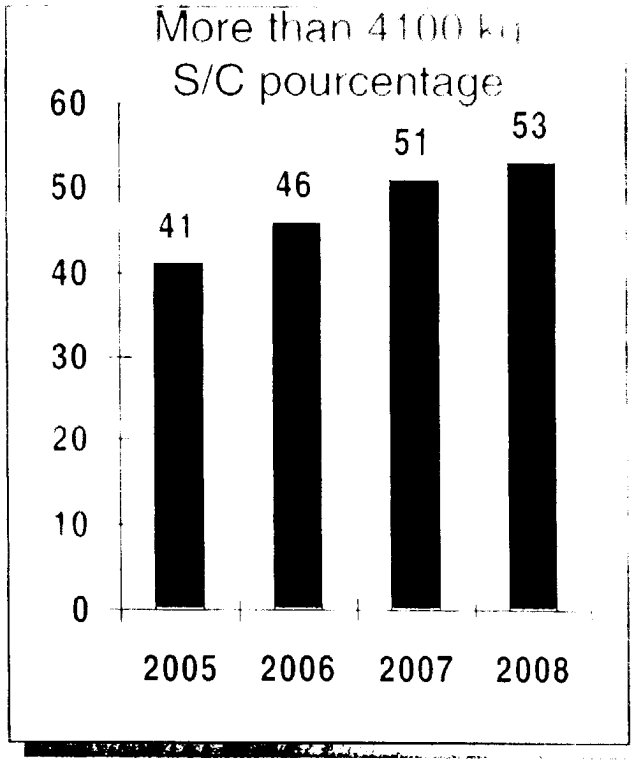
- The Science segment will remain constant low

esa

GTO S/C Mass will continue to increase

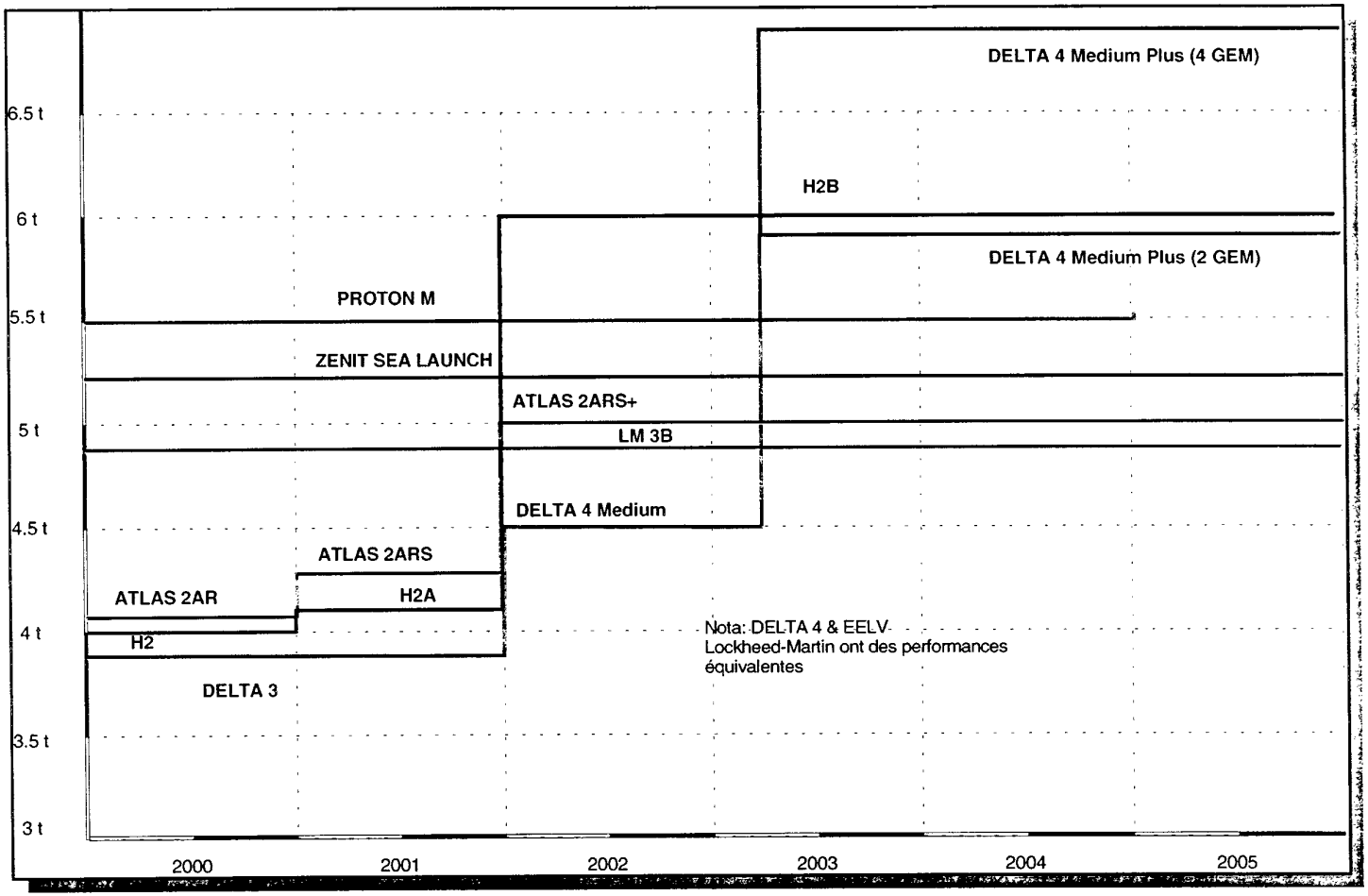


Source: Arianespace



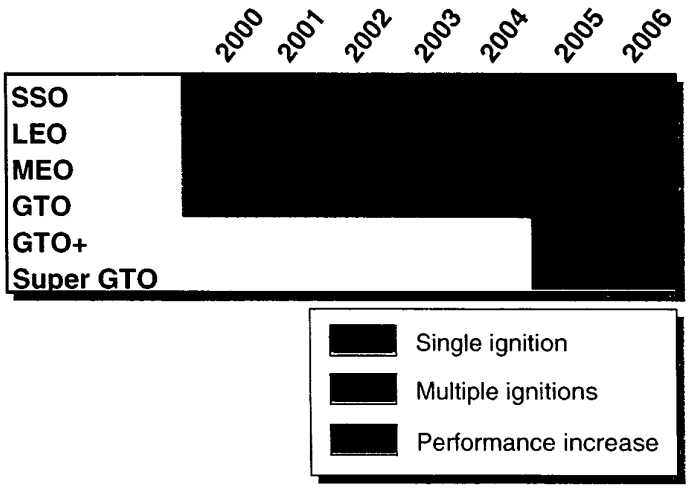
Source: COMSTAC "1997 Update of Commercial Spacecraft Mission Model" 14/05/97

AR5 competitors in the 5 - 6 t GTO range



esa

Multiple ignition capability and performance increase are distinct before 2005



- Multiple ignitons for less energetic missions (LEO, MEO, scientific) needed as soon as 2001
- Multiple ignitions for most energetic missions (GTO+, GEO) needed in 2005 as well as performance increase

Market Evolutions Summary

The main Ariane 5 commercial market is getting more demanding:

- GEO missions capability means now: GTO, super GTO and GTO+ injections
- MEO and LEO mission for constellations.

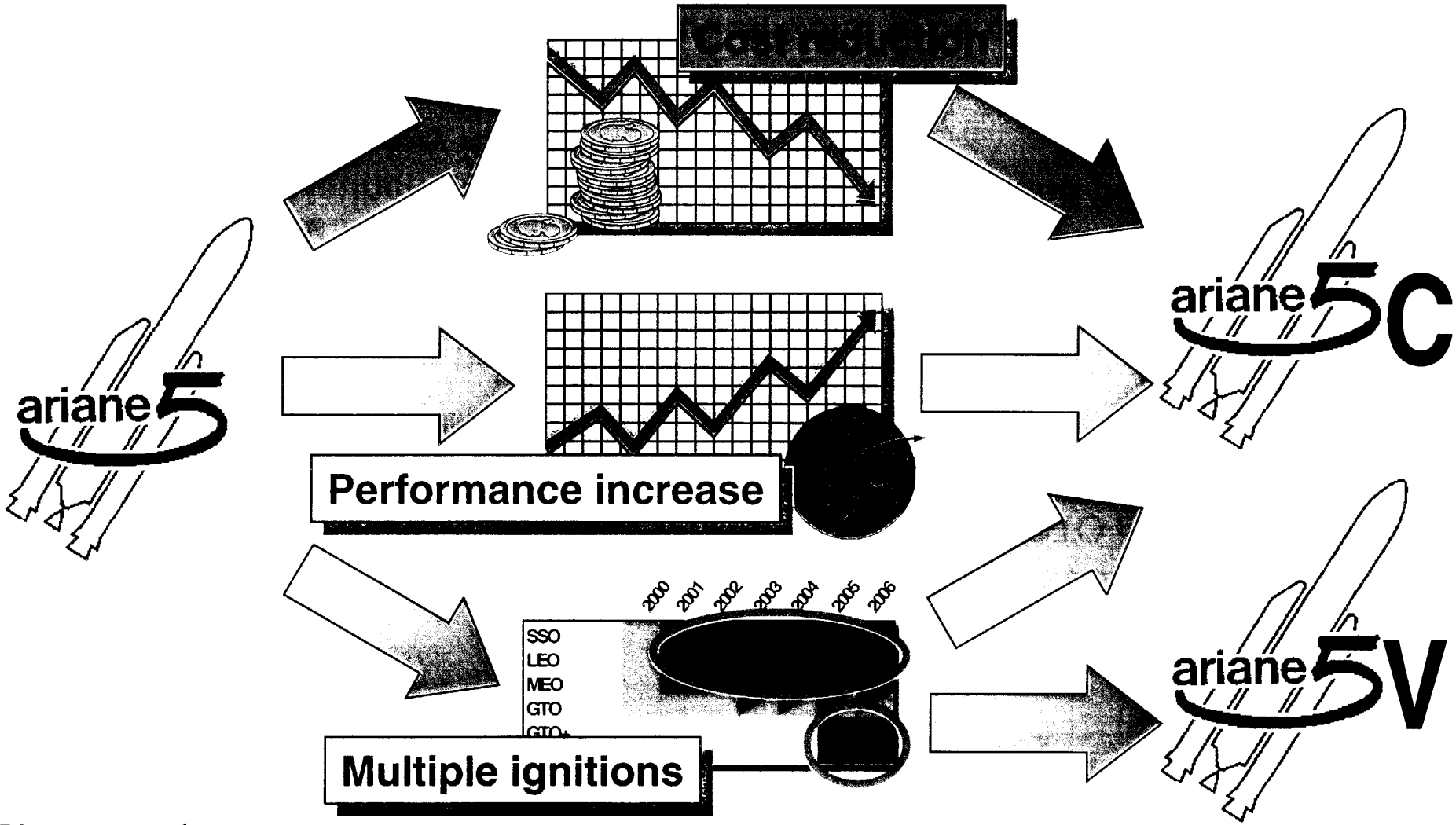
> A higher mission flexibility must be the answer to fulfil customer needs.

> Increasing competition on launcher side leads to decreasing specific launch prices, therefore cost reduction and performance increase are key issues.

> Ariane 5 core performance is tailored to a double launch capability for GEO missions, mass evolution trend to be covered

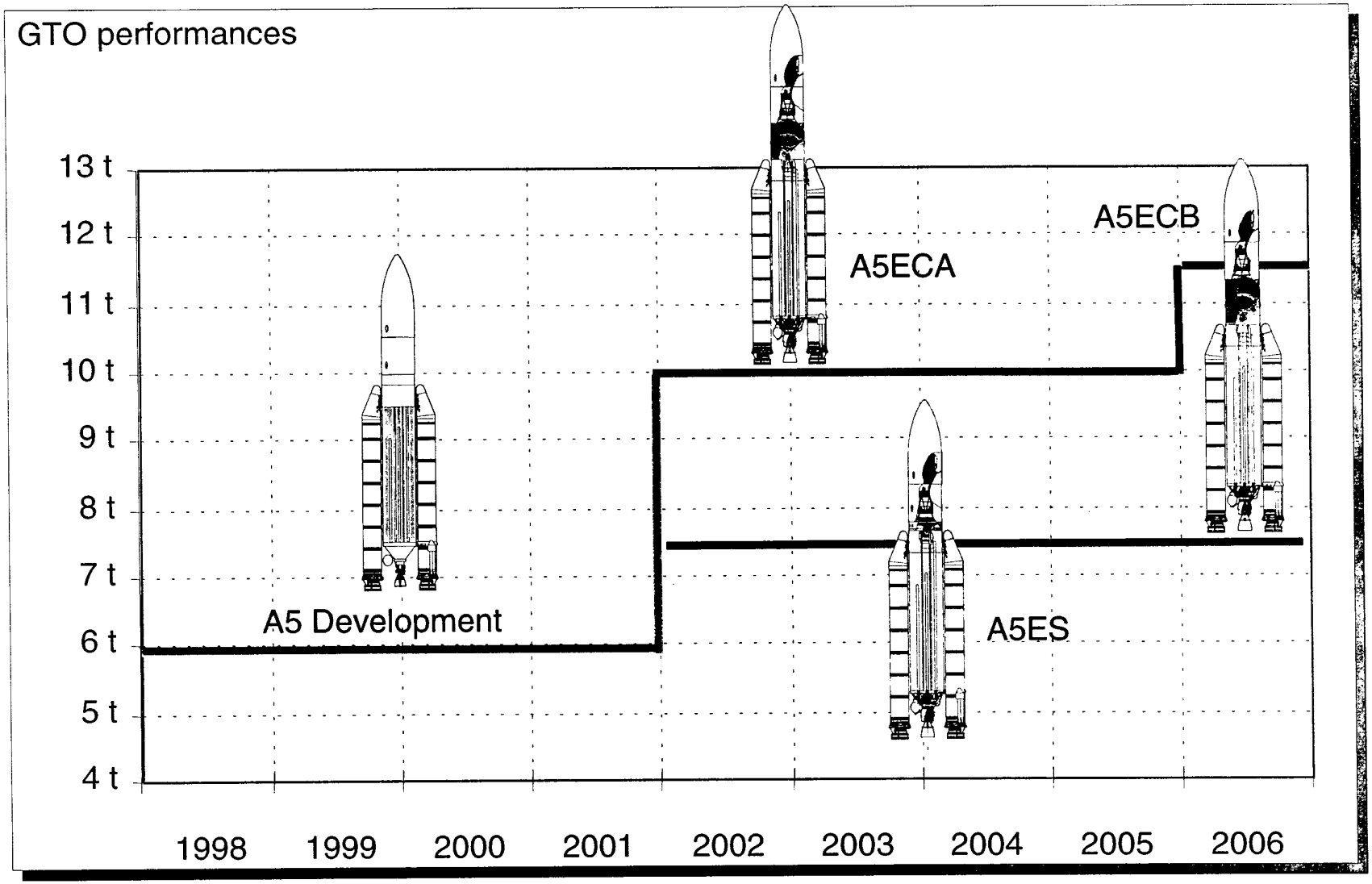
esa

ARIANE 5 EVOLUTION AXIS



Ariane 5 and its evolutions until 2005

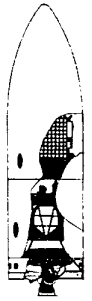
Ariane 5 Performance in GTO



19/01/00

After 2002, both ESC and EPS will be used

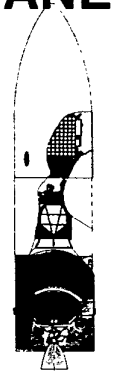
ARIANE 5V



Etage à Propergols Stockables

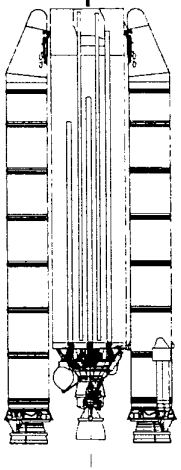
EPSV will be used for LEO, MEO and low performance GTO missions

ARIANE 5C



Etage Supérieur Cryotechnique

ESC will be used for high performance GTO, GTO+ and super GTO missions



Ariane 5 Evolution plus Perfo 2000 lower composite

esa

Perfo 2000 abstract

Foreseen in year 2000

CASE

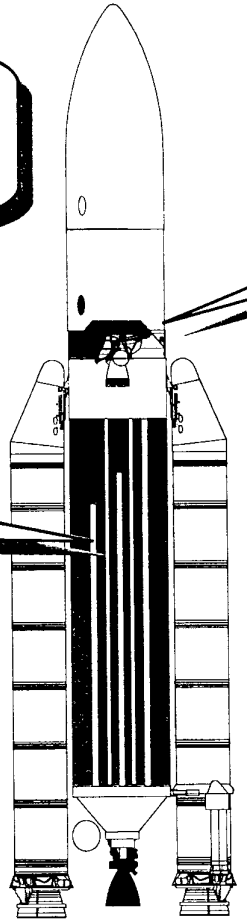
- composite structure
- pyro-cutting system

EPS

- RM: 2,05 -> 1,9
- MMH tank volume increase
- nozzle length increase (10 cm)

EPC

- switch VGC
- RIE common bulkhead lowering (17 cm)



- Perfo 2000
- ARIANE 5 EVOLUTION
- ARIANE 5V
- ARIANE 5C/ESC-A
- ARIANE 5C/ESC-B

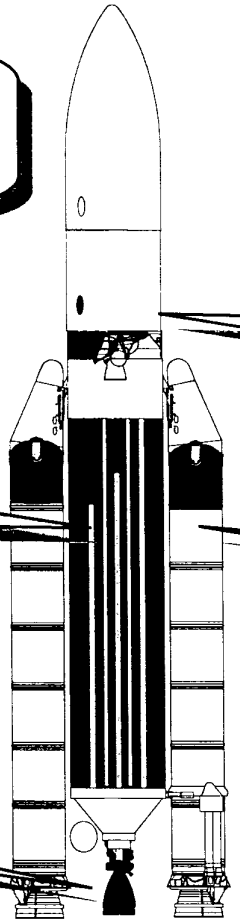
esa

ARIANE 5 EVOLUTION
abstract

Foreseen in year 2002

CASE
- composite structure
- pyro-cutting system

EPS
- RM: 2,05 -> 1,9
- MMH tank volume increase
- nozzle length increase (10 cm)



EPC
- RIE common bulkhead lowering (60 cm)

MPS
- welded joints in plant

Vulcain
- MK2 with 1350 kN thrust

- Perfo 2000
- ARIANE 5 EVOLUTION
- ARIANE 5V
- ARIANE 5C/ESC-A
- ARIANE 5C/ESC-B

esa

ARIANE 5V abstract

Foreseen in year 2002

CASE

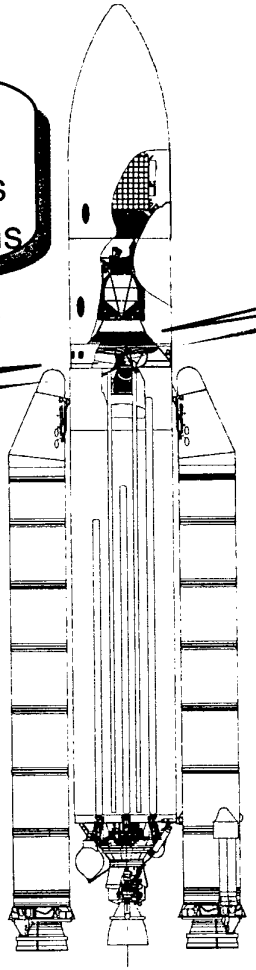
- SCA adaptations
- Electric system adaptations
- Thermal system adaptations

System

- flight program modifications

EPS

- tank pressure new algorithm



- Perfo 2000
- ARIANE 5 EVOLUTION
- ARIANE 5V
- ARIANE 5C/ESC-A
- ARIANE 5C/ESC-B

esa

ARIANE 5C/ESC-A abstract

Foreseen in year 2002

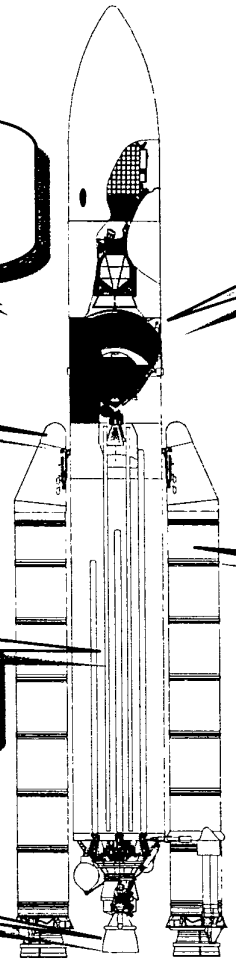
CASE
- composite structure

ESC-A
- AR4 LOX tank
- LOX+ LH2: 14 tons
- HM7B propulsion bay

EPC
- Reinforced JAVE (TBC)

MPS
- welded joints in plant

EPC
- RIE common bulkhead lowering (60 cm)



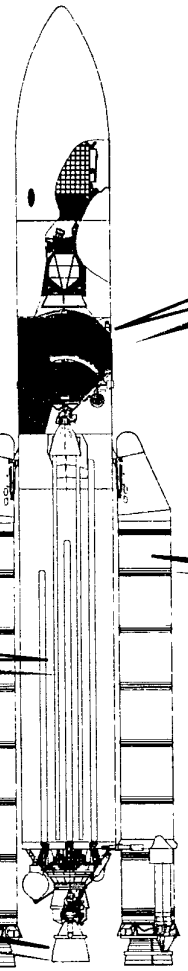
Vulcain
- MK2 with 1350 kN thrust

- Perfo 2000
- ARIANE 5 EVOLUTION
- ARIANE 5V
- ARIANE 5C/ESC-A
- ARIANE 5C/ESC-B

esa

ARIANE 5C/ESC-B abstract

Foreseen in year 2006



CASE

- composite structure

ESC-B

- LOX+ LH2: 25 tons
- Vinci engine

EPC

- Reinforced JAVE (TBC)

MPS

- welded joints in plant

EPC

- RIE common bulkhead lowering (60 cm)

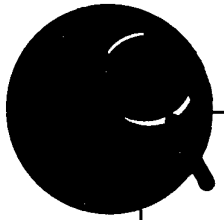
Vulcain

- MK2 with 1350 kN thrust

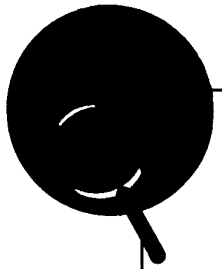
Perfo 2000
ARIANE 5 EVOLUTION
ARIANE 5V
ARIANE 5C/ESC-A
ARIANE 5C/ESC-B

esa

Ground installations must be adapted to Ariane 5 cryogenic upper stage



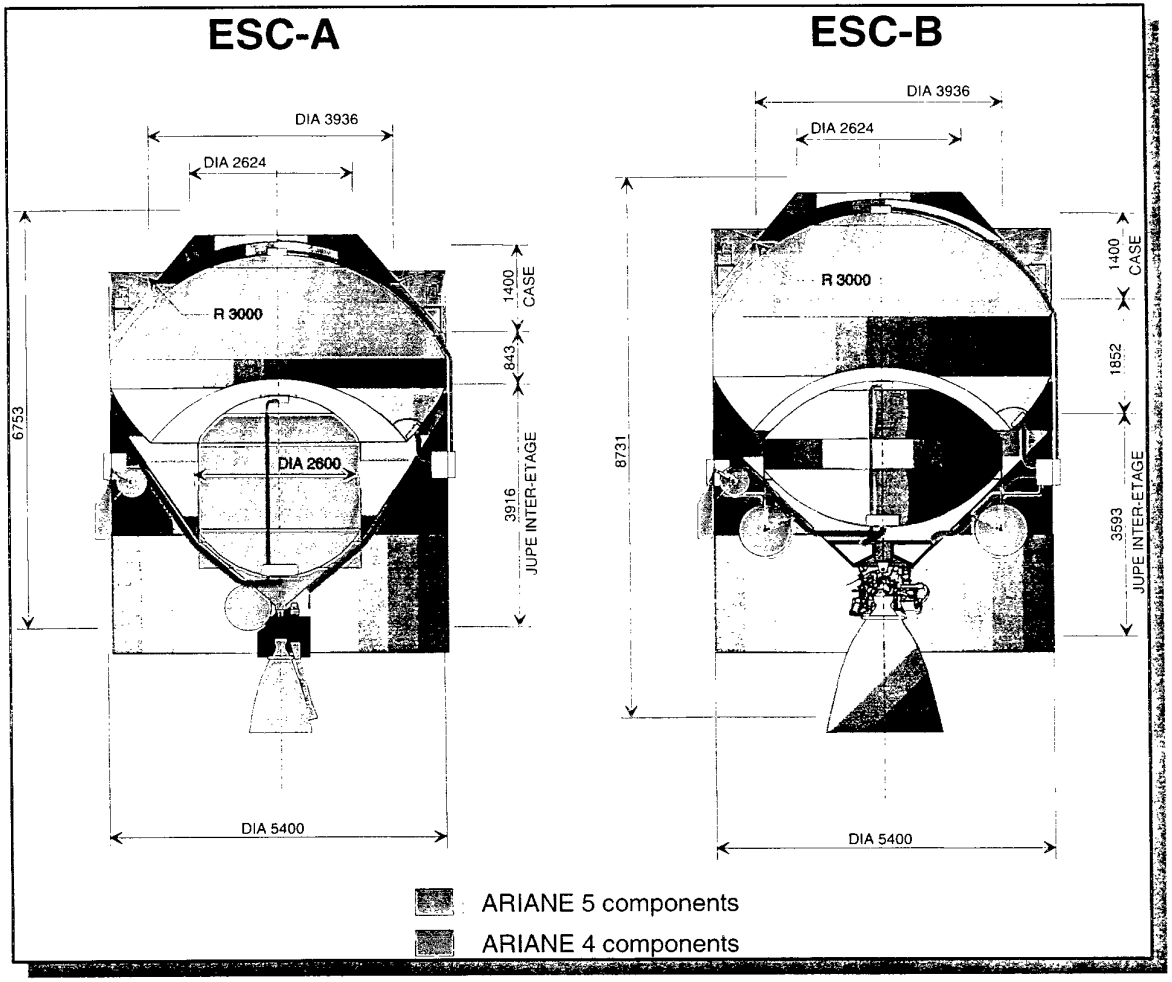
- Engine tests on existing benches
- Engine sub-assembly tests on existing benches



- Upper stage cryogenic propellant feeding located in altitude: interfaces with launch pad
- Ground/board disconnection in positive time (after lift off)
- BIL door height increase to allow launcher transfer up to the BAF

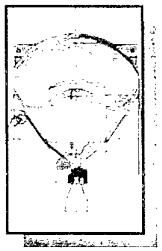
Ariane 5 new upper stages

AR4 and AR5 component re-use leads to lower costs



esa

ESC-A Architecture/ Characteristics



- LOX tank taken from Ariane 4 H10
- Engine bay taken from A4 H10
- LH2 tank design driven by length limitation
  - Upper dome is used from EPC
  - Tank cylinder considered made from flat sheet
  - Lower bulkhead is a isogrid with a height of about 25 mm
  - Lower bulkhead is a section of EPC dome

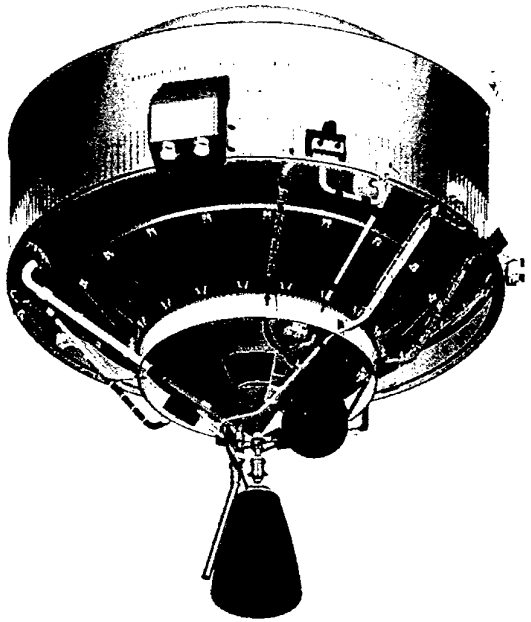
LOX tank Propellant loading capacity	14000 kg
Stage dry mass	4500 kg
Engine thrust	64 kN
Specific impulse	~ 446 s
Number of Ignitions	1

ESC- A development constraints

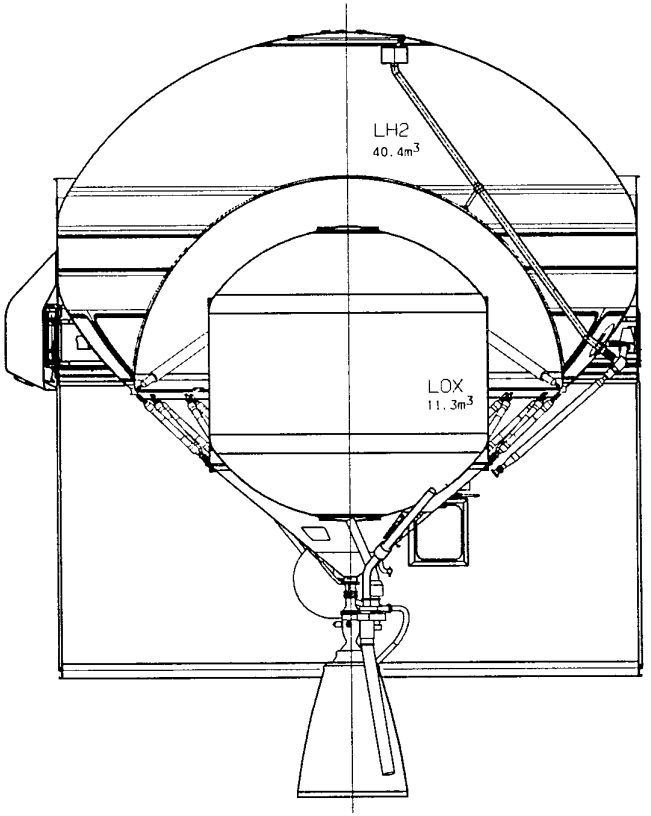
- Limited cost and short time development needs adapted methods, concerning the reviews and decision points.
- System loops for general specification establishment and stage design run in parallel. Refinement limited.
- Maximum re-use of existing hardware, mainly the propulsion system including the engine.
- Parallel development of major subsystems, development phases overlap.
- Two full scale models for the stage and system qualification including dynamic, vibration, acoustic, electric and fuelling/ground operations tests.
- No stage hot firing test, no qualification flight.

Ariane 5 ESC-A





ESC-A Stage Architecture



Main Characteristics

-Stage height H = 4750,7 ± 63mmNew
(between EPC/VEP I/F)

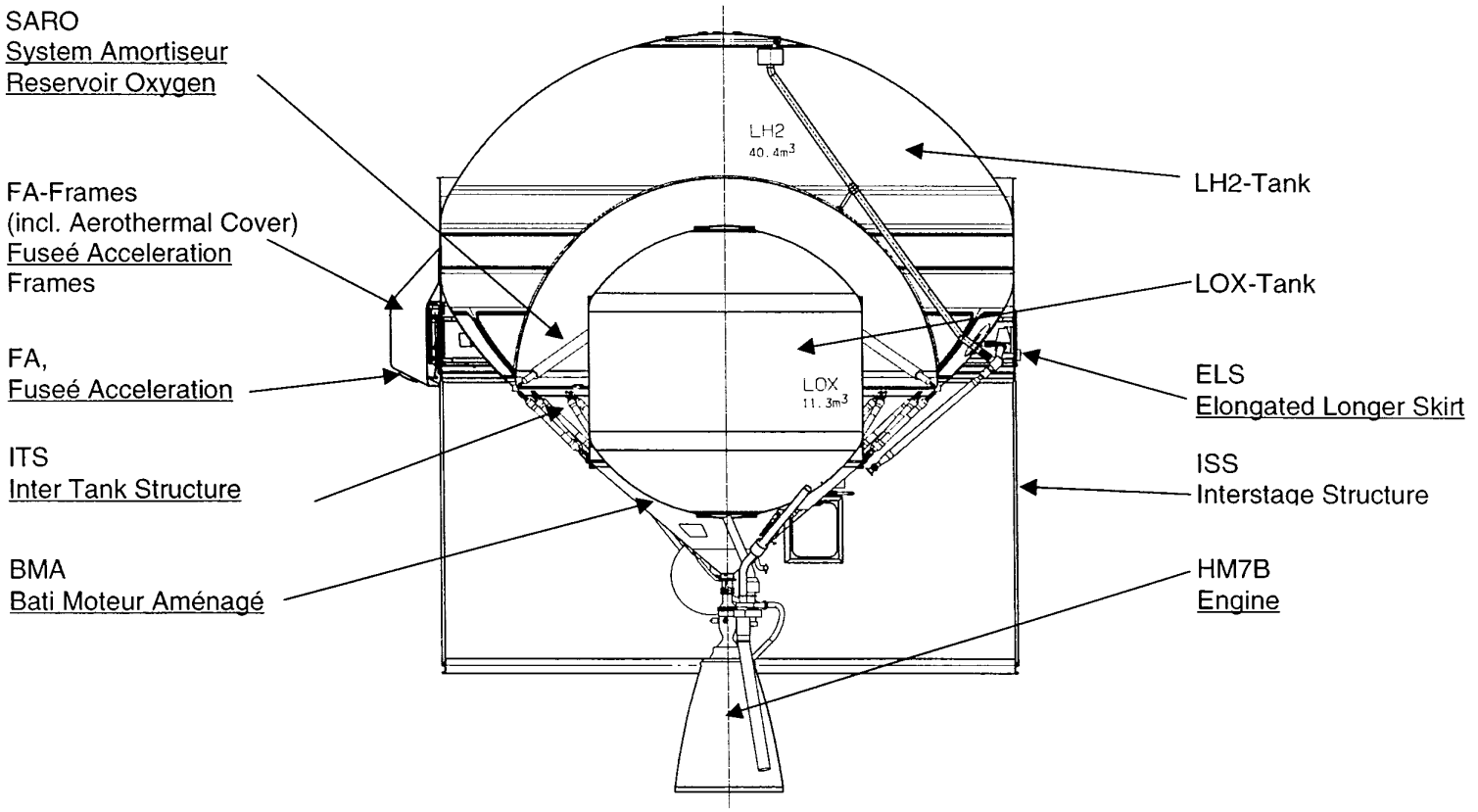
-Stage Separation System in ISS

-Propellant Tank Volume
V_{LH2} = 40,4m^3 V_{LOX} = 11,3m^3

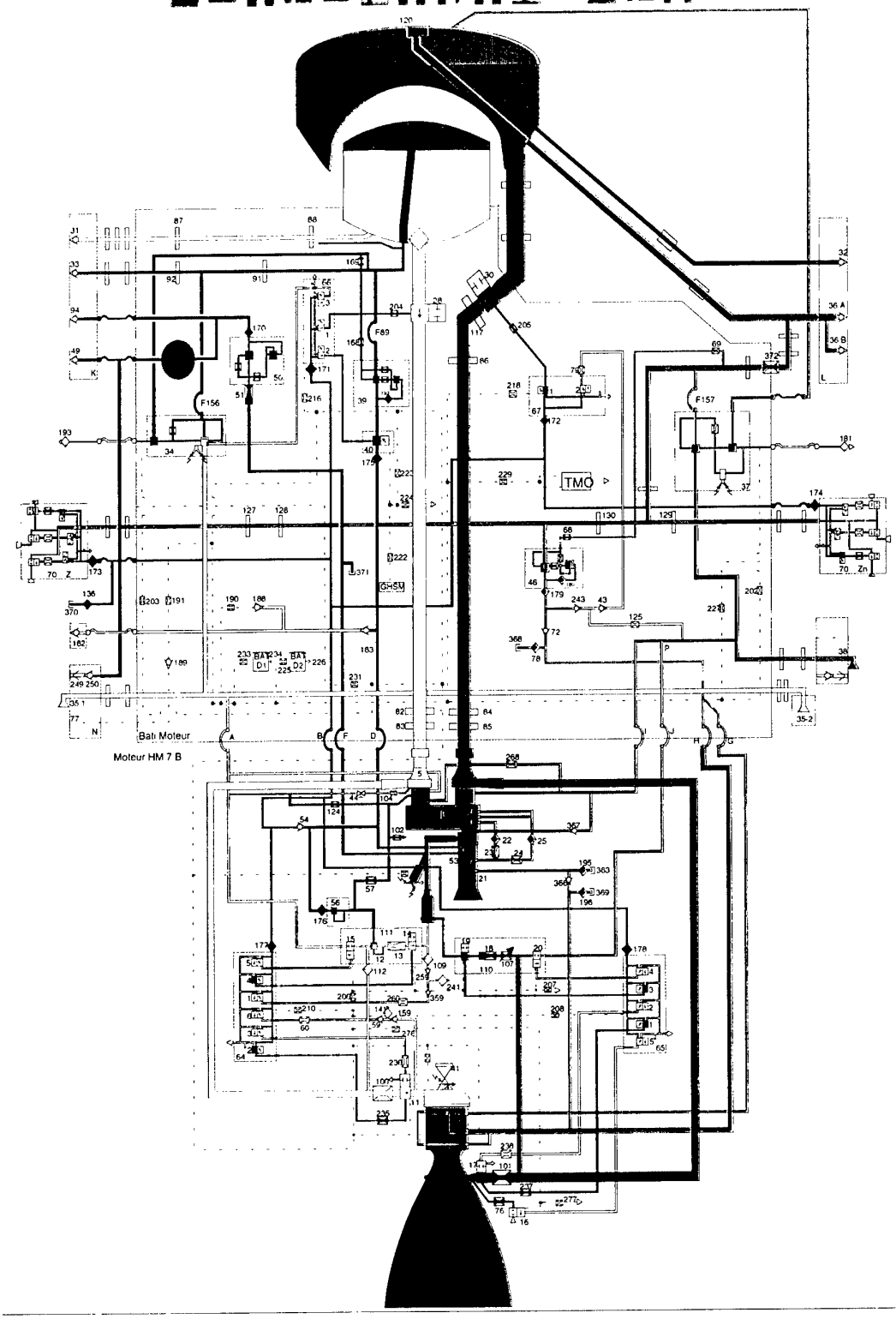
-ITS Ring Fixation at 45° to LH2-Tank

-Damping System: SARO

ESC-A Stage Nomenclature



ESC-A Propulsion System



Any modification on this synopic has to be done by means of a new edition of the A5-NT-130 0000-A-0012-SEPV

Oxygène
Hydrogène Liquide
Hydrogène gazeux
Gaz chauds
Hélium de commande
Hélium
Hélium + oxygène gazeux

Etage Supérieur Cryotechnique ESC A

DaimlerChrysler Aerospace snecma

A5E-NT-130-0000-A-0012(4)-SEPV

REPRESENTATION PHASE PROPULSEE

Edition : 8 septembre 19

HM 7B engine major characteristics

- LOX - LH2 turbo-pump gas generator engine
- Thrust 64.8 kN
- Isp: 445 s
- Chamber pressure 36 bar
- Total mass flow 14.4 kg/s
- Mixture ratio 5.6
- Regenerative cooled nozzle
- ESC-A application: 170s increased burn duration, new dynamic environment, new inter stage environment, higher Helium temperature required.

esa

ESC-B Architecture / Characteristics



- **New re- ignitable high performance cryogenic engine called Vinci to be developed**
- LH2 tank as used for ESC-A version but the cylinder of the tank is elongated to obtain a higher volume
  LOX tank is different from ESC-A LOX tank will be supported on the engine thrust frame

Propellant loading capacity	25000 kg
Final dry mass	5900 kg
Engine thrust	150 - 200 kN
Specific impulse	~ 460 s
Maximum ignition number	5
Maximum ballistic phase duration	6 h
Minimum ballistic phase duration	180 s

Vinci major Requirements

- Upper stage cryogenic engine with high specific impulse
- Thrust level: 150kN with growth potential
- Burn duration <= 770s
- Limited length in stowed condition (below 2.3m)
- Re- ignitable (5 ignitions in total)
- Able of long ballistic flight phases (up to 6h)
- Mass below 480 kg

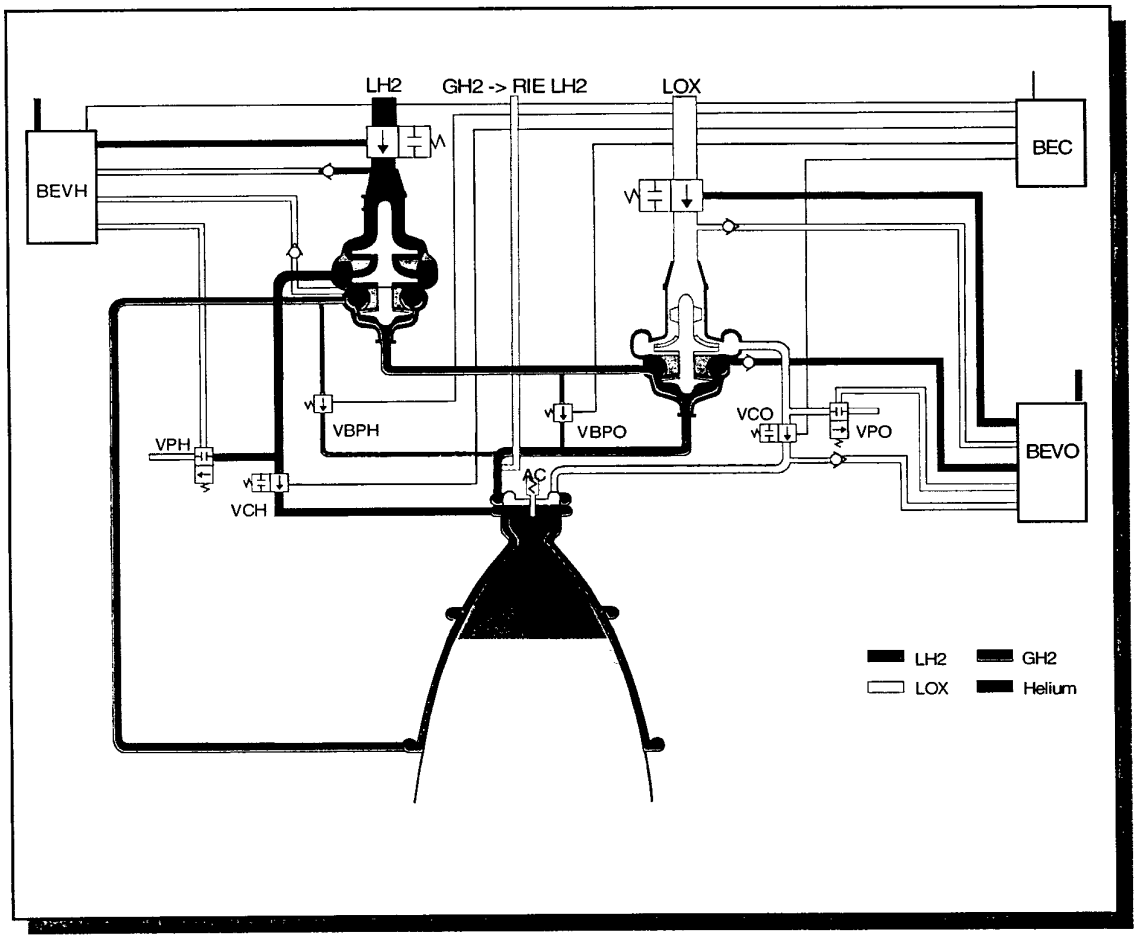
Vinci development constraints

- Development in less than 5 years with a limited budget, so specific subsystem tests limited to the necessary minimum.
- Lowest recurrent cost is major design driver.
- All critical technologies to be mastered by European Industry
- High reliability of final product
- No dedicated qualification flight

Vinci engine main characteristics

- Expander cycle LOX - LH2 engine (no gas generator)
- Low temperature highly efficient separated turbopumps sequentially fed by reheated gaseous hydrogen.
- Two stage LH2 pump and single stage LOX pump
- By pass valves on both turbines.
- Nozzle with regenerative and radiative cooled part
- Electrical system for re-ignition capability
- Isp: 465 s
- Chamber pressure 60bar
- Thrust 155 kN to 200kN

Vinci Expander cycle and preliminary design





Conclusion

- Mission flexibility, cost and time to market are actually the driving parameters for commercial launcher evolutions.
- Ariane 5 follows a sound roadmap of major developments to stay in very good competitive position
- Parallel to the big steps a continuos improvement process is running adding also small (cost and perfo) benefits.
- Ariane 5 is a young and living product with still great evolution potential ahead.
- Time to market is a key factor concerning future evolutions of the propulsion system.

RELIABILITY OVERVIEW OF FIRST-&-SECOND-STAGE ENGINES OF CHINA LONG MARCH LAUNCH VEHICLE

Jinrong Zhang

The 11th Research Institute of China Aerospace Science & Technology Corporation
Xi'an, China, 710100

Abstract

Based on a general analysis of the reliability of rocket engines, the paper mainly overview the reliability of the first-&-second-stage liquid rocket propellant engines of China Long March launch vehicle (Here after called "LMRE"). It displays the features of the LMRE and further illustrates the keys to the breakthrough of utilizing reliability technology, and contents concerning reliability assurance, reliability test and reliability evaluation. The paper aims to show the inevitability of 100% success ratio.

1. Introduction

With the continuous development of aerospace technology, in all countries in the world, design capacity and production quality of launch vehicle makes unceasing progress, and its reliability has greatly raised. From the fifties of the 20th century up to now, aerospace cause in the world makes brilliant achievements, but various failure and accident is often seen. For aerospace technology, reliability is still a question not to be ignored. Liquid propellant rocket engine is the chief dynamical device of launch vehicle. The reliability of engines plays a keyrole in the flight of launch vehicle, especially for the manned space flight. All the countries in the world, laying emphasis on it, have defined reliability target as the major technology target and quantified it. Thus, improving the reliability of launch vehicle has always been the goal for the space research in all countries. The LMRE carried out all 60 flights of the Long March launch vehicle with excellent performance and 100% success ratio. To ensure its high reliability, we employed all reliability design technology, such as redundancy design, fault-tolerant design, fault mode and effect analysis (FMEA), fault tree analysis (FTA), and solved the problems like: high-frequency combustion instability of combustion chamber, low-frequency combustion instability of gas generator, intermediate-frequency flow-rate-model vibration, environment protection and others. Through breaking many technological problems, we ensured the quality of the LMRE.

2. A Summary to the Reliability of Rocket Engines

The reliability of rocket engines means the ability of engines to fulfill required function under required conditions and within required time limits. It involves structure reliability and performance reliability. In order to reach the reliability target, a full consideration must be given to the reliability of the whole process, from engine design, manufacture, test, storage and transportation to maintenance.

A high reliability of engines suggests low ineffective rate and fewer faults, whereas a low reliability indicates high ineffective rate and more faults, which may lead to the delay of scheduled task and failure in vehicle launching, and a tremendous loss. Therefore, no country can be exempted from the task of improving the reliability of engines.

The reliability of engines can be described with the help of inherent reliability and service reliability. Inherent reliability is determined by design and manufacture; service reliability refers to practical use, which is different from inherent reliability, and is related to the conditions of storage and transportation and maintenance, which applies to the formula (1):

$$R_u = k \cdot R_I \quad \text{.....} \square 1 \square$$

Where

Ru — the service reliability of engines;

R_I — the inherent reliability of engines;

k — coefficient.

Once the engine is designed and manufactured, its inherent reliability is fixed, and its operation and maintenance are to keep its inherent reliability; since coefficient is determined by operational conditions and maintenance level,

what really matters is still engine's inherent reliability. Therefore, the key to the reliability engineering should be its design.

According to incomplete statistics on failures of launch vehicles, most failures happened in propulsion system. Such as, the second-stage-engine of Proton-K vehicle took place 2 times failure in 4 flights only in 1999, because there were swarf and ore particle in the engine. SL-16 vehicle exploded because there were foreign bodies in fuel pipe of РД-120 engine in August, 30, 1991. The VikingD engine appeared unstable combustion in L02 flight of Ariane1 in May, 23,1980 and led launch failure. Because a cloth stopped pipeline for cooling, the water valve of viking4 engine was stopped, led thrust not enough and launch failure of Ariane4 in February, 22,1990. Because of failure of HM-7 engine, it led L5 flight of Ariane1 failed in September, 10,1982, and led V15 flight of Ariane3 and V18 flight of Ariane3 failed in May, 30,1986, and in September, 13,1985. Because of failure of the MN-3 engine, it led the H-1 vehicle failed in March, 12,1986. But F-1 engine kept 100% success ratio in all 13 flights of SaturnV launch vehicle, and the LMRE keeps 100% success record in all 60 flights of Long March launch vehicle.

To ensure a high inherent reliability, every country has done a lot, especially valued the choice of design project and the reliability verification.

The design of F-1 engine solves the problem of combustion instability in engines with great thrust. The first F-1 engine design program involved 44 tests, 20 of which appeared the phenomenon of combustion instability, peak equaling to or exceeding average pressure. These vibrations caused severe erosion and ablation of injector, indicating a radial and tangential pressure fluctuation. To overcome the combustion instability, design centered on improving injector and baffle, and the improved F-1 engine successfully went through a great deal of combustion instability rating test.

To ensure high reliability of the LMRE, the research from very beginning focuses on its reliability, It can be illustrated as following:

Inheritance[7]**:** The theory is applied to the whole procedure of the LMRE manufacture. We inherit successful experiences, and improve only the necessary; try our best to draw on the experience of established and advanced technology home & abroad. Only after we do strict test which involve vibration test and engine test for the integrity can we finally decide their design, insisting on the principle of advanced technology adapting to the reality level, which should be fully practical in production.

Research Based on the Theory of Reliability[7]**:** We stick to "quality first" and "reliability first". After summing up some common faults during hot-firing test, and during production, we carry out FMEA and make further improvements. Based on design-test-improving design-test again steps, we successfully guarantee that engine's reliability increased step and step up to the require value.

Hard and Strict Hot-firing Test[1]**:** Hot-firing test points at not only the reliability of the engine, but also its technique. The LMRE is tested with load, which involved enhancing thrust, increasing propellant mixture ratio, delaying test time, increasing pump inlet pressure and swinging, so as to expose its weak points thoroughly. Then improvement is carried out pointing to these weak points to ensure its reliability.

Stress on Reliability Evaluation[1]**:** The best way to check engine's reliability is to test, and evaluate according to test result. We use normal distribution (two-sided allowable limit) method to assess the performance reliability, and use Weibull method to assess the structure reliability.

3 A Brief Introduction to the LMRE

First-stage engine consists of four units, and second-stage engine involves main engine and vernier engine, which consists of four engine units.

3.1 Design Feature of the LMRE

3.1.1 Simply but Reliable System Plan[3]

Start and cutoff valve use electroexplosive actuated valve, which is simple in structure, and need no gas. This enables a take-off without gas and thus guarantees its high reliability.

Flow rate control elements utilize calibration orifice and cavitating venturi. There are all together 20 cavitating

venturi in first-&-second-stage engines, which requires fewer components than a regulator and has simple structure but high accuracy.

The engine uses solid start cartridge, which enables a quick and stationary start. The prevalve is placed in front of the pump, and other valves are always open, thus, at the time when propellant is injecting or stops injecting, the propellant cannot enter the systems of the engine, which prevents each assemblage from being soaked or corroded. When the engines starts, it can certainly work well, provided the prevalve is open as usual.

The engine uses two-stage cut-off. First, shuts off gas generator oxidizer feed line; then, shuts off two main lines. By this way there come less hydraulic pressure, Faster deceleration time, less cutoff impulse and easier separation.

As different systems, the second-stage main and vernier engine is designed individually. Though they share same group of prevalve, each uses its own main valve. Main engine and vernier engine can work together, or work individually, in particular, vernier engine utilizes turbopump-fed system, which is useful for long time gliding and meets the requirements of rocket attitude control.

The LMRE chooses simple design scheme, which well guarantees its high reliability.

3.1.2 Engine Swing

First-stage engine adopts the plan of swing in front of pump. Each engine swings in an angle of 10 degree along the tangential direction to provide the control moment for rocket flying. The advantages of such a plan lie in the following points: by combining the turbopump equipment with the thrust chamber, it fully uses the horizontal space of the rocket and reduces the length of the rocket; each engine is comparatively independent of the others, so it is convenient for developing, checking, and accepting individually; swing and thrust transmission are achieved by installing a gimbal mount assembly with dry-film lubricant in the front of the thrust chamber, such installation is simple in structure and reliable in working; the fixing of a inner casing flexible hose assembly in front of the pump avoid the problems in developing the high pressure hose assembly at the back of the pump.

Second-stage main engine doesn't swing but four units of vernier engine swing. In adopting such a plan of only swinging thrust chamber, which can be connected with the rocker frame assembly through bearing and sleeves and make up a swing engine unit. This engine unit can swing in an angle of 60 degree along the tangential direction of rocket. The dynamic sealing device between the swing axle and sleeve is make by rubber sealing washer and F4 anti-extrusion circle. Such a swing pattern has a small moment of inertia and is suitable for multi-chamber rocket engine.

3.1.3 Thrust Chamber Plan

Horizontal orifice injector is adopted in the thrust chamber, which body uses the small contract ratio corrugated plate with regenerative cooling baffle device.

3.1.4 Turbopump Plan

First-stage and second-stage main engine use co-axial vertical turbopump. Oxidant pump is in the upper place, fuel pump in the middle, and turbine in the lower place. Such an arrangement saves much space in horizontal direction and leaves much space for engine's swing. Because of high oxidant saturation vapor pressure, oxidant pump is placed on the top so that it can reduce the loss of the inlet pressure.

Turbopump of the vernier engine adopts the plan that turbine is among and double face-riding seal.

3.1.5 Valve

Electroexplosive actuated valves and check valves are used here. They are simple in structure and need no gas source. Without carrying any gas, they are reliable in working.

3.1.6 Self-Pressurize System

Evaporator and cooler self-pressurize system are installed in order to maintain a normal working of the propellant feed system, to keep the inlet pressure of the pump, to avoid cavitation in pump. N_2O_4 evaporator loads the oxidant tank's pressure through some N_2O_4, which heated by turbine waste gas. Through cooling the some turbine gas by flow rate to the baffle. Gas cooler loads pressure for the fuel tank. Self pressurize system is carefully designed and tends to be more reasonable both in the aspect of structure sharing with the other systems and in residual-heat utilization.

3.2 Major Parameters for the LMRE

The propellant is N_2O_4/UDMH, which transmitted by turbopump-fed system, gas generator cycle. The following are the major parameters.

Table1 Major Parameters for the LMRE

No.	Parameters	First-stage Engine	Second-stage Engine		Remarks
			Main Engine	Vernier Engine	
1	thrust(kN)	740.4×4	742.04	47.1	vacuum thrust in second stage
2	specific impulse(m/s)	2550	2922.4	2834	vacuum specific impulse in second stage
3	mixture ratio	2.12	2.181	1.57	
4	total flow rate(kg/s)	290.4×4	254.95	16.69	
5	combustion chamber pressure(MPa)	7.70	6.74	3.29	

4. Reliability Design

4.1 Reliability Design Principles[2]

a. After satisfying the design requirement, performance reliability should be subordinated to structure reliability. Meanwhile the more simple the design is, the better.

b. Reliability block diagram and mathematical model should be adapted to reliability distribution and prediction.

c. Fault mode, effect and casualty analysis should be made in the development of each period in order to find out the weak points and take necessary measures to improve them. On the basis of the analysis key projects should be determined.

d. Redundancy technique should be adopted in designing key component. Fault-tolerant plan should also be adopted in designing for the convenient of manufacturing and installing.

e. Under the condition of satisfying the requirements, design should be simplified. Good experiences in previous design should be carried on in the improvement of rocket engine's design. Re-designed components should adopt the successful technique.

f. New technique and material should be fully proved and tested before designing. Plan demonstration, design, and test of the re-designed components should be strictly controlled in order to succeed once.

g. Enough design allowance should be given.

4.2 Reliability Block Diagram

Because each components of the engine has its own function and structure. And the reliability of the rocket engine is the product of the reliability of each component. Failure of each one will result in the failure of the rocket engine. The following block diagram is the series system of each component.

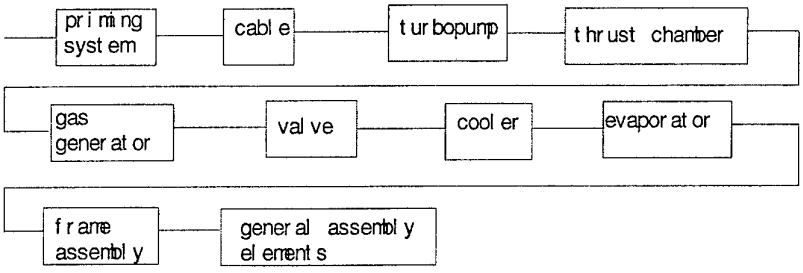


Fig.1. Reliability block diagram of the LMRE

Reliability of the rocket engine can be indicated in the following formula:

$$R_e = \prod_{i=1}^{n} R_i \quad \text{.....} \square 2 \square$$

Where

Re — engine's reliability;

Ri — the reliability of component i;

n — the number of components.

Figure 1 and formula 2 indicate that component reliability is the basis of the whole engine's reliability. In the early period of engine's development, each component must have its own share of reliability according to the requirement of the engine's reliability. Each component must have an acceptable designing plan and be fully tested before engine test for the integrity, in order to meet the reliability requirement.

4.3 Application of the Reliability Design Engineering

Reliability design is a design means to meet the proposed requirement of the reliability. It consists of reliability design analysis and reliability engineering design[5].

Reliability design analysis mainly refers to reliability probability analysis. It includes reliability prediction and distribution. Its emphasis lies in the three-F analysis. Reliability engineering design is a practical design plan and technical measures to guarantee a high reliability for the product. In designing the product reliability must be fully considered.

4.3.1 Reliability Design Analysis

1) Fault Mode, Effect, and Casualty Analysis (FMECA)

FMECA is a lower-to-upper way to identify all the possible failure modes. In identifying single-point failure, it analyzes each effect of fault modes made to the working condition of the engine. All the fault modes are put in order according to their seriousness and probability of occurrence to find out the weak points in design. Preventing and improving measures are taken to eliminate or reduce the possibility of failure occurrence so as to guarantee the reliability of each product. The following listed key items are the results of the FMECA.

After analysis and break through in hot-firing test, the LMRE have the following major failure models: turbopump failure, propellant feed line failure, valve failure, thrust chamber structural damage, jointing loosing, etc. Among them, turbopump failure is the most disastrous one. It has the following failure forms: turbine explosion, face-riding seal of turbopump ineffective, turbine vane break, turbine shroud falling off, bearing damage, pump cavitating, pump inducer break, etc. Fire leaking, liquid leaking, foreign matter plugging, structural fatigue break, rotating parts seizing-up, ablative, component ineffectiveness, component parts misapplication, supporting parts loosing, turbine wheel crack, etc., all occurred in the LMRE former or later, no matter how serious the effect they have brought to the engine, each aroused engineers' great attention. Measures have been taken to improve it so as to eliminate the possibility of failure re-occurrence.

In viewing the occurrence of engine failure, it needs a certain period of time for the possible failure source to develop into an occurred failure. This period of time is called failure occurrence time. If failure occurrence time is less than 0.05s, it is called sudden failure, others are called gradual failure. Sudden failures are catastrophic failures because they occur very quickly and are hard to detect. So such failures must be eliminated. Gradual failures can be detected and controlled by measuring the pressure, rotating speed, and mechanical vibration.

According to the result of the FMECA, importance degree and features of a component determine the key items of the LMRE. These items are installation sealing structure, electroexplosive cartridge, and turbine wheel.

In manufacturing, testing, and accepting, these items must be controlled strictly.

2) Fault Tree Analysis (FTA)

FTA is a method by using square diagram to analyze the lower class failures. It uses logic order to locate the direct cause for the failure. It is a kind of upper-to-lower level analysis method. FTA in the LMRE aims at the failures related to safe. As for rocket engine, failures, which effect security of an engine, are mainly the following: engine explosion, performance parameter severely dropping, and no thrust. These failure modes are regarded as the top incident. The bottom incident can be found according to the failure occurrence mechanism. Then a fault tree of an engine is drawn.

According to this fault tree, qualitative and quantitative analysis for and engine's security can be made.

4.3.2 Reliability Engineering Design

4.3.2.1 Redundancy Design

Redundancy design is to achieve reliability by way of surplus resources, which is an important aspect in reliability design.

The key to the design is the selecting of redundant quantity. Reliability of parallel redundancy parts is:

$$R_n = 1 - \prod_{i=1}^{n}(1 - R_i) \quad \square 3 \square$$

where

Rn— the reliability of redundancy system;

R_i — the reliability parts i;

n — the number of parts.

Suppose reliability of each part is the same, with each to 0.8. When double redundancy (n=2) is used, reliability R2 should be 0.96. While R3 and R4 will field to 0.992 and 0.9984 respectively if three redundancies and four-redundancy are applied. And the reliability gain will appear respectively by:

R_2/R_1=120% R_3/R_2=103% R_4/R_3=100.6%

It is clear that the overall reliability increases as the redundancy quantity goes up, while the reliability gain decreases as the quantity becomes more.

Taking all these into consideration, we know that the quantity increase will cause complexity of the system and partly counteract the superiority of multi-redundancy. In overcoming this, the double redundancy will be used to increase the system's reliability.

By way of this design philosophy for higher reliability in key components and key parts of engines, parallel redundancy design is conducted. That is, double lock plan is used for the lock mechanism of prevalve, double face-riding seal are used in turbopump.

1) Double-lock Mechanism of Prevalve[11]

The prevalve is a constantly closed, butterfly-type electroexplosive valve. When directed order for starting, electroexplosive cartridge will explode to open the valve plate, and position-locking mechanism will lock diaphragm at the set position. In testing, failures occur position-locking mechanism to make valve plate deviate its set position, which increases pressure loss of valve and causes cavitating in pump and decrease engines performance. In improving the locking reliability, one more locking system is added to the former to form a new double-lock system, with each working independently. According to formula (3), if reliability R1 of single-lock is 0.9, the double-lock reliability R2 will be 0.99, thus greatly improving the reliability.

2) Double Face-riding Seal of Turbopump[8]

Oxidant and fuel pump of second-stage vernier engine is separately located in both sides of turbine. Turbine working fluid is fuel-rich gas. If oxidant leaks into the turbine, explosion will occur. At the earlier stage, face-riding seal of oxidant pump was completed by one line of spring. Failure in sealing occurred due to the components, assembling error and occasional cause. To ensure safety, sealing by spring-typed and bellows face-riding seals are conducted, with non-circulable Fluorenone filled between the two seals. The first sealing control oxidant and the second seals gas. According to formula (3), if reliability of each face-riding seal is 0.99, the reliability of double face-riding seal should yield to 0.9999, which improves much more than single seal.

4.3.2.2 Fault-tolerant Design

In assembling an engine, many components are needed in the connections. Measures have been taken in the design to improve assembling reliability — different sizes and types of connections for inlet and outlet to meet the flow-direction requirement which cavitating venturi, calibration orifice, check valve demand. Therefore an end is put to the wrong assembling.

4.3.2.3 Protection Design for Environment

In manufacturing, storing, transporting and operating, engines may encounter high or low temperatures and wet conditions, with temperature ranging from –40□ to +50□ and maximum relative humidity (RH) 98%. To ensure the engine to meet requirements in different conditions, measures have been taken in design to avoid decreases in reliability on account of adverse circumstances.

1) Protection Design for Low-temp

Design requirement for low-temp are put forward to all components and parts, which are considered low-temp performance when designed.

The low-temp circumstance may not be appropriate for powder in the solid start cartridge. Therefore, powder proportion must be selected suitable for low temperatures. Non-metal materials must undergo low-temp experiments for their properties.

2) Water & Moisture Proofing Design[12]

The engine cable is the key part in water & moisture proofing design. The cable is composed of master plug, wire beam and branch plug. The weak parts of water-resistant measure are: connection between master plug of engine cable and controlling cable of rocket; between wire beam and master plug; between wire beam and branch plug; between branch plug and electroexplosive cartridg. Different measures have been taken for different parts. Resin sealing washer is designed for cable master plug, with its tailor part filled with rubber. The root of branch plug is wrapped and covered with nitro-glue soluting. For the welding point of cable wire beam and branch plug, the point is designed inside tailor cover and filled with seal rubber. For the connection of branch plug and electroexplosive cartridge, seal spacer is applied to.

3) Vibration-Protecting Design[9]

It is important in design for the components and installing conduit to stand strong vibration of engines. Therefore one aspect is set stricter demand of vibration environment, another is demand all installing conduit avoiding main frequency of the engine. The following introduces vibration-resistance and vibration- attenuation designs for installing conduit.

The major measures taken for vibration-resistance of the installing conduit is to operate overall position welding of it. For the requirement of sealing and fatigue-resistance of high-temp (to 850□) gas conduit and normal-temp conduit, automatic impulse argon arch welding is applied to the installing conduit. Because of adding no filling, weld bead is smooth and there isn't lumped mass; because of heating discontinuously, grain crystal of weld bead are in small particles and there is no crystal-boundary corrosion, therefore performance of fatigue-resistance has been greatly improved. In selecting shapes of conduit, stationary requirement is demanded for decreasing rigidity to eliminate stress by being out of shape, while dynamic requirement is demanded its natural vibration frequency avoiding main frequency of the engine and not occurring harmonic oscillation.

4.4 Reliability Design Engineering for Problem-shooting

The LMRE have developed 3 series (LM-2, LM-3, and LM-4), 9 models in the past 30 years. It has good heritage and better improvement. New techniques have been applied to perfect the design and manufacturing, and to increase reliability of the engine. It is keynote to solve unstable combustion.

The combustion instability may be due to spraying, breaking of liquid-drop, fogging, turbulent mixture and other chemical reactions. There is high-frequency combustion instability like acoustic oscillation, coupled and low frequency combustion instability, among which high frequency combustion instability is the most destructive one.

It is clear to note combustion instability in the chamber pressure, with oscillation frequency ranging from below 100Hz to thousands, pressure oscillation ranging from 10% to 1000% of chamber steady-state pressure. And it is also apparent to see the change in mechanical vibration with high-energy order.

The unstable combustion can cause serious vibration, decrease the performance, creating uncontrollable impulse and even the destruction of thrust chamber and injector. Under any of the conditions, the engine will not work properly. The problem must be solved to ensure reliable work of the engine.

If damping progress is strong enough to cause to exhaust energy faster than is provided, the oscillation will fall weak. Therefore the adding of damping and decease the coupling with exciting force can prevent the unstable combustion.

4.4.1 To Solve Transverse High-frequency Combustion Instability[4]

One of the most important subjects in manufacturing liquid propellant rocket engines is to do away with high

frequency unstable combustion in the combustion chamber. It is most destructive and difficult to control.

Destroy modality of high-frequency unstable combustion is follow:

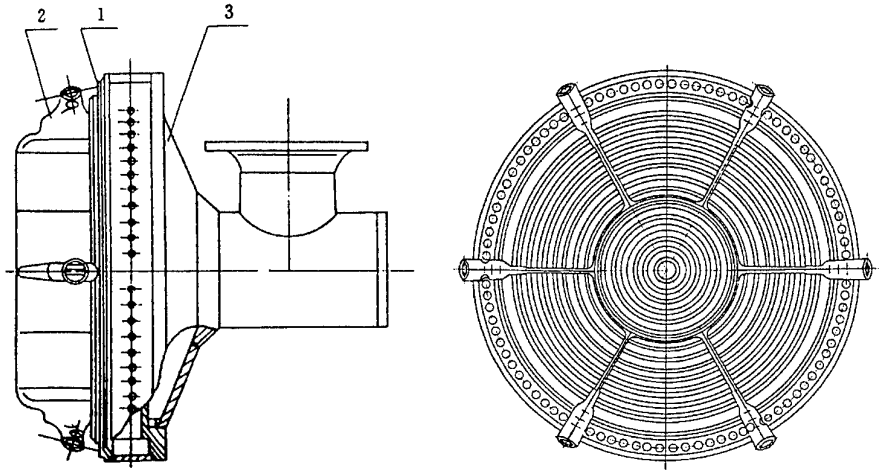
a. Burn-down around the injector and interior wall of chamber.

b. Destruction of engine components, including tear-away of weld bead, breakout of line and loosening of connections.

The combustion system affects stability with high frequency in two aspects. One is the magnitude of energy supporting oscillation under the given disturbance of pressure; the other is relationship between the time of energy supporting supply oscillation and the period of the disturbance.

Both aspects are associated with the design of injector and baffle. Therefore an excellent injector, a good baffle suitable to the injector type is of great importance. Great care has been taken to the LMRE in solving unstable combustion, taking the design of injector and hub-type baffle into great consideration.

The schematic diagram of the structure of the combustion chamber head is shown in fig.2.



1—injector 2—baffle 3—top cover assembly

Fig.2. Schematic Diagram of Structure of the Combustion Chamber Head

1) Design of Injector

The design quality and machining precision of an injector have a great influence on the stability, efficiency of combustion in the combustion chamber and the lifetime of the chamber. For this reason, particular regard is paid to design and production of an injector in the course of development of a combustion chamber. The discussion in this paper will center on its design.

A good injector shall meet the following requirements:

a . Comparatively good combustion stability.

b . Comparatively properties in combustion.

c . Good starting, cutoff and cooling properties.

d . Good technique.

Among these things, to ensure the combustion stability is one of the fundamental but most important requirements. To meet this, principles of designing injector of the LMRE are set as follows:

a . To Adopt an Adequate Radial Flow Rate Intensity Distribution

The distribution of flow rate intensity from an injector has a heavy effect on the transverse high-frequency stability. It is contrary to the distribution of pressure amplitude of possible high-frequency instability combustion mode, namely, the minimum flow rate intensity is distributed close to the antinode, whereas the maximum one near the wave node. In order to restrain the radial and tangential combustion instability, a rather fast-rise double-humped wave distribution of flow rate intensity in radial is adopted and a projecting flow rate intensity distribution in the central area and the middle of the fan section in the injector surface. The projecting flow rate intensity is 1.2 to 1.9 times the mean flow rate intensity.

b. To Adopt Liquid-phase Zoning

In order to improve combustion stability, such a particular nozzle as to divide the injector into some subzones is adopted in design of an injector. Adopting a particular nozzle, which differs from basic one aim to form non-uniformity of flow rate intensity, resulting out of accord of burning surfaces.

Based on these principles, the injector elements and their configuration, the distribution of flow rate intensity, the distribution of excess oxidizer coefficient α and the sizes of subzones of the head are all meticulously designed. The following is a brief description of the distribution of flow rate intensity in chamber of the LMRE:

The flow rate intensity is highest and the energy releasing is most concentrated at the radial position of a radius of 145.3mm in the fan section of the baffle, which is simply close to the pressure node.

The flow rate intensity is considerably high in the area around the center of the circumferential baffle. This area is just the pressure node, which conforms to the design principles.

There are small holes for cooling fuel in either the baffle or around the chamber wall, causing an area of low excess oxidizer coefficient. Such a design, on one hand, meets the requirement for cooling and, on the other hand, keeps the energy releasing rate under control at the position of pressure amplitude, meeting the requirement of combustion stability.

From eleven schemes is selected an optimum one for injector which is a layout in the form of two-direct orifice like-impinging element with concentric circles. Such a layout makes up a concentric circle flame surface, which brings a powerful restraint on the transverse pressure oscillation.

Hosts of hot-firing tests and flights prove that high-frequency combustion instability has never happened to any LMRE.

2) Setting Baffle

The baffle is a damping device, which is installed on the injector. It achieves the aim at restraint on the low-order transverse high frequency oscillation by varying the acoustic performance of the chamber, limiting the oscillatory Flow State and restraining the oscillation.

Much attention has been paid to the combustion instability even since the very beginning of development of the LMRE. In the original scheme was adopted a hub-type baffle which involves a circumferential baffle and six radial baffle with a height of 100mm, hence simply the name of 6×1-100 baffle, which is connected to an injector by welding. Introduction of the baffle has the process of atomization, mixing and initial burning of the propellant completed separately in a number of parts, thus changing the characteristics of the acoustic oscillation of the gas in the main combustion space of a combustion chamber and strengthening the damping effect on the acoustic oscillation. The baffle's functions are generalized as follows:

a. It can greatly raise the natural frequency of a combustion chamber, sharpen its ability against transverse combustion oscillation and reinforce its inherent stability.

b. It can obviously strengthen the dissipation function of the chamber. The change of its height and number directly affects the whole process of fragmentation, atomization, mixing and burning of propellant so that the pressure wave's dissipation at the density medium interfacing consequently changes. This effect is comprehensively expressed by a change in mean sound velocity of the gas, and in the end embodied by a change in oscillation frequency and amplitude.

The following is a brief analysis of how the baffle raises the oscillation frequency:

The acoustic oscillation modal frequency in a combustion chamber is:

$$f = \frac{c}{2}\sqrt{\left(\frac{\alpha_{m,n}}{r_c}\right)^2 + \left(\frac{q}{L_c}\right)^2} \quad \text{.....} \square 4 \square$$

Where

f — acoustic oscillation modal frequency in the chamber, Hz;

$L_c \square r_c$ — reduced length and radius of the chamber respectively, m;

c — sound velocity of the gas, m/s;

$\alpha_{m,n}$ — coefficient of tangential-radial combination mode of vibration;

q — order of longitudinal vibration mode.

a. Natural Oscillation Frequency in Combustion Chamber without the Baffle

Each order oscillation frequency in the chamber without a baffle is found in Table2 listed below in accordance with equation (4):

Table2 Each Order Oscillation Frequency(Hz) in Combustion Chamber without Baffle

Order number	Tangential	Radial	Longitudinal
1	1729	3598	1130
2	2868	6588	2260
3	3945	9553	3390
4	4993	12511	4520

b. Natural Oscillation Frequency in Combustion Chamber with the Baffle.

The mode of oscillation in the fan section of 6×1-100 baffle fitted onto the combustion chamber, corresponds theoretically to the mode of combination of third order tangential oscillation with fourth order radial oscillation in the chamber without baffle, and the natural oscillation frequency is :

$$f = \frac{c}{2}\sqrt{\left(\frac{\alpha_{m,n}}{r_c}\right)^2 + \left(\frac{q}{L_c}\right)^2} = \frac{c}{2}\frac{\alpha_{m,n}}{r_c} \quad \text{.....} (5)$$

Where

c=1180m/s, $\acute{A}_{m,n} = 5.6624$ r_c=0.2m.

The frequency in the fan section outside the circumferential baffle is 16704Hz.

In the same way, the natural oscillation frequency in the central area(diameter D≤0.178m) inside the circumferential baffle can also be found(see Table 3).

Table 3 Oscillation Frequency (Hz) in Areas in Combustion Chamber with Baffle

Order number	Central area inside circumferential baffle			Fan section
	Tangential	Radial	Longitudinal	Combination type (third-ordered tangential with fourth-ordered radial)
1	4117	8567	1130	16704
2	6829	11920	2260	16704

The energy which maintains the oscillation is determined by the oscillation frequency and the minimum initial amplitude, i.e.,

$E=A^2f$ ..... (6)

Where

E — oscillation energy;

f — oscillation frequency;

A — minimum initial amplitude.

In order to keep on an oscillation, there must be minimum initial amplitude, which relates nothing to the frequency. So the minimum energy used to maintain the oscillation is of a direct proportion to the oscillation frequency. That is, the amount of the frequency straightly relates to the generating strength of combustion instability. After equipped with 6×1-100 baffle in the combustion chamber, the lowest-stage-frequency increases suddenly, the least energy to keep on a oscillation is great then to decrease the possibility of transverse oscillation.

4.4.2 Overcome the Coupling Intermediate Frequency Flow-rate-model Vibration[6]

In the design of the combustion, the transverse vibration is primarily considered, for it can be a great danger. Although adopting a reasonable flow rate intensity distribution and a regenerative cooling baffle can effectively restrain the transverse (including the radial and tangential) vibration, it has no effect on restraining the longitudinal vibration.

In the research and production of the LMRE, the pressure pulsation of the propellant feed line system and the pressure oscillation of the thrust chamber once coupled, which is presented by a leading mode of vibration of 800-1000Hz in the hot-firing test. The transient parameter of the different mechanical vibration, of the pressure pulsation in the line and of dynamic strain in the combustion chamber cylindrical section, as well as the column dynamic strain, etc., all show this vibration frequency. The pressure pulsation in the combustion chamber is strengthened together with the fluid pressure pulsation of liquid in the line, stimulating strong oscillation combustion, bringing an effect on the combustion chamber and the whole engine's work. After a careful research on the hot-firing test, in case of a coupling vibration, the features would be:

a. Each part, assembly or subassembly will be damaged to a different degree.

b. If the vibration becomes more violent, it will lead to the failure of the hot-firing test and produces effect on the reliability of the engine.

c. The oscillograph used to measure vibration presents a clear sine wave. Its frequency tends to be single. The frequency splitting acceleration is fairly near to the comprehensive acceleration.

d. Performance is reduced and specific impulse lowers greatly.

e. The pressure oscillation in the combustion chamber is usually 20% of the steady pressure.

f. The flame is of group of red color with turbid light. Sometime it throws out from out-let of the nozzle, and the shock wave is not clear, sometimes long, sometimes short, very unstable.

g. The sound tends to be screaming. There is "buzzing" and "humming" sound in it.

When these phenomena last for a rather long time, some weak parts of the engine structure will be partially fatigue failure, then the fire will be leaking and the engine will lose its ability.

It is analyzed that the 800~1000Hz prominent vibration frequency in the hot-firing test is mainly due to the coupling with the first-order vibration frequency in the combustion chamber. First-order vibration frequency in the combustion chamber is about 850~1000Hz after calculation and acoustic experiment. Since the main vibration resource of the engine is the combustion chamber, and its first-order longitudinal vibration frequency is the leading frequency of the engine. This leading frequency's strong expression covers the natural vibration frequency of the other assembly. Hence, the first-order longitudinal pressure pulsation in the combustion chamber plays an important role in the vibration of the engine.

The feature of the first-order longitudinal vibration in the combustion chamber is a pressure peak existed on the surface of the injector. If there is only a simple first-order longitudinal vibration appeared, the vibration would be gradually decreased because of the existence of a damping. It is analyzed that the premise to continual vibration energy is that there should be a standing wave in the oxidizer main line, which can be proved both in theory and by experiment. In theory, it can be deduced by setting up a standing wave equation. If there is a pressure pulsation coming from the combustion chamber, and there is a perfect line length and reflecting surface, the standing wave can be produced. Actually, there is an 800~1000Hz standing wave mode pressure pulsation in the oxidizer main line, which can be proved by the water acoustic experiment.

Because of the both-sided effectiveness of the two dynamic characteristics of the propellant feed system and the combustion chamber, this coupling vibration, in the end, shows a great change of flow rate. The vibration frequency is the first-order longitudinal intermediate frequency, the energy used to go on this vibration is the great pulsation of the flow rate, so this is called an intermediate frequency flow-rate-model vibration.

To improve reliability of the engine, the intermediate frequency flow-rate-model vibration must be overcome. So it needs to take a measurement of vibration-resistance and vibration-attenuation. According to the generation mechanism and development mechanism of the intermediate frequency flow-rate-model vibration, measures should be adopted in the combustion chamber and in the propellant feed system.

a. The Scheme of Improving the Injector

In the design, except the combustion efficiency, protection with baffle and the anti-high frequency combustion instability is considered, it is emphatically considered to restrain intermediate frequency flow-rate-model vibration, and the injector of the "K" scheme is selected from many schemes. In detail, it is to lower the injector pressure loss and adjust its pressure loss ratio, to use an outstanding cone-shaped flow rate intensity distribution and have big flow rate intensity in both sides of the baffle, to reduce the jet stream's knocking angle rightly. Just because of the above measure, when the geometric size is certain, the acoustic oscillation frequency will change with the changing of the gases parameter, it will lower 50~100Hz on the basis of the former one. This will miss the responding frequency of the oxidizer main line.

b. To Take a Vibration-damping Measure in Propellant Feed System

Add a calibration orifice for the fixed throttle pressure in the oxidizer main line. After that, the vibration-damping will become a reality. However, with different position of the calibration orifice, there will be different damping affection. When the calibration orifice is placed in the pressure wave node (that is, flow rate wave loop), it will have the best effect. Furthermore, the bigger the throttle pressure, the more outstanding effect it has. Since the distance away from it reduces the amplitude of the flow rate forced vibration caused by the combustion chamber, to set the calibration orifice in the flow rate wave loop nearest to the chamber will have the best result. At present, the throttle pressure of the calibration orifice is 0.686MPa.

The above two measures are called "OK" scheme in the LMRE.

4.4.3 To Solve the Low Frequency Combustion Instability of Gas Generator[7]

The excess oxidizer coefficientα of the first-stage and second-stage main engine's gas generator in the LMRE is 0.067. One part of the released energy by combustion under a low coefficient is to maintain the normal combustion, the other part is for the evaporation, the vaporization of un-combustioned fuel and the mixture with gas. Therefore, the time is comparatively long which fuel stay at gas generator, it is easy to cause low-frequency vibration and low-frequency combustion instability. For this reason, it should take the following measurements in the gas generator.

a. Use a high excess oxidizer coefficient αdistribution in the central area of the gas generator head, then a high temperature strong flame is produced in this area.

b. Select a fitful gas generator capacity to shorten the delay of the combustion product.

c. Increase the injector's pressure loss, improve the quality of the mixed and atomization, increase the ability of resisting pressure pulsation in the generator and effectively avoid the low frequency combustion instability.

4.5 The Measures of Improving Performance Reliability[10]

The reliability of an engine includes two aspects---structure reliability and performance reliability. We have mainly introduced the measures of improving the structure reliability above. In fact, the engine's performance precision which decides the rocket whether could finish the duty exactly is the key index. During the research of the LMRE, we always pay attention to the improvement of performance precision.

On the design, we used calibration orifice and cavitating venturi as flow rate regulation unit, the second-stage engine was equipped with full cavitating venturi design. Because of its work character, its pressure fluctuation of downstream could not influence the upstream, therefore, the engine's flow rate could control exactly on condition that pressure behind pump is stable and the thrust chamber pressure fluctuation could not influence flow rate change of propellant feed system.

The flow rate control precision of calibration orifice is about 3~5%, the flow rate precision of cavitating venturi is about 2~3%.

On the test, some main assembling unit connected with the performance of engine such as thrust chamber, turbopump, gas generator, calibration orifice, cavitating venturi and cooler have been test by hydraulic test, so that we can get precision flow resistance data of all assembling units. Then, according to the flow resistance data, we can adjust the working parameter of engine, such as speed, combustion chamber pressure etc. Furthermore, in order to keep the stability of the test system, we should check the test system, and in order to ensure data correct, standard cavitating venturi is prepared for its hydraulic test to check the test system.

5 Measures for Reliability Assurance

The reliability of the components is the basic guarantee of the reliability of the engine, so the design scheme for the components should first be carefully drawn up and then be fully tested and verified. The design scheme is guaranteed by the means of production. The production quality provides a key basis for the reliability guarantee of the engine.

In order to ensure high reliability of the LMRE, a series of effective measures for production and management have been employed after years of exploration and have played an important role in guaranteeing the inherent reliability.

The major measures are as follows[1]:

a. Strictly control the working accuracy of all the units.

b. Perfect the technology standards, and advance the working accuracy of small hole of the injector.

c. Employ advanced technological methods to guarantee the design conditions.

d. Strictly control welding status, optimize welding parameters, advance and stabilize welding qualities.

e. The nozzle extension of the second stage main engine is a channeling and brazing structure, with its structure being compact, its mould being double circular arc, and its cooling channel being of small flow resistance. The method of power spinning is employed to make semifinished product of channeling section in interwall of tail nozzle of thrust chamber of the second-stage main engine, improve the production quality and solve its problem of butt-joint misplacement and non-synchronize of welding contract with ahead section.

f. Improve the molding technique and the casting quality on the basis of the casting techniques available.

g. Improve the quality of the forge pieces and stabilize the performance of the machinery.

h. Strictly control the alteration of the design conditions and technological conditions. All the altered parts should undergo evaluation and can only then be carried on.

6 Reliability Test and Evaluation

6.1 Reliability Test

Since the research of first-stage engine of Long March launch vehicle has been hot-firing test 98 times and add up to 24992.3 seconds, second-stage main engine has been hot-firing test 100 times and add up to 23473.42 seconds, second-stage vernier engine has been test 77 times and add up to 51279.77 seconds. After a lot of test, all kinds of faults of engines are found. In order to keep high reliability, it is necessary for fault-parts to be improved design, based on design-test-improving design-test steps.

The reliability tests consists of the reliability test of the assembling unit and the reliability test of the engine, mainly including the turbopump linkage test, the reliability test of the ignition of the electroexplosive cartridge, the vibration test of each component, the combustion stability rating test of the combustion chamber, the engine reliability test for the integrity, the performance hot-firing test of the engine, engine test under simulated high/ low ambient temperature condition, etc. The following discussions are focused on the reliability hot-firing test for the integrity.

The aim of the reliability hot-firing test is as follows: expose the defects of the engine in its design, technology, and raw material, etc., through improving design and manner and then improve it to eliminate defects or faults, thus gradually increasing the reliability of the engine.

In order to fully expose the defects of the engine, the LMRE is put to a reliability hot-firing test, which employs the method of altering the operating parameter and prolonging its working time, with choosing the thrust and the mixture ratio as its working parameters. The condition of the reliability hot-firing test is shown in figure below.

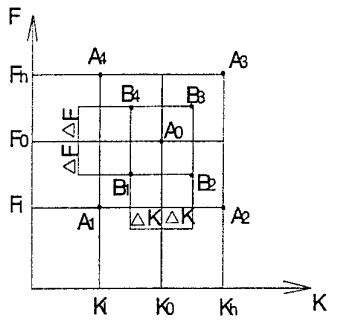


Fig.3. The conditions of the reliability hot firing test
A0 refers rated condition;
A1,A2,A3,A4 refer border condition;
B1,B2,B3,B4 refer reliability demonstration condition.

In figure 3:

A_0 represents the rated condition of the engine, determined by the nominal thrust F_0 and the nominal mixture ratio K_0.

ΔF,ΔK are the allowable thrust deviation and mixture ratio deviation respectively both of which as well as the rated condition determine the four work mode points $B_1B_2B_3B_4$. With these four points as the vertexes, a square is thus formed. Obviously, under any condition determined by the thrust and the mixture ratio indicated by any point within the square, the engine should operate with reliability. The reliability of the engine refers to the reliability of any point within this square.

In order to expose better the weak links of the engine, the Square $A_1A_2A_3A_4$ that is much larger than the Square $B_1B_2B_3B_4$ is taken into account in the hot-firing test of the LMRE. If the engine can operate with reliability within the Square $A_1A_2A_3A_4$, it is certain that the engine will operate with higher reliability within the Square $B_1B_2B_3B_4$. The vertexes of the Square $A_1A_2A_3A_4$ are generally determined by + 10~15% of the nominal number. The hot-firing test time is 3~4 times the nominal working time, and can also be determined by the capacity of test-bed.

The engine's reliability will not increase through the reliability test itself. The test is carried out mainly to expose the weak links and faults, then analyze the cause of the faults exposed in the test and put forward some measures to make improvements, and then verify it through tests. Thus it is a process of "test—improvement—retest—re-improvement". The verification of the measures for improvements will prove an increase in the reliability of the engine, Furthermore, the reliability test is also carried out to provide information and basis for the reliability estimation.

6.2 Reliability Evaluation

To evaluate the reliability, such method is employed: a method for the evaluation is determined according to the sub-samples of the reliability available and then is employed to calculate the reliability of the engine. The normal distribution method is adopted to evaluate the performance reliability of the LMRE and the Weibull distribution method to evaluate the structure reliability.

6.2.1 Performance Reliability Evaluation [2]

Performance reliability refers to the probability of parameters of the engine, such as thrust, specific impulse, and mixture ratio etc., within the designated allowance belt. Obviously, performance reliability is connected with the size of the allowance belt, that is, the broader the allowance belt, the higher the calculated performance reliability will be.

The normal distribution method is adopted to evaluate the performance reliability of the LMRE.

The probability of performance parameter within the interval $[\mu - l\sigma \le \chi \le \mu + l\sigma]$ is named the performance reliability R, namely,

$$P[\mu - l\sigma \le \chi \le \mu + l\sigma] = R \quad \square 7 \square$$

Where

μ— the expected value of the parameter;

σ— the standard deviation of the parameter;

l — be traced from the normal distribution table and R.

Under the few times of hot-firing test, both μandσare unknown numbers, so the following formula is used to evaluate the interval $[\mu - l\sigma, \mu + l\sigma]$

$$P[\bar{x} - kS \le \mu \pm l\sigma \le \bar{x} + kS] = 1 - \alpha \quad \square 8 \square$$

Where

$1-\alpha$ — degree of confidence;

$\bar{x}$ — average value, $\bar{x} = \sum_{i=1}^{n} x_i / n$;

S — variance, $S = \sqrt{\frac{\sum_{i=1}^{n}(x_i - \bar{x})^2}{n}}$.

Probability of the parameter x within the interval $[\bar{x} - kS, \bar{x} + kS]$ is named the reliability R of the degree of confidence $1-\alpha$.

6.2.2 Structure Reliability Evaluation [2]

Structure relaibility evaluation consists of two units as the assembling units and the engine. The reliability test for some assembling units is carried out with the engine, while some assemblies as the electroexplosive cartridge and the prevalve estimating individually.

Prevalve reliability is determined by whether butterfly plate can be opened correctly and captured reliability. Clearly, it has nothing to do with the length of engine's working time. So, the prevalve can test and evaluate its reliability independmently apart from the engine.

The structure reliability evaluation for the engine is based on the Weibull distribution method. It is hard for the engine to test the failure point because of the limited time of test-bed. So, hot-firing test is usually taken the timing truncation method. According to this, Weibull-Bayes method is used to evaluate the reliability.

The following is accounting formula for the reliability probability.

$$R_L(t_0) = \exp\left[-\frac{t_0^m \chi_\gamma^2(2r+2)}{2T}\right] \quad \square 9 \square$$

where

m — shape parameter in Weibull distribution, m≈3, according to the year's tested statistic analysis;

t_0 — normal working time of the engine;

$T = \sum_{i=1}^{n} t_i^m$;

n — times of the hot-firing test or flying time;

t_i — actual hot-firing time or flying time of the engine, i=1,2,...,n;

$\chi_\gamma^2(2r+2)$ — underside number of χ^2 distribution when freedom degree is 2r+2, read from standard;

γ — degree of confidence;

r — failure times.

7 Conclusion

It is the basis to guarantee the reliability of the LMRE, along with thirty years development, whose design, production and test have been becoming riper gradually. Thus, the engine's inherent reliability level makes steady progress through continuously adopting the reliability engineering. In the respect concerned with maintenance for the engine, which has few items for surveying and testing after delivering. There mainly has the installation of priming system, the electronic system test, which improve the maintenance reliability, and ensure the engine's inherent reliability. Since having been employed many measures for ensuring the reliability, the engine hot firing test has basically already eliminated failures, then the success ratio is up to 100% in all Long March vehicle flight missions.

In spite of above success, at the present time, the main aim of the LMRE is still to guarantee its reliability, and then perfects its engine's design, production and test.

References

[1] Baokun Zhang "Several Problems in Development of the LMRE"

[2] Baokun Zhang "Works on the LMRE Reliability"

[3] Hongming Sun "Summary Report on Systematic Designing and Developing of the LMRE"

[4] Bingcheng Fu, Ziqiang Chen "Combustion Stability rating test of combustion chamber"

[5] Zhijun Wang "Reliability and Maintenance of the Missile and Weapon system"

[6] Zhijun Wang "Report on Intermediate Frequency Flow –model Vibration of the High Power Liquid Rocket Engine"

[7] Hongchao Zhao "The Development of Liquid Rocket Engine in China"

[8] Shaokang Yang "Development and manufacture of double face-riding seal of the Turbo-pump"

[9] Xinlin Wang " Summary Report on Engine's Texture Design and Development"

[10] Xubai Shen " Suggestions on Improving the Performance reliability of the LMRE"

[11] Zhanchen Guo " Demonstrational Report on Prevalve Redundancy Plan"

[12] Yunyan Wang "Evaluating Report on Performance and Test of Cable's moisture & water proofing"

esa

LIQUID SPACE PROPULSION AT ESTEC

prepared by:
F.Felici, J. M. Muylaert,
I. Kaelsch, H. Schoeyer

Date: 13 March 2000
Ref : TOS-MP/2622/tw

- **Where is propulsion in ESA ?**
- **Institutional tasks**
- **System studies**
  - **Propulsion 2000**
  - **STOTS**
- **Technology for Spacecraft**
  - **Rocket engines**
  - **New "clean"Propellants**
  - **Cold gas micropropulsion**
- **Tools & Verification**
  - **Rocflam**

Experimental /CFD activities

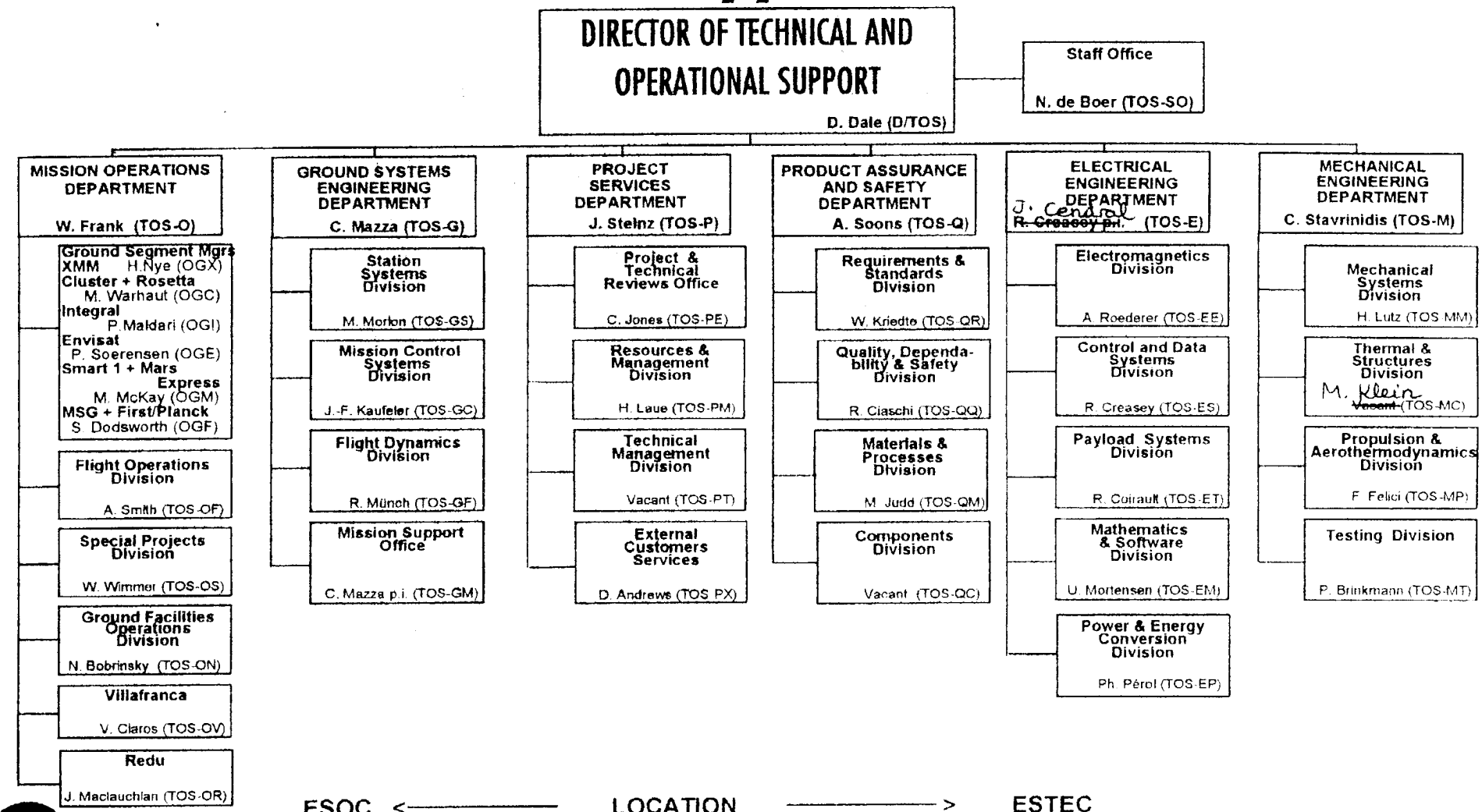
A) Propulsion jet / External flow interaction

- **Basic**
- **Generic**
- **Ariane 5**

B) Nozzle separation / Cooling studies

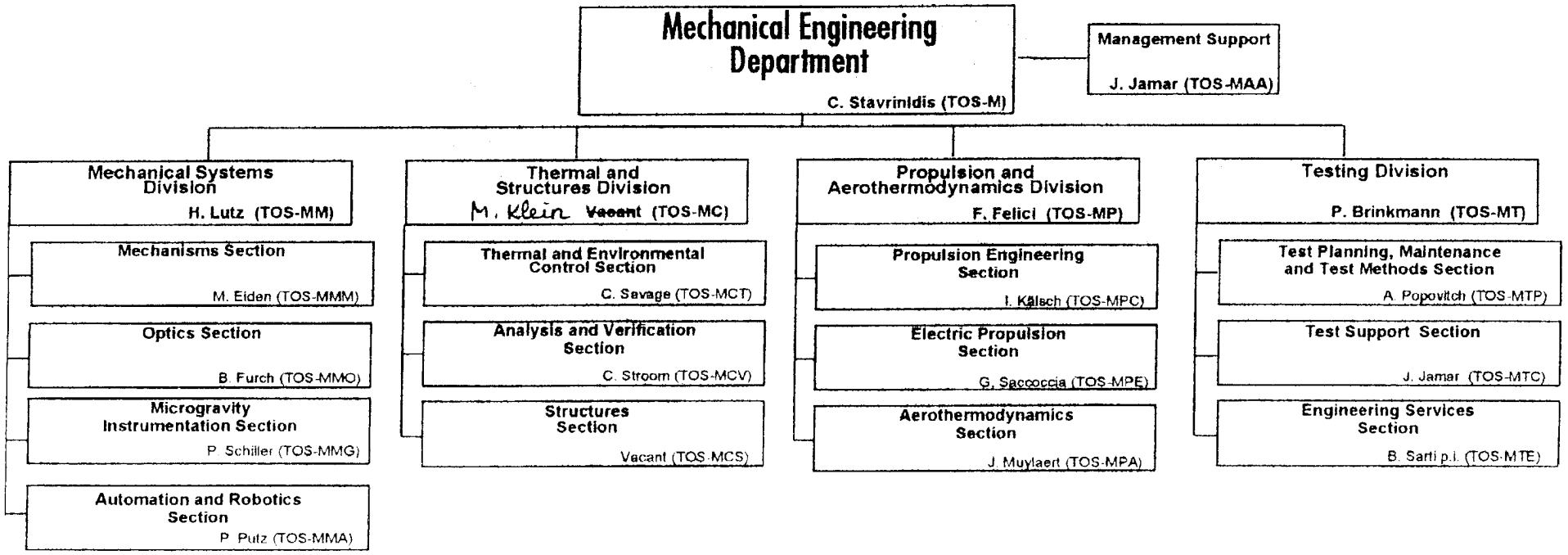
C) Plug nozzles

Directorate of Technical and Operational Support

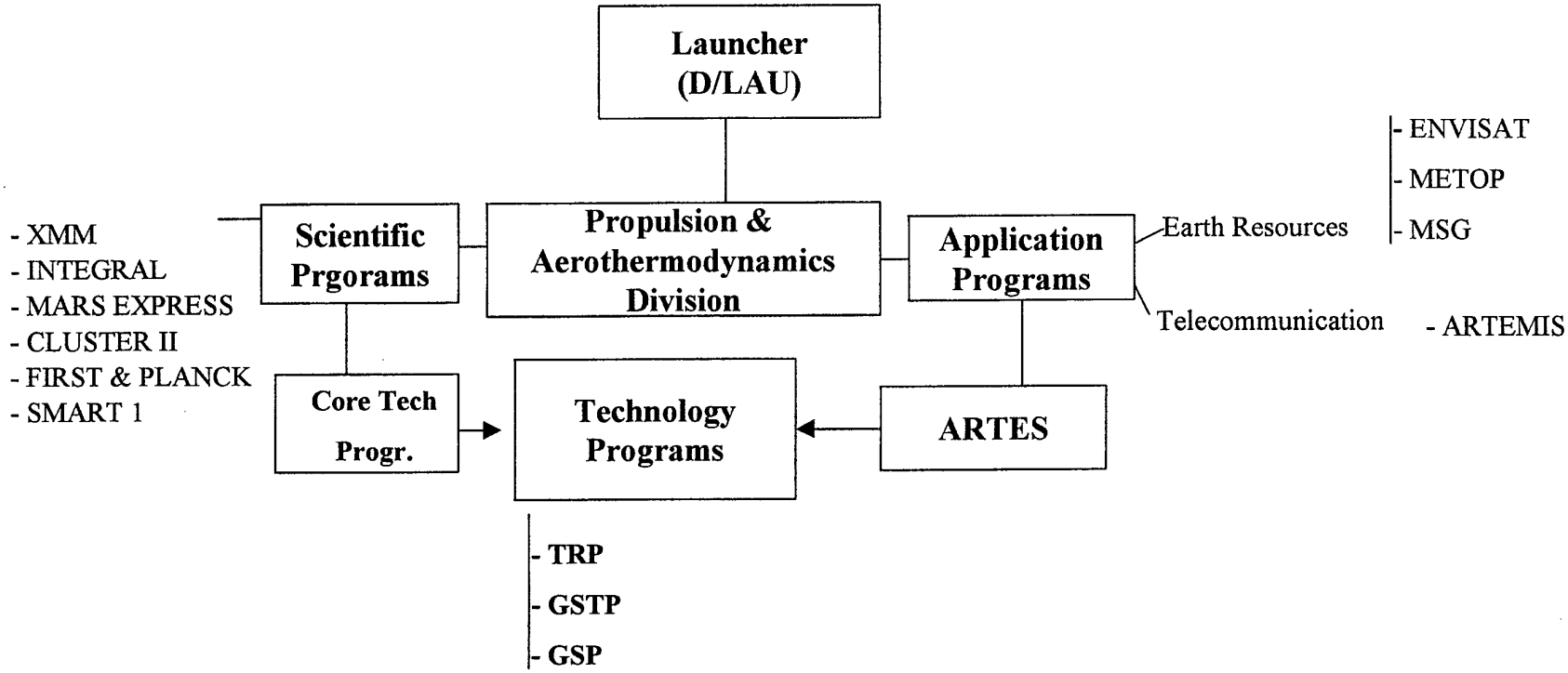


esa

Directorate of Technical and Operational Support



INTERFACES


Launcher
(D/LAU)
Propulsion &
Aerothermodynamics
Division
Scientific
Prgorams
- XMM
- INTEGRAL
- MARS EXPRESS
- CLUSTER II
- FIRST & PLANCK
- SMART 1
Core Tech
Progr.
Technology
Programs
- TRP
- GSTP
- GSP
Application
Programs
Earth Resources
- ENVISAT
- METOP
- MSG
Telecommunication
- ARTEMIS
ARTES

Institutional Tasks

Spacecrafts

- Conceptual designs, tradeoffs, layout of pre-Phase A and Phase A of new missions.
- Support to ESA satellite projects in requirements definition, technology assessment, procurement.
- In orbit performance assessment and troubleshooting (Soho).
- RCS / Spacecraft interactions (plumes, charging, passivation, contamination...)
- Development of new technologies and tools in the propulsion field, based on lessons learned, future missions requirements and European competitiveness.
- Support to launchers in the fields of aerothermodynamics and propulsion analysis.

In the framework of the General Study Programme of ESA, the Propulsion and Aerothermodynamics Division has initiated a study to perform an assessment of new needs for advanced space propulsion systems of the next two decades.

The Study covers the areas of spacecraft, launcher and upper-stage propulsion systems.

A Selection of promising propulsion technologies will be performed on the basis of technical, operational, cost effectiveness and programmatic criteria.

The results of the study will be used to initiate new R&D activities and to set-up a European policy, in consultation with other Agencies and Industries, for future programmes in the area of space propulsion systems.

The study will be completed in mid 2001

Solar-Thermal orbit Transfer Stage (STOTS) technologies have been recognised as one of the most promising area of investigation for new upper stage concepts and propulsion technologies capable of providing large velocity increments.

In the framework of the General Study Programme of ESA, the Propulsion and Aerothermodynamics Division has initiated a study to perform an assessment of STOTS for future launcher generations.

The Study will address design, development and other critical issues for all the technologies involved in a STOTS and will also assess the European capability to engage in a programme of development for these technologies.

The study will be completed in mid 2001.

TECHNOLOGY DEVELOPMENT ACTIVITIES

- Spacecraft Rocket Engines (Thrusters)
- Propellant Tank Diaphragm
- Exhaust Plume Characterisation Testing of European Reaction Control Thrusters

SPACECRAFT ROCKET ENGINES

- Bi-Propellant Rocket Engines for Application in "Dual Mode" Systems
  - Propellant Combination:
    - Anhydrous Hydrazine (N_2H_4) as Fuel
    - Mixed Oxides of Nitrogen (MON) as Oxidiser
- Bi-Propellant Rocket Engines for "Standard" Bi-Propellant Systems
  - Propellant Combination:
    - MonoMethyl Hydrazine (MMH) as Fuel
    - Mixed Oxides of Nitrogen (MON) as Oxidiser

"DUAL MODE" ROCKET ENGINES
ARC UK Ltd, Westcott, UK

LEROS 1D

- 4th generation of successful LEROS 1 Apogee Engines
- Use of high temperature resistant material (Ir/Re) for the combustion chamber
- Major design parameters:
  - Thrust Level 458 N (103 lbf)
  - Specific Impulse > 330 sec
  - Mixture Ratio 0.8
  - Area Ratio 270:1
  - Life 25 000 sec
  - Throat operating temperature of 1800 C
  - Columbium Exit Cone
- 15 months Development and Design Verification Test Program, completion in 2001

"DUAL MODE" ROCKET ENGINES
ARC UK Ltd, Westcott, UK

- LEROS 20Ha
- Engine for Reaction Control and back-up for LEROS 1
- Use of Platinum / Rhodium Alloy for combustion chamber
- Major design parameters:
  - Thrust level, nominal 22 N (5 lbf) at 240 psi feed pressure
  - Specific Impulse 308+ sec
  - Mixture Ratio 0.8
  - Area Ratio 150:1
  - Life: Impulse tot. 2.8 * 10^6 Ns, 1 000 000 pulses
- Development ongoing

BI-PROPELLANT ROCKET ENGINE
DaimlerChrysler Aerospace (D)

- 3rd Generation 400N High Performance Bi-Propellant Engine
- Use of advanced materials technology for combustion chamber and expansion nozzle and ROCFLAM software for achievement of high performance goal
- Major Design Parameters:
  - Thrust 400N range at 15 bar feed pressure
  - Specific Impulse 325+ sec (target)
  - Area Ratio 300+ (TBC)
  - Life 15 000 sec min.
- Development started on
  - High Performance Injector
  - Advanced Materials
  - High Area Ratio Nozzle / Thruster

PROPELLANT TANK DIAPHRAGM

- DaimlerChrysler Aerospace (D)
- Development of an Elastomeric Silica Free Diaphragm
  - Diaphragm material is compatible with Hydrazine fuels and NitrogenTetroxide (NTO) oxidisers
  - Diaphram manufacturing process developed
  - Long term propellant exposure and functional testing on tank level initiated
  - Completion of development program and availability of diaphragm tanks scheduled for 2003
- IAB Consulting (UK)
- Testing of an enhanced hydrazine compatible diaphragm material ongoing

New "clean" mono propellants

Presently the commonly used mono-propellant on satellites is *Hydrazine*

Disadvantages:

- Carcinogeneous
- Poisonous
- Vapours are susceptible to uncontrolled decomposition during adiabatic compression

Relatively low specific impulse: ~2200 m/s

Requires caution and safety measures in handling and loading of spacecraft.

Cost of Purified Anhydrous Hydrazine is high.

Potential solution:

"clean mono propellants"

ESA has two research and development efforts on this topic:

- Swedish Space Corporation
- TNO-Prins Maurits Laboratory

New "clean" mono propellants

Swedish Space Corporation

Mono propellant based on

ADN (Ammonium DiNitramide, $NH_4N(NO_2)_2$)	60,8%
Water (H_2O)	26,1% and
Glycerol ($C_3H_8O_3$)	13,1%

This yields an I_{sp} ~ 2400 m/s theoretically; in practice it will be ~ 2200 m/s
The flame temperature T_c ~ 1900 K. For comparison, the Hydrazine decomposition temperature ~900 K.

Initial experiments show that ignition is well possible
Steady state performance is close to what is expected.

New "clean" mono propellants

TNO Prins Maurits Laboratory

Here a group of mono-propellants is being investigated. All are based on HNF (Hydrazinium Nitroformate, $H_5CN_5O_6$)

Low performance group:

$HNF+CH_3OH+H_2O$ I_{sp}~ 2200 – 2300 m/s, Flame temperature ~ 1500 K

$HNF+NH_3+H_2O$ I_{sp}~ 2200 – 2300 m/s, Flame temperature ~ 1500 K

The volumetric specific impulse is ~ 35% higher than for Hydrazine

Medium performance group:

$HNF+N_5H_5+H_2O$ I_{sp}~ 2600 m/s, Flame temperature ~ 1900 K

$HNF+CH_3NO_2+H_2O$ I_{sp}~ 2700 m/s, Flame temperature ~ 2000 K

The volumetric specific impulse is ~ 50% higher than for Hydrazine.

Catalytic ignition demonstrated to be effective and rapid at ambient pressures.

Catalytic ignition, thermal bed ignition and electrolytic ignition will be evaluated.

New "clean" mono propellants

The New Oxidisers used in clean propellants

ADN is a relative new oxidiser, originally developed in Russia, but during the 1980's also made (in small quantities) in the USA for use in solid propellants.

It is presently being made in Sweden by Bofors, ~ 1000 kg/yr.

It is a white monoclinic crystal that dissolves well in water.

HNF was discovered in the 1950's in the USA and is presently being developed as an oxidiser for high performance solid propellants. It is being manufactured in the Netherlands by APP, ~ 300 kg/year

It is a yellow monoclinic crystal that dissolves well in water. For use as a monopropellant one does not have to make HNF first, but one may dissolve the two basic ingredients: Hydrazinehydrate and Nitroform in water, which is very beneficial for the costs.

The figure next shows a sample of HNF



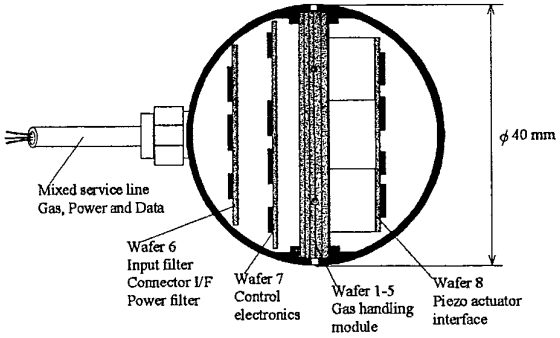
Cold gas micropropulsion

- ACR Electronic AB (Trosa-Sweden) has been developing, under ESA contract, silicon microtechnology to achieve highly proportional, very small thrusts, in an integrated package.

- Phase 1 of the four phases activity has been completed successfully. (components manufacturing). Phase 2 has started (module integration).

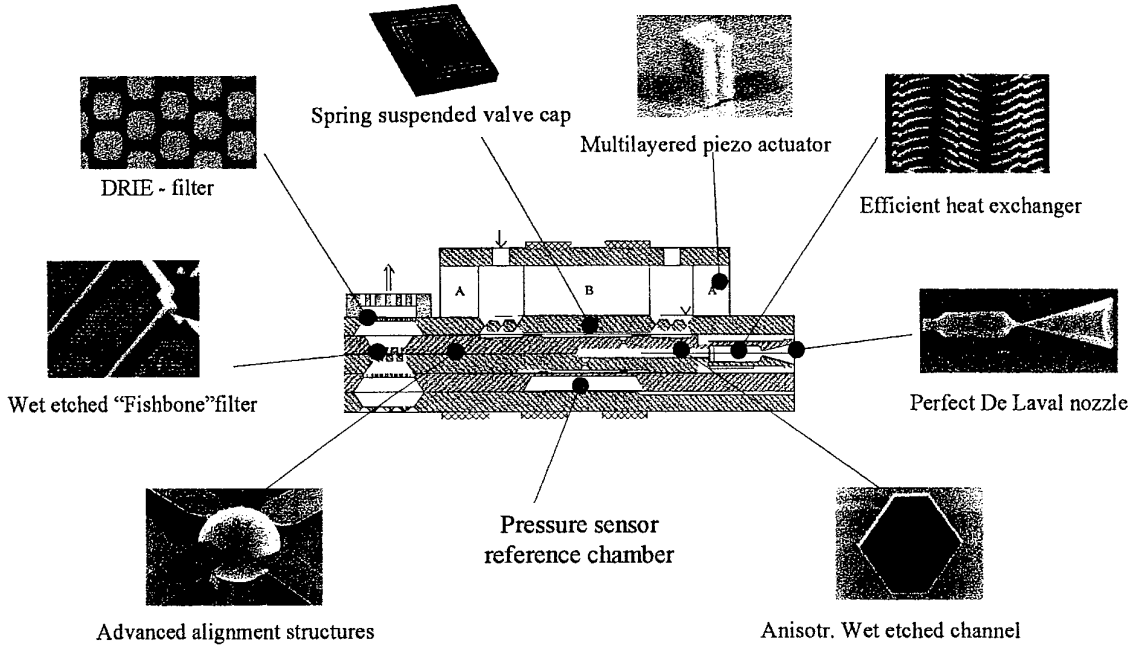
- This type of propulsion may fly on the ESA GOCE (Gravity Field and Ocean Circulation Mission) spacecraft, recently approved.

Micro Propulsion Cold Gas Thrusters



Features:

4 nozzles in each pod
Thrust range: 0,1 – 10 mN
Proportional control
Low power consumption
Low weight: ~ 80 g



Cross-section through the micro-machined gas handling device

The ROCFLAM Code

The ROCFLAM code is presently being developed for ESA by DaimlerChrysler Aerospace (D).

It is an engine design tool, reducing experimental development of bi-propellant thrusters by computer modelling.

The code assumes a certain injector behaviour. The injector characteristics cannot be properly modelled by the code. For a given injector behaviour: droplet size, velocity (magnitude and direction), the code solves for:

- The flow field
- The droplet trajectories (inclusive break-up, splashing on, sticking to, or bouncing back from the wall)
- The establishment of a coolant film
- The combustion reaction
- The nozzle flow

Output from the code include the outside wall temperature distribution, thrust, specific impulse, thrust coefficient, chamber pressure, characteristic velocity, etc.
These parameters allow to verify the code results with actual engine performance.

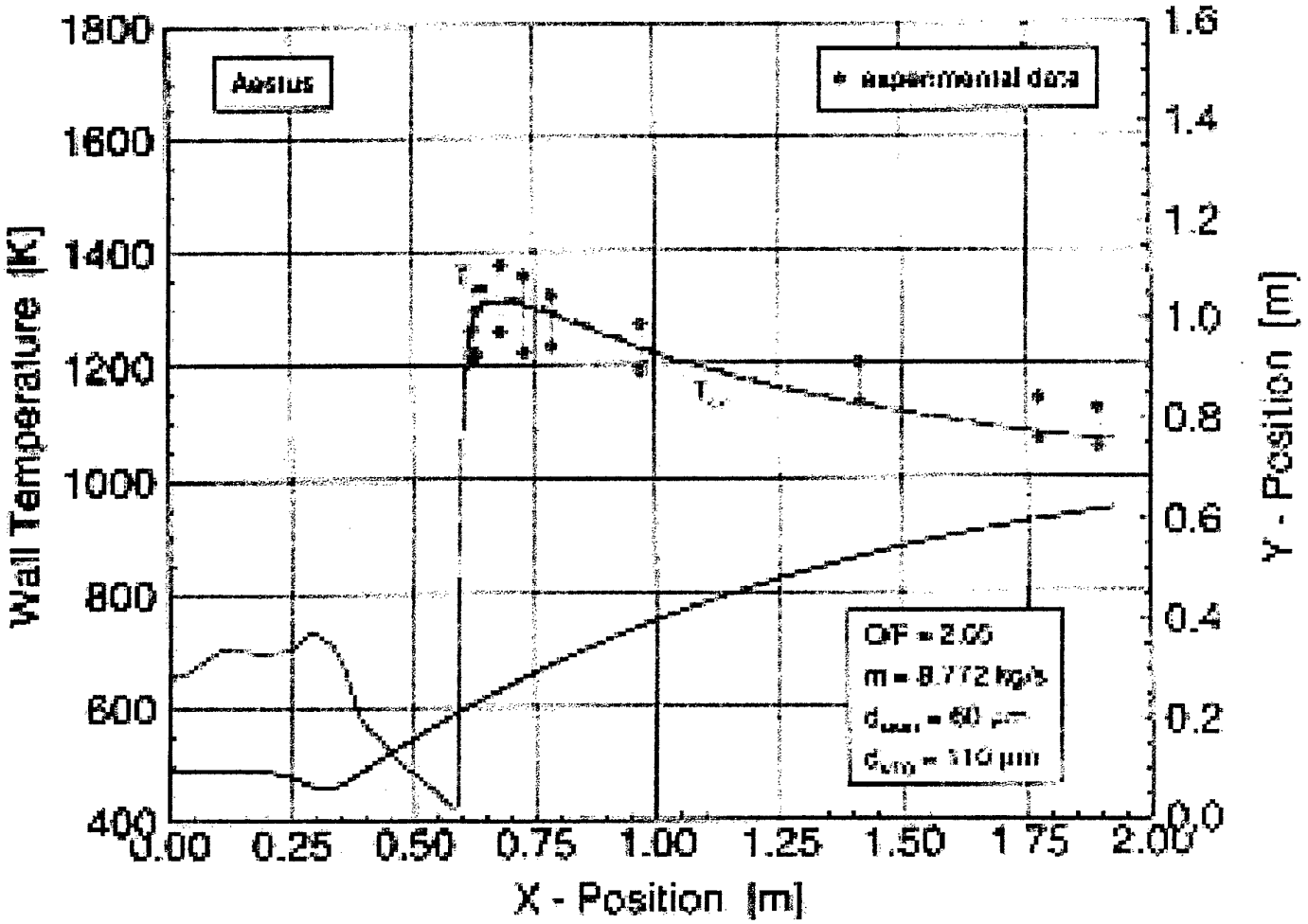
The ROCFLAM Code ('ctd)

- Once an experimental engine has been tested under a range of conditions, the injector pattern is modelled such that over a range of experimental conditions the code calculations match experimental (overall) measurements.

- Thereafter, modifications to the engine may be made: different geometries, different mass flow rates, different mixture ratio's, etc. The ROCFLAM code will make reliable predictions. This reduces the amount of experimental development efforts by engine manufacturers substantially.

- The ROCFLAM Code has been tested on the DaimlerChrysler 400 N engine and the ARC-UK LEROS II engine. In addition to the DaimlerChrysler 400N and the ARC-UK LEROS II engine Rocflam has been applied to analyse a number of different engines: The Aestus (Ariane 5 Upperstage engine), the DaimlerChrysler 22N and the DaimlerChrysler/Boeing Rockwell RS 72.

The ROCFLAM Code ('ctd)



Propulsive Jet/ External Flow Interaction Studies

Basic studies

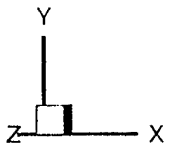
Base pressure/ jet entrainment
Steady and unsteady effect

1. Validation exp. Using simplified models at TU Delft /ONERA/FFA (cold) for underexpanded (blockage region) and overexpanded flow (aspiration region): effects.

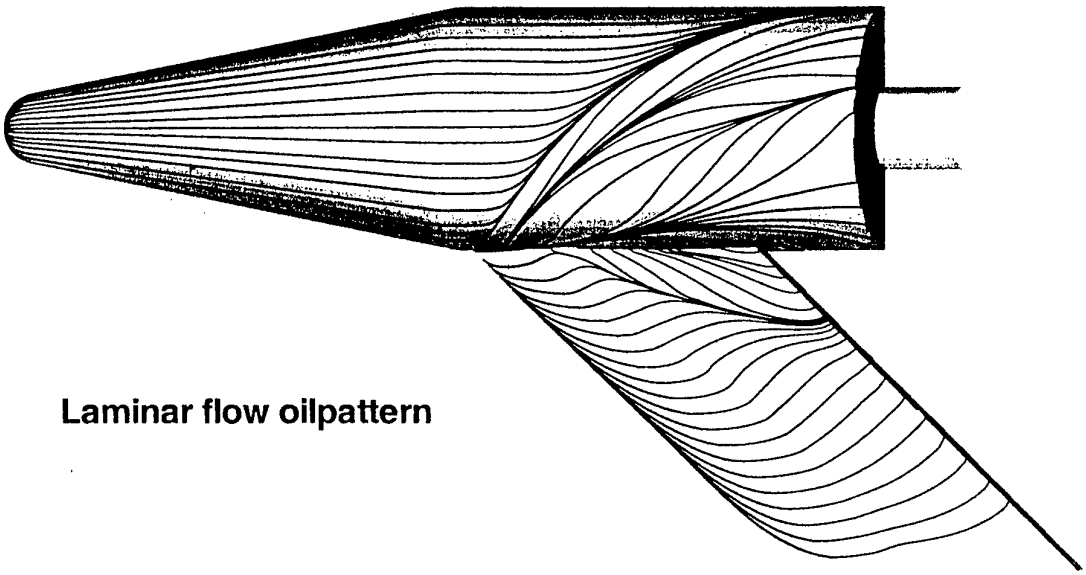
2. Influence of hot plumes.
- **TNO experiments (future)**
- **Flight data (Russian lessons learned)**

Festip BCCC.0

Mesh 1 (353,026 cells)

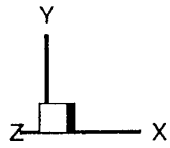


M_∞=2.98
Plume-off
Perfect gas

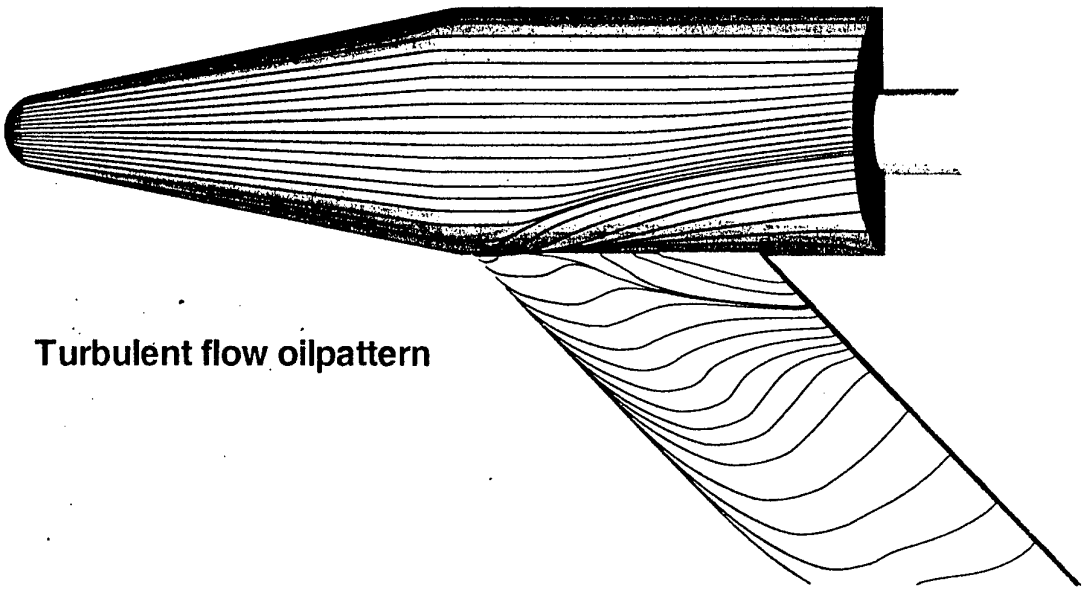


Laminar flow oilpattern

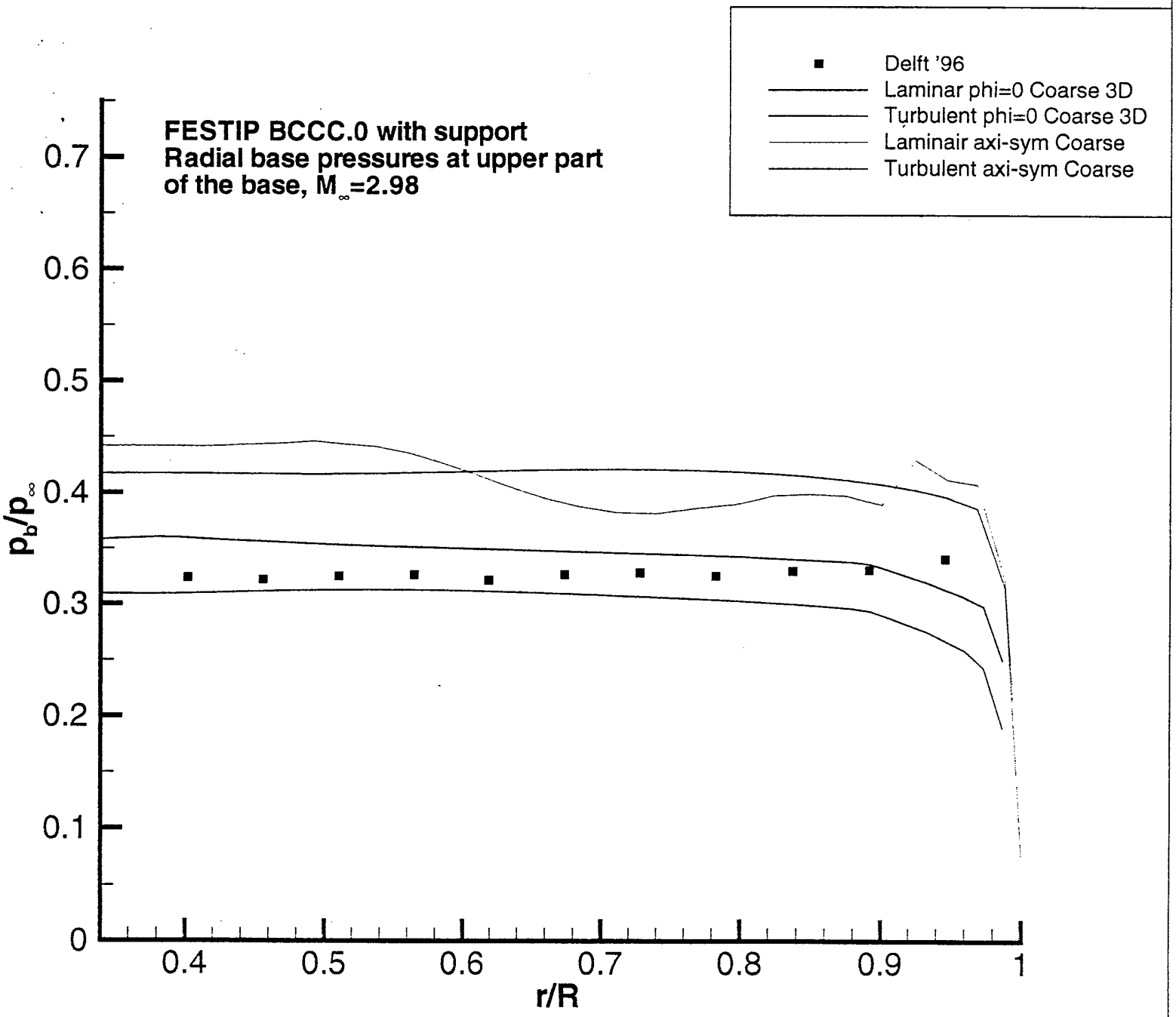
Mesh 1



M_∞=2.98
Plume-off
Perfect gas



Turbulent flow oilpattern

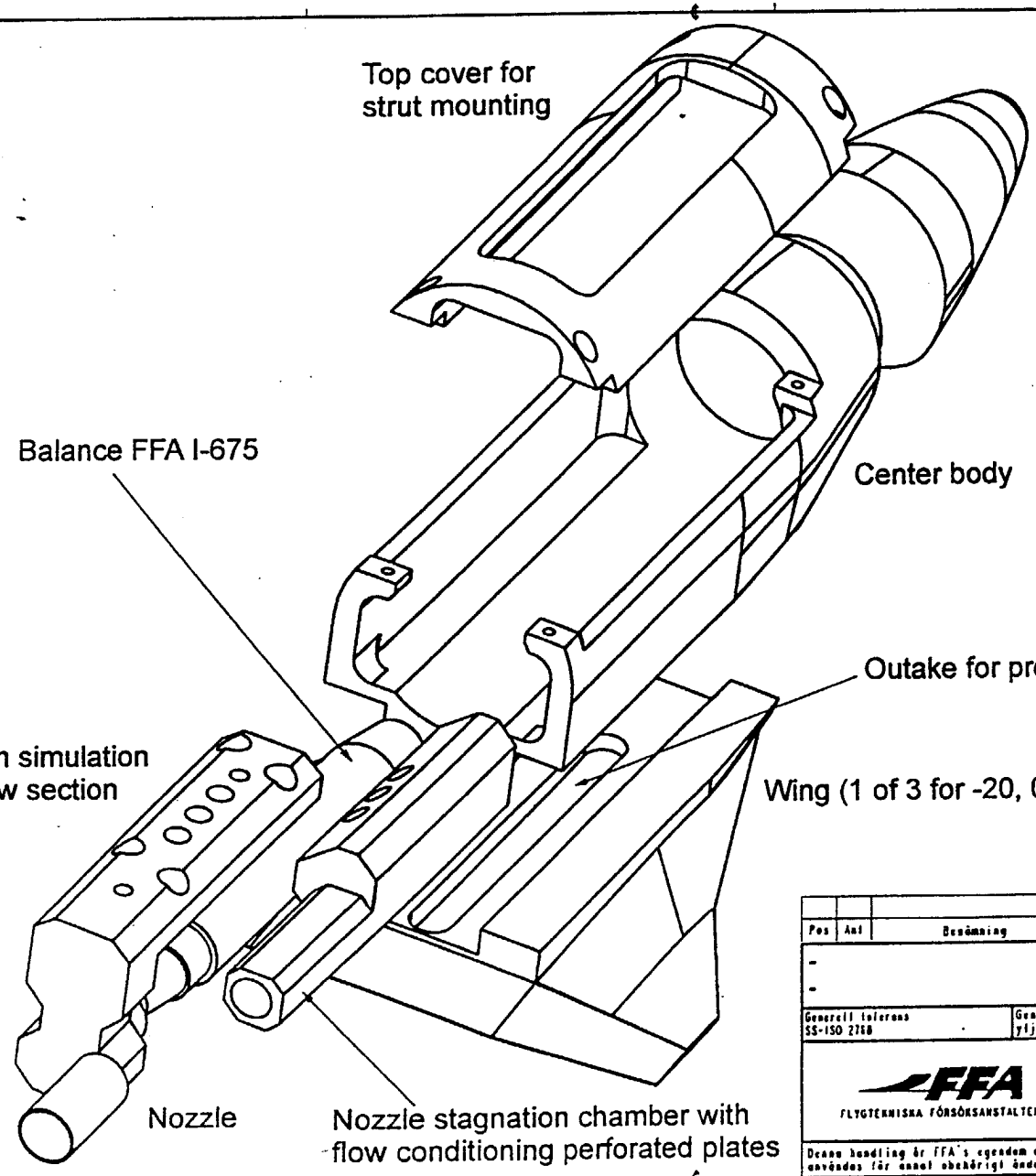

FESTIP BCCC.0 with support
Radial base pressures at upper part of the base, M∞=2.98
Delft '96
Laminar phi=0 Coarse 3D
Turbulent phi=0 Coarse 3D
Laminair axi-sym Coarse
Turbulent axi-sym Coarse
pb/p∞
0
0.1
0.2
0.3
0.4
0.5
0.6
0.7
0.4
0.5
0.6
0.7
0.8
0.9
1
r/R

Generic Studies

EXTV; Exp. FFA, S4 facility
Comp: ESTEC, EPFL, DLR

Issues: Twin plume interaction on base + body flap + external flow + flight extrapolation

△	Ändringens art	Datum	Sign	Godk



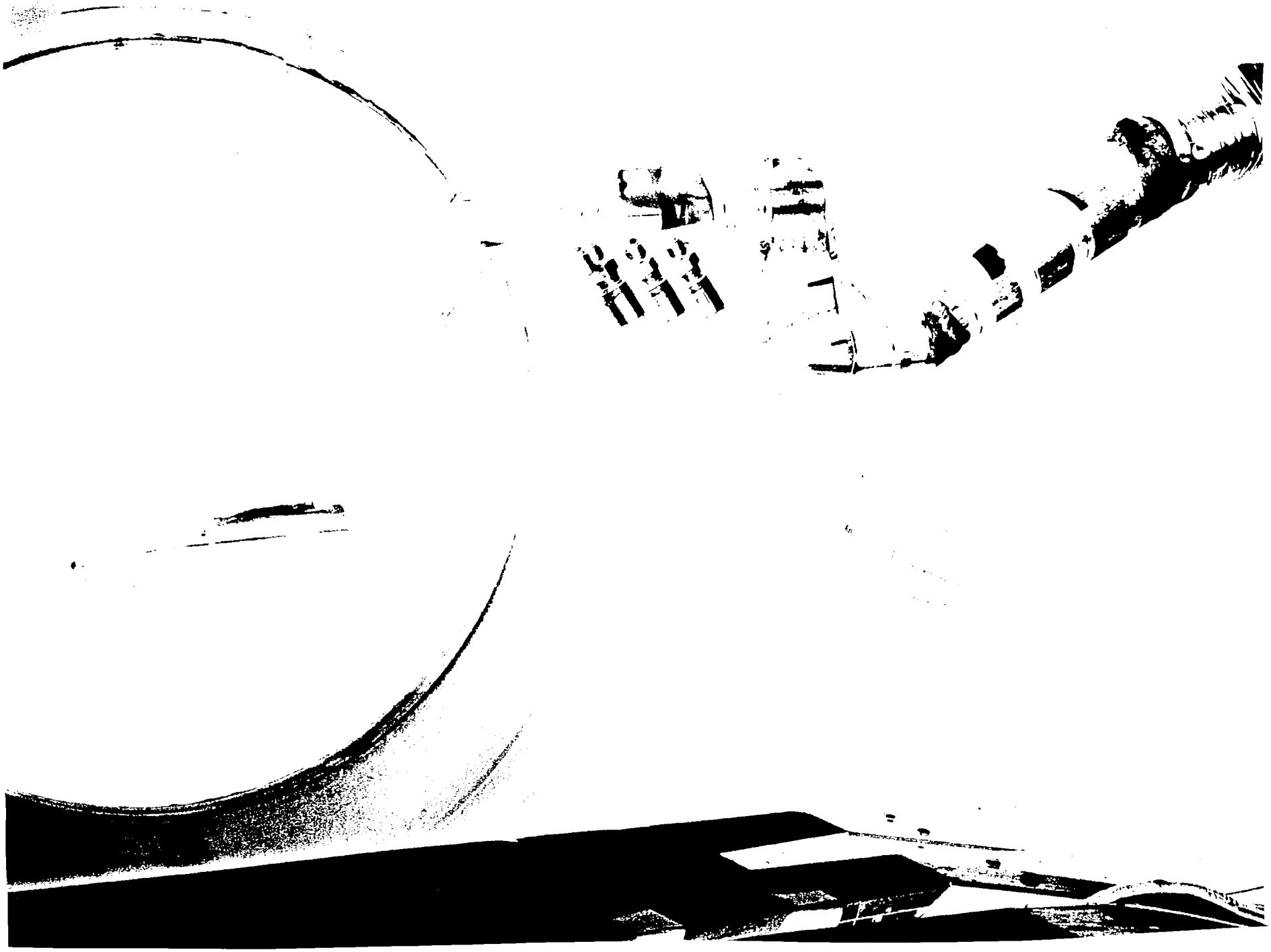
Pos	Ant	Benämning	Material
-			
-			

Skala		Uppdrag	
Generell tolerans SS-ISO 2768	Generell ytjämnhet Ra	Vikt kg	Ytbehandling

FFA FLYGTEKNISKA FÖRSÖKSANSTALTEN

CAD-modell	EXTV		
Slyckt	Pos	Smst	
Ritad d.		År	
Kontr	Godk		

Denna handling är FFA's egendom och får ej utan FFA's skriftliga medgivande kopieras, delges tredje man eller användas för annat obehörigt ändamål.
COPYRIGHT Flygtekniska Försöksanstalten



Specific

- **ARIANE 5 : Base flow / jet interaction numerical /experimental activities**

  Exp. NLR/FFA/ONERA
  Numerical analysis : ONERA, AML, ESTEC ,

- **ARIANE 5 : Buffeting correlation activities**

  Exp.: FFA,ONERA
  Numerical analyses: ESTEC,ONERA,FFA,AML

EXHAUST PIPE FLOW INTERACTION

- VERIFICATION OF NO LOCAL FLOW SEPARATION IN LEO/LEH EXHAUST PIPE AFTER EAP SEPARATION

- 70 KM (EAP SEPARATION)
  M = 8 (V = 2020 $m/_{sec}$)
  Ts = 230 K
  $\rho s = 7.10^{-5}\ kg/_{m2}$

TRP/GSTP Activities on nozzle Technologies

I TRP (DASA, SNECMA, UNIROME, TU Delft, TU Dresden)

- Experimental & Numerical Analysis of Flowfield

- Optimization / effect of Plug Shape/cut off

- Influence of external flow

- Influence of side fences (3d effects)

- Trust vector control

Engineering Performance Model for flight configuration

II GSTP (VAC, FFA)

- **High quality axisymmetric validation data for CFD on similar plug configuration**

- **Investigation of unsteady flow phenomena/ side loads for e.g.**

  - **Extendible bell nozzle**

  - **Dual bell nozzle**

Experimental & Numerical Prediction + Performance model construction and validation

III TRP (DASA, ...)

- **Performance Analysis + Modeling for Expansion/ Deflection nozzle Concept**

- **Concept/System trade-off:**

  - **Performance**

  - **System engineering issues; mass, length, engine**

Basic investigation of usefulness of alternative concepts

Nozzle Separation/Cooling Activities

Numerical/Experimental (on ground)

Start up/shut down shock patterns

Influence of chemistry
- **Frozen flows**
- **No equilibrium flow**

Influence of film cooling

Influence of 3D effects

Influence of surface roughness

Post combustion

Interaction with external flow (numerically in flight)

CONCLUSIONS

NEED TO FURTHER USE CFD FOR THE DESIGN OF EXPERIMENTS, THE DEFINITION OF THE TEST ENVIRONMENT INCLUDING MEASUREMENT TECHNIQUES, THE INTERPRETATION OF THE RESULTS AND FINALLY THE EXTRAPOLATION TO FLIGHT

PULSED DETONATION ROCKET ENGINES

Rajendran Mohanraj*
Houshang Ebrahimi**
Charles L. Merkle***

The University of Tennessee Space Institute
Mechanical, Aerospace, and Engineering Sciences
Tullahoma, TN

and

Arnold Engineering Development Center
Tullahoma TN37388

Abstract

Pulsed detonation engines give promise of improved efficiency and reduced pumping requirements for space transportation. The overall operation of a pulsed detonation engine is discussed and multi-cycle performance estimates are presented using a quasi one dimensional model with a single progress variable equation to represent chemical reaction. The one-dimensional results are verified against a multi-dimensional model. The emphasis is on application to rockets burning hydrogen and oxygen at stoichiometric conditions. The effects of adding a variable area nozzle are shown to improve performance at altitude conditions but to penalize performance at low altitudes. The improvement in specific impulse at altitude increases with area expansion ratio in much the same manner as for a conventional rocket engine. Increasing the length of the nozzle while keeping the overall engine length fixed decreases the specific impulse indicating that the detailed shape of the nozzle may be of importance. Variations in the fraction of the tube that is filled with propellant cause minor variations in the specific impulse suggesting that detailed changes in the unsteady wave dynamics can have a measurable effect on performance. Detailed physics are exemplified in *x-t* diagram.

Introduction and Background

Pulsed Detonation Engines (PDE's) have received a considerable amount of attention in the past several years as potential advanced propulsion engines for air and space travel[1-4]. PDE's differ from conventional propulsion engines in two basic ways. First, as their name implies, they produce thrust in an intermittent or 'pulsed' manner as contrasted with the continuous thrust produced by most conventional propulsive systems. Second, they use a detonation instead of the more familiar deflagration process to convert the chemical energy of the propellants to thermal energy. Potential implementations of PDE's encompass both air-breathing and non-air-breathing applications. The air-breathing versions collect air from

* Post Doctoral Research Associate, UTSI
** Research Scientist, AEDC
*** Arnold Chair in Computational Mechanics and Professor of Mechanical Engineering, UTSI

the surrounding atmosphere to serve as the oxidizer, while the non-air-breathing versions carry their oxidizer on board. In the latter case, the device is sometimes referred to as a Pulsed Detonation Rocket Engine (PDRE) although both air-breathing and non-air-breathing devices are included in the generic category, pulsed detonation engine. Although PDE's have been considered for a variety of applications, their ultimate use will depend upon their weight, cost and propulsive performance as compared with competing conventional systems.

In its simplest form, a pulsed detonation engine is composed of a long tube (the detonation tube) that is closed at one end and open at the other. The propellants are fed into the tube through valves placed at or near the closed end, or perhaps through a series of valves distributed along the length of the tube. The propulsive cycle starts by filling the tube with fuel and oxidizer in such a manner as to provide a uniformly mixed, detonable mixture throughout the length of the tube. When the tube is filled, the mixture is detonated by a spark or other device at some appropriate location in the tube. The detonation can be initiated at the closed end, the open end, or somewhere in between. Practical implications appear to favor initiation from the closed end, although intermediate locations including open-end initiation provide similar thermodynamic performance. After the detonation wave has propagated the entire length of the tube, the hot gases are exhausted through the open end to provide thrust during a blow-down phase. Following the blow-down, the valves are again opened to fill the tube and the process repeats.

Detonations differ substantially from the more commonly observed deflagration process. They provide a large pressure rise as the reactants are burned and they propagate at supersonic speeds (few kilometers per second). The pressure rise afforded by a detonation represents one of the attributes that make a pulsed detonation device attractive for propulsive applications. The pressure rise from the combustion should allow a reduction in the pumping requirements for a given engine pressure level. The high speed of the detonation process implies that the combustion takes place so rapidly that it is essentially a constant volume process. The constant volume process represents a potentially more efficient thermodynamic cycle than a constant-pressure deflagration process and provides a potential increase in performance. In addition, the relative simplicity of the engine offers promise of potential lower costs and lighter weights.

The concept of using pulsed detonation devices for propulsive purposes has been around since the sixties, but improved understanding of the physics of detonation initiation has recently led to a resurgence of interest in the concept. Initial studies of the PDE concept conducted during the 60's and 70's consistently resulted in experimental measurements for which the predicted pressure rise fell far below analytical estimates. As a result, interest in the concept waned and development efforts ceased. Recent findings have suggested that the apparent reason for the poor pressure rise in these earlier experiments was that most failed to produce detonations and so could not achieve the advantages that come from the detonation process. Improved understanding of the initiation process and improved diagnostics to verify that detonations are achieved have recently allowed detonations to be produced in a reliable and repeatable manner[5]. This success has once more attracted interest in PDE's as a potential propulsion device.

Reviews of previous works on PDE's in the literature can be obtained from Eidelman *et al.*[1] and Bratkovich and Bussing[2]. Kailasanath *et al.*[3] present a review of computational studies

of PDE's. A recent study by Cambier and Tegner[4] focuses on optimization of PDE performance by analyzing the effects of different cycling parameters, fueling strategies and nozzle geometry. The present paper is aimed at addressing PDE operational characteristics from a global perspective to identify the significant trends that can be expected in a propulsive environment. The paper presents parametric studies of a variety of effects including ambient pressure, nozzle geometries and non-ideal effects such as performance penalties associated with purge mass injection.

Model Formulation

The literature on PDE's contains projected performance levels that differ by nearly a factor of two in specific impulse. This has created a substantial amount of uncertainty in the true attributes of such a system. Reliable mission studies are needed to identify those arenas where this new propulsive system can contribute but, before they can be useful, these mission studies require both higher fidelity performance estimates as well as parametric predictions of the effects of altitude and Mach number on performance. The focus of the work described in the present paper is addressed toward these issues.

Because the emphasis in the present study is on obtaining parametric performance estimates, it is important that the resulting model provide rapid turnaround time. Accordingly, the focus is on capturing the dominant physical effects with simple, global models. The primary characterizing feature of PDE's is the dominant unsteady, wavelike nature of its operation. To simulate these unsteady effects, the parametric studies are based upon the unsteady equations. Two levels of modeling are used. In the first, the quasi-one-dimensional equations are solved along with simplified chemistry to provide qualitative design estimates of the performance characteristics[6]. The global character of the chemistry is incorporated by means of single-step reaction, and constant specific heat. In the second, a two-dimensional unsteady analysis with full kinetics is used[7]. This allows selected observations from the one-dimensional results to be calibrated. Finally, we have used a one-dimensional steady analysis of conventional rocket engines with the same heat release and specific heats as in the PDE calculations to give back-to-back comparisons between the PDE predictions and conventional engines. Overall, comparisons between the present single-step formulation and the full-chemistry computations indicate the trends predicted by the two different formulations are essentially identical and that it takes relatively little effort to select heat release rates and specific heat ratios that also provide realistic levels of performance.

PDE Operation

It is convenient to divide the processes occurring in a single cycle of a pulsed detonation engine into three phases: (a) the *fill time* during which the chamber is filled with reactants; (b) the *detonation travel time* during which the detonation is initiated and traverses through the chamber consuming the reactants; and (c) the *blowdown time* during which the bulk of the combustion products are expelled by a system of compression and rarefraction waves. After the blowdown process, the fill process starts again and the cyclic operation continues. Included in the cycle are additional effects such as finite valve response rates and purge gases as discussed below. Note that these three phases are not mutually exclusive since the

blowdown process occurs continually throughout the cycle and is not limited to only the blowdown phase.

Periodic operation requires that all of these processes be properly sequenced by some control mechanism. For the results in the present paper we have controlled the global sequencing by specifying the valve opening time. For finite response valves, this specified time corresponds to the time at which the signal is given to open the valve. The valve thus opens in a precisely periodic manner. The timings for the remaining processes in the cycle (such as valve closing or detonation initiation) are then determined from the solution and so vary slightly from cycle to cycle.

Two valve closing procedures have been used. In the one, a chemical 'sensor' is placed at a particular location in the tube that senses the arrival of the reactant-product interface and gives a signal to close the valve. In the second, the total mass of propellants in the tube is computed and the signal to close the valves is given when the desired amount of propellant has been delivered. For either of these criteria, the valve closing time involves some judgement. First fresh propellants continue to flow into the chamber after the signal for closing the valve has been given (unless the valve is infinitely fast). Second, even though the detonation moves very rapidly, it takes a finite amount of time to traverse the tube. In this time the fresh reactants continue to move through the tube and can be lost to the outside before the detonation arrives. Consequently, the signal to close the valve must anticipate both the valve closing interval and the detonation propagation time while striving to fill the desired fraction of the tube.

The propellant flow rate through the inlet valve is determined by specifying the stagnation pressure and temperature of the incoming gas along with its chemical composition and a valve orifice area. The reservoir conditions are analogous to a pump feed into a reservoir. These key geometric parameters are summarized in Fig. 1.

A very simple model is used for finite-rate valves. During the opening process, the valve area is increased linearly with time from zero to the full area in a specified valve response time, τ_{valve}. Valve closing is treated in an analogous manner.

In conjunction with the valve opening process, we also make allowance for a purge gas that places a slug of inert buffer gas between the hot, burned gases, and the cold incoming propellants. This purge gas ensures that the hot products do not come in contact with the freshly injected reactants and initiate combustion prior to the detonation. The amount of purge gas injected is specified as a percentage of the total mass injected during the fill phase.

A final important issue in PDE modeling is the method used for initiating the detonation. It is not practical to simulate the initiation process in design-level studies. It is, however, imperative that a detonation be initiated. In the present computations, detonation initiation has been attained by increasing the temperature of a volume of gas adjacent to the injector region to 2500 K and simultaneously increasing the pressure of the gas in this volume by a factor of 30. For the present computations, this length of this initiation zone was generally chosen as 1.2 mm.

Results

A series of computations has been performed to assess the effects of a wide variety of parameters including ambient pressure, nozzle geometry, the amount of purge mass flow, characteristic valve operating times etc. All computations shown are for periodic conditions obtained by starting from some arbitrary initial condition and continuing until periodic cyclic operation is reached. This typically requires three to four cycles. In most cases the initial cycle was started with the chamber filled with reactants at atmospheric pressure and a temperature of 300 K except for the region near the closed end where high pressure and temperature conditions for initiating the detonation are specified. The eventual periodic results are independent of the initial conditions. After periodic conditions have been reached, performance quantities such as specific impulse, thrust, frequency of operation, etc are computed for the multicycle PDE operation at the chosen operating conditions.

The gas properties are specified using $\gamma = 1.25$, $C_p = 2771.4$ $J/Kg\ K$, and a heat content of 7.77×10^6 J/Kg. The length (L) for all computations is 0.5 m. The thrust and total mass flow rate are computed on the basis of a circular tube with a diameter of 4.0×10^{-2} m. For most of the results, the reservoir pressure (P_r) is 5×10^5 Pa and the maximum valve area is ten percent of the cross sectional area at the PDE inlet. Unless mentioned otherwise, the valve is closed at a time such that the detonation wave and the reactant-product interface reach the exit at approximately the same time. Some results are presented for which only a portion of the tube was filled.

For the computations presented, the length of the detonation chamber was taken as 0.5 m, and was represented by 2500 equally spaced grid points. This corresponds to a cell width of 0.2 mm. This resolution was chosen on the basis of computations on grids of 625, 1250, 2500, 5000 and 10,000 points. This grid resolution study indicated that the results at 2500 points are reasonably independent of the grid spacing. The finer grids give minor improvements in the diffusion of contact surfaces, but the results are globally similar and the present grid is ample for deducing PDE operational trends. As a quantitative example of the changes observed as a result of grid refinement, we quote here the thrust levels for a case with a diverging nozzle for which the results are most sensitive to grid refinement. On three successive grids (2500, 5000 and 10,000 points respectively) the calculated values for the thrust [N] computed were 183.7, 182.6 and 182.8 for a back pressure ,$P_{amb} = 0.0$, and 127.9, 126.8 and 127.1 for a back pressure, $P_{amb} = 1.0$ atm, respectively.

Effects of Ambient Pressure

One possible application for pulsed detonation rocket engines is as an upper stage propulsion system for space flight. For such applications, an issue of interest is the dependence of PDE performance on the ambient pressure (P_{amb}). The implications of operating a PDE at low ambient pressures are of particular interest. To investigate the manner in which PDE operation changes with altitude, we begin by presenting the results of a parametric study of the effects of ambient pressure.

To introduce the study, we first consider the results for a reference case with nominal values for all parameters whose effects are studied. Subsequent solutions of the effect of changing the various parameters are studied by varying one at a time with respect to this reference case.

The reference case involves a constant area duct with no area variation in the nozzle. The valve opening process is controlled by the injection pressure, P_{inj} which is set to one atmosphere. As soon as the pressure at the closed end falls below the threshold value of 1.0 atm, the signal is given to open the valve. Instantaneous valve action (i.e., $\tau_{valve} = 0$) was assumed. To complete the definition of the reference case, a purge rate of 5% of the total injected mass was used.

As noted above, we have divided the period of operation into three phases. The times attributed to these three phases are given in Fig. 2a for PDE operation of this reference case. A cursory inspection of the plot indicates that the fill time is the largest of the three phases of the cycle, while the detonation travel time is the shortest. This is characteristic of most PDE operations. The results show that the overall cycle time gradually decreases (the frequency increases) as P_{amb} is decreased from 1.0 *atm* toward the vacuum limit. This decrease is a direct result of using the injection pressure as the valve opening signal. In terms of the three phases of the cycle, we also see that both the blowdown time and the fill time decrease with reduced pressure. It is the changes in these two portions of the cycle that causes the frequency to increase. The reason for this behavior is that the overall pressure in the chamber decreases with the ambient pressure. Lower ambient pressures imply faster mass efflux. Lower chamber pressures also imply that less mass is required to fill the chamber, and so the (essentially) constant mass inflow rate is terminated in less time. The fill time therefore decreases because the valves need to be open for a shorter time to inject the smaller amount of mass per pulse required to fill the chamber volume. In addition to the changes in the fill time, the blowdown time (determined by the time required for the head end pressure to drop to 1.0 atm) also decreases because the lower chamber pressure decreases to the fixed injection pressure in less time since it started from a lower pressure.

The variation of the specific impulse (I_{sp}), thrust, frequency and average mass flow rate, with the ambient pressure are shown on Fig. 2b-e for the reference and a number of other cases. First looking at the reference case, the results show that the specific impulse increases substantially as the ambient pressure is lowered (Fig. 2b). This behavior is similar to that seen for rocket engine operation and arises because of the increased impulse per pulse from the pressure-area term. The corresponding increase in thrust (Fig. 2c) arises primarily because the frequency increases (Fig. 2d). Figure 2e also shows that the mass flow rate of the reference case decreases slightly as the pressure is reduced. This decrease arises because the fill time decreases more rapidly than the cycle time (i.e., T_{fill}/T_{osc} decreases, where T_{fill} and T_{osc} are the fill time and the total oscillation period, see Fig. 2a).

Inherent in the results discussed above is an important effect of the impact of the backpressure. When the ambient pressure is one atmosphere, the PDE experiences inflow over a substantial fraction of the cycle. As the ambient pressure is lowered below 1.0 atm, the fraction of the cycle during which reverse flow occurs diminishes. At sufficiently small values of P_{amb} all reverse flow disappears and the proportion of time that the flow is choked increases. This choked flow portion of the cycle eventually prevents the pressure in the tube from decreasing further and enables a finite pressure to remain in the tube even at vacuum conditions. Since the mean chamber pressure is relatively higher than P_{amb}, more thrust is obtained. Note that unlike the frequency and I_{sp} which monotonically increase when P_{amb} is lowered, the thrust first decreases (dominated by the decrease in the mass flow rate) and then increases (dominated by the increase in the frequency).

Purge Gas Effects

Purge gases are needed between the hot burned gases and the incoming unburned propellants to prevent pre-mature combustion before the detonation arrives. The effect of increasing the purge flow rate from 5 to 10% of the total mass injection is also shown in Figs. 2(b-e) (compare triangles to squares). On average, this 5% increase in purging results in roughly a 4% decrease in the specific impulse. Similarly, when the purge was increased from 5% to 15% (not shown), the average decrease in I_{sp} was about 8%. Thus the fractional decrease in I_{sp} caused by adding a fraction of purge gases to the propellant mass injected into the chamber, is marginally lower than the fractional increase in the purge. To first order, the variation is percent for percent, indicating that the penalty associated with buffer gases between charges is not severe so long as all propellants are already carried on board. The slight difference from a straight proportionality can possibly be attributed to thrust generated from the cold gas as it is injected into the chamber.

Effect of Injection Pressure

Next, the changes obtained by decreasing the threshold injector end pressure (P_{inj}) from 1 atm to 0.4 atm are studied (compare diamond symbols with square symbols on Figs. 2(b-e)). Note that changing this control parameter causes a very minor decrease in the specific impulse at lower pressures (Fig. 2b). Since the injection process is not started till the pressure at the head end falls to a lower value, reducing this threshold value increases the blowdown time and as expected, the frequency of the PDE operation decreases resulting in lower thrust. These changes are a measure of $\Delta T_{bl}/T_{bl}$ where T_{bl} is the blowdown time in the reference case and ΔT_{bl} is the time interval during which the closed end pressure decreases from 1 atm to 0.4 atm.

Effects of Variable Area Nozzle

Variable area nozzles are staple components on conventional steady-flow propulsion systems. Their behavior in this unsteady application is clearly of much interest. The major issue in PDE nozzle design is to identify a 'pressure ratio' for the widely varying levels of pressure that are seen throughout the cycle. The effect of adding a variable area section is first studied by considering a divergent conical nozzle at the exit. The area expansion ratio is 4.0 and the length of the nozzle section is one-third of the total PDE length, which is maintained at 0.5 m. (The constant area section is 0.33 m while the nozzle length is 0.17 m.) The impact of the divergent nozzle on the specific impulse shown on Fig. 2b and can be compared to the constant area device by comparing the circles with the squares. At high ambient pressures, the nozzle is seen to be detrimental. The presence of the nozzle causes the I_{sp} to decrease. On the other hand, at low values of P_{amb}, the nozzle results in a significant increase in I_{sp}. This occurs because the divergent nozzle acts like a diffuser at high back pressures and decelerates the flow and decreases the thrust, while at low back pressures it acts as a nozzle and accelerates the flow and increases the thrust. In addition, at high back pressures, the presence of the nozzle increases the fraction of time the exit pressure drops below the ambient value and reverse flow into the PDE occurs, while the opposite is true at low backpressures.

One implication of operating the PDE at low P_{amb} is that the chamber pressure decreases significantly during the blow down process. In the reference case, for low P_{amb} the exit flow is sonic throughout the PDE operation. One way to retain a higher average pressure in the chamber is through placing a convergent section in the nozzle. This, of course, raises issues with heat transfer and cooling, but the potential benefits appear promising. Computations with a convergent divergent nozzle have also been completed and are given on Fig. 2b-e by the x's. The converging portion of the nozzle was defined by a cubic equation with second derivative continuous matching to the constant area section. The converging section was allowed to run between $(2/3)L < x < (5/6)L$. A matching divergent portion was added as a mirror image about the throat location to bring the entire PDE length again to L. Thus the nozzle exit area for this converging-diverging nozzle is the same as the inlet area. For the results shown here, the throat area was chosen as half the inlet area.

The first observation of the effects of the converging-diverging nozzle is that the specific impulse remains essentially unchanged at high back pressures (as compared to the constant area case), but the impulse is significantly higher at low back pressures. The presence of the convergent section aids in obtaining a higher chamber pressure and this increases the blow down time causing both the frequency (see Fig. 2(d)) and the thrust (Fig. 2c) to decrease. As compared to the divergent nozzle, the C-D nozzle is slightly less effective at low backpressures, but a fair comparison would entail also looking at a C-D nozzle whose exit area was equal to that of the divergent area. At high ambient pressures, the convergent divergent nozzle has negligible influence on the frequency but due to the reduction in the chamber volume associated with the use of the convergent divergent nozzle (the volume is 83% of the volume for the reference case), the fill process is characterized by lower amount of mass injection per unit time resulting in reduced thrust (see Figs. 2(c,e)). Note, however, that taking the ratio of Figs. 2d and e shows that the mass per pulse is increased, so the throat section raises the pressure sufficiently to offset the decrease in volume. Overall, the impact of adding a throat downstream of the PDE appears attractive.

Effect of Nozzle Area Expansion Ratio

As a second set of examples we consider the performance changes associated with variations in the expansion ratio of a conical divergent nozzle. These computations were performed at vacuum conditions where the presence of the nozzle is expected to yield the maximum gain in I_{sp}. One significant difference with respect to the previous examples is that the control parameter used for opening the valve was determined by specifying the PDE frequency at 500 Hz instead of being determined by the injector head end pressure (i.e., instead of bootstrapping the PDE operation). In reality constraints due to valve response time (τ_{valve}) etc. dictate the frequency of operation. In this example, no purge gas is injected.

Note that during the fill phase one attempts to fill the volume of the PDE with reactants, and the mass of reactants injected during the fill process depends on (a) the chamber pressure, its spatial variation during the fill process, and (b) the velocity of the reactant-product interface (note that as this velocity increases, the valve closing should occur earlier to ensure that the detonation and the interface reach the exit around the same time). Since the above two factors are significantly altered by the use of a nozzle, we compare two different degrees of filling the chamber ('partial' and 'total' filling) to better understand the effect of including the nozzle.

In comparing these two cases, we define 'total' filling, as the fill process used in the previous examples. Specifically, the fill process is ended at a time such that the detonation and the interface reach the exit of the nozzle at approximately the same time. The 'partial' filling case is defined in an identical manner except that the fill process was terminated at a time that would cause the detonation and the interface to reach some location partially along the tube. Thus, the tube was 'partially' filled. The results for partial filling were chosen so that the detonation reached the interface at the nominal location of the start of the nozzle ($x=0.67L$).

There are several phenomena relevant to the case involving partial filling. For the partial filling fraction chosen ($(2/3)L$), the inlet injection valve had to be closed when the reactant-product interface reached approximately $x/L = 0.5$. The low back pressure induces large flow velocities throughout the entire chamber for at least a portion of the cycle. When convected at these high speeds, the interface travels a significant distance downstream before the detonation reaches it. Subsequently, due to the lack of reactants, there is no detonation downstream of that location and the detonation transitions to a shock that traverses to the exit. These high velocities caused difficulties in ensuring proper filling of the tube to the desired lengths, and increases the error bands on the present results.

The I_{sp}, thrust and mass flow rates for the total and partial filled cases are shown as a function of the nozzle area expansion ratio in Fig. 3(a-c) for expansion ratios ranging from 1 to 12. Comparing the specific impulse of partial and total filling in Fig. 3(a) shows that in general a higher specific impulse is obtained for the case of partial filling than for the case of total filling. An increase in I_{sp} due to filling a smaller fraction of the chamber has also been observed in earlier analysis of PDE performance[4]. At present we are still studying this trend to understand the precise reasons for these differences.

Note that due to operation at a lower mass flow rate, the partial filling case which has a higher I_{sp} is characterized by a lower thrust. In both the cases of partial and total filling, when the area expansion ratio approaches unity (i.e., the constant area case) the thrust increases (see Fig. 3(b)).

For a large area expansion ratio, the velocity of the reactant-product interface is large enough such that the fill process stops before the interface reaches the nozzle region (to ensure that the detonation and the interface reach the exit around the same time). Thus, although the presence of the nozzle results in a larger PDE volume, this volume is not filled with the reactants for the chosen nozzle length (one-third of the total length).

Effects of Partial Filling

The periodic operation of a pulsed detonation engine requires the specification of a large number of parameters and each cycle involves many complicated wave interactions. One parameter of interest is the percent of the tube that is filled with combustible mixture prior to each detonation. Although the entire tube could be filled in each cycle, it is of interest to assess performance when the tube is only partially filled. We present in Figs. 4, 5, and 6 the results of a series of computations for a fixed tube length, L, in which the fraction of the tube that was filled with propellants, Ld, was treated as a parameter. In particular, the ratio, Ld/L,

was varied from 0.4 (the first 40% of the tube was filled) to 1.0 (the entire tube filled with propellants). Results for four sets of computations are presented on these figures. The four sets involve two different fixed periods of oscillation, 5.0 ms (200 Hz) and 8.0 ms (125 Hz), and two different ambient temperatures. The two ambient temperatures correspond to two extremes. In the first, it is assumed that the gas that is re-ingested through the open end when the pressure falls below ambient is at the temperature of the outside environment. In the second case, it is assumed that the re-ingested gas is comprised of the hot gas that has just been expelled. It is to be expected that the real (multi-dimensional, multi-pulse) operation will fall between these two limits so that these two calculations bracket the physical result. All results correspond to an ambient pressure of one atmosphere. Figure 4 shows the mass of propellants used per pulse; Fig. 5 shows the thrust level; and Fig. 6 shows the specific impulse. We consider the mass per pulse first since its variation is the most straightforward.

The mass per pulse given on Fig. 4 shows that increasing the fill fraction increases the mass per pulse almost proportionately independently of the pulse repetition rate or the ambient temperature. Thus, for a fill fraction of 50% the mass per pulse is approximately half that for a fill fraction of 100%. This implies that the pressure level in the tube (at the end of each pulse) is nearly independent of the period, or the ambient temperature. To be sure, there are minor differences when either of these are changed, but the results are reasonably consistent.

The thrust variation with fill fraction follows directly from the mass per pulse and the pulse rate as Fig. 5 shows. Increasing the frequency (compare the two 8.0 ms data sets with the two 5.0 ms sets) increases the thrust in a nearly proportional manner. In addition, for a given period, increasing the fill fraction increases the thrust in a nearly proportionate manner. Since the mass per pulse is to a first approximation independent of the pulse rate for a given value of Ld/L and varies linearly with Ld/L as Ld increases, the impulse per pulse is nearly constant and the thrust scales directly with both the number of pulses per second and the fill fraction.

The results for the specific impulse (Fig. 5) are, however, more complex. Looking first at the 5.0 ms case with cold ambient gas (square symbols connected by solid line), we see that increasing the fill fraction from 0.4 to about 0.7 increases the specific impulse, but that continued increases to 1.0 cause the specific impulse to decrease again. Thus, at this condition, a fill fraction of 0.75 represents a local maximum. The increase in Isp at the lower values of Ld/L, is correlated with an increased magnitude of inflow into the open end of the tube, but it is not clear is this is a cause or an effect. When the period is increased to 8.0 ms (circular symbols with long-dashed line) the same general trend is observed, except the entire curve is shifted downward by about 5-7 seconds. In addition, the peak now shifts from 0.75 to 0.70. These results show that stopping the cycle sooner improves performance, but this trend is not followed at all conditions.

The two remaining sets of data on Fig. 6 are more convoluted than these first two. In general, re-ingesting hot gas increases the specific impulse as opposed to the cold ingestion condition, but there are some conditions for which the change in ambient gas temperature has no effect. Similarly, there is a general tendency for the shorter period case to exhibit higher specific impulse, but for some values of Ld/L, the Isp is the same for both periods. Overall, the results shown on this figure indicate that the specific impulse is subject to 'tuning' to the details of a specific condition. Further, the Isp variation caused by this tuning effect is

approximately 10% of the total Isp. Such results suggest that practical implementations of PDE's will need to be carefully controlled to provide operation at the maximum specific impulse, and that failure to do so will result in substantial penalties.

A further indication of the complexity of the flow dynamics inside the cycle is given by the *x-t* diagram on Fig. 7. This figure corresponds to the $Ld/L = 0.4$ results of Figs. 4, 5, and 6, and shows the left- and right-running characteristics along with representative particle paths in the vicinity of the location where the detonation overtakes the interface between the fresh propellant and the burned gas from the previous cycle (at the $x \approx 0.2$ location). As can be seen, the discontinuity slows from a detonation to a shock at this interface, and reflects as an expansion fan propagating toward the left-hand (closed) end. The streamlines between the shock and the interface are very closely spaced indicating high density in this region, and lower densities elsewhere. The complexities of this single relatively simple interaction are clearly multiplied throughout the cycle and give rise to many possible parametric effects whose understanding requires detailed analysis of a specific engine configuration. In addition they are strongly dependent upon the ambient pressure (and the ambient temperature as noted above) as well as the pulse repetition rate, the fill-fraction, etc. The addition of a variable area nozzle would also affect local events dramatically. These minute differences inside a given cycle clearly indicate the necessity of using one-dimensional unsteady analyses, while also pointing out the need for assessing multi-dimensional effects to validate the one-dimensional models.

Effects of Nozzle Geometry

As a final example, we consider some results at the low ambient pressure limit. The results on Figs. 8, 9, 10 and 11 show the performance at vacuum conditions for a family of conical nozzles. The variations used in defining the nozzle family are shown in Fig. 8. Here we define the parameter, *Xnoz/L*, where *Xnoz* is the location at which the divergent section starts, and *L* is the total length of the engine. Note that as *Xnoz/L* goes to zero, the geometry approaches a geometry that diverges over its entire length. In all cases, the inlet area, the constant area section, and the exit area were held fixed. The exit area was four times the area of the constant area section. As the value of *Xnoz* is decreased, the volume of the nozzle increases as shown in Fig. 9. Note that as the nozzle volume increases the mass per pulse (also shown on Fig. 9) changes in the manner opposite to the nozzle volume. (Note the entire geometry—constant area plus nozzle—is filled with propellant in these examples.) The opposite trends between mass per pulse and chamber volume implies that the average pressure and the velocity in the chamber at the end of the fill period off-set the volume increase. (This opposite trend between mass per pulse and chamber volume highlights the importance of comparing results from the periodic state, not from the first pulse. For the first pulse condition, the mass in the chamber will be proportional to the chamber volume.)

The thrust and specific impulse for these cases is shown on Figs. 10 and 11. As can be seen, both the thrust and the specific impulse continue to increase as the conical nozzle is shortened and its angle is increased (to reach the same final area). These nozzle effects are strongly dependent on altitude as noted previously[6], but suggests that the nozzle geometry represents a very important area for additional research. Optimizing a nozzle for unsteady flow is much different than optimizing a nozzle for steady flow.

Summary and Conclusions

Pulsed detonation engines offer a potential new propulsive concept for space propulsion applications. The engines differ from current rocket engines in two dominant ways. They are intermittent rather than continuous, and they burn the fuel by means of a detonation rather than a deflagration. The detonation provides a significant pressure rise that holds promise of reducing pumping requirements thereby simplifying the engine and possibly reducing weight and cost. Proponents have also suggested that the constant volume combustion might give improved specific impulse, but this remains speculative.

The present paper uses results from an unsteady one-dimensional computational model of the PDE to obtain the general performance trends that can be expected for pulsed detonation operation. Because of the many parameters involved, a constant specific heat, single step reaction thermodynamics is used to provide more intuitive understanding of the results and to allow a broader range of parameters. These simplified one-dimensional results are compared with those from a two-dimensional, full kinetics, model to assess primary shortcomings from the simplifications.

The results indicate that it is imperative to include the effects of multicycle, as opposed to single pulse, operation to obtain meaningful trends. In all cases considered, multi-cycle operation is readily attained after some three to four pulses. The operational cycle for a PDE is divided into three parts, the detonation travel time, the blowdown time, and the fill time. At high pulse repetition rates the fill time dominates, while at low rep rates (which are more typical of envisioned hardware operation) the blowdown time dominates.

Some of the characteristics associated with the use of variable area nozzles have been discussed. In general, the nozzle provides performance benefits at high altitudes, but leads to a performance deterioration at low altitudes. Holding the nozzle length fixed and increasing the expansion ratio improves specific impulse at high altitudes expressing the well-known benefits of increased expansion ratio for conventional rocket engines. Fixing the nozzle expansion ratio and changing the nozzle length while holding the overall engine size fixed (shortening the constant area section of the detonation tube) results in a decrease in the specific impulse.

Finally, changing the percent of the tube that is filled with propellant can change the specific impulse by on the order of 10%. This appears to be the result of self-tuning in various portions of the cycle so that there is some possibility of finding an optimum Isp at various conditions. The analysis needed for establishing and making use of such tuning mechanisms can certainly be accomplished for a given engine, but it is difficult to make general observations as to preferred regions of operation.

References

1. Eidelman, S., Grossmann, W., and Lottati, I., "Review of Propulsion Applications and Numerical Simulations of the Pulse Detonation Engine Concept," Journal of Propulsion and Power, Vol. 7, No. 6, pp.857-865, 1991.

2. Bratkovich, T. E., and Bussing, T. R. A., "A Pulse Detonation Engine Performance Model," AIAA paper 95-3155, July 1995.

3. Kailasanath, K., Patnaik, G., and Li, C. "Computational Studies of Pulse Detonation Engines: A Status Report," AIAA Paper 99-2634, June 1999.

4. Cambier, J.-L. and Tegner, J. K., "Strategies for Pulsed Detonation Engine Performance Optimization," Journal of Propulsion and Power, Vol. 14, No. 4, pp.489-498, 1998.

5. Brophy, C. M. and Netzer, D. W., "Effects of Ignition Characteristics and Geometry on the Performance of a JP-10/O_2 Fueled Pulse Detonation Engine," AIAA Paper 99-2635, June 1999.

6. Mohanraj, R. and Merkle, C.L., "A Numerical Study of Pulse Detonation Engine Performance," AIAA paper 2000-0325, January 2000.

7. Ebrahimi, H. B. and Merkle, C. L., "A Numerical Simulation of the Pulse Detonation Engine with Hydrogen Fuels," AIAA paper 99-2259, June 1999.

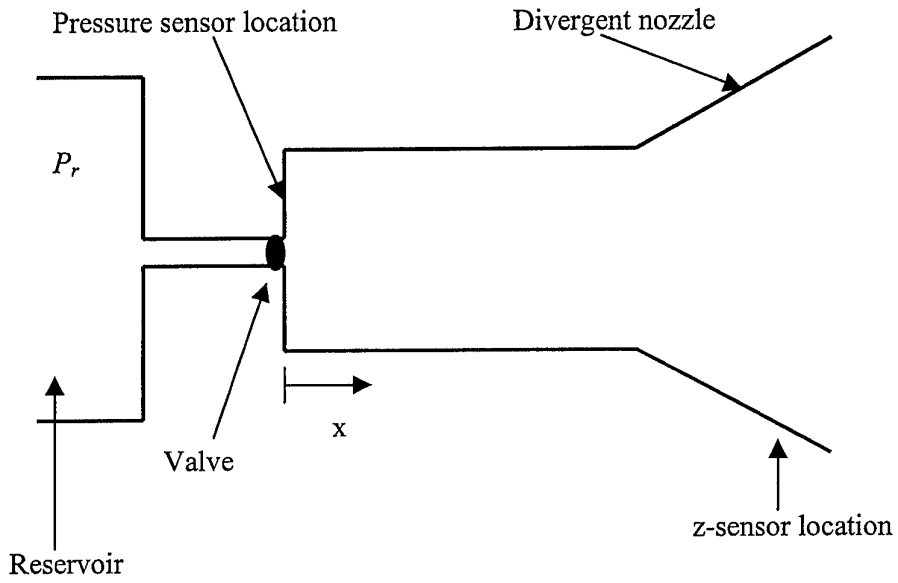
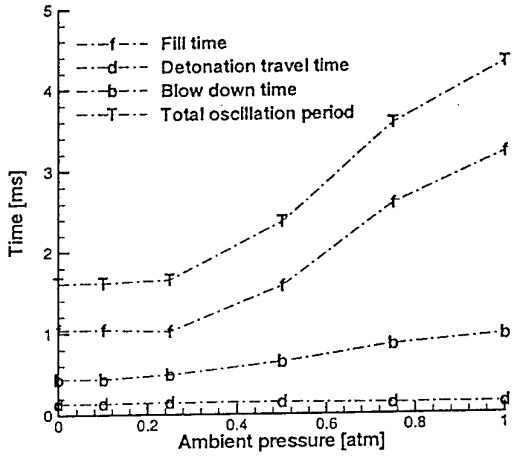
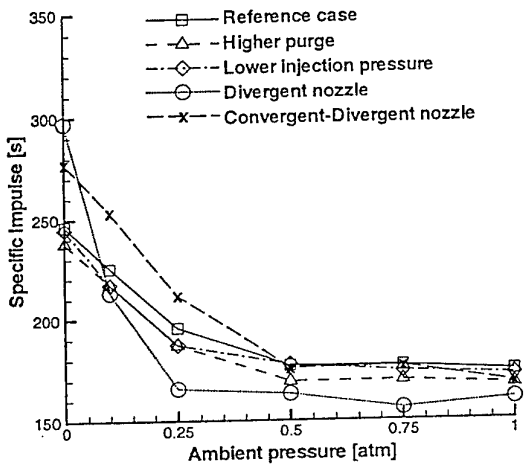


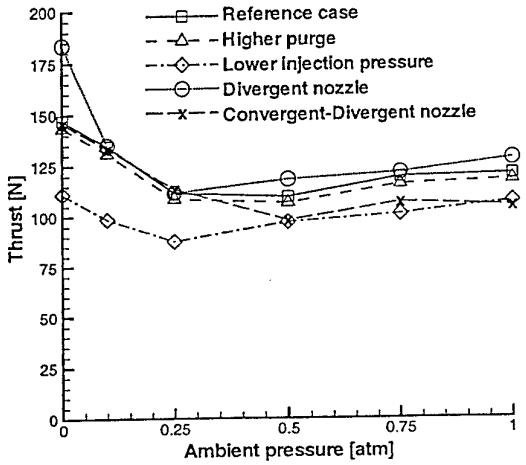
Figure 1: A Schematic of the Pulse Detonation Engine.



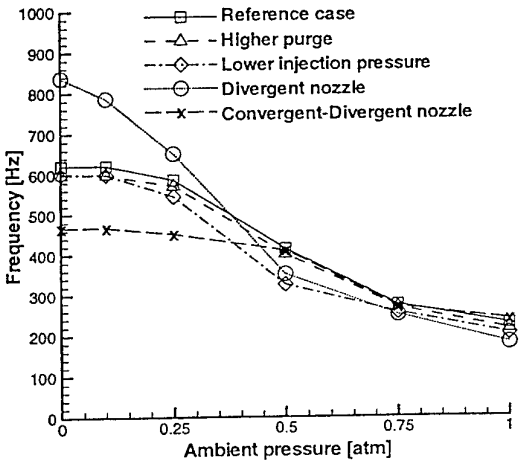
(a) The different characteristic times associated with the PDE operation for the reference case.



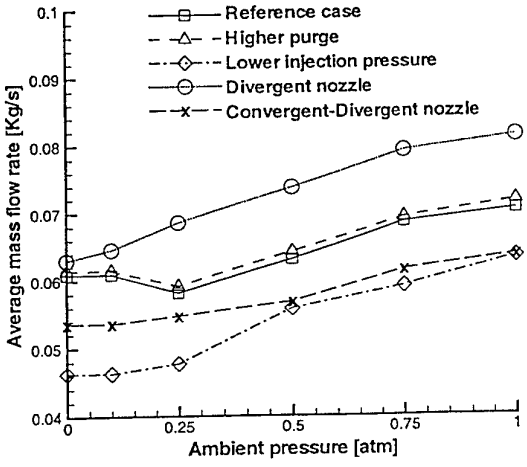
(b) Specific impulse



(c) Thrust

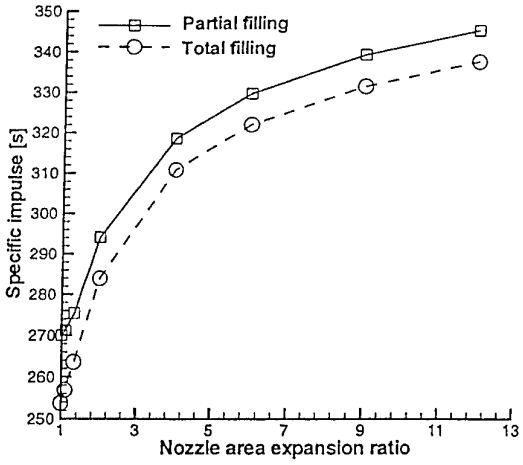


(d) Frequency of PDE operation

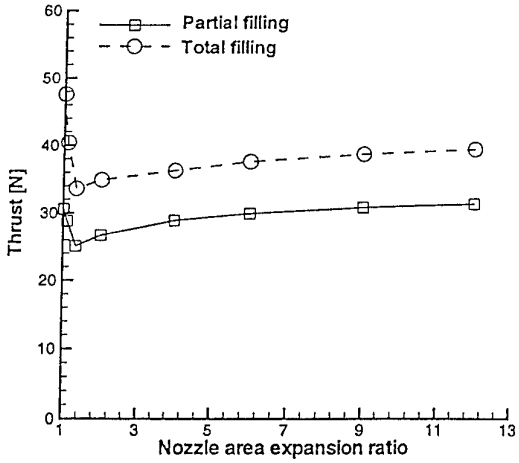


(e) Average mass flow rate

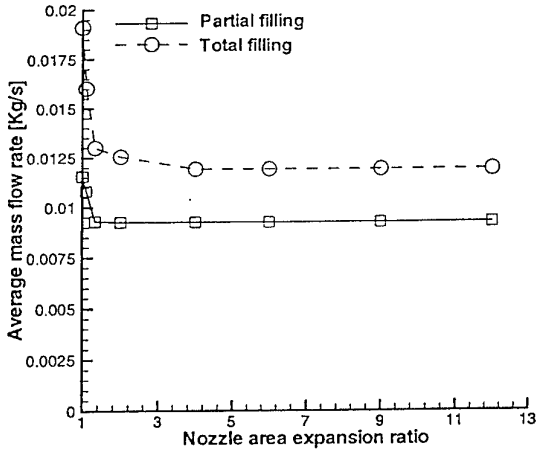
Figure 2: The effect of ambient pressure on the performance of the PDE for different cases: (i) reference case - constant area geometry, 5% purge, P_{inj} = 1.0 atm; (ii) 10% purge; (iii) P_{inj} = 0.4 X 105 *Pa*; (iv) conical divergent nozzle - area expansion ratio of 4; (v) convergent divergent nozzle - area contraction ratio of 0.5 at the throat.



(a) Specific impulse



(b) Thrust



(c) Average mass flow

Figure 3: The effect of nozzle area expansion ratio: Conical divergent nozzle, P_{amb} = 0.0, PDE operated at 500 Hz, no purge.

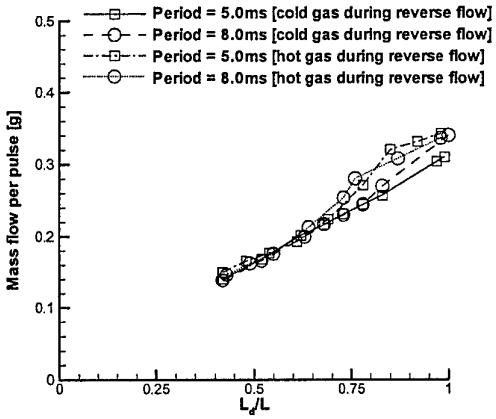


Fig. 4 Mass injection per pulse as a function of chamber fill fraction for two periods and two re-ingestion conditions.

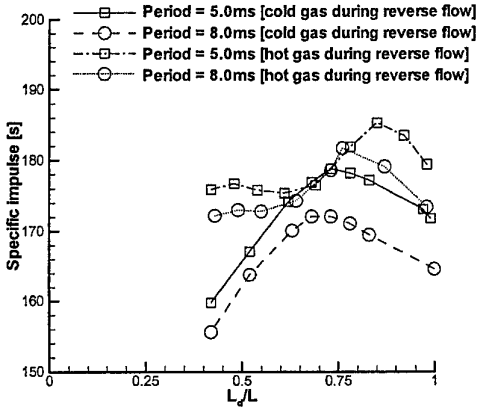


Fig. 6. Specific impulse as a function of chamber fill fraction for two periods and two re-ingestion conditions.

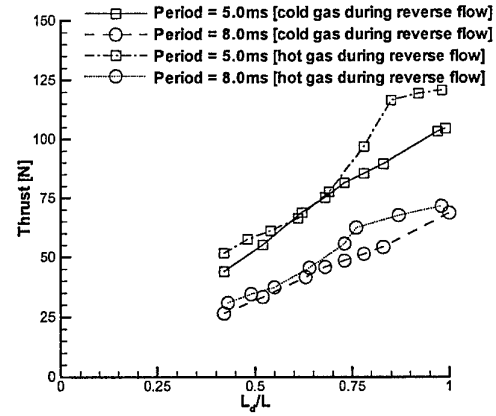


Fig. 5. Thrust as a function of chamber fill fraction for two periods and two re-ingestion conditions.

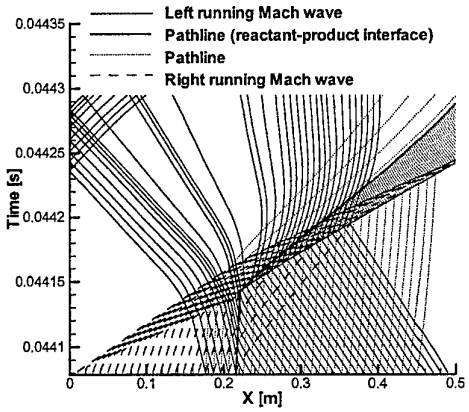


Fig. 7. *x-t* diagram for detonation transitioning to shock wave at an interface between cold unburned propellant and hot burned gases.

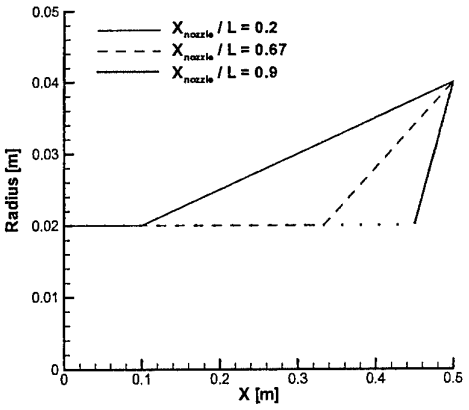


Fig. 8. Geometric configurations for parametric study of nozzle shape.

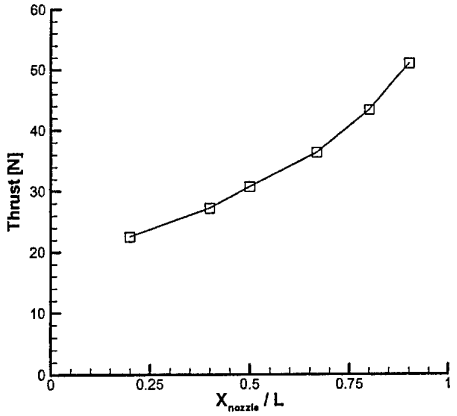


Fig. 10. Variation of thrust as a function of nozzle shape parameter in Fig. 8.

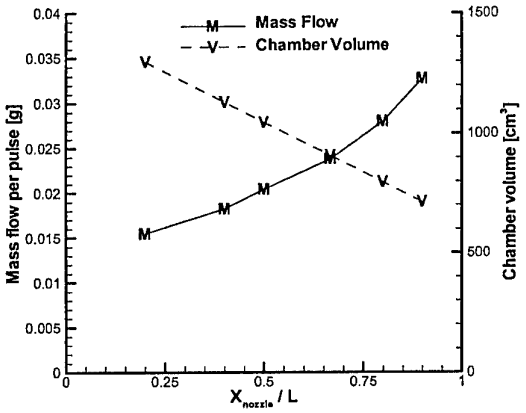


Fig. 9. Variation of mass per pulse and chamber volume as a function of nozzle shape parameter in Fig. 8.

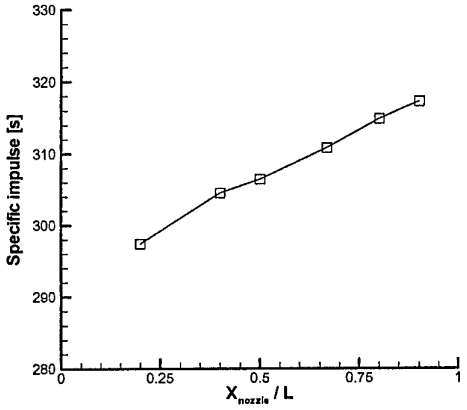


Fig. 11. Variation of specific impulse as a function of nozzle shape parameter in Fig. 8.

In-Flight LOX Collection : System Aspects and Experimental Studies

P. Hendrick
Royal Military Academy
Applied Mechanics Dept.
Ave de la Renaissance, 30
1000 Brussels
Belgium
Hendrick@mapp.rma.ac.be

F. Breugelmans
von Karman Institute
Turbomachinery Dept.
Chaussée de Waterloo, 72
1640 Rhode-Saint-Genèse
Belgium
fb@vki.ac.be

C. Promper & M. Saint-Mard
Techspace Aero
Space Dept.
Route de Liers, 121
4041 Milmort
Belgium
cpromper@techspace-aero.be

P. Ngendakumana
University of Liège
Applied Thermodynamics
Chemin des Chevreuils, 7, Bldg B49
4000 Sart Tilman (Liège)
Belgium
pngendakumana@ulg.ac.be

D. Bizzarri
University of Liège
Industrial Chemistry Laboratory
Allée de la Chimie, Bldg B6
4000 Sart Tilman (Liège)
Belgium
d.bizzarri@ulg.ac.be

ABSTRACT

The in-flight LOX collection concept, consisting in collecting air during the atmospheric phase of a launch and storing the liquefied oxygen enriched air ("LOX") after separation from nitrogen for the subsequent rocket propulsion phase, is applied to a HTOHL Two Stage To Orbit (TSTO) with a high supersonic staging. The staging occurs between Mach 4 and 5 and the collection phase takes place mainly in cruise at Mach 2.5 with a moderate collection ratio (maximum 3.0). The 1st stage is propelled with turbofan-ramjet engines and the LOX collection plant is highly integrated with the turbofan part. The 2nd stage can be reusable or expendable.

The paper will present three aspects of the launcher study : the first stage propulsion (von Karman Institute), the LOX collection plant pre-design (Techspace Aero) and the integration of the results of these two studies in a pre-design tool used to evaluate the performance of such a launch vehicle (Royal Military Academy).

The feasibility of the integrated collection-propulsion system is analysed through cycle studies and examination of performance in design and off-design engine operation. Different engine configurations and LOX collection plant variants are investigated and their performance along the entire trajectory are calculated. After the definition of the most appropriate engine and collection cycle, a complete turbomachinery design is performed and a collection plant mass and volume evaluation is made.

Another application of in-flight LOX collection is also presented : a large subsonic airplane collecting LOX at subsonic speed and belly-launching an orbiter at a subsonic speed as well.

Finally, experimental developments related to in-flight LOX collection are shown, especially the existing Vortex Tube separation device (University of Liège) and the Rotary Distillation Separator now under development in Belgium (University of Liège and Royal Military Academy).

NOMENCLATURE

LOX	Liquid oxygen
LCP	LOX collection plant
BPR	Bypass ratio
CR	Collection ratio
Ao	Orbit altitude (km)
Cox	LOX purity (%)
$LOGW_2$	2nd stage mass at staging (t)
Oinc	Orbit inclination (°)
RTW	Thrust-to-Weight ratio at take-off (-)
TOGW	Take-Off Gross Weight (t)
Vppl	Volume of propellants (m^3)
Wdry	Dry mass (t)
Wcol	Collection plant mass (t)
W_{LOX}	Mass of LOX in the stage (t)
Lto1	1st stage wing loading at take-off (t/m^2)
μstr	average stage structural index (kg/m^2)
tau	Küchemann's parameter (Volume/Aerodynamic reference area $^{1.5}$) (-)

INTRODUCTION

The Air Collection and Enrichment System (ACES) concept, also called In-Flight LOX Collection has been the subject of studies and technology demonstrations since the 60's. It consists in collecting air during the atmospheric phase of a launch, to enrich its oxygen content by separating and rejecting the nitrogen and to store the liquefied oxygen enriched air in the tanks for a subsequent rocket propulsion phase. Air pre-cooling and liquefaction are realised in heat exchangers thanks to the high cooling capacity of hydrogen. This concept is here applied to a Two Stage To Orbit (TSTO) in a rather different way than what has been proposed by the Wright Laboratory of the USAF in the '60 and early '90.

With a staging (separation) Mach number between 4 and 5, it can provide a very interesting launcher solution, even if

the collection phase takes place only during a cruise at a relatively "low" Mach number (about 2.5) and with a "moderate" Collection Ratio (i.e. the ratio of collected LOX mass flow rate per kilo of hydrogen used in the launcher, e.g. CR=3 or less, even if values around 5 are frequently quoted in the literature). Indeed, the ACES TSTO concept allows to take-off with a much lighter vehicle (no LOX in the tanks) which induces a lighter landing gear, a lighter propulsion plant, a quicker climb phase (with less drag) and, last but not least, a lower planform area (Spfl) (which means a lighter structure) for a given planform loading at take-off. The second stage can be reusable or expendable making the whole transportation system fully reusable or semi-reusable.

This paper is a summary of a study funded by ESA in the frame of the FESTIP 2 program, (Technology Studies, Heat Management, WP8). The launcher first stage is propelled by turbo-engines from take-off up to Mach 3.8. It is followed by ramjet propulsion up to the staging Mach number (e.g. Mach 5.0). The paper will present three aspects of the launcher study : the first stage propulsion (von Karman Institute), the LCP pre-design (Techspace Aero) and the integration of the results of these two studies in a pre-design tool used to evaluate the performances of such a launch vehicle (Royal Military Academy). One of the challenges of this study is to integrate the propulsion and the LCP.

Indeed the LCP requires an air intake, a compressor to overcome the high pressure losses in the heat exchangers and in the N_2-O_2 separator, and a nozzle to reject the oxygen depleted air and recover a part of the collection drag. As these elements are already present for the air-breathing propulsion of the first stage, an interesting idea is to integrate the LCP with the propulsion engines by using the bypass flow of a turbofan engine (low bypass ratio) as the incoming air to the collection plant during the collection phase of the flight. The outer part of the LP compressor is then also the compressor of the LCP. The depleted air is reintroduced into the bypass to be mixed with the core flow of the engine and expanded in the main nozzle with the possibility of afterburning. This could decrease the additional drag induced by LOX collection. The system is represented in the schematic of figure 1.

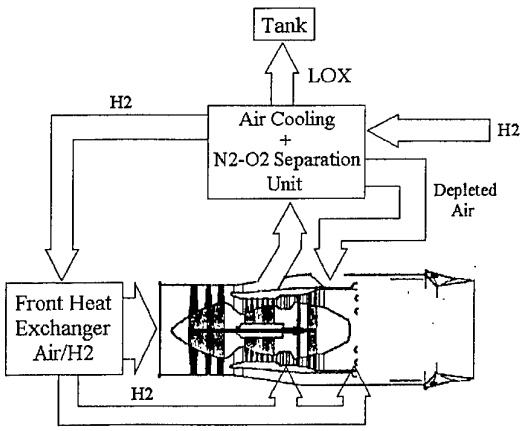


Figure 1 : Integrated propulsion + LOX collection engine (engine schematic taken from [1])

The feasibility of this original system is analysed through cycle studies and examination of performances in design and off-design engine operation. Different engine configurations and LCP variants are investigated and their performances along the entire trajectory are calculated. One difficulty is that the sub-systems and the vehicle studies interact strongly with each other. For example, the hydrogen used in the LCP has to correspond to the fuel consumption of the engines that produce the thrust required by the vehicle.

COMBINED PROPULSION – COLLECTION PLANT

Definition of the problem

A constant dynamic pressure trajectory at 43 kPa is chosen for this study, giving the relation between altitude and Mach number for engine cycle calculations. The mission of the first stage is mainly an acceleration mission from take off to staging at Mach 5 although a cruise is envisaged at Mach 2.5. This cruise phase provides the necessary time for LOX collection and ensures a stable and on-design operation of the LCP for a large part of the collection phase.

The turbo-engines must be used from take off to Mach 3.8 while ramjet propulsion ensures the final acceleration, the pull-up manoeuvre for separation and the first part of the return flight, before gliding. LOX collection takes place within the 1.8 to 3 Mach number range, including the cruise phase at Mach 2.5.

For the definition of the combined turbofan engines, thrust requirements must be specified. As a first guess, a mission and vehicle sizing calculation is performed using an engine performance database created from the performance of the Saënger turboramjet engines. This provides the minimum thrust required for the propulsion of the designed vehicle and the defined mission. The thrust requirements per engine are plotted in figure 2, given that 8 combined turbofan engines are used. It appears that an important throttle-down will be necessary for cruising.

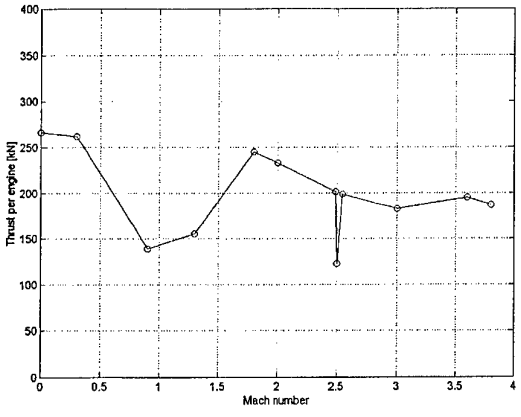


Figure 2 : Thrust requirements per engine

The turbofan engine design is also subjected to several constraints due to its combination with the collection plant. The hydrogen used for cooling and liquefaction in the heat exchangers of the collection plant is burned after for propulsion. The fuel consumption of the engine must be

therefore adjusted depending on the hydrogen requirements of the collection plant. The LP compressor inlet temperature as well as the reinjection temperature of the depleted air must also be in agreement with the thermodynamic capabilities of the LCP.
The mixing condition of the primary and secondary flows of the turbofan engine (i.e. the equality of pressure before the afterburner) has also to be carefully considered. Indeed, this condition could be difficult to realise because of the large differences in the bypass pressure losses between the LOX collection phase and the rest of the flight. The expansion ratio through the collection plant is evaluated to 2.5.

Different mixed turbofan configurations are examined.

Fully pre-cooled turbofan

For this first configuration, all the air entering the LP compressor is pre-cooled by the front heat exchanger as represented in the schematic of figure 1. Cycle studies are performed in order to determine the best adapted HP compressor pressure ratio and bypass ratio. The criteria are to maximise the engine thrust – as the mission is mainly an acceleration mission (with moderate acceleration) – and to minimise the internal power required (i.e. minimise the engine size). The conclusions of the cycle studies are that a relatively low HP compressor pressure ratio around 2.5 must be chosen (for Mach 2.5 cruise conditions) while the bypass ratio must be as low as possible for high acceleration performances. The lower bound of the bypass ratio is however fixed by the thermodynamics of the LCP. Indeed, for a given LOX mass flow rate, the lower the bypass ratio, the higher the amount of pre-cooled air which is not used for collection (core flow). Furthermore, the cooling capabilities of the pre-cooler depend on the available hydrogen mass flow rate, i.e. the fuel consumption. It follows therefore that the bypass ratio must be at least 0.8. This value is already low from the collection plant point of view and allows only a limited temperature drop in the pre-cooler.
In order to achieve the required thrust, the mass flow rate through each engine must be around 235 kg/s (for Mach 2.5 cruise conditions). With a bypass ratio of 0.8, each engine can supply the LCP with 105 kg/s of air. As a minimum total LOX production of 70 kg/s is specified (with a separator efficiency of 0.65), the bypass flow of 4 engines is sufficient. This configuration requires therefore the installation of two different types of turbo-engine (4 combined with the LCP and 4 pure propulsion) on board of the vehicle.

An engine cycle is determined for cruise conditions and the engine operation during the whole acceleration mission is analysed by off-design calculations using typical performance maps for compressors and turbines. The main difficulty lies in the high increase of pressure losses in the bypass flow during the collection phase. That means that the pressure ratio of the LP compressor must increase at once to satisfy the mixing condition. This is possible mainly due to the inlet temperature decrease (pre-cooling) inducing higher rotor Mach numbers and therefore higher pressure ratio for the same rotational speed. Note however that the density and therefore the inlet mass flow rate increase also. The pressure ratio evolution of both LP and HP compressors is shown in figure 3 for the whole mission. The lower value at Mach 2.5 is due to the necessary throttle-down during the cruise (see figure 2). The increasing of the LP compressor pressure ratio during the collection phase is well visible. Note also that the turbofan mixing condition is satisfied for all flight conditions.

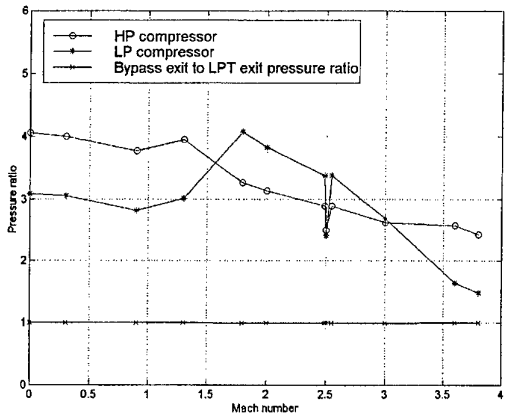


Figure 3 : Pressure ratio evolution – fully pre-cooled system

The general decrease in pressure ratio with Mach number for both compressors is due to the mechanical speed reduction because of the limited turbine inlet temperature (1800 K from materials considerations) while the engine inlet temperature is higher and higher. This phenomenon is however partly compensated by the use of the pre-cooler even outside the collection phase.

The high integration level of the propulsion engines with the collection plant induces that they are both constrained by each other. The main constraint is the limitation on the bypass ratio which must be high for LOx collection and low for propulsion. The chosen compromise of 0.8 limits significantly the temperature drop in the pre-cooler and reduces the acceleration performances of the engine. Furthermore, two different types of engine are necessary, which is not convenient. The system can be therefore improved if this constraint on the bypass ratio is removed. This is achieved by a modification of the pre-cooler, resulting in a system named *the ring pre-cooler system.*

Ring pre-cooler system

The constraint on the bypass ratio was imposed because of the pre-cooling of the whole inlet flow. This constraint disappears if the pre-cooling is applied only on the bypass flow of each engine with a ring-shaped pre-cooler. This can be achieved providing that the core flow and the bypass flow are well separated before and along the LP compressor. The flow separation through the LP compressor is physically realised by fins placed on the rotor blades such as the currently used part span shrouds and on the stator blades with eventually some labyrinth connections between the rotating and static parts. The front part of the turbofan engine with the ring pre-cooler system is sketched in figure 4.

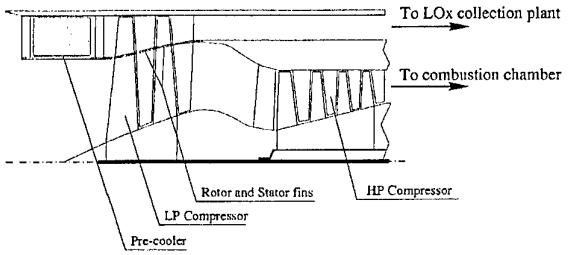


Figure 4 : The ring pre-cooler system

Following the cycle study, the HP compressor pressure ratio is still around 2.5 in cruise while the bypass ratio can now be decreased to a value around 0.22. For a given mechanical LP spool speed, the mass flow rate in the outer part will be higher when pre-cooling because of the increase in density, resulting in a natural increasing of the bypass ratio until 0.35 for a temperature drop of 200 K at Mach 2.5. This allows to supply the required mass flow rate to the LCP with an engine designed to have a lower bypass ratio for propulsion only operation (without pre-cooling). With this low bypass ratio, 8 identical combined engines can be used as each one supplies the collection plant with 53 kg/s of air for an engine mass flow rate of 205 kg/s (note that this value is lower than for the fully pre-cooled system because of the lower bypass ratio giving higher thrust capabilities).

For the same rotational speed of the LP compressor, the lower temperature when pre-cooling induces higher Mach numbers in the outer part of the blades, naturally increasing the outer compression ratio while the inner part operation does not change. This is advantageous to overcome the simultaneous increasing of the pressure losses experienced by the bypass flow going through the collection plant. The pressure ratio evolution for both LP (inner and outer parts) and HP compressors is given in figure 5. The consequences of the different operating conditions of the inner and outer parts of the LP compressor are well visible. The ring pre-cooler system has then the capability of natural adaptation to the requirements of the combined propulsion – collection plant.

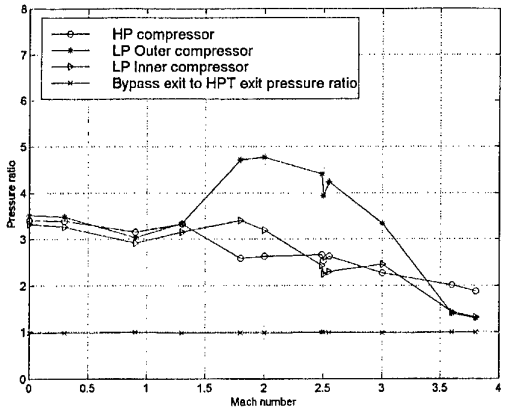


Figure 5 : Pressure ratio evolution – ring pre-cooler system

Furthermore, the higher pre-cooling capacity induces a higher increase of the LP outer pressure ratio. The attention must be put however on the fact that the Mach numbers in the outer part of the compressor must not become too high and therefore, the rotational speed of the LP spool must be reduced for some conditions.
The general diminution with Mach number of the achievable pressure ratio, for the LP as well as for the HP compressor, is more important in this case because no pre-cooling is possible anymore outside the collection phase (and is even never available for the core flow).

The total thrust capability of the 8 combined engines equipped with the ring pre-cooler system is given in figure 6 for stoichiometric reheat. The thrust diminution during the LOX collection phase is due to the lower amount of oxygen available for afterburning and to the necessary throttle-down for the reduction of the LP rotational speed because of the reason explained above.

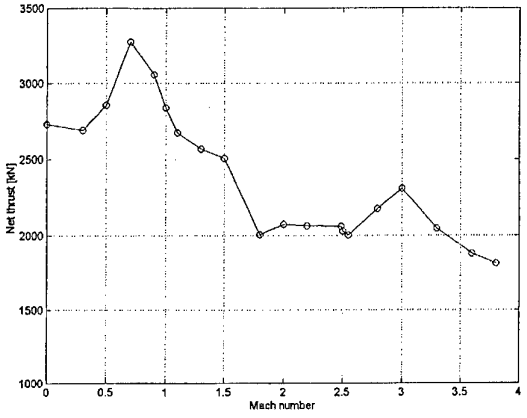


Figure 6 : Maximum thrust capability – turbofan engine with ring pre-cooler system

COLLECTION PLANT PERFORMANCE

The LCP is located in the by-pass duct of a "mixed turbofan". In the first option investigated, a pre-cooler is installed in front of the fan. This configuration has the advantage of sharing the same compressor between the LCP and the engine. The pre-cooling advantages are a lower work consumption for the fan and a higher fan pressure ratio. A pre-cooling allows also a higher mass flow rate and a higher airbreathing Mach number with the same engine technology. There is however a drawback with this configuration : for the propulsion, the ideal BPR should be between 0.2 and 0.5 while for the LCP, the BPR should be much higher (an a priori value was 1.5). Indeed, with a high BPR the cooling capacity of hydrogen is mainly used for the collection plant, allowing better performances (collection ratio) and lighter heat exchangers. Therefore, other integration solutions were examined.

In a less integrated system, the fan and the nozzle are still common but only the bypass air is cooled, after the fan compression. In this case, the work consumed by the fan to compress the bypass flow is relatively high especially since the pressure drop in the LCP is higher than for the usual turbofan. Anyway, in this case the bypass ratio has no influence on the collection plant performance as only the LCP processed air is cooled.
In a still lower integration only the intake and the nozzle

are common; there could be also power transmission between the engine and the collection plant compressor. In this case there is an additional compressor but it should compress the collection plant pre-cooled air.
None of these solutions was estimated very promising. Here is therefore an other reason to come to the ring pre-cooler system
As the pre-cooling of all the propulsion air flow causes problem to the LCP, the idea is to pre-cool only the bypass air. The two flows (bypass and core flow) would be separated, the bypass flow would go through a ring shaped heat exchanger. A good separation between the flows seems possible. The schematic of figure 7 shows the combined LCP-engine architecture.
Some advantages are :

- The LCP takes advantage of the engine turbomachinery;
- The pre-cooling of the bypass air reduces the power extracted from the propulsion engine
- And consequently reduces also the heat to remove from the air to be processed;
- As the core air is not pre-cooled, it does not impact negatively on the LCP performances.

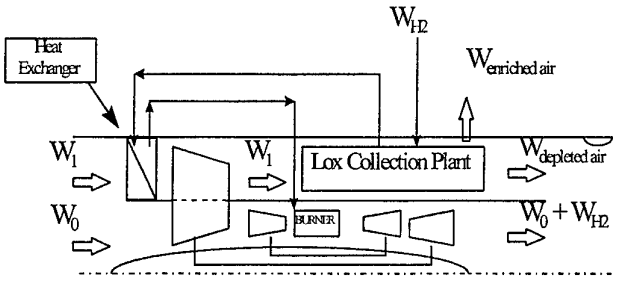


Figure 7 : Integrated LCP-engine architecture

The input parameters of the LCP thermodynamic calculations are adapted to the data provided by the propulsion plant study presented above. These data correspond to an 8 engines launcher. The air processed through the LCP for each engine is approximately 50 kg/s and the enriched air (LOX) production is about 8 kg/s. The main data provided by the propulsion study are the outer fan pressure ratio and the bypass air mass flow rate.

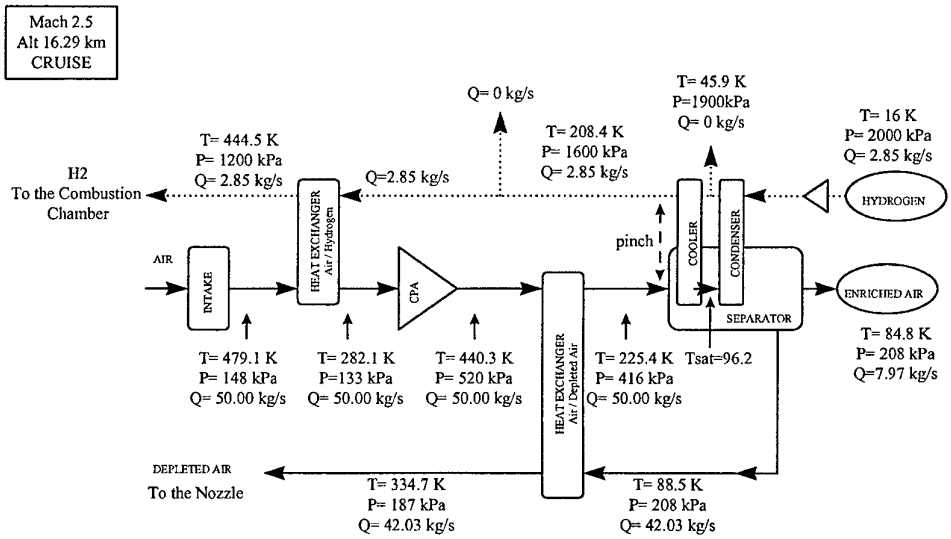


Figure 8 : Ring heat exchanger configuration, LCP main parameters

The first task was to pre-design a LCP able to process 50 kg/s of air, with a given fan pressure ratio and good performances for an acceptable mass and volume (but this is not a very critical point for a TSTO). After a few iterations (thermodynamic and components analysis) a solution was selected for which the main thermodynamic parameters are shown in figure 8 : after the ring heat exchanger (air/H2), the air goes through the fan and then in a second heat exchanger (Air/Depleted Air); the air enters the "separation" unit at a relatively high temperature (225 K) and has to be cooled down to the saturation temperature in the so-called "cooler"; after the condenser, the air enters the separator strictly speaking; the depleted air is heated in the air/DA heat exchanger before being injected into the nozzle.

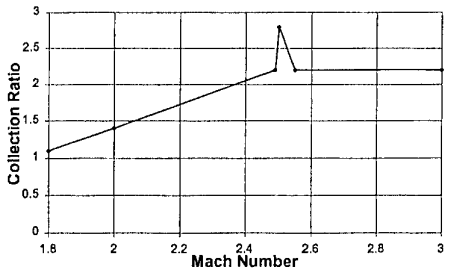
The design has been made for the cruise conditions. The results presented correspond to a collection ratio of 2.8.

The thermodynamic analysis has been made in parallel with component evaluation, mainly heat exchangers. One important point also is the separator performances : the oxygen separation efficiency is taken equal to 0.65 (65 % of the oxygen of the entering air is separated and collected). In our case, it is the main limitation for a higher collection ratio. The value of 0.65 has been chosen because it corresponds roughly to the value obtained with the rotary distillator demonstrated in the USA [2]. An other reason is that for a too high separation efficiency, the poor oxygen content in the depleted air would decrease the afterburning possibilities.
The extension of LOX Collection outside the cruise phase, between Mach 1.8 and Mach 3 has been studied. This collection extension implies heat exchangers mass increase as they have to resist to higher temperatures. Heat exchangers (cross counterflow shell and tubes) mass evaluation has been made in both cases (table 1).

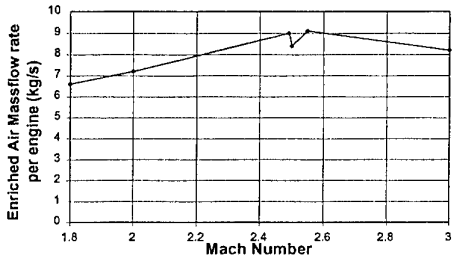
MASS (kg)	Design for cruise at Mach2.5	Design for Mach 3
Air/ H2 pre-cooler	242	361
Air/DA	147	189
Air/H2 deep cooling	123	123
Total	512	673
Total per kg/s of EA	64.2	84.4

Table 1

The performance is optimised for the cruise. So, at lower and higher speed, during acceleration, the performances somewhat deteriorates as it is shown on figures 9a and 9b. Anyway LOX collection is possible during acceleration but necessitates additional control equipment.



(a)



(b)

Figure 9 : LCP performances in off-design

VEHICLE SIZING RESULTS

The results of the sub-systems detailed studies have to be integrated in a pre-design vehicle-sizing tool. This sizing tool integrates the propulsion, aerodynamics and in-flight LOX collection aspects using the results provided by the sub-systems studies with a complete vehicle trajectory calculation and a mass & volume model of both stages [3].

The first results are for a fully reusable HTOHL (Horizontal Take-Off Horizontal Landing) TSTO with a staging at Mach 5.0 and a CR of 2.8. Collection takes place in acceleration (between Mach 1.8 and 3.0) but mainly in cruise (at Mach 2.5 and 16.7 km altitude). For the first stage airbreathing propulsion, the ring pre-cooled turbofans are used from take-off up to Mach 3.8 followed by ramjets up to staging. The first stage shows a blended-body configuration and the second stage has a winged-body configuration. The average structural index of both stages is equal to 21 kg/m². Both stages are very well integrated (2nd stage mated to the 1st stage). The table 2 shows some vehicle sizing parameters for three different values of the purity of the LOX stored inside the 2nd stage tanks in flight. The all-rocket (LOX-LH_2 engines) 2nd stage propulsion is assumed to loose 1.5 second of vacuum ISP per percent of LOX impurities (with a Mixture Ratio of 6.5, ref. [4]).
It is shown that, with a purity of 90%, the launch of a payload of 7 tons on an equatorial LEO (ESA FESTIP requirement, ref. [5]) requires a TOGW as low as 370 t with a 1st stage dry mass of 200 t for a fully reusable TSTO (with a take-off from Kourou). In all these launch vehicles, the collection plant mass represents only less than 2% of the 1st stage dry mass. The specific mass of the collection plant (and thus mainly of the different heat exchangers) is therefore not so critical (not like in a SSTO with in-flight LOX collection).

SIZING PARAMETER	Cox = 95% (ref.)	Cox = 92%	Cox = 90%
TOGW (t)	333.4	353.0	369.2
$Wdry_1$ (t)	185.0	195.4	203.9
Cruise (s)	2279	2409	2507
τ_0 (-)	0.0523	0.0510	0.0500
$W_{LH2,1}$ (t)	90.6	96.9	102.2
$Vppl_1$ (m^3)	1264	1352	1426
$LOGW_2$ (t)	178.1	189.2	198.5
$Wdry_2$ (t)	30.1	31.7	33.0
τ_2 (-)	0.0764	0.0743	0.0727
W_{LOX2} (t)	122.1	130.3	137.2

Table 2

The second results are for a semi-reusable TSTO (thus with an expendable 2nd stage). One of the objectives of using an expendable 2nd stage is to be able to reduce the staging Mach number with still a low TOGW and a low 1st stage dry mass. The results are shown in table 3 where two fully reusable TSTO concepts analysed in detail in other European studies ([6] & [7]) are also indicated. One can see that in-flight LOX collection allows to reduce much the TOGW. This large reduction will also offer more margin for the whole structural design : for example, for a staging at Mach 4.0, (Wdry1 / TOGW) = 176/361 vs. 188/431 for a FSS-12 launcher configuration without LOX collection.

TSTO TYPE	Sänger	FSS-12D	½ reuse	½ reuse	½ reuse
Collection	No	No	Yes	Yes	Yes
Mach staging	6.7	4.0	5.0	4.5	4.0
TOGW (t)	372	431	254	286.9	361
RTW (-)	0.74	0.84	0.84	0.84	0.84
Ao (km)	463	250	250	250	250
Oinc (°)	28.5	5	5	5	5
Wdry1 (t)	188	188	130	139.5	176
Wdry2 (t)	24	31	25	30.3	32.2
Wcol (t)	0	0	3.5	3.5	3.5
Staging time (s)	3190	520	2883	3176	3520
Coll cruise (s)	--	--	2034	2325	2726
Lto1 (t/m²)	0.25	0.453	0.30	0.32	0.38
μstr1 (kg/m²)	21	19	20	19	18
Tau0 (-)	0.0305	0.1134	0.0853	0.0926	0.128
Payload (t)	7.0	7.0	7.0	7.0	7.0

Table 3
(CR = 2.8, Cox = 90%, μstr2=20 kg/m², Lto2 = 0.50 t/m²)

In tables 2 and 3, the indices 0, 1 and 2 refer respectively to the whole vehicle, the 1st stage and the 2nd stage.

Large subsonic ACES launcher

The next to come development of very powerful turbofans (115.000 lbf., maybe even more) and of the large twin engine planes they will power make it possible to consider jumbo carriers that could be derived at moderate development costs and risks for airborne space launch.
The Molnya company has been proposing such kind of plane (the Herakles-1000) for 5 years, announcing a 450 t maximum cargo capacity for this 900 t GTOW special design plane, powered with conventional kerosene fuelled turbofans of PW4084 class. Using such kind of plane for airborne launching and the full development of synergies between LOX collection and hydrogen fuelled turbofans would raise to unsuspected summits the advantages already identified at the scale of a B747 (ref. 8).
The advertised data for Herakles-1000 (Jane's 98-99) are summarised below:

G.T.O.W = ~ 900 t and OEW = ~ 300 t
Engines : 6 × PW4084 class
Max fuel capacity : 360 t kerosene
Range with Max. PL (450 t): > 1 200 NM
Range with max fuel & 240 t PL : > 4 000 NM

Hydrogen burning turbofans

Substituting hydrogen to kerosene will drastically reduce the equivalent maximum fuel mass from 360 Mg down to less than 140 Mg but the volume is multiplied by a factor 4.0-4.5 and LH2 cannot be stored in conventional wings tanks. A twin fuselage rather than a twin-boom-like (Herakles) fuselage architecture will be needed (ref. 12).
Fifty percent (70 Mg), at least, of this LH2 load can be used to collect 210 Mg. of LOX with CR = 3.0. That would authorise to design a 300 Mg initial mass LOX/LH2 launch vehicle of more than 360 Mg with LOX/Kerosene propulsion (configurations C and D in Table 4). An improved LCP achieving CR = 4.0 would similarly allow to collect 280 Mg of LOX and launch much heavier vehicles (configurations E and F). Increasing the percentage of LH2 used for Lox-collection (earlier operation and/or shorter flight after LV release) would also provide a significant increase of the LOX mass available, whatever the CR achieved. Configuration (G) illustrates this point with 58% of the LH2 load instead of 50%.

LOX-Collection flow rate

Maximising the total mass of collected LOX introduces an important operational constraint : flow-rate is strictly proportional to the burn-rate of the turbofans. As an average hydrogen burn-rate of ≈10 Mg/hour can be expected the maximised Lox-collection will extend over ≈7 hours. One deriving advantage is the possibility to take-off as far as 3600 NM away from the selected L.V release point. One drawback could be to have to loiter for a few hours around the L.V. release point until the required mass of LOX has been collected. In fact, operational flexibility will be provided with additional LCP modules and dumping the hydrogen that is not burnt by the turbofans.

Mass comparison

Table 4 summarises a series of data that have been estimated with four different sets of assumptions :
- with kerosene fed turbofans and without LOX collection
- with hydrogen burning turbofans and with the number of LCP-modules required to collect within less than 4 hours
- same as above but with an improved LCP achieving CR = 4.0 (at the cost of a 100 % increase of its mass)
- same as above but collection starts earlier, allowing a larger (58%) share of the LH2 load for collection.

To simplify the discussion, the Operational Empty Weight (O.E.W) of the basic plane is kept constant. Consequently the mass of hydrogen (to collect oxygen and feed the turbofans) is also constant.

	Conven tional		H2 fed eng.// basic LCP		H2 feed and impr. LCP		
(All masses in Mg)	(A)	(B)	(C)	(D)	(E)	(F)	(G) *
LV propulsion	LOX/LH2	LOX/KER	LOX/LH2	LOX/KER	LOX/LH2	LOX/KER	LOX/LH2
CARRIER PLANE							
OEW (basic)	300	300	300	300	300	300	300
Fuel							
Kerosene	290	230					
LH2			140	140	140	140	140
GTOW	900	900	540	596	575	646	591
Weight at LV release	687	725	652	708	757	828	817
LOX. COLL. PLANT							
System	0	0	10	10	20	20	20
LOX mass collected	0	0	210	210	280	280	324
LAUNCH VEHICLE							
LV at release	300	356	300	356	395	466	455
LV mass at take-off	300	356	90	146	115	186	131
Propellants (total)	245	300	245	300	326	400	378
Mission Range (NM) **	3200	2500	5000	4500	4500	4000	4500

* Common hypothesis is 50% of LH2 used for Lox-collection but 58% for configuration (G).
** Distance from take-off to release point. // 20% of fuel burnt before LOX-collection phase.

Table 4 – Mass comparison of various possible design possibilities

As expected Lox-collection provides spectacular reductions of the GTOW, even after part of the gross reduction has been used for a heavier but more efficient LCP to collect more LOX.
It would be possible to push the performance even further up, beyond configuration (G) of Table 4, and still remain well below the 900 Mg GTOW limit, but other advantages seem to be preferred:
- more opportunities to reuse structures and parts from ageing aircraft;
- not more than 4 engines;
- shorter take-off distance;
- acquiring experience progressively with increasing LH2 loads, etc.

Experimental aspects

Among the various devices that Air Collection and Enrichment System vehicles need to operate, one crystallises the unknowns of the concept: the separation device that extracts oxygen from air in order to fill up the LOX tanks during flight. To address this issue, the FESTIP programs of ESA have financed the development of an experimental test bench for testing vortex tube separation. But another concept will also be tested within the GSTP 3 technological program of ESA (in the period 2000-2002) where a significant effort will be devoted to the experimental study of a centrifugal distillation column.
One needs also to look attentively at the Integrated LCP - Turbofan unit presented here before. Experimental work is planned in the ESA FLTP1 (2000-2001).

Vortex Tube (VT) separation experiments

In the frame of FESTIP 1 & 2 from 1997 till 1999, the Thermodynamics Laboratory of the University of Liège (with the initial support of V. Balepin) has designed and built a test bench able to produce "dried" compressed air (up to 7 bar) and to cool it down to a two-phase flow state. Then, a demonstration of the air oxygen separation by means of a vortex tube (figure 9) with air compressed up to only 6 bar has been successfully achieved. There is here no need to compress air above its critical pressure (≈ 37.7 bar). A small vortex tube (6-7 g/s capacity) as well as a vortex tube of higher capacity (factor 4) have been designed, built and tested successfully. An intensive experimental work devoted to study the influence of the geometry and the operating conditions of a vortex tube on the air oxygen separation efficiency has been carried out.

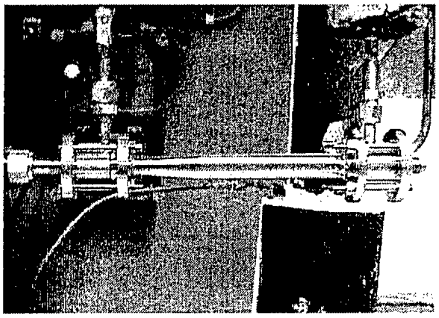


Figure 9 : VT on test bench

The influence of the following parameters has been investigated: the heat gain from the environment, the scale of the vortex tube, the relative diameter of the depleted air orifice, the vortex tube length, the size and number of the inlet nozzle(s), the air vapour quality and the enriched air fraction. The main parameters that seem to play a key role on the vortex tube performance are : the air vapour quality at the inlet of the vortex tube and the enriched air fraction. That is illustrated in figure 10 which gives the oxygen mass concentration (y_{O2}) of the enriched air stream versus the air vapour quality ($x_{a,su}$) for different enriched air ratios (f).

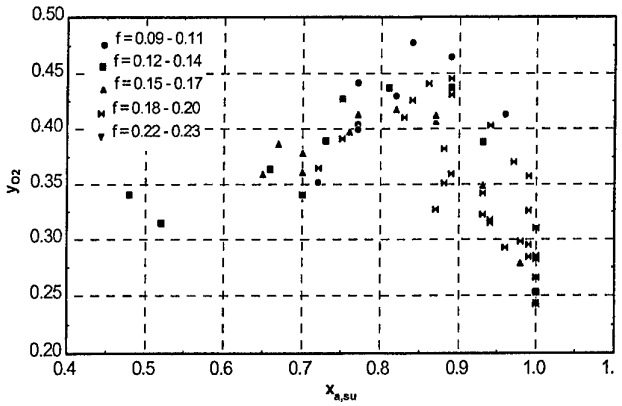


Figure 10 : Measured performance of VT separator

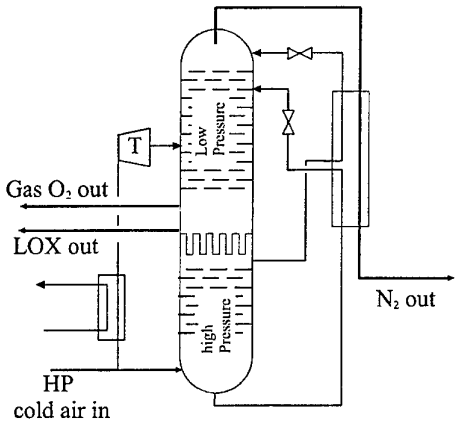
Oxygen concentrations up to about 90% have also been recorded in the enriched air stream just downstream of the vortex tube, but the flux composition was not uniform at that location.

Rotary Distillation Separation (RDS) experiments

Distillation on Board, the Technological Choices for a Rotary Distillator

Supplied with a substantial amount of air near saturation, the separation device of the full size vehicle has the challenging task of separating oxygen from nitrogen. Of course, in practice, that process will be incomplete and neither will the oxygen enriched fraction be pure, nor will it contain all the available oxygen. The main reason for choosing fractional distillation is that among the technologies available to separate miscible fluids, it is a rather attractive solution. Indeed, it is widely used in industry and, in most cases, it can separate fluids from each others with a given efficiency and to a given purity provided their properties are sufficiently different. Moreover, performance estimates are possible since the process is well known and is mainly based on the thermodynamics of liquid-vapour phase equilibria.
Looking at industrial separation systems, the most common arrangement is a combination of two columns operating at different pressures and separated by a reboiler-condenser (figure 11). However, these concepts are optimised for energy efficiency and low cost production of oxygen. In the onboard oxygen collection plant, simpler systems will be preferred even at the cost of a less efficient use of the cold source (hydrogen), see, for example, the arrangement of figure 12 that uses a centrifugal arrangement to avoid the excessive bulkiness of classical columns. Looking inside the 'column', two main options remain possible: a classical

plate type column or a packing type of column (packings are wrinkled perforated sheets bonded together into compact blocks that force the contact between the liquid and the vapour that are flowing in opposite direction). Although packings will almost certainly give better performances, the particular choice for the experimental setup, will mainly be based on manufacturing considerations.



gaseous outflows are used to precool air inflow

Figure 11 : The industrial production of oxygen (T denotes a turbine)

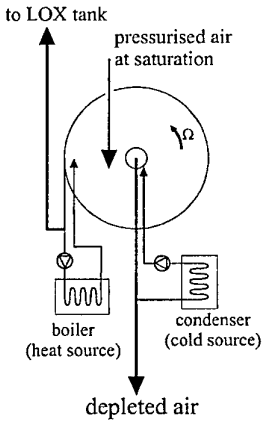


Figure 12: Scheme of in-flight rotary distillation device.

The Test Rig for ESA GSTP3

The test rig will consist of a cylindrical rotor of 400 to 500 mm in diameter rotating in a casing and working with a limited mass flow. For practical reasons, a simplified version of the complex flow chart presented on figure 12 will be used, but the ability of the column to operate at a limited efficiency and purity will be kept. To facilitate future extrapolations from the experimental results, the rig will be able to control the major parameters: rotational speed of the rotor, mass flow, composition, temperature and pressure of the supplied fluid. On the other side, composition and relative mass flow of outgoing fluids will be measured to check the performances. The supply air will be a synthetic mixture of oxygen and nitrogen, mainly to avoid potentially tricky icing problem. It will be possible to add argon later by mixing it with the oxygen in the tank.

Objectives

Although strong theoretical and experimental basis are available about distillation columns, only few tests have been carried out on their centrifugal equivalents (references 9, 10 & 11), which means that many unknowns are still present. The present goal is, starting from synthetic air, a purity of 80% and a collection efficiency (fraction of total oxygen recovered) of 60%. These performances, once reached with a significant throughput, are an excellent basis for an ACES concept separator. Concerning argon, one percent of the air composition, it is expected that, once it will be added, it will almost entirely follow the oxygen, causing a serious limitation on oxygen purity (95% at best from air) unless an additional argon separator is used.

Integrated Turbofan – LCP experiments

In the FESTIP 2 vehicle study, the TSTO with supersonic separation takes advantages of the integration of the LCP within the turbofan used for the first stage propulsion.
The logical next step is now to simulate this integration and this interaction of the LOX collection plant on an existing turbofan engine. Therefore, it is proposed to use an existing LBPR turbofan which will be specially modified to allow a bleed from the secondary flow (by-pass duct) and a re-injection of nitrogen or depleted air (figure 13). The goal is to check the engine behavior when implementing the collection plant by introducing pressure drop, bleed and nitrogen re-injection (instead of air) into the secondary flow and thus in the afterburner.

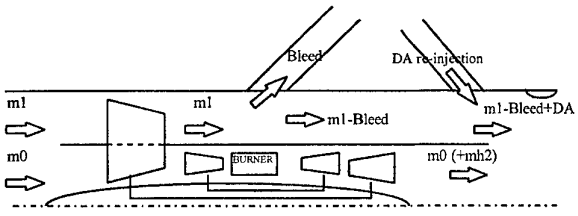


Figure 13 : LCP – turbofan experimental set-up

The bleed simulates the air extracted for the collection plant (up to 30%) and the re-injection simulates the depleted air coming from the separator (vortex tube, rotary separator or other)[1].

This demonstrator allows mainly to show how an turbofan can work with an air collection system : to control the influence on the surge margin and on the performance of the engine itself.
From these experimental data, the model of the engine (with the integration of the LCP) will be refined and the model will be extrapolated to the same engine running with hydrogen as fuel instead of kerosene.
In parallel, tests on heat exchangers should be performed in order to see how the icing problem can appear for cruise thermodynamic conditions. Therefore, we should reproduce the thermodynamical properties of the air at Mach 2.5 (cruise) in front of the heat exchanger (working with

[1] The VT, the RDS and their complementarity will also be studied in parallel in the ESA GSTP3 study.

nitrogen as coolant instead of hydrogen). Additionally, this should be done with different values of the air humidity. Afterwards, we should determine the influence of the air humidity (so, influence of the icing) on the air pressure drop, flow rate, thermal exchange...
This study shared in FLTP1 and GSTP3 programs aims at a global validation of the integrated system propulsion/collection and the development of a reliable air separation device.

CONCLUSIONS

A TSTO with supersonic staging is first presented. The originality of the study is to integrate all the different aspects related to a TSTO with in-flight LOX collection, mainly by coupling the engine and LCP design calculations. The engines have been specifically designed considering their interaction with the LCP, satisfying its requirements in terms of air mass flow rate and pressure ratio.
The fully pre-cooled turbofan showed a too high level of interaction with the LCP, constraining the performance of both systems. More freedom has been obtained by using the ring pre-cooler system. This system has also additional advantages due to its capability of natural adaptation to the requirements of the LCP, by the increase in pressure ratio and mass flow rate in the outer part when pre-cooling, while the inner part operation stays unchanged.
The LCP has been designed to correspond to the engines flow capacity and compression ratio during the cruise at Mach 2.5. Then off-design calculations have shown that LOX collection is possible during the acceleration phase of the flight between Mach 1.8 and 3 at the cost of additional control equipment and heat exchanger mass (for the higher speed).
From a vehicle point of view, the ring pre-cooled turbofan assures very high performance to a fully reusable TSTO using in-flight LOX collection. Even with a collected LOX purity of 90%, the TOGW and the 1st stage dry mass are as good as what was expected for Sänger but with a staging at Mach 5.0 instead of 6.7-6.8.
For a semi-reusable TSTO (expendable 2nd stage) with staging at Mach 4, the in-flight LOX collection concept used with a LOX purity of 90% allows to size a vehicle with a much lower TOGW (and a lower 1st stage dry mass) than the FSS-12D concept.
The option of a subsonic air-launched orbiter from a specially designed large subsonic transport aircraft has been presented too. This represents certainly the ideal first step into the development of a launcher using in-flight LOX collection, with other possible uses of the same subsonic carrier.
Experiments centred on the Vortex Tube separation principle have already performed. More are planned within the next two years but mainly centred on the development and the testing of a Rotary Distillation Separation unit. Tests of an integrated LCP – turbofan installation will also be carried out, with JP-8 as a fuel.

ACKNOWLEDGEMENTS

This work has been performed in the frame of the **ESA** FESTIP Technology Phase 1 & 2 Program – Part Heat Management lead by ESTEC & Techspace Aero.
We want to thank Jean Vandenkerckhove for his spiritual inheritance and some others for their continuous support.

REFERENCES

[1] Kurzke J., "GasTurb Version 8.0 User's Manual, A program to calculate design and off-design performance of gas turbines", 1998.
[2] Leingang J.L., Maurice L.Q. and Carreiro L.R, Wright Laboratory, "In-Flight Oxidiser Collection Systems for Airbreathing Space Boosters", Developments in High-Speed-Vehicle Propulsion Systems, AIAA, Progress in Astronautics and Aeronautics, Vol. 165, Ch. 7, pp 333-384, 1996.
[3] Balepin V., Hendrick P., Pelloux-Gervais P and Saclier F., "O2/N2 Separation Processes for LOX Collection with Airbreathing Propulsion Systems", AAAF Space Launchers Symposium, Paris, 24 May 1996.
[4] Hendrick P. and Saint-Mard M., "Sänger-type T.S.T.O. using in-flight LOX collection", AIAA 97-2858, Seattle, 6-9 July 1997.
[5] OHB System, Report FSS-OHB-SC-2130-001, 28 March 1995.
[6] Kuczera H. et al., FESTIP System Concepts description, DASA, August 1998.
[7] Grallert H., "FSSC-12 re-configuration and performance – Evaluation & Synthesis", Final Report, 30 June 1998.
[8] Johnson C & Hendrick P., "LOX Collection : a Highly Synergistic Technology", AIAA 99-4830, Norfolk, 1-5 November 1999.
[9] R. Drnevich & J. Nowobilski, "Airborne Rotary Separator Study", NASA CR-191045, December 1992.
[10] Gottzmann C. et al., "Airborne Rotary Air Separator Study", Union Carbide Industrial Gases Inc., NASA-CR-189099, December 1990.
[11] Leingang J. & Maurice L., "In-Flight Oxidizer Collection Systems for Airbreathing Space Boosters", Developments in High-Speed-Vehicle Propulsion Systems, Vol. 165 Progress in Astronautics and Aeronautics, AIAA, November 1996.
[12] L. Jenkinson, P. Simpkin and D. Rhodes, "Civil Jet Aircraft Design", AIAA book, 1999.

JAPHAR

Joint Airbreathing Propulsion for Hypersonic Application Research

WG2 Activities

Supersonic Combustion Modeling



Numerical Method
DLR / RWTH Aachen Code

- Finite-Element Algorithm on Unstructured Grids
- Galerkin weighted Residual Formulation

$$\int_\Omega N_J \left(\frac{\partial \widetilde{U}}{\partial t}\right) d\Omega = \int_\Omega \frac{\partial N_J}{\partial x_j} \widetilde{F}_j d\Omega + \int_\Omega N_J \widetilde{H}_j d\Omega - \int_\Gamma N \widetilde{F_j} n_j d\Gamma$$

- Triangular Elements with Linear Form Functions

$$\widetilde{U} = \sum_{K=1}^{3} N_K \widetilde{U}_K \quad \widetilde{F} = \sum_{K=1}^{3} N_K \widetilde{F}_K \quad \widetilde{H} = \sum_{K=1}^{3} N_K \widetilde{H}_K$$

- Time-Integration by a Runge-Kutta Five-step Scheme

$$U_J^{(\nu+1)} = U_J^n + \alpha_\nu \cdot \Delta t_J \cdot \left[M_{L_J}^{-1} R_J \left(U_J^{(\nu)}\right) + D_J^{(2)} - D_J^{(4)}\right]$$

Combustion Modeling



- Very fast reaction with a presumed PDF Approach
- Chemistry is described through one global reaction step

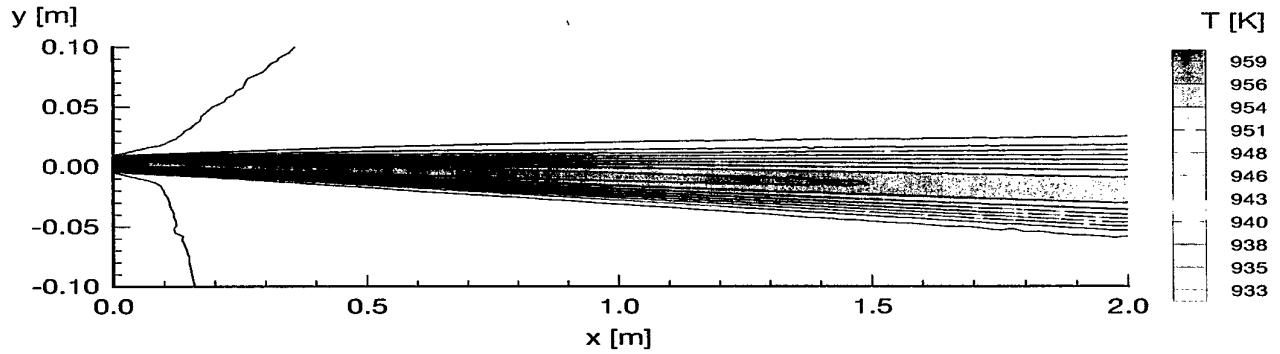
$$fuel + r_f \cdot oxidizer \rightarrow (1 - r_f) \cdot product$$

- Mutual influence between turbulence and chemistry described by Probalistic Euler Langrangian model developed by Borghi, Vervisch et al.
- Coupling of combustion and turbulence by application of a Beta function for the PDF

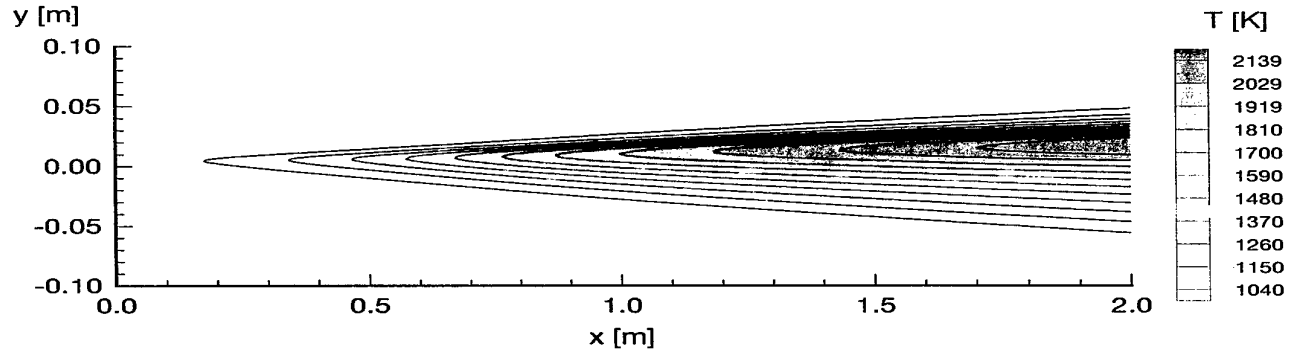
$$\widetilde{Y}\left(\widetilde{Z}, \widetilde{Z''^2}\right) = \int Y(Z)\, P\left(Z, \widetilde{Z}, \widetilde{Z''^2}\right) dZ$$

with the dependance on two parameters:
  - Mixture fraction $\widetilde{Z}$
  - Variance $\widetilde{Z''^2}$

Non-reactive and reactive Mixing Layer
TEMPERATURE DISTRIBUTION

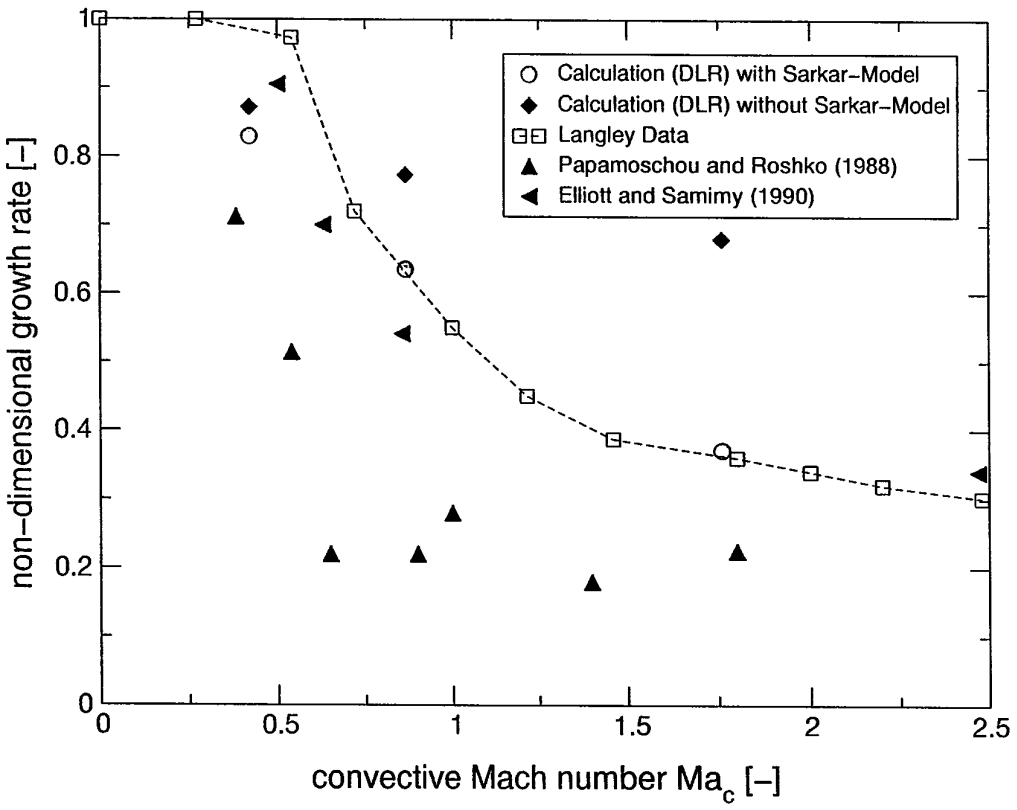


- non reacting shear layer

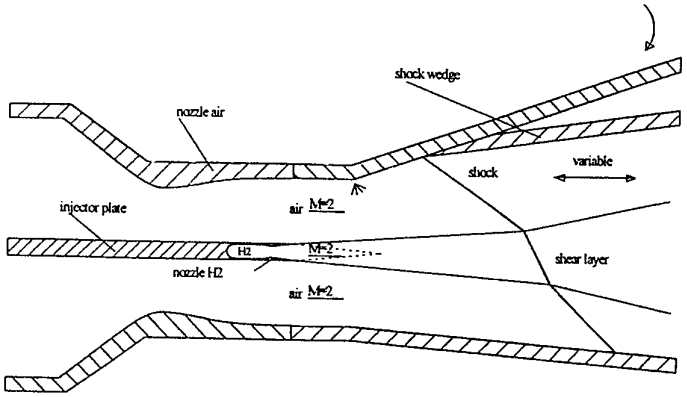


- reacting shear layer

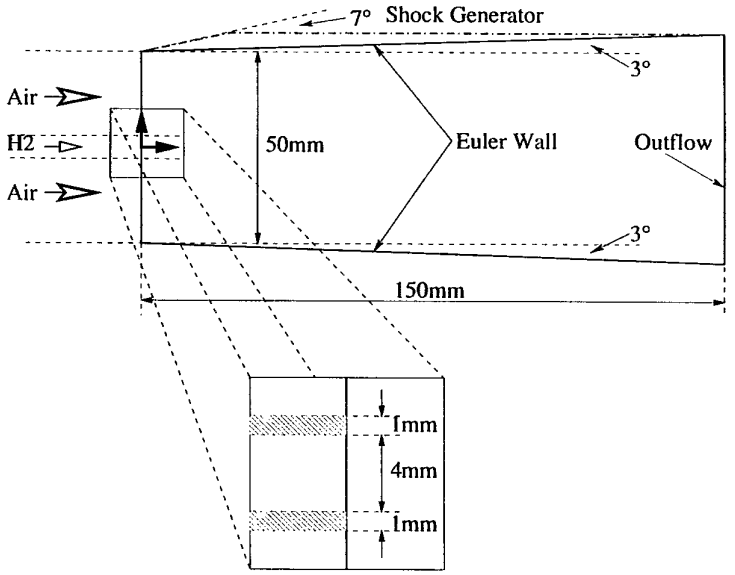
Non-dimensional Mixing Layer Growth



Test Case Geometry
DLR EXPERIMENT



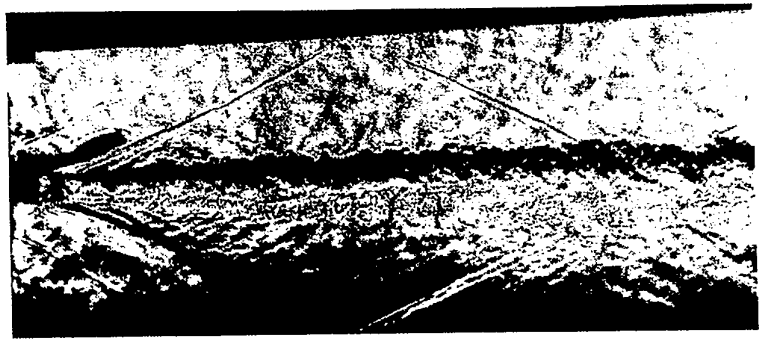
(a) Sketch of experiment



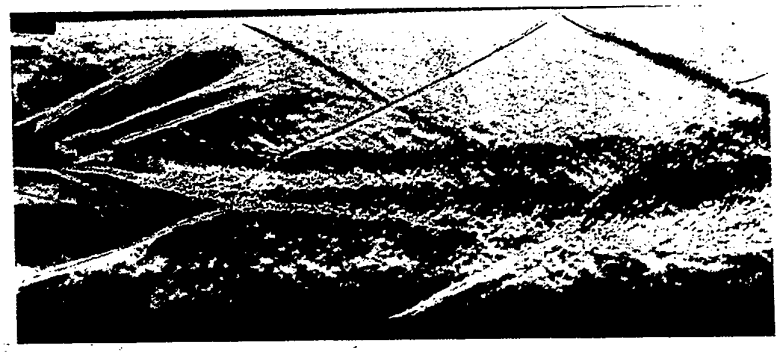
(b) Boundary of computational domain

$\Rightarrow$ Inlet Mach number $Ma = 2.0$ for airflow and injected hydrogen

Schlieren Pictures of DLR Experiment



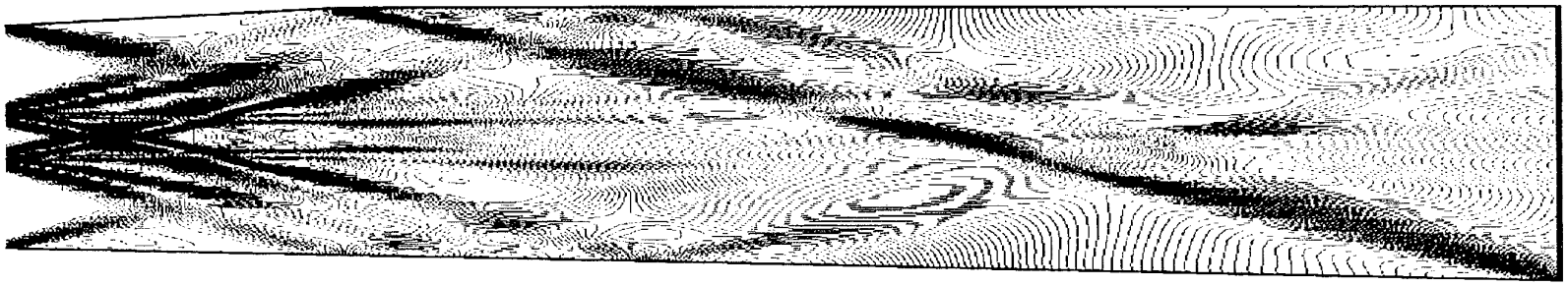
(a) without shock



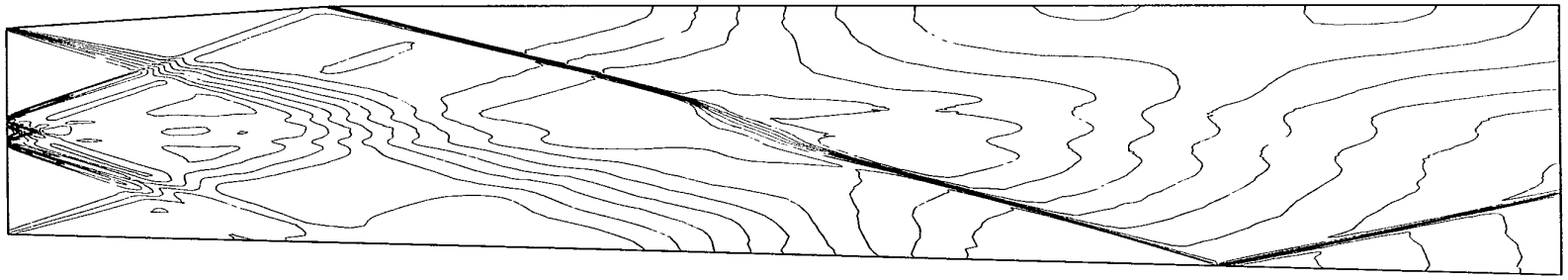
(b) with shock

Schlieren pictures for $Ma_c = 1.1$ without shock interaction (a) and with shock interaction (b)

Shock - Mixinglayer Interaction
PRESSURE DISTRIBUTION

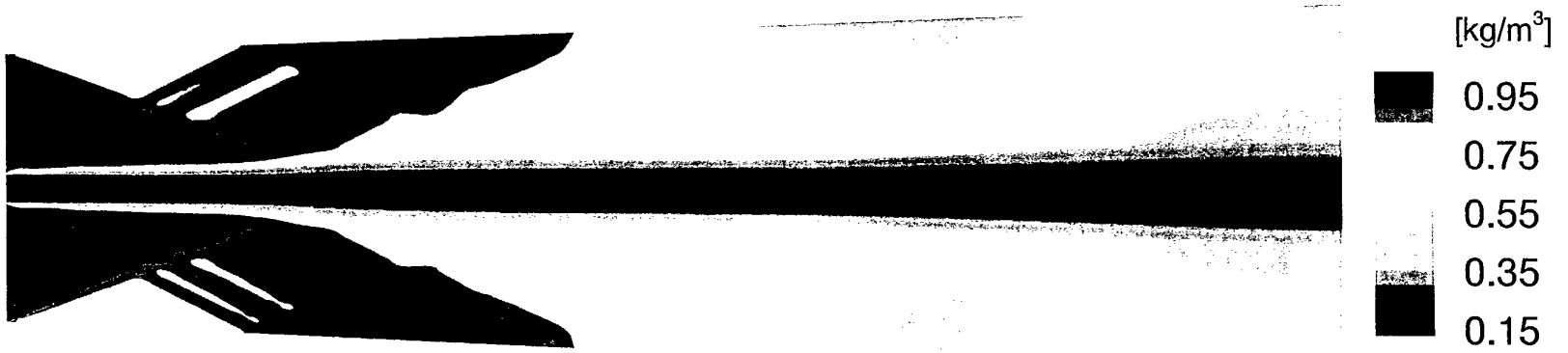


- Calculation ONERA (MSD Code)



- Calculation DLR / RWTH Aachen

Shock - Mixing Layer Interaction
DENSITY DISTRIBUTION



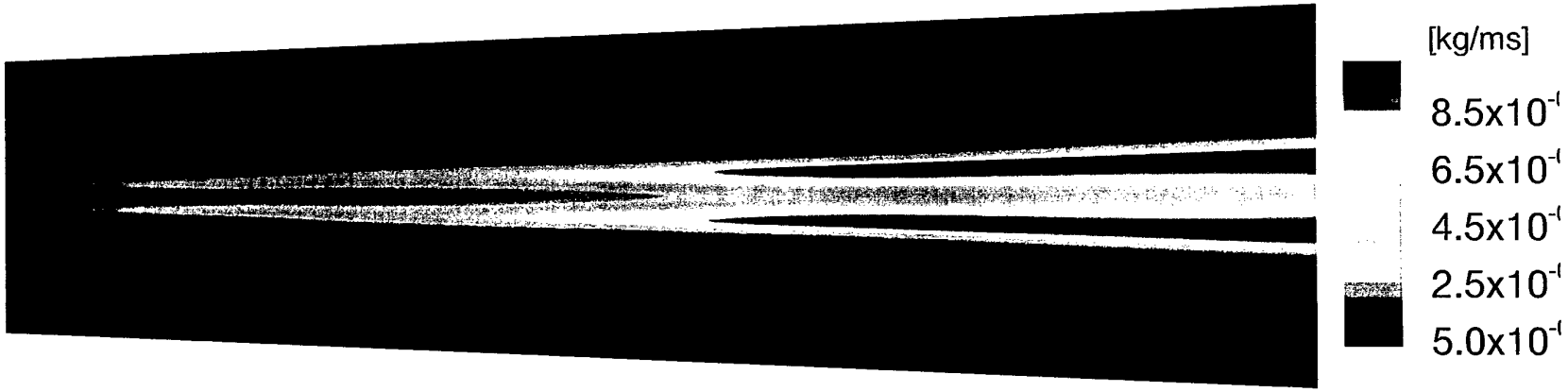
- without shock



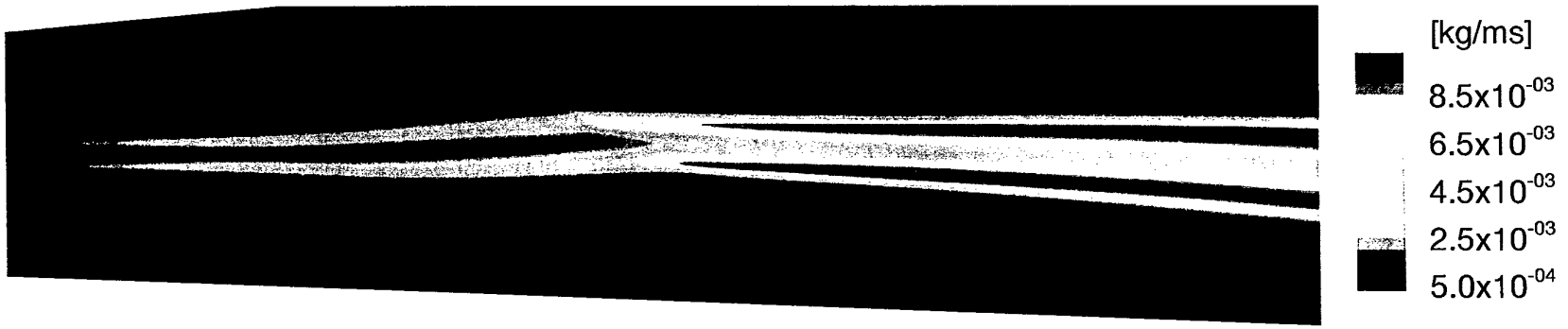
- with shock

Shock - Mixing Layer Interaction

DISTRIBUTION OF TURBULENT VISCOSITY

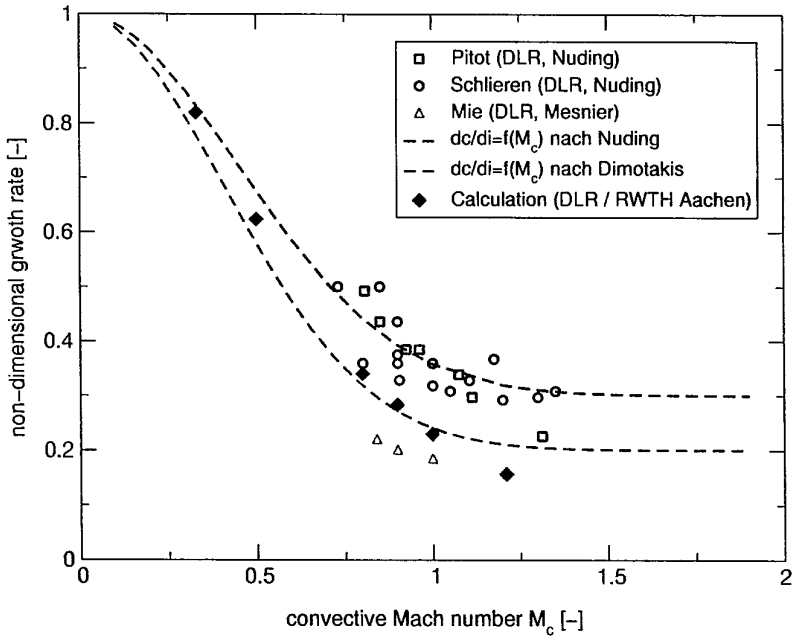


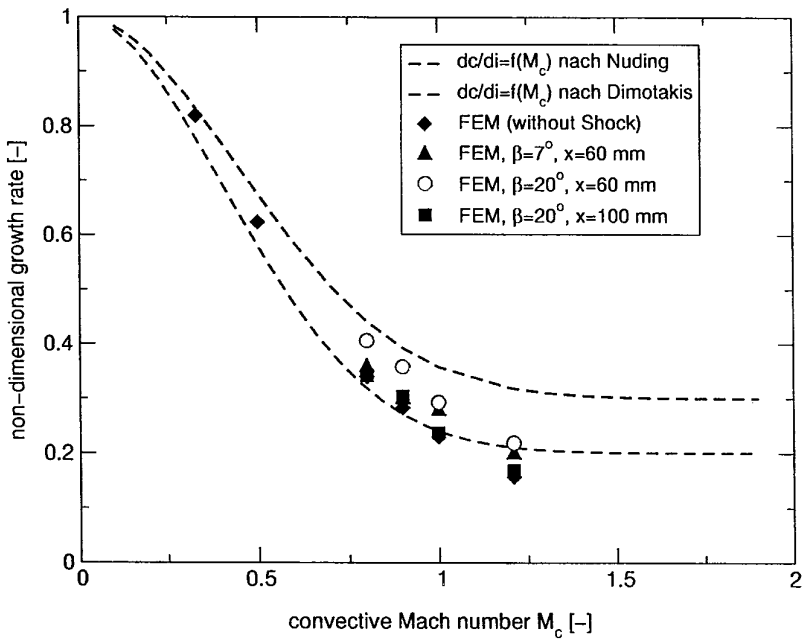
- without shock



- with shock

Non-dimensional Mixing Layer Growth

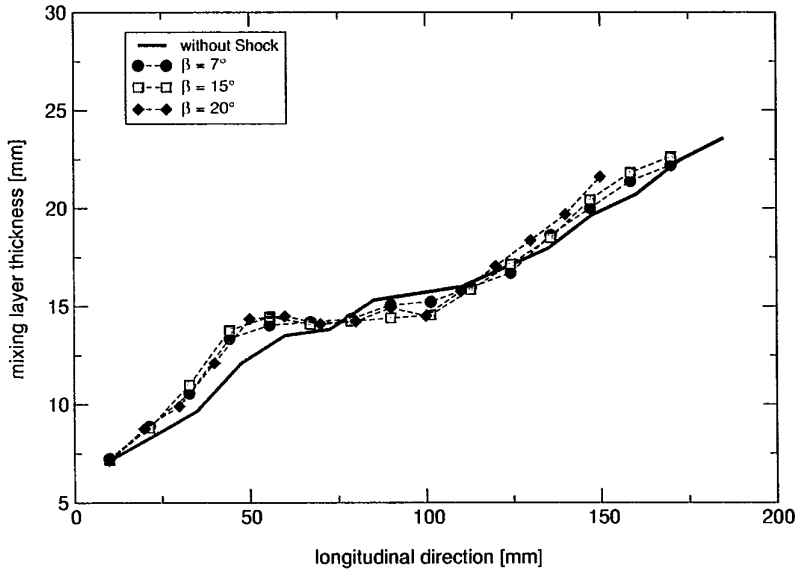




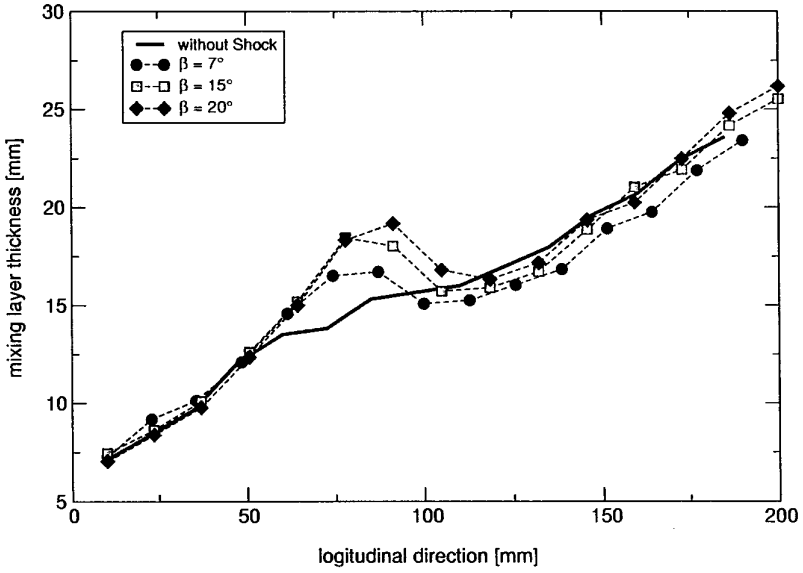
⇒ Shock interaction increases growth rate

Absolute Mixing Layer Growth

Shock position x_0 = 60mm



Shock position x_0 = 100mm



WG 2 ACTIVITIES
SUPERSONIC COMBUSTION MODELING

DLR

ONERA

ONERA - DLR cooperation on High Speed Airbreathing Propulsion

OBJECTIVE OF THE BASIC STUDIES



Improve the physical models used to describe the turbulent and reactive flows in a scramjet combustor.

Evaluate these new approaches on elementary 2D reactive and non reactive supersonic flows.

- **Study of the 2D supersonic reactive and non reactive mixing layer**

Validate the compressible turbulence and combustion models on 3D experiments.

- **Supersonic combustion experiment of LAERTE laboratory.**
- **DLR experiment on shock-mixing layer interaction.**

DLR

ONERA

Compressible turbulence modeling

Turbulent kinetic energy k :

$$\frac{\partial \bar{\rho} k}{\partial t} + \frac{\partial}{\partial x_j}(\bar{\rho}\tilde{U}_j k) = -\overline{\rho u_i'' u_j''}\tilde{d}_{ij} - \bar{\rho}\varepsilon + \frac{\partial}{\partial x_j}\left(\overline{\tau_{ij} u_i''} - \overline{p' u_j''} - \frac{1}{2}\overline{\rho u_i'' u_i'' u_j''}\right) + \boxed{\overline{u_j''}\frac{\partial \bar{P}}{\partial x_j} + \overline{p' u_{j,j}''}}$$

Viscous dissipation of k (Sarkar & Zeman approach)

$$\varepsilon = \varepsilon_s + \varepsilon_d$$

$$M_t = \frac{\sqrt{k}}{c}$$

DLR

ONERA

Turbulent combustion modeling



Classical combustion models (based on infinitely fast chemistry assumption) are not adapted to the representation of supersonic combustion cases.

- *Coherent flame model adapted to supersonic combustion*

- *Multi-dimensional pdf approach*

$$K + s\left[O_2 + \beta\ N_2\right] \longrightarrow \left[1 + s\right]P + s\beta\ N_2$$

Have been adapted to supersonic combustion.

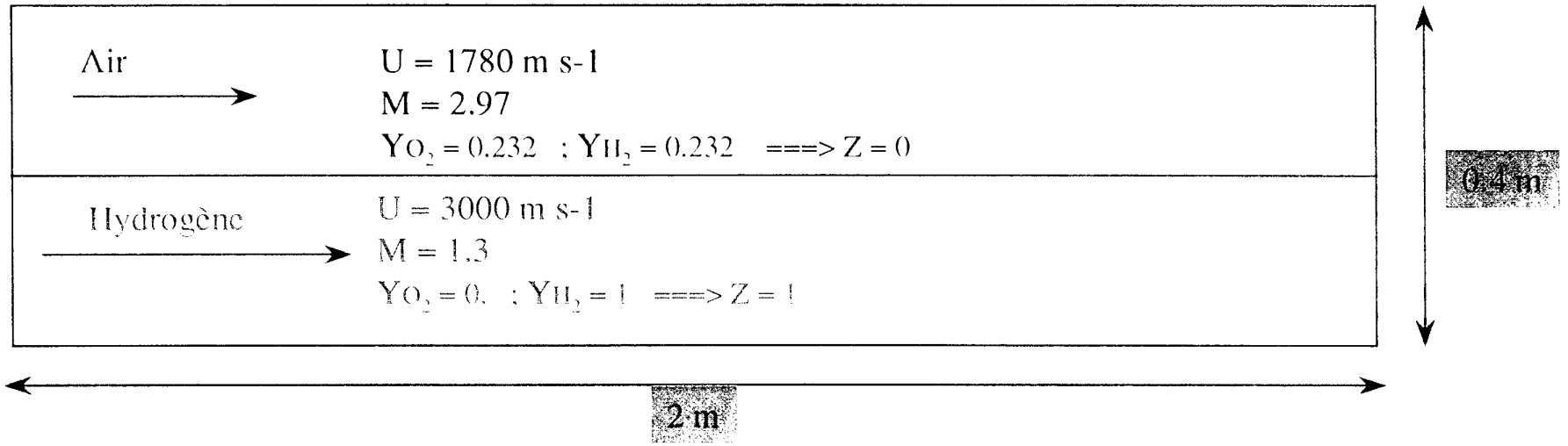
- *Generalized kinetics model (partially coupled with turbulence)*

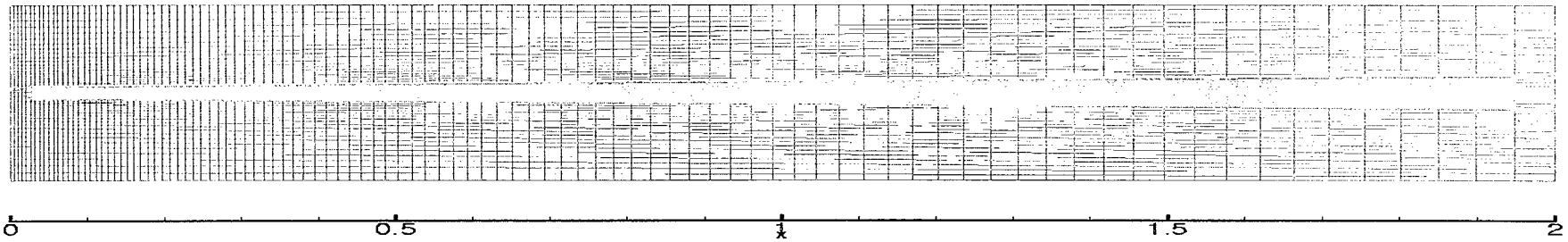
$$\sum_{k=1}^{n} \upsilon_{k,kr}^{(1)} \left[S\right]^k \longleftrightarrow \sum_{k=1}^{n} \upsilon_{k,kr}^{(2)} \left[S\right]^k \quad k_r = 1,\ldots,k_r$$

DLR

ONERA

2D TURBULENT AND REACTIVE MIXING LAYER





Mesh of the mixing layer : main domain (100 x 50) + subdomain (94 x 30)

DLR

ONERA

ONERA - DLR cooperation on High Speed Airbreathing Propulsion



Air → U = 1780 m s-1
M = 2.97
$Y_{O_2} = 0.232$; $Y_{H_2} = 0.00$ ===> Z = 0

Hydrogène → U = 3000 m s-1
M = 1.3
$Y_{O_2} = 0.$; $Y_{H_2} = 1$ ===> Z = 1

Air → U = 1200 m s-1
M = 1.93
$Y_{O_2} = 0.232$; $Y_{H_2} = 0.00$ ===> Z = 0

Hydrogène → U = 3800 m s-1
M = 1.58
$Y_{O_2} = 0.$; $Y_{H_2} = 1$ ===> Z = 1

Air → U = 800 m s-1
M = 1.37
$Y_{O_2} = 0.232$; $Y_{H_2} = 0.00$ ===> Z = 0

Hydrogène → U = 4300 m s-1
M = 1.94
$Y_{O_2} = 0.$; $Y_{H_2} = 1$ ===> Z = 1

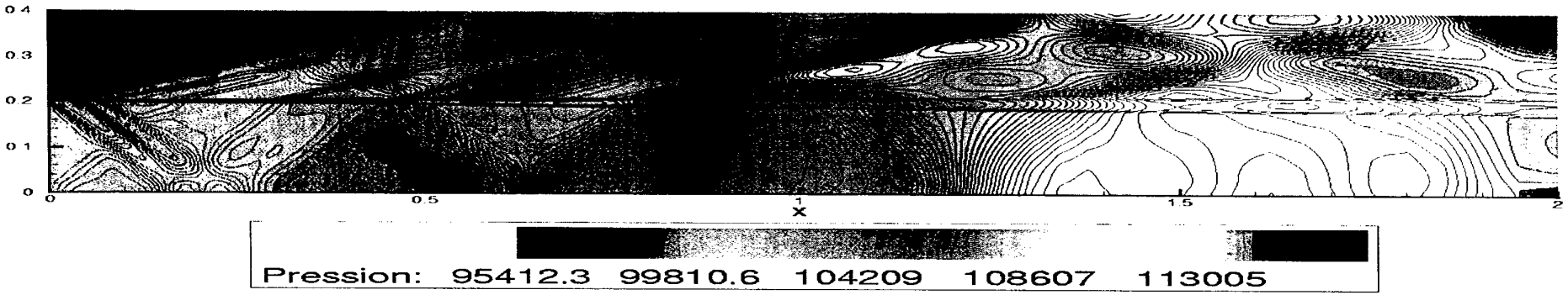
$$M_c = \frac{M_1 \sqrt[2]{\rho_2} - M_2 \sqrt[2]{\rho_1}}{\sqrt[2]{\rho_2} + \sqrt[2]{\rho_1}}$$

DLR

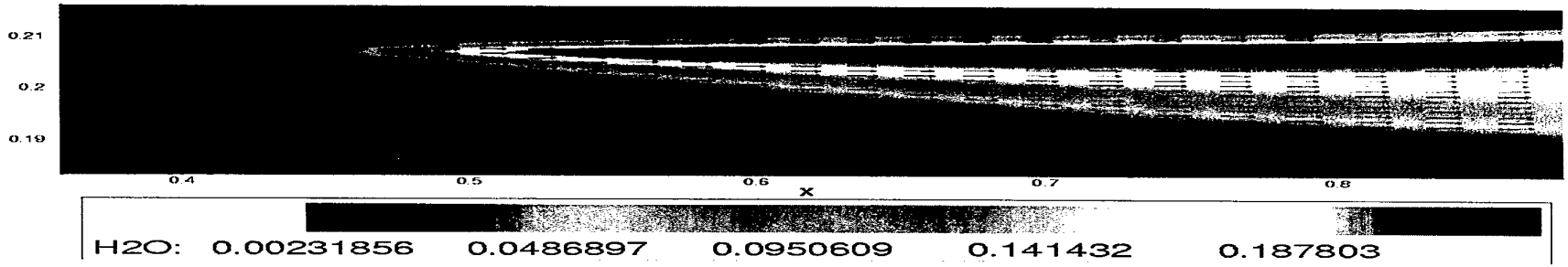
ONERA

ONERA - DLR cooperation on High Speed Airbreathing Propulsion

- Closure assumptions of the compressibility terms.



- Ignition of H_2 in the supersonic mixing layer .

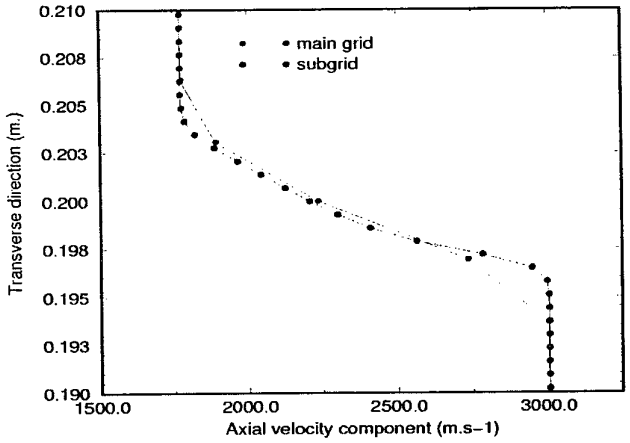


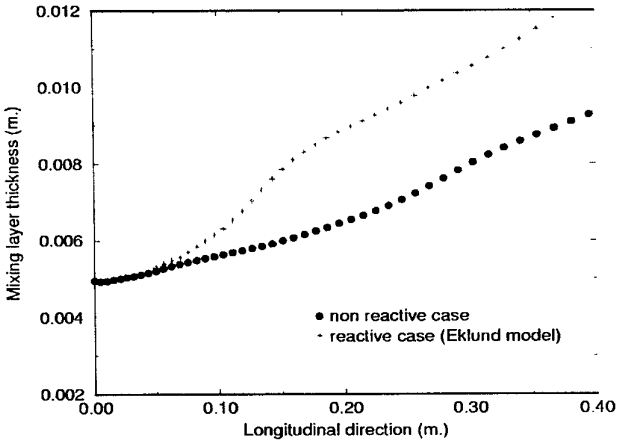
DLR

ONERA

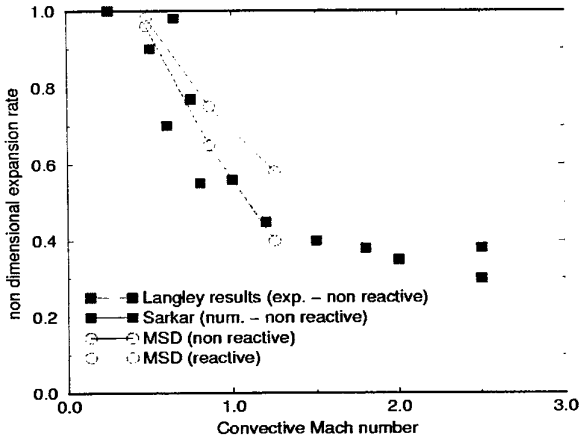
ONERA - DLR cooperation on High Speed Airbreathing Propulsion

The combustion process increases the expansion of the supersonic jet.





$$\delta'\omega^* = \frac{\frac{d\omega}{dx}}{\left.\frac{d\omega}{dx}\right|_{inc}}$$

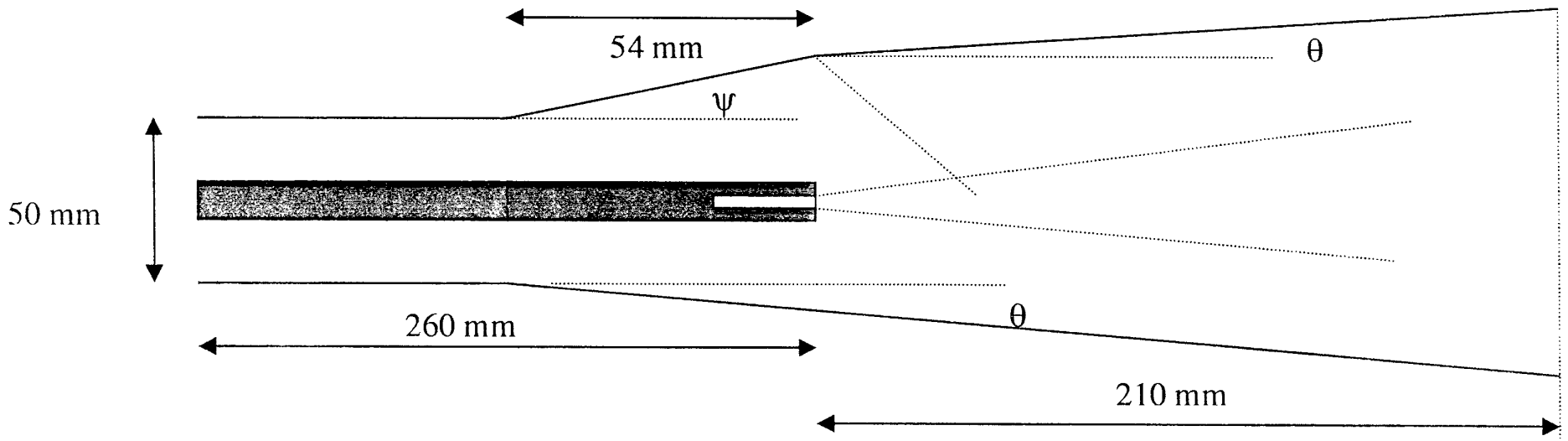


DLR

ONERA

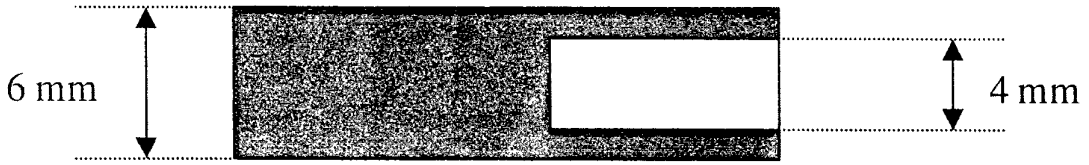
ONERA - DLR cooperation on High Speed Airbreathing Propulsion

NUMERICAL STUDY OF THE SHOCK - MIXING LAYER INTERACTION



$$\Psi = 7 - 15 - 20 \quad ^{o}$$

$$\Theta = 3 \quad ^{o}$$

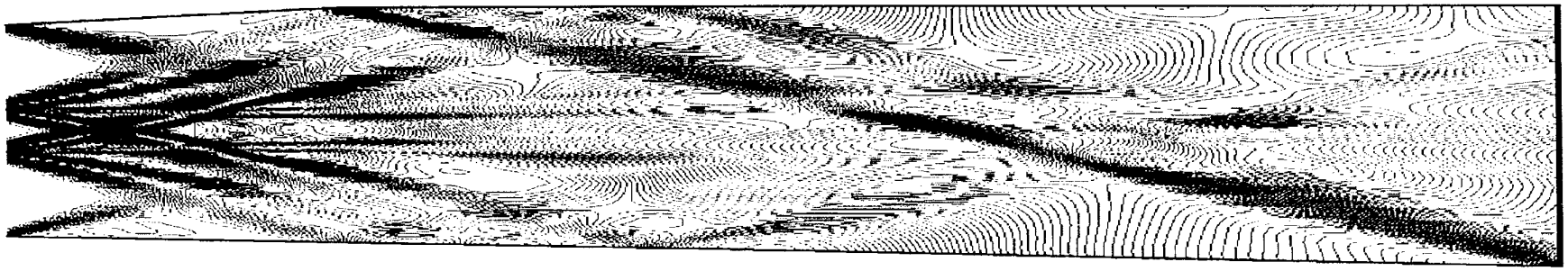


DLR

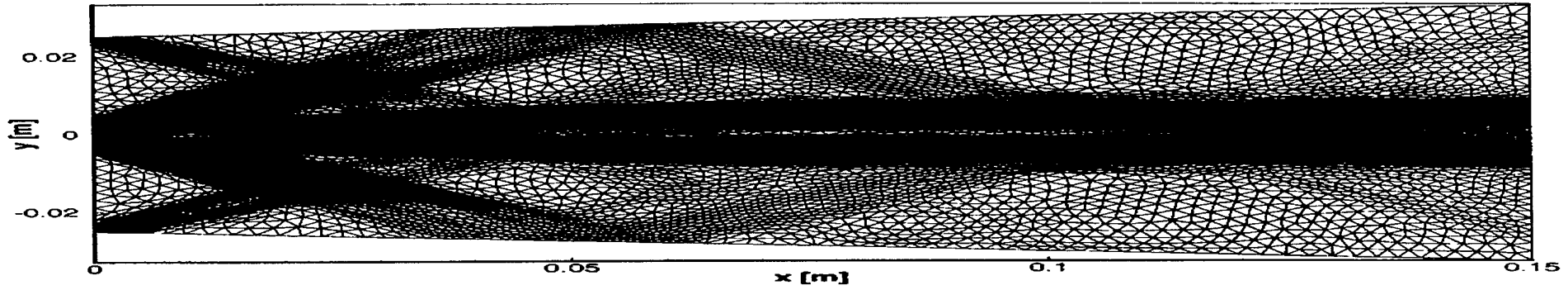
ONERA

ONERA - DLR cooperation on High Speed Airbreathing Propulsion

❁ Shock - Supersonic mixing layer interaction



Calcul ONERA (MSD)



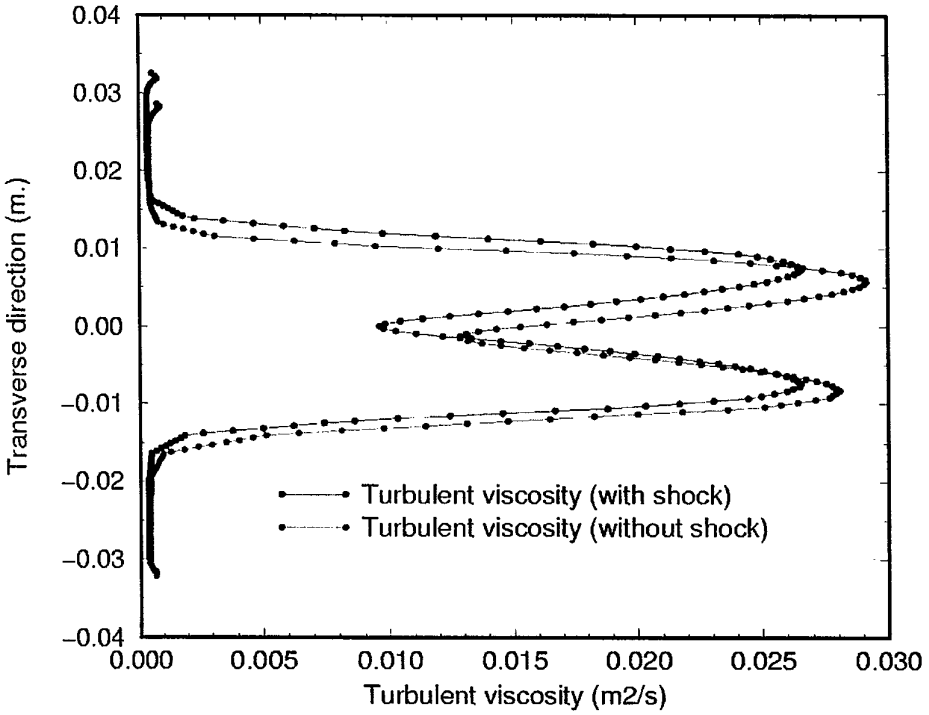
Calcul DLR/Lampoldshausen

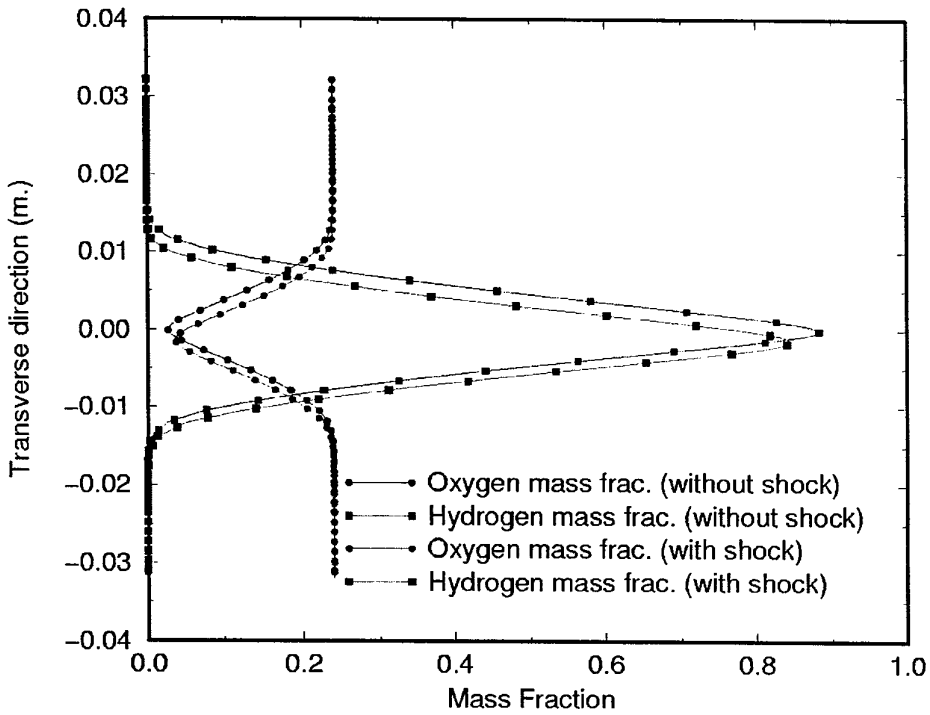
DLR

ONERA

ONERA - DLR cooperation on High Speed Airbreathing Propulsion

Comparison of numerical results obtained on both configurations (with and without shock)





DLR

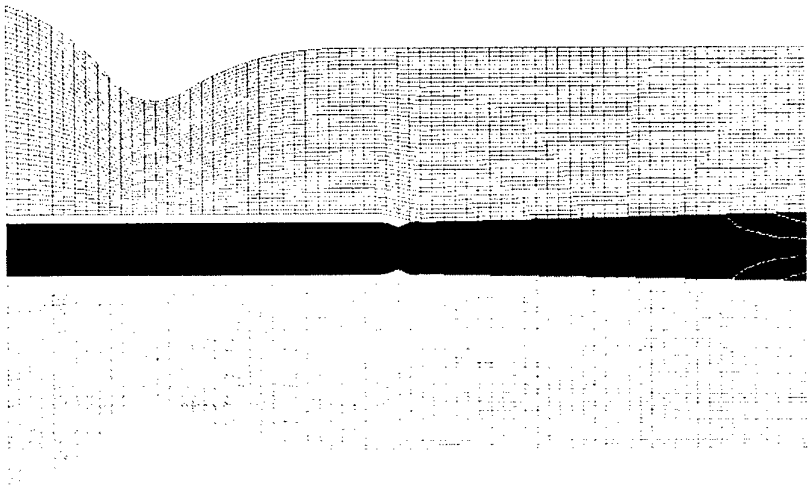
ONERA

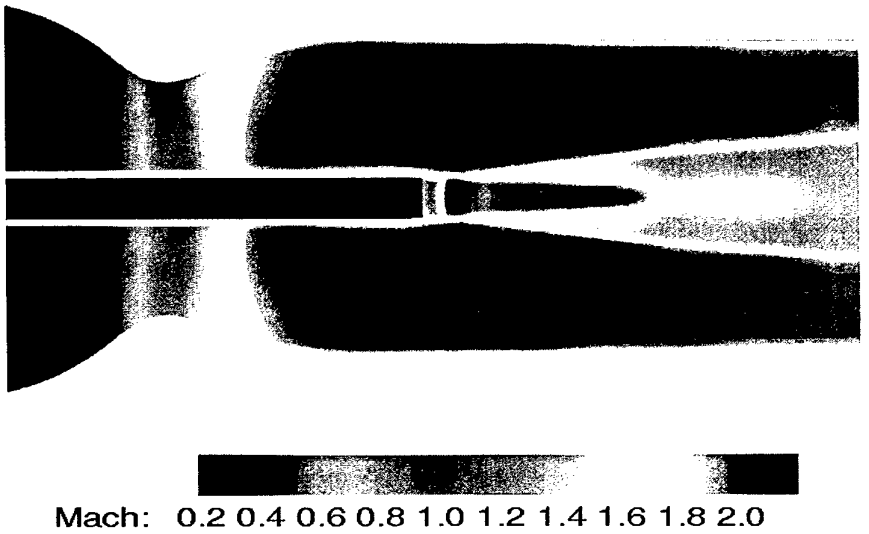
ONERA - DLR cooperation on High Speed Airbreathing Propulsion

Supersonic combustion experiment in ONERA / LAERTE laboratory

Parallel Supersonic Hydrogen injection discharging in a Mach 2 air flux :

Wall pressure distribution - OH mass fraction profiles (PLIF)
CARS Temperatures - LDV velocity field



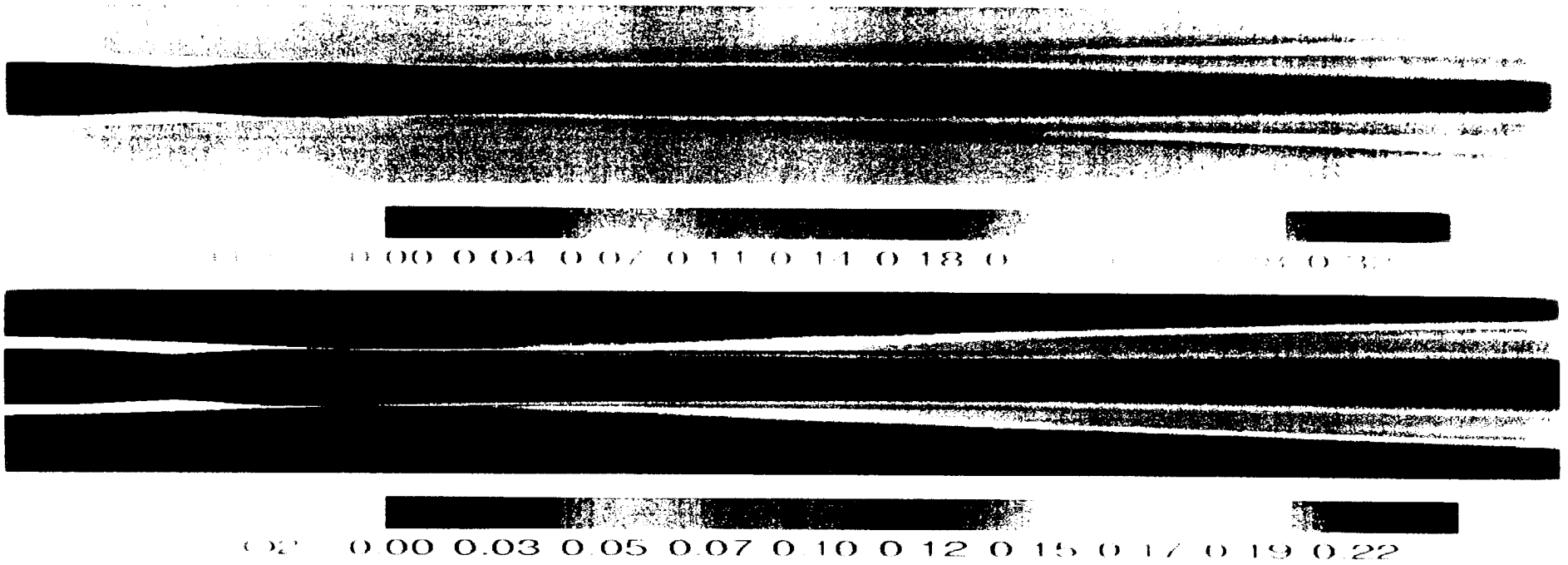


DLR

ONERA

ONERA - DLR cooperation on High Speed Airbreathing Propulsion

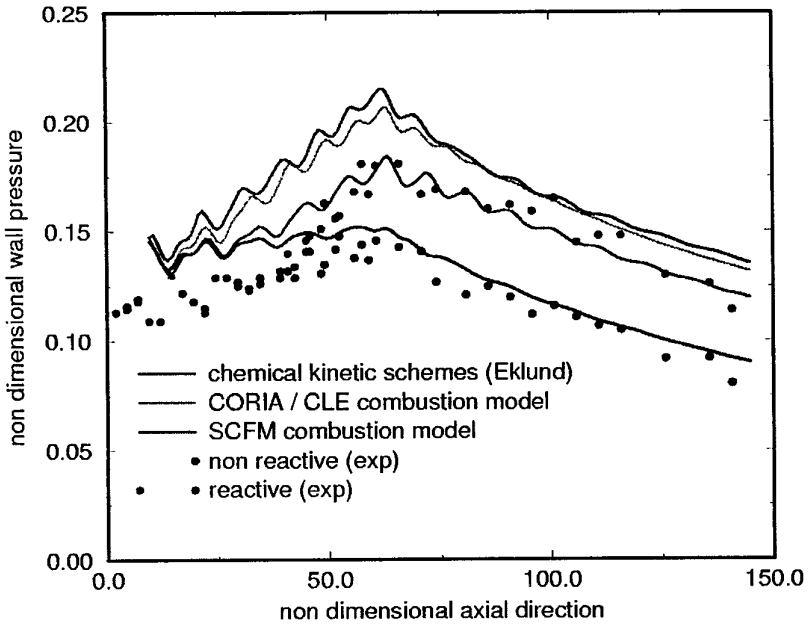
The mesh is refined in strongly sheared mixing layer in order to capture with a good accuracy the turbulent mixing and the chemical phenomena.

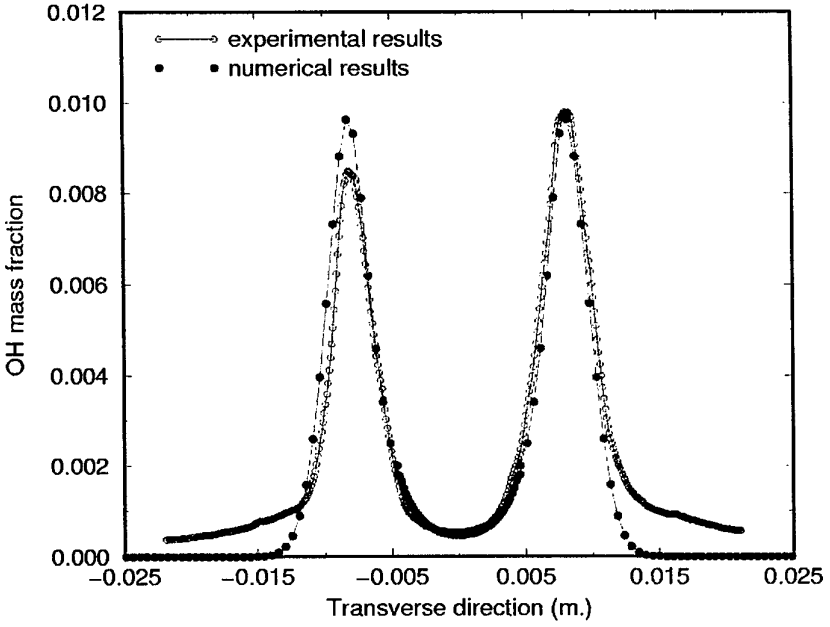


DLR

ONERA

2D MSD Results (LAERTE experiment)





Wall pressure axial distribution

OH mass fraction

DLR

ONERA

ONERA - DLR cooperation on High Speed Airbreathing Propulsion

Conclusions



- Compressible equation turbulence models used in DLR and ONERA numerical codes are well adapted to the description of the supersonic mixing layer.

- Coupling between turbulence and heat release has to be improved.

- Chemical kinetics approach using Eklund scheme has given very good results on the LAERTE experiment with a very refined grid.

DLR

ONERA

A STUDY ON COMBUSTION STABILITY OF A BIPROPELLANT LIQUID ROCKET ENGINES FOR ORBIT TRANSFER

Hong Xin, Zhang Zhongguang

Shanghai Academy of Spaceflight Technology

Shanghai

People's Republic of China

Abstract

To assure operational reliability of liquid rocket engines, the issue of high-frequency combustion instability of a newly developed 2500N-thrust NTO/MMH engine was studied both experimentally and numerically. During the early stage of development, high-frequency combustion instability phenomenon was encountered in hot firing of the engine with initial injector configuration. Finally a high combustion stability margin was obtained through the modification of injector configuration, including incorporation of acoustic cavity and rearrangement of injection element. The final injector configuration demonstrated very stable combustion characteristic in many stability evaluation hot firings under a wide range of operation parameters. To get more thorough understanding of combustion instability and help design, numerical study with modern CFD methods was carried out along with the experiments. The numerical study mainly involve following several topics: analysis of physical sub-process in combustion chamber such as propellant atomization, vaporization, mixing and chemical reacting, numerical methods for unsteady spray combustion, and stability evaluation technology. The important issues include modeling of propellant atomization, droplet vaporization/combustion, acoustic cavity and hypergolic propellant chemical reaction were treated carefully to obtain credible prediction. To catch the development of unsteady spray flow field, a new unsteady two-phase flow algorithm was developed based on the gaseous PISO algorithm. Finally, the effect of unsteady atomization, dynamic vaporization of droplet and acoustic cavity on the combustion stability was examined.

Subject: Bipropellant Liquid Rocket Engines, Combustion Instability, CFD

Nomenclature

A, B, C	= coefficient	ϕ	= general variable
c_p	= constant pressure specific heat	ω	= circular frequency
F	= force	ρ	= density
G', H', M'	= operator	$\mathfrak{R}$	= droplet state
K	= coefficient of elasticity	*superscript*	
M	= mass	*	= interim value
$\dot{m}$	= vaporization rate	'	= fluctuation value
P	= pressure	-	= average value
P_c	= chamber pressure	n	= n time layer
Q	= atomization rate	n+1	= n+1 time layer
r	= radius	*subscript*	
R	= damping factor	0	= reference state
r_m	= mixing ratio	A	= amplitude
S	= area	*ac*	= acoustic cavity
t	= time	*ato*	= atomization
T	= temperature	d	= droplet
u, v	= velocity	f	= fuel
x	= displacement	g	= gas
Y	= mass fraction	m	= mass
Z	= impedance	o	= oxidizer
α	= coefficient	s	= droplet surface
θ	= impact angle of jet	u	= velocity
ϑ	= momentum angle of jet	*vap*	= vaporization
η_c	= combustion efficiency	∞	= ambient

I. Introduction

Great progress has been made in liquid rocket engines technology during the past half century. Unfortunately, there were still some problems that were not completely solved. For example, high frequency combustion instability[1~3]. Due to its serious harm to engine and spacecraft, propulsion society has made a great effort to solve this problem, and some engineering methods were found which could suppress the combustion instability successfully in practice. However, since we still have not got an deep understanding about this extremely complex phenomenon up to now, solving combustion instability problem usually need engineering experience and a great amount of hot firing, which were very expensive and sometimes lead to iterative modification of the design of engine. So for long time propulsion society has been studying the mechanism and the suppression measurement of combustion instability in order to found an effective stability theory to guide the design of engine since the initial stage of development.

In the first hot firing of a hypergolic bipropellant (MMH/NTO) liquid rocket engines developed by Shanghai Academy of Spaceflight Technology (SAST) recently, high frequency combustion instability phenomenon were encountered, which lead to the destruction of thrust chamber. Subsequently an experimental study project was carried out in order to eliminate the combustion instability phenomenon of the engine and to insure a sufficient combustion stability margin for the engine in operation. Based on the experimental study, some numerical study was also carried out to deepen the understanding of this phenomenon. The main characteristic of the engine was listed in table 1.

Table 1 Main characteristic of the engine

Item	Unit	
Propellant		NTO/MMH
Thrust in vacuum	N	2500
Chamber pressure	MPa	0.75
Specific impulse	Ns/kg	2900
Mixing ratio		1.65
Cooling mode		Liquid film/Radiation

II. Experimental Study of Combustion Stability

To get sufficient combustion stability margin of the engine, a great amount of hot firing were needed to help designer to find out the stability characteristics of engine with various configuration and design parameters. During the development of the engine, three candidate injectors with different configuration were tested. The main parameters of these injectors were listed in table 2.

Table 2 Main design parameters of injector

Item	Unit	Config. I	Config. II	Config. III
Number of orifice row		1	1	2
Number of injection element		48	48	48
Diameter of oxidizer orifice	mm	0.85	0.85	0.85
Diameter of fuel orifice	mm	0.65	0.65	0.61
Impinge angle of orifice, θ_o/ θ_f	°	47/33	47/33	25/45, inner row
		17/63	17/63	35/45, outer row
Number of cooling orifice		24	24	32
Number of acoustic cavity		—	24	28
Diameter of acoustic cavity	mm	—	6.5	5
Depth of acoustic cavity	mm	—	20.4	20/23

A. Design and test of initial injector (config. I)

To obtain a high combustion performance with relatively short characteristic length of combustion chamber, unlike doublet injection element were adopted in initial injector configuration. Two types of injection element with different integrated momentum angle (ϑ), one is positive (deflected to chamber wall) and the other is negative (departed from chamber wall), were adopted to smooth the profile of propellant mass flux in combustion chamber cross section. Two types of injection element were arranged one by one in single row. The cooling fuel orifices were located near the perimeter of injector to form liquid film on the wall, which protect the wall from high temperature core gas. To find out the maximum possible acoustic mode of combustion instability in the engine, no acoustic cavity was adopted in initial injector configuration. A sketch of initial injector was shown in figure 1.

The thrust chamber with initial injector was hot fired under nominal operation condition. The test was ceased abnormally due to high frequency combustion instability, which resulted in two ablation spot in chamber wall near throat, one of which was burnout. Frequency spectrum analysis of the chamber vibration measurement indicated a prominent frequency of 6768 hertz (see figure 2), which is correspond to the theoretical prediction of first tangential acoustic mode. The maximum acceleration measured under this frequency is as high as 39.2 g, from which one can know that the first tangential mode combustion instability was happened in the thrust chamber during hot firing.

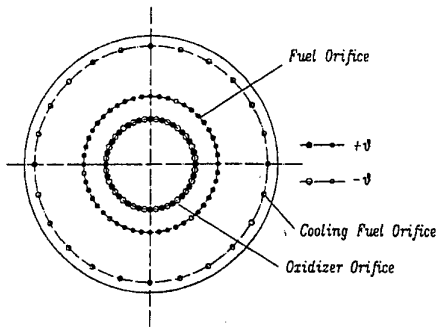


Fig.1 Injector configuration I

B. Design and test of modified injector (injector config. II and III)

Due to the combustion instability hazard of initial injector configuration, two modified injector configuration were proposed (see figure 3 and 4). As a conventional way to eliminate combustion instability, 24 acoustic cavities were adopted in injector configuration II and 28 for configuration III. In configuration II all acoustic cavities are identical and designed to prevent first tangential acoustic mode. In configuration III two types of acoustic cavities with different depth were adopted, both were designed to prevent first tangential acoustic mode. However the longer one was aimed at combustion instability during start-up stage and the shorter one for stable operation stage. Besides, the single-row arrangement of injection element in initial configuration was replaced by double-row arrangement in configuration II.

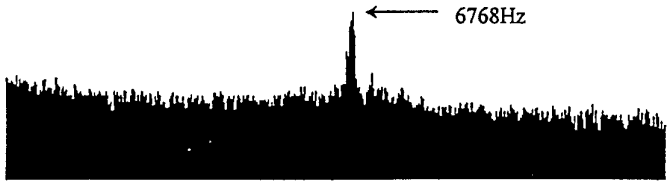


Fig.2 Power spectrum of the measurement of chamber vibration

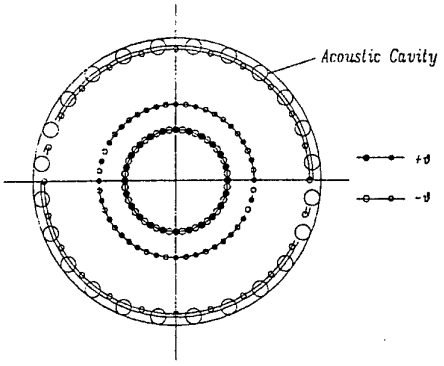


Fig.3 Injector configuration II

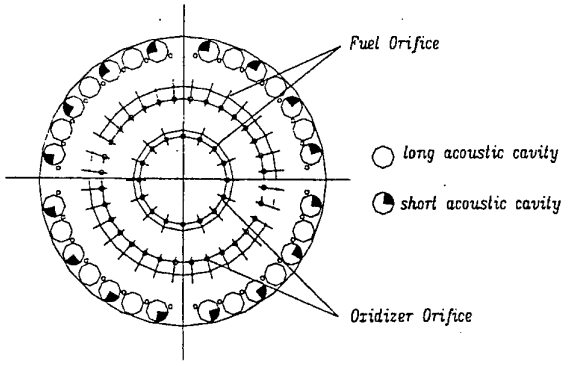


Fig.4 Injector configuration III

To examine the stability characteristics, hot firing under various chamber pressure and mixing ratio were carried out for both modified configuration. The hot firing were completed successfully and no combustion instability was observed. Since the combustion efficiency of chamber with configuration III is slightly higher than that with configuration II, the configuration III was chosen as the final injector configuration. Subsequently the stability evaluation hot firings were conducted for this final configuration.

C. Evaluation of dynamic stability

The dynamic stability of thrust chamber was evaluated by pulse gun test. The charge used in pulse gun is RDX. In each test generally two pulse gun was used, one installed tangentially and another radially (figure 5). About twenty tests with different operation parameter of engine (mixing ratio, chamber pressure, temperature of propellant) and different pulse gun charge mass were conducted to examine the stability margin of thrust chamber. In all tests the

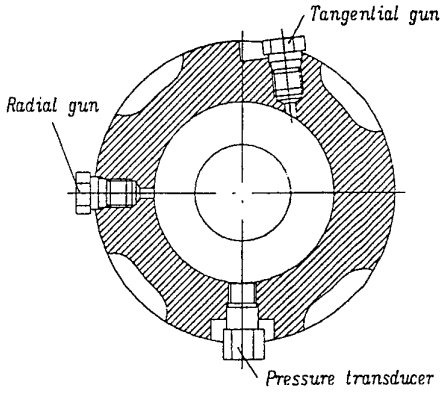


Fig.5 Cross section of hot firing chamber

tangential pulse gun was fired firstly, then the radial one. A high frequency pressure transducer was mounted flush in inner wall to monitor the combustion process.

Some parameters of the test were listed in table 3. In most tests the pulse disturbance was decayed in 10 milliseconds. In all tests no instability was observed, and the chamber is in good condition after hot firing, which indicated that the engine has a good stability characteristic. Some typical chamber pressure histories with pulse gun disturbance were shown in figure 6 and 7.

Table 3 Parameters in pulse gun test

Test No.	P_c MPa	r_m	η_c	T_o/T_f ℃	charge mass of pulse gun mg		dimensionless pressure peak		decay time ms	
					T	R	T	R	T	R
1	0.795	1.75	0.919	ambient	120	120	2.6	1.6	6	6
2	0.764	2.235	0.902	ambient	120	120	5.0	2.5	10	17.5
3	0.759	1.18	0.952	ambient	120	120	2.1	1.9	4	3
4	0.608	2.269	0.93	ambient	120	120	5.1	1.9	40	47
5	0.643	1.331	0.949	ambient	120	120	2.9	2.2	8	7.5
6	0.749	1.625	0.921	40.8/37.2	120	120	2.6	1.6	4.5	7.5
7	0.627	1.299	0.945	42/39	120	120	1.7	—	4.5	—
8	0.731	2.067	0.89	43.6/40	120	120	2.9	2.0	6.5	10
9	0.919	1.571	0.948	ambient	120	120	1.75	1.8	1.5	1.8
10	0.892	2.077	0.909	ambient	120	120	4.6	2.0	5	4.9
11	0.633	1.695	0.946	ambient	120	120	3.7	—	7.3	—
12	0.616	2.205	0.948	ambient	120	120	4.7	2.8	31	30
13	0.778	1.656	0.942	ambient	60	60	1.75	1.6	5.7	2.3
14	0.779	1.633	0.945	ambient	120	120	2.5	2.1	7.3	5.4
15	0.777	1.637	0.944	ambient	180	120	6.0	1.7	7	6.3
16	0.775	1.647	0.944	ambient	240	240	5.1	2.7	7.5	7.5
17	0.775	1.643	0.944	ambient	120	120	5.7	—	4.3	—

T-tangential; R-radial

III. Numerical Study of Combustion Stability

Computation fluid dynamics (CFD) has been applied to combustion instability analysis as early as 1960's. However, limited by the low level of computer hardware and numerical algorithm of that time, the early application of CFD in combustion instability analysis was too simplified to provide useful information for combustor design. Promoted by the development of the technology of computer software and hardware since 1980's, CFD methods has boomed rapidly and are widely applied to most engineering fields today. Since 1990's the combustion instability numerical analysis has been developing quickly[4-10].

. Based on the combustion instability phenomenon arisen in SAST engine and its suppression measure, a numerical study was carried out to get more understanding of this complex problem.

A. Physical model

1.Propellant atomization Up to now no precise analytical description of propellant atomization process was available due to the extremely complex interaction between liquid jet and ambient gas. In recent years the direct numerical simulation of atomization process has been developed quickly, however, such study is aimedmainly at investigation of atomization process itself and can't be directly adopted for combustion analysis. Now the spray property needed for numerical simulation of combustion process was obtained either from the measurement of spray or from engineering empirical correlation which was drawn out based on a great deal of measurements of spray property of specific type injector.

1.1 Droplet size distribution

The droplet size distribution was described with Nukiyama-Tanasawa distribution for impinge jet atomization. The mass mean diameter of oxidizer and fuel were determined from literature.

1.2 Droplet velocity distribution

The distribution of the velocity and injecting angle of droplet was assumed to be Gaussian. The injecting angle and the magnitude of velocity of spray, which can be calculated based on the design parameters of the injector, the flux and density of propellant, were taken as the expectation of the distribution of injecting angle and velocity of droplet respectively. The variance of both distributions was determined empirically. When the equivalent annular chamber model was adopted in computation, the expectation of the injecting angle of droplet should be set to zero.

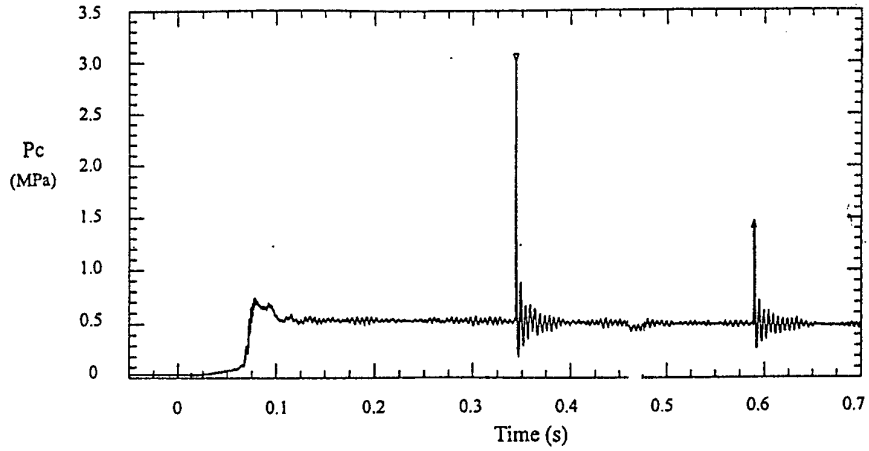


Fig.6 History of chamber pressure in pulse gun test

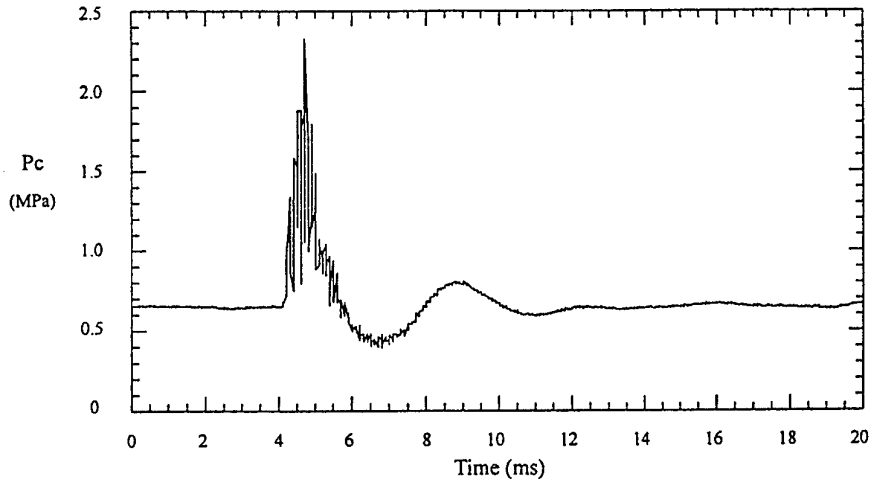


Fig.7 History of chamber pressure in pulse gun test

2.Droplet vaporization/combustion The state of droplets in combustion chamber is very complex. However, in most spray combustion relevant studies the phase-transition of propellant droplet was treated as a pure vaporization process. Recently several authors investigated multiple-mode droplet model. Jiang and Hsu[11] compared three droplet model: ① Droplet evaporation model (DEM), droplet was assumed in pure vaporization state; ② Droplet combustion model (DCM), droplet was assumed in combustion state;③ Modified droplet combustion model (MDCM), both vaporization or combustion state are possible, the state of droplet was determined by its condition and certain ignition criterion. Jiang and Hsu[11] concluded that the MDCM is the most preferable model. Base on this study, Jiang and Chiu[12] studied the bipropellant combustion with MDCM. Huang and Chiu[13] investigated the vaporization, ignition, blow off, extinction and recurrence of n-octane in air with numerical method, and developed a criterion for droplet state estimation base on Damkohler number *Da*. However, their study was conducted for specific fuel and the results were difficult to be applied to this study.

Due to the complex chemical property, the vaporization/combustion process of hypergolic propellant has a significant difference with that of liquid oxygen or hydrocarbon, and this difference was hardly considered in previous studies concerning the hypergolic propellant. To eliminate the limitation of single mode vaporization model and model the real process of hypergolic propellant droplet more accurately, multiple mode vaporization/combustion models for MMH/NTO propellant was developed in this paper. The droplet mode considered included pure vaporization of MMH/NTO droplet, dissociation reaction of MMH droplet, oxidation reaction of MMH droplet, and combustion of NTO droplet in gaseous MMH. The transient heating process of droplet was also considered.

2.1 Droplet vaporization model

● MMH

The vaporization behavior of MMH droplet is far different from liquid oxygen or hydrocarbon droplet because MMH is a monopropellant that will decompose and a flame surround the droplet will be formed due to the heat released during vaporization. Zhuang et al[14] have studied this type process for a long time. Their model will be incorporated in this study.

The physical model for the vaporization of MMH droplet was illustrated in figure 8, where r_s, r_f and r_∞ is radius of droplet, decomposition reaction flame and effective film respectively. The detail of computation can be found from ref.[14].

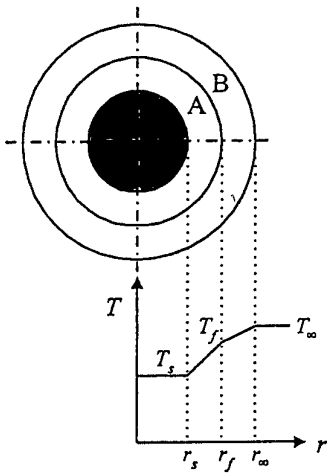


Fig. 8 Physical model of vaporization of MMH droplet

● NTO

Contrary to MMH, NTO droplet will undergo endothermal dissociation reaction during vaporization. However, the temperature needed for the dissociation reaction is low, and the vaporization system is easy to reach equilibrium state. The endothermal dissociation reaction is assumed to happen at the surface of droplet. The heat absorbed by dissociation reaction could be treated as latent heat of liquid. So the vaporization of NTO can be calculated by MMH model with proper modification.

2.2 Droplet combustion model

When the ignition condition was satisfied, the vapor of one propellant will react with the vapor of other propellant and a diffusive flame surrounded the droplet will be formed. Thus there will be two flame for MMH droplet and one for NTO droplet.

● MMH

The physical model based on the forementioned hypothesis was illustrated in figure 9. where r_s, r_{f1}, r_{f2} and r_∞ is radius of droplet, decomposition reaction flame, diffusive flame and effective film respectively. The details of calculation can be found from ref.[14].

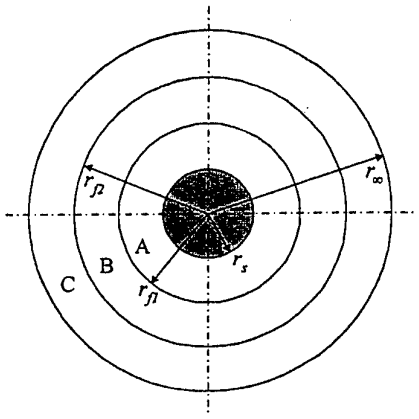


Fig. 9 Physical model of combustion of MMH droplet

● NTO

Like its vaporization model, the combustion of NTO droplet can also be calculated by MMH model with proper modification. The main difference between the combustion model of MMH and NTO lie in that the NTO droplet has no decomposition flame.

2.3 Criterion for droplet state

For case of MMH, the droplet was assumed burning if the following condition were satisfied.

① The ambient gas was oxidizer-rich;

② $D_a > D_{al}$.

The expression of droplet Damkohler number D_a and ignition Damkohler number D_{al} can be found from [15].

The case of NTO can then be deduced from above.

3.Chemical reaction rate The equilibrium chemistry is assumed in this study because no reduced reaction scheme are available for bipropellant due to its complex chemical property. The equilibrium chemistry is feasible in view of the shorter time scale of chemical process compared to atomization or vaporization.

Although only four elements (C, H, O and N) were involved in the reaction system comprised of NTO and MMH, many species are involved in practical system. Based on the results of combustor thermochemistry calculation, The following ten species with highest concentration are included in the study: H_2, O_2, N_2, CO, NO, OH, CO_2, H_2O, H, O. Additionally, CH_4 was also included to facilitate the droplet model. All rest species were ignored in the chemistry model in view of their very low concentration (less than 10^{-5}) in system.

The chemical reaction rate of species was calculated by iterative algorithm under the constraint condition that the species in system and relevant parameters should satisfy the chemical equilibrium condition. The detailed algorithm of reaction rate in equilibrium chemistry can be found from[16]。

4.Acoustic cavity model The lumped parametric governing equation of the motion of gas in acoustic cavity should be derived in order to determine the response characteristic of the gas under fluctuant environment. The

approach adopted in this study is similar to that of Helmholtz resonator. The gas in cavity was simulated by a mass-spring-damping system. So we should know the characteristic of this system.

Denote the mass of mass-spring-damping system as M_{ac}, the coefficient of elasticity as K_{ac}, the damping factor as R_{ac}. A sinusoidal driving force F_{ac} was assumed,

$$F_{ac} = F_A \cos \omega t \tag{1}$$

Then the governing equation of the motion of the system can be written as

$$M_{ac} \frac{d^2x}{dt^2} + R_{ac} \frac{dx}{dt} + K_{ac} x = F_A \cos \omega t \tag{2}$$

Based on vibration theory, the amplitude of velocity vibration of the system can be written as

$$v_A = \frac{F_A}{|Z_{ac}|} \tag{3}$$

where Z_{ac} is impedance of the system. The modulus of impedance is

$$|Z_{ac}| = \sqrt{R_{ac}^2 + (\omega M_{ac} - \frac{K_{ac}}{\omega})^2} \tag{4}$$

From equation (3) and (4) one can know that the mass, coefficient of elasticity and damping factor of system can be determined if the dependency of v_A on F_A with various ω value was obtained. Then the acoustic cavity source terms in flow governing equations can be determined through vibrator equation (2).

Numerical method was adopted to obtain the response of the motion of gas in cavity to the fluctuation of pressure outside the cavity. The computational domain was illustrated in figure 10 by dotted line.

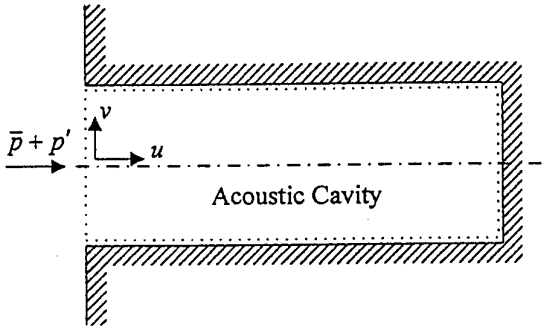


Fig. 10 A sketch of acoustic cavity

The pressure outside the acoustic cavity assumed to be sinusoidal:

$$p' = p'_A \cos \omega t \tag{5}$$

The response of system on pressure fluctuation was measured by the velocity of gas at the inlet if cavity. However, the numerically calculated gas velocity will not be uniform along the cross section of the cavity. So the following cross section averaged value of gas velocity was used in acoustic cavity model,

$$\bar{u} = \frac{1}{S_{ac}} \iint_A u dA \tag{6}$$

where S_{ac} is the area of cross section of cavity. Once the dependency of $p'_A S_{ac}$ on $\bar{u}$ with various ω was obtained, the characteristic parameters of acoustic cavity model can be determined.

B. Numerical approach

1.Governing equations Two types of governing equations, two-dimensional cylindrical coordinate equations or the so-called equivalent annular chamber equations firstly developed by Habiballah et al[4], were adopted in the study depend on the research object. The annular chamber equations used for the problems involved tangential mode instability and the cylindrical equations for others.

The motion of liquid phase was described in Lagrangian frame and the effect of turbulent dispersion was considered in the code.

2.Grid generation A boundary-fitted curvilinear grid was generated with TTM method for the case of cylindrical equations. Some orthogonalization treatment was conducted for the boundary node to facilitate the treatment of boundary condition and improve the convergence of code. As to the case of annular chamber equations, the rectangle grid was adopted.

3.Algorithm for unsteady two-phase flow Based on the idea in ref[17] and the original PISO algorithm[18,19], a two-phase PISO algorithm for the computation of unsteady spray combustion was developed to improve the efficiency and accuracy of computation. In this newly developed algorithm the concept of time-split are adopted in droplet phase as well as in gaseous phase. The calculation procedure from time layer t to time layer $t+\Delta t$ was described below. The interim values of variables were denoted by superscript $*$, and the gaseous source term and liquid source term were denoted by subscript g and d respectively.

① Prediction of droplet phase

Based on the flow field variables ϕ^n and droplet information $\Re^n$ (such as the number, place, mass, velocity and temperature of computational droplet) at t time layer, the droplet information $\Re^*$ at $t+\Delta t$ time layer was calculated through the droplet dynamics. Then the droplet source term S_d^* in prediction step can be obtained through the concept of PSIC[20].

② Prediction of gaseous momentum

The prediction of gas velocity u_i^* was obtained through the implicit iterative solution of differential form of gaseous momentum equation with the pressure and density of old time layer:

$$(\frac{1}{\delta t}-\frac{A_0}{\rho^n})\rho^n u_i^* = H'(u_i^*)-\Delta_i p^n + S_{g,u} + S_{d,u}^* + \frac{\rho^n u_i^n}{\delta t} \tag{7}$$

③ First correction of droplet phase

The droplet information $\Re^{**}$ at $t+\Delta t$ time layer was calculated based on u_i^*, ϕ^n and $\Re^n$. At the same time the droplet source term in first correction step S_d^{**} can be got.

④ First correction of gaseous phase momentum

Transform the differential form momentum equation to following explicit correction form:

$$(\frac{1}{\delta t}-\frac{A_0}{\rho^n})\rho^* u_i^{**} = H'(u_i^*)-\Delta_i p^* + S_{g,u} + S_{d,u}^{**} + \frac{\rho^n u_i^n}{\delta t} \tag{8}$$

With equation (7), equation (8) can be written as following incremental form:

$$\rho^* u_i^{**} - \rho^n u_i^* = -(\frac{1}{\delta t}-\frac{A_0}{\rho^n})^{-1}\left[\Delta_i(p^*-p^n)+(S_{d,u}^*-S_{d,u}^{**})\right] \tag{9}$$

Through state equation we got

$$\rho^* = p^*\phi(p^n, T^n) \tag{10}$$

Combine equation (9), (10) and continuum equation, the following pressure equation can be yielded,

$$\left\{\Delta_i\left[(\frac{1}{\delta t}-\frac{A_0}{\rho^n})^{-1}\Delta_i\right]-\frac{\phi(p^n,T^n)}{\delta t}\right\}(p^*-p^n)$$

$$= \Delta_i\left[(\frac{1}{\delta t}-\frac{A_0}{\rho^n})^{-1}(S_{d,u}^{**}-S_{d,u}^*)\right]+\Delta_i(\rho^n u_i^*)-S_{g,m}-S_{d,m}^{**} \tag{11}$$

Solve the equation above, we got the prediction of pressure p^*. Then the prediction of density ρ^* and the first correction of velocity u_i^{**} can be calculated with equation (9) and (10).

⑤ Prediction of gaseous scalar

The temperature and species fraction can be obtained by implicit iteration of the equations of species and energy,

$$(\frac{1}{\delta t}-\frac{B_0}{\rho^*})\rho^* T^* = G'(T^*)-\frac{1}{c_p}\Delta_i(p^* u_i^{**})+S_{g,T}+S_{d,T}^{**}+\frac{\rho^n T^n}{\delta t} \tag{12}$$

$$(\frac{1}{\delta t}-\frac{C_0}{\rho^*})\rho^* Y^* = M'(Y^*)+S_{g,Y}+S_{d,Y}^{**}+\frac{\rho^n Y^n}{\delta t} \tag{13}$$

⑥ Second correction of droplet phase

Based on the updated field variable ϕ^*, u_i^{**} and droplet information $\Re^n$, calculate the droplet information $\Re^{***}$ at $t+\Delta t$ time layer and the droplet source term S_d^{***} of second correction step.

⑦ Second correction of gaseous phase momentum

Calculate the following equations explicitly with the latest value of relevant variables.

Momentum equation:

$$(\frac{1}{\delta t}-\frac{A_0}{\rho^*})\rho^{**} u_i^{***} = H'(u_i^{**})-\Delta_i p^{**}+S_{g,u}+S_{d,u}^{***}+\frac{\rho^n u_i^n}{\delta t} \tag{14}$$

Continuum equation:

$$\Delta_i(\rho^{**} u_i^{***}) = -\frac{1}{\delta t}(\rho^{**}-\rho^n)+S_{g,m}+S_{d,m}^{***} \tag{15}$$

State equation:

$$\rho^{**} = p^{**}\phi(p^*, T^*) \tag{16}$$

Combine above three equations we got the following equation for the pressure correction p^{**}:

$$\left\{\Delta_i\left[(\frac{1}{\delta t}-\frac{A_0}{\rho^*})^{-1}\Delta_i\right]-\frac{\phi(p^*,T^*)}{\delta t}\right\}p^{**}$$
$$=\Delta_i\left[(\frac{1}{\delta t}-\frac{A_0}{\rho^*})^{-1}(H'(u_i^{**})+S_{g,u}+S_{d,u}^{***}+\frac{\rho^n u_i^n}{\delta t})\right]-\frac{\rho^n}{\delta t}-S_{g,m}-S_{d,m}^{***} \quad (17)$$

Based on equation (17), (16) and (14), p^{**}, ρ^{**} and u^{***} can be calculated. Now the latest values of all variables being calculated were taken as the value at $t+\Delta t$ time layer.

⑧ Calculation of turbulent variables

The calculation of turbulent variables such as k and ε was also comprised of prediction and correction. The detail of calculation procedure is identical to that of gaseous PISO algorithm and can be found from literature[18,19].

C. Stability study

In many numerical studies of combustion instability a disturbance was added on the steady operation value of flow field variables to simulate the flow field disturbed by bomb or pulse gun. In fact the initial flow field generated with such numerical disturbance may be far from the reality. To simulate the realistic physical process more closely the effect of pulse gun on flow field was considered by adding short duration source terms of mass, momentum and energy to gaseous governing equations in this study.

1.Effect of dynamic response of vaporization The droplet model based on quasi-steady hypothesis will give a questionable results when flow field parameters in combustion chamber were oscillatory such as the case of combustion instability. So the influence of oscillatory environment on droplet vaporization should be considered in combustion instability study. The key problem is the dynamic response expression of droplet vaporization model under oscillatory environment. Limited by computation resource, the complete numerical model of dynamic vaporization could not adopted in numerical study of combustion chamber. In this paper the following general phenomenological analytical expression was adopted,

$$\dot{m}=\dot{m}_0(1-\alpha_{vap}\frac{dp}{dt}\Big/\left(\frac{dp}{dt}\right)_0) \quad (18)$$

where $\dot{m}_0$ is stable state vaporization rate calculated with quasi-steady model, $\left(\frac{dp}{dt}\right)_0$ is a reference value of pressure derivative and set as constant for given propellant, α_{vap} is coefficient of dynamic term used to regulate the intensity of dynamic response.

The simulation of combustion stability was conducted with various α_{vap}. To simplify the computation a monodisperse droplet was assumed and the droplet generation rate was set to constant. The results were illustrated in figure 11 to 13. The Y-axis in the figures indicated the pressure at the center of injector face. From these figures one can know that the combustion stability is fairly good since the oscillation of chamber pressure decay quickly when the dynamic response of droplet vaporization is not significant which indicated by small α_{vap}. With the increasing of α_{vap}, The decay rate of pressure oscillation decreased obviously. When α_{vap} increased to an enough large value, combustion instability that indicated by sustaining pressure oscillation would be observed. The study confirmed that the couple between vaporization and chamber pressure oscillation would be a significant driving factor of combustion instability.

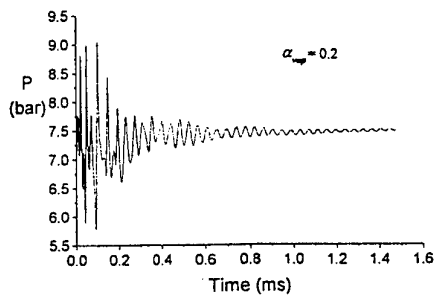


Fig. 11 History of pressure at injector center

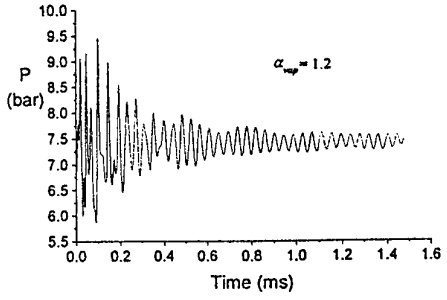


Fig. 12 History of pressure at injector center

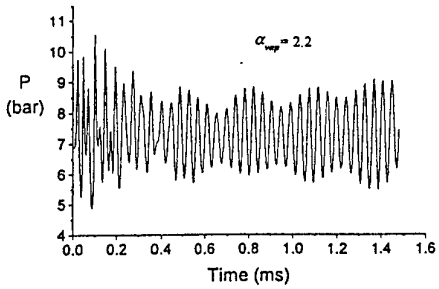


Fig. 13 History of pressure at injector center

2.Effect of unsteady atomization Based on experiment observation and theoretical analysis, the atomization of impinging jet was known as an unsteady process and the formation of droplet was a periodic process. The periodicity of droplet formation could have a significant influence on combustion process and could become an important driving factor of combustion instability. This problem was seldom considered in previous combustion instability analysis. Since the detail mechanism of atomization was not understood well up to now, this problem was discussed by the way of parametric study in this study. To consider the temporal nonuniform of atomization rate, the following expression was adopted to describe the droplet generation rate as a function of time,

$$Q_{ato} = \overline{Q}_{ato}[1 + \alpha_{ato} \sin(\omega_{ato} t)] \tag{19}$$

where Q_{ato} is atomization rate, i.e. the mass of droplet injecting to chamber per unit time, Q_{ato} is the steady value of atomization rate, α_{ato} is a coefficient between 0 and 1, which was used to regulate the fluctuation intensity, and circular frequency ω_{ato} was adopted to regulate the time scale of atomization periodicity.

Through equation (19), the effect of atomization periodicity on combustion stability was investigated. Two-dimensional cylindrical form of gaseous governing equations was employed and monodisperse droplet was assumed. The pressure history with various α_{ato} and ω_{ato} were illustrated in figure14 to 17, the pressure was sampled at axial position one fifth of the length of combustion chamber downstream the injector. From these figures one can know that the periodical injection of droplet formed a driving factor of the oscillation in chamber. This driving factor would achieve its maximum at certain ω_{ato}. When the driving factor exceeded the damping factor, the parameter oscillation would be amplified and resulted in combustion instability. When the atomization periodicity was not significant, which was indicated by small α_{ato}, parameter oscillation in combustion chamber was decayed quickly to small amplitude oscillation with the frequency identical to atomization oscillation. However, the parameter oscillation would be amplified when α_{ato} is large enough and atomization frequency is located in certain range.

3.Effect of acoustic cavity In order to examine the effect of acoustic cavity on combustion stability, computation of tangential mode stability of the chamber, which has encountered combustion instability during development, was carried out without acoustic cavity (injector I) and with acoustic cavity (injector II). The equivalent annular chamber equations were adopted for tangential mode instability simulation with current computation resource. Since the details of dynamic response of vaporization and the periodicity of atomization are not understood well up to now, the parametric study was carried out in stability simulation. More than one value was specified for each affect factor of sub-process in order to cover the uncertainty of atomization and vaporization. Eight calculations were conducted with different parameters that were listed in table 4. The calculation cases listed in the table were arranged in the order of increasing instability factor. In the table, n was the droplet uniformity parameter. With the greater n, the droplet size is more uniform. The computation results were also listed in the table.

Case 1 and 2 were the most stable case. In these two cases, the vaporization of droplet was assumed to be quasi-stable and without dynamic response to the ambient oscillation, the atomization rate was assumed to be constant. Thus the combustion were stable in the chamber both with acoustic cavity and without acoustic cavity. However, the result indicated that the decay rate of the oscillation in chamber were slightly higher in the case with acoustic cavity than the case without acoustic cavity.

When the dynamic response of vaporization was taken into account in case 3, the parameter oscillation decay rate was slower than that of case 2. However, the combustion in case 3 was still stable even without acoustic cavity probably because the dynamic response of vaporization was not great enough. The computation result of case 3 still indicated that the acoustic cavity accelerated the decay of oscillation. When the dynamic response of vaporization was increased to certain value, the combustion instability was appeared as indicated in case 4. However, the combustion instability was suppressed by the acoustic cavity in this case.

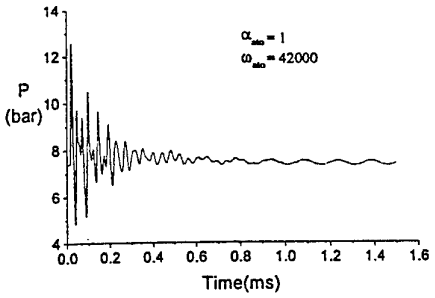


Fig. 14 History of chamber pressure

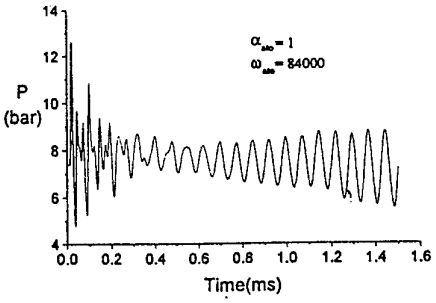


Fig. 15 History of chamber pressure

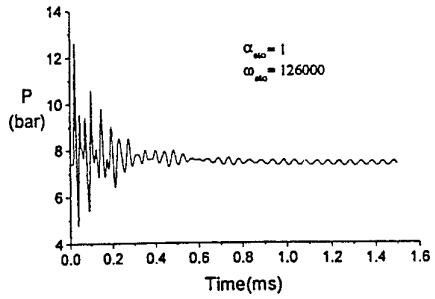


Fig. 16 History of chamber pressure

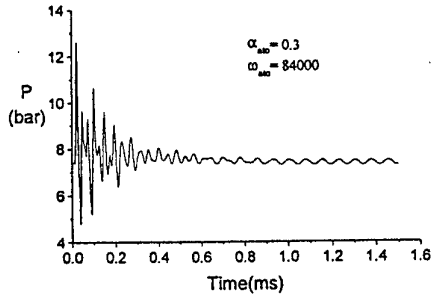


Fig. 17 History of chamber pressure

Table 4 Combustion stability under different condition

case	n	α_{vap}	α_{ato}	ω_{ato}	Stability	
					injector I	injector II
1	1.5	0	0	—	S	S
2	3	0	0	—	S	S
3	3	0.5	0	—	S	S
4	3	2.5	0	—	U	S
5	3	2.5	0.5	30000	U	S
6	3	2.5	1	30000	U	S
7	3	2.5	1	50000	U	S
8	3	2.5	1	40000	U	U

S-Stable U-Unstable

Since case 5 the instability driving factor of atomization, i.e. atomization periodicity, was taken into account. The results shown that the combustion were unstable without acoustic cavity in case 5~8. However, the instability were suppressed by acoustic cavity in case 5~7. Case 8 is the case including the most instability-driving factor. In this case the combustion instability would happen even with acoustic cavity. This is not the fact, so one can know that the instability-driving factors considered in case 8 were more than reality, or the damping factor of the system considered was less than reality.

IV. Conclusion

Limited by computation resource, only a fraction of atomization and vaporization problems were studied in the paper. Based on the study one can find that the periodicity of atomization and the dynamic response of vaporization to ambient oscillation both are important combustion instability driving factors, and the combustion instability could be triggered when these factors is great enough. However, the possibility of such instability, or how much the influence of atomization periodicity and vaporization dynamic response on the instability are in reality would not understand until the thorough investigation of atomization, vaporization and their coupling mechanics with combustion are carried out. For high frequency combustion instability, the parameter oscillation in chamber has a minor influence on propellant feeding process, the main problem of atomization should lie in the coupling between the breakup of liquid jet and ambient environment.

The stability design of the engine developed by SAST was validated both experimentally and numerically.

The effect of acoustic cavity to suppress the combustion instability is evident. To understand the combustion instability phenomenon more deeply, a great deal of thorough study effort concern the sub-process of spray combustion process should be conducted.

Acknowledgement

The authors want to express their sincere thanks to Academician Sun Jingliang and Professor Cheng Huier, Zhang Baojiong, Han Hongyin, Zhuang Fengchen, and Dr Liu Weidong for their great support and important advice to the study. The authors also want to thank all friends who presented very helpful ideas and provided good research condition for the study.

Reference

[1] Harrje, D.T., and Reardon, F.A.(ed.), *Liquid Propellant Rocket Combustion Instabilities*, NASA SP-194,1972

[2] Culick,F.E.C.,"Combustion Instabilities in Liquid-Fueled Propulsion Systems—An Overview,"AGARD CP-450 (also AD-A211109),1988.

[3] Yang,V.,and Anderson,W.(eds.),*Liquid Rocket Engine Combustion Instability*, Progress in Astronautics and Aeronautics, Vol.169,AIAA,1995

[4] Habiballah,M.,*et al.*, "High Frequency Combustion Instabilities in Liquid Propellant Rocket Engines—A Review of Studies Carried Out at ONERA for the Ariane Launcher," AIAA 92-0774.

[5] Kim,Y.M.,*et al.*, "Numerical Simulation of Combustion Instabilities in Liquid-Fueled Engines," AIAA 92-0775.

[6] Grenda,J.M.,and Merkle,C.L., "Computational Fluid Dynamic Analysis of Liquid Rocket Combustion Instability," AIAA 91-1609.

[7] Litchford,R.J.,and Jeng,S.M., "Liquid Rocket Spray Combustion Stability Analysis," AIAA 92-3227.

[8] Liu Weidong, *A Numerical Model Study of Liquid Rocket Engines Combustion Instability*, Ph.D. Dissertation, National Univ. of Defense Technology,1996

[9] Zhao Wentao, *A Nonlinear Analysis of Liquid Rocket Engines Combustion Instability*, Ph.D. Dissertation, National Univ. of Defense Technology,1997

[10] Nie Wansheng, *A Study on Combustion Stability of Hypergolic Propellant Liquid Rocket Engines*, Ph.D. Dissertation, National Univ. of Defense Technology,1998

[11] Jiang,T.L.,and Hsu,W.J., "Comparison of Droplet Combustion Models in Spray Combustion," AIAA-91-2203.

[12] Jiang,T.L.,and Chiu,H.H., "Bipropellant Combustion in a Liquid Rocket Combustion Chamber," J. of Propulsion and Power,Vol.8,No.5,1992,pp.995-1003.

[13] Huang,J.S.,and Chiu,H.H., "A New Droplet Model for Spray Combustion," AIAA 95-2427.

[14] Zhuang Fengchen, *Theory, Model and Application of Liquid Rocket Engines Spray Combustion*, National Univ. of Defense Technology Press, 1995

[15] Law,C.K.,and Chung,S.H., "An Ignition Criterion for Droplets in Sprays," Combustion Science and Technology, Vol.22,1980, pp.17-26.

[16] Ramshaw, J.D. and Amsde, A.A., "Improved Iteration Scheme for Partial Equilibrium Flow", J. Computational Physics. Vol.59,No.3, p484-489,1985

[17] Chen.C.P.,*et al.*, "An Efficient Pressure-Velocity Procedure for Gas-Droplet Two-Phase Flow Calculations," Int. J. Numerical Methods in Fluids,Vol.15,1992,pp.233-245

[18] Issa,R.I., "Solution of the Implicity Discretized Fluid Flow Equations By Operator-Splitting," J. Comp. Phys.,Vol.62, 1986,pp.40-65

[19] Issa,R.I.,*et al.*,"The Computation of Compressible and Incompressible Recirculating Flows by a Non-Iterative Implicit Scheme," J. Comp. Phys.,Vol.62,1986,pp.66-82

[20] Crowe. C.T.,et al., "The Particle-Source-in Cell(PSI-CELL) Model fro Gas Droplet Flows," J. Fluids Engineering, Vol.99,1977,pp.325-332

Experimental method of effectiveness estimation of different damped measures for oscillations in LRE combustion chambers and gas generators

Lebedinsky[1] E. Mosolov[2] S.
Keldysh Research Center, Moscow, Russia

Abstract

The principles of acoustic modeling of dynamic properties of the combustion chamber and gas generator are considered in the article.

The concept of the acoustic facility intended for experimental definition of the frequency characteristic of the combustion chamber is adduced.

The examples of practical application of a method are given.

1. Operating principles of the acoustic facility

On modern oppinion [1], [2] appearance of burning instability arises from joint operation of the two dynamic elements: the burning zone and the acoustic link (see Fig. 1).

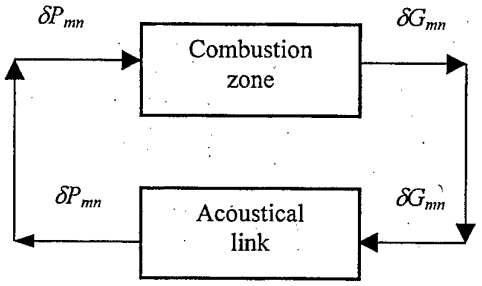


Fig.1

The chain of actions shown in Fig. 1 is a closed self-excited circuit. In this circuit δP_{mn} and δG_{mn} are dimensionless amplitudes of pressure pulsation, $\delta P_{mn} = \frac{P'_{mn}}{\bar{P}}$, and of mass flux density pulsation, $\delta G_{mn} = \frac{\rho'_{mn}}{\bar{\rho}} + \frac{u'_{mn}}{\bar{u}}$ of mode (m, n) at the burning zone end.

The system shown in Fig. 1 be at the stability boundary under the following condition:

$$H\theta = 1 \qquad (1)$$

or

$$|H||\theta| = 1 \qquad (2)$$

$$\sin(\varphi_H + \varphi_\theta) = 0, \qquad (3)$$

where $H = \frac{\delta G_{mn}}{\delta P_{mn}} = |H| e^{i\varphi_H}$ is a frequency characteristic of the burning zone;

$\theta = \frac{\delta P_{mn}}{\delta G_{mn}} = |\theta| e^{i\varphi_\theta}$ is an acoustic frequency characteristic.

If modulus $|\theta|$ decreases at a constant modulus $|H|$, the system becomes stable:

$$|H| < \frac{1}{|\theta|}.$$

If modulus $|\theta|$ increases at a constant modulus $|H|$, the system goes into the instability zone:

$$|H| > \frac{1}{|\theta|}.$$

Therefore, in order to increase the stability reserve, it is necessary to reduce the combustion chamber acoustic frequency characteristic modulus. This conclusion is valid both for a "soft" mode of oscillations excitation and for a "hard" one [2].

The acoustic frequency characteristic is unequivocally connected to an impedance, widely used in acoustics [3].

$$Z = \frac{P'_{mn}}{\bar{\rho}\bar{c}u'_{mn}}$$

[1] Chief of section, professor
[2] Leading researcher

$$\theta = \frac{\gamma MZ}{1 + MZ} \quad \left(M = \frac{\overline{u}}{\overline{c}} \right)$$

where γ is the adiabatic exponent

Let's break the self-excited circuit shown in Fig. 1 by omitting the burning zone. Then, the remaining acoustic link have the mass flux (mass flow-rate) density pulsation at the burning zone end (at the injection head) as an input coordinate and the pressure pulsation at the same section as an output coordinate.

So, in order to simulate an acoustic link operating mode under unstable burning properly, it is necessary artificially to generate mass flow rate harmonic oscillations of amplitude δG_{mn} and to measure the amplitude of the appearing pressure pulsation δP_{mn} at the same section. Then, dividing δP_{mn} by δG_{mn}, we can determine the combustion chamber acoustic frequency characteristic.

A schematic of this idea realization is shown in Fig. 2 and has been described in Ref. [4].

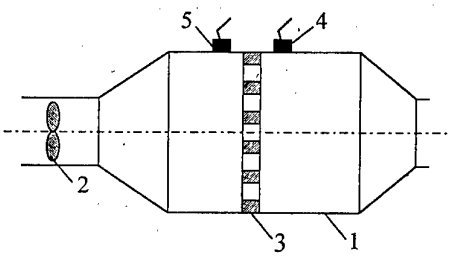


Fig. 2

1- the investigated object (the acoustic link); *2* – a source of harmonic disturbances in the stream (a pulsator); *3* – a grate installed at the inlet of the investigated acoustic link and providing supersonic pressure drop (hereinafter it is named methodical grate); *4* – a gauge of pressure pulsation downstream of the grate (p_1'); *5* – a gauge of pressure pusation upstream of the grate. (p_2')

The methodical grate performs the following functions:

- the disturbances generated by the pulsator are supplied through it into the investigated acoustic link;
- due to a supersonic pressure drop, the grate separates (isolates) dynamic properties of the investigated object from acoustic properties of the flow upstream of it;
- the grate allows of measuring the mass flow rate pulsation introduced into the investigated link by measuring the pressure pulsation upstream of the grate;
- using the grate, we can excite not only longitudinal oscillation modes in the acoustic link under investigation, but also higher oscillation modes.

Let's consider, that wavelength of the analyzed oscillations is substantially greater than the methodical grate channels length. Then, neglecting a gas accumulation in the grate channels, we obtain:

$$G_2 = G_1 \quad \text{or} \quad \overline{G}_2 = \overline{G}_1;\ G_2' = G_1', \qquad (4)$$

where $G = \rho u$ is density of the gas mass flux through the grate.

Due to the same reason, we can consider the unsteady gas flow through the grate channels as a quasi-steady process, therefore, under the supersonic pressure drop, we have:

$$\delta G_2 = \frac{G_2'}{\overline{G}_2} = \frac{\gamma + 1}{2} \cdot \frac{P_2'}{\overline{P}_2}, \qquad (5)$$

where γ is the adiabatic exponent.

Since, according to (1.4), $\delta G_1 = \delta G_2$, the combustion chamber acoustic frequency characteristic is equal to

$$\theta = \frac{\delta P_1}{\delta G_1} = \left(\frac{2\gamma}{\gamma + 1} \right) \cdot \frac{\delta P_1}{\delta P_2} = \frac{2\gamma}{\gamma + 1} \cdot N, \quad \text{where}$$

$$N = \frac{\delta P_1}{\delta P_2} \qquad (6)$$

i. e., it is proportional to the ratio of the dimensionless pressure pulsations in the combustion chamber and upstream of the methodical grate.

A principle point of the acoustic facility is realization of a certain oscillation mode in the combustion chamber. Numerous methodical experiments had shown that the mode structure of acoustic disturbances in the combustion chamber can be changed simply by redistributing the methodical grate orifices on its plane (Fig. 3):

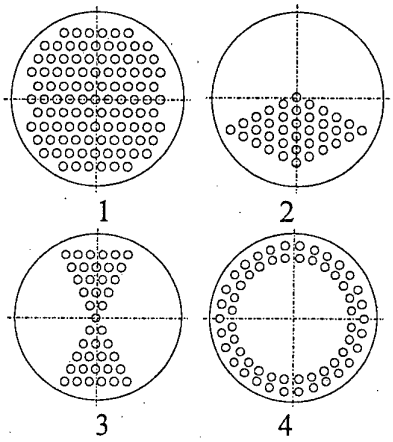


Fig. 3

grate 1 generates plane disturbances;

grate 2 generates disturbances of the first tangential mode of transverse oscillations;

grate 3 generates disturbances of the second tangential mode of transverse oscillations;

grate 4 generates disturbances of the first radial mode of transverse oscillations.

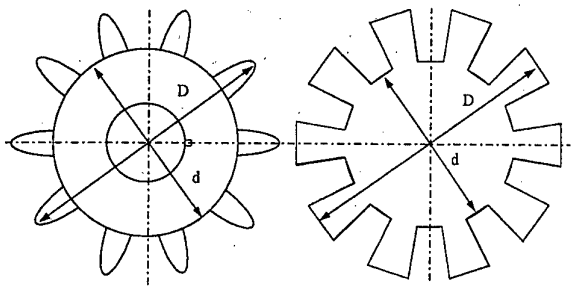
But it is relevant to note here, that these (shown in Fig. 3), methods of exciting various oscillation modes disturb the combustion chamber steady stream pattern.

As numerous tests had shown, the combustion chamber steady stream pattern disturbances don't change the combustion chamber dynamic properties fundamentally.

A source of harmonic disturbances, i. e., the pulsator is an important element of the acoustic facility. The following main requirements are specified for the pulsator:

- possibility of passing through it the total steady mass flow rate of the gas passing through the combustion chamber;
- generation of the heeded mass flow rate pulsation amplitudes;
- possibility of varying the mass flow rate pulsation amplitudes.

The hydraulic (flow passage) part of the pulsator is a throttle element whose flow passage cross area varies in time in a harmonic law due to rotation of the pulsator sprocket (the rotor) against the motionless pulsator pylons (the stator). Contours of the sprocket and of the pylong for a ten-petal pulsator are shown in Fig. 4 [5].



D=108 mm d= 69 mm

а) sprocket б) pylons

Fig. 4

The pulsation amplitudes of mass flow rate can be changed discretely through changing the sprocket dimension D.

2. Criteria of the acoustic simulation

The acoustic tests are model tests, since to realize a high-temperature combustion chamber operation under conditions of the acoustic tests is impossible because of low thermal resistance of the experimental hardware and the pulsator in particular. Because of that, a model gas (air heated up to about 550 K) is used in the acoustic facility. In connection with switching over to the model gas, questions on adequacy of the combustion chamber and pulsator acoustic characteristics under the model conditions and under the full-scale ones arise. The adequacy criteria for the combustion chamber are:

1. $\left(\frac{\omega D}{2C}\right)=\left(\frac{2\pi fD}{2C}\right)=const$ is frequency criterion;

2. $\left(\frac{D_{th}}{D}\right)^2=const$ is Mach number at the nozzle subsonic part inlet;

3. $\left(\frac{l}{L}\right)=const$

4. $\left(\frac{D}{L}\right)=const$

(are geometric criteria).

Here:

f is oscillations frequency (Hz);

D is diameter of the combustion chamber cylinder;

D_{th} is diameter of the nozzle throat;

L is length of the combustion chamber cylinder;

l is length of the nozzle subsonic part;

C is reference sonic velocity in the combustion chamber.

As the nozzle subsonic part is a variable cross area channel, criteria 3 and 4 are equivalent to the requirement of similarity of the full-scale and model nozzle subsonic contours.

In the acoustic simulation it is convenient to use a combustion chamber model of full-scale dimensions. At that, according to frequency criterion 1, the operating frequency range under the model conditions is equal to:

$$f_M = f_R \frac{D_R}{C_R} \frac{C_M}{D_M} = f_R \frac{C_M}{C_R},$$

so at C_M=480 m/s and C_R=1200 m/s

$$f_M = f_R \cdot 0.4$$

subscript $_M$- model conditions

subscript $_R$ - real conditions

3. Schematic of the acoustic facility

A schematic of the acoustic facility is shown in Fig. 5. The facility includes the following units:

1 - the investigated object, i. e. a combustion chamber with a resonator;

2 - the methodical grate whose functions have been described above;

3 - a pulsator being a source of harmonic disturbances in the flow;

4 - a hydroturbine intended for rotating the pulsator;

5 - a mechanical reduction gear intended for increasing the number of pulsator revolutions;

6 - an alcohol/air burner intended for heating the air used as a facility working body;

7 - an adapter (spacer) connecting the pulsator with the combustion chamber;

8 - connecting manifolds.

When a heated air having γ=1.4 and C=578 m/s ($T \approx 550$ K) is used as a facility working body at the combustion chamber pressure of $P_c=2\cdot10^5$ Pa and at the nozzle throat area of $F_{th}=14.52\cdot 10^{-3}$ m^2, the total mass flow rate of the gas flowing through the facility is equal to about 5 kg/s.

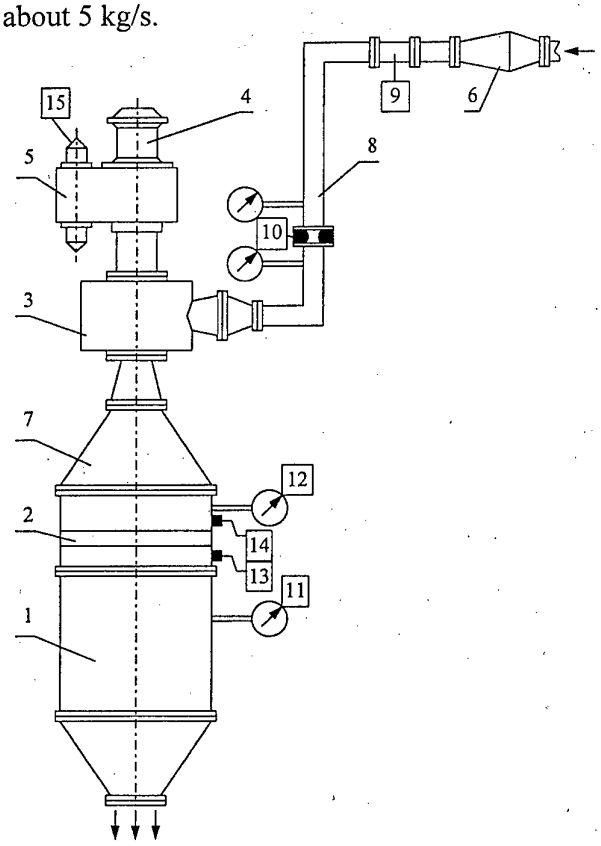


Fig. 5

4. Measuring system of the acoustic facility

The measuring system used in the facility (see Fig. 5) records both steady facility parameters and fast-changing ones. The steady parameters measured in the facility are:

9 – air temperature downstream of the burner;

10 – air mass flow rate;

11 – combustion chamber pressure;

12 – pressure upstream of the methodical grate.

The unsteady parameters measured in the facility are:

13 – combustion chamber pressure pulsation;

14 – pressure pulsation upstream of the methodical grate;

15 – frequencies of the oscillations generated by the pulsations generated by the pulsator (so-called position gauge).

The combustion chamber frequency characteristic within the frequency range under investigation is determined in one test through

smooth variation of the pulsator revolutions number.

Filtering signals coming from the pressure gauges installed in the combustion chamber and upstream of the grate within a narrow frequency range near the frequency determined by the position gauge and dividing them by one another in accordance with equation (6), we can determine the combustion chamber frequency characteristic modulus and phase.

5. Examples of results received on the acoustic facility

Examples of practical use of an offered method are resulted below.

Their purpose to show on the one hand, capabilities of an experimental technique, and on another hand - to estimate influence of the geometry of a variable cross-section channel and gas stream mode on dynamic properties of a flow.

The first example concerns gas flow in a cylindrical channel of 1640 mm length and 80 mm diameter, with the right exit lattice of a supercritical pressure drop (7 apertures of diameter 10.7mm).

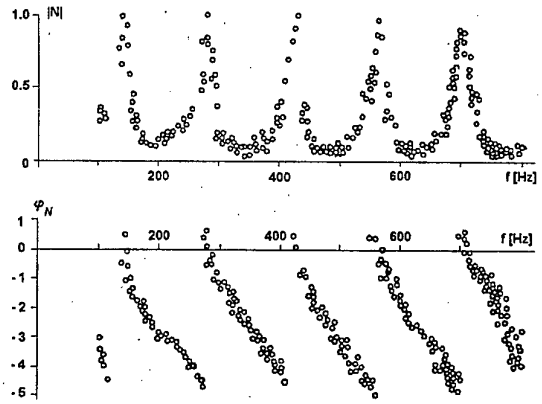


Fig. 6. The amplitude phase characteristic for a flow in a cylindrical pipe

The case of flat disturbances was investigated. The results of experiments are adduced in a fig. 6.

In the investigated frequency range from 100 up to 800 Hz at speed of a sound 470 m/s were realized 5 longitudinal resonances of a pipe. As we see, the condition of quasistationary of the efflux through a lattice begins slightly to be upset only from the fifth resonant maximum.

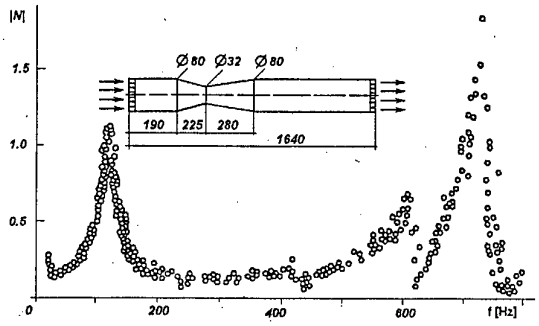


Fig. 7. The amplitude characteristic for a flow in a channel with subsonic contraction

The second example shows change of dynamic properties of a flow, when in the same pipe the segment of stream with smooth subsonic contraction of a flow (see fig. 7) is organized.

In a series of tests submitted in fig. 7, the Mach number ~0.47 was realized in narrow contraction section.

The value of total pressure losses in diffuser of a part was equal to ~0.45 %.

As it is visible from comparison of fig. 6 and fig. 7 this change of geometry has essentially changed dynamic properties of the flow. The full disappearance of resonant maxims in frequency range of 200 , 500 Hz and their increase on frequencies 120 and 725 Hz is observed practically.

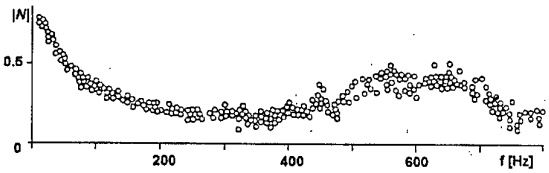


Fig. 8. The amplitude characteristic for the flow in a channel with supercritical cross-section contraction

The value of a module of the frequency characteristic is shown In fig. 8 when in narrow cross-section of a channel the supercritical mode of the stream was realize. The presence of a zone of sound velocity in narrow section of channel leads to independence of dynamic properties of the flows up to contraction and after contraction.

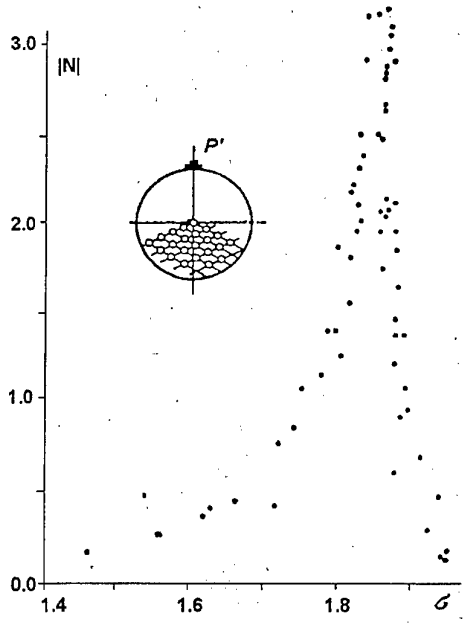


Fig. 9. The amplitude characteristic for the first tangential mode of transversal oscillations

The results adduced in a fig. 9 illustrate possibilities of using of the offered experimental technique for research of tangential shapes of oscillations in the combustion chamber of 240 mm diameter, 90 mm diameter of a nozzle throat, length up to a nozzle throat 660 mm.

As we see, on frequency close to critical $\left(\sigma = \frac{\omega R}{\bar{c}} = 1.84\right)$ It is observed good enough resonant maximum of the frequency characteristic. It testifies to significant decreasing of acoustic energy expiration via the nozzle in comparison with flat disturbances (compare to fig. 8).

The important practical application of the acoustical modeling method is assessment of efficiency of various design measures, directed to reserves of stability increasing of combustion in LRE combustion chambers and gas generators, which coupled with change of their acoustic characteristics.

As was already spoken above, if the measure results to decrease of a maximum of the frequency characteristic, it unequivocally promotes improvement of stability characteristics.

The question about necessary level of this decrease can be decided only by experimental check in fire test conditions. At the same time the realization of comprehensive optimization analysis of the design sizes of various damping devices on the acoustic facility reduces up to a minimum a volume of their subsequent fire tests.

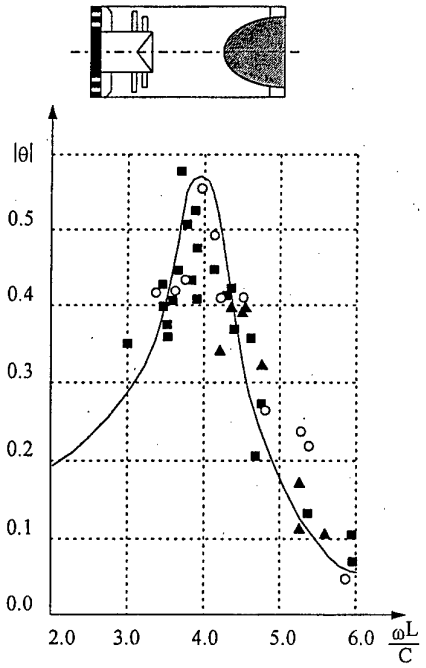


Fig. 10 (a)

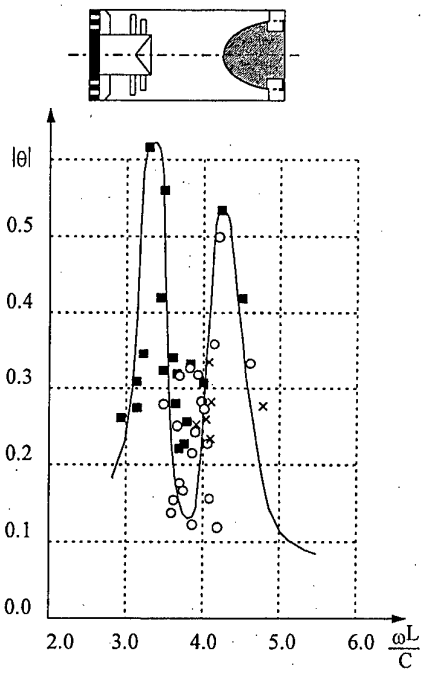


Fig. 10 (b)

The following examples illustrate this idea.

Two frequency characteristics of the gas generator in case of longitudinal oscillations are adduced for comparison on fig. 10 (a) and 10 (b): a) - without measures; b) - the resonator Helmholtz without passage is installed in the turbine nozzle lattice. As it is visible from fig. 10 (a) the measure in whole has appeared inefficient, since the stabilizing effect of absorbent is shown in very narrow frequency range near the resonance of a parent version.

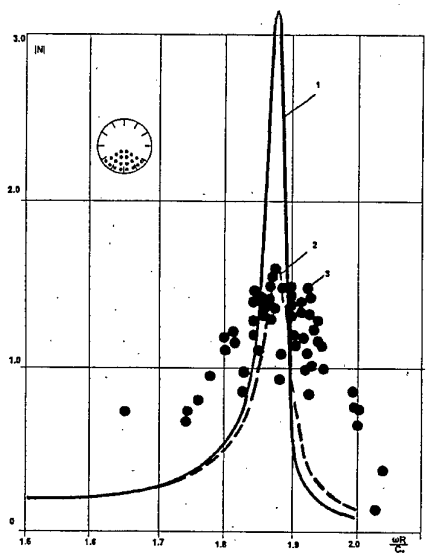


Fig. 11. The figures designate: 1 - without edges, 2 - with edges, 3 - experiment with edges

The example of the acoustic characteristics change for the first tangential mode of transversal oscillations in the combustion chamber is shown on fig. 11 for the case when some metal edges of a small altitude were installed on its lateral surface. From comparison of fig. 9 and 11 it is possible to see efficiency of this measure. In the further metal edges were replaced on rigid burning one, and the conducted firing tests with this design have confirmed stabilizing effect of burning dividing walls on a mode of start-up.

The frequency characteristic of the same combustion chamber with antipulsation dividing walls (6- partition of length 40 mm) is adduced on fig. 12.

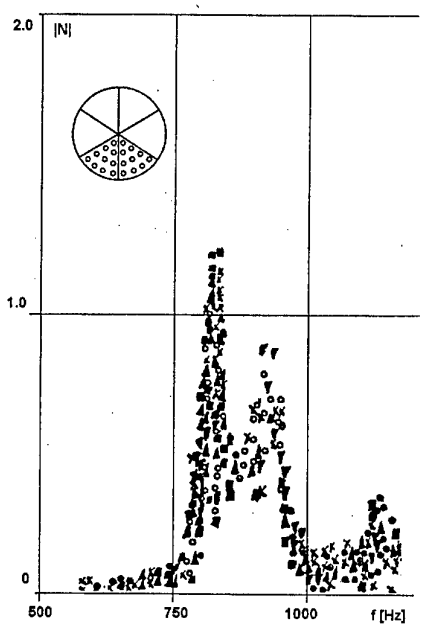


Fig. 12.

The results adduced on fig. 12 indicate an acoustic nature of stabilizing influence of antipulsation dividing walls.

References

1. Liquid Propellant Rocket combustion instability. Editor David T. Harrje. Associate Editor Frederick H. Reardon. National Aeronautics and Space administration. Washington, 1972
2. Natanzon M. S. "Instability of combustion". - Moscow, Mashinostroenie, 1986.(in Russian).
3. Lebedinsky E. V., Natanzon M. S., Nikiforov M. V. An experimental method of determining dynamic properties of gas streams. Acoustic Journal, 1982, v. XXVIII, issue 2, pp. 660-664 (in Russian).
4. Lebedinsky E. V., Natanzon M. S., Yarlykova Y.I. Acoustic, entropy and vortex disturbances in a channel of variable cross-section. – News of USSR Academies of sciences. Series: The mechanics of fluid and gas, 1982, #1, p.91-98. (in Russian).
5. Konokhov V. N. Lebedinsky E. V. Reflection of acoustic disturbances from a multihole grate with supersonic pressure drop – in "Cavitational oscillations and dynamics of two-phase flows", Kiev, "Naukova Dumka", 1985. (in Russian).

On the Nature of Combustion "Noise- to- Auto-Oscillation" Transition in Liquid Rocket Engines

K.P. Denisov*, V.N. Ivanov**, V.P. Pikalov***

Research Institute of Chemical Machine Building

(NIICHIMMASH)

Sergiev Posad, Russia

Abstract

Results of investigation of combustion dynamic bistability in liquid rocket engine (LRE) chambers are given.

Some manifestations of combustion instability to pressure high-frequency oscillation can not be adequately interpreted within the framework of a well-known model of potentially self-oscillating system with a hard excitation.

It is shown that a set of phenomena of auto-oscillation excitation suggests a consistent explanation based on a possibility of realization of combustion zone multiple stationary states under fixed conditions of propellant feed. Depending on the stationary states being stable or unstable to small acoustic disturbances, one or another type of dynamic transition is realized.

Results of the performed investigation may be of a principal meaning in development of dynamic transition models and search of factors responsible for low reproducibility of the phenomenon of acoustic auto-oscillation excitation in combustion.

---

*Vice – General Director.

**Senior Research Engineer.

***Head, Research Division.

Nomenclature

f =frequency

h =potential barrier

P_c = static combustion chamber pressure

P' = pulsating pressure component

$\dot{m}$ = mass flow rate

P_{st} = stationary probability density function

Q = heat release rate

$R(\tau)$ = autocorrelation function

$\vec{r}$ = radius vector

SLC = stable limit cycle

ULS = unstable limit cycle

Y = parameter of state

z = eigen function

α = equivalense ratio (oxygen excess relative to the stoichiometric ratio)

β = decay coefficient

v = oscillation decrement

$\delta(\tau)$ = Dirac delta function

λ = amplitude (envelope) of narrow-band signal

λ_{SLC} = SLC amplitude

λ_{ULC} = ULC amplitude

$\xi(t)$ = normal delta – correlated (white) noise

τ = temporal interval

φ = oscillation phase

ϕ = potencial function

ω = oscillation angular frequency

ω_o = natural angular frequency

$\langle \ldots \rangle$ - averaged value

Introduction

A possibility of dynamically bistable combustion mode realization in liquid rocket engine (LRE) under fixed condition of propellant feed is an established fact.

The dynamical bistability manifests itself in transitions (which can be spontaneous or induced by artificial pulsed disturbance) from a state of small random oscillation ("noises") to a state of regular self-oscillation of an amplitude which is an order of magnitude higher than the initial noise level (Fig.1).

A widespread explanation of the dynamical bistability consists in treating the chamber process as a potentially self-oscillating system being in the mode of self-oscillation hard excitation.

In the framework of this concept, an idea was conceived of estimating the margin of combustion dynamical stability by introducing artificial pulsed disturbance into the combustion chamber.

At present the assessment of combustion process dynamical stability by applying artificial pulsed disturbance is an integral part of engine development testing.

The concept of "hard" excitation of a potentially self-oscillating system is based on postulating unstable limit cycle (ULC) existence. The unstable limit cycle is actually a pressure oscillation amplitude boundary that separates the states of noise and self-oscillation. In this conceptual framework, dynamical stability margin can be treated as a measure of spacing between the unstable limit cycle amplitude λ_{ULC} and the amplitude of chamber natural acoustic noise λ_{NOISE} (for example, $\lambda_{ULC}=n\lambda_{NOISE}$) The larger n, the higher the stability margin is.

However the experience gained in the course of testing and operating some engines having sufficient dynamical stability margin (in the sense specified above) showed that sometimes self-oscillation spontaneous excitation is observed in operation stationary modes. The self - excitation occurs in a natural ("soft") mode, starting with chamber noises, no pulsed disturbance preceded the auto-oscillation excitation. It is essential that oscillation self-excitation in the cases under consideration was not attributed to chamber operating parameter reaching the boundary of stable operation region. Auto-oscillation self-excitation was of statistical nature, with strictly fixed conditions of propellant feed.

An attempt is made in the present paper to analyze the above phenomena. The proposed treatment is not exhaustive, it is rather hypothetical and may be a subject foe discussion.

1. Basic concept: combustion chamber as a potentially self-oscillating system (single-mode approximation)

An excitation of a natural oscillation single mode is often observed in combustion chambers.

Let us consider a simplest model of a potentially self-oscillating system. This model major values are its simplicity and a possibility to identify parameters.

An analysis of acoustic narrow-band noise in LRE chambers showed that signals recorded in the vicinity of resonant frequency can be presented in the following form:

$$P'(\vec{r},t) = Z(\vec{r}) \cdot X(t), \qquad (1)$$

where: $Z(\vec{r})$ is a real function of coordinates;

$X(t)$ is a random function of time that can expressed as follows:

$$X(t) = \lambda(t) \cdot \cos(\omega_0 t + \varphi(t)). \qquad (2)$$

Here:

$\lambda(t)$ and φ(t) (amplitude and phase) are functions, slowly changing in comparison to cos. $\omega_0 t$

ω_0 is a resonant frequency.

The auto-correlation function of the process, $X(t)$, has generally the following form,

$$R(\tau) \cong \sigma^2 \exp(-\beta|\tau|) \cdot \cos\omega_0 \tau . \qquad (3)$$

The above facts suggest that $X(t)$ obeys the following stochastic differential equation:

$$\frac{d^2X}{dt^2} + 2\beta\frac{dX}{dt} + \omega_0^2 x = \omega_0^2 \xi(t), \qquad (4)$$

where $\xi(t)$ is stationary delta-correlated (white) noise;

β = *const* is a coefficient of acoustic energy dissipation in the chamber volume($\beta << \omega_0$).

The model (4) is widely used in experimental estimation by statistical methods of the decrement of low oscillation decay, for example, from the spectral spike width in the vicinity of the resonant frequency ω_0 [1].

For model (4) to describe a potentially self-oscillating system of a hard excitation mode, the existence of $\beta=\beta(x)$ (or $\beta=\beta(\lambda)$) relationship should be postulated. This relationship provides the existence of self-oscillation unstable limit cycles (ULC) and stable limit cycles (SLC).

The existence of such relationship was experimentally found in some model combustion chambers burning gaseous propellants and in some actual liquid engine chambers. [2]

Deductive devising of Equation (4) applied to gas-liquid engines is described in [2].

To the first approximation, the evolution of oscillation amplitude $\lambda(t)$ of system (4) can be presented in a form of stochastic equation [2];

$$\frac{d\lambda}{dt} = -\beta(\lambda)\cdot\lambda + \omega_0^2 N_0 / 8\lambda + \varepsilon(t), \qquad (5)$$

where

$N_0 = const.$ is spectral intensity of random noise signal $\xi(t)$ in the vicinity of the natural frequency ω_0;

$\varepsilon(t)$ is stationary random delta-correlated function:

$$R = <\varepsilon(t)\cdot\varepsilon(t+\tau)> = \omega_0^2 N_0 \cdot \delta(\tau)/4;$$

$\delta(\tau)$ is Dirac delta function.

Statistical and dynamic features of model (5) are presented in Fig. 2:

- Hypothetical relationship $\beta=\beta(\lambda)$, meeting the conditions for ULC and SLC existence;
- Potential function: $$\phi(\lambda) = -\sigma^2\left[\int_0^{\lambda}\frac{a(\lambda)}{b(\lambda)}d\lambda\right]; \qquad (6)$$

$$a(\lambda) = -\beta(\lambda)\cdot\lambda + \omega_0^2 N_0 / 8\lambda; \qquad (7)$$

$$b(\lambda) = \omega_0^2 \cdot N_0 / 4; \qquad (8)$$

$$\beta_0 = \beta(\lambda), \ \lambda \to 0; \qquad (9)$$

$$\sigma^2 = \omega_0^2 \cdot N_0 / 8\beta_0; \qquad (10)$$

- Stationary probability density of states (of oscillation amplitude):

$$P_{st}(\lambda) = c\cdot\exp\left[-2\phi(\lambda)/\sigma^2\right] = c_1\cdot\lambda\cdot\exp\left\{-\frac{1}{\beta_0\sigma^2}\cdot\int_0^{\lambda}\lambda\cdot\beta(\lambda)d\lambda\right\}. \qquad (11)$$

Model (5) allows the following dynamic transitions:

- <<noise→ auto-oscillation>>

a) a spontaneous transition, induced by turbulent combustion noise; the transition occurs at a random moment t_i corresponding to the realization of condition: $\lambda(t_i)>\lambda_{ULC}$;

b) a determinate transition induced by pulsed disturbance; the transition occurs when the following condition is realized: $\lambda(t_i)>\lambda_{ULC}$;

- <<auto-oscillation→ noise>>

c) a spontaneous transition, induced by noise; the transition occurs at a random moment t_i corresponding to the realization of condition: $\lambda(t_i) < \lambda_{ULC}$;

d) a determinate transition induced by pulsed disturbance; the transition occurs when the following condition is realized: $\lambda(t_i) < \lambda_{ULC}$

Model (5) is a methodological basis for combustion dynamical stability estimation by a method of artificial pulsed disturbance [1].

This model adequately describes the non-linear oscillating dynamics of some model combustion chambers burning gaseous propellant [3].

Fig.3 shows a typical experimental set-up. An external positive feedback was used for the signal amplitude self - adjustment to resonance with natural oscillation.

Bifurcation diagram for the dynamic system under consideration is shown in Fig.4: chamber oscillation amplitude versus fuel flow rate.

Fig. 5 shows the dependence of chamber pressure pulsation amplitude on the amplitude of the input harmonic signal. This dependence is shown for two sections of the bifurcation diagram: 1-1 and 2-2 (Fig.4)

Fig.6 illustrates a reproduced dependence of the coefficient on oscillation amplitude (for section 1-1 of bifurcation diagram)

Model (5) allows a quantitative estimation of combustion chamber susceptibility to oscillation self-excitation, that is of a probability of engine unstable operation in the specified regime during a time period of t_p.

Let assume that at certain initial time t_0, the process $\lambda(t)$ has a definite value $\lambda(t_0) = \lambda_0$ which is in the vicinity of the left minimum of the potential $\phi(\lambda)$, Fig.2. The estimate of a probability of the system transition through the potential barrier h for time $t \leq t_p$, is equal to [4]:

$$P(t) = 1 - e^{-tp/T_1}; \qquad (12)$$

where $T_1 = 2\langle T \rangle$ and $\langle T \rangle$ is mean time on the expiry of which the random process $\lambda(t)$ will reach the boundary λ_{ULC} corresponding to the amplitude of unstable limit cycle:

$$\langle T \rangle = 2 \int_{\lambda_0}^{\lambda_{\text{пред}}} e^{-\Psi(x)} \cdot \int_0^x \frac{e^{\Psi(x)}}{b(Y)} dY dx, \qquad (13)$$

$$\text{where } \Psi(x) = 2 \int_0^{\lambda} \frac{a(\lambda)}{b(\lambda)} d\lambda, \qquad (14)$$

and $a(\lambda)$ and $b(\lambda)$ are defined by (7) and (8).

As an illustration, calculation data of the mean time in which the random Markov process $\lambda(t)$ will first reach an amplitude of $\lambda_{ULC} = 12\sigma$ are given in Table 1 for a set of hypothetical relationships $\beta(\lambda)$:

$$\beta = \beta_0 = const; \qquad \beta = \beta_0\left(1-\frac{x}{12}\right);$$

$$\beta = \beta_0\left(1-\frac{x^2}{12^2}\right); \qquad \beta = \beta_0\left(1-\sqrt{x/12}\right).$$

The estimation of a probability of auto-oscillation self-excitation in an initially undisturbed system is given for $\beta = 100$ an $t_p = 500$ s. As can be seen, a probability of «noise→ self-oscillation» transition depends, to a large extent, on the function $\beta(\lambda)$ form.

Table 1

Function $\beta(x)$	$P=t_p/T$
$\beta = \beta_o$	$1.75 \cdot 10^{-25}$
$\beta = \beta_o\left(1-\frac{x^2}{12^2}\right)$	$0.536 \cdot 10^{-10}$
$\beta = \beta_o\left(1-\frac{x}{12}\right)$	$0.537 \cdot 10^{-5}$
$\beta = \beta_o\left(1-\sqrt{\frac{x}{12}}\right)$	$0.387 \cdot 10^{-1}$

Thus in an ideal case, for practical estimation of a probability of self-excitation of potentially self-oscillating system exposed to a random wide-band noise, the following experimental estimates are to be available:

- root- mean square value of acoustic noise, σ, in the pass band $\Delta\omega$ of the resonance maximum ω_i being studied;
- decay coefficient β_0 at $\lambda \rightarrow 0$;
- amplitudes λ_{ULC};
- relationship $\beta = \beta(\lambda)$ in the $0 < \lambda \leq \lambda_{ULC}$ range;

Values of σ and β_0 can be estimated from narrow-band noise realization:

$$X = \lambda(t)\cos(\omega_0 t + \varphi(t)).$$

Estimates of λ_{ULC} and $\beta = \beta(\lambda)$ can be obtained in some cases by using active methods of harmonic or pulsed disturbances.

In the case the anticipated amplitude of unstable limit cycle exceeds σ level only moderately (for example, $\lambda_{ULC} \approx (5...6)\sigma$) the relationship $\beta(\lambda)$ can be estimated and amplitude λ_{ULC} can be predicted by a passive method (from "noise") based on an expression obtained from (11):

$$\frac{\beta(\lambda)}{\beta_0} = \sigma^2 \left\{ \frac{1}{\lambda^2} - \frac{1}{P_{st}} \cdot \frac{dP_{st}(\lambda)}{d\lambda} \right\} \qquad (15)$$

In this case the procedure of estimating $\beta = \beta(\lambda)$ includes the following steps:

- a complex filtration of narrow-band noise in the vicinity of the resonance maximum ω_i being studied, with obtaining of an envelope (amplitude), $\lambda(t)$;
- smoothed estimation of probability density of envelope distribution, $P(\lambda)$;
- estimation of $\frac{\beta(\lambda)}{\beta_0}$ from (15) with predicting the amplitude λ_{ULC}.

Let us use the above approach to the estimation of dynamical stability margin of actual liquid rocket combustion chambers

2. Liquid Rocket Engine with Gas-Generator Gas Burning (Development Testing History)

Propellant: UDMH + Nitrogen Tetroxide (hypergolic)

Injection element configuration is shown in Fig. 7.

There were no cases of spontaneous excitation of self-oscillation in the course of the engine tests at a horizontal stand.

A series of stand tests with application of pulsed disturbance to the chamber was carried out for the purpose of estimating the margin of combustion process dynamical stability.

Those tests statistical data and working regimes are shown in Fig.8. It can be seen that introduction of pulsed disturbances into engines with injection element basic configuration resulted in excitation of self-oscillation actually in the whole region of working parameters within the square ($Pc - K\dot{m}$), excluding the left upper angle.

Typical variants of response to the pulsed disturbances in the nominal regime are given in Fig.9. The character of the responses suggests a presence of self-oscillation unstable limit cycle, λ_{ULC}.

Estimation of λ_{ULC} for the nominal regime will be carried out based on the data, given in Fig.10. Empty dots are maximum values of relative amplitude of the decaying responses to the disturbance (first tangential mode, frequency component is 2 400 Hz); solid dots show minimum values of relative amplitude of responses to disturbance resulting in self-oscillation excitation.

It follows from the examined statistics of responses to pulsed disturbances that

$$65 > \frac{\lambda_{ULC}}{\sigma} > 24$$

Let us take λ_{ULC}/σ=24 as a lower estimate of unstable limit amplitude

As decaying responses to pulsed disturbance are usually amplitude-modulated, it is very difficult to estimate correctly the relationship $\beta = \beta(\lambda)$.

To obviate the difficulty, assume that the worst variant of relationship $\beta = \beta(\lambda)$ is realized, i.e. the one mostly promoting system self-excitation. According to Table 1, such a relationship corresponds to the following expression:

$$\beta = \beta_o \sqrt{1 - \frac{1}{\lambda_{ULC}}} \ .$$

The duration of engine operation in the nominal regime is t_p=300 s. The value of β_0 at $\lambda \to 0$, estimated from "noise" (from resonance spectral peak width at f= 2400 Hz) is β_0=125.

In this case a probability of oscillation self-excitation during $t \leq 300$ s was estimated as $P=0.8 \cdot 10^{-20}$, that is vanishingly small. Similar estimates were obtained for other regimes as well.

Thus in the framework of dynamic model (5), auto-oscillation self-excitation during the time of engine operation in the nominal regime can be considered as actually improbable.

First spontaneous excitation of self-oscillation was recorded in tests of that engine at a vertical stand.

Self-oscillation occurred in 3 s after the engine reached the nominal operating regime.

Spontaneous excitation of high-frequency self-oscillation reoccurred in subsequent tests. As in the first case, self-oscillation was excited in 1.6...3 s after the engine reached the nominal operating regime and had low reproducibility in an assemble of similar tests. Later some cases of spontaneous excitation were also recorded during tests at a horizontal stand.

The statistical analysis of the tests performed at the vertical stand showed that two outcomes were possible when the engine reached the nominal regime:

- realization of a noise state with an average decrement of chamber pressure oscillation of $\bar{\nu} \approx 0.2$, at a frequency of f=2.4 kHz, and rms fluctuations of $\varepsilon_v \approx 20\%$ (common case);
- realization of a noise state with an average decrement $\bar{\nu} \approx 0.1$, and rms fluctuations of $\varepsilon_v \approx 60\%$ (rare cases).

It was the realization of the second case that led to subsequent self-excitation of auto-oscillation (Fig. 11)

The analysis of abnormal tests showed that no disturbance of a pulsed character preceded the self-oscillation excitation. The self-oscillation was excited "softly" from the chamber noise level and did not follow the scenario, predicted by the dynamic model (5). Search of any differences in test procedure that could lead to abnormal results, were unsuccessful. The test program was ceased and work on injection head improvement was started with an aim of stability margin increase. The above test results can not be explained by the dynamic model (5).

Within the approximation under consideration, the dynamic model of a potentially self-oscillating system does not account of a possibility of parametric fluctuations of combustion zone structure, which fluctuations result in $\beta(\lambda)$ fluctuation. In other words, it is assumed the 'landscape" of the potential function $\phi(\lambda)$ exhibits no fluctuations in time. Naturally, such fluctuation would reduce a possibility of engine stable operation. However there is some doubt about the fluctuation hypothesis, taking into consideration the fact that cases of oscillation self- excitation were observed mostly in tests at a vertical stand. It seems likely that, the discrepancy between the estimated probability of unstable operation and the real situation has deeper roots.

An attempt to explain the observed discrepancy is made below.

3. Parametric bistability concept

While devising the dynamic model (5) it was implicitly postulated that the stationary space structure of the combustion zone is unambiguously defined by injection system design parameters and propellant feed regime.

The suggestion that with identical values of parameters governing liquid rocket combustion chamber stationary regime, a generation of multiple space structures (patterns) is possible was first made in [5]. The realization of one or another flame space structure may depend on a combination of random factors that take place in the course of engine starting and subsequent operation in the specified stationary regime. A random realization of a particular flame initial space structure may lead to a statistical character of auto-oscillation self- excitement.

In other words: the regime of propellant feed is not a factor that unambiguously defines combustion zone spatial structure and sensitivity to acoustic disturbances. This hypothesis leads us to a problem of bifurcations of combustion stationary modes and their ability to give rise to dynamic ambiguity [6].

Bifurcations of stationary combustion modes with variation of one of the controlling parameters were found while investigating an open diffusion flame of some injection elements used in liquid rocket engines [1,7].

A possibility of combustion stationary mode bifurcations is directly connected with the "mechanism" of flame stabilization in liquid rocket combustion chamber equipped with the given injectors types (Fig.7). In this case fuel jets that penetrate oxidizer jets act as flame natural stabilizers. Specific features of the formed recirculating flows seems to cause space ambiguity of the flame structure. Let us consider the dynamic aspect of the problem.

Suppose that combustion zone space structure can be described with a set of "state parameters" $\{Y_i\}$ satisfying nonlinear evolution equations of the following form:

$$\frac{\partial Y}{\partial t} = F[Y(\vec{r},t)] + q(\vec{r},t). \qquad (16)$$

Here: $\{Y(\vec{r},t)\}$ is a vector of state parameters Y_i;

$F[Y(\vec{r},t)]$ is a vector of non-linear functional relations, representing local evolution of Y_i components in time t and space $\vec{r}$

Among the state parameters Y_i; there can be: temperature fields, concentration fields, velocity fields and so on.

Propellant flow rates, combustion chamber static pressure, propellant temperature and so on can act as controlling parameters γ.

The term $g(\vec{r},t)$ simulates the combustion zone exposure to random hydrodynamic actions.

Stationary states are defined by the solutions of:

$$F[Y(\vec{r},t)]=0 \qquad (17)$$

Assume that in some range of controlling parameters γ the solution of (17) is multi-valued that is, as an example, a realization of three states is possible: Y_1, Y_2, Y_3 (Fig. 12)

Assume further that states Y_1, and Y_3 are locally stable while Y_2, is unstable. The acoustic equation (4) with a certain functional β (that is of different extent of stability to acoustic disturbances) can be assigned to each of the locally stable stationary states Y_1, and Y_3.

$$Y_i \rightarrow Q_i(\vec{r}t) \rightarrow \beta_i \qquad (18)$$

Here: $Q_i(\vec{r}t)$ is a rate of combustion chamber heat release given by the state Y_1;

A possibility of realization of parametrically bistable stationary states of the combustion zone with different extent of stability to low acoustic disturbances was confirmed by experiments in a model combustion chamber with a single coaxial injector [7].

Parametrically bistable system allows both spontaneous and pulsed disturbance-induced excitation of self-oscillations, with external controlling parameters remaining unchanged. However the scenario of excitation may differ from the corresponding scenario described my model (5) (unstable limit cycles may be absent). In particular, a dynamic transition «noise→self-oscillation» may occur if one stationary state, acoustically stable, is replaced by another state, acoustically unstable. Such change of states can be performed, among others ways, by an artificial disturbance of parameters of combustion zone structure.

In this case, unlike model (5), which assumes dynamic transitions of only "noise→self-oscillation' type, a parametrically bistable system allows also transitions

of «noise→noise» type, that is a replacement of one acoustically stable state by other one, also acoustically stable.

Occurrence of such transition may serve as a diagnostic indication of parametrically bistable system with combustion.

4. Model chamber with gas-liquid combustion

The hypothesis of possible realization of parametrically bistable stationary states of the combustion zone, that are characterized by different extent of sensitivity to acoustic disturbances, received further support in a series of experiments carried out in a model combustion chamber running kerosene and gaseous oxygen [7]

The model combustion chamber (Fig.13) is equipped with four elements injecting radial jets of kerosene into a gaseous oxygen axial jet. A device for applying artificial pulse disturbances is mounted on the chamber.

The distinguishing feature of the chamber dynamic behavior were as follows:

1. On igniting and the chamber reaching the steady regime (P_c=0.4 MPa, α=0.7), one of the two dynamically stable noise state was realized usually:

- state 1 – with the oscillation effective amplitude λ_{rms}= 9.0 arbitrary units and a decrement of ν_1=0.04 at a frequency of the first tangential –first longitudinal mode (f=6200 Hz): (Fig. 14).;
- state 2 – with the oscillation effective amplitude λ_{rms}= 23.3 arbitrary units and a decrement of ν_2=0.01 at a frequency of f=6290 Hz,: (Fig. 15).;

The frequency of state 1 and state 2 occurrence in an ensemble of similar tests was approximately the same.

Depending on the realized stationary state (1 or 2) artificial pulsed disturbance introduction into the combustion chamber resulted in:

- transition from state 1 to state 2 (Fig.16)
- transition from state 2 to state 1 (F ig.17)
- to resetting of the initial state 1 or state 2 (Fig. 18)

2. On chamber operation augmentation, by pressure (P_c=0.7 MPa, α=0.7), the two-valued property (ambiguity) of the stationary states was persisting and in this case:

- if state 1 occurred, it persisted, as a rule, during the whole test (t=20 s);
- if state 2 occurred, then in some random time interval, spontaneous excitation of regular auto-oscillation was observed at a frequency close to the frequency of the first tangential –first longitudinal mode (f=6400 Hz); (Fig.19).
- the auto-oscillation either persisted up to the test completion or terminated in some random time with transition to state 1 (without any subsequent excitation, Fig. 20) or to state 2 (with subsequent self-excitation) , (Fig. 21)

3. The use of the procedure of $(\beta = \beta(\lambda))$ relationship estimation described in section 2 above (from noises) revealed for (P_c=0.7 MPa, α=0.7) that:

- in the case of state 1 realization there were no indications of unstable limit cycles presence, at least in the $\lambda \leq 3.5\sigma$ range. State 1 corresponds to linear narrow-band noise with envelope distribution following Rayleigh law (Fig. 22)
- in the case of state 2 realization, there were indications of unstable limit cycles presence, with the same values of P_c and α. State 2 corresponds to nonlinear narrow-band noise with envelope distribution deviating from Rayleigh law (Fig.23).

Unstable limit cycles presence is in agreement with subsequent evolution of the system that is in state 2 initially: auto-oscillation spontaneous excitation

Thus, in the considered range of the controlling parameter P_c chamber combustion process shows evidence of parametric bistability (noise states 1 and 2). Stationary state 1 is stable to acoustic disturbance. State 2 realized with the same values of parameter P_c is characterized with unstable limit cycle of acoustic auto-oscillation, i.e. the state is metastable.

The realized stationary states 1 and 2 have different margins of stability to acoustic disturbances.

It seems that with the initial metastable state 2 spontaneous transitions «noise→ auto-oscillation» occur following a scenario dictated by model (5). In the case of realization of state 1, another acoustically stable state, the transitions «noise→noise» (that are induced by pulsed disturbance) are of a parametric (not acoustic) nature. By this we mean that artificial disturbances destroy the combustion zone initial stationary structure for some time, after which the disturbed structure relaxes either to dynamically stable state 1 or to state 2.

5. Liquid rocket engine with gas-generator gas burning (development testing history continuation)

Within the framework of a potentially auto-oscillating system with parametrically bistable states, the test outcomes, described in Section 2, can be easily interpreted.

Assume that on the engine reaching the nominal regime, realization of both state Y_1 or state Y_3 is possible (Fig. 12). In this case, due to some specific features of engine start at a horizontal stand, a probability of state Y_1 is much higher than that of Y_3.

Change to tests at a vertical stand promoted an increase of the probability of state Y_3 realization. Provided the state Y_1 has a higher margin of stability to acoustic disturbance, we get the picture of test outcomes just considered.

The engine injection head modification was carried out in two ways:

- anti-pulsation baffles made of extending injection elements were installed on the face plate;
- peripheral injection elements were modified (change of injector number and fuel nozzle diameter).

Subsequent tests showed that anti-pulsation baffles eliminated a possibility of pulsed excitation of auto-oscillation: all responses to pulsed oscillation were of decaying character (Fig.24). However this design was not implemented (for some other reasons not connected with combustion instability)

Modification of peripheral injection elements failed to change the margin of combustion chamber stability to pulsed (hard) excitation of auto-oscillation. However cases of spontaneous excitation terminated. This modified injection head was accepted for fabrication. Engine multiple ground tests and many-year operation in a rocket showed no cases of unstable combustion.

Conclusion

The success in diagnostics of liquid rocket engine combustion stability is to a great extent caused by an adequacy of the model used. A diagnostic model based on the traditional concept of a combustion zone as a monostable space structure can not explain, in some cases, combustion high-frequency instability observed in liquid rocket engines. The revealed parametric bistability of combustion zone structure may give rise to dynamic ambiguity that manifests itself in random excitation of auto-oscillations in one or other engine stationary operation regime.

The data presented in this paper show that a possibility of bifurcation of combustion stationary regimes is to be taken into consideration while devising diagnostic models of pulsating combustion in LRE chambers and developing methods of stability margin estimation.

References

1. Agarkov A.F., Denisov K.P., Dranovsky M.L. et al. "Jnjector Flame Stabilization Effects on Combustion Jnstability". Progress in Astronautics and Aeronautics, Vol. 169, 1993.

2. Ilchenko M. A. and others. Operating Process Stability in Spacecraft. M. Mashinistroenie, 1995. (Rus.)

3. Ivanov V.N. Investigation of Model Combustion Chamber Nonlinear Dynamics. NIICHIMMASH Report, 1980. (Rus)

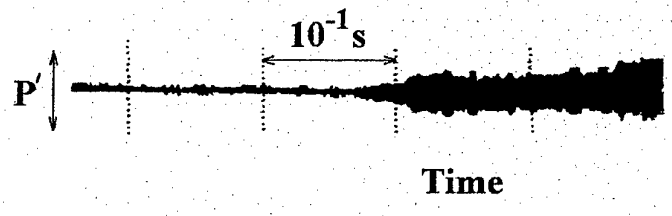
4. Stratonovich R. L., Landa P.S. Noise Action on a Hard-Excited Generator. IVUZ . Radiophysics, v.2, №1, 1959. (Rus.)

5. Dubinkin B.N., Natanzon M.S. Chamian A.E. "On Two Modes of Combustion with Recirculation Zone". The Physics of Combustion and explosion, №6, 1978.(Rus).

6. Culick F.E.C. "Some Possible Consequences of Bifurcations in Combustors". Jnternational Workshop on Research Status and Perspectives in Liquid Rocket Combustion Chamber Flow Dynamics". Paris France MAY 27-28, 1999.

7. Denisov K.P., Jvanov V.N., Pikalov V.P. "Some Aspects of Nonreproducibility of Self-oseillation Excitation in Combustion Chamber of Liguid Rocket Engine". Jnternational Workshop on Research Status and Perspectives in Liquid Rocket Combustion Chamber Flow Dynamics". Paris France MAY 27-28, 1999.

(a)



(b)

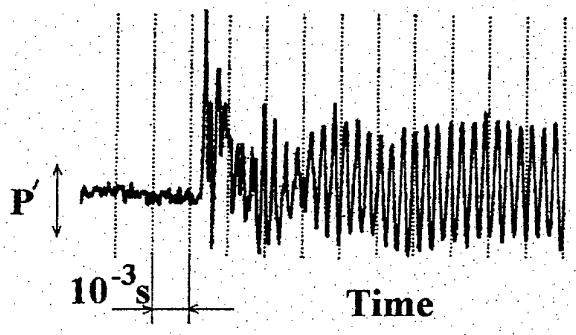


Fig. 1. Spontaneous (a) and pulsed disturbance-induced (b) transitions «Noise→Auto-oscillation»

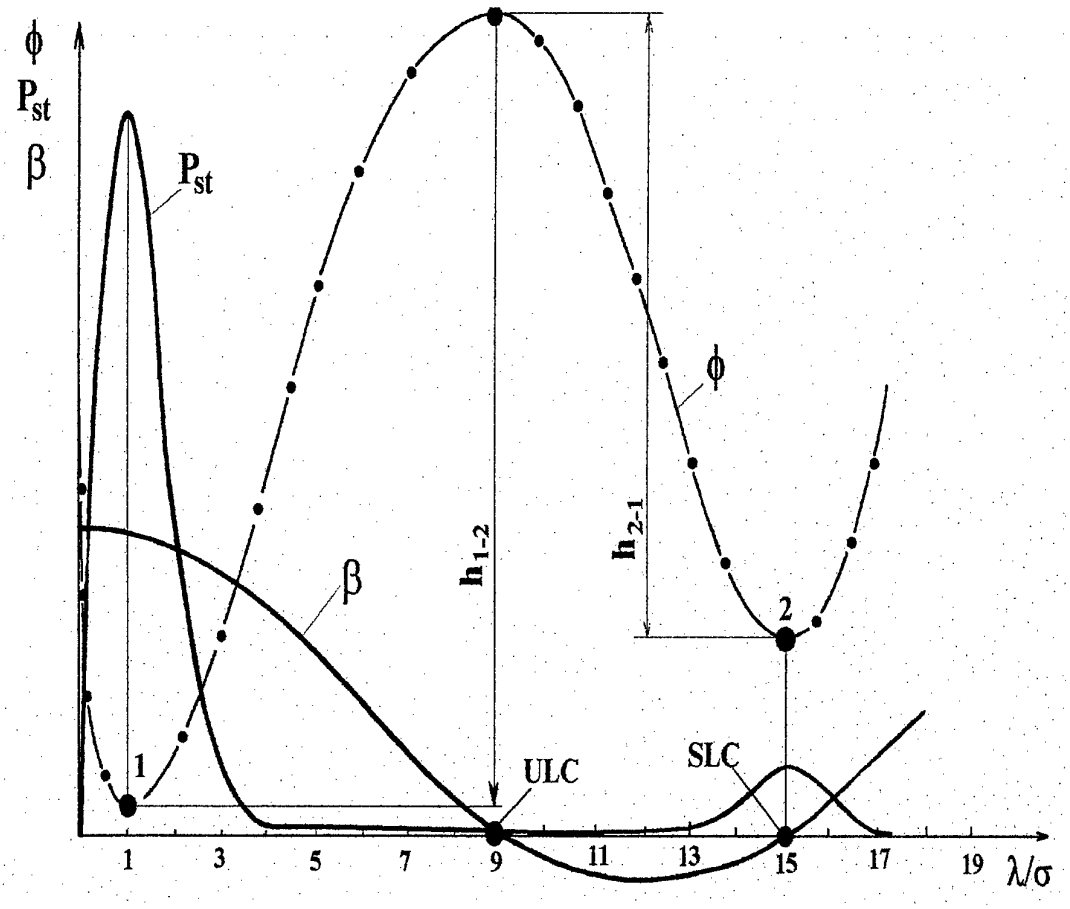


Fig.2. Decay coefficient β, probability density P_{st} and potential ϕ versus oscillation relative amplitude:

h_{1-2}: Potential barrier of the transition from state 1 to state 2

h_{2-1}: Potential barrier of the transition from state 2 to state 1

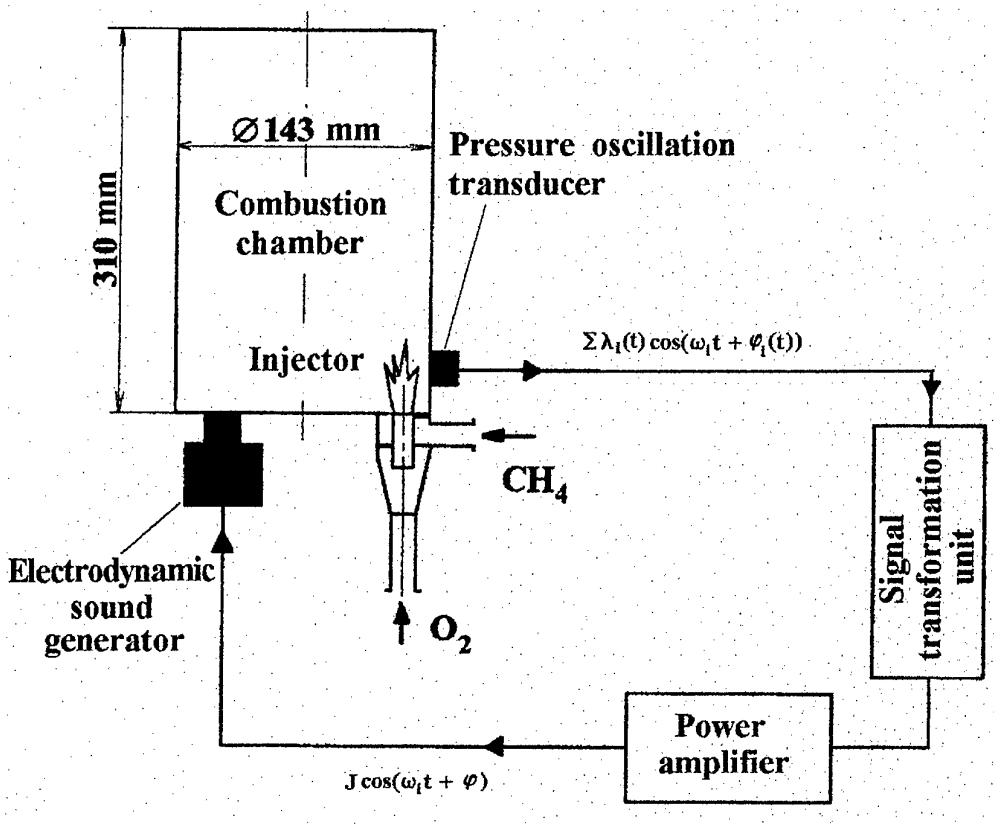


Fig.3. Typical experimental set-up

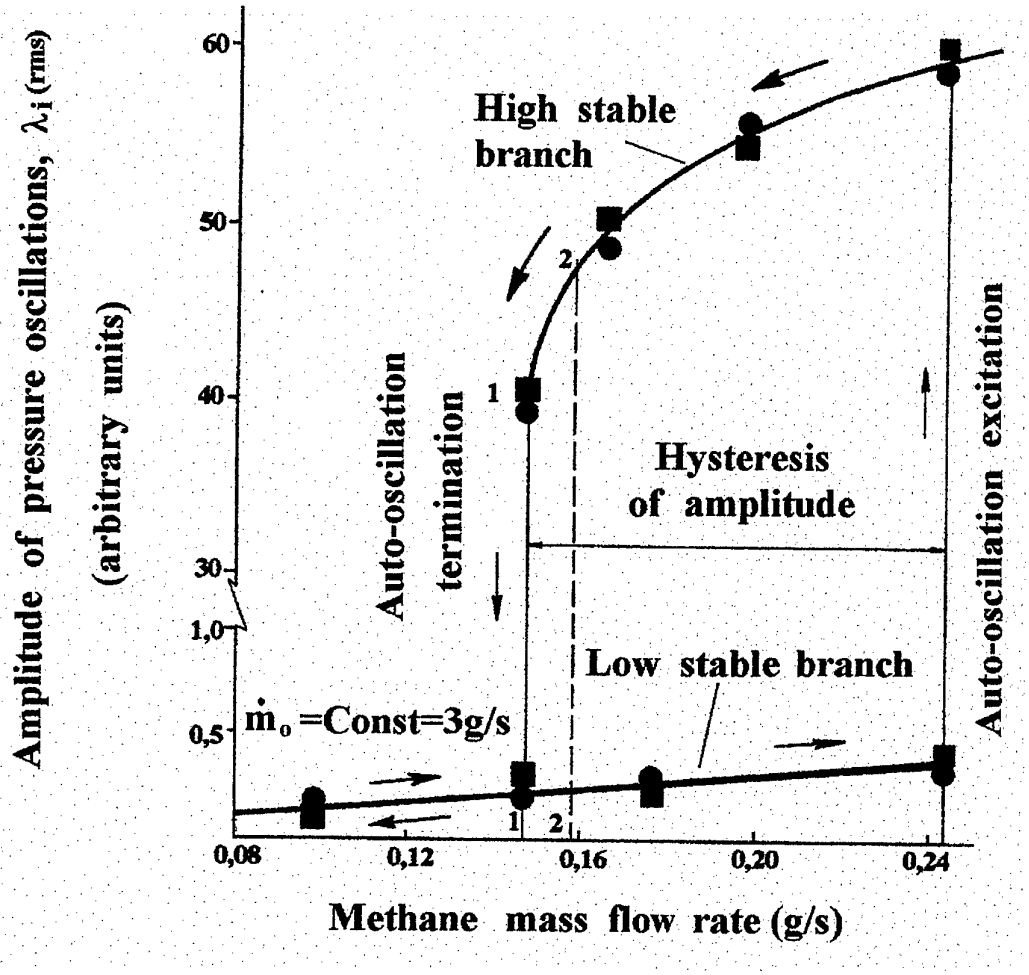


Fig.4. Bifurcation diagram

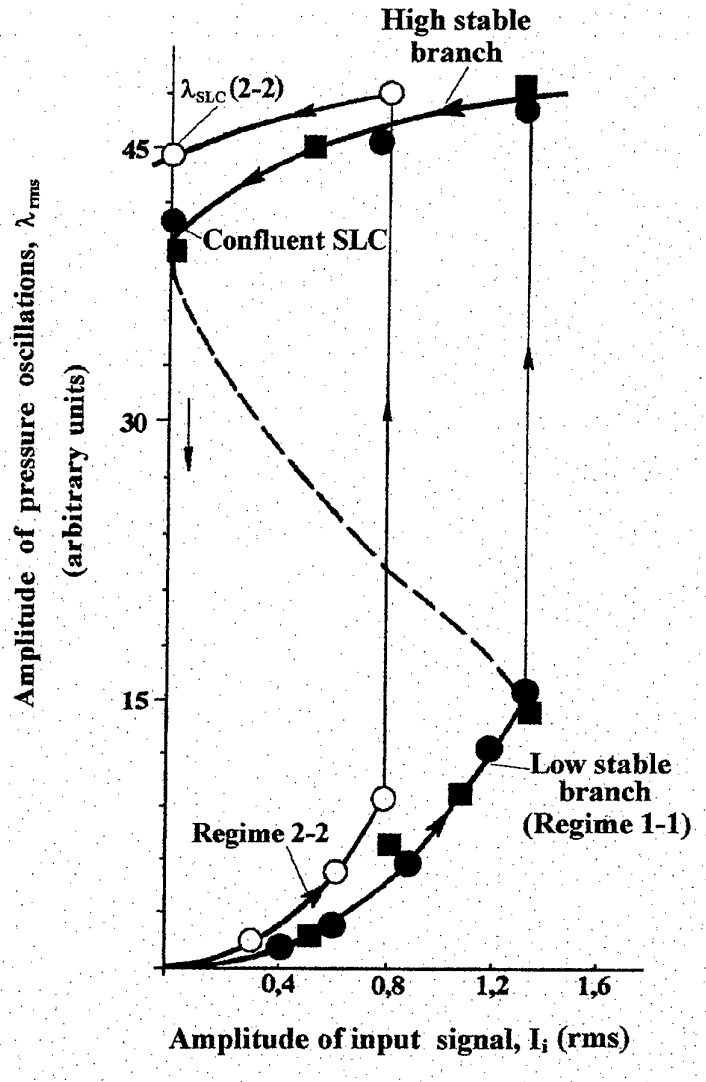


Fig.5. Dependence of forced oscillation amplitude on the amplitude of the input harmonic acoustic signal

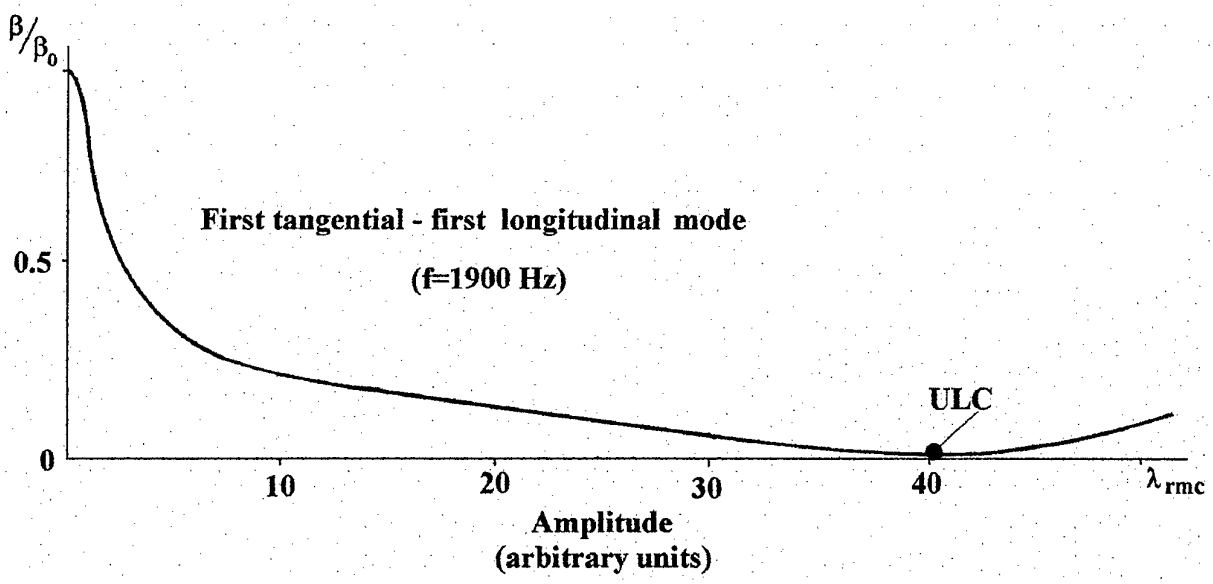


Fig.6. Reproduced dependence of the coefficient on oscillation amplitude (for section 1-1 of bifurcation diagram)

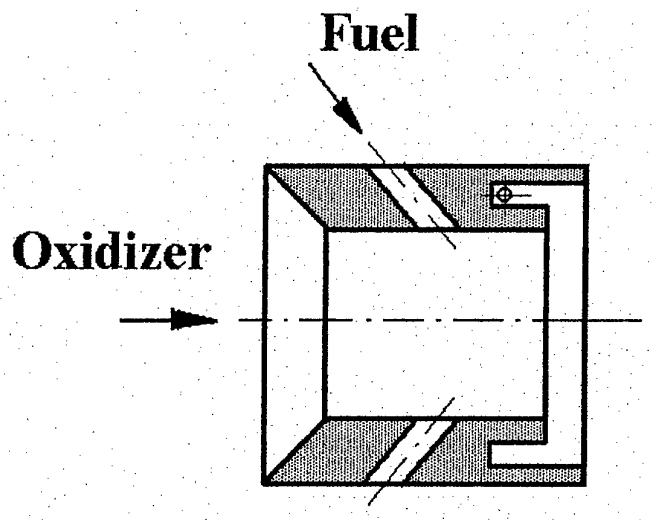


Fig.7. Injector

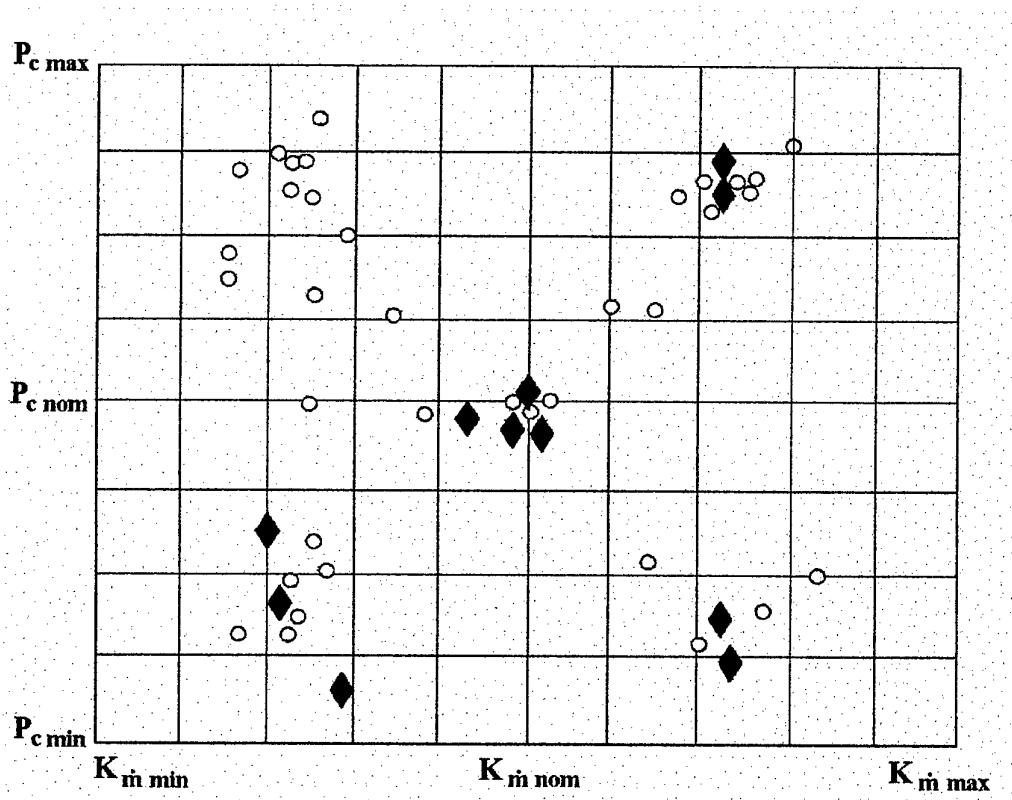
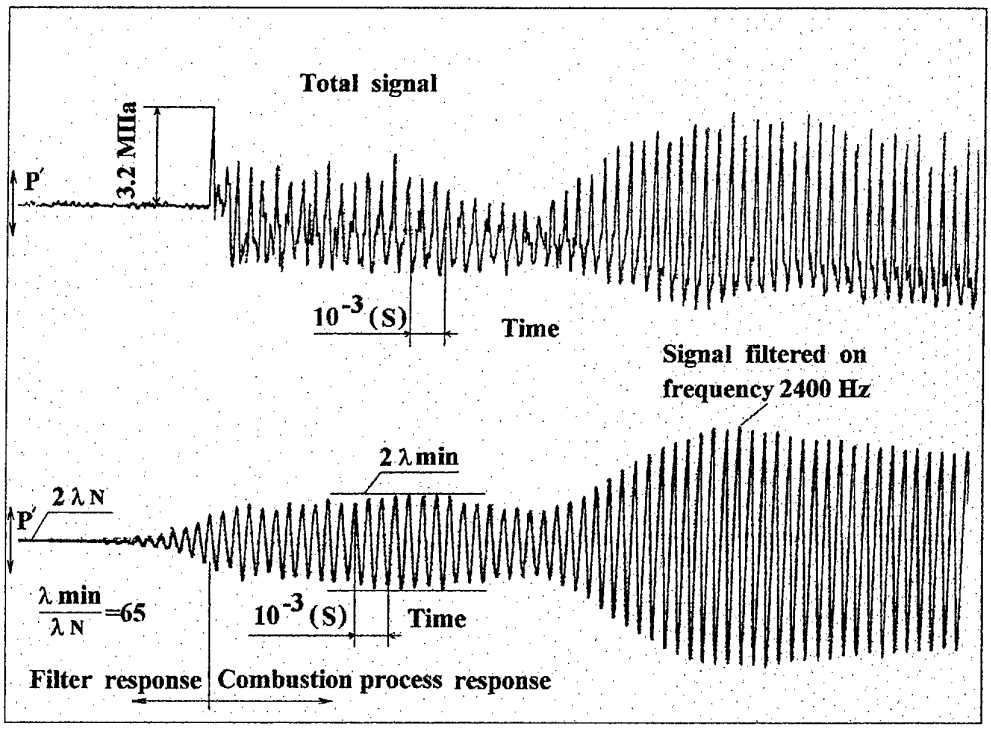


Fig.8. Engine test parameters with pulsed disturbance application

(a)



(b)

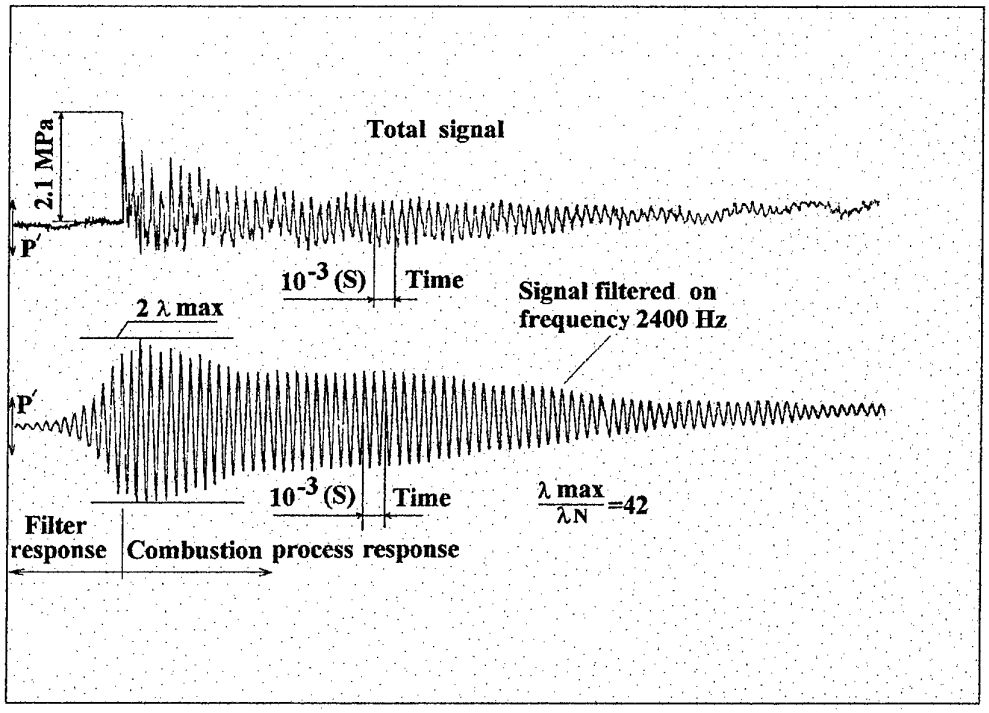


Fig.9. Combustion process response to artificial pulsed disturbances:

a) self-oscillation pulsed excitation;

b) decaying response

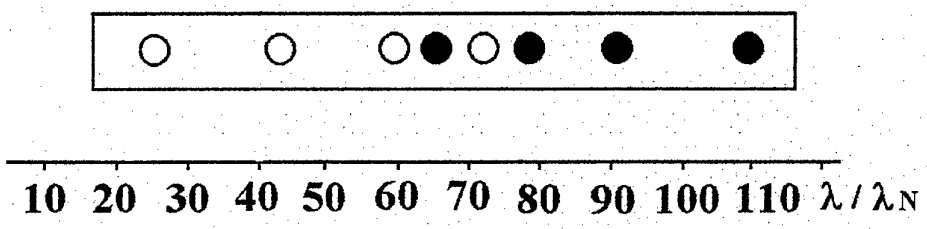


Fig.10. Diagram of responses to pulsed disturbance

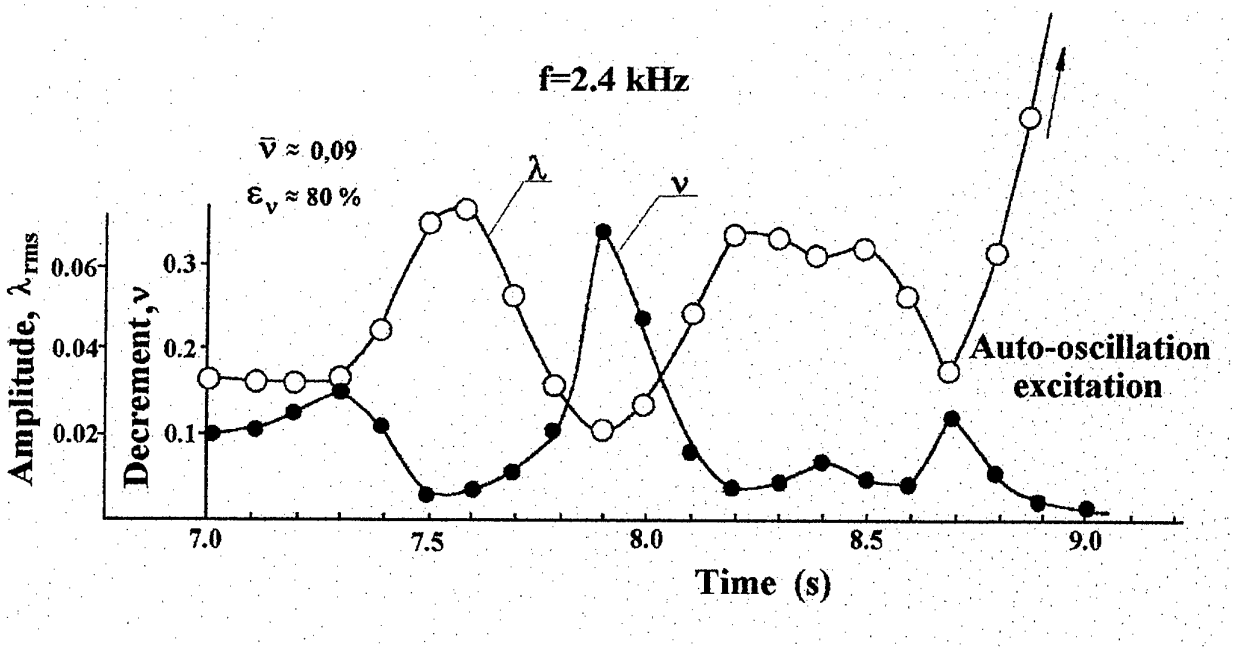


Fig.11. Variation of noise amplitude and oscillation decrement on a frequency of $f = 2.4$ kHz in the time interval preceding spontaneous excitation of self-oscillation

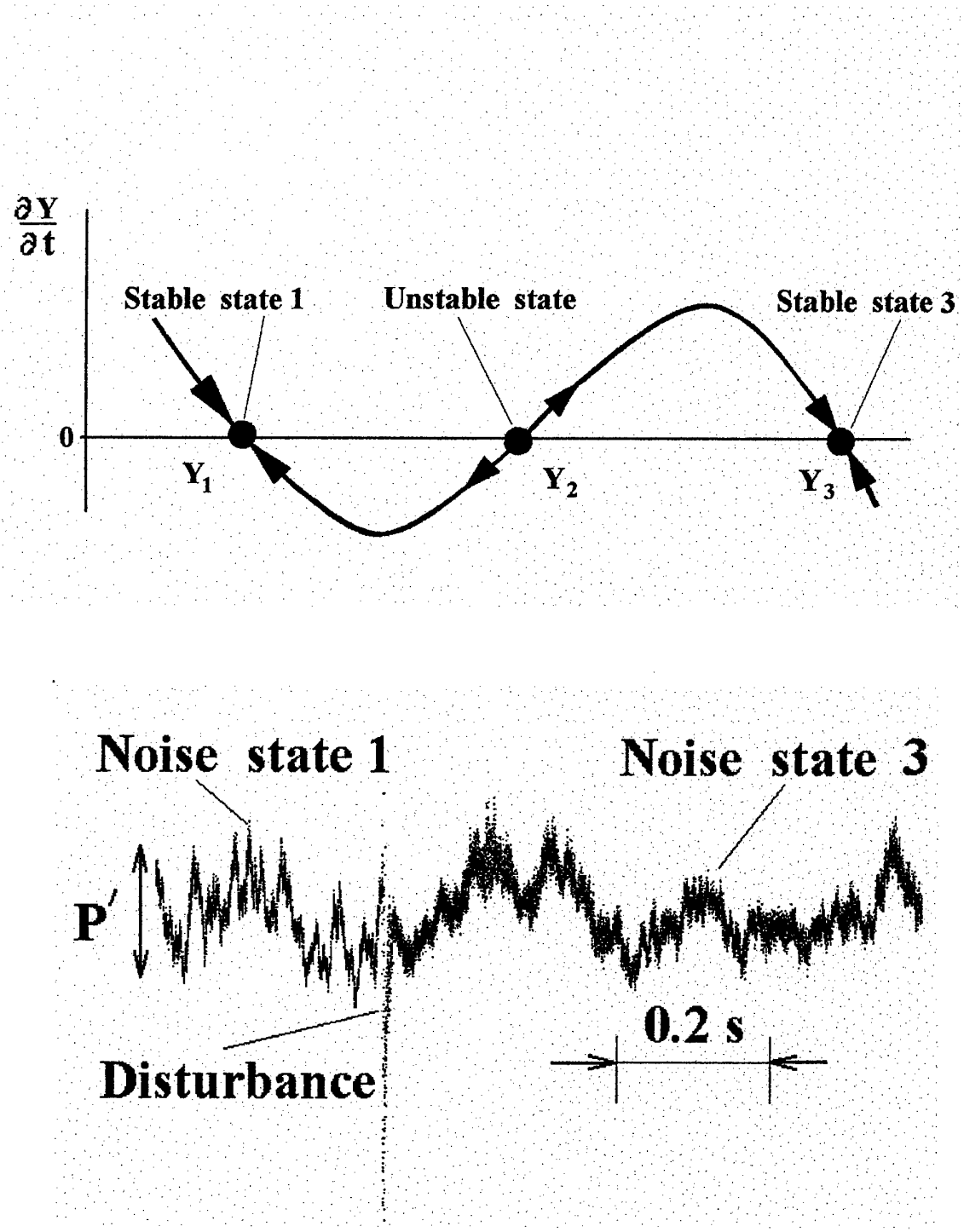


Fig. 12. Bifurcation diagram of stationary states

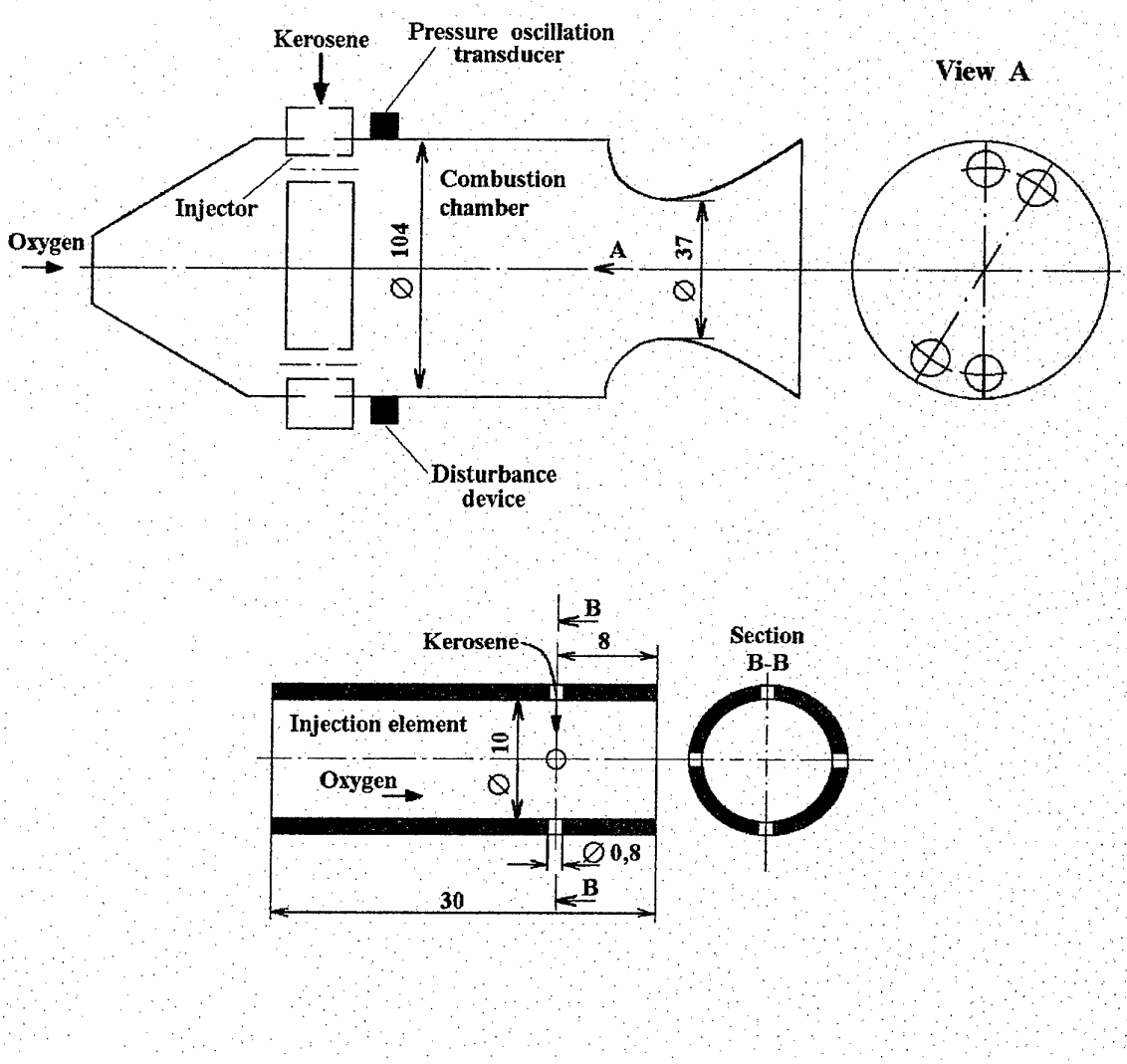


Fig.13. Model combustion chamber

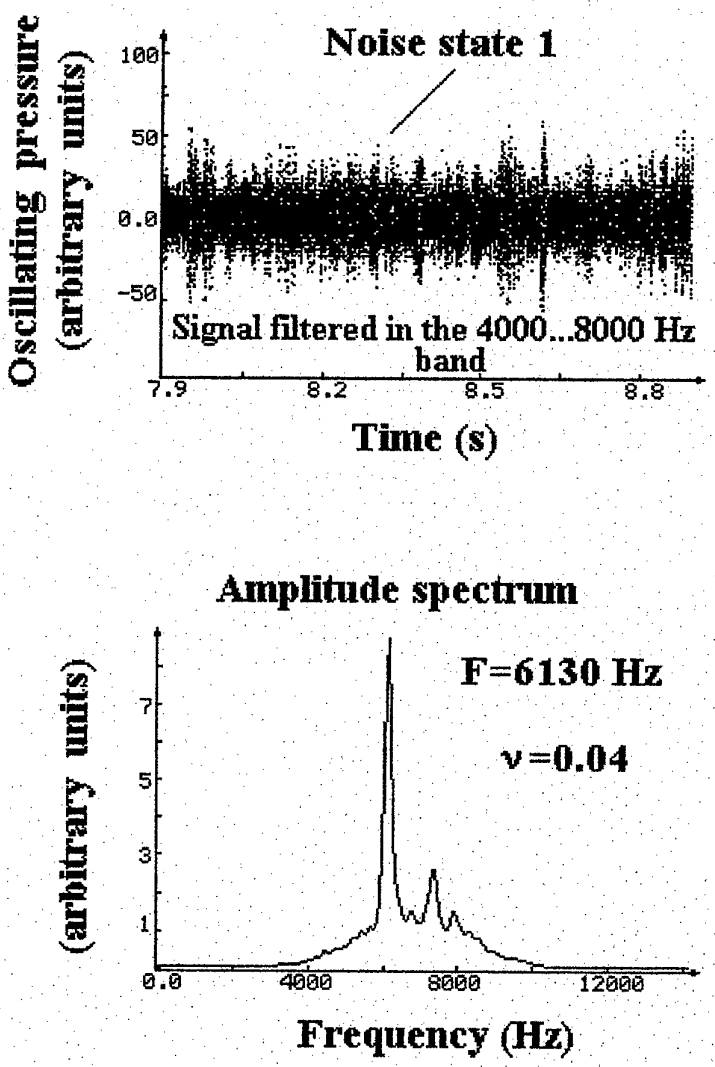


Fig.14. Noise state 1

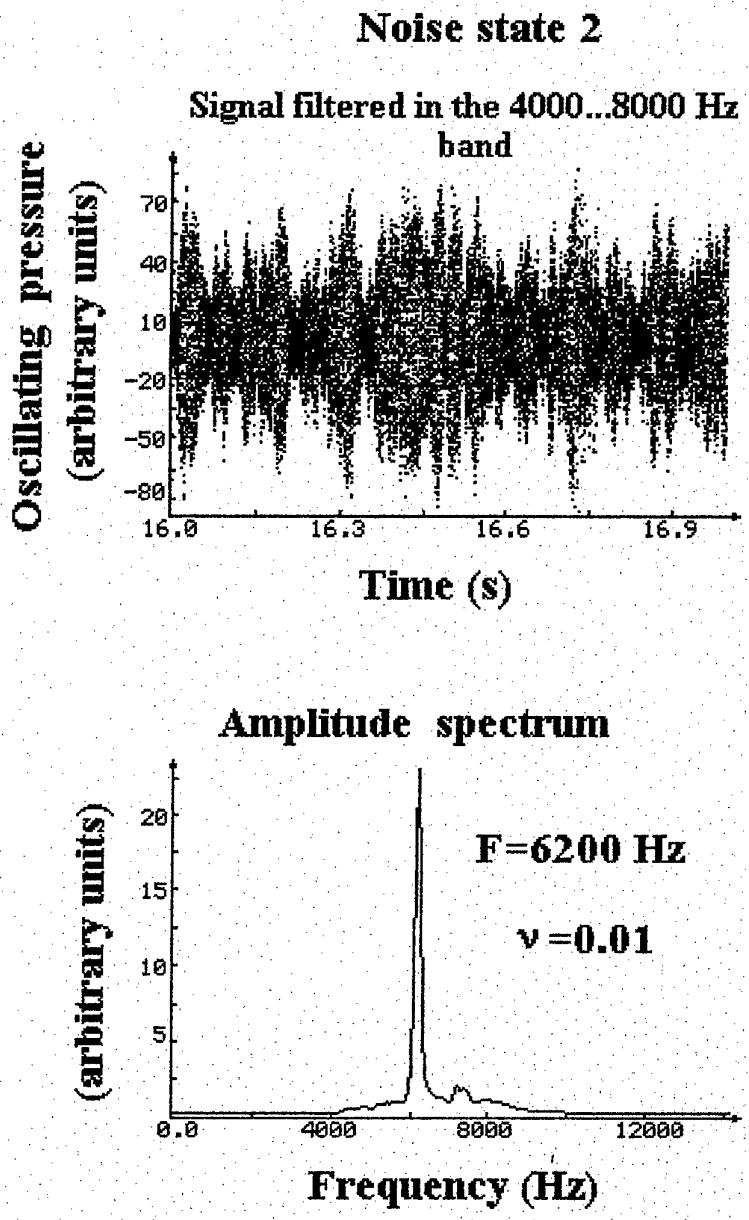


Fig.15. Noise state 2

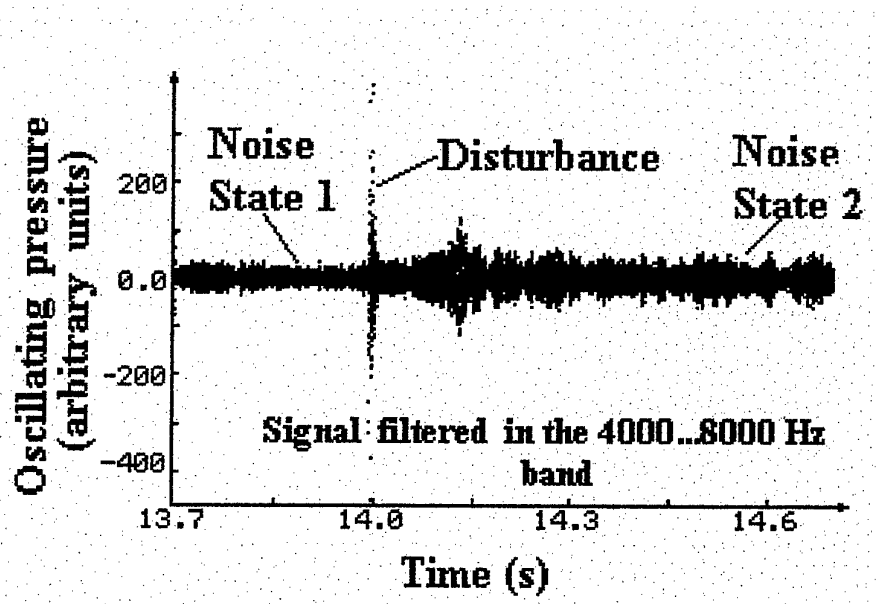


Fig.16. «Noise 1→Noise 2» transition induced by pulsed disturbance

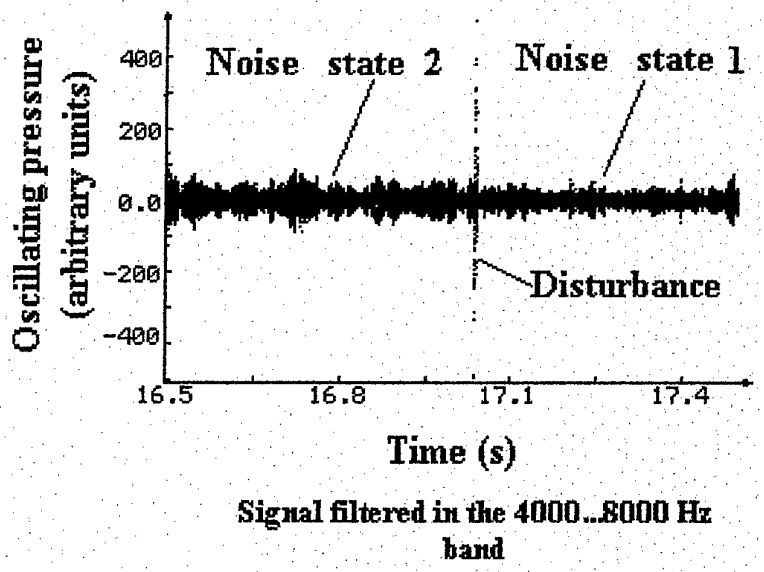


Fig.17. «Noise 2 →Noise 1» transition induced by pulsed disturbance

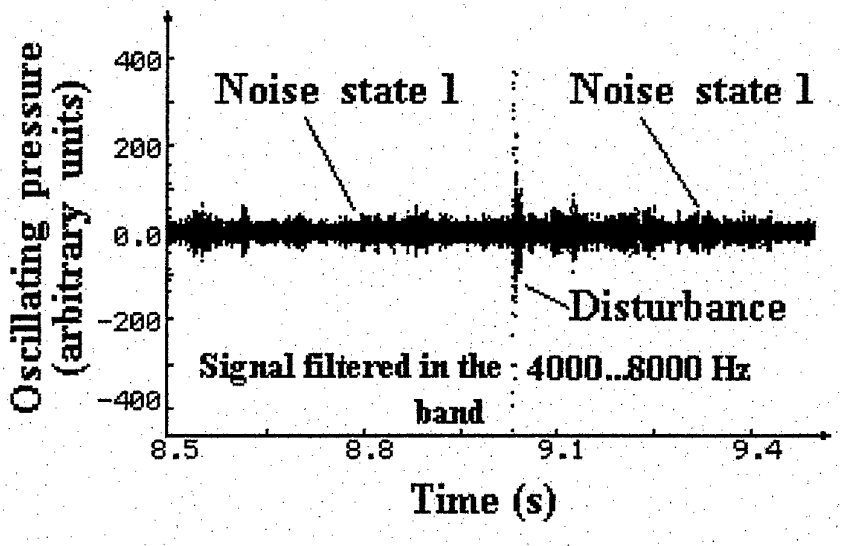


Fig. 18.Recovery of initial noise state after pulsed disturbance application

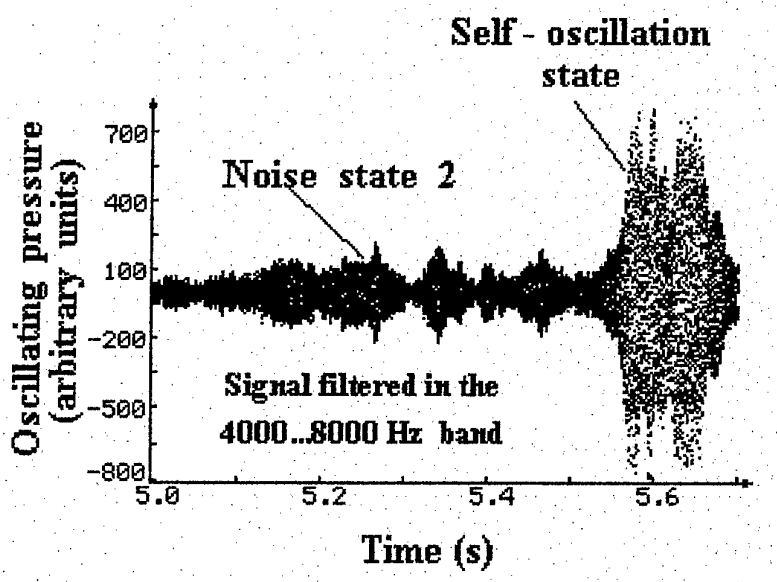


Fig.19. Spontaneous dynamic transition «Noise 2 →Auto-oscillation»

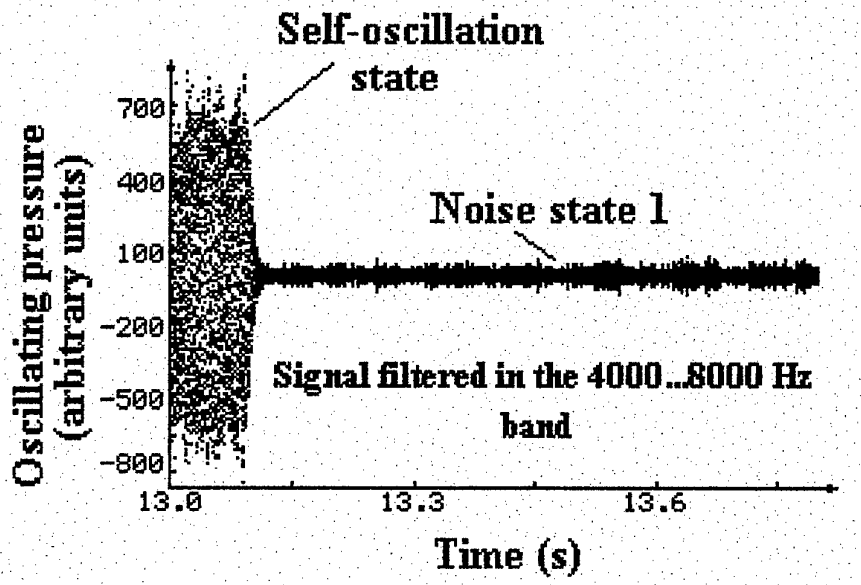


Fig.20. Spontaneous dynamic transitions:

«Auto-oscillation→Noise1»

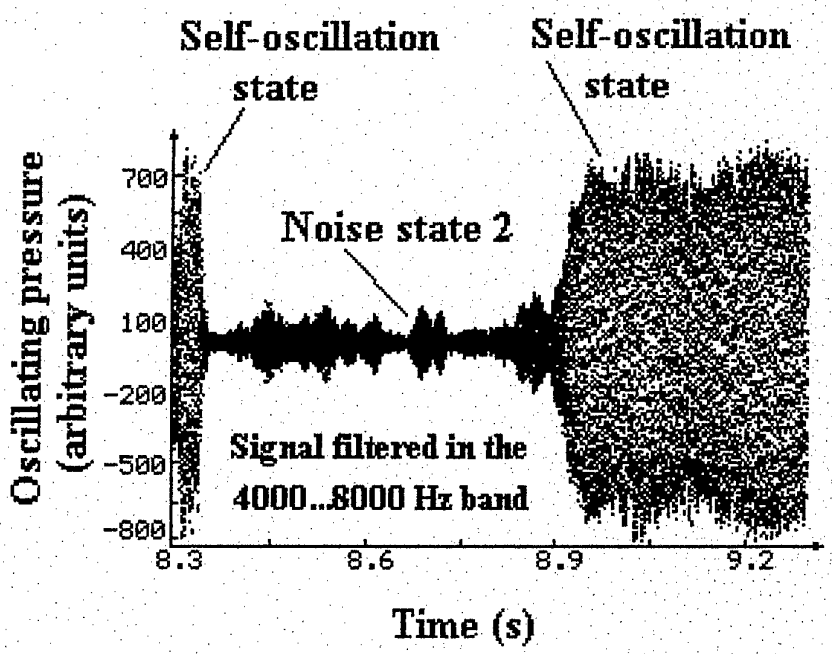
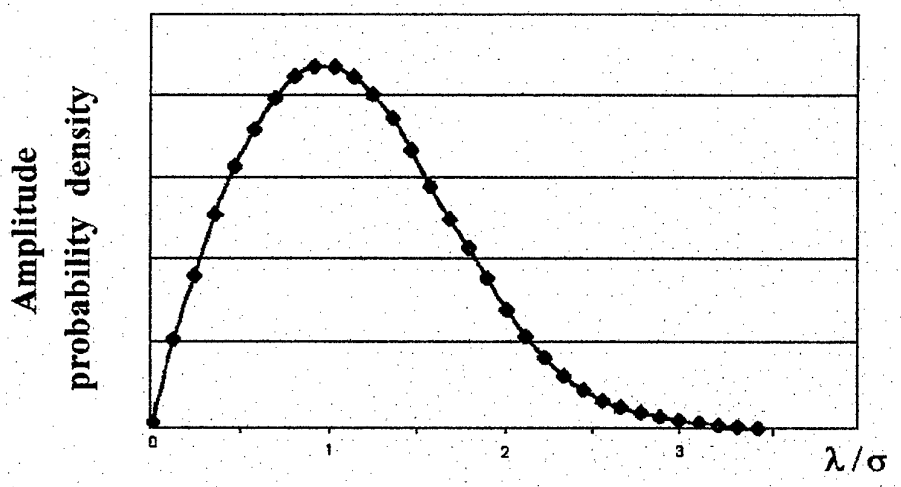


Fig.21. Spontaneous dynamic transitions:

«Auto-oscillation→Noise2→Auto-oscillation»

(a)



(b)

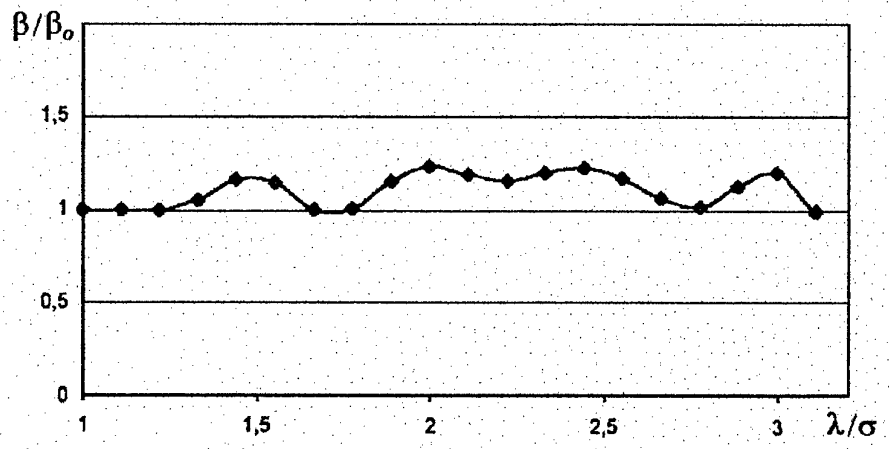
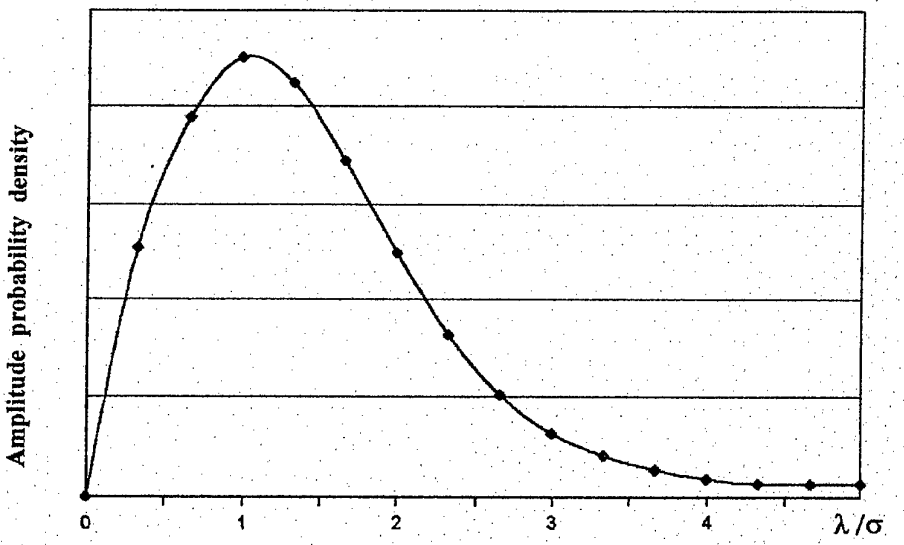


Fig. 22. Estimate of probability density of noise amplitude (a) and reconstructed relation «decay coefficient – amplitude» (b) (Noise state 1)

(a)



(b)

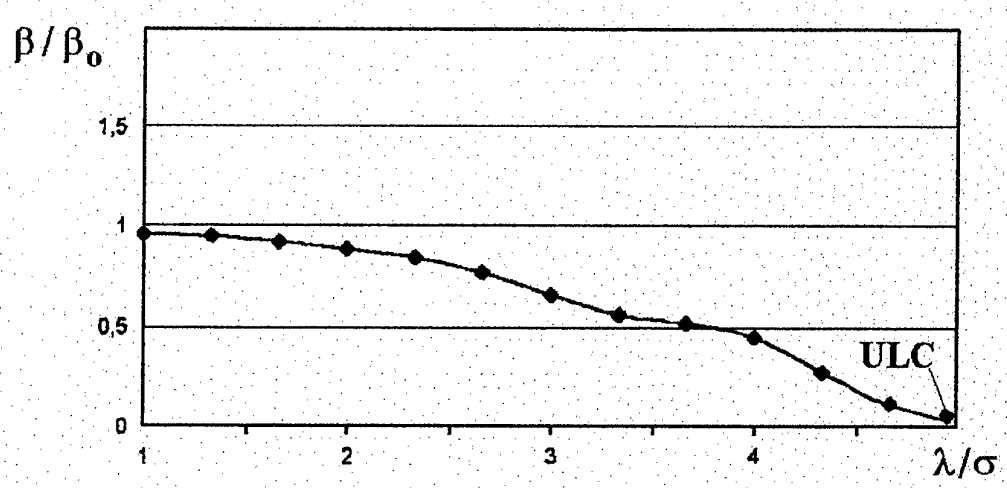


Fig. 23. Estimate of probability density of noise amplitude (a) and reconstructed relation «decay coefficient – amplitude» (b) (Noise state 2)

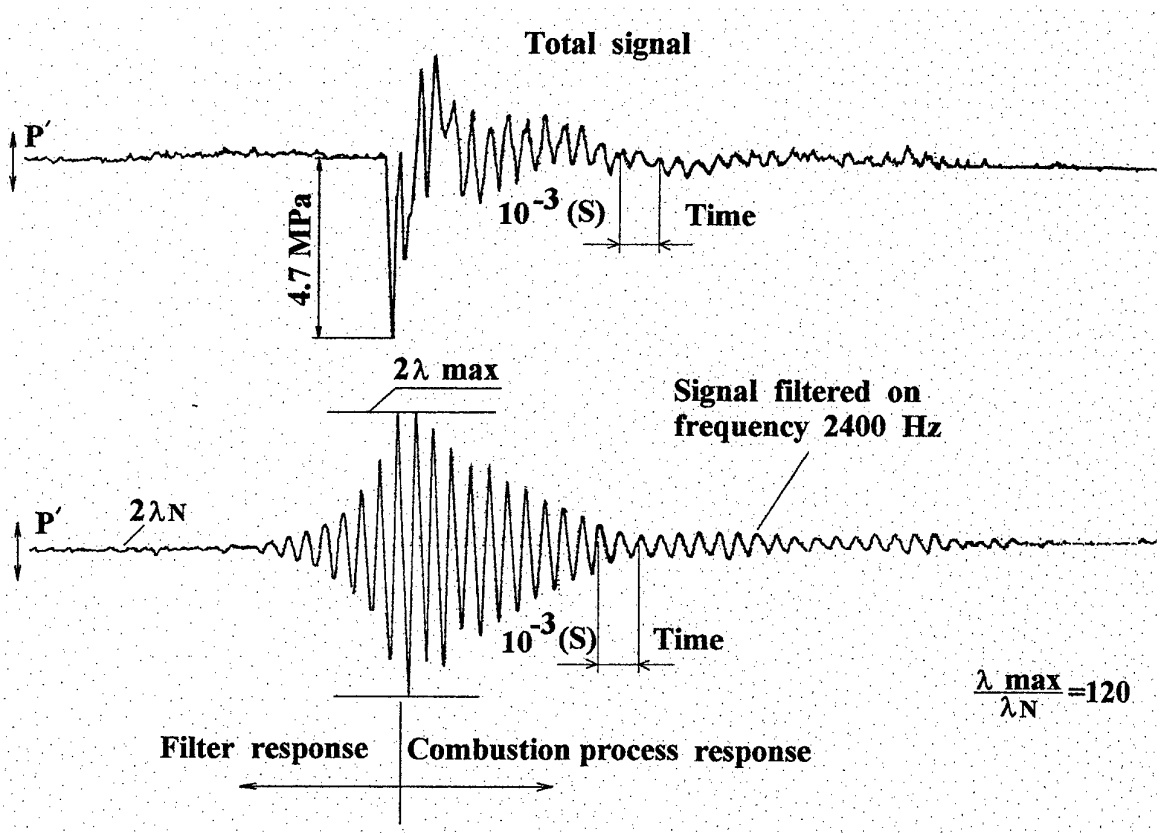


Fig.24. Combustion process response to artificial pulsed disturbances (chamber with anti-pulsation baffles)

Paper presented at the 4th International Symposium on Liquid Space Propulsion, March 12-15, 2000, DLR Lampoldshausen

Flow Separation and Side-Loads in Rocket Nozzles

Gerald Hagemann, and *Michael Terhardt,*
Dasa, DaimlerChrysler Aerospace, Space Infrastructure, 81663 Munich, Germany

Manuel Frey,
DLR, German Aerospace Centre, Space Propulsion, 74239 Hardthausen, Germany

Philippe Reijasse,
ONERA, Fundamental and Experimental Aerodynamics Department, Meudon, France

Marcello Onofri, and Francesco Nasuti,
University di Roma "La Sapienza", Roma, Italy

Jan Östlund,
VAC, Volvo Aero Corporation, Trollhättan, Sweden,
KTH, Royal Institute of Technology, Stockholm, Sweden

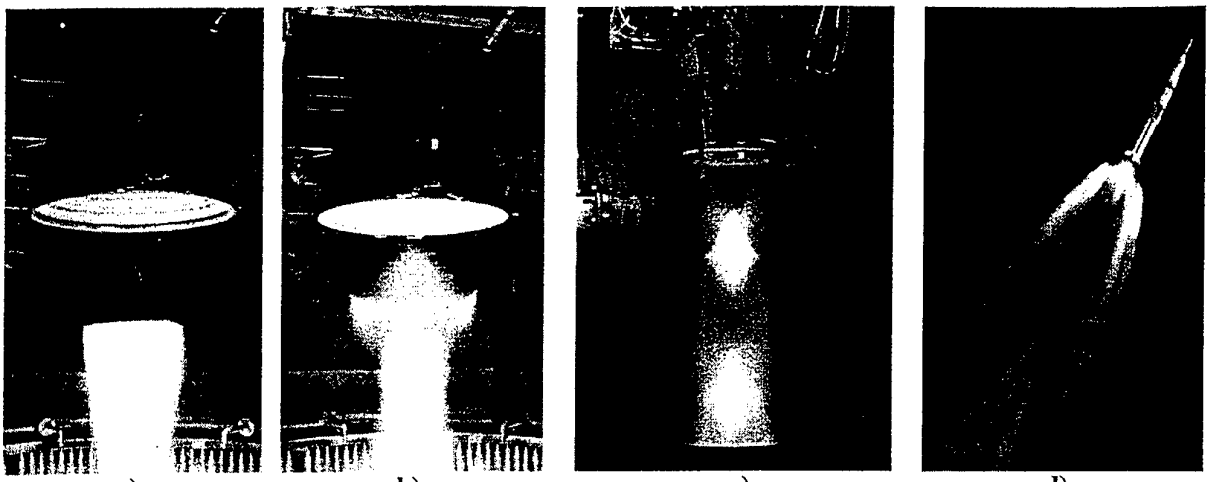
Abstract

During the transient start-up of a rocket engine operating against an ambient pressure, the exhaust flow separates from the nozzle wall at a certain pressure ratio of wall pressure to ambient pressure. Furthermore, if the chamber pressure at nominal operation condition is not high enough to reach full flowing in overexpanded flow condition, flow separation will occur even for steady state operation. Flow separation is a strongly three-dimensional instationary process, and lateral forces may be generated, the so called side-loads.
The physical origins of flow separation and side-loads and its theoretical prediction have been the key objectives for several experimental and theoretical studies in the past decades. This paper addresses the physical background of flow separation and side-loads, and gives an overview on the state-of-the-art prediction for both phenomena.

1. Introduction

Rocket nozzles of high performance rocket engines in use for first- or main stage propulsion, e.g. the American SSME, the European Vulcain, or the Japanese LE-7, operate from sea-level with one bar ambient pressure up to near vacuum. At ground, these types of engines operate in an overexpanded flow condition with an ambient pressure higher than the nozzle exit pressure. During the ascent as ambient pressure decreases, the initially overexpanded exhaust flow becomes adapted, and then finally underexpanded.
Figures 1 and 2 show photographs of nozzle exhaust flows during these two off-design operations. In the case of overexpanded flow, oblique shocks emanating into the flowfield adapt the exhaust flow to the ambient pressure. Further downstream, a system of shocks and expansion waves leads to the characteristic barrel-like form of the exhaust plume. Different shock patterns in the plume of overexpanded rocket nozzles have been observed, including the singular shock reflection generating the classical Mach disk, and the apparent regular shock reflection at the centreline.* In addition to these two plume pattern, a third pattern,

* In case of axisymmetrical flow, a pure regular reflection at the centreline is not possible. Instead, a very small normal shock exists at the centreline.[1]



a) b) c) d)

Fig. 1: Exhaust plume pattern: a) Vulcain, overexpanded flow with classical Mach disk, b) Vulcain, overexpanded flow with cap-shock pattern, c) RL10-A5, overexpanded flow with apparent regular reflection, and d) underexpanded flow, photographed during launch of Saturn 1-B (Courtesy photos: SNECMA, CNES, NASA).

the cap-shock pattern, is observed in the plume of thrust-optimised or parabolic nozzle contours featuring an internal shock, which limits the high Mach number field at the centreline. Figure 1 proves the existence of this specific flow pattern in the exhaust plume of the Vulcain nozzle.[2-4] Recent subscale experiments performed within the European FSCD[†] group also confirmed the stable existence of this shock pattern in the plume of thrust-optimised or parabolic subscale rocket nozzle.[5-8] As example, Fig. 2 shows Schlieren images of the exhaust plume of parabolic subscale nozzles tested at DLR, ONERA, and FFA. For comparison, the exhaust plume of a truncated ideal nozzle is also shown, in where the classical Mach disk is clearly visible.[8]

At high altitudes, the underexpansion of the flow results in a further expansion of the exhaust gases behind the rocket, as impressively illustrated in Fig.1 (right), taken during a Saturn 1-B launch. However, this post-expansion does not yield any thrust contribution, since it appears outside the nozzle.

Any off-design operation with either overexpanded or underexpanded exhaust flow induces performance losses. These inherent losses due to non-adapted flow condition for fixed geometry nozzles may rise up to 15%, compared to a continuously adapted exhaust flow.[9] In principle, a first- or main stage rocket nozzle could be designed for a much higher area ratio to achieve higher vacuum performance, but the flow would then separate inside the nozzle during low altitude operation, with high risk for side-load generation. And the strong requirements of a stable nozzle operation on ground, and a high vacuum performance lead to the design of a highly overexpanded, but operationally full flowing nozzle at sea level condition.

It becomes obvious, that a most accurate prediction of flow separation is essential during the definition of a new rocket nozzle. Furthermore, accurate prediction of expected side-loads during transients is a further decisive task, needed to mechanically define the thrust chamber structure to ensure mechanical integrity under worst case condition.

Therefore, flow separation and side-loads in overexpanded nozzles have been the subject of several studies in the past decades. In the following, a literature review and the state-of-the-art for both the understanding of the physical phenomena involved and the prediction of flow separation and side-loads is given.

[†] FSCD: Flow Separation Control Device, research group with members from industry (Dasa, Snecma, Volvo Aero) and institutes (CNES, ESA, DLR, ONERA, LEA Poitiers), which investigates flow separation and side-load origins in nozzles by means of experiments and numerical analyses.

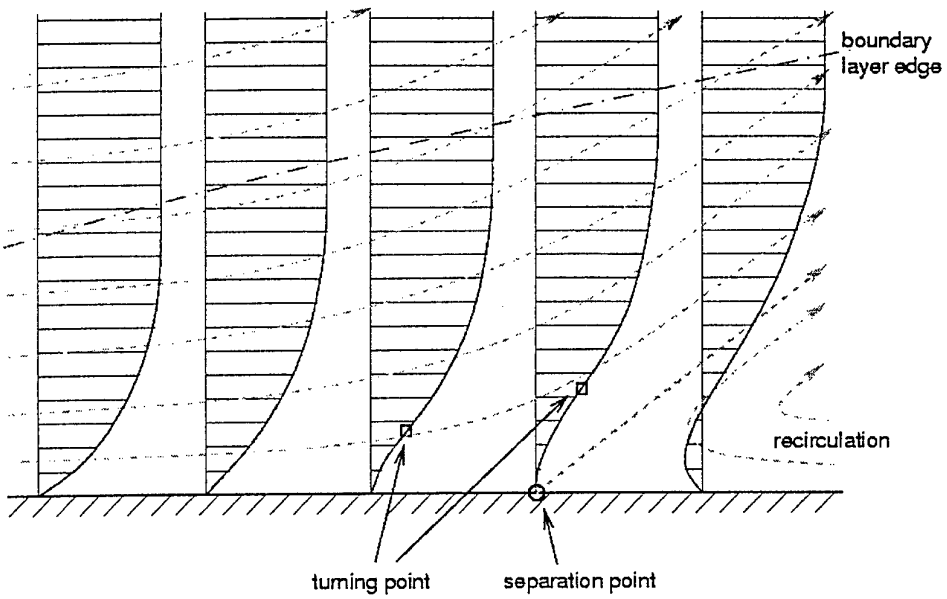


Fig. 3: Streamwise velocity profiles (solid lines), streamlines (dashed line) and boundary layer thickness dot-dashed line) near and at the separation point.

2. Flow Separation

In 1904, Prandtl [10] showed that flows with low friction in the vicinity of bodies can be subdivided into two regions: a thin layer close to the body, the so-called boundary layer (originally called *friction layer* due to the predominance of friction), and the remaining flow, the potential flow where friction effects can be neglected. In the boundary layer itself, the flow at the wall must follow a no-slip condition. Hence, the boundary layer is decelerated by the wall, but accelerated by the outer flow. The static pressure, constant across the boundary layer, is governed by the main flow.

In flows with favourable or zero wall pressure gradient, the boundary layer is attached to the wall. This can be different in the case of an adverse wall pressure gradient. If the wall pressure increases in the main flow direction, kinetic energy of the fluid particles is transformed into potential energy. However, fluid particles close to the wall only have a small kinetic energy because of their lower velocity. Therefore they are stopped by the pressure rise, and may be even forced to flow in the reverse direction, see Fig. 3. In this case the boundary layer is separated from the wall, and the recirculation region is developed in the vicinity of the wall.

Flow separation requires the existence of both friction and an adverse wall pressure gradient in a flow along a body. If one of these two conditions is suppressed, flow separation can be prevented. Prandtl proved this with different experiments, e. g. with a flow around rotating cylinders or with a diffuser with boundary layer suction. [11] Also, flow separation might not occur if the adverse pressure gradient is weak. In this case, the normal exchange of momentum inside the boundary layer can be sufficient to transport momentum from the mean flow to the wall; consequently, the kinetic energy of the particles close to the wall can be high enough to withstand the pressure rise without separation. Turbulent boundary layers with their characteristic high lateral exchange of momentum therefore separate much later than laminar boundary layers, where the momentum transport only consists of molecular movements.

At the separation point of two-dimensional boundary layers, planar or axisymmetric, the wall shear stress becomes zero,

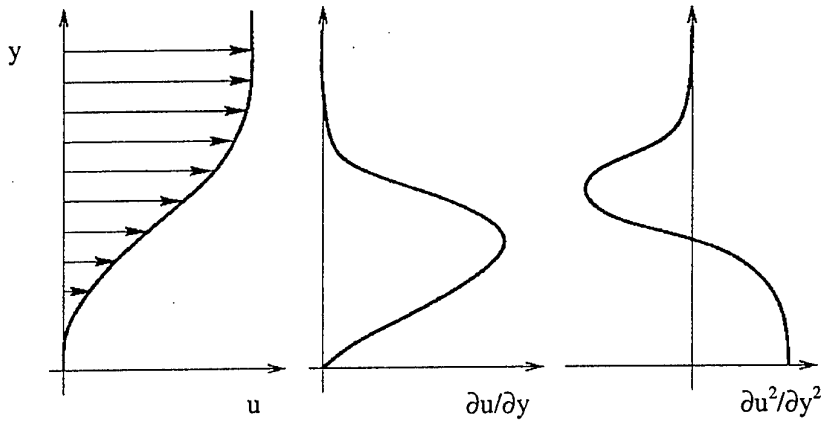


Fig. 4: Velocity profile, and first and second derivative in wall normal direction at the separation point.

$$\tau_w = \mu \cdot (\partial u/\partial y)_w = 0 \,. \tag{1}$$

From this equation, and the velocity profile sketched in Fig. 3, the behaviour of the derivatives of u in wall-normal direction can be estimated, see Fig. 4.
In order to get a closer understanding of the separation processes, the momentum equation in wall-parallel direction is considered. The chosen non-conservative formulation is valid for a Newtonian fluid in a Cartesian co-ordinate system, neglecting volumetric forces:

$$\begin{aligned} &\rho\left(\frac{\partial u}{\partial t}+u\frac{\partial u}{\partial x}+v\frac{\partial u}{\partial y}+w\frac{\partial u}{\partial z}\right)= \\ &-\frac{\partial p}{\partial x}+\frac{\partial}{\partial x}\left[2\mu\cdot\left(\frac{\partial u}{\partial x}-\frac{div\ \vec{v}}{3}\right)\right]+\frac{\partial}{\partial y}\left[\mu\left(\frac{\partial u}{\partial y}+\frac{\partial v}{\partial x}\right)\right]+\frac{\partial}{\partial z}\left[\mu\left(\frac{\partial u}{\partial z}+\frac{\partial w}{\partial x}\right)\right] \end{aligned} \tag{2}$$

If an arbitrary point at the wall is considered, the non-slip condition yields $u = v = w = 0$ for all velocity components as well as for their derivatives with respect to time and to the wall-parallel directions x and z. Substituting $div\ \vec{v} = \partial u/\partial x + \partial v/\partial y + \partial w/\partial z$, and by assuming a constant viscosity across the boundary layer, the expression is simplified as follows:

$$0=-\frac{\partial p}{\partial x}-\frac{2}{3}\mu\cdot\frac{\partial}{\partial x}\left(\frac{\partial v}{\partial y}\right)+\mu\frac{\partial^2 u}{\partial y^2} \tag{3}$$

Because of $\partial/\partial x\ (\partial v/\partial y) = \partial/\partial y\ (\partial v/\partial x)$, the second term on the right side of Eq.(3) becomes zero. Consequently, the following formula is valid for an arbitrary location at the wall:

$$\mu\left(\frac{\partial^2 u}{\partial y^2}\right)_w=\frac{\partial p_w}{\partial x} \tag{4}$$

In this context, Eq.(4) was derived directly from the momentum equation (2), only assuming a constant viscosity in the boundary layer, and is therefore valid for any point at the wall, including separation and recirculation zones. Schlichting[12] derived Eq.(4) from the classic boundary layer equations, which only

represent an approximation of the flow. The aforementioned derivation from the momentum equation shows that Eq. (4) is not only an approximation, but an exact solution for the flow at the wall.
As showed in Fig. 4, Eq. (1) can be used to show that $(\partial^2 u/\partial y^2) > 0$ at the separation point. Since the dynamic viscosity is always positive, Eq. (4) yields that in order to have separation the wall pressure gradient must be adverse:

$$\left(\frac{\partial p_w}{\partial x}\right)_{x,\,separation} > 0 \qquad (5)$$

In order to provide scientists and engineers with more information on this wall pressure rise and the exact shock location, many experimental measurements have been carried out both in the past and recently for full scale and subscale overexpanded nozzles, see e.g. Ref. 5-8, 13-21. Furthermore, a significant support to the analysis of the flow separation has been provided by means of numerical simulations.[2, 4, 5, 22-25]
Two different separation patterns have been observed, the classical free shock separation, and the restricted shock separation, in the following respectively called by their acronyms FSS and RSS. Figure 5 shows a schematic for both separation pattern with the definition of characteristic points. In addition, Figure 6 compares measured and numerically calculated wall pressures for both separated flow patterns, and also includes the numerically calculated Mach number distribution for FSS and RSS, respectively.

2.1 Free shock separation

In the classical free shock separation condition, the overexpanded nozzle flow fully separates from the wall at a certain ratio of wall- to ambient pressure. The resulting streamwise wall pressure evolution is mainly governed by the physics of shock / boundary layer interactions occurring in any supersonic flow separation. The first deviation of the wall pressure from the vacuum profile is commonly named *incipient separation pressure*, p_{sep} in Fig. 5. The wall pressure then quickly rises from p_{sep} to a *plateau pressure* p_p, which is in general slightly lower than the ambient pressure p_a. Analyses of subscale tests in nozzles and at forward facing steps have shown, that the steep pressure rise is caused by a shock front fluctuating at typical high frequencies in the order of ~1-2 kHz in between the incipient separation point x_{sep} and the point where the plateau pressure is reached, x_p.[26] This observation, although not completely new, is in contrast to the classical view of a stable and well defined separation point, in where the pressure rise from p_{sep} to p_p has the origin in compression waves focussing to the oblique separation shock.[15, 27]
From many cold gas tests in the past decades it has been noticed, that the boundary layer effectively separates from the nozzle wall shortly before reaching the plateau pressure p_p. In the recirculation zone downstream of the separation point, the wall pressure increases slowly from p_p to $p_{w,e}$. This gradual pressure rise can be explained with the inflow of gas from the ambience into the recirculation region at a total pressure equal to ambient pressure. The acceleration of the ambient gas inside the nozzle before it is mixed with the exhaust gas in the turbulent shear layer results in a decrease of measured static pressure, and an increase in dynamic pressure. Considering the direction of the main exhaust flow, this yields the gradual pressure rise.
To predict the axial separation location inside a nozzle, the ratio of separation to ambient pressure p_{sep}/p_a must first be known. Using the vacuum wall pressure profile of this nozzle, the separation location can then easily be determined. Of course, the separation pressure ratio p_{sep}/p_a includes the influence of both the pressure rise at the separation location itself and the gradual pressure rise in the recirculation region. To simplify the physical interpretation of the separation pressure ratio p_{sep}/p_a, it should be subdivided into two factors $(p_{sep}/p_p)\cdot(p_p/p_a)$, where each part refers to a single physical phenomenon, the former for the separation itself, the latter for the subsequent open recirculation with inflow of ambient gas.

It was noticed very early, that the separation pressure ratio decreases during the start-up of nozzle flows, as the separation point moves downstream with increasing pressure ratio p_c/p_a.[13-19] This was soon attributed to the Mach number influence, as experiments in wind tunnels had shown the separation pressure ratio to decrease with increasing Mach number.

However, there is a deviation from this regular behaviour as the separation point reaches the vicinity of the exit.[19, 20] At a location where the local area ratio of the nozzle has reached about 80% of its final value, the separation pressure ratio p_{sep}/p_a reverses its previous trend and increases as the pressure ratio p_c/p_a is

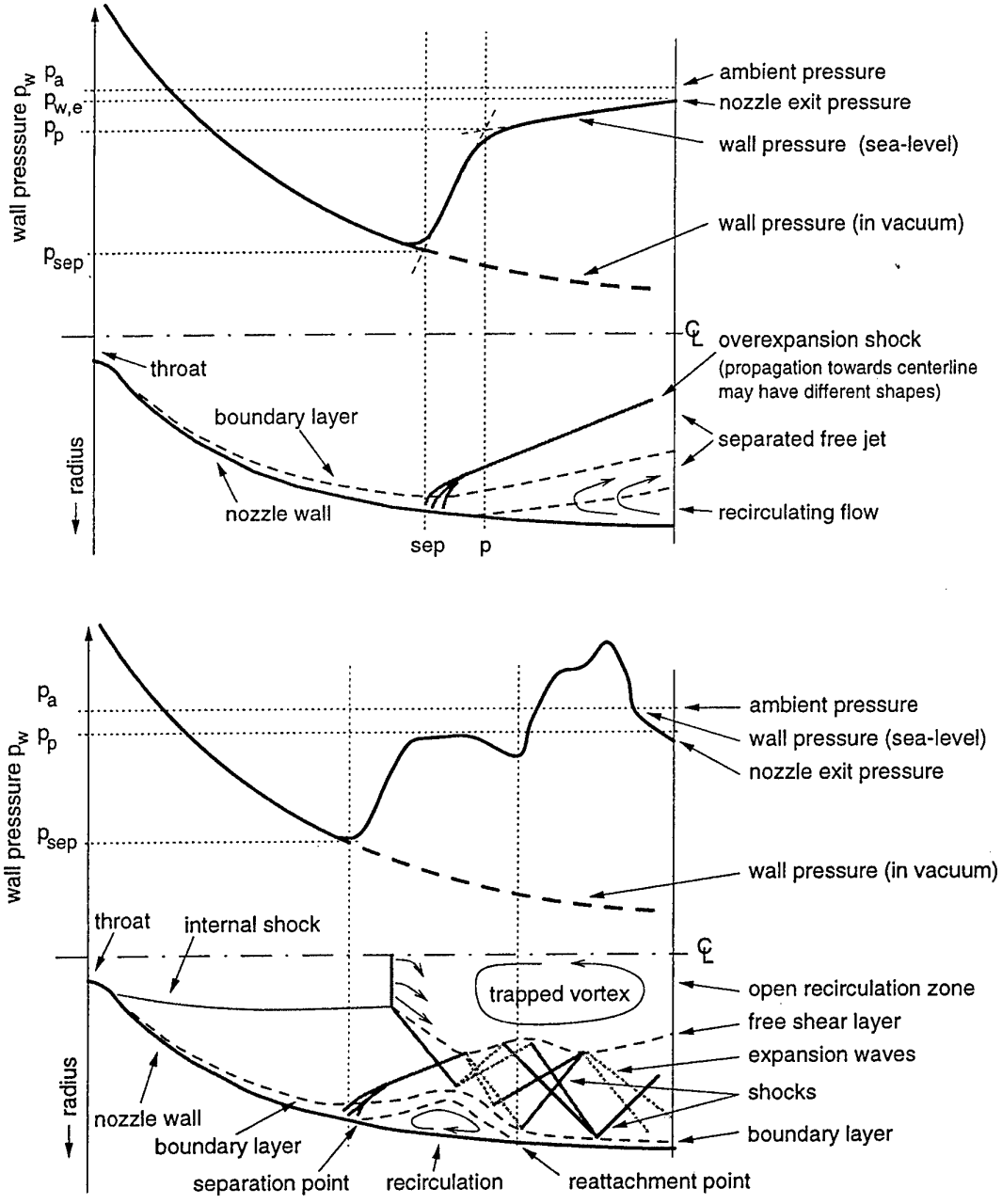


Fig. 5: Phenomenological sketch of free shock separation (FSS, top), and restricted shock separation (RSS, bottom).

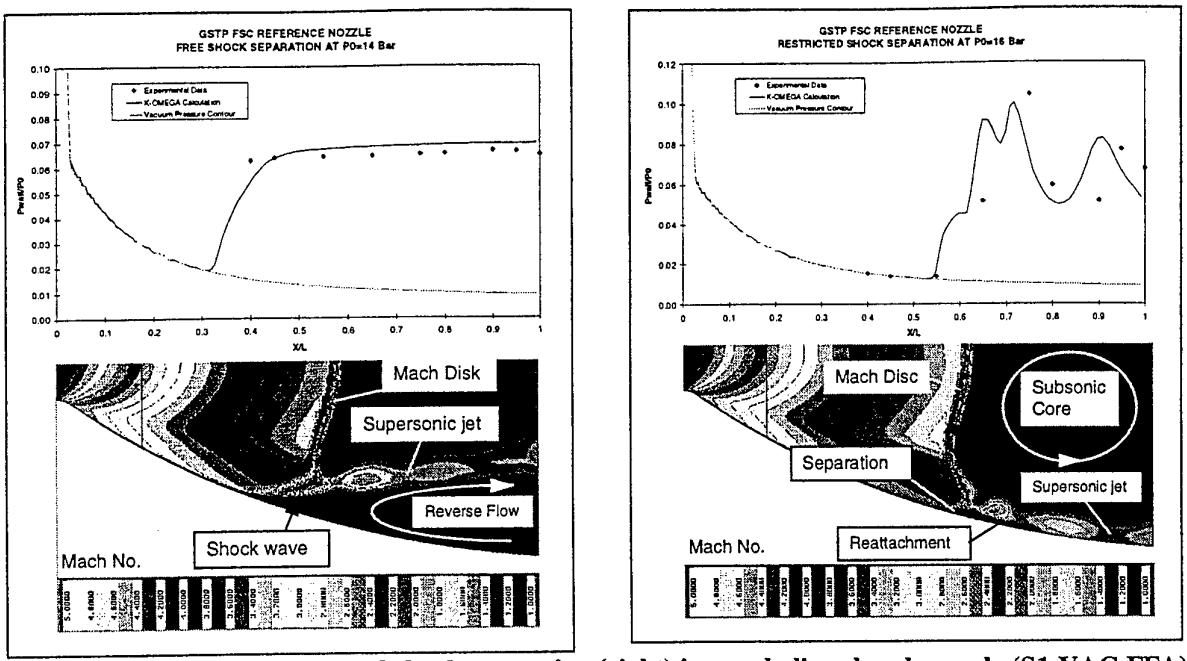


Fig. 6: Free (left) and restricted shock separation (right) in parabolic subscale nozzle (S1 VAC FFA), comparison of measured and calculated wall pressures, and calculated Mach number distribution.

increased. An explanation given for this behaviour in Ref. 20 is that close to the nozzle exit the plateau pressure increases to ambient pressure. For a constant pressure ratio p_{sep}/p_p in this last part of the nozzle, this would cause then an effective increase in separation pressure p_{sep}, and thus in p_{sep}/p_a. As the point p reaches the nozzle exit, the flow can be attached until the exit despite a clear pressure rise detected by sensors in the vicinity of the exit. This means there is no effective flow separation, but only incipient separation.

A further contribution to the observed pressure increase for an effectively full flowing nozzle might be due to the subsonic part of the boundary layer, which allows information from the ambient to be carried upstream into the nozzle.

2.2 Restricted shock separation

During cold-flow subscale tests for the J-2S engine development in the early 70s, a different kind of separated nozzle flow at strongly overexpanded conditions was observed, which had not been known before.[28] In this flow regime, which only occurred at certain pressure ratios, the pressure downstream of the separation point showed an irregular behaviour and partly reached values above the ambient pressure. This is attributed to a reattachment of the separated flow to the nozzle wall, inducing shocks and expansion waves. Due to the very short separated region, this flow regime was called *restricted shock separation*. The separation characteristic of *restricted shock separation*, as observed in the literature,[28] and recently confirmed for subscale[5, 7, 8] and full-scale rocket nozzles[2-4] is described in the following.

During the start-up of the nozzle flow, featuring initially pure free shock separation, the transition from FSS to RSS occurs at a well defined pressure ratio.[4,5] A closed recirculation zone is formed, with static pressures significantly below the ambient pressure level. Thus, the transition from FSS to RSS is connected with a sudden downstream movement of the separation point. Beyond the reattachment point in RSS, supersonic flow propagates along the nozzle, thereby inducing shocks that result in the aforementioned wall pressure peaks above ambient pressure. By further increasing the thrust chamber pressure ratio, the closed recirculation zone is pushed towards the nozzle exit. Finally, the reattachment point reaches the nozzle exit,

and the recirculation zone opens to the ambience. This is connected with a pressure increase in the recirculation zone behind the separation shock, which pushes the separation point again further upstream. Thereby it occurs, that the recirculation zone closes again, connected with a drop in static pressure which results again in a downstream movement of the separation point. A pulsating process is observed, connected with the opening and closing of the separation zone. This re-transition from RSS back to FSS is in the literature also referred to as the end effect.[4, 5]
The same phenomena can be also observed during shut-down. While the end-effect, and thus the transition now from FSS to RSS occurs at the same pressure ratio as the RSS- to FSS transition during start-up, the re-transition from RSS to FSS occurs in general at a different lower pressure ratio than the corresponding transition FSS-RSS during start-up.[2-6]

The theory of reattached flow in the J-2S sub-scale nozzle was first confirmed by numerical simulations of Chen et al. in 1994, Ref. 22. In addition, their calculations revealed a trapped vortex behind the central normal shock, but they did not provide any explanation about the generation of such flow structure.
Later, Nasuti and Onofri [23-25] stressed the role played by the centreline vortex on the separation pattern and side-load generation, and suggested a possible explanation of its formation mainly based on the key role played by the flow gradients behind the recompression shock in the nozzle core. According to their explanation, an *inviscid mechanism* leads to the generation of the vortex. In particular, the driving role is played by the non-uniformity of the flow impinging on the recompression shock, as that carried by the internal shock in parabolic nozzles. Because of this upstream flow non-uniformity, the shock cannot be straight, and its strength cannot be constant along the shock profile. As a consequence, a rotational flow occurs behind the recompression shock with velocity and entropy gradients, that becomes larger for increasing flow non-uniformity upstream, and thus is able to generate vortical structures. Once the centreline vortex is generated, it acts as an obstruction for the exhausting jet, that therefore deviates towards the wall. As a consequence a radial flow component is generated that tends to reattach the separated region to the wall, thus switching the flow structure of the separated region from FSS to RSS.
A further explanation of the reattached flow has been given by Frey and Hagemann based upon experimental observations and numerical simulation.[2,3] According to their results, key driver for the transition from FSS to RSS and vice versa is the specific cap-shock pattern. As conclusion, a transition from FSS to RSS can only occur in thrust-optimised or parabolic nozzles featuring an internal shock. Based on their findings, the cap-shock pattern results from the interference of the separation shock with the inverse Mach reflection of the weak internal shock at the centreline.[3] Key feature of this inverse Mach reflection is the trapped vortex downstream of it, driven by the curved shock structure upstream of it which generates a certain vorticity in the flow.[3, 29, 30] Thus, the vortex would be a result of the curved shock structure, which is partially in contrast the explanation given by Nasuti and Onofri, that includes also an effect of flow gradients upstream. Further experimental and numerical verification are planned to finally conclude on the interesting vortex phenomenon.
However, it is interesting to note, that both hypotheses of Nasuti and Onofri, and Frey and Hagemann identify the curved cap-shock profile as driver for the transition from FSS to RSS, which is meanwhile proven by experiments.[4-8]

2.3 Flow separation - Steady state vs. transient analysis

Numerical attempts to simulate transients with either impulsive[22] or smooth [24, 25] chamber pressure variations were carried out in the literature, to study the potential effect of transient phenomena on the separation behaviour. In the smooth variations, the transients were still assumed to be one order of magnitude faster than real, lasting only 100 milliseconds. This choice of reducing the time of transient duration was forced by the huge amount of computational time needed for such simulations. The comparison of solutions computed at different times during the transient with quasi-steady analysis obtained as a sequence of steady solutions showed no significant difference until the obstruction created by the recirculating region in the core of the

divergent section becomes so large as to squeeze the separated region at the wall.[24] In particular, the transient flow simulation of Ref.24 showed that the unsteady character of the main jet in this phase influences the evolution of the flow reattachment. However, the observed qualitative behaviour was similar, with the evolution from free to restricted flow separation and the generation of the vortex in the core flow. Keeping in mind, that typical start-up sequences of full scale rocket engines require approx. 1-2 seconds up to nominal operation condition, steady state flowfield analyses to study the separation behaviour are justified.

2.4 Flow separation - Prediction models

The theoretical prediction of free shock separation is the case which has been most extensively studied in the past since, historically, almost all experiments have been performed in conical and truncated ideal nozzle contours only featuring this separation pattern. Experimental data have been used to develop a number of empirical and semi-empirical criteria in order to give the nozzle designer a prediction tool for the separation point, although knowing that in reality there is no exact point of separation because it fluctuates between two extreme locations. But even today, an exact prediction cannot be guaranteed because of the wide spectrum of parameters involved in the boundary layer – shock interaction such as nozzle contour, gas properties, wall temperature, wall configuration and roughness.

As previously described, the FSS phenomenon can be subdivided into two separate mechanisms, one associated with the boundary layer separation from the nozzle wall, p_{sep}/p_p, and a second one associated with the aspirated ambient gas in the recirculation region, p_p/p_a. The whole pressure rise from incipient separation- to ambient pressure can therefore be described as $p_{sep}/p_a = (p_{sep}/p_p)\cdot(p_p/p_a)$.

Probably the most classical and simple criteria for FSS purely derived from nozzle testing is the one given by Summerfield et al., Ref. 15, which is based on extensive studies on the separation phenomenon in conical nozzles in the late 1940's:

$$p_{sep}/p_a \approx 0.4 \qquad (6)$$

A first approach to include the Mach number influence was published by Arens and Spiegler in the early 1960's.[19] However, the major formula derived turned out to be too complex for engineering application.

Based on experiments with conical and truncated ideal nozzles, Schilling derived in 1962 a simple expression accounting for the increase of separation pressure ratio p_{sep}/p_a with increasing Mach number,

$$p_{sep}/p_a = k_1\cdot(p_c/p_a)^{k2}, \qquad (7)$$

with $k_1 = 0.582$, and $k_2 = -0.195$ for contoured nozzles, and $k_1 = 0.541$, and $k_2 = -0.136$ for conical nozzles.[17] In 1965, based on Schilling's expression Kalt and Badal chose $k_1 = 2/3$ and $k_2 = -0.2$ for a better agreement with their experimental results.[18]

NASA adopted a correlation similar to the one of Schilling for truncated contoured nozzles as a state of the art indication at the mid 1970's.[31]

Later investigations performed by Schmucker[27] lead NASA to recommend the semi-empirical criteria by Crocco and Probstein which accounts for the property of the boundary layer, the gas and the inviscid Mach number at the onset of separation.[32] The NASA recommendation from 1976 was to use this criteria with an additional margin of 20% from the predicted separation occurrence. An inherit from this time is also the purely empirical criterion proposed by Schmucker:[27]

$$p_{sep}/p_a = (1.88\cdot M - 1)^{-0.64}, \qquad (8)$$

which has similar characteristics as the Crocco and Probstein criterion and is still widely used.

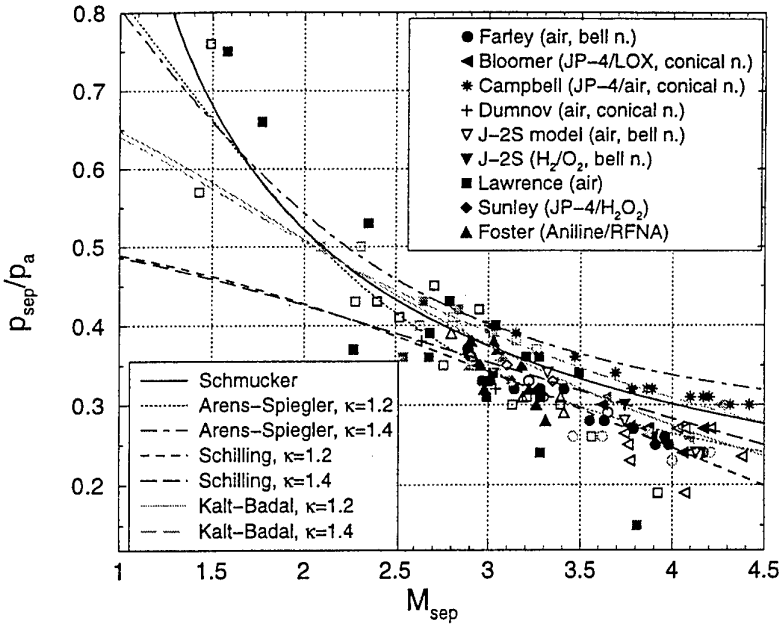


Fig. 7: Comparison of simple separation prediction models for p_{sep}/p_a with experimental results.

By comparing these different criteria with test data a significant scatter of the data points around the criteria is observed, see Figure 7. This enlightens the NASA advice of a 20% margin and also points out the necessity of new and more reliable criteria. One of the major reasons for the rather poor agreement is that all above criteria included the two separate mechanisms involved in the pressure rise of the flow in one single expression. This fact was realised already 1966 by Carriere[33] and 1967 by Lawrence[21] who suggested to establish a criterion where the pressure recovery p_{sep}/p_a is subdivided into two parts, one part for the critical pressure rise, p_{sep}/p_p, over the separation shock and a second for the pressure rise in the recirculation zone, p_p/p_a.

It has been shown by many experiments, that the shock / boundary layer interaction properties are nearly independent of the cause having induced the separation.[7,34] The critical pressure rise over shocks, p_{sep}/p_p, formed under boundary layer separation in front of forward facing steps, or ramps has been extensively studied and several theoretical and purely empirical criteria exist e.g. the one by Panov and Shvets,[35] or the one by Zukoski.[36] As example, Zukoski found the following simple relation to be in good agreement with experimental results, with the inviscid Mach number of the attached flow upstream of the separation point, M_{sep}:

$$p_{sep}/p_p = (1 + 0.5\, M_{sep})^{-1}, \qquad \text{for the Mach number range of } M_{sep} = 1.4 \text{ to } 6. \quad (9)$$

In Ref. 2 it was shown, that the oblique shock angle and the deflection angle of the separated flow can be easily correlated with the inviscid Mach number M_{sep}. This correlation can then be used to model the critical pressure rise, p_{sep}/p_p.

For the pressure recovery in the separated region, p_p/p_a, the situation is very different, because models are lacking. Experimental data indicate that the wall contour downstream the separation point has a significant influence on the pressure increase in this zone.[21] As reported in Ref. 2, it seems that in addition to the wall contour the length of the separated region, the curvature of the wall downstream of the separation and the radial size of the recirculating zone between the wall and the jet are further parameters influencing the pressure rise p_p/p_a. A clear indication of this can be found in Fig. 8. Thus, it is obvious that to be able to

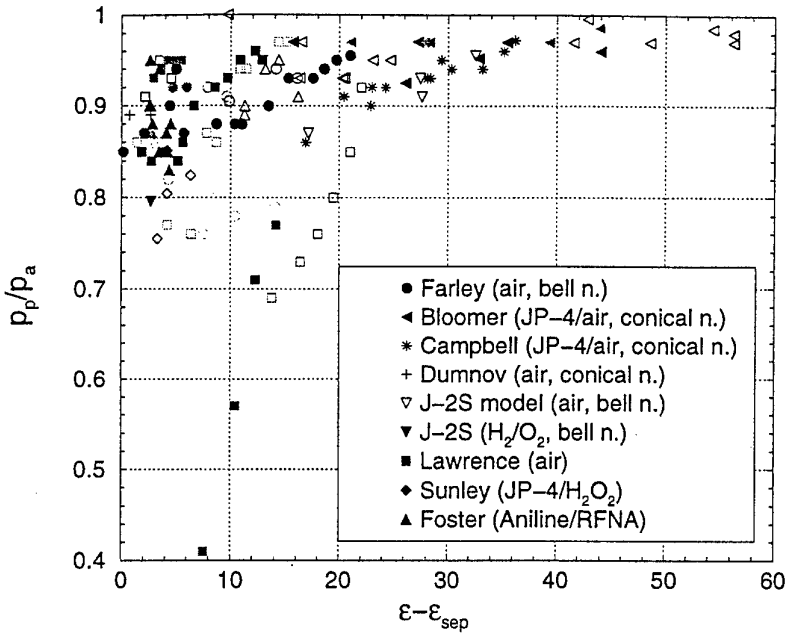


Fig. 8: Experimental results for the pressure rise p_p/p_a as function of separation location.

predict the location of separation successfully, a new separation criterion must be developed where first of all the shock-boundary layer interaction is properly described and secondly a model where the pressure rise in the recirculating zone is included which accounts for downstream conditions and nozzle geometry. The development and validation work of such models is currently ongoing at the different partners of the FSCD group. E.g., Reijasse[7] has recently developed a physical model taking into account the recirculation in the separated region.

The prediction of restricted shock separation has only been addressed in the last years, see Ref. 3, 6. The key point for the prediction of RSS is to predict the location where the transition from FSS to RSS takes place. The driving force for reattachment of the flow is the radial momentum balance in the separated jet induced by the cap-shock pattern. By quantifying this momentum balance the transition point can be determined. Based on this Östlund and Bigert proposed a simple empirical criterion for the prediction of transition from FSS to RSS, showing very good results considering its simplicity.[6]
Frey and Hagemann have developed a more sophisticated and physical model.[3] In this model the FSS shock system is always prevailing before a possible reattachment is defined. Based on numerical flowfield data, the cap shock pattern is re-calculated by a shock-fitting technique. By calculating the momentum balance across the cap shock pattern and the corresponding direction of the jet downstream of the cap shock pattern, the driving force for reattachment is evaluated and the location where the transition takes place is determined. Both models account for the sudden pressure drop of the plateau pressure and the subsequent jump of the separation point when the flow reattaches and the separated region becomes enclosed by supersonic flow. Due to the complexity of the flow downstream of the reattachment point, which is characterised by subsequent compression and expansion waves, no models for this pressure recovery process yet exist. Instead a constant value of the plateau pressure based on test data experience is often used. This value is kept until the RSS is transformed back into FSS and FSS criteria are applicable again. This transformation occurs either when the cap-shock is converted into the Mach disc or when the enclosed separation zone is opened up at the nozzle exit.
Based on numerical simulations of the cap shock pattern with the trapped vortex, Reijasse[7] has proposed a further transition prediction model based on an effective area ratio for the RSS condition, estimated with the

effective nozzle exit area occupied by the re-attached annular jet, and the throat area. Thus, the remaining exit area filled with the recirculating flow of the trapped vortex is ignored in this approach.

3. Side-Loads – Physical Origins and Models for Prediction

Side-loads have been observed either in subscale or full-scale rocket nozzles during transient operations like start-up or shut-down, and during stationary operation with separated flow inside the nozzle. The first important report dealing with side forces was published within the frame of the J-2S testing, Ref. 28.
These forces acting lateral to the main thrust direction are an undesired phenomenon, and may feature as severe design constraint for new rocket engine concepts. Despite of significant effort spent by space industries and research establishments on the side-load research, its analytical prediction in general still lacks of sufficient accuracy to the authors knowledge.



Fig. 9: The three Space Shuttle Main Engines SSME at transient start-up process (Photo NASA).

Side-loads in rocket nozzles are caused by a three-dimensional pressure distribution inside the rocket nozzle, either highly transient or steady state. As example, Fig. 9 shows a time instant during the transient start-up of the Space Shuttle Main Engines, SSME, shortly prior to lift-off. The three-dimensional separation line is clearly visible due to water vapour condensation on the wall of cryogenic cooled nozzle extension.
Potential origins for side-loads generated by asymmetric wall pressure evolution inside the nozzle are:

- tilted separation line,
- pressure pulsation at separation location and in recirculation zone,
- aeroelastic coupling,
- transition in separation pattern, FSS to RSS and vice versa.

Furthermore, pressure pulsation acting from the outside on the nozzle shell, asymmetric hardware, or asymmetric injection conditions may generate lateral forces, which however are not further considered in this discussion.
Several models have been developed based on the different origins. They are briefly discussed in the following.

3.1 Side-loads due to tilted separation line

The assumption of a tilted separation line in pure free shock condition is the basis of several side-load models, e.g. of Pratt and Whitney, Rocketdyne, and Schmucker.[27] The principle of this basic idea is

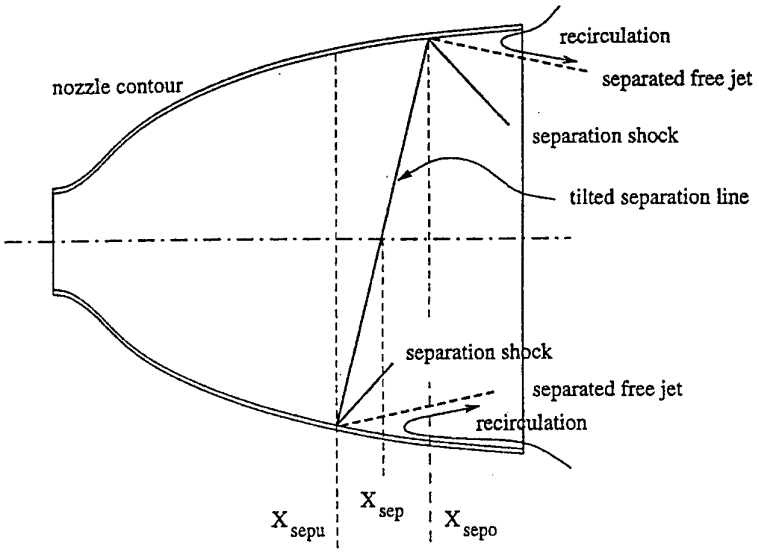


Fig. 10: Principle idea of a tilted separation line.

illustrated in Figure 10. It is reported in the literature, that model applications to specific engine tests, e.g. the Schmucker model to J2 engine test data, showed reasonable agreement. But it should be mentioned, that this specific has been developed by exploiting J2-S data.
Recent comparison of experimental data with the model approach of a tilted separation line have shown, that none of the models correctly predict the side-load behaviour of different rocket nozzles, indicating that this simplified underlying assumption of a tilted separation plane is not fully correct. It seems that the models based on this assumption yield acceptable predictions only for special nozzle families. As soon as one of the models is applied to a nozzle which is very different in shape, the agreement between predicted and measured forces is rather poor. This indicates that the simple underlying assumption of a tilted separation line does not account for the real physics.

3.2 Side-loads due to random pressure pulsation

Random oscillation of the separation line and random pressure pulsation in the separated flow region are the basic idea of the Dumnov side-load model.[37] The method is based on a statistical generalisation of empirical data for the pulsating pressure field at the wall. The empirical data are mainly based on sub-scale cold-gas experiments with separated nozzle flows. For these experiments, only conical and truncated ideal nozzles were used. The application of the Dumnov-model to Russian rocket nozzles, like RD-0120, gave reasonable agreement between measured and predicted side-loads.[37]

3.3 Side-loads due to aeroelastic coupling

It is known that slight variations in wall pressure may cause significant distortion of the contour. This distortion in turn results in a further variation in wall pressure and the system forms a closed loop, which may result in a significant amplification of the initial load. The study of the closed-loop effects of jet separation has not been attacked vigorously due to the complexities involved in generating accurate asymmetric dynamic models of the nozzle-engine support system, the jet boundary layer separation, and interaction at the boundary of the two subsystems. However, a technique for handling these difficult coupling problems has been developed by Pekkari.[38, 39] The model consists of two main parts, the first dealing with the equation of motions of the thrust chamber as aerodynamic loads are applied, and a second part modelling the change of the aerodynamic loads due to the distortion of the wall contour. The wall pressure in the attached region is the nominal vacuum pressure profile with a pressure shift due to the

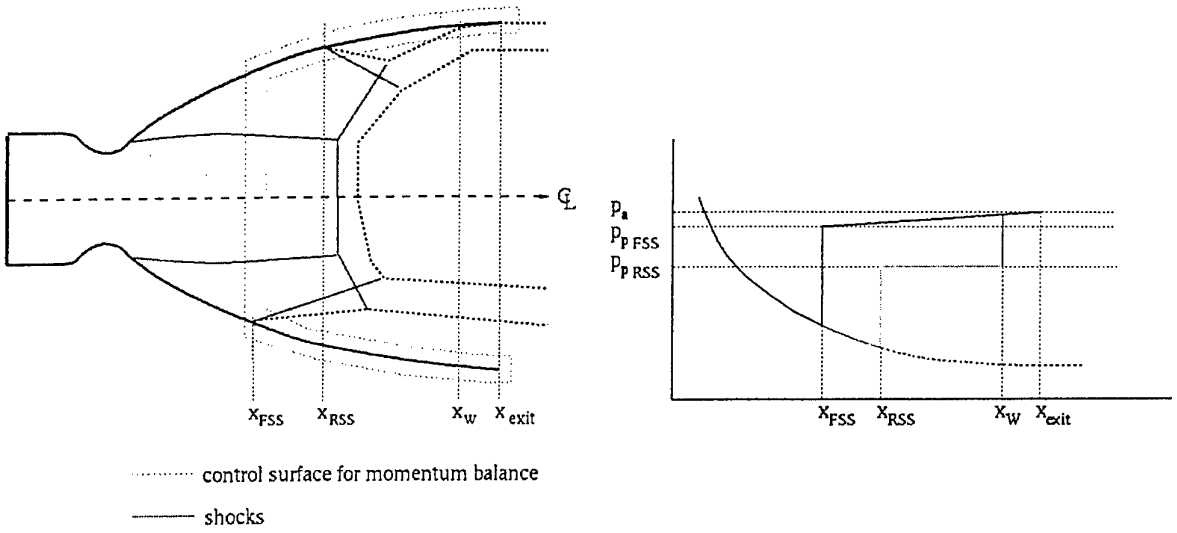


Fig. 12: Asymmetric flowfield inside nozzle at instant of FSS-RSS transition for worst case side-load prediction. Control surface for momentum balance included. Momentum of impinging jet on wall taken into account at x_w.

half of the nozzle features FSS-, while the other half shows already RSS flow condition. For this case, the side-load calculation is purely physically motivated, and comes from a momentum balance across the complete nozzle surface, as illustrated in Fig 12. Comparison of predicted values with maximum measured values in subscale and full-scale experiments revealed an astonishing agreement.

3.5 Influence of further transient phenomena on side-loads

Although steady flow analysis helps in understanding the flow structure at the instant of side-loads maxima, only transient analysis can simulate the actual highly transient phenomenon. A peculiar behaviour that has been detected in the few transient simulations published in the literature is the development and evolution of so-called shocklets in the narrow jet circumventing the centreline vortex in RSS flow condition.[22-25] In particular, the quick displacement of such strong pressure waves along the nozzle wall was indicated as a possible responsible of side-loads, also because of their improbable circumferential symmetry. Indeed, this flow structure is intrinsically weak, as it can easily degenerate towards a strongly 3D structure, because

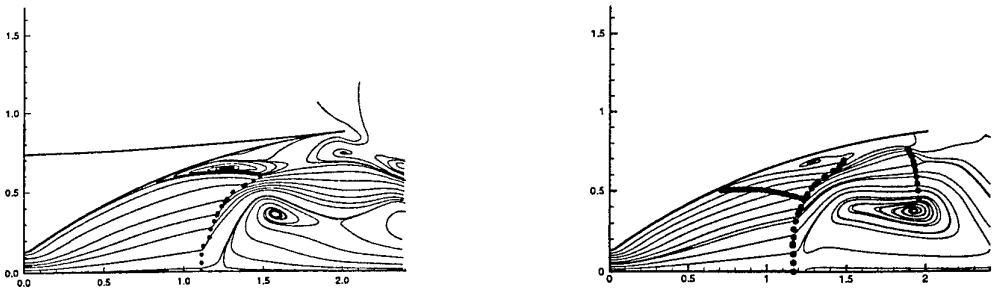


Fig. 13: Transient simulation of nozzle flow, with generation of shocklets in main jet at the wall.

even small non-uniformities in the incoming flow yield unsymmetrical distribution of shocklets and thus of pressure loads. The time-dependent analyses published in Ref. 22-25 show that an unsteady behaviour takes place with shocklets and sometimes stronger shocks that temporarily appear and disappear in the main jet. A typical example of this behaviour is given by the quick variation of the solution at two close times, as shown in Fig. 13.

4. Conclusion

Flow pattern observed in the exhaust plumes of subscale and full-scale rocket nozzles have been discussed, including the classical Mach disk, the apparent regular reflection, and the cap-shock pattern. The latter flow pattern is only observed for special type of rocket nozzles featuring an internal shock emanating out of the nozzle before being reflected at the centreline.

Within various experiments and numerical simulations, two different flow separation phenomena have been observed, the free shock separation and restricted shock separation. It has been shown, that the cap-shock pattern is the driver for the transition from free- to restricted shock separation.

For the classical free shock separation, various simplified prediction models for the pressure rise from wall pressure with attached flow to ambient pressure that are published in literature show qualitative agreement with experimental data. Higher accuracy in quantitative prediction can only be achieved by de-coupling the two different physical phenomena associated with the flow separation, namely the pressure increase due to oblique shocks and the one in the separated recirculation region.

For the transition from free- to restricted shock separation, models have been recently developed. Results obtained with these new models are encouraging.

In the second part of the paper, different origins for side-loads and corresponding prediction models published in the literature are discussed. Potential side-load origins include a tilted separation line, random pressure pulsation in the separating region, an aeroelastic coupling, and a transition in separation pressure from free- to restricted shock separation. Stimulated by recent test results with parabolic nozzles, side-load models for the transition from free- to restricted shock separation and vice versa have recently been developed within the European space community with encouraging accuracy in matching experimental results.

No special emphasis was given in this paper to numerical methods applied to nozzle flowfield prediction under separated flow condition, although these tools are meanwhile frequently used in the space community. Obtained results show in general a good qualitative and quantitative agreement with experimental data. In addition to the high confidence level achieved for separation prediction, these simulations give a most valuable insight into the physical phenomena involved inside the nozzle.

5. Nomenclature

5.1 Abbreviations

FFA	The Aeronautical Research Institute of Sweden
FSCD	Flow Separation Control Device
FSS	Free Shock Separation
ONERA	Organisation Nationales des Etudes et Recherches Aérospatiales
RSS	Restricted Shock Separation

M	Mach number
p	pressure
u, v, w	velocity components
x, y, z	co-ordinates

ε	area ratio A_{exit}/A_{throat}
μ	viscosity
τ	wall shear stress

5.2 Sub- and Superscripts

a	ambient
e	exit
p	plateau
sep	separation
w	wall

6. Literature

[1] Moelder, A., Gluamhussein, A., Timofeev, E., and Voinovich, P.,'' Focusing of Conical Shocks at the Centreline of Symmetry'', Paper 5601, *Proceedings of the 21st International Symposium on Shock Waves*, Great Keppel Island, Australia, July 1997

[2] Frey, M. and Hagemann, G., ''Status of Flow Separation Prediction in Rocket Nozzles'', AIAA 98-3619, 1998

[3] Frey, M. and Hagemann, G., ''Flow Separation and Side-Loads in Rocket Nozzles'', AIAA 99-2815, 1999

[4] Terhardt, M., Hagemann, G., and Frey, M., ''Flow Separation and Side-Load Behaviour of the Vulcain Engine'', AIAA 99-2762, 1999

[5] Mattsson, J., Högman, U., and Torngren, L., ''A Sub-Scale Test Programme on Investigation of Flow Separation and Side-Loads in Rocket Nozzles'', *Proceedings of the 3rd European Symposium on Aerothermodynamics of Space Vehicles*, ESA-ESTEC, Netherlands, November 24-26, 1998

[6] Östlund J., Bigert M., ''A Subscale Investigation on Side-Loads in Sea Level Rocket Nozzles", AIAA 99-2759, June 1999

[7] Reijasse, P.,Servel, P., and Hallard, R., ''Synthesis of the 1998-1999 ONERA Works in the FSCD Working Group'', ONERA RTS 49/4361 DAFE/Y, December 1999

[8] Frey, M., Stark, R., and Ciezki, H., ''Subscale Nozzle Testing at the P6.2 Test Stand'', AIAA paper, to be published at the 36th Joint Propulsion Conference, July 2000

[9] Hagemann, G., Immich. H., Dumnov, G., and Nguyen, Th., ''Advanced Rocket Nozzles'', *Journal of Power and Propulsion*, Vol. 14, No. 5, September – October 1998

[10] Prandtl, L., ''Ueber Fluessigkeitsbewegung bei sehr kleiner Reibung'' (On Fluid Movement at Low Friction, in German), International Mathematical Congress, Heidelberg, 1904

[11] Prandtl, L., ''Fuehrer durch die Stroemungslehre'' (Text Book on Fluid Dynamics, in German), Friedrich Vieweg & Son, Braunschweig, 1960

[12] Schlichting, H., and Gersten, K., ''Boundary Layer Theory'', Springer, Berlin Heidelberg, 1997

[13] Foster, C., and Cowles, F., ''Experimental Study of Gas Flow Separation in Overexpanded Exhaust Nozzles for Rocket Motors'', JPL Progress Report 4-103, May 1949

[14] Green, L. ''Flow Separation in Rocket Nozzles, *ARS Journal*, Vol. 23, No. 1, January – February 1953

[15] Summerfield, M., Foster, C., and Swan, W., ''Flow Separation in Overexpanded Supersonic Exhaust Nozzles'', *Jet Propulsion*, Vol. 24, September-October 1954

[16] Campbell, C. and Farley, J., ''Performance of Several Conical Convergent-Divergent Rocket Type Exhaust Nozzles'', NASA TN D-467, September 1960

[17] Schilling T. W., ''Flow Separation in Rocket Nozzle'', M.S. Thesis, University of Buffalo, June 1962

[18] Kalt S., and Badal D., ''Conical Rocket Nozzle Performance Under Flow Separated Condition'', *Journal of Spacecraft and Rockets*, Vol. 2, No. 3, May 1965

[19] Arens, M., and Spiegler, E, Shock-Induced Boundary Layer Separation in Overexpanded Conical Exhaust Nozzles'', *AIAA Journal*, Vol. 1, No. 3, March 1963

[20] Sunley, H., and Ferriman, D., ''Jet Separation in Conical Nozzles'', *Journal of the Royal Aeronautical Society*, Vol. 68, December 1964

[21] Lawrence, R.A., ''Symmetrical and Unsymmetrical Separation in Supersonic Nozzles'', Research report 67-1, Southern Methodist University, April 1967

[22] Chen, C., Chakravarchy, S., and Hung, C., "Numerical Investigation of Separated Nozzle Flows", *AIAA Journal*, Vol. 32, No. 9, September 1994
[23] Nasuti, F., and Onofri, M., "Viscous and Inviscid Vortex Generation During Nozzle Flow Transients", AIAA 96-0076, June 1996
[24] Nasuti, F., and Onofri, M., "Viscous and Inviscid Vortex Generation During Start-Up of Rocket Nozzles", *AIAA Journal*, Vol. 36, No. 5, May 1998
[25] Onofri, F., and Nasuti, M., "The Physical Origin of Side-Loads in Rocket Nozzles", AIAA 99-2587, July 1999
[26] Kistler, M., "Fluctuating Wall Pressure under a Separated Supersonic Flow", *Journal of the Acoustical Society of America*, Vol. 36, No. 3, March 1964
[27] Schmucker, R., "Flow Processes in Overexpanding Nozzles of Chemical Rocket Engines" (published in German), Report TB-7,-10,-14, Technical University Munich, 1973
[28] Nave, L. H., and Coffey, G. A., "Sea-Level Side-Loads in High Area Ratio Rocket Engines", AIAA 73-1284, 1973
[29] Gribben, B., Cantariti, F., Badcock, K., and Richards, B., "Numerical Study of an Underexpanded Jet", *Proceedings of the 3rd European Symposium on Aerothermodynamics of Space Vehicles*, ESA-ESTEC, Netherlands, November 24-26, 1998
[30] Welsh, F., "Electron Beam Fluorescence Measurements of Shock Reflection Hysteresis in an Underexpanded Supersonic Jet", *Proceedings of the 21st International Symposium on Shock Waves*, Great Keppel Island, Australia, July 1997
[31] NASA Space Vehicle Design Criteria (Chemical Propulsion), "Liquid Rocket Engine Nozzles", SP-8120, July 1976
[32] Crocco, L., and Probstein, R., "The Peak Pressure Rise Across an Oblique Shock Emerging from a Turbulent Boundary Layer Over a Plane Surface", Princeton University (Princeton. NJ), March 1964
[33] Carriere, P., " Remarques sur les Méthodes de Calcul des Effets de la Viscosité dans les Tuyères Propulsives" (Comments on computational methods of viscous effects in propulsion nozzles, in French), DGRR/WGLR Symposium, Bad Godesberg, also published as ONERA TP 408, October 1966
[34] Delery, J., and Marvin. J.G., "Shock-Wave Boundary Layer Interactions", AGARD No. 280, February 1986
[35] Panov, Yu A., and Shvets, A.I., "Separation of Turbulent Boundary Layer in Supersonic Flow", Prikladnaya meklanika 1, 1966
[36] Zukoski, E.E., "Turbulent Boundary Layer Separation in Front of a Forward Facing Step", *AIAA Journal*, Vol. 5, No. 1, January 1967
[37] Dumnov, G.E., "Unsteady Side-Loads acting on the Nozzle with Developed Separation Zone", AIAA 96-3220, 1996
[38] Pekkari, L.-O., "Aeroelastic Stability of Supersonic Nozzles with Separated Flow", AIAA 93-2588, June 1993
[39] Pekkari, L.-O., "Aeroelastic Analysis of Side-Loads in Supersonic Nozzles with Separated Flow", AIAA 94-3377, June 1994

THRUST NOZZLE PROFILING

G.Dumnov, N.Ponomarev, I.Eliseev
Keldysh Research Center, Moscow, Russia

M.Terhardt
DASA, Ottobrunn, Germany

Abstract

Three methods (of variational exit characteristic, of uniform exit characteristic, and of direct optimization) user for profiling rocket nozzles are compared with each other in nozzle delivered performance of an Ariane-5-class launcher 2nd stage sustainer oxygen/hydrogen rocket engine. Three versions of restrictions imposed on nozzle contours (specifying the nozzle exit point, providing attached nozzle flows, and restricting side loads acting on nozzle during engine startup) are under consideration. Besides, three methods (ideal gas with integral boundary layer, ideal gas with differential boundary layer, and TDK) are used for predicting nozzle performance. The results obtained show that all the three performance prediction methods produce nearly the same performance rating of the nozzles profiled with the three contour design methods, where the direct optimization method is best if the nozzle exit point is not fixed.

Introduction

Varying the supersonic nozzle contour, as well as the nozzle envelope (i.e., length and expansion ratio), one can highly affect the engine specific impulse, both in vacuum and in the ground conditions. For definiteness and correctness, we split the nozzle contour design procedure into the two procedures: designing the nozzle contour shape as a curve connecting the nozzle throat and the specified nozzle contour exit point and selecting the nozzle length and expansion ratio. Both the designing parts are important and coupled with one another. So, varying the nozzle contour shape and the nozzle length, one can affect the vacuum specific impulse losses due to divergence, boundary layer (friction with regeneration), and nozzle mass (for the so-called effective vacuum specific impulse taking the nozzle mass into account through the specific-impulse/payload-mass equivalent for the launch vehicle stage under consideration), whereas, varying the nozzle expansion ratio, one can affect, besides the abovementioned specific impulse losses, the ideal (i.e., thermodynamic) vacuum specific impulse and the term scaling the delivered vacuum specific impulse to the delivered ground (or altitude) specific impulse (if the engine operates under non-zero ambient pressures).

It is evident that the optimum nozzle contour providing the maximum payload gain (in some cases, e.g., for upper vehicle stages, this target can be replaced by the maximum effective delivered vacuum specific impulse) and satisfying the imposed

restrictions (e.g., on the nozzle length, and/or requirements of providing a fully attached nozzle flow during engine operation, etc.) depends on both the method used for designing the one and the method used for predicting the delivered (maybe effective) vacuum specific impulse governing the target function behaviour when the nozzle contour is varied. The following three methods are used for contouring nozzles at present: the uniform exit characteristic method [1,2], the variational exit characteristic method [3-5], and the direct optimization method [6,7]. All of them are under consideration in this paper.

As for the methods used in this paper for predicting the delivered vacuum specific impulse, they are: two methods using the same code [8] for calculating the inviscid supersonic nozzle flow core as an axisymmetric ideal gas flow and approach [9] for calculating the specific impulse loss due to finite rate kinetics and differing from one another by the boundary layer calculation approach: one of them, [10], calculates the boundary layer with V.S.Avduevsky integral method (through solving two ordinary differential equations) and the other, [11], does that with a differential method (through solving the boundary layer equations in partial derivatives); the third method is widely known code TDK [12].

Nozzle contour design methods

The first method (VC) used for the supersonic nozzle contour design is the variational method [3-5]. To obtain contour with this method, a fan of expansion waves (characteristics of the 2nd family) is calculated around an arc specifying the initial part of the supersonic nozzle contour and a variational exit characteristic of the 1st family, outcoming from this expansion fan and coming to the specified nozzle contour exit point with providing the minimum vacuum specific impulse loss due to divergence, is constructed. Then the Goursat problem is solved with the method of characteristics between the fan last characteristic and the variational exit characteristic, so the supersonic nozzle contour is obtained.

The second method (UC) used for the supersonic nozzle contour design is the classic method of characteristics with a uniform exit characteristic of the 1st family, see [1,2]. To obtain contour with this method, a fan of expansion waves (characteristics of the 2nd family) is calculated around an arc specifying the initial part of the supersonic nozzle contour, so the specified exit Mach number must be attained at the last fan characteristic at the nozzle axis. Then the uniform exit characteristic of the 1st family with this Mach number is emanated from this axial point and the Goursat problem is solved with the method of characteristics between the last characteristic of the fan and the uniform exit characteristic, so the supersonic nozzle contour is obtained. If the nozzle contour exit point is specified, the exit characteristic Mach number is varied until the designed contour passes through this point.

The third nozzle contour design method (DO) is the direct optimization method [6,7]. According to this method, the optimum supersonic nozzle contour is searched among analytically specified curves having free parameters governing the contour. The optimization is reduced to searching the optimum values of these N parameters, providing the needed extremum of the target function (e.g., the minimum, if the target function is the total specific impulse loss, or the maximum, if the target function is the delivered specific impulse). As the obtained extremum is not

global, i.e., only in the chosen N-parametric family of analytical curves, the problem can be widened by searching the optimum family of curves, see [7]. In this paper, basing on our experience, we have chosen the 2-parametrical family of 2-order curves. If the nozzle contour exit point, as well as the arc defining the initial (just downstream of the nozzle throat) part of the contour is specified, then this family has two free parameters for optimization, for which it is convenient to use the initial (i.e., at the end point of the arc) and exit (i.e., at the nozzle exit) contour angles.

Nozzle performance prediction methods

The first two methods (M1 and M2) of predicting the delivered vacuum specific impulse uses the same code [8] for calculating the inviscid supersonic nozzle flow core, which is considered as an axisymmetric ideal gas flow with a constant nozzle-average adiabatic exponent. This code provides the core flow parameters needed for the boundary layer calculation and determination of the vacuum specific impulse loss due to flow divergence, ξ_d. These methods also use the same approach [9] for calculating the vacuum specific impulse loss due to finite rate kinetics, ξ_{kin}, and the same code [9] for calculating the ideal (thermodynamic) vacuum specific impulse, I_{vi}. They differ from one another by the boundary layer calculation approach. The first of them, M1, calculates the boundary layer with a differential method [11] through solving the boundary layer equations written in partial derivatives. To close these equations, a well-known Cebeci-Smith algebraic model of turbulence with a small correction of model numerical constants is used. The second, M2 method calculates the boundary layer with the modified V.S.Avduevsky integral method [10] through solving a set of two ordinary differential equations written for the boundary layer momentum loss thickness and for the boundary layer energy loss thickness. Both M1 and M2 methods use various semi-empirical constants providing satisfactory agreements of predictions, performed with these methods, with available model and full-scale experimental data. As a result of the boundary layer calculation, both the methods predict the vacuum specific impulse loss due to boundary layer, ξ_{bl}, being the difference between the loss due to friction and the vacuum specific impulse addition due to heating the propellant component in the nozzle cooling jacket (i.e., due to the heat regeneration).

The third method is widely known code TDK [12]. It consists of several modules computing all the specific impulse losses related to the nozzle. The core flow is computed by a method of characteristics with finite rate kinetics. The boundary layer is calculated through finite differences with taking finite rate kinetics into account and using a Cebeci-Smith eddy viscosity turbulence model.

In all three methods (M1, M2, and TDK) the solutions of the core flow and the boundary layer are connected with one another through iterations taking the boundary layer displacement thickness into account.

As for satisfying the requirements of fully attached nozzle flow in the nominal engine operating mode, we have used the pressure critical rise approximation of Refs. [13,14] without taking the nozzle firing wall temperature and roughness into account, which produce the results being close to the ones obtained with approximation [15].

Initial data for optimization

The calculations have been performed for the following initial data. We have considered an oxygen/hydrogen rocket engine having throat radius of R_{th}=120 mm and operating under the combustion chamber pressure of P_{cc}=100 bar with the combustion chamber propellant mixture ratio of K_m=6.0. The nozzle wall firing surface temperature and the nozzle wall firing surface roughness were specified equal to 800 K and 30 μm, accordingly, over the whole nozzle, including the combustion chamber, in all the calculations. The nozzles were assumed fully regeneratively cooled. To estimate the nozzle mass and the effective vacuum specific impulse taking the nozzle mass change into account, the specific (i.e., per a unit surface area) nozzle divergent wall surface mass was specified equal to 20 kg/m^2, and the nozzle mass equivalent of the vacuum specific impulse gain was specified equal to 150 kg/s. We have assumed that this engine is a sustainer engine of the second stage of an Ariane-5 - class launch vehicle (with initial parallel operation of the first and second stages), so it begins to operate in the nominal operating mode at the sea (ground) level and continues to operate up to a very high altitude.

When optimizing the supersonic nozzle contour we have specified the initial contour part (just downstream of the nozzle throat) in all the cases as the arc of radius $R_{d\,th} = R_{th}$.

Optimization with a specified nozzle exit point

This optimization has been performed for the nozzles having specified exit point X_e/R_{th}=27, Y_e/R_{th}=10 in order to investigate influence of nozzle profiling methods on vacuume specific impulse in this case. Contour N1 was profiled with the VC method. Contour N2 was profiled with the UC method and Contour N3 was profiled with the DO method.

Comparison of these nozzle contours shows that contour No.1 is more convex than contour No.2. Calculations performed in a more wide range of X_e,Y_e had shown that all nozzle contours designed with the VC method had this feature in contrast to the contours designed with the UC method. The contour designed with DO method lies between these two nozzles.

The engine thrust performances provided by these contours are presented in Table 1. As these contours have the same exit point, the vacuum specific impulse losses are presented in this table only. They are the loss due to flow divergence, ξ_d, the loss due to boundary layer, ξ_{bl}, the total loss $\xi_\Sigma = \xi_d + \xi_{bl}$ (the losses of the other kinds are the same in this case), and the total losses difference with respect to contour No.1. One can see that contour No.1 (VC) provides the minimum ξ_d , but that is compensated by increased ξ_{bl} , so the total loss is close to the one provided by contour No.2 (UC). Contour No.3 (DO) provides the minimum ξ_Σ . These trends are produced by all the methods (M1, M2, and TDK). As the differences between ξ_Σ provided by the obtained contours are too small, we can conclude that all the nozzle contour design methods considered here provide practically the same engine thrust performance in the case under consideration.

If additionally to take the nozzle mass into account, this does not change the final results, as these contours are close to each other, so the conclusion stated above remains true.

The same conclusions were done in Ref.[7] on the basis of the calculations performed there.

Optimization providing attached flows

If we consider a case of designing the nozzle supersonic contour for an engine operating beginning from the ground (sea) level, then we have to impose the restriction that the contour must provide fully attached nozzle flow in the engine nominal operating condition. Otherwise, the nozzle will suffer substantial unsteady side loads at the sea level and low altitudes, so the engine can fail, or, in any case, its reliability decreases substantially.

The optimum contours of the specified relative length X_e/D_e=1.4, designed with the three methods under the above-mentioned restriction have been built: VC contour No.4, UC contour No.5, DO contour No.6. The DO contour has the highest area ratio, whereas the UC contour has the lowest area ratio. That is due to optimizing the DO contour exit angle, so lowering this angle allows of increasing the available DO contour area ratio providing the specified nozzle exit wall pressure needed for an attached nozzle flow and, by that, increasing the ideal vacuum specific impulse. In contrast to that, the exit angles of the UC and VC contours can't be freely changed, so, as the UC contours have the highest exit angles, the specified exit wall pressure causes the lowest maximum available area ratio of the UC contours in comparison with the other contours, whereas the VC contours, having somewhat lower (than the UC contours) exit angles governed by minimizing the specific impulse loss due to divergence, accordingly have somewhat higher (than the UC contours) maximum available area ratio, so provide somewhat higher vacuum specific impulse.

The engine thrust performances provided by these contours are presented in Table 2. As the nozzle area ratio has been optimized in this optimization, the target function of this optimization was the delivered vacuum specific impulse, I_v , and the vacuum specific impulse kinetic loss depending on the nozzle area ratio was taken into account additionally to the abovementioned losses. Correspondingly, the delivered and ideal vacuum specific impulses, as well as the kinetic loss, are included in Table 2. One can see that the DO contour provides the maximum delivered vacuum specific impulse, whereas the UC contour produces the lowest delivered vacuum specific impulse.

The differences between the contours in the delivered vacuum specific impulse slightly depend on the method (M1, or M2, or TDK) used for predicting the delivered vacuum specific impulse.

As in real cases the nozzle contour optimization changes the nozzle mass, so influencing the vehicle stage mass, this effect was taken into account through adding the vacuum specific impulse loss due to changing the nozzle supersonic wall mass, ξ_m , to the abovementioned specific impulse losses and considering the effective vacuum specific impulse, I_{vm} , obtained by that, instead of the delivered vacuum specific impulse. The corresponding values of ξ_m and I_{vm} are presented in Table 2 too. One can see that the DO contour provides the maximum effective vacuum specific impulse,

whereas the UC contour produces the lowest effective vacuum specific impulse but the difference in effective specific impulse between them is decreased.

Flow patterns in nozzles No. 4, 5, and 6 are presented accordingly in Fig. 1, 2, and 3 in the form of Mach number isolines. One can see that the flow patterns in the VC (No.4) and UC (No.5) nozzles are nearly similar, whereas the DO (No.6) nozzle flow pattern has a pronounced shock wave emanating from the region of joining the throat contour arc with the further contour part specified by the analytical curve.

Fixing the absolute nozzle length at $X_e/R_{th}=18.12$ instead of fixing the relative nozzle length at $X_e/D_e=1.4$, we obtain the results presented in Table 3. Here, optimum contours No. 7, 8, and 9 have been obtained with the VC, UC, and DO methods, accordingly. As in the previous case, the DO contour provides the highest area ratio and the highest delivered and effective vacuum specific impulses, whereas the UC contour produces the lowest ones. Accordingly, the DO contour has the lowest relative length ($X_e/D_e=1.13$), whereas the UC contour has the highest one ($X_e/D_e=1.39$), resulting in lower differences between the delivered and effective vacuum specific impulses, as ξ_Σ increases when X_e/D_e decreases.

Optimization providing restricted side loads

Using relatively high area ratio DO contours providing maximum vacuum specific impulse and fully attached nozzle flows in nominal operating modes under the ground conditions causes substantial unsteady side loads acting on nozzles during engine startup and shutdown under the ground conditions. Appearance of such side loads can be explained only through asymmetrical nozzle flow separation from the nozzle walls during engine startup or shutdown. This fact was first published in Ref.[16]. A high level of side loads was also observed during Vulcain engine startup and shutdown [17,18] although this engine nozzle hadn't the maximum available area ratio. Relationships allowing of estimating level of these side loads in the nozzles of such type were proposed in Ref.[15].

Unsteady side loads acting on an engine during long-duration operation with a developed separation zone had been revealed in Russia in firing tests of engine RD0120 (Ref.[13]). The nozzle of this engine had been contoured with the UC method. An experimental investigation of side loads acting on nozzles contoured with the UC method had been conducted in Refs. [13, 14]. It was shown that turbulent gas flow pulsations are the main source of side loads appearance. In the case of nozzle flow separation the turbulent pulsation is substantially amplified by the separation flow shock. Even in the case of an attached nozzle flow the unsteady side loads are non-zero and increase when the combustion chamber pressure rises, that once more validates that the turbulent pulsation is the main cause of side loads appearance. In Refs. [13, 14] it was shown that from the mathematical viewpoint the unsteady side loads are stationary wide-band random processes. Physical and mathematical model of side loads appearance had been developed in these works on the basis of model experiments. A comparison of the predictions performed with this model with the RD0120 engine test data had shown their good agreement.

If to suggest that the side loads appearing in nozzles contoured with the UC and DO methods are of the same nature, then the maximum side loads would be observed in the RD0120 engine, as this engine nozzle had the highest area ratio,

therefore highest exit diameter and highest side area on which the side loads act, comparing with engines J2-S, SSME, Vulcain. But a comparison of the side loads measured in firing tests of engines RD0120 [13] and Vulcain [17,18] had shown that the RD0120 engine undergoes the side loads which in several times less than the side loads acting on the Vulcain engine nozzle. That indicates different natures of the side loads acting on nozzles contoured with the UC and DO methods. As long as the nature of the side loads appearing in nozzles contoured with the UC method had been determined in Refs. [13, 14], the nature of the side loads appearing in nozzles contoured with the DO methods is investigated at present.

Using computational methods, authors of Refs. [18,19] have shown that separated nozzle flows of an untraditional type appear during startup and shutdown of Vulcain engine having a nozzle contoured with a DO method. These separated flows feature by a reattachment of the separated flow to the nozzle wall with forming a bubble-shaped separation zone. As the combustion chamber pressure rises, this bubble moves to the nozzle exit. As a result, side loads in nozzles of this kind have two peaks: the first one corresponds to appearance of the bubble-shaped separation zone and the second one appears during breakdown of this bubble at the nozzle exit. As at these moments the separated zone changes asymmetrically, the separation line slant has scale of the "bubble" length instead of the boundary layer thickness in the case of nozzles contoured with the UC method. Naturally, not all nozzles contoured with a DO method produce this feature of separated nozzle flows, but, apparently, only those, which have low exit angles, as a result of nozzle contour optimization under the specified nozzle exit wall pressure.

Let's consider an effect of the restriction imposed on the side loads level during engine startup and shutdown in the case of contouring the nozzle with the DO method. Let's specify that the side load mustn't exceed 30...35 kN and estimate the side loads with method [15].

If to specify X_e/D_e=1.4, then after optimization we obtain contour No.10 whose performance is presented in Table 4. Comparing this contour performance with the one of contour No.6, presented in Table 2, one can see that the restriction imposed on the side loads has reduced the nozzle area ratio, the delivered vacuum specific impulse by 28.1 m/s, and the effective vacuum specific impulse by 23.2 m/s.

If to fix the absolute nozzle length X_e/R_{th}=18.12 and impose the same restriction on the side loads, then, using the DO method, we obtain contour No.11 presented in Table 4. Comparing with DO contour No.9 presented in Table 3, contour No.11 produces the less by 14.4 m/s delivered vacuum specific impulse and the less by 13 m/s effective vacuum specific impulse.

Thus, the restriction imposed on the side loads reduces vacuum specific impulse gain over the nozzles contoured with the VC and UC methods. So, the delivered vacuum specific impulse gain over the UC contour has decreased to 23.5 m/s and the effective vacuum specific impulse gain has decreased to 22.6 m/s, the corresponding gains over the VC contour have decreased to 12.7 m/s and 11.8 m/s, accordingly. At X_e/R_{th}=18.12 the gains over the UC contour have decreased to 18.6 m/s and 17.9 m/s, accordingly, and over the VC contour - to 6.6 m/s and 6.4 m/s, accordingly.

Altitude performance of the optimized nozzles

Vacuum performance of the optimized nozzles have been considered and presented above. But as the engine under consideration must operate in a wide altitude range beginning from the sea (ground) level, its altitude performance is important.

Effects of the vehicle flight altitude and the nozzle contour choice (of contours No. 4 (VC), 5 (UC), and 6 (DO)) on the delivered altitude specific impulse are shown in Fig.4. One can see that the nozzle with contour No.6 provides the gain of about 50 m/s in the delivered vacuum specific impulse over the nozzle with contour No.5, whereas the nozzle with contour No.5 provides the gain of about 500 m/s in the delivered ground specific impulse over the nozle with contour No.5. The altitude at which these contours provide the same delivered altitude specific impulse is equal to about 17 km. Table 5 presents for contours No. 4, 5, 6, and 10 the delivered ground specific impulse, I_H, the specific impulse ground loss, ξ_H, and the altitude, H, at which the contour under consideration provides the same delivered altitude specific impulse, as DO contour No.6.

These characteristics for contours No. 7 (VC), 8 (UC), 9 and 11 (DO) designed to the specified absolute nozzle length are presented in Fig.5 and in Table 6. One can see that contour No.9 provides the gain of about 30 m/s in the delivered vacuum specific impulse over contour No.8, whereas contour No.8 provides the gain of about 460 m/s in the delivered ground specific impulse over contour No.9. The altitude at which these contours provide the same delivered altitude specific impulse is equal to about 20 km.

From Tables 5 and 6 one can see that for about half of the ascent trajectory the nozzles contoured with the UC and VC methods gain in the delivered altitude specific impulse over the nozzle contoured with the DO method. Although the effect of specific impulse gain at this trajectory part on payload mass gain for the engine under consideration is in several times less than the one at the upper trajectory part, nevertheless, that decreases the payload mass gain provided by the DO nozzle contour. More precisely the payload mass gain can be estimated with ballistic calculations only.

The ballistic calculations have been performed for the Ariane-5 - class launch vehicle with the engine under consideration instead of Vulcain engine and the target orbit of 200 km altitude and 28.5° inclination. The calculation have shown that

- for the VC and DO contour nozzles of the X_e/D_e=1.4 relative length the payload mass gain over the UC contour nozzle reaches 1...3 % (see Table 7);
- for the VC and DO contour nozzles of the X_e/R_{th}=18.12 length the payload mass gain over the UC contour nozzle reaches 1...2 % (see Table 8);

From the results presented in Tables 7 and 8 one can see that the DO contour nozzles, in spite of their substantial disadvantages in the delivered ground specific impulse, provide the maximum payload mass gain.

Conclusion

The performed computational investigations have shown that the optimal contours designed with the three nozzle contour design methods under consideration and having the same exit point provide practically the same vacuum specific impulse.

The performed comparison of the three nozzle contour design methods under consideration, being applied to contouring nozzles of a launch vehicle second stage engine operating from the sea (ground) level to a high altitude has shown that

- the maximum vacuum specific impulse of the engine having a nozzle of the X_e/D_e=1.4 relative length is provided by a nozzle contoured with the DO method, at that the maximum vacuum specific impulse gain over the nozzle contoured by the UC method is equal to 52.4 m/s, and the gain is equal to 23.5 m/s if the additional restriction is imposed on the admitted side load level ($F_{SL} \leq 30$ kN);
- if the nozzle length is fixed (X_e/R_{th}=18.12), the maximum vacuum specific impulse gain provided by the DO method nozzle over the UC method nozzle is equal to about 33 m/s, and, if the admitted side load is restricted, the gain is equal to 18.6 m/s;
- although the ground specific impulse provided by the DO method is substantially less than the one provided by the UC method contour, the ballistic calculations performed for an Ariane-5 – class launch vehicle have shown that using the X_e/D_e=1.4 length nozzle contoured by the DO method provides the payload gain of about 3% over the UC method nozzle. If the side load mustn't exceed F_{SL}=30 kN, than the payload gain decreases down to 1.9 %;
- the VC method contour provides the payload gain of about 0.9 % over the UC method contour.

References

1. Mel'nikov D.A. Contouring Round Supersonic Nozzles of Jet Propulsions. Keldysh Research Center, Technical Report, 1955 (in Russian).

2. Mel'nikov D.A., Pirumov U.G., and Sergienko A.A. Nozzles of Jet Propulsions. In: Aeromechanics and Gas Dynamics, M., "Nauka", 1976 (in Russian).

3. Guderley K.G., Hantsch E. Beste Formen fur achsensymmetrische Ubershallschubdusen. – Z. Fliegwiss., v.3, No.9, 1955 (in German).

4. Shmyglevsky Yu.D., Some Variational Problems of Gas Dynamics of Axisymmetric Supersonic Flows. Prikladnaya Matematika i Mechanika, v.21, No.2, 1957 (in Russian).

5. Rao G.V.R. Exhaust Nozzle Contour for Optimum Thrust. Jet Propulsion, v.28, No.6, 1958.

6. Allman J.G., and Hoffman J.D. Design of Maximum Thrust Nozzle Contours by Direct Optimization Methods. AIAA Paper 78-1048.

7. Ponomarev N.B. Direct Optimization of Rocket Engine Nozzle Contours. In: " Space-Rocket Technique: Rocket Engines and Power Plants", Keldysh Research Center, issue 2 (135), 1992 (in Russian).

8. Ponomarev N.B. Program Package for Computation of Two-Dimensional Ideal Gas Flow in Nozzles - PEGAS. State Fund of Algorithms and Programs, No. S00053, 1985 (in Russian).

9. Alemasov V.E., Dregalin A.F., Tishin A.P., Hudyakov V.A. Thermodynamical and Thermophysical Properties of Combustion Products. Edited by V.P.Glushko, M., "Izd. AN SSSR", 1971 (in Russian).

10. Kuz'mina L.F., Mel'nikov D.A., and Nikulin G.Z. Specific Impulse Loss due to Friction in Nozzles. In: "Space-Rocket Technique: Rocket Engines and Power Plants", Keldysh Research Center, issue 2 (135), 1992 (in Russian).

11. Voinov A.L. and Mel'nikov D.A. Performance of Rocket Engine Nozzles with Slot Injection. AIAA Paper 96-3218.

12. Nickerson G.R., Berker D.R., Coats D.E., and Dunn S.S. Two-Dimensional Kinetics (TDK) Nozzle Performance Computer Program, Users Manual. Software and Engineering Associates, Inc., March 1993.

13. Dumnov G.E. Unsteady Pulsating Transversal Loads on Rocket Engine Nozzles Operating in Off-Design Exhaust Flow Regimes. In: "Space-Rocket Technique:

Rocket Engines and Power Plants", Keldysh Research Center, issue 2 (135), 1992 (in Russian).

14. Dumnov G.E. Unsteady Side Loads Acting on the Nozzle with Developed Separation Zone. AIAA Paper 96-3220.

15. Schmucker R.H., Braitinger M.E. Ein vereinfachtes verfahren zur abschatzung der leistungsgrenzen von triebwerken fur kernstufen parallelgestufter raketen und einstufige trager. Zeitschrift fur Flugwissenschaften und Weltraumforschung, v.13, No. 3, 1989.

16. Nave L.H., and Coffey G.A. Sea Level Side Loads in High-Area-Ratio Rocket Engines. AIAA Paper 73-1284.

17. Pekkari L.-O. Aeroelastic Analysis of Side Load in Supersonic Nozzles with Separated Flow. AIAA Paper 94-3377.

18. Terhardt M., Hagemann G. Flow Separation and Side-Load Behavior of the Vulcain Engine. AIAA Paper 99-2762.

19. Hagemann G., and Frey M. Status of Flow Separation Prediction in Rocket Nozzles. AIAA Paper 98-3619.

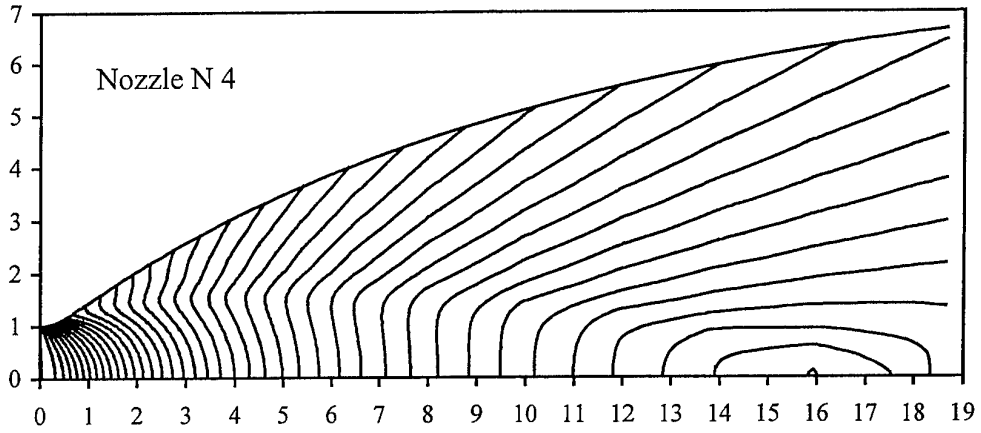


Fig.1. Mach level lines for nozzle N 4(VC)

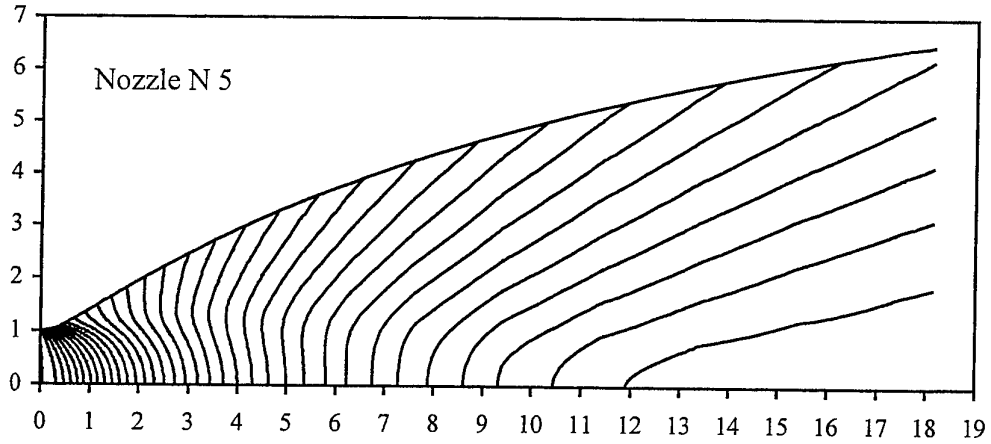


Fig.2. Mach level lines for nozzle N 5(UC)

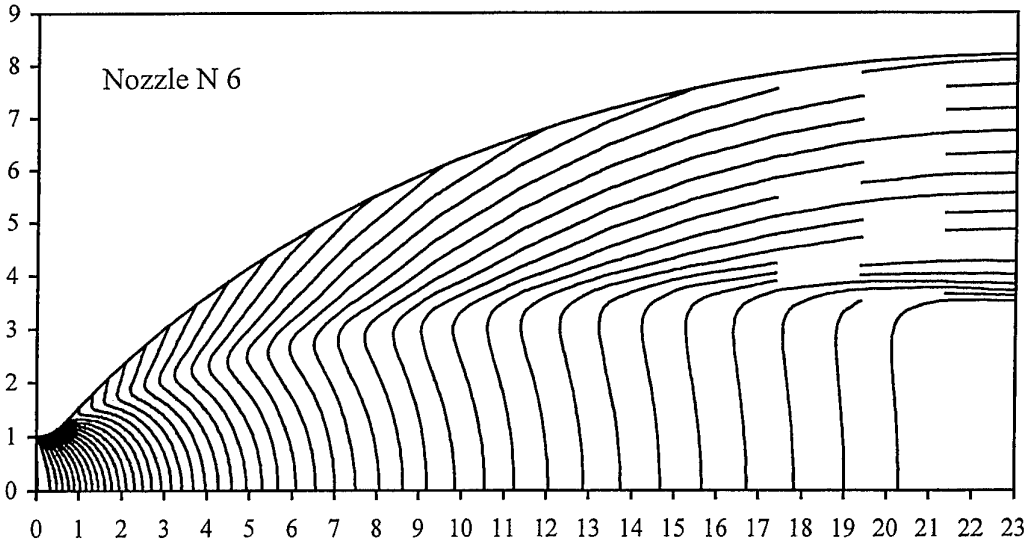


Fig.3. Mach level lines for nozzle N 6(DO)

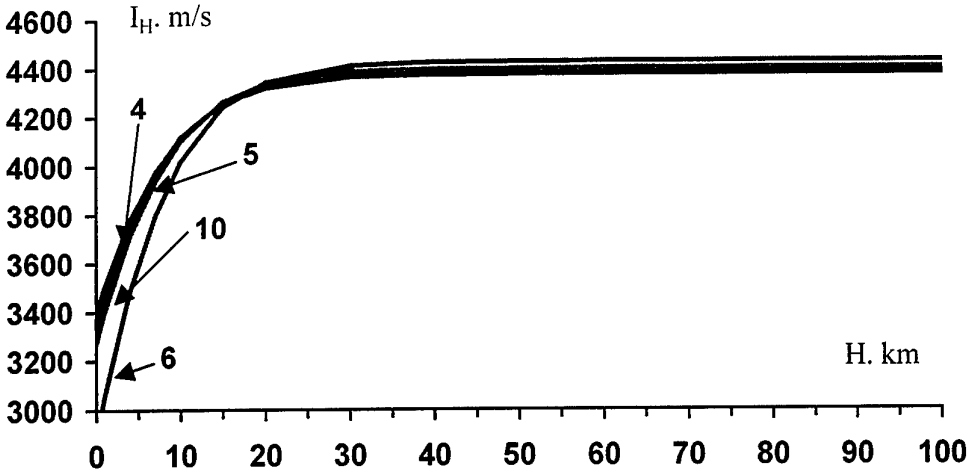


Fig.4. Effect of altitude on the delivered specific impulse

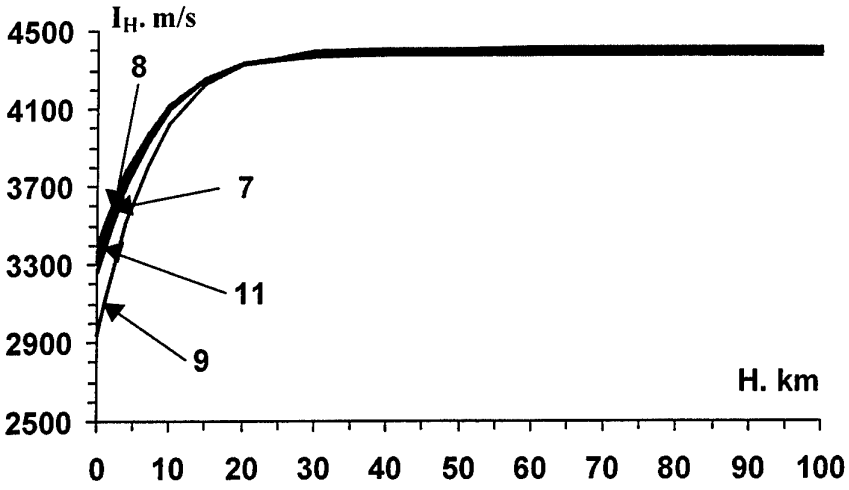


Fig.5. Effect of altitude on the delivered specific impulse

Table 1

N	Method	ξ_d,%	ξ_{bl},%	ξ_Σ',%	$\Delta\xi_\Sigma'$,%	θ_e, ^{0}	M_{ew}
1	M1	0.67	0.93	1.60	0	8.01	4.49
	M2	0.71	0.66	1.40	0		
	TDK	0.76	1.81	2.56	0		4.41
2	M1	0.74	0.91	1.65	0.05	9.49	4.55
	M2	0.76	0.68	1.42	0.02		
	TDK	0.87	1.76	2.63	0.07		4.56
3	M1	0.67	0.91	1.57	-0.03	8.5	4.52
	M2	0.72	0.68	1.40	0		
	TDK	0.76	1.80	2.56	0		4.52

Table 2

N	Method	F_e	I_{vi},m/s	ξ_d,%	ξ_{bl},%	ξ_{kin}%	ξ_Σ,%	I_v,m/s	ξ_m,%	I_{vm},m/s	ΔI_{vi},m/s	ΔI_v,m/s	ΔI_{vm},m/s	M_w	θ_e,°	X_e/R_{th}
4	M1	44.98	4458.8	0.42	0.98	0.15	1.54	4390.5	0.23	4380.3	0	0	0	3.986	6.75	18.773
	M2		4458.8	0.44	0.77	0.15	1.35	4398.4	0.23	4388.2	0	0	0			18.773
	TDK		4486	0.47	1.66	0.12	2.25	4386	0.23	4375.8	0	0	0	3.95		18.773
5	M1	42.64	4448.4	0.46	0.97	0.14	1.57	4379.3	0.21	4369.8	-10.4	-11.2	-10.5	3.987	7.73	18.284
	M2		4448.4	0.46	0.76	0.14	1.36	4387.9	0.21	4378.4	-10.4	-10.5	-9.8			18.284
	TDK		4475	0.51	1.64	0.12	2.27	4374	0.21	4364.5	-11	-12	-11.3	3.95		18.284
6	M1	67.24	4531.7	1.01	1.04	0.17	2.22	4431.7	0.36	4415.5	72.9	41.2	35.2	3.991	0.2	22.96
	M2		4531.7	1.08	0.85	0.17	2.10	4436.5	0.36	4420.3	72.9	38.1	32.1			22.96
	TDK		4563	1.07	1.92	0.16	3.15	4419	0.36	4402.8	77	33	27	3.95		22.96

Table 3

N	Meth.	F_e	θ_e,°	I_{vi},m/s	ξ_d,%	ξ_{bl},%	ξ_{kin}%	ξ_{Σ}',%	I_v,m/s	ξ_m%	I_{vw},m/s	ΔI_{vi},m/s	ΔI_v,m/s	ΔI_{vm},m/s	M_{ew}	L
7	M1	46.24	7.6	4464.1	0.57	0.94	0.15	1.66	4390.3	0.22	4380.4	0	0	0	3.984	1.33
	M2			4464.1	0.59	0.74	0.15	1.48	4398.2	0.22	4388.4	0	0	0		
	TDK			4494.7	0.62	1.65	0.13	2.4	4386.9	0.22	4377	0	0	0	3.94	
8	M1	42.51	7.9	4447.8	0.48	0.95	0.14	1.57	4378.1	0.21	4368.7	-16.3	-12.2	-11.7	3.981	1.39
	M2			4447.8	0.49	0.82	0.14	1.45	4383.3	0.21	4374.0	-16.3	-14.9	-14.4		
	TDK			4478.1	0.54	1.63	0.12	2.29	4375.8	0.21	4366.4	-16.6	-11.1	-10.6	3.96	
9	M1	64	7.2	4523.2	1.43	0.88	0.17	2.48	4411.2	0.25	4399.7	59.1	20.9	19.3	3.988	1.13
	M2			4523.2	1.49	0.71	0.17	2.37	4416.0	0.25	4404.7	-59.1	17.8	16.3		
	TDK			4554.8	1.47	1.64	0.15	3.26	4405.9	0.25	4394.4	60.1	19	17.4	3.93	

Table 4

N	Method	F_e	θ_e,deg	I_{vi},m/s	ξ_d%	ξ_{bl},%	ξ_{kin}%	ξ_Σ',%	I_v,m/s	ξ_m,%	I_{vm},m/s	M_{ew}	L
10	M1	49	5.1	4475	0.49	0.95	0.15	1.59	4403.6	0.25	4392.3	3.983	1.4
	M2			4475	0.53	0.79	0.15	1.47	4409.2	0.25	4398.0		
	TDK			4505.6	0.51	1.73	0.13	2.37	4398.8	0.25	4387.5	3.96	
11	M1	49	7.2	4475	0.68	0.92	0.15	1.75	4396.7	0.23	4386.6	3.983	1.29
	M2			4475	0.71	0.73	0.15	1.59	4403.8	0.23	4393.5		
	TDK			4505.6	0.71	1.64	0.13	2.48	4393.9	0.23	4383.8	3.95	

Table 5

N	I_H,m/s	ξ_H,%	ΔI_H,m/s	H,km	L	F_e
4	3355.3	23.2	0	17.8	1.4	44.98
5	3398.0	22.0	42.7	16.8	1.4	42.64
6	2884.2	34.2	-471.1	-	1.4	67.24
10	3275.9	25.2	-79.4	18.9	1.4	49

Table 6

N	I_H,m/s	ξ_H,%	ΔI_H,m/s	H,km	L	F_e
7	3326.1	23.8	0	22.1	1.33	46.24
8	3399.8	22.0	73.7	19.8	1.39	42.51
9	2938.3	32.6	-387.8	-	1.13	64
11	3269.0	25.2	-57.1	22.0	1.29	49

Table 7

N	4	5	6	10
Δm_{pl},%	0	-0.94	2.04	0.91

Table 8

N	7	8	9	11
Δm_{pl},%	0	-0.93	0.81	0.45

Causes of Thrust Performance Loss in a Clustered Linear Aerospike Nozzle

Takeo TOMITA Hiroshi SAKAMOTO Mamoru TAKAHASHI Masaki SASAKI
Takuo ONODERA Hiroshi TAMURA
National Aerospace Laboratory, Kakuda Research Center

Abstract

Combustion tests were carried out on a 14 kN clustered linear aerospike nozzle composed of 6 rectangular-cell-nozzles with a 20%-length truncated spike nozzle. The thrust coefficient efficiency obtained at sea level condition was only 87.5%, which was remarkably low in comparison with the predicted values of 97%. To clarify causes of loss qualitatively and quantitatively, cold-flow tests were conducted with a 3-cell-clustered nozzle model which simulates the 14 kN clustered aerospike nozzle. Based on the observed results, a thrust performance model for clustered linear aerospike nozzles, which can roughly estimate the loss due to clustering of cell nozzles, is proposed. Using this model, the loss due to clustering for the 14 kN clustered nozzle was estimated to be 2.5%

Nomenclature

A_g : Gap area
A_t : Throat area of cell nozzle
$C_{Fcluster}$:Thrust coefficient of clustered nozzle, Eq. (5)
C_{FMcell} :Theoretical thrust coefficient of cell nozzle for momentum force
$C_{F,E}$: Thrust coefficient of aerospike nozzle, Eq. (1)
$C_{F\varepsilon=5}$: Theoretical thrust coefficient at $\varepsilon = 5$
$F_{cluster}$:Thrust of clustered nozzle
NPR: Nozzle pressure ratio, Pcell/Pa
P_{cell} : Plenum pressure of cell combustor
$P_{cell,exit}$: Pressure at cell nozzle exit
$P_{cell,E}$: Calculated pressure which is attained if the cell exhaust expands to the gap space
P_W : Pressure on the spike surface
P_a : Ambient pressure
P_B : Pressure at truncated nozzle base surface
P_E : Calculated pressures at the end of the full-spike nozzle
P_g : Pressure on the surface of the gaps
P_T : Calculated pressures at the truncated point

ε_B: Ratio of truncated nozzle base area and total throat area

ε_{cell} : Expansion area ratio of cell nozzle

ε_E : Expansion area ratio of spike nozzle

θ_{cell} : Tilt angle of cell nozzle to the spike axis

η_{CF}: Thrust coefficient efficiency

η_{Isp}: Specific impulse efficiency

Introduction

For future fully reusable SSTOs, reusable rocket engines characterized by light weight and high performance from low altitude to high altitude are essential. Engines with aerospike nozzles are drawing attention as promising candidates which satisfy these requirements, and such engines have been adopted in the USA for use in the X-33 vehicle. The National Aerospace Laboratory has studied aerospike nozzles for the past few years.[1-8] Cold flow tests, CFD analysis and combustion tests have been conducted to clarify the flows behind the truncated spike-nozzle base, the methods of secondary injection, the necessity of side-fences and required sizes, cell-to-cell interaction of the exhaust jets and so on.[1-8]

The purpose of this paper is to clarify the causes of thrust performance loss in a clustered linear aerospike nozzle. A 14 kN thruster with a clustered linear aerospike nozzle composed of six rectangular cell nozzles and a two-dimensional truncated spike nozzle was fabricated and fired at ground-level condition. To acquire detailed information on the loss due to the clustering of cell nozzles, cold flow tests with a subscale model which simulates the clustered cell nozzles were also conducted.

Performance of Linear Aerospike Nozzles

Theoretical Performance of Linear Aerospike Nozzles

Before discussion of clustered linear aerospike nozzles, the theoretical performance of a two-dimensional linear aerospike nozzle is presented with our experimental results.[5,6] The theoretical thrust coefficient of aerospike nozzles can be calculated by the following equation:[8]

$$C_{F,E} = C_{FMcell}\cos\theta_{cell} + \varepsilon_{cell}\cos\theta_{cell}\frac{P_{cell,exit}}{P_{cell}} + \frac{\int P_w dy}{P_{cell}A_t} + \varepsilon_B\frac{P_B}{P_{cell}} - \varepsilon_E\frac{P_a}{P_{cell}} \qquad (1)$$

Here, the first term on the right-hand side represents the momentum of the exhaust jets from the cell nozzles, the second term is the pressure at the exit planes of the cell nozzles, the third term indicates the pressure on the spike wall, the fourth term represents the pressure at the base of the truncated spike nozzle, and the fifth term is the atmospheric pressure.

Pw in the third term can be evaluated by the method of characteristics. P_B in the fourth term cannot be analytically obtained, so an empirical relation or CFD analysis is required. The value

of P_B changes according to the flow pattern formed behind the base. When the pressure ratio, Pc/Pa, is small, an open wake is formed, and P_B nearly equals the ambient pressure. When Pc/Pa exceeds a certain value, the wake pattern changes from an open wake to a closed wake, and the value of P_B no longer equals the ambient pressure but has a certain value depending on the geometry of the spike nozzle. Fick[9] showed the following empirical equation for annular truncated spike nozzles at the closed wake condition with no secondary injection.

$$P_B = 0.5 (P_T + P_E) \qquad (2)$$

where P_T and P_E are the calculated pressures at the truncated point and at the end of the full spike nozzle based on the Prandtl-Meyer fan emanating from the tip of the cell nozzle, respectively. For the linear aerospike nozzles, we found that the constant in the equation needed to be changed from 0.5 to 0.3 based on our cold flow data.[5,6]

$$P_B = 0.3 (P_T + P_E) \qquad (3)$$

Hagemann[10] detailed how to determine the transition point from an open wake to a closed wake with the method of characteristics by tracing the right-running characteristics emanating from the sonic throat toward the centerline. The transition occurs when this characteristic meets the point on the lower shear layer in the wake of plug, where trailing shock is induced. In the present paper, a rough estimation for the transition point was used.[10]

Cold Flow Tests with a Linear Full-Spike Nozzle

Figure 1 shows the linear full-spike nozzle used in our cold flow tests. The expansion ratio of the cell nozzle, ε_{cell}, was 2.0 and the nozzle pressure ratio, NPR, of optimum expansion for the cell nozzle was 10.7. The expansion ratio of the spike nozzle, ε_E, was 8.0 and the NPR of the optimum expansion for the spike nozzle was 97.9. The tilt angle of cell nozzle, θ_{cell}, was 29.6°. The full-spike nozzle used in the tests, was actually truncated at a length 80% that of the theoretical nozzle length due to a manufacturing difficulty. The loss by this truncation, however, is estimated to be negligible. Height of the cell nozzle throat was 3.5 mm, and width of the cell nozzle was 42.4 mm. In the design of cell nozzle contour, a parabolic curve was employed. The axial length of the cell-nozzle from the throat to the exit plane was 80% that of an equivalent 15-deg-half angle wedge nozzle, the initial wall angle of the parabola was 30°, and cell-nozzle exit wall angle was 0.76°. No reflection condition was used in designing the contour of the spike wall, assuming uniform flows from the cell nozzle.

Figure 2 shows the observed thrust coefficient efficiency, η_{CF}, as a function of NPR with the theoretical efficiency calculated by equation (1). The figure includes a conventional Bell nozzle efficiency without loss with the same expansion ratio as that of the spike nozzle. The theoretical value of η_{CF} for the full spike nozzle was around 0.99 ~ 1.00 for all operating conditions, which confirms an excellent altitude compensation of full-spike nozzles. The observed η_{CF} for the full-spike nozzle was 0.99 around NPR= 100 and 0.94 around NPR= 10.7.

Figures 3 and 4 show a typical comparison of a visualized image using a shadowgraph and computed Mach number contours under the inviscid flow assumption for the full-spike nozzle at

NPR= 100, respectively.[7] These figures indicate the existence of an oblique shock wave emanating from the inside of the cell nozzle. The oblique shock wave which was incident on the spike surface showed a typical flow structure: a reflected shock, a separation of laminar boundary layer and a reattachment and a recompression shock. The present CFD only predicted a simple reflected shock. The generation of the oblique shock inside the cell nozzle was originated due to an excessively large initial wall angle of the cell nozzle contour.

Figure 5 shows a comparison of the η_{CF} from the CFD results and the observed data.[6] It can be seen that the value of the computed η_{CF} agrees well with the experimental data. The computational and experimental data show a tendency to decrease as the NPR goes down. Based on a simple modeling, the η_{CF} loss due to the total pressure loss by the oblique shock was calculated. Figure 6 shows the estimated relations between η_{CF} and NPR for the test condition[7] The figure indicates that η_{CF} decreases as NPR goes down as expected. Needless to say, there may be many causes for the decline of nozzle efficiency, but it is qualitatively thought that the oblique shock may be one of them.

Cold Flow Tests with a Linear Truncated Spike Nozzle

The η_{CFS} for a linear truncated spike nozzle are shown in Figure 7. The nozzle configuration is the same as the previous full-spike nozzle but truncated, at a length of 20% that of the theoretical nozzle length. The figure shows the cold flow data and the predicted efficiency based on equations (1) and (3). At NPR= 10, the predicted η_{CF} was about 0.91 and measured η_{CFS} were about 0.85. At NPR= 100, the predicted η_{CF} was about 0.98 and measured η_{CFS} were about 0.95. At NPR ~ 25, a sharp drop of η_{CF} was observed both on the predicted line and in the cold flow data. This drop was caused by the change of the flow pattern behind the base from an open wake to a closed wake. The base pressure P_B is nearly equal to Pa at an open wake and $P_B = 0.3 (P_T + P_E)$ shown in equation (3).

The loss of truncation in the present cold flow model was 0.085 for the theory and 0.05 ~ 0.10 for the experiment at NPR= 10.7, and 0.02 for the theory and 0.04 for the experiment at NPR= 100. The observed magnitude of loss due to the truncation showed reasonable agreement with the predicted loss.

Combustion Tests with a 14 kN Clustered Linear Aerospike Nozzle Thruster

The experiments and the analysis shown above treated only the linear aerospike nozzle composed of two-dimensional cell nozzles. In reality, high cooling requirements because of the greater surface area to be cooled rule out this simple configuration. To overcome this difficulty, clustered rectangular-cell- nozzles are used.

Design of a 14 kN Clustered Linear Aerospike Nozzle

Table 1 indicates the specifications of the 14 kN linear aerospike nozzle thruster and Fig. 8

shows the dimensions of the thruster. LOX and methane were selected based on considerations of low heat load to the chamber wall and of visibility of shock patterns in exhaust jets. In the design of the aerospike nozzle, a parabolic curve was used in the cell nozzle contour: nozzle length: 80% of the 15-deg-half angle wedge nozzle; initial wall angle: 30°; exit wall angle: 5.3°. Generation of an oblique shock was again suspected, but in this case, the cell-nozzle-contour almost coincided with a contour with no reflection condition, so generation of an oblique shock was not observed in either the following experiments nor in the CFD analysis.

Gaps between cell nozzles are known to cause a considerable loss of nozzle efficiency.[11] In the case of clustered annular aerospike nozzles, a geometrical restriction requires a certain length of gaps.[11] On the other hand, clustered linear aerospike nozzles do not require such a geometrical restriction. So the length of gaps can be reduced to the limit of structure design. In the present study, a cooling channel for the cell combustor was the cause of nozzle gaps. We concluded that some length of gaps necessarily exist even in linear clustered aerospike nozzles, thus accepted the existence of gaps and considered them to be an important cause of performance loss. In the design of the spike surface contour, these gaps were neglected and a simple two-dimensional flow was assumed.

Combustion Test Results with the 14 kN Clustered Linear Aerospike Nozzle

Figure 9 shows a photograph of the combustion test with the 14 kN clustered linear aerospike nozzle. Chamber pressure of the six cells coincided within 1%. Figure 10 shows the measured η_{CF} as a function of NPR with the predicted η_{CF} with no secondary injection from equation (1) and (3). The conditions tested correspond to the optimum NPR of the cell nozzles. The obtained η_{CFS} were only 0.875, which was remarkably low in comparison with the predicted values, 0.97. The causes of this large loss will be discussed in the following section.

Gaps between cells not only cause a loss of thrust performance but also induce a high heat load on the spike surface. The effect of the gaps was investigated by conducting combustion tests with a rectangular three-cell combustor with a heat sink flat-plate spike nozzle. The photographs in Fig. 11 was taken just after ignition, and that in Fig. 12 was taken a few second after ignition. The first picture shows an expansion wave emanating from the cell nozzle tip, and wakes behind the gaps can be clearly seen in Fig. 11. Figure 12 shows heat spots behind the gap, indicating an enhanced heat load on the spike surface due to the gaps.

3-Cell-Clustered Cold Flow Model Tests

The main causes of the loss observed in the 14 kN clustered aerospike nozzle were considered to be the loss from the flow characteristics of linear aerospike nozzles shown in the section entitled "Performance of a Linear Truncated Aerospike Nozzle," and performance loss due to the gaps between cell nozzles. To clarify the cause of the loss due to the clustering qualitatively and quantitatively, cold-flow tests were carried out with the 3-cell-clustered nozzle model which simulates the 14 kN clustered aerospike nozzle.

Design of the 3-Cell-Clustered Cold Flow Model

The cold flow model was composed of a rectangular 3-cell nozzle with a flat-plate outer nozzle. The expansion ratio of the cell nozzle, ε_{cell}, was 5.0, which was the same as that of the combustion test model, and the optimum NPR for the cell nozzle was 47.6. Height of the cell nozzle was 25.0 mm and width of the cell nozzle throat was 4.0 mm. The thrust-cells were arrayed and separated by 5 mm gaps. The ratio of the width of the cell nozzle exit and the gap width was nearly the same as that of the combustion test model. If we define expansion ratio, $\varepsilon_{cell+gap}$, as the ratio of the sum of the cell nozzle exit area and the gap area and the cell-throat area, it becomes 5.83 and the optimum NPR for this is 60.5. The contour of the cell nozzle was designed with the method of characteristics.

A flat-plate outer nozzle, 100 mm in length, was used to simulate the first part of the contoured spike nozzle. The flat part of the contoured spike-nozzle starts from the cell exit and ends at the point where the characteristic line emanating from the upper end of cell nozzle exit is incident on it. The length of the flat part of this cold flow model is 75 mm. Pressure on the flat nozzle was measured at more than 100 points. Side fences were as high as the height of the cell exit. The co-ordinate of the test models is defined as shown in Fig. 13. The x-axis was directed downstream, the y-axis was on the flat plate, and the z-axis was normal to the flat plate. The origin of the axis was at the exit of the cell nozzle at the center of the center cell.

Flow Field in the Cell Nozzle

To confirm the designed contour of the cell nozzle, flow field in the cell nozzle was computed with a two-dimensional invicid compressible code. Figure 14 shows the contour of the Mach number in the cell nozzle. No oblique shock was observed. Variation of the Mach number at the cell nozzle exit plane was within 0.66%.

Pressure Distribution on the Flat Plate Nozzle at the Optimum NPR of the Cell Nozzle

The lower half of Fig. 15 shows a visualized image using the shadowgraph technique, and the upper half of Fig. 15 shows NDP distribution on the flat plate nozzle at the optimum NPR of the cell nozzle. NDP was defined as NDP= $(P_w - P_a)/P_{cell}$. Based on this definition, the positive value of NDP (red region in Fig. 15) produces thrust and the negative value (blue region in Fig. 15) produces drag.

The observed visualized image was similar to the wake pattern usually seen behind a back step. That is, jet boundaries, a recirculation zone, and a re-compression shock wave were observed behind the gap between the cells. Characteristic lines, the expansion wave in this case, emanating from the edges of cell exit to the center of the cell axis were also observed. In the NDP distribution, regions of negative value were observed in recirculation regions behind the gap. Fan-shaped negative NDP regions were observed from the edge of the cell nozzle exit. An increase of pressure was observed downstream of re-compression shocks. Based on these

observations, the flow field can be explained as follows. The exhaust which flows from cell nozzles produce wakes behind gaps, the pressure of which is low. This low pressure produces expansion fans emanating from the edge of cell nozzle exit, these expansion fans corresponding to the fan-shaped negative NDP regions, and pressure recovers by re-compression shocks generated behind the gaps.

The pressure force which acts on the surface of the gap directly affects the thrust in the present test configuration. This force will be discussed in the section "Pressure on the Gap Surface." On the other hand, the pressure on the flat plate spike-surface does not affect the thrust in the present test configuration. This force will be discussed in the section "Pressure on the Flat Plate Region." Although re-compression shock increases the pressure on the surface on the flat nozzle, it results in total pressure loss. As was discussed in the section "Performance of Linear Full Spike Nozzle," total pressure loss due to oblique shocks results in performance loss. This will be discussed in the section "Total Pressure Loss Due to Re-compression Shock."

Pressure Force on the Surface of the Gap

The pressure on the surface of the gap, P_g, was lower than the cell nozzle exit pressure, $P_{cell,exit}$. P_g was also lower than P_a and thus produced drag force. P_g may be estimated by using an empirical equation (3) as $P_g = 0.3(P_{cell,E}+P_{cell,exit})$. Where $P_{cell,E}$ is the pressure if the exhaust gas from a cell expands isentropically to an area from the center of a cell nozzle to the center of a gap. The expansion ratio for this condition was defined as $\varepsilon_{cell+gap}$, and the optimum NPR for this is 67.2. Loss in a cell nozzle is assumed to be zero. Thus, the thrust of the 3-cell-clustered nozzle, $F_{cluster}$, is estimated to be

$$F_{cluster} = C_{F\varepsilon=5} P_{cell} A_t + (P_g - P_a)A_g \qquad (4)$$

Thrust coefficient, $C_{Fcluster}$, is

$$C_{Fcluster} = F_{cluster}/(P_{cell} A_t) \qquad (5)$$

Since the upper side of the wake behind the gap is open, flow in and out of this side is possible. This flow should affect the value of P_g, so some change in the above estimation is required to improve the accuracy of prediction.

Figure 16 shows $\eta_{CFcluster}$ as a function of NPR. Observed η_{CFexp}s are also shown in this figure. Where $\eta_{CFcluster} = C_{Fcluster}/C_{F\varepsilon=5.83}$ and $\eta_{CFexp} = C_{Fexp}/C_{F\varepsilon=5.83}$. η_{CFexp} had the lowest value of 98% at NPR $>$ 30, then increased with an increase of NPR. Estimated $\eta_{CFcluster}$ was about 99 ~ 99.5 over NPR. It can be seen that $\eta_{CFcluster}$ shows reasonable agreement with η_{CFexp} and that the two almost coincide at NPR > 70. Causes of losses are considered to be drag due to the pressure acts on the gap surface, the boundary layer loss in the cell nozzle and on the flat plate surface, and the real gas effect. In this model, however, only the first effect (drag due to pressure acting on the surface of the gap) was taken into account.

Pressure on the Flat Spike Surface

To clarify the contribution of the pressure on the flat spike to the thrust, the average pressure

along the y-axis at each x was obtained by the summation

$$P_{w,ave}/P_{cell} = \Sigma\ (P_{w,i}/P_{cell} \times A_i) / \Sigma\ A_i, \qquad (6)$$

where $P_{w,ave}$ is the average pressure at each x, $P_{w,i}$ is the pressure at each pressure port, and A_i is the area around each pressure port. Figure 17 shows $P_{w,ave}/P_{cell}$ as a function of x with a parameter of NPR. In the figure, $(P_w/P_{cell})_{\varepsilon cell}$ and $(P_w/P_{cell})_{\varepsilon cell+gap}$, the pressures that are attained if the cell nozzle flow isentropically expands to ε_{cell} and $\varepsilon_{cell+gap}$, respectively, are also shown as references. In the figure, it can be seen that $P_{w,ave}/P_{cell}$ was around $(P_w/P_{cell})_{\varepsilon cell}$ for all NPRs in the range of $x < 50$. In the range of $x > 50$, the observed $P_{w,ave}/P_{cell}$ increased or decreased with an increase of x, depending on NPR$<$ 50 or NPR$>$ 50, respectively. The observed behavior can be considered to have been caused by the expansion waves or shock waves emanating from the upper side of the cell nozzle exit. In an ideal situation, those waves should be incident at x= 75. However, they shifted upstream. The shift may have been caused by a lower Mach number distributed on the flat nozzle due to the oblique shocks. The fact that $P_{w,ave}/P_{cell}$ is nearly equal to $(P_w/P_{cell})_{\varepsilon cell}$ means that the our design procedure, in which gap spaces are ignored when calculating the contour of the spike surface, may be proper.

Total Pressure Loss Due to Re-compression Shock

The wake behind a gap is modeled as shown in Fig. 18. Here, $P_2 = P_g$ and $\theta_2 + \theta_a = \theta_3 \equiv \theta$. From the visualized shadowgraph image, it was found that $\theta \cong 8^\circ$ and $(\beta - \theta) \cong 14^\circ$. On the other hand, θ and $(\beta - \theta)$ can be calculated as follows: M_2 and θ are calculated by the equation of Prandtl-Mayer using $P_g = 0.3(P_{cell,E}+P_{cell,exit})$, and β is calculated by oblique shock equations. The calculated results were $M_2 = 3.64$, $\theta \cong 7.7^\circ$, $\beta \cong 21.7^\circ$, and $(\beta - \theta) = 14^\circ$. Thus, the observed and calculated angles of θ and $(\beta - \theta)$ agreed well. Total pressure loss, P_{02}/P_{01}, calculated from oblique shock equations was 0.971. The total pressure loss of this model can be calculated from the nozzle design, which is independent of NPR.

Thrust Performance Model For Clustered Linear Aerospike Nozzles

Based on the results discussed above, a simple model to estimate thrust performance for clustered linear aerospike nozzles is proposed. The model uses only the design values of nozzles. The model is as follows:

(1) Loss in cell nozzles is caused only by the divergent loss. Thus, a correction factor for the thrust of a cell nozzle is $\lambda = \sin\theta_a/\theta_a$, where θ_a is a cell nozzle wall exit angle.

(2) The thrust contribution from the gap surface is calculated using $(P_g - P_a)A_g$, where $P_g = 0.3(P_{cell,E}+P_{cell,exit})$.

(3) The performance loss due to the total pressure from re-compression shock, P_{02}/P_{01}, is calculated using the model shown in Fig. 18.

(4) The pressure on a flat spike surface is constant at $P_w = P_{cell,exit}$

Based on the model, C_{Fmodel} can be calculated as follows:

$$C_{Fmodel} = \lambda C_{FMcell} \cos\theta_{cell} + \varepsilon_{cell} \cos\theta_{cell} \frac{P_{cell,exit}}{P_{cell}} + \frac{\cos\theta_{cell} (P_g A_g)}{P_{cell} A_t} + \frac{P_{02} \int P_w dy}{P_{01} P_{cell} A_t} + \varepsilon_B \frac{P_B}{P_{cell}} - \varepsilon_E \frac{P_a}{P_{cell}} \quad (7)$$

We apply this model to the 14 kN clustered linear aerospike nozzle. The pressure behind the gap can be calculated by $P_g = 0.3(P_{cell,E}+P_{cell,exit})$, thus, $P_g/P_{cell} = 0.01646$. By using Fig. 18, $\theta_2 = 10.1°$ and $\beta = 29.9°$. On the other hand, observed angles from Fig. 11 were $\theta = \theta_2 + \theta_a = 16.3°$ and $\beta - \theta = 20°$. Since $\theta_a = 5.3°$, $\theta_2 = 11.0°$ and $\beta = 36°$. The experimental and calculated values of β and θ showed reasonable agreement, considering the assumption of the model and the ambiguity inherent in reading the angles from the combustion photographs. Using calculated total pressure loss, $P_{02}/P_{01} = 0.890$, $\eta_{CFmodel} = 0.945$. The difference between $\eta_{CFmodel}$ (= 0.945) and η_{CF} (= 0.970) was 0.025. It should be remembered that η_{CF} and $\eta_{CFmodel}$ were defined in equation (1) and (7). By the definition of equation (7), the difference indicates the loss due to the clustering of cell nozzles. The observed η_{CFexp} for the 14 kN aerospike nozzle was only 0.875, and thus the cause of the loss of about 7% is still unknown.

Conclusion

Causes of thrust performance loss on a clustered linear aerospike nozzle were investigated by conducting cold flow tests with a linear aerospike nozzle composed of two-dimensional cell nozzles, combustion tests with a 14 kN thruster having a clustered linear aerospike nozzle, and by cold flow tests with a clustered cold flow model which simulated the 14 kN thruster. The findings of the study are as follows:

(1) Observed thrust coefficient efficiency for the 14 kN thruster with a clustered linear aerospike nozzle was 87.5% at a ground level operation, which was about 10% less than the expected efficiency, 97.5%, calculated by a semi-theoretical equation derived by the authors.

(2) The loss due to the clustering of cell nozzles was predicted by a simple proposed model. The main causes of this loss were the drag force due to the lower pressure acting on the gap surface between cells and the loss due to the total pressure loss caused by the re-compression shock generated behind the gap.

(3) The predicted efficiency including the loss by the clustering, was estimated to be 94.5%, and thus the cause of loss about 7% is still unknown. This type of large performance loss has already been noticed even in two-dimensional full-spike nozzle at low NPR. To clarify the cause of this loss, further study is required.

Reference

1) Tomita, T., et. al. "An Experimental Evaluation of Plug Nozzle Flow Field," AIAA paper 96-2632, 1996.
2) Tomita, T., et. al. "Plug Nozzle Flow Field Characteristics," The Proceeding of 20th ISTS, pp. 82-87, 1996.
3) Tomita, T., et. al. "Flow Field of Clustered Plug Nozzles," AIAA paper 97-3219, 1997.
4) Tomita, T., et. al. "Observation of Shock Wave Interaction on the Surface of Aerospike Nozzles," ISTS paper 98-a-1-07, 1998.
5) Tomita, T., et. al. "Visualization of Shock Wave Interaction on the Surface of Aerospike Nozzles," AIAA paper 98-3523, 1998.
6) Tomita, T., et. al "Effects of Base Bleed on Thrust Performance of a Linear Aerospike Nozzle." AIAA paper 99-2586, 1999.
7) Onodera, T., et. al. "Numerical Investigation of the Flow Field Around Linear Aerospike Nozzles," AIAA paper 99-2588, 1999.
8) Tamura, H., et. al. "An Experimental Study With a 14kN Linear Aerospike-Nozzle Combustor," AIAA paper 99-2761, 1999
9) Fick, M. and Schmucker, R. H., "Performance Aspects of Plug Cluster Nozzles," Journal of Spacecraft and Rockets, Vol. 33, No. 4, July-August 1996.
10) Hagemann, G., et. al. "Flow Phenomena in Advanced Rocket Nozzles - The Plug Nozzle," AIAA paper 98-3523, 1998.
11) Aerojet Liquid Rocket Company: "Unconventional Nozzle Tradeoff Study," NASA CR-159520, 1979

Table 1. Specification of 14 kN Clustered Linear Aerospike Nozzle Thruster

Propellants:	LOX/Methane
Number of cells:	6
Maximum chamber pressure:	5.0 MPa
Expansion ratio of cell nozzle:	5
Optimum pressure ratio of cell nozzle:	31.3
Expansion ratio of engine:	45
Optimum pressure ratio of engine:	556.3
Specific heat ratio of combustion gas:	1.20
Size of cell throat:	35.4 mm x 7.86 mm
Theoretical full spike length:	1361 mm
Theoretical thrust coefficient:	1.813 (Frozen)
Nominal thrust (Vac.) :	14.4 kN

Fig. 1 Photograph of a linear full-spike nozzle model used in the cold flow tests.

Fig. 2 Observed thrust coefficient efficiency, η_{CF}, for the linear full-spike nozzle as a function of NPR with the theoretical efficiency calculated by equation (1).

Fig. 3 Visualized image using the shadowgraph technique for the linear full-spike nozzle at NPR= 100

Fig. 4 Calculated Mach number contour for the linear full-spike nozzle at NPR= 100

Fig. 5 Comparison of thrust coefficient efficiencies, η_{CF}, between calculation and experiment

Fig. 6 The effect of oblique shock waves on the spike nozzle to the thrust coefficient efficiency (η_{CF2} :after the incident oblique shock, η_{CF3}: after the reflected oblique shock)

Fig. 7 Observed thrust coefficient efficiency, η_{CF}, for the 20%-truncated-spike nozzle as a function of NPR with the theoretical efficiency calculated by equation (1)

Fig. 8 Schematics of the 14 kN clustered linear aerospike nozzle thruster

Fig. 9 Photograph of the combustion test with the 14 kN clustered linear aerospike nozzle (LOX/methane, Pcell = 4.6 MPa)

Fig. 10 Observed thrust coefficient efficiency, η_{CF}, as a function of NPR with the predicted η_{CF} with no secondary injection from equation (1) and (3)

Fig. 11 Photograph of the flat spike surface taken just after ignition (NPR= 4.6 MPa, LOX/methane)

Fig. 12 Photograph of the flat spike surface taken 4 seconds after ignition (NPR= 4.6 MPa, LOX/methane)

Fig. 13 Definition of the co-ordinate on the 3-cell cold flow test models

Fig. 14 Calculated contour of the Mach number in the cell nozzle

Fig. 15 Observed NDP distribution (upper-half) and visualized image using the shadowgraph technique (lower-half) on the 3-cell cold flow model at the optimum NPR of the cell nozzle.

Fig. 16 Observed η_{CF} of the 3-cell-clustered cold flow model with the predicted η_{CF} by the proposed prediction model

Fig. 17 Average pressure distribution on the flat-spike surface, $P_{w,ave}/P_{cell}$, as function of x with a parameter of NPR

Fig. 18 Schematics of the wake model behind a gap

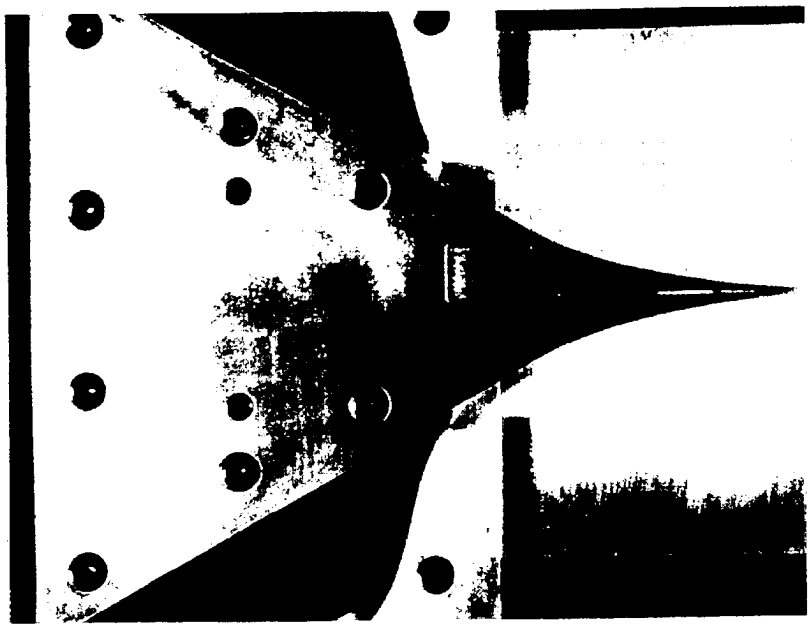


Fig. 1 Photograph of a linear full-spike nozzle model used in the cold flow tests.

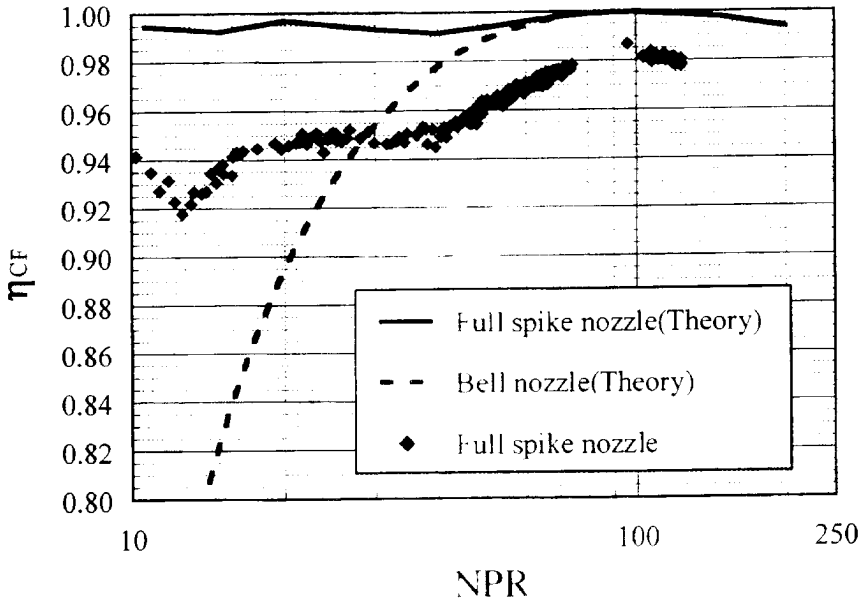


Fig. 2 Observed thrust coefficient efficiency, η_{CF}, for the linear full-spike nozzle as a function of NPR with the theoretical efficiency calculated by equation (1).



g. 3 Visualized image using the shadowgraph technique for the linear full-spike nozzle at NPR= 100



ig. 4 Calculated Mach number contour for the linear full-spike nozzle at NPR= 100

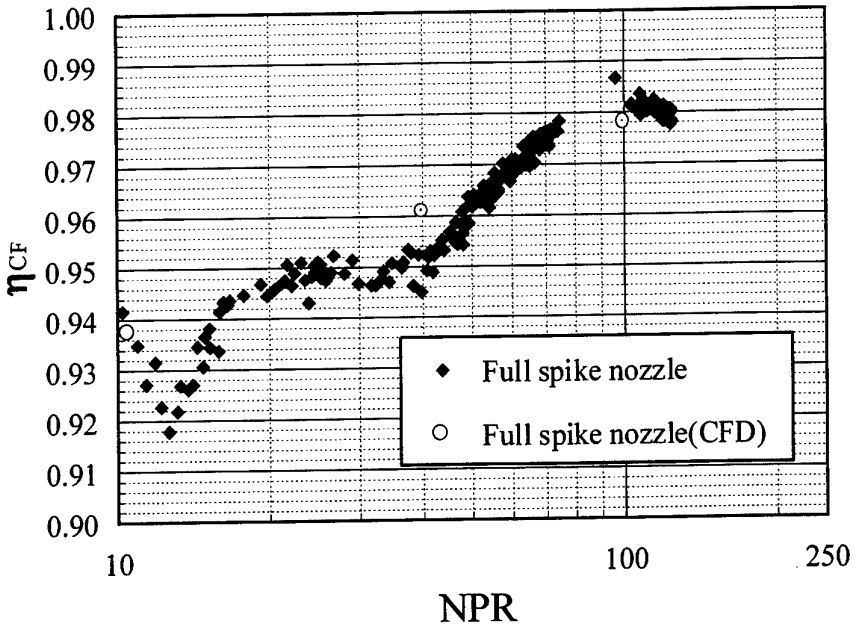
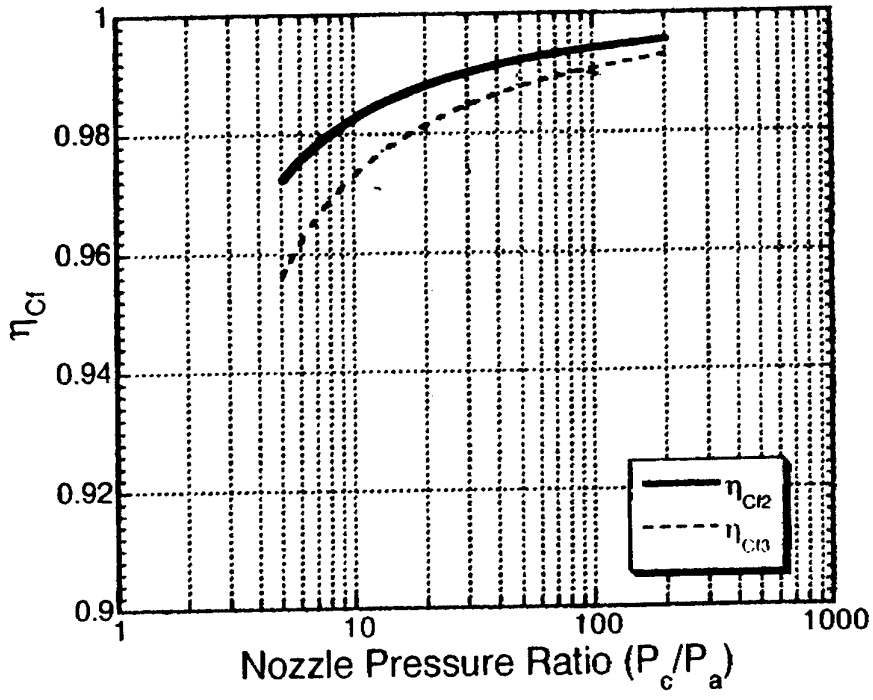


Fig. 5 Comparison of thrust coefficient efficiencies, η_{CF}, between calculation and experiment



FFig. 6 The effect of oblique shock waves on the spike nozzle to the thrust coefficient efficiency (η_{CF2} :after the incident oblique shock, η_{CF3}: after the reflected oblique shock)

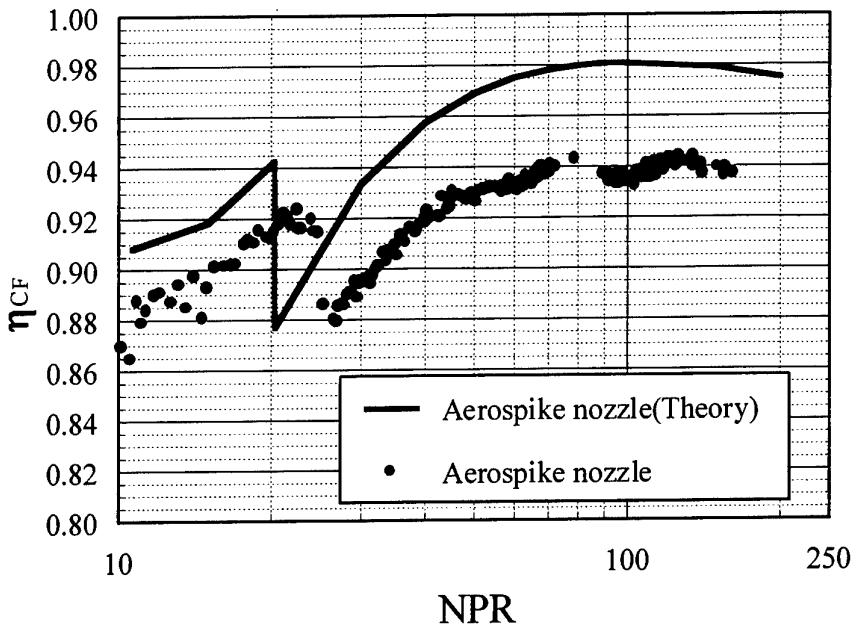


Fig. 7 Observed thrust coefficient efficiency, η_{CF}, for the 20%-truncated-spike nozzle as a function of NPR with the theoretical efficiency calculated by equation (1)

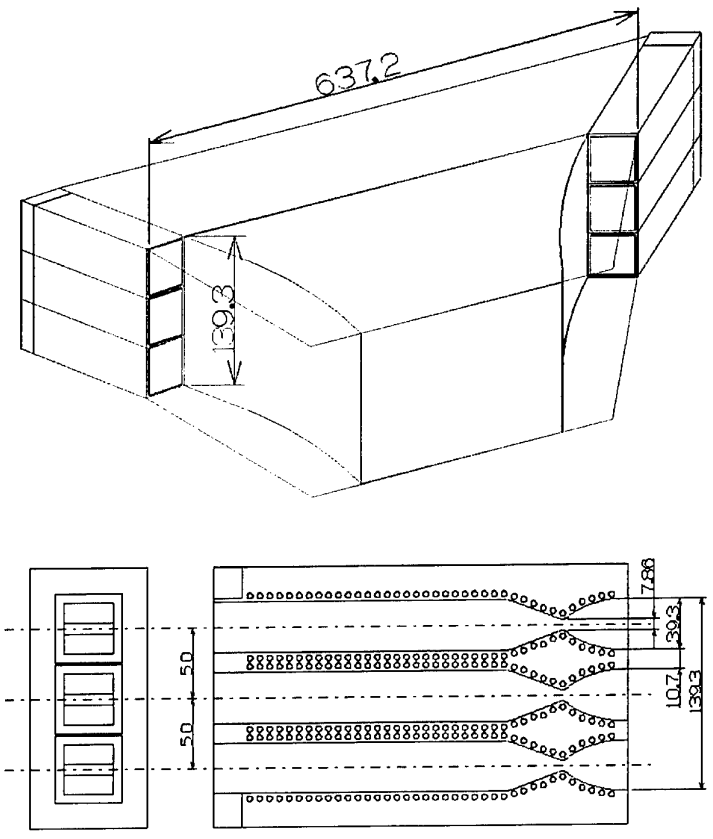


Fig. 8 Schematics of the 14 kN clustered linear aerospike nozzle thruster

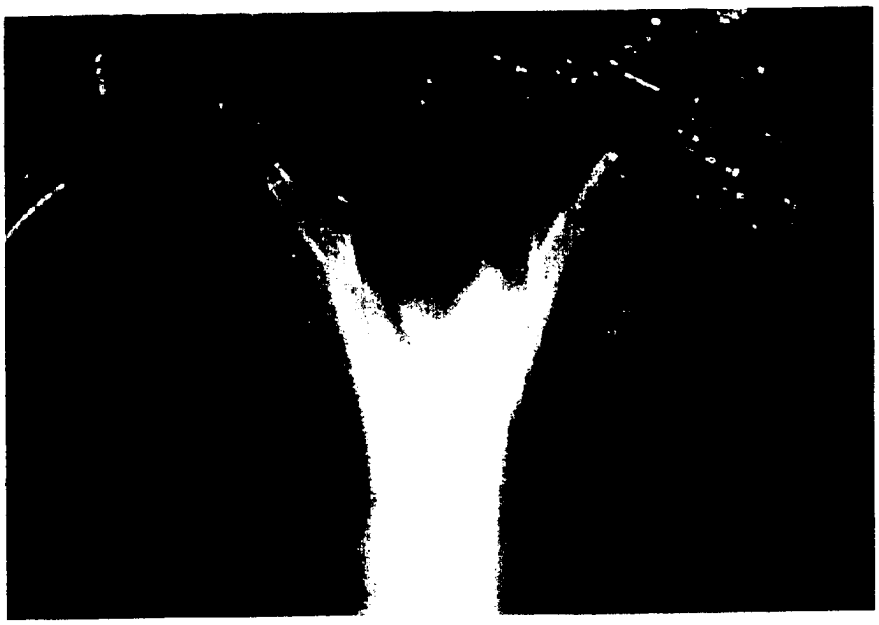


Fig. 9 Photograph of the combustion test with the 14 kN clustered linear aerospike nozzle

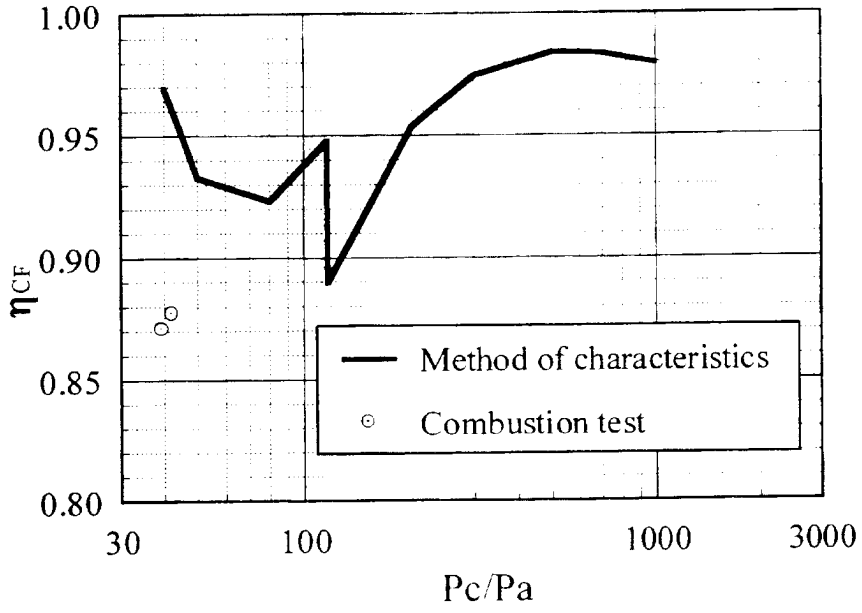
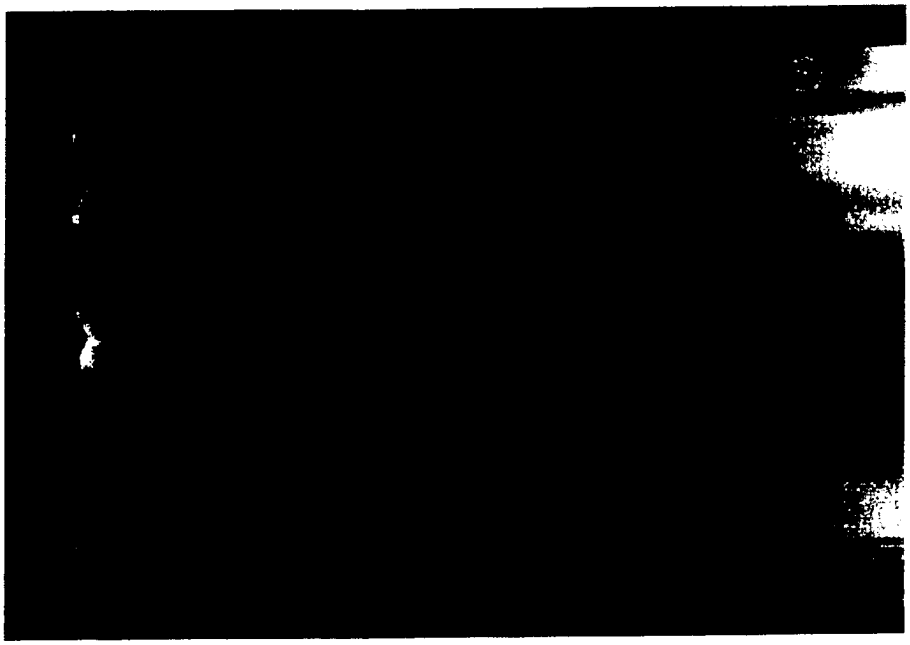


Fig. 10 Observed thrust coefficient efficiency, η_{CF}, as a function of NPR with the predicted η_{CF} with no secondary injection from equation (1) and (3)



g. 11 Photograph of the flat spike surface take[illegible] after ignition
(NPR= 4.6 MPa, LOX/methane)

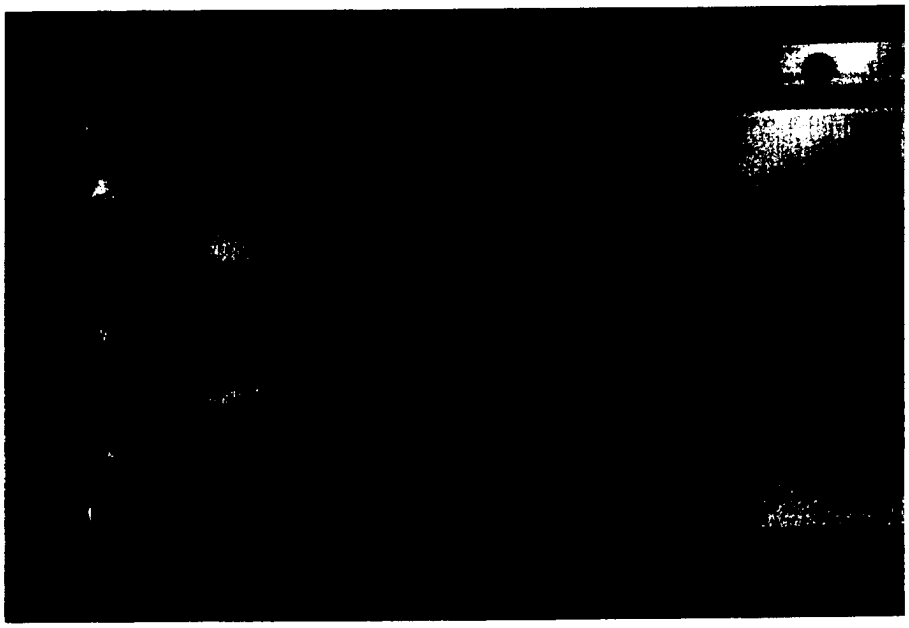


Fig. 12 Photograph of the flat spike surface take[illegible] seconds after ignition
(NPR= 4.6 MPa, LOX/methane)

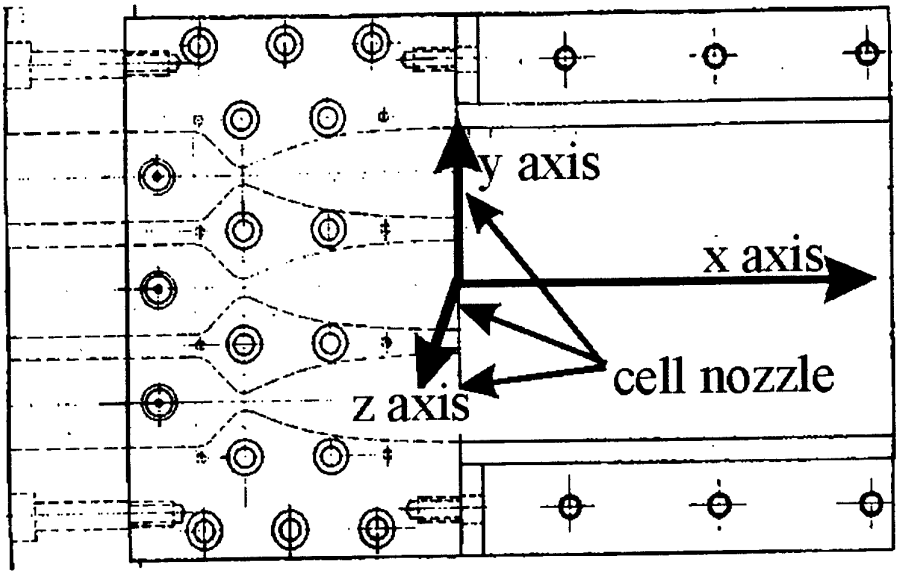


Fig. 13 Definition of the co-ordinate on the 3-cell cold flow test models

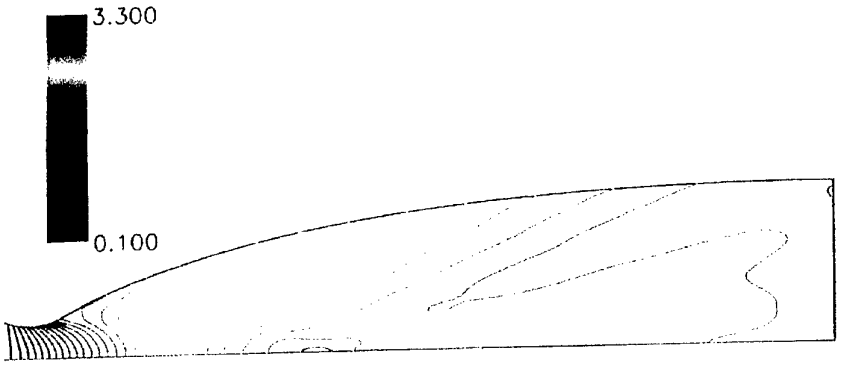


Fig. 14 Calculated contour of the Mach number in the cell nozzle

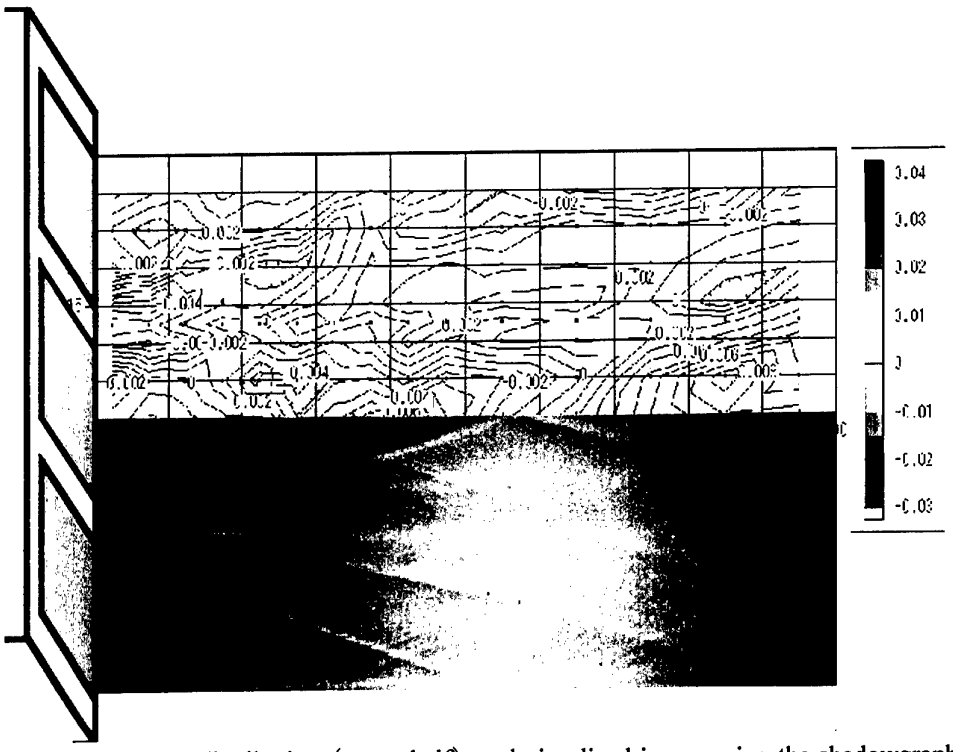


Fig. 15 Observed NDP distribution (upper-half) and visualized image using the shadowgraph technique (lower-half) on the 3-cell cold flow model at the optimum NPR of the cell nozzle.

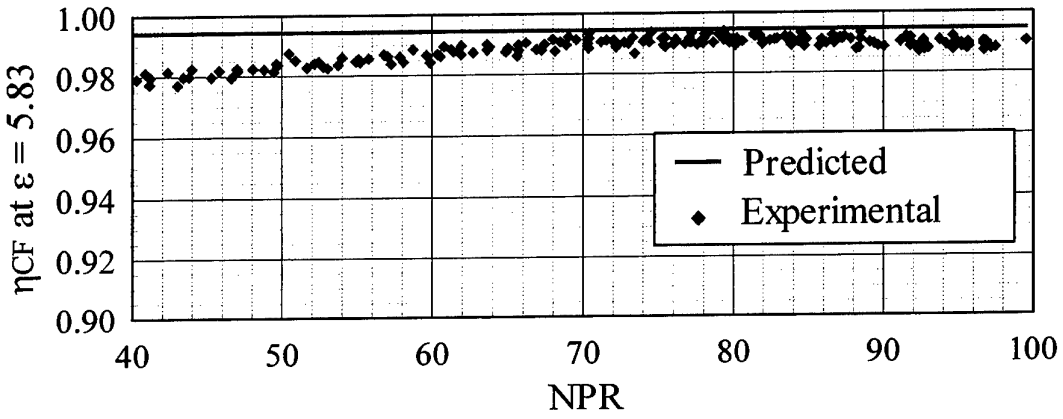


Fig. 16 Observed η_{CF} of the 3-cell-clustered cold flow model with the predicted η_{CF} by the proposed prediction model

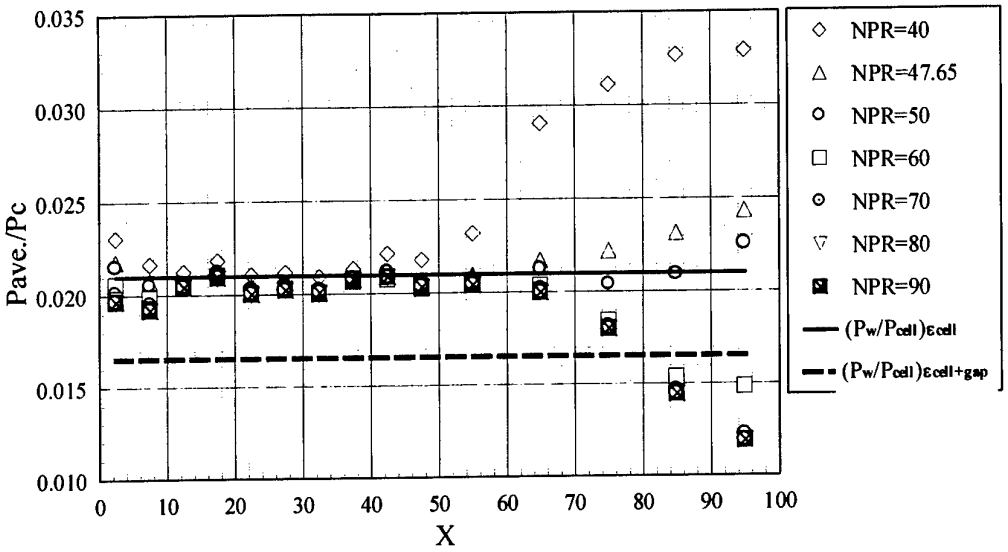


Fig. 17 Average pressure distribution on the flat-spike surface, $P_{w,ave}/P_{cell}$, as function of x with a parameter of NPR

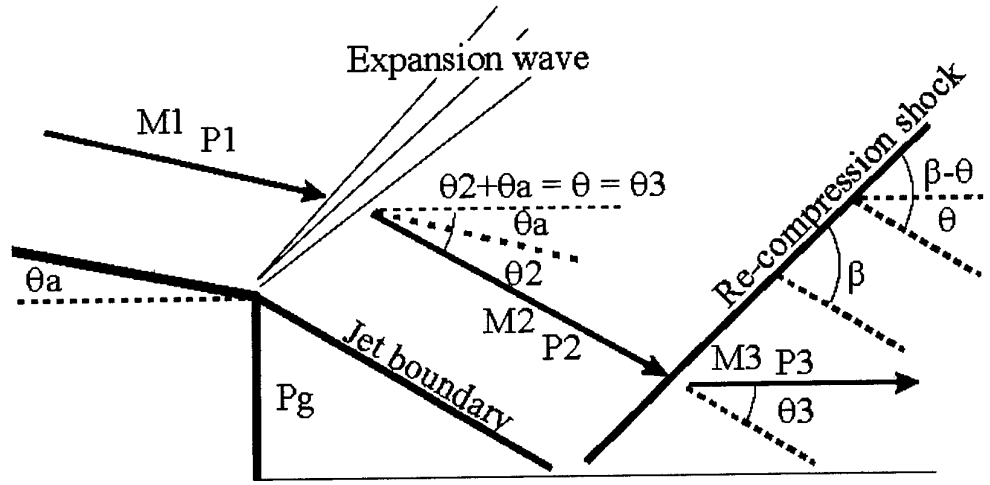


Fig. 18 Schematics of the wake model behind a gap

NOZZLE DIFFERENTIAL FACILITY FOR HIGH ACCURACY INVESTIGATIONS OF NOZZLE PERFORMANCE.

G.Dumnov, G.Nikulin

Keldysh Research Center, Moscow, Russia

Abstract

Nozzle Differential Facility (NDF) are usually used for determination of performance of rocket engine nozzles of different configurations. There are a principal scheme and brief description of the main characteristics of this rig in the paper. The main idea of thrust performance measuring of nozzle under consideration is based on comparison of its thrust with the trust of reference nozzle under the same mass flow rates. Such differential measuring scheme of trust performance allows to have its value with minimum errors (0.08...0.05%). Some experimental results of thrust performance of Laval's nozzles with roughness wall, axisymmetric and plane plug nozzles are presented in paper. NDF has been equipped with low pressure chamber which allows to test different nozzles with Mach number up to 6. Efficiency of thrust vector control elements (injection in supersonic nozzle part, aerodynamic blades of different configurations and ets.) can be investigated on NDF too. NDF has been equipped with sub- and transonic wind tunnel (M_∞~0.1...1.4) which allows to investigate an influence of ambient flow on thrust characteristics. Usual nozzle tests (determination of pressure and heat flux distributions along the wall) are performed on NDF also.

Numerical Approaches to Spray Combustion

E. Gutheil[a]*, D. Schlotz[a], F.X. Demoulin[b], R. Borghi[b]**

[a]Interdisziplinäres Zentrum für Wissenschaftliches Rechnen
Universität Heidelberg
Im Neuenheimer Feld 368, 69120 Heidelberg, Germany
***e-mail: gutheil@iwr.uni-heidelberg.de**

[b]IRPHE
UMR 6594 CNRS - Université d'Aix-Marseille I et II - ESM2
Technopôle de Château Gombert
13451 Marseille Cédex 20, France
****e-mail: demoulin@esm2.imt-mrs.fr**

Abstract

The paper concerns both laminar and turbulent spray combustion modeling. In the first part detailed numerical computations of structures of laminar spray diffusion flames in the counterflow configuration are presented. Here the emphasis lies on including detailed chemical reaction systems. Both mono- and bidisperse sprays are considered. Liquid oxygen/hydrogen spray flames for high subcritical, cryogenic conditions are investigated, and the model is extended to include transport coefficients for the gas phase for cryogenic temperatures and elevated pressure. The formulation of thermodynamic equilibrium at the droplet surface includes both temperature and pressure dependence of the binary mixture. The formulation of the gas phase equations includes detailed transport and detailed chemical reactions which enables the investigation of both the inner flame structure and the extinction of these flames. At high strain droplet reversal and oscillation are observed; moreover, condensation of the oxygen occurs near the gas stagnation plane. The laminar spray flame structures may be included in the flamelet model for turbulent spray diffusion flames.

In practical systems spray flames typically are turbulent. Droplets are local sources of vapour randomly distributed in space. Thus they produce additional local fluctuations of equivalence ratio. In order to represent the mixing process, these fluctuations must to be taken into account. Such situation can be modeled with the PDF (*P*robability *D*ensity *F*unction) approach, with convenient particular features. The combustion is described using two different models, one assuming infinitely fast chemistry and the other is based on the MIL model [4] and presumes sudden chemistry. Both models are tested to represent the auto-ignition and the combustion of a turbulent fuel spray penetrating into a hot oxidizing atmosphere.

1 Introduction

The modeling of both laminar and turbulent spray flames is relevant to various technical combustion systems such as internal engine combustion, liquid rocket propulsion, gas turbine combustors as well as liquid fueled industrial furnaces.

The focus in the last years has been the modeling of the interaction of chemical reactions and the laminar or turbulent flow field where a vaporizing spray is present. The liquid processes in these configurations are fairly well understood. The same is true for pure gas

phase combustion. The focus of the present paper is the interaction of vaporization, droplet motion (within either a laminar or a turbulent flow field) and chemical reactions.

The first part of the paper concerns the structure and extinction of laminar liquid oxygen (LOX)/hydrogen spray flames in the counterflow configuration. This setup has various advantages. First, the boundary conditions are well defined and easy to vary. Moreover, the system is accessible to experiment. The counterflow configuration also has relevance to turbulent spray flame modeling since the flame structures obtained in this setting are being used in flamelet computations for turbulent (spray) diffusion flame models.

Experiments in liquid rocket propulsion where the highly reactive chemical system hydrogen/oxygen is relevant are very rare due to safety aspects. This makes numerical studies very attractive. The combustion in liquid rocket propulsion concerns both the high subcritical and supercritical pressure regime as well as cryogenic inlet temperatures. The present study focuses on the high subcritical regime which is relevant to current upper stage engines of the ARIANE IV and V that operate in the range between 3 and 4 MPa. Moreover, research combustion chambers such as the micro combustion chamber M3 [38] of the DLR as well as the MASCOTTE [16] are developed for pressures up to 2 MPa and 6 MPa, respectively. Thus, the first part of the present paper investigates structures of laminar LOX/hydrogen spray flames for use in turbulent spray flame models such as the flamelet model for turbulent spray diffusion flames [23, 24]

The vaporization process that is basic to spray flames considerably affects the flame structure as well as the models for these flames. The second part of the present study concerns the modeling of turbulent spray diffusion flames using a presumed PDF (*P*robability *D*ensity *F*unction) approach. The turbulent flow field is described with a standard type of $k-\epsilon$ model, and the fluctuations of chemcial reactions and of turbulent mixing are modeled using the PDF. The probability density function is formulated to account for drolet vaporization. The model developed here is basic to turbulent spray flame modeling, and various chemical reaction models may be included.

The first part of the paper presents the modeling of laminar LOX/hydrogen spray flames in the counterflow configuration whereas the second one concerns a numerical approach to turbulent spray combustion.

2 Structures of Laminar Liquid Oxygen/Hydrogen Spray Flames

The counterflow configuration has been widely used to model both gas [33, 39, 14] and spray [10, 8, 11, 19] flames. On the one hand the configuration easily allows variation of well definded boundary conditions, and on the other hand the configuration has been used in experiment [26, 7, 9] as well. In the recent decade, more research groups have been concerned with the study of laminar spray flames in this configuration. Both non-reacting and reacting sprays have been studied experimentally whereas numerical computations emphasis on reactive sprays.

Most papers concern situations where the spray does not show significant interaction with the reaction zone [10, 11, 19, 27]. This condition is related to the injection of very small droplets at low injection velocity. The spray does not penetrate into the reaction zone but vaporizes as it enters the regime of somewhat elevated gas temperature. Moreover, most studies concern spray combustion at atmospheric pressure where the temperature of the

injected liquid is not far away from its boiling temperature if standard inlet conditions are considered. However, experimental studies do show that in both non-reactive sprays [27] and in reactive high-strain situations [17] the spray deeply penetrates the configuration, and it shows both droplet crossing the gas stagnation plane and reversal towards their injector – in the reactive case strong interaction between the vaporization and the combustion processes occurs.

Most studies so far concerned atmospheric fuel spray flames. There is one experimental study concerning laminar hydrogen/air gas flame at low strain, and the present model perfectly predicts the flame structure [37]. Moreover, a paper of Sohn *et al.* [40] concerns extinction characteristics of laminar high pressure gas flames where the reactants are hydrogen and oxygen, and the present model is suitable to predict their results reasonably well.

The focus of the present study is the structure of high-pressure liquid oxygen/hydrogen spray flames in dependence of strain. Moreover, the flame structures for various boundary conditions such as dispersity of the spray and initial equivalence ratio are presented.

2.1 Mathematical Formulation

The mathematical formulation includes both the gas and the liquid processes which are strongly coupled. The present model assumes a thin spray which is represented by the discrete droplet model. Thus, the gas phase equations include additional source terms that account for the interaction of the gas and the liquid. The set of two-dimenstional Navier-Stokes equations is non-dimensionalized [10, 21], and a similarity transformation [10, 21] converts the two-dimensional equations into one-dimensional form. The model includes variable density, the low Mach number assumption, and the boundary layer approximation. The final form of the equations then yields

Mass

$$v = -\frac{1}{\rho}([\alpha+1]f + f_\mathrm{v}) \quad \text{with } f_\mathrm{v} = -\int_0^\eta \frac{1}{\rho}\sum_{j=1}^{J} S_{\mathrm{v},j}\mathrm{d}\eta\,, \quad \alpha = \begin{cases} 0 & \text{planar} \\ 1 & \text{axisymmetric} \end{cases} \tag{1}$$

Momentum

$$\frac{\mathrm{d}}{\mathrm{d}\eta}\left(\rho\mu\frac{\mathrm{d}f'}{\mathrm{d}\eta}\right) + ([\alpha+1]f + f_\mathrm{v})f'' = (f')^2 - \sum_{j=1}^{J}\frac{1}{\rho}\frac{S_{\mathrm{m},j}}{\rho x} \tag{2}$$

Energy

$$\frac{\mathrm{d}}{\mathrm{d}\eta}\left(\lambda\rho\frac{\mathrm{d}\theta}{\mathrm{d}\eta}\right) + C_P([\alpha+1]f + f_\mathrm{v})\frac{\mathrm{d}\theta}{\mathrm{d}\eta} = \rho\sum_{\mathrm{k}=1}^{\mathrm{K}} V_{\mathrm{k}\eta}C_{P\mathrm{k}}\frac{\mathrm{d}\theta}{\mathrm{d}\eta} + \frac{1}{\rho}\sum_{\mathrm{k}=1}^{\mathrm{K}} h_\mathrm{k}\dot{\omega}_\mathrm{k} - \sum_{j=1}^{J}\frac{1}{\rho}S_{\mathrm{e},j} \tag{3}$$

Species Mass Fractions

$$-\frac{\mathrm{d}}{\mathrm{d}\eta}(\rho V_{\mathrm{k}\eta}) + ([\alpha+1]f + f_\mathrm{v})\frac{\mathrm{d}Y_\mathrm{k}}{\mathrm{d}\eta} = -\frac{1}{\rho}\dot{\omega}_\mathrm{k} - (\delta_{\mathrm{ik}} - Y_\mathrm{k})\frac{1}{\rho}\sum_{j=1}^{J} S_{\mathrm{v},j}\,, \quad \delta_{\mathrm{ik}} = \begin{cases} 1 & \text{for } O_2 \\ 0 & \text{otherwise} \end{cases} \tag{4}$$

In the above equations x and y denote physical coordinates in radial and axial directions, respectively, and y is transformed into the nondimensional variable η [10, 21]; u and v are the

corresponding velocities. ρ denotes the gas density, θ is the nondimensional gas temperature. Y_k is the mass fraction of species k, $\dot{w}_\mathrm{k}$ and h_k are their specific chemical reaction rate and specific enthalpy, respectively. Here K different species and J different droplet size groups are considered. c_P is the specific heat capacity at constant pressure, λ the thermal conductivity, and μ the dynamic viscosity of the fluid. Mass, momentum, and energy source terms for droplet size group j are $S_{v,\mathrm{j}}$, $S_{m,\mathrm{j}}$, and $S_{e,\mathrm{j}}$. The ideal gas law $\rho = \overline{M}/\theta$ is used to close the equations, where $\overline{M}$ is the mean molar mass of the gas mixture. The ideal gas law may be replaced by the modified Soave-Redlich-Kwong equation of state [18] or Saur's equation [15] to account for real gas effects. However, for the present conditions at 3 MPa, the real gas effects are extremely small [15], and they are neglected. Note that a real gas equation is used to evaluate the phase equilibrium at the droplet surface as discussed below.

The diffusion velocity $V_{\mathrm{k}\eta}$ is given by

$$V_{\mathrm{k}\eta} = -\frac{\rho D_\mathrm{k}}{\overline{M}} \frac{\mathrm{d}(\overline{W} Y_\mathrm{k})}{\mathrm{d}\eta} - \frac{D_\mathrm{T}}{\theta} \frac{\mathrm{d}\theta}{\mathrm{d}\eta}, \tag{5}$$

where D_k and D_T are the molecular and thermal diffusion coefficients, respectively. Thermal diffusion is considered for the light species H and H_2.

The boundary conditions for the gas phase equations are

$$\eta = -\infty: \qquad f = f_{-\infty} \quad f' = 1; \qquad Y_\mathrm{k} = Y_{\mathrm{k}-\infty}; \qquad \theta = 1 \tag{6}$$

$$\eta = +\infty: \qquad f' = \sqrt{\rho_{-\infty}/\rho_{+\infty}}\,; \qquad Y_\mathrm{k} = Y_{\mathrm{k}+\infty}; \qquad \theta = T_{+\infty}/T_{-\infty}. \tag{7}$$

The total phase exchange terms $\sum_{\mathrm{j}=1}^{\mathrm{J}} S_{v,\mathrm{j}}$, $\sum_{\mathrm{j}=1}^{\mathrm{J}} S_{m,\mathrm{j}}$, and $\sum_{\mathrm{j}=1}^{\mathrm{J}} S_{e,\mathrm{j}}$ appearing in the gas phase equations are obtained through solution of the appropriate terms for each droplet size group j, and they are added up. This requires the solution of the equations to describe droplet heating, vaporization, and motion separately for each droplet size group. In the following equations, the index j is omitted.

Vaporization

$$\frac{d\xi_s}{d\tau} = -1/9 \; c_1 \rho_f D_f \tilde{\mathrm{Sh}} \ln(1 + B_M) \tag{8}$$

Droplet Heating

$$\frac{\partial \theta_l}{\partial \tau} - \frac{\xi}{\xi_s} \frac{d\xi_s}{d\tau} \frac{\partial \theta_l}{\partial \xi} = \frac{1}{\xi_s \xi^2} \frac{\partial}{\partial \xi} \left(\xi^2 \frac{\partial \theta_l}{\partial \xi} \right) \tag{9}$$

Droplet Velocity Equation in x-Direction

$$\frac{\partial^2 x_l}{\partial \tau^2} - \frac{1}{\xi_s} \left(\frac{d\xi_s}{d\tau} - c_1 \mu \right) \frac{dx_l}{d\tau} = c_1 c_2 \mu \frac{df}{d\eta} x_l + c_2^2 \xi_s^2 g_x \tag{10}$$

Droplet Velocity Equation in η-Direction

$$\frac{\partial^2 \eta_l}{\partial \tau^2} + \rho \frac{d\rho^{-1}}{d\tau} \frac{d\eta_l}{d\tau} - \frac{1}{\xi_s} \left(\frac{d\xi_s}{d\tau} - c_1 \mu \right) \frac{d\eta_l}{d\tau} = c_1 c_2 \mu (-([\alpha + 1] f + f_v)) + \rho c_2^2 \xi_s^2 g_\eta. \tag{11}$$

In the above equations, $c_1 = 6\pi (M^\star / M_l^\star)(L_l^\star / L^\star)(t_l^\star / t^\star)$ and $c_2 = t_l^\star / t^\star$.

The boundary conditions are

$$\xi_s(0) = 1; \qquad \frac{\partial \theta_l}{\partial \xi} \mid_{\xi=0} = 0; \qquad \frac{\partial \theta_l}{\partial \xi} \mid_{\xi=1} = \frac{\dot{q}}{3\xi_s}; \qquad \eta_l(0) = \eta_{l0}; \qquad \eta_0'(0) = \eta_{l0}' \tag{12}$$

with

$$\dot{q} = \dot{m} \left[\frac{c_{Pf}}{c_{Pl}} \left(\frac{T^\star}{T_l^\star} \theta - \theta_{ls} \right) / B_T - L \right]. \tag{13}$$

Here $\dot{m}$ and L denote the non-dimensional mass vaporization rate and the enthalpy of vaporization, respectively. B_M and B_T are the Spalding transfer numbers for mass and for energy, respectively.

Droplet number density and source terms of the gas equations are given by

Droplet Number Density

$$n = n_0 s_0 \eta_{l0}' \rho \; / \; (s \eta_l' \rho_0); \qquad s = x_l / u_{l0} \tag{14}$$

Mass Source

$$\frac{S_v}{\rho} = -\frac{M_l^\star}{M^\star} \frac{t^\star}{t_l^\star} \frac{n}{\rho} \, 3 \, \xi_s \, \frac{d\xi_s}{d\tau} \tag{15}$$

Momentum Source

$$-\frac{S_u}{\rho x} = \frac{M_l^\star}{M^\star} \left(\frac{t^\star}{t_l^\star} \right)^2 \frac{n}{\rho s} \left[\xi_s \frac{d^2 s}{d\tau^2} + 2 \, \frac{d\xi_s}{d\tau} \, \frac{ds}{d\tau} - 3 \, \frac{t_l^\star}{t^\star} f' s \, \xi_s \, \frac{d\xi_s}{d\tau} \right] \tag{16}$$

Energy Source

$$-\frac{S_e}{\rho} = \frac{c_{Pf}}{\bar{c_P}} \frac{M_l^\star}{M^\star} \frac{t^\star}{t_l^\star} \frac{n}{\rho} \dot{m} \left(\theta - \frac{T_l^\star}{T^\star} \theta_{ls} \right) \frac{1 + B_T}{B_T} \tag{17}$$

The present formulation implies that each droplet size group, j, maintains its own characteristics.

The description of the gas phase includes a detailed chemical reaction mechanism [43] for the hydrogen/oxygen system that has been used in earlier studies of gas flames for pressures up to 100 MPa [15, 40]. The gas phase transport coefficients are computed from the NASA polynomials which cover the temperature range between 300 and 5000 K. The transport coefficients for the species H_2 and O_2 which are predominantely present at lower temperatures (80 K $\leq$ T $\leq$ 300 K), considerably differ from extrapolated NASA polynomials in this temperature range. Moreover, they show a strong pressure dependence as the critical point is approached. Therefore, the transport properties for the components hydrogen and oxygen are determined from JSME tables [30] for the temperature range between 80 and 300 K and for pressures up to 20 MPa.

For the determination of the pressure and temperature dependent binary composition at the droplet surface, thermodynamic equilibrium is assumed between the liquid and the gas phase [28, 25, 45]. This assumption is more accurate than the use of Raoult's law, since the latter describes the equilibrium of a liquid component and its own vapor not taking into account further species. A modified Soave-Redlich-Kwong equation of state [18] is used to

perform the equilibrium calculation, and the mixing rules of Prausnitz *et al.* [35] are adopted. Moreover, both the pressure and temperature dependence of the heat of vaporization are included in the model [28].

The convective droplet heating and vaporization for the LOX/hydrogen system is modeled using the equations derived by Abramzon and Sirignano [1] which were developed for fuel droplets vaporizing in a convective air stream. In the present study this model is formulated and used for the vaporization of liquid oxygen droplets in a convective hydrogen stream. If the ambient pressure is in the low subcritical range, calculated droplet life times using the reformulated two-film model of Abramzon and Sirignano [1] neglecting convection are in good agreement with computed data of Nicoli et al. [29] for a stagnant surrounding. At pressures beyond 3 MPa there are significant differences in the predicted droplet life times. Experimental data for both stagnant and convective droplet vaporziation for the LOX/H_2 system are not available. Up to date the model of Abramzon and Sirignano [1] for convective droplet heating and vaporization is the most advanced model in the literature and therefore, it is applied here even though it was validated only for fuel sprays in air up to 1 MPa.

Delplanque and Sirignano [12] found that the combustion of LOX in hydrogen at supercritical conditions is affected by droplet stripping. However, under the high subcritical conditions studied here, the ratio $We/\sqrt{Re}$ is well below the critical value of 0.5, and droplet stripping is not included in the present model.

The numerical solution procedure is a hybrid scheme. First the droplet equations are solved. They determine the source terms of the gas equations which are solved next within a cycle of roughly 100 to 1000 iterations depending on the variation of the parameter investigated. The numerical grid is variable and shows a fine resolution within both the vaporization and the chemical reaction zone. The number of grid points goes up to 2000. The time step for the iterations is of the order of 10^{-6} s because of the small time scale of the chemical reaction system. The small Lewis number of molecular hydrogen causes a very broad spray flame, and the computational domain for these flames is large even for the high-pressure situation studied here. Thus, the compuations are very expensive, and the parameter study presented in the next section needs to be evaluated extremely carefully.

2.2 Results and Discussion

The present study concerns liquid oxygen/hydrogen spray flames at high subcritical pressure (p = 3 MPa). The inlet temperature of the liquid oxygen is 80 K, and both the carrier gas hydrogen and the hydrogen gas stream that is directed against the spray has an initial temperature of 100 K.

Figure 1 shows the effect of the variation of the initial equivalence ratio on the flame structure. The initial gas strain rate is 3,000/s, and the equivalence ratio is increased from $E_r = 1$ (left) to 10 (right). Since the oxidizer is liquid in the present system, and increase of equivalence ratio corresponds to a decrease of liquid mass which is associated with a drastical reduction of the width of the spray flame. However, the width of the vaporization zone is almost 2 mm in both the situations. The reduced liquid mass consumes less energy from the gas phase for the vaporization resulting in the elevated gas temperature shown on the RHS of Fig. 1. The two reaction zones that are typical for LOX/hydrogen spray flames at low strain are maintained. The enhanced chemical reactions at high equivalence ratio cause a higher level of H_2O concentration. The reduced level of O_2 mole fraction seen on the RHS of Fig. 1 results from the reduced amount of liquid oxygen mass. Both conditions show a gas diffusion

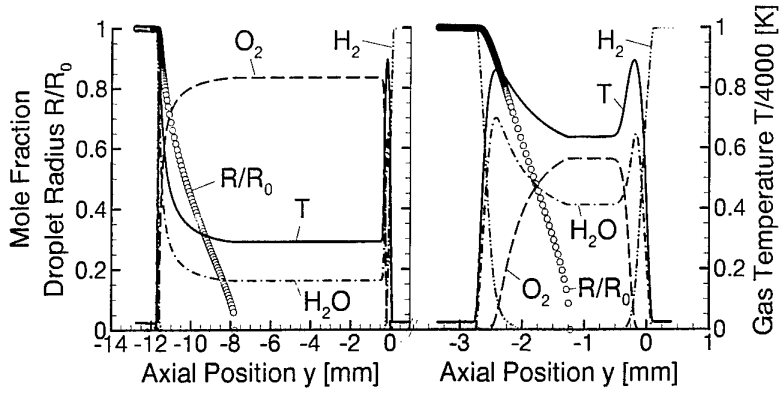


Figure 1: Structure of a liquid oxygen/hydrogen spray flame at low strain: $a = 3,000/\mathrm{s}$; $E_r = 1$ (left) and $E_r = 10$ (right).

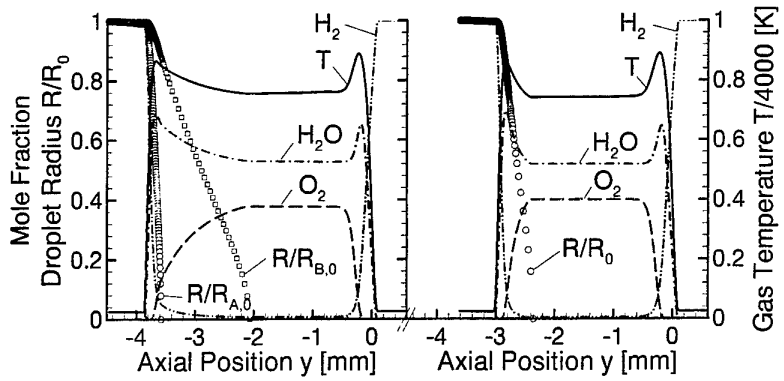


Figure 2: Structure of a bidisperse (left) and monodisperse (right) liquid oxygen/hydrogen spray flame at low strain: $a = 3,000/\mathrm{s}$ and $E_r = 6$.

flame occurring near the gas stagnation plane of the configuration (at $y = 0$ mm) and a spray flame near the injector of the liquid.

Figure 2 shows the effect of dispersity of the spray on flame structure. This condition is discussed in more detail in [37], and it is summarized here for completeness. For the low strain situation here which is studied for the equivalence ratio of six, the principal structure of the spray flames with a bidisperse spray ($R_{0A} = 25\mu$m and $R_{0B} = 10\mu$m) is the same as for the corresponding monodisperse flame structure with the Sauter mean radius $R_0 = 14.3\mu$m. The figure shows that the level of all major profiles as well as gas temperature are the same. The major difference is the width of both the reaction and the vaporization zones. The large droplets of the bidisperse spray have an increased momentum which causes them to deeper

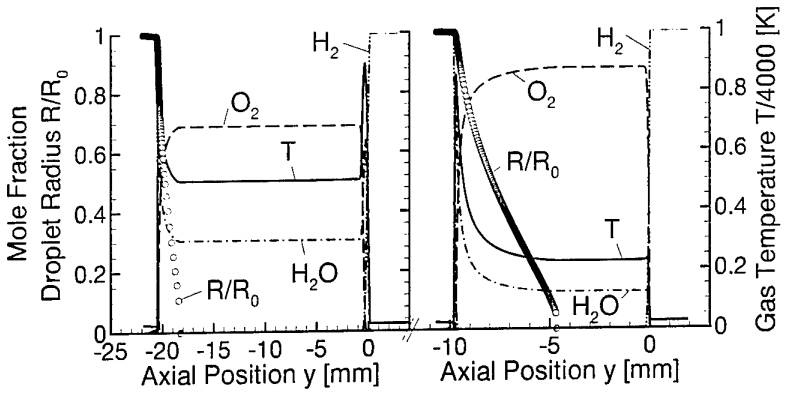


Figure 3: Structure of a liquid oxygen/hydrogen spray flame at low strain: $a = 1,000/\mathrm{s}$ (left) and $a = 5,000/\mathrm{s}$ (right).

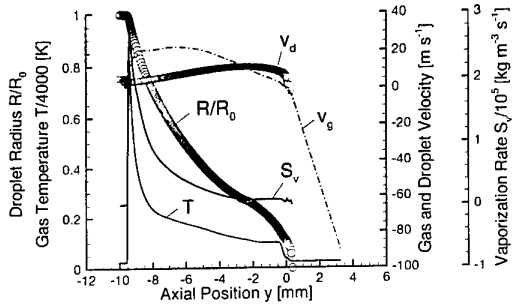


Figure 4: Structure of a liquid oxygen/hydrogen spray flame at elevated strain: $a = 30,000/\mathrm{s}$.

penetrate into the flame and thus to enlarge the vaporization regime by more than a factor of two. This effect smoothens the profiles of all gas phase profiles within the vaporization zone, but it does not alter their order of magnitude. The entire spray flame, however, is only broadened by about 20%. For relatively small values of gas strain rate with no droplet reversal and oscillation, c.f. Figs. 5-7, it may be concluded that the principal structures of the bidisperse and the monodisperse spray flame with the Sauter mean radius are the same.

Figure 3 shows the effect of increasing strain on the flame stucture. The equivalence ratio for the remainder of the study is unity and the initial droplet radius of the monodisperse spray is 25 μm. The gas phase strain rate on the spray side of the configuration is increased from a value of 1,000/s (left) to 5,000/s (right) which causes the breakdown of the reaction zone near the gas stagnation plane. The residence time of the species becomes too small to maintain a flame. This effect is particular to LOX/hydrogen spray flames at high pressure, and it has not been observed in fuel/air sprays at atmospheric pressure. In principal, the hydrogen/oxygen flames are extremely stable [40], and any fuel/air flame would have completely extinguished at this level of strain [21].

A further increase of the strain rate to 30,000/s causes the spray to cross the stagnation plane of the gas phase which is shown in Fig. 4. The gas temperature near the gas stagnation

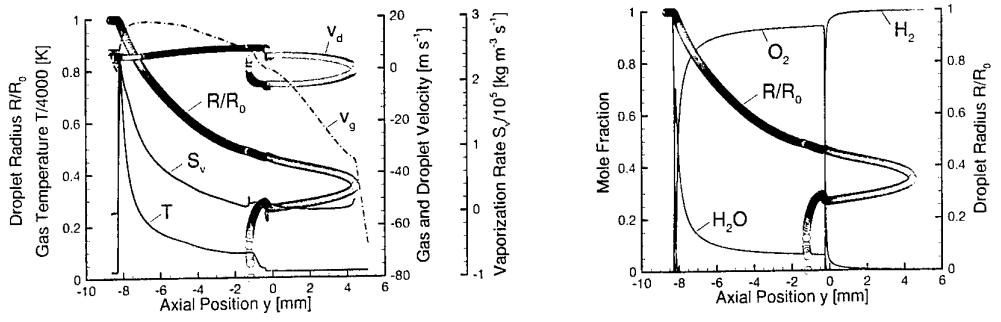


Figure 5: Structure of a liquid oxygen/hydrogen spray flame at high strain: $a = 50,000/\text{s}$.

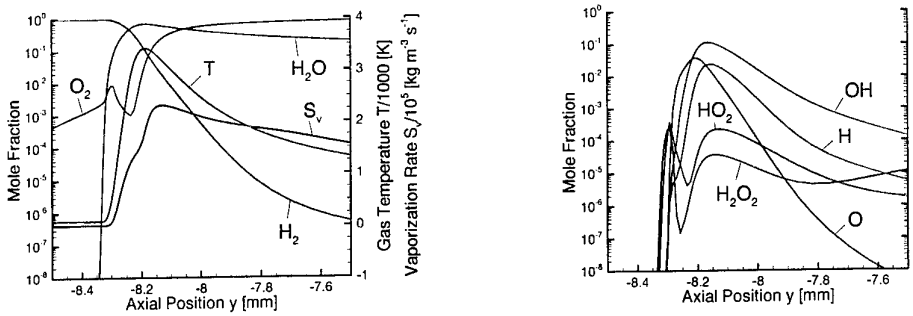


Figure 6: Nonmonotonicity of some profiles in a liquid oxygen/hydrogen spray flame at high strain: $a = 50,000/\text{s}$.

plane is about 400 K and thus, it is high enough to vaporize the liquid but too cold to sustain chemical reactions. The figure also shows the big difference of gas and droplet velocities due to drag.

The droplets start reversing their direction and oscillating around the stagnation plane at higher strain rates. Figure 5 displays the flame structure at 50,000/s where a complex picture of the spray flame structure is obtained. The droplet oscillation causes the spray to show dispersity, that is more that one droplet size group coexist in the same axial direction. Note that the droplets' position differ in radial direction due to their differences in droplet drag within the frame of the similarity analysis. The direction of droplet motion can best be seen from the absolute values of the droplet velocity plotted in the left part of Fig. 5. The droplets change their direction of motion twice so that there are regions in the spray flame where three different size groups coexist. In course of time (corresponding to their Lagrangian way of motion) their size decreases due to vaporization. The profile of the gas temperature shows a second drop near the gas stagnation plane which is associated with the abrupt vaporization of small droplets in this region. The RHS of Fig. 5 displays the profiles of the major species. The reactants move towards each other and meet at the gas stagnation plane without reacting chemically which is due to the low gas temperature. The H_2O profile attains a maximum value close to where the gas temperature peaks, and it follows the profile of the gas temperature.

Figure 6 shows a zoom of the major and minor species mole fractions within the chemical

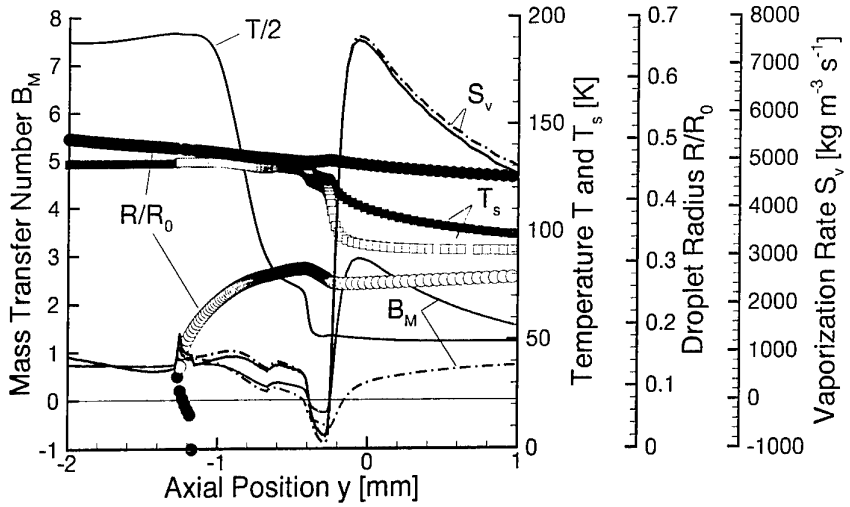


Figure 7: Condensation in a liquid oxygen/hydrogen spray flame at high strain: $a = 50,000/\mathrm{s}$.

reaction zone. It is seen that the oxygen profile is strongly affected by both vaporization and chemical reactions, and it shows nonmonotonicity. This effect is also found at low strain [37] in both mono- and bidisperse spray flames, and it is characteristic for LOX/hydrogen spray flames. The local maximum in the profile occurs in regions of strong vaporization whereas the local minimum stems from chemical reactions overweighing the vaporization process. This phenomenon is typical for the LOX/hydrogen system as mentioned above, and the reason for it to occur is the high chemical reactivity of that system leading to the profile shown in Fig. 6. The production of HO_2 and H_2O_2 comes directly from O_2 or from its direct reaction products as discussed in [37], and their principal profile follows that of the gaseous oxygen.

Another interesting feature of the LOX/hydrogen spray flames at high strain can be seen in Fig. 7. The figure shows a zoom of the situation near the gas stagnation plane. First the gas temperature is shown. Moreover, the figure shows the normalized droplet size (and position of droplets) for the injected droplets as well as for the reversing drops. Also, their droplet surface temperature, T_s, their vaporization rate, S_v, and their mass transfer number, B_M, are displayed.

The mass transfer number $B_\mathrm{M} = (Y_{\mathrm{O}_2} - Y_{\mathrm{O}_2,\mathrm{s}}) \,/\, (1 - Y_{\mathrm{O}_2,\mathrm{s}})$ is negative near $y = -0.25$ mm which means that condensation of the gaseous oxygen occurs. In this region, the vaporization rate of both the droplet groups attains a negative value as well. The profile of droplet surface temperature jumps to a considerably lower value which is associated with the condensation process. The gas temperature attains a value of 100 K which is the boundary condition of the gas side of the configuration – the droplet surrounding is too cold to sustain vaporization.

The flame structure shown in Figs. 5-7 is typical for LOX/hydrogen spray flames at high strain. A further increase of gas strain rate does not change the principal flame structure. The increase of strain, however, is associated with an increase of injected liquid mass, and the droplet momentum is enhanced. The droplet oscillation therefore is more pronounced as strain is further increased, and at a value of 250,000/s, the droplets return to their point of injection. This flame structure, however, is not physically reasonable, and the computations

were stopped. A breakdown of all chemical reactions due to strain may be anticipated if the absolute value of the initial spray velocity is decreased (decreasing the strenght of droplet oscillation) since the spray flame structure strongly depends on this variable [21].

The present study shows that the LOX/hydrogen spray flames are extremely stable, and for the conditions investigated here, the liquid processes (in particular droplet motion) dominates the flame structure at high strain. At low strain rates, however, chemistry is important since flame extinction on the gas side of the configuration is obtained.

The effect of varying initial spray velocity has not been studied here, but its reduction will lead to even more stable flames since the strength of droplet oscillation is relaxed. For too low initial spray velocities, however, the flame will not be sustained and extinctiion will occur at lower strain rate or the flame sits at the burner.

A recent study of ethanol/air spray flames [20] at atmospheric pressure shows that the Sauter mean radius of bidisperse sprays is not suitable to represent flame extinction for sprays where droplet reversal and oscillation occurs. This is also true for the LOX/hydrogen flames studied here. In consequence, a flamelet model for turbulent spray diffusion flames has to represent each droplet size group of the turbulent spray by its own laminar flamelet.

3 PDF-Approach to Turbulent Spray Combustion

Most often two-phase flow combustion occurs in turbulent medium. We want to extend the approach usually developed from the pure gaseous combustion to the spray combustion. Even if the medium is premixed at large scale, the presence of fuel droplets prevents the medium to be perfectly premixed at small scale. To describe the mixing state of two-phase flows accurately, it is important to consider the new behaviour encounter in sprays.

3.1 Study of the New Fluctuations Induced by the Liquid Phase

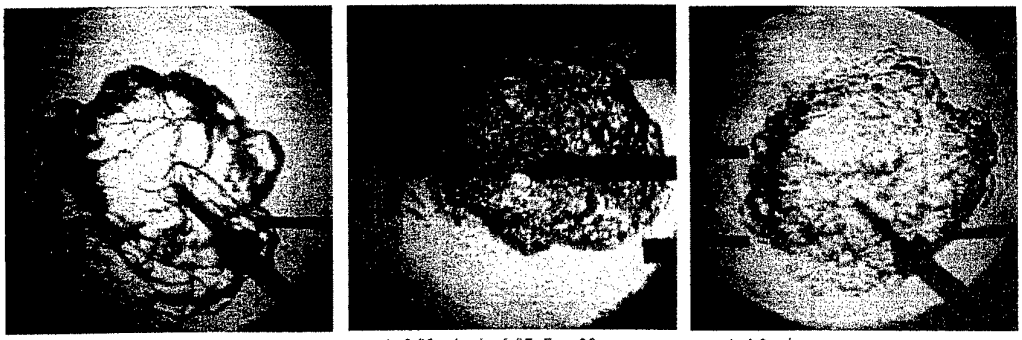


Figure 8: Turbulent spherical flames visualised by schlieren, $\Phi = 1.0$ [3, 6]

One of these characteristic features is illustrated in Fig. 8, where spherical turbulent flames are represented. The combustion takes place in a bomb where a premixed medium is agitated by electric fans and then ignited [3, 6]. The left and the right pictures represent a turbulent flame propagating in a pure gaseous medium. The turbulence due to the fans was measured and the r.m.s. turbulent velocity is equal for the left picture to $u' = 0.6$ m/s and for the right

picture to $u' = 1.2$ m/s. It is well known that the flame is wrinkled by the turbulence, and one could see that the structures on the flame are smaller and more numerous when the turbulence is higher. The central picture represents a case where a part of the fuel is condensed to a spray of liquid droplets, the r.m.s. turbulent velocity is equal to $u' = 0.83$ m/s. It is possible to see that although the turbulence intensity is not at the highest level the flame is more wrinkled. This is an effect of the droplets that we must consider.

The maximum fuel concentration is located at the droplet surface and decreases far away from it. Since the droplets are randomly distributed in space they induce a medium composed by rich pockets around droplets and a poor medium far away from them. These fluctuations of equivalence ratio appears naturally by considering the equations which describe the vaporisation and the mixing:

- Mass equation:

$$\frac{\partial \overline{\rho}}{\partial t} + \frac{\partial \widetilde{u_\alpha}\overline{\rho}}{\partial x_\alpha} = \overline{\rho}\widetilde{\omega_v} \tag{18}$$

- Mixture fraction Z equation:

$$\frac{\partial \overline{\rho}\widetilde{Z}}{\partial t} + \frac{\partial \overline{\rho}\widetilde{u_\alpha}\widetilde{Z}}{\partial x_\alpha} = \frac{\partial}{\partial x_\alpha}\left(\overline{\rho}D\frac{\partial \widetilde{Z}}{\partial x_\alpha}\right) + \overline{\rho}\widetilde{\omega_v}. \tag{19}$$

The first one is the mass equation where the right hand side is a special term, which introduces the vaporisation of the droplets. It is also possible to write the equations for the mass fraction of all the species. By combining them we get the second equation for the mixture fraction Z. This variable is equal to zero in pure air and unity in pure fuel vapour. The last term of this equation is due to the vaporisation and represents the increasing of Z due to the augmentation of fuel mass fraction during the vaporisation. Since the medium is turbulent we have written these equations in an average form. The two vaporisation terms are identical. They are classically modelled by using a stochastic Lagrangian approach to describe the liquid part of the flow [31]. This approach is already implemented in a code based on the KIVA II code [2].

To obtain an evaluation of the equivalence ratio fluctuation intensity we consider the variance of Z, $\widetilde{Z''^2}$. An equation for this equation is classically written for turbulent gaseous flows. The same approach is extended here to the two-phases flow case and leads to the following equation:

$$\begin{aligned}\frac{\partial \overline{\rho}\widetilde{Z''^2}}{\partial t} + \frac{\partial \overline{\rho}\widetilde{u_\alpha}\widetilde{Z''^2}}{\partial x_\alpha} &= -\frac{\partial \overline{\rho}\widetilde{u''_\alpha Z''^2}}{\partial x_\alpha} + \frac{\partial}{\partial x_\alpha}\left(\overline{\rho}D\frac{\partial \widetilde{Z''^2}}{\partial x_\alpha}\right) - 2\overline{\rho}\widetilde{u''_\alpha Z''}\frac{\partial \widetilde{Z}}{\partial x_\alpha} - 2\overline{\rho}D\frac{\partial \widetilde{Z''\partial Z''}}{\partial x_\alpha \partial x_\alpha} \\ &\quad +2\left(\widetilde{Z\dot{\omega}_v} - \widetilde{Z}\widetilde{\dot{\omega}_v}\right) + \widetilde{Z^2\dot{\omega}_v} - \widetilde{Z^2}\widetilde{\dot{\omega}_v}\end{aligned}$$

In this equation the last four terms are characteristics of the vaporisation. The first and the second are due to the vaporisation term in the mass equation. The third and the fourth are due to the vaporisation term in the $\widetilde{Z}$ equation. These terms represent the fluctuations of equivalence ratio due to the vaporisation of the droplets. Two of them are in an unclosed form. Nevertheless by considering the local equation it is possible to rewrite them by using the value of Z at the liquid surface, Z_s [5, 13]:

- $\widetilde{Z\omega_v} = \widetilde{Z_s\omega_v}$,
- $\widetilde{Z^2\omega_v} = \widetilde{Z_s^2\omega_v}$.

We assume that the value Z_s is unique for a given droplet. We can compute its value for each stochastic particle representing the droplets. Both correlations are then computed for each cell of the mesh by summing up the contributions of all the stochastic particles representing the droplets in the computational cell.

3.2 The Maximum Concentration of Fuel Vapour

The second aspect specific of spray mixture that we have to consider concerns the value corresponding to the maximum concentration of fuel vapour. For the gaseous case this value is well known and always corresponds either to an input condition or to an initial condition. But in case of spray the maximum value of fuel mass fraction is located at the liquid surface. It depends on several characteristics of the droplet considered and of the gas around the droplet (e.g. droplet temperature and pressure). Therefore, this maximum is not known and must be determined.

The value Z_s is defined only at the liquid surface. Nevertheless it also corresponds to the initial state of mixing, Z_I, of fluid particles just evaporated. This new variable stays as a characteristic of the vapour fluid particles. Since the maximum of vapour concentration is located at the surface these variables describe also the upper part of the permitted Z domain. Since each droplet has its own characteristics which fluctuate, initial values of Z_i fluctuate. Although it is possible to write an equation for the PDF of Z_I, our first attempt was to describe the effect of this new variable simply by using its mean value, $\overline{Z_I}$. An equation for this value was written in [13]:

$$\frac{\partial \overline{\rho}\widetilde{Z}\overline{Z}_i}{\partial t} + \frac{\partial \overline{\rho u_\alpha}\widetilde{Z}\overline{Z}_i}{\partial x_\alpha} = \frac{\partial}{\partial x_\alpha}\left(\overline{\rho}D_t\frac{\partial \widetilde{Z}\overline{Z}_i}{\partial x_\alpha}\right) + \overline{\rho}\int_0^1 Z_i\widetilde{\omega_{v|Z_i}}dZ_i. \tag{20}$$

We approximate the shape of the PDF of Z by using a shape which is valuable for a Partially Stirred Reactor (PaSR). We assume that this shape is quite general and stays a realistic shape even for practical cases. In order to completely determine the PDF of Z by using this presumed shape we need to know the following parameters: $\widetilde{Z}$, $\widetilde{Z''^2}$, and $\overline{Z}_I$. Both $\widetilde{Z}$ and $\widetilde{Z''^2}$ are usually also used in case of a pure gaseous medium whereas $\overline{Z}_I$ is characteristic for two-phase flows, and it describes the state of mixing at the liquid surface. For pure gaseous flows this value exists but it is just the value of mixture fraction at the fuel entrance, usually this value is equal to unity, and it stays constant.

Figure 9 shows the shapes of the PDF corresponding to different segregation rate expressed in percentage. By definition the segregation rate is equal to:

$$S = \frac{\widetilde{Z''^2}}{\widetilde{Z}\left(1-\widetilde{Z}\right)} \tag{21}$$

It is equal to unity when the medium is completely non-premixed and zero when the medium is perfectly mixed. The left side of the picture corresponds to a value of $Z_I = 1.0$ and the right side to a value of $\overline{Z_I} = 0.8$. This variable strongly influences the shape of the PDF, therefore it must be taken into account.

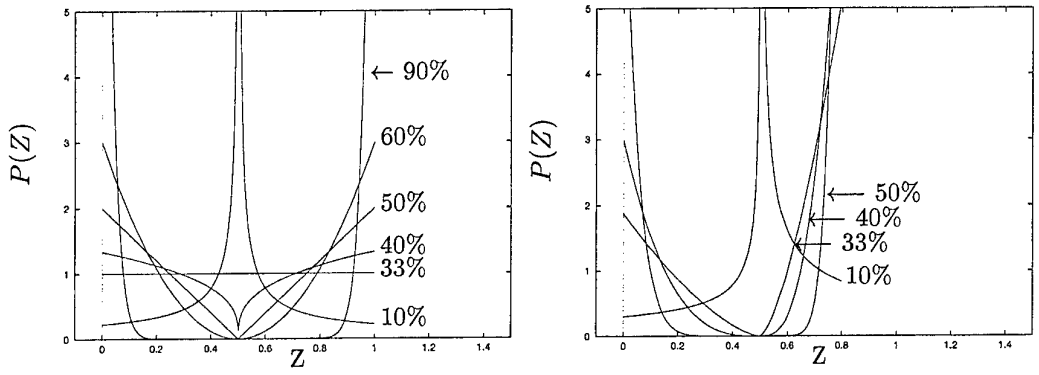


Figure 9: Shape of $P(Z)$ for different values of S on the right side $\overline{Z}_i = 1.0$ and on the left side $\overline{Z}_i = 0.8$.

3.3 The MIL Model

In order to completely describe the medium we must consider the chemistry. If we assumed that the chemistry is infinitely fast, an accurate description of the mixing is sufficient to completely desribe the thermo chemical medium. But in order to take into account interactions between the chemistry and the mixing, we have to use a less restrictive hypothesis. We shall use the MIL model of Borghi and Gonzalez [4], which assumed a sudden chemistry, by adapting it in case of two-phase flows.

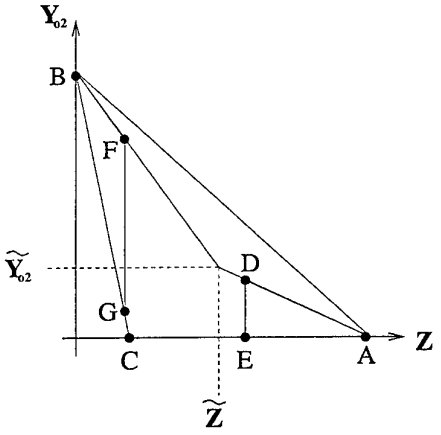
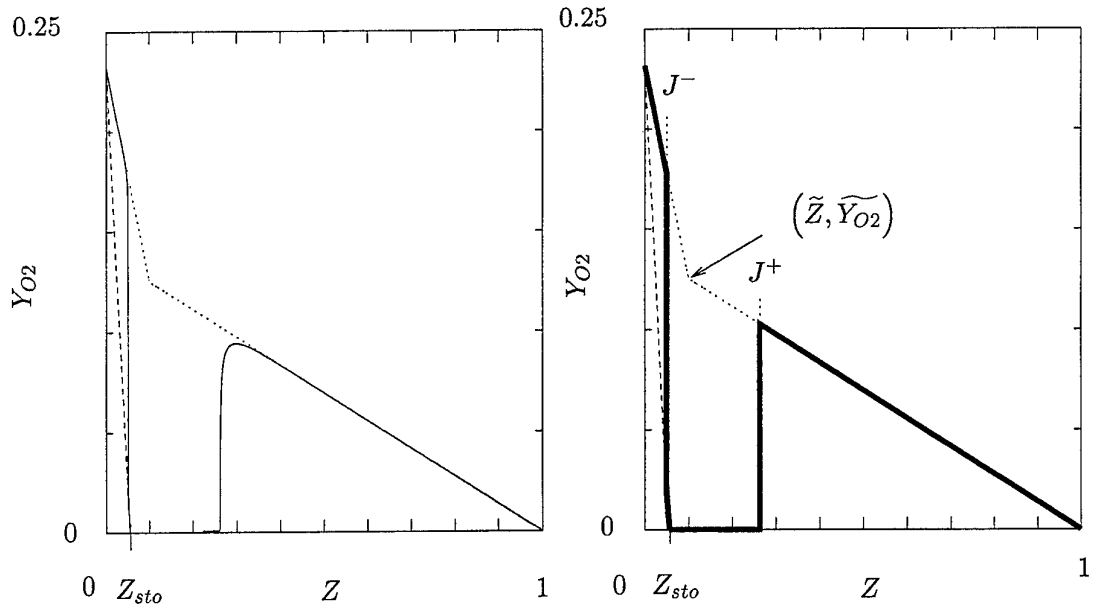


Figure 10: Phase diagram (Z, Y_{O2}), with the skeleton of fluid particle trajectories

In order to completely describe the thermo chemical medium and assuming a unique global reaction, we need to know two variables. One of them is the mixture fraction Z and we choose to take the other one as the oxygen mass fraction Y_{O2}. Since we know the statistics of the Z variable we need either to determine the PDF of Y_{O2} or find a relation between these two variables. For the determination of the relation between Z and Y_{O2} we look at the phase diagram (Z, Y_{O2}) which is represented in Fig. 10. The possible domain of realisation is comprised between the segment AB corresponding to a pure mixing without any



Computed phase trajectory Approximate trajectory

Figure 11: Scheme of the approximation used in the sudden chemistry assumption

reaction, and the two segments AC and CB corresponding to a completely burnt mixture. The simplest relation is to consider that all the fluids particles are completely burnt by assuming an infinitely fast chemistry, then we could define the function $Y_{O2}^b(Z)$ which describes the two segments BC and AC.

Nevertheless this hypothesis is often too restrictive, and it does not permit to include any interactions between the mixing and the chemistry. The MIL model proposed by Borghi and Gonzalez [4] is based on a less restrictive hypothesis, which is sudden chemistry. It means that a fluid particle needs a finite time to be ignited and then burns instantaneously and completely. This idea leads to the trajectory composed by the segments AD, DE, EC, and BF, FG, GC. Along segments:

- AD and BF, a fluid particle does not react, it is only mixed with the whole fields of fluid particles. Globally its characteristics tend to the mean characteristics of the medium.
- DE and FG, suddenly the reaction begins and the particle instantaneously reaches the completely burnt line.
- EC and FC the particle stays along the completely burnt line.

We call $Y_{O2}^{MIL}(Z)$ the function which corresponds to these trajectories. Moreover these segments are completely defined providing that we know the location of the jumps corresponding to the positions of points D, E, F, and G.

As a first approximation the values of Z corresponding to this jump are solutions of the following equation:

$$\tau_Z \frac{\omega_c\left(Y_{O2}, Z, \widetilde{Z}, \widetilde{Y_{O2}}\right)}{\widetilde{Y_{O2}} - Y_{O2}} = O(1). \tag{22}$$

This equation is simply a comparison between the chemical time, here the reciprocal of the global reaction rate, and the mixing time taken proportional to the integral turbulent time scale.

The assumption of the sudden chemistry means that the activation energy of the global reaction is high. Figure 11 presents on the right hand side the trajectories computed in a case of a PaSR with an unique global reaction used to represent the chemistry and the IEM [42] model used to represent the micro-mixing. The chemical reaction rate of the fuel, here the methane, is computed by using an Arrhenius law, with an activation energy given in [44], $E_a = 30$ kcal/mole. The left side corresponds to the approximated trajectories obtained by using the MIL model, which are very close to the computed values.

3.4 Application of the PDF Approach to Represent the Self-Ignition of a Spray of Fuel Penetrating a High Temperature Atmosphere

The whole modelling permits to simulate the self-ignition of a spray of fuel penetrating a high temperature medium. Comparison with the experiment permits us to test the availability of this approach and to discuss the importance of each step of the model.

3.4.1 Description of the Experiment

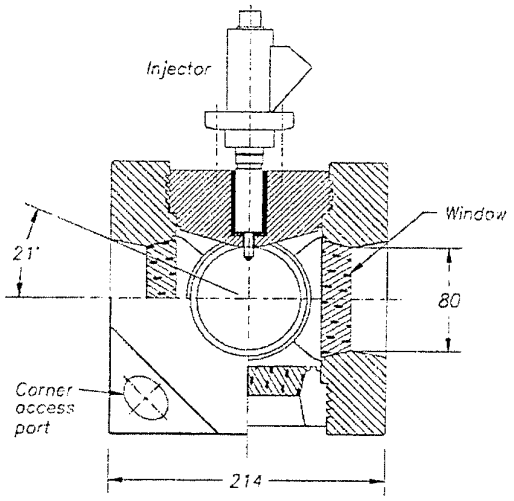


Figure 12: Scheme of the combustion chamber used by IFP

The experiment is conducted by the IFP and is devoted to the self-ignition of a spray of fuel penetrating a high temperature atmosphere. A scheme of the bomb is represented in Fig. 12. This experiment is mainly qualitative and for the moment the combustion is studied just by direct visualisation of the flame. Nevertheless it is interesting since many phenomena interact

with each other, and at least three time scales are involved: one for the evaporation, one for the mixing, and one for the combustion. Moreover, to avoid questioning input conditions concerning the spray, many studies were done by IFP [22]. In particular, experiments were done in a "cold" case, where the bomb is fed with a gas mixture not containing oxygen in order to prevent the combustion. These experiments permit improvement of the atomisation model in the KIVA code, and the results of the computation meets the experimental data for the cold case. The same atomisation model is incorporated in the present computation, with the same constants.

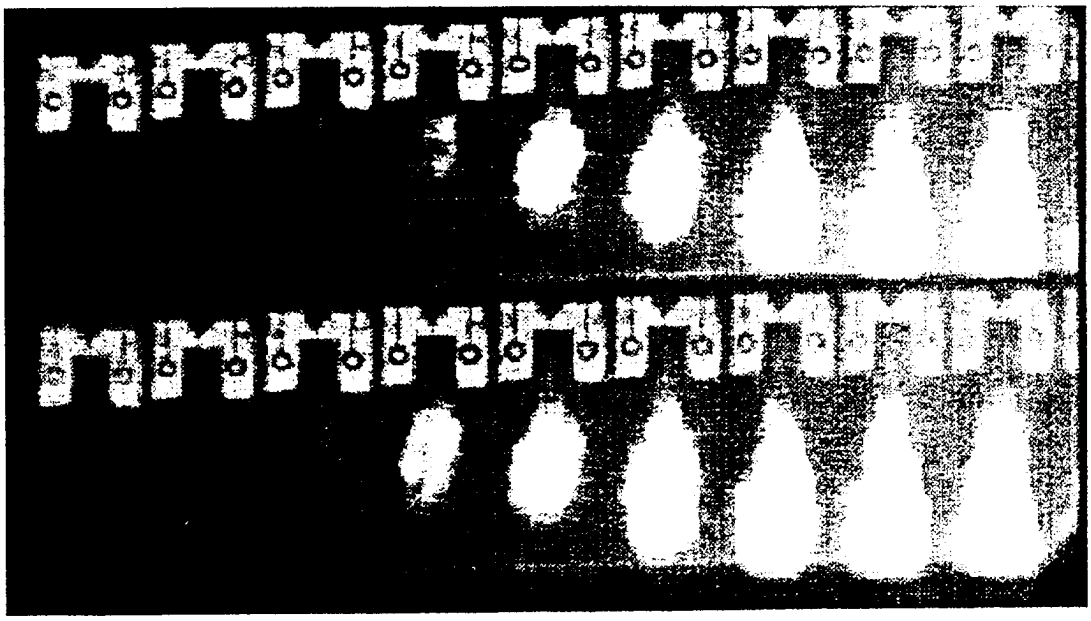


Figure 13: Ignition and propagation of the flame in the IFP bomb. [41]

FIgure 13 presents images of the direct emission of the flame. These images, recorded at about 10,000 images per second, show roughly the 1.5 ms of combustion [41]. The order of these images is from top to bottom and from the left to the right. In this example the first light emitted by the flame appears at the fifth image which corresponds to about 0.5 ms after injection. The delay of the self-ignition of the flame is taken as the delay needed for the appearance of the first perceptible light emission of the flame. Measurements done over many experiments lead to a mean ignition delay time of 0.73 ms. The images of Fig. 13 also permit to see the main features of the flame. The flame is shifted down from the injector for a few millimeters. The ignition takes place on the edge of the spray and then the initial flame grows until it covers completely the spray. Finally the flame is completely developed and it has a "blob" shape.

3.4.2 Utilisation of the Model

Our results will strongly depend on the three phenomena atomisation, mixing, and the chemical reactions. For each submodel there are constants which must be discussed:

The first one concerns the representation of the atomisation and evaporation. Here we do use the models and the constant adjusted by IFP and RENAULT. The liquid phase is classically represented in KIVA by a set of stochastic particles. The initial size of these particles is given by the input injector diameter. Then these particles are represented by parcels of liquid which are atomised. The surface wave instability atomisation (Wave) model of Reitz [36] is coupled to the break-up model (FIPA) which is based on the experimental correlations of Pilch et al. [34, 22]. The mass of dodecane injected is 14 mg and the injection time is 1.92 ms. The injector is supplied with fuel at 80.0 MPa, and liquid fuel temperature at the injector exit is estimated to be 373 K. The initial temperature in the combustion chamber is 800 K and the initial pressure is 6.1 MPa. Figure 14 presents the visualisation of the spray done by the IFP using laser sheet imaging of Mie scattering. They used a technique in which the spray was illuminated by a "step" laser sheet with low intensity in the liquid region of the spray and a high intensity in the vapour region. This picture is taken at 1.22 ms after injection. It is possible to discern the liquid penetration as same time as the vapour penetration. These measurements were performed without oxygen, therefore without combustion, in order to calibrate the model constants.

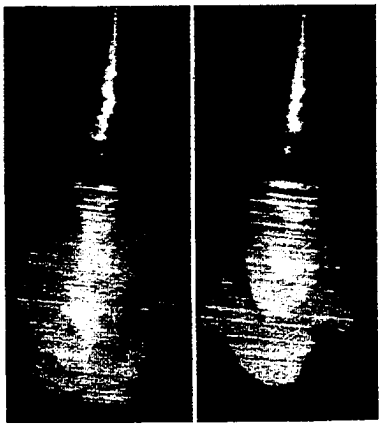


Figure 14: Visualisation at the same time for the spray and of the vapour of fuel, 1.22 ms after injection [22].

- The second constant to be determined concerns the modelling of the scalar fluctuation dissipation. Here we use a classical model:

$$D\frac{\widetilde{Z''}}{x_\alpha}\frac{\widetilde{Z''}}{x_\alpha} = -\frac{\widetilde{Z''^2}}{\tau_Z}. \tag{23}$$

In this model the scalar mixing time τ_Z is taken proportional to the integral turbulent time $\tau_t = k/\varepsilon$, $\tau_Z = C_Z\tau_t$. The constant C_Z is usually taken between 0.5 and 1.5. We do not know if this model is still valuable in case of a spray. In fact during their vaporisation the droplets create fluctuation of equivalence ratio at a length scale corresponding to

Fuel	A	a	b	E_a kcal/mole
Dodecane	3.0^{11}	0.25	1.5	30.0

Table 1: Table of chemical constants used for the dodecane

the mean space interval between droplets. This length scale can be independent of turbulence. The introduction of this new scale in the model could be done in further work, for the moment we use the classical model with $C_Z = 0.6$.

- The last point of the modelling concerns the chemistry. In order to calculate the position of the ignition points in the Z space, we have to estimate the global reaction rate. Although it is possible to build a library of these jump positions as a function of the mixing time, as it was done in [32], here we used a simpler approach. We assumed that the chemistry can be represented by a single step reaction:

$$F + \nu_{O_2} O_2 \rightarrow \nu_{CO_2} CO_2 + \nu_{H_2O} H_2O.$$

Moreover, we assumed that it is possible to compute the reaction rate using an Arrhenius law:

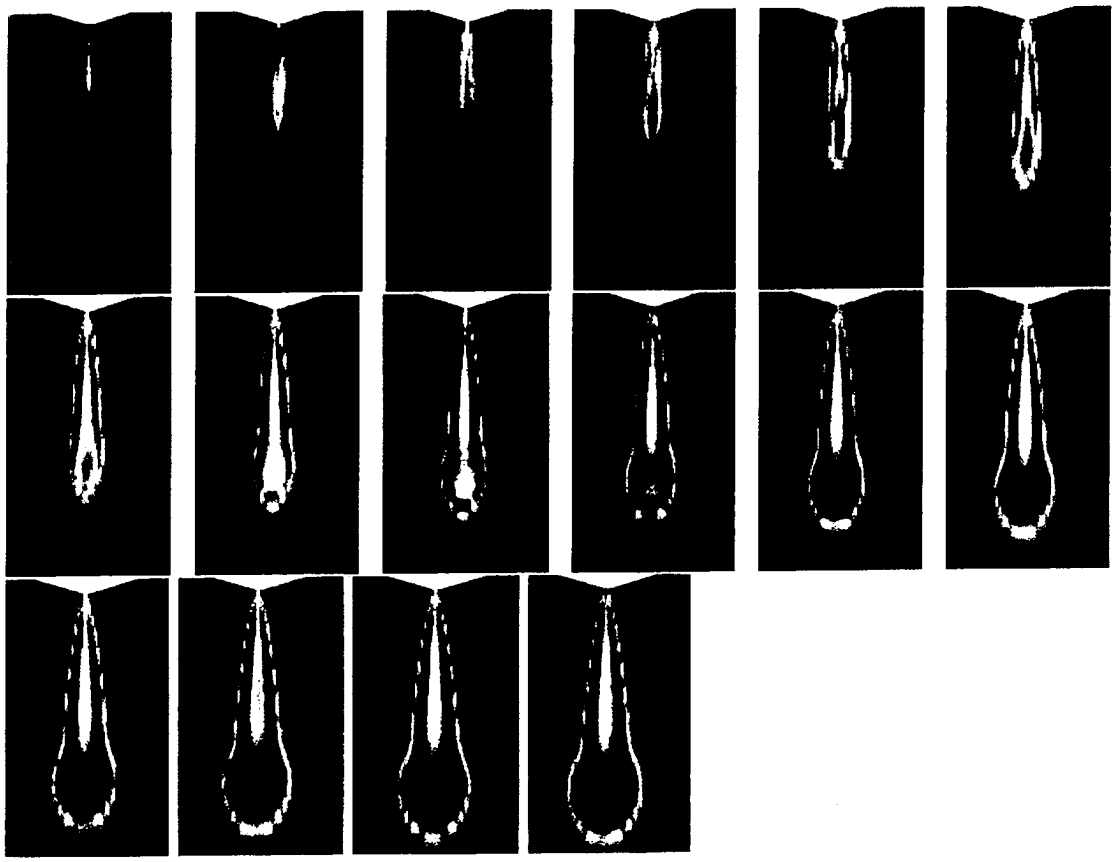
$$\frac{d[F]}{dt} = \omega_c(F) = A\,[F]^a\,[O_2]^b\ e^{-\frac{E_a}{RT}}. \tag{24}$$

The constants would have to be adjusted to find a good self-ignition delay. Nevertheless we do not know such set of constants and we use those proposed by Westbrook *et al.* [44], which were used to find the right burning velocity. The chemical constants used for the dodecane are recapitulated in Tab. 1.

3.5 Results

We have tested this model first in its simplest form, assuming an infinitely fast chemistry. Figure 15 presents the mean temperature field in a centre plane of the combustion chamber at different times from the beginning of the injection. The global shape of the flame is well reproduced. But since there is no chemical time involved this is mainly due to an accurate prediction of the injection, atomisation and mixing. Of course there is no delay of self-ignition, since as soon as the fuel is evaporated and mixed it burns. This could be improved simply by using a model like the *Shell* model at the beginning until the ignition takes place. Later the flame reaches the injector tip, which is in contrast to the experiment. Even with the addiction of a model for the self-ignition, this point will not be improved. Therefore it is necessary to use a model taking account some aspect of the interaction between the chemistry and the mixing.

The same kind of picture is presented in Fig. 16, for a computation using the MIL model. These pictures look like to the photos of the flame. The ignition of the spray takes a certain time and then the flame appears on the edge of the spray. Then the initial flame grows until it completely covers the spray. But even at the end of the injection the flame does not reach the injector tip.



ure 15: Mean temperature field during the first 2 ms, computed by assuming an infinitely
chemistry

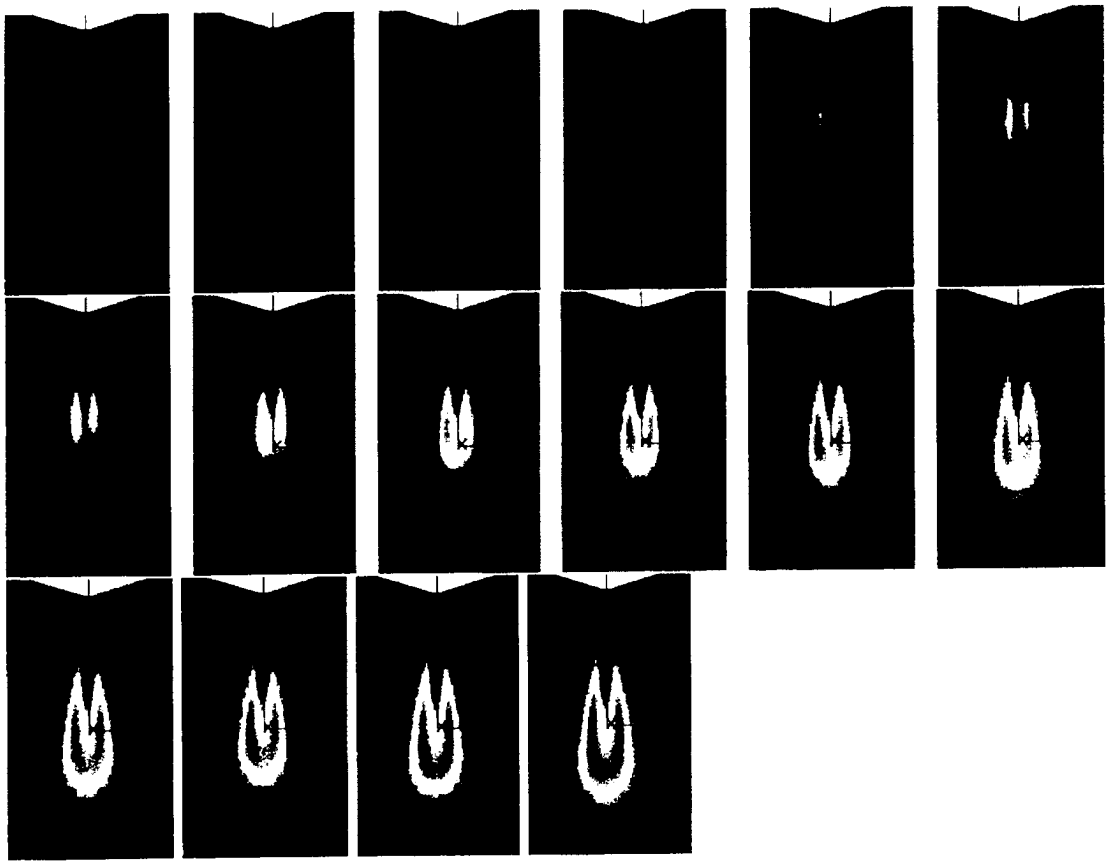


Figure 16: Self-ignition and evolution of the flame computed using the MIL model

Concerning the delay of self-ignition it is difficult to conclude since it is not easy to estimate the temperature corresponding to the first light emitted by the flame. Assuming that the soot is produced and sufficently heated to produce light for a mean temperature equal to 1600 K, the delay of self-ignition in our calculation is about 0.5 ms. This is a good order of magnitude but somewhat too early. This could be improved by modifying the pre-exponential constant, A, in the global chemical reaction rate.

3.6 Discussion

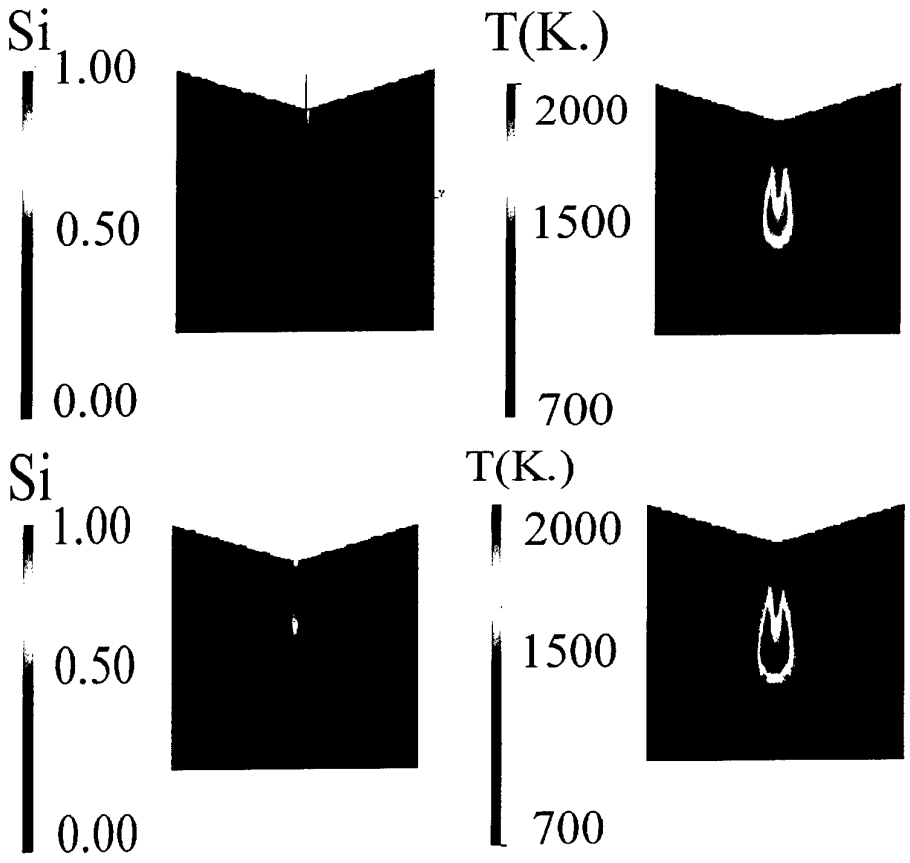


Figure 17: Effect of terms due to the evaporation in the equation of $\widetilde{Z''^2}$. Mean segregation rate, S_i, (left) and mean temperature field (right), without these terms (top) and with these terms (bottom).

Figure 17 presents a comparison of the mean temperature field computed when the new terms induced by the droplet evaporation in the equation for $\widetilde{Z''^2}$ were neglected (top) and when there are not neglected (bottom). These terms are clearly terms of production of fluctuations of Z since the mean segregation is higher for the computation including these terms. There is also an effect on the mean temperature since with these terms the local temperature is 100 K higher. This dependence of the temperature on the segregation rate emphasises the

importance of accurately modelling the scalar dissipation. It is probable that by modifying the constant C_Z we will change the level of temperature.

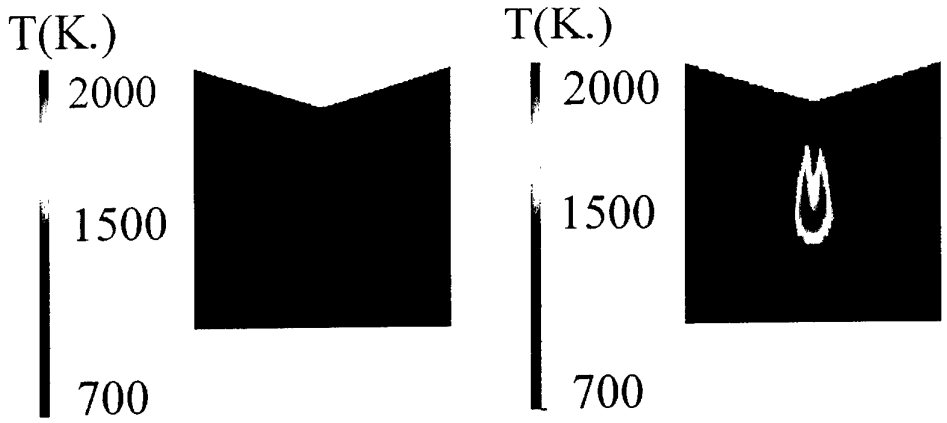


Figure 18: Influence of the new variable $\overline{Z_i}$, at 1.6 ms. $\overline{Z_i}$ is taken constant and equal to unity (left) and $\overline{Z_i}$ is computed by using its transport equation (right).

We have also tested the influence of the new variable $\overline{Z_i}$. We have made a computation where this variable is taken constant and equal to unity as in a pure gaseous case. The terms due to the vaporisation for the scalar fluctuation are take into account. Figure 18 presents the mean temperature field at 1.6 ms after the beginning of injection, on the left side with $\overline{Z_i}$ equal to unity and on the right side $\overline{Z_i}$ is computed using Eq. (20). The difference is obvious: if we do not take into account the variation of this variable the flame does not exist. Figure 19 shows the mean field of $\overline{Z_i}$ in the case where it is computed. The whole field of $\overline{Z_i}$ is considerably lower than unity, which can be explained by the fact that the fuel used here, the dodecane, is a heavy fuel, which under these conditions is far away from boiling. If we look at the phase domain Z, one can see that the equivalence ratio which could permit a good combustion corresponds to an interval of Z near to zero. By computing a low value of the upper limit of the possible Z, we increase the probability to be in this interval, and then we increase the combustion.

4 Conclusions

The paper presents numerical approaches to both laminar and turbulent spray flames. The structure of laminar liquid oxygen/hydrogen spray flames has been studied, and droplet reversal and oscillation has been identified in these flames. There are two phenomena that are unique and typical for these flames: First, the profile of the gaseous oxygen shows nonmonotonicity with distance. This is due to the high reactivity of the hydrogen/oxygen system where the local chemical reaction rates may be larger than the local vaporization rate. Moreover, condensation of the gaseous oxygen is found near the gas stagnation plane where the gas temperature drops due to complete vaporization of droplets, and vaporization no longer occurs.

Moreover, a PDF model has been developed for turbulent diffusion flames where the effect

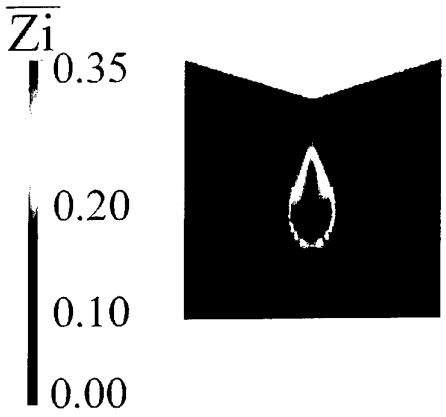


Figure 19: $\overline{Z_i}$ field , at 1.6 ms.

of vaporization has been included in the formulation of the probability density function. The developed approach is generel in the sense that various models for chemcial reactions may be included. The present study considers infinitely fast chemistry and a fast chemistry approach. However, finite rate chemistry as developed and used in Chapter 2 of this paper may be included either within the formulation of a flamelet approach or as a tabulated subroutine containing detailed chemical reaction rates and species profiles.

Acknowledgements

Part of the research presented in Chapter 2 was financially supported by the DARA (DLR Lampoldshausen) and the DFG within the SFB 359.

References

[1] G. Abramzon and W.A. Sirignano. Droplet vaporization model for spray combustion calculations. *Int. J. Heat Mass Transfer*, 9:1605-1618, 1989.

[2] A.A. Amsden, P.J. O'Rourke, and T.D. Butler. KIVA II: A computer program for chemically reactive flows with sprays. *Los Alamos National Laboratory report LA-11566-MS*, 1989.

[3] F. Atzler. *Fundamental studies of aerosol combustion.* PhD thesis, University of Leeds, 1999.

[4] R. Borghi and M. Gonzalez. A lagrangian model for predicting turbulent diffusion flames with chemical kinetic effects. *Combustion and Flame*, 63:239–250, 1986.

[5] Roland Borghi. The links between turbulent combustion and spray. In S.H. Chan, editor, *Transport phenomena in combustion*, volume 1, pages 1–18. Taylor and Francis, 1995.

[6] D. Bradley, M. Lawes, and C.G.W. Sheppard. Study of turbulence and combustion interaction: Measurement and prediction of the rate of turbulent burning. Technical report, University of Leeds, 1994.

[7] G. Chen and A. Gomez. Charge-induced secondary atomization of droplets in diffusion flames of electrostatic sprays. In *Twenty-Fourth Symposium (International) on Combustion*, pages 1531–1539, 1992.

[8] N.-H. Chen, B. Rogg, and K.N.C. Bray. Modelling laminar two-phase counterflow flames with detailed chemistry and transport. In *Twenty-Fourth Symposium (International) on Combustion*, pages 1513–1521, 1992.

[9] Z.H. Chen, T.H. Liu, and S.H. Sohrab. Combustion of liquid fuel spray in stagnation-point flow. *Combust. Sci. and Tech.*, 60:63–77, 1988.

[10] G. Continillo and W.A. Sirignano. Counterflow spray combustion modeling. *Combust. and Flame*, 81:325–340, 1990.

[11] N. Darabiha, F. Lacas, J.C. Rolon, and S. Candel. Laminar counterflow spray diffusion flames: A comparison between experimental results and complex chemistry calculation. *Combust. Flame*, 95:261–275, 1991.

[12] J.-P. Delplanque and W.A. Sirignano. Boundary-layer stripping effects on droplet transcritical convective vaporization. *Atomization and Sprays*, 4:325–349, 1994.

[13] F.X. Demoulin and R. Borghi. Presumed pdf modeling of turbulent spray combustion. *Combust. Sci. and Tech.*, 2000. to appear.

[14] G. Dixon-Lewis. Structure of laminar flames. In *Twenty-Third Symposium (International) on Combustion*, pages 305–324, 1990.

[15] M. El-Gamal, E. Gutheil, and J. Warnatz. The structure of laminar premixed H_2-air flames at elevated pressures. *Zeitschrift fuer Physikalische Chemie*, 214(4):419–435, 2000.

[16] P. Gicquel and L. Vingert. Experimental investigations of cryogenic sprays in combustion. In *ILASS – Europe'99*, July 5-7 1999.

[17] A. Gomez, 1999. Personal Communication.

[18] M.S. Graboski and T.E. Daubert. A modified soave equation of state for phase equilibrium calculations. 1. hydrocarbon systems and 2. systems containing CO_2, H_2S, N_2, and CO. *Industrial and Engineering Chemistry Process Design and Development*, 17:443–454, 1978.

[19] J.B. Greenberg and N. Sarig. *Combust. Flame*, 104:431–459, 1996.

[20] E. Gutheil. Structure and extinction of laminar ethanol/air spray flames. *ZAMM*, 2000. to be submitted.

[21] E. Gutheil and W.A. Sirignano. Counterflow spray combustion modeling including detailed transport and detailed chemistry. *Combustion and Flame*, 113:92–105, 1998.

[22] C. Habchi, D. Verhoeven, C. Huynh Huu, L. Lambert, J.L. Vanhemelryck, and T. Baritaud. Modeling atomization and break up in high-pressue diesel sprays. *SAE Technical paper series*, (970881), February 1997.

[23] C. Hollmann and E. Gutheil. Flamelet-modeling of turbulent spray diffusion flames based on a laminar spray flame library. *Combust. Sci. and Tech.*, 135 (1-6):175, 1998.

[24] C. Hollmann and E. Gutheil. Flamelet-modeling of turbulent spray diffusion flames based on a laminar spray flame library. *Combust. Sci. and Tech.*, 135:175–192, 1998.

[25] K.C. Hsieh, J.-S. Shuen, and V. Yang. Droplet vaporization in high-pressure environments. i: Near critical conditions. *Combust. Sci. and Tech.*, 76:111–132, 1991.

[26] S.C. Li, P.A. Libby, and F.A. Williams. Spray structure in counterflowing streams with and without a flame. In *Twenty-Fourth Symposium (International) on Combustion*, pages 1503–1512, 1992.

[27] S.C. Li and F.A. Williams. In *Twenty-Sixth Symposium (International) on Combustion.* The Combustion Institute, 1996.

[28] R.J. Litchford and S.-M. Jeng. LOX vaporization in high-pressure, hydrogen-rich gas. *AIAA*, (90-2191), 1990.

[29] C. Nicoli, P. Haldenwang, and J. Daou. Substitute mixtures for LOX droplet vaporization study. *Combust. Sci. and Tech.*, 112:55–74, 1996.

[30] JSME Data Book: Thermophysical Properties of Fluids. 1983.

[31] P.J. O'Rourke and A.A. Amsden. Three dimensional numerical simulations of the UPS-292 stratified charge engine. *SAE Technical paper series*, (870597), 1987.

[32] M. Oubounou, M. Gonzalez, and R. Borghi. A Lagrangian model for predicting turbulent diffusion flames with chemical kinetic effects. In *Twenty-Fifth Symposium (International) on Combustion*, pages 1107–1113. The Combustion Institute, 1994.

[33] P. Peters and B. Rogg. *Reduced Kinetic Mechanisms for Applications in Combustion Systems.* Springer, 1993.

[34] M. Pilch and C.A. Erdman. Use of breakup time data and velocity history data to predict the maximum size of stable fragments for acceleation-induced breakup of liquid drop. *Int. J. Multiphase flow*, 13(6):741–757, 1987.

[35] J. M. Prausnitz, R.N. Lichtenthaler, and E.G. de Avezedo. *Molecular Thermodynamics of Fluid-Phase Equilibria.* Prentice Hall, 1986.

[36] R.D. Reitz. Modeling atomisation processes in high-pressure vaporizing sprays. *Atomization and Spray Technology*, 3:309–337, 1987.

[37] D. Schlotz and E. Gutheil. Modeling of laminar mono- and bidisperse liquid oxygen/hydrogen spray flames in the counterflow configuration. *Combustion Science and Technology*, 2000. to appear.

[38] J. Sender, R. Lecourt, M. Oschwald, and O.J. Haidn. Application of droplet-tracking-velocimetry to lox/gh_2 coaxial-spray combustion with varying combustion chamber pressures. In *Proceedings of the 13th Annual Conference on Liquid Atomization on Spray Systems, Florence, Italy*, pages 145–154, 1997.

[39] M.D. Smooke. *Reduced Kinetic Mechanisms and Asymptotic Approximations for Methane-Air Flames.* Springer, 1991.

[40] C.H. Sohn, S.H. Chung, S.R. Lee, and J.S. Kim. Structure and acoustic-pressure response of hydrogen/oxygen diffusion flames at high pressure. *Combustion and Flame*, 115(3):299–312, 1998.

[41] D. Verhoeven, J.L. Vanhemelryck, and T. Baritaud. Macroscopic and ignition characteristics of high-pressure sprays of single-componet fuels. *SAE Technical paper series*, (981069), February 1998.

[42] J. Villermaux. Micromixing phenomena in stirred reactors. pages 707–768, West Orange, 1986.

[43] J. Warnatz, U. Maas, and R.W. Dibble. *Combustion.* Springer, 1996.

[44] Charles K. Westbrook and Frederick L. Dryer. Simplified reaction mechanisms for the oxidation of hydrocarbon fuels in flames. *Combust. Sci. and Tech.*, 27:31 43, 1981.

[45] V. Yang, N.N. Lin, and J.-S. Shuen. Vaporization of liquid oxygen droplets in supercritical hydrogen environments. *Combust. Sci. and Tech.*, 97:247–270, 1994.

"Cryogenic Combustion: Effects of Pressure and LOX Injector Recess"

by

A. Tripathi, M. Juniper,
P. Scouflaire, C. Rolon, and S. Candel,
EM2C-Laboratory, Ecole Central Paris,
and L. Vingert, ONERA,
Palaiseau, France

Paper was not available

Theoretical and Practical Issues of CARS Application to Cryogenic Spray Combustion

V.V.Smirnov
General Physics Institute
Academy of Sciences of
Russia
Vavilov Street 38

W. Clauss, M.Oschwald
Deutsches Zentrum für Luft-
und Raumfahrt e.V.
Langer Grund
74239 Hardthausen

F.Grisch
Département Mesures Physiques
Office National d'Études et de Recherches Aerospatiales
Fort de Palaiseau
91761 Palaiseau Cedex

Abstract

In reactive two phase flows like the cryogenic LOX/GH2 combustion, there is a complex interaction of injection, atomization, vaporization, mixing and combustion processes. It is desirable to develop numerical CFD-codes for better understanding of these combustion chambers. Currently, there is a need for experimental data that are reliable and that can be used to develop a better understanding of the different mechanisms controlling the various processes. In particular, knowledge of combustion species and temperature is necessary for accurate modeling of cryogenic propellant reaction mechanisms and their effect on the macroscopic behavior of the propellant.

In this report, the general potential of Coherent Anti-Stokes Raman Scattering (CARS) as a diagnostic tool not only for temperature measurement is demonstrated.

Presented is basic research ranging from the measuring of spectral line shape and line broadening to the temporal distribution of molecular energy between the internal degrees of freedom as well as special applications in high pressure cryogenic combustion, where all the data from the basic research are needed for high accuracy measurement.

1. Fundamental basis for CARS diagnostics of chemical composition, temperature and density

The achievements in nonlinear optics and quantum electronics have significantly broadened concepts of the interaction of emission (light) with matter, thereby opening the way on a number of fundamentally new spectroscopic techniques based on the physical principles of nonlinear optical phenomen that employ tunable lasers as the excitation sources.

Prominent nonlinear spectroscopic techniques utilizing the third order nonlinear susceptibility resonances when the frequency difference of the interacting fields lies within the range of frequencies of the Raman-active transitions of the test medium include the stimulated Raman scattering technique proposed by B. Stoicheff et al. with amplification of the Stokes waves [1] and the case with attenuation of the anti-Stokes waves [2] that was than further developed in the studies by A. Owyoung [3-5], A. Lau et al. [6,7] and E. Yeung [8] together with the ellipsometry and coherent scattering polarization spectroscopy method for Raman resonance developed by S.A. Akhmanov at al. [9, 10] and the quadratic Kerr effect induced in Raman resonance as developed by R. Hellwarth [11].

CARS (Coherent Anti-Stokes Raman Scattering) is a direct four photon parametric interaction process in a medium with the third order nonlinear suszeptibility $\chi^{(3)}(\omega)$ [12]. Three photons of frequencies ω_1, ω_1 und ω_2 are send into a probe volume in this medium where a fourth photon ω_{CARS} is generated. This new wave results from the inelastic scattering of ω_1 by the molecular vibrations of the third order nonlinear suszeptibility $\chi^{(3)}(\omega)$ which are coherently and resonant driven by the waves ω_1 and ω_2 if the frequency difference $\Delta\omega = \omega_1 - \omega_2$ is equal to a Ramanactive molecular transition of a specific molecule.

All other molecules present in the probe volume emit a nonresonant CARS signal which is not just an offset of the resonant signal, but interferes with it. Therefore, the nonresonant signal has to be taken account of in the CARS theory.

The directly-measured quantities (scattered emission power, its polarisation or phase state) are characterized by the dispersion of the squared modulus determined by experimental conditions and the linear combination of $\chi^{(3)}$ tensor components as a function of detuning $\omega_1 - \omega_2$, and bear information on the microscopic characteristics of the medium, including the cross-sections, the frequencies and the characteristic spectra of different molecules, the linewidths of the transitions and gas density, the function of density population of the probe energy levels and in case of equilibrium of the media-about the temperature, etc.

The spectral intensity of the CARS signal is given by the equation:

$$I_{CARS}(\omega) = I^2{}_{\omega 1} \bullet I_{\omega 2}(\omega) \bullet \left|\chi^{(3)}(\omega)\right|^2 \bullet L^2 \bullet ph$$

(I = laserintensites, L = length of probe volume, ph phasing factor, takes into account the conservation of impulse)

The third order nonlinear suszeptibility $\chi^{(3)}(\omega)$ has a resonant and a nonresonant part:

$$\chi^{(3)}(\omega) = \chi_R{}^{(3)}(\omega) + \chi_{NR}{}^{(3)}(\omega)$$

Deducing the temperature from experimental CARS spectra is done by analyzing the spectral profile formed by the different intensities of the excited rovibrational transitions of the molecules.

The resonant suszeptibility $\chi^{(3)}(\omega)$ is calculated for the specific molecule as a function of temperature. Here, specific molecular data like polarizability, transition probability and linewidth broadening with pressure effects must be included.

A convolution taking into account the influences of the CARS apparatus, the apparatus function, gives a library of theory spectra. This library has a multidimensional grid of spectra sorted after temperature, pressure and $\chi_{NR}^{(3)}(\omega)$ - value.

The experiment spectra now are compared to the theory spectra using the Marquard least squares fit method. The CARS code searches for a minimum of the sum of the least squares. The temperature, pressure and $\chi_{NR}^{(3)}(\omega)$ - values of the theory spectra with the best fit to the experimental spectral are then attributed to the experiment.

The accuracy of the temperature fit depends on the precise simulation of the CARS spectra.

In a first approximation, this can be calculated by summing isolated line contributions. This requires knowledge of the molecular parameters and in particular the Doppler and pressure broadenings of the rotational lines.

However, when the pressure increases so that adjacent lines are pressure broadened to an extend that they overlap, such a simple model does not predict that the spectral shape will collapse to a narrower bandwidth. The overlap refelcts rotational energy transfer between lines which causes a drastic change in the shape of the Q-branch. Simulation of this so called 'motional narrowing' phenomenon requires sophisticated models.

In order to employ CARS as a diagnostic tool at high pressure technical combustion, much basic research is needed to have the data for such models.

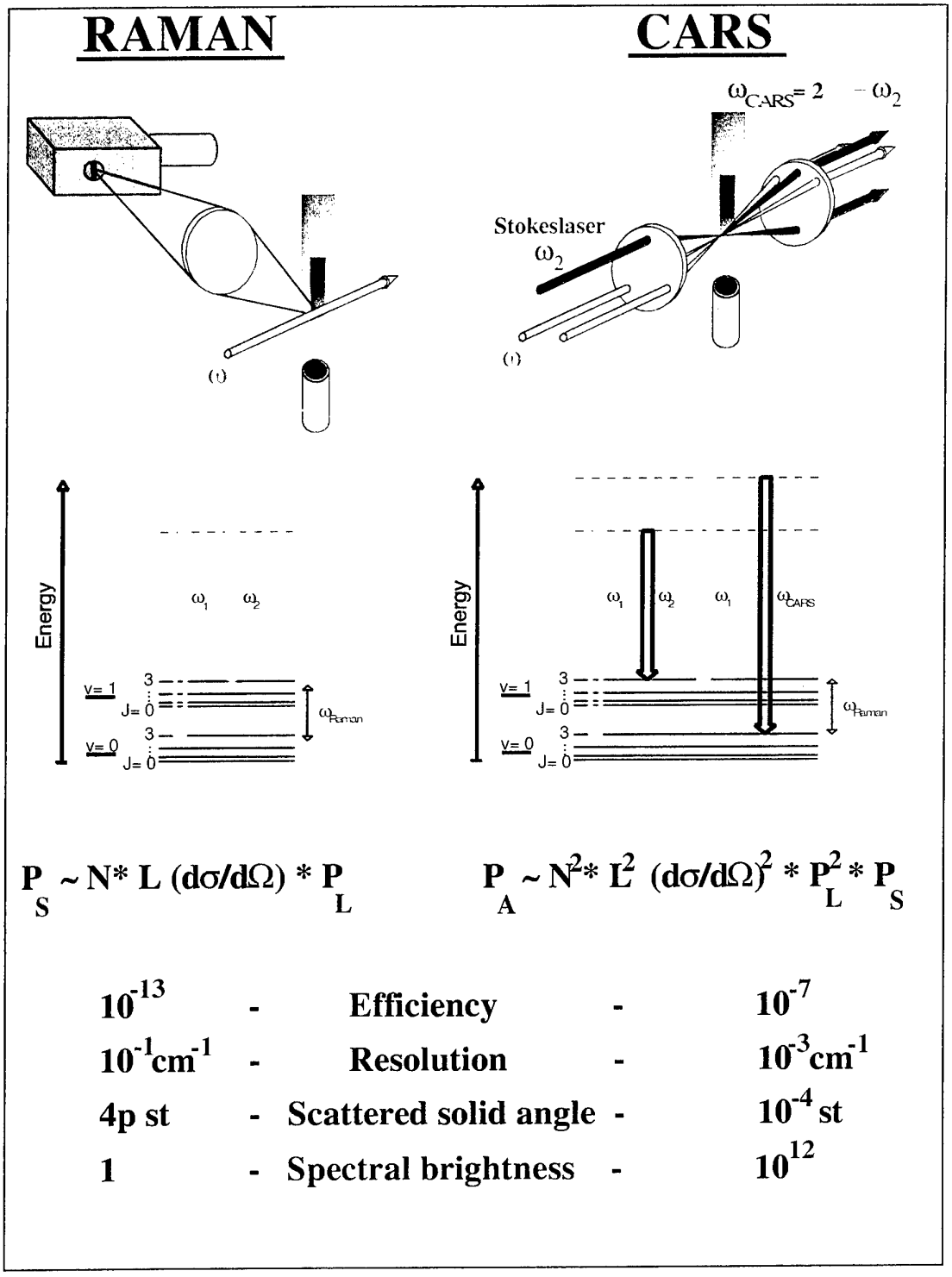


Fig. 1
Comparison of spontaneous Raman effect with CARS. The main advantages of CARS are listed.

1.1 Characteristic features of Coherent Anti-Stokes light scattering method

- Universality: the CARS spectrometers, using broadband Stokes lasers, allow to cover the whole frequency range of the vibrational-rotational transitions of molecules with a single laser shot.
- Locality: The scattered emission intensity I_{CARS} is proportional to the quantity $I^2_{\omega 1} \bullet I_{\omega 2}(\omega) \bullet \left|\chi^{(3)}(\omega)\right|^2$. By using high peak power pulsed lasers for $I_{\omega 1}$ and $I_{\omega 2}$,transformation factors exceeding those obtained in Spontaneous Raman Scattering (SRS) by 4-8 orders of magnitude are possible. Focussing the laser beams creates a strong nonlinear dependence of the scattering process efficiency on the pump field intensity and makes it possible to obtain information on the parameters of the medium with high spatial resolution (20×20×500 μm).
- Brightness: The anti-Stokes emission is coherent, propagates in the direction $2k_1$-k_2, as established by the pump wave vectors, and has a divergence of ~10^{-6} steradians, determined by the pump laser emission divergence. The emission brightness in CARS exceeds that of SRS by a factor of 10^{10}-10^{14} times. Both these facts make it possible effectively collect the scattered CARS emission and to significantly simplify its detection in investigating processes accompanied by powerful self-luminescence like discharge, combustion, chemical reactions, etc. Only two small windows positioned opposite to eachother in line of sight are needed in a combustion chamber.
- Selectivity: At the same time that the equipment resolution that may be achieved using continuous tunable lasers is 0.0001 cm^{-1}, the actual resolution is limited by Doppler broadening at the frequency of the test transition (~0.01 - 0.002 cm^{-1}). Due to this it is possible to obtain a new information about structure of energy levels and spectral data for molecules that was previously inaccessible for Raman-active transition.
- High time resolution: use of broadband CARS spectrometer with laser pulse duration of about 3 ns and single pulse signal detection with multichannel detectors, allows to record panoramic scattering spectra during a single laser pulse.
- Limitation: One of important drawback of the CARS process as a spectroscopic method is caused by the nonresonance (at these transitions) contribution ($\chi^{(3)}_{NR}$) to the susceptibility from remote electron resonances. Intensity fluctuations in this background caused by amplitude instabilities in the pump sources may are usually not significant, since at exact resonance the $\chi^{(3)}_{NR}/\chi^{(3)}_{max}$ ratio is ~10^{-2} - 10^{-3}. However, investigating low concentration molecular fragments or those having small scattering cross-section this fact significantly limits the applicability of the method. In diagnostics of turbulent combustion, were species concentration changes from one laser shot to the next, with the possibility that the resonant molecule is of low concentration, this nonlinear background must be included in the CARS modeling. Today some number of methods have been developed that make it possible to significantly reduce the contribution of $\chi^{(3)}_{NR}$ due to the difference in the polarization, phase or temporal properties of the signal caused by the resonance and nonresonance parts of the susceptibility. The nonresonance signal level here been reduced a factor of 10-10^3.

1.2 Selected examples of basic research aimed to obtain information necessary for diagnostic application.

Depending on the processes to be studied, different kind of molecules can be used as a probe molecule to determine gaseous parameters. In connection with this the knowledge of molecular spectral data as well as linewidth shift and broadening are very important. With this aim, the unique high-resolution CARS spectrometers have been created at GPI [13]. With this device the extensive information on the structure of vibrational-rotational energy levels of many molecules has been obtained, supplying the necessary database for quantitative analysis and gas thermometry [14].

A fully resolved spectra of the ν_1 band Q-branch spectra CH_4 is presented in fig.2. For comparison on upper trace also presented spectra, obtained by means conventional Raman technique.

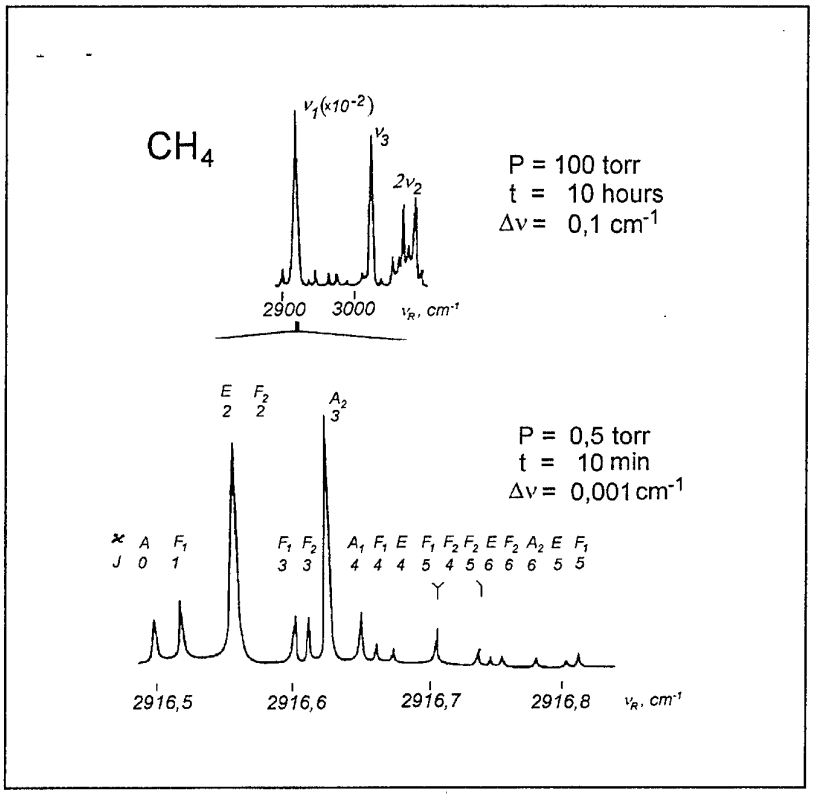


Fig. 2
the ν_1 band Q-branch spectra of CH_4

The collisional dynamic of molecules has been studied through the investigation of the spectral line broadening in the gas pressure range from 0.01 to 100 atm [14] with high precision of the spectral line shape measurements, and the observation of Dicke and "collisional" narrowing effects. Fig.3 presents results of Q_0 and Q_2 lines investigation for D_2 molecule occurring the region with Dicke narrowing effect.

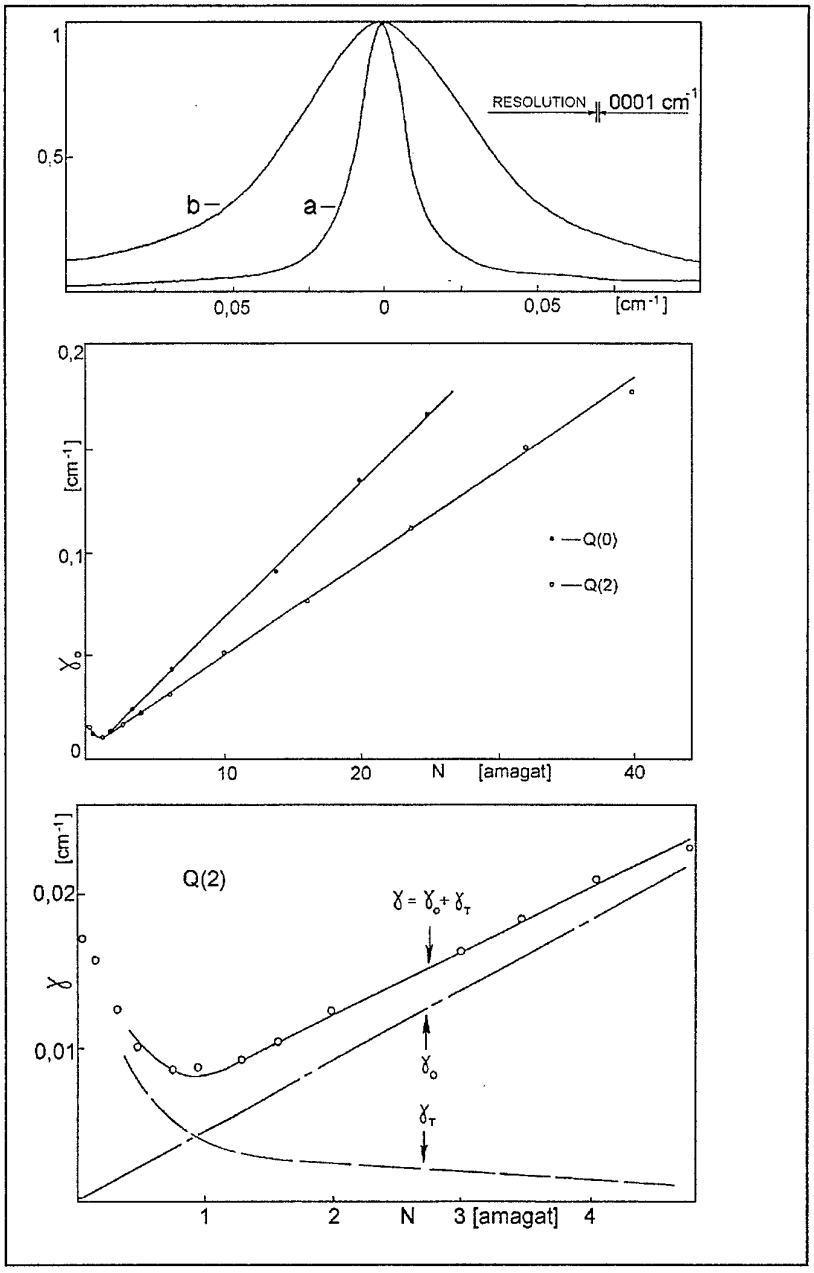
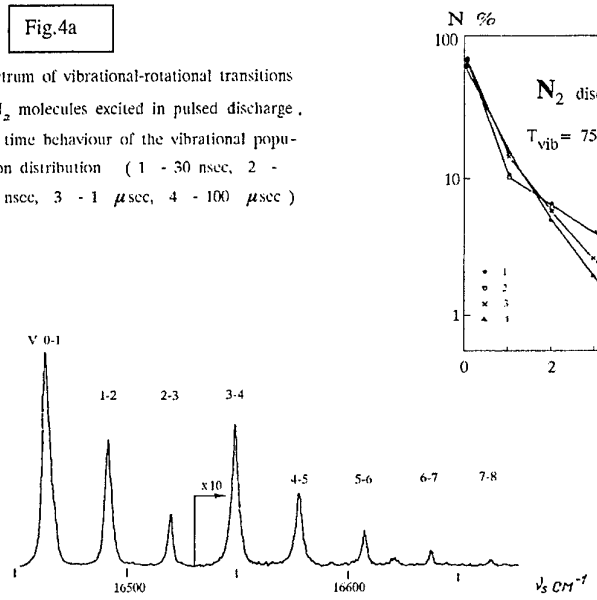


Fig. 3
Collisional narrowing of spectral lines at high pressure

The developed techniques of pulse excitation and CARS probing (with temporal resolution of 10^{-8} sec) proved to be very effective for the studies of temporal transformation of the distribution of molecular energy between the internal (vibrational and rotational) degrees of freedom, and of the level-to-level kinetics of excited molecular systems [15]. It is sufficient to mention that the rate constants of vibrational-vibrational exchange of N_2 and SF_6 have been measured, these constants being respectively, the lowest and the highest of the rates of these processes (as known from the literature). As an illustration Fig.4a shows the spectra of the vibrational-rotational transitions of nitrogen molecules, excited to a non-equilibrium conditions in a discharge, along with temporal behaviour of distribution function off the populations of vibrational levels with vibrational temperature of T_V=7500 K. The spectra with resolved (presented on fragment of Figure 4b) allow to measure in the same place of the discharge the rotational distribution function and to obtain the rotational (at 100 torr translational) temperature Tr = 328 K.

Fig.4a

Spectrum of vibrational-rotational transitions of N_2 molecules excited in pulsed discharge. The time behaviour of the vibrational population distribution (1 - 30 nsec, 2 - 100 nsec, 3 - 1 μsec, 4 - 100 μsec)



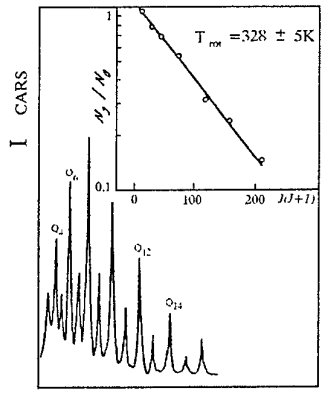


Fig.4b

Fragment of CARS spectra V (3→4) with resolved rotational structure. The insert shows the population distribution of the rotational states of N_2 molecules in discharge.

Fig.5 presents the results of remote nonperturbing measurement of the distribution of local value of temperature and static pressure along the axis of a supersonic jet of nitrogen. Here M is the Mach number, T - temperature, p - pressure, the solid line show the calculations, using the gas-dynamic functions for ideal gas. The accuracy of measurements was 1% for temperatures and 2% for pressures.

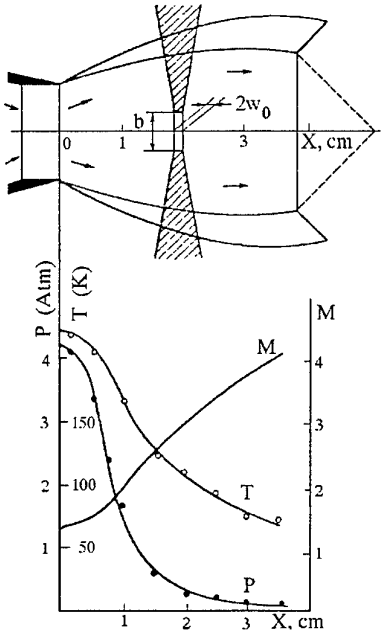


Fig. 5

CARS-probe configuration for a supersonic flow (above) and the temperature and pressure distribution in the flow (below).
b = 300 μm, $2w_0$ = 30 μm.

The characteristic features of strongly cooled (down to 10 K) supersonic jets with different values of Knudsen number also were studied. The Knudsen number values being changed, the transformation of the flow type from the rotational non-equilibrium (rotational temperature is not equal to translational and moreover were different for odd and iven spin modifications of a nitrogen molecules see fig. 6) to the type with strong condensation processes was experimentally observed.

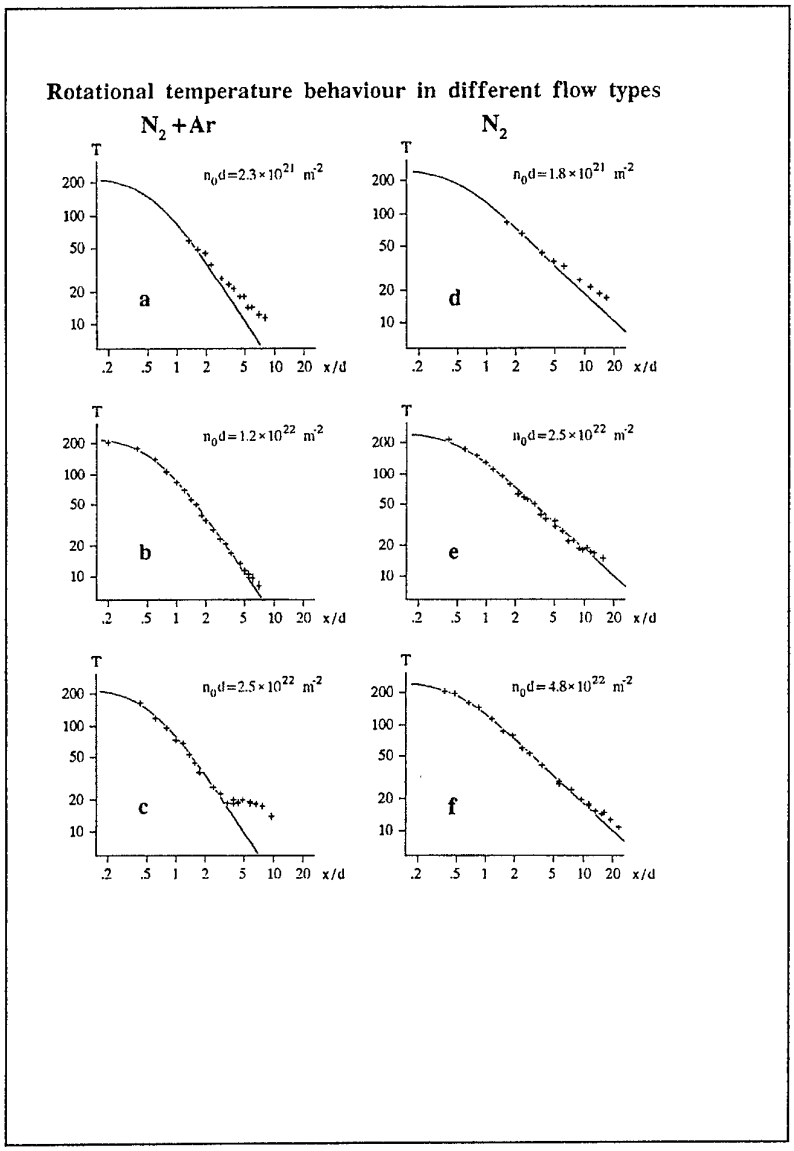


Fig. 6
Rotational nonequilibrium at flows of different Knudsen number

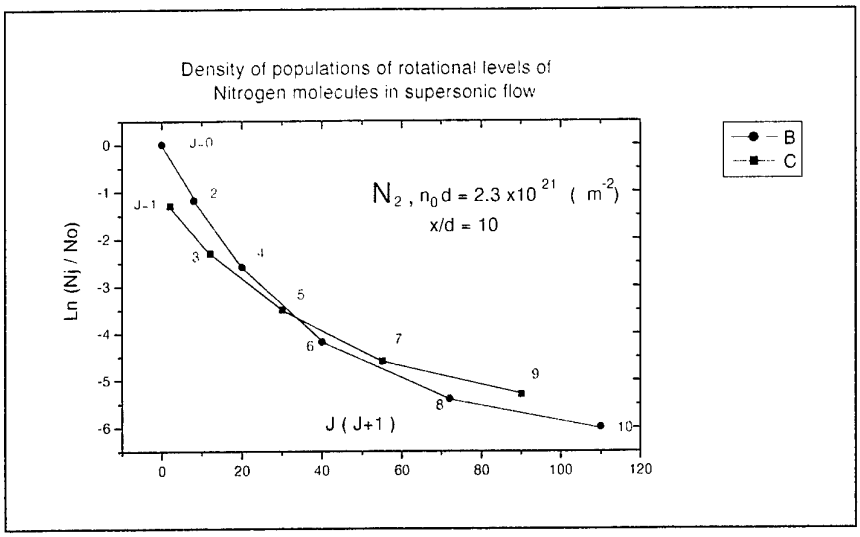


Fig. 7

2. CARS as a diagnostic tool for combustion thermometry

Temperature measurements in combustion by means of nonlinear optical techniques can provide investigations of turbulence fields existing in real scale technical combustors. For this, pulsed lasers must be employed that allow the recording of CARS spectra from each single laser shot of about 10 ns pulse duration. Of special importance is the question of the precision achievable in such a single laser shot.

The serious problem of combustion thermometry by CARS is to find the compromise between the sensitivity, the signal-to-noise ratio, the time of data acquisition, and the precision of temperature measurements. Due to the nonlinear and coherent nature of CARS process, beatings of pump lasers frequency components lead to strong fluctuations in the intensity distribution of a CARS spectrum which in turn result in errors in temperature determination. The only way to overcome this difficulty is to perform some sort of averaging: either over time – that means to perform accumulations of consecutive CARS signals, or spectral averaging. The latter approach allows not to loose available temporal resolution and to achieve reasonable precision in single-shot temperature measurements which is basically necessary for successful employment of CARS at turbulent combustion. There exist two ways to perform spectral averaging: one is to average the measured parameters over the molecular transitions in a broad frequency range (broadband CARS); the other – to use many spectral components of two broadband pump lasers for averaging over the spectrum of the driving force, exciting Raman-active molecular transitions. This approach, first proposed for vibrational CARS [16] and later on developed for rotational CARS [17-19], is known as the *d*ual-*b*road*b*and CARS (DBB CARS) technique.

In most of the previous flame temperature measurements by CARS nitrogen was used as a probe gas. Due to the significant number of rotational components in the Q-branches there is an efficient averaging over the spectra of

molecular transitions (see, e.g. [20-22]). Therefore, broadband CARS spectroscopy can be employed at N_2 molecules with precision of ~ 3% RSD for single shot temperature measurements.

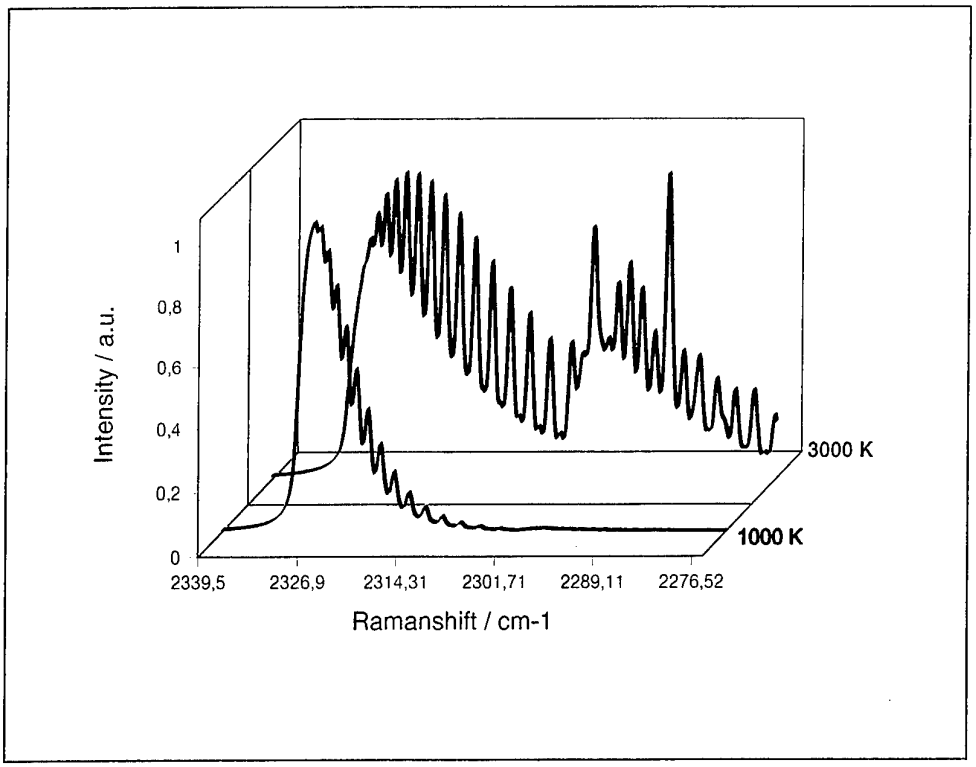


Fig. 8
Temperature signature of nitrogen (simulation) for 1000 K and 3000 K

3. CARS thermometry at the H_2 and H_2O molecules

3.1 Hydrogen

In hydrogen-oxygen combustion hydrogen may be used to measure temperature [23,24]. However, spectral averaging over the transitions is not so efficient for broadband measurements using H_2, because only a few narrow lines are observed in a CARS spectrum even at temperatures as high as 2000-3000 K, that greatly limits attainable precision of temperature determination.

One approach to eliminate this problem, which can be attributed to the stochastic dyelaser mode structure, is to recored this dyelaser structure for each single shot and then use this signal to normalize the corresponding CARS spectra from the combustion. For this 'online referencing', an argon filled cell is placed in the laser beam path. The nonresonant signal from argon represents the dyelaser mode structure transformed to the anti-Stokes side of the spectrum. The online referencing requires two spectrographs and detectors.

Another approach is Dual Broadband CARS, where two Stokeslasers are employed to get a more effective averaging over the laser driving fields. Especially if the Stokeslasers are modeless lasers, which eliminates the noise due to mode competition and reduces the noise in energy and spectral shape of CARS, caused by amplitude and phase fluctuations of the laser fields, a very efficient averaging over the spectra of laser radiation can be achieved. This greatly improves the precision of temperature measurements at the hydrogen molecule and ~ 3% RSD are also possibly for H_2.

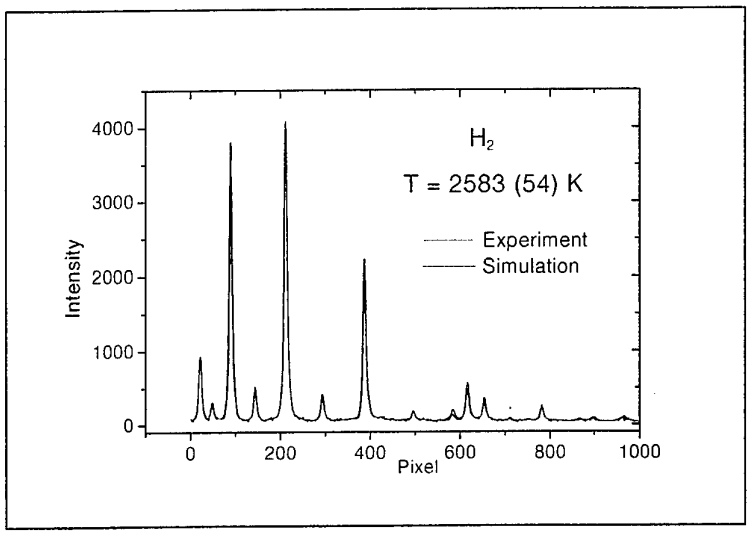
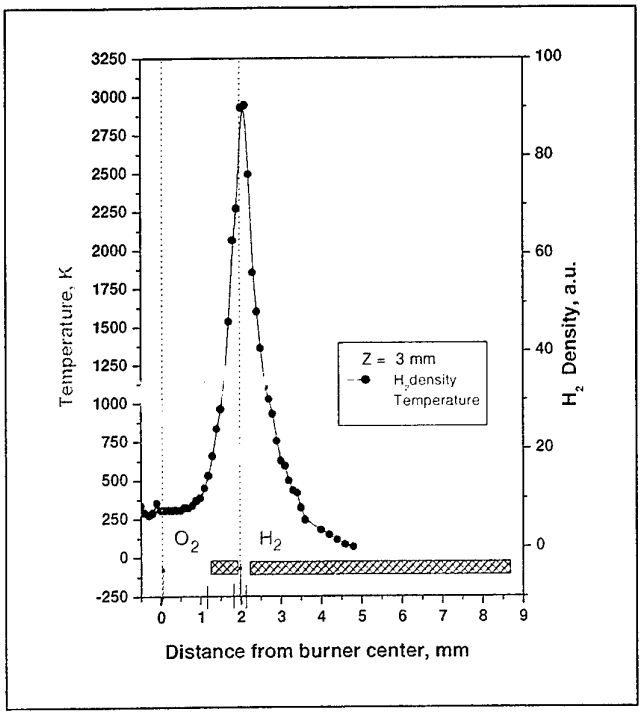


Fig. 9
Experimental hydrogen CARS spectra acquired with a DBB-CARS setup and simulation of the spectra

In an atmospheric coaxial burner operated with GO2 and GH2, the DBB-technique was demonstrated with very good results. The following figures show an extensive temperature mapping at such a burner in two heights above the burner plate.



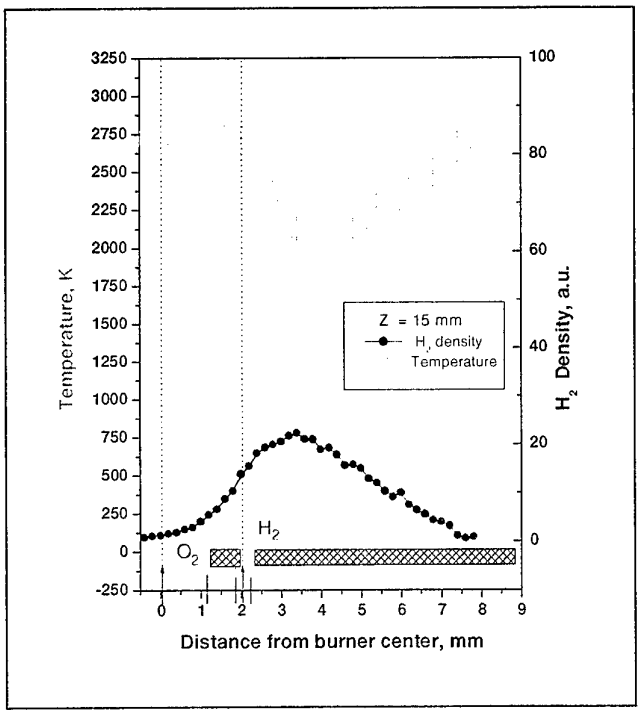


Fig. 10 a and Fig 10. b
Temperature mapping and H_2 density measurement at a H_2/O_2 burner

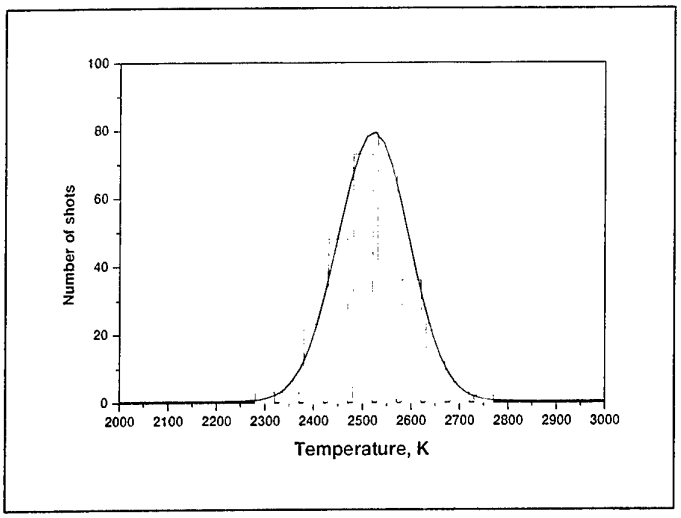


Fig. 11
Coaxial hydrogen-oxygen flame.
Histogram of single shot temperatures
Z = 15 mm
T= 2522 K+-73 K (3% RSD)

3.2 Water

In hydrogen/oxygen combustion, the water molecule can also be used for CARS thermometry. Similar to the nitrogen molecule, water has many closely spaced rovibrational transitions. Rotional energy transfer by elastic collisions affects the spectral shape. The vibrational relaxation is fast, even faster than for the nitrogen molecule. This leads to fast thermal equilibrium.

The molecular data for water are presently known to an extend that the ν_1 band can be modeled. Water is an asymmetric top molecule with three vibrational modes. The ν_1 (symmetric stretch) and ν_3 (antisymmetric stretch) are at 3657,1 and 3755,9 cm^{-1}, respectively, and the ν_2 (bending motion) mode frequency is 1594.7 cm^{-1}. Among these modes, only the ν_1 is strong enough to be used for CARS

Spectral averaging with conventional broadband Stokeslasers is efficient enough and it is not necessary to employ the more complicated 'online referencing'-CARS or DBB-CARS .

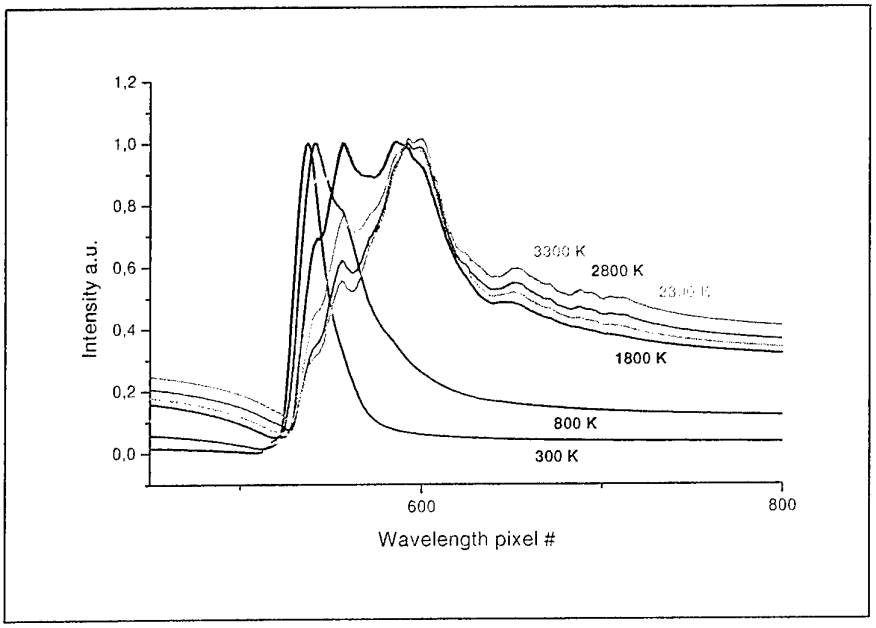


Fig. 12
Simulation of H_2O CARS spectra for different temperatures

4. CARS-Thermometry on H_2 and H_2O in high pressure cryogenic combustion

Modern cryogenic rocket engines like the Vulcain have typical combustion efficiencies exceeding 99 %. Nevertheless, knowledge about the complex interaction of the liquid injection related processes like atomization, vaporization, mixing and combustion is still very poor.

Up to now, no modern laser diagnostics have been performed in this field due to the condition encountered in such engines. The sound and vibration induced stresses at a big test bench prohibit the application of delicate laser diagnostic equipment.

But the increasing demands on performance, reliability and reusability together with the need to have a database of reliable experimental data for design of next generation engines raised the need for more detailed knowledge about the physical phenomena in cryocombustion.

To achieve this goal, the MASCOTTE test bench at Onera Palaiseau and the P8 test bench at DLR Lampoldshausen have been built up as scientific test sites for cryogenic hydrogen/oxygen high pressure combustion with emphasis to the application of laser diagnostics. Both test benches provide hardened diagnostic rooms close to the test cell to accomodate the laser apparatus.

Some optical diagnostics have already been applied at high pressure cryocombustion, largely emission and laser-induced fluorescence on the OH radical. However, the analysis of the data is difficult because the quenching rates are often not known to sufficient accuracy for the high pressure environment and absorption of the excitation laser beam by the liquid phase.

A notable exception is CARS. In the last two decades, much basic research has been done and the intramolecular processes appearing with high pressure like energy transfer and linebroadening effects are theoretically understood and experimental data exist to describe this.

Therefore, it was decided to employ CARS for the cryocombustion diagnostics.

The fuel H_2, the oxidizer O_2 and the combustion product H_2O are potential CARS probe molecules. Since CARS is not accurate enough if the resonant molecule is of low concentration, O2 as a minority species was ruled out.

4.1 Water CARS at P8

At DLR Lampoldshausen, a CARS temperature mapping at 6 Mpa inside the 'combustion chamber C' was done using H2O as a probe molecule.

The P8 test bench has the operating parameters:

Mass flow LOX 0.2... 8 kg/s at 100K

Mass flow GH2 0.05...1.5 kg/s at T between 100 and 150 K or fixed at 300 K.

Combustion chamber operating conditions 1..300bar at 30s run time

The 'combustion chamber C' , a single coaxial injector design with a rectangular layout of 50mm x 50mm, was tested at the following conditions at 6MPa:

Mass flow LOXw 300 g/s and mass flow GH2 60 g/s.

Window cooling mass flow GH2 230 g/s

Two points about 5 mm from the middle axis were probed at 32 mm and 88 mm distance from the injector. The water temperatures at 88 mm/5 mm were around 1100K, at the other position, almost no signal could be recorded.

The CARS system was a conventional broadband system with a Nd :YAG pumplaser delivering the two photons at ω_1 and a dyelaser for the Stokes frequency ω_2 . A whole spectra was generated with each laser pulse, dispersed in a 1 m spectrograph and recorded by a gated multichannel detector. The beam geometry was USED-CARS with a probe volume length of 2.5 mm.

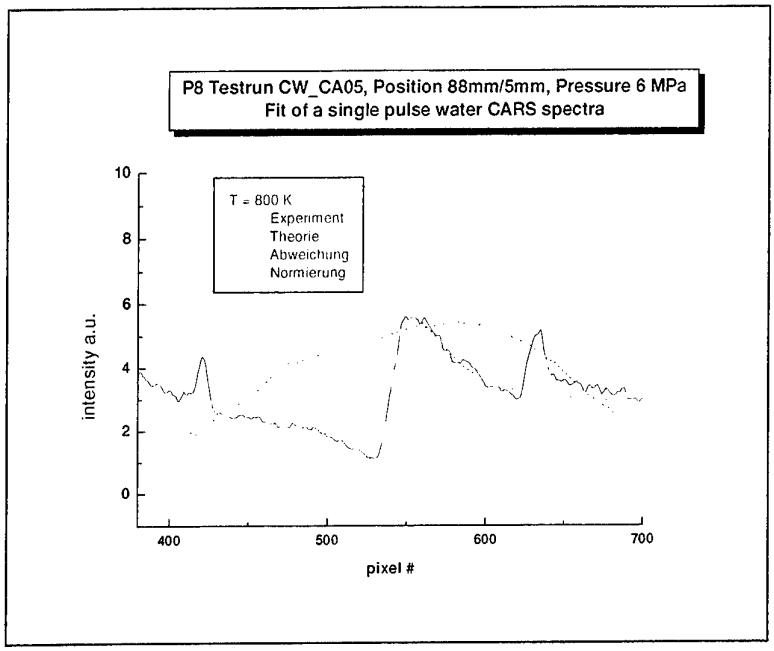


Fig. 13
Simulation of experiment CARS spectra acquired in P8 at 6 Mpa.

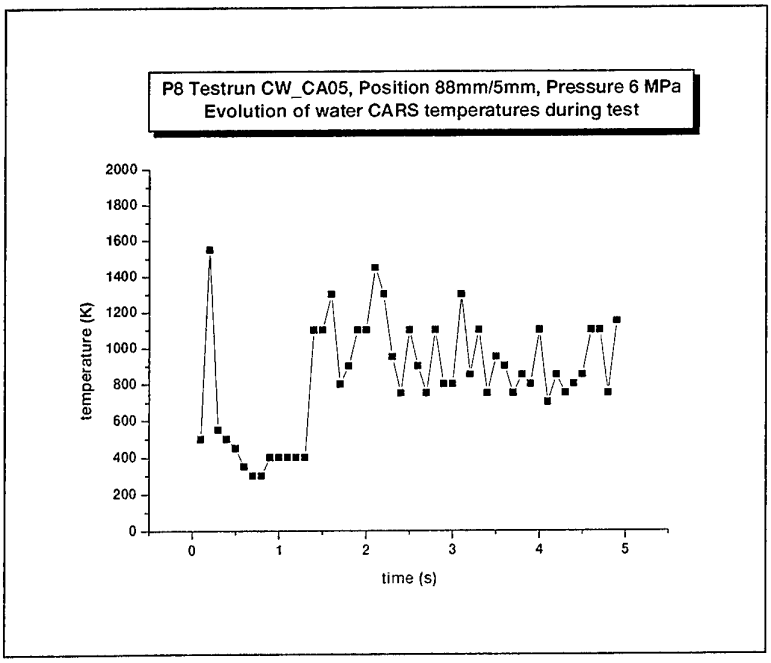


Fig. 14
Water CARS temperatures at P8 recorded with 10 Hz during the test run

4.2 Simultaneous two species CARS at MASCOTTE

At Onera Palaiseau, an extensive temperature mapping inside the MASCOTTE combustor was performed as a joint diagnostics task by Onera and DLR. Here, pressures from 0.1 Mpa up to 6.5 Mpa were probed.

At MASCOTTE, three diagnostics groups from Onera, DLR Lampoldshausen and GPI teamed together to perform a simultaneous two species CARS. The reasons for this were the following:

When performing CARS on the H2 molecule alone at a turbulent combustion, there was during a test run quite often a loss of signal even at the same measurement point. In this case, the hydrogen concentration was low with high water concentration. Therefore, a simultaneous CARS at H2 and H2O would always get a least one signal giving a much increased understanding of combustion processes. Obligatory for this approach was the synchronization of two laser beams in time and space and the synchronization of the detection systems so that each pair of recorded spectra could be identified.

The MASCOTTE testbench („Montage Autonome Simplifié pour la Cryocombustion dans l'Oxygéne liquide et Toutes Techniques Expérimentales") has the following operating parameters:

Mass flow LOX 10..400g/s at 85 K and 200bar

Mass flow GH2 5..75g/s GH2 at 100K up to ambient

Combustion chamber operating conditions 1..100bar at 30s run time

The combustion chamber itself was a rectangular channel of 45 mm x 45 mm built of modular sections. One section was equipped with quartz windows for optical diagnostics like CARS, LIF, OH-imaging and Schlieren-Imaging. The main windows were 100 mm long and 40 mm high, the two windows on top and bottom of the module were only 10 mm wide and intended for laser light sheet entrance and exit. The windows were cooled and protected from hot gases by a helium flow.

The injector was a single element coaxial injector with the LOX coming through the inner tube and the GH2 through the coaxial slit surrounding the tube. Two combustion conditions A and B were probed at ambient pressure, at 1 Mpa, 3 Mpa and 6.5 MPa.

The two CARS systems employed at MASCOTTE were built on separate optical benches. The first optical bench comprised a frequency-doubled injection-seeded Nd:YAG laser and a broadband dye laser that generated the pump and the Stokes beams required for the multiplex CARS measurements. The Stokes was centered at 683 nm to excite the Q-branch of hydrogen with a 200 cm-1 bandwidth. An online referencing was employed successfully. The second laser bench used to probe water vapor consisted of a broadband dye laser pumped by a multi-mode Nd:YAG laser. Both laser pulses were synchronized with a delay of 100 ns and a temporal jitter of 200 ns. A planar BOXCARS arrangement was used for the H2-CARS system in which referencing is applied systematically. For the H2O-CARS system, a USED-CARS beam geometry was used. All the beams were combined and focused in the combustion chamber using a 200 mm focal length achromat yielding a typical 1 mm long, 100 µm diameter, probe volume.

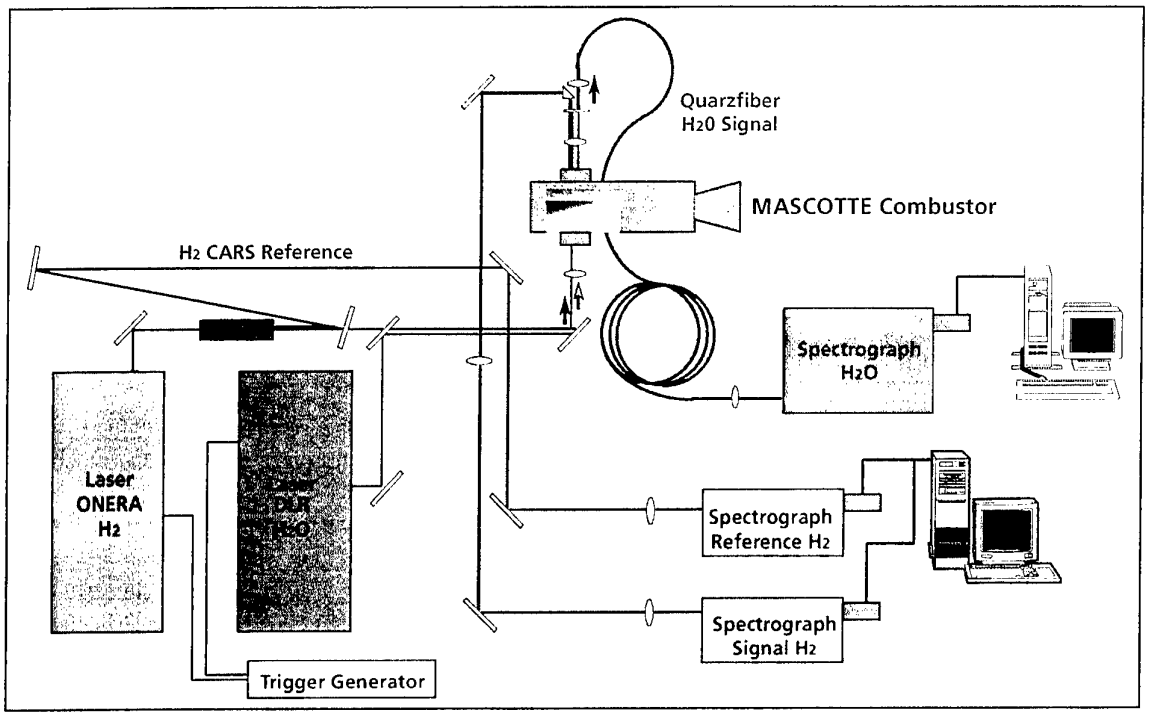


Fig. 15
The synchronized CARS systems for two species detection at MASCOTTE

Measurements were performed at several pressures covering the 1-65 bar pressure range. For each species, an analytical procedure has been developed and employed to reduce CARS spectra to useful temperature despite the unknowledge of the mixture composition of the probe volume. A library of pre-calculated theoretical spectra was generated at 50 K increments over a range encompassing the expected flame temperature. Libraries were generated for different molar fractions of H2 and H2O in order to characterize the effect of the linewidths on the resulting CARS spectral shape. The temperatures were evaluated by a weighted least squares of the measured CARS spectra with the theoretical spectra. The accuracy of the temperature was assumed to be equal to 10 % for both CARS spectra. In the same time, the H2O molar fraction is deduced from the ratio between the resonant part and the nonresonant of the H2O CARS spectra.

For each condition of pressure, an ensemble of about 100 instantaneous measurements were recorded during each run of the burner. The temperature distributions displayed the degree of burnout which depended primarily on the mixing of H2 and H2O. Agreement between the temperature profiles deduced from the H2 and the H2O CARS spectra, in terms of the mean and the standard deviations, was good especially in the zone where the combustion is partially finished. The high validation rates, defined as the ratio between the number of spectra successfully processed and the total number of laser shots, demonstrate the feasibility of CARS measurements in those severe conditions, even at supercritical pressures. Analyzing the complete set of data provided an insight of

the flame structure and of the evolution with the pressure. The main conclusions are the followings. The flowfield was extremely turbulent as indicated by the standard deviation of the instantaneous temperatures. The decreasing of the validation rate on H2 near the axis showed that the stratification of the flowfield is very important near the injector, but vanishes further downstream when mixing was achieved. The location of the local temperature maximum indicates that increasing the pressure brings the flame nearer to the injection plate.

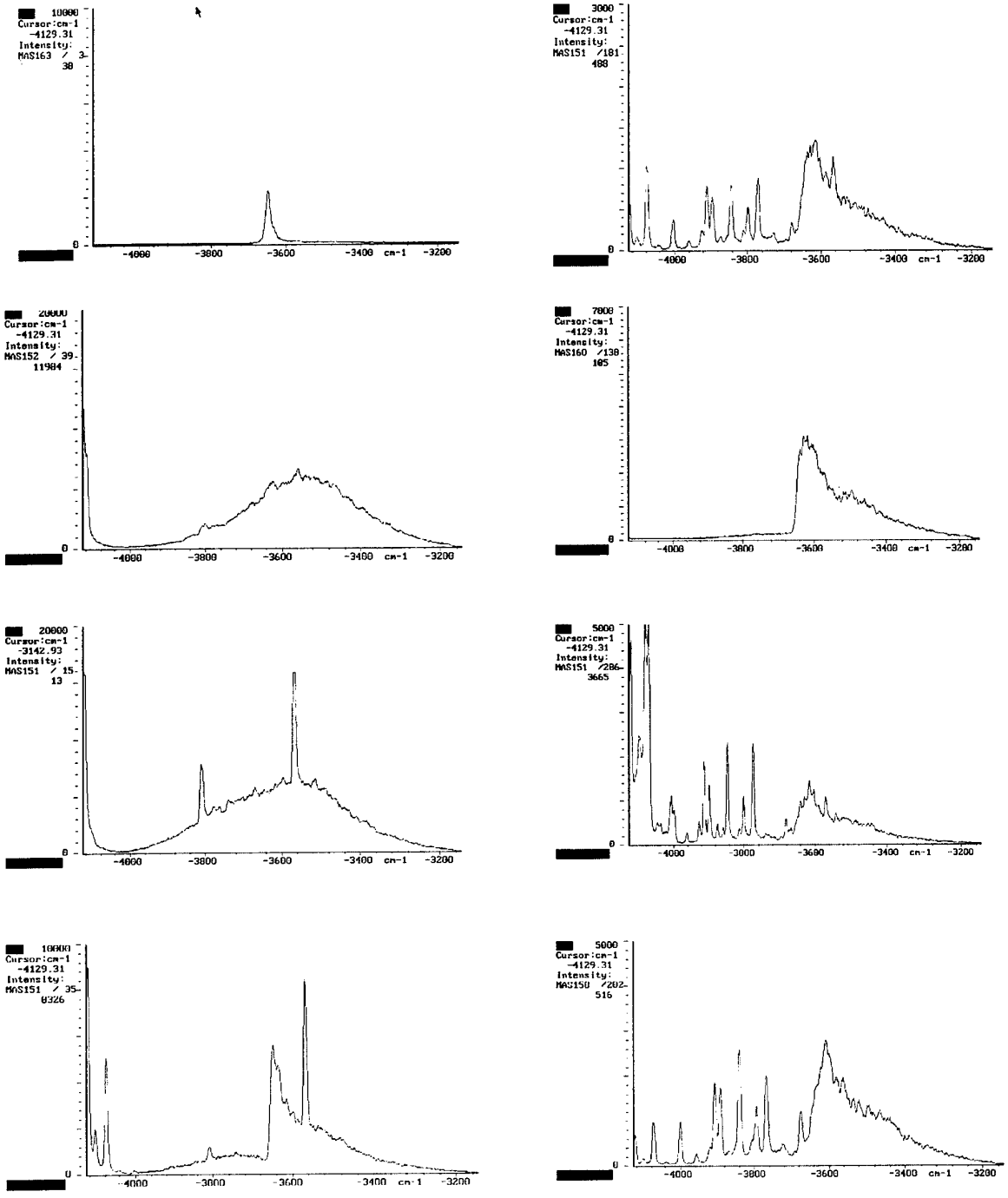


Fig. 16
Different spectra from MASCOTTE showing ignition phase and strong variation of spectra during test run

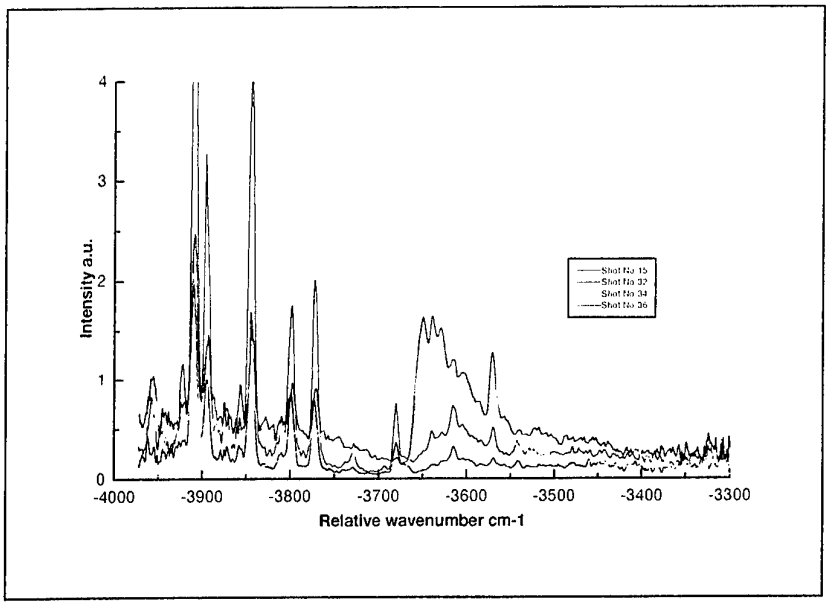


Fig. 17
Water CARS spectra taken at MASCOTTE. Some hydrogen lines are to the left. These cannot be simulated due to low excitation energy.

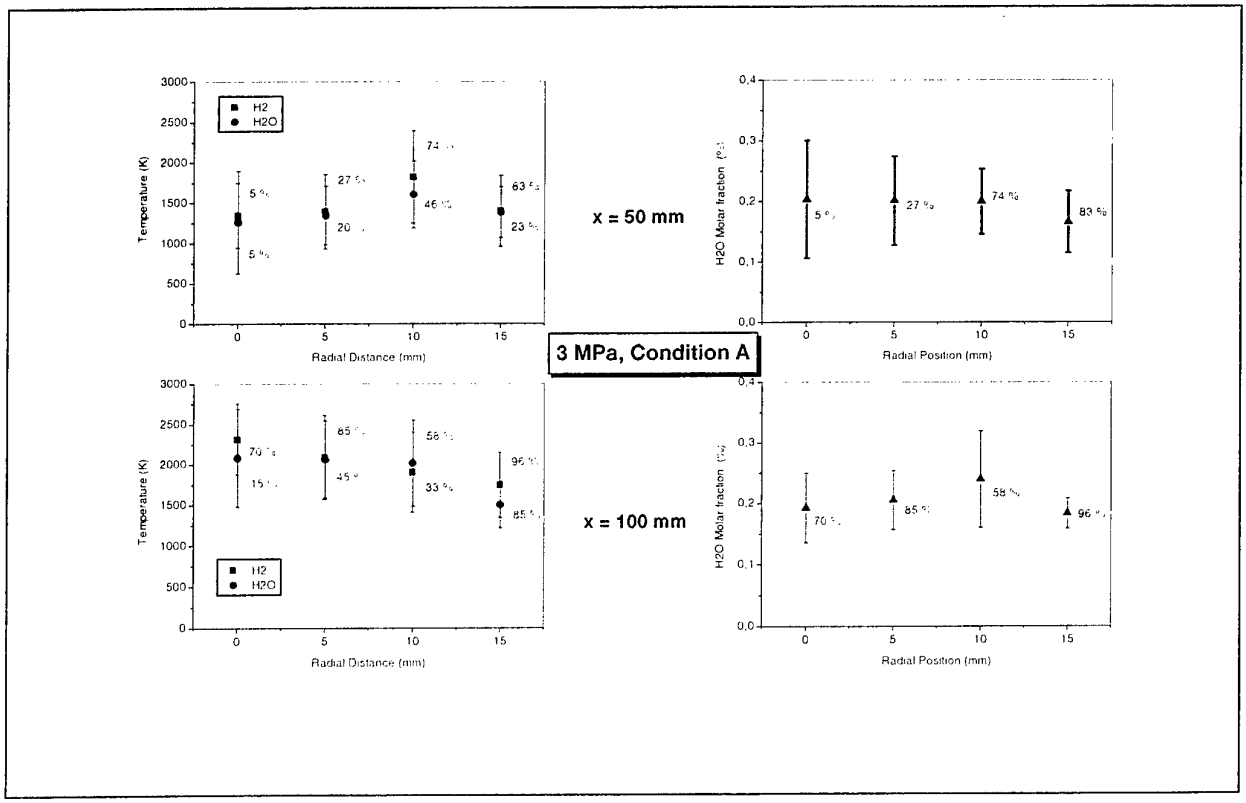


Fig. 18
Results from MASCOTTE at 3 Mpa.

5. Conclusion

- CARS is a powerful diagnostic tool. For the successful application of CARS to technical combustion, basic molecular data must be acquired at first.

- GPI, DLR and ONERA have the knowledge and experience and possess the necessary equipment to provide CARS-spectroscopy with qualitative and quantitative information in fundamental research as well as to apply CARS in diagnostics of chemical compositions, of population density and temperature measurements at discharges, chemical rectors, gas flows and technical combustion.

- By mutual efforts CARS approaches for simultaneous measurement H_2 and H_2O spectra in high pressure cryocombustion were developed. The instrumental precision RSD 3% for single shot temperature measurement was achieved.

References

1. Stoicheff, B.P. Characteristics of stimulated Raman radiation generated by coherent light. Phys. Lett., 1963, Vol. 7, pp186-188.
2. Lallemand, P. Simova, P. Bret, G. Pressure-induced line shift and collisional narrowing in hydrogen gas determined by stimulated Raman emission. Phy. Rev. Lett., 1966, Vol. 17, pp. 1239-1241
3. Owyoung, A., Esherick, P. Inverse Raman spectroscopy: Porto memorial conf. On laser and applications. Rio de Janeiro, Brazil, 1980, pp. 37-38
4. Owyoung, A. Jones, E.D. Stimulated Raman spectroscopy using low power cw laser. Optics Lett., 1977, Vol. 1, pp. 152-154
5. Owyoung, A. Coherent Raman gain spectroscopy using cw laser sources. IEEE J. Quant. Electron., 1978, Vol. QE-14, pp. 192-197.
6. Gadow, P. ,Lau, A.,Thuy, Ch. T. et al. The inverse Raman scattering in mixture. Opt. Commun., 1971, Vol. 4, pp. 226-227.
7. Werncke, W., Klein, J., Lau, A. et al. Investigation of inverse Raman scattering using the method of intracavity spectroscopy. Opt. Commun.., 1974, Vol. 11, pp. 159-163.
8. Yeung, E.S. Inverse Raman effect: A quantitative spectroscopic technique. J. Mol. Spectrosc., 1974, Vol. 53, pp. 379-392.
9. Akhmanov, S.A., Bunkin, A.F., Ivanov, S.G. et al. Polarization active spectroscopy and coherent Raman ellipsometry. ZhETF, 1978, Vol. 74, No. 4, pp. 1271-1294.

10. Bunkin, A.F., Ivanov, S.G., Koroteev, N.I. Coherent polarizational Raman spectroscopy. DAN SSSR, 1977, Vol. 233, pp. 338-341.
11. Heiman, D., Hellwarth, R., Levenson, M.D. et al. Raman induced Kerr effect. Phys. Rev. Lett., 1976, Vol. 36, p.189.
12. Druet, S.A.J, Taran, J.P.E. CARS Spectroscopy, Prog. Quant. Electr, 1981, Vol. 7, pp. 1-72
13. Bulatov, E.D., Kozlov, D.N., Otlivanchik, E.A. et al. A computerized high resolution CARS spectrometer and coherent Raman spectroscopy of tetrahedral molecules. Kvantovaya elektron, 1980, Vol. 7, pp. 1294-1298.
14. Volkov, S.Yu., Kozlov, D.N., Prokhorov, A.M., Smirnov, V.V., Fabelinskij, V.I. High resolution CARS spectroscopy of molecular gases in "Laser-Induced Raman Spectroscopy in crystals and gases" ed. By P.P. Pashinin. NOVA SCIENTIFIC PUBLISHERS, COMMACK 1988, pp.91-164.
15. Valjanskij, S.I., Verschagin, K.A., Volkov, A.Yu., Ilyukhin, A.A., Pashinin, P.P., Smirnov, V.V., Fabelinskij, V.I. Local noninvasive Diagnostics of Gaseous Media in "Laser-Induced Raman Spectroscopy in crystals and gases" ed. By P.P. Pashinin. NOVA SCIENTIFIC PUBLISHERS, COMMACK 1988, pp.165-190.
16. Eckbreth, A.C., Anderson, T.J., Appl. Opt. 24, 2731 (1985)
17. Eckbreth, A.C., Anderson, T.J., Opt. Lett. 11, 496 (1986)
18. Alden, M., Bengtsson, P.-E., Edner, H. Appl. Opt.25. 4493 (1986)
19. M. Aldén, P.-E. Bengtsson, H. Edner, S. Kroll, and D. Nilsson: Appl.Opt. 28, 3206 (1989).
20. M. Aldén, P.-E. Bengtsson, H. Edner, S. Kroll and D. Nilsson: Appl.Opt. 28, 1068 (1989).
21. P. Snowdon, S.M. Skippon, and P. Ewart: Appl.Opt., 30, 1008 (1991).
22. W. Stricker, M. Woyde, R. Luckerath, V. Bergmann: Ber.Bunsenges.Phys.Chem. 97, 1608 (1993).
23. W. Clauss and R. Sontgen: Single shot CARS in H_2: Diagnostics Group Meeting DLR, Stuttgart, April 16, 1991.
24. V. Bergmann, W. Stricker: Appl.Phys. B61, 49 (1995).
25. Grisch, F., Péalat, M. Journal of Raman Spectroscopy, Vol. 25, pp 145-151, (1994)

Deutsches Zentrum für Luft- und Raumfahrt e.V. German Aerospace Center

Advanced Materials for Thrust Chamber Technologies

E. Serbest, K. Fritscher, O.J. Haidn,
H. Hald, G. Korger, and P. Winkelmann

German Aerospace Center (DLR)

Outline

- Motivation
- Numerical Tool for Transient Heat Transfer Prediction
- Thermal Barrier Coatings
  - Coating Characteristics
  - Preliminary Results
- Porous C/C for Effusion Cooling
  - Material Properties
  - Experimental Results
- Transpiration Cooling with C/C Structures
- Summary and Outlook

DLR

Thrust Chamber Requirements for Future Space Propulsion Systems

- Higher Engine Performance
- Increased Component Reliability
- Enhanced Chamber Life Time
- Damage Tolerance Capabilities
- Increased Thrust-to-Weight Ratio
- Reduced Manufacturing Costs

Motivation

Characteristic Figures of Current and Future European Large Cryogenic Engines

		VULCAIN	VULCAIN 2	VULCAIN 3*	ACE*
Cycle		GG	GG	GG	SC
Propellants		LOX/LH2	LOX/LH2	LOX/LH2	LOX/LH2
Pressure	[bar]	105	115	135	150
Mass Flow	[kg/s]	265	320	380	440
Mixture Ratio	[-]	5.9	6.1	6.4	6.5
Heat Flux	[MW/m2]	80	100	115	125
Thrust (vac)	[kN]	1120	1350	1550	1750
Isp (vac)	[sec]	431	434	442	462
Weight	[kg]	1630	1850	2100	2500
T/W-Ratio	[-]	68.3	72.9	73.8	70.0

DLR

Candidate Techniques to Fulfill these Requirements

- High Aspect - Ratio Cooling Channels
- Elastic Liner Concepts
- Injector Trimming (Film Cooling)
- Thermal Barrier Coatings
- Effusion Cooling Applying Fiber Re-Inforced Ceramics

Motivation

Basic Characteristics of Candidate Techniques

- Thermal Barrier Coatings
  - Reduction of heat load to metallic surfaces
  - (Increase of component life)
  - Reduction of regenerative cooling pressure losses
  - Comparatively lower costs (micro channels, elastic liners, etc)
- Transpiration Cooling with C/C Structures
  - Minimum coolant mass flow rates
  - Reduced pressure coolant pressure losses
  - Reduced weight
  - Failure tolerance capabilities

Motivation

Tasks and Problems to be Solved (1)

- Engineering Tool for Transient Heat and Mass Transfer Prediction
  - Determination of temperature induced stresses at the interface of coating and substrate during transients
  - Prediction of pressure differences across porous structures during engine startup and shut-down
  - Prediction of heat and mass transfer especially for startup transient
- Thermal Barrier Coating Technique
  - Tuning of sub-layers between substrate and final coating
  - Favorable coating technique
  - Verification and qualification

Tasks and Problems to be Solved (2)

- Porous Ceramic Structure
  - Pre- and post-processing treatment of fiber and porous structure (precursors, infiltration technique)
  - Application oriented process and pore structure optimization
  - High pressure and temperature qualification
- Transpiration Cooling
  - Engineering tool for cooling parameter prediction
  - Determination of operational parameters
  - Verification under engine conditions

Flow through Porous Walls

General Assumptions

$\frac{\partial}{\partial z}$=0;$\frac{\partial}{\partial \Theta}$=0;$u_z = 0; u_\Theta = 0$

Darcy-Velocity

$v = \epsilon u$

Porosity

$\epsilon = \frac{V_f}{V_{tot}}$

Continuity Equation

$\epsilon \frac{\partial \rho_f}{\partial t} + \frac{1}{r}\frac{\partial}{\partial r}\left(r \rho_f v\right) = 0$

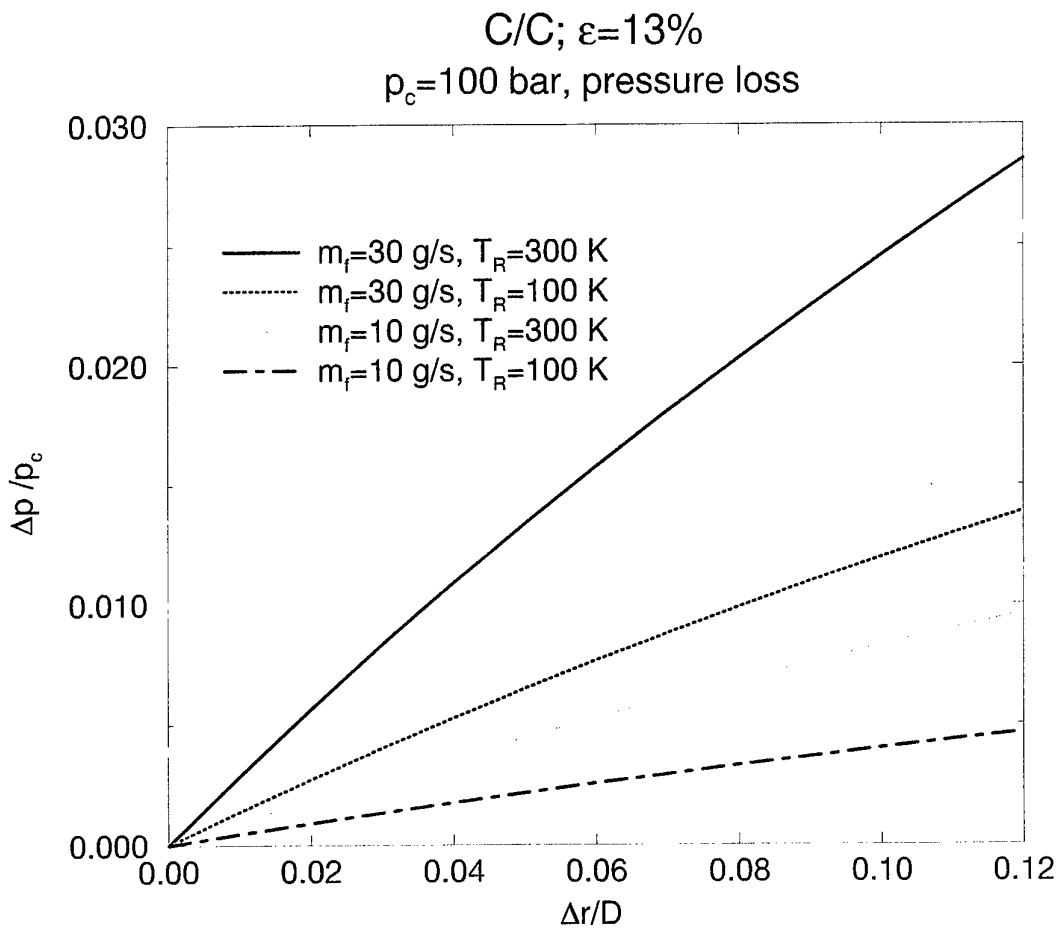
Momentum Equation (Darcy,experimental on porous flat plate, Re$\leq$ 1)

$\frac{dp}{dx} = -v\frac{\eta}{K}$

Modified Darcy-Equation(Re$\geq$ 1)

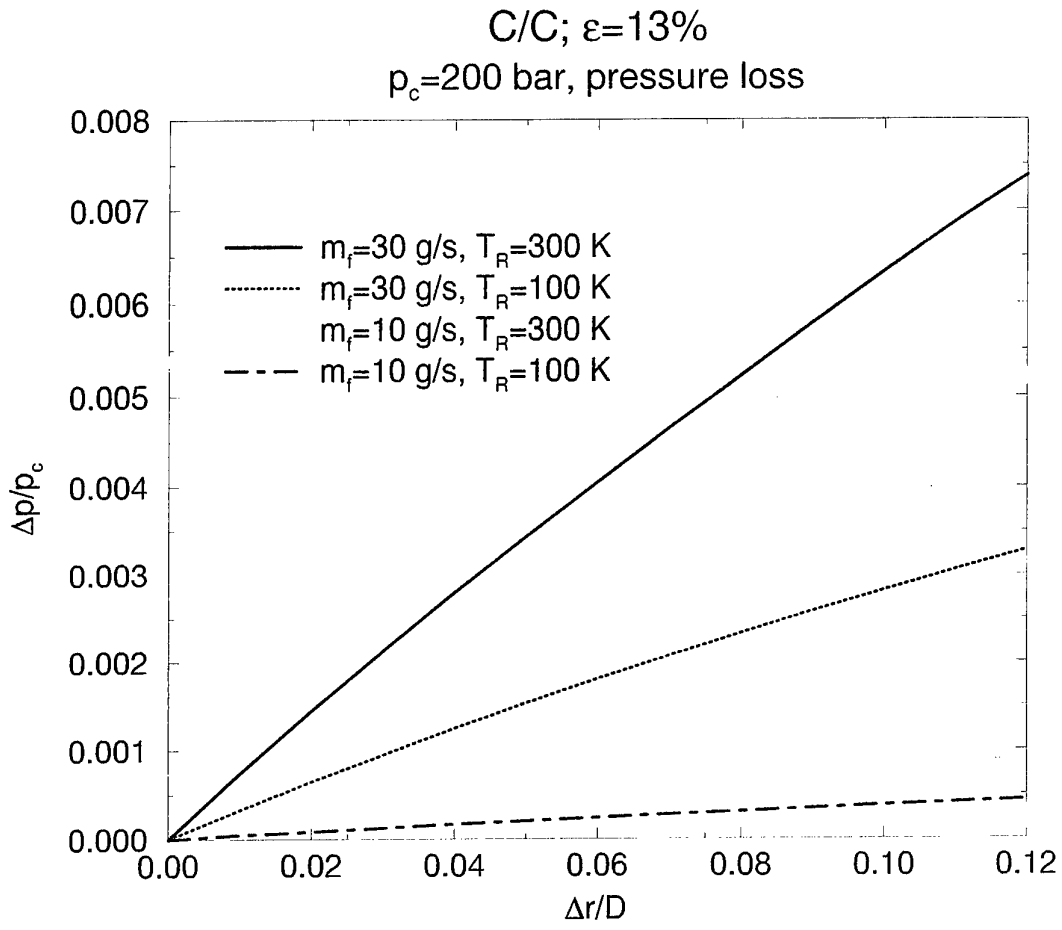
$\frac{1}{\epsilon}\frac{\partial \rho_f v}{\partial t} = -\left(\frac{\partial p}{\partial r} + \left(\frac{\eta}{\alpha} + \frac{\rho_f}{\beta}|v|\right)v\right)$

DLR



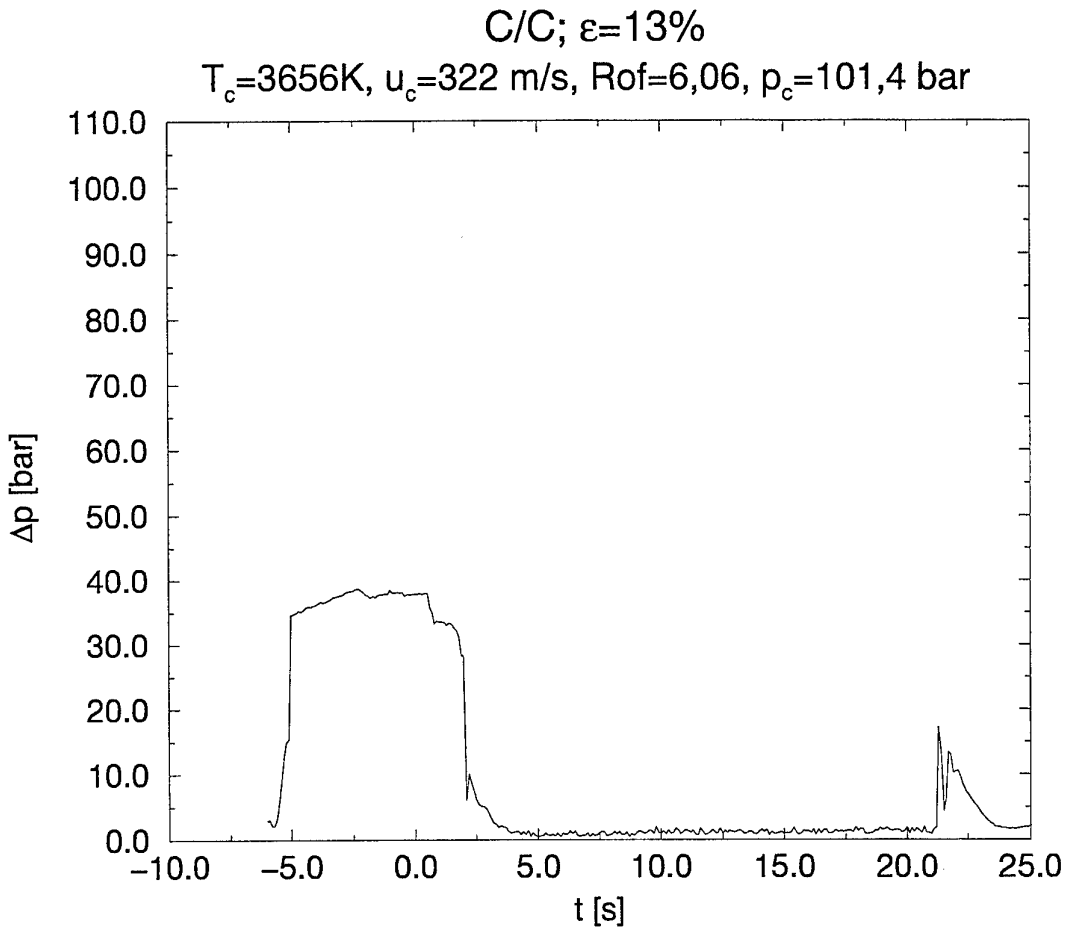
Pressure loss over the porous wall stationary condition

DLR



Pressure loss over the porous wall stationary condition

DLR



Pressure loss over the porous wall during ignition, stationary condition and shut off

DLR

Heat and Mass Transfer in Porous Walls

Properties of Porous Material

$$\rho_s = (1-\epsilon)\rho$$

$$cp_s = (1-\epsilon)cp$$

$$\lambda_s = (1-\epsilon)\lambda$$

Energy Equation Solid

$$\rho_s cp_s \frac{\partial T}{\partial t} = \frac{1}{r}\frac{\partial}{\partial r}\left(r\lambda_s \frac{\partial T}{\partial r}\right) - \frac{\alpha_{sf}}{A}\frac{dA_{sf}}{dr}\left(T_s - T_f\right)$$

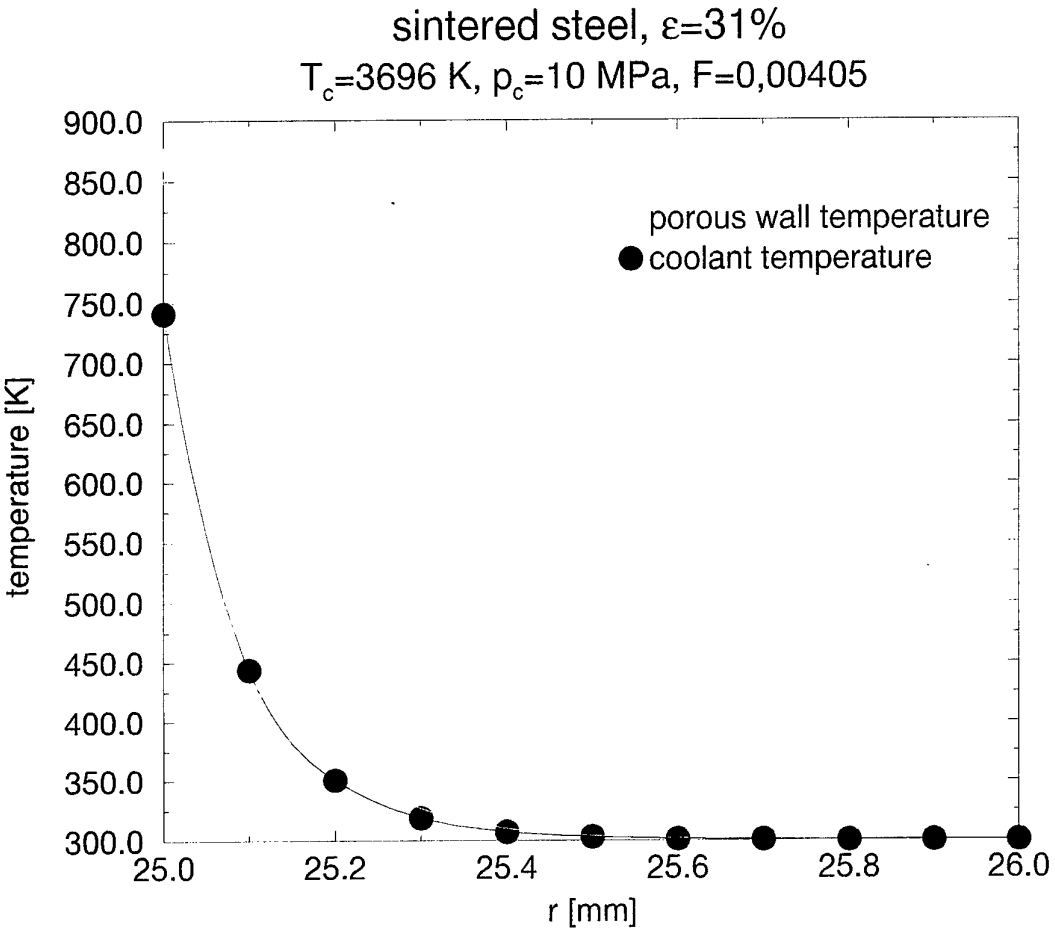
Energy Equation Fluid

$$\rho_f cp_f \frac{dT}{dt} = \frac{dp}{dt} + \frac{1}{r}\frac{\partial}{\partial r}\left(r\lambda_f \frac{\partial T_f}{\partial r}\right) + \frac{\alpha_{sf}}{A}\frac{dA_{sf}}{dr}(T_s - T_f) + \Phi$$

Convective Heat Transfer

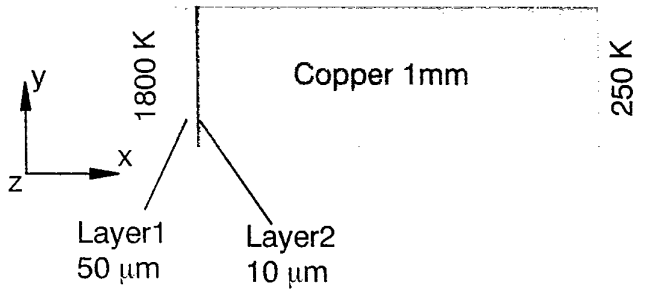
$$\frac{d\dot{q}_{konv}}{dr} = \frac{\alpha_{sf}}{A}\frac{dA_{sf}}{dr}(T_s - T_f)$$

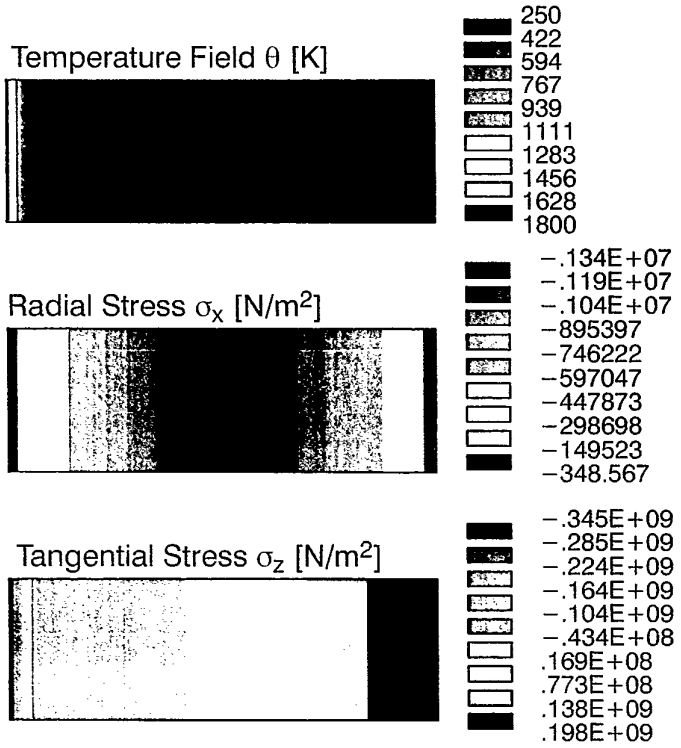
DLR

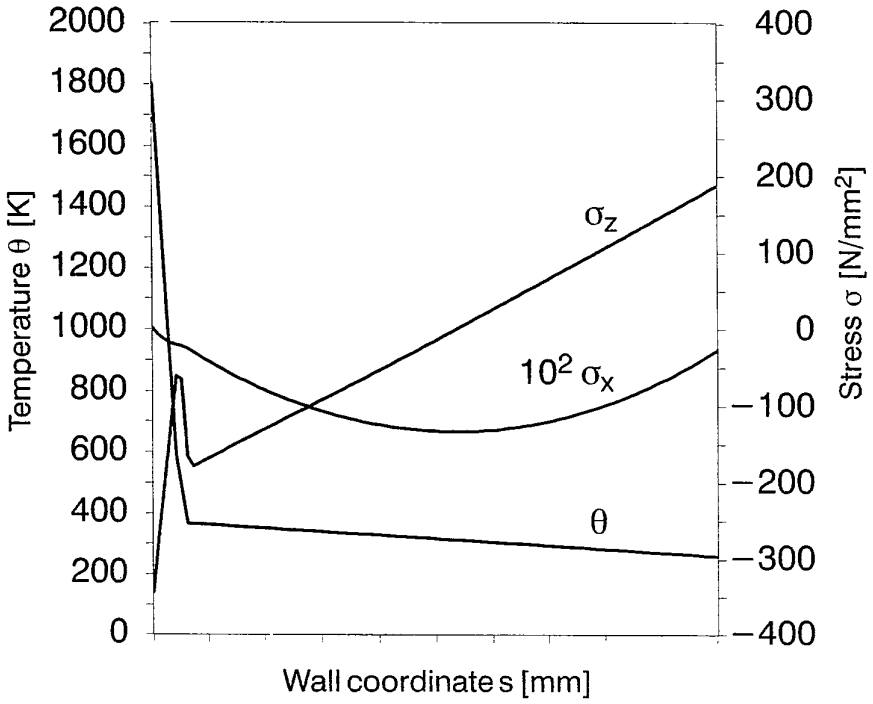


sintered steel, λ = 3-4 W/mk

DLR







Thermal Barrier Coating

DLR

Combustion Chamber Technologies

Material: Stabilized Zirkonia (Y_2O_3, MgO, CeO_2)

Processing Technique: Electron Beam Physical Vapour Deposition

Material and Layer Pretesting at M3 Micro Combustor Facility

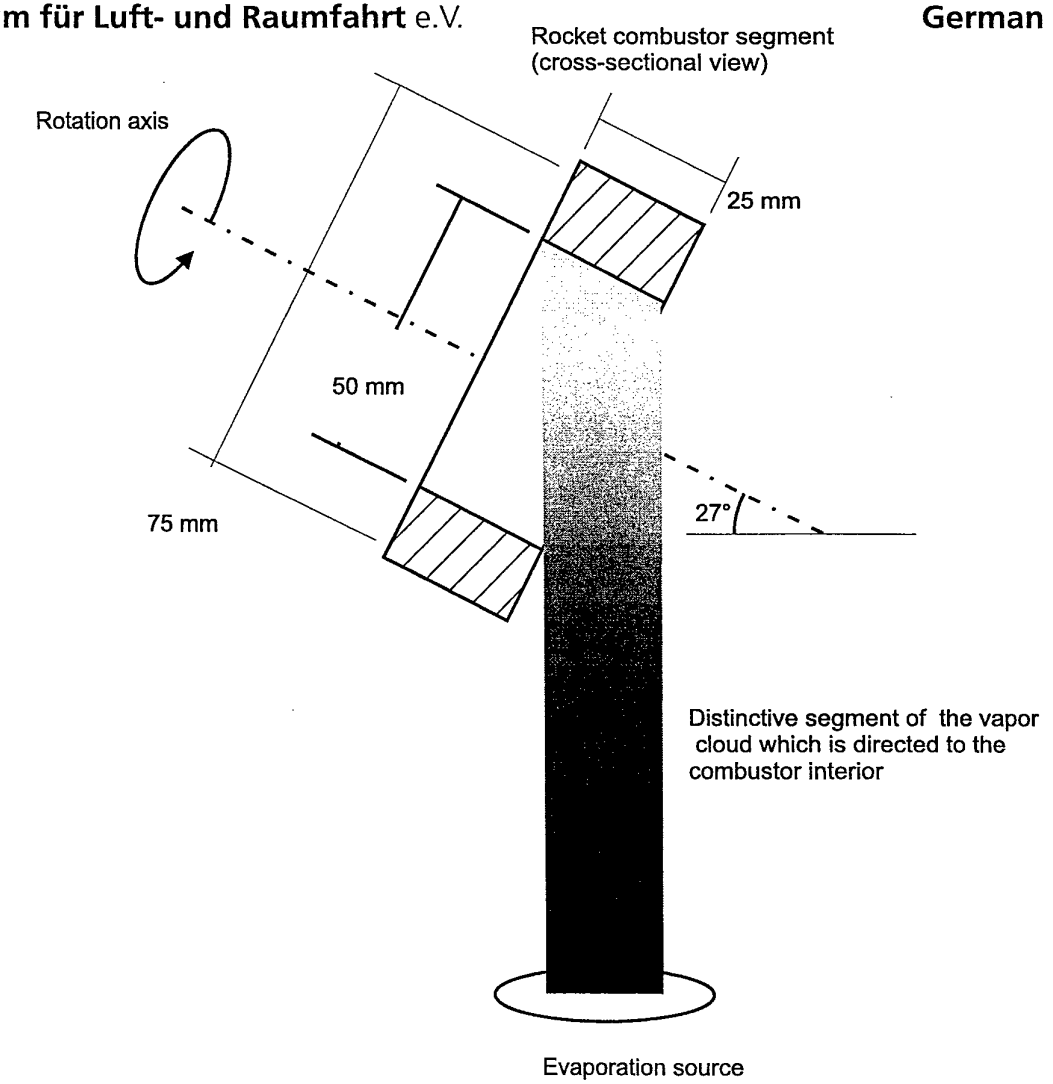
• Operating Conditions:	0.1 – 1 MPa	500 K – 1400 K	No Cooling

Subscale Testing at P8 Facility

• Operating Conditions:	5 – 15 MPa	500 – 1400 K	Water Cooling LH_2 Cooling

Thermal Barrier Coating Strategy

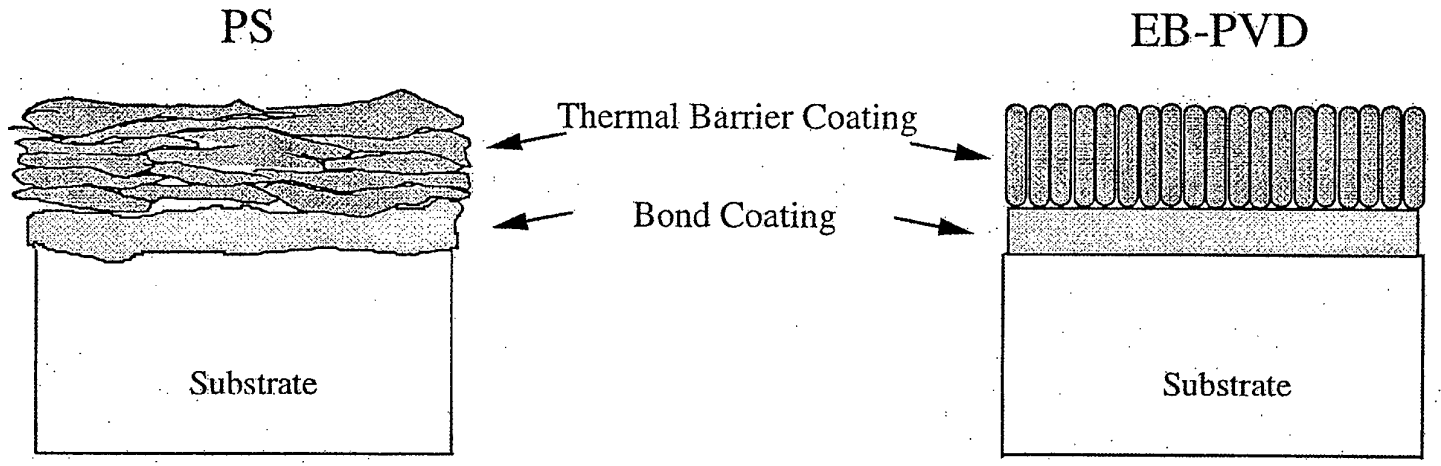
DLR



Processing of EB-PVD TBC for combustion chamber

DLR

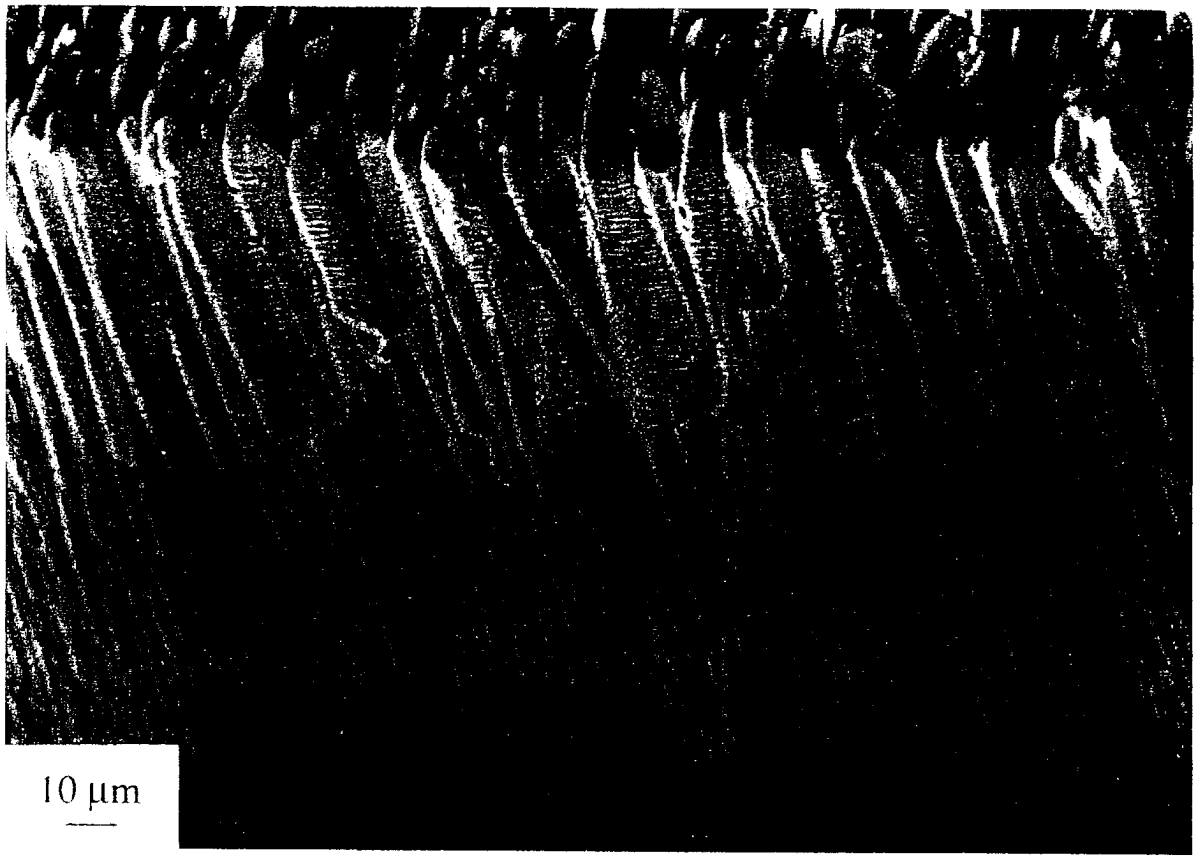
Comparison Plasma Spraying (PS) and Electron Beam – PVD



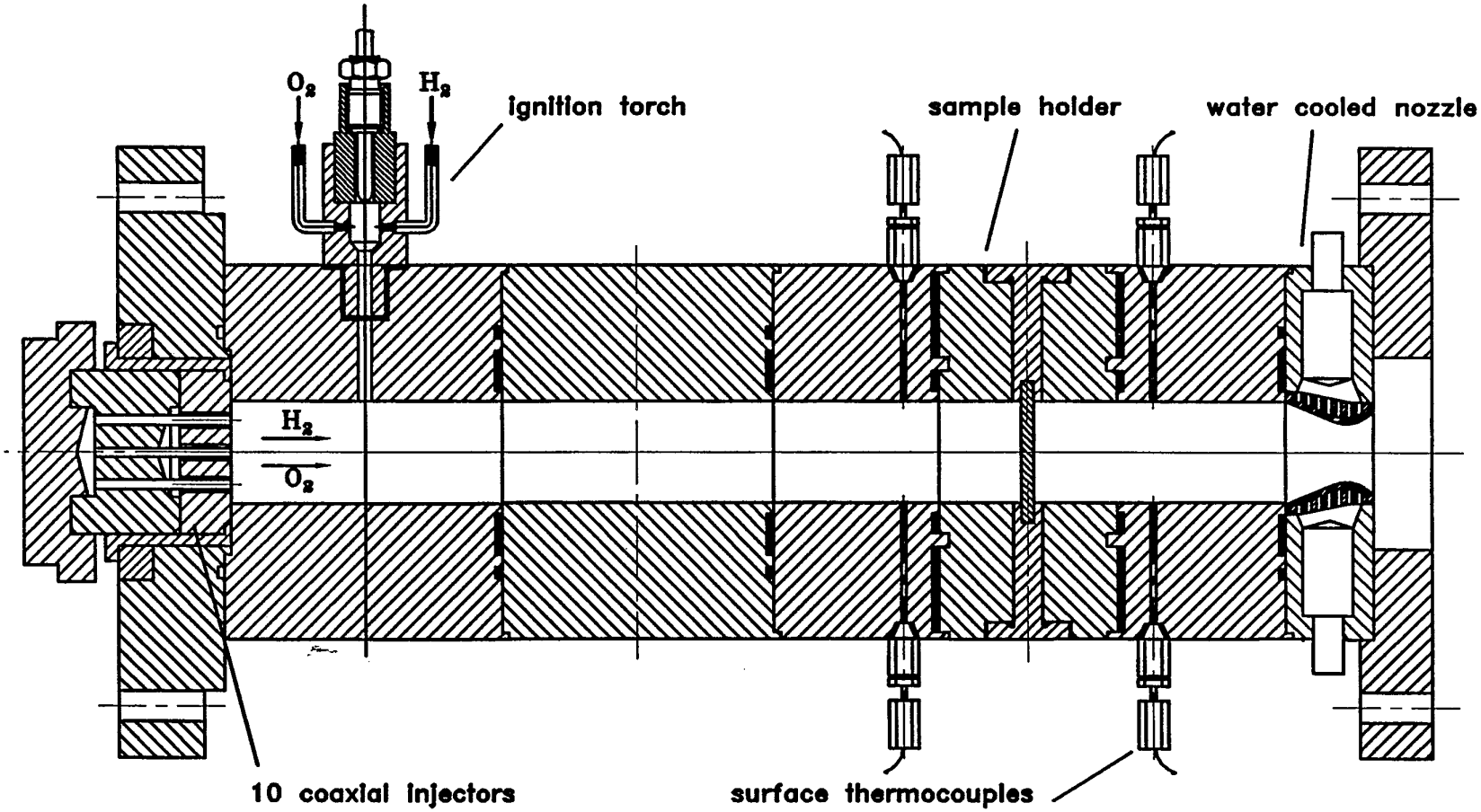
Horizontal Splat Structure,
Thickness 0.2 – 3 mm,
Mechanical Bonding,
Rough Surface,
Flexible Coating Chemistry,
Low Thermal Conductivity,
(Normal to Coating)

Columnar Structure,
Thickness 0.1 – 0.3 mm,
Chemical Bonding,
Smooth Surface,
Superior Erosion Restistance,
Low Elastic Modulus,
(Normal to Coating)
Increased Life Time

DLR

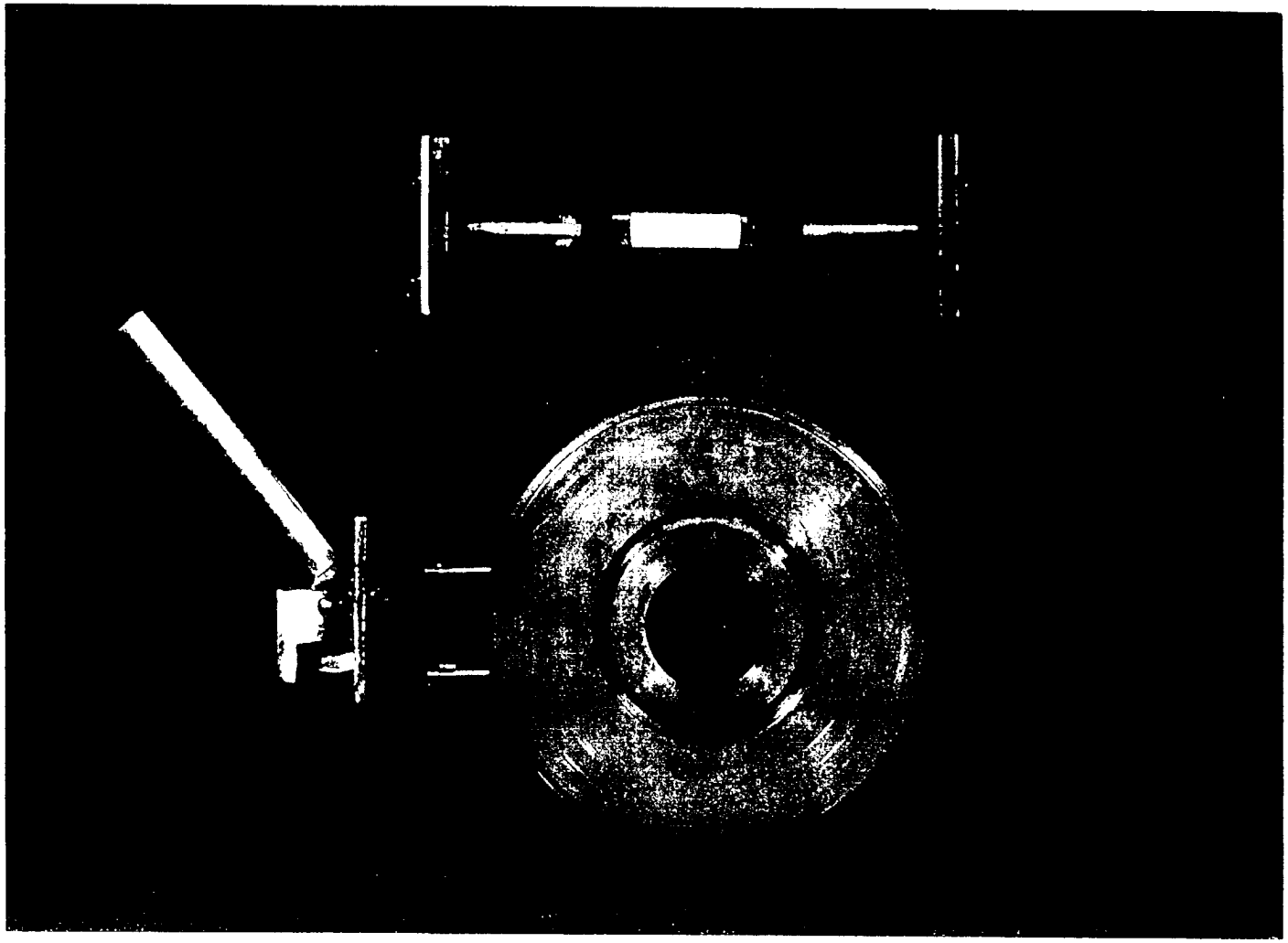


Columnar Structure of EB-PVD Thermal Barrier Coating

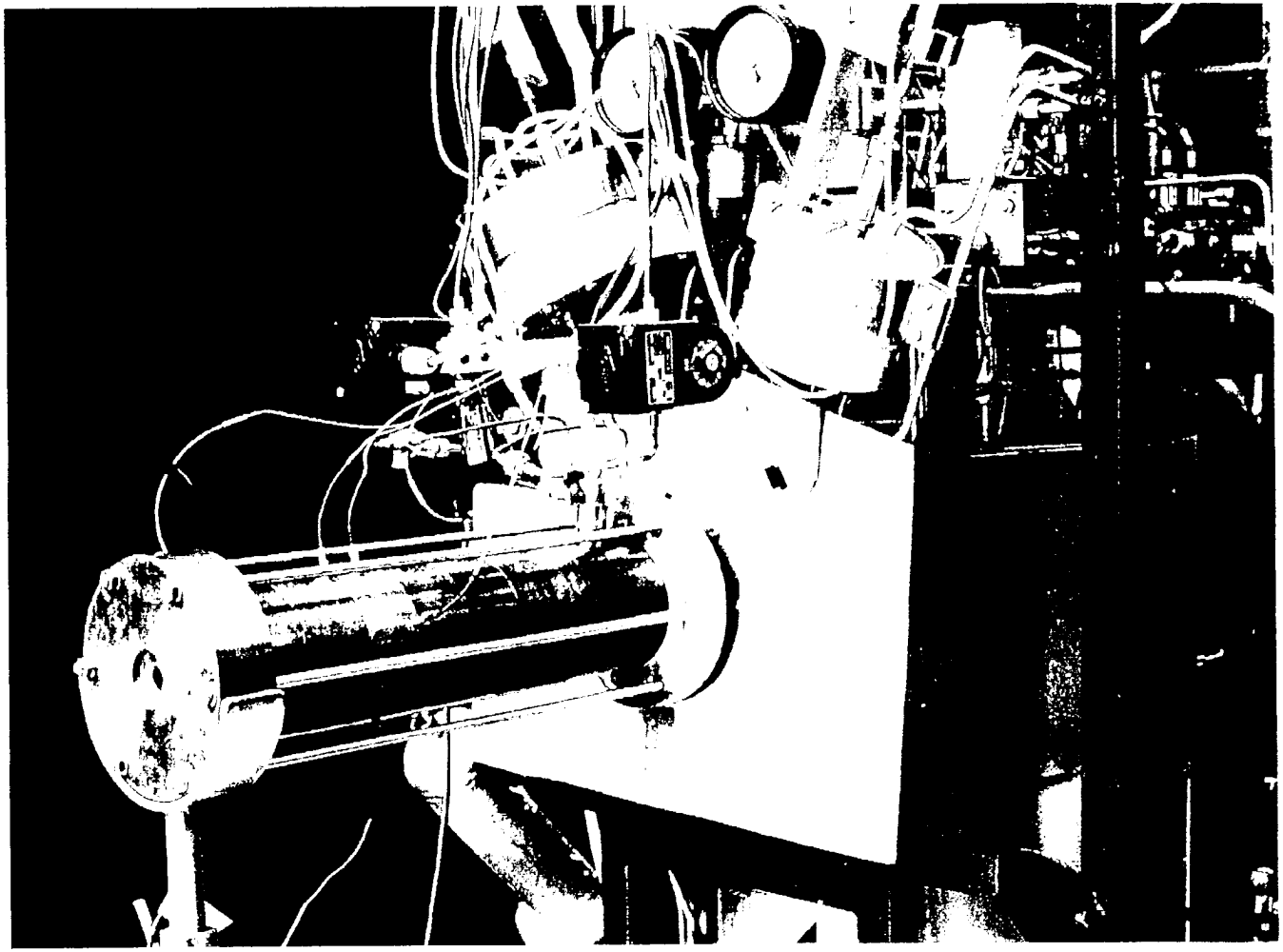


Micro-Combustor for material tests

DLR



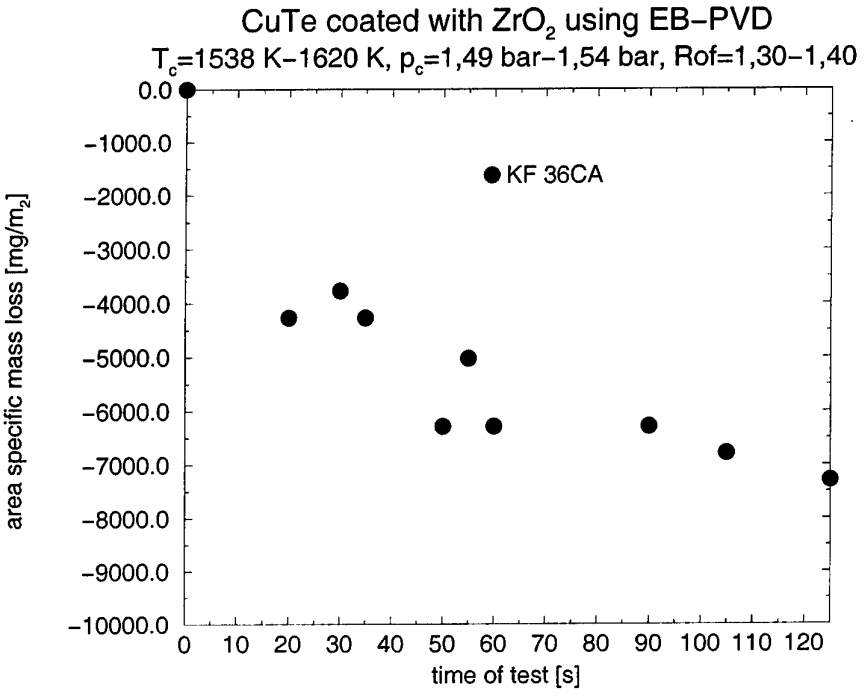
Specimen holder with ZrO_2 coated specimen



M3 Micro Combustor: Setup for Preliminary Material Testing

T_C [K]	1334-1660
p_C [MPa]	0,11-0,185
Rof [-]	1,06-1,45

Operating conditions for the coated copper segments



Specific mass loss of the coating surface

DLR

Combustion Chamber Technologies

Material: Porous C / C, C / Si C

Processing Technique: Resin Transfer Moulding, Liquid Silicon Infiltration

Pretesting of the Material

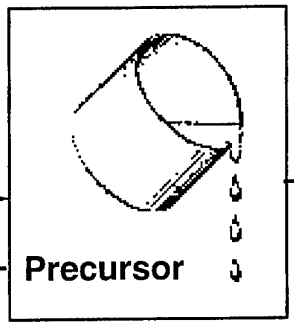
- Plasma Wind Tunnel (PWK)
- M3 Micro Combustor

Functional Tests with Hydrogen Cooling

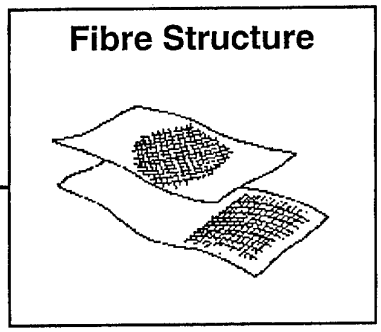
- M3 Micro Combustor
- P8 Test Facility

Fiber Re-Inforced Ceramics Strategy

Manufacturing of C/C



Precursor



Reinfiltration (0 - 1), only for Comb.- Ch.

CFRP - Manufacturing

Resin Transfer Moulding / Autoclave Technique

Conversion to C/C

Pyrolysis, T>900°C, Inert Gas

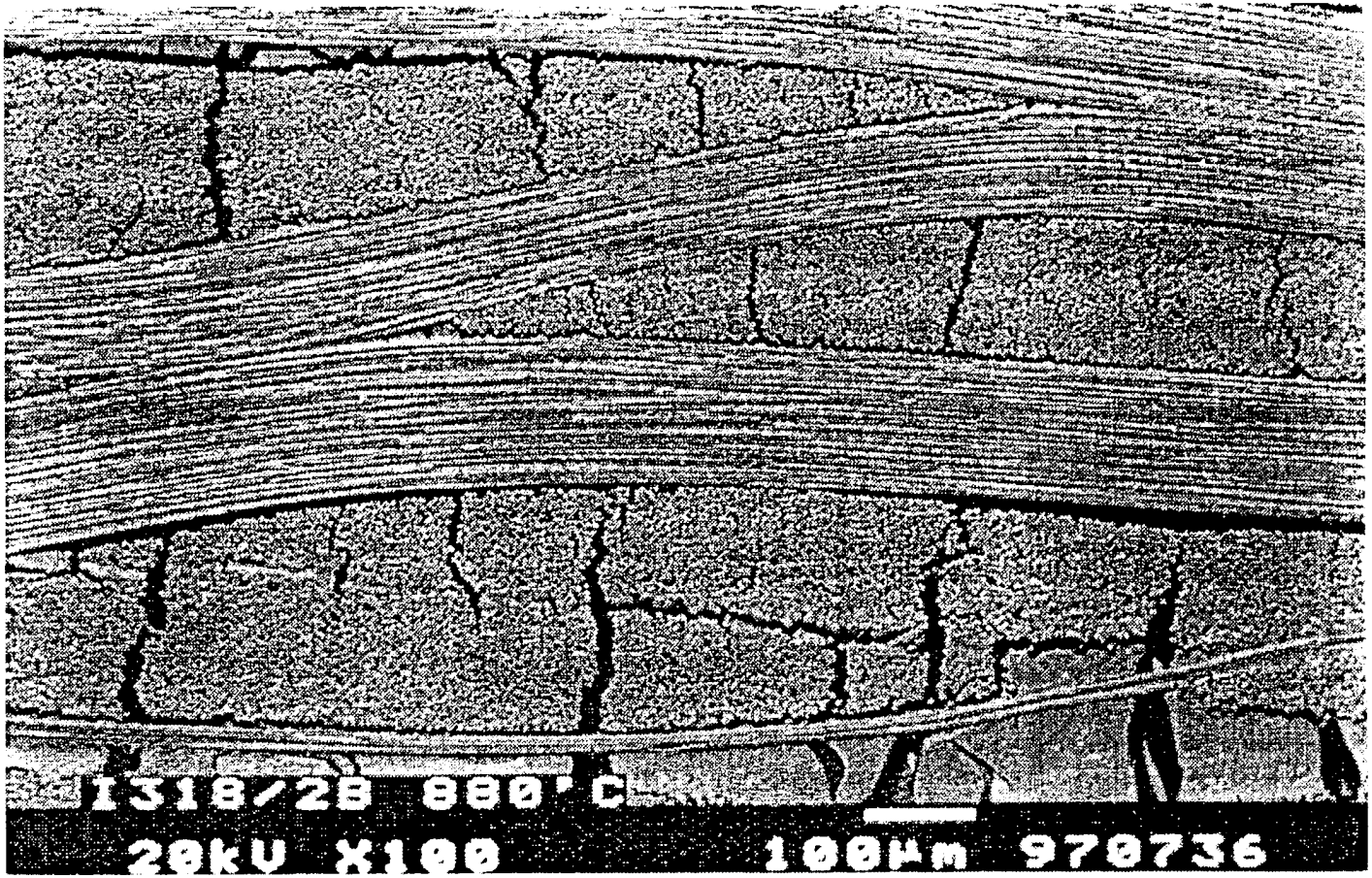
Combustion Chamber

(Effusion Cooling)

Conversion to Ceramics
Siliconizing, ~1600°C
(Liquid Silicon Infiltration)

Thermal Protection
Systems, Hot Structures

DLR



C / C Properties and Microstructure

2D -Fabric Re-Inforcement
Fibre Volume Fraction 55 – 65 %

Density: ~ 1.4 g / cm
Open Porosity: ~ 15 % – 25 %

DLR

Ceramic Material Pretesting

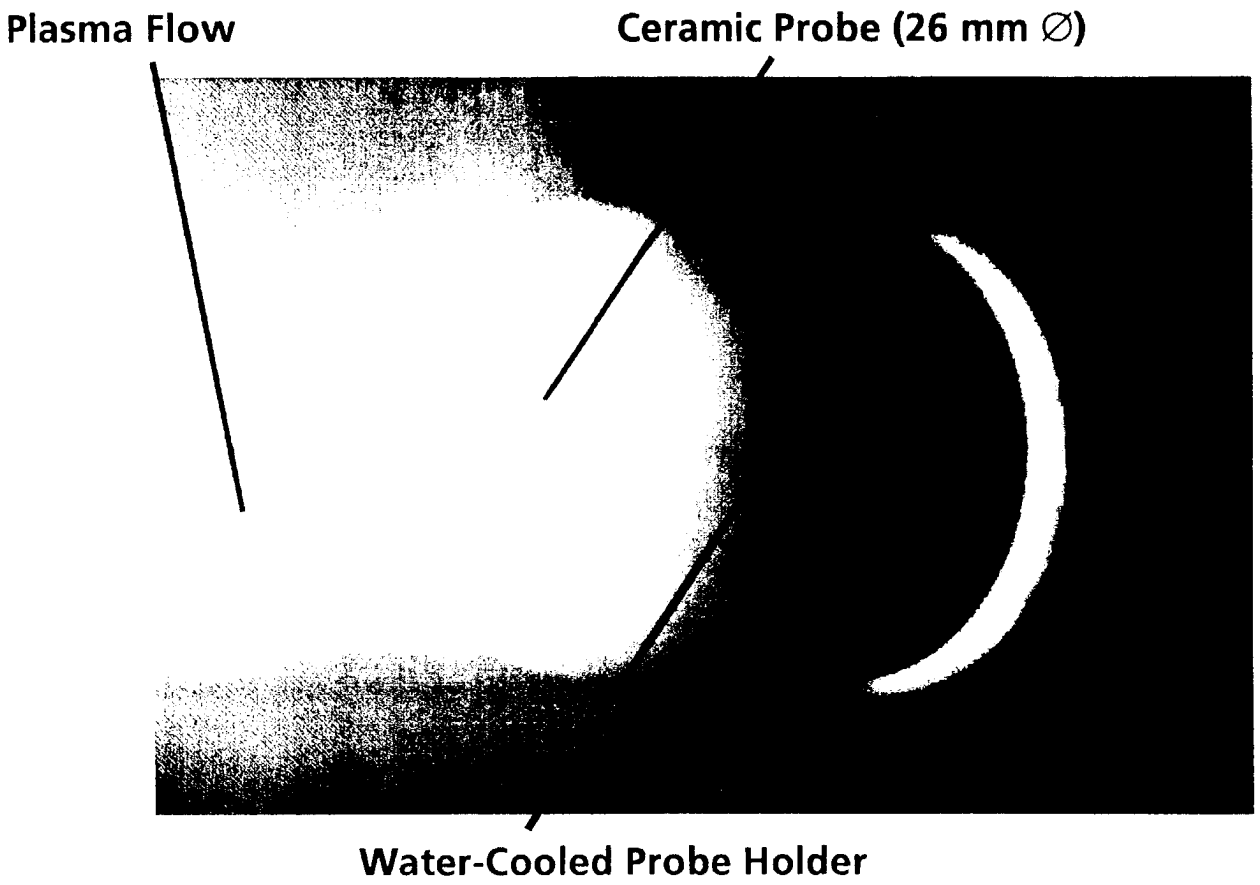
Plasma Wind Tunnel Operating Conditions

- Low Pressure P = 0.0015 MPa
- High Temperature T = 1970 K
- Different Environments H_2, H_2/O_2, $H_2/O_2/N_2$

DLR M3 Micro Combustor Facility Operating Conditions

- Moderate Pressures P = 0.2 - 1.05 MPa
- High Temperatures T = 1700 - 3000 K
- Environments H_2/H_2O (Variation of Mixture Ratio)

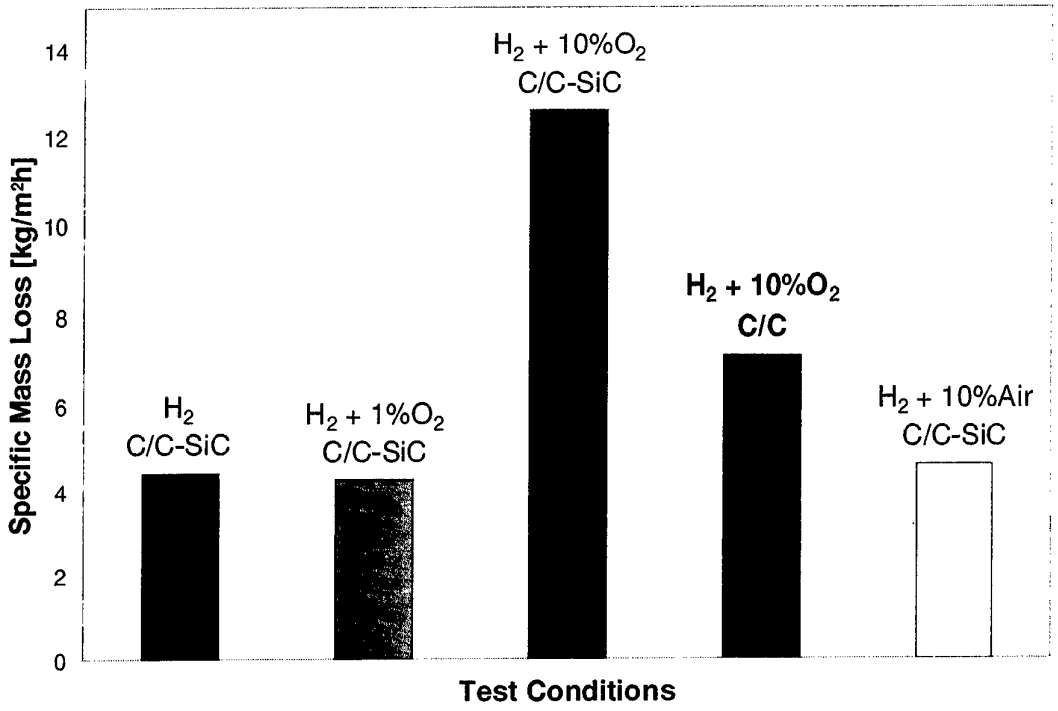
DLR



Fiber-Ceramic Probe in the Plasma Wind Tunnel

DLR

Material Tests in PWK[1] (FESTIP)



C/C-SiC shows significant mass loss rate in H_2-plasma
(⟶ no oxidation effect possible)

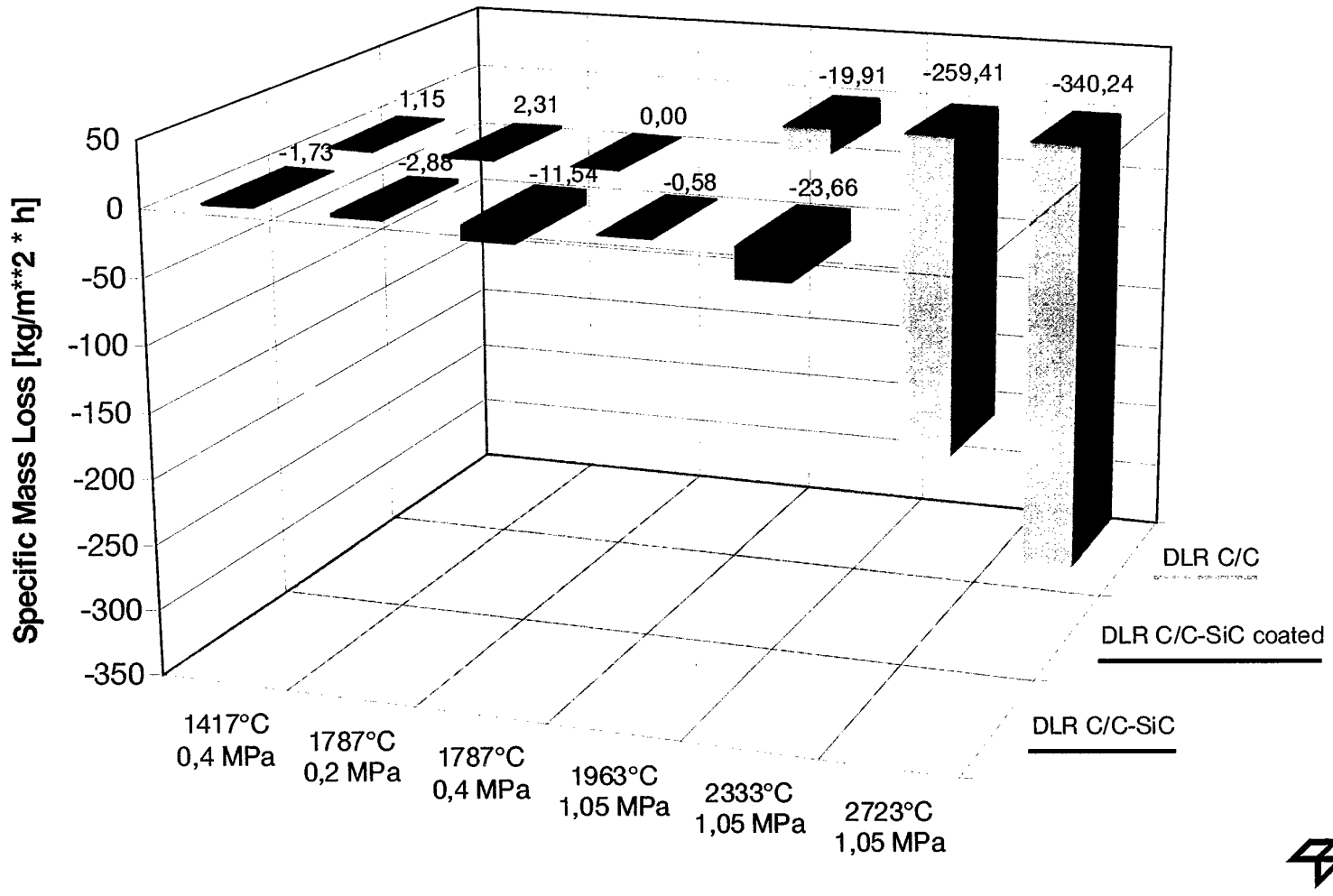
Admixture of O_2: very high mass loss rates
(⟶ water vapour corrosion)

Admixture of O_2: C/C-SiC shows higher mass loss rate than C/C
(⟶ oxidation not dominant)

[1] Inst. für Raumfahrtsysteme, Universität Stuttgart

DLR

Material Tests in Combustion Chamber M3



DLR

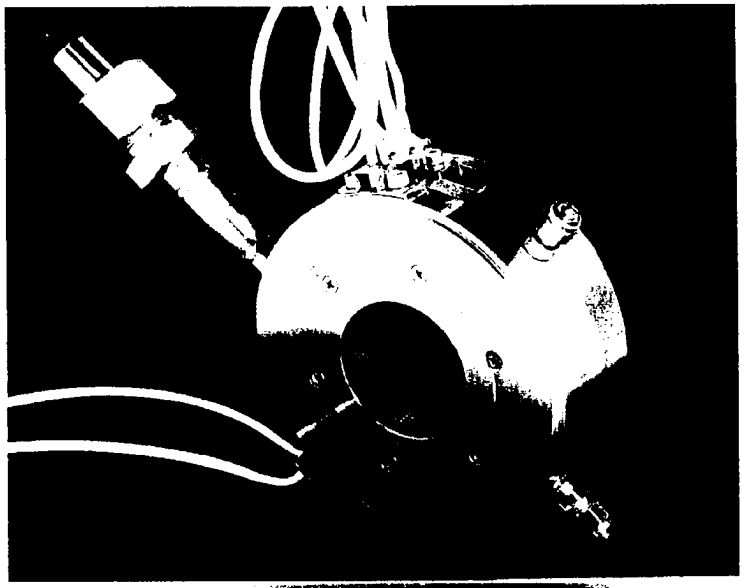
Ceramic Functional Tests with Transpiration Cooling

M3 Micro Combustor

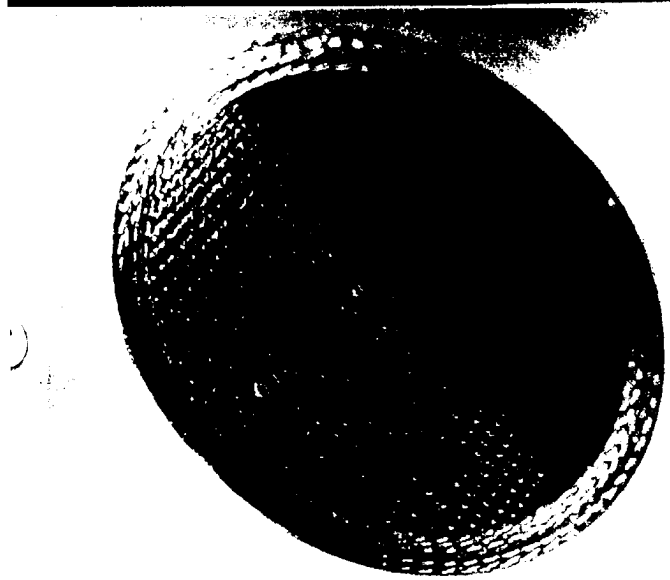
- Establishment of Data Base for Development and Verification of Numerical Design Tool
- Cyclic Testing for Component Life
- Determination of Minimum Coolant Mass Flow Rate

P8 Subscale Facility

- Determination of Operating Parameters at High Pressures (< 15 MPa)
- Technology Verification
  - relevant combustion chamber pressures
  - relevant coolant temperatures (GH2 : 100 K, LH2)

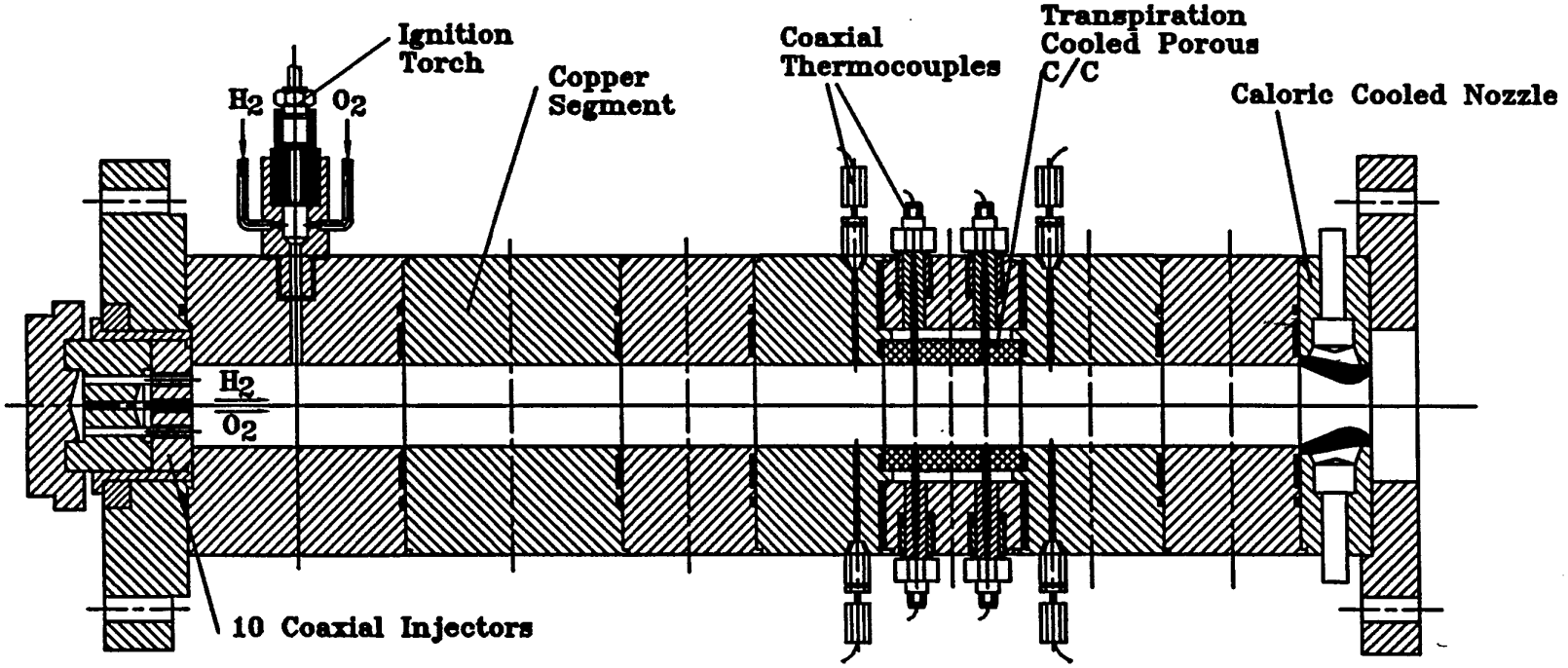


Combustor B Segment for Transpiration Cooling with Porous C/C



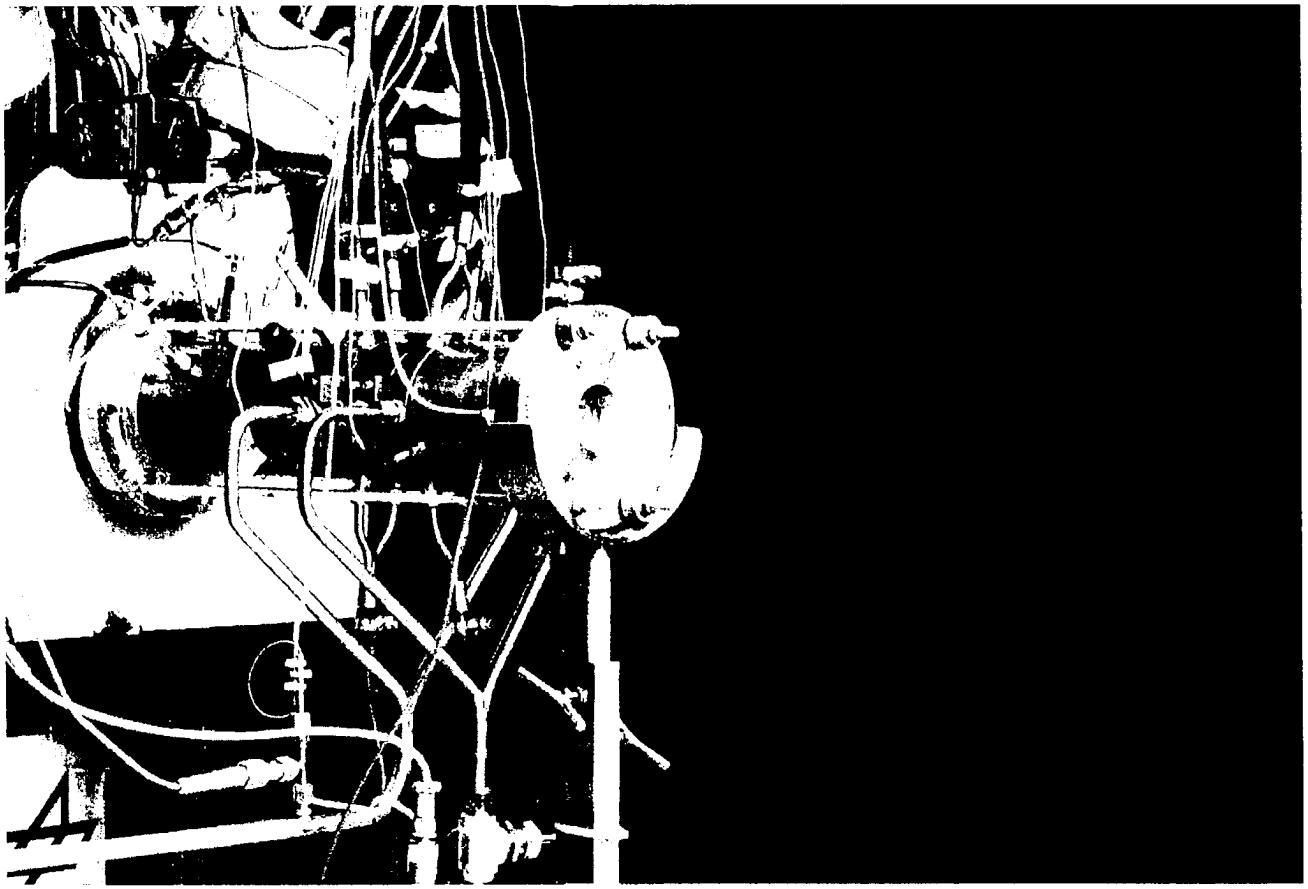
C/C-Segment Equipped with Thermocouples for Coolant Film Temperature Measurements

DLR



Micro-Combustor with C/C for effusion cooling

DLR



M3 Micro Combustion Facility with Effusion Cooled Segment

Operating Conditions for Effusion Cooling at M3

$Rof = 6.50$, $Pr = 0.58$, $u_c = 260\ m/s$				
T_c [K]	3207	3300	3360	3396
ρ_c $[kg/m^3]$	0.153	0.298	0.436	0.559
cp_c [kJ/kgK]	17.58	15.85	15.13	14.54
Re_D $[10^3]$	15.51	28.6	42.27	53.1
p_c $[MPa]$	0.30	0.605	0.875	1.16
$Rof[-]$	6.44	6.50	6.74	6.70

Total of 100 tests with

- C/C porous segments with 15%, 20 %, 22%, 25% porosity
- Blowing ratio varying between 0,007 and 0,03

DLR

Governing Equations

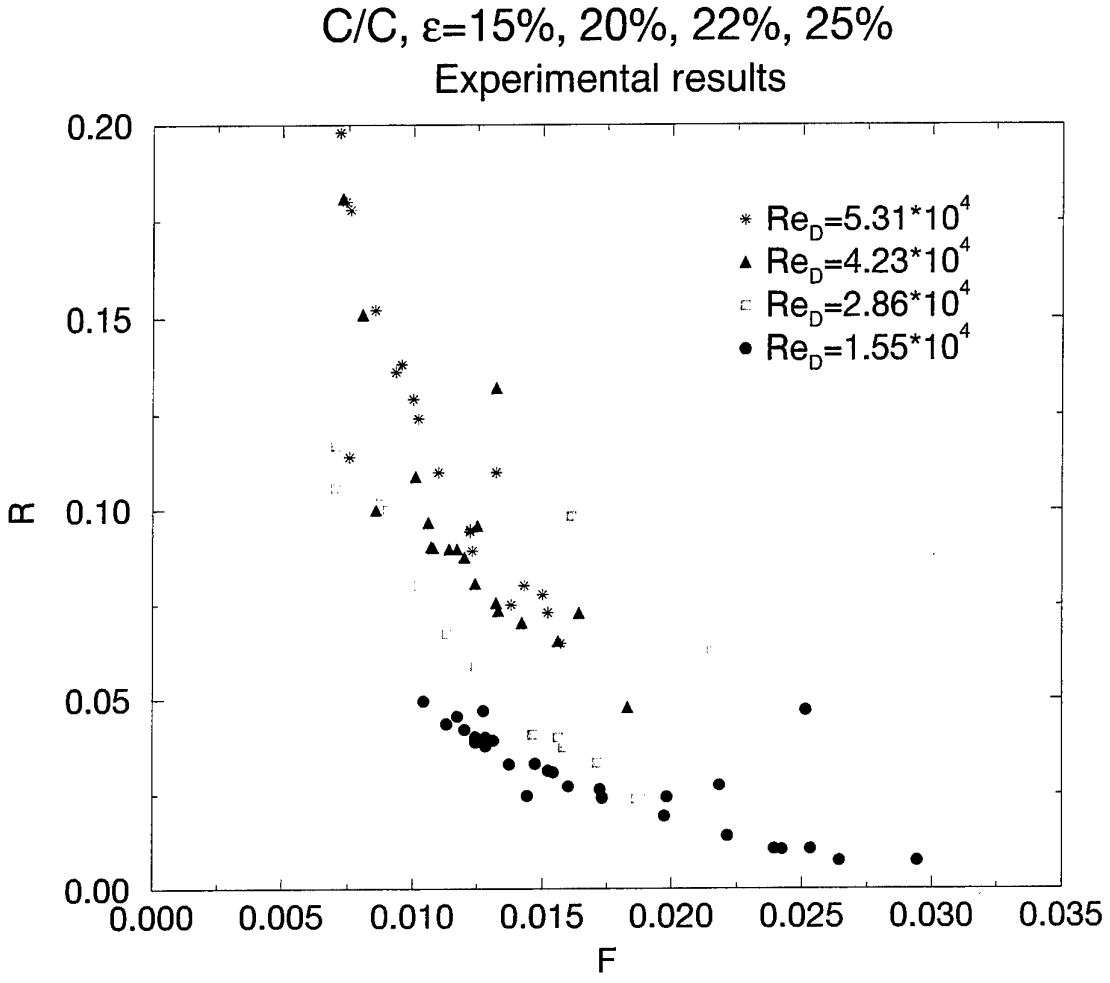
$$Re_D = \frac{u_c D}{\nu}; \qquad St_0 = \frac{Nu_0}{PrRe_D}$$

$$Nu_0 = \frac{\alpha_0 D}{\lambda} = 0.0205 \cdot Re_D^{0.82} Pr^{0.82} \left(\frac{T_{ad}}{T_W}\right)^{0.35} F_g(x)$$

$$F = \frac{\rho_f v_f}{\rho_c u_c}; \qquad \eta = \frac{St}{St_0}$$

$$R = \frac{T_W - T_R}{T_c - T_R}$$

DLR



Temperature ratio as a function of blowing ratio, experimental results micro combustion chamber M3

DLR

Operating Conditions for Cyclic Testing of Effusion Cooled C/C Structures

T_c~	3379 K	ρ_c	0.538 kg/m^3
c_p	14.22 kJ/kgK	u_c	274 m/s
p_c	1.13 MPa		
Re	5.27 x10^4	R_{of}	6.32

A total of 50 tests (10 sec duration) were performed with the same porous segment (21.6% porosity) at a blowing ratio of about 0.003.

- After each serie of 5 tests the segment was optically controlled with an endoscope to check for erosion and surface roughening.
- The pressure drop across the C/C structure was surveilled to check for cracks and delamination.

⇒ No damage could be detected.

DLR

Operating Conditions for Functional Test at P8

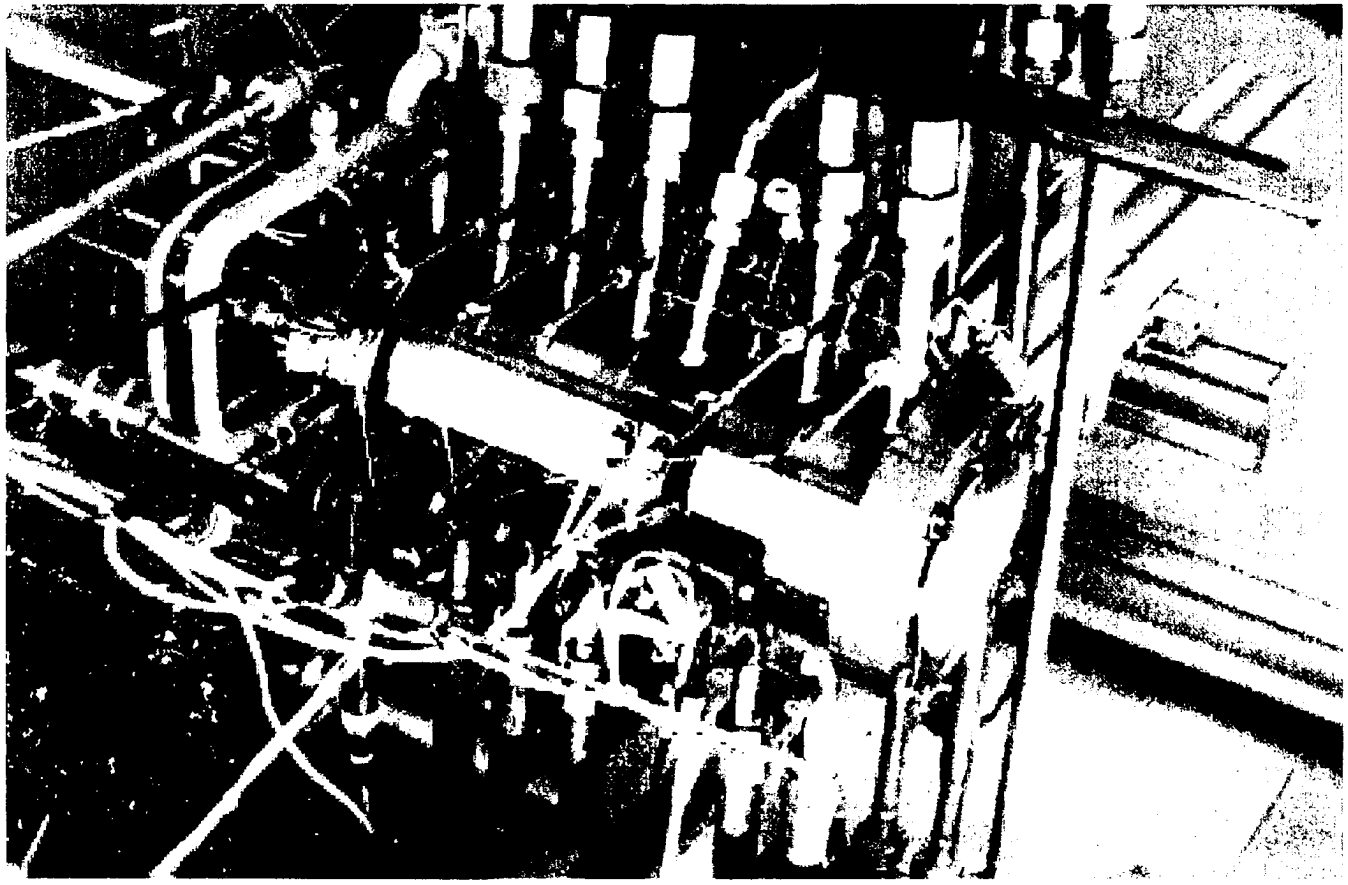
p_c	9 MPa	10 MPa
Re	6.6×10^5	7.3×10^5
m_{tot}	2.0 kg/s	2.3 kg/s

A total of 10 tests have been performed with DLR Model Combustor B (GH2 / LOX) operated at a mixture ratio of 6.0 with a C/C segment having a porosity of 13%.

The blowing ratio F has been varied between 0.002 and 0.0025 with 2 different coolant temperatures T_{GH2} 300 K and 160 K.

Again, at the very low end of the blowing ratio, material losses at the surface could be detected.

DLR



Functional Tests of Porous C /C for GH2 Transpiration Cooling Applying DLR Model Combustor at P8

DLR

Operating Conditions for Tests to Determine Minimum Coolant Mass Flow Rate

T_c~	3379 K	ρ_c	0.538 kg/m^3
c_p	14.22 kJ/kgK	u_c	274 m/s
p_c	1.13 MPa		
Re	5.27 x10^4	R_{of}	6.32

A total of 10 tests (10 sec duration each) was performed with the same porous segment (21.6% porosity) and the blowing ratio was reduced step by step from 0.003 to 0.0023.

⇒ Only at the very low end of the blowing ratio a minor material loss could be detected.

DLR

Summary

- Overview on the Motivation for our Work
- Problems to be solved
- Current Status
  - Engineering Design Tool
  - Thermal Barrier Coatings
  - Ceramic Structures for Transpiration Cooled Components

Outlook

- Qualification of TBC at P8 with water-cooled components and LH2 cooled components
- Enlarge Data Base for Transpiration Cooled Porous Ceramic Structures at P8 with LH2

Thermomechanical Fluid-Structure Analysis and Mathematical Optimization Techniques Applied to Cryogenic Liquid Rocket Engine Design

Detlef Kuhl
Ruhr-University Bochum, Institute for Structural Mechanics
Universitätsstraße 150, D-44780 Bochum, Germany

Jörg Riccius and Oskar J. Haidn
German Aerospace Center, Institute of Space Propulsion
D-74239 Hardthausen, Germany

Abstract

A coupled finite element fluid-structure interaction analysis of regeneratively cooled rocket combustion chambers, which allows the computation of the coolant flow and the heat conduction between the coolant and the combustion chamber structure, will be presented. Furthermore, the resulting elastoplastic deformation of the combustion chamber under cyclic thermal and mechanical loading will be analyzed by the Finite Element Method. The developed solution strategy of the thermo-mechanically coupled field problem will be studied and applied to the prediction of the heat transfer and thermal load induced deformation process of the European rocket engine 'Vulcain'. Based on this results, the failure mechanism and the parameters of failure of the combustion chamber can be indicated which allows some proposals of improved combustion chamber design concepts reducing the plastic strains and consequently increasing the life time of the rocket engine.
Beside the conceptual design given by the engineer, a mathematical optimization procedure based on the Finite Element model of the combustion chamber is investigated. This optimization method allows the improvement of an initial design of the combustion chamber with respect to a finite number of design variables such that the stress, plastic strain or temperature level is decreased and accordingly, the life time will be increased. The main advantage of the presented method is that a design change will be determined automatically and the improvement of the structure with respect to a user defined objective is guaranteed.

Key words

fluid flow simulation, thermal fluid-structure analysis, thermo-elasto-plasticity, non-linear finite element method, rocket combustion chamber, cyclic loading, optimization, conjugate direction methods

1 Introduction

The cryogenic hydrogen/oxygen powered Vulcain engine is the main stage of the European Ariane 5 space transportation system. Figure 1 shows the scheme of this regeneratively cooled gas generator cycle engine. At the nominal operating point of 11 MPa, the peak heat load in the throat area exceeds 80 MW/m^2. The regenerative cooling introduces an enormous temperature gradient across the combustion chamber walls yielding large heat fluxes and induced thermal stresses. The resulting plastic deformations of the wall material limit the combustion chamber life. Experimental investigations by QUENTMEYER [34, 35] have demonstrated that low-cycle-fatigue and creep are the main reasons for material failures. Figure 2 shows a sketch of a combustion chamber cross section emphasizing characteristic features of a regeneratively cooled combustion chamber such as cooling channel geometry, failure location, chamber wall and outer liner materials.

1.1 Motivation

The increasing requirements regarding the performance of cryogenic liquid rocket engines in combination with the need to continuously reduce the operational cost has led to the idea of reusable space transportation systems. Since all reusable systems are based on an increased combustion chamber life, the current research and technology activities at DLR Lampoldshausen aim at

- a detailed understanding of the failure mechanisms,
- the development of a tool for the prediction of the combustion chamber life
- an optimized design of the combustion chamber.

Prior to the realization of these items, the general problem of heat and mass transfer in a combustion chamber of a liquid rocket engine has to be solved: The prediction of injection, atomization, mixing and combustion of the propellants as well as the hot gas flow in the combustion chamber, the heat transfer from the hot gas side to the wall, further into the structure and into the coolant, and, finally, the coolant flow itself. The basis for a deeper understanding of the failure mechanisms of current combustion chamber designs are detailed experimental data, material and failure laws, and numerical simulations of the structural behaviour, compare KUHL, WOSCHNAK &HAIDN [22] and KUHL [20]. Improved and validated models for low-cycle-fatigue and creep have to be implemented in a finite-element-code together with the appropriate boundary conditions in order to realize a tool for combustion chamber life prediction. The automatic design optimization requires the solution of the inverse thermo-mechanical problem. Therefore, mathematical programming or optimization methods will be applied to improve future developments of combustion chambers, see KUHL ET AL. [21]. It is expected that the combination of the obtained design tools and results yields an improvement of both, coolant side heat transfer and the combustion chamber geometry and will increase the life time of cryogenic liquid rocket engines.

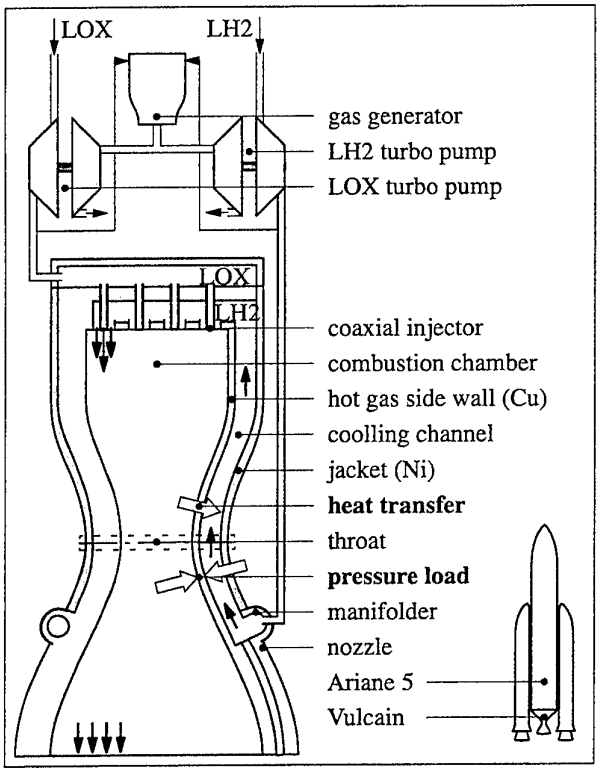


Figure 1: Schematic view of the regeneratively cooled combustion chamber Vulcain

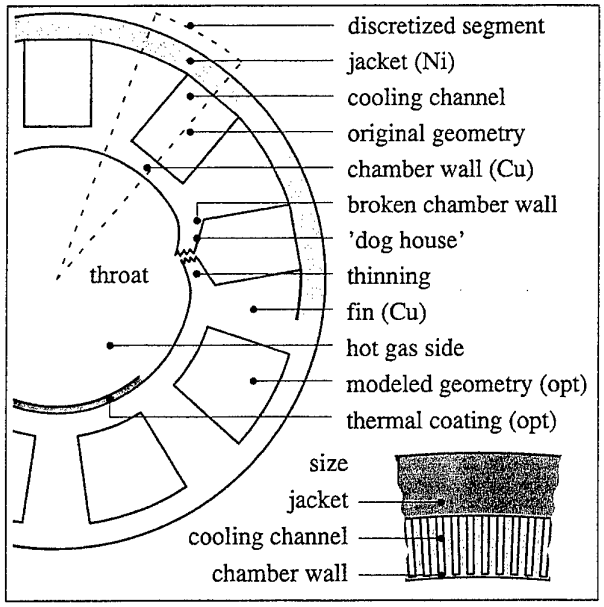


Figure 2: Throat of the combustion chamber: modeling, characteristic failure and optimization model (opt)

1.2 Direct thermo-mechanical problem

The modeling and the simulation of the direct thermo-mechanical problem is focused on the coolant flow and the deformation of the combustion chamber wall. The effect of the combustion chamber flow and heating on the hot gas side is introduced due to prescribed boundary conditions, namely the combustion chamber pressure p_h and the hot gas side heat flux $q_h = \alpha_h(\theta - \theta_h)$, obtained from experiments by FISCHER, POPP&QUENTMEYER[10]. The thermo-mechanical fluid-structure model is subdivided in the coupled fluid-flow and thermal field problem and the thermo-mechanical structural problem, whereby the parts are connected by the heat transfer $q_c = \alpha_c(\theta_c - \theta)$ and the pressure p_c. For the sake of simplicity the geometry of the combustion chamber wall and the cooling channel is substituted by a representative geometry, given by a three dimensional straight cooling channel and thermal structural model and a plane stress thermo-mechanical structural model as sketched in Figure 3.

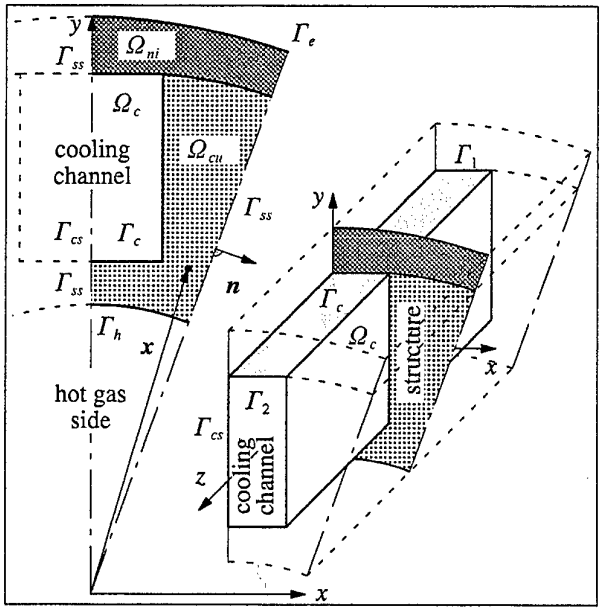


Figure 3: Computational model of the combustion chamber

1.3 Optimization

Based on the direct problem described in section 1.2 the inverse problem can be solved. Within the framework of the inverse problem, loads and material as well as manufacturing restrictions are given and the design of the combustion chamber should be generated in away to obtain an optimal behavior with respect to a well defined objective. The inverse problem is solved by methods of mathematical programming where the solution of the direct problem is included in order to determine the objective and the sensitivity of the objective with respect to the design parameters. Practically, the application of optimization methods are restricted to an additional optimization loop in the program code including the solution procedure of the direct problem. Consequently, these methods may be simply applied in order to calculate the optimal design of combustion chambers. Within this paper, optimization methods and their application to the optimization of combustion chamber design is investigated by means of a linear thermo-mechanical model problem of the combustion chamber are presented.

2 Governing equations

The thermo-mechanically coupled boundary value problem of the interacting coolant flow and the combustion chamber's structure is governed by the conservation laws of mass, momentum and energy as well as the related boundary conditions, whereby the conservation of mass is explicitly satisfied for the solid approach. First, four essential simplifications are made in order to obtain a system of differential equations which can be solved robustly and effectively by Finite Element discretization techniques:

Assumption 1: The system behavior is independent of time, a steady state formulation is sufficient.

Assumption 2: The fluid flow is incompressible.

Assumption 3: The fluid properties dynamic viscosity μ and density ρ are independent on the temperature.

Assumption 4: The isotropic conductivity λ of the fluid and the structure are independent on the temperature.

Assumption 5: The deformations of the structure are small, a geometrically linear description is sufficient.

The computational model of the combustion chamber, the solid and fluid subdomains and the boundaries for the formulation of the thermo-mechanical fluid-structure-interaction problem are illustrated in Figure 3. Based on the the Assumptions 1 the 5 to thermo-mechanical system of the combustion chamber is uniquely described by the velocity field of the fluid $\dot{\boldsymbol{u}}$, the coupled temperature field of the fluid and the structure θ, the displacement field of the structure $\boldsymbol{u}$ and the local history variables of the non-linear material law $\boldsymbol{\epsilon}^p$ and $\boldsymbol{\alpha}$. For the formulation of the differential equations in the following sections compare the related literature (see e.g. MALVERN[28], MARSDEN&HUGHES[29], HIRSCH[17] and LEWIS ET AL.[25]).

2.1 Mechanical fluid field

If the Assumptions 1-3 are considered, the Navier-Stokes equations, explicitly the conservation of mass and momentum, circumstantiate that the fields of the velocity vector $\dot{\boldsymbol{u}}(\boldsymbol{x}, p)$ and the pressure $p(\boldsymbol{x}, \dot{\boldsymbol{u}})$ are

independent of the temperature field $\theta(\boldsymbol{x}, \dot{\boldsymbol{u}}, p)$. The conservation of mass is given by the divergence free velocity field.

$$\nabla \cdot \dot{\boldsymbol{u}} = 0 \quad \forall \quad \boldsymbol{x} \in \Omega_c \tag{1}$$

If no external forces are applied, the equation of motion

$$\nabla \cdot (\rho\, \dot{\boldsymbol{u}} \otimes \dot{\boldsymbol{u}} - \boldsymbol{\sigma}) = \boldsymbol{0} \quad \forall \quad \boldsymbol{x} \in \Omega_c \tag{2}$$

is given as a function of the density ρ, the velocity vector $\dot{\boldsymbol{u}}(\boldsymbol{x})$ and the stress tensor $\boldsymbol{\sigma}(\boldsymbol{x}, \dot{\boldsymbol{u}})$. The stress tensor $\boldsymbol{\sigma}$ is defined by the constitutive law including the pressure $p(\boldsymbol{x})$, the isotropic dynamic viscosity μ and the viscous shear tensor $\boldsymbol{\tau}(\boldsymbol{x}, \dot{\boldsymbol{u}})$ of a Newtonian fluid.

$$\begin{aligned} \boldsymbol{\tau} &= 2\,\mu\, \nabla^{sym} \dot{\boldsymbol{u}} = \mu\, [\nabla \dot{\boldsymbol{u}} + (\nabla \dot{\boldsymbol{u}})^T] \\ \boldsymbol{\sigma} &= -p\, \boldsymbol{I}_2 + \boldsymbol{\tau} \end{aligned} \tag{3}$$

Herein, $\boldsymbol{I}_2$ denotes the rank-2 unit tensor. The pressure can be determined for a prescribed velocity field by the evolution of the divergence of equation (2) considering equations (1) and (3).

$$\nabla^2 \cdot (\dot{\boldsymbol{u}} \otimes \dot{\boldsymbol{u}} + p\, \boldsymbol{I}_2) = 0 \tag{4}$$

Dirichlet boundary conditions are given by the velocities at the inlet, the non-slip condition at the cooling channel wall, the symmetry conditions and the pressure at the outlet.

$$\begin{aligned} &\dot{\boldsymbol{u}} \cdot \boldsymbol{n} = \dot{u}_1 \quad \dot{\boldsymbol{u}} \times \boldsymbol{n} = \boldsymbol{0} && \forall \quad \boldsymbol{x} \in \Gamma_1 \\ &\dot{\boldsymbol{u}} = \boldsymbol{0} && \forall \quad \boldsymbol{x} \in \Gamma_c \\ &\dot{\boldsymbol{u}} \cdot \boldsymbol{n} = 0 && \forall \quad \boldsymbol{x} \in \Gamma_{cs} \\ &p = p_2 && \forall \quad \boldsymbol{x} \in \Gamma_2 \end{aligned} \tag{5}$$

2.2 Thermal fluid field

If no heat sources and external forces are applied and assumption 1 is considered, the conservation of energy is given in terms of the convective heat flux of the specific total energy $h(\boldsymbol{x}, \dot{\boldsymbol{u}}, \theta)$, the diffusive flux of energy $\boldsymbol{q}(\boldsymbol{x}, \theta)$ and the work performed by the internal stresses $\boldsymbol{\sigma} \cdot \dot{\boldsymbol{u}}$.

$$\nabla \cdot (\rho\, \dot{\boldsymbol{u}}\, h + \boldsymbol{q} - \boldsymbol{\sigma} \cdot \dot{\boldsymbol{u}}) = 0 \quad \forall \quad \boldsymbol{x} \in \Omega_c \tag{6}$$

Herein, the total energy is given by the sum of the kinetic energy $\dot{\boldsymbol{u}}^2(\boldsymbol{x})/2$ and the internal energy $e(\boldsymbol{x}, \theta)$.

$$h = \frac{1}{2}\, \dot{\boldsymbol{u}} \cdot \dot{\boldsymbol{u}} + e \tag{7}$$

Furthermore, the constitutive laws connect the temperature field to the diffusive heat flux and the specific internal energy to the temperature field,

$$\boldsymbol{q} = -\lambda\, \nabla \theta\,, \quad e = c\, \theta \tag{8}$$

where λ represents the isotropic conductivity and c the specific heat coefficient. Thermal boundary conditions are given at the in- and outlet, the cooling channel wall and the symmetry plane Γ_{cs}.

$$\begin{aligned} &\theta = \theta_1 && \forall \quad \boldsymbol{x} \in \Gamma_1 \\ &\theta = \theta_s && \forall \quad \boldsymbol{x} \in \Gamma_c \\ &\boldsymbol{q} \cdot \boldsymbol{n} = 0 && \forall \quad \boldsymbol{x} \in \{\Gamma_{cs}\,,\, \Gamma_2\} \end{aligned} \tag{9}$$

2.3 Thermal structural field

Assuming a stationary temperature field $\theta(\boldsymbol{x})$ (assumption 1), the energy balance law, given for the heat source free case, connects the heat flux $\boldsymbol{q}(\boldsymbol{x}, \theta)$ to the internal dissipation $\mathcal{D}_{\text{int}}(\boldsymbol{x}, \boldsymbol{u}, \theta)$ resulting from the plastic deformation of the material.

$$\nabla \cdot \boldsymbol{q} = \mathcal{D}_{\text{int}} \quad \forall \quad \boldsymbol{x} \in \{\Omega_{cu}\,,\, \Omega_{ni}\} \tag{10}$$

The constitutive law, namely the Fourier law, defines the heat flow as a function of the temperature field. With the assumption of an isotropic conductivity λ, the heat flux of the combustion chamber's structure is given by the gradient of the temperature field.

$$\boldsymbol{q} = -\lambda\, \nabla \theta \tag{11}$$

All the boundary conditions of the thermal field are Neumann boundary conditions, described by symmetry conditions, adiabatic conditions at the environment surface, the experimentally evaluated film coefficient α_h with respect to the bulk temperature θ_h at the hot gas side (representing the normal heat flux $q_h = \boldsymbol{q} \cdot \boldsymbol{n}$) and the numerically evaluated film coefficient α_c at the coolant side with respect to the bulk temperature θ_c (representing the normal heat flux q_c).

$$\begin{aligned} &\boldsymbol{q} \cdot \boldsymbol{n} = 0 && \forall \quad \boldsymbol{x} \in \{\Gamma_{ss}\,,\, \Gamma_e\} \\ &\boldsymbol{q} \cdot \boldsymbol{n} = q_h = \alpha_h\, (\theta - \theta_h) && \forall \quad \boldsymbol{x} \in \Gamma_h \\ &\boldsymbol{q} \cdot \boldsymbol{n} = q_c = \alpha_c\, (\theta - \theta_c) && \forall \quad \boldsymbol{x} \in \Gamma_c \end{aligned} \tag{12}$$

2.4 Mechanical structural field

Considering Assumptions 1 and 5, the deformation of the combustion chamber's structure is described by the displacement field $\boldsymbol{u}(\boldsymbol{x}, \theta)$, dependent on the position vector and the applied temperature field $\theta(\boldsymbol{x})$. For the quasi-static case, the displacement field in absence of prescribed body forces is determined by Cauchy's equation of motion.

$$\nabla \cdot \boldsymbol{\sigma} = \boldsymbol{0} \quad \forall \quad \boldsymbol{x} \in \{\Omega_{cu}\,,\, \Omega_{ni}\} \tag{13}$$

Herein, $\boldsymbol{\sigma}(\theta, \boldsymbol{\epsilon}, \boldsymbol{\alpha})$ represents the Cauchy stress tensor, given as a function of the temperature field, the Green strain tensor $\boldsymbol{\epsilon}(\boldsymbol{x}, \boldsymbol{u})$ and the internal variables $\boldsymbol{\alpha}(\boldsymbol{x}, \boldsymbol{u}, \theta)$. The stress tensor is related to this field variables by the constitutive or material law as described in section 2.5. According to a geometrically linear description (assumption 5), the strain tensor is defined by the symmetric part of the gradient operator applied to the displacement field.

$$\boldsymbol{\epsilon} = \nabla^{sym}\boldsymbol{u} = \frac{1}{2}\left[\nabla\boldsymbol{u} + (\nabla\boldsymbol{u})^T\right] \tag{14}$$

In order to solve the system of differential equations (13), the mechanical boundary value problem should be completed by the associated boundary conditions. These are symmetry conditions, the pressure free environment, the experimentally evaluated hot gas side pressure p_h and the cooling channel pressure p_c.

$$\begin{aligned} \boldsymbol{u}\cdot\boldsymbol{n} &= 0 \quad && \forall \quad \boldsymbol{x} \in \Gamma_{ss} \\ \boldsymbol{n}\cdot\boldsymbol{\sigma}\cdot\boldsymbol{n} &= 0 && \forall \quad \boldsymbol{x} \in \Gamma_{e} \\ \boldsymbol{n}\cdot\boldsymbol{\sigma}\cdot\boldsymbol{n} &= p_h && \forall \quad \boldsymbol{x} \in \Gamma_{h} \\ \boldsymbol{n}\cdot\boldsymbol{\sigma}\cdot\boldsymbol{n} &= p_c && \forall \quad \boldsymbol{x} \in \Gamma_{c} \end{aligned} \tag{15}$$

2.5 Non-linear material law

The solution of the equation of motion (13) requires the calculation of the stress tensor as a function of the total strains and the temperature. Therefore, a material model has been chosen, which can be characterized by the von Mises yield function, associative small strain plasticity, a linear kinematic hardening rule and temperature dependent material properties. The thermal field is assumed to be constant within the deformation process. Consequently, only the temperature dependent material properties and the thermal strains couple the thermal and the mechanical field. The basic theory described e.g. in HILL[16], LEMAITRE& CHABOCHE[24], LUBLINER[26], SIMO&HUGHES[39], SIMO[38] and KLEIBER[19] will be summarized and applied to the calculation of the rocket combustion chamber.

As a basis for the definition of the non-linear material behavior, the infinitesimal strain tensor $\boldsymbol{\epsilon}$ is additively splitted in an elastic $\boldsymbol{\epsilon}^e(\boldsymbol{x}, \boldsymbol{u}, \theta)$, a thermal $\boldsymbol{\epsilon}^\theta(\boldsymbol{x}, \theta)$ and a plastic part $\boldsymbol{\epsilon}^p(\boldsymbol{x}, \boldsymbol{u}, \theta)$.

$$\boldsymbol{\epsilon} = \nabla^{sym}\boldsymbol{u} = \boldsymbol{\epsilon}^e + \boldsymbol{\epsilon}^\theta + \boldsymbol{\epsilon}^p \tag{16}$$

Thermal strains of isotropic materials are determined by the thermal expansion coefficient α and the difference between the current temperature θ and the reference temperature $\underline{\theta}$ representing the temperature of manufacturing.

$$\boldsymbol{\epsilon}^\theta = \alpha\ (\theta - \underline{\theta})\ \boldsymbol{I}_2 \tag{17}$$

The stress tensor is described by the elastic stress strain relation and the constitutive tensor $\boldsymbol{C}(\theta)$

$$\boldsymbol{\sigma} = \boldsymbol{C} : \boldsymbol{\epsilon}^e = \boldsymbol{C} : (\boldsymbol{\epsilon} - \boldsymbol{\epsilon}^p - \boldsymbol{\epsilon}^\theta) \tag{18}$$

given in terms of the temperature dependent Lamé material parameters $\lambda(\theta)$ and $\mu(\theta)$ and the rank-4 unit tensor $\boldsymbol{I}_4$

$$\boldsymbol{C} = \lambda\ \boldsymbol{I}_2 \otimes \boldsymbol{I}_2 + 2\,\mu\,\boldsymbol{I}_4 \tag{19}$$

or the Young modulus $E(\theta)$ and the Poisson ratio ν.

$$\lambda = \frac{E\,\nu}{(1-2\,\nu)\,(1+\nu)}\ , \quad \mu = \frac{E}{2\,(1+\nu)} \tag{20}$$

Plastic deformations are characterized by the von Mises yield function and the linear kinematic hardening rule.

$$f(\boldsymbol{\sigma}, \boldsymbol{\alpha}, \theta) = \|\mathrm{dev}\boldsymbol{\sigma} - \boldsymbol{\alpha}\| - \sqrt{\frac{2}{3}}\,\sigma_Y \tag{21}$$

Herein, $\boldsymbol{\alpha}$ are the second order tensor valued internal hardening variables defining the center of the von Mises yield surface with $\boldsymbol{\alpha} : \boldsymbol{I}_2 = 0$, $\sigma_Y(\theta)$ is the temperature dependent yield stress and the deviator of a tensor is defined as follows:

$$\mathrm{dev}(\bullet) = (\bullet) - \frac{1}{3}\,(\bullet) : \boldsymbol{I}_2\ \boldsymbol{I}_2 \tag{22}$$

The flow rule and the linear kinematic hardening law for associative plasticity are formulated in evolution equations by means of the consistency parameter $\dot{\gamma}$,

$$\dot{\boldsymbol{\epsilon}}^p = \frac{\partial \boldsymbol{\epsilon}^p}{\partial t} = \dot{\gamma}\,\frac{\mathrm{dev}\boldsymbol{\sigma} - \boldsymbol{\alpha}}{\|\mathrm{dev}\boldsymbol{\sigma} - \boldsymbol{\alpha}\|} = \dot{\gamma}\,\boldsymbol{n} \tag{23}$$

where $\boldsymbol{n}$ defines the normal tensor of the yield surface including the direction of the plastic flow. The evolution of the kinematic hardening variables is defined in terms of the kinematic hardening modulus $H(\theta)$ related to the material parameters evaluated by the uniaxial tension test, namely the Young modulus $E(\theta)$ and the tangent modulus $T(\theta)$.

$$\dot{\boldsymbol{\alpha}} = \dot{\gamma}\,\frac{2}{3}\,H\,\boldsymbol{n} = \dot{\gamma}\,\frac{2}{3}\frac{E\,T}{E-T}\,\boldsymbol{n} \tag{24}$$

Furthermore, the Kuhn-Tucker loading/unloading conditions and the consistency condition

$$\dot{\gamma} \geq 0,\ f \leq 0,\ \dot{\gamma}\,f = 0,\ \dot{\gamma}\,\dot{f} = 0 \tag{25}$$

have to be satisfied. With $\dot{\gamma} > 0$, the consistency condition, the time derivative of the yield function (equation (21)) and the assumption of an associative flow rule, the consistency parameter can be determined.

$$\dot{\gamma} = \frac{3\,\mu}{3\,\mu + H + \sigma_Y}\,\boldsymbol{n} : \dot{\boldsymbol{\epsilon}} \tag{26}$$

Applying equations (18,23,26) yields the rate of the stress tensor related to the rate of the total strain tensor

$$\dot{\sigma} = \boldsymbol{C} : (\dot{\epsilon} - \dot{\epsilon}^p - \dot{\epsilon}^\theta) = \boldsymbol{C} : (\dot{\epsilon} - n\dot{\gamma}) = \boldsymbol{C}^{ep} : \dot{\epsilon} \quad (27)$$

by the continuum elastoplastic tangent operator $\boldsymbol{C}^{ep}$ which is identical to $\boldsymbol{C}$ given in equation (19) for $\dot{\gamma} = 0$ and calculated by

$$\boldsymbol{C}^{ep} = \boldsymbol{C} - \frac{6\,\mu^2}{3\,\mu + H + \sigma_Y}\, \boldsymbol{n} \otimes \boldsymbol{n} \quad (28)$$

for plastic deformations defined by $\dot{\gamma} > 0$. Finally, the influence of the plastic deformation to the thermal field $\theta(\boldsymbol{x})$, the internal dissipation $\mathcal{D}_{\text{int}}$ included in the conservation law of energy (10), will be determined. The internal dissipation is given in terms of the work done by the stresses and the plastic strains $\boldsymbol{\sigma} : \dot{\boldsymbol{\epsilon}}^p$ as well as in terms of the hardening variables $\boldsymbol{\alpha}$ and the derivative of the yield function $f(\boldsymbol{\sigma}, \boldsymbol{\alpha})$ (equation (21)) with respect to the hardening variables.

$$\mathcal{D}_{\text{int}} = \boldsymbol{\sigma} : \dot{\boldsymbol{\epsilon}}^p + \boldsymbol{\alpha} : \frac{\partial f(\boldsymbol{\sigma}, \boldsymbol{\alpha})}{\partial \boldsymbol{\alpha}}\, \dot{\gamma} = (\boldsymbol{\sigma} - \boldsymbol{\alpha}) : \dot{\boldsymbol{\epsilon}}^p \quad (29)$$

3 Solution technique

The previously described multiple field boundary value problem, governed by the fluid problem of the coolant flow, the thermal fluid-structure interaction and the thermo-mechanical problem of the combustion chamber structure, a coupled field solution strategy and the Finite Element discretization will be applied.

3.1 Coupled field problem

Summarizing previous sections, the coolant flow, the heat transfer and the structural deformation are completely described by the differential equations and coupling fields or coupling boundary values illustrated in Figure 4. In the middle of this diagram the differential equations are shown. The left side demonstrates the coupling of these equations from the top to the bottom, whereas the right side shows the coupling in the opposite direction. As mentioned before, the velocity field of the coolant flow is independent of the other fields but influences the thermal field of the fluid as well as the displacement field of the structure. Remember, that this one-way-coupling is based on assumptions 2-5. In contrast to this, the other fields are fully coupled. However, if a further assumption is introduced, the solution process will be significantly simplified.

Assumption 6: In comparison to the high thermal loading of the combustion chambers structure within the boundaries the influence of the internal dissipation $\mathcal{D}_{\text{int}}$ to the thermal field is negligible .

Assumption 6 leads to an only one-way-coupled thermo-mechanical problem of the structure, see Figure 4 for $\mathcal{D}_{\text{int}} = 0$ and consequently to a sequential coupled fluid-structure problem. Finally, the previously explained simplifications yield the following sequential solution strategy:

1. Solve the non-linear system of differential equations (1,2) for the velocity field $\dot{\boldsymbol{u}}(\boldsymbol{x})$ of the fluid.
2. Solve the coupled energy equations (6, 10) of the fluid and the solid domain for the temperature field $\theta(\boldsymbol{x}, \dot{\boldsymbol{u}})$.
3. Solve non-linear equation of motion (13) for the displacement field $\boldsymbol{u}(\boldsymbol{x}, \theta)$ of the structure.

Note, that steps 1 and 3 require only standard discretization and non-linear solution methods, whereas the execution of step 2 enforces the coupled solution of the thermal fields of the fluid and the structure. This problem results in linear differential equations if the dynamic viscosity μ and and the conductivity λ of the fluid are assumed to be constant within the the considered temperature range (assumtions 3 and 4).

The coupling of the thermal fields $\theta(\boldsymbol{x}) \;\forall\; \boldsymbol{x} \in \{\Omega_c, \Omega_{cu}, \Omega_{ni}\}$ can be realized based on the equivalence of the type of the differential equations (6) and (10). Consequently, the coupled field problem can be solved by a pure fluid code introducing the restriction

$$\dot{\boldsymbol{u}} = 0 \quad \forall \quad \boldsymbol{x} \in \{\Omega_{cu}\ ,\ \Omega_{ni}\} \quad (30)$$

as proposed by EMERY, COCHRAN & PEPPER [8]. It is worth to note, that alternative strategies for the solution of the combustion chambers thermal fluid-structure problem are discussed by KUHL, WOSCHNAK & HAIDN [22] and WOSCHNAK & KUHL [40] whereby the method characterized by equation (30) was refereed by the adjectives effective and accurate.

Based on above given statements, the thermal field of the combustion chamber can be calculated in a single calculation. However, with respect to the following Finite Element solution technique the complete three dimensional temperature distribution of the combustion chamber is calculated by the fluid analysis and the heat flux q_h at the position of the plane structural analysis is determined by a post-processing procedure, firstly, and used as thermal boundary condition to the one-way coupled plane thermo-mechanical structural problem, secondly. This step by step strategy is favored, because it allows the combined three and two dimensional analysis as well as different adapted Finite Element meshes for the fluid and structural analysis of the combustion chamber (compare Figure 6).

3.2 Modeling of turbulence

Note, that the previous sections 2.1 and 2.2 constitute a complete description of the fluid, which can be solved directly for laminar and also for turbulent flows. Nevertheless, for the direct solution of turbulent flows a very fine discretization is required which is not realizable

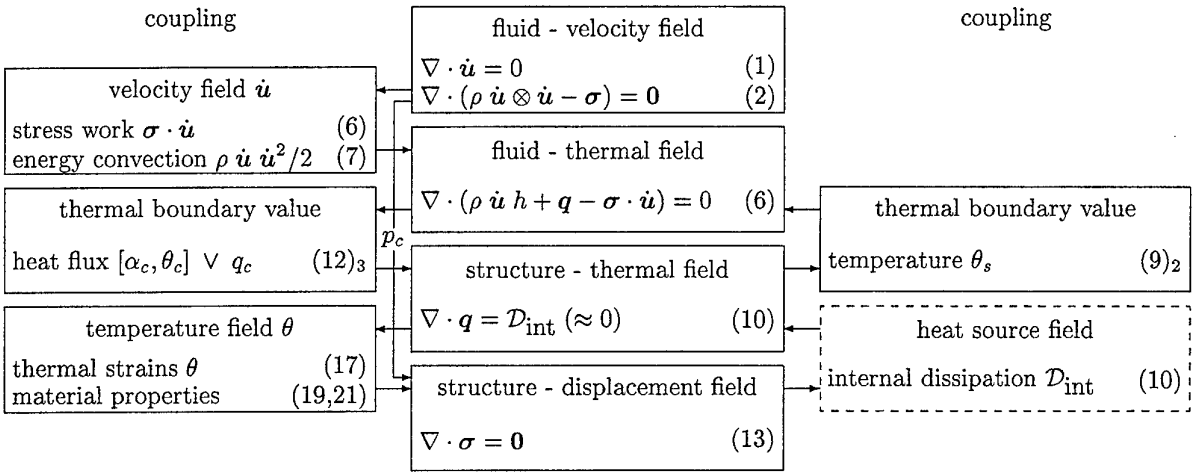


Figure 4: Coupling of the thermomechanical fluid-structure problem

jet even on super computers for the complete cooling channel flow. In order to solve this kind of flow with a finite discretization, the effect of the turbulent motion will be described by the averaging of the turbulent quantities and the additional modeling of turbulence by the k-ε model (see LAUNDER & SPALDING [23]). Herein, the state variables $\dot{u}, p, \theta$ in equations (2, 4, 6) are averaged quantities and the dynamic viscosity μ in equation (3) and the conductivity λ in equation (8) have to be substituted by the related effective values μ_e and λ_e calculated as the sum of the molecular and turbulent quantities.

$$\mu_e = \mu + \mu_t\ , \quad \lambda_e = \lambda + \lambda_t \tag{31}$$

The turbulent diffusive transport coefficients μ_t and λ_t are defined by

$$\mu_t = \frac{C_4\, k^2\, \rho}{\varepsilon}\ , \quad \lambda_t = \frac{C_4\, k^2\, \rho\, c}{\varepsilon\, \mathrm{Pr}_t} \tag{32}$$

where C_i are empirical constants, Pr_t is the turbulent Prandtl number, $k(\boldsymbol{x}, \dot{u}, \varepsilon)$ is the turbulent kinetic energy and $\varepsilon(\boldsymbol{x}, \dot{u}, k)$ represents the turbulent energy dissipation. k and ε are defined by coupled transport equations.

$$\begin{aligned} \dot{u} \cdot \nabla k = {} & C_4\, \frac{k^2}{\varepsilon}\, \nabla \cdot \left(\nabla \dot{u} + \nabla^T \dot{u}\right) \cdot \dot{u} \\ & - \varepsilon + \nabla \cdot \left(\frac{C_4\, k^2}{\mathrm{Pr}_t\, \varepsilon}\, \nabla k\right) \end{aligned} \tag{33}$$

$$\begin{aligned} \dot{u} \cdot \nabla \varepsilon = {} & C_1 C_4\, k\, \nabla \cdot \left(\nabla \dot{u} + \nabla^T \dot{u}\right) \cdot \dot{u} \\ & - C_2\, \frac{\varepsilon^2}{k} + \nabla \cdot \left(\frac{C_4\, k^2}{C_3\, \varepsilon}\, \nabla \varepsilon\right) \end{aligned} \tag{34}$$

The boundary conditions

$$\begin{array}{llll} k = k_1 & \varepsilon = \varepsilon_1 & \forall & \boldsymbol{x} \in \Gamma_1 \\ k = 0 & \varepsilon = 0 & \forall & \boldsymbol{x} \in \Gamma_c \\ \boldsymbol{n} \cdot \nabla k = 0 & \boldsymbol{n} \cdot \nabla \varepsilon & \forall & \boldsymbol{x} \in \{\Gamma_2\ ,\ \Gamma_{cs}\} \end{array} \tag{35}$$

complete the turbulence model. Notice, that the turbulence modeling requires the additional solution of state variables k and ε. However, the global solution technique described above is not influenced by the turbulence modeling, only the solution of the velocity field has to be extended by the transport equations (33) and (34). Consequently, equations (2, 33, 34) have to be solved being coupled, whereas the energy equation (6) is only one-way coupled to the turbulence quantities k and ε by the effective dynamic viscosity μ_e and effective conductivity λ_e.

3.3 Discretization of the fluid

The solution algorithm for the fluid flow analysis applys a Galerkin Finite Element approach to transform the set of partial differential equations into a system of algebraic equations for the primary unknowns. For each degree of freedom, the transport equation can be formulated as a stationary problem. In this analysis the transport equations consist of an advective and a diffusive term. For the discretization of the advective term and due to stabilization requirements the streamline upwind approach (see e.g. RICE & SCHNIPKE [36]) has been used. For the discretisation of the diffusion terms the standard method of the weighted residuals (see e.g. ZIENKIEWICZ & TAYLOR [41]) is applied.

The solution of the resulting algebraic equation system of the fluid flow uses an uncoupled approach. This means, that each field variable is solved in a sequential way with intermediate values of the other quantities from the previous global iteration. A segregated velocity-pressure solution algorithm, called Fractional Step Method, is applied (compare HIRSCH [17]).

3.4 Integration of the material law

The numerical solution of material evolution laws for the plastic strain tensor ϵ^p and the internal variable tensor α is realized as proposed by SIMO & HUGHES [39] and SIMO [38]. Therefore, the initial value of the the internal variable tensor has to be defined and its evolution within the time should be integrated in a numerical manner. The application of the implicit backward Euler integration to the evolution equations (23) and (24) yields the time discrete description of the plastic strains and the hardening variables. The calculation of the stresses and strains at the end of the time step is realized in a common manner by an operator split in a purely elastic step and a closest-point projection of the so called trial state onto the yield surface. By this procedure the current stress tensor and the algorithmic elasto-plastic tangential will be obtained.

3.5 Discretization of the structure

The solution of the local differential equations describing the thermal and the mechanical field of the combustion chamber's structure is realized by the Finite Element Method. As the mechanical problem is nonlinear, the thermal and mechanical load is applied step wise and the iterative Newton-Raphson solution strategy is used in every load step. As the mentioned methods are familiar to the reader, we only refer to the related literature (see e.g. HUGHES [18], ZIENKIEWICZ & TAYLOR [41], CRISFIELD [5, 6], BATHE [1], LEWIS ET AL. [25] and KLEIBER [19]).

4 Thermomechanical analysis of the rocket engine Vulcain

In order to demonstrate the performance and efficiency of the proposed solution strategy it will be applied to the analysis of the currently employed liquid hydrogen/oxygen main engine 'Vulcain' of the European space transport system 'Ariane V'. The geometry of the cooling channel and the structural model are summarized in Figure 5. In order to avoid the transfer of high-tech knowledge of the producing industry (Daimler-Crysler Aerospace), the given data set represents only a qualitative model of the combustion chamber, generated by informations available from the literature, published by FRÖHLICH ET AL. [13], FISCHER, POPP & QUENTMEYER [10] and POPP & SCHMIDT [33]. The applied material properties of the copper alloy and the nickel, obtained from POPP & SCHMIDT [33], and the additional assumption of linear varying material properties as a function of the temperature and the material properties of the hydrogen are summarized in Table 1.

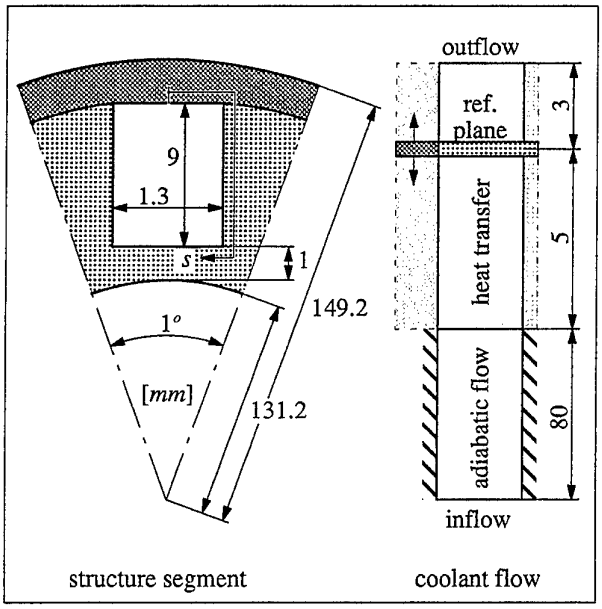


Figure 5: Geometry of the combustion chamber

4.1 Fluid flow simulation

For the analysis of the velocity and temperature fields of the coolant flow (and the structure) the model problem given in Figure 5 is discretized by three dimensional 8-node finite elements. In the first part of the cooling channel an adiabatic flow is assumed, the length of this part is chosen such that the velocity boundary layer is fully developed. In the second part the thermal flow between the coolant and the structure is considered. The position reference plane is chosen according to the thermal boundary layer. The flow conditions, the parameter and the boundary conditions of the turbulence model are given as follows (compare LAUNDER & SPALDING [23]).

$$\begin{aligned} &\theta_1 = 60\,K, \quad u_1 = 160\,\tfrac{m}{s}, \quad p_2 = 14.5\,MPa \\ &\mathrm{Pr}_t = 1.0, \quad k_1 = 3.84\,\tfrac{m^2}{s^2}, \quad \varepsilon_1 = 12800\,\tfrac{m^2}{s^3} \\ &C_1 = 1.44, \quad C_2 = 1.92 \\ &C_3 = 1.3, \quad C_4 = 0.09 \end{aligned} \tag{36}$$

4.2 Thermal field and heat transfer analysis

If the boundary conditions at the hot-gas side of the thermal fluid model

$$\alpha_h = 28\,\frac{kW}{m^2K}, \quad \theta_h = 3538\,K \tag{37}$$

are recruited, the thermal field of the fluid and structure can be analyzed. Figure 7 demonstrates the evolution of the temperature field with the longitudinal position z. Figure 8 shows the circumferential distribution of

		hydrogen	copper alloy	nickel
modeling		Newtonian fluid	von Mises lin. kinematic hardening	Saint Venant-Kirchhoff
Young's modulus	$E[GPa]$	-	$148 - 0.073\ \frac{\theta}{K}$	193
tangent modulus	$T[MPa]$	-	$602 - 0.690\ \frac{\theta}{K}$	-
yield stress	$\sigma_Y[MPa]$	-	$232 - 0.138\ \frac{\theta}{K}$	∞
Poisson's ratio	$\nu[-]$	-	0.3	0.3
dynamic viscosity	$\mu\left[\frac{Ns}{m^2}\right]$	$6.5173\ 10^{-6}$	-	-
density	$\rho\left[\frac{kg}{m^3}\right]$	49.72	(9130)	(8910)
thermal expansion	$\alpha\left[\frac{1}{K}\right]$	-	$1.72\ 10^{-5}$	$1.22\ 10^{-5}$
conductivity	$\lambda\left[\frac{W}{mK}\right]$	0.10657	310	75
specific heat	$c\left[\frac{J}{kgK}\right]$	15125	(373)	(444)

Table 1: Material properties of hydrogen, copper alloy and nickel

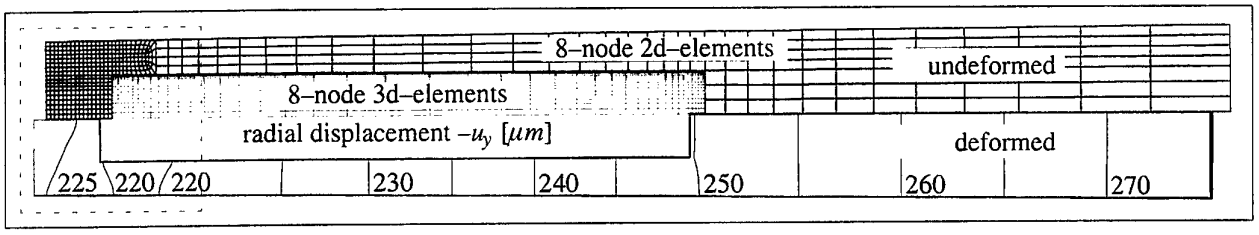


Figure 6: Finite element discretization, deformation and displacement field

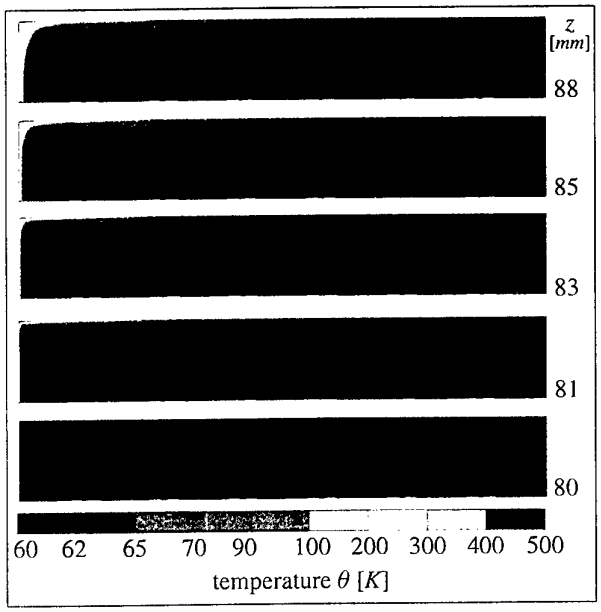


Figure 7: Temperature field of the coolant

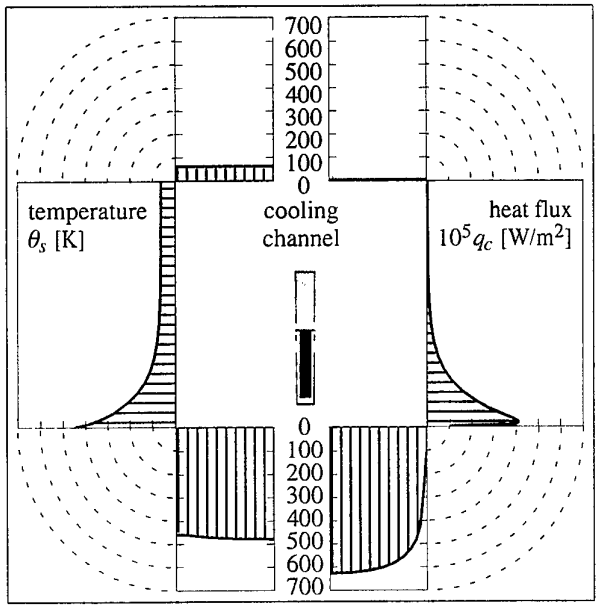


Figure 8: Heat transfer at $z = 85\ mm$

the local wall temperature and the wall heat flux, used as boundary condition of the structural analysis in the context of a convective heat transfer model, at the longitudinal position $z = 85\ mm$. From previous results it can be interpreted, that the local heat transfer is influenced by the thickness of the flow boundary layer and the of the effective conductivity within a cross section of the cooling channel. The interference of the orthogonal channel wall's thickens the boundary layer and therefore a lower thermal gradient coupled with a decrease of the local heat transfer coefficient can be observed.

4.3 Structural deformation by single loading

For the non-linear structural analysis of the combustion chamber by a load controlled Newton-Raphson iteration, where 1000 steps are applied to reach the full pressure and thermal loads characterized by the load factor $\lambda = 1$ and the interval $\lambda \in [0, 1]$ defines the successive loading process. Figure 6 illustrates the discretization and the displacement field as the result of the single loading by the thermal field and the pressures. The deformed structure clearly shows the shrinking as a result of the decreasing temperature of the nickel-jacket. The effect of the high pressure inside the combustion chamber and the thermal strains related to the increase of the temperature of the combustion chamber wall are suppressed by the very stiff jacket. The displacement field confirms this observation. Nevertheless, the largest radial displacements are not on the hot gas side but in the region of the cooling channel's corner. Therefore, hot gas side pressure driven bending deformations of the chamber wall arise. A detailed analysis of the deformation process is necessary in order to understand the complex structural response. Therefore, the evolution of the tangential component subdivided in thermal, elastic and plastic parts at four characteristic positions of the structure are analyzed as a function of the load factor in Figure 9, compare also the strain field $\epsilon_x^e + \epsilon_x^p$ of the first loading in Figure 10. All points demonstrate positive linear thermal strains representing the increasing thermal field caused by the increase of the load factor. The tangential and radial elastic strains vary linearly until the yield stress is reached. After the beginning of the plastification, small linear changes of the elastic strains related to the temperature dependent yield stress can be observed. As a result of the global shrinking of the structure, negative tangential plastic strains are generated at the four chosen points. On the other hand, the radial total and plastic strains are positive. This observation describes the effect of the deviatoric plastic deformation connecting the tangential and radial strains. A special effect of the combustion chamber's structure can be observed by means of the plastic and total tangential strains of the positions on the hot gas side boundary (point 1-3). As expected, at point 1 high negative plastic and total strains occur. However, only a small negative plastic strain component and a positive total strain can be identified at point 2. The reason for this unexpected effect is the high pressure gradient between the hot gas side and the cooling channel ($\Delta p = p_c - p_h > 0$) leading to bending like deformation of the chamber wall and consequently to the reduction of the compressive tangential plastic strains in the region of points 3 and 4. The evolution of the tangential strains within the successive loading procedure, as presented in Figure 10 for the small region of the combustion chamber wall, demonstrates clearly the above discussed influence of the additional compression effects driven by the shrinking liner and the bending

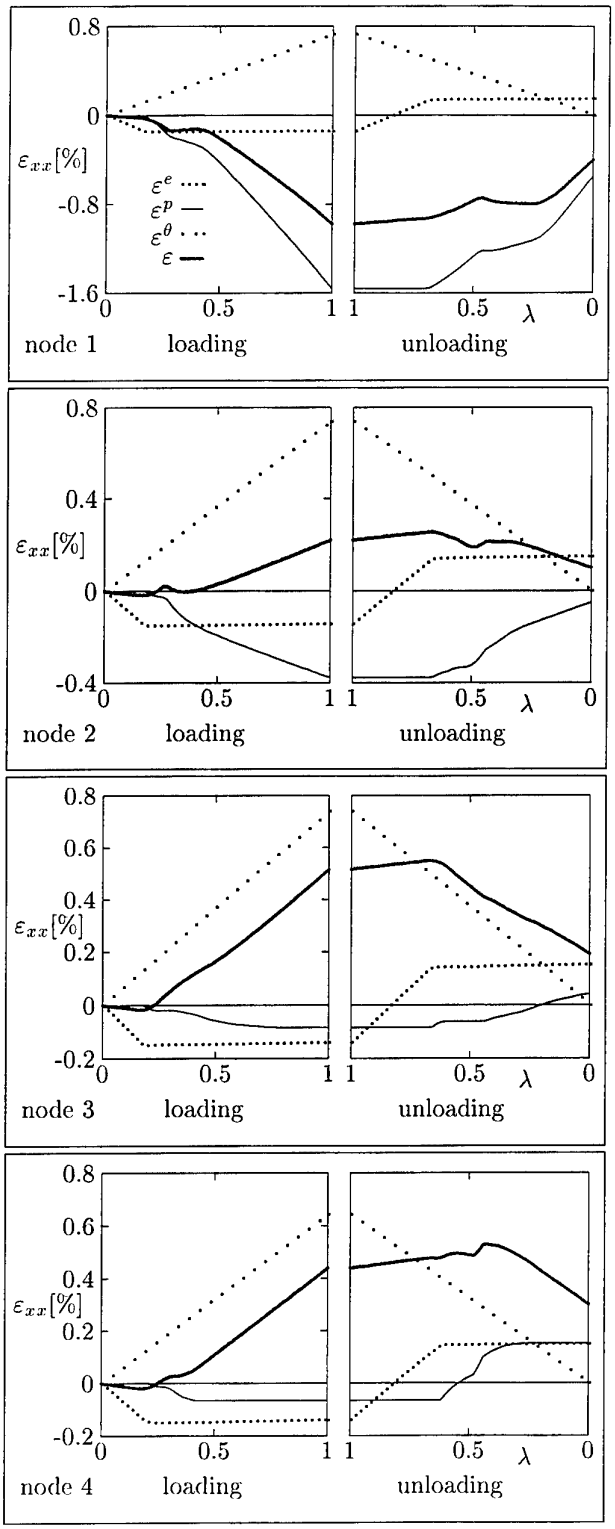


Figure 9: Evolution of the tangential strain parts

effect as a result of the pressure difference Δp. It is worth to note, that the 'bending effect' is negligible in a linear structural analysis. Only the combination of the high pressure difference Δp and the plastic flow yields the observed significant change in the tangential strain component.

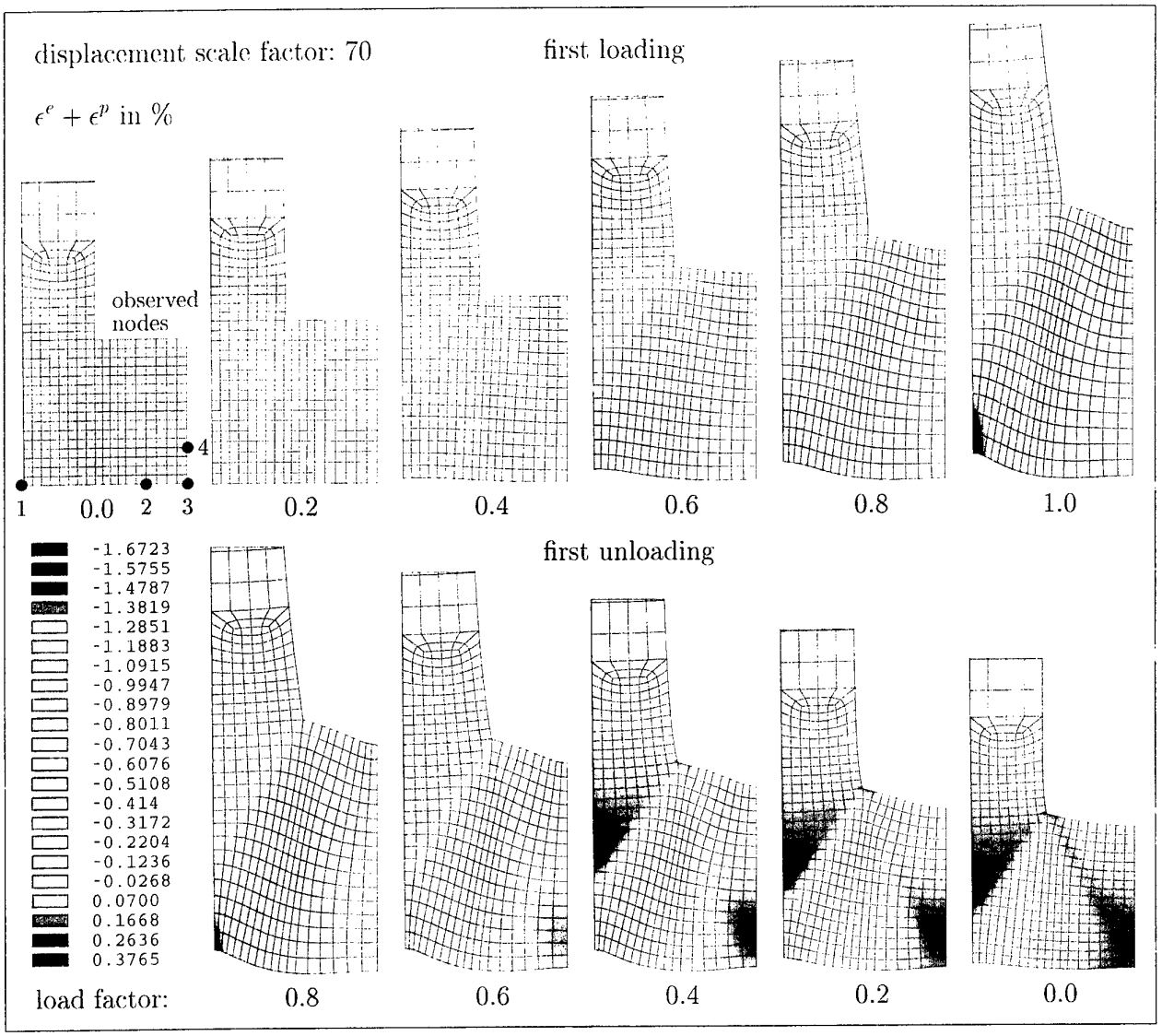


Figure 10: Evolution of the tangential strains $\epsilon_x^e + \epsilon_x^p$ for the first loading cycle

As a result of the structural behavior of the chamber wall, the highest plastic strain for the single loading process is obtained at point 1. If classical life time analysis is applied on the basis of this single loading analysis the failure of the structure occurs at point 1. This is in a sharp contrast to experimental observations presented by QUENTMEYER[34, 35] and POPP &SCHMIDT[33] which describes the thinning of the combustion chamber wall, the evolution of a 'dog-house' and finally the the structural failure by a crack in the region of point 3 which is driven by fatigue, compare the sketch given in Figure 2. Consequently, the analysis of the single loading is not a sufficient basis for the prediction the life time of combustion chambers. In order to dissolve this seemingly contradictory results of experimental and numerical investigations the unloading and the cyclic repetition of the loading/unloading process should be studied.

4.4 Structural deformation by cyclic loading

Now the thermo-mechanical structural analysis is extended to cyclic loading whereby each cycle consists of the loading process similar to the single loading analysis and the unloading process described by a decreasing load factor $\lambda \in [1, 0]$. As the life time of the combustion chamber is primarily restricted by the total value and the range of local plastic strains, the interpretation of the mechanical simulation is focused on the plastic strains. The evolution of the tangential strain component of four specified points within the first unloading process is illustrated in Figure 9. Furthermore, the distribution of the sum of elastic and plastic tangential normal strain components of the first load cycle is plotted in Figure 10.

The expansion of the global structure during the unloading as the consequence of vanishing thermal strains and mechanical boundary conditions leads to elastic unloading and plastic deformation in the opposite direction of the primary plastic deformation of the material. As in points 3 and 4 the total changes of the plastic strains of the unloading process are larger than the change of the strains related to the loading process, the cyclic repetition of the loading/unloading process leads to increasing positive plastic strains within every loading cycle. Considering the stress-strain relation given in Figure 11, the failure mechanism observed by the means of experiments can be well understood. The initiation of a crack at point 3 is associated with the increase of plastic strains of the unloaded state within every load cycle. In contrast to this, the increase of $\epsilon^e_{xx} + \epsilon^p_{xx}$ at point 2 is smaller compared to the critical points and at point 1 nearly a repetition of the first loading cycle is obtained, the evolution plastic strain of the unloaded structure is stable at this point.

4.5 Failure phenomenon

Experimental investigations on regeneratively cooled rocket combustion chambers as described in section 1.1 have demonstrated the limiting of the life time due to the failure mechanism characterized by the so called 'dog-house' as a result of a plastic bending deformation of the wall, the thinning of the wall and finally a radial crack in the middle of the wall. The evolution of this kind of failure can qualitatively be explained by a detailed numerical analysis of the heat transfer and the elastoplastic deformation phenomenon, presented in sections 4.1 to 4.4. This analysis allows the interpretation of the deformation process as well as the indication of the reason for the crack initiation in the chamber wall.

The deformation of the combustion chamber structure is primarily driven by the shrinkage of the jacket as a result of the temperature reduction by the cryogenic coolant in this region. On the other side, the temperature of the hot gas side wall is significantly increased with respect to the reference state of the combustion chamber. As a consequence of both superposed effects a large plastic tangential compression of the material is obtained at the hot gas side wall. Furthermore, a seemingly secondary deformation effect was established as an essential property concerning the cyclic operation and the restriction of the life time of the combustion chamber. The pressure difference between the cooling channel and the combustion chamber reduces the constrained deformation and consequently also the plastic strains in the middle of the chamber wall within the loading process. Nevertheless, the global expansion of the structure within the unloading process enforces large tangential strains leading, first, to an elastic compression unloading and, second, to an elastic and plastic tangential tension loading. As the result of this, the

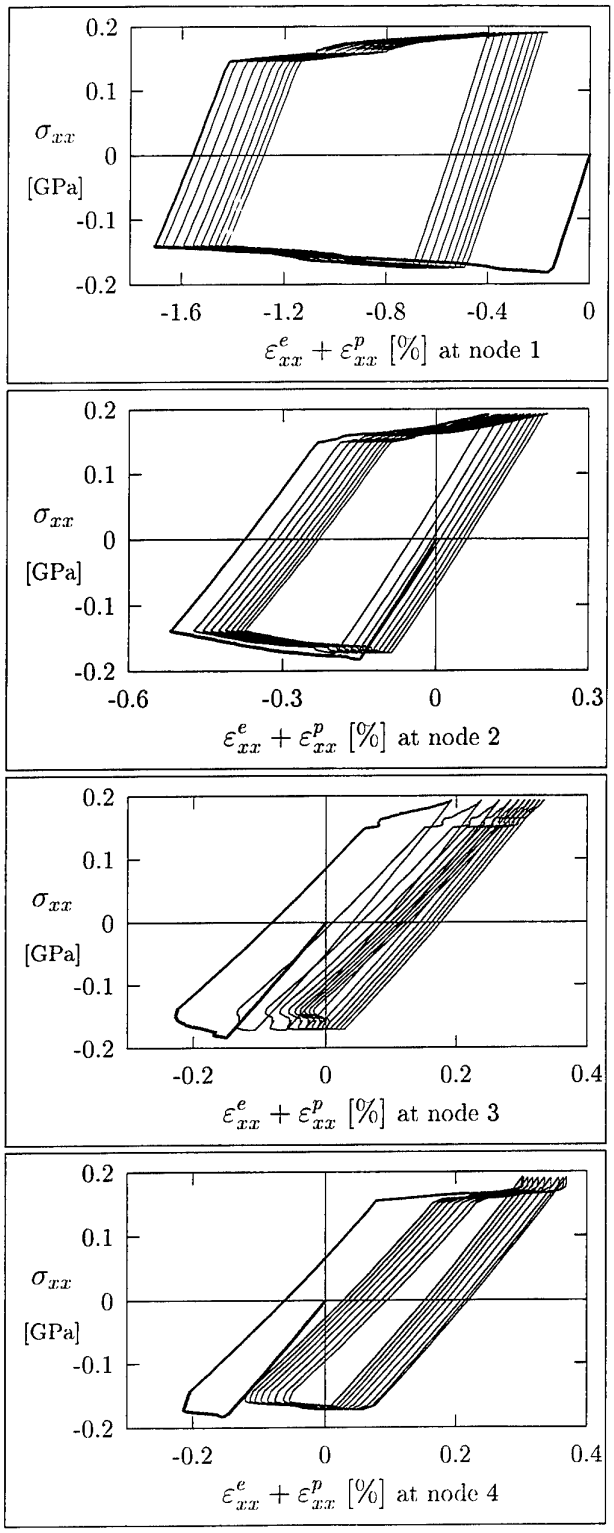


Figure 11: Stress-strain relation for cyclic loading

sign of the plastic strains in the middle region (compare Figure 2 where 'dog house' failure occurs) changes during unloading. Consequently, the cyclic repetition of this deformation leads to an increasing of the remaining positive plastic strains within every loading/unloading process and the evolution of the 'dog house', see Figure

11. This mechanism is finally responsible for the failure of the combustion chamber wall.

If the above mentioned failure phenomenon is summarized, it can be stated, that

- the combustion chamber failure is mainly controlled by the temperature difference $\Delta\theta = \theta_h - \theta_e$ of the hot gas side wall Γ_h and the jacket of the combustion chamber Γ_e
- and the pressure difference $\Delta p = p_c - p_h$ is responsible for the increase of the plastic strains in the crack zone within every load cycle.

4.6 Design improvements

After the main structural failure mechanisms and parameters of combustion chambers were indicated in the previous section, some system improvements reducing $\Delta\theta$ and Δp or avoiding the enforced compressive strains of the combustion chamber wall are now proposed. Firstly, the temperature difference $\Delta\theta$ may be reduced significantly by the following design concepts:

- The improvement of the heat transfer between the combustion chamber wall and the coolant will reduce the temperature level of the hot gas side wall and consequently the thermal and compressive plastic strains. This may by realized by increasing α_c due to a higher surface roughness or additional fins (see Figure 13), for example. It should be noted, that as consequence of the proposed design concept, a higher pressure loss in the cooling channels, requiring a higher Δp, will be obtained.
- $\Delta\theta$ can be decreased by increasing the temperature of the jacket. This may be realized by an external heating of the jacket due to the combustion products of the gas generator (gas generator cycle). As a disadvantage of this technique, the additional heating of the coolant has to be mentioned. Alternatively the jacket temperature can be increased by application of a thermal barrier coating on selected surfaces of the cooling channel (see Figure 13). The thermal isolation of regions of the cooling channel with a low heat transfer (compare Figure 8) yields the heating of the jacket due to heat conduction. As the heat transfer is slightly reduced by this modification, this concept requires additional constructive measures increasing α_c.
- $\Delta\theta$ can be also decreased by decreasing the temperature θ_h of the copper alloy. This can be realized due to a soft thermal barrier coating at the hot gas side (see Figure 13). It should be noted, that this design concept reduces the heat transfer significantly. Consequently, it is nor suitable for the expander cycle.

Secondly, the negative influence of the pressure difference Δp to the cyclic thermo-mechanical behavior of the combustion chamber may be avoided by the following measures:

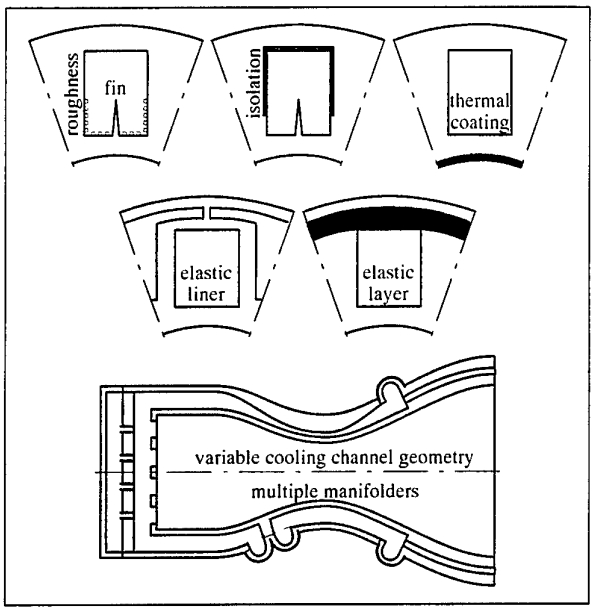


Figure 13: Advanced design concepts increasing the life time of rocket combustion chambers

- Controlling of the cooling channel pressure during the shut down process of the combustion chamber such that it is adapted to the thermo-mechanical state of the material, which means that the pressure difference should vanish $\Delta p = 0$ in this situation.
- Reduction of the cooling channel pressure in critical regions by an adaption of the cooling channels cross section which increase also the heat transfer characterized by α_c.
- Reducing the necessary entrance cooling channel pressure by the use of more manifolders for shorter cooling channels allowing an unchanged injection pressure.

Thirdly, the damaging impact of the temperature difference $\Delta\theta$ can be reduced by changing the mechanical design of the combustion chamber:

- If the coupling of the deformations $\boldsymbol{u}$ of the hot gas side wall and the nickel jacket is reduced, the compressive plastic strains of the hot gas side wall will be decreased. The mechanical decoupling can be realized by the design concept of an elastic liner, decoupling inner and outer deformation due to the geometric design, or by the low stiffness compressible material layer between the copper alloy and the nickel jacket (see Figure 13).

5 Optimization

Previously summarized experimental and numerical studies allow the following statement: The principle failure phenomenon of combustion chambers can be qualitatively simulated and understood by the interpretation

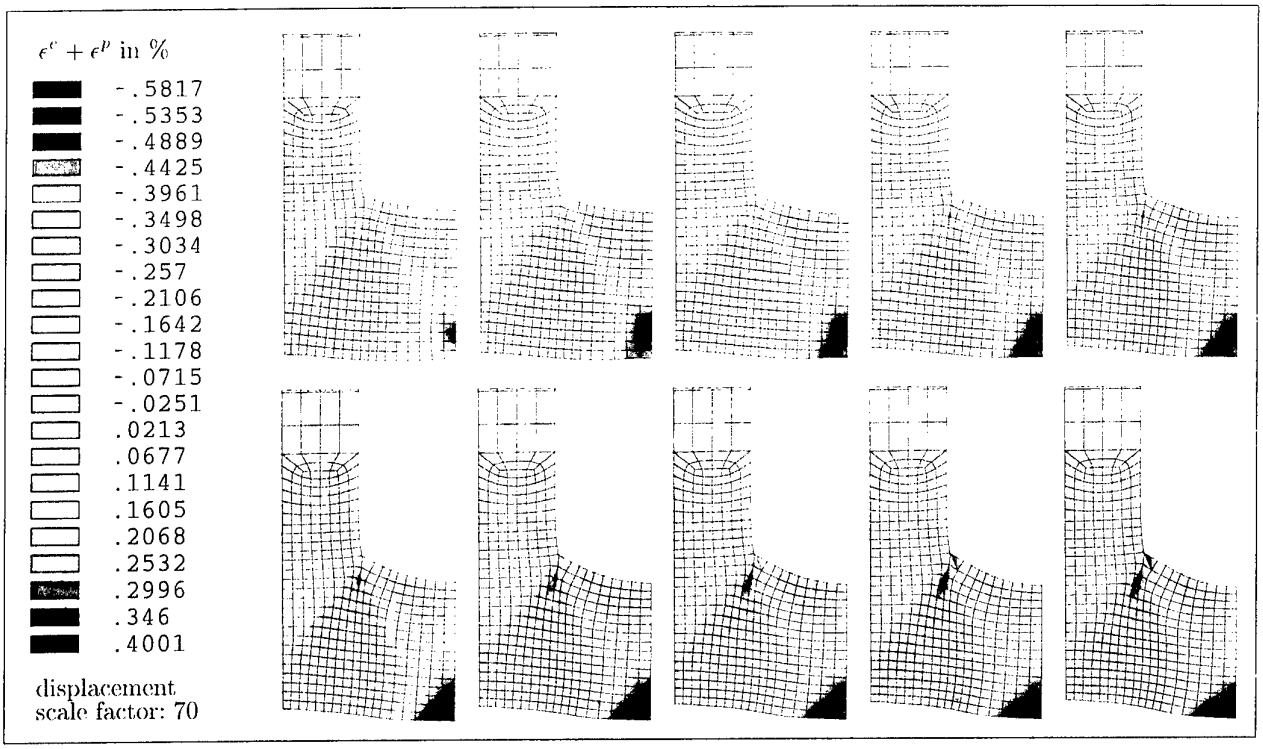


Figure 12: Evolution of deformation within an increasing number of load cycles at the end of the loading cycles

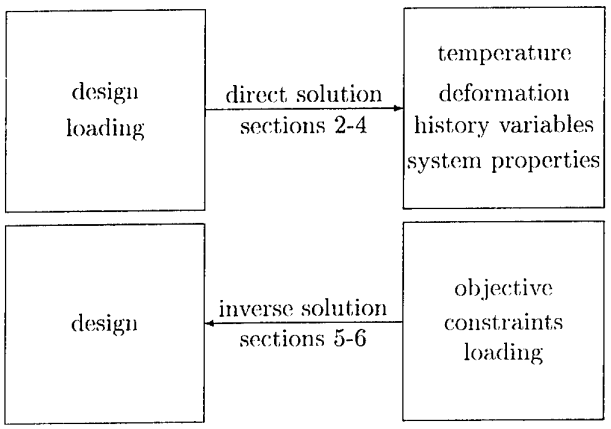


Figure 14: Classification of direct and inverse problems

of the numerical results. However, the direct simulation of the thermo-mechanical deformation process is not suited to lead to an answer of the following engineering question: Which design leads to an improved or optimal thermo-mechanical behavior and finally maximizes the life time of the structure or optimizes any other property of the combustion chamber? In order to answer this question, the inverse thermo-mechanical problem has to be solved. This kind of problem is characterized by a given loading and the unknown design which minimizes a chosen objective function such that simultaneously several constraints are satisfied, compare Figure 14. The inverse problem is classically solved by the engineer who developes the structure, analyzes the structural behavior, checks constraints and finally changes the design and repeats the procedure until the structure fulfills all demands and the objective criterion is improved.

A similar procedure is used within the mathematical design optimization process defined by the three essential columns of optimization strategies as shown in Figure 15. The initial design of the structure is defined by a set of design variables $\boldsymbol{s}_n = \boldsymbol{s}_0$, whereas the type of the geometry description by the design parameters distinguishes between the three optimization disciplines illustrated in Figure 16 by means of a combustion chamber's structure. These principle optimization techniques are, firstly, the sizing handling only modifications of the geometrical dimensions, secondly, shape optimization combining sizing and modifications of the shape and, finally, the topology optimization allowing additionally the generation of new boundaries within the structure. If the geometry is completely described by fixed parameters and the initial design variables, the direct solution is applied in order to check the constraints $\boldsymbol{g}(\boldsymbol{s}_n)$ and to determine the objective function $f(\boldsymbol{s}_n)$ which characterizes the quality of the design. In addition to the direct solution, a sensitivity analysis is carried out. The sensitivity $\nabla_s f(\boldsymbol{s}_n)$ is required by the 'mathematical programming' procedure in which the criterion of the optimal design is checked and the design variables are modified systematically. The above mentioned mathematical optimization cycle will be repeated until the optimization criterion $\nabla_s f(\boldsymbol{s}_n) = \boldsymbol{0}$ is satisfied. In contrast to the typical engineering optimization approach which relays more or less on the educated guess, every design

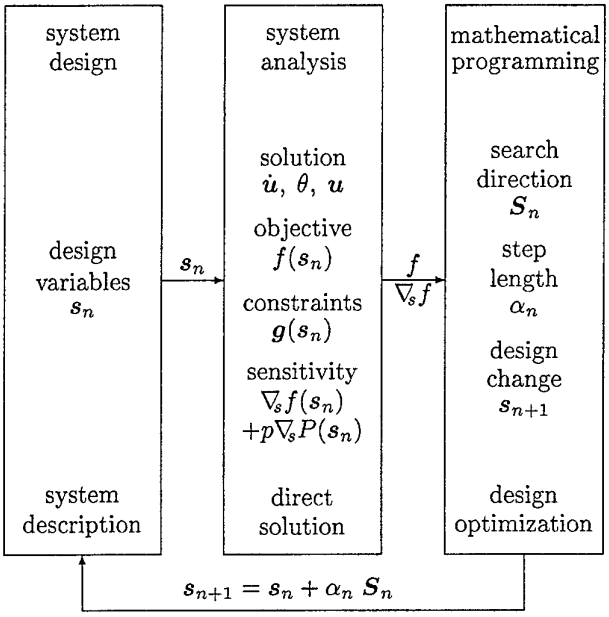


Figure 15: Optimization strategy - three columns of design optimization

change by mathematical programming does guarantee an improvement of the design and the (locally) optimal construction can be found as a result of the sensitivity analysis and the formulation of the necessary criterion of an optimal design.

The optimization of the combustion chamber structure is organized as follows: Firstly, the constrained optimization problem is defined and secondly, it will be transformed into the unconstrained optimization problem by its penalty formulation and finally solved by mathematical programming methods. These methods consist of the determination of the search direction, the computation of the sensitivities and the determination of the step length. For a detailed discussion of optimization methods the authors refer to DENNIS&SCHNABEL[7], LUENBERGER[27], POLAK[31], HAFTKA, GÜRDAL &KAMAT[15], BENDSØE[2], ESCHENAUER, OLHOF&SCHNELL[9] and KLEIBER[19].

5.1 Constraint optimization problem

A constrained optimization model of the combustion chamber is given by the vector s of design parameters of the combustor and the definition of the objective function

$$f(s) = \min, \quad s = [s_1, s_2, \ldots, s_k]^T \tag{38}$$

which should be minimized simultaneously satisfy the constraints

$$g(s) \geq 0, \quad g = [g_1, g_2, \ldots, g_l]^T \tag{39}$$

characterizing the feasible design domain. In general, the objective is an arbitrary scalar valued function of the design variables s which can be determined through

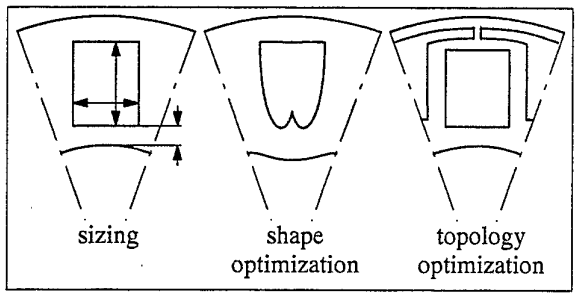


Figure 16: Optimization disciplines

the direct analysis of the combustion chamber discussed in sections 2-4. For example, this may be the maximum plastic strain of the structure after one or after a series of direct calculated loading cycles, the predicted life time, the temperature difference of the chamber wall and the jacket, the pressure loss in the cooling channel or the increase of the coolants internal energy due to heat exchange (expander cycle), only to point out a few possible objectives. The optimization problem is completed by the definition of the constraints including the restrictions of the design variables $\underline{s}, \overline{s}$ characterizing for example bounds of manufacturing or process parameters and $l - 2k$ further scalar constraints calculated by the direct analysis of the problem.

$$\begin{aligned} g_{2i-1}(s) &= s_i - \underline{s}_i \quad i \in \{1, \ldots, k\} \\ g_{2i}(s) &= \overline{s}_i - s_i \quad i \in \{1, \ldots, k\} \\ g_j(s) & \qquad\quad j \in \{2k+1, \ldots, l\} \end{aligned} \tag{40}$$

Herein g_j may be the maximum wall temperature defined by the melting temperature of the copper alloy and the minimal cross section of all cooling channels wich is necessary for the transport of the fuel with an acceptable pressure loss, respectively.

5.2 Unconstraint optimization problem

Introducing the exterior penalty function $P(s)$ defined by

$$P(s) = \overline{g}(s) \cdot \overline{g}(s), \quad \overline{g}_i(s) = \max(0, g_i(s)) \tag{41}$$

and the penalty factor p, the constrained optimization problem given by equations (38) and (39) can be transformed to an unconstrained one by using the penalty method.

$$Q(s) = f(s) + p\, P(s) = \min \tag{42}$$

The Gâteaux derivative of $Q(s)$ with respect to the design variables yields the necessary or Kuhn-Tucker condition of an optimal design.

$$\frac{\partial Q(s)}{\partial s} = \nabla_s Q(s) = \nabla_s f(s) + p\, \nabla_s P(s) = 0 \tag{43}$$

The sufficient condition for a minimum is, that the second derivative of the unconstrained objective function

with respect to the design variables $\nabla_s^2 Q(s)$, representing the curvature or the Hessian of the objective function $Q(s)$, has to be positive definite. However, as equation (43) determines only one vanishing tangential of the objective function, $\nabla_s Q(s) = \mathbf{0}$ characterizes a local and not the global optimum of a non-convex objective Q.

5.3 Optimization algorithms

Numerical methods solving the non-linear optimization problem described by equation (42) are in general based on the solution of the necessary condition of an optimum (43) by the multidimensional Taylor expansion of $\nabla_s Q(s)$ about a given design vector s_n.

$$\nabla_s Q(s_{n+1}) = \nabla_s Q(s_n) + \nabla_s^2 Q(s_n)\,(s_{n+1} - s_n) \quad (44)$$

As the Hessian $\nabla_s^2 Q(s_n)$ is invertible, the Newton iteration, first proposed by CAUCHY[4], is described by

$$s_{n+1} = s_n - \left(\nabla_s^2 Q(s_n)\right)^{-1} \nabla_s Q(s_n) \quad (45)$$

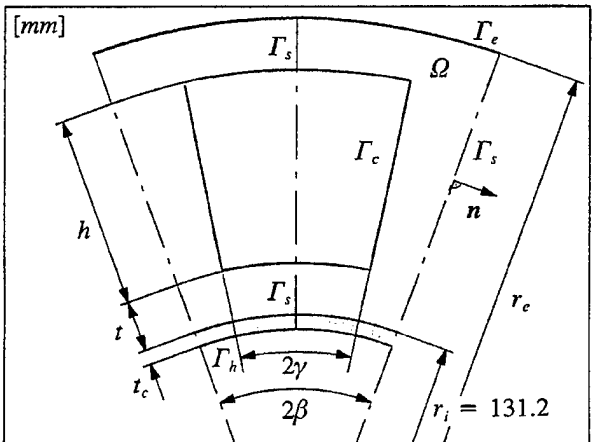
where $s_{n+1} - s_n$ is the Newton correction. Unfortunately, the Hessian $\nabla_s^2 Q(s_n)$ is not known in general. Therefore, the inverse Hessian $\left(\nabla_s^2 Q(s_n)\right)^{-1}$ is approximated by $\alpha_n \boldsymbol{B}_n$

$$s_{n+1} = s_n - \alpha_n\, \boldsymbol{B}_n\, \nabla_s Q(s_n) = s_n + \alpha_n\, \boldsymbol{S}_n \quad (46)$$

where $\boldsymbol{B}_n$ is generated by evolution equations in every step of the Quasi-Newton iteration. Furthermore, the iterative change of the vector of design variables is interpreted as the product of the search direction $\boldsymbol{S}_n = -\boldsymbol{B}_n\, \nabla_s Q(s_n)$ and the step length α_n. The approximated Hessian can be calculated by the conjugate direction methods developed by FLETCHER & REEVES [12] and POLAK & RIBIÉRE [32] or, alternatively, by the symmetric rank-two update proposed by BROYDEN [3], FLETCHER [11], GOLDFARB [14] and SHANNO [37]. Furthermore, the iterative solution of the optimization problem requires the knowledge of the sensitivity $\nabla_s Q$ and the step length α_n for every design set s_n. These quantities are calculated numerically by the forward difference method and line search procedure (see e.g. KUHL ET AL. [21]), respectively.

6 Optimization of the rocket engine Vulcain

In order to demonstrate the idea and the problems concerning the application of mathematical optimization techniques to the design of rocket combustion chambers, the proposed method will be applied to the analysis of the hydrogen/oxygen combustion chamber illustrated in Figure 17. In order to avoid further complexity of the description and calculation, the computational model of the combustion chamber wall presented in the



design variables s		$\beta[^0]$	$\gamma[^0]$	t	h	r_e	t_c
standard design	s_*	.5	.25	.6	5	151.2	0
lower bound	$\underline{s}$	.2	.02	.1	1	134.2	.01
upper bound	$\overline{s}$	2	1.8	2	10	155.2	.05

Figure 17: Optimization model (design set s_*)

previous sections will be significantly simplified by the following assumptions:

- The heat transfer coefficients and the related bulk temperatures describing the hot gas side and cooling channel heat transfer are given.
- The heat transfer coefficients are independent of the design parameters and constant on the surfaces Γ_h and Γ_c.
- The deformations of the material are purely elastic and described by the Saint Venant Kirchhoff material law ($\sigma_Y \to \infty$).
- The shape of the cooling channel is slightly modified for a simpler parametric description of the geometry in polar coordinates and a simpler meshing procedure. Furthermore, the combustion chamber is constructed by monolythic copper alloy.

Note, that this model is not suited to handle the complex behavior of the combustion chamber because the cooling channel heat transfer is crucially influenced by the geometry and the resulting stresses are much higher

		copper	ceramic
Young's modulus	$E[GPa]$	148	12
Poisson's ratio	$\nu[-]$	0.3	0.3
thermal expansion	$\alpha\left[\frac{10^{-5}}{K}\right]$	1.72	0.2
conductivity	$\lambda\left[\frac{W}{mK}\right]$	310	2
temperature	$\underline{\theta}[K]$	293	293
		hot gas	coolant
film coefficient	$\alpha_i\left[\frac{kW}{m^2K}\right]$	32	100
bulk temperature	$\theta_i[K]$	3528	50
pressure	$p_i[MPa]$	10	14.2

Table 2: Optimization model - input data

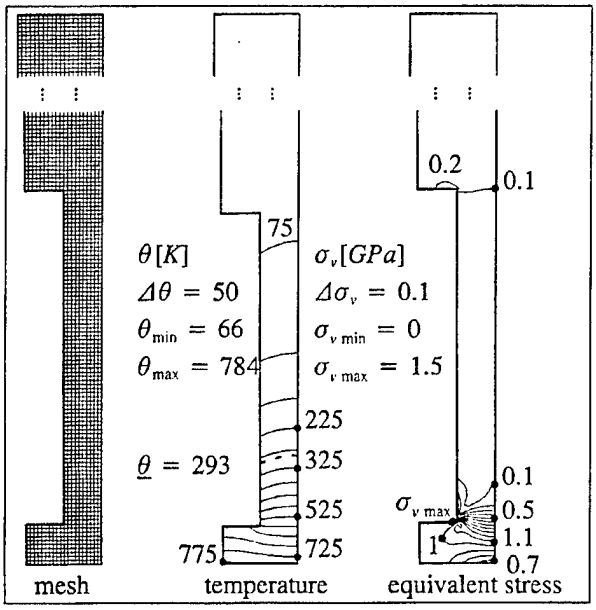


Figure 18: Direct solution for design $s_\star$

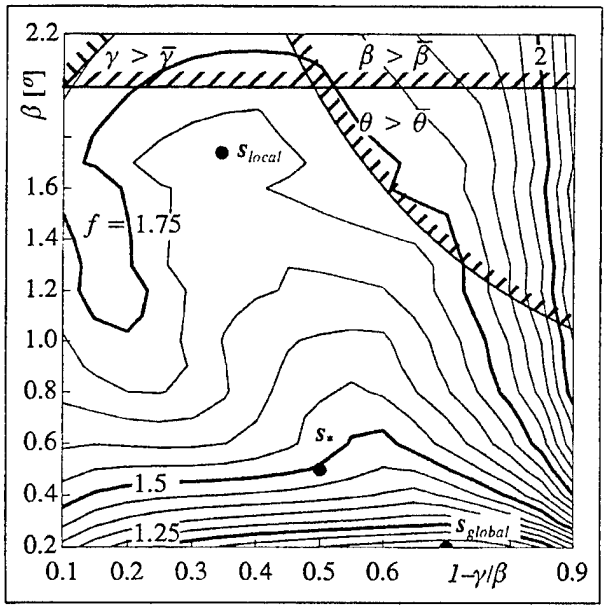


Figure 19: Character of the Objective function $f(\beta, 1-\gamma/\beta)$ $[GPa]$

than the yield stress. Furthermore, it is well known, that the optimal design calculated by an elastic structural model is not identical to the optimal design obtained by considering a non-linear material formulation within the solution of the direct problem and sensitivity analysis (see e.g. MAUTE, SCHWARZ & RAMM [30]). Nevertheless, this simple model is used in order to introduce mathematical programming methods as design tools for rocket combustion chambers and to study the properties of these methods saving computer time for the calculation of the heat transfer and the successive iterative solution of the material non-linear mechanical model.

Material properties of the copper alloy used for the optimization procedure are obtained from POPP & SCHMIDT [33], see Table 2. If a thermal barrier coating is applied, it is modeled by the material data given in column 'ceramic'. Furthermore, the thermal and mechanical boundary conditions are given in Table 2. For the studied model of a combustion chamber, the design variables with upper and lower bounds as summarized in Figure 17 are chosen.

$$s = [\beta, \gamma, t, h, r_e, t_c]^T \tag{47}$$

As the maximal scalar-valued equivalent von Mises stress

$$\sigma_v = \sqrt{\frac{2}{3}}\,\|\mathrm{dev}\sigma\| \tag{48}$$

within the domain Ω should be optimized, the objective function is given by

$$f(s) = \max_{\Omega} \sigma_v(s) \tag{49}$$

whereby the local character of the objective σ_v is mentioned. As additional constraints the maximal wall temperature $\overline{\theta} = 1000\ K$ and the minimal total cross section of all cooling channels given by 80% of the original cross section $A(s_\star)$ are introduced.

$$\begin{aligned} g_{2k+1}(s) &= g_{l-1}(s) &&= \overline{\theta} - \max_{\Gamma_h} \theta(s) \\ g_{2k+2}(s) &= g_l(s) &&= A(s) - 0.8\,A(s_\star) \end{aligned} \tag{50}$$

6.1 Characterization of the objective

Before optimization techniques are applied, the standard design given by the design vector $s_\star$ will be analyzed in detail. Furthermore, the character of the chosen objective function and the optimization problem will be studied by means of systematical studies performed by the solution of direct thermo-mechanical problems with different design sets.

Figure 18 demonstrates the discretization by 4-noded plane stress finite elements and the distribution of the temperature and the equivalent von Mises stress within the structure. As expected after the discussion of the direct problem in the previous sections, the maximal equivalent stress is obtained in the region of the chamber wall.

The objective function $f(s)$ will be studied by means of the parameter variation $\beta \in [0.2, 2.2]$ and $1-\gamma/\beta \in [0.1, 0.9]$. The calculated objective $f(s)$, the temperature constraint $\overline{\theta} - \max_{\Gamma_h} \theta(s) > 0$ for $\overline{\theta} = 1000\ K$, the standard design set $s_\star$ and the geometrical restrictions $\overline{\beta} - \beta > 0$, $\overline{\gamma} - \gamma > 0$ are plotted in Figure 19. This representation of the objective characterize the associated optimization problem:

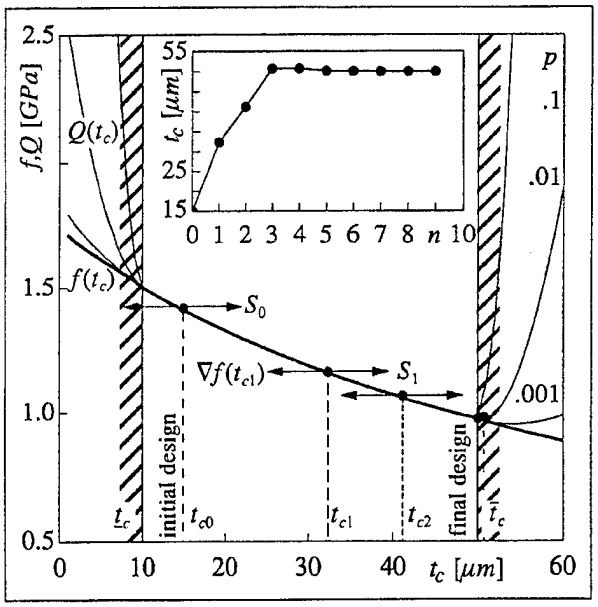


Figure 20: Optimization of thermal coating

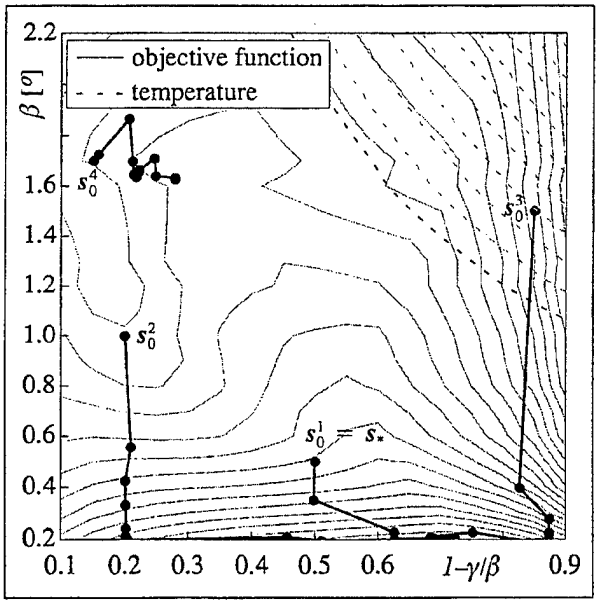


Figure 21: Optimization $f(\beta, 1-\gamma/\beta) = \min$

- The objective function $f(s)$ is not convex.
- One local and the global minimum are indicated in the design space.
- In some regions of the feasible design space, the Hessian $\nabla^2 f(s)$ may be indefinite or negative definite.

It is well known, that Quasi-Newton methods require, that the type of definiteness of the Hessian or the approximated Hessian does not change during the iteration process. As the satisfaction of this necessary convergence condition can not be guaranteed in general, the conjugate direction methods, in particular the Polak-Ribiére method combined with an exact line search, are favored for the optimization of the presented thermo-mechanical problem.

6.2 Thermal Coating

The application of the presented optimization strategy to the improvement of the thickness of a thermal coating is illustrated in Figure 20. As this problem is described only by one design parameter t_c, the constrained objective function $f(t_c)$, the unconstrained objective function $Q(t_c)$ associated to different penalty factors p and the iterative change of the design t_c can be simple visualized. The optimization problem is convex and consequently, it is easy to find the global optimum ($p = 0.01$, $t_c = 50\ \mu m$). The good convergence to the optimal design is illustrated by the evolution of the thickness t_c versus the number of iterations.

6.3 Two dimensional optimization

The comparison between the parametric study and optimization methods is demonstrated by means of the two-parameter optimization problem, minimize $f(\beta, 1-\gamma/\beta)$, such that the constraint $\overline{\theta} > \max_{\Gamma_h} \theta(s)$ is satisfied. The optimization paths for different initial design sets are plotted in Figure 21. The optimization of the standard design (No. 1) leads directly to the solution of the inverse problem given by the global optimum. On the other hand, the optimization paths 2 and 3 strictly reducing the parameter β until the related penalty term is activated. Then, the search direction changes significantly and, finally, the global optimum is obtained. The first search direction $\boldsymbol{S}_0^3$ of optimization No. 3 is seemingly not the steepest descent direction. But, if the temperature constraint $1000K - \max_{\Gamma_h} \theta(s) > 0$ is considered, it becomes clear, that the first search direction is primary controlled by the penalty function related to this constraint. As a local optimum is expected on the basis of the parametric study, initial design sets near this minimum have been tested. In one of these tests, the optimization of initial design number 4 results in a local 'optimum' far away from the global optimum. In general, the investigated studies allow the statement, that optimization methods are able to improve an initial design significantly with respect to a user defined objective but do not guarantee, that the global minimum can be found for every initial design set.

6.4 Chamber wall design

The simultaneous optimization of the design parameters $s = [\beta, \gamma, t, h, r_e]^T$ is composed of the inverse problem, minimize $f(s)$, such that the constraints $\overline{\theta} > \max_{\Gamma_h} \theta(s)$ and $A(s) > 0.8\ A(s_*)$ are satisfied. The application of the Polak-Ribiére method combined to the exact line search results in the evolution of the objective function and the constraints within the iterative

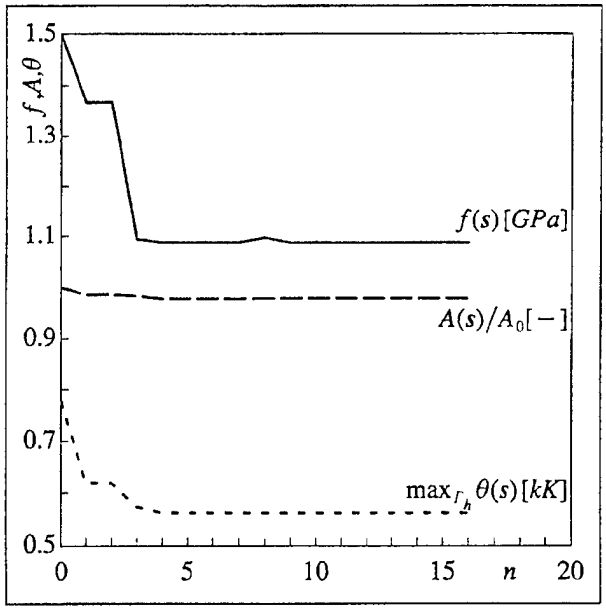


Figure 22: Evolution of objective and constraints

solution process as shown in Figure 22. It can be observed, that the maximal equivalent von Mises stress and the maximal wall temperature are reduced about 27% with respect to the initial design whereas the total cross section of the cooling channels is approximately constant.

7 Conclusion

A solution strategy of the coupled thermo-mechanical fluid-structure-interaction boundary value problem of rocket combustion chambers was been developed on the basis of some permissible simplifications (Assumptions 1-6) applied to the general governing differential equations. In the framework of the presented method, the discretization and solution of the fluid and solid equations was realized by non-linear finite element methods. The application to the combustion chamber 'Quasi-Vulcain' has demonstrated the ability of the presented strategy to compute the cooling channel flow, the heat transfer phenomenon and the deformation process of the structure. Finally, the failure mechanism of the combustion chamber during cyclic thermal and mechanical loading was discussed and improved design concepts were proposed.

In addition to the solution strategy of the direct problem, a design concept for the geometry of a rocket combustion chamber wall, based on mathematical programming techniques, has been suggested and investigated by means of the sizing of a combustion chamber model. The solution of the inverse problem by mathematical optimization schemes has been presented. The practicability of the optimization strategy has been demonstrated in the context of the sizing of a combustion chamber cooling channel. However, it has also been pointed out, that the final design may strongly depend on the chosen initial design and being only a local minimum. In summary, optimization methods are well suited for the improvement of a good initial rocked engine design, but are not able to substitute the engineers education and knowledge which are essential in order to interpret the numerical results and to generate a appropriate initial design, respectively.

Acknowledgements

The presented study is supported by grant from the 'Bundesministerium für Forschung und Technologie' within the research project 'Nationales Technologieprogramm kryogene Raketenantriebe'. This support is gratefully acknowledged.

References

[1] Bathe, K.-J.: Finite Element Procedures. Prentice Hall, Englewood Cliffs (1996).

[2] Bendsøe, M.P.: Optimization of Structural Topology, Shape, and Material. Springer-Verlag, Berlin (1995).

[3] Broyden, C.G.: The Convergence of a Class of Double-Rank Minimization Algorithms. Parts I & II. Journal Institute of Mathematics and its Applications Vol.6, 76-90, 222-231 (1970).

[4] Cauchy, A.: Méthode Générale Pour la Résolution des Systémes d'Equations Simultanées. Centre de Recherche de l'Académie des Siences de Paris Vol. 25, 536-538 (1847).

[5] Crisfield, M.A.: Non-Linear Finite Element Analysis of Solids and Structures. Volume 1. John Wiley & Sons, Chicester NewYork (1991).

[6] Crisfield, M.A.: Non-Linear Finite Element Analysisi of Solids and Structures. Volume 2 Advanced Topics. John Wiley & Sons, Chicester NewYork (1997).

[7] Dennis, J.E.; Schnabel, R.B.: Numerical Methods for Unconstrained Optimization and Nonlinear Equations. Society for Industrial and Applied Mathematics, Prentice Hall, Englewood Cliffs (1983).

[8] Emery, A.F., Cochran, R.J., Pepper, D.W.: Current Trends in Heat Transfer Computations. Journal of Thermophysics and Heat Transfer, Vol. 7, 193-212 (1993).

[9] Eschenauer, H.; Olhof, N.; Schnell, W.: Applied Structural Mechanics. Structural Optimization. Springer-Verlag, Berlin (1997).

[10] Fischer, S.C.; Popp, M.; Quentmeyer, R.J.: Thrust Chamber Cooling and Heat Transfer. Second International Symposium on Liquid Rocket Propulsion, ONERA, June 19-21 (1995).

[11] Fletcher, R.: A New Approach to Variable Metric Algorithms. Computer Journal Vol. 13, 317-322 (1970).

[12] Fletcher, R.; Reeves, C.M.: Function Minimization by Conjugate Gradients. Computer Journal Vol. 7, 149-154 (1964).

[13] Fröhlich, A.; Popp, M.; Schmidt, G.; Thelemann, D.: Heat Transfer Characteristics of H_2/O_2-Combustion Chambers. 29th Joint Propulsion Conference, AIAA-93-1826 (1993).

[14] Goldfarb, D.: A Family of Variable-Metric Methods Derived by Variational Means. Mathematics of Computations Vol. 24, 23-26 (1970).

[15] Haftka, R.T.; Gürdal, Z.; Kamat, M.P.: Elements of Structural Optimization. Kluwer Academic Publishers, Dordrecht (1993).

[16] Hill, R.: The Mathematical Theory of Plasticity. Clarendon Press, Oxford (1950).

[17] Hirsch, Ch.: Numerical Computation of Internal and External Flows. Volume 1 & 2. John Wiley & Sons, NewYork (1988).

[18] Hughes, T.J.R.: The Finite Element Method. Linear Static and Dynamic Finite Element Analysis. Prentice-Hall, London (1987).

[19] Kleiber, M.: Handbook of Computational Solid Mechanics. Survey and Comparison of Contemporary Methods. Springer-Verlag, Berlin (1995).

[20] Kuhl, D.: Thermomechanical Analysis of Rocket Combustion Chambers. Proceedings of the Fourth World Congress on Computational Mechanics. Buenos Aires, Argentina, 29 June - 2 July (1998).

[21] Kuhl, D.; Haidn, O.J.; Josien, N.; Coutellier, D.: Structural Optimization of Rocket Engine Cooling Channels. 34th Joint Propulsion Conference, AIAA-98-3372 (1998).

[22] Kuhl, D.; Woschnak, A.; Haidn, O.J.: Coupled Heat Transfer and Stress Analysis of Rocket Combustion Chambers. 34th Joint Propulsion Conference, AIAA-98-3373 (1998).

[23] Launder, B.E.; Spalding, D.B.: The Numerical Computations of Turbulent Flows. Computer Methods in Applied Mechanics and Engineering, Vol. 3, 269-289 (1974).

[24] Lemaitre, J.; Chaboche, J.L.: Mechanics of Materials. Cambridge University Press, Cambridge (1990).

[25] Lewis, R.W.; Morgan, K.; Thomas, H.R.; Seetharamu, K.N.: The Finite Element Method in Heat Transfer Analysis. John Wiley & Sons, Chicester (1996).

[26] Lubliner, J.: Plasticity Theory. Macmillan Publishing Company, NewYork (1990).

[27] Luenberger, D.G.: Introduction to Linear and Nonlinear Programming. Addison-Wesley, NewYork (1984).

[28] Malvern, L.E.: Introduction to the Mechanics of a Continuous Medium. Prentice-Hall, Englewood Cliffs (1969).

[29] Marsden, J.E.; Hughes, T.J.R.: Mathematical Foundations of Elasticity. Dover Publications, New York (1983).

[30] Maute, K.; Schwarz, S.; Ramm, E.: Adaptive Topology Optimization of Elastoplastic Structures. Structural Optimization 15, 81-91 (1998).

[31] Polak, E.: Optimization. Algorithms and Consistent Approximations. Springer-Verlag, Berlin (1991).

[32] Polak, E.; Ribiére, G.: Note sur la Convergence de Méthodes de Direction Conjuguées. Revue Francaise d'Informatique Recherche Opertionelle, Serie Rouge, No. 16, 35-43 (1969).

[33] Popp, M.; Schmidt, G.: Advanced Cryogenic Thrust Chambers. 5th International Symposium, Propulsion in Space Transportation, AAAF, Paris (1996).

[34] Quentmeyer, R.J.: Experimental Fatigue Life Investigation of Cylindrical Thrust Chambers. 13th Propulsion Conference, AIAA-77-893 (1977).

[35] Quentmeyer, R.J.: Rocket Combustion Chamber Life-Enhancing Design Concepts. 26th Joint Propulsion Conference, AIAA-90-2116 (1990).

[36] Rice, J.G.; Schnipke, R.J.: A Monotone Streamline Upwind Finite Element Method for Convection-Dominated Flows. Computer Methods in Applied Mechanics and Engineering, Vol. 48, 313-327 (1985).

[37] Shanno, D.F.: Conditioning of Quasi-Newton Methods for Function Minimization. Mathematics of Computations Vol. 24, 647-656 (1970).

[38] Simo, J.C.: Numerical Analysis and Simulation of Plasticity. In: Ciarlet, P.G.; Lions, J.L.: Handbook of Numerical Analysis. Volume VI, North-Holland, Amsterdam (1998).

[39] Simo, J.C.; Hughes, T.J.R.: Computational Inelasticity. In: Marsden, J.E.; Sirovich, L.; Wiggins, S.: Interdisciplinary Applied Mathematics. Springer-Verlag, NewYork (1998).

[40] Woschnak, A.; Kuhl, D.: Simulation of Heat Transfer in Regeneratively Cooled Rocket Combustion Chambers. Proceedings of the Fourth ECCOMAS Computational Fluid Dynamics Conference, Athens, Greece, September 7-11 (1998).

[41] Zienkiewicz, O.C.; Taylor, R.L.: The Finite Element Method. Fourth Edition – Volumes 1 & 2. McCraw-Hill Book Company, London (1989).

PERFORMANCE INVESTIGATION OF THE PRE-BURNER USED IN OXYGEN HYDROGEN ROCKET ENGINE

Wang, J. Cheng, S. Q. Hu, P. X.
China Academy of Launch Vehicle Technology
Wang, Z. G. Zhou, J. Liu, W. D.
University of National Defense Technology

Abstract

A new-type tri-coaxial injector of the pre-burner used in oxygen hydrogen rocket engine has been investigated in this paper. Cold spray measurements, comparative test of four candidate injectors, flow field analysis and performance test of the pre-burner have been performed to reveal the tendency of exhaustive gas temperature distribution and transient behavior. By optimizing the operating condition and configuration of the pre-burner, it was possible to obtain fairly uniform gas temperature distribution during the transient and steady state off-nominal operation period.

Introduction

The pre-burner is the essential component for the staged combustion cycle rocket engine. Comparing with the traditional gas generator, the pre-burner has higher chamber pressure and larger mass flow rate. Overall performance of the pre-burner largely depends upon the parameters of operation and configuration. The transient and steady state off-nominal operation of the pre-burner may result in turbine blade pitting and erosion due to incomplete mixing and downstream after-burning.

The injectors in use today are coaxial swirl and shear injectors, as shown in figure1.1 and figure1.2. The two are commonly used in the pre-burner of oxygen hydrogen rocket engines and have the advantages of easy manufacture and high operating reliability. But the coaxial injectors can not eliminate the free oxygen at downstream while combustion happen at low mixture ratio. In addition, it was suggested [1]that providing a portion of the injection area, where the mixture ratio is near stoichiometric, would be a good approach to obtain assured ignition. However, this stoichoimetric region produces a hot temperature streak in the gas generator due to the bad downstream mixing. Moreover, it was difficult to organize effective downstream mixing due to the increase of the oxygen flow rate under the pre-burner conditions. As a result, the author has designed a new-type tri-coaxial injector that can effectively enhance the downstream mixing, as shown in figure1.3. In this case, The hydrogen enters the inside and outside injectors, simultaneously. Combustion happens with near stoichiometric only in the inner injector (1st stage injector). In the meantime, the remaining hydrogen enters the outside injector (2nd stage injector) as a diluent to reduce the combustion gas temperature. The stoichiometric combustion can lessen the downstream free oxygen and benefit the incomplete mixing and after-burning.

Cold spray measurements and six hot fire tests were performed to reveal the difference of four candidate injectors and select the injector with the best spray behavior and combustion performance. Cold spray measurements using the phase Doppler particle analyzer (PDPA) can measure the size and velocity of the spray

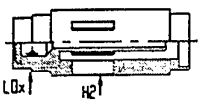


Fig.1.1 Coaxial swirl (A)

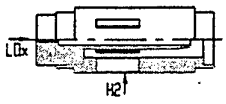


Fig.1.2 Coaxial shear (B)

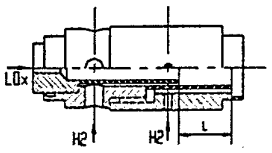


Fig.1.3 Tri-coaxial C L=17mm D L=27mm

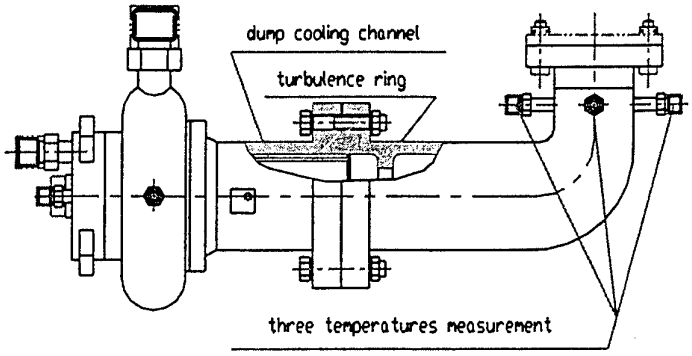


Figure 1.4 Preburner structure

particles simultaneously. It can also get the downstream distribution of the injector mixture ratio from the data analysis. In addition, the data of the cold spray measurements after properly conversion can provide the initial atomization field for the theoretical calculation. It is not enough to optimize the pre-burner injector only using the information of the cold spray measurements. Consequently, six hot fire tests were conducted using gaseous hydrogen and liquid oxygen as propellants for four candidates. Each test unit of the sub-scale pre-burner consists of four injector elements. Combustion efficiency, mechanical vibration, igniting stagnation and exhaustive gas temperature distribution have been obtained to manifest the differences between these injectors.

Furthermore, a corrective pre-burner with tri-coaxial injector, dump cooling channel, turbulence ring, and elbow exit was designed to improve the combustion performance of the pre-burner during the transient and steady state off-nominal operating period, as shown in figure 1.4. The dump cooling channel is set up at the forward section of the pre-burner to improve the burning resistant ability, and increase the average mixture ratio in the central ignition zone as well. The percentage of the dump cooling flow rate to the total hydrogen flow rate will change with the operating conditions, therefore the effect of the percentage of the dump cooling flow rate on the performance of the pre-burner was investigated with the fixed height of the turbulence ring. The turbulence ring is located downstream of the dump cooling channel exit to enhance the downstream mixing. The test of the turbulence ring consists of the open and the closed turbulence ring. The structure of the closed turbulence ring is a mesh arch. Both the straight exit and the 90° elbow exit are investigated. The performance test of the pre-burner was performed using liquid hydrogen and liquid oxygen as propellants. Three tri-coaxial injector elements are installed in the pre-burner for performance test.

The theoretical analysis was performed using the PHOENIX commercial software. The objective of the theoretical calculation is to obtain the limitation of the dump cooling flow rate, the best configuration of the turbulence ring and the optimum mixture ratio of the inner tri-coaxial injector. The percentage of the dump cooling

flow rate has been studied range from one percent to 25 percent. The mixture ratio of the inner tri-coaxial injector has been investigated by varying from rich-hydrogen to rich-oxygen. The flow field analysis has been conducted by calculating the concentration distribution of the propellants and the temperature distribution in the pre-burner.

Experimental Facilities

High Pressure Spray Rig System. Cold spray measurements were performed using Aerometrics' PDPA with high pressure chamber, as shown in figure 2.1. This chamber is capable of operating at pressures as high as 3.5MPa. The spray chamber has an inner diameter of 320mm and is about 1200mm long. Four viewing / optical port 100mm in diameter are provided on the chamber. For phase Doppler applications, the optical ports at the transmitter and receiver ends were fitted with 25mm thick optical quality quartz windows. The two other windows were fitted with 50mm thick soda lime glass windows for flow visualization purposes. A two axes traverse system was located within the chamber for moving the injector axially and in a radial direction. Several ports were available on the bottom of the spray rig for draining the accumulated liquid and for exhaustive gas.

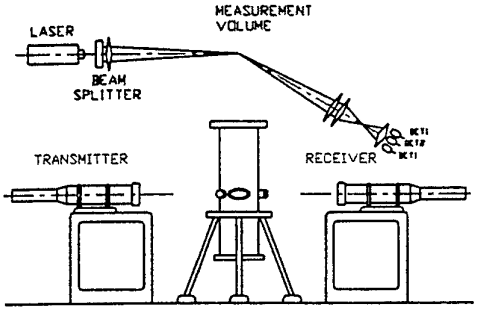


Fig.2.1 High pressure spray rig system

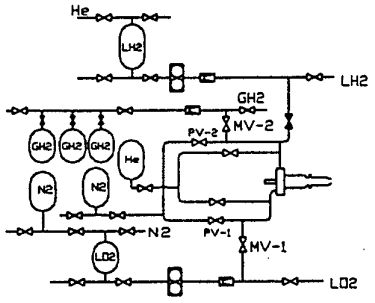


Fig.2.2 Burning Test Schematic

Burning Test Set-up. The propellant system schematic is shown in figure 2.2. Liquid oxygen and liquid hydrogen were supplied to the pre-burner from jacketed tanks through heavy wall pipes. The venturi tube was used for flow rate control. For all tests, the tank was pressurized with gaseous nitrogen for oxygen and Helium for hydrogen. Gaseous hydrogen used for fuel on the comparative tests was supplied from the 18MPa supply system. The feed line was a pipe of 40mm in diameter. The sonic nozzle was used for flow rate measurement.

The parameters from the hot fire testing measured by various types of transducers were converted to a digital form by a data acquisition system. The digital system had a capacity of 32 channels of pressure, temperature and flow rate. Mechanical vibration was recorded and stored on magnetic tape. Three thermocouples used to measure exhaustive gas temperature distribution were located center, half radius and inner wall of exit section of the pre-burner.

Theoretical Description

The theoretical framework used in this paper was a set of conservation equations of mass, momentum, total energy, and species concentration for gas and droplet, respectively. The analogy-fluid model was used to simulate the multiphase flows. As a result, the general form of the conservation equations could be written as:

$$\frac{\partial(\rho_k \Phi_k)}{\partial t} + \frac{\partial}{\partial x_j}(r_k \rho_k u_j^k \Phi_k) = \frac{\partial}{\partial x_j}(r_k \Gamma_\Phi \frac{\partial \Phi_k}{\partial x_j}) + \frac{\partial}{\partial x_j}(\Phi_k D_\Phi \frac{\partial r_k}{\partial x_j}) + s_{\Phi,k} + s_{m,\Phi,k} + s_{c,\Phi,k}$$

Where Φ = u,v,w,h,r,y_f,y_{ox},k, ε ,p, k=1,2 represents gas and liquid, respectively. $S_{\Phi,k}$,$S_{m,\Phi,k}$ and $S_{c,\Phi,k}$ represent remainder resource term, two-phase interaction resource term and chemical reaction resource term, respectively. The droplet vaporization rate can be calculated based on the high vaporization model[5]. The k- ε equations are applied to the model of the turbulent flow. Spalding's EBU model and Arrehnius formula are used to calculate chemical reacting rate.

In order to obtain the stable results, the resource terms have been linearized as follows: $S_{m,\Phi} = C_P T(V_P - \Phi_P)$, $V = S_m/C_P + \Phi_P$

The static enthalpy $h = C_P T + \Sigma Y_i H_i$ is used as a variable in energy equation to avoid the negative temperature which may result in divergence of calculation. Reasonable boundary conditions are very vital for accuracy and divergence of the calculation results. Boundary conditions in this paper are given as follows:

Entrance conditions: Assume U1=V1=0, other velocities are fixed by numerical boundary conditions.

Exit conditions: Mach number=1, all of variables can be calculated by extrapolation.

Assuming wall is adiabatic, impermeable and fixed. The 1st order derivative of all variables at centerline is zero.

Results and Discussion

Spray Characteristics. The PDPA measurements were restricted to the measurement plane at an axial location of 110mm downstream. The cold flow measurements were performed using water and air as simulative medium for liquid oxygen and hydrogen, respectively. The atomization process was completed at this axial location by performing a weight average of the radial D_{32} distributions. A single cumulative D_{32} can characterize the overall spray distribution using the following equation:

$$D_{32} = \frac{\int_0^R N_d(r) D_{30}(r) dr}{\int_0^R N_d(r) D_{20}(r) dr}$$

The cumulative Sauter mean diameter is found to decrease with the increase of the air/liquid pressure drop ratio. A linear increase of the cumulative Sauter mean diameter can be seen with the increase of back pressure and water mass. A little difference of the Sauter mean diameter between these injectors can be seen as shown in figure 4.1 through 4.4. In addition, assuming the gaseous volume flux was viewed as uniform in radial direction, the radial variation of the volume flux showed that the spray of the swirl coaxial injector is close to the periphery whereas the volume flux of

the shear coaxial injector concentrates the central region. The periphery distribution of the spray is benefit to the mixing and ignition of the propellants. The spray behavior of the tri-coaxial injector is approximately the same as the shear coaxial injector, its cumulative D_{32} will decrease when the oxygen post recess increases. It is difficult to tell the performance differences existing in these candidate injectors just according to the cold flow spray measurement. But the size and velocity of the spray particle can disclose the variation of the spray characteristics with the operating condition in detail. The significance of the cold flow spray measurement is to provide the initial data for the theoretical calculation. Unfortunately, the data conversion from cold flow to hot fire has not formed a satisfied formula and the simulation is still approximate.

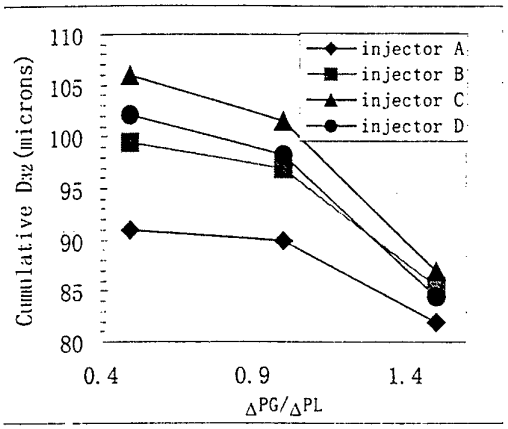


Figure 4.1 D_{32} variation with pressure drop ratio

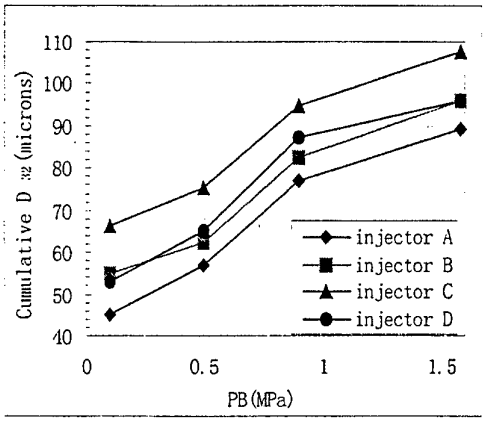


Figure 4.2 D_{32} variation with back pressure

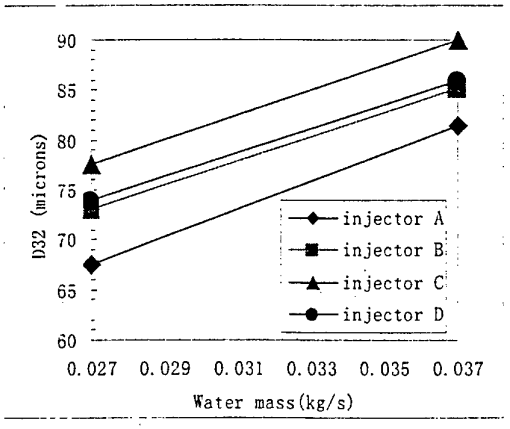


Figure 4.3 D_{32} variation with water flow rate

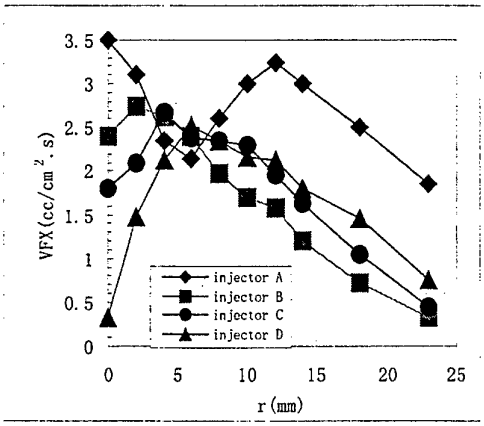


Figure 4.4 Distribution of volume flux

In this study, the simulation of the gaseous hydrogen injection density and the liquid oxygen surface tension and viscosity is considered to be crucial to obtaining atomization results that are directly relevant to gaseous hydrogen and liquid oxygen injector sprays. However, since the surface tension of the droplet vanishes at supercritical point. The Reynolds and Weber Numbers can not describe supercritical spray. According to our experience, the momentum ratio of gas and liquid propellant is a crucial parameter for determining the combustion performance. The parameter can be expressed as follows: $R=(\rho_g v_g^2)/(\rho_l v_l^2)$. Other parameters, such as back pressure, have a much greater effect on atomization. The parameters relating to the

spray characteristics of the injectors can be written as: $D_{32}=f(R, P_b)$. For the swirl coaxial injectors, the geometrical characteristics should be considered.

Comparative Test. Six hot fire tests have been performed for four candidate injectors. The candidate B and the candidate D were experimented for two times, respectively. The second test for the candidate D was not ignited due to low mixture ratio of 0.6 during the start-up period. The results show that the combustion efficiency for each test is close to 1 except the test of non-ignition. Comparing with four types of injectors, the candidate D has the highest value of 0.998 and the candidate B has the lowest combustion efficiency of 0.98.

Three thermal-coupling transducers are used to measure the exhausting gas temperature distribution. The temperature difference between them can indicate the uniformity of the exhausting gas temperature distribution. The results show that the candidate D has the best temperature distribution with difference of $\Delta T=20.09K$. The candidate B has a maximum temperature difference of $\Delta T=50.23K$.

The igniting stagnation is defined as the time interval between hydrogen entrance and igniting. The test data show that the candidate A has shorter time interval of 0.9 second and the longest time interval is 1.4 second for the candidate B. The short igniting stagnation of the candidate A can be attributed to the ability of oxygen transversal penetrability of the swirl coaxial injector. Therefore, the behavior of the volume flux close to the spray's periphery can effectively improve the mixture ratio distribution and ignition performance.

The mechanical vibration data indicate that the candidate D has the lowest accelerating amplitude of mechanical vibration. The synthetic acceleration of the candidate D is 325.4 m/s^2 and the value of the partial acceleration is 36.8m/s^2 with frequency of 3025HZ. The synthetic acceleration and the partial acceleration are 686m/s^2 and 196.4m/s^2 with frequency of 5575HZ for the candidate B, respectively.

To sum up, the candidate D has the advantage of the high combustion efficiency, good combustion stability and uniform temperature distribution over all candidate injectors. But the candidate D has a longest igniting stagnation, hence, the igniting performance of the tri-coaxial injector should be further improved.

Theoretical Analysis. In this study, the flow field is 3-D and the liquid oxygen and hydrogen entering the pre-burner from three tri-coaxial elements were a compressible turbulent reacting multiphase fluid. Complicated physical phenomena such as atomization and spray combustion were included and the analogy-fluid model was used to deal with the multiphase flow. Liquid drop vaporization under high pressure was adopted the theory of Spalding's formula[3] that assume the drop vaporization in the inertia gas surroundings and the process is sphere-symmetrical. The grid mesh size used in this study was 75 by 30 by 25 in axial, circular and radial direction, respectively.

The results of the study show that the mixture ratio of the inner tri-coaxial injector and the percentage of the dump cooling flow rate is vital to obtain gas temperatures as uniform as possible at the pre-burner exit. The distributions of the oxygen and hydrogen concentration are shown in figure 4.5 and figure 4.6. There is a circulation zone near injector where the concentration of the hydrogen is high. The

temperature variation with radius at different axial locations shows that the temperature is less than 800 K near the injector. The chemical reaction can not happen in the circulation zone due to the low mixture ratio. The concentration of the hydrogen becomes the higher due to the addition of the diluting hydrogen. There is not a strong mixing process before the gas exhaust.

The concentration of the oxygen can represent the length of the flame for relative compare purpose. The flame length is about 70mm long at the inner injector's mixture ratio of 6 as shown in figure 4.6. The length of the flame does not increase until the mixture ratio of the inner tri-coaxial injector excess the stoichiometric. In the meantime, the flame length decreases when the mixture ratio of the inner injector varies from 6 to the stoichiometric. The shorter the flame length could be, the better the uniformity of the exhausting gas temperature distribution is.

The figure 4.7 shows the gas temperature distribution. There is a high temperature flame region in the central jet of the inner tri-coaxial injector. The highest temperature changes in the range of 30 to 70mm downstream where a strong combustion zone exists. The oxygen reacts immediately with the hydrogen due to the local high mixture ratio. The combustion temperature in this region can reach as high as 3000 K. The chemical reaction stops after excess of 90mm downstream injector and the gas temperature are gradually close to uniformity. There is an initial temperature peak in radial direction, then the peak move gradually toward the centerline. Moreover, the elbow can enhance the uniform of the exhausting gas temperature that can be seen in figure 4.7. The uniformity of the exhausting gas temperature becomes worse with the increase of the dump cooling flow rate. The diluting hydrogen exhausting from the exit of the dump cooling channel can not mix with the main flow immediately. There is a limitation of the dump cooling flow rate that the exhausting gas temperature distribution can satisfy the temperature limitations of the turbine blade. Both the turbulence ring and the elbow exit is benefit to improve the uniformity of the exhausting gas temperature distribution.

Performance Test. Though the tri-coaxial injector shows satisfied combustion performance, there is still a concern that propellants may not be ignited well due to inappropriate oxidizer/fuel mixture ratio during start-up. In addition, the stoichiometric mixture ratio region may produce a hot temperature streak in the pre-burner. To alleviate these problems, the pre-burner should be redesigned to enhance the mixing capability of combustion gases and further improve the ignition performance and exhausting gas temperature distribution. The objective of performance test is to define a pre-burner configuration that can be reliably ignited during the off-nominal operation period and produces a uniform temperature at exit. The performance test in this study consists of the open and the close turbulence ring, the mixture ratio of the tri-coaxial inner injector, the percentage of the dump cooling flow rate and the forms of the pre-burner exit.

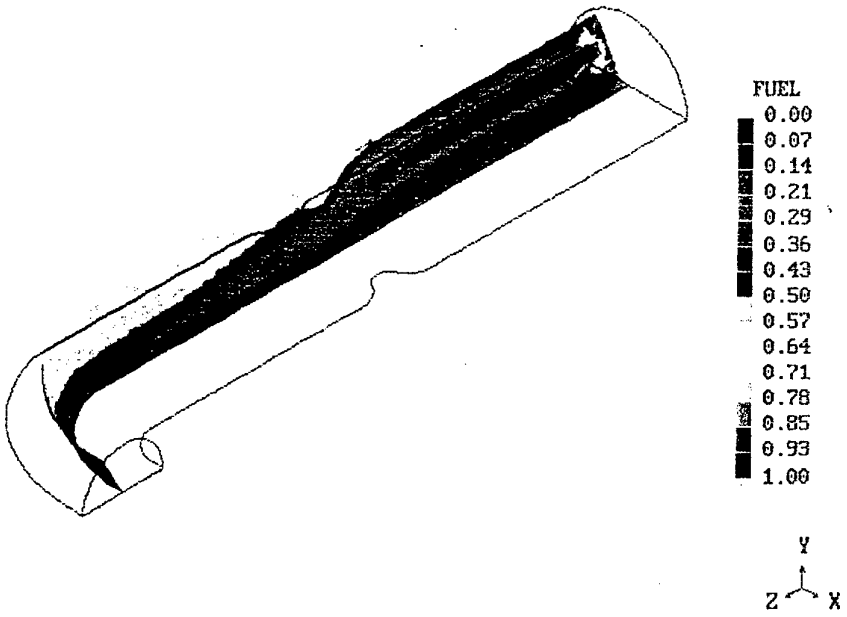


Figure 4.5 Concentration of the hydrogen

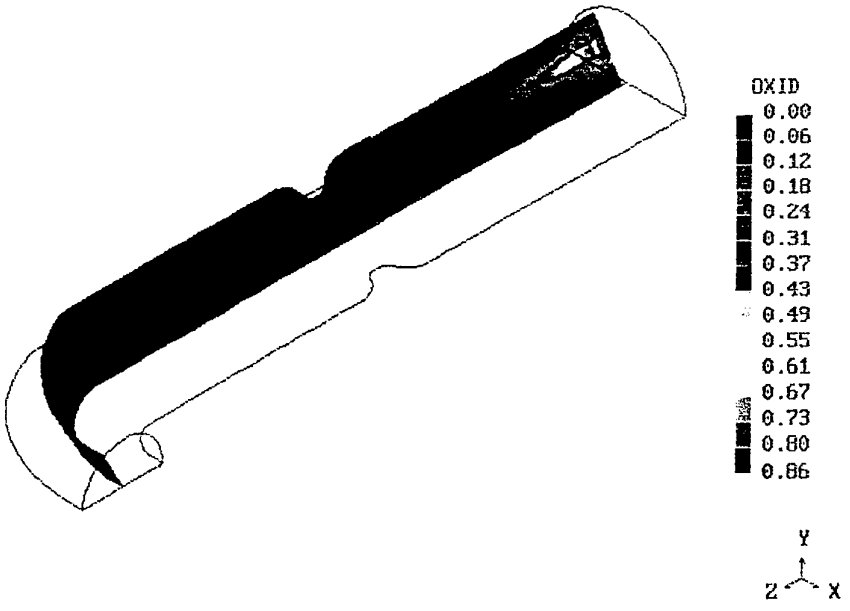


Figure 4.6 Concentration of the oxygen

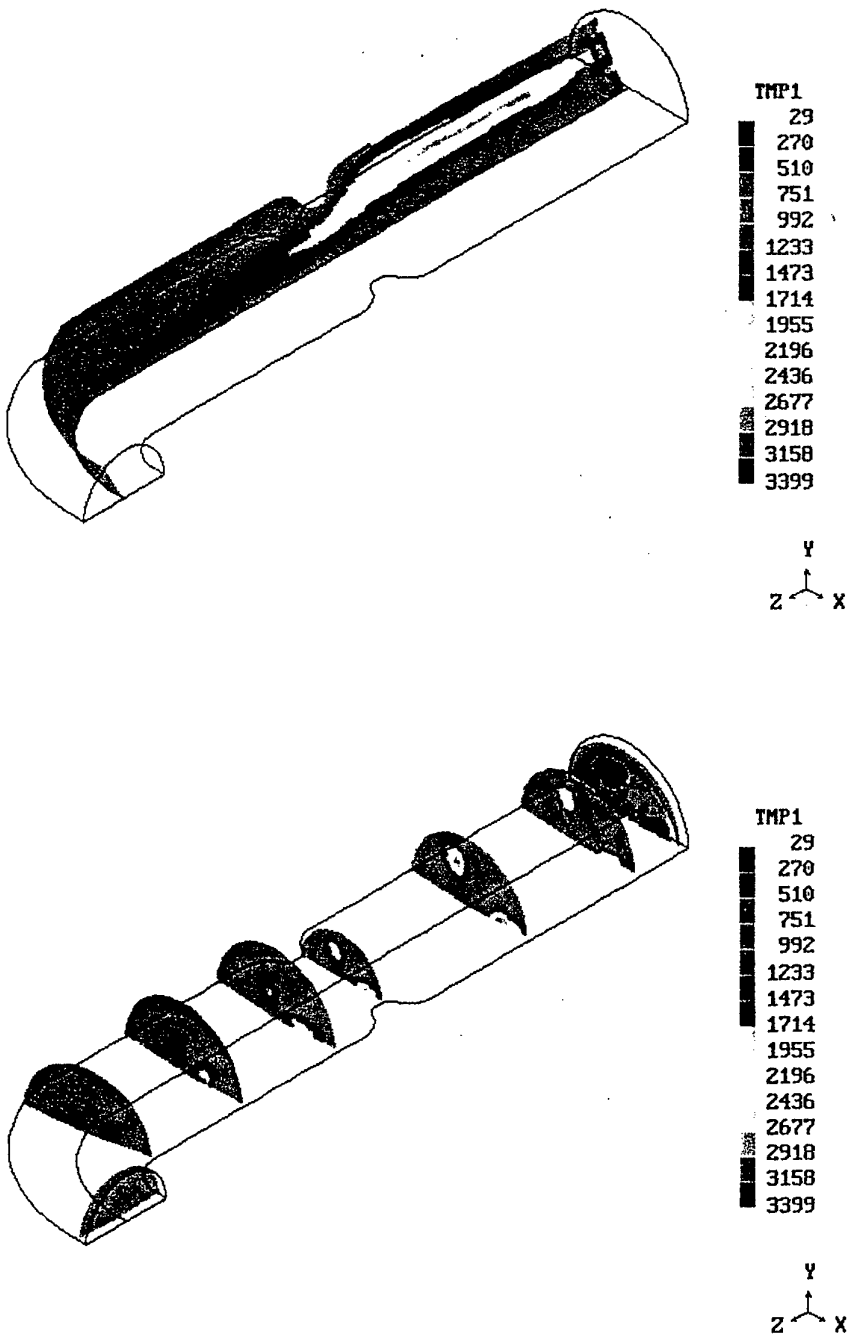


Figure 4.7 Temperature distribution of fluid in the pre-burner

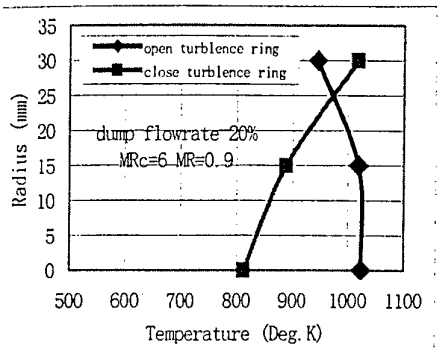


Fig. 4.8 Open/close turbulence ring

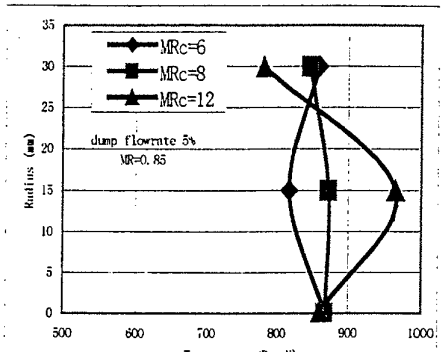


Fig. 4.9 Mixture ratio of inner injector

The open/close turbulence ring test results are shown in fig.4.8. It can be seen that the open turbulence ring as an enhancing device is good enough to improve the exhausting gas temperature distribution. The temperature difference can satisfy the definite temperature limitations of the turbine blade. The close turbulence ring was found being burned down during shut down due to the higher central mixture ratio. There is a contradiction between cool ability to protect close turbulence ring and improving ignition performance by increase of central mixture ratio. Therefore the close turbulence ring has been given up.

The exhausting gas temperature distribution varied with the mixture ration of the inner tri-coaxial injector, as shown in figure 4.9. When the mixture ratio of the inner tri-coaxial injector changes from rich-hydrogen to rich-oxygen, more and more free oxygen move downstream after-burning which is not benefit to the mixing of gases. Therefore the mixture ratio of the inner tri-coaxial injector should be less than the stoichiometric mixture ratio.

The uniformity of the exhausting gas temperature distribution becomes poor while increasing the dump cooling flow rate, as shown in figure 4.10. The non-uniformity of exhausting gas temperature distribution would be excess definite temperature limitations of the turbine blade when the percentage of dump cooling flow rate is greater than 10%. Generally speaking, the percentage of the dump cooling flow rate is proportional to the height of the turbulence ring. Moreover, the pressure drop of the

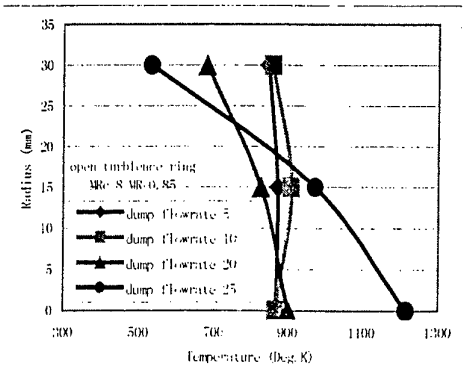


Fig.4.10 Dump cooling flow rate

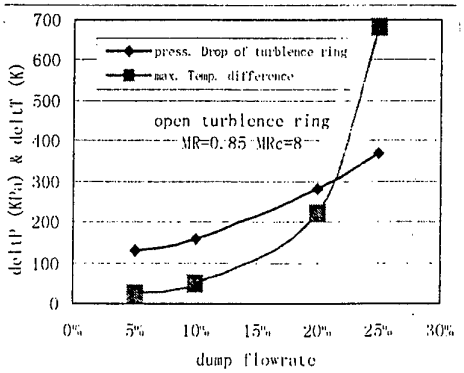


Fig.4.11 Temp uniformity : Pressure drop of turbulence ring

turbulence ring would slightly increase with the increase of the percentage of dump

cooling flow rate. It is shown in figure 4.11. This is the reason that the density of gaseous hydrogen ejected from cool channel is lower than the density in central region. The pressure drop of turbulence ring is more susceptive to the height of turbulence ring.

Finally, the figure 4.12 shows that the elbow exit can improve the uniformity of exhausting gas temperature distribution. It is recommended that a designer should adopt it for the allowable engine assembly.

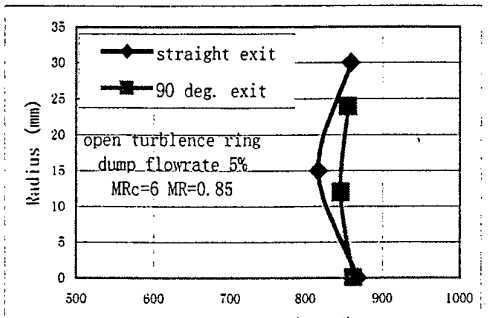


Fig. 4.12 Straight exit / elbow exit

Conclusion

The new-type tri-coaxial injector has been selected to be the pre-burner injector from four candidate injectors. The tri-coaxial injector has advantages of high combustion efficiency, good combustion stability, and uniform exhausting gas temperature distribution over other types of injectors. But the tri-coaxial injectors should be improved on the igniting performance. The optimum pre-burner configuration has been established to enhance the mixing capability of combustion gases and eliminate the hot temperature streak during start-up. The mixture ratio of the inner tri-coaxial injector should be less than the stoichiometric and the percentage of the dump cooling flow rate should not be excess 10% of the total hydrogen flow rate. The author recommends that a designer should employ the open turbulence ring and the elbow exit to assure the reliable operation of the pre-burner during the off-nominal operation period and the uniformity of the exhaustive gas temperature.

References

[1] D. Morgan, R.. Beichel, "Stoichiometric Gas Generator— A Strategic Departure", AIAA-91-2584

[2] S. Kim, H. P. Trinh, "Design Study of an Advanced Gas Generator", AIAA-93-2158

[3] N. J. Sekas, L. W. Acker, "Design and Performance of Liquid-Hydrogen, Liquid-Oxygen Gas Generator for Driving 1000-Horsepower Turbine", Technical Note D-1317

[4] M. C. Yost, et al, "Pre-burner of Staged Combustion Rocket Engine", NASA CR-135356

[5] J. M. Bommie, et al, "Thermodynamic Properties 6000K for 210 Substances Involving the First 18 Elements", NASA SP-3001

[6] S. V. Sankar, J. Y. Zhu and W. D. Bachalo, "Experimental Studies on the Behavior of Coaxial Rocket Injector Spray", Aerometrics Inc., Sunnyvale, CA, U. S. A., 1994

[7] A. H. Levebvre, "Atomization and Spray", Hemisphere Pub., XO, 1989

Heat Flux Management and Cooling Techniques in Rocket Thrust Chambers

D. Haeseler, D. Preclik

DaimlerChrysler Aerospace AG

Space Infrastructure Propulsion, Munich, Germany

4th International Symposium on Liquid Rocket Propulsion

13 - 15 March 2000, Heilbronn, Germany

This document is the property of DaimlerChrysler Aerospace and is not to be disclosed or reproduced without prior written consent.

Overview on Presentation

- General Requirements for Thrust Chamber Cooling
- Current Examples of Rocket Engines in Operation
  - ➤ Gas Generator Cycle
  - ➤ Staged Combustion Cycle
  - ➤ Expander cycle
- Cycle-Specific Requirements on TC Heat Transfer Management
- Goals for Thrust Chamber Heat Transfer Management
- Hot Gas Side Heat Transfer Management Methods
- Summary and Conclusions

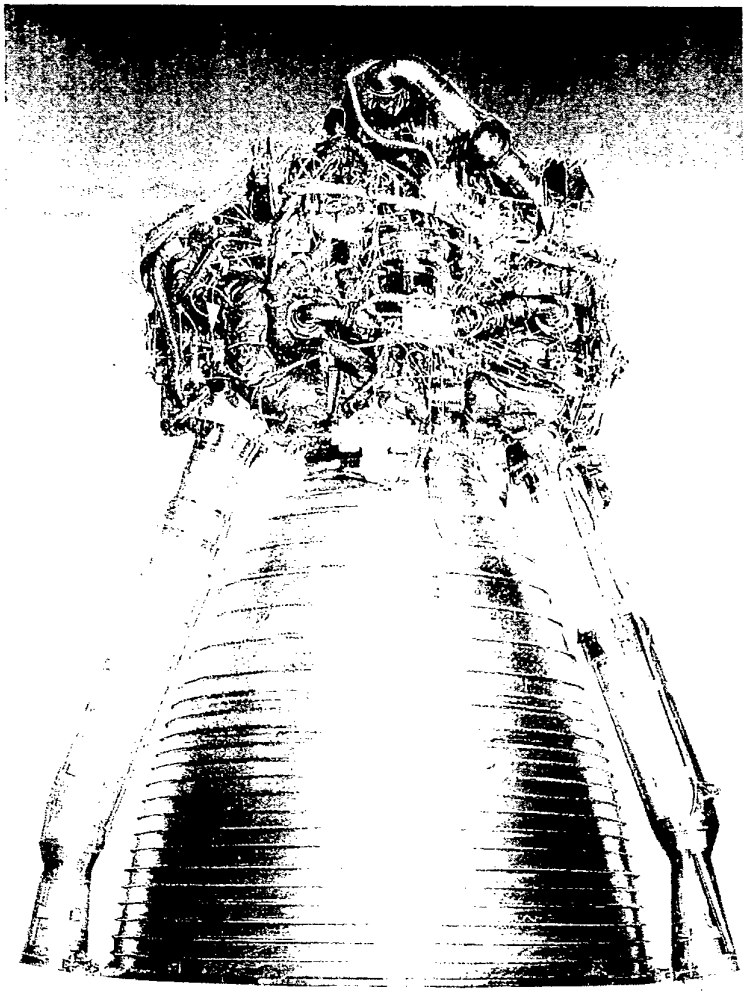
This document is the property of DaimlerChrysler Aerospace and is not to be disclosed or reproduced without prior written consent.

General Requirements for Thrust Chamber Cooling

- Hot-gas wall temperature limit given by lifetime requirements and wall material properties.
- The rational for the coolant flow rate is defined by the engine cycle
- The rational for the coolant pressure budget is defined by the engine cycle

This document is the property of DaimlerChrysler Aerospace and is not to be disclosed or reproduced without prior written consent.

Current Status of Gas Generator Cycle Thrust Chamber Cooling



Example: Vulcain (Snecma Moteurs, Dasa)

Propellants:	LOX-LH2, Mixture ratio in chamber 5.9
Vacuum thrust:	1140 kN (256 klb)
Chamber pressure:	110 bar (1595 psia)
Application:	Ariane 5 Central Stage EPC

Cooling System Requirements and Functions:

- Minimum coolant pressure drop in combustion chamber cooling circuit.
- Minimum coolant flow rate in nozzle cooling circuit.
- Hydrogen heating for better combustion.

Combustion Chamber Cooling:

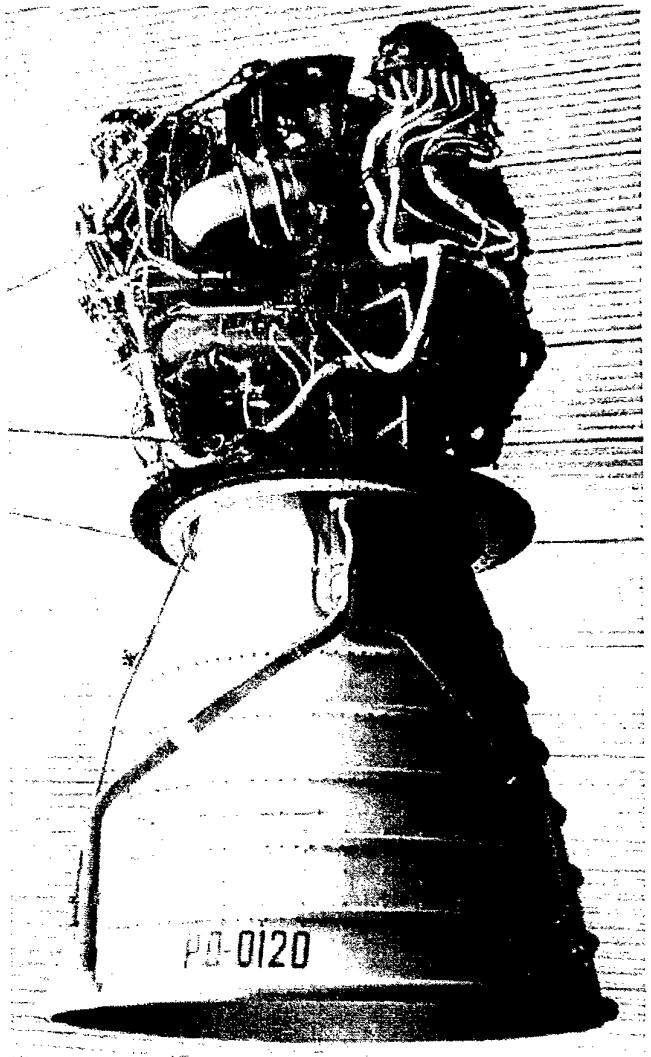
- Regenerative cooling with LH2, coolant pressure 150–120 bar, coolant temperature 35–100 K.
- High-aspect coolant channels to carry total hydrogen flow.
- Reduced mixture ratio in outer injector row.

Nozzle Extension Cooling :

- Dump-cooling with LH2, coolant pressure 45–15 bar.

This document is the property of DaimlerChrysler Aerospace and is not to be disclosed or reproduced without prior written consent.

Current Status of Staged Combustion Cycle Thrust Chamber Cooling



Example: RD-0120 (КБХА)

Propellants:	LOX-LH2, Mixture ratio in chamber 6.0
Vacuum thrust:	1961 kN (441 klb)
Chamber pressure:	218 bar (3162 psia)
Application:	Energia Central Stage

Cooling System Requirements and Functions:

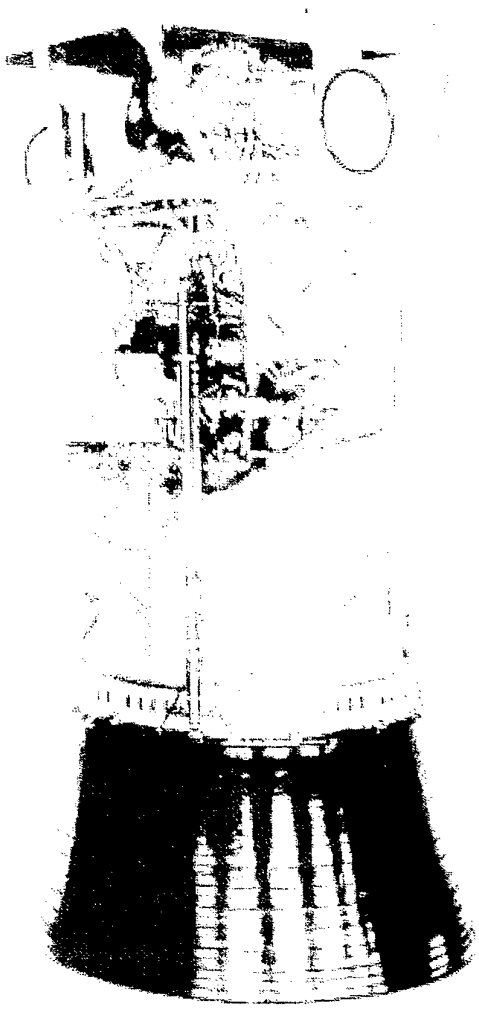
- Cooling circuit parallel to fuel-rich preburner and turbine expansion.
- Minimum coolant flow rate in thrust chamber cooling circuit (bypassing main turbine) within available pressure drop (given by turbine pressure ratio).
- Hydrogen heating to drive LH2-boost-pump turbine.

Thrust Chamber Cooling:

- Regenerative cooling with LH2, coolant pressure 430–314 bar, coolant temperature 55–500 K.
- Reduced mixture ratio in outer injector row (~3.8)
- Hydrogen film-cooling (1.4 %) at injector.
- Ni+Cr thermal barrier coating.

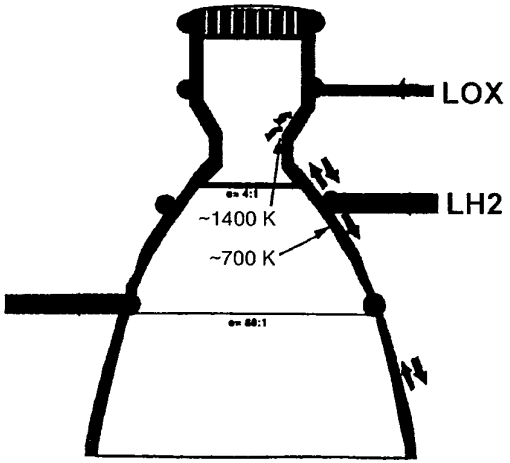
This document is the property of DaimlerChrysler Aerospace and is not to be disclosed or reproduced without prior written consent.

Current Status of Staged Combustion Cycle Thrust Chamber Cooling



Example: RD-57 (Saturn-Lyulka)

Propellants:	LOX-LH2, Mixture ratio in chamber 5.8
Vacuum thrust:	397 kN (89 klb)
Chamber pressure:	115 bar (1668 psia)
Application:	N-1M Upper Stages



Cooling System Requirements and Functions:

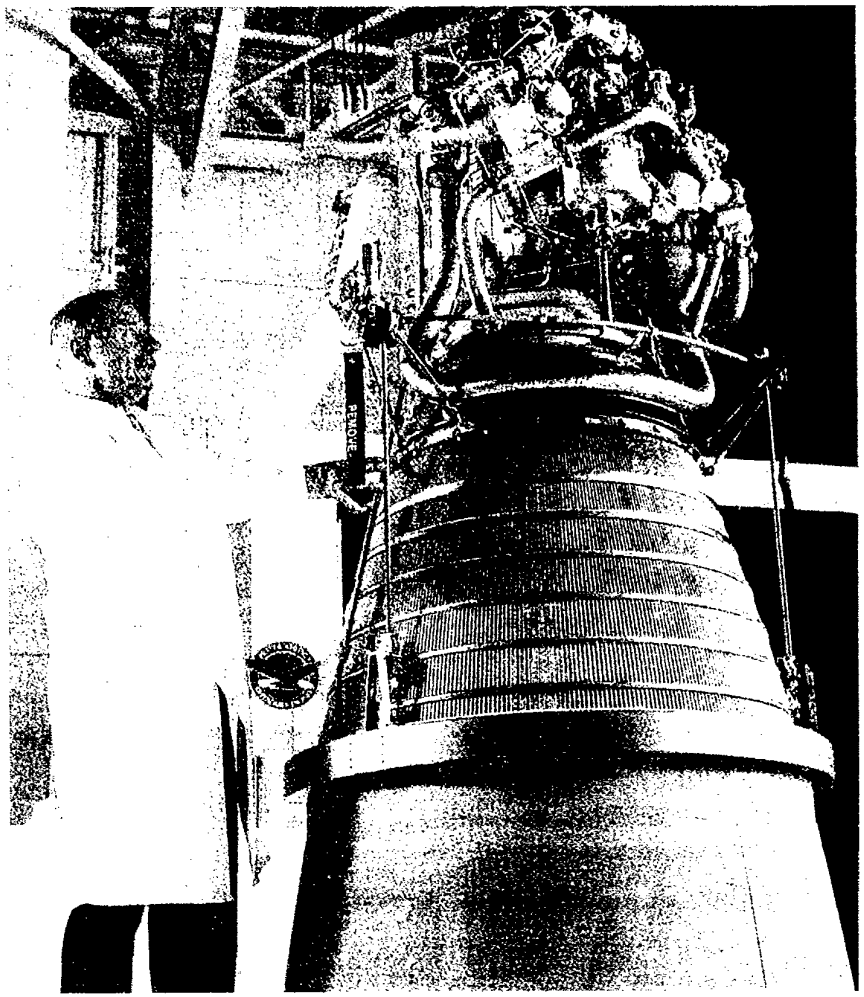
- Cooling circuits parallel to fuel-rich preburner and turbine expansion.
- Minimum coolant flow rate in thrust chamber cooling circuit within available pressure drop (given by turbine pressure ratio).

Thrust Chamber Cooling:

- Regenerative cooling of throat region and nozzle with LH2.
- Regenerative cooling of chamber barrel with LOX to reduce fuel cooling pressure drop, and thus required fuel pump discharge pressure.
- Hydrogen film-cooling at chamber barrel end near throat.
- ZrO_2 thermal barrier coating.

This document is the property of DaimlerChrysler Aerospace and is not to be disclosed or reproduced without prior written consent.

Current Status of Expander Cycle Thrust Chamber Cooling



Example: RL10A-4-1 (Pratt&Whitney)

Propellants:	LOX-LH2, Mixture ratio in chamber 5.5
Vacuum thrust:	99 kN (22.3 klb)
Chamber pressure:	42 bar (610 psia)
Application:	Centaur Upper Stage

Cooling System Requirements and Functions:

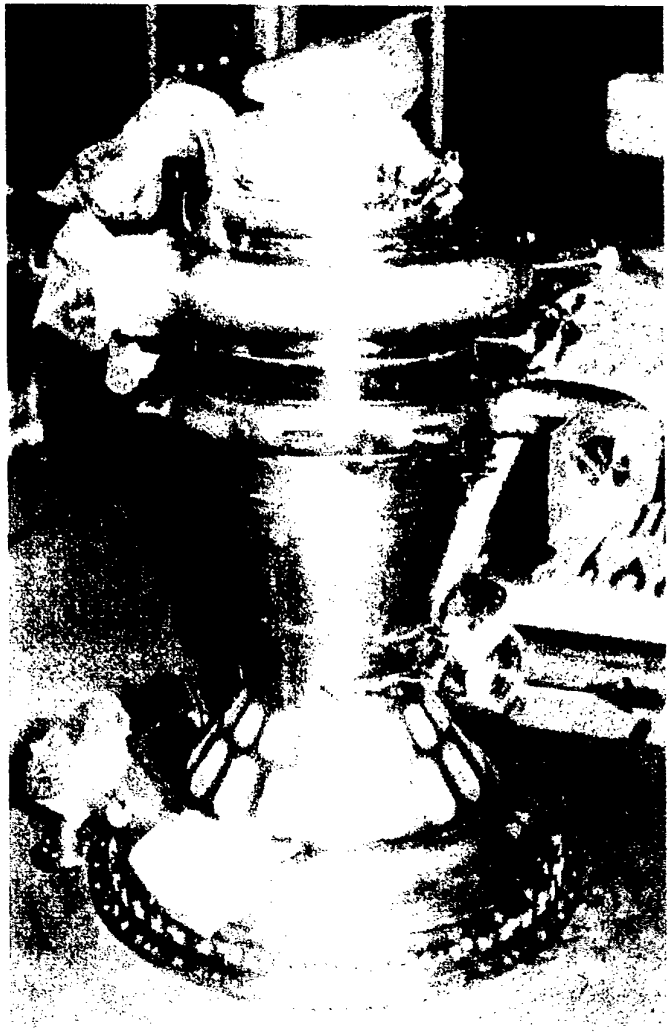
- Maximum coolant heating with total coolant flow rate in thrust chamber cooling circuit at limited pressure drop.
- Hydrogen heating is only power source for turbopumps.

Thrust Chamber Cooling:

- Regenerative cooling with LH2, coolant pressure 91–75 bar, coolant temperature 35–230 K.
- Thin-walled tubular chamber liner (steel material)

This document is the property of DaimlerChrysler Aerospace and is not to be disclosed or reproduced without prior written consent.

Current Status of Expander Bleed Cycle Thrust Chamber Cooling



Example: LE-5A (NASDA/Mitsubishi)

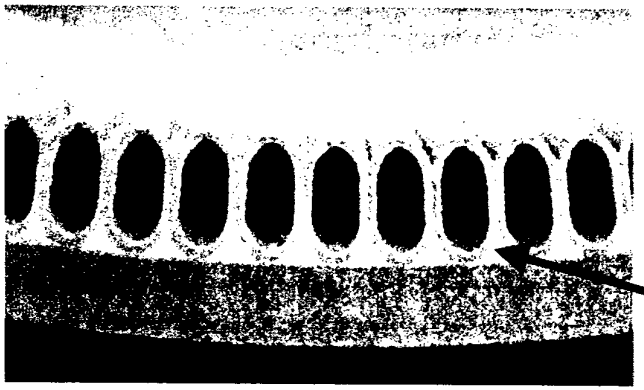
Propellants:	LOX-LH2
Vacuum thrust:	121.6 kN (27.34 klb)
Chamber pressure:	39.8 bar (577 psia)
Expander-cycle:	heating in nozzle cooling, turbine exhaust bleed into nozzle
Application:	H-II Stage 2

Combustion Chamber Cooling:

- Cut-outs in outer shell for mass reduction

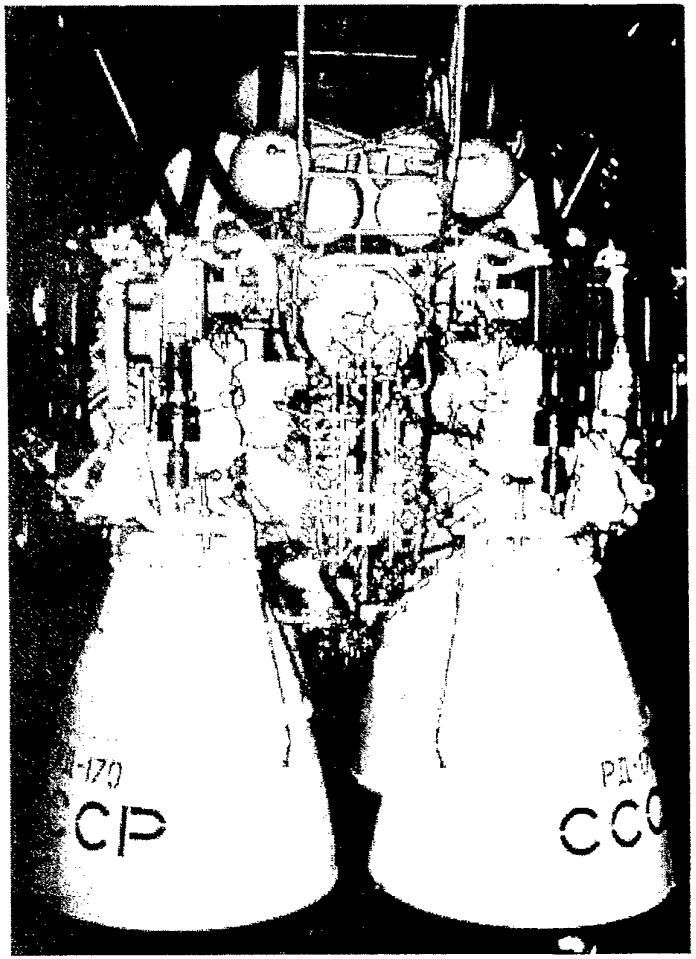
➔ Leak in test with hot spots

➔ Failure during flight H2-5



This document is the property of DaimlerChrysler Aerospace and is not to be disclosed or reproduced without prior written consent.

Current Status of Staged Combustion Cycle Thrust Chamber Cooling



Example: RD-170 (NPO Energomash)

Propellants:	LOX-Kerosene, Mixture ratio in chamber 2.6
Vacuum thrust:	7903 kN (1777 klb)
Chamber pressure:	245 bar (3553 psia)
Application:	Zenit Stage 1, Energia Booster

Cooling System Requirements and Functions:

- Cooling circuit parallel to ox.-rich preburner and turbine expansion.
- Sufficient cooling for required lifetime while avoiding overheating of coolant (avoid decomposition)

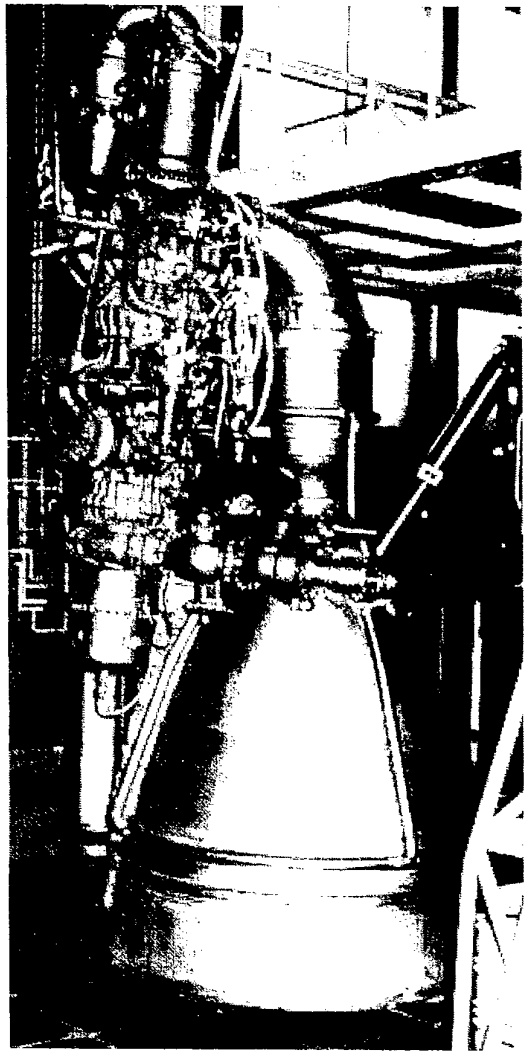
Thrust Chamber Cooling:

- Regenerative cooling with kerosene, coolant pressure 412–258 bar, coolant temperature 280–430 K.
- Faceplate cooled regeneratively with kerosene.
- Kerosene film-cooling (~9 %) in chamber barrel near throat.
- Increased injection mixture ratio near wall to counterbalance reduction by kerosene from film-cooling.
- Ni+Cr thermal barrier coating.

→ $q_{w,max} \approx 50$ MW/m² $T_{wg} < 780$ K $T_{wcool} < 620$ K

This document is the property of DaimlerChrysler Aerospace and is not to be disclosed or reproduced without prior written consent.

Current Status of Staged Combustion Cycle Thrust Chamber Cooling



Example: NK-33 (Kuznetsov)

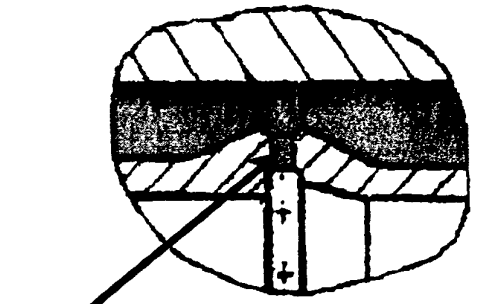
Propellants:	LOX-Kerosene, Mixture ratio in chamber 2.6
Vacuum thrust:	1745 kN (392 klb)
Chamber pressure:	157 bar (2277 psia)
Application:	N-1 Stage 1

Cooling System Requirements and Functions:

- Cooling circuit parallel to ox.-rich preburner and turbine expansion.
- Sufficient cooling for required lifetime while avoiding overheating of coolant (avoid decomposition)

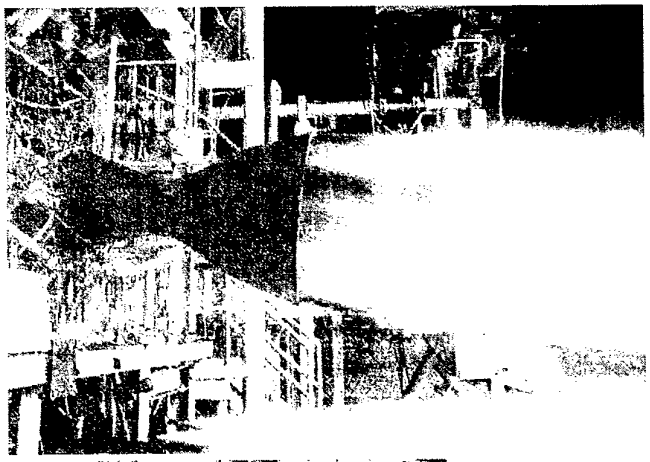
Thrust Chamber Cooling:

- Regenerative cooling with kerosene, coolant pressure 290–165 bar.
- Faceplate cooled regeneratively with kerosene.
- Kerosene film-cooling in chamber barrel near throat.
- Mixture ratio bias in outer injector row.

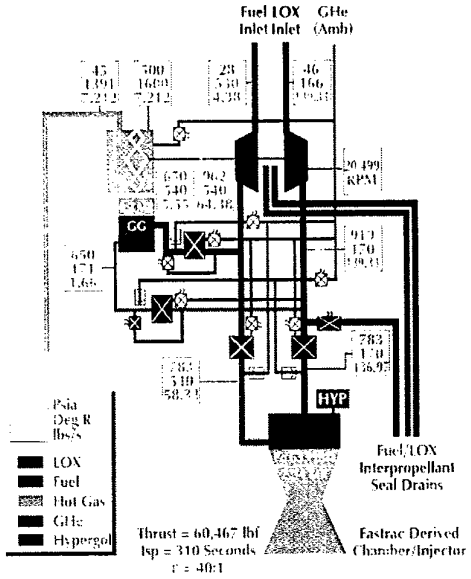


This document is the property of DaimlerChrysler Aerospace and is not to be disclosed or reproduced without prior written consent.

Current Status of Low-Cost Gas Generator Cycle Thrust Chamber Cooling







Example: Fastrac (NASA MSFC)

Propellants:	LOX-Kerosene, Mixture ratio in chamber 2.35
Vacuum thrust:	269 kN (60.5 klb)
Chamber pressure:	44 bar (633 psia)
Application:	X-34 RLV-Demonstrator

Cooling System Requirements and Functions:

- Minimum coolant pressure drop in combustion chamber cooling circuit.

Thrust Chamber Cooling:

- Ablative cooling using silica phenolic material.
- Alternatively:
  regeneratively cooled chamber made from copper-based metal-matrix composite material

This document is the property of DaimlerChrysler Aerospace and is not to be disclosed or reproduced without prior written consent.

Cycle-Specific Requirements on TC Heat Transfer Management

	Gas Generator Cycle	Staged Combustion Cycle	Expander Cycle	Expander Bleed Cycle
Example	Vulcain, HM7-B	SSME, RD-0120, RD-170	RL10A	LE-5A, LE-5B
Coolant flow rate	Total chamber fuel flow (except nozzle dump-cooling)	Minimum necessary for sufficient chamber cooling	Total chamber fuel flow	Balance between flow rate, pressure drop, and heat pick-up
Coolant pressure budget	Minimum possible	Given by turbine expansion ratio	Minimum possible	
Coolant heating	Minimum necessary for stable combustion	Maximum tolerable (to minimise flow rate)	Maximum possible	Maximum possible

- An optimum compromise between coolant flow rate, coolant flow routing (chamber vs. nozzle circuit), coolant heating, and coolant pressure budget is to be found for each engine design.
- Additional necessities like pre-pump turbine drive further complicate the lay-out.

This document is the property of DaimlerChrysler Aerospace and is not to be disclosed or reproduced without prior written consent.

Goals for Thrust Chamber Heat Transfer Management

Meet cooling requirements for future reusable long-life chambers for gas generator, expander, and staged combustion cycle chambers

1 Reduce heat flux to chamber wall for gas generator and staged combustion cycle chambers

➔ Lower wall temperature or pressure drop or flow rate (or any combination).

2 Reduce coolant pressure drop per coolant flow rate for given cooling task (heat flux, coolant-side wall temperature).

➔ Lower flow rate for given pressure drop and upper wall temperature limit (SC-cycle).

➔ Lower pressure drop for given upper wall temperature limit and flow rate (GG-cycle).

3 Increase heat flux to coolant for expander cycle chambers.

➔ Enhanced available turbine power
(trade-off heat pick-up vs. coolant pressure drop necessary).

This document is the property of DaimlerChrysler Aerospace and is not to be disclosed or reproduced without prior written consent.

Reduction of Heat Flux to Chamber Wall

(For gas generator and staged combustion cycle chambers)

- Reduced chamber pressure ($q_w \sim p_c^{0.8}$):
  - Reusable engines require highest chamber pressure for high performance within available engine installation envelope.

- Injector mixture ratio bias near wall, e.g. SSME, Vulcain, RD-0120:
  - May lead to performance loss.
  - Reduced mixture ratio near wall causes high mixture ratio for core flow.
  - Different injection elements for core and periphery required.

- Film cooling, e.g. RD-170:
  - May lead to performance loss.
  - Limited effectiveness for film injection at injector faceplate.
  - Design complications for film injection through chamber wall (through cooling structure).

This document is the property of DaimlerChrysler Aerospace and is not to be disclosed or reproduced without prior written consent.

Reduction of Heat Flux to Chamber Wall - 2

(For gas generator and staged combustion cycle chambers)

- Transpiration cooling:
  - May lead to performance loss.
  - Design complications for porous chamber wall sections and transpirant supply.
  - Active transpirant flow control may be necessary.

- Thermal barrier coating, e.g. Viking, RD-0120, RD-170:
  - Reusability of coatings may be critical.
  - No performance reduction (even slight increase due to reduced boundary layer losses due to higher temperature on coating surface).
  - Provides also protection against chemical attacks.

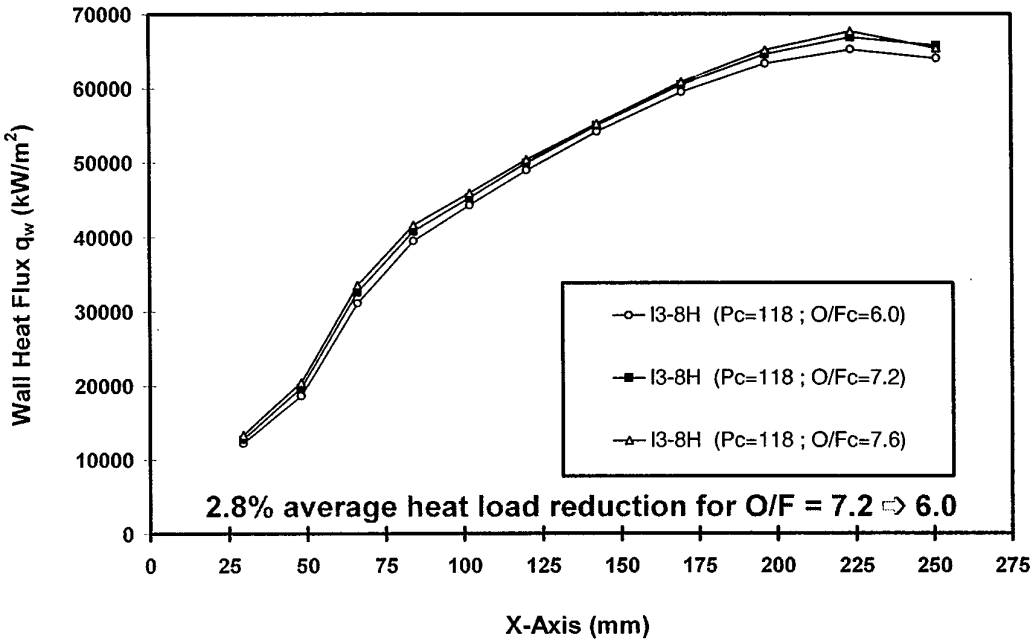
This document is the property of DaimlerChrysler Aerospace and is not to be disclosed or reproduced without prior written consent.

Hot Gas Side Heat Transfer Management Methods

- Film Cooling Concepts (Jet Holes, Slots)
- Wall Injector Element Mixture Ratio Biasing
- Transpiration Cooling
- Thermo-Chemical Protection Systems
- Surface Roughening
- Injector Element-to-Wall Distance
- Surface Contouring (Ribs)

This document is the property of DaimlerChrysler Aerospace and is not to be disclosed or reproduced without prior written consent.

Hot Gas Wall Heat Transfer Reduction with Injection Element O/F-Biasing



(axial length of calorimeter combustor barrel section)

Experiments Performed by Dasa

Propellants:	GH2/LOX
Chamber pressure:	100 ÷ 120 bar
Mixture ratio O/F	6.0 ÷ 7.6
Local heat flux reduction:	< 10 %

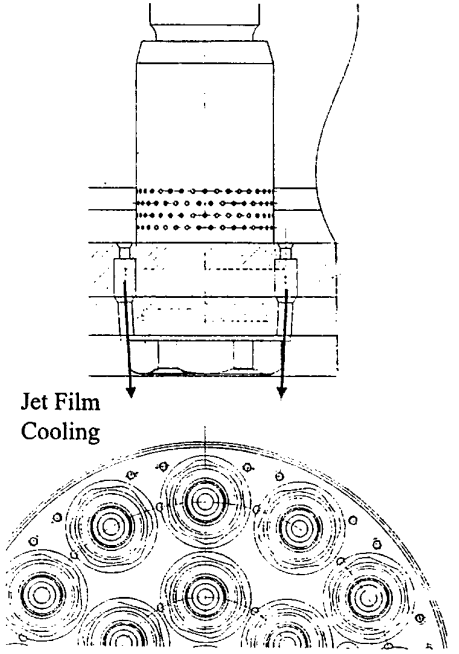
Fullscale Situation	Total	Core	Wall	$\Delta m_{H,wall}$
O/F - Biasing (case 1)	7.2	7.7	5.0	4.8%
> Flame Temperature	100%	100.3%	91.0%	
O/F - Biasing (case 2)	7.2	7,4	6.0	2.2%
> Flame Temperature	100%	100.2%	97.0%	
Film Cooling (altern.)	7.2	7.3	7.3	1.5%
> Flame Temperature	100%	100.1%	100.1%	

- O/F-biasing primarily aims at reducing the injection element's flame temperature near the wall.
- O/F-biasing may create an unfavourable high core element mixture ratio.
- Inhomogeneous radial mixture ratio distribution at injector leads to performance loss.

This document is the property of DaimlerChrysler Aerospace and is not to be disclosed or reproduced without prior written consent.

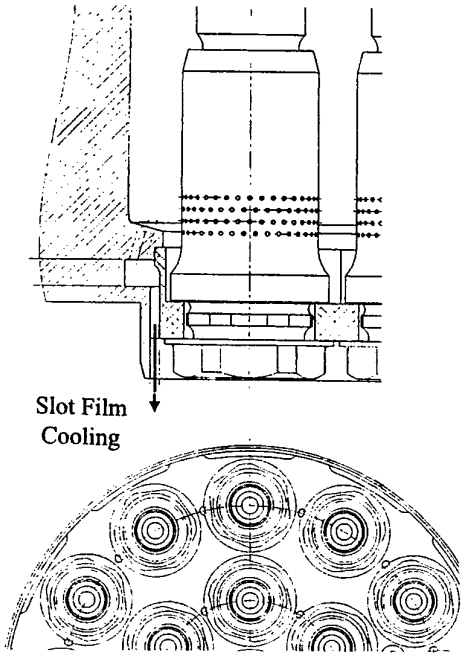
Hot Gas Wall Heat Transfer Reduction with Film Cooling

2 Jets / Wall Element (high H_2-velocity)



Jet concept effective only up to jet/wall impact point (≈ 55% of CC-barrel section)

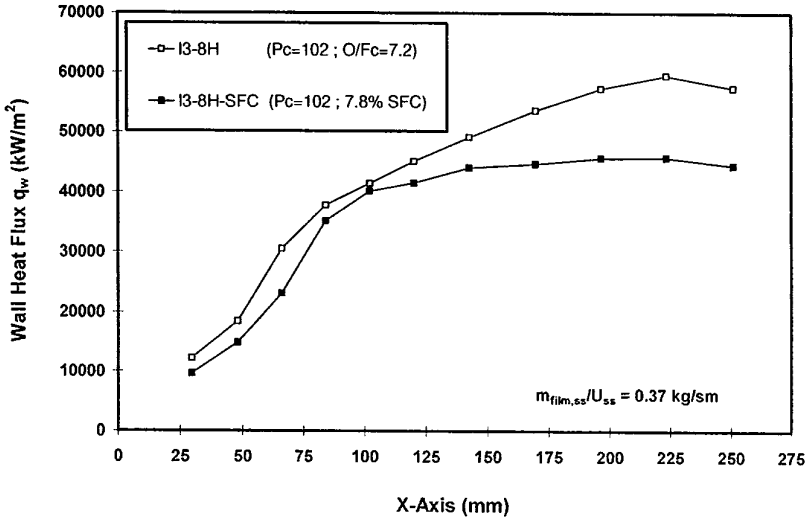
1 Slot / Wall Element (low H_2-velocity)



Slot concept effective in both sub- and supersonic sections of subscale combustor

Experiments Performed by Dasa

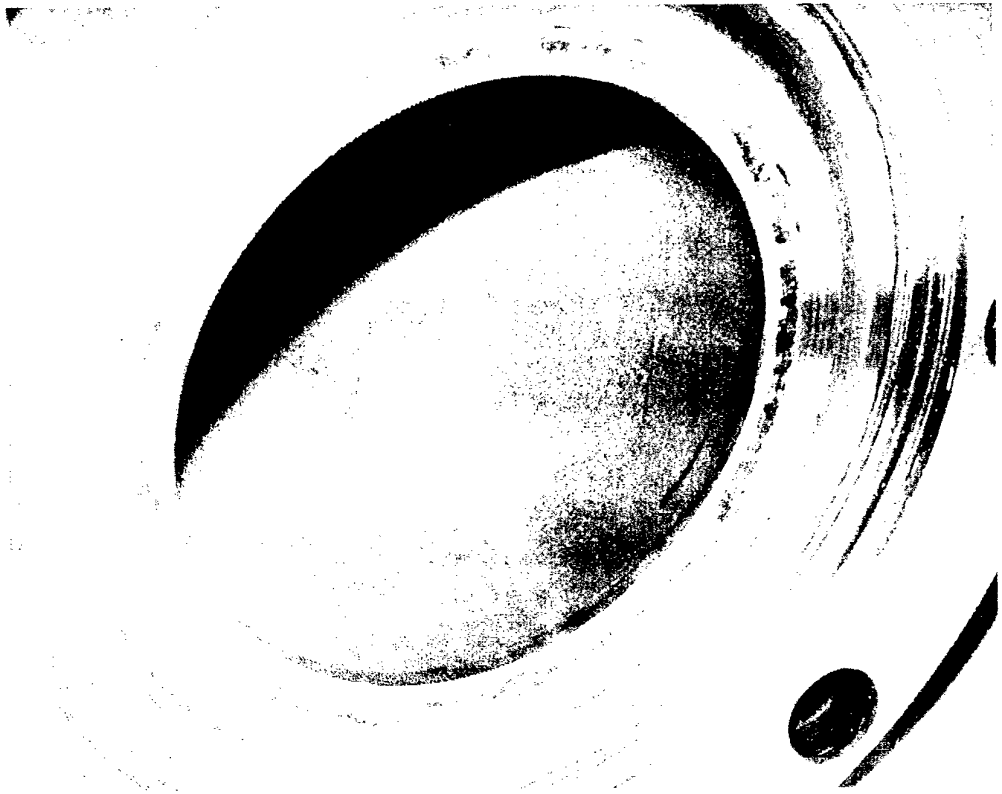
Propellants:	GH2/LOX
Chamber pressure:	100 ÷ 120 bar
Mixture ratio O/F	6.0 ÷ 7.2
Local heat flux reduction:	< 25 %



(axial length of calorimeter combustor barrel section)

This document is the property of DaimlerChrysler Aerospace and is not to be disclosed or reproduced without prior written consent.

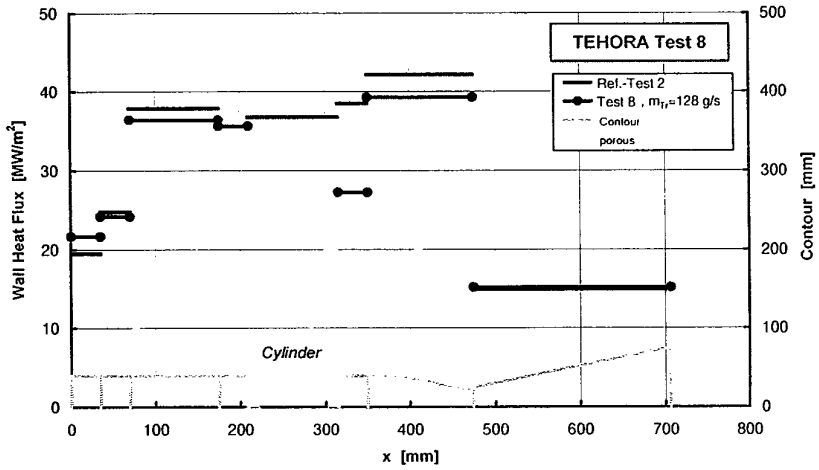
Hot Gas Wall Heat Transfer Reduction with Transpiration Cooling



GH2 transpiration-cooled chamber throat segment (Ni-based alloy, HIP powder technology, length: 124 mm, diameter: 80 - 46 mm)

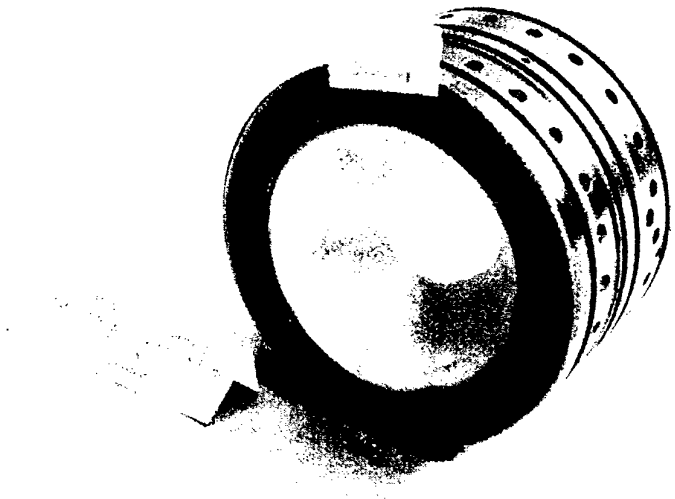
Experiments Performed by Dasa and КБХА

Propellants:	GH2/LOX
Chamber pressure:	100 bar
Mixture ratio O/F	5.0 ÷ 7.0
Heat flux reduction:	< 40 %

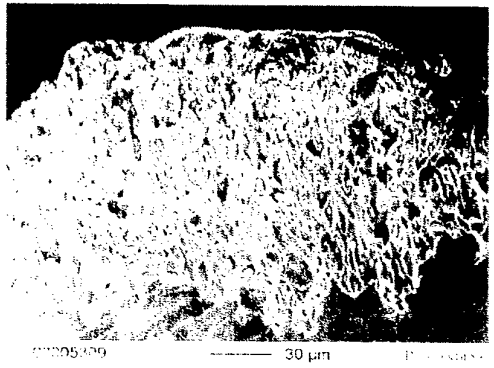


This document is the property of DaimlerChrysler Aerospace and is not to be disclosed or reproduced without prior written consent.

Hot Gas Wall Heat Flux Reduction with Thermo-Chemical Barrier Coating



Ceramic HVOF-ZrO_2 coated throat segment



Cu-liner O_2-blanching without surface protection

Experiments Performed by Dasa

Propellants:	GH2/LOX
Chamber pressure:	100 bar
Mixture ratio O/F:	5.0 ÷ 6.0
Heat flux reduction:	< 50 %

Cryogenic H_2-cooled segments currently in preparation

Goals of Using Thermo-Chemical Protection

- Reduce thermal heat load of wall structure ($T_{wall,copper}$ ↘ ⇨ Cu-liner O_2-blanching ↘)
- Reduce liner material erosion and porosity (surface roughness ↘ ⇨ q_{wall} & $T_{wall,copper}$)
- Reduce liner overall degradation process (liner life-time ↗)

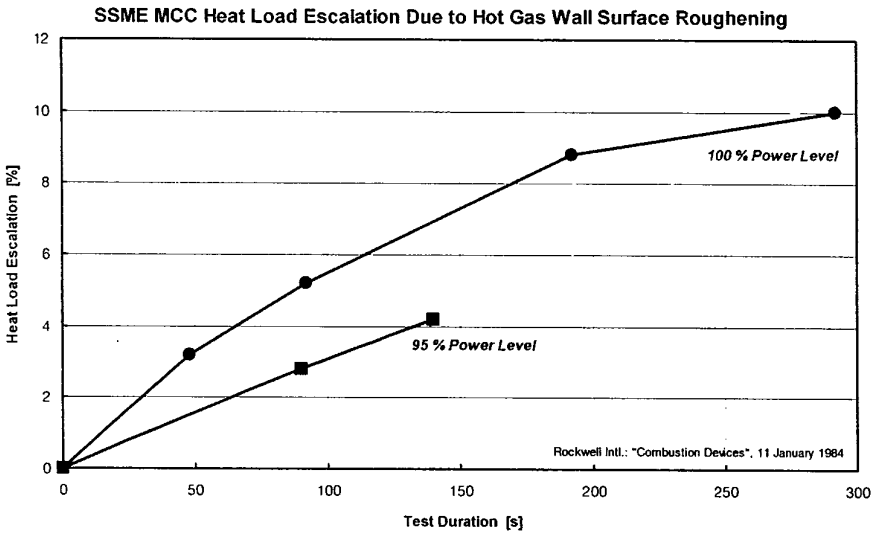
This document is the property of DaimlerChrysler Aerospace and is not to be disclosed or reproduced without prior written consent.

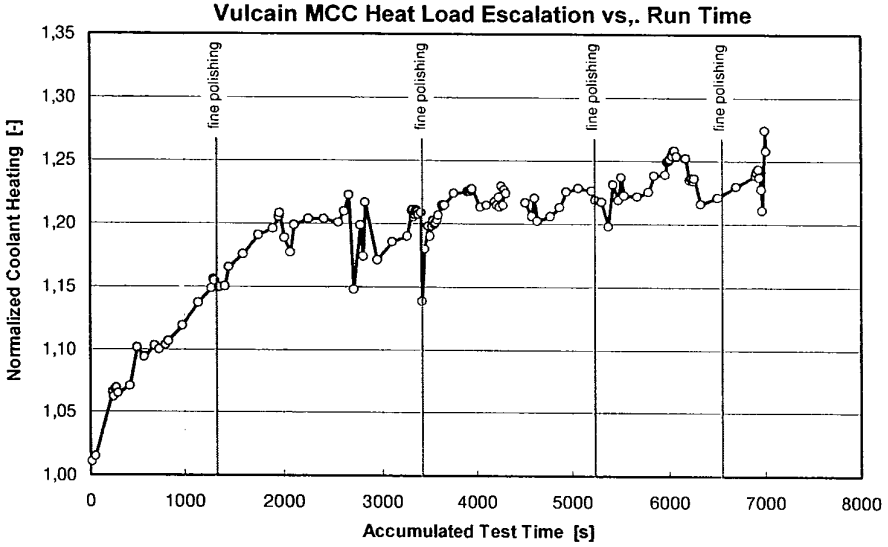
Increased Heat Flux to Coolant For Expander Chambers

- Increased heat transfer surface area:
  - Fins or ribs on chamber wall.
  - Tubular liner structure
- Increased surface roughness:
  - Occurs by itself during runtime, observed limit at ~25% heat transfer increase.
  - May be introduced by special geometrical designs or from manufacturing.
- Reduced injection element-to-wall distance:
  - May enhance liner degradation.

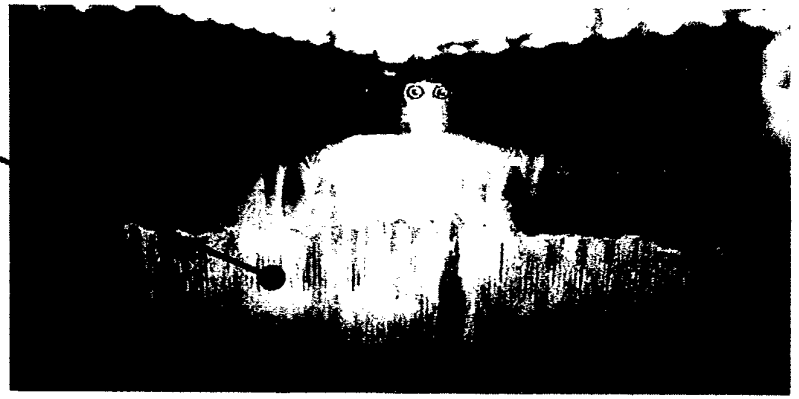
This document is the property of DaimlerChrysler Aerospace and is not to be disclosed or reproduced without prior written consent.

Hot Gas Wall Heat Transfer Increase Due to Surface Roughening



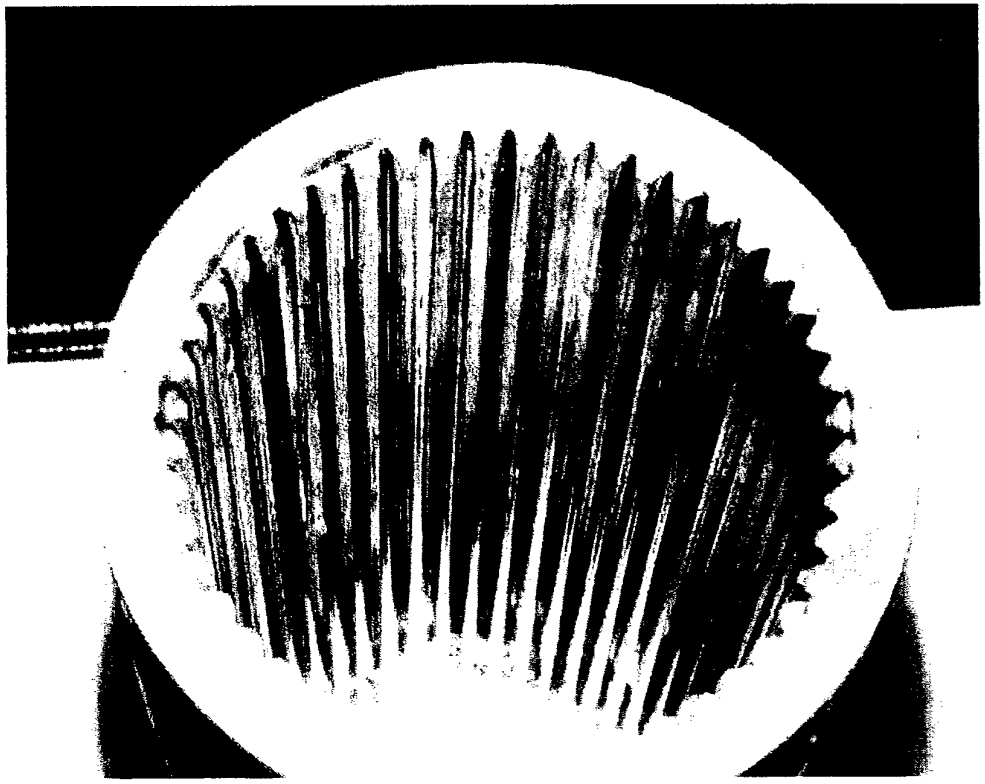


- Surface roughness increases with chamber run-time.
- Polishing can temporarily diminish the roughening effect.
- Coolant heating escalation seems to stabilize at approximately 125 % of initial value.



This document is the property of DaimlerChrysler Aerospace and is not to be disclosed or reproduced without prior written consent.

Hot Gas Wall Heat Transfer Enhancement Using Ribbed Surface Contour

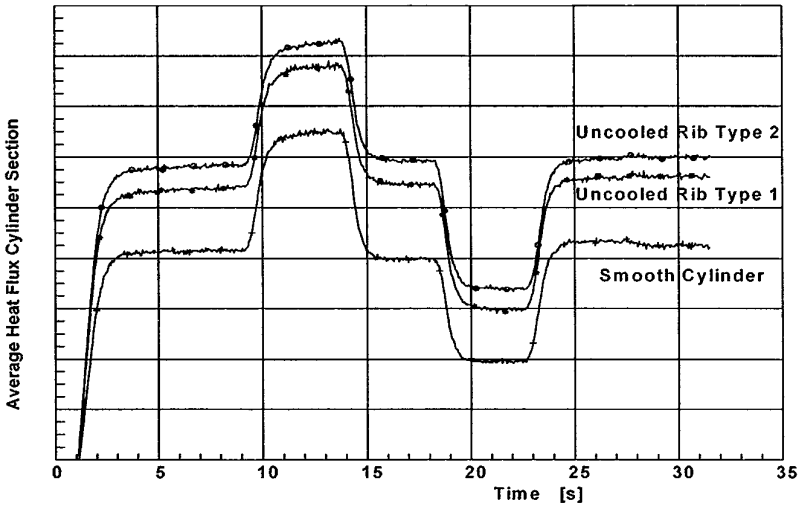


Water-cooled, ribbed barrel segment (length: 240 mm)

6 different configurations tested

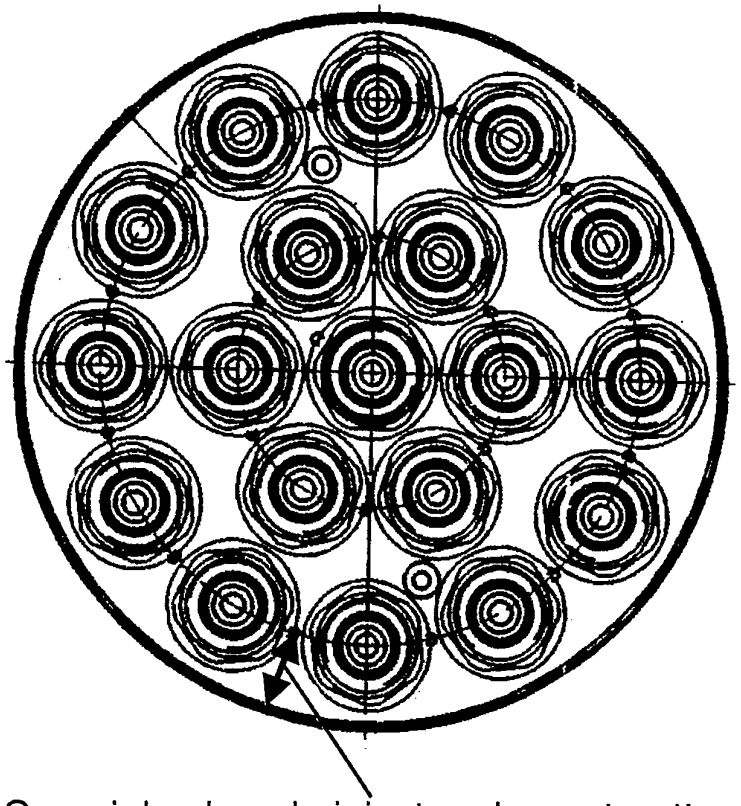
Experiments Performed by Dasa

Propellants:	GH2/GO2
Chamber pressure:	40 bar
Mixture ratio O/F	5.0 ÷ 7.0
Accumulated life time for a single specimen	>300 s
Heat flux enhancement:	15 ÷ 30%



This document is the property of DaimlerChrysler Aerospace and is not to be disclosed or reproduced without prior written consent.

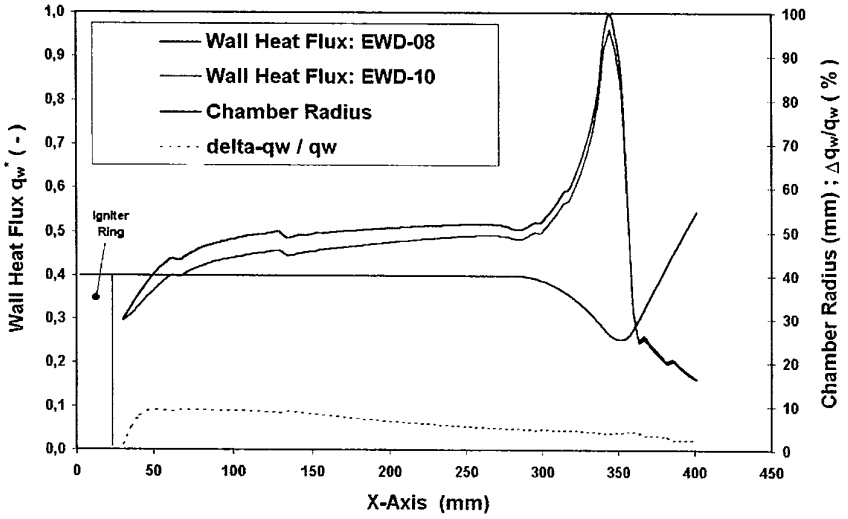
Hot Gas Wall Heat Transfer Enhancement with Reduced Injection Element-To-Wall Distance



Co-axial subscale injector element pattern with element-to-wall distance (EWD)

Experiments Performed by Dasa

Propellants:	GH2/LOX
Chamber pressure:	35 ÷ 70 bar
Mixture ratio O/F	5.0 ÷ 7.0
Heat flux reduction: **(EWD-08 ⇨ EWD-10)**	< 10 %



This document is the property of DaimlerChrysler Aerospace and is not to be disclosed or reproduced without prior written consent.

Summary and Conclusions

- Current engines in operation typically use one or several of the presented techniques to achieve the required thrust chamber reliability and lifetime.
- Film-cooling and/or O/F-biasing are most widely used around the world (*SSME, VULCAIN 2, RD-0120, etc.*).
- Transpiration cooling has not yet been realized on a operational engine up to now (complex, no low-cost technique), but may become of specific interest in the context of new liner materials (*Ceramics, Metal-Matrix-Composites*).
- Thermal barrier coating needs to be further developed (*ultra-thin layers*) in order to demonstrate sufficient reliability for re-usable propulsion systems.
- Surface contouring (*ribs*) is a very promising technique for advanced expander cycle concepts, but has not yet reached the required technology readiness level.
- Effective heat transfer management in thrust chambers remains a central design task and mandatory for any future expendable or re-usable rocket engine.

This document is the property of DaimlerChrysler Aerospace and is not to be disclosed or reproduced without prior written consent.

Impact of Intentional and Unintentional Combustion Chamber Porosity on Rocket Engine Characteristics

J. Görgen, O. Knab[‡], D. Haeseler[‡], D. Wennerberg[¶]

DaimlerChrysler Aerospace AG
Space Infrastructure, Engineering Engine Components, RIA54
PO Box 801168, 81663 Munich, Germany

Abstract

The CryoROC (**Cryo**genic **RO**cket **C**ombustion) software, a sophisticated multi-phase Navier-Stokes code developed by DaimlerChrysler Aerospace AG (Dasa) is used to analyze complex flows in combustion chambers and nozzles of cryogenic hydrogen/oxygen rocket engines. The paper focuses on the impact of intentional and unintentional combustion chamber porosity on engine characteristics. Numerical simulations of engines with porous walls are presented with special regard to heat flux development on one hand and performance losses on the other hand. They reveal the capability of the CryoROC tool to support the design and optimization process of engines using advanced porous wall concepts like transpiration cooling. They also prove the capability to estimate the impact of unintentional porosity as, for example, cracks in the chamber wall on the engine characteristics. Available test data such as chamber pressures, heat flux distributions as well as engine performance data like thrust and specific impulse are used to evaluate the CryoROC results. Experimental investigations of the transpiration cooling concept were conducted on subscale level in the frame of a German-Russian cooperation for future thrust chambers. The tests have been performed on a test bench at the Russian industrial company *Chemical Automatics Design Bureau* (CADB) in Voronezh. For the assessment of CryoROC crack simulations, the test campaigns of the Ariane 5 Vulcain engine are used.

1 Introduction

Cryogenic hydrogen/oxygen launcher propulsion systems are important business fields of the Propulsion & Transportation Systems Division of DaimlerChrysler Aerospace AG (Dasa). Products representing Dasa's experience in this field are the thrust chambers of the Vulcain and HM-7 engine systems, developed, manufactured and tested for the European Space Agency (ESA). VINCI, the future cryogenic upper stage engine of Ariane 5, is currently under development. Nevertheless, with increasing commercialization and hence increasing need for cost-optimized development and design, the space transportation and propulsion industry is forced to open up for new technologies and concepts. One of these concepts currently under discussion is the realization of reusable spacecrafts. Large development programs are started both in the U.S. (e.g. X-33) and Europe (e.g. Phönix) with the aim to demonstrate the feasibility of such a vehicle. Due to the design for reentry, those reusable vehicles possess a larger inert mass in comparison to common expendable launchers in use today. This drawback has to be balanced in order to realize payload mass fractions similar to present launchers. Thus, general accordance exists upon the need for future rocket engines with long lifetime (for reusability) and high performance that actually means very high chamber pressures and nozzle area ratios. Novel technologies will be required in order to achieve these targets, especially for the engine components combustion chamber and expansion nozzle [1].

One of the main problem areas for thrust chambers is the extreme heat flux due to the envisaged high chamber pressure. The near-throat region is supposed to be the thermally highest loaded section of the combustion chamber which can't be handled any longer by customary regenerative cooling systems, unless very high coolant pressure drops are accepted. Therefore, alternative concepts are demanded. Among these, one promising concept is transpiration cooling with gaseous hydrogen [2].

Increasing competition has forced rocket propulsion industry to reduce trial and error approaches associated with expensive experimental testing programs and to search more resource effective ways in developing new propulsion systems. In this context Dasa has recognized the application of computational fluid dynamics (CFD) as unique possibility to reduce development costs.

[‡] Member AIAA

[¶] Dasa Consultant

Copyright ©2000 by Dasa. Published by the American Institute of Aeronautics and Astronautics, Inc., with permission.

While nowadays the employment of numerical methods to predict rocket engine performance is state-of-the-art, their use to determine heat loads in thrust chambers is still at the beginning. The reason is that for heat fluxes steep gradients have to be resolved which especially in combustion chambers depend on the complex interaction of multiple physical phenomena such as turbulence and spray combustion.

In recent years Dasa has therefore developed the Navier-Stokes code CryoROC (**Cryo**genic **RO**cket **C**ombustion), which is a derivative of the ROCFLAM (**R**Ocket **C**ombustion **F**low **A**nalysis **M**odule) code family [3,4]. This tool comprises state-of-the-art models of many physical disciplines such as aerothermodynamics, multi-phase flows, turbulence and multi-species chemistry. The objective is not to resolve each single subprocess occurring in thrust chambers in too far-reaching detail but to reflect the global operational behavior of cryogenic rocket motors. Balancing model accuracy and computational effort, the major assignment of this sophisticated engineering tool is to provide heat flux distributions along regeneratively cooled combustion chamber walls allowing for multi-phase effects.

Test data obtained by means of Dasa's calorimeter model combustor [5] has been used to anchor and adapt CryoROC simulations to experimental results. The main objective of that subscale chamber is to characterize the heat transfer behavior of various co-axial injection element configurations under different operational conditions. Injector and combustor design are chosen in such a way that crucial parameters, such as contraction ratio, element to wall distance and element loading, are representative also for envisaged fullscale chamber layouts. By recomputing diverse of these test campaigns, the CryoROC code has been validated comprehensively. The capability of the tool to reproduce also fullscale conditions accurately has been verified by HM-7, Vulcain and Vulcain 2 engine simulations.

Lately, an extended version enabled the CryoROC code to simulate quantitatively mass flow injected through the chamber wall boundaries. This means that the code now provides the analysis of heat flux distributions and performance losses in combustion chambers

- with porous walls (transpiration cooled chamber walls)
- with small cracks which will lead to a leakage of hydrogen into the chamber

This paper presents and discusses first applications of the CryoROC software to rocket engines characterized by porous walls. The objective is to demonstrate the potential of the tool to evaluate the impact of intentional thrust chamber porosity such as transpiration cooling technology as well as unintentional chamber cracks on the engine characteristics.

2 CryoROC Features

Thrust chamber flows of cryogenic hydrogen/oxygen rocket engines are characterized by the coexistence and complex interaction of various physical phases. A reactive multi-species gas mixture (1st phase), together with a dispersed oxygen droplet phase (2nd phase) have to be resolved efficiently. CryoROC treats the gaseous phase by solving the Favre-averaged Navier-Stokes equations extended by the species continuity and k-ε turbulence equations. The latter include appropriate modifications accounting for compressibility effects and handle the near wall region optionally by a logarithmic wall function approximation or by a two-layer approach. The set of equations is discretized according the finite-volume methodology for non-orthogonal, boundary fitted grids and solved by an implicit algorithm. Hereby, both central and upwind differencing schemes are applied. The reaction mechanism of cryogenic hydrogen/oxygen systems is represented by 5 species (H_2, O_2, H_2O, H and OH). Up to now, a single-step, global reaction scheme is employed ($H_2 + xO_2 \Rightarrow aH_2O + bH + cOH$) basing on a turbulence (EDC) and/or kinetically (Arrhenius) controlled combustion model

In addition to solving transport equations for the continuous gas phase, CryoROC allows to simulate multiple discrete phases in a Lagrangian frame of reference. These second phases consist of spherical particles representing propellant droplets of different sizes being dispersed in the continuous gaseous phase. CryoROC computes the trajectories of these discrete phase entities by integrating their force balance. In particular for LH_2/LOX systems, CryoROC allows for transient LOX heat-up, supercritical LOX gasification, as well as droplet-to-gas phase turbulent interaction.

The latest feature incorporated in CryoROC includes the capability to simulate an additional mass flux coming into the combustion chamber through the chamber wall at various positions. On the boundary, the injected amount of mass as well as the injection velocity and thermodynamic properties of the injected media can be prescribed. In this way, CryoROC enables to consider multiple cracks and porous walls and analyze their impact on engine characteristics like heat flux distribution and global performance.

Table 1: Technical specification of the CryoROC (**Cryo**genic **RO**cket **C**ombustion) code

Capabilities

- compressible - sub-, trans- and supersonic
- turbulence models
  - standard k - ε with wall functions
  - 2 layer model
  - compressibility effects
- multi-gaseous species consideration (H_2, O_2, H_2O, H, OH, N_2, CO_2, CO, ...etc.)
- chemical reaction models
  - turbulence controlled (Eddy Dissipation Concept)
  - kinetically controlled (Arrhenius)
  - multi-step global reaction schemes
    - * hydrogen/oxygen
- Lagrangian particle tracking (Stochastic Separated Flow model)
  - multi-class, bi-propellant, discrete particle injection and sequential tracing approach
  - mass, momentum and heat coupling with gas phase
  - supercritical LOX gasification model

Capabilities (cont.)

- viscous heating, species diffusion
- standard Jannaf property data base for gaseous combustion species (Gordon&McBride)
- porous walls and crack simulation
- coupling with Dasa's RCFS (**R**egenerative **C**oolant **F**low **S**imulation) code

Numerics

- 2D, axisymmetric, finite volume
- Favre-averaged
- SIMPLE algorithm (pressure correction)
- implicit Stone solver

Grid

- structured
- non-orthogonal
- curvilinear

Gaseous and dispersed phase calculations are coupled in a loosely manner, i.e. source terms in the respective governing equations are not updated simultaneously. As a thumb rule, oxygen droplet tracking is performed every 70 to 200 gas phase iterations. Table 1 gives a survey on the most important modeling features of the CryoROC software. For a more detailed description of the models the reader is referred to [3,4,5].

3 Intentional Chamber Porosity: the Transpiration Cooling Concept

In order to avoid high wall temperatures and heat transfer rates in the combustion chamber, which both run down the engine's life-time, transpiration cooling is regarded to be one of the more promising cooling concepts. Hereby, the combustion chamber walls are cooled by gaseous hydrogen coming into the chamber through a porous wall.

Since 1994 Dasa cooperates on the common development of technologies for advanced thrust chambers with the Russian industrial company *Chemical Automatics Design Bureau* (CADB) in Voronezh, who developed the SSME-like cryogenic engine RD-0120 for the Energia launcher [6]. Theoretical and experimental work on transpiration cooling have been realized in the frame of the TEHORA project in the years 1995-98. The corresponding tests have been performed on a test bench at CADB in Voronezh, Russia. This cooperation has been supported by the two national space agencies RKA in Russia and DLR (former DARA) in Germany. Notice that the transpiration cooling technology was developed and demonstrated on subscale level only.

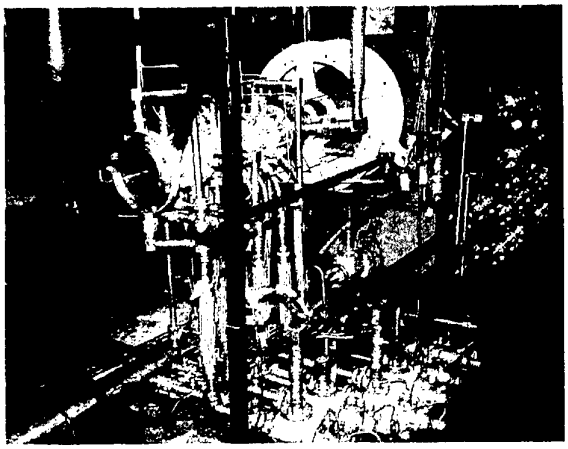


Figure 1: Subscale chamber on the CADB test bench in Voronezh

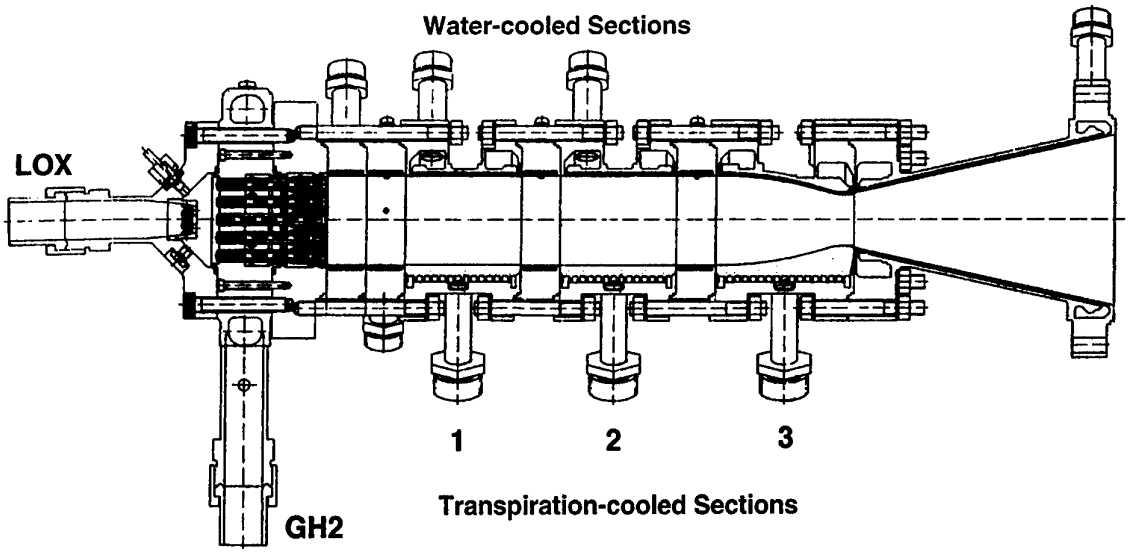


Figure 2: Subscale chamber schematic: Water cooled configuration (upper half) and positions of the transpiration cooled sections (lower half)

Fig.1 shows the subscale chamber on the test bench in Russia using a Dasa injection head. The chamber is mounted fixed to a thrust frame. The nozzle exit is fixed to the test bench only vertically allowing for horizontal movements for thrust measurements. Many flexible connections are used to feed the water cooling of the various sections. The hydrogen supply for the chamber is visible to the right of the injection head. A schematic of the subscale chamber is given in Fig.2.

Based upon former results of material characterization and the performance predictions of selected material and design concepts, the addressed transpiration cooling concept was tested under realistic conditions at 100 bar chamber pressure using gaseous hydrogen and liquid oxygen with a mixture ratio of around 6 as propellants [2].

The CryoROC capability to give accurate prediction of the wall heat flux distribution in regenerative cooled engines has already been demonstrated [5]. In the present paper, available subscale and fullscale test data are used to validate the code's extension towards porous walls. Notice that CryoROC is an efficient engineering tool balancing computational effort and accuracy. Grid resolutions have therefore been chosen following previous experience. Convergence has been achieved by a residual drop of three orders of magnitude.

The subsequent discussion starts with a basic investigation made for the thrust chamber without transpiration cooling (test 2) which is used as the reference case for both measurements and numerical calculations. Then, following tests are analyzed which were conducted with one transpiration cooled insert at position 2 (see Figure 2). Two different transpiration flow rates are taken into account: $\dot{m}_{Trs}$=0.128 kg/s (test 8) and $\dot{m}_{Trs}$=0.080 kg/s (test 11). The transpiration flow rate in Test 8 corresponds to 10.5% of the total hydrogen flow rate whereas that of Test 11 to 7.0%.

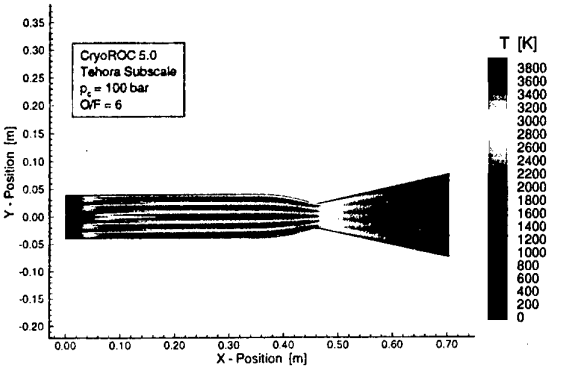


Figure 3: Reference case (test 2), temperature contours

Figure 3 shows the computed temperature contours determined for the reference case. It gives a good impression of the temperature stratification resulting from the propellant spray injection and evaporation. Figure 4 shows the heat flux evolution for these three cases. As it is clearly to see the test with higher transpiration flow rate (test 8) leads to the highest reduction of the wall heat flux behind the transpiration cooled area. In the throat section, the maximum heat fluxes could be reduced about 22% and 18% respectively.

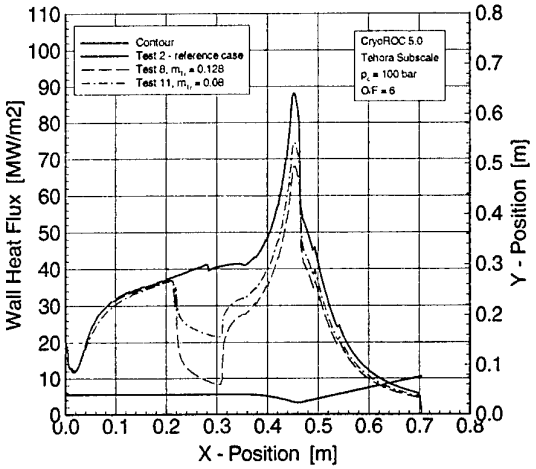


Figure 4: Computed wall heat fluxes for the tests 2, 8 and 11

Unlike to real fullscale engines, where the hydrogen, used as transpiration medium, is missing in the injector head, here the injector conditions are not influenced by the transpiration cooling process. Therefore, the heat flux distributions upstream the transpiration cooled section is nearly identical for all three cases (if the hydrogen were tapped off the injector head, the resulting mixture ratio increase would actually lead to an increase in the wall heat flux distribution.).

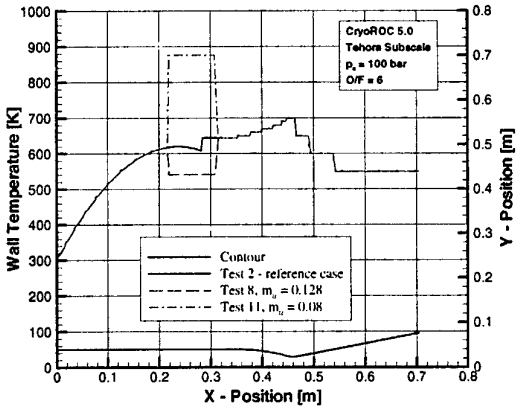


Figure 5: Prescribed temperature distributions along the wall for the three test cases 2, 8 and 11

The corresponding wall temperatures are depicted in Figure 5. These hot gas wall temperatures along the regenerative cooled part of the combustion chamber have been determined by Dasa's RCFS (Regenerative Coolant Flow Simulation) code [7] and then prescribed as boundary condition in the CryoROC simulations. As it is apparent from Figure 5, these prescribed wall temperatures differ only in the transpiration cooled insert due to the different hydrogen infiltration conditions. The other parts adopt it from the reference case. Thus, the influence of the developing hydrogen film on the wall temperature evolution downstream of the transpiration cooled insert has not been taken into account.

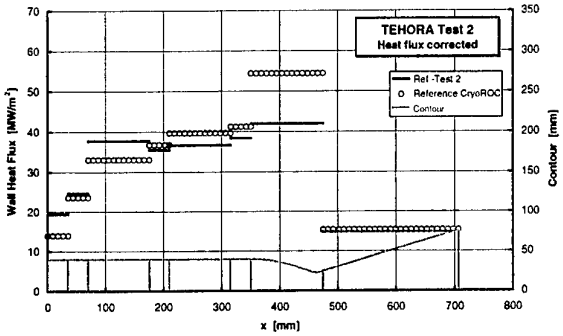


Figure 6: Reference wall heat flux distributions (Test 2) – CryoROC simulation and measurement

A comparison with the measurement data for the reference case is given in Figure 6. To be compliant with the experiment, the heat fluxes are averaged for short cylinder sections, shown at the contour plot in Figure 6. Fairly good agreement is obvious along the cylindrical and supersonic part of the combustion chamber. Somewhat questionable seems to be the relatively low heat load measured in the throat section. Dasa's subscale experience gained with a calorimetric nozzle part revealed heat flux maxima in the throat which are about a factor of two higher than the heat flux at the end of the cylindrical part of the combustor (see Figure 4). The reader may notice that the measurement data are corrected due to distinct gaps at the interface between two adjacent sections, which cause disturbances of the hot gas boundary layer and which could not be considered in the simulations. Figure 7 depicts measurement values and numerical predictions for the wall heat fluxes of test 8.

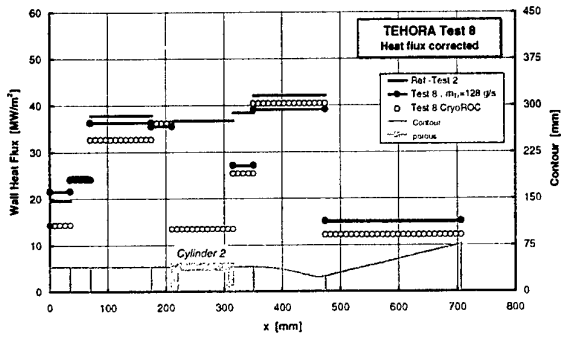


Figure 7: Wall heat flux distribution for Test 8 – CryoROC simulation and measurement

One can recognize that there is an excellent agreement for the heat flux drop behind the transpiration cooled area. Moreover, here the computed and measured head loads of the throat section almost coincide.

Figure 8 shows the mixture ratio profiles shortly downstream of the transpiration cooled insert, at x = 358.9 mm. Apparently, there isn't much a difference in the stratified core flow, but near the wall exists a distinct drop for the two test cases with transpiration cooling (about 50%). This comes, of course, from the higher hydrogen concentration in this area.

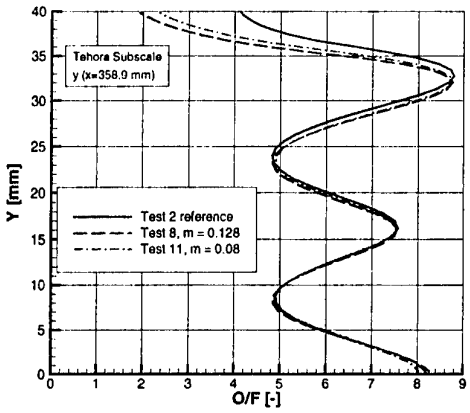


Figure 8: Mixture ratio (O/F) downstream the transpiration cooled insert at x = 358.9 mm

Finally , the Figures 9 and 10 presents the performance losses for the entire test campaign in dependance of increasing hydrogen leakage, related to the reference case without transpiration cooling.

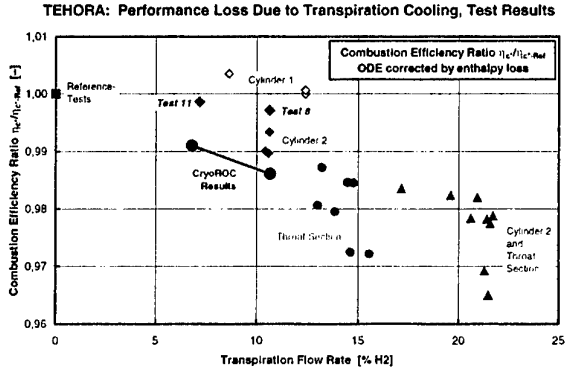


Figure 9: Reduction of combustion chamber efficiency (characteristic velocity) in dependence of increasing H_2 leakage

As can be seen are the CryoROC predictions in good agreement with the measured data. Additionally, there is a hint in both measurements and numerical simulation, that the losses in the characteristic velocity (Figure 9) are higher than the global engine performance losses like thrust and specific impulse (Figure 10). This characteristic behavior will be observed even more clearly in case of unintentional porosity (cracks). An explanation will be given in the next section.

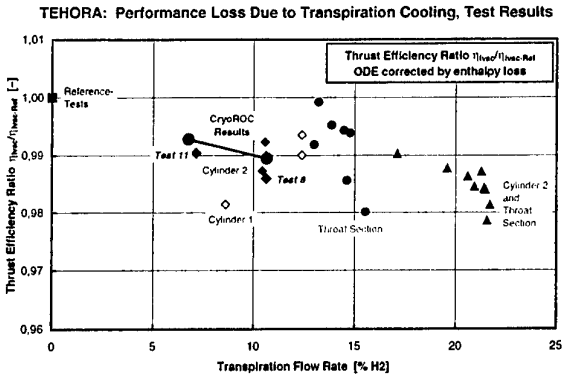


Figure 10: Reduction of thrust chamber efficiency (specific impulse) in dependence of increasing H_2 leakage

4 Unintentional Porosity: Cracks

Extensive testing of the Vulcain engine revealed, that small cracks may develop in the combustion chamber. This will lead to a leakage of hydrogen into the combustion chamber at a position downstream of the injection plate due to the regenerative hydrogen cooling along the combustion chamber wall. In order to investigate quantitatively the consequences of such cracks, representative leakage inflow conditions were modeled and numerically analyzed with the CryoROC code. Since the pressure outside the combustion chamber, i.e. in the cooling channels, is always higher than the pressure on the hot gas side of the wall, an infiltration of the cooling media into the chamber occurs.

The development of (up to several hundred) cracks in the combustion chamber will lead to three-dimensional flow. Since the CryoROC code can be applied only to 2D axisymmetric geometries, the assumed crack area has been modeled as a circumferential slot with an

	Δx_{Crack} [mm]	m_{inj} [kg/s]	$\approx n_{Cracks}$
1	-	-	0
2	**0.34**	**3.0**	**150**
3	**0.57**	**5.0**	**250**
4	**0.80**	**7.0**	**350**

Table 2: Specification of the different crack parameters for the four test cases

equivalent area and mass influx. In this way, the local conditions around the cracks will not be completely representative, but the effect of different crack sizes on the global performance parameters can still be estimated. The injected hydrogen flow at the injector plate is corrected by subtracting the inflow at the crack location. The consequences are higher mixture ratios in the vicinity of the injector head.

Four different test cases of the Vulcain engine at 100 bar were computed and compared: one without cracks as the reference case and three cases with increasing amount of infiltrated mass flow rate (see Table 2).

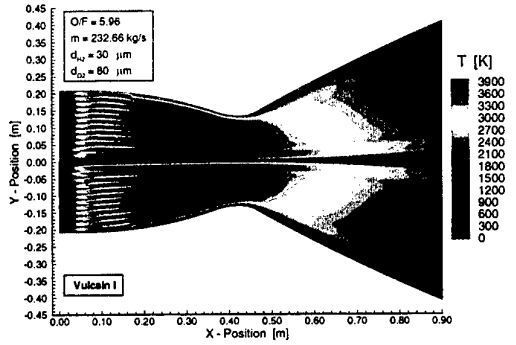


Figure 11: Temperature contours for the Vulcain combustion chamber

An overview of the temperature contours with the characteristic stratification due to Vulcain's 12 injector rows is given in Figure 11. As can be further seen, the crack position has been chosen to reflect the so-called wall impact point, where the propellant jet of the outer injector row hits the chamber contour and supports crack formation (x=0.17 m). Along the wall the cooling effect of the infiltrated hydrogen is clearly visible. As exspected, this amount of hydrogen does not burn any more but heat up and expand through the nozzle.

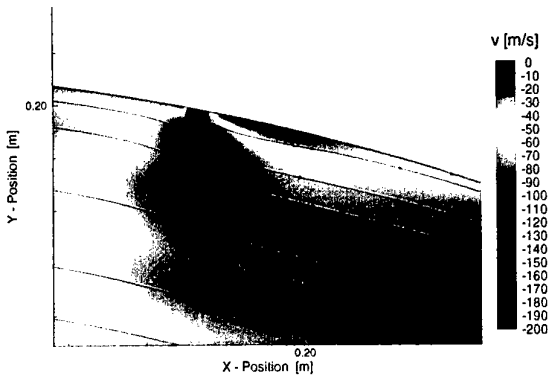


Figure 12: Flow field around the crack position: contours of radial velocity component

A more detailed zoom into the flow field with streamlines around the crack area is shown in Figure 12. One can clearly recognize the strong inflow impulse of the small crack slot.

In order to evaluate the influence of the crack width and mass inflow rate through the crack, the calculated global performance parameters are related to the first reference case without cracks. The Figures 13 and 14 reveal the reduction of the characteristic velocity (c^*/c^*_{ref}) and vacuum specific impulse ($I_{sp}/I_{sp,ref}$) in dependence of increasing hydrogen leakage. One can clearly recognize that the c* –losses differ distinctly from the performance losses. The reduction of the characteristic velocities (Fig.13), is much more relevant than the plain specific impulse losses (Fig.14).

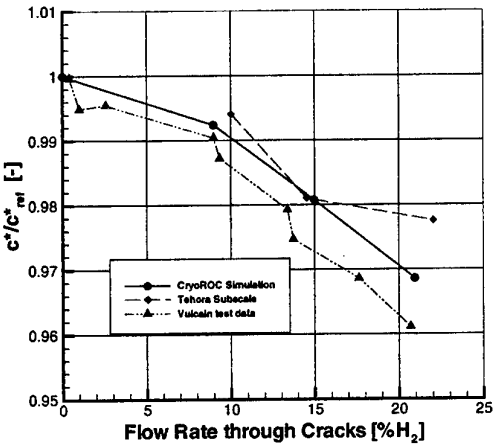


Figure 13: Reduction of characteristic velocity in dependence of increasing H_2 leakage

This is due to the fact, that the hydrogen coming through the cracks does not contribute to the combustion process, but nevertheless getting heated and thus contribute to the thrust development. In addition to the CryoROC results, the Figures 13 and 14 contain experimental data obtained from Vulcain engine test evaluations. Unfortunately, here thrust measurements are not available. For comparison, also test data from the previously discussed TEHORA campaign has been included. Those thrust measurements confirm the predicted CryoROC tendency of reduced specific impulse losses compared to more severe losses in the characteristic velocity. This is crucial for operating an engine with a certain amount of cracks. A fairly good agreement between computational and experimental results is visible, proving the CryoROC potential for such complex applications.

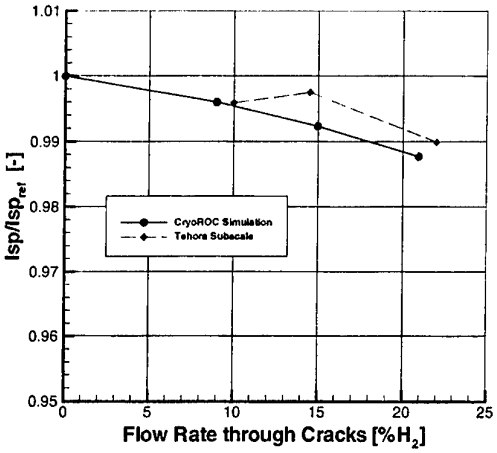


Figure 14: I_{sp} performance losses in dependence of increasing H_2 leakage

5 Summary and Conclusions

In this paper several CryoROC (**Cryo**genic **RO**cket Combustion) simulations have been introduced and discussed. Thereby, the objective was to show the code's capability to numerically analyze thrust chamber flows with porous walls.

Concluding this work the most important results obtained are summarized and assessed:

- the presented CryoROC analyses the wall heat flux distribution in a transpiration cooled thrust chamber on subscale level
- investigating different transpiration inflow rates, a comparison with available test data showed that the predicted reduction of the heat transfer downstream the transpiration cooled insert is in very good accordance with the measurements
- further simulations have been performed for a Vulcain fullscale thrust chamber considering cracks in the chamber wall
- the CryoROC calculations showed that there are distinct differences between the reduction of characteristic velocity and the global performance losses. The hydrogen coming through the cracks do not contribute to the combustion process, but nevertheless getting heated and thus contribute to the thrust development. As a consequence, the performance losses are much lower than the c* - losses

To sum up, this paper describes the first steps towards a numerical analysis of thrust chamber flows including porous walls. A comparison with available test data on both subscale and fullscale level proved the code's capability to resolve qualitatively the main physical flow phenomena. Also, the quantitative predictions of the wall heat flux development as well as performance losses in transpiration cooled thrust chambers or chambers with cracks are in good agreement with the measurement data.

Acknowledgements

The TEHORA project was performed in the frame of a German-Russian cooperation, funded by the German Aerospace Center (DLR) and the Russian Space Agency (RKA). The Vulcain test campaigns were performed within the Vulcain 2 evolution – Perfo 2000 project. For the supply of test data, the authors would like to thank Mr. Oechslein and Mrs. Lex.

References

[1] Popp, M., and Schmidt, G., Advanced Thrust Chambers, 5th AAAF International Symposium "Propulsion in Space Transportation", Paris, France, 22-24 May 1996, Paper 10.1.

[2] Haeseler, D., Mäding, C., Rubinskiy, V., Gorokhov, V., and Khrisanfov, S., Experimental Investigation of Transpiration Cooled Hydrogen-Oxygen Subscale Chambers, AIAA 98-3364, 1998.

[3] Preclik, D., Estublier, D., and Wennerberg, D., An Eulerian-Lagrangian Approach to Spray Combustion Modelling for Liquid Bi-Propellant Rocket Motors, AIAA 95-2779, 1995

[4] Knab, O., Fröhlich, A., and Wennerberg, D., Design Support for Advanced Storable Propellant Engines by ROCFLAM Analyses, AIAA 99-2459, 1999.

[5] Preclik, D., Wiedmann, D., Oechslein, W., and Kretschmer, J., Cryogenic Rocket Calorimeter Chamber Experiments and Heat Transfer simulations, AIAA 98-3440, 1998

[6] Rachuk, V.S., Goncharov, N.S.., Martynyenko, Y.A., Barinshtein, B.M., and Sciorelli, F.A., Design, Development and History of the Oxygen /Hydrogen Engine RD-0120, AIAA/ASME/SAE/ ASEE, 31st Joint Propulsion Conference, San Diego, Ca, 1995, AIAA-95-2540.

[7] Fröhlich, A., Popp, M., Schmidt, G., and Thelemann, D., Heat Transfer Characteristics of H_2/O_2 Combustion Chambers, AIAA 93-1826, 1993.

4. International Symposium on
Liquid Space Propulsion
Heilbronn, Germany, 13-15.3.2000

DaimlerChrysler Aerospace

Session 8: Progress on CFD and Health Monitoring

Impact of Intentional and Unintentional Combustion Chamber Porosity on Rocket Engine Characteristics

J. Görgen*, O. Knab*, D. Haeseler*, D. Wennerberg¶

* DaimlerChrysler Aerospace AG
Space Infrastructure
P.O. Box 80 11 68
81663 München
Germany

¶ Tecosim GmbH
- Dasa Consultant
Im Eichfeld 3
65428 Rüsselsheim
Germany

This document is the property of DaimlerChrysler Aerospace and is not to be disclosed or reproduced without prior consent

DaimlerChrysler Aerospace

Features of Dasa's Spray Combustion Codes

ROCFLAM

ROcket Combustion FLow Analysis Module

- turbulence (EDC) or kinetically (Arrhenius) controlled combustion model
  - hydrazine/NTO
  - MMH/NTO
- secondary droplet break-up
- annular film cooling model
- advanced droplet-to-wall / film interaction model
- heat conduction in solid walls
- multi-block

- finite volume method, 2d and axisymmetric, compressible, sub- and supersonic flows
- Favre-averaged Navier-Stokes solver (implicite Stone solver)
- k - ε turbulence model
  - 2 layer model
  - logarithmic wall function
  - compressibility effects
- multi-species global chemistry model (CH_4, NO_2, H_2O, N_2, H_2, OH, H, CO_2, CO, HCN)
- Lagrangian partical tracking (Stochastic Separated Flow model)
  - multi-class, bi-propellant, discrete particle injection and sequential tracking approach
  - mass, momentum and heat coupling with gas phase
- viscous heating, species diffusion
- standard Jannaf property data base

CryoROC

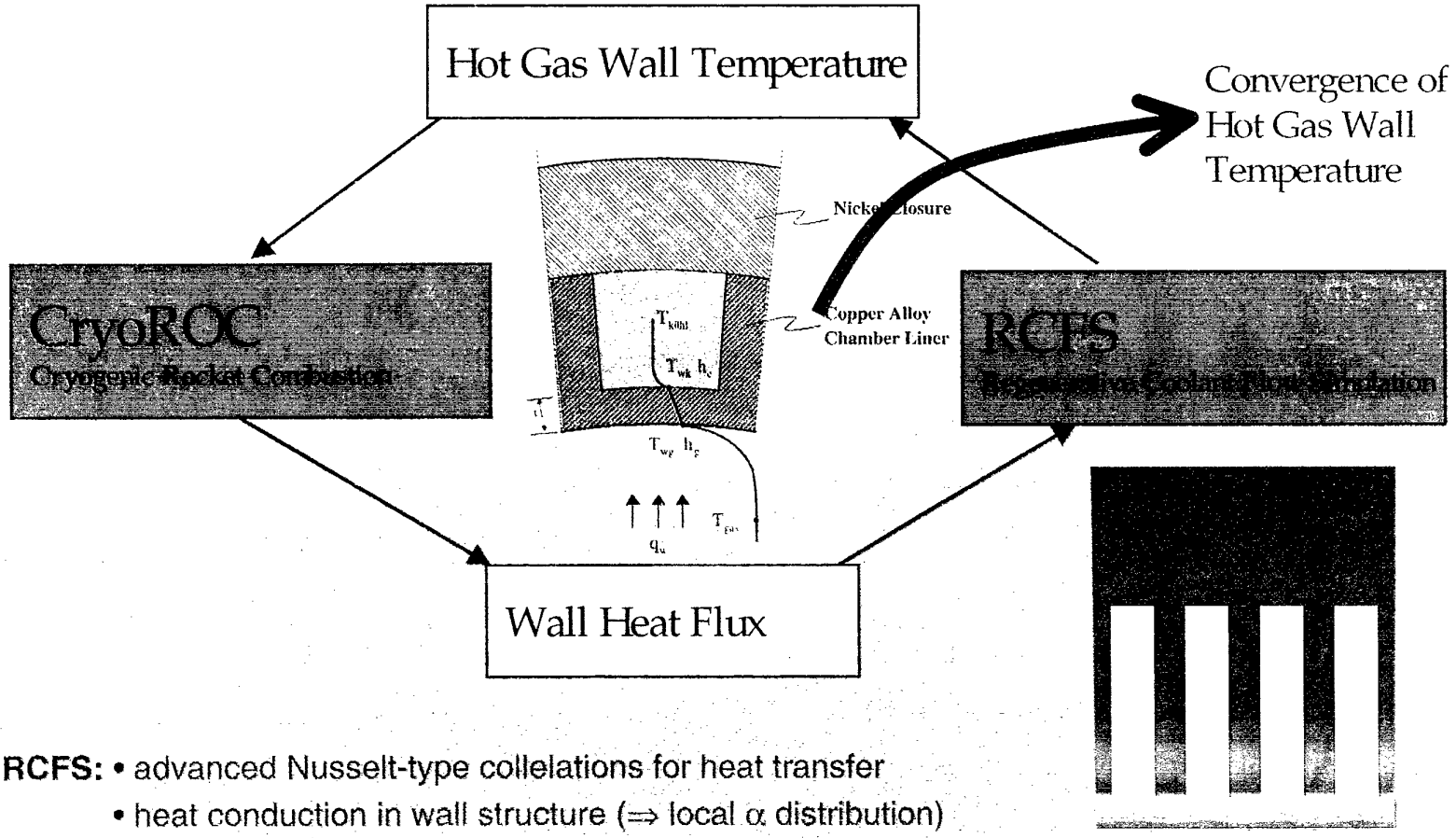
Cryogenic ROcket Combustion

- turbulence (EDC) or kinetically (Arrhenius) controlled combustion model, $H_2 + xO_2 \Rightarrow aH_2O + bH + cOH$
- supercritical LOX gasification model
- coupling with Dasa's RCFS code (Regenerative Coolant Flow Simulation)
- crack simulation

This document is the property of DaimlerChrysler Aerospace and is not to be disclosed or reproduced without prior consent

DaimlerChrysler Aerospace

CryoROC / RCFS Coupling Strategy

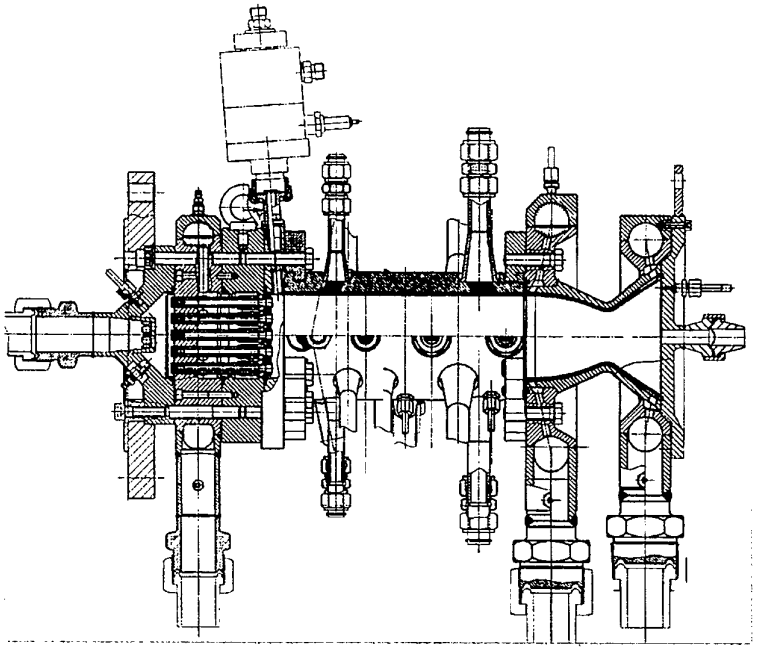


RCFS: • advanced Nusselt-type collelations for heat transfer
• heat conduction in wall structure (⇒ local α distribution)

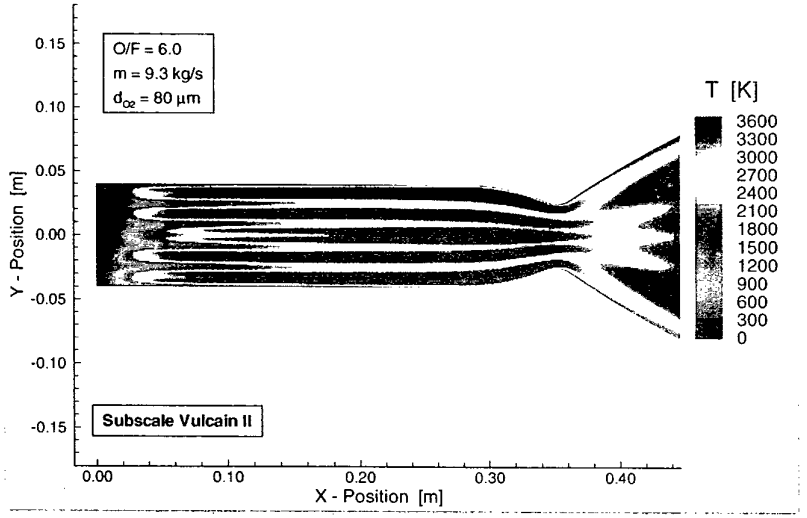
DaimlerChrysler Aerospace

CryoROC / RCFS Simulation: Vulcain 2 Subscale

p_c = 100 bar, O/F = 6.0



Schematic of Caloric Model Combustor

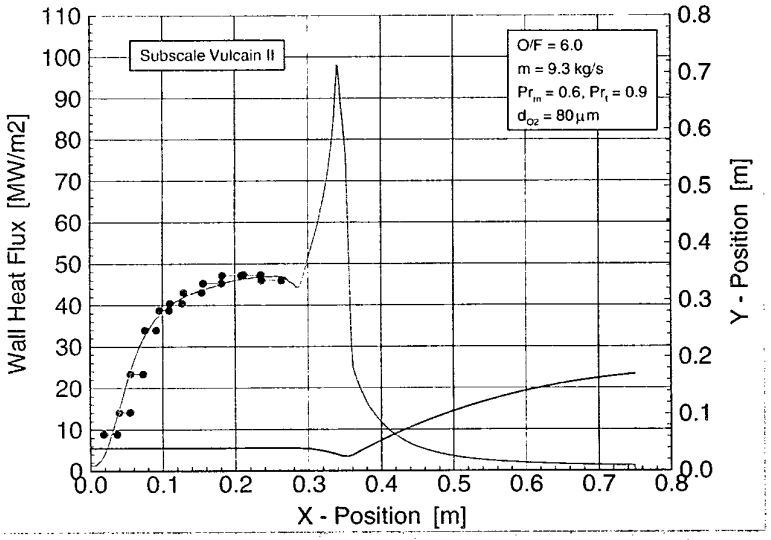


Temperature Contours

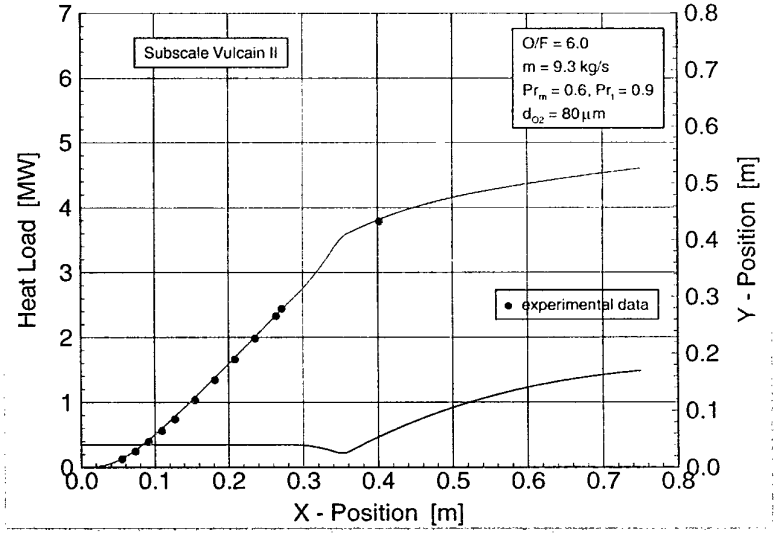
This document is the property of DaimlerChrysler Aerospace and is not to be disclosed or reproduced without prior consent

CryoROC / RCFS Simulation: Vulcain 2 Subscale

p_c = 100 bar, O/F = 6.0



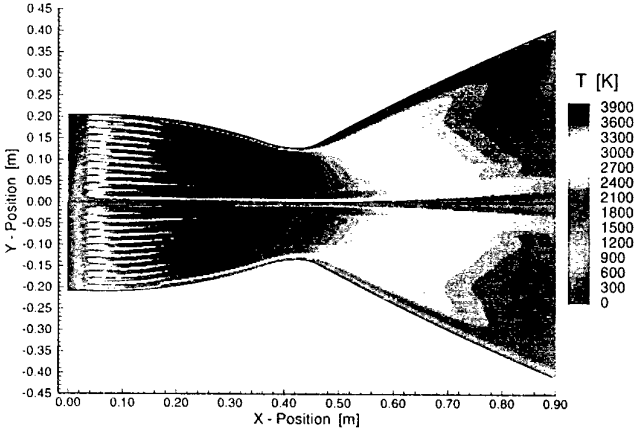
Wall Heat Flux Distribution

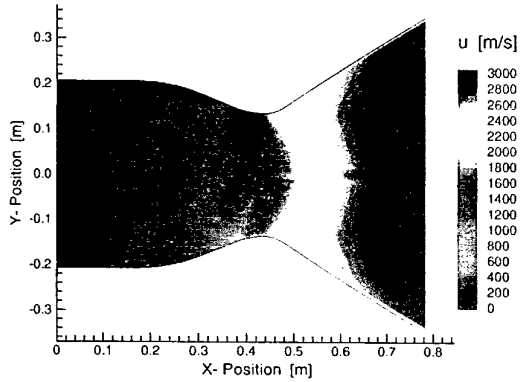


Heat Load

Selection of CryoROC Simulations

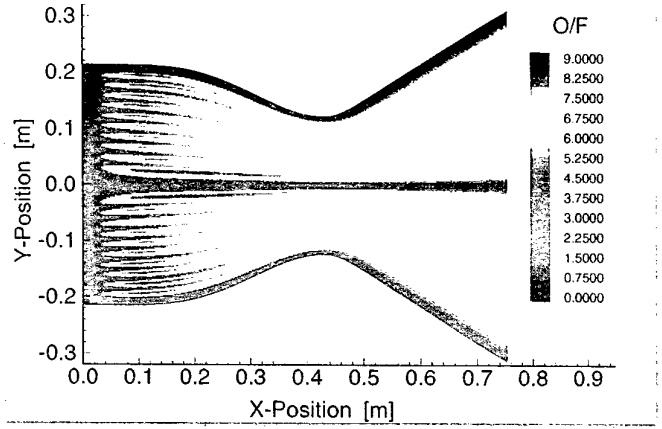
Vulcain
(100 bar)

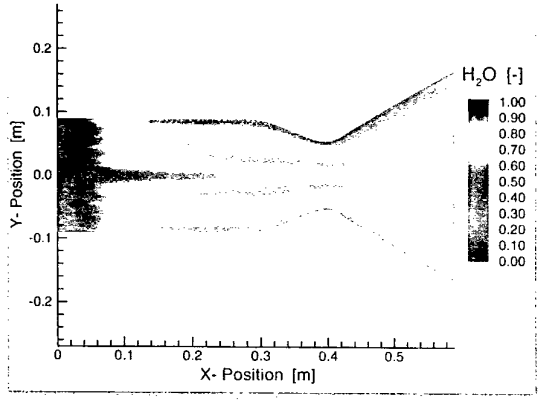




Vulcain 2
(116 bar)

RD-0120
(206 bar)





HM 7
(35 bar)

DaimlerChrysler Aerospace

Unintentional Chamber Cooling :

Cracks

- trickling of gaseous fuel through many small cracks in the wall

Combustion Chamber incl. porous walls

Combustion Chamber Cooling Concepts:

Regenerative cooling

- standard
- with established design for coolant channels
- upper limit for maximum heat load

Liquid film cooling

- development of a separating layer between hot combustion gas and wall

Transpiration cooling

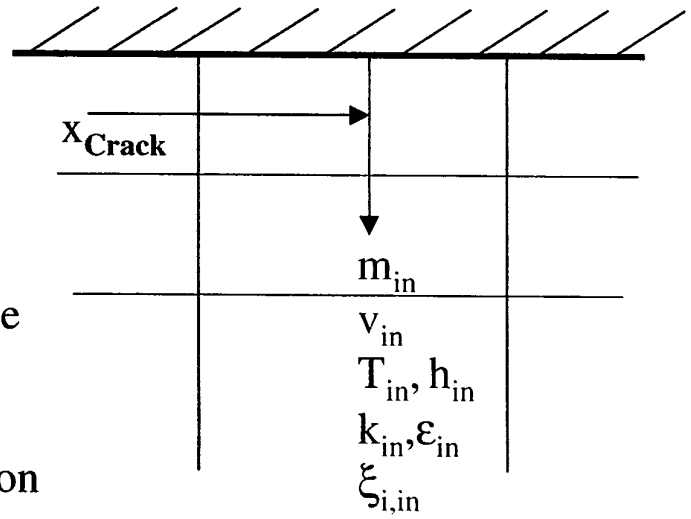
- trickling of gaseous fuel through a porous part of the wall

This document is the property of DaimlerChrysler Aerospace and is not to be disclosed or reproduced without prior consent

CryoROC 5.0: Modelling of Combustion Chamber Porosity

Numerical Implementation:

- Adaptation of source terms in the corresponding equations for mass, momentum and energy conservation



Boundary Conditions:

- Specification of the injected mass flow rate
- Specification of the injection velocities and the thermodynamic and transport data
- Specification of the turbulence
- Specification of the injected species distribution

⇒ Possible simulation of (locally appearing) intentional and unintentional combustion chamber porosity.

⇒ Investigation of the impact on global engine characteristics like thrust and specific impulse

This document is the property of DaimlerChrysler Aerospace and is not to be disclosed or reproduced without prior consent

DaimlerChrysler Aerospace

CryoROC 5.0 Computations - Transpiration cooled wall

Inflow Conditions:

$p_c \approx 100$ bar

O/F ≈ 6

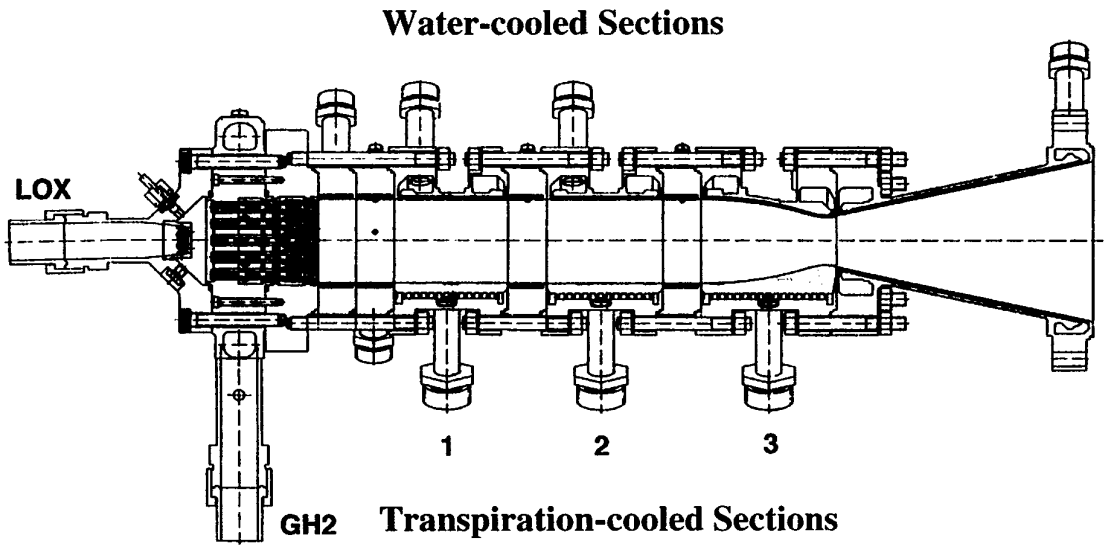
m_{inj} (O_2) ≈ 6.0 kg/s

m_{inj} (H_2) ≈ 1.07 kg/s

Transpiration Flow Rate:

Test 8: m_{tr} (H_2) = 0.128 kg/s

Test 11: m_{tr} (H_2) = 0.08 kg/s



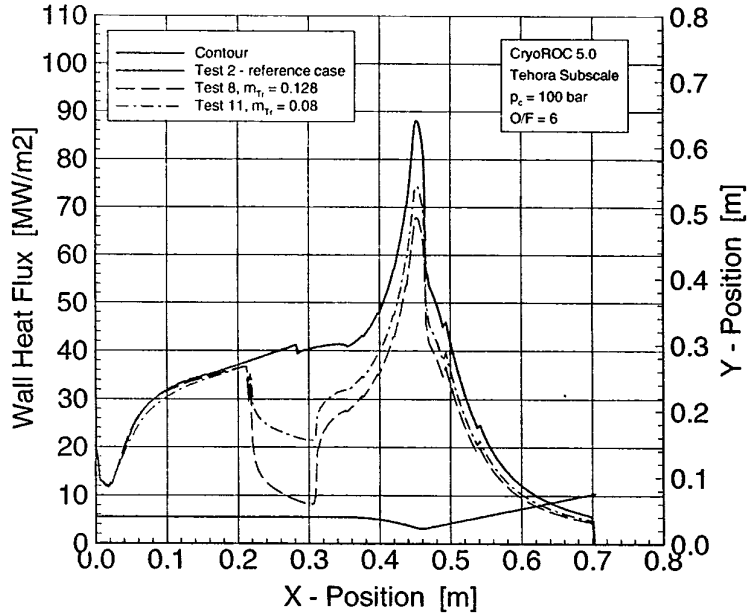
Sketch of the transpiration cooled TEHORA Subscale chamber

This document is the property of DaimlerChrysler Aerospace and is not to be disclosed or reproduced without prior consent

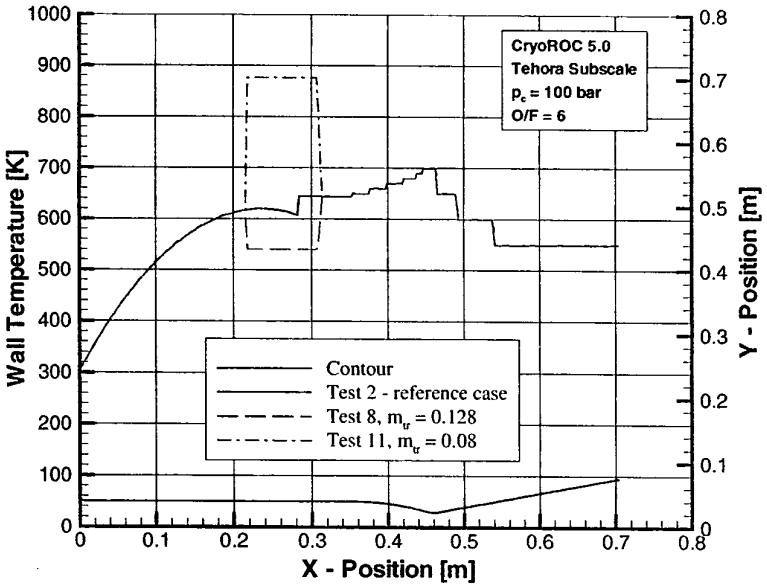
DaimlerChrysler Aerospace

CryoROC 5.0 Computation - Transpiration cooled wall

Different injection flow rates: 0.128 kg/s (Test 8), 0.08 kg/s (Test 11)



Heat Flux along the Wall



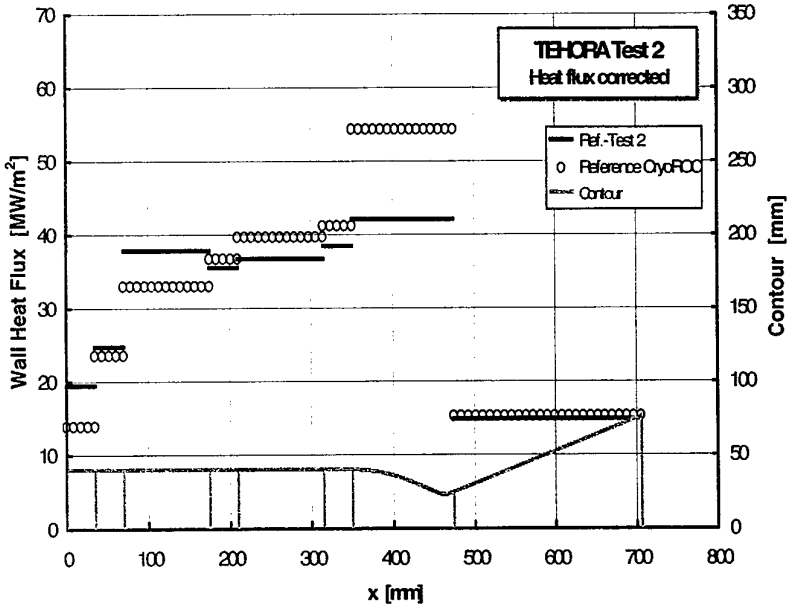
Corresponding Wall Temperatures

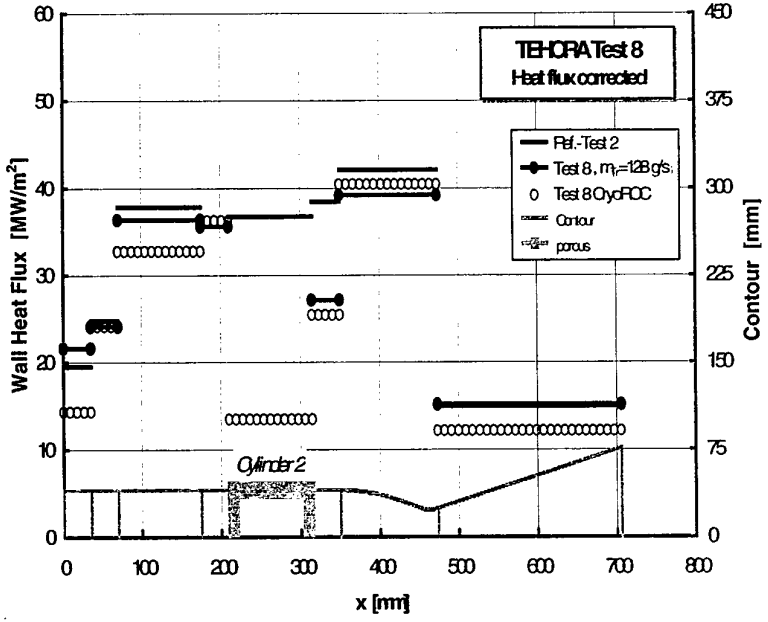
This document is the property of DaimlerChrysler Aerospace and is not to be disclosed or reproduced without prior consent

DaimlerChrysler Aerospace

CryoROC 5.0 Computation - Transpiration cooled wall

Tehora Subscale, p_c = 100 bar, O/F = 5.62





Averaged Wall Heat Flux (Test 2)

without transpiration cooling insert

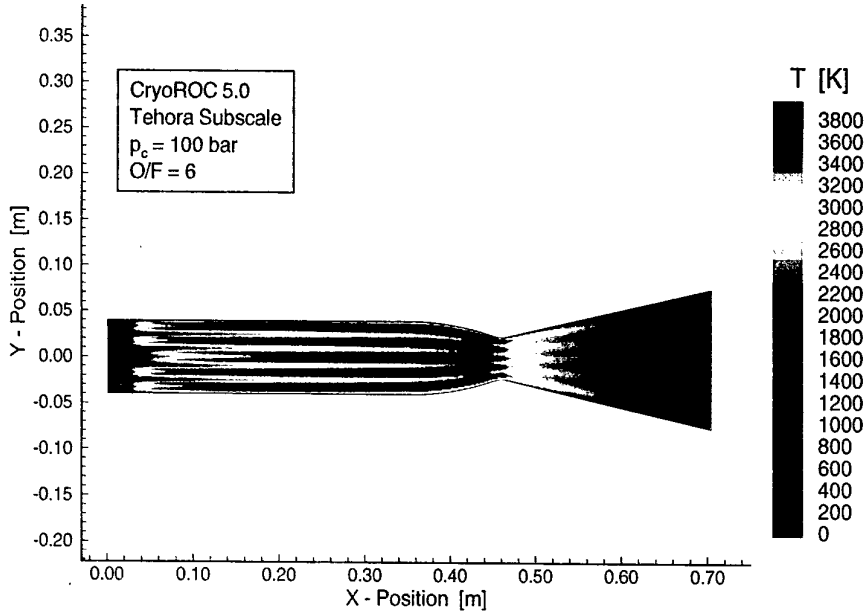
Averaged Wall Heat Flux (Test 8)

transpiration mass flow rate: 0.128 kg/s

DaimlerChrysler Aerospace

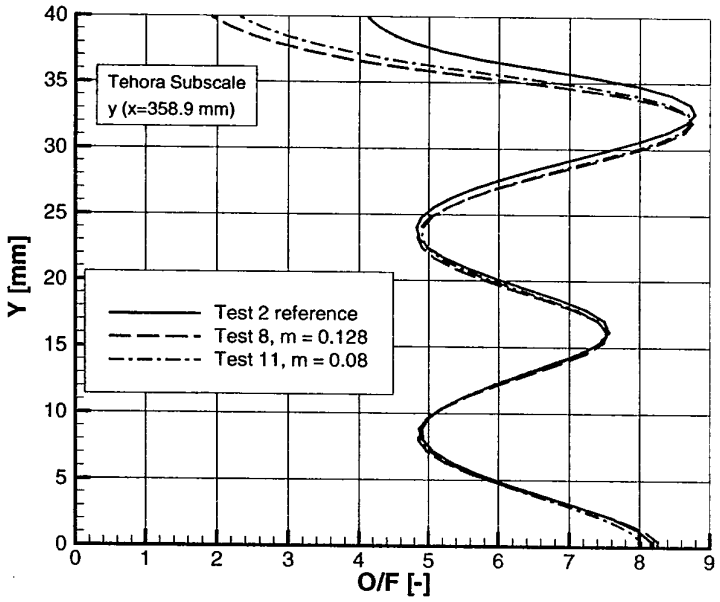
CryoROC 5.0 Computation - Transpiration cooled wall

Tehora Subscale, p_c = 100 bar, O/F = 5.62



Temperature Flow field

without transpiration cooling insert



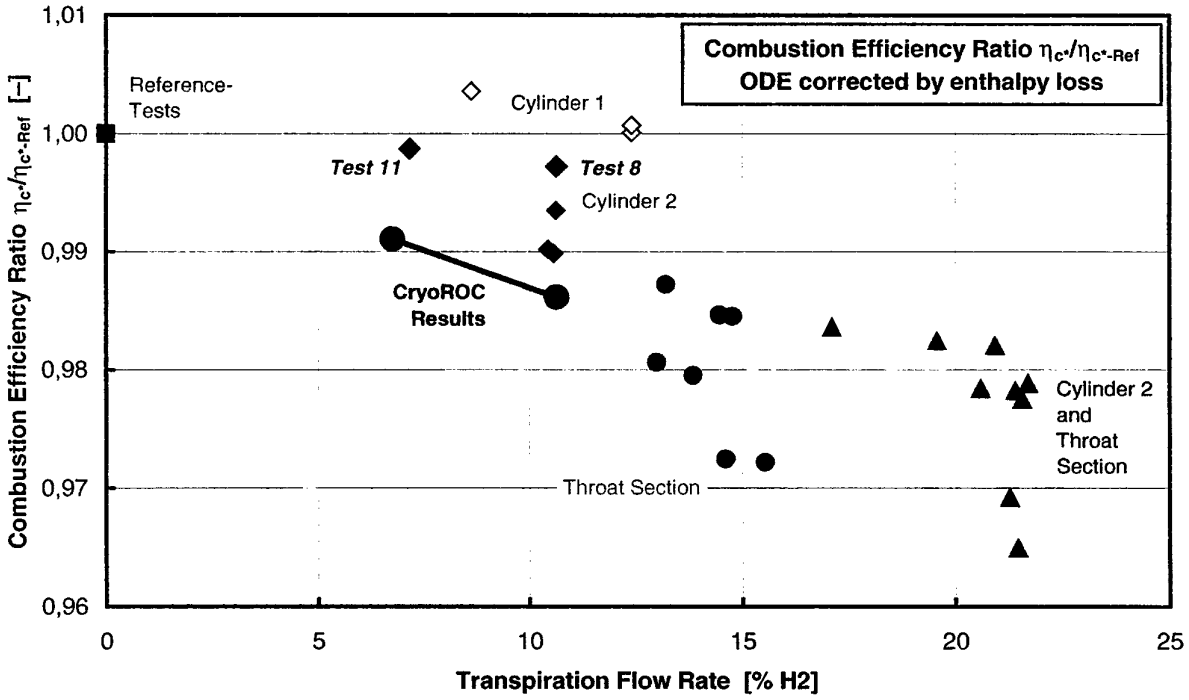
Profile of the Mixture Ratio O/F downstream the transpiration cooled insert

This document is the property of DaimlerChrysler Aerospace and is not to be disclosed or reproduced without prior consent

CryoROC 5.0 Computation - Transpiration cooled wall

Tehora Subscale, p_c = 100 bar, O/F = 5.62

TEHORA: Performance Loss Due to Transpiration Cooling, Test Results

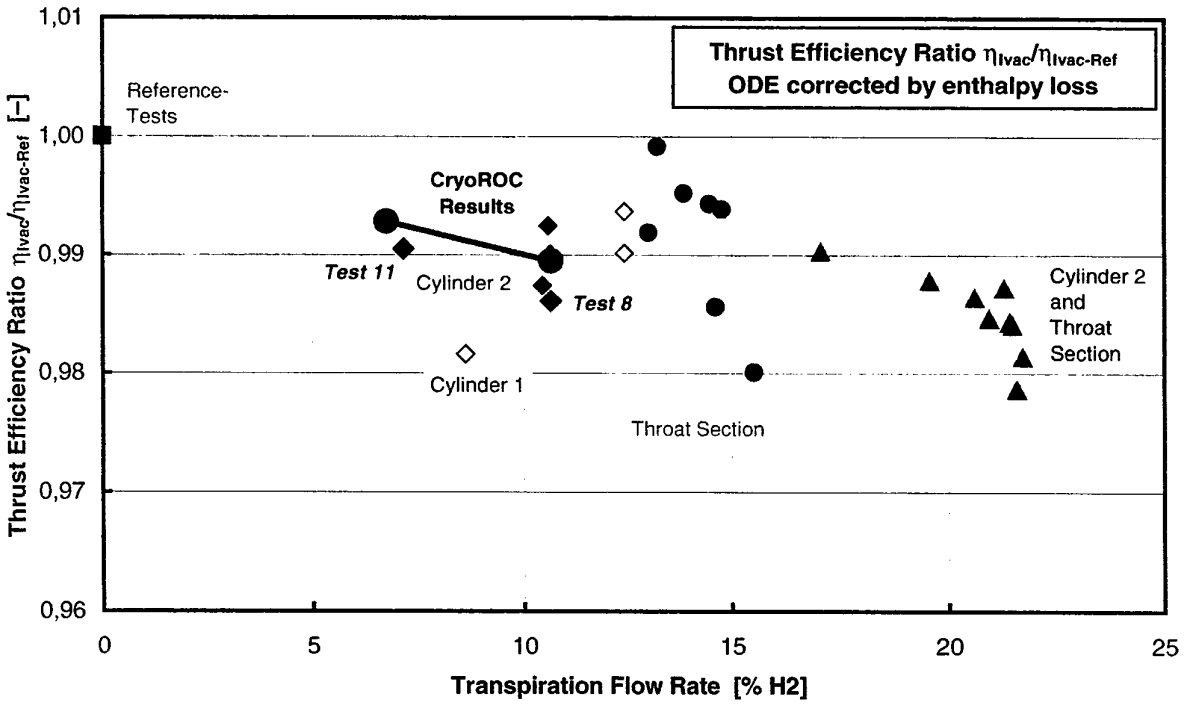


Reduction of <u>characteristic velocity</u> in dependence of Transpiration Flow Rate

CryoROC 5.0 Computation - Transpiration cooled wall

Tehora Subscale, p_c = 100 bar, O/F = 5.62

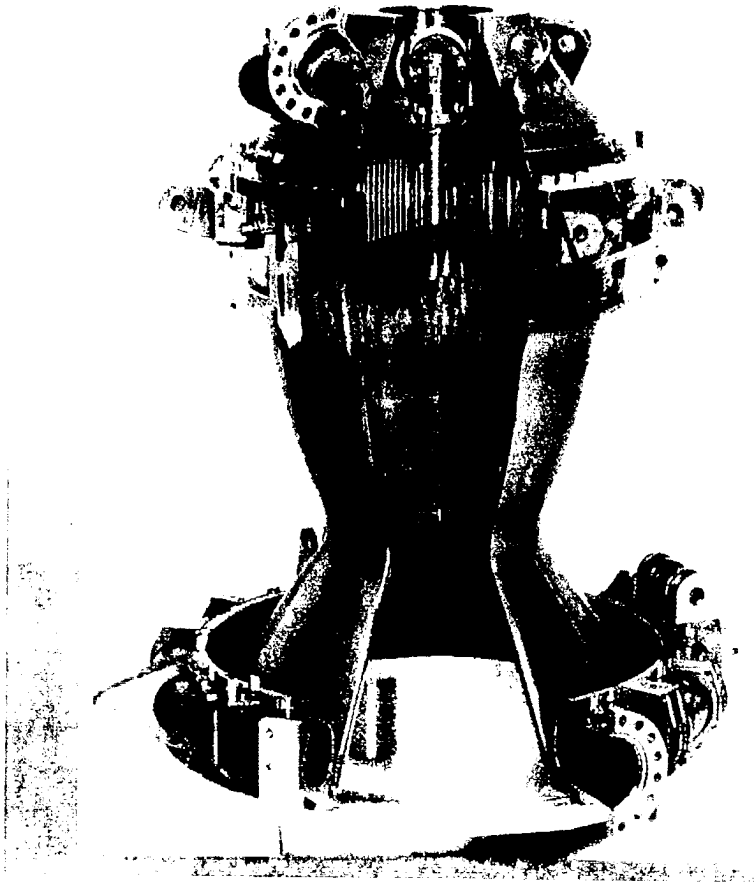
TEHORA: Performance Loss Due to Transpiration Cooling, Test Results



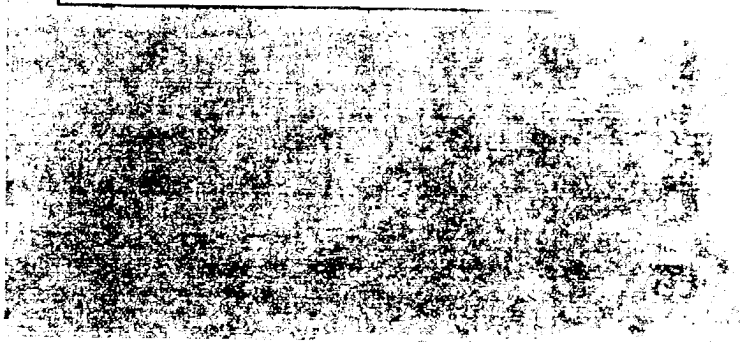
Reduction of <u>specific impulse</u> in dependence of Transpiration Flow Rate

DaimlerChrysler Aerospace

Vulcain Thrust Chamber Modelling:



	Δx_{Crack}	m_{inj}	$\approx n_{Cracks}$
1	-	-	0
2	**0.34 mm**	**3.0 kg/s**	**150**
3	**0.57 mm**	**5.0 kg/s**	**250**
4	**0.80 mm**	**7.0 kg/s**	**350**

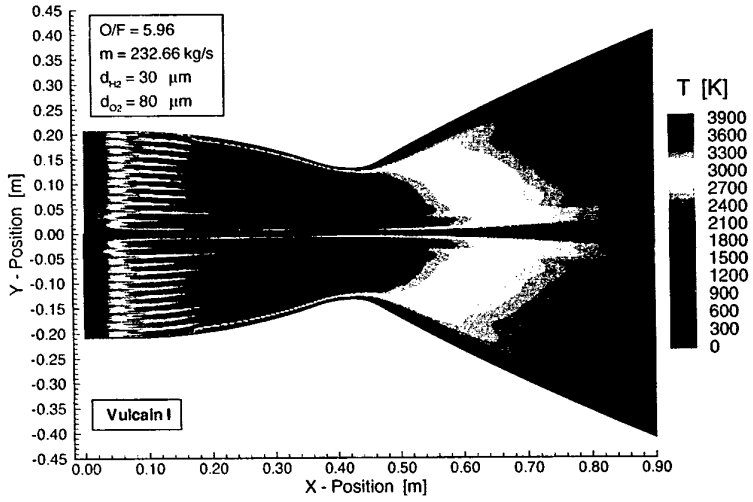


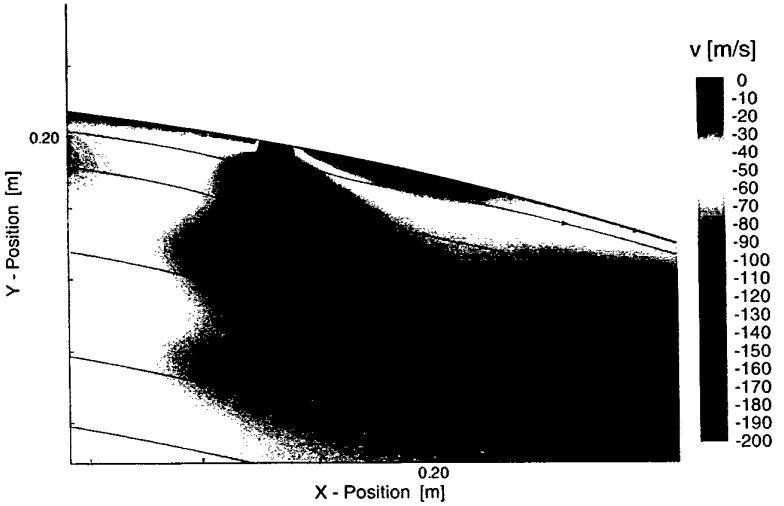
This document is the property of DaimlerChrysler Aerospace and is not to be disclosed or reproduced without

DaimlerChrysler Aerospace

CryoROC 5.0 Simulation - Modelling of Combustion Chamber Porosity

(Vulcain engine with cracks, p_c = 100 bar, O/F = 6)





Temperature Flow Field

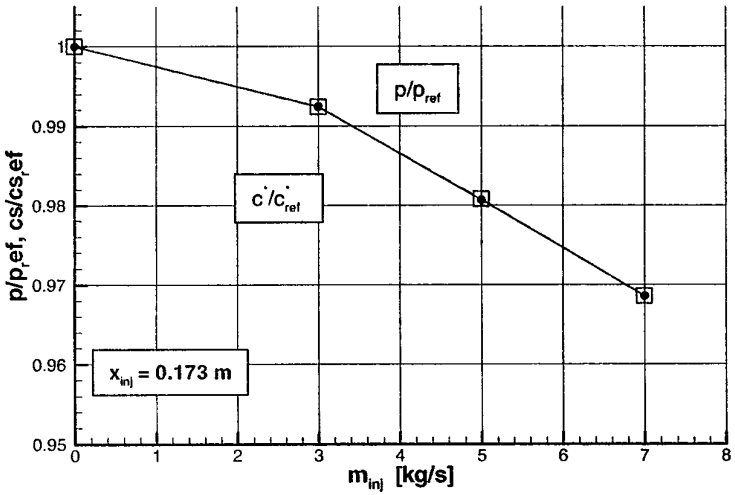
Radial Velocity Component, Streamlines

This document is the property of DaimlerChrysler Aerospace and is not to be disclosed or reproduced without prior consent

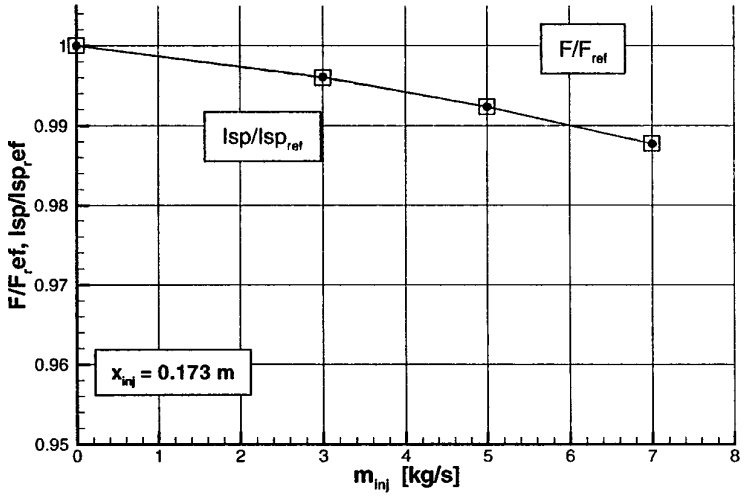
DaimlerChrysler Aerospace

CryoROC 5.0 Simulation - Modelling of Combustion Chamber Porosity

(Vulcain engine with cracks, p_c = 100 bar, O/F = 6)



Chamber Pressure and c*



Vacuum Thrust and specific Impulse

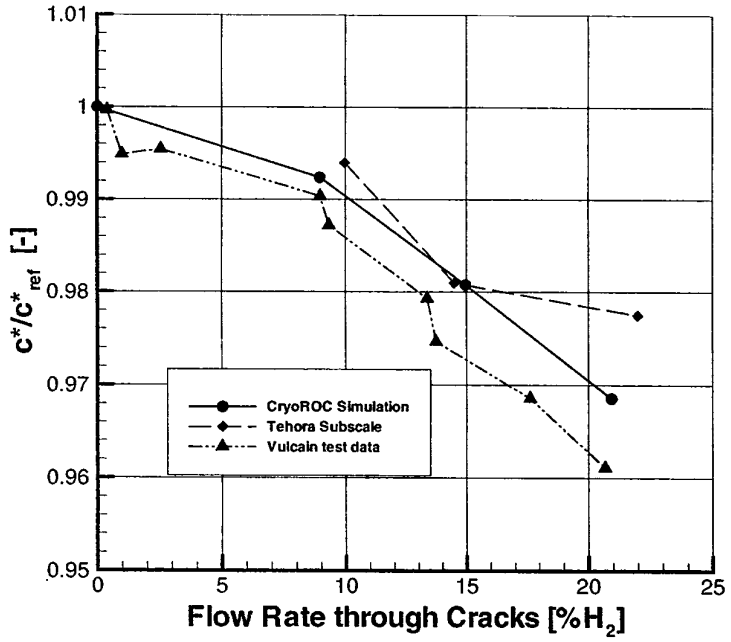
⇒ **performance losses in dependence of increasing H_2 leakage**
⇒ **η^*_c – losses differ distinctively from the performance losses**
⇒ **heated hydrogen contributes to the thrust development**

This document is the property of DaimlerChrysler Aerospace and is not to be disclosed or reproduced without prior consent

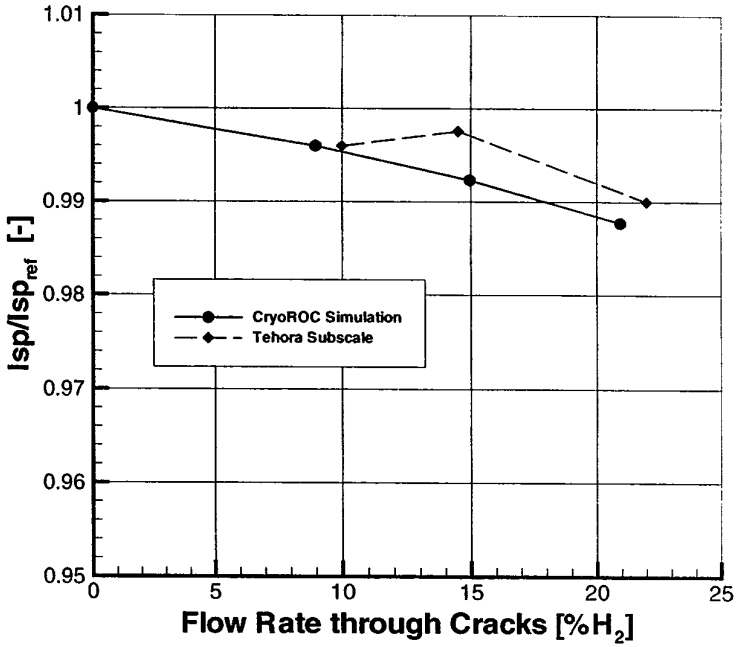
DaimlerChrysler Aerospace

CryoROC 5.0 Simulation - Modelling of Combustion Chamber Porosity

(Vulcain engine with cracks, p_c = 100 bar, O/F = 6)



Characteristic Velocity c*



Specific Vacuum Impulse

This document is the property of DaimlerChrysler Aerospace and is not to be disclosed or reproduced without prior consent

Concluding Remarks:

First applications of the CryoROC software to rocket engines characterized by porous walls are presented:

- ➤ intentional porous wall in the combustion chamber based on the transpiration cooling concept
- ➤ unintentional porosity due to (up to several hundred) cracks in the chamber wall

Comparison of CryoROC with available test data on subscale and fullscale level showed the code's potential for such complex flows:

- ➤ excellent reproduction of the heat flux drop behind a transpiration cooling insert
- ➤ c*-losses differ distinctively from the vacuum performance losses
- ➤ heated hydrogen contributes to the thrust development

ENGINE HEALTH MONITORING WITH EXHAUST PLUME EMISSION SPECTROSCOPY

F. S. Zavelevich, Yu. M. Golovin, Yu. P. Matsitsky, K. B. Moshkin, A. S. Romanovsky

Keldysh Research Center, Moscow, Russia

Abctract

Experimental optoelectronic equipment was developed featuring the following characteristics: spectral range of measurement – 320÷800 nm (unit measurement interval – 30 nm); maximum spectral resolution – 0.02 nm; measurement rate – 3÷100 spectra/s. To simulate ablation of structural materials when an LRE is operating, an experimental plant was developed which allowed one to inject small doses of lean concentrated metal salt solutions in the combustion chamber of subscale LRE operating on oxygen-ethanol or oxygen-kerosene components at propellant consumption rate of ~ 100 g/s. Experimental data were obtained on the detection limit of such metals as Fe, Al, Mn, Cr, Ni, and Cu in the exhaust plume. Radiation spectra of the "Proton" second stage engine exhaust plume were measured.

1. Introduction

Methods of LRE health monitoring based on exhaust plume emission spectroscopy technology received a development effort late in the nineties. An experimental plant for simulation of structural material losses with the engine operating was developed at Keldysh Research Center, and with participation of the Bauman State Technical University quick-operating spectroscopic instrumentation was developed. The task was to determine detection limit of the spectroscopic method based on metal vapours and to use spectral data for monitoring the spectral signatures of eroding engine components in test and/or flight operations. Monitoring the material losses is extremely important not only to evaluate lifetime of LRE various elements, but, primarily, for the objective of ignition prevention.

The detection of metal traces in LRE exhaust plumes using emission lines and determination of their concentration is not a trivial task. A number of factors hinder extracting metal line emission and measurement of their intensity: the band emission from thermally and chemically excited molecules of combustion products, the continuous background emission, the absorption by the environment, etc.

The idea of extracting chemical data from the analysis of the electromagnetic spectrum and using them for LRE health monitoring is not new. Engine health monitoring with exhaust plume emission spectroscopy is under intensive study at NASA [1 – 4].

2. Theory

In the isothermal equilibrium flame of thickness L at the temperature T the emission intensity of non-reabsorbed line J ($W/m^2 \cdot sr$) is equal to

$$J = N \cdot L \cdot A \cdot g \cdot h \cdot c \cdot \exp(-E_b/k \cdot T)/4\pi \cdot \lambda \cdot n, \quad (1)$$

where: N – volumetric concentration, m^{-3};

A – the Einstein transition probability for spontaneous emission, s^{-1};

g – statistical weight;

n – sum for states;

T – absolute temperature;

h – Planck's constant, $6.62 \cdot 10^{-34}$ J·s;

c – velocity of light, $3 \cdot 10^8$ m/s;

k – Boltzmann constant, $8.621 \cdot 10^{-5}$ eV/K;

E_b – energy of high level, eV;

λ – wavelength, m.

Formula (1) is true only for an optically thin emitter, when the optical width is

$$\tau = A_i \cdot g_i \cdot \lambda^4 \cdot N \cdot L/n \cdot 8\pi \cdot c \cdot \Delta\lambda \quad (2)$$

is less than a unity. Here $\Delta\lambda$ is the half-width of spectral line.

Formula (2) is true for the majority of lines with the lower main level. Limiting N·L values for strong lines of some metals are presented in Table 1.

Table 1.

Limiting N · L values for strong lines of some metals

Metal	Line wave-length (λ), nm	$A \cdot g \cdot 10^8$, s^{-1}	n	Halfwidth of line ($\Delta\lambda$), nm	N·L, m^{-2}
Al	396	1.3	5.9	$3 \cdot 10^{-3}$	$4 \cdot 10^{16}$
Cr	425	2.0	10.6	$2.3 \cdot 10^{-3}$	$3 \cdot 10^{16}$
Cu	324	4.1	2.4	$1.6 \cdot 10^{-3}$	$0.65 \cdot 10^{16}$
Fe	372	2.5	28.5	$2 \cdot 10^{-3}$	$9 \cdot 10^{16}$
Ni	352	4,6	30,6	$2 \cdot 10^{-3}$	10^{17}

3. Spectroscopic Instrumentation

Spectroscopic instrumentation (Fig. 1) consists of an optical system, a grating monochromator, a photodetector and a PC.

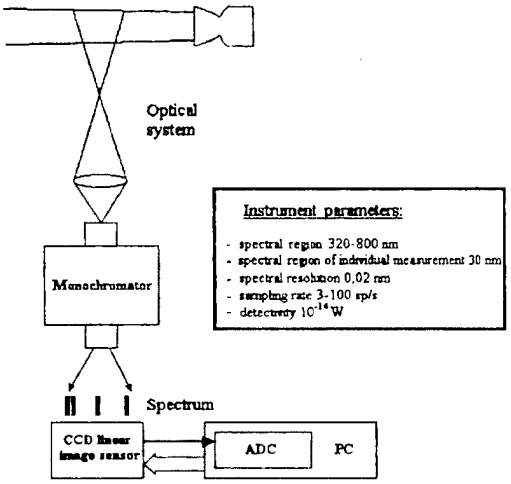


Fig. 1

Various optical systems were used for measurements. A quartz condensor of D=55 mm, focal distance f = 70 mm, was used on the experimental plant with a subscale engine. In testing of the "Proton" launching vehicle engine (PE) a focusing spherical mirror of D = 120 mm (diameter) and F = 1.2 m (focal distance) was used.

The monochromator comprises a plane diffraction grating of n = 1200 lines/mm; two spherical mirrors of 600 mm focal distance.

The monochromator effective range as to spectrum is 300÷1000 nm, the reverse linear dispersion is 1.3 nm/mm.

The photodetector incorporates a 2048-pixel CCD linear image sensor, a controller and buffer operational amplifiers.

Characteristics of the 2048-pixel CCD linear image sensor (TCD142D): number of image sensing elements – 2048, image sensing element size – 14 μm ×14 μm; dynamic range – 1500 (integration time = 10 ms).

Spectroscopic instrumentation main characteristics:

- Spectral region – 320÷800 nm
- Spectral region of individual measurement – 30 nm
- Maximum spectral resolution – 0.02 nm
- Detectivity (integration time is 170 ms, light source wavelength is 500 nm) – 10^{-14} W
- Temporal resolution – 0.01÷0.3 s.

In order to refer accurately to the wavelength, the instrumentation was calibrated by the Hg-lamp. Using the light source of T = 3000 K the detectivity was determined and the spectral responsivity was measured (Fig. 2).

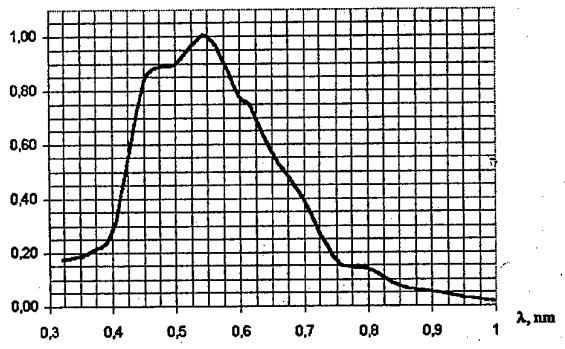


Fig. 2

4. Experimental Plant

Losses of small quantities of material from engine structural members were simulated by injection of small quantities (1.3÷15.0 %) of dilute solutions of metal salts and alkalis into the combustion chamber of a subscale ethanol-oxygen LRE. The subscale engine was fitted with a volume doser to feed small quantities of weak salt solutions into the combustion chamber. The solution was expelled from the doser tank by high-pressure nitrogen. The salt consumption was controlled by the pressure differential in the tank and the combustion chamber.

Main experiments were run on the subscale engine with the total flow rate of propellants (ethanol + oxygen) of ~ 100 g/s. The typical operation mode of the engine during tests: oxidizer flow rate G_0 = 82.25 g/s; fuel flow rate G_a = 39.6 g/s; α = 1.017; combustion chamber pressure P_c = 17.7 kg/cm^2; salt solution flow rate – 1÷15 g/s; relative metal content (mass) – $(2\div15)\cdot10^{-4}$.

5. Experiments on Subscale Engine

The objective of these experiments is optimization of measuring procedures and determination of instrument sensitivity as to metal vapours in conditions close to nonsimulated conditions as to the plume chemical content.

The instrumentation was pointed to the near nozzle region of plume where the design

temperature was 2200÷2400 K, the pressure P = 0.1 MPa. The width of the monochromator entrance slit was prescribed to be equal to 0.15 mm that provided the spectral resolution of 0.2 nm.

The results of measurements presented in Fig. 3 were obtained when small quantities of $KMnO_4$ additive were injected in the subscale LRE combustion chamber. The water solution of $KMnO_4$ was added directly to the fuel (ethanol). The concentration of $KMnO_4$ in the ethanol was ~ $5 \cdot 10^{-5}$ that, when converted to K and Mn in the gas mixture, gives

~ $4 \cdot 10^{-6}$ and ~ $6 \cdot 10^{-6}$, respectively. One can easily see the K doublet (404.414 and 404.72 nm) and the Mn triplet (403.076; 403.307 and 403.443 nm).

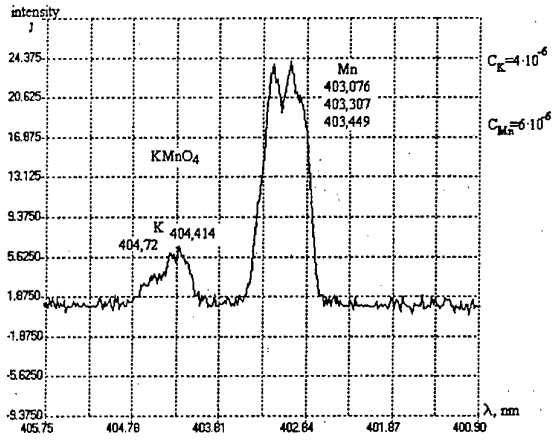


Fig. 3

The plume emission spectrum with injection of 1.5-percent water solution of $K_2Cr_2O_7$ in the combustion chamber is presented in Fig. 4. During the tests the consumption of salt solution amounted to ~ 5 % of the total component consumption that gives the Cr content in the plume equal to $2 \cdot 10^{-4}$. On the plot the most prominent are the chrome lines at 425.435; 427.480 and 428.372 nm.

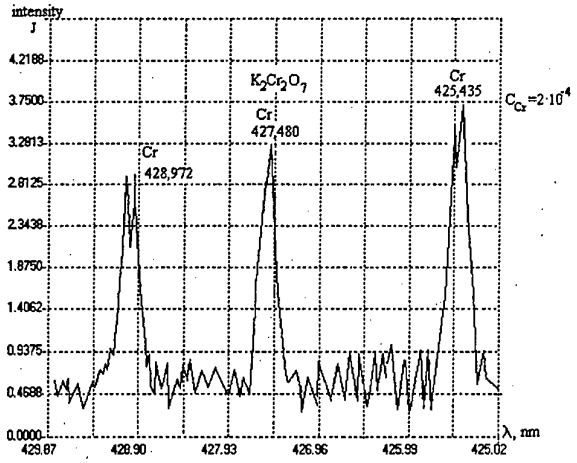


Fig. 4

More detailed investigations were carried out using the copper salt $Cu(NO_3)_2$. Measurements with 8-percent water solution of $Cu(NO_3)_2$ were taken in three spectral intervals where lines at 324.754, 327.396, 510.554 (Fig. 5, 6). In doing so the line at 510.554 nm was observed against a background of molecular bands.

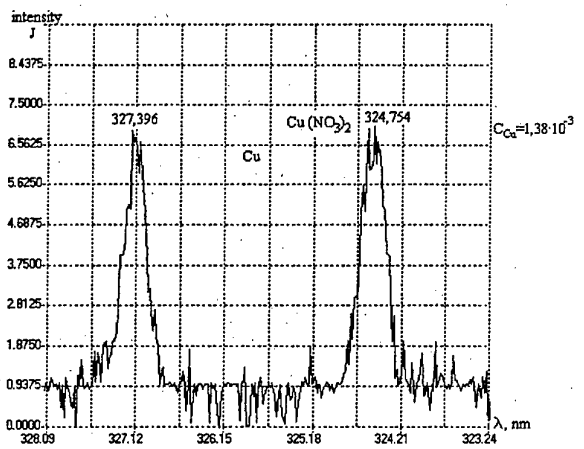


Fig. 5

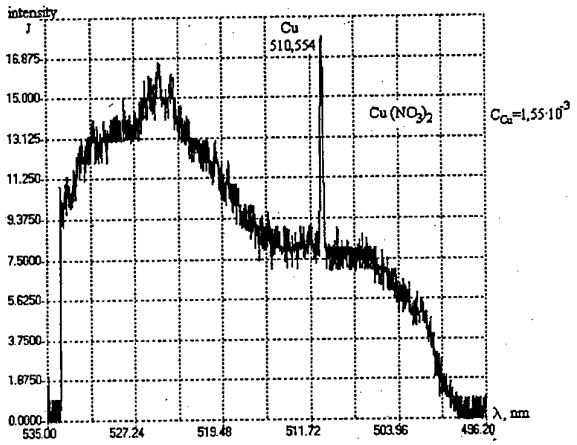


Fig. 6

Besides, in order to check the assumption on the non-reabsorbity of lines for the line at 510.554 nm, measurements were taken at different copper concentrations in the plume ($1.9 \cdot 10^{-4}$; $2.9 \cdot 10^{-4}$; $8.2 \cdot 10^{-4}$ and $2.2 \cdot 10^{-3}$). Within the range of precision of measurements, which is caused mainly by variability of engine operation modes from startup to startup, the intensity of line depends linearly on copper concentration that suggests that formula (1) can be applied to the results obtained on the subscale engine.

Iron can be the main component of structural materials of the overwhelming majority of LRE elements. Nickel enters into the composition of practically all stainless steels that are used in LRE. Besides, nickel is widely used for coatings of contacting turbine elements which are the most susceptible to ignition. That is why these metals are the most interesting for LRE health monitoring.

Shown in Fig. 7 are spectra of subscale engine plume emission when 12-percent solution of $Ni(NO_3)_2$ is injected in the combustion chamber. The content of Ni in the plume therewith amounted to $1.5 \cdot 10^{-3}$. On the spectra a whole set of nickel lines is presented of which the most interesting are lines at 361.939; 380.714 and 385.830 nm.

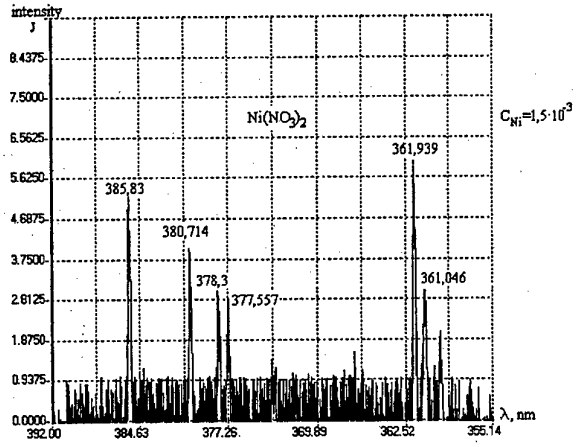


Fig. 7

The iron lines in the subscale LRE plume spectra (Fig. 8) were obtained when 10-percent solution of $FeSO_4 \cdot 7H_2O$ was injected in the chamber. The content of iron in the LRE plume amounted to $7.5 \cdot 10^{-4}$.

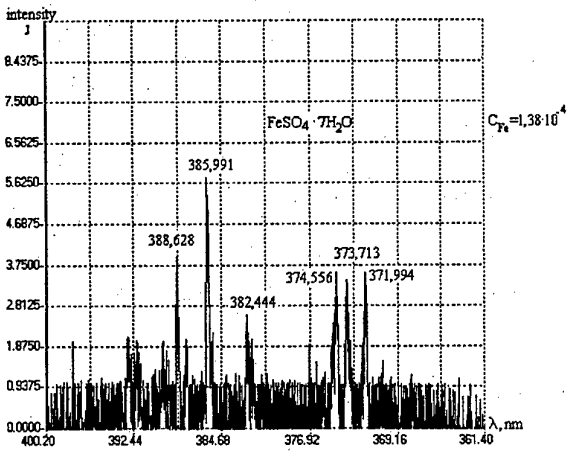


Fig. 8

6. Measurements of Emission Plume Spectrum of "Proton" Launching Vehicle Second Stage Engine

Seven tests of "Proton" launching vehicle second stage engines (PE) were performed in January-February 2000 on the test stand of the Chemical Automatics Design Bureau. To investigate the influence of strange particles (impurities) on the engine operability, in a number of tests powders of an aluminium alloy and steel were injected in fuel manifolds at certain periods of time.

Main characteristics of the engine:

- propellants: oxidizer – N_2O_4; fuel – nonsymmetrical dimethylhydrazine $(CH_3)_2N_2H_2$;
- mixture ratio $K_m = G_0/G_f = 2.6$;
- propellant flow rate $G_\Sigma = 180$ kg/s;
- combustion chamber pressure P_c=15 MPa;
- nozzle expansion ratio – 8.4.

The tests were run in the atmosphere, i.e. the jet was overexpanded. The instrumentation was pointed to the plume region at a distance of ~ 0.7 m from the nozzle exit immediately after the Mach disk as shown by TV recording. The design gas temperature in this region under condition of thermochemical equilibrium is ~ 3100 K, the pressure is ~ 0.2 MPa. During tests the measurement rate was 6 or 3 lines per second. The width of monochromator enterance slit was set 0.2 mm that provides spectral resolution of 0.25 nm.

Shown in Fig. 9 is a typical spectrum of plume emission which is characteristic of standard engine operation mode. In the course of the whole period of testing (t = 320 s) the spectrum does not undergo essential changes. Against the background of continuous emission two strong Fe lines are seen at 385.99 and 388.63 nm. The emission intensity in the lines does not change over time that attests that the iron flow rate is constant. The most probable cause of iron occurring in the plume is the presence of iron in the propellant that is confirmed by results of the chemical analysis which is made before each testing. The content of Fe in the fuel, which was measured before this test, amounted to ~ 10^{-7} that corresponds to the flow rate of ~ 20 mg/s.

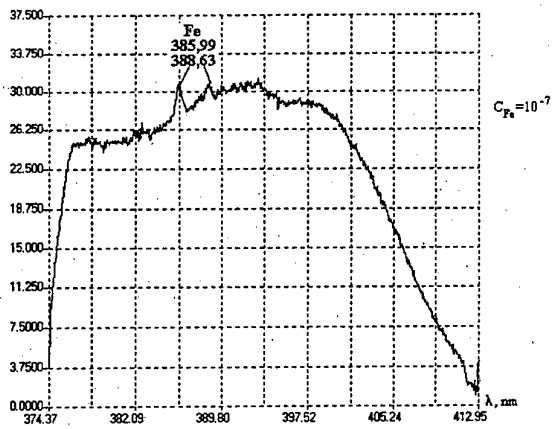


Fig. 9

Fig. 10 illustrates the spectrum of plume emission when 2.5 g steel powder (70 % Fe, 18 % Cr, 10 % Ni, 1 ÷ 2 % Mn) are injected in the fuel manifold. When comparing results shown in Figs. 11 and 8, one can see that the intensity of emission in Fe lines at 385.99 and 388.63 nm increases sharply, and new lines

have appeared: Fe lines at 376.72, 382.59, 388, 389.97, 392.29, 392.79 nm and the Mn line at ~ 403.1 nm.

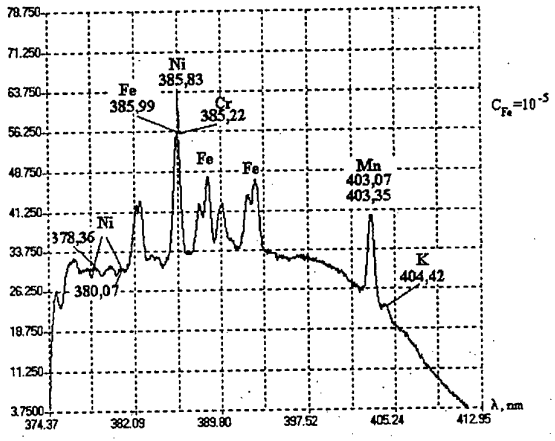


Fig. 10

Under condition of thermochemical equilibrium the relative content of Cr atoms at 3100 K temperature is only ~ 3 %. That is why in this spectra the intensity of relatively strong Cr lines (385.22, 385.52, 388.68 nm) is disguised by intensive Fe lines due to inadequately high spectral resolution.

The relative content of Ni atoms is ~ 0.85. The Ni line (λ = 385.83 nm) is concealed by the strong Fe line (λ = 385.99 nm). Ni lines (λ = 378.35 and 380.7 nm) are present in the spectrum.

It might be well to point out that if the concentration of iron increases more than 100 times, the intensity of strong Fe lines at 385.99 and 388.63 nm is only approximately 10 times as much. This is related to self-absorption in the central part of lines. This is corroborated by the magnitude N·L which is determined from the Fe flow rate. It turned to be equal to $N \cdot L_{Fe} = 3 \cdot 10^{19}$ m^{-2}. This magnitude is 2 orders as much as the magnitude at which relationship (1) is true (see Table 1).

Figs. 11 and 12 show spectra of plume emission when 700 mg of aluminum alloy powder are injected which contains 0.5 ÷ 0.8 % Mn. The powder was injected in the fuel manifold (Fig. 11) and in the oxidizer manifold (Fig. 12). About 10 % (for mass) of the most large-sized particules were retained by filters and did not reach the combustion chamber and, consequently, the plume.

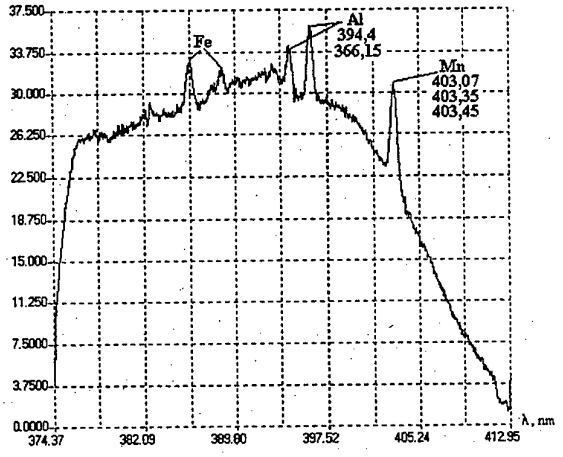


Fig. 11

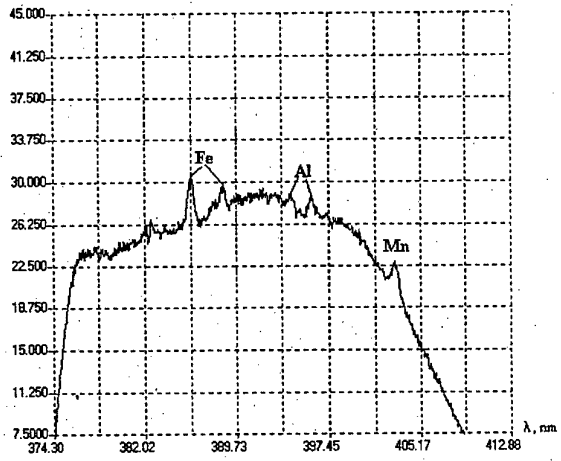


Fig. 12

As is seen from the results presented, when the powder is injected, emission occurs in Al lines (394.4 and 396.15 nm) and in Mn lines (~ 403.1 nm). The intensity of emission and, consequently, the concentration of Al and Mn atoms strongly depend on what manifold the powder is injected in: oxidizer or fuel ones. When the powder is injected in the oxidizer manifold, the most part of Al and Mn is oxidized.

The luminiscence in Al and Mn lines is observed within ~ 1 second. It means that the registered intensity of emission corresponds to the Al flow rate of ~ 600 mg/s, the Mn flow rate of ~ 4 mg/s or to the relative concentration of $3 \cdot 10^{-6}$ and $2 \cdot 10^{-8}$, respectively. In fact, only a small part of initial material is contained in the plume as atoms which form spectral lines. Thus, under condition of thermochemical equilibrium after the Mach disk at T = 3100 K only 3 % of all Al and 50 % Mn are contained as atoms.

In summary we shall indicate minimum recordable relative concentrations C_{min} and mass flow rates G_{min} of different metals in the PE plume.

Table 2.

Minimum recordable relative concentrations C_{min} and mass flow rates G_{min}

Element	Wavelength, nm	Proton engine	
		C_{min}	G_{min}, g/s
Al	394.4/396.15	$5 \cdot 10^{-7}$	0.1
Fe	371.99/373.6/374.8 385.99/388.63	$5 \cdot 10^{-8}$	0.01
Ni	352.454/361.94	$5 \cdot 10^{-9}$	0.001
Mn	403.08/403.31/403.45	$3 \cdot 10^{-9}$	0.0006

References

1. G. Madzsar. "Digital filtering of plume emission spectra", AIAA 90-1994. 1990.

2. R. Bickford, G. Madzsar. "Fabry-Perot interferometer development for rocket engine plume spectroscopy", AIAA 90-2234, 1990.

3. G. D. Tejwani et al. "Space Shuttle main engine health monitoring with exhaust plume emission spectroscopy". J. Spac. Rock., № 3, 1998.

4. D. A. Benzing, K. W. Whitaker. "Approach to Space Shuttle main engine health monitoring using plume spectra". J. Spac. Rock., № 6, 1998.

Theory of drop formation

Jens Eggers

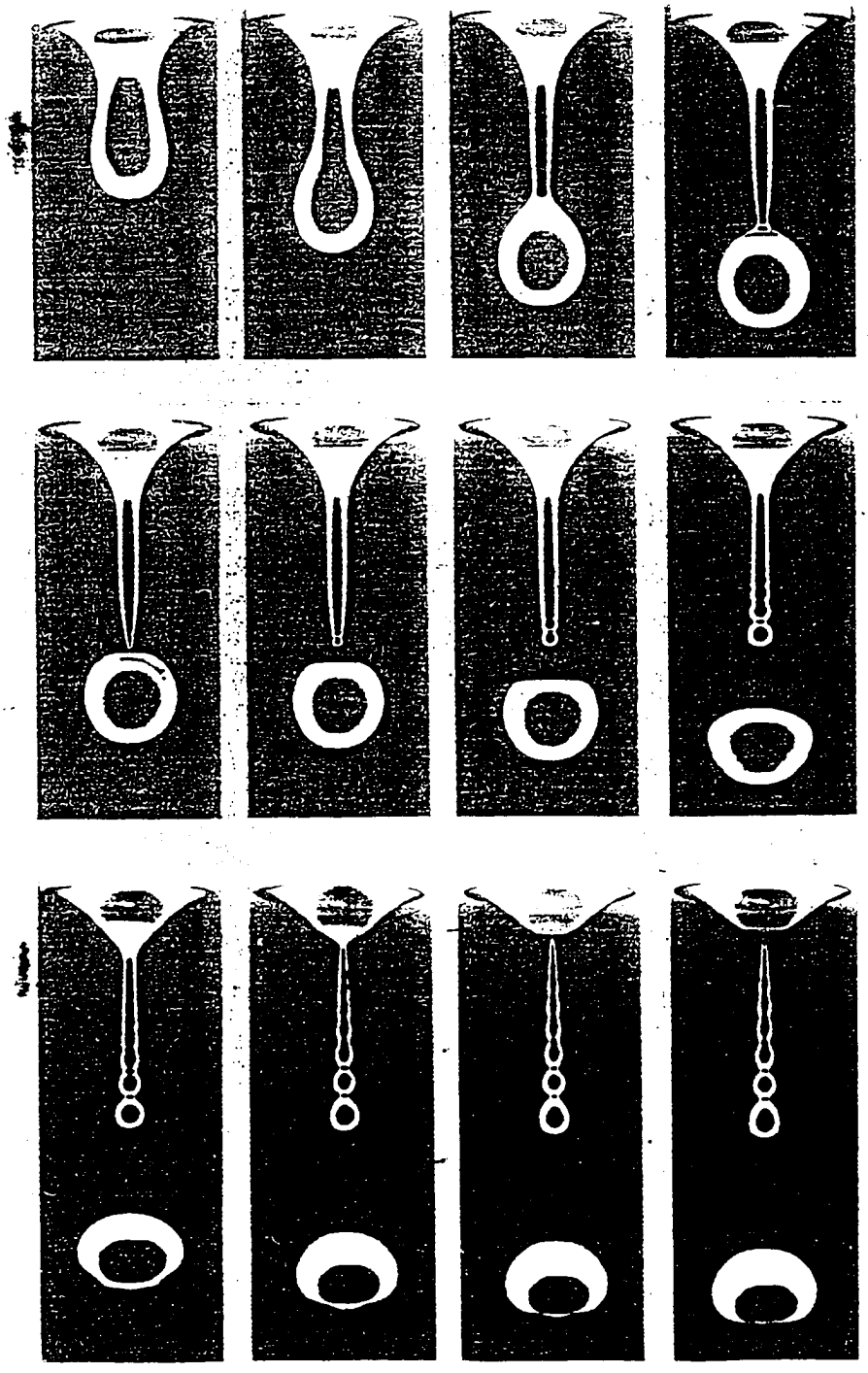
Lampoldshausen, March 2000

Thanks: Michael Brenner, MIT
John Lister, Cambridge
Howard Stone, Harvard

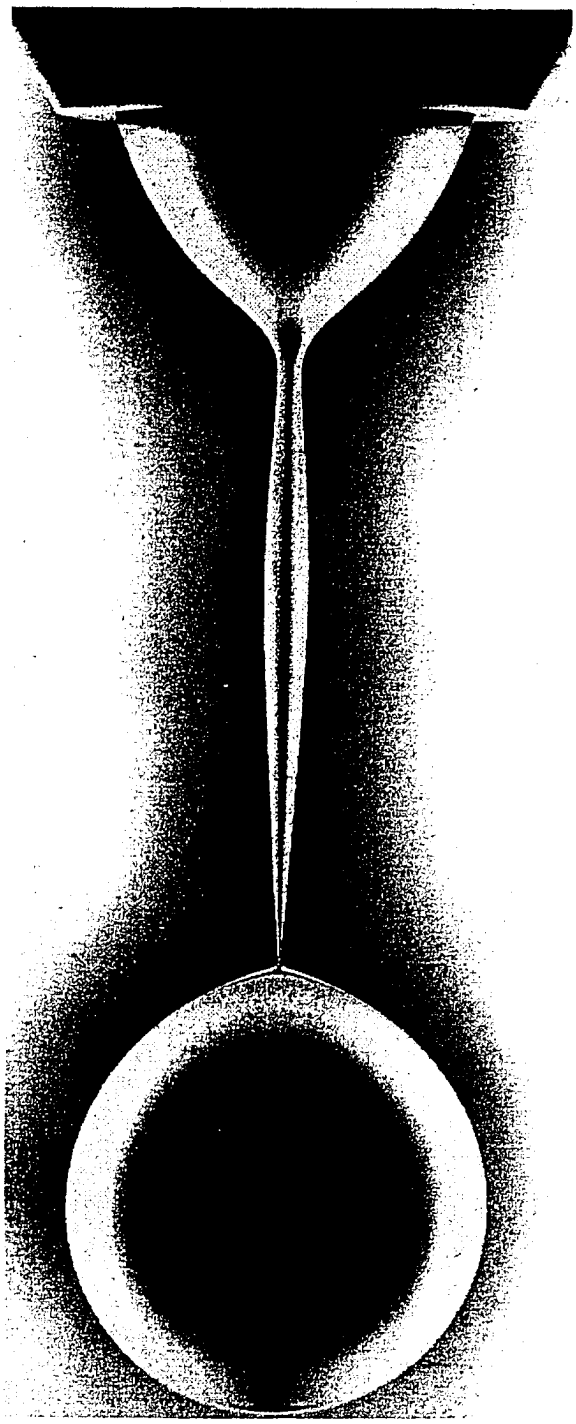
AMERICAN
ASSOCIATION FOR THE
ADVANCEMENT OF
SCIENCE

SCIENCE

8 JULY 1994 $6.00
VOL. 265 • PAGES 157–288

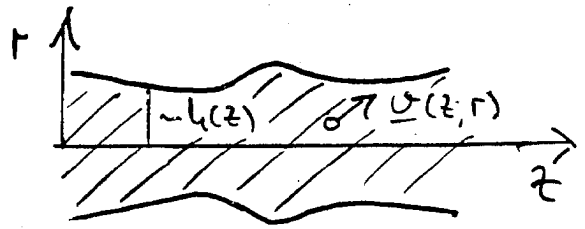


Lavalamp



Hei Coiner

Navier - Stokes dynamics



$$\underline{v}(z,r) = v_r \underline{e}_r + v_z \underline{e}_z$$

$$\partial_t \underline{v} + (\underline{v}\,\underline{\nabla})\underline{v} = -\underline{\nabla} p + \nu \Delta \underline{v} \qquad \text{NSE}$$

$$\underline{\nabla}\,\underline{v} = 0 \qquad \text{I}$$

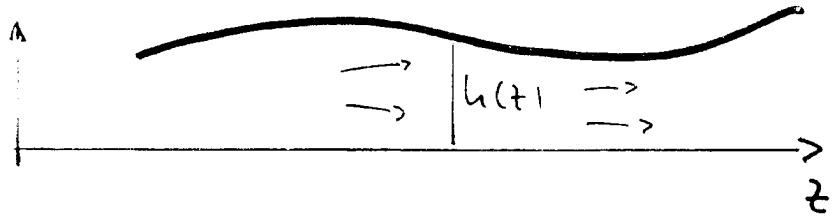
$$\underline{n}\,\underline{\underline{\sigma}}\,\underline{n} = \frac{\gamma}{s}\left(\frac{1}{R_1} + \frac{1}{R_2}\right)$$

$$\underline{n}\,\underline{\underline{\sigma}}\,\underline{t} = 0 \qquad \text{BC}$$

$$\partial_t h = \sqrt{1 + h_z^2}\;\underline{n}\,\underline{v} \qquad \text{S}$$

2 + 1 dimensional, nonlinear moving boundary problem!

1-D models: radial expansion



Taylor expansion

$$v_z(z,r) = v_0(z) + v_2(z)\, r^2 + \cdots$$

In NSE: (prime is ∂_z)

$$\partial_t v_0 + v_0 v_0' = -\frac{1}{\rho} P_0' + \nu\left(4 v_2 + v_0''\right)$$

P_0: normal force balance

v_2: tangential force balance

momentum
$$\partial_t v_0 + v_0 v_0' = -\frac{\gamma}{\rho}\frac{1}{h} + 3\nu\frac{(v_0' h^2)'}{h^2}$$

mass
$$\partial_t h + v_0 h' = -\frac{1}{2} h v_0'$$

Closed set of equations at leading order in $l_r \ll l_z$!!

Higher order systems ($h, v_0, v_2, \ldots v_{2n}$) possible.

Simulation with lubrication models

$$\partial_t h + v h_z = -\frac{1}{2} v_z h$$

$$\partial_t v + v v_z = \frac{1}{s} P_z + 3\nu \frac{(v_z h^2)_z}{h^2}$$

$$P = \gamma \left[\frac{1}{h\sqrt{1+h_z^2}} - \frac{h_{zz}}{\sqrt{1+h_z^2}^3} \right]$$

a) Full curvature term assures good agreement with linear theory

b) Singularities reproduced exactly

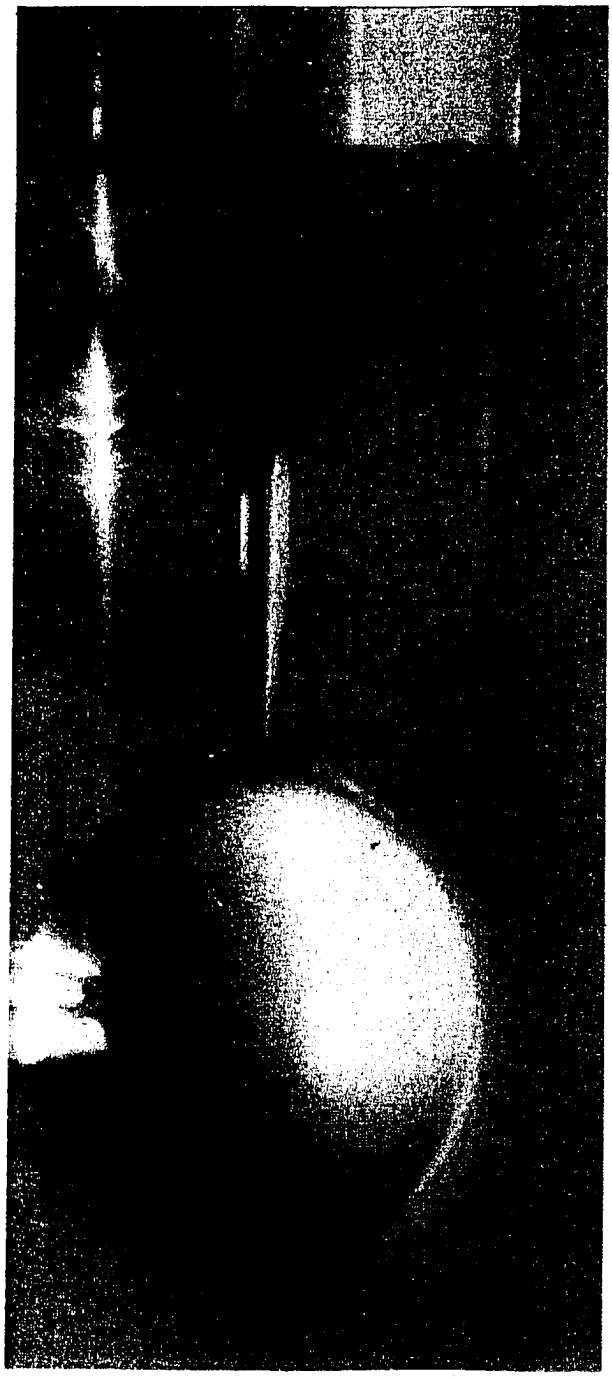
c) Physical boundary conditions at the nozzle

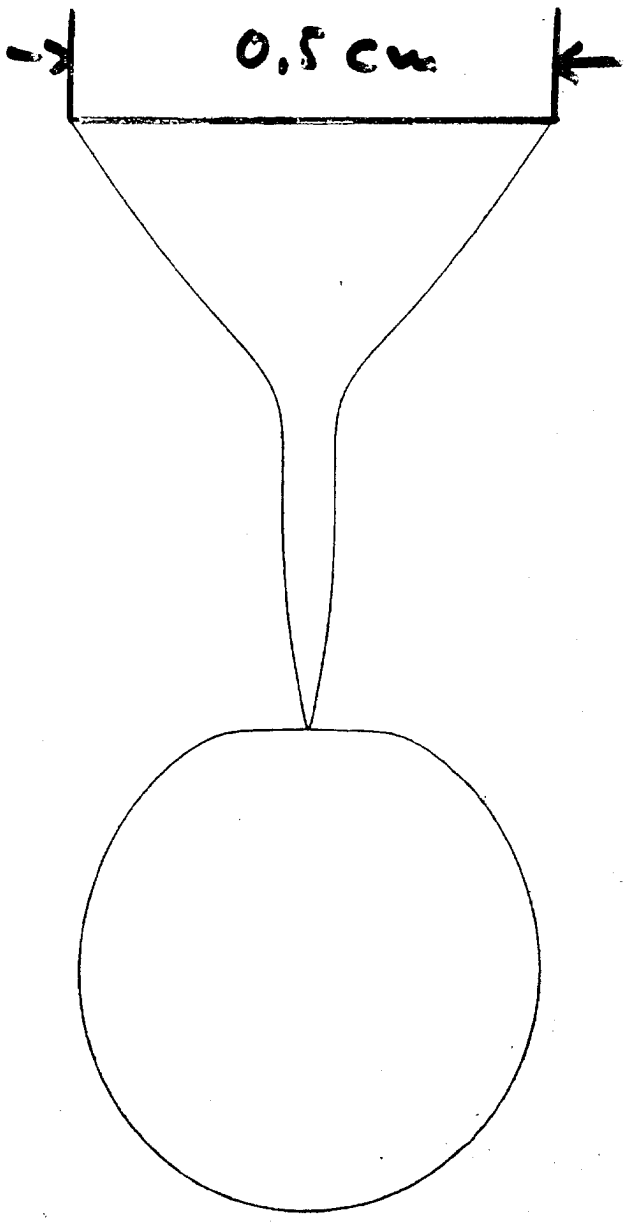
d) Fluid is broken if $h_{min} < 10^{-3} r_{nozzle}$

e) Implicit code, automatic grid refinement

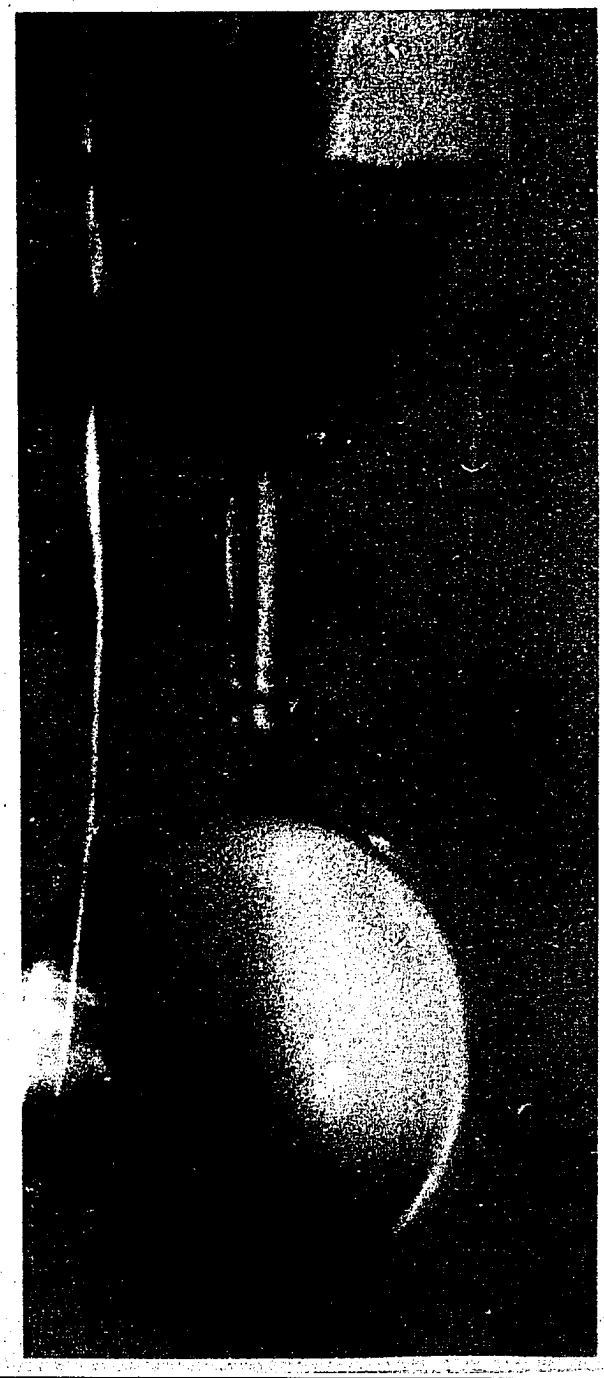
Peregrine 1990

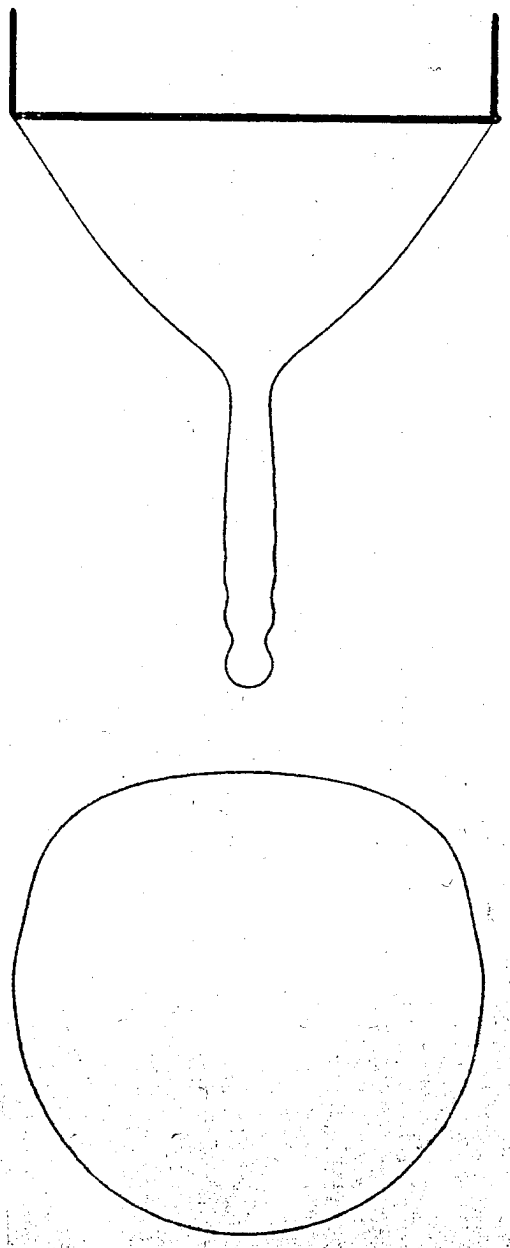
Simulation der Näherungsgleichungen mit
Michael Brenner und Todd Dupont





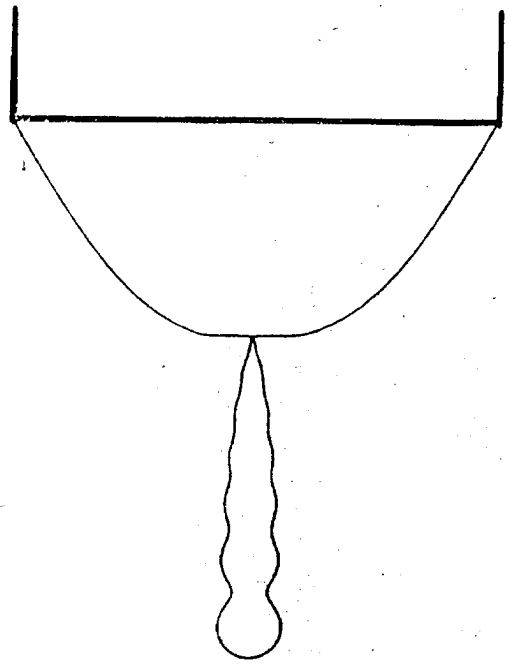
0,9 msec

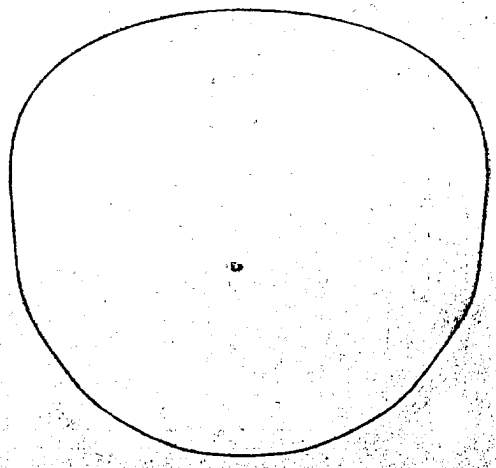




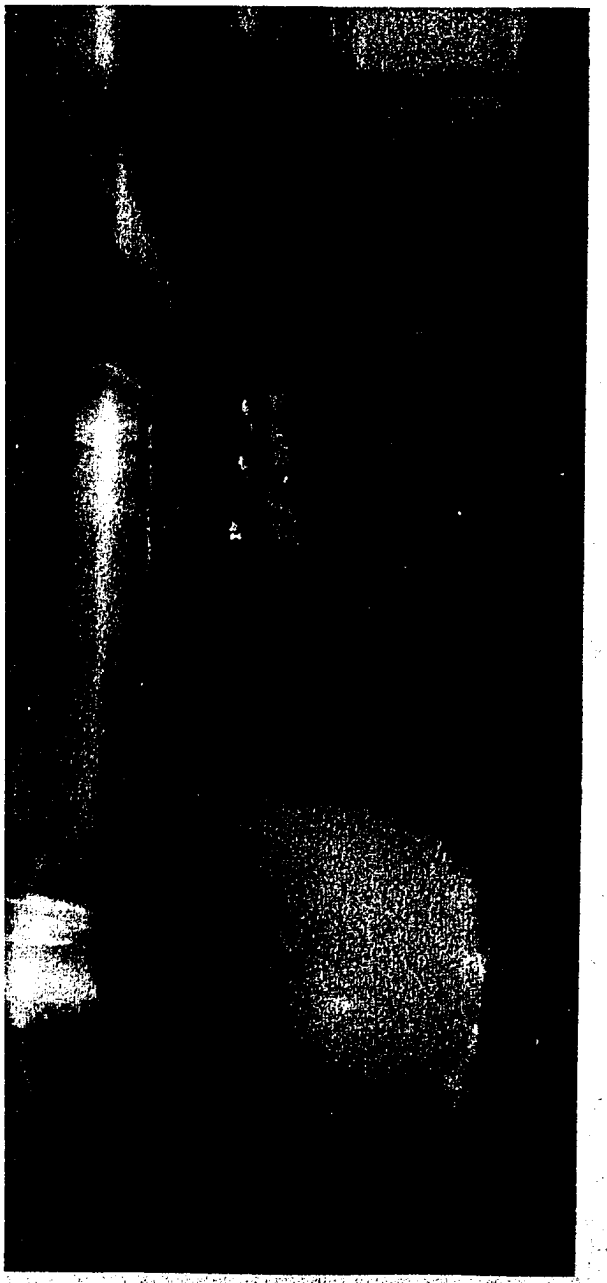
1,7 msec

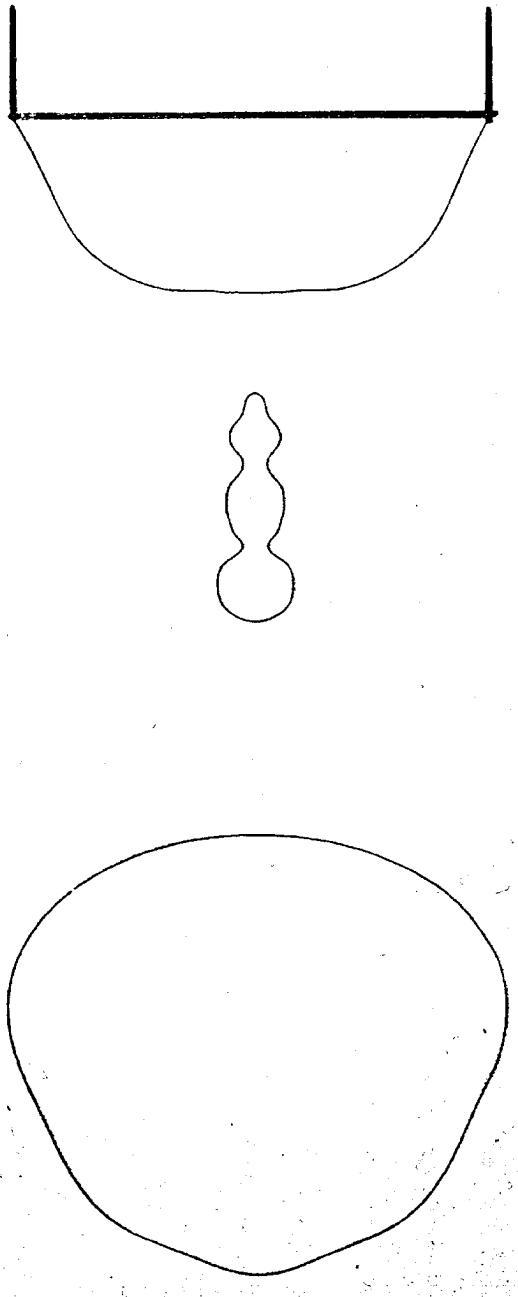






2,9 msec





Scaling solution

r : scale : $\frac{\ell^2 \rho}{\gamma}$

t : $\frac{\ell^3 \rho^2}{\gamma^2}$ | universality!

use surface tension, inertial, and face tension forces:

$$\left.\begin{aligned} (z,t) &= |t-t_0|\,\phi(\xi) \\ (z,t) &= |t-t_0|^{1/2}\,\psi(\xi) \end{aligned}\right\} \quad \xi = \frac{z-z_0}{|t-t_0|^{1/2}}$$

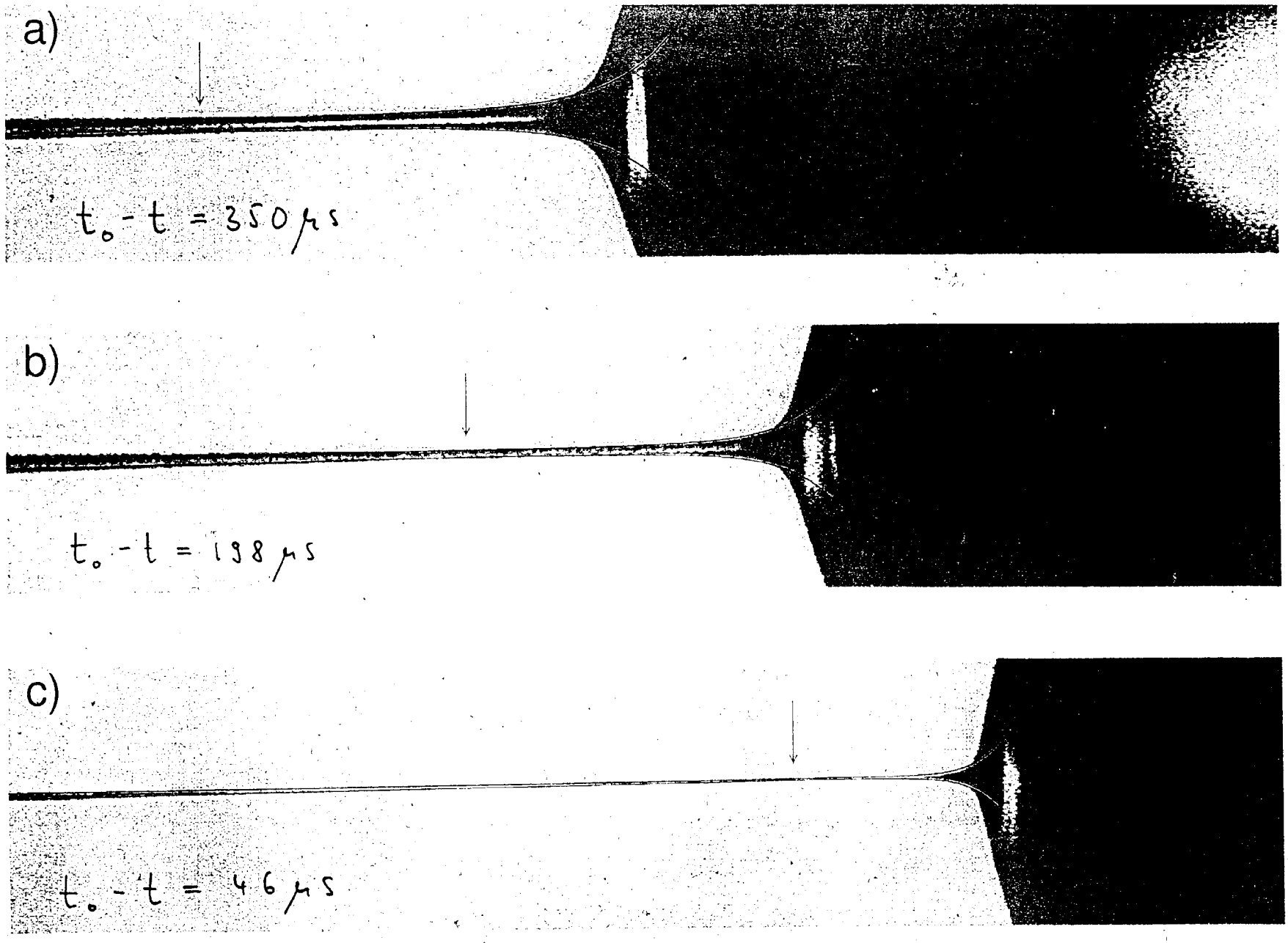
$r \sim |t-t_0|$, $\ell_z \sim |t-t_0|^{1/2}$!

$$\cdot + \xi\frac{\psi'}{2} + \psi\psi' = \frac{\phi'}{\phi^2} + 3\frac{(\psi'\phi^2)'}{\phi^2} + O(t')$$

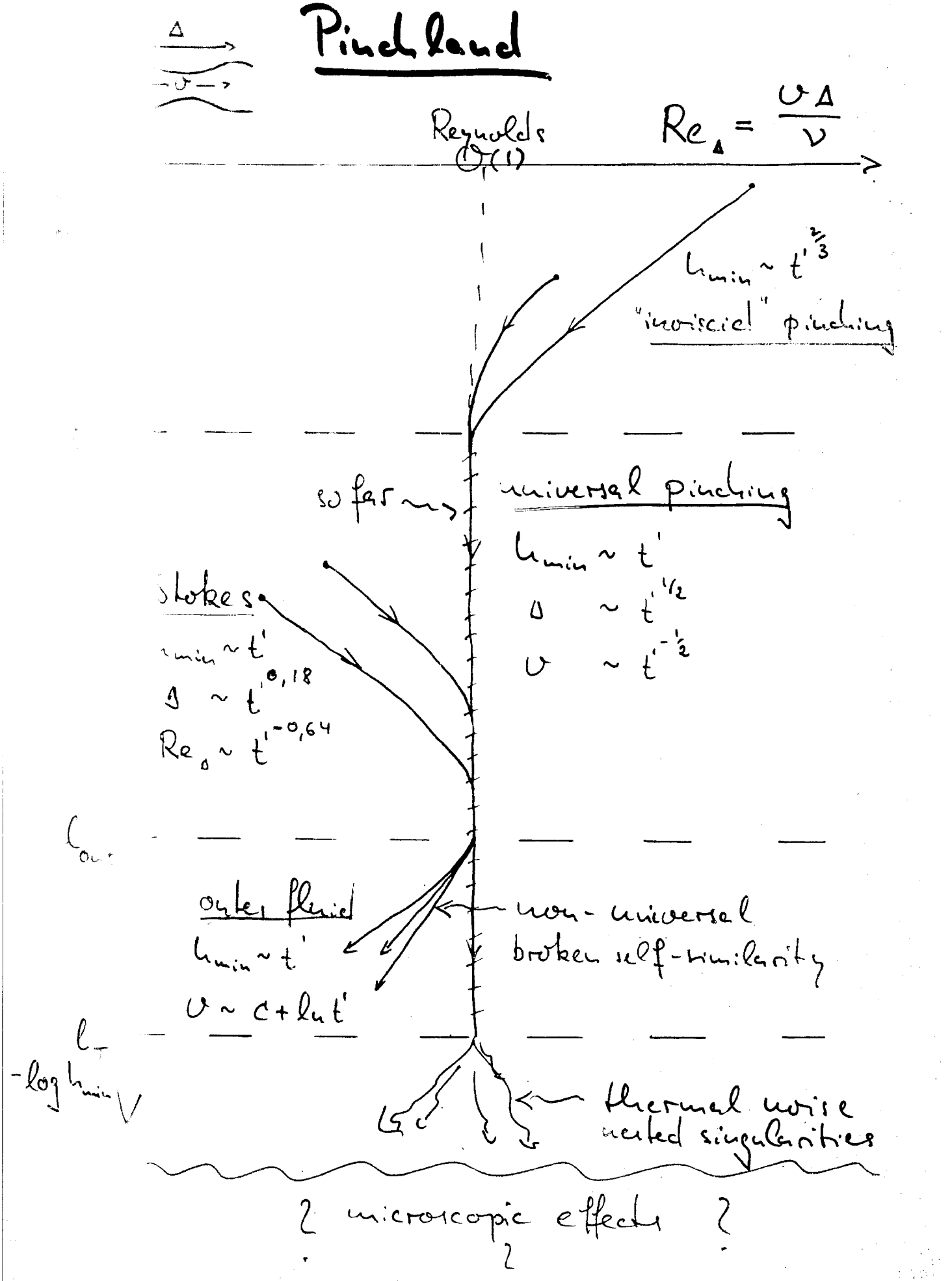
$$\phi + \xi\frac{\phi'}{2} + \psi\phi' = -\frac{\psi'}{2}\phi + O(t')$$

unique solution with $\phi(\xi) \underset{\xi\to\pm\infty}{\sim} \xi^2$

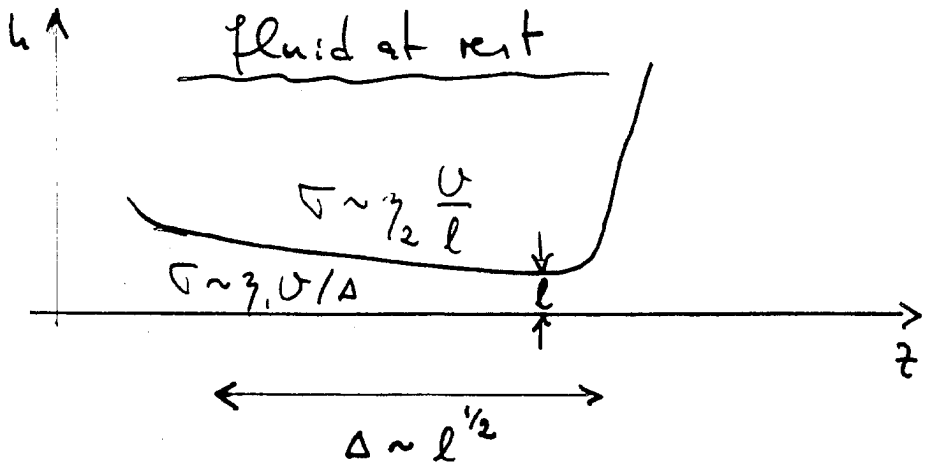
Pinching solution independent of init. cond.!



T. A. Kowalewski


Δ
-v→
Pinchland
Reynolds
$Re_\Delta = \frac{v\Delta}{\nu}$
O(1)
$h_{min} \sim t'^{2/3}$
"inviscid" pinching
so far ~>
universal pinching
$h_{min} \sim t'$
$\Delta \sim t'^{1/2}$
$v \sim t'^{-1/2}$
Stokes
$h_{min} \sim t'$
$\Delta \sim t'^{0,18}$
$Re_\Delta \sim t'^{-0,64}$
l_{out}
outer fluid
$h_{min} \sim t'$
$v \sim c + l_{out} t'$
non-universal
broken self-similarity
l_-
$-\log h_{min}$
thermal noise
nested singularities
? microscopic effects ?

Outer fluid (Cohen, Nagel, Brenner)



New scaling for $\ell \lesssim \left(\frac{\eta_2}{\eta_1}\right)^2 \ell_\nu$!

v finite, $Re = \frac{v\Delta}{\nu} \to 0$

Stokes equation $\quad \underline{\nabla} p = \eta \Delta \underline{u}$

Integral representation : $(\eta_1 = \eta_2)$

$$\underline{u}(\underline{r}_1) = -\frac{1}{8\pi} \int_S \underline{f}(\underline{r}_2) \left[\frac{\underline{I}}{r} + \frac{\underline{r} \otimes \underline{r}}{r^3} \right] d^2\sigma_2$$

$$\underline{f} = \gamma \left(\frac{1}{R_1} + \frac{1}{R_2} \right) \underline{n} = \gamma \kappa \underline{n}$$

long-ranged interaction !

Logarithmic singularities

$$\partial_t h(z,t) + v_z \partial_z h = v_r$$

$$\underline{v}^{(s)}(z,t) = -\frac{\gamma}{\eta} \int_S \mu(z') \underline{n}(z') \underline{\underline{J}}(z,z')\, dz'$$

Scaling analysis:

$$\left.\begin{aligned} h(z,t) &= t' H(\zeta) \\ v(z,t) &= V(\zeta) + b \ln t' \end{aligned}\right\} \quad \zeta = \frac{z'}{t'} + b \ln t'$$

$$V(\zeta) = -\int_{z_-/t'}^{z_+/t'} \underbrace{\mu(\zeta')\underline{n}(\zeta')\,\underline{\underline{J}}(\zeta,\zeta')}_{\sim \frac{1}{\zeta'} \text{ f. } |\zeta'| \to \infty} d\zeta' - b \ln t' \underline{e}_z$$

choose b to cancel logarithmic singularity!

$$\rightsquigarrow\ b = -\frac{1}{4}\left[\frac{S_+}{\sqrt{1+S_+^2}} + \frac{S_-}{\sqrt{1+S_-^2}}\right] \qquad H = S_\pm \zeta \quad (|\zeta| \to \infty)$$

Comparison with experiment

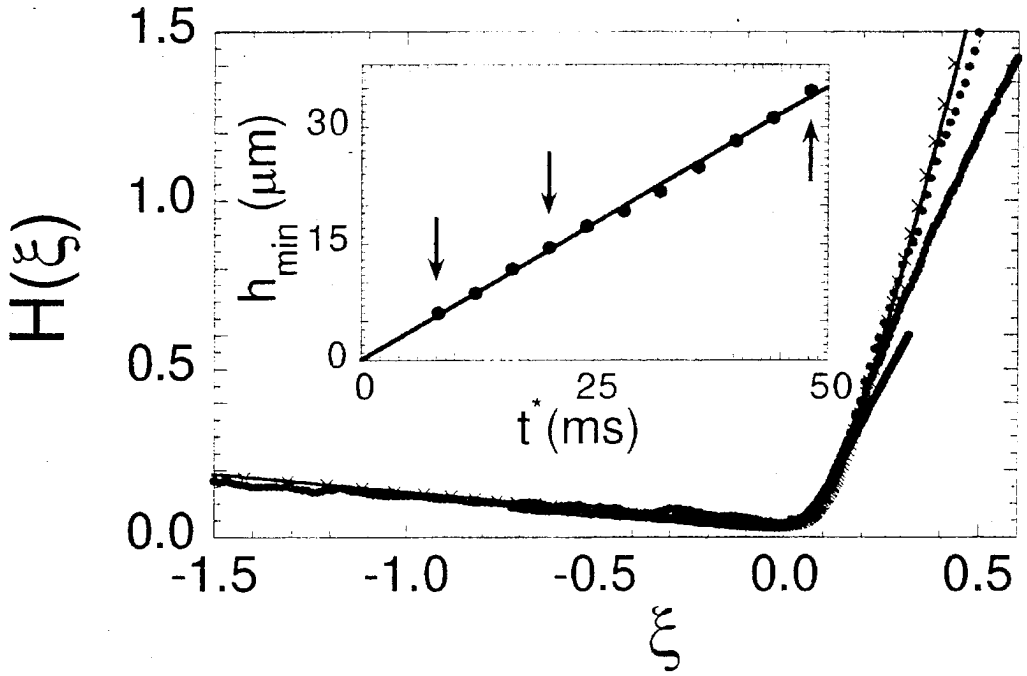


FIG. 2. The inset shows the minimum radius, $h_{min}(t)$, as a function of time for the drop shown in Fig. 1. The solid line is the theoretical prediction. The main figure shows the similarity function $H(\xi)$ as defined by (4). The dots are rescaled experimental profiles corresponding to the times indicated as arrows in the inset. The solid line is the theory, and the x's mark the final simulation profile.

$$h(z,t) = t' H\left(z'/t' + b \ln t'\right)$$

$$H_{min} = 0,0328$$

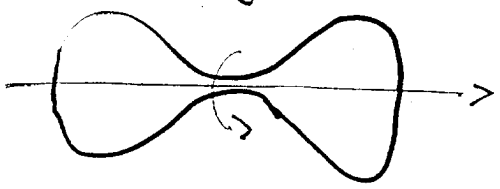
$$S_+ = 4,81$$

$$S_- = -0,105$$

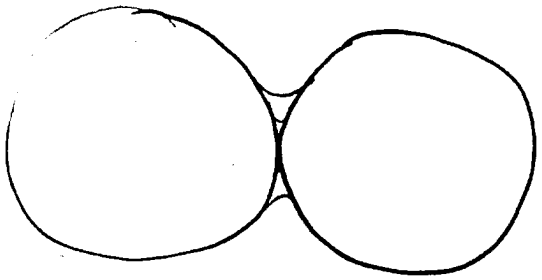
broken self-similarity ! non-universality !

Outlook

1) spinning drops

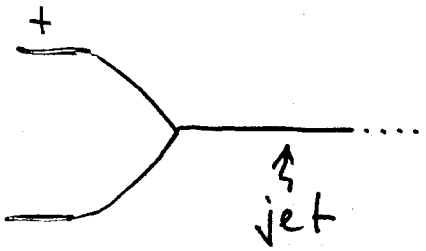


2) Coalescence



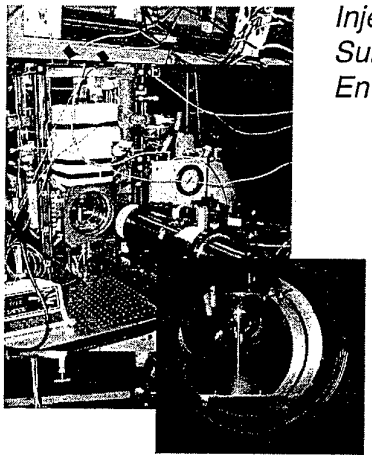
with J. Lister, H. Stone

3) Electric jets



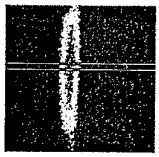


Fourth International Symposium on Liquid Space Propulsion
DLR – Lampoldshausen, Germany
March 13 - 15, 2000

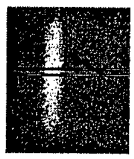


Injection of Cryogenic Jets into Subcritical and Supercritical Environments: Raman Measurements

B. Chehroudi, A. Badakshan, R. Cohn, and D. Talley



Subcritical N_2 Jet



Supercritical N_2 Jet

Objectives

AFRL

Overall

- Determine the mechanisms which control the breakup, transport, mixing, and combustion of sub- and super-critical droplets, jets, and sprays.

This Presentation

- Determine the structure of subcritical and supercritical cryogenic jets using quantitative Raman imaging.

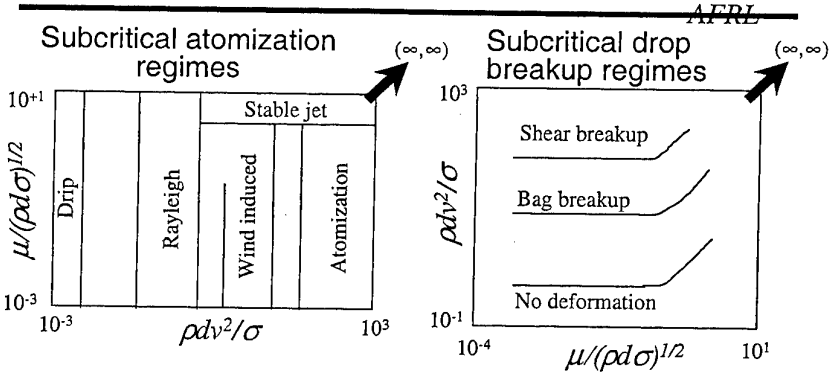
Background

AFRL

- In engines having chamber pressures exceeding the critical pressure *(SSME, Vulcain, etc.)*, the distinct difference between a "gas" and a "liquid" disappears.
- The resulting flows are influenced by factors not present in conventional sprays:
  - Vanishing surface tension and enthalpy of vaporization.
  - Equivalent gas and liquid phase densities.
  - Strongly enhanced gas / liquid solubility.
  - Liquid-like gas phase diffusivity.
  - Mixing induced critical point variations.
  - Enhanced gas phase unsteadiness.
- *Unknowns contribute to potentially large uncertainties in making design predictions.*

Background (2)

AFRL



Surface tension σ vanishes at supercritical conditions. Conventional atomization and breakup parameters become *infinite*, where no data exists.

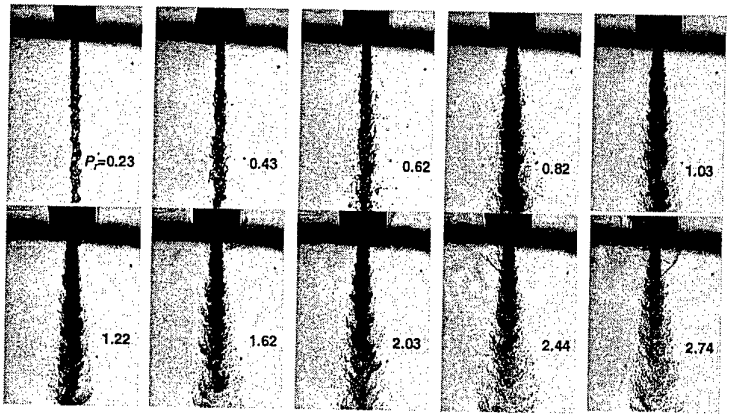
Supercritical atomization and breakup regimes are largely unknown

Shadowgraph Results - N_2 into N_2

AFRL

P_{cr} = 3.39 MPa T_{amb} = 300 K Re = 25,000- 75,000

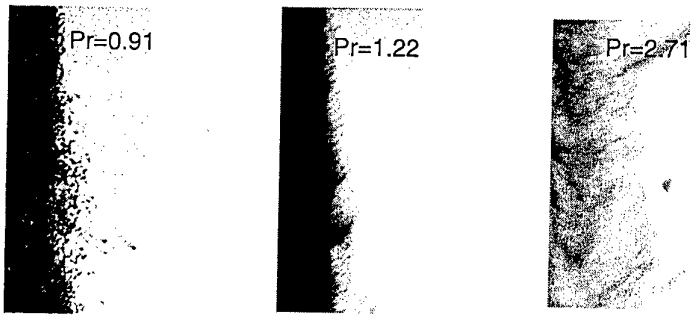
T_{cr} = 126 K T_{inj} = 99-120 K V_{inj} = 10-15 m/s



Mixing Layer Structure - N_2 into N_2

AFRL

P_{cr} = 3.39 Mpa, T_{cr} = 126 K, T_{inj} = 128 K, T_{amb} = 300 K



Low Pres. Subcritical Droplets

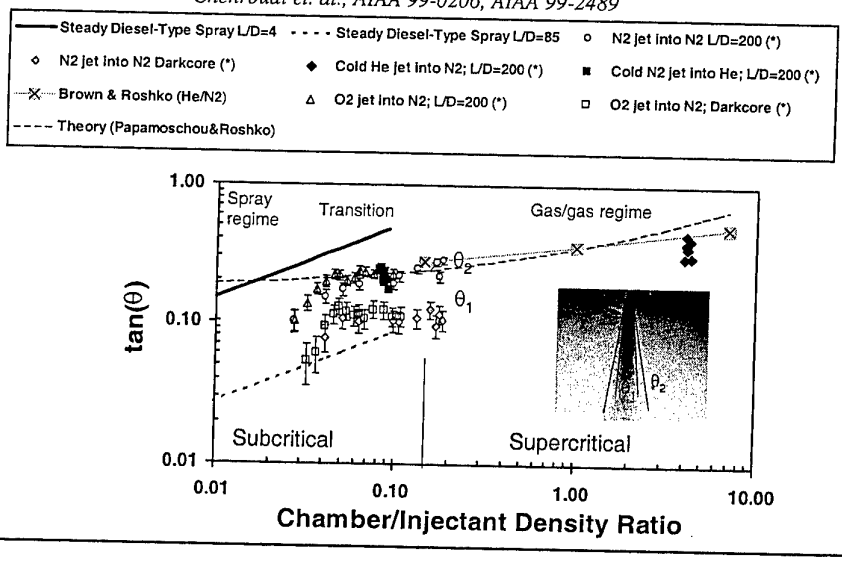
Mod. Pres. Supercritical Transition

High Pres. Supercritical Gas layers

Jet Spreading Angles

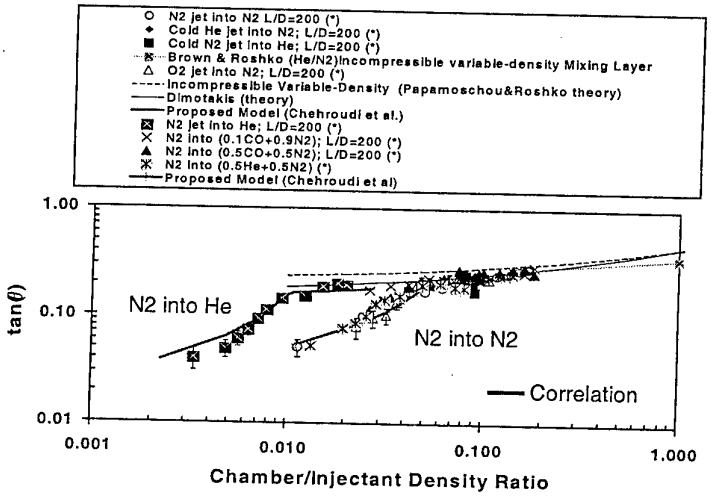
AFRL

Chehroudi et. al., AIAA 99-0206, AIAA 99-2489



Empirical Correlation

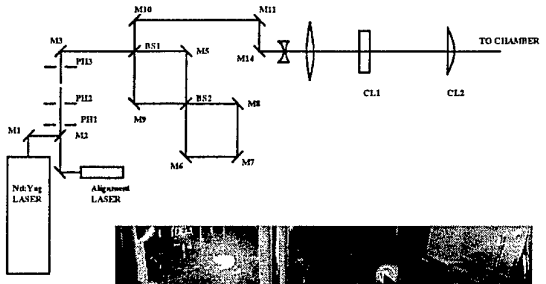
AFRL

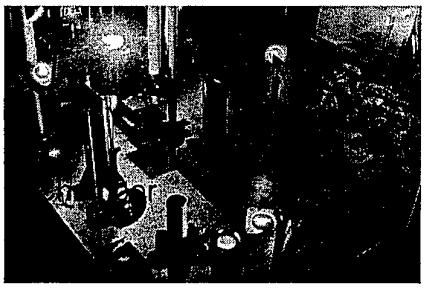


Raman Imaging Approach

AFRL

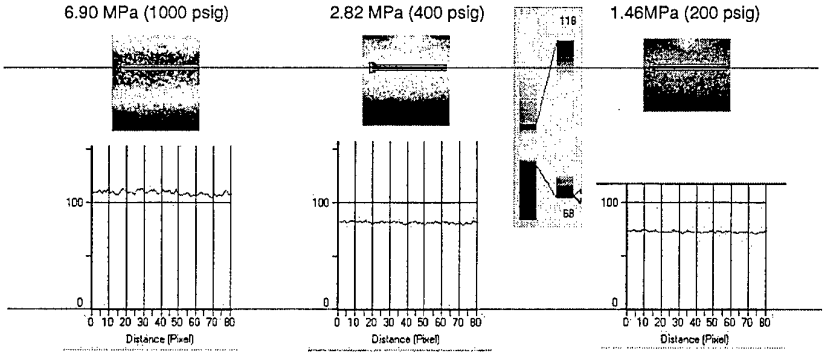
- Nd-Yag laser in 2nd harmonic at 532 nm produces Raman signal at 607 nm.
- Double loop optical delay to extend pulse from 10 ns to 30 ns.
- Notch filter at 532 nm, plus band pass and hi-pass filters.
- Princeton Instruments N_2 cooled ICCD camera
- Sheet forming optics to various sheet widths.
- Average data for 4 center lines, over 40 shots.





Results in Isothermal N_2 at 273 K

AFRL

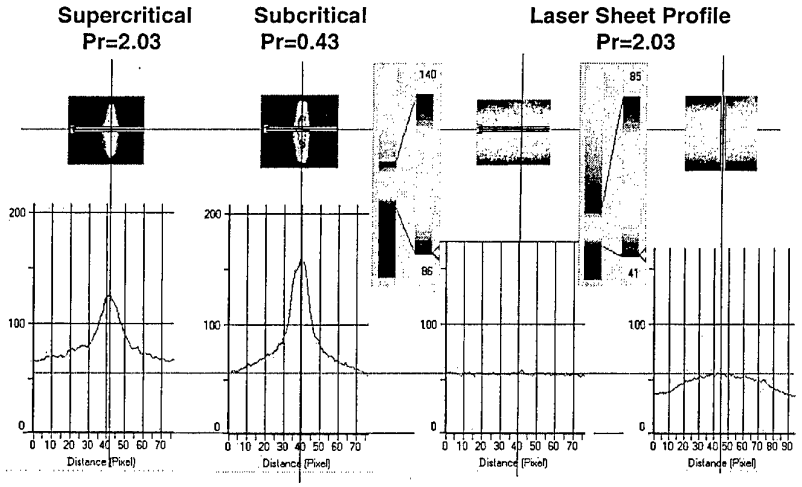


Chamber Pressure Mpa	Density Ratio Based on P-Measurement & Ideal Gas Nitrogen	Dark-background-corrected Camera-measured Intensity Ratio Nitrogen
6.90	4.73	4.78
2.82	1.93	1.89
1.46	1.00	1.00

2-D Raman Images, N_2 into N_2

AFRL

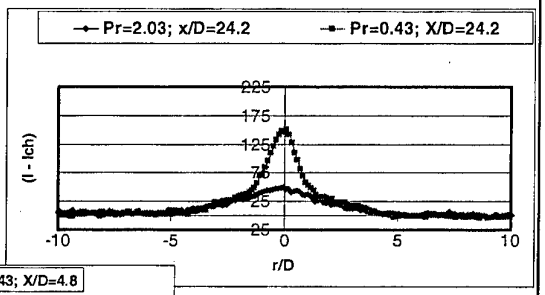
Re= 12,000 to 35,000; X/D = 2.44; sheet center

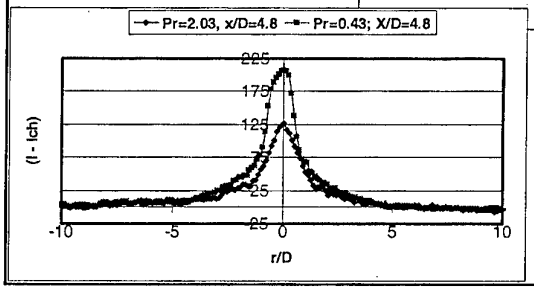


Intensity Defect vs Normalized Radius

AFRL

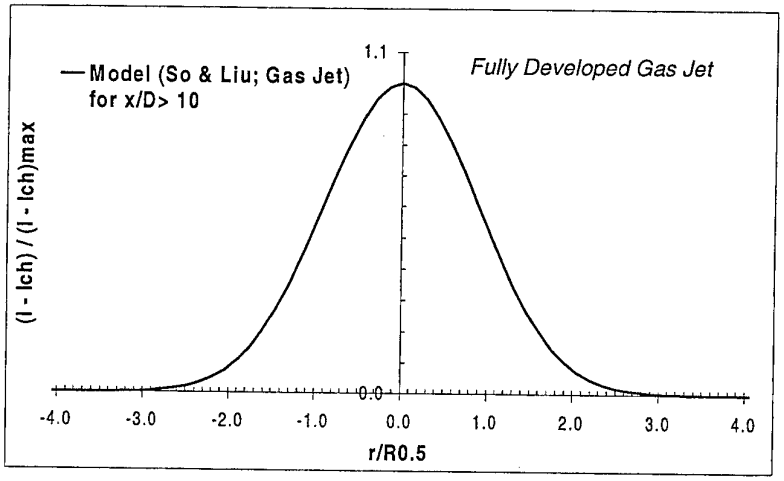
N_2 into N_2





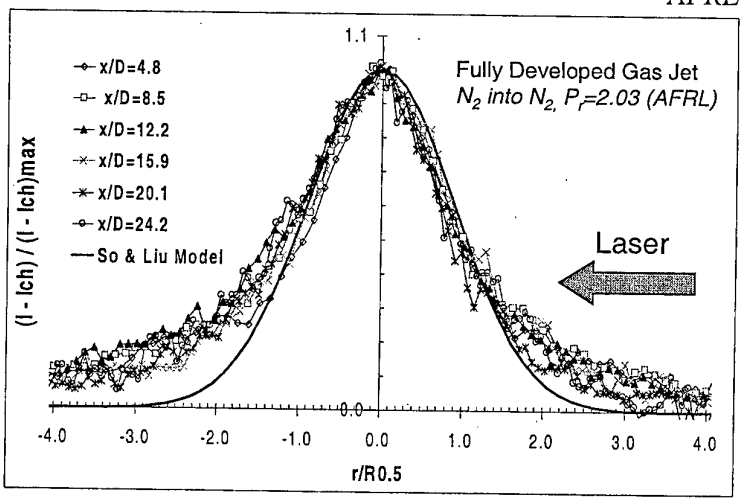
Normalized Intensity Defect Plot: Reference Case

AFRL



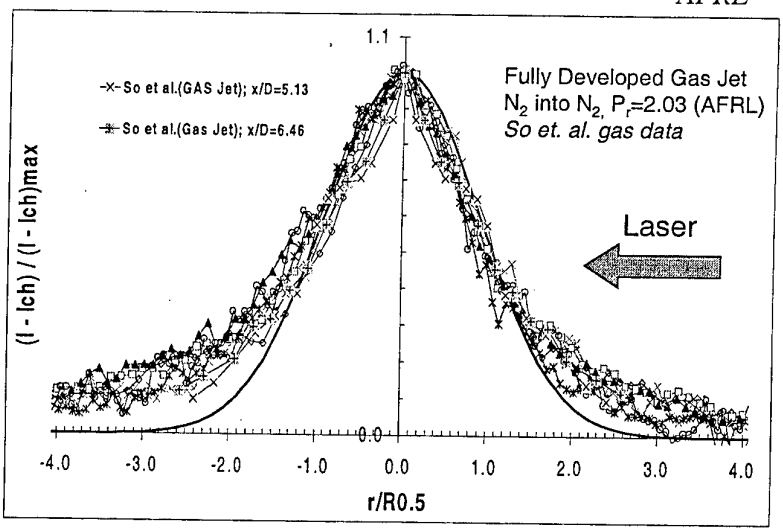
Normalized Intensity Defect Plot: Supercritical Regime

AFRL



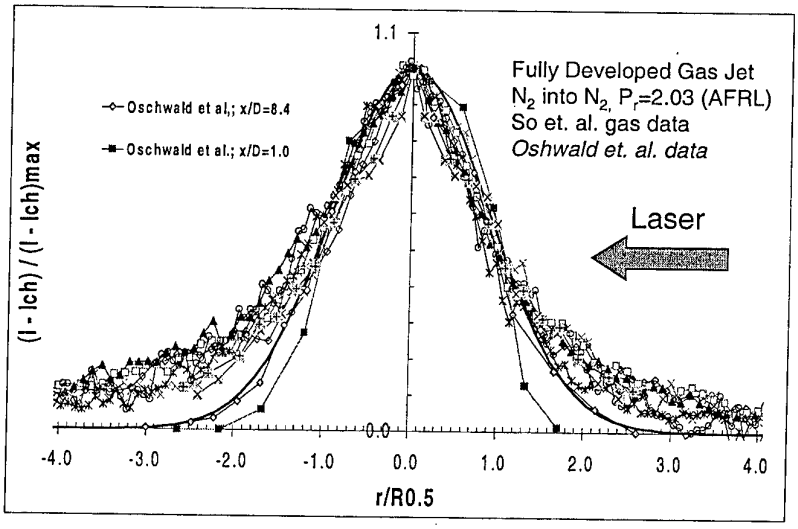
Normalized Intensity Defect Plot: Supercritical Regime (2)

AFRL



Normalized Intensity Defect Plot: Supercritical Regime (3)

AFRL



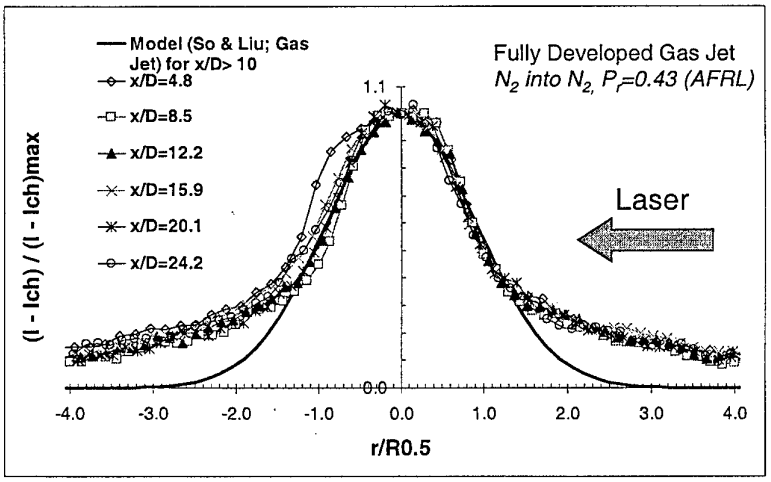
Normalized Intensity Defect Plot: Supercritical Regime (4)

AFRL

	X/D	Pch	Pr	Inj. Temp	Inj. Vel	Re	Inj/Cham
		MPa		K	m/s		density ratio
Oschwald et al.	1.0	4.0	1.2	140	5.0	115000	3.3
Oschwald et al.	8.4	4.0	1.2	118	5.0	126000	12.5
Chehroudi et al.	4.8 to 24.4	6.9	2.0	95	8.0	35000	7.1
Chehroudi et al.	4.8 to 24.4	1.5	0.4	110	8.0	12000	40.6
So et. al.	5.13	.1			11.16	4300	.64
So et. al.	6.46	.1			11.16	4300	.64

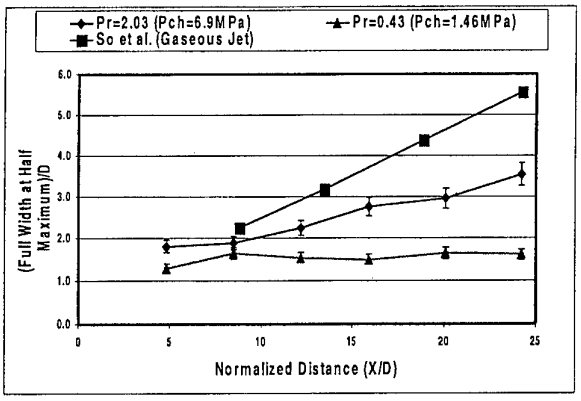
Normalized Intensity Defect Plot: Subcritical Regime

AFRL



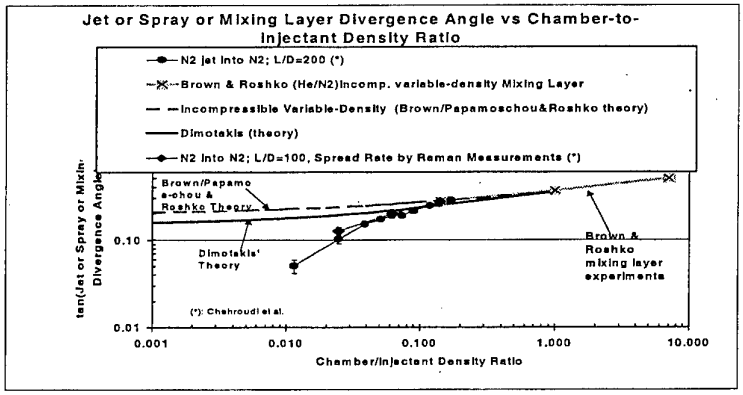
Growth Rates

AFRL



Comparison of Shadowgraph Measurements with Raman Measurements

AFRL



- Setting $\theta = 2 \times$ FWHM produces agreement with shadowgraph measurements.
  - Consistent with the observations of Brown and Roshko

Summary & Conclusions

AFRL

- Measurement system integrity has been established by performing Raman measurements of isothermal N_2 at different pressures.
- Measurements were constrained to the near-field in order to maintain large Froude numbers (minimize buoyancy).
- Growth rates measured from Raman profiles measured at 2 x FWHM point agree well with shadowgraph measurements.
  - Brown and Roshko observed a similar result at similar points in the distribution for gas jets at near unity density ratio.
- To within experimental error, the near-field plots appear to reduce to self-similar shapes for both the supercritical and subcritical cases.
  - Not the same profile as for fully developed turbulent gas jets.
- The near-field supercritical profile more closely approaches that of fully developed turbulent gas jets than the near-field subcritical profile.

Future

AFRL

- Complete N_2-into-N_2 analysis.
- Reduce and analyzise N_2-into-N_2/He data.

"Hot-Fire Studies of LOX Primary Atomization from Rocket Engine Coaxial Injectors"

Y. Boniface, A.B. Reeb, R.D. Woodward, S. Pal, and R.J. Santoro

Propulsion Engineering Research Center
and
Department of Mechanical and Nuclear Engineering
The Pennsylvania State University

and

W. Mayer

Deutsche Forschungsanstalt für Luft- und Raumfahrt e.V. (DLR)
Lampoldshausen, Germany

Outline

I. Introduction

II. Experiment Description

- Cryogenic Combustion Laboratory
- Rocket Chambers
- Shadowgraph Diagnostic
- Experimental Conditions

III. Results and Discussion

- Dense Core Length
- Near-Injector Characterization
- Mid-Core Region
- Fragmentation Region
- Interaction Flame-Dense Core

IV. Conclusions

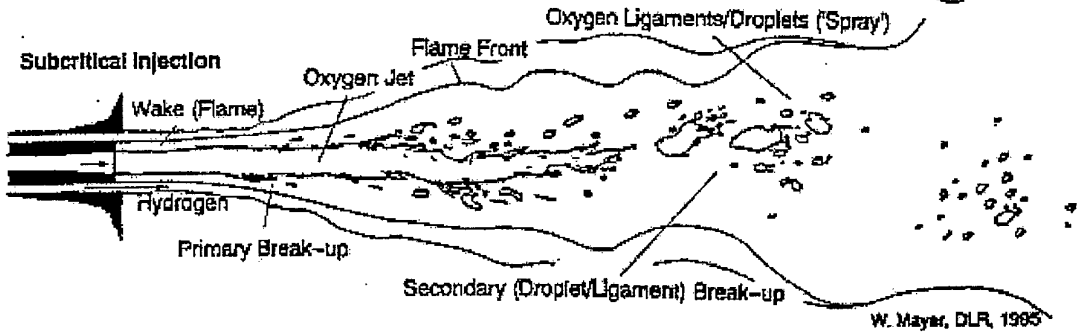
V. Ideas for Future Experiments

Introduction (1)

◆ Fundamental jet breakup research:

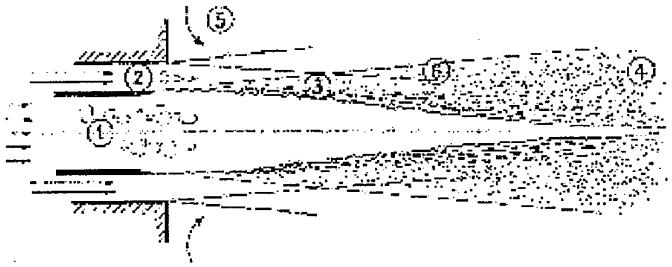
⇒ Large amplitude helical waves can be responsible for high Reynolds number jet disintegration.

Batchelor and Gill (1962), Hoyt and Taylor (1977), Andrews (1993).



⇒ Nevertheless, intense shearing action of the high velocity annular gas jet could prevent the large amplitude wave mode of fragmentation.

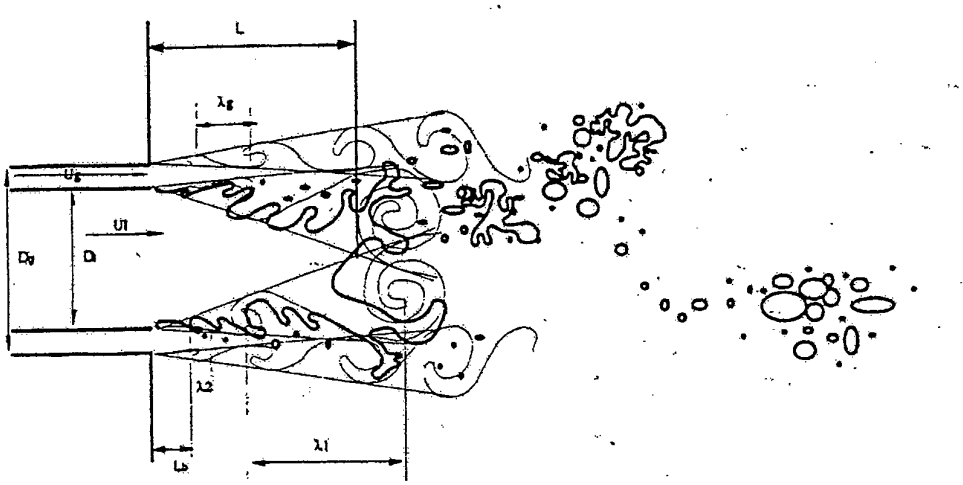
Chuech et al. (1991).



W. Mayer and G. Krülle, DLR, 1994

Introduction (2)

$\Rightarrow$ Dense Core Length Depends on the Regime of Atomization.
High Velocity Ratio (e.g. 200) and High Momentum Flux Ratio (e.g. 40)
Have Been Observed to Disintegrate the Core Rapidly.



Lasheras and Hopfinger, 2000

Introduction (3)

- Numerical models of LOX atomization:

  ⇒ *Sutton et al (1974), Chuech et al (1991):*
  Droplet aerodynamic stripping occurs until the LOX jet is consumed, creating a narrowing LOX core and expanding spray field.

- Hot-fire results:

  ⇒ *Woodward (1993), Beisler et al. (1994), Mayer and Tamura (1995):*
  Large oscillation waves dominate the atomization process.

  ⇒ *Herding et al. (1996):*
  Droplet stripping rules the atomization process.

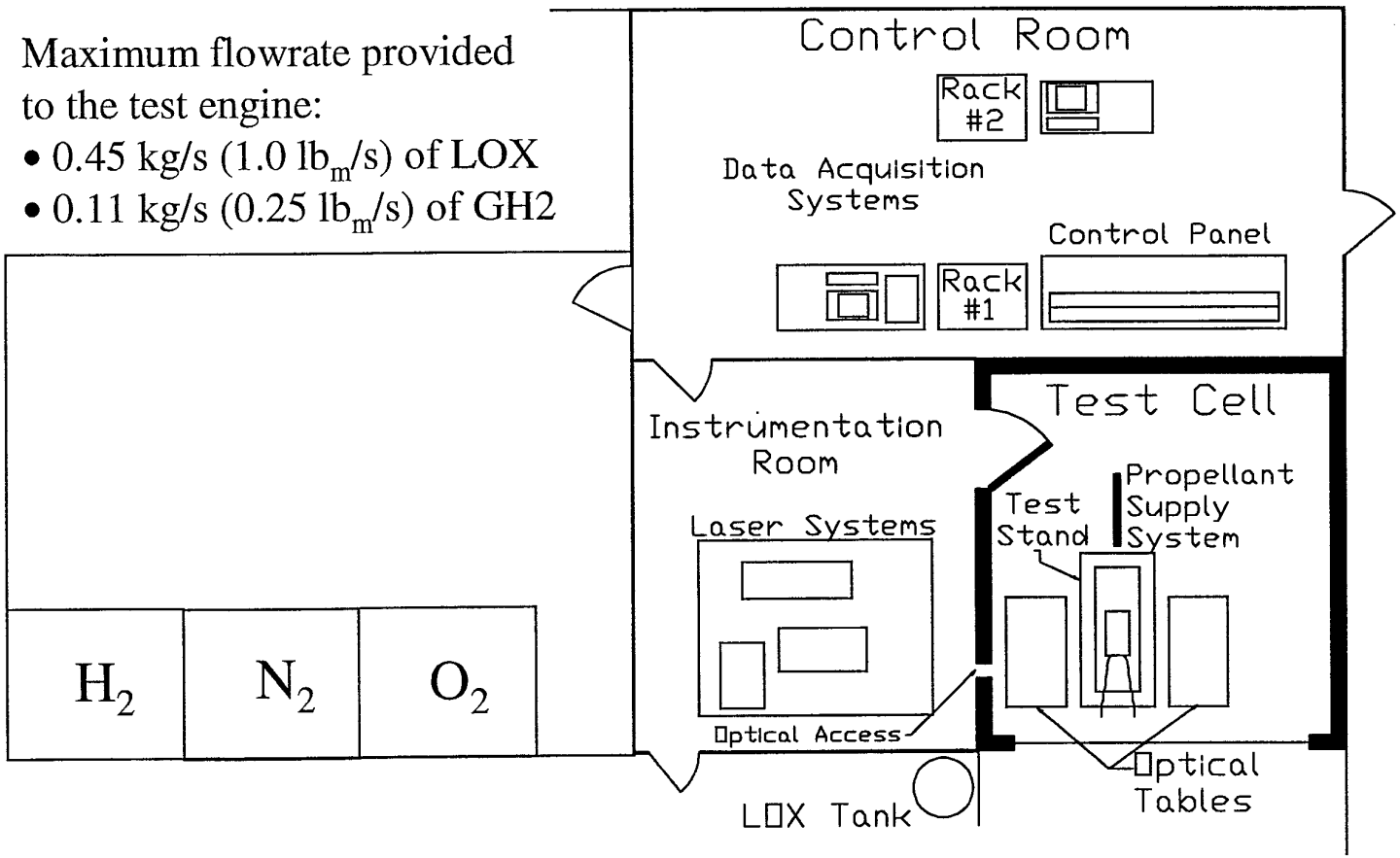
Motivation

- Study the Influence of the Chamber Mach Number on the Atomization Process Under Hot-Fire Test Conditions for Single-Element Coaxial Injectors.
- Evaluate the Effects of Momentum Flux Ratio Variation.
- Examine the Effect of Chamber Pressure on Jet Breakup Mechanisms.
- Study the Flame-Dense Core Interaction.
- Give a Realistic Description of the LOX/GH2 Injection Phenomena in a "Typical" Rocket Engine. (subcritical)

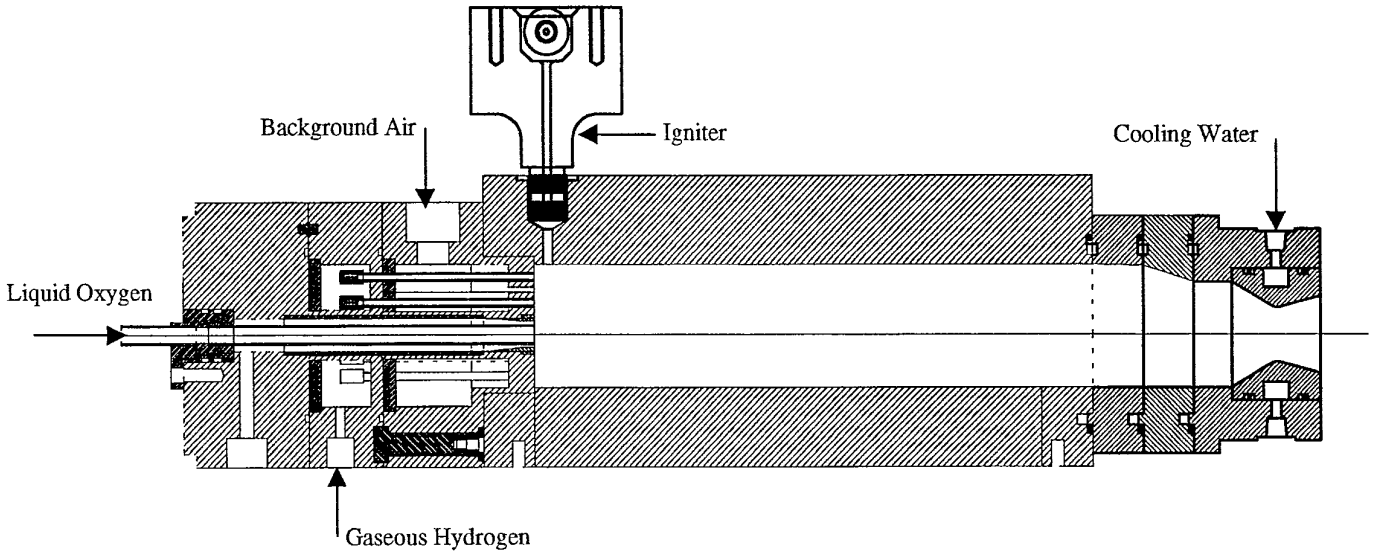
Cryogenic Combustion Laboratory Top View

Maximum flowrate provided to the test engine:

- 0.45 kg/s (1.0 lb_m/s) of LOX
- 0.11 kg/s (0.25 lb_m/s) of GH2



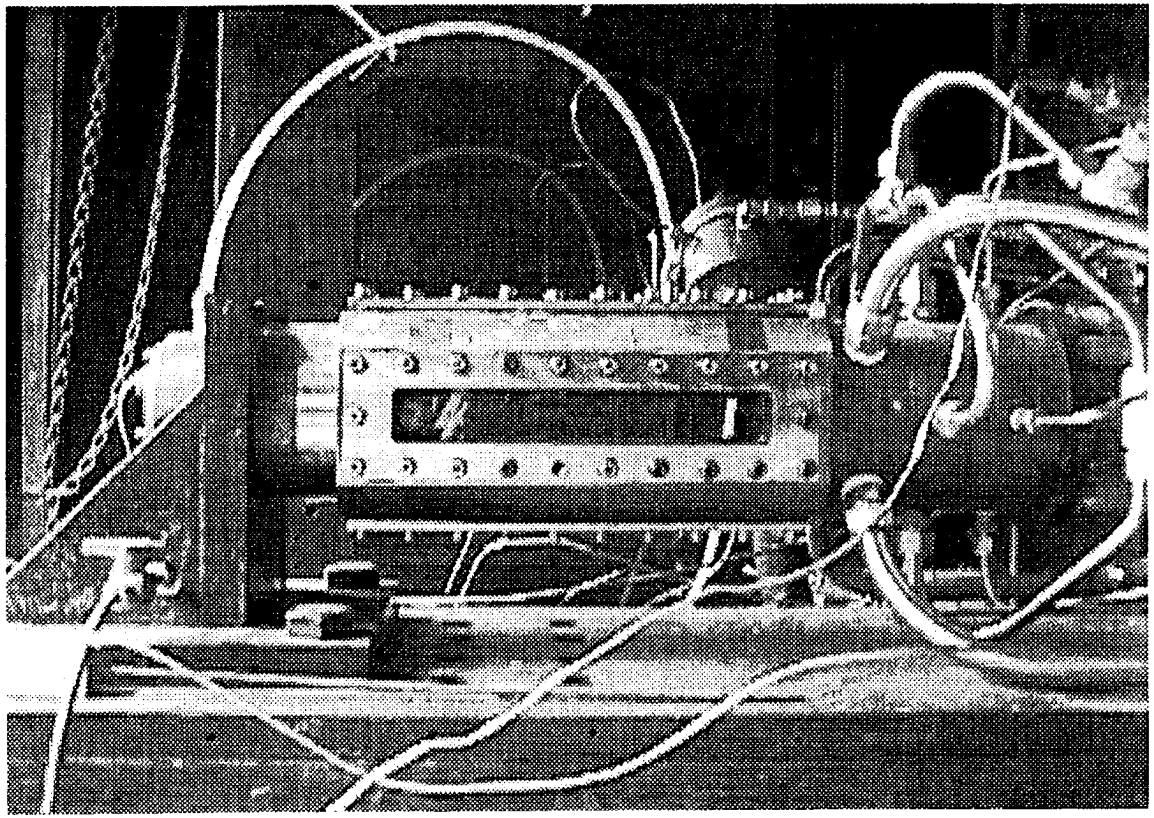
Engine Used to Conduct the Mach = 0.3 Experiments



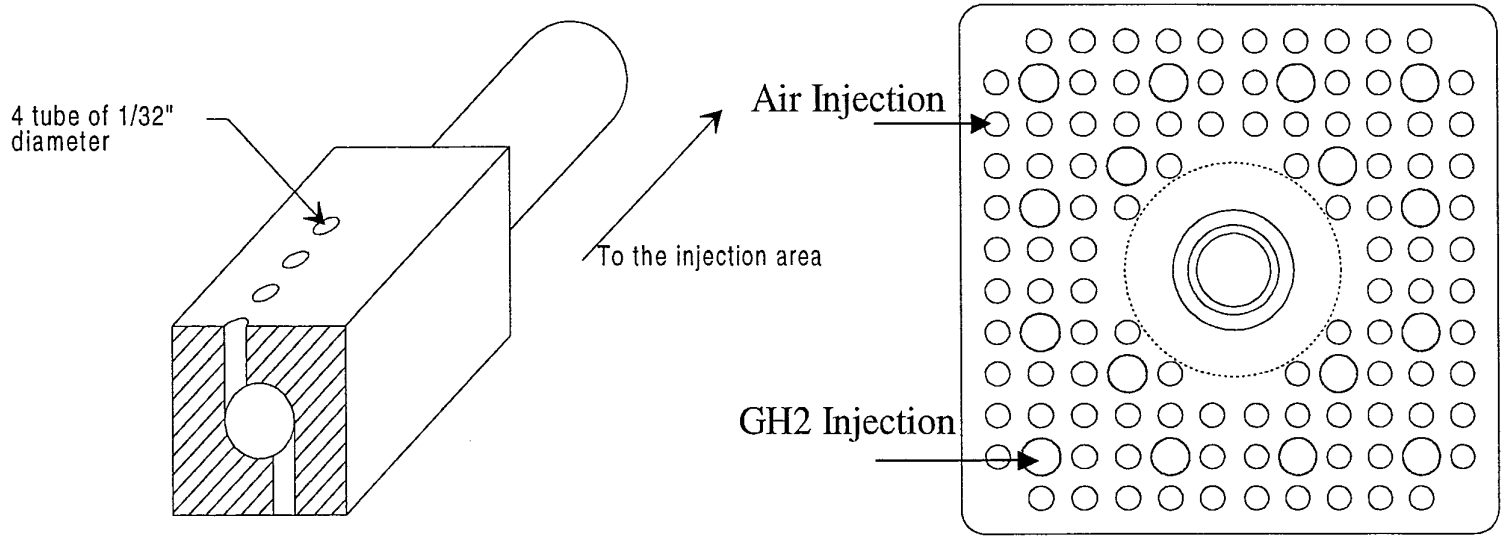
Injector Geometry	
LOX Tube Inner Diameter	3.43 mm (0.135 in)
GH_2 Annulus Inner Diameter	4.19 mm (0.165 in)
GH_2 Annulus Outer Diameter	7.11 mm (0.280 in)

Chamber Properties	
Chamber Pressure	1.22 MPa (180 psi)
Chamber Length	371.1 mm (14.6 in.)
Chamber Cross Section	51mm x 51mm (2in x 2in)
Throat Diameter	39.6mm (1.6 in)

High Mach Rocket Engine at the Cryogenic Laboratory



Injector Head of the High Mach Number Rocket Engine

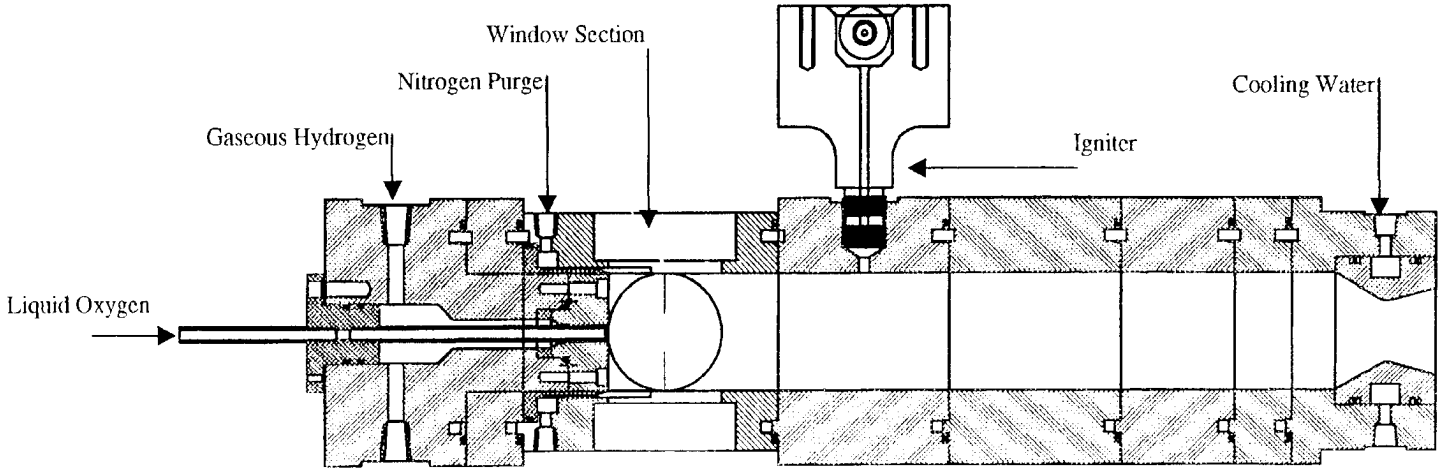


Swirl Injector for GH2 Background Injection

End View of the Injector Face

Injector Face Characteristics	
LOX Tube Inner Diameter	3.43 mm (0.135 in)
GH2 Annulus Inner Diameter	4.19 mm (0.165 in)
GH2 Annulus Outer Diameter	7.11 mm (0.280 in)
GH2 Swirl Injector Diameter	2.54 mm (0.100 in)
Air Tube Diameter	2.54 mm (0.100 in)

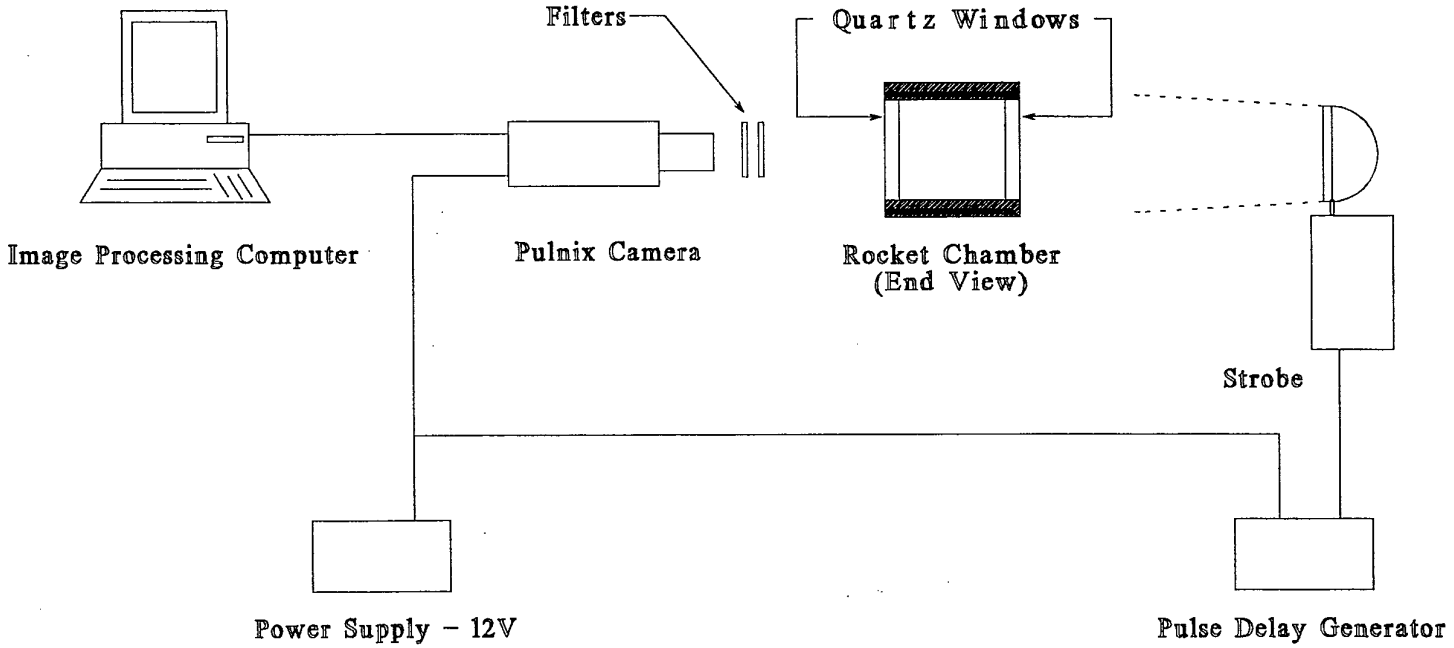
Single Element Rocket Engine
Used for Low Mach Number Experiments



Injector Geometry	
LOX Tube Inner Diameter	3.43 mm (0.135 in)
GH_2 Annulus Inner Diameter	4.19 mm (0.165 in)
GH_2 Annulus Outer Diameter	7.11 mm (0.280 in)

Chamber Properties	Higher Pc	Lower Pc
Chamber Pressure	2.99 Mpa (440 psi)	1.77 MPa (260 psi)
Chamber Length	345.6 mm (13.6 in.)	345.6 mm (13.6 in.)
Chamber Cross Section	51mm x 51mm (2in x 2in)	51mm x 51mm (2in x 2in)
Throat Diameter	13.7 mm (0.538 in)	18.3 mm (0.722 in)

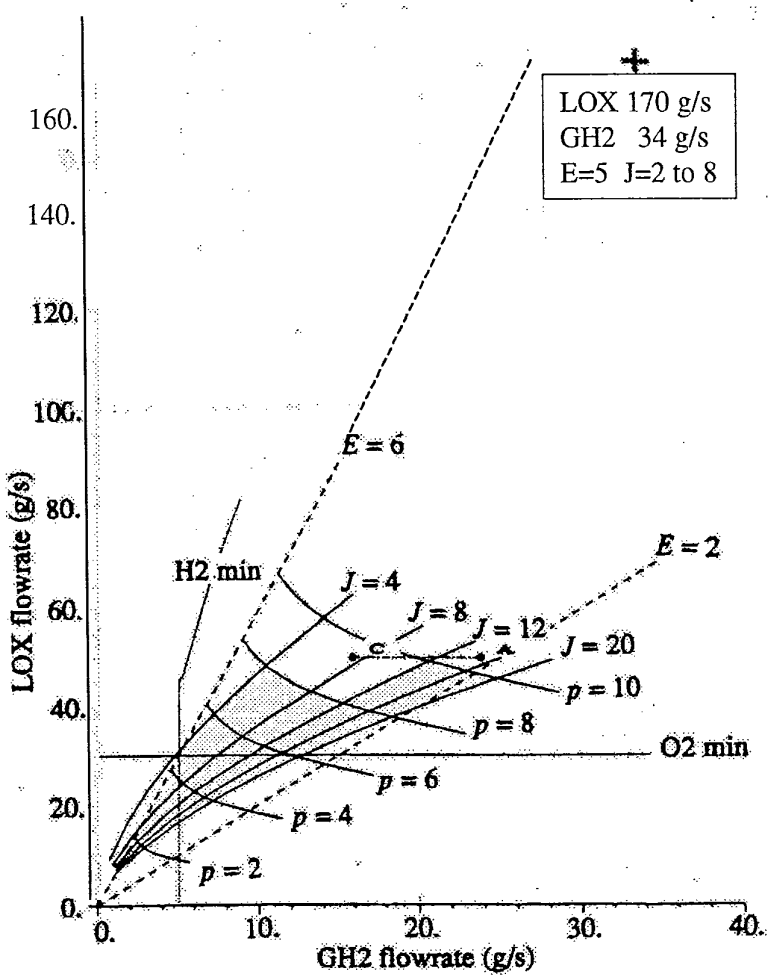
Image Acquisition Setup



Run Conditions

	Mach = 0.3 Testing, J=4.85	Mach = 0.3 Testing, J=8.00	Mach = 0.026, Higher P_c	Mach = 0.061, Lower P_c
Oxidizer Properties				
LOX Mass Flow Rate	0.17 kg/s (0.375 lb_m/s)	0.17 kg/s (0.375 lb_m/s)	0.17 kg/s (0.375 lb_m/s)	0.17 kg/s (0.375 lb_m/s)
Background Air Mass Flow Rate	0.93 kg/s (2.05 lb_m/s)	0.93 kg/s (2.05 lb_m/s)	N/A	N/A
LOX Temperature	122 K (-240 °F)	122 K (-240 °F)	122 K (-240 °F)	122 K (-240 °F)
LOX Velocity	19.1 m/s (63 ft/s)	19.1 m/s (63 ft/s)	18.9 m/s (62 ft/s)	19.0 m/s (62 ft/s)
Fuel Properties				
Hydrogen Mass Flow Rate	0.034 kg/s (0.075 lb_m/s)	0.034 kg/s (0.075 lb_m/s)	0.034 kg/s (0.075 lb_m/s)	0.034 kg/s (0.075 lb_m/s)
Background GH_2 Mass Flow Rate	0.009 kg/s (0.020 lb_m/s)	0.009 kg/s (0.020 lb_m/s)	N/A	N/A
Nitrogen Mass Flow Rate	N/A	0.020 kg/s (0.044 lb_m/s)	N/A	N/A
Hydrogen Temperature	298 K (77 °F)	298 K (77 °F)	298 K (77 °F)	298 K (77 °F)
Hydrogen Velocity	1312.5 m/s (4305 ft/s)	1312.5 m/s (4305 ft/s)	542.2 m/s (1778 ft/s)	913.0 m/s (2994 ft/s)
Non-dimensional Parameters				
Main Propellant Mixture O/F	5.0	3.2	5.0	5.0
Total Propellant Mixture O/F	25.9	17.5	5.0	5.0
Main Injection Velocity F/O	68.07	70.9	18.88	19.01
Main Propllt Momentum Flux F/O	4.85	8	2.01	3.37
LOX Reynolds Number	6.66E+05	6.66E+05	6.42E+05	6.58E+05
LOX Weber Number	1.02E+06	1.58E+06	4.05E+05	6.96E+05

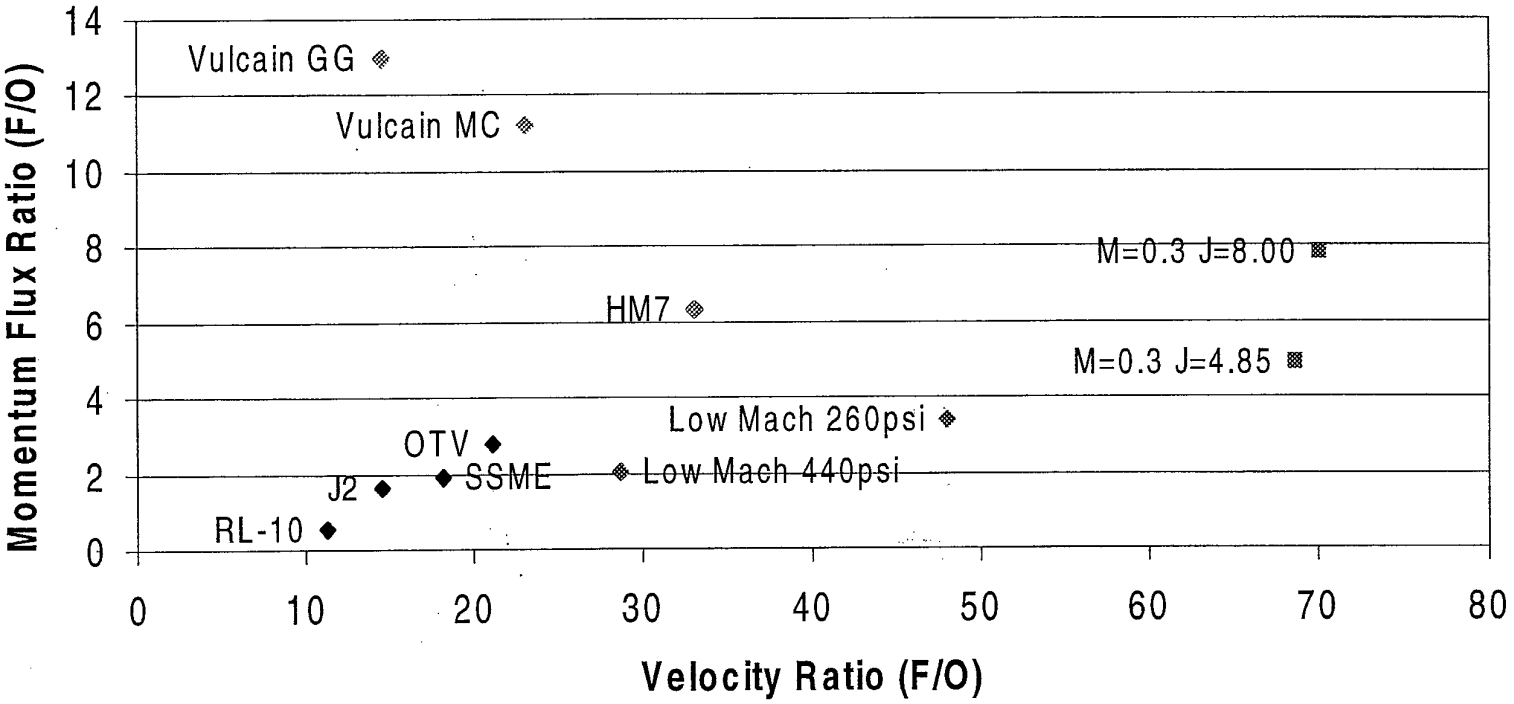
Comparison of run conditions



E: Mixture Ratio O/F
J: Momentum Flux Ratio F/O

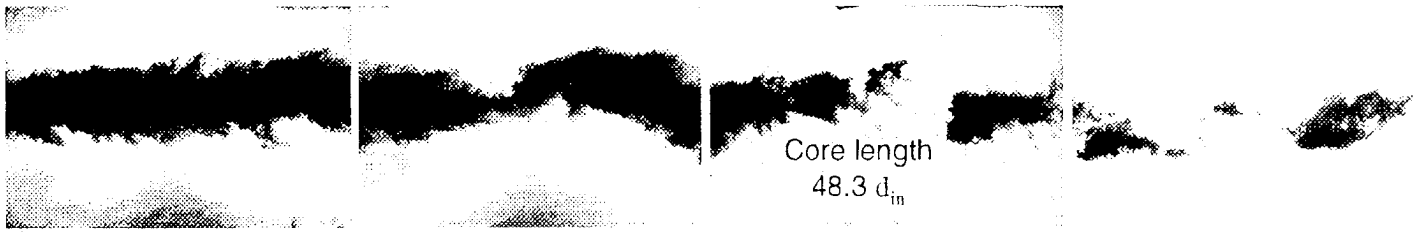
Adapted from
Candel et al. 1998

Comparison of Different Rocket Engine Operating Conditions with Cryo Lab Run Characteristics



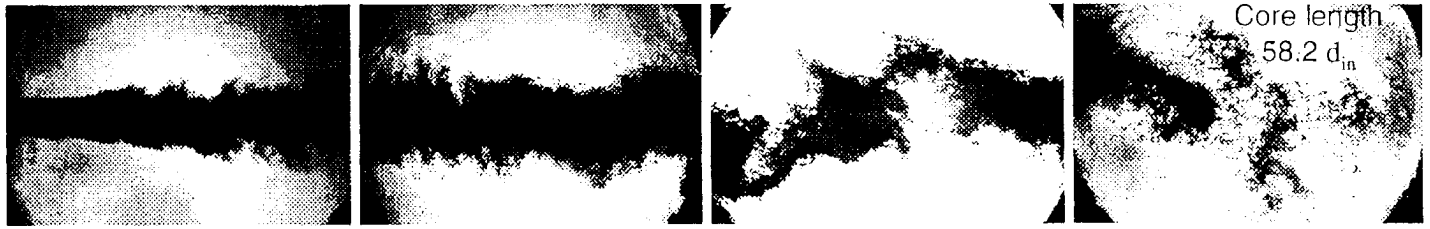
Dense core downstream from the injector
Influence of the chamber Mach number and chamber pressure

1.22MPa - M=0.3 → 51 mm Field of View

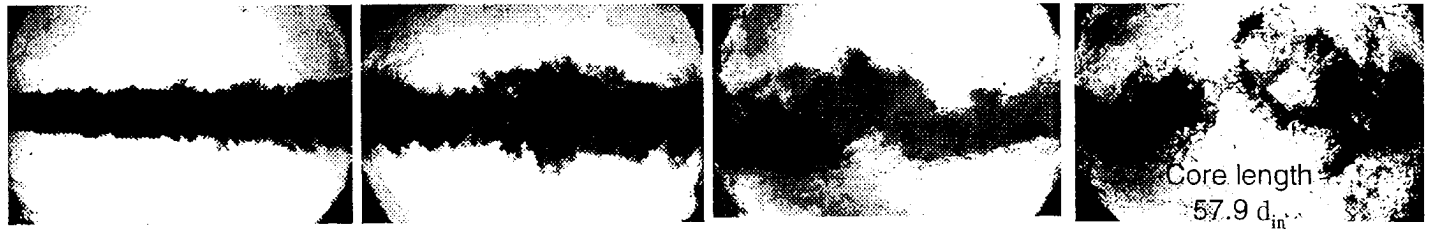


11 d_{in} 37 d_{in} 45 d_{in} 52 d_{in}

1.77MPa - Low Mach →



2.99MPa - Low Mach →



7 d_{in} 22 d_{in} 45 d_{in} 60 d_{in}

Core Length Calculations Results

	High Mach			Low Mach		
	J=4.85	J=8.00	average both conditions	1.77 MPa	2.99 MPa	average both conditions
L/d	44.9	42.2	**44.2**	**55.1**	**59.8**	56.9
Conf. Int. 95%	0.96	2.48	0.97	3.73	2.61	2.52
Number of measurements	38	13	51	12	8	20
Breakup out of Field of View				15>52 9<52 1>67	15>52 1<52 6>67	

Existing Correlations* for Core Length (L_b/D)

	Results for Hot-Fire Conditions of This Study			
	High Mach J=4.85	High Mach J=8.0	Low Mach P=2.99MPa	Low Mach P=1.77Mpa
Measured Value	**44.9**	**42.2**	**59.8**	**55.1**
Woodward (1993) $0.0025\left(\frac{\rho_g}{\rho_\ell}\right)^{-0.44} Re_D^{0.76} We_g^{-0.22}$	**65.8**	**48.4**	**53.5**	**60.6**
Chigier & Eroglu (1991) $0.66 Re_D^{0.6} We_g^{-0.4}$	**8.1**	**6.8**	**11.5**	**9.4**
Rehab et al. (1997) $\frac{6}{\sqrt{J}}\left(\left\|1-\frac{U_\ell}{U_g}\right\|\right)^{-1}$	**2.7**	**2.2**	**4.3**	**3.3**
Raynal et al. (1997) $\frac{6}{\sqrt{J}}\left(\left\|1-\frac{0.001\sigma}{\mu_g U_g}\right\|\right)^{-1/2}$	**2.7**	**2.2**	**4.2**	**3.2**

* All are based on cold-flow experiments

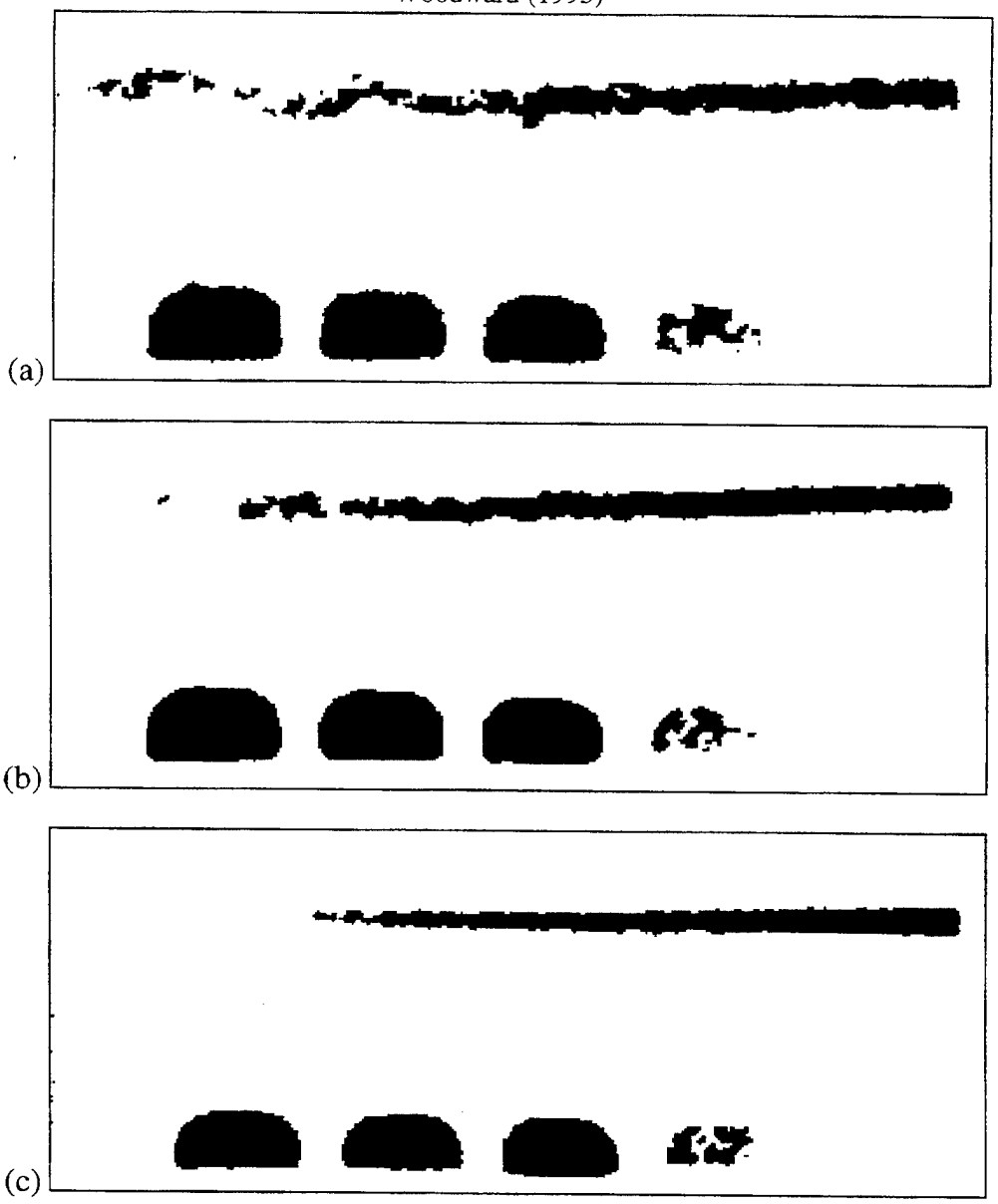
Existing Correlations* for Core Length (L_b/D)

	Results Using Bulk Chamber U_g and ρ_g from CEA Code Analysis			
	High Mach	High Mach	Low Mach	Low Mach
	J=0.37	0.37	0.012	0.022
	We_g=6.9x10^4	6.9x10^4	1.1x10^3	3.0x10^3
Measured Value	**44.9**	**42.2**	**59.8**	**55.1**
Woodward (1993)				
$0.0025\left(\frac{\rho_g}{\rho_\ell}\right)^{-0.44} Re_D^{0.76} We_g^{-0.22}$	**105.7**	**103.2**	**259.5**	**264.7**
Chigier & Eroglu (1991)				
$0.66 Re_D^{0.6} We_g^{-0.4}$	**23.9**	**23.9**	**124.1**	**83.4**
Rehab et al. (1997)				
$\frac{6}{\sqrt{J}}\left(\left\|1-\frac{U_\ell}{U_g}\right\|\right)^{-1}$	**10.5**	**10.5**	**83.9**	**50.3**
Raynal et al. (1997)				
$\frac{6}{\sqrt{J}}\left(\left\|1-\frac{0.001\sigma}{\mu_g U_g}\right\|\right)^{-1/2}$	**9.9**	**9.9**	**56.0**	**40.9**

* All are based on cold-flow experiments

X-Ray Radiography of Cold-Flow Aqueous KI Solution

Woodward (1993)



Threshold technique for determining intact core applied to different types of radiographic images at same flow conditions:

(a) single instantaneous image
(b) image that is average of 10 instantaneous images
(c) single time-averaged (ungated) video image

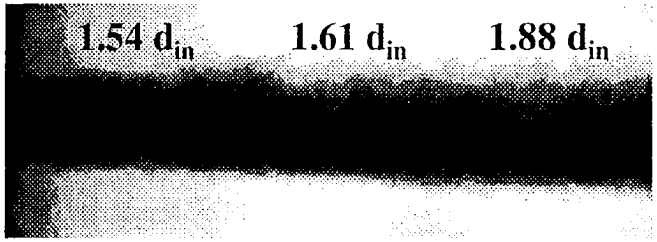
$$U_l = 15\text{m/s},\ U_g = 95\text{m/s},\ P = 10\text{ atm}$$

$$Re_D \approx 1\text{x}10^5,\ We_g \approx 5\text{x}10^3,\ L_b/D \approx 22$$

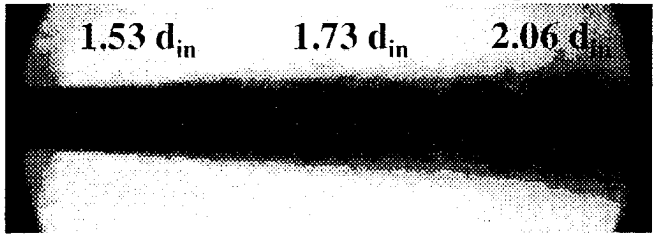
Dense Core Diameter on Averaged Pictures

7 d_{in} location - 51 mm Field of View

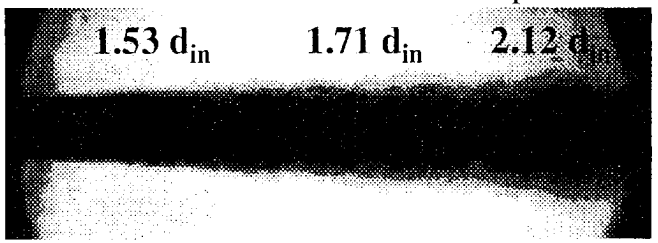
1.22 MPa - M=0.3 14 pictures



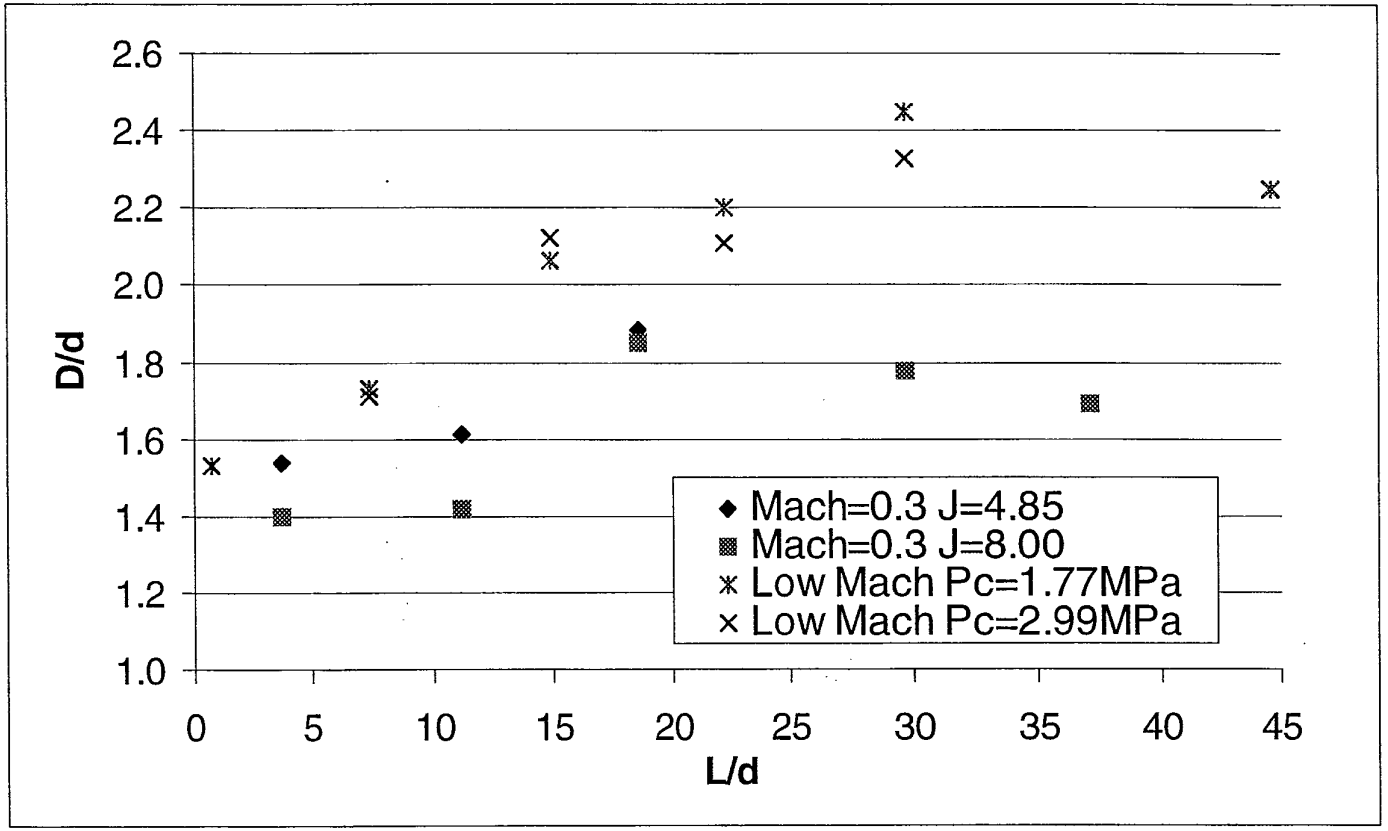
1.77 MPa - Low Mach 16 pictures



2.99 MPa - Low Mach 17 pictures



Evolution of the Core Diameter along the Chamber



Near-Injector Region

51 mm Field of View

1.22 MPa - M=0.3 →



11 d_{in}

1.77 MPa - Low Mach →



7 d_{in}

2.99 MPa - Low Mach →

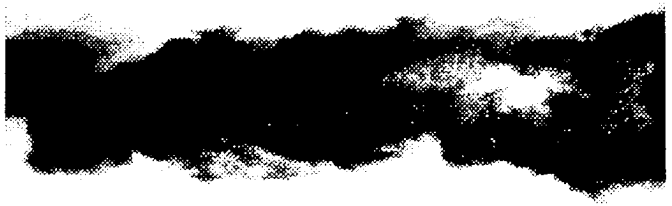


7 d_{in}

Mid-Core Region (1)

51 mm Field of View

1.22 MPa - M=0.3 ⟶



37 d_{in}

1.77 MPa - Low Mach ⟶



22 d_{in}

2.99 MPa - Low Mach ⟶

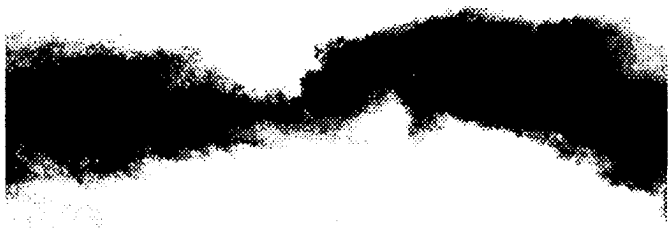


22 d_{in}

Mid-Core Region (2)

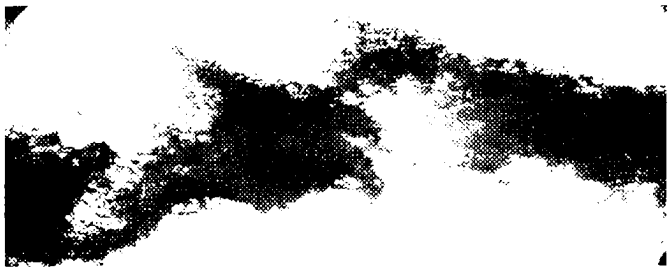
51 mm Field of View

1.22 MPa - M=0.3 →



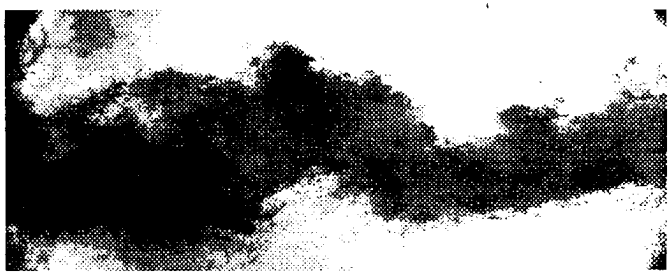
37 d_{in}

1.77 MPa - Low Mach →



45 d

2.99 MPa - Low Mach →



45 d_{in}

Breakup Region

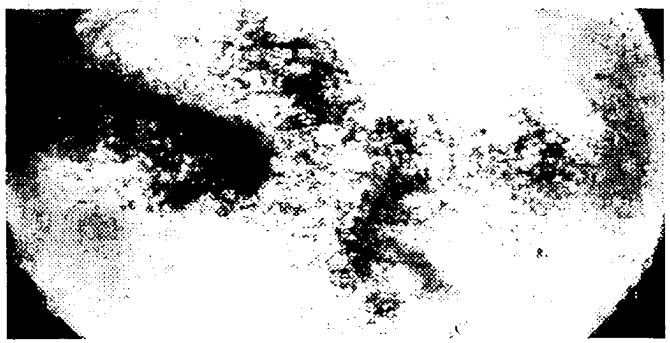
51 mm Field of View

1.22 MPa - M=0.3 →



45 d_{in}

1.77 MPa - Low Mach →



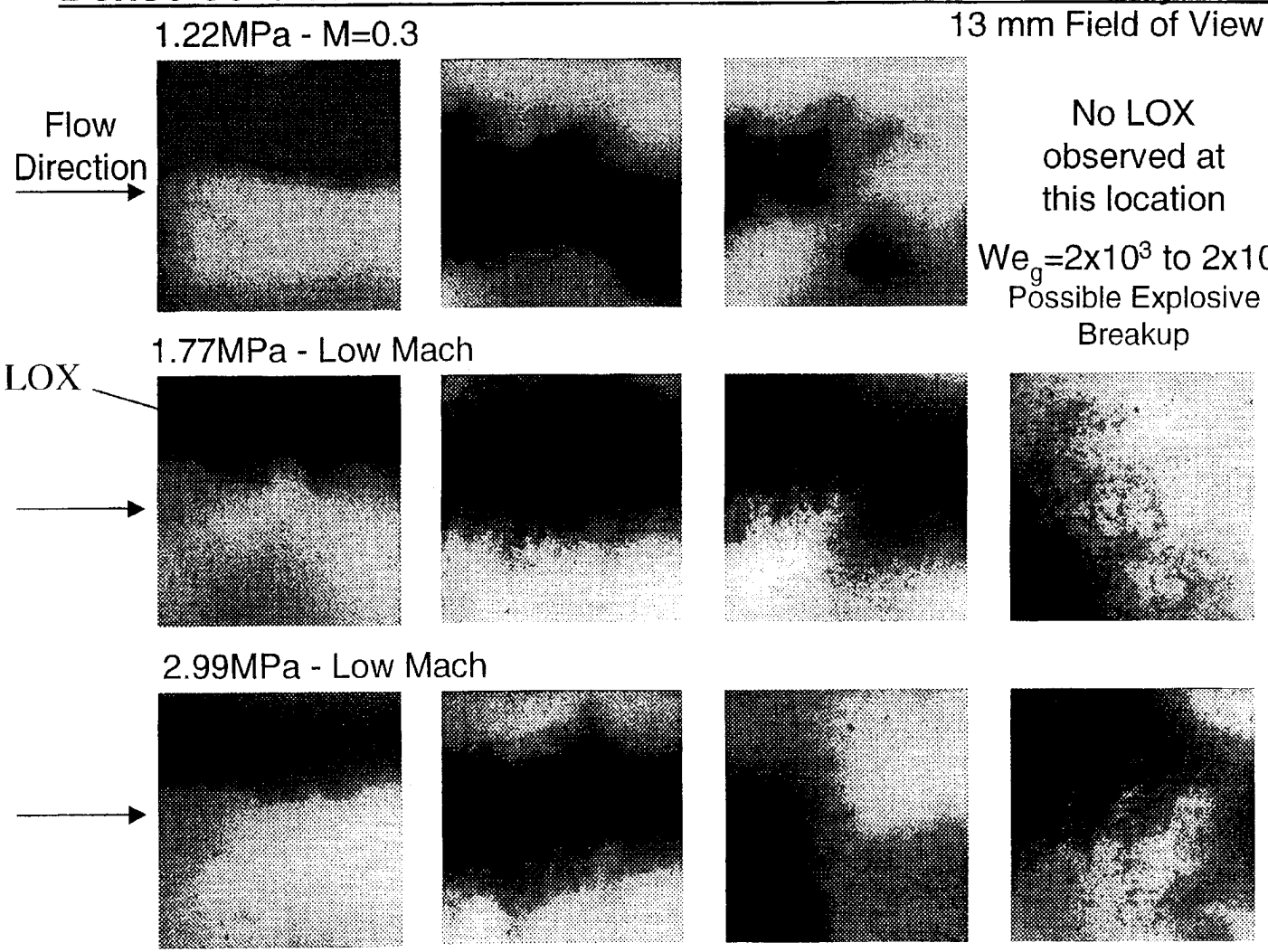
60 d_{in}

2.99 MPa - Low Mach →



60 d_{in}

Dense core surface character downstream from the injector



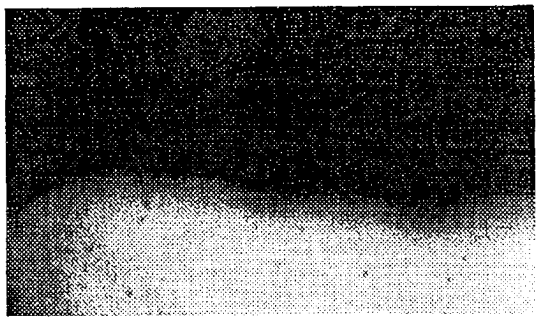
Core Surface Distinctiveness

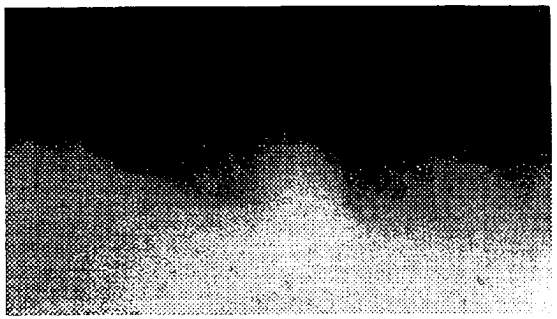
13 mm Field of View

1.22 MPa - M=0.3

1.77 MPa - Low Mach

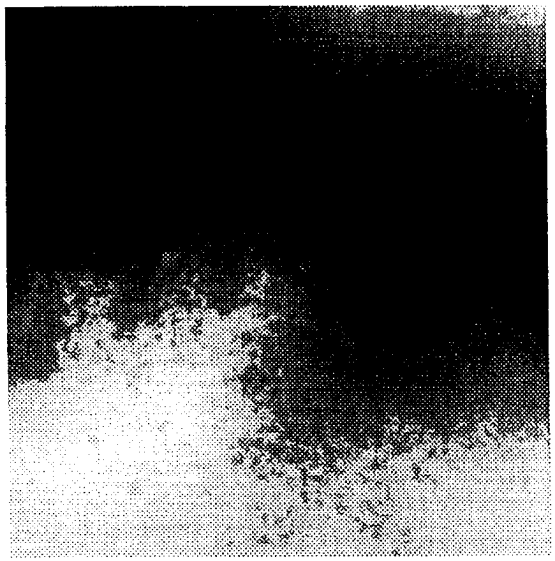
7 d_{in}





45 d_{in}





Droplet Production in the Breakup Region

13 mm Field of View

1.77 MPa - Low Mach ⟶



60 d_{in}

2.99 MPa - Low Mach ⟶

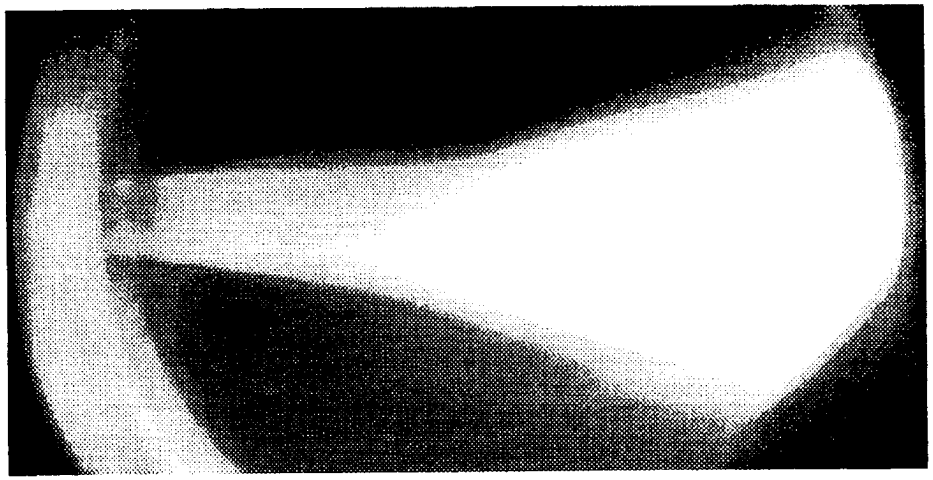


60 d_{in}

OH emission at the injector plate

51 mm Field of View

1.77 MPa - Low Mach averaged picture

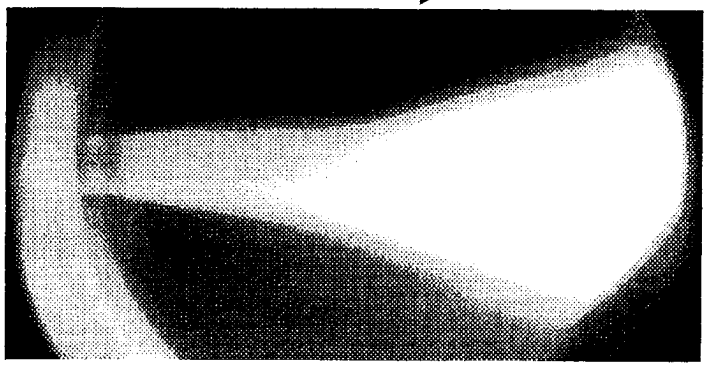


- The flame is almost cylindrical (spreading angle 5°) in the near-injector region until 3 d_{in}, then it expands itself and becomes conical (spreading angle 14°).
- Reaction is starting at the injector plate and seems anchored to the LOX post.
- Further downstream, the flame occupies the whole chamber.
- No influence of pressure in our range of conditions (1.77 to 2.99 MPa).

Interaction flame-dense core

51 mm Field of View

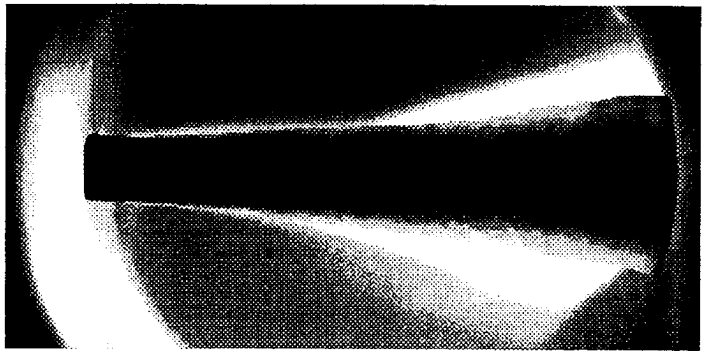
1.77 MPa - Low Mach - averaged picture



- The flame is surrounding the dense core as an outer layer.
- Thin reacting layer close to the injector.
- Further downstream:
  - Formation of a spray at the surface of the jet.
  - External group combustion.
  - The reacting zone expands itself around the dense core.

(cf. Candel et al. 1998)

Dense core in the flame shell



Conclusions

⇒ For Both Low and More Realistic Chamber Mach Number Conditions of This Study, LOX Core Disintegration is Ultimately Caused by large Amplitude Helical Oscillations. Droplet Stripping has a Secondary Effect on Core Breakup.

⇒ In the Low Mach Case, the Core Fragments Produce Ligaments and then Droplets Along a Classical Spray Process. Explosive Breakup May Occur Under Realistic Chamber Conditions.

⇒ High H_2 Injection Velocity Affects Only the Near Field Atomization Due to Rapid Expansion.

⇒ Attention Should Be Paid to Creating a Realistic Chamber Mach Number (Bulk Velocity) in Single Injector Element Experimentation.

Conclusions (2)

⇒ For Rocket Engine Conditions, Probably Not Suitable to Correlate Core Length or Far-field Drop Distribution Based on Injection Momentum Flux Ratio and/or Weber Number Due to Rapid Relative Velocity Relaxation.

⇒ Existing Correlations are Inadequate at Providing Realistic Jet Breakup (Core) Length Prediction Over More Than a Narrow Range of Conditions for Which They Were Created. Don't Extrapolate Well Especially in Terms of Jet Reynolds Number.

Ideas for Future Experiments

⇒ Expand Momentum Flux Ratio Regime to 10-12; LOX Heat Exchanger Required to Run at Lower Flow Rates.

⇒ Laser-Sheet Droplet Scattering Images on Surface of Large Scale Structures or Laser-Spark Shadowgraphy ....Obtain Nanosecond Scale Images of Droplets.

⇒ View Jet Rotation Due to Helical Instability by Cutting Jet with Laser Sheet Perpendicular to Axis.

⇒ High Speed Imaging (1 Million Frames per Second) of Core Breakup Event to Record Rapid Disintegration Sequence.

Acknowledgements

⇒The authors thank Mr. Larry Schaaf for his assistance in conducting the experiments at the Cryogenic Combustion Laboratory.

⇒Y. Boniface gratefully acknowledges the financial support of SNECMA (SEP division).

SECONDARY ATOMIZATION MODELLING IN THESEE

Bruno Vieille, Christian Chauveau,

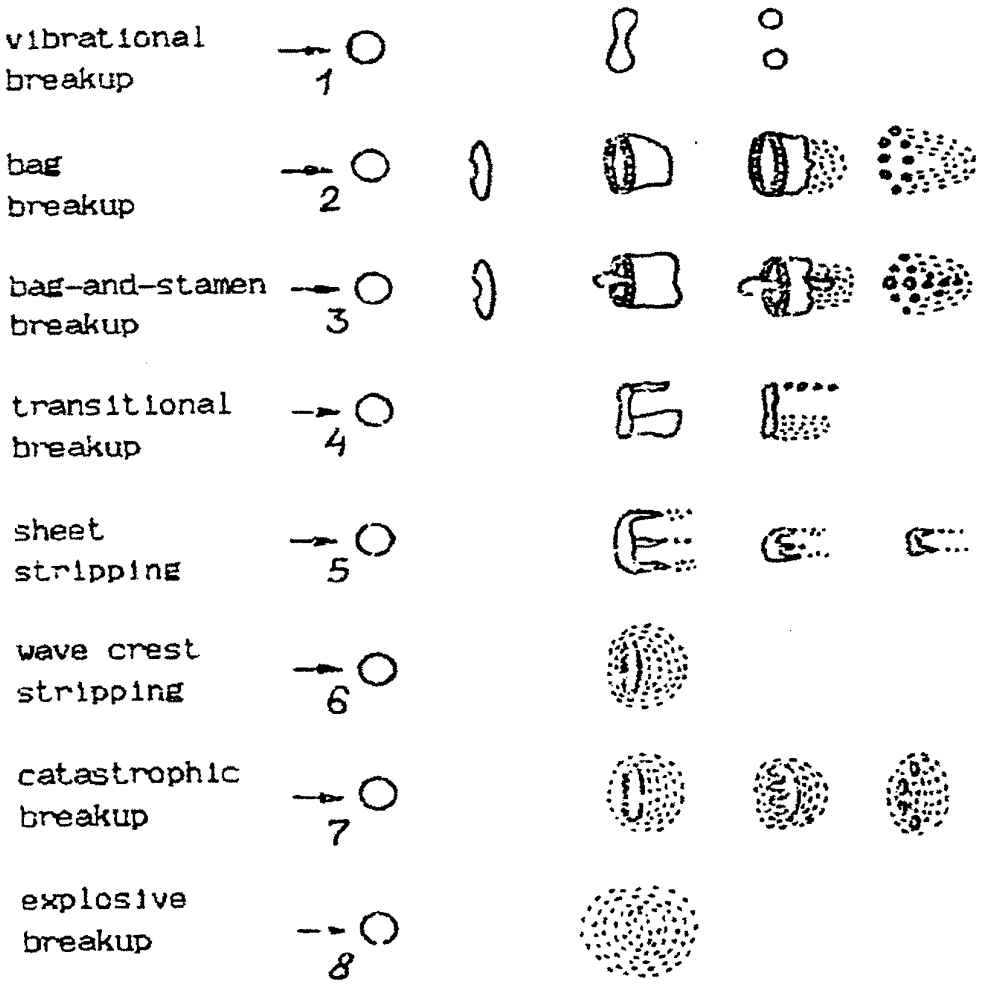
Raphaël Cousty, Stephan Derhay, Ivan Fedioun, Iskender Gökalp, LCSR, CNRS, Orléans, F

Didier Saucereau, Stephan Zurbach, SNECMA Division Moteurs Fusée, Vernon

OBJECTIVES

- To develop a secondary atomization model in THESEE (Bruno Vieille's thesis).
- To develop a vaporization model which takes care of the pressure and turbulence effects.

BREAK-UP REGIMES IDENTIFICATION



SECONDARY ATOMIZATION CONTROL PARAMETERS

- aerodynamic shear forces
- surface tension forces
- gas and liquid viscosity forces

$$We = \frac{\rho_g D U^2}{\sigma} = \frac{aerodynamic\ shear\ force}{surface\ tension\ force}$$

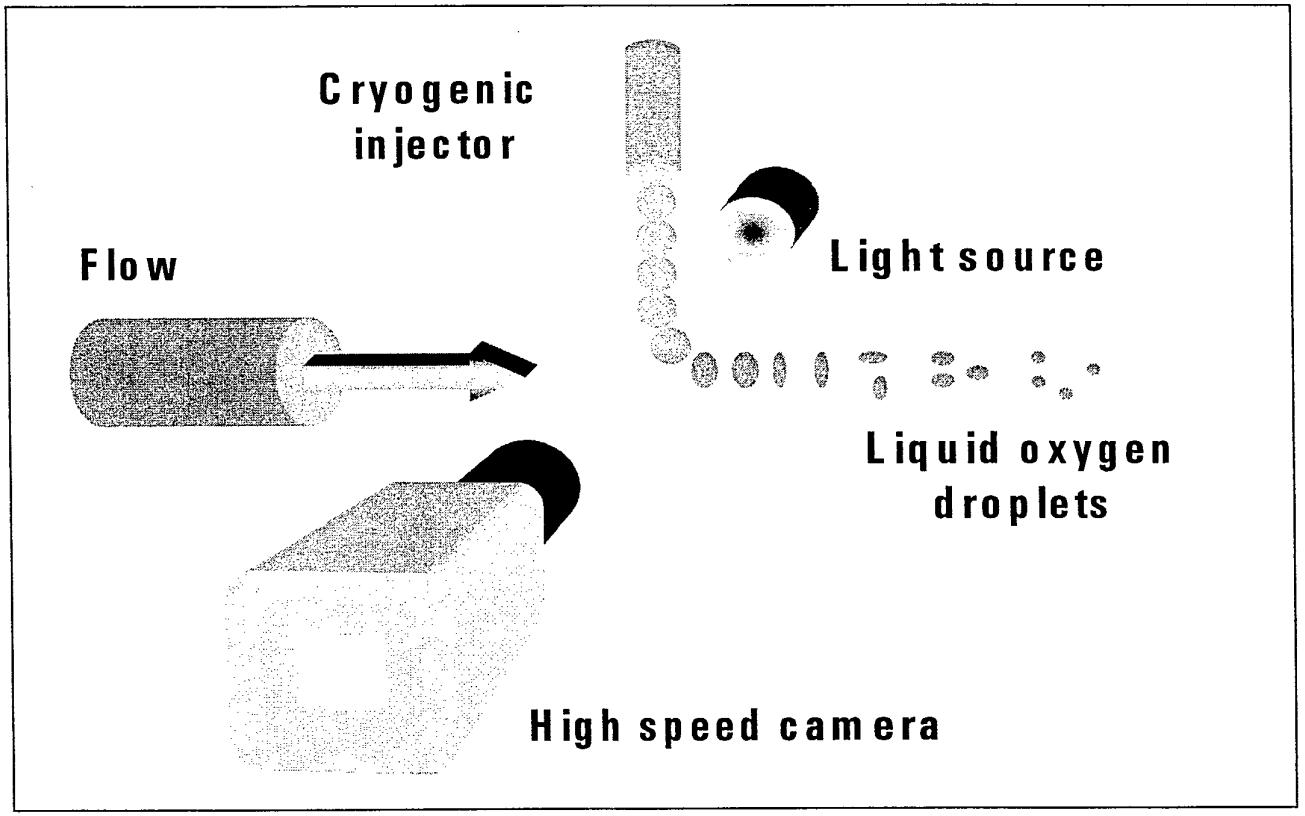
$$Re = \frac{\rho_g D U}{\mu_g} = \frac{aerodynamic\ shear\ force}{gas\ viscosity\ force}$$

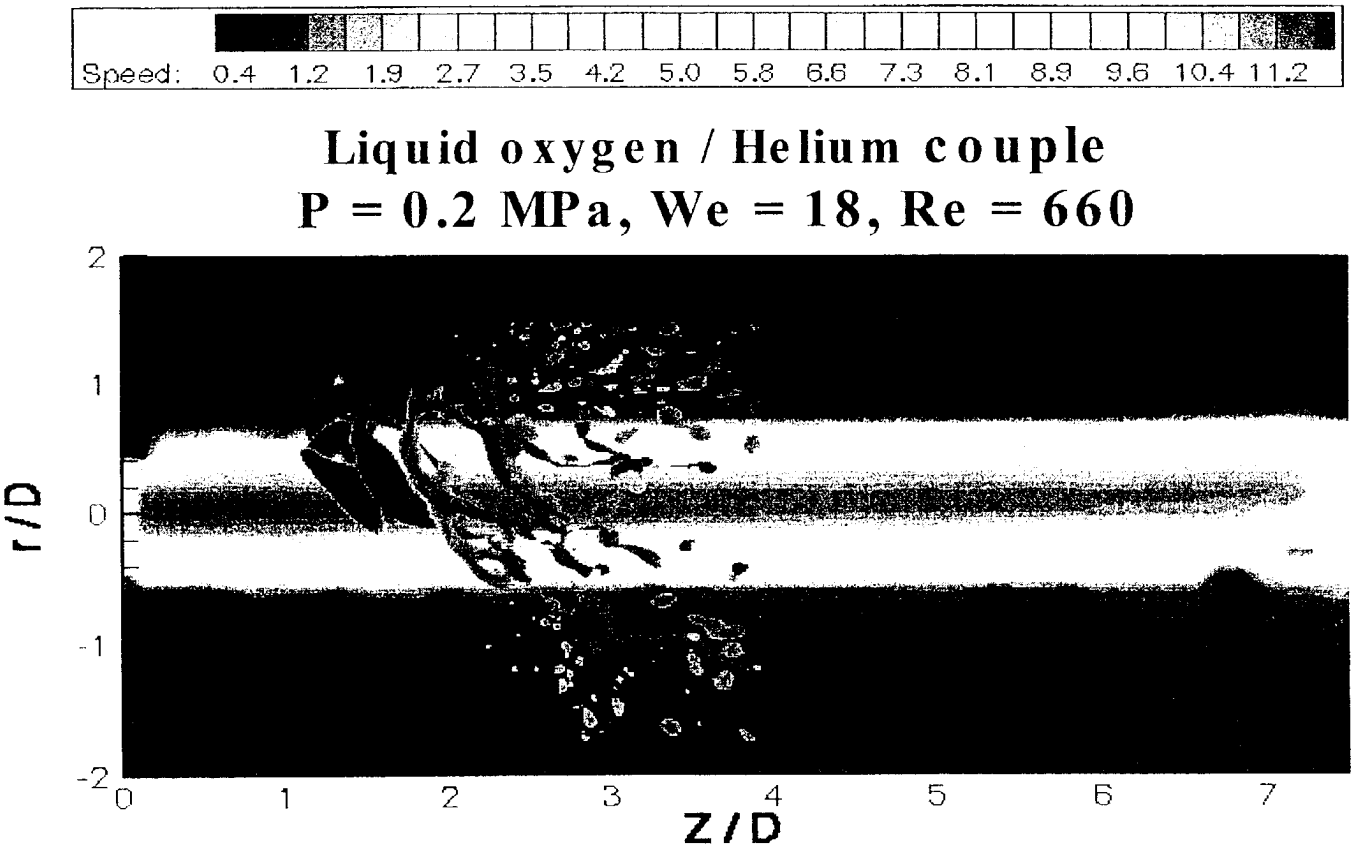
$$Oh = \frac{\mu_l}{\sqrt{\rho_l D \sigma}} = \frac{fluid\ viscosity\ force}{(aerodynamic\ shear\ force\ .\ surface\ tension\ force)^{1/2}}$$

OBJECTIVES OF BRUNO VIEILLE'S EXPERIMENTAL STUDY

- To identify and charactarize the break-up regimes and their transition criteria.
- To document the characteristic break-up times.
- To quantify the secondary droplets distributions.

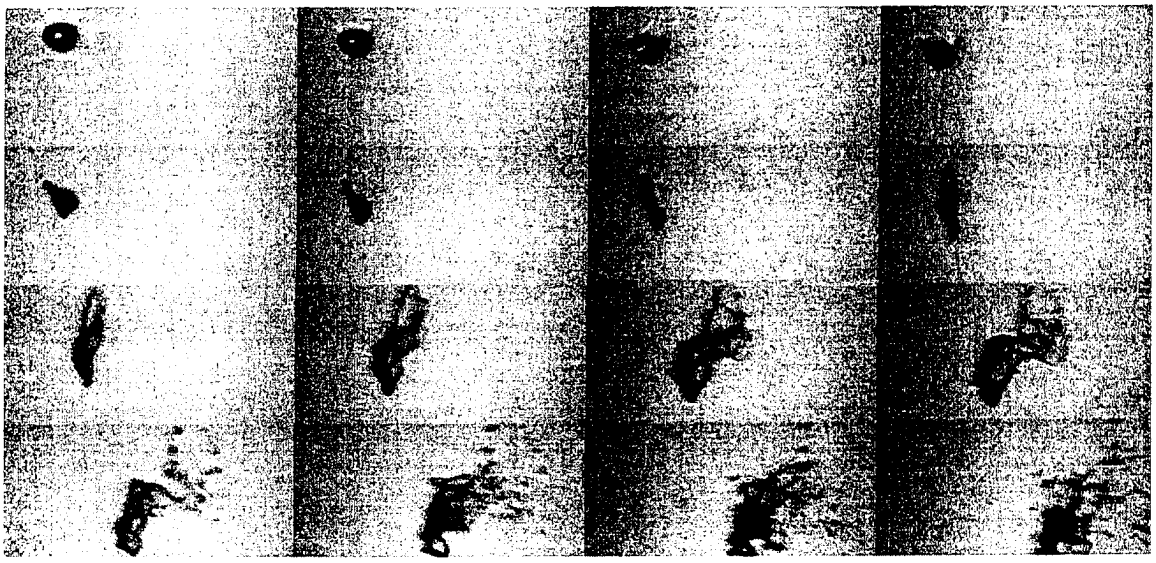
Schematic view of the experimental configuration



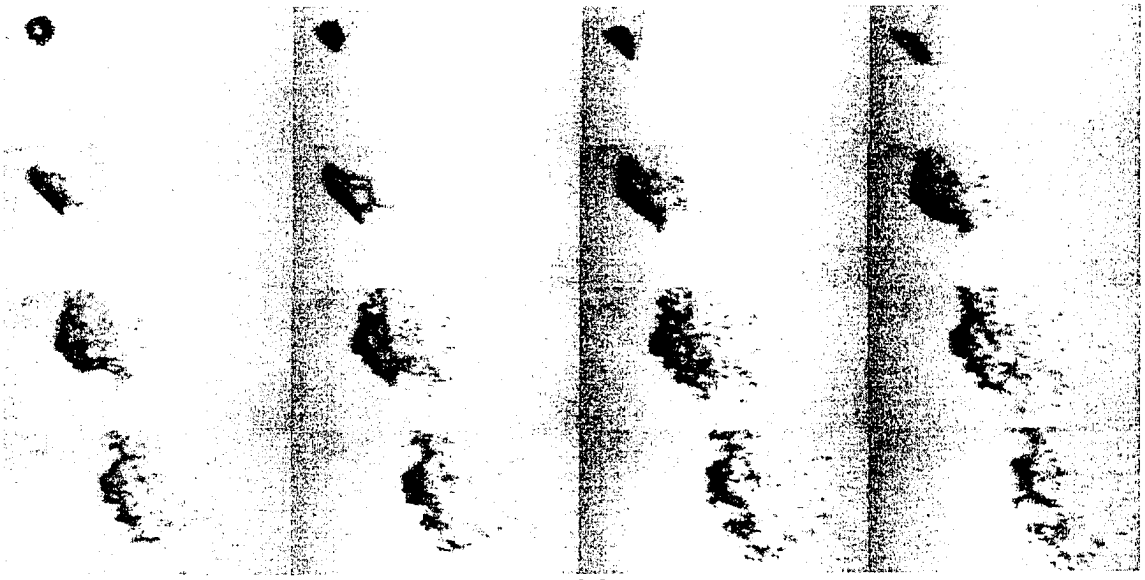


Superimposition of the aerodynamic field and droplet break-up images

DOPLET BREAK-UP VISUALIZATION

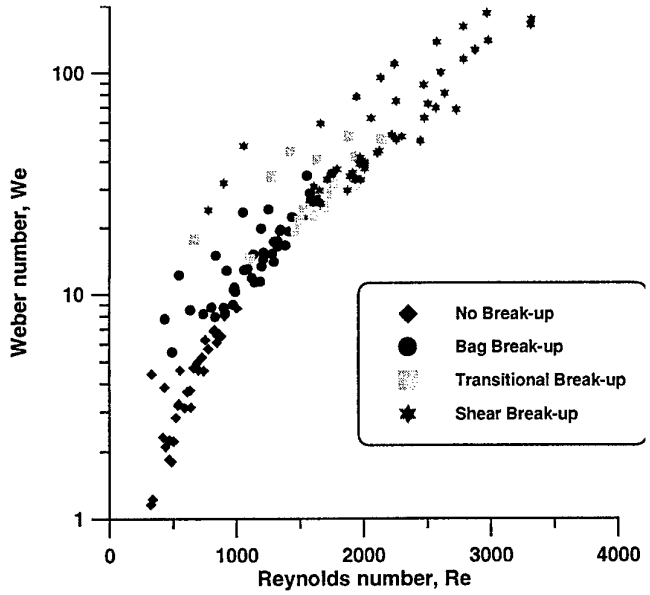


First Series

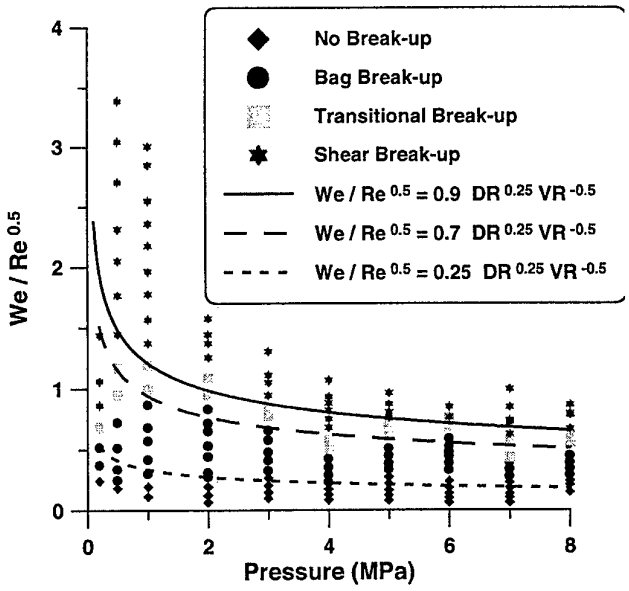


Second Series

Visualisation of secondary atomisation of LOX droplets in Helium



Experimental droplet-jet interaction regimes for LOx droplets – helium jet



Experimental data and the corresponding correlations for LOx droplet break-up regime limits

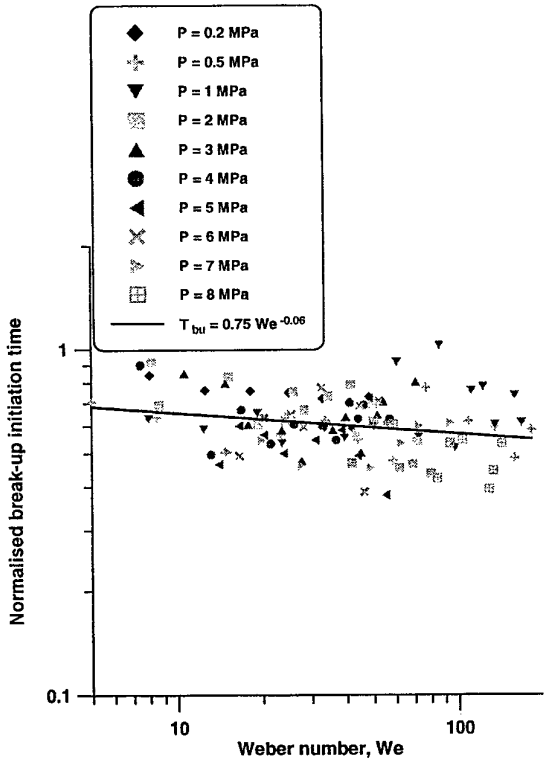
BREAK-UP REGIME TRANSITION CRITERIA

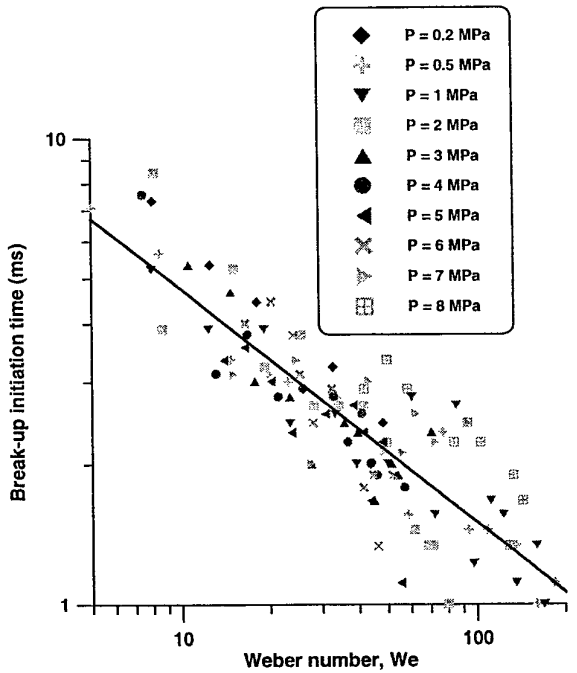
Transition to the regime of	Transition corrélations
Bag breakup	$\frac{We}{\sqrt{Re}} = 0{,}25 \cdot DR^{0{,}25} \cdot VR^{-0{,}5}$
Transitional breakup	$\frac{We}{\sqrt{Re}} = 0{,}7 \cdot DR^{0{,}25} \cdot VR^{-0{,}5}$
Shear breakup	$\frac{We}{\sqrt{Re}} = 0{,}9 \cdot DR^{0{,}25} \cdot VR^{-0{,}5}$

Bruno Vieille's correlations obtained for the break-up regime transitions

LOX DROPLET BREAK-UP INITIATION TIMES IN HELIUM

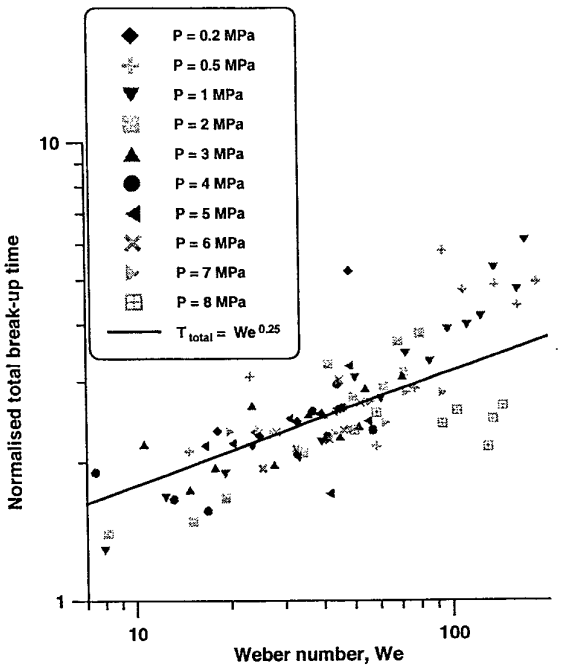
$$Tini = 0.75\frac{D}{U}\left(\frac{\rho_l}{\rho_g}\right)^{0.5} We^{-0.06}$$

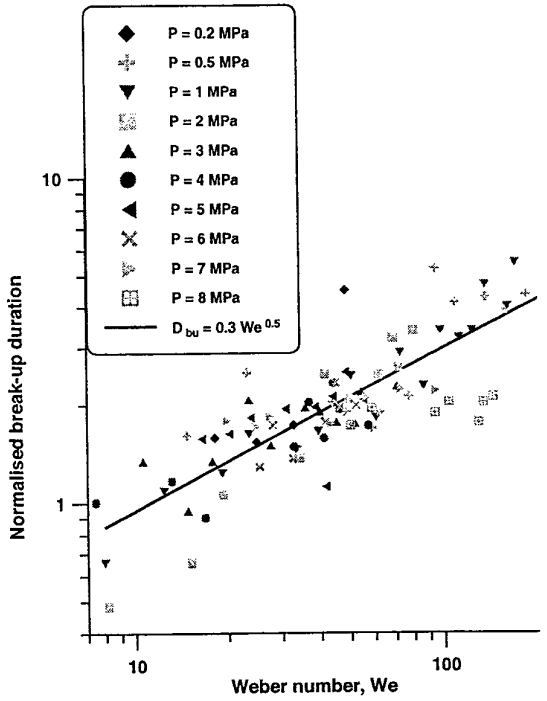




LOX DROPLET TOTAL BREAK-UP TIME IN HELIUM

$$Tini = 0.3\frac{D}{U}\left(\frac{\rho_l}{\rho_g}\right)^{0.5} We^{0.5}$$





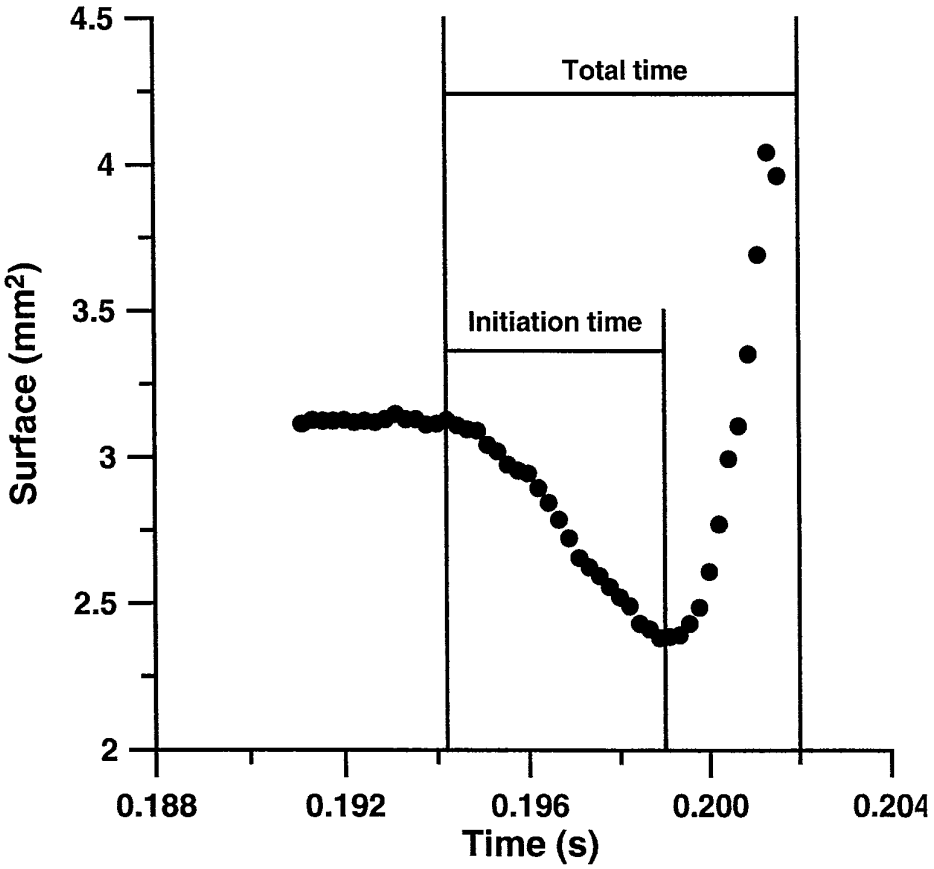
CHARACTERISTIC BREAKUP-UP TIMES CORRELATIONS FOR LIQUID OXYGEN / HELIUM COUPLE

Initiation time : $$Tini = 0{,}75 \cdot T \cdot We^{-0{,}06}$$

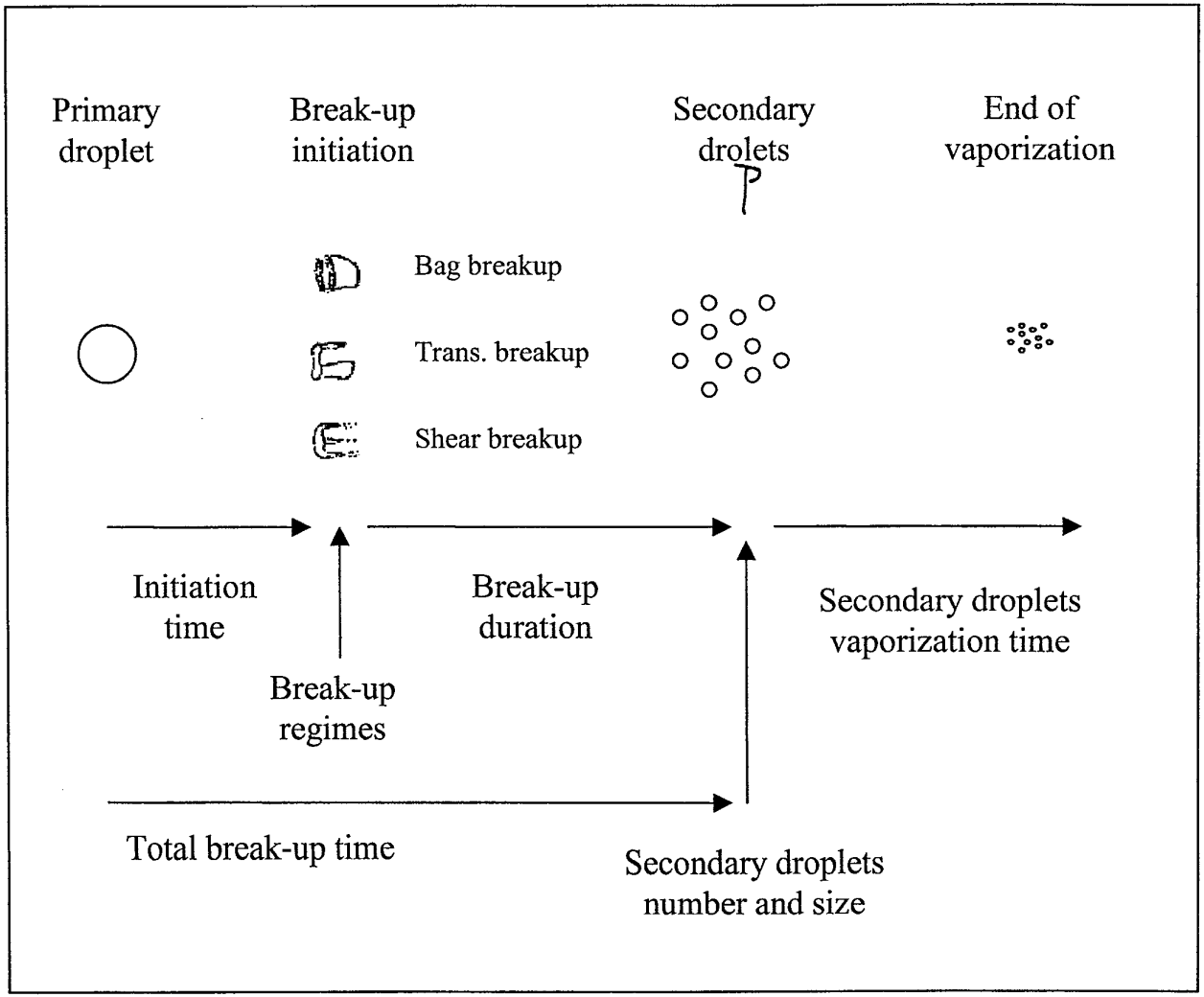
Characteristic time : $$T = \frac{D_0}{U}\sqrt{\frac{\rho_l}{\rho_g}}$$

Break-up duration : $$Tcass = 0{,}3 \cdot T \cdot We^{0{,}5}$$

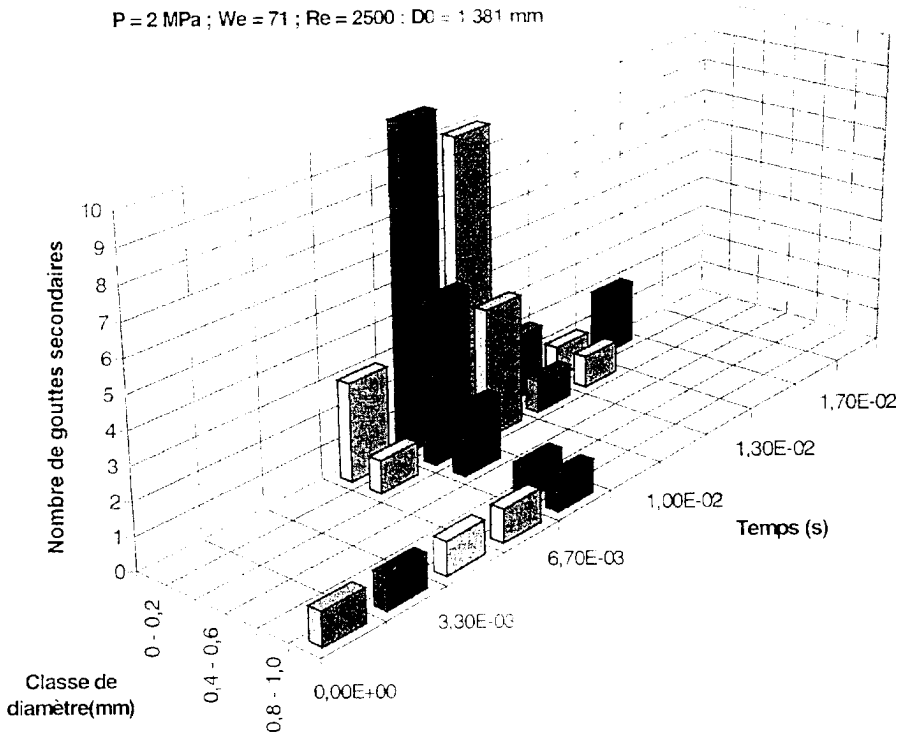
INITIATION TIME DETERMINATION

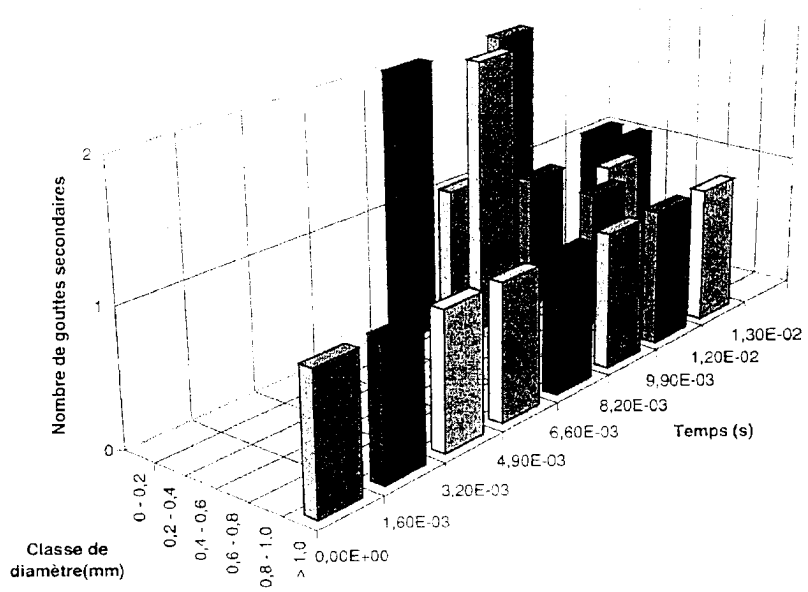


CHARACTERISTIC BREAK-UP TIMES



SECONDARY DROPLET DISTRIBUTIONS OBTAINED BY BRUNO VIEILLE





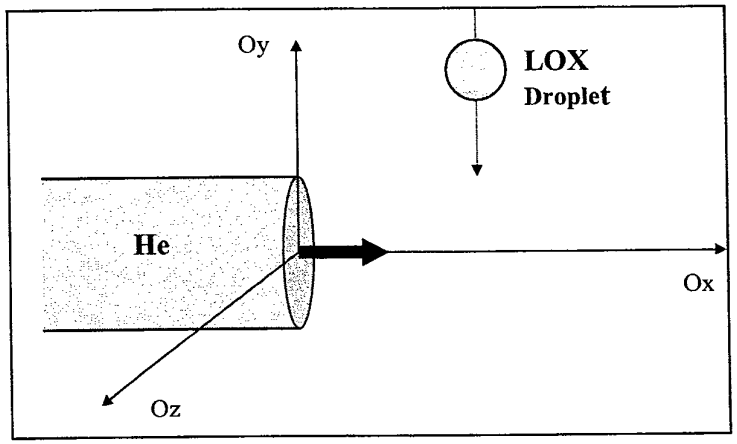
P = 2 MPa ; We = 20 ; Re = 1350 ; D_0 = 1,49 mm).

THESEE

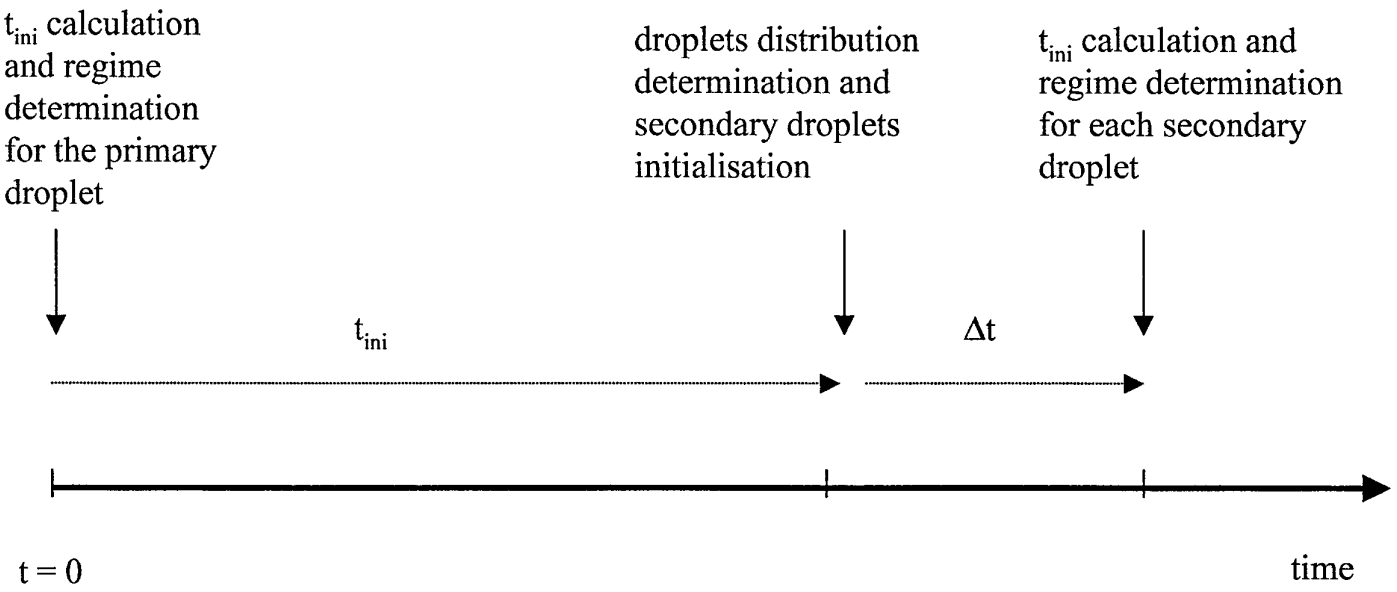
- mono or multi-phase flows
- 2D or 3D flows
- laminar or turbulent flows
- mass and heat transfer with phase change
- chemical reactions
- combustion
- vaporization (D^2 law, Sirignano-Delplanque model)

NUMERICAL SIMULATION

- Liquid Oxygen / Helium couple
- mono-droplet configuration (LOX)
- non-reactive flow (Helium)
- vaporisation model (D^2 law)
- turbulence model
- Bruno Vieille's experimental configuration



SECONDARY ATOMISATION MODEL PRINCIPLE



THE ATOMIZATION MODEL PRINCIPLE

Break-up regime determination

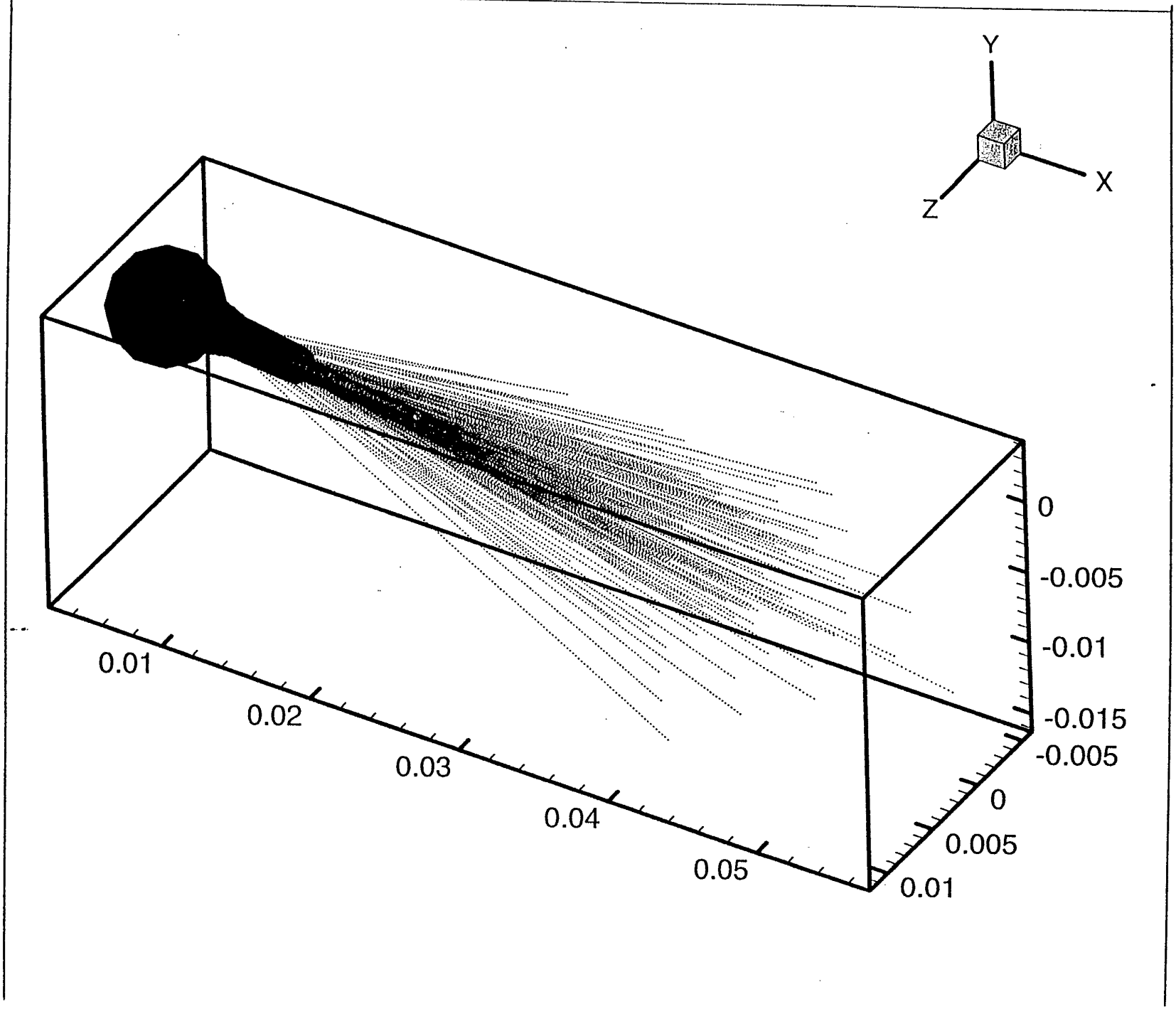
Transition to the regime	Correlations obtained
Bag breakup	$\frac{We}{\sqrt{Re}} = 0{,}25 \cdot DR^{0{,}25} \cdot VR^{-0{,}5}$
Transitional breakup	$\frac{We}{\sqrt{Re}} = 0{,}7 \cdot DR^{0{,}25} \cdot VR^{-0{,}5}$
Shear breakup	$\frac{We}{\sqrt{Re}} = 0{,}9 \cdot DR^{0{,}25} \cdot VR^{-0{,}5}$

Initiation time calculation

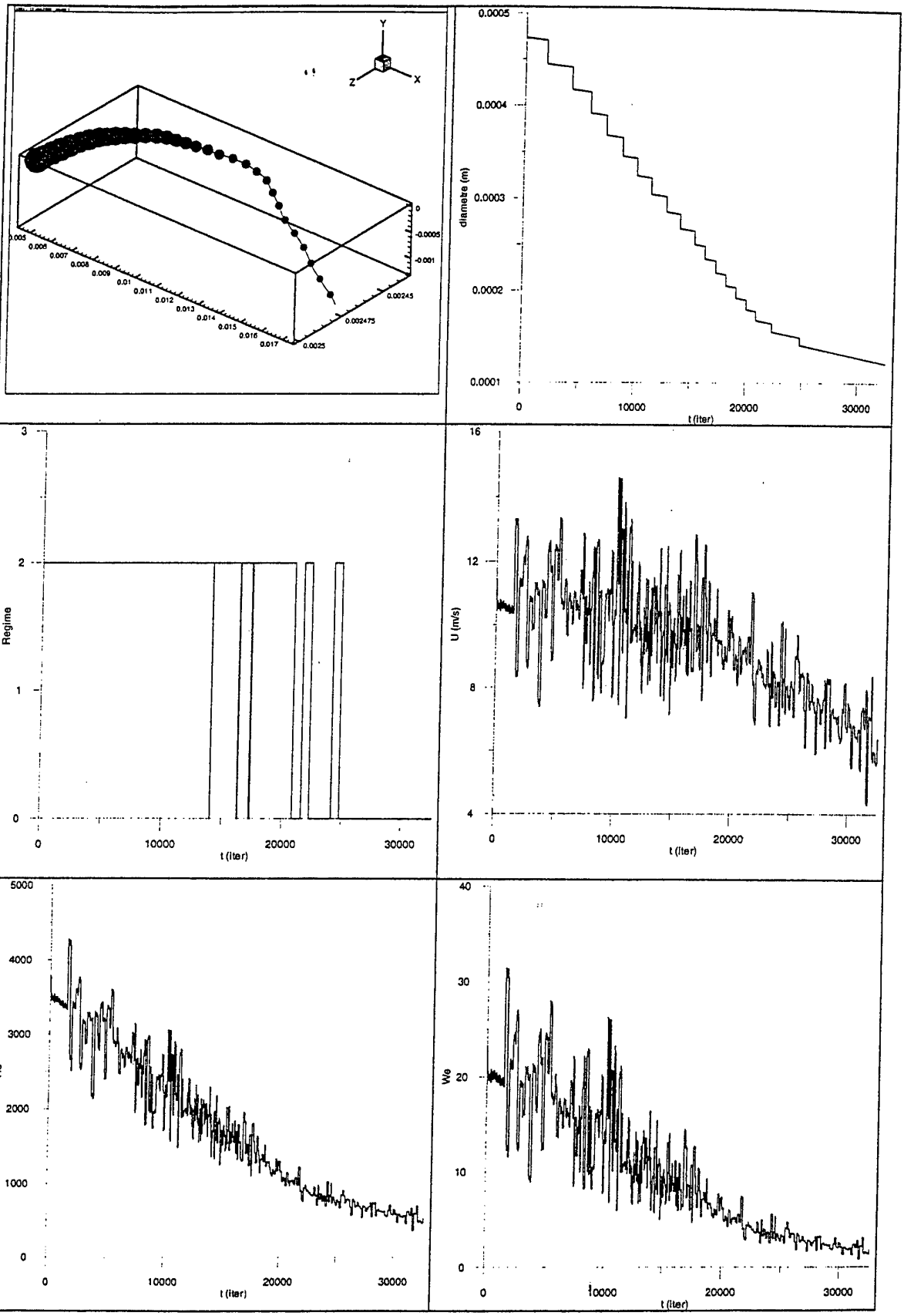
$$Tini = 0{,}75.T.We^{-0{,}06} \qquad T = \frac{D_0}{U}\sqrt{\frac{\rho_l}{\rho_g}}$$

Secondary droplets distribution determination

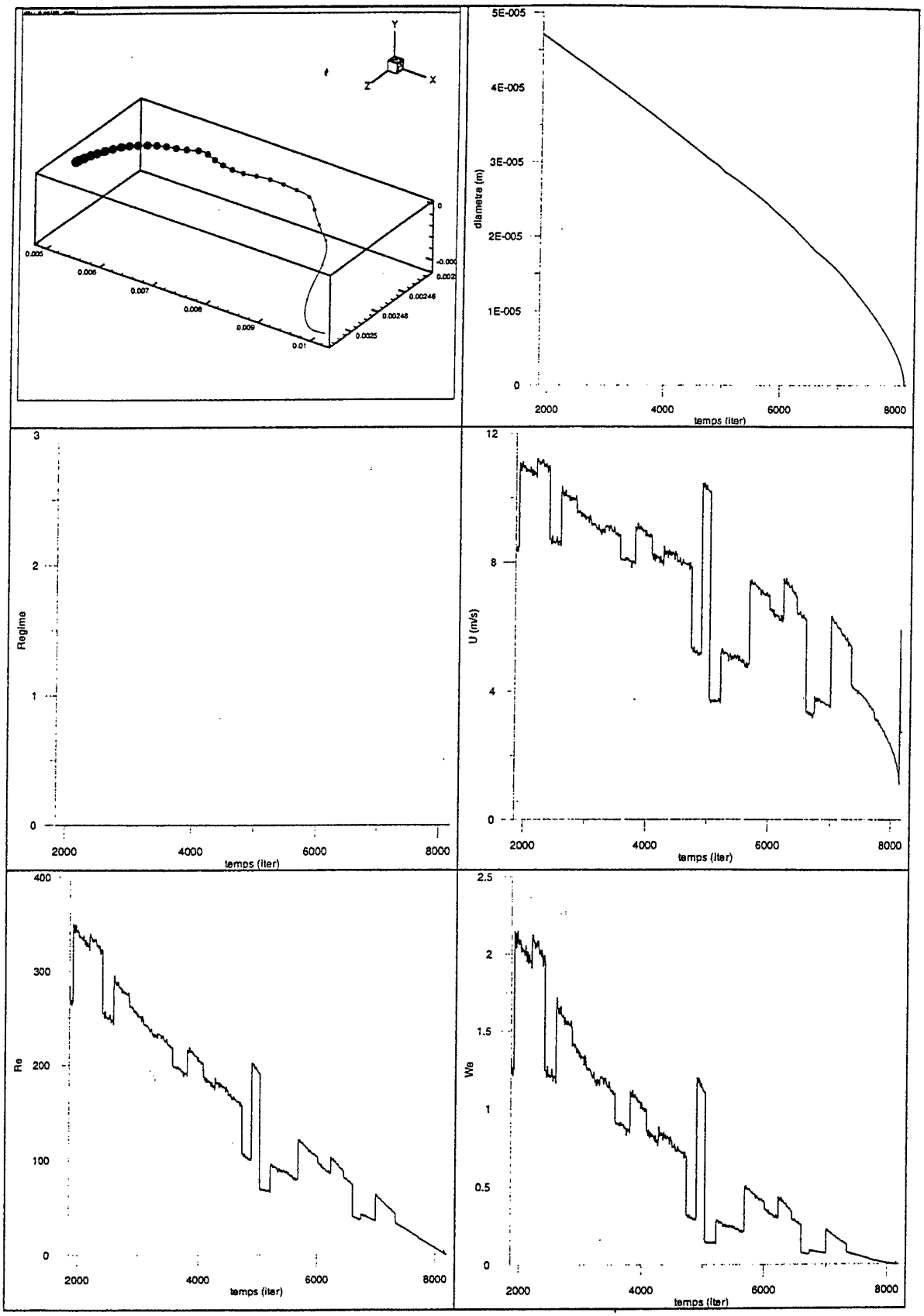
Regime	% function of the mother droplet diameter		
	10 %	30 %	50 %
Bag	2	2	1
Trans	3	1	1
Shear	4	2	2


Y
X
Z
0
-0.005
-0.01
-0.015
0.01
0.02
0.03
0.04
0.05
-0.005
0
0.005
0.01

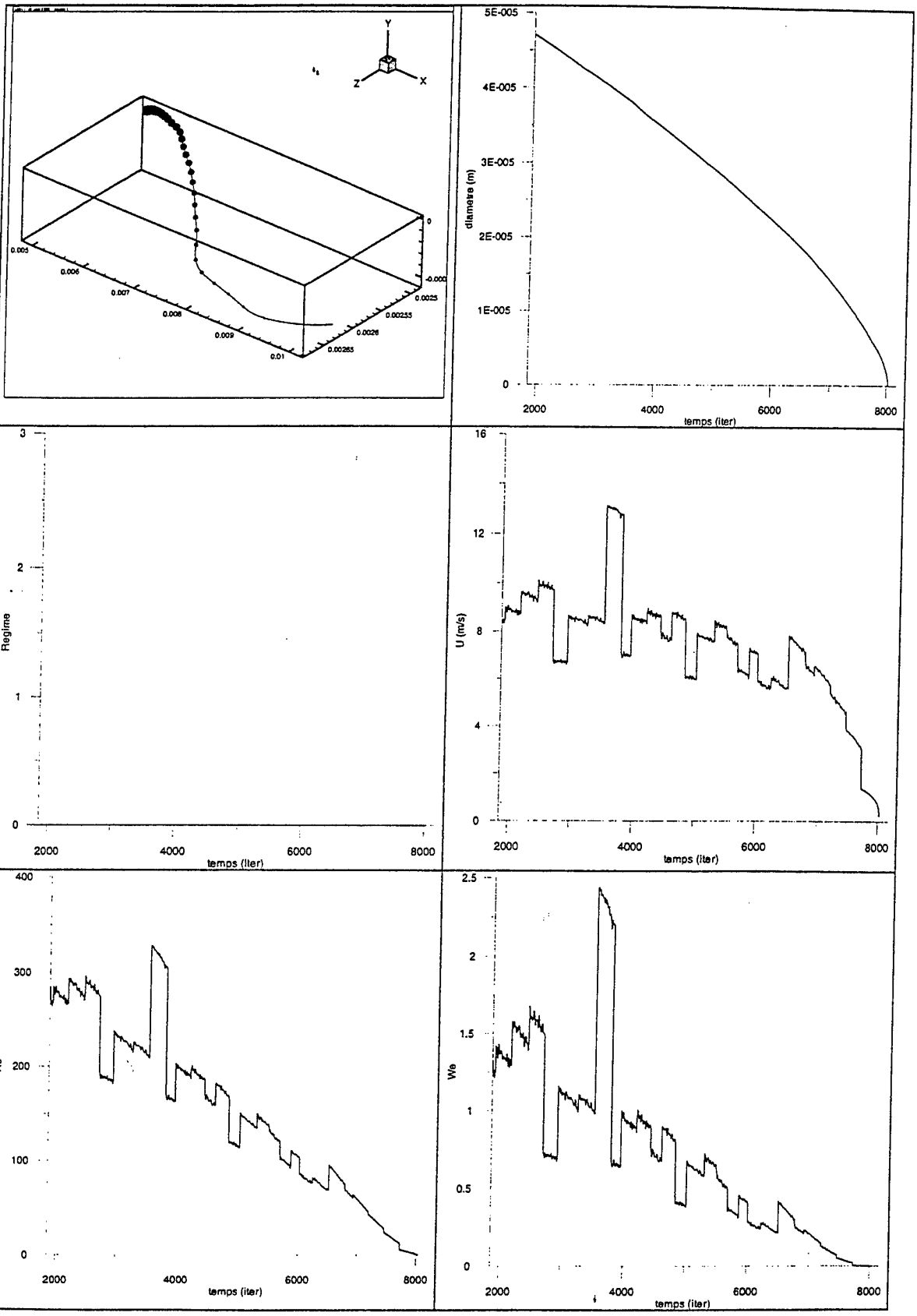
Goutte n°1


Y
Z
X
0.005
0.006
0.007
0.008
0.009
0.01
0.011
0.012
0.013
0.014
0.015
0.016
0.017
0.0025
0.00245
0.002475
0
-0.0005
-0.001
0.0005
0.0004
0.0003
0.0002
0.0001
diamètre (m)
0
10000
20000
30000
t (iter)
3
2
1
0
Regime
0
10000
20000
30000
t (iter)
16
12
8
4
U (m/s)
0
10000
20000
30000
t (iter)
5000
4000
3000
2000
1000
0
Re
0
10000
20000
30000
t (iter)
40
30
20
10
0
We
0
10000
20000
30000
t (iter)

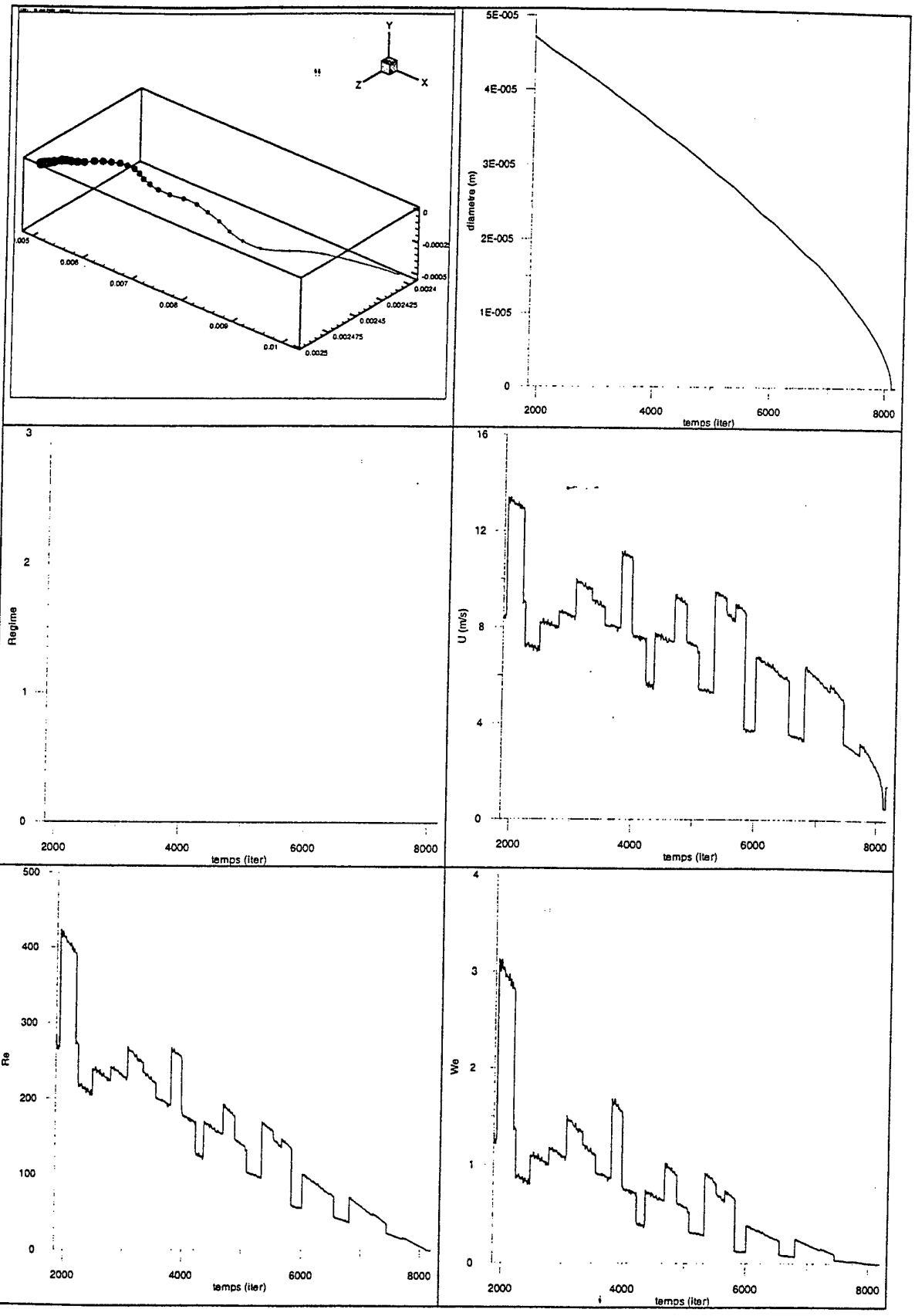
Goutte n°2


Y
X
Z
0.005
0.006
0.007
0.008
0.009
0.01
0.0025
0.00248
0.00246
0
5E-005
4E-005
3E-005
2E-005
1E-005
0
diametre (m)
2000
4000
6000
8000
temps (iter)
Regime
3
2
1
0
U (m/s)
12
8
4
Re
400
300
200
100
We
2.5
2
1.5
1
0.5

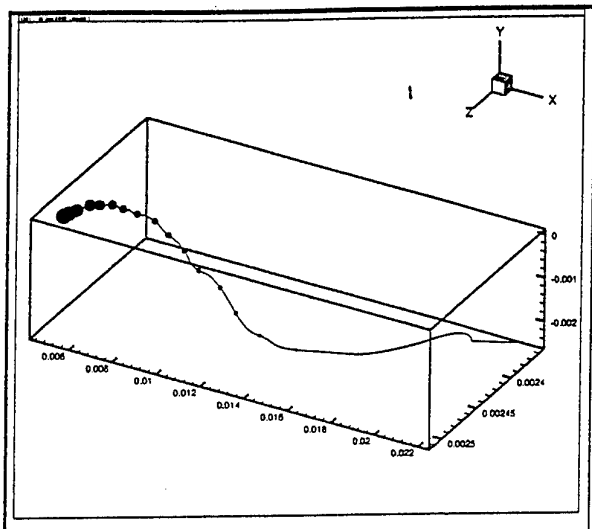
Goutte n°3

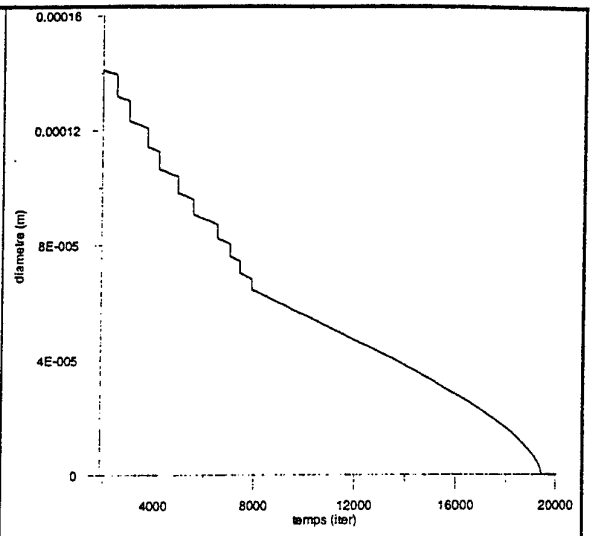

Y
Z
X
0.005
0.006
0.007
0.008
0.009
0.01
0.0025
0.00255
0.0026
0.00265
0
-0.000
5E-005
4E-005
3E-005
2E-005
1E-005
0
diametre (m)
2000
4000
6000
8000
temps (iter)
3
2
1
0
Regime
2000
4000
6000
8000
temps (iter)
16
12
8
4
0
U (m/s)
2000
4000
6000
8000
temps (iter)
400
300
200
100
0
Re
2000
4000
6000
8000
temps (iter)
2.5
2
1.5
1
0.5
0
We
2000
4000
6000
8000
temps (iter)

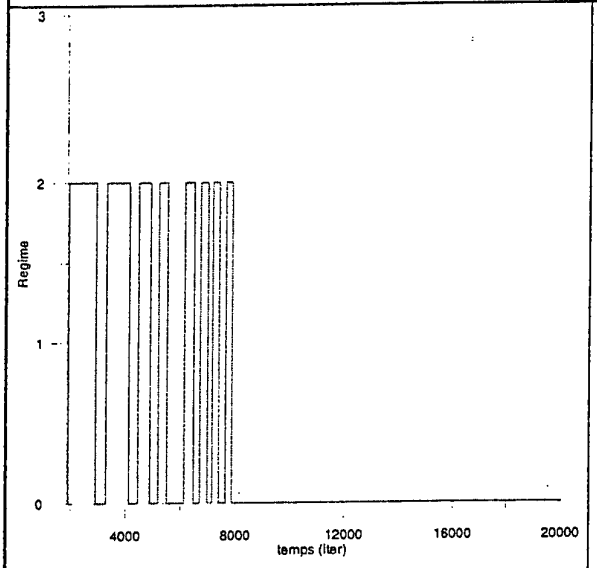
Goutte n°4

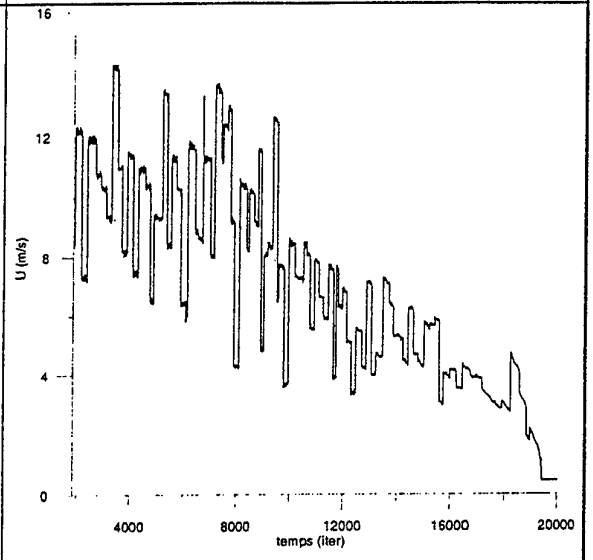

Y
Z
X
0.005
0.006
0.007
0.008
0.009
0.01
0.0025
0.002475
0.00245
0.002425
0.0024
0
-0.0002
-0.0005
5E-005
4E-005
3E-005
2E-005
1E-005
0
diamètre (m)
2000
4000
6000
8000
temps (iter)
3
2
1
0
Regime
16
12
8
4
U (m/s)
500
400
300
200
100
Re
4
3
2
1
We

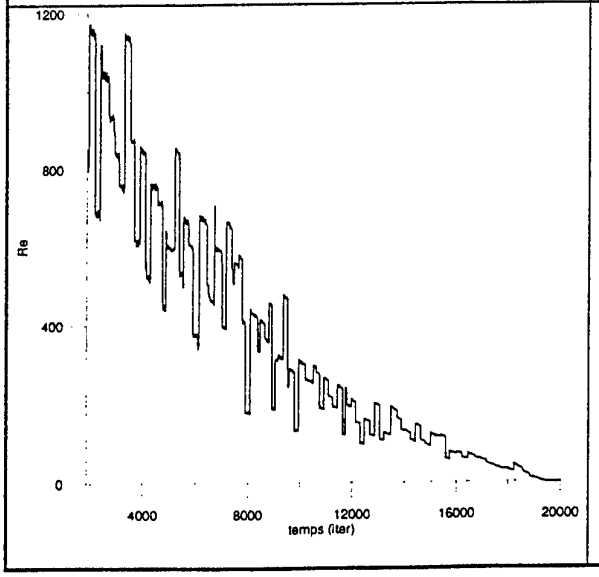
Goutte n°5

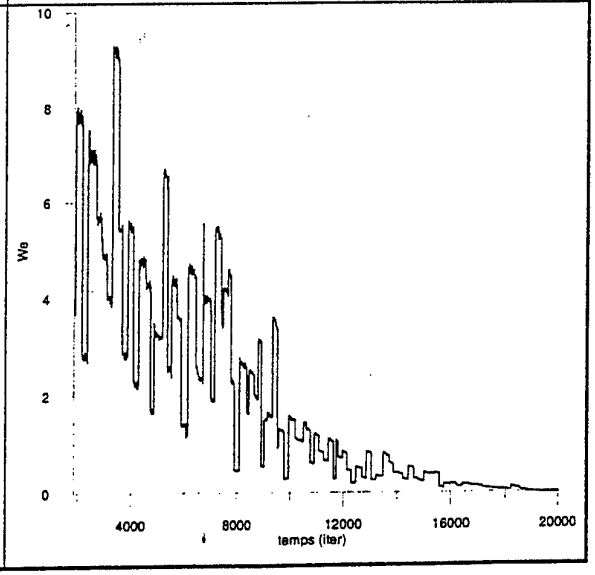

Y
X
Z
0
-0.001
-0.002
0.006
0.008
0.01
0.012
0.014
0.016
0.018
0.02
0.022
0.0024
0.00245
0.0025


0.00016
0.00012
8E-005
4E-005
0
diamètre (m)
4000
8000
12000
16000
20000
temps (iter)

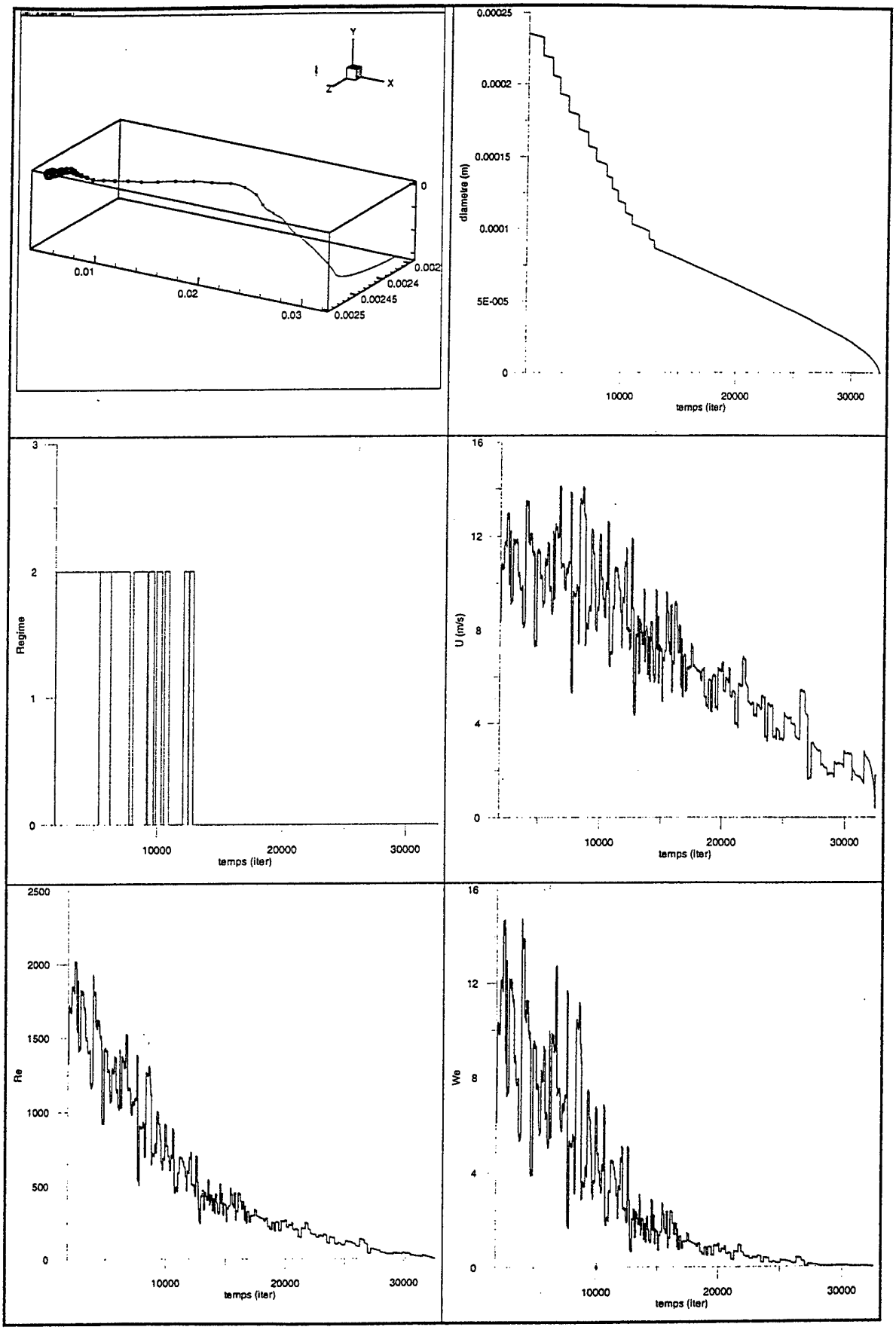

3
2
1
0
Regime
4000
8000
12000
16000
20000
temps (iter)


16
12
8
4
0
U (m/s)
4000
8000
12000
16000
20000
temps (iter)

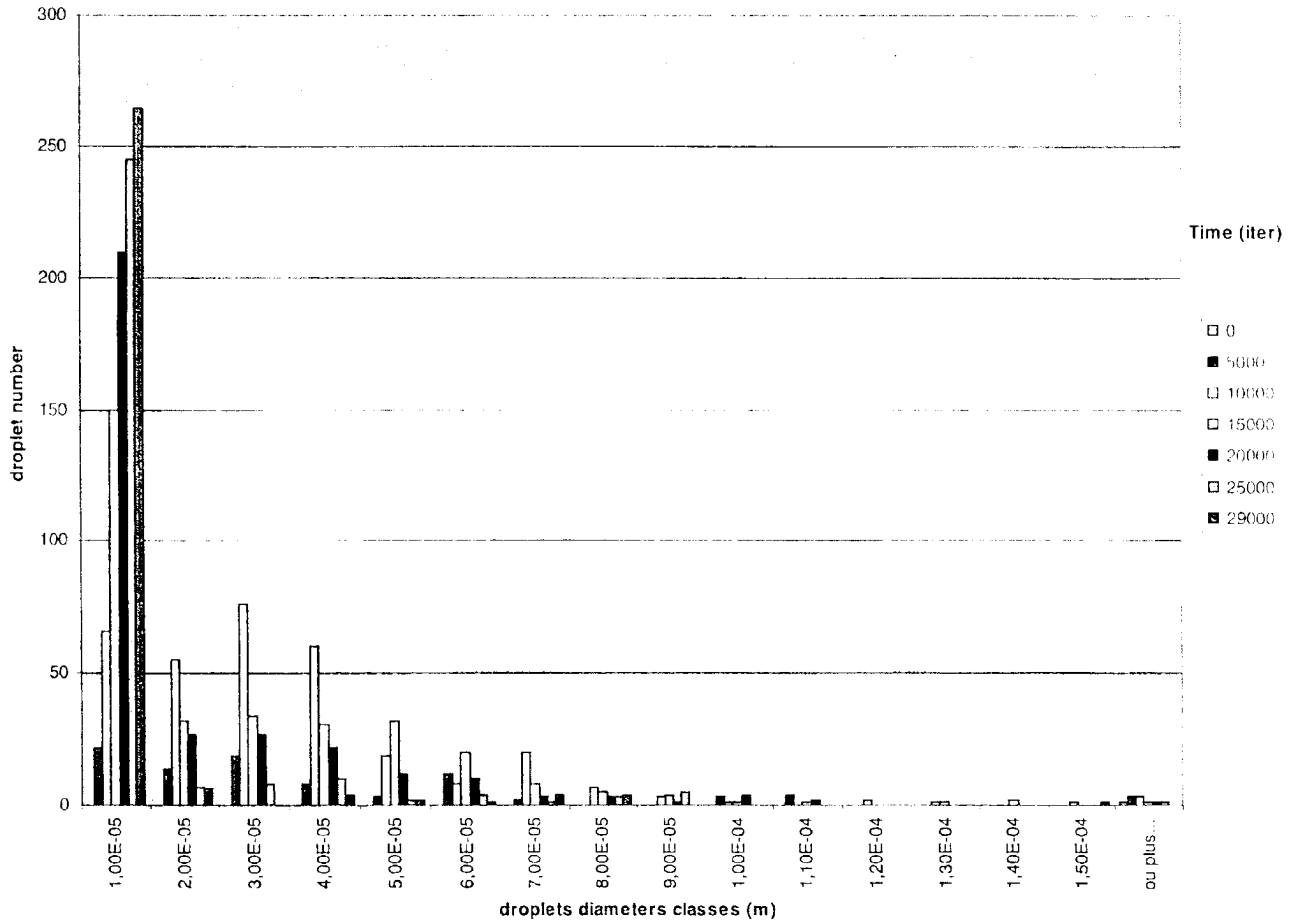

1200
800
400
0
Re
4000
8000
12000
16000
20000
temps (iter)


10
8
6
4
2
0
We
4000
8000
12000
16000
20000
temps (iter)

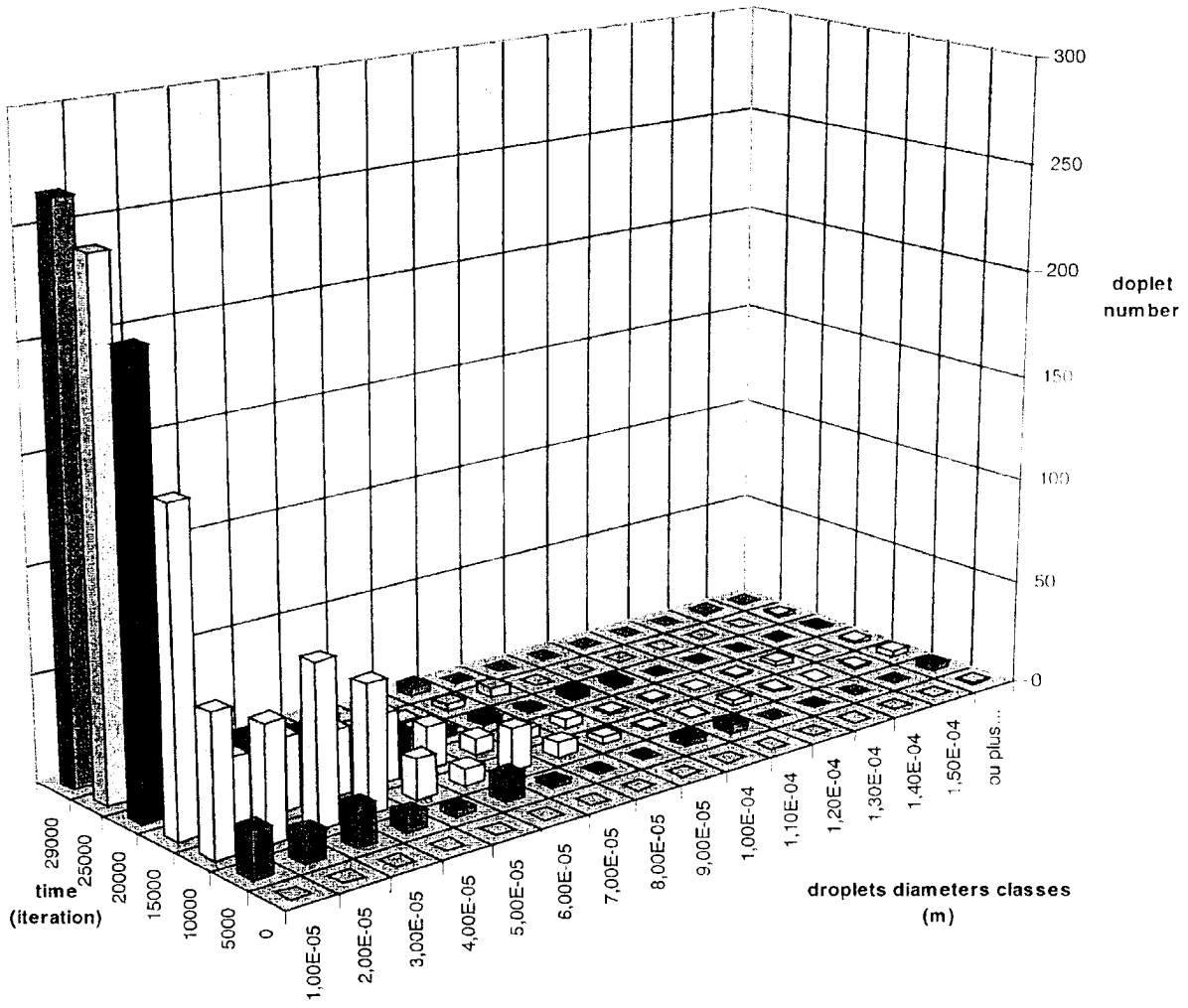
Goutte n°6


Y
X
Z
0
0.01
0.02
0.03
0.002
0.0024
0.00245
0.0025
0.00025
0.0002
0.00015
0.0001
5E-005
0
diametre (m)
10000
20000
30000
temps (iter)
3
2
1
0
Regime
10000
20000
30000
temps (iter)
16
12
8
4
0
U (m/s)
10000
20000
30000
temps (iter)
2500
2000
1500
1000
500
0
Re
10000
20000
30000
temps (iter)
16
12
8
4
0
We
10000
20000
30000
temps (iter)

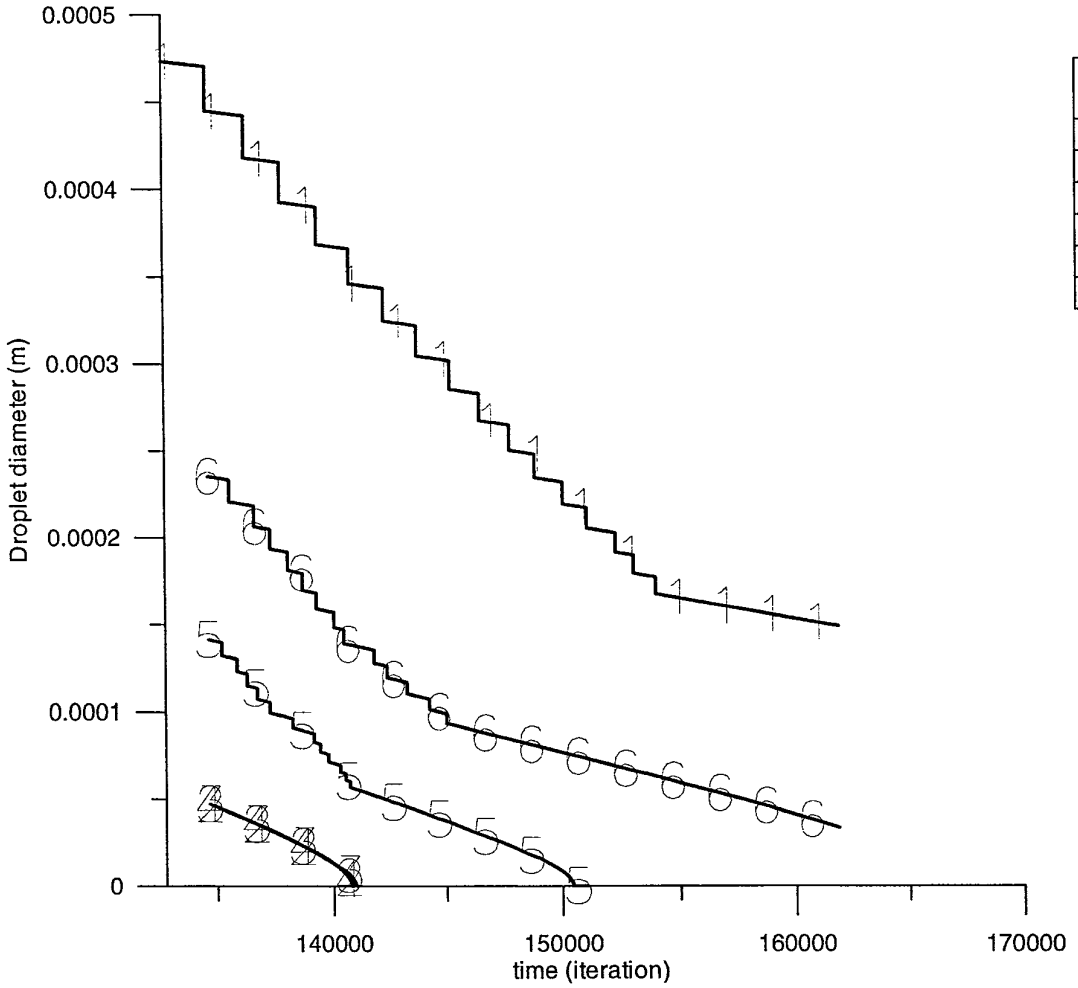
SECONDARY DROPLET DISTRIBUTION DURING THE WHOLE ATOMIZATION PROCESS SIMULATION



SECONDARY DROPLET DISTRIBUTION DURING THE WHOLE ATOMIZATION PROCESS SIMULATION



DIAMETER EVOLUTION OF THE PRIMARY DROPLET AND THE SECONDARY DROPLET



Droplet number	initial diameter	Number of break-up
1	4.71E-04	16
6	2.35E-04	13
5	1.41E-04	12
2	4.71E-05	0
3	4.71E-05	0
4	4.71E-05	0

CONCLUSIONS

- Starting with an initial mono-droplet configuration, the secondary atomization model developped manages to generate a distribution of secondary droplets

- During the break-up process, the droplet diameter evolution results mainly from the atomization model and not from the vaporization model.

- Once the droplet diameter is small enough, its evolution results from the vaporisation model and the break-up processes end.

- A dispersion of the small droplets can be visualized.

PERSPECTIVES

- To test different primary droplet distributions and visualize their effects on the secondary droplet distributions.
- To apply the model to a spray configuration
- To study the atomization model in a spray flame configuration
- To introduce a vaporization model which takes care of the pressure and turbulence effects.

IMPINGING INJECTOR ATOMIZATION RESEARCH AND APPLICATION

Zhang Mengzheng Li ao
The 11th Research Institute of China Aerospace Science & Technology Corporation
Xi'an, China

Abstract

In this article, the development of impinging injector atomization research was reviewed, and some of the research results conducted in China on the injector impingement and atomization by means of laser holography and image processing were also introduced. The effects of impingement angle, injector orifice diameter ratio and momentum ratio of oxidant jet to fuel one on the distribution of drop size and the performance of atomization had also been considered. In the research, the impingement angle varied from 40° to 90°, injector orifice ratio ranges from 1.0 to 1.8, momentum ratio ranges from 1.0 to 2.2. The results suggest that the increase of impingement angle, the decrease of diameter ratio or momentum ratio will result in the decrease of atomization broken length and drop size. In the initial spray region, the velocity of liquid film and liquid ligament is approximately the same as the jet. The empiric formula for predicting droplet Sauter mean diameter size was also provided. The comparison analysis between the water test injector atomization performance and the injector fire test efficiency were made, and it suggested the feasibility of predicting injector hot fire test efficiency and injector selection by cold test atomization experiment.

Nomenclature

D = orifice diameter
D_m = mass median diameter
D_{30} = volume mean diameter
D_{32} = Sauter mean diameter
I = jet momentum
I_{sp} = Specific impulse
K = injecting orifice diameter ratio
Lp = broken length
n = Rosin-Rammler drop size distribution parameter
V = velocity
α = impingement angle
β = spray cone angle
δ = deviation of double jet center
γ = momentum ratio
σ = surface tension
ρ = density
μ = absolute viscosity
η_c = combustion efficiency

Subscripts
f = fuel
g = gas
l = liquid
o = oxidant
p = propellant
ref = reference
x = direction x
y = direction y

Introduction

Injector is the most important part in the thrust chamber of liquid propellant rocket engine. Its function is to realize propellant atomization and mixture so as to produce high efficiency and stable combustion. The distributions of atomization and mixture ratio of propellant in the thrust chamber determine the combustion efficiency, the distribution of the temperature field and the thermal flux to the chamber wall in the thrust chamber.

The selection of injector style is determined by many factors, such as the propellant combination, the mix ratio of oxidant and fuel, the pressure drops of the injectors, the combustion chamber dimension, the performance level demanded, the simplicity of manufacture, the designer's experience and so on. The best design should have the demanded performance, good stability throughout all running range and low manufacture cost.

The impinging injector unit has the characters of sample structure, promptly respondent, rapidly mixing and

combustion, and have been widely used in storable and hydrocarbon propellant liquid rocket engine. The impinging injector can be divided into like-on-like injectors (impinging streams have the same properties in geometry and kinetics) and unlike injectors (oxidant jet impinges fuel jet). The injector can also be divided into double streams style (like-on-like or unlike), three streams style, four streams style, five streams style and so on, depending on the number of impinging streams.

The like-on-like and unlike injector are element unit of impinging injector. Like-on-like injector use the same propellant impinges on each other then mixing with the other kind of propellant. It can produce a dispersed combustion area. Like-on-like unit is widely used in large thrust engine. The unlike injectors use the impingement of oxidant and fuel to realize the atomization and mixture of propellant, is widely used in low thrust engine. The impinging injector has been widely studied and much achievement has been obtained. But because the complication of atomization and lack of advanced experiment technology, till now there isn't a good model of atomization and mixture. The design of injector was depended on the experience method. It is necessary to deeply study the principle of the atomization, especially of the initial atomization, to study the relationship between the atomization performance and the affective factors. It can optimize the injector design.

In this article we have reviewed the development of impinging injector atomization research, and especially introduced our study on double jet impinging injector. The experiment obtained relationship between the impingement angle, the diameter ratio, momentum ratio and spray structure, drop size and distribution, drop velocity. The empiric formula for Sauter mean diameter D_{32} was provided. In our study the impingement angle range is 40°~90°, the orifice ratio range is 1.0~1.8, the momentum ratio range is 1.0~2.2. The comparison analysis between cold test atomization characteristics and fire test efficiency results were made, and proved the possibility to evaluate inject fire test performance and select injector from cold test atomization characteristics.

Review on atomization research

1 Common features of impinging injectors

The design parameters of impinging injector include impingement angle, orifice diameter, diameter ratio and the flow parameter. The geometry and flow parameters of injector that used in practice engine are shown on Table 1. The aperture cross section of injector is usually round. Injector orifice are typically fabricated by twist drilling, electrical discharge machining or laser drilling. The orifice entrance edge is usually sharp. The impingement point length to diameter ratio is typically about two to five. The angle between two jets is generally about 60°.The injection pressure drops range from about 0.5 to 3.0 MPa. A vena contract zone is usually formed by the stream at the downstream of the injector element entrance region and subsequently the stream reattaches to the wall. The typical orifice discharge coefficients range within the thin orifice limit of 0.6 and 0.9. Based on orifice diameter and liquid properties, Reynolds numbers are on the order of 10^5~10^6 under typical rocket operation conditions. Weber numbers ($W_{er} = \rho_l u_j^2 d_o / \sigma$), indicating the balance between liquid inertial forces which tend to fragment the propellant and surface tension forces which tend to maintain the integrity of the liquid drop, are on the order of 10^5.

Table 1 Key features of impinging injector used by practice engine

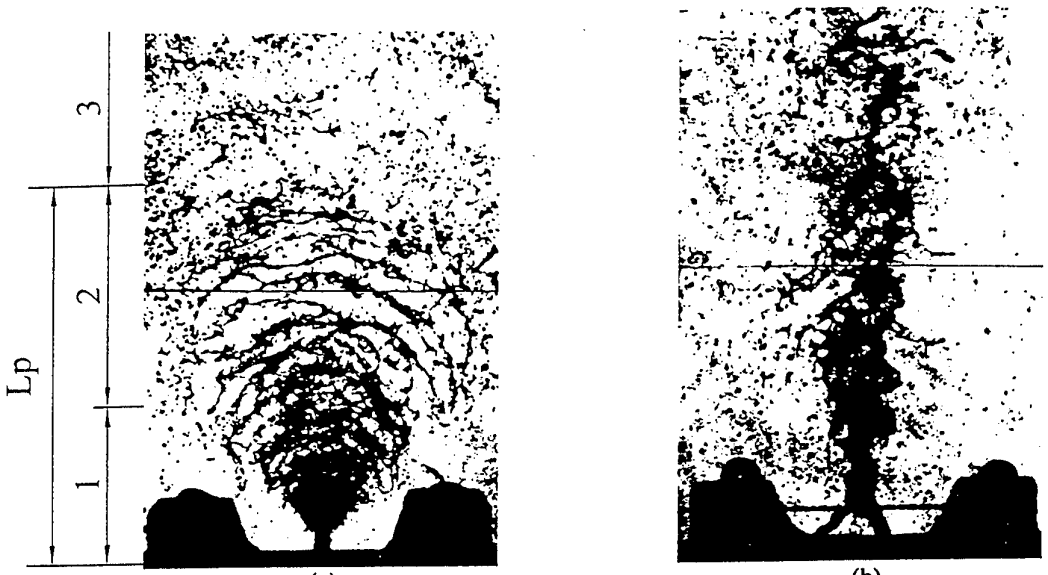
Engine	Propellant	Thrust	Number of main unit	Type	Orifice diameter (mm)		D_o/D_f (only for UD)
		KN			Ox	Fu	
Gemini 1st Stage	NTO/A-50	956*	Ox: 568 Fu: 516	L D	3.05	2.03	
Gemini 2nd Stage	NTO/A-50	445**	Ox: 1319 Fu: 818	Quadlets	1.27	1.02	
Apollo LEMDE	NTO/A-50	47**	165	F-O-F	1.96	1.24	
Apollo LEMA	NTO/A-50	16**	177	U D	1.28 0.92	1.01 0.81	1.27 1.14
Titan II Booster	NTO/A-50	954*	Ox: 1319 Fu: 818	Quadlets	3.02	2.08	
Lance (XRL) Booster	IRFAN/UDMH	187*	460	U D	1.85	1.31	1.41
Lance (XRL) Sustainer	IRFAN/UDMH	18**	108	U D	1.52	1.52	1.0
AGENA	HDA/UDMH	75**	Ox: 88 Fu: 176	Triplets	2.85	1.24	
Long March 3 YF-20	NTO/UDMH	697*	Ox: 607 Fu: 605	L D	2.70	2.30	

Long March 4 YF-40	NTO/UDMH	5*	Ox: 100 Fu: 105	L D	1.35	0.9	
YF-90	NTO/UDMH	0.025**	1	U D	0.54	0.37	1.47
YF-92	NTO/UDMH	0.010**	1	U D	0.028	0.026	1.08
Ariane Viking V	NTO/UH25	680*	Ox: 216 Fu: 216	L D	4.3	2.9	
Space Shuttle OME	NTO/MMH	27**	Ox: 272 Fu: 272	L D	0.81	0.71	
Redstone, A-7	LOX/EtOH	347*	Ox: 355 Fu: 355	L D	2.87	2.58	
Titan I Booster	LOX/RP-1	801*	Ox: 560 Fu: 610	L D	3.02	/	
Titan I 2nd Stage	LOX/RP-1	356*	Ox: 328 Fu: 392	L D	2.16	1.45	
Saturn 1B, H-1	LOX/RP-1	91*	Ox: 365 Fu: 612	L D & T R	3.05	2.08	
Saturn 1C, F-1	LOX/RP-1	6730*	Ox: 714 Fu: 702	L D	6.15	7.14	
Atlas MA-5 Booster	LOX/RP-1	734* (each TCL)	Ox: 335 Fu: 582	L D & T R	2.87	1.61	
Atlas MA-5 Sustainer	LOX/RP-1	254*	Ox: 144 Fu: 175	T R	3.05	2.37	
Jupiter	LOX/RP-1	667	Ox: 361 Fu: 361	L D	2.87	2.26	
Thor, MB-3	LOX/RP-1	756	Ox: 335 Fu: 582	L D & T R	2.87	1.61	

*Seal level value **Altitude value

2 The atomization of injector

Figure 1 is the photos taken along the spray fan and perpendicular to the spray fan respectively. The atomization mechanism is analyzed in this way: In the typical case of dynamically similar impinging jets, double jet impinge each other with high speed, both jets converge and stagnate at the impingement point where a very high-pressure region is formed. The kinetic energy of jet transform into potential energy. The ideal static pressure at this point is equal to the total pressure of the propellant main fluid after deceleration at the stagnate point. Then the fluid is accelerated nearly close to the jet initial velocity. The potential energy of jet transform into kinetic energy. The measurements of Anderson[1] and this paper on the liquid film and liquid ligament and droplets under variable geometry condition and flow condition are the evidence of above phenomenon. The high pressure in the stagnation region also causes the jet spread laterally to create a fan, the shear occurs in the region between the stagnation streamline along the jet axis and the constant pressure streamline that defines the outer boundary of impinging jet system. The impinged jets produced impingement wave and high-pressure make fluid scatter and form liquid film. The impingement wave is the main energy source for two impinging jets, it makes the spray fan produce sine-wave-like pulse. At present, although the wavelength, frequency and transmit velocity of the wave have been measured, but the study is still inadequate. Then, the liquid film is split by surface tension and disturb force and turned into liquid ligament and droplets. Droplets continued to split under the effects of surface tension and disturb force until the kinetic balance is reached between droplets and around atmosphere. The Weber number can be used to judge if the droplet would be split further. For the atomization process shown in Fig. 1, the atomization field can be divided into three region: The impingement wave and liquid fan region, the liquid film and liquid ligament region, the second atomization and full atomized region. In the impingement wave and liquid fan forming region, the procedure is the transform between kinetic energy and potential energy, and impingement wave forming, oblige jets scattering and producing liquid fan. This region was mainly effected by initial condition (such as impingement angle, velocity) of jets, it is the main region to affect combustion stability. In the liquid film and liquid ligament atomization field, the main affect factor is atmosphere kinetics, viscosity, inertia force and surface tension, split is mainly determined by the initial condition of liquid film and liquid ligament. Weber number determines whether the droplet will continue split. In the second atomization and full atomization region, the drop is affected by gas dynamic forces, viscosity, inertia force and surface tension. The gas dynamic forces make drop shape changing, the inertia force and surface tension safeguard the drop shape. When balance of two forces is broken, the droplet split would happen.



(a) (b)

Fig. 1 The impinging injector photo taken in the surface parallel to fan surface (a) and perpendicular to spray fan (b)

To understand the relative order of effect of stresses that can disrupt the intact liquid provides insight into the physics of atomization. Following Ranz[2], order of magnitude estimates of the atomization process active stresses of a like double fuel element in the F-1 engine are presented in the Table 2. For this injector, the injection velocity v_j was 17 m/s and the impingement angle was 30 degree. To estimate interfacial shear effects, the relevant length L was calculated by using turbulent boundary layer dimensionless thickness δ /d that grows as $0.16Re^{-1/7}$, where x was scaled by the orifice diameter d_o. This leads to a boundary-layer depth estimate of $\delta \sim 0.06d_o$, or L~0.4mm for both liquid and gas. To estimate ambient fluid inertia, a maximum relative velocity is used with the assumption that quiescent atmosphere surrounds the jets, thus V~17m/s. The liquid inertial forces is depended on the relative velocity of two jets, here, the relative velocity of the two jets is 8.8m/s. The liquid's cohesive forces were estimated with injector diameter d being equal to 7.1mm and surface tension of kp-1 in air, σ being equal to 1.5mg/s.

Table 2 Force on a liquid element (using F-1 quadlets injector as case study)

Viscous forces			
	Ambient fluid, N/m^2,	$\mu_g V/L$	0.04
	Liquid boundary layer, N/m^2	$\mu_l V/L$	3.6
Inertia forces			
	Ambient fluid, N/m^2	$\rho_g V^2$	2.0
	Liquid, N/m^2	$\rho_l V^2$	62
Cohesive force	N/m^2	σ/d	0.0002

* Quote from [4]Anderson. W.E., Ryan H.M. and Stantoro R. J., "Impinging injector Atomization", in "Liquid Rocket Engine Combustion Instability", published by AIAA.

It is seen from Table 2 that the magnitude of liquid inertial forces are one order higher than that of the aerodynamic stress. Only when length scales become extremely small do surface tension effects become important. The condition of the jet before impingement is very important in determining atomization characteristics. The jet dynamics will play the major role in the breakup of the liquid sheet. For injector design scheme compare and performance qualitative evaluate, it is adequate if only jet dynamic is taken account.

2.1 Effects of geometry and flow course on atomization

Injector geometry parameters include impingement angle, orifice diameter, diameter ratio. The major flow parameters is momentum(or injector velocity, drop of pressure). The atomization parameters that the designers interested are the spray structure, split length, droplet size and distribution, droplet velocity, mixture efficiency of propellant.

2.2.1 Effects of geometry and flow course on spray structure

Spray structure produced by straight flow style injector, co-axis style injector or centrifugal styled injectors are usually simple. But spray structure produced by impinging injector is variable. Heidmann[5] had extensively studied the effects of geometry and flow course on spray structure, include orifice diameter d_o , jet velocity v_j , impingement angle α , pre-impingement length L_j and liquid properties. Liquid velocities between 4 and 30 m/s were studied for orifice diameters of 0.64,1.02 and 1.45mm, with L_j/d_o ratios of 80, 50 and 35 respectively. Impingement angle range was from 30 to 100

degree, viscosity and surface tension effects were studied by using various glycerol solutions, varsol and water.

From these studies, Heidmann[5] determined that the liquid jet velocity and impingement angle were critical parameters in determining spray structure and also identified four spray regions: 1) For low-velocity jet (v_j < 4m/s), liquid sheet was initially formed then was subsequently contracted into a cylindrical stream. A closed rim region could be observed. 2) At higher velocities (4< v_j < 6m/s), waves were appeared on liquid sheet. The drops peeled off from the periphery of the main sheet rim with regularly circle distance, a periodic drop region was displayed. 3) At higher velocities (6< v_j < 9m/s), waves were seen on the surface of the sheet and drops. Liquid sheet displayed an open rim region. 4) At jet velocities between 5 and 10 m/s. Both open rim and periodic drop patterns were seen. For higher viscosity liquid, periodic phenomena was more pronounced. Above 10m/s till the highest tested velocities (~30m/s), spray patterns were displayed as a fully deployed regions, with which the periodic wave motion of drops projecting from the point of impingement was apparent.

Heidmann[5] Reported that sheet breakup length increased with jet velocity for the periodic wave motion and closed rim state, then approached a constant value for open rim state. The breakup length in the fully developed region was not able to measure with any certainty. Figure 1 shows a spray structure of impinging injector, the orifice ratio is 1.4 and the momentum ratio of the two jets along horizontal direction is 1.0.

In fact, the spray structure formed by impinging injector not only depends on the impingement angle and jet velocity, but also depends on two diameter ratio and momentum ratio of the double jets, usually when diameter ratio and momentum ratio of double jets come close to 1.0, the spray structure formed by injector is fan-shape-like in the surface perpendicular to the outlet surface of the injector and ellipse shaped in the plane parallel to injector outlet surface. When the diameter ratio comes close to1.0 but the momentum ratio far exceed 1.0 or momentum ratio comes close to 1.0 but diameter ratio far exceed 1.0, the spray shape in the plane parallel to injector outlet surface will not be ellipse shaped. The accurate shape of spray will be changed with orifice ratio and momentum ratio. For unlike unit, when diameter ratio or momentum ratio far exceed 1.0 , the mixture distribution of propellant will be worse.

2.2.2 Effect of geometry and flow course on drop size

Ingebo[6] used heptane as media to studied droplet size and distribution of like-on-like injector with the impingement angle of 90° under various orifice jet velocity and air velocity. He obtained the volume mean diameter of droplets like

$$D_{30} = D/(2.64\sqrt{DV} + 0.97DV) \tag{1}$$

Zajac[7] mass median diameter formula of the like-on-like injector at 60° impingement angle for melt wax media was:

$$D_m = 1.6\times10^5 \times V_j^{-1} \times \left(P_c/P_j\right)^{-0.1} \times d_j^{0.57} K_{prop} \tag{2}$$

where,

V_j = injection velocity, ft/sec
d_j = orifice diameter, inch
K_{prop} = correction factor for propellant physical properties

Zajac[7] provided the empiric formula of mass median diameter of unlike double jet injector at 60° impingement angle like:

$$D_m = 2.9\times10^4 \times V_f^{-0.766} \times \left(P_c/P_f\right)^{-0.65} \times d_f^{0.293} \times P_D^{0.165} \times \left(d_o/d_f\right)^{0.023} \times K_{prop} \tag{3}$$

where

D_m = mass median drop size, microns
V = injection velocity, ft/sec
P_c/P_j = velocity profile parameter, dimensionless
P_c = dynamic pressure at center of jet, psi
P_j = mean dynamic pressure, psi
d = orifice diameter, inch
P_d = dynamic pressure ratio $\rho_f V_f^2/\rho_o V_o^2$, dimensionless
K_{prop} = correction factor for propellant physical properties
ρ = density, lbm/ft^3

Lourme[8] gave the empiric formula of Vikin engine of Ariane vehicle as

$$D_m = 150\times\left[V_l/30\right]^{-0.95}\left[d_l/2\right]^{0.3}\left[LL_l/5\right]^{-0.8}\left[\rho_g/5\right]^{-0.2}\left[\sigma_l/7.35\times10^{-2}\right]^{-0.5}\left[u_l/10^{-3}\right]^{-0.04} \tag{4}$$

Studies of the effect of the primary impingement angle on drop size for like-on-like impinging jets are reported in references 7 and 9, the relation can be expressed as

$$D_m = \left(1.44 - 0.00734\alpha\right)\times D_{m.60} \tag{5}$$

where α is impingement angle expressed in degree and $D_{m.60}$ is the value for drop mass volume diameter obtained form Eqs. (2).

Experimental study in China

1 Experimental description

Figure 2 shows the scheme and coordinate of our injector studies. The laser holography and image processing system was used to analysis the impinging jet atomization. The hologram of the spray was taken in from Z-axis and Y-axis. The record range of hologram was 120mm. The system resolution is 10 micron. The replicated image was handled by image processing system to obtain the spray characteristics, such as spray cone angles, the spray split length, the drop size and distribution, the drop velocity, Rosin-Rammler drop size distribution parameter (n), number of drops (N), maximum drop diameter, minimum drop diameter, volume-surface mean diameter (D_{30}), mean median diameter and Sauter mean diameter (D_{32}), etc.

The fuel orifice diameter of injector was 1.0mm, water mass flow-rate was 20.8 g/s, injector velocity was kept at constant V_f = 26.6 m/s. Reynolds number was 0.26×10^5, Weber numbers was 0.95×10^4. The oxidant orifice diameter was varied from d_o = 1.0mm to d_o = 1.8mm. The impingement angle of double jet was change from 40° to 90°. The range of momentum ratio of oxidant orifice to fuel was 1.0 to 2.2. The orifice injection velocity range was v_o=14.7 m/s ~ 38.5 m/s. Jets Reynolds numbers range from Re = $0.26\sim0.4\times10^4$. The Weber number range was $0.6\sim2.2\times10^4$.

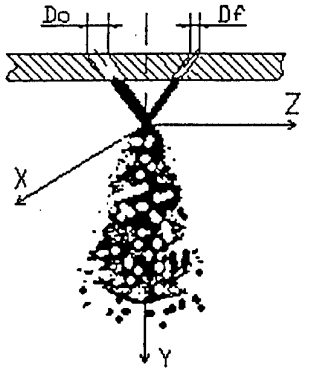


Fig. 2 The scheme of structure and coordinate system of injector

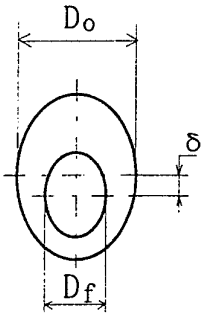


Fig. 3 The deviation of double jet center

2 Test result and typical test analysis

2.1 Spray cone broken length analysis

The spray distribution region could be described by spray cone angles in XOY and ZOY planes, which depend on impingement angles, ratio of diameter and momentum of double jet. A boundary between liquid and air was formed after the expansion of jet atomization. When impingement angles and injection velocity were small, the outlines of boundary between liquid and air were regular and clear. When impingement angles and injection velocity were big, the impinging jet was full atomized, the definition of outlines of boundary was difficult.

In our research, two straight lines can be defined along double side wave peals of liquid sheet in the impingement wave and liquid fan region. The included angle of two straight lines in XOY plane is defined as β_z that one in YOZ plane is defined as β_x, as shown in Fig. 1. Figure 4 shows the α effects on the β_x and β_z for k=1.4, γ =1.0. Figure 5 shows the effects of K on β_x and β_z for γ =1.0, α =40°. It can be shown from Fig. 4, when impingement angle α increased, the momentum of jet along z-axis is also increased, the distribution width of the impinging produced liquid film becomes wider in XOY plane and β_z increased. β_x changed slightly for k=1.0. When k>1.0, since oxidant diameter was bigger than fuel one, part of oxidant jet was not impinged by fuel jet, it would move along original direction. The momentum of oxidant taken part in impingement was smaller than fuel momentum. Therefore the combined spray flow would incline to the side of oxidant orifice. β_x would be increased with the increase of α. The increase of K could lead to the increase of

β_x and β_z, but amplitude of the effects was less that of α for β_x and β_z, as shown in Fig. 4. The trend of effects of k and α on β_x and β_z was the same as shown in Fig. 4 and Fig. 5 for other γ values.

It should be noted that β_x will be increased with the increase of deviation δ. δ was caused by manufacture quality.

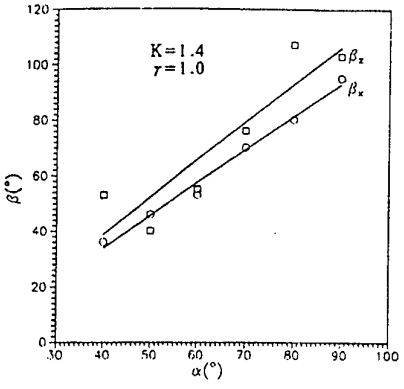


Fig. 4 Effects of α on β_x and β_z

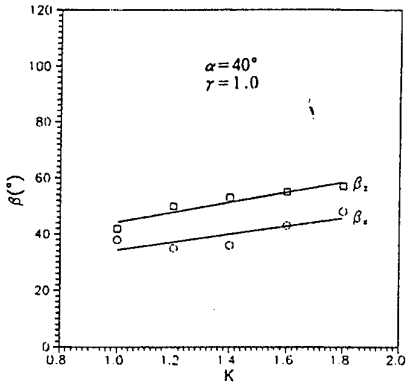


Fig. 5 Effects of K on β_x and β_z

The atomization of liquid sheet and liquid ligament will go through a distance. The distance from impingement point to the point where the liquid ligaments completely broke and turned into droplets defined as the spray broken length, as shown in Fig. 1. Figure 6 shows the effect of k and γ on L_p. Figure 7 shows the effect of α and γ on L_p. The spray broken length is an average value of many laser holograph obtained data.

When α and γ were fixed, the increase of k would lead to the reduction of part of oxidant jet took part in impingement, therefore the broken length increased, as shown in Fig. 6. When k, γ were fixed, the increase of α could lead to the increase of momentum of jet along z-axis, the liquid film thickness decreased, the split become easier, therefore the broken length decreased. The broken length was the smallest one when γ =1.0 in all K. It should be noted that the L_p could be affected by the deviation of double jet center and outside environment.

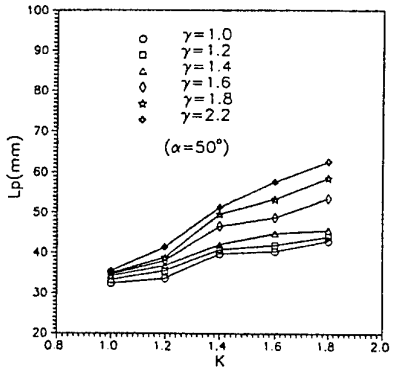


Fig. 6 Effect of k and γ on L

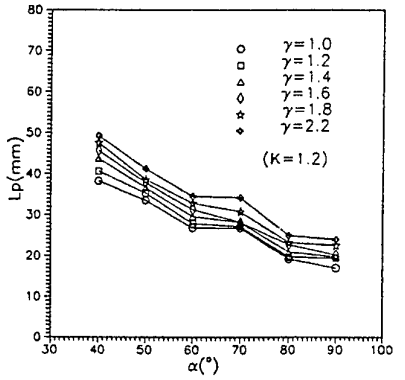
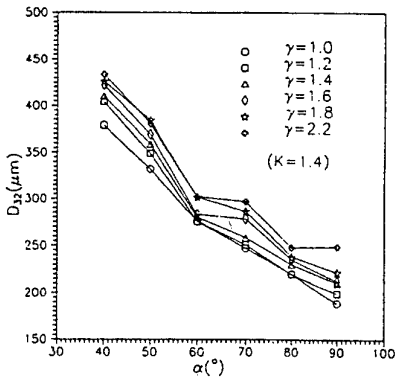


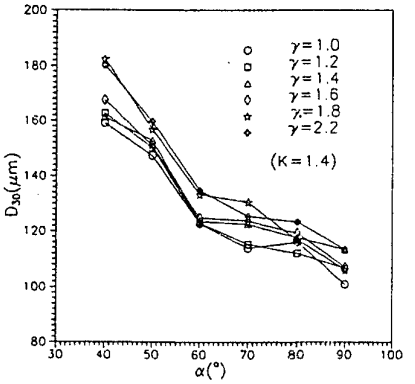
Fig. 7 Effect of α and γ on L

2.2 Drop size and distribution

2.2.1 The effects of α and ratio of jet momentum



(a)



(b)

Fig. 8 Effect of α and γ on D_{32} (a) and D_{30} (b)

Figure 8 shows the effects of α, γ on D_{30} and D_{32} for k=1.4. It has been found in the study that when K and γ were fixed, the increase of α would lead to the reduction of liquid film thickness and the drop size split from film. D_{30} and D_{32} were also decreased. When impingement angles was greater than 60°, for big momentum ratio ($\gamma \geq 1.8$), the trend of drop size decreasing became slower. For K and α were constants, the increase of momentum ratio would lead to the drop size increase. The minimum values of D_{30} and D_{32} would be obtained under any K for γ =1.0. The effect trends of α and γ on D_{30} and D_{32} are the same for other ratio of double jet diameter.

2.2.2 The effects of jet diameter ratio and impingement condition

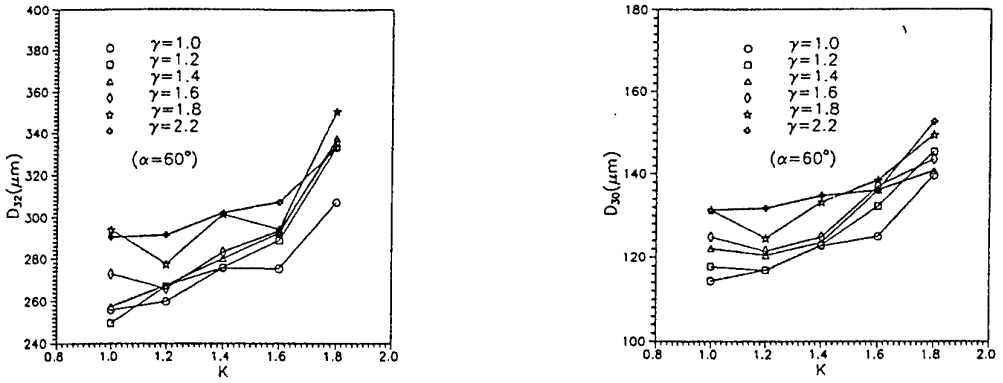


Fig. 9 Effect of K and γ on D_{32} (a) and D_{30} (b)

Figure 9 shows the effect of K and γ on D_{30} and D_{32} for α =60°. Following Fig. 9, the increase of K would lead to the increase of drop size for all γ. When K>1.0, D_{30} and D_{32} would increase more quickly, the Rosin-Rammler size distribution parameter decrease. Based on the deviation of double jet center, the jet impingement condition could be divided into two kinds, the central impinging(δ =0) and the eccentric impinging($(d_o-d_f)/2 \geq \delta > 0$), as shown in Fig. 3. If the effects of liquid dynamic viscosity and surface tension were ignored and assume that the momentum was uniform distributed on the jet cross section, then the momentum was divided equally by jet cross section area. The momentum of jet per unit cross section area could be obtained. The momentum of part of oxidant jet not taken part in impingement could be calculated. The proportion of momentum of part of oxidant jet not taken part in impingement in full oxidant jet momentum was shown in Table.3, for four ratio of diameter, when δ =0 and δ =$(D_o-D_f)/2$.

Table 3 Effects of γ and δ on proportion of momentum not take part in impingement

K	δ =0	δ =$(D_o-D_f)/2$
1.8	33.1%	42.9%
1.6	26%	34.3%
1.4	17.5%	23.6%
1.2	8%	11%

The calculation indicates: When the ratio of diameter increasing, the part of not take part in impingement of oxidant jet increase. When the ratio of diameter is larger than 1.2, the proportion of the oxidant jet momentum not taken part in impingement is 8% for the central impinging. The experiment result indicates: When K>1.4, D_{32} and D_{30} increase quickly. The Rosin-Rammler size distribution parameter decrease. The variation trend for other K and γ condition is the same.

It should be noted: The atomization of impingement injector is realized by the double jet impingement, which also bring about the mixture of double liquid. The proportion of the jet mass not taken part in mixture will be 8% for the central impinging when K=1.2; the spray quality and mixture quality will become worse for eccentric impinging. The increase of K and δ would lead to spray quality and the mixture quality become bad simultaneously. At the same time, spray angle increased, the spray cone is twisted and the combustion efficiency is decreased, combustion chamber wall would be burn out in seriously condition. Therefore the diameter ratio of double jet and manufacture quality is very important. The experimental result has also indicated: the spray split length and D_{30}, D_{32} are smaller in small diameter ratio for all α and γ, therefore, the proposal is fair and reasonable that diameter ratio should be kept less than 1.2 for impinging injector special for unlike unit.

Following above experiment data, the drop size is affected by impingement angle, diameter ratio, and momentum ratio. From the analysis of the experimental data, we have obtained following empirical formula for D_{32}.

$$D_{32} = 849.8 \times \gamma^{-0.4047} \times (3.14159/180 \times \alpha)^{-0.7015} \times K^{0.0026} \times I_o^{-0.1936} \times D_o^{0.3079} \qquad (6)$$

There:

D_{32} = Sauter mean diameter (μ m)

α = Impingement angles (degree)
I = jet momentum per unit across area ($g.m/s^2$)
D = jet diameter (mm)

This equation illustrates the relevance of D_{32} with K, γ, α, I_o and D_o. A good prediction result could be obtained by this empirical formula for impinging injector when parameters of geometry and flow course is within the framework of this paper. When impingement half angle of oxidant is not equal to fuel one, the momentum ratio γ in formula should be taken as momentum ratio of double jets along z direction. The effect level of D on D_{32} is close to the results of formula (2) and (5). It is clear that the impingement angle is the most important parameter of all affective parameters. For the same propellant, small jet diameter, high jet injection velocity, large impingement angles could lead to good spray and mixture quality. Therefore, it is true that the selections of large jet diameter, high injection velocity in large liquid rocket engine may result in good atomization. Because the combustion chamber length is short in low thrust engine, high injection velocity would lead to droplet incomplete combustion, therefore small jet diameter should be chosen. Impingement angle affects propellant atomization quality, back flow of droplet and thruster head temperature, therefore, impinging angle should not be kept too large. The reasonable range of impingement angle is 50°~70°.

2.3 Droplet velocity

Droplet velocity is measured by double pulse laser photography, the pulse interval range from 1 μs to 100 μs. The experiment result illustrates that the droplet velocity in spray field depends on the impingement angles, the ratio of double jet diameter, momentum ratio and jet initial velocity. In the same spray field, drop size and velocity are slightly bigger in initial spray region than in spray region. In general, when the orifice diameter and jet velocities of the two jets (like-on-like injector) are the same, the velocity of the liquid film and ligament are almost the same as the jet initial velocity. This indicates that the momentum of the impinging produced liquid film and liquid ligament have almost reached to the whole dynamic head of the jet. The droplet velocity is slightly smaller than jet velocity in the initial spray region. The big droplet velocity is slightly higher than small one in this spray region. This result is the same as part of results obtained by Anderson, Ryan, etc. in "Fundamental Studies of Impinging Liquid Jets".

When oxidant jet velocity is not equal to fuel one. The impinging produced liquid film and ligament would decrease with the decrease of oxidant jet velocity, but it's value is between oxidant jet velocity and fuel jet velocity. Therefore, the droplet velocity can be replaced by jet injection velocity in digital simulating program. Figure 10 shows the droplet velocity obtained by double pulse photography, the pulse interval was 5 μs. Figure 11 shows the variation of droplet velocity with oxidant jet injection velocity in the initial spray region. The droplet velocity is the average velocity of the velocities of random sampled one hundred droplets.

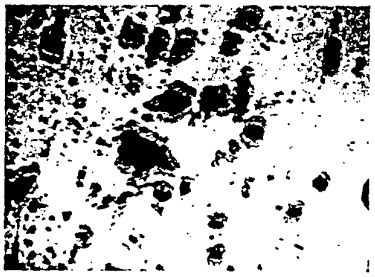


Fig. 10 Holographic photo of droplets taken by double pulse laser

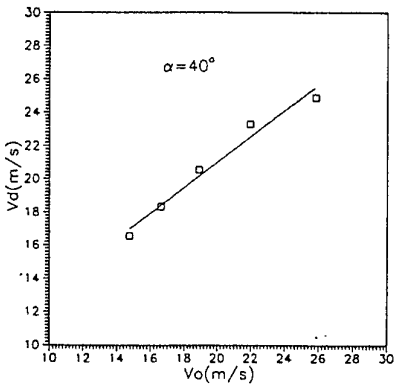


Fig. 11 Effects jet velocity on drop velocity

Application of cold test spray study

As it has been already mentioned above, the impingement deviations of double jet center could lead to the spray and mixture quality deteriorated. Therefore, at least in theory, it is reasonable that based on a large number of cold spray and hot run experimental data statistics and comparison analysis, cold test spray characters could be used to evaluate results of injector fire test. Figure 12 is a photo of spray fan along y-axis, it shows impinging jet doesn't form a gather liquid flow as Fig. 1(b), impinging jet was diffusion. Spray fan produced twirl. This injector was of the same as one shown in Fig. 1(b). The fire test condition was also the same; it's combustion efficiency was 76%. But efficiency of injector shown in Fig. 1(b) was 90%. The fire test results and cold test spray characteristics of double injector are shown in Table 2. The serial number of the double injector are SN02, SN03 respectively.



Fig. 12 Spray photo of an unlike injector taken in YOZ plane

In our study seven injector were tested in sequence, the serial number of the seven injector was SN12, SN03, SN15, SN17, SN19, SN20, SN02. In cold test water was used, spray characteristics were obtained, include β_x and β_z, spray split length, droplet size and distribution, D_{30}, D_{32}, drop distribute parameter, etc. Because β_x represents the impinging phenomenon and manufacture quality; it also reports the mixture quality qualitatively. The spray split length represents the velocity of jet broken, it also reports the combustion deathtrap length, and spray speed level. D_{32} represents and drop distribution indictor n represents atomized drop size and uniformity. Because the experiments were conducted by using water under atmosphere conditions, injection could lead to the air movement, this may, in turn, affect spray. To reduce this effects, the part of spray region of 50×60 mm^2 at x = 0mm, y = 25mm was selected to mention. D_{32}, D_{30} and n had been obtained in this region. Seven injectors had been fire tested after cold test. The fire test results and cold test spray characteristics of seven injectors are shown in Table 4.

As shown in Table 4, the good agreement has been achieved between fire test results and cold test spray characteristics in the condition listed below. The fire test specific impulse $I_{sp} \geq 2600$ m/s but with good combustion efficiency.

1. $\beta_x < 40°$
2. $L < 16$ mm
3. $D_{32} < 150$ μm

The three parameters were used as complexes evaluate index. Based on above complex evaluation index. In the following test, two injectors(SN24, SN25) were selected from five injectors for high altitude simulation fire test. Good agreement had been achieved between fire test results and predicted result. The idea has been proved. The fire test result and cold test spray characteristics are shown in Tab.4.

Table 4 Fire test results against spray characteristics

Injector No.	L(mm)	β (°)	D_{32}(μm)	N	I_{sp}(m/s)	η
SN12	10	33	140	5.45	2780	95%
SN03	12	35	124	5.20	-	90%
SN15	14	30	132	5.14	2700	89%
SN17	16	25	143	5.24	2650	89%
SN19	18	46	158	4.43	2480	81%
SN20	16	40	157	4.75	2400	80%
SN02	10	50	118	4.60	-	76%
SN25	15	30	145	5.04	2625	88%
SN24	13	35	147	5.06	2622	88%

The number of SN02, Sn03 was fire tested on ground.

Conclusions

Our study illustrates:

1.Increase impingement angle, decrease the ratio of double jet diameter and ratio of double jet momentum could lead to the reduction of spray split length and droplets size. The relationship between D_{32} and above perimeter was provided as

Eqs. (6).

2. Double jet diameter ratio should be less than 1.2; the ratio of double jet momentum should be equal to 1.0.

3. Liquid film and liquid ligament velocities are the same as jet injects velocity in initial spray region, the droplet velocity is slightly less than inject velocity.

4. Double jet impingement precession is very important for impinging injector. It would affect spray characteristics and mixture efficiency. For low thrust liquid rocket engine, the fire test results could be predicted by cold test obtained spray characteristics.

Concluding remarks

The purpose of this paper is to provide a concise report on the current state of knowledge on the spray mechanisms of impinging liquid jets. First, a brief report about relationship between perimeters of geometry and flow course and atomization performance is provided. Then, the experimental result of spray structure and drop size affected by impingement angle, diameter ratio and momentum ratio is shown. The empiric formula for D_{32} is provided. Last, the comparison analysis of the injector atomization performance using water test and the result of injector fire test efficiency is made. The possible proposed of injector hot fire test efficiency prediction and injection selection by cold test atomization has be proved by real hot test.

Injector atomization and mixture research has not finished yet. Effects of diameter ratio on propellant mixture, distribution should be further researched. It should also be further studied how the liquid properties and outside environment effect on spray structure and atomization performance. Based on these studies we will be albe to designers with a frame on selection of the design parameter and a method to forecast atomization performance and structure forecast through cold test.

References

[1]Anderson W.E., Ryan H.M., Pals, and Santoro R. J., "Fundamental Studies of Impinging Liquid Jets", AIAA 30th Aerospace sciences Meeting, AIAA paper 92-0458, Reno, NV, Jan. 6-9, 1992.

[2]Ranz, W.E., "Some Experiment on Orifice Spray", *Candian Journal of Chemical Engineering*, Aug. 1958.

[3]Anon, " Liquid Rocket Engine Injectors", NASA sp-8089, 1976.

[4]Anderson, W.E., Ryan, H.M. and Stantoro, R. J., "Impinging injector Atomization", in "Liquid Rocket Engine Combustion Instability", published by AIAA.

[5]Heidmann, M. F., Priem, R. J., and Humphrey, J. C., "A Study of Sprays Formed by Two Impinging Jets", NASA, TN3835, 1957.

[6]Ingebo, "Rocket Motor Injector Performance, Port, Correlation of Experimental Data", Northern Research and Engineering Corporation Report, No. 1045-2,1962.

[7]Zajac, L. J., "Correlation of Injector Spray Dropsize Distribution and Injectors Variables", Final Rep. R-8455, Rocketdyne Div., North American Rockwell Corp., Dec. 15, 1971.

[8]Lourme, D., "Like-on-like Injector Spray Characterization for the Ariane Viking Engine", AIAA Paper 86-1444, 1986.

[9]Knykendahl W. R., "The Effect of Injector Design Variables on Average Dropsize for Impinging Jets", AFRPL-TR-70-73, Air Force Rocket Propulsion Lab. (Edwards, CA), May 1970.



AIAA 99-2888

The Effects of LOX Post Biasing on SSME Injector Wall Compatibility

P. A. Strakey and D. G. Talley
Air Force Research Laboratory
Edwards AFB, CA

L. K. Tseng and K. I. Miner
Boeing Rocketdyne Propulsion & Power
Canoga Park, CA

35th AIAA/ASME/SAE/ASEE Joint Propulsion Conference and Exhibit
20–24 June 1999
Los Angeles, California

For permission to copy or to republish, contact the American Institute of Aeronautics and Astronautics, 1801 Alexander Bell Drive, Suite 500, Reston, VA, 20191-4344.

THE EFFECTS OF LOX POST BIASING ON SSME INJECTOR WALL COMPATIBILITY

P. A. Strakey* and D. G. Talley†
Air Force Research Laboratory, 10 E. Saturn Blvd. Edwards AFB, CA 93524
&
L. K. Tseng‡ and K. I. Miner§
Boeing Rocketdyne Propulsion & Power, Canoga Park, CA

Abstract

An experimental investigation has been carried out to examine the effects of LOX post biasing of a shear coaxial injector on the behavior of the spray near a chamber wall. The experimental work was performed with inert propellant simulants in a high-pressure chamber. Injector flow rates and chamber pressure were designed to match the Space Shuttle Main Engine (SSME) injector gas-to-liquid density and velocity ratio at the point of propellant injection. Measurements of liquid mass flux, gas phase velocity and droplet size were made using mechanical patternation and phase Doppler interferometry techniques. The measurements revealed that the liquid mass flux distribution shifts away from the wall with increasing LOX post bias away from the wall. The shift in the liquid flux distribution was much greater than that caused by the angling of the LOX post alone. Gas velocity near the wall simultaneously increased with increasing LOX post bias away from the wall. The increase in wall side gas velocity was due to the higher fraction of gas injected on the wall side of the injector as a result of the eccentricity at the injector exit. The net result was a decrease in mixture ratio near the wall. Estimates of heat transfer and engine performance relative to the unbiased case are presented.

Introduction

The thrust of rocket propulsion technology today is to reduce engine costs while maintaining engine life and performance. One area of potential improvement in propulsion efficiency and engine lifetime is injector wall compatibility. In an effort to increase engine performance, chamber pressures have historically been increasing. The rate of heat transfer from the hot combustion gasses to the chamber wall is proportional to chamber pressure and in many cases results in a chamber wall temperature that is unacceptably high using regenerative cooling alone. This results in a need for additional wall cooling which is typically accomplished by increasing the fuel flow near the inside wall of the combustion chamber. The increased fuel flow reduces the mixture ratio near the wall, thereby decreasing the temperature of the combustion gasses. The increased fuel flow also provides a protective barrier against oxidizer attack on the chamber wall.

A number of methods have been developed and successfully implemented to provide gas or liquid film cooling protection for the combustion chamber wall. A commonly used method is the introduction of a row of holes in the injector faceplate very close to the chamber wall. These holes provide a curtain of protective film coolant, which can be either gaseous or liquid in phase. This technique can be applied to almost any type of injector configuration and has been used successfully for years in many LOX/kerosene impinging injector engines.

Another method of wall cooling which is particularly applicable to coaxial types of rocket injectors involves operating the outer row of injectors at a reduced mixture ratio either by increasing the fuel flow or by decreasing the oxidizer flow. The lower mixture ratio decreases the temperature of the combustion products near the wall. This is one type of wall protection that is employed in the SSME, which uses LOX/gH_2 shear coaxial injection elements. Another form of wall protection used in the SSME is the angling or "biasing" of the outer row of LOX posts inward, away from the combustion chamber wall. The biasing of the LOX post creates an eccentricity of the fuel annulus providing for a larger flowrate of gaseous fuel on the outer side of the injector. This arrangement, in conjunction with the decreased mixture ratio for the

---

* Research Scientist, Member AIAA
† Research Scientist, Member AIAA
‡ Engineer/Scientist, Combustion Analysis
§ SSME Development Engineer
This paper is declared a work of the U.S. Government and is not subject to copyright protection in the United States.

outer row elements has been proven to provide adequate wall protection.

The price that is paid for protecting the wall by these methods is a loss in specific impulse (I_s) due to deviation in mixture ratio near the wall of the combustion chamber. It has been shown in a number of theoretical and experimental studies that any digression from the average mixture ratio in a combustion chamber results in a loss of performance, as measured by I_s.[1,2] This is true even when the overall engine mixture ratio is not at the optimum mixture ratio for maximizing I_s, as long as the I_s versus mixture ratio curve is parabolic or similar in shape. This is the case with hydrogen and oxygen and most other propellant combinations. The sensitivity of performance to mixture ratio distribution in the combustion chamber is due to the relatively poor rate of mixing in the radial direction as a result of high axial acceleration rates of the combusting propellants, and short chamber lengths in comparison to the chamber diameter.

A study has been conducted at the Air Force Research Laboratory (AFRL) high-pressure cold-flow facility to increase the understanding of the injector wall interaction of a SSME shear coaxial injector. The goal was to provide a detailed understanding, through cold-flow simulations, of the effects of LOX post biasing on the liquid and gas phase distribution near a wall. Understanding the effects of LOX post biasing on the spray characteristics will allow injector designers to minimize the performance loss while still providing adequate wall protection.

Experimental Setup

Water and gaseous nitrogen were used as simulants for LOX and gaseous hydrogen. In order to simulate the conditions inside the actual engine, the tests were performed at elevated pressure and at flow rates which match the hot-fire injection gas-to-liquid density and velocity ratios. Spray characteristics which were measured include liquid mass flux distribution, gas phase velocity and droplet size.

The experimental facility is capable of characterizing full scale single element rocket injectors in cold flow at pressures to 13.8 MPa. Water, which is used as a simulant for liquid oxygen, is stored and pressurized in a 1 m^3 tank. Nitrogen is stored in a 6 m^3 tank at 40 MPa. The injector gas and liquid flow rates are controlled with throttling valves and measured with turbine flow meters to an accuracy of +/- 1%. Chamber pressure is measured to within +/- 0.5%. The maximum water flow rate is 1.8 kg/s and the maximum

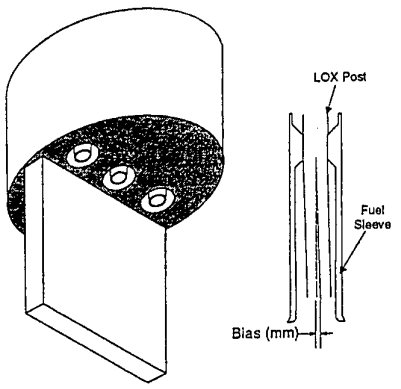


Figure 1: Schematic of the 3-element SSME injector and wall test article along with a cutaway of an injector element.

nitrogen flowrate is 0.18 kg/s. The chamber consists of a 0.5 m diameter stainless steel, optically accessible pressure vessel containing a 27 tube linear array mechanical patternator which can be traversed through the spray. The patternator tubes are 6.35 mm square in dimension. A mechanical shutter prevents liquid from entering the tubes until the spray conditions are obtained at which time the shutter is opened and liquid is collected for a specified amount of time in a series of stainless steel bottles connected to the patternator tubes. After the shutter has closed, the bottles are de-pressurized and the liquid is emptied into beakers and weighed. The mass flux is simply the mass of collected fluid divided by the collection time and cross sectional are of the collection tubes. The patternator was traversed through the spray at 6.35 mm steps, thus yielding a two-dimensional map of the liquid mass flux distribution.

Three 50 mm and one 120 mm sapphire windows provided optical access to the chamber for spray imaging and for droplet size and velocity measurements using phase Doppler interferometry (PDI).

The injector, which was designed and manufactured by Boeing Rocketdyne, consisted of a stainless steel manifold containing three SSME fuel sleeves and LOX posts. The manifold provided separate inlet ports for gas and liquid delivery. A wall was mounted on the face of the manifold at 6.35 mm from the outside edge of the fuel sleeves to simulate the presence of the combustion chamber wall. The LOX posts had an internal diameter of 4.77 mm and the fuel gap annulus was 2.24 mm with the LOX post centered in the annulus. Figure 1 is a schematic of the injector manifold along with a cross sectional view of one of the

injector elements. The LOX posts were biased by angling the posts away from the wall. Bias was measured as the displacement of the tip of the LOX post from the unbiased condition.

Injector Scaling Parameters

Chamber pressure and flow rates were chosen to match the following SSME injector hot fire similarity parameters at the point of injection: gas-to-liquid velocity ratio, density ratio, momentum ratio and mixture ratio, while the maximum gas flowrate was limited by the maximum facility flowrate. Table 1 contains the single element run conditions used in this study along with conditions for the SSME at full power level. The most notable difference between cold-flow and the SSME hot-fire conditions was the lower liquid Reynolds number for the cold-flow tests, which was lower by a factor of 25 due to the lower injection velocity and a seven-fold higher viscosity for water. The results should still provide qualitative information on spray behavior because the Reynolds number for the cold-flow tests was still well into the fully turbulent regime. For all of the results presented here, all three injectors were flowing gN_2 at the flow rate specified in Table 1, however, water was flowed through only the central injector. This was an effort to reduce the optical thickness of the spray field in order to facilitate the droplet size and velocity measurements. The gas flow in the outer two injectors was designed to simulate the aerodynamic confinement encountered in the actual engine.

Table 1 : Scaling parameters for cold-flow and engine operating conditions.

Parameter	SSME (LOX/ gH_2+H_2O)	Cold-Flow (H_2O/ N_2)
Chamber Pressure (MPa)	19.3	0.74
Liq. Flowrate (kg/s)	0.63	0.18
Liq. Injection Vel. (m/s)	31.3	10.0
Liq. Density (kg/m^3)	1117	1002
Liq. Reynolds Number	1.1×10^6	4.3×10^4
Gas Flowrate (kg/s)	0.193	0.056
Gas Injection Vel. (m/s)	360.6	115.9
Gas Density (kg/m^3)	9.47	8.48
Gas Reynolds Number	9.0×10^5	2.4×10^5
Density Ratio (liq/gas)	117.6	117.6
Velocity Ratio (liq/gas)	0.087	0.087
Momentum Ratio (liq/gas)	0.286	0.286
Mixture Ratio (liq/gas)	3.25	3.25

Results and Discussion

Strobelight Imaging

Spray imaging experiments were conducted at a variety of test conditions using a 5 μs duration strobelight to back-light the spray and a CCD camera and VCR to capture and store images of the spray. These images yielded qualitative information on the shape of the sprays. A series of images were taken at the conditions listed in Table 1 for an unbiased injector and for a biasing of 0.48 mm away from the wall. The images in Figure 2 show the spray from the edge on and span an axial distance of 0 to 45 mm (top row) and 45 to 110 mm (bottom row). Note that each image in the top and bottom row series of images was captured at a different instance in time and are therefore representative of typical spray behavior. The dark areas on the image are areas with a high liquid concentration. These images indicate that biasing the LOX posts tended to shift the liquid flow away from the wall.

Liquid Mass Flux Results

Mechanical patternation measurements of liquid mass flux were made with all three injectors flowing N_2 and only the central injector flowing water. Tests were conducted with the LOX posts unbiased (centered in the fuel sleeve) and with the LOX post tips biased away from the wall 0.25, 0.48 and 1.02 mm. Figure 3 contains contour plots of measured liquid mass flux at axial locations of 51, 83 and 127 mm from the injector exit plane. The wall was located at 0.0 mm and the center of the injector was located at 10 mm from the wall. These results show a decrease in liquid flux near the wall and a shift in the peak mass flux away from the wall as the LOX posts were biased away from the wall. The shift in the peak flux was largely due to an increase in gas flow on the wall side of the biased injectors, which will be discussed in a later section.

Figure 4 is a plot of liquid mass flux as a function of distance from the wall through the centerline of the spray. The size and location of the injector is shown in the figure. Figure 4 clearly shows the shift in the peak of the liquid flux distribution away from the wall with increasing LOX post bias. It is interesting to note that the maximum liquid flux displacement occurs for a biasing of 0.48 mm. Further biasing to 1.02 mm did not shift the liquid flux any further away from the wall. Also note that the effect of LOX post biasing diminished with increasing axial distance from the injector.

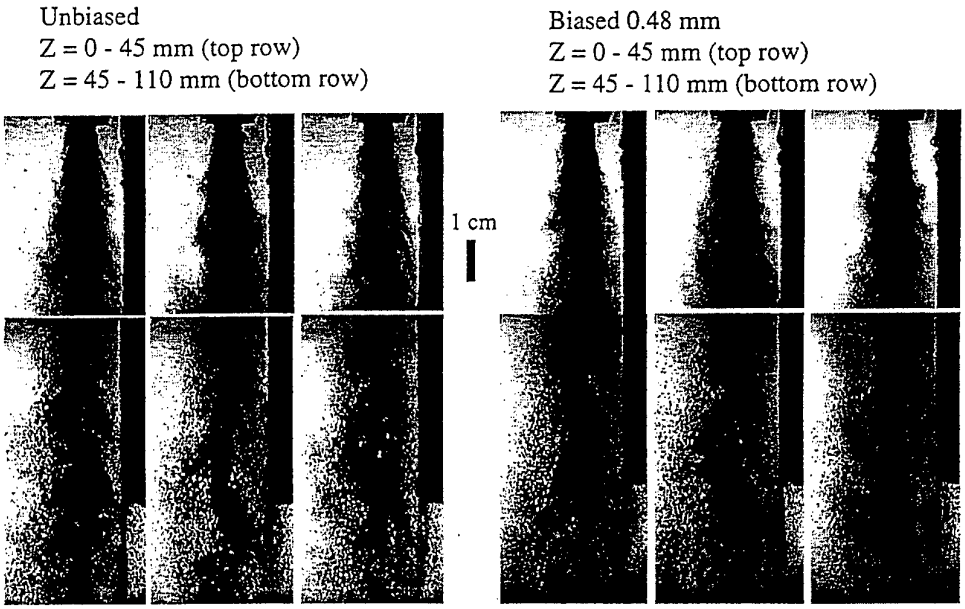


Figure 2: Strobe back-lit images of the unbiased injector spray (left) and biased injector spray (right) at two axial locations. The wall is the dark object located on the right hand side of each image.

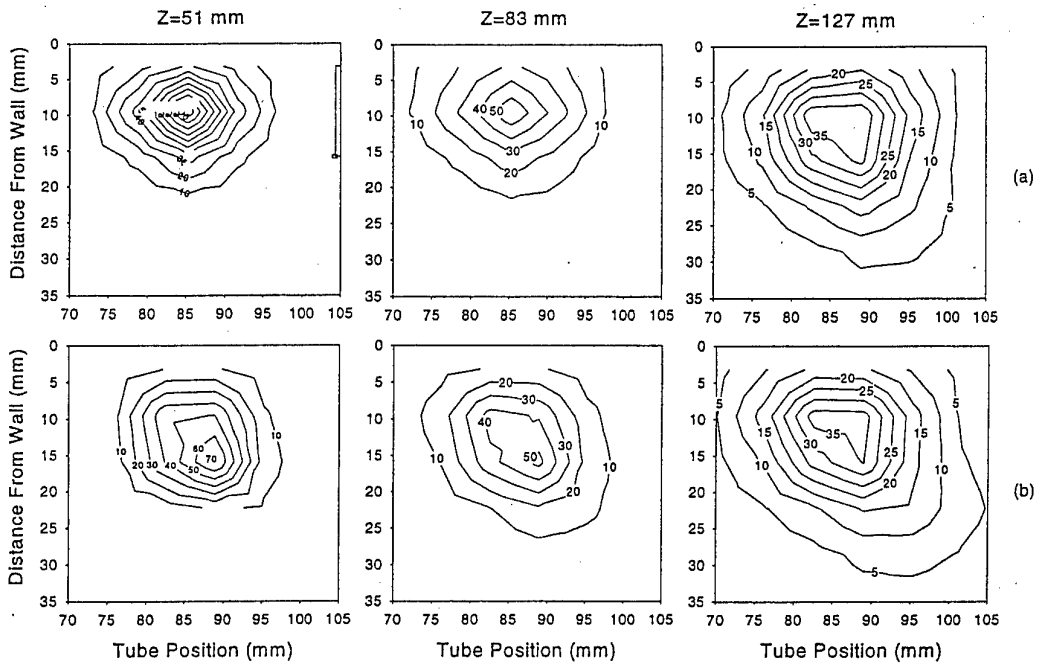


Figure 3: 2-D liquid mass flux distributions at Z=51, 83 and 127 mm, for the test conditions in Table 1 for the (a) unbiased injector and (b) injector biased 0.48 mm away from the wall. The wall is at 0 mm and contours are in gm/s/cm^2.

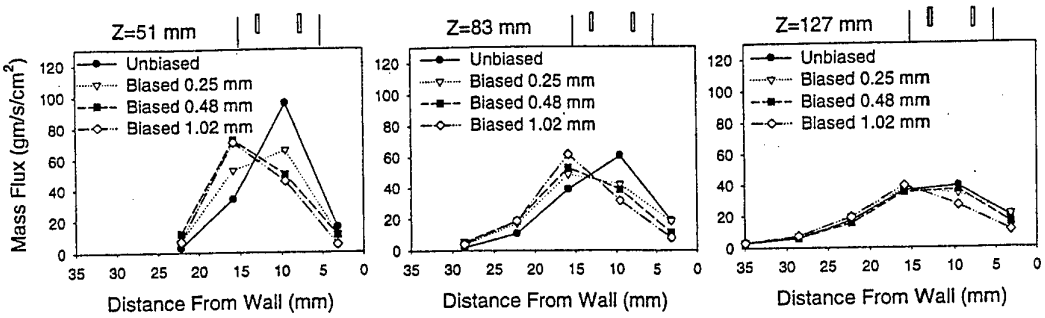


Figure 4: Liquid mass flux distribution through the centerline of the spray as a function of LOX post biasing and axial distance. Run conditions listed in Table 1.

The shift in the peak of the liquid mass flux distribution was much greater than that caused by only the angling of the LOX post. For the case of 0.48 mm bias, the LOX post biasing angle was 0.69°, which would result in a shift of 0.61 mm away from the wall at an axial location of 51 mm. The actual shift in the peak as determined by curve fitting the liquid flux data to a Gaussian profile was 3.9 mm.

Estimation of Error

Several repeat runs were made with the injector biased at 0.48 mm in order to assess the repeatability of the liquid mass flux measurements. The error associated with repeatability varied slightly through the spray but the average standard deviation in liquid mass flux was about 7%. Another error associated with mechanical patternation measurements is rejection of droplets at the entrance of the patternaor tubes due to the formation of a stagnation zone. The patternator bottles were vented back to chamber to allow the gas that enters the collection tubes to return to the chamber. There was, however a pressure drop through the patternation system that generates a stagnation zone at the entrance to the patternator tubes. The smaller droplets tend to follow the gas streamlines around the patternator entrance and are not collected. Larger droplets, which carry most of the mass flux in the spray have enough momentum in the axial direction to overcome the streamlines formed by the stagnation zone and enter the patternator. The amount of error associated with droplet rejection can be assessed by integrating the total mass flux over the extent of the spray and comparing to the injected mass flow rate. The result is a collection efficiency, which will always be less than 100%. The measured collection efficiency for the unbiased and biased runs were similar, but varied in the axial direction. The average collection efficiency was 71%, 80% and 87% for the axial locations of 51, 83 and 127 mm respectively. Collection efficiency increased with increasing axial distance from the injector as the local gas velocity decreased.

Velocity Measurements

Gas phase velocity and liquid droplet size measurements were made with a 2-component phase Doppler interferometer (PDI). Measurements were made with the PDI at axial locations of 51, 83 and 127 mm. The PDI was optically configured to measure the smallest droplets possible. It was calculated that droplets less than about 6 μm in diameter would be following the mean flowfield completely and could be used as "seed" particles for making measurements of the gas phase velocity. The requirement was that the droplet relaxation time, τ_D, be much less than the characteristic mean timescale for the flowfield, τ_F. The relationship used here was;

$$\frac{\tau_D}{\tau_F} < 0.1 \qquad (1)$$

The droplet relaxation time is the time lag for a droplet to accelerate from the injected liquid velocity to the mean flowfield velocity. τ_F and τ_D are calculated as follows.

$$\tau_F = \frac{Z}{V} \qquad (2)$$

$$\tau_D = \frac{\rho_l \cdot D^2}{18 \cdot \mu_g} \qquad (3)$$

In Equation 2, Z is the minimum distance from the injector and V is the maximum flowfield velocity. At a distance of 51 mm the maximum flowfield velocity was estimated to be 50 m/s from initial

experiments. This yielded a time constant, τ_f, of 1.02 ms and a droplet size, D, of 5.7 μm for $\tau_D/\tau_F = 0.1$

Measurements were also made as close as 5 mm from the injector face, but there were very few droplets available for making velocity measurements here, therefore the gas stream being fed to the injector was seeded with a dilute spray of very small droplets to act as tracer particles. The introduction of droplets to the gas flow was far enough upstream of the injection point to ensure that the droplets were following the flowfield.

The PDI was configured with a 500 mm focal length transmitter and receiver lens. A 60 μm beam waist and a 50 μm slit were used in order to facilitate measurements in the anticipated high number density sprays. A ten-to-one intensity validation scheme was implemented to reject erroneous measurements associated with the relatively small beam waist in comparison to the droplet sizes being measured ($2<D<350$ μm).[3]

The PDI was fixed in location with respect to the chamber windows and the injector was traversed through the probe volume at 1 mm steps for the axial location of 5 mm and 3 mm steps for all other axial locations. This yielded a radial profile of the gas phase velocity and droplet diameter from the outside edge of the spray to the wall, through the centerline of the spray as defined by the center of the LOX post. At each location in the spray, 5000 measurements were recorded. Velocities are reported as the average velocity of droplets less than 6 μm in diameter. It was found, however, that there was very little correlation between droplet size and velocity, indicating that velocity was independent of droplet size.

Figure 5 contains plots of gas phase axial velocity as a function of distance from the wall at axial locations of 5, 51, 83 and 127 mm for the test conditions listed in Table 1. The relative size and location of the injector is shown on each plot. Figure 5 shows that near the exit of the injector (Z=5 mm) the gas phase velocity was only slightly higher on the wall

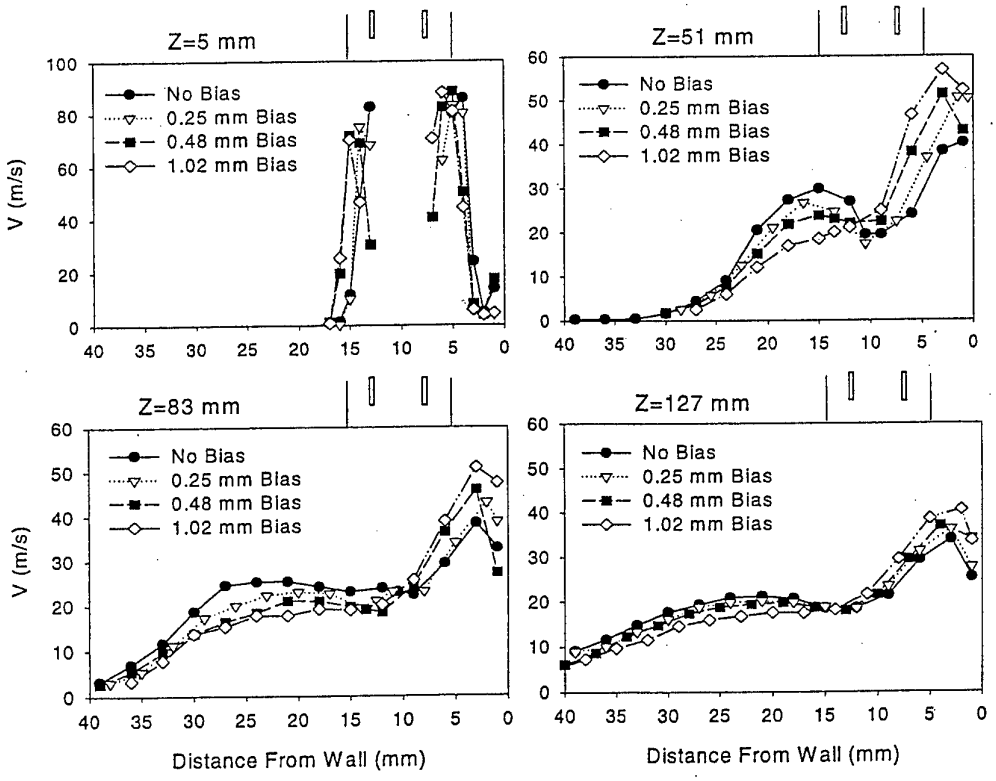


Figure 5: Gas phase axial velocity profiles versus distance from the wall at axial locations of 5, 51, 83 and 127 mm. Profiles are through the centerline of spray as defined by the LOX post and the injector is shown schematically in the plots.

side of the injector than the far side of the injector. Note that at the axial location of Z=5 mm, no data is shown in the center of the spray. This is due to the fact that at this axial location the liquid core of the spray was still intact and data validation rates at these locations were very low. Further downstream from the injection point the gas phase axial velocities were much higher on the wall side of the spray than the far side of the spray. This is because the spray was physically confined by the presence of the wall at 0 mm and was aerodynamically confined by the injectors operating on either side of the spray. The far side of the spray was not confined and was free to expand, thus resulting in a lower velocity.

The most interesting feature of Figure 5 is the increase in velocity near the wall with a corresponding decrease in velocity on the far side of the spray for the runs with the LOX post biased away from the wall. The ratio of wall side velocity to far side velocity increased with increasing LOX post bias. The velocity gradient was caused by the unequal exit areas of the gas annulus at the injector exit, with a larger flow area on the wall side of the injector. Since the flow was physically confined on the wall side of the injector, the wall side velocity must increase as the injector exit area and hence flow rate increased with bias. The effect of biasing was most prominent at the 51 mm axial location, with a decrease in relative effect as the spray evolved in time (axial distance) from the point of injection. The decrease in influence of the LOX post bias on the velocity distribution with increasing axial distance was a result of transport and mixing of the unevenly distributed gas on the wall side of the spray to the far side of the spray due to the large axial velocity gradient in the radial direction. This was the driving force behind the shift in the liquid phase away from the wall in Figure 4.

In order to calculate the liquid-to-gas mixture ratio from the liquid flux and gas phase velocity data, which were collected at different spatial resolutions, the liquid flux data were curve fit to a Gaussian profile and the mixture ratio was calculated at the data points corresponding to the gas phase velocity measurements. The mixture ratio distribution for the unbiased and biased injectors is shown in Figure 6. The shift in mixture ratio away from the wall was most prominent at the axial location of 51 mm, but persisted even at the 127 mm location. The shift in mixture ratio was due to the combined effect of the shifting of the liquid flux distribution away from the wall, and the increased gas flow near the wall. The total measured mixture ratio for each run was significantly less than the injected mixture ratio of 3.25 due to entrainment of chamber gas into the spray. The amount of entrained gas increased with increasing distance from the point of injection.

Heat Flux Analysis

One of the goals of the present investigation is to use the experimental cold-flow data to estimate the effects of LOX post biasing on wall heat transfer and engine performance in the SSME. Since the engine operates fuel rich, any reduction in mixture ratio near the wall might imply a decrease in hot gas temperature and heat transfer to the wall. Two approaches were used to predict relative changes in heat transfer between the unbiased and biased injector data. The first approach incorporated a flat plate turbulent heat transfer correlation (Equation 4) using the measured gas velocity and mixture ratio near the wall.[4]

$$q^{"} = 0.0296 \mathrm{Re}_z^{\frac{4}{5}} \mathrm{Pr}^{\frac{1}{3}} \frac{k_g}{Z}(T_g - T_w)$$

$$\mathrm{Re}_z = \frac{V_g \rho_g Z}{\mu_g} \qquad (4)$$

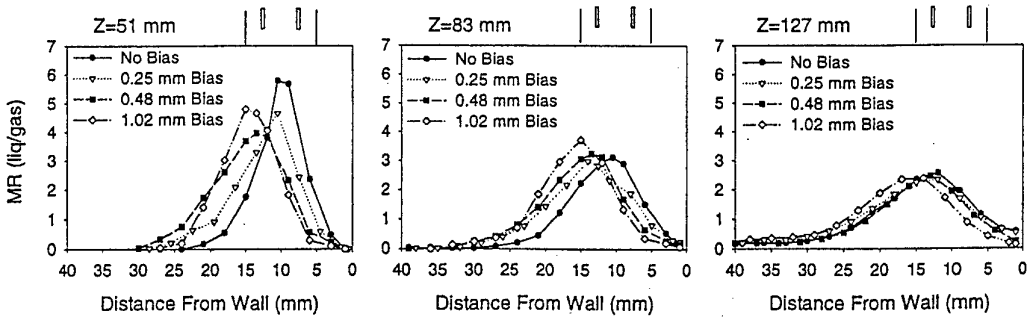


Figure 6: Mixture ratio distribution for unbiased and biased injectors at axial locations of 51, 83 and 127 mm. Injector size and location is shown on the plots. Test conditions are given in Table 1.

Table 2: Relative change in heat transfer for biased data.

Biasing (mm)	Δq" @Z=51 mm	Δq" @Z=83 mm	Δq" @Z=127 mm
0.25	-8%	-4%	-4%
0.48	-7%	-20%	-14%
1.02	-11%	-28%	-29%

Local gas temperature and transport properties were calculated using the NASA CEA chemical equilibrium code using the mixture ratio data from Figure 6. A constant wall temperature of 600 K was assumed in the calculation for both the unbiased and biased data. The heat flux was averaged from 1 to 6 mm from the wall, which was estimated to be the extent of the thermal boundary layer at the throat of the SSME using Equation 5.

$$\delta_t = 0.37 \cdot Z \cdot \mathrm{Re}_z^{\frac{-1}{5}} \qquad (5)$$

The average Reynolds number in the SSME combustion chamber is estimated to be about 5×10^6 which yielded a boundary layer thickness of 6 mm at the throat. The calculated heat fluxes for the biased runs were expressed as a percent change from the unbiased data and are tabulated in Table 2.

It is interesting to note that the maximum reduction in heat transfer occurred further downstream with increasing LOX post bias. In the SSME the outer row of injectors contain LOX posts which are biased 0.48 mm inward. The predicted decrease in heat transfer from the cold-flow data is 7% at the 51 mm axial location, increasing to 20% then dropping off to 14% at the 127 mm axial location.

The second method of predicting heat transfer from the cold-flow data involved a manipulation of sub-scale hot-fire test data obtained with a calorimeter test chamber and unbiased injectors. The calorimeter test data provided a profile of heat flux as a function of axial location between the injector faceplate and the chamber throat. Heat flux data obtained with unbiased injectors was adjusted by the relative change in gas velocity and mixture ratio near the wall between the biased and unbiased cold-flow data. The effect of mixture ratio and velocity on heat transfer was assumed to be similar to the previous method using a flat plate heat transfer correlation. The effect of biasing (for the 0.48 mm biased data), as measured with the cold-flow experiments was then extrapolated to the chamber throat to obtain an integrated heat load reduction of 7.1%, which agrees very well with full-scale engine test data. The main difference between these two methods of predicting heat transfer is that method 1 provides a measure of relative heat flux at several axial locations, while method 2 provides a prediction of overall heat load change.

Performance Analysis

The most commonly used method of estimating the performance impact of mixture ratio non-uniformity in a rocket engine is stream-tube analysis. The assumption is that there is negligible mixing between adjacent injectors and therefore the performance of each injector can be calculated separately and summed to obtain the total engine performance, which can be measured by specific impulse. The use of stream-tube analysis to predict engine performance has been validated with a large database of experimental hot-fire data.[5] A schematic representation of stream-tube analysis is given in Figure 7 which shows that each injector element is assumed to operate over an equal area of the combustion chamber and does not mix with adjacent elements.

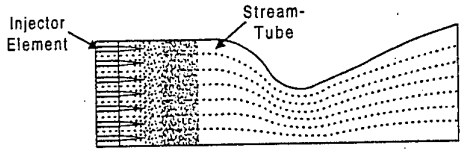


Figure 7: Schematic representation of stream-tube analysis.

The SSME injector consists of 600 elements, 515 of which are unbiased "core" elements and 85 of which are biased "wall" elements. Each of the core elements constituted 1 stream-tube, while each of the wall elements was subdivided into two sub-stream-tubes representing the wall side of the spray and the far side of the spray. The dividing line that defines the center of the spray was taken to be at the point of maximum liquid flux as measured with the cold-flow experiments. Since the shape of the liquid flux distributions for all of the runs was very similar, the relative amount of gas flow on each side of the spray was assumed to be the only factor in skewing the mixture ratio from the unbiased condition. I_s was calculated by assuming that the unbiased data represented a case of perfect mixing at the injected mixture ratio, and the biased data represented a deviation from perfection by the amount of gas flow on

each side of the spray relative to the unbiased condition. Vacuum I_s was calculated using the NASA CEA chemical equilibrium code for the injected propellants. The oxidizer was LOX at 122 K, while the fuel is a mixture of 55% gaseous hydrogen and 45% water vapor by weight at approximately 800K. Note that the mixture ratio was defined as the ratio of oxidizer to fuel, not oxygen to hydrogen. The calculated vacuum I_s as a function of mixture ratio and LOX to H_2 ratio is provided in Figure 8. In the SSME the outer row of injectors operate at a LOX to hot gas mixture ratio of 3.0 while the core injectors operate at 3.4. The overall LOX to H_2 ratio for the SSME is about 6.0.

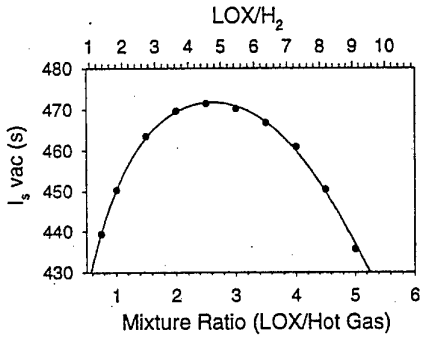


Figure 8 : Vacuum I_s versus mixture ratio and LOX-to H_2 ratio for the SSME.

The calculated vacuum I_s for each side of the spray was multiplied by the mass fraction (m_f) of propellant on each side of the spray and summed to obtain the total I_s within the stream-tube. The total I_s for the engine was calculated in a similar fashion, by summing the $I_s \cdot m_f$ of all 600 individual stream-tubes.

The calculated I_s, expressed as a change from the unbiased condition is given in Table 3 as a function of LOX post biasing at each axial location. Each axial location represents a calculation of performance assuming that location represents the overall state of mixing in the engine. Many researchers have made direct comparisons between cold-flow and hot-fire data at equivalent axial locations. A study with gaseous oxygen and gaseous hydrogen propellants has suggested that the fraction of heat released in an engine is roughly equal to the cold-flow mixing efficiency at equivalent residence times from the point of injection.[6] For the SSME, the total chamber residence time is approximately 1 ms, which would most closely match the cold-flow data at the 51 mm location. The I_s calculations at other axial locations are provided as an estimation of the range of I_s losses that could be expected with LOX post biasing.

Also provided in the last column of Table 3 is an estimate of I_s loss from a method similar to the one just described, but where the amount of gas flow on each side of the spray was assumed to be equal to the relative cross-sectional area of the gas annulus at the LOX post tip. The flow was divided at the center of the LOX post. This analysis did not use any of the cold flow data. It is interesting that this simple analysis agrees well with the analysis based on cold-flow data (highlighted in bold) at an axial location that decreases with increasing LOX post bias. All of the performance loss estimates for the case of 0.48 mm (SSME) show that the amount of I_s loss is very small and is probably too small to verify with full scale engine test data.

In an effort to find the optimum LOX post bias for minimizing heat transfer while maximizing I_s, the heat transfer data from Table 2 was normalized by the percent decrease in I_s from Table 3, and is shown in Figure 9 for the three different axial locations. The peak of each curve in Fig. 9 represents the LOX post bias at which the heat transfer to I_s loss ratio is optimized. Although the 83 and 127 mm data were optimized at a bias of 0.48 mm, the 51 mm data was optimized at a bias of 0.25 mm. It is possible that the overall injector optimum operating point is somewhere between the two.

Droplet Size Measurements

Droplet size measurements were made with the PDI technique described previously. Droplet size data is presented for the axial location of 127 mm in Figure 10 in the form of the volume mean diameter, D_{30}. Droplet size data is shown only for the locations where the data validation rates where relatively high (> 60%) and the PDI measured mass flux agreed

Table 3: I_s change from unbiased condition from cold-flow data analysis and from injector area analysis (last column).

Biasing (mm)	ΔI_s (s) @Z=51 mm	ΔI_s (s) @Z=83 mm	ΔI_s (s) @Z=127 mm	ΔI_s (s)
0.25	-0.2	-0.25	**-0.13**	-0.14
0.48	-0.63	**-0.50**	-0.27	-0.45
1.02	**-2.18**	-1.08	-0.87	-2.10

relatively well with the patternator data. In the core of the spray at Z=127 mm, as well as with the shorter axial locations, the presence of large, non-spherical ligaments was believed to be the cause of low data validation rates. The presence of large ligaments is supported by the images in Figure 2.

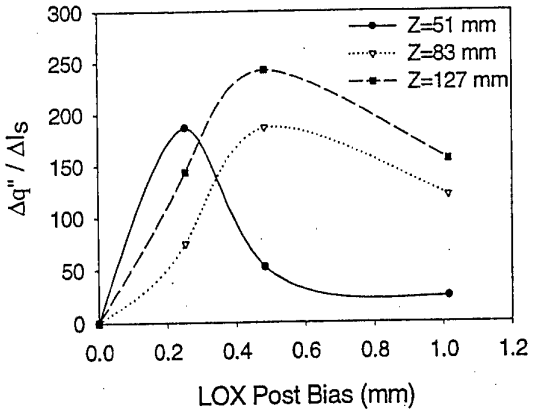


Figure 9: Percent change in heat flux normalized by the percent change in I_s as a function of LOX post bias at Z=51, 83 and 127 mm.

Figure 10 shows an increase in D_{30} on the side of the spray away from the wall with increasing LOX post bias. This was believed to be due to the decrease in gas velocity, and hence, Weber number on this side of the spray as shown in Figure 5. There was also a corresponding decrease in droplet size on the wall side of the spray with increasing LOX post bias.

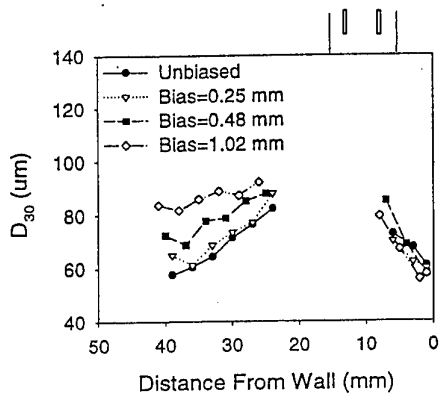


Figure 10: Volume mean diameter versus distance from wall as a function of LOX post bias at Z=127 mm. Test conditions from Table 1. Size and location of injector shown on plot.

Conclusions

The cold-flow measurements have shown a pronounced effect of LOX post biasing on the mixture ratio distribution near the wall. This was largely the result of the increased gas flow on the wall side of the injector. It is this decrease in mixture ratio, and hence combustion temperature, along with a decrease in LOX flow near the wall that provides the protection to the wall of the SSME combustion chamber.

The optimization curves in Figure 9 provide the injector designer with information on how to design a biased injector but do not guarantee that an optimized injector will provide adequate wall protection. Maximum tolerable wall temperature might dictate that the injector be designed far from optimum. The implication for the SSME is that some reduction in the amount of biasing in the outer of injectors might recover some performance loss while still maintaining an acceptable wall temperature.

Droplet size measurements showed a decrease in droplet size near the wall with increasing LOX post bias and a corresponding increase in droplet size on the far side of the spray. The effect on droplet size is probably too small to have a measurable impact on engine performance or heat transfer.

These results will allow injector designers to better predict heat transfer and performance impact in new engines and reduce the amount of time spent in the hot-fire testing and redesign phase of an engine development program.

Nomenclature

D	droplet size (m)
h	heat transfer coefficient ($W/m^2/K$)
I_s	specific impulse (s)
k_g	thermal conductivity (W/m/K)
m_f	mass fraction
MR	mixture ratio (liq/gas)
Pr	Prandtl number
q"	heat flux (W/m^2)
T_g	gas temperature (K)
T_w	wall temperature (K)
V_g	gas velocity (m/s)
Z	axial distance (from injector) (m)
ρ_l	liquid density (kg/m^3)
ρ_g	gas density (kg/m^3)
μ_g	gas viscosity ($N\ s/m^2$)

Acknowledgments

The authors would like to thank Mr. Mike Griggs and Mr. Timothy Auyeung for their assistance in operating the facility and collecting data.

References

1. K. Ramamurthi and A. Jayashree, "Optimization of Mixture Ratio Distribution in Liquid Propellant Rocket Thrust Chamber", *Journal of Propulsion and Power*, Vol. 8, No. 3, May-June, 1992, pp. 605-608.

2. J. L. Pieper, L. E. Dean and R. S. Valentine, "Mixture Ratio Distribution- Its Impact on Rocket Thrust Chamber Performance", *Journal of Spacecraft and Rockets*, Vol. 4, No. 6, June 1967, pp. 786-789.

3. P.A. Strakey, D.G. Talley, W.D. Bachalo and S.V. Sankar, "The Use of Small Probe Volumes with Phase Doppler Interferometry" Presented at the 12th International Conference of ILASS-Americas, Sacramento, CA, May 17-20, 1998.

4. Fundamentals of Heat and Mass Transfer, Incropera and DeWitt, Wiley and Sons, New York, 1985, pg. 319.

5. Nurick, W. H. And Clapp, S. D., "An experimental Technique for Measurement of Injector Spray Mixing", *Journal of Spacecraft and Rockets*, Vol. 6, No. 11, Nov. 1969, pp. 1312-1315.

6. D. F. Calhoon, D. L. Kors and L. H. Gordon, "An Injector Design Model for Predicting Rocket Engine Performance and Heat Transfer" AIAA Paper No. 73-1242, AIAA/SAE 9th Propulsion Conference, Las Vegas, Nevada, Nov. 5-7, 1973.

EFFECTS OF OXIDIZER SWIRLING ON COMBUSTION CHARACTERISTICS OF COAXIAL INJECTORS

Hiroshi TAMURA, Hiroshi SAKAMOTO
National Aerospace Laboratory, Kakuda Research Center

Takao INAMURA, Kei MIYATA
Hirosaki University

Saburo YUASA
Tokyo Metropolitan Institute of Technology

ABSTRACT

Effects of oxidizer swirling on combustion characteristics of coaxial injector were investigated. First, for the coaxial injectors with oxygen-swirl, the thickness of the liquid film at the injector exit was investigated theoretically and experimentally. The empirical equation of a sheet cone angle was deduced from the potential theory of swirl flow of swirl atomizers. Second, the effects of swirl intensity and fuel annulus area on combustion characteristics were investigated with LO_2/GH_2, LO_2/LH_2, GO_2/GH_2 and GO_2/GCH_4 propellants. The progress of combustion was estimated by measuring the chamber pressure distribution and heat flux distribution for the LO_2/GH_2 and LO_2/LH_2 studies. The flame structure and the flame intensity distribution in the combustion chamber were observed for the GO_2/GH_2 and GO_2/GCH_4 studies. It was found that applying swirl to the oxygen jet greatly enhances the combustion near the injector exit. A decrease of fuel annulus area with oxygen-swirl injectors further enhances atomization and mixing near the injector exit, thus reducing the chamber length to complete combustion.

INTRODUCTION

For coaxial injectors, in which oxygen is injected through a central tube and fuel is injected through an outer annulus, the introduction of swirling on the oxygen jet greatly changes the jet configuration. That is, the configuration of the oxygen jet changes due to the swirling motion from a cylindrical jet to a hollow cone jet. The oxygen jet impinges on the surrounding fuel jet intensively near the injector exit, which promotes intense mixing and fine atomization of the propellants. Atomization with oxygen-swirl injectors is reported in [1] to [3] and combustion characteristics are examined in [4] to [9]. Reports on visualization of burning spray can be found in [10] and [11], and oscillating flow with injection elements and instability characteristics are discussed in [12] to [14].

The authors have investigated the effect of oxygen-swirling on coaxial injectors with gas-liquid propellants[6] , liquid-liquid propellants[7] and gas-gas propellants.[8,9] The purpose of the present paper

is to summarized these results and reinvestigate the effect of oxygen-swirling on the combustion characteristics. First, a cold flow study to investigate the spray characteristics of coaxial injectors with oxygen-swirl was conducted. Liquid film behavior in a central oxygen tube, spray angle, and atomization by the oxygen-swirling were investigated. Second, combustion test results with uni-element thrusters and a 9-element thruster with LO_2/GH_2 and LO_2/LH_2 propellants, respectively, were examined. The effect of oxygen-swirl and the effect of the size of annulus fuel area were studied. Axial pressure distributions and wall temperature distributions were measured for these studies to estimate the axial progress of combustion in the chamber. Third, combustion test results with uni-element thrusters employing GO_2/GCH_4 and GO_2/GH_2 propellants were examined. The effect of swirl intensity was investigated. The progress of combustion in the combustion chamber was estimated by observing the flame configuration and the emission spectra from the flame through small quartz glass windows for these studies. Finally, based on these observations, the effects of oxidizer swirling on combustion characteristics were reexamined

ATOMIZATION CHARACTERISTICS OF SWIRL INJECTOR

Experimental Apparatus and Conditions

The structure of the swirl coaxial injector is shown in Fig. 1. Liquid is introduced tangentially into the center post through three holes with a diameter of 0.81 mm. Then liquid flows spirally on the inner wall of a center post tube, and exits in the form of a hollow cone sheet due to the swirling motion. The high speed gas stream is injected axially through the annular slit around the center post, and impinges on the conical liquid sheet. The spray characteristics were measured by PDA (DANTEC, 10 Mw He-Ne Laser) . The behavior of the hollow cone sheet issued from the injector exit was observed by the still back-lighted photograph. The film thickness at the injector exit was measure by the contact needle method[15]. The fundamentals of the contact needle method is illustrated in Fig. 2. When the needle touches the film the electric circuit is closed, and the voltage difference across a resistance is produced. The accuracy of the needle positioning is 1 μm. The experimental conditions are summarized in Table 1. Water was employed as the atomizing liquid and the nitrogen gas was employed as the atomization gas.

Theoretical Analysis of Film Thickness

The film thickness at the injector exit is one of the factors which govern the spray characteristics, and is the important parameter for the design of the injector. In the present study the liquid film thickness was analyzed theoretically. The coordinate system and the variables were defined as shown in Fig. 3. Prior to the analysis, the following assumptions were made;

(1) The liquid flow is two-dimensional.

(2) The laminar boundary layer originates at x= 0, and is maintained up to the injector exit.

(3) The velocity distribution across the laminar boundary layer can be approximated by the biquadratic equation by Ishigai et al..[16]

(4) The liquid velocity outside the laminar boundary layer can be approximated by the constant

velocity, Uo.

(5) The effects of the air flow upon the liquid film and the gravity on the film behavior can be ignored.

(6) The liquid constant velocity, Uo and the liquid film thickness, hi at x= 0 can be determined by the potential theory proposed by Tanasawa and Kobayashi.[17]

The momentum equation of two-dimensional laminar boundary layer is given as follows;

$$K = \sqrt{\frac{1}{k^2} - 1} - k \ln\left(\frac{1}{k} + \sqrt{\frac{1}{k^2} - 1}\right) \qquad (1)$$

where ν_l indicates the liquid kinetic viscosity and $f(\eta)$ indicates the velocity distribution across the laminar boundary layer.[16] In the present study, the distance from the origin to the injector exit along the spiral stream line is much greater than xo which indicates the streamwise position where the laminar boundary layer arrives at the film surface. Equation (1) is solved by Newton-Raphson method, and the film thickness at the injector exit, ho is given by the following equation;

$$U_0 = \frac{U_a}{\sqrt{1 - k^2}} \qquad (2)$$

where, constant, A and Reynolds number, Re is defined as follows;

$$U_0 = \frac{U_a}{\sqrt{1 - k^2}} \qquad (3)$$

$$U_a = \frac{W_l}{\rho_l} \frac{1}{\pi d_e h_i} \qquad (4)$$

Where Q_l indicates the liquid volume flow rate par unit width and α is defined by Eq. (5). The sheet cone angle is expressed by 2α which is given by the following equation:[17]

$$\frac{d}{dx}\left[\rho_l U \delta \int_0^1 \left\{U_0 f(\eta) - U f(\eta)^2\right\} d\eta\right] = \rho_l \nu_l \left(\frac{\partial u}{\partial y}\right)_{y=0} \qquad (5)$$

where, k is a cavity factor which equals to dc/de. The above equation was deduced from the potential theory by Tanasawa and Kobayashi,[17] it should be corrected using the Reynolds number and the center post length. The authors propose the following empirical equation for the sheet cone angle;

$$f(\eta) = 2\eta - 2\eta^3 + \eta^4 \qquad (6)$$

In the present study, the adjustable constants, a and b were determined as 18.9 and 670, respectively.

Disintegration Phenomena of Swirling Hollow Cone Sheet

Figure 4 shows the disintegration phenomena of a conical sheet issued from the injector. The nitrogen gas is not injected. The conical sheet greatly fluctuates and disintegrates into ligaments and droplets at the tip of the sheet. The angle of the sheet cone increases as the liquid flow rate increases due to the increase of the liquid momentum. The breakup point of the sheet approaches the injector as the liquid flow rate increases.

Film thickness and sheet cone angle

Figures 5, 6 and 7 show the comparisons of a film thickness between the theoretical analysis and measurements. The nitrogen gas is not injected. The film thickness decreases monotonously as the water flow rate increases in all L/de conditions. As the center post tube lengthens, the film thickness increases. Since the momentum loss between the inlet and the exit of an injector increases as the center post length increases, consequently, the film thickness increases. In the case of L/de= 8.33, the theoretical equation almost agrees with the measurements. On the other hand, in the case of long center post tubes (L/de= 11.67 and 16.67), the measurements show the larger values than the theory. This result shows that the momentum loss of liquid along the stream line is larger than the predictions. In the case of L/de= 11.67, the predictions underestimate the film thickness about 150 μm and 220 μm at L/de= 16.67. These discrepancies for long center post tubes seem to be due to the simplification of a film flow model, especially assumptions (2) and (5). Figure 8 shows the comparisons of a sheet cone angle without nitrogen gas injection. The empirical equations agree with the measurements for larger cone angle than about 55 degree. The discrepancies for small cone angle seem to be due to the surface tension. When the tangential momentum of liquid is small the conical sheet is deflated by the surface tension in the azimuthal direction, and the cone angle decreases. In the range of small cone angle, the surface tension affects the cone angle greatly.

Droplet diameter

The following results are the measurements by phase Doppler particle analyzer for the center post of L/de= 11.67 with nitrogen gas injection. Figure 9 shows the effects of the liquid mass flow rate on the Sauter mean diameter (SMD). The measuring point is the axial distance from the injector exit, z= 150 mm, and the radial distance from the center line, r= 0 mm. The measurements are widely scattering, but the trend that SMD increases with the increase of the liquid flow rate may be recognized except at large liquid flow rate and small gas flow rate. Figure 10 shows the effects of the nitrogen gas mass flow rate on SMD. SMD decreases

monotonously as the gas flow rate increases except at M_l= 43.6 g/s. This shows the general trend of an airblast atomizer. At M_l= 43.6 g/s SMD increases slightly against the gas flow rate. In the vicinity of the injector exit, the spray shows the hollow cone type. Therefore, the point where SMD becomes maximum is apart from the center. As it goes downstream, the large droplets are drawn near the center due to the lower pressure of the center. The pressure of the center decreases as the gas flow rate increases. Consequently, the point where the large droplets are drawn near the center approaches to the injector exit with the increase of the gas flow rate. This phenomena affects the trend of SMD against the gas flow rate at M_l= 43.6 g/s. Figure 11 shows the radial profiles of SMD at z= 135 and 250 mm and r= 0 mm. The radial profiles have peaks at the center for every experimental condition. As the axial distance of the measuring point increases, the radial profile approaches to a flat profile due to the turbulent dispersion of droplets.

Summary of atomization characteristics of swirl injector

The film flow on the inner wall of a center post tube of swirl coaxial injector was investigated theoretically and experimentally. From the comparisons of film thickness at the injector exit between theory and experiments, it was clarified that the theoretical analysis underestimates the film thickness for long center post tubes. These discrepancies seem to be due to the imperfection of the flow model. Therefore, in order to predict the film thickness in the post tube more precisely, further development of the flow model is necessitated. The empirical equation of a sheet cone angle was deduced from the potential theory of swirl flow in a simplex swirl atomizer proposed by Tanasawa and Kobayashi. The spray characteristics of the swirl coaxial injector were investigated by phase Doppler particle analyzer. The effects of the liquid flow rate and the gas injection velocity on the droplet diameter almost resemble those of a conventional airblast atomizer qualitatively.

LO_2/GH_2 and LO_2/LH_2 COMBUSTION

Experimental Apparatus and Test Condition

Figures 12 and 13 show the configuration of uni-element thrusters and 9-elements thruster, respectively. Tables 2 and 3 list the sizes of injectors and combustion chambers and a nominal operating condition for each thruster. Swirl characteristics number, K, defined in Eq. (1) and cavity factor, k= dc/de, were listed in Table 2 and 3. The injection temperature of gaseous fuel was at room temperature, that of liquid oxygen was about 100 K, and that of liquid hydrogen was about 50 K. The fuel annulus area was changed to study the effect of fuel injection velocity. The exit diameter of oxygen tubes was about 5 mm. Combustion chamber pressures were 2.6 and 3.5 MPa. Mixture ratio, O/F, was changed from 4 to 9. Chamber pressure distribution in the cylindrical section was measured to estimate the progress of combustion in the combustion chamber. Heat flux distributions along the chamber axis were also measured.

Performance Evaluation

Figures 14 and 15 show c*s measured with the uni-element thrusters listed in Table 2. The measured c*s were corrected for momentum pressure loss. Figure 14 shows results with a short chamber (180 mm). Figure 15 shows results with a long chamber (287 mm). Theoretical c* reached maximum at about O/F = 2.8 (equivalence ratio, ϕ , = 2.86), so it monotonously decreased with an increase of O/F in the present test range. Measured c*s also monotonously decreased with an increase of O/F.

ηc* are shown in Figs. 16 and 17. (In the figures, injectors were classified by COAX, SW-9.0, SW-10.0 and so. COAX indicates coaxial injectors without oxygen-swirl (we call them shear-coaxial injectors). SW indicates coaxial injectors with oxygen-swirl (we call them oxygen-swirl injectors). And the following number indicates the fuel annulus diameter. Thus, the larger the number, the larger the fuel annulus area.) The obtained ηc*s with the short chamber, Fig. 16, showed a trend similar to that obtained with the gas-gas propellant studies of Figs. 34 and 35. The ηc*s of the shear-coaxial injector were significantly lower than those of the oxygen-swirl injectors. This means oxygen-swirling is effective for improving combustion performance. The ηc*s of the shear-coaxial injector decreased with an increase of O/F. On the other hand, the ηc*s of the oxygen-swirl injectors improved with an increase of O/F. The obtained ηc*s with the long chamber showed similar trends but were different in detail (Fig. 17). That is, the ηc*s of the oxygen-swirl injectors also increased with an increase of O/F. However, for the ηc*s of the shear-coaxial injectors, they showed almost the same ηc* as those of the oxygen-swirl injectors, and did not decrease with an increase of O/F.

In this study, the outer fuel annulus area was changed as listed in Table 2. With the both chambers, the highest ηc*s were obtained with the smallest annulus area. To show this trend clearly, the variation of ηc* as a function of fuel annulus area was estimated from these figures and is represented in Fig. 19. The figure indicates that the ηc* monotonously increased with a decrease of fuel annulus area.

The ηc*s with the 9-element thruster are shown in Fig. 18. The chamber length of the 9-element thruster was 307 mm, which is comparable of that of the long chamber of the uni-element thruster. The contraction ratio of the chamber was 2.32 which is also comparable to that of the long chamber. The obtained ηc*s showed a large scatter caused by the some erroneous factor in this test, namely, a limitation of the test duration with the heat sink chamber with cryogenic propellants LO_2/LH_2 and deformation of the throat area during the combustion tests. These effects were carefully corrected but introduced some degree of error. The very narrow gap of the fuel annulus, only 0.2 mm in the minimum case shown in Table 3, was also the cause of some error due to inaccuracy of manufacturing. The data shown in Fig 18 included only the results which seemed to be reliable. The ηc* of the shear-coaxial injector was as high as those of the oxygen-swirl injectors. Similar trends were observed in the results with the long chamber of uni-element thruster. However, they appreciably decreased with an increase of O/F as was the case with short chamber. The ηc*s of the oxygen-swirl injectors, on the other hand, increased with an increase of O/F. The effect of the fuel annulus area was estimated from Fig. 18 and is shown in Fig. 20. The figure indicates that the ηc* tends to increase with an increase of

fuel annulus area. The observed trend is opposite that of the one with the uni-element results.

Pressure Distribution along the Chamber Axis

A pressure drop in the cylindrical section of the chamber is mainly caused by a momentum pressure loss, and is thus related to the progress of combustion along the chamber axis.[18] So the pressure gradient is related to the rate of combustion and the point on the steep pressure gradient corresponds to a site where combustion take place actively. The chamber pressure distributions normalized by the difference between the maximum pressure and the minimum pressure along the chamber are shown in Figs. 21 to 24. The pressure distributions measured with the shear-coaxial injector for the uni-element thruster are shown in Fig. 21. The effect of O/F change from 4.4 to 7.8 is shown. It can be seen that the position of the maximum pressure gradient shifts downstream as O/F increases. Figure 22 shows the typical pressure distributions measured with the oxygen-swirl injectors. It can be seen that due to oxygen-swirling, the site where combustion takes actively drastically shifts upstream. A change of O/F results in only a small change in the pressure distribution. Figure 23 shows that the change in the fuel annulus area change at O/F was about 6. A change of fuel annulus area has also only a small effect on the pressure distribution. The chamber pressure distribution with the multi-element thruster is shown in Fig. 24. The distributions with the shear-coaxial injector and with oxygen-swirl injectors of various fuel annulus areas were compared at O/F of about 6. The obtained results are similar to the results of uni-element thrusters.

To compare the pressure distributions quantitatively shown in the above figures, the length required for chamber pressure to decrease to the mean value of the chamber pressure is denoted as L50 and was obtained from the previous figures. L50 roughly indicates the site where combustion actively takes place. Figures 25 and 26 show the L50 for the shear-coaxial injectors as a function of O/F for the uni-element thruster and the multi-element thruster, respectively. The L50 increased linearly as O/F increased. When O/F changed from 5 to 7, the L50 for the uni-element thruster increased from 93 mm to 111 mm. Figures 27 and 28 show the L50 for the oxygen-swirl injectors as a function of O/F. The fuel annulus area changed parametrically. Although the change of L50 due to the change of O/F was small, it showed a monotonous decrease with an increase of O/F for both cases. For example, due to a change of O/F from 5 to 7, the L50 for the uni-element thruster changed from 53 mm to 51 mm, and the L50 for the multi-element thruster, changed from 45 mm to 43 mm. The increase of fuel area increased L50.

Heat Flux Distribution along the Chamber Axis

Heat flux distribution along the chamber axis was estimated by measuring the wall temperature distribution of the heat-sink chamber of the 9-element thruster. Thermocouples were mounted at 57, 147, 237 mm from the injector face plate, and at the nozzle throat. The tip of the thermocouple was placed 1 mm from the hot-gas-side. Figure 29 shows measured temperature distributions at 1.5 seconds after combustion, O/F is about 6. The figure indicates that the wall temperature with the shear-coaxial injector increased downward. On the other hand, the wall

temperatures for the oxygen-swirl injectors reached a maximum at 150 mm from the face plate and then decreased downward in the cylindrical section. The figure also indicates that the smaller the fuel annulus area of the oxygen-swirl injectors, the higher the wall temperature was at 57 mm from the injector face.

GO_2/GH_2 AND GO_2/GCH_4 COMBUSTION WITH UNI-ELEMENT INJECTORS

Figure 30 shows the water-cooled thruster used in this study. It contained a single-coaxial injector with fuel, and an inner swirling oxygen jet and two optical ports for viewing the combustion process and measuring spectra from a flame in the combustion chamber. Figure 31 shows a schematic of the coaxial injector. Gaseous fuel (GH_2 or GCH_4) was supplied axially through an outer annulus. GO_2 was supplied axially through a central hole or tangentially through tangential slots. Table 4 shows dimensions of injectors and chambers used in the study. Geometric swirl numbers of the oxygen jet defined as

$$Sg = \frac{\text{Angular momentum of oxygen jet}}{\text{Linear momentum of oxygen jet} \quad x \quad \text{Exit radius of oxygen jet}} \qquad (7)$$

are tabulated with nominal chamber conditions in Table 4.

Thruster Performance

Figures 32 and 34 show Isp and c* efficiency, ηc^*, as functions of mixture ratio, Mo/Mf, for GO_2/GCH_4. Figure 33 and 35 shows Isp and ηc^* for GO_2/GH_2. Here, Isp and ηc^* were not corrected for the effects of heat loss and other losses. When the shear-coaxial injectors were used, the chamber pressure did not attain the designed points. The attained maximum pressures for both gaseous propellants were only 0.29 MPa. The low levels of ηc^* indicate incomplete combustion. For shear-coaxial injectors, ignition did not occur when O/F was smaller than 2.5 with GO_2/GCH_4. The ηc^*s of the shear-coaxial injectors were low compared to those of the ηc^*s of the coaxial injectors with oxygen-swirl (we call it oxygen-swirl injectors). The ηc^*s of the shear-coaxial injectors were decreased with an increase of O/F. On the other hand, the ηc^*s of the oxygen-swirl injectors were increased with an increase of O/F. The injectors with higher swirl intensity showed slightly higher ηc^*s than those of lower swirl intensity injectors (Fig. 34 and Fig. 35).

Flame Behavior in the Combustion Chamber

The shape of the combustion flames formed in the chamber was observed at positions of 0 mm to 30 mm and 90 mm to 120 mm downstream from the injector face. Stable flames, attached to the injector rim between the oxygen jet and the fuel jet, were observed with the shear-coaxial injectors. The flame without oxygen-swirl was generally similar in shape to ordinary turbulent jet diffusion flames. Even near the nozzle entrance, combustion was confined to a narrow region on the central axis. Introduction of swirl to the oxygen jet increased the diverging angle of the flame

and decreased flame length.

For GO_2/GH_2, only a stable attached flame was observed in the test range. For GO_2/GCH_4, an attached flame and a lifted flame were observed. Figure 36 shows boundaries of an attached flame and a lifted flame on a map of the angular momentum of the oxygen jet to the linear momentum of the fuel jet, MOR, defined as:

$$MOR = \frac{Mo\ Uo\ Ro}{Mf\ Uf\ 2\sqrt{Af/\pi}}\ Sg \qquad (8)$$

and an equivalence ratio, ϕ (= (O/F) stoich/ (O/F))

The attached flame was observed where MOR was smaller than 1.06. The lifted flame was observed where MOR was larger than 1.57. Between these values, both flames were observed alternatively. Where Mo is the oxidant mass flow rate, Mf is the fuel mass flow rate, Uf is the fuel injection velocity, Ro is the exit radius of the oxygen port, and Af is the area of the fuel injector port. For comparison, the momentum ratio for the GO_2/GH_2 is also shown. The figure shows that with a decrease of ϕ , the oxygen angular momentum increases. Corresponding to this, the rim stability decreases. This relation implies that the radial velocity component of the oxygen jet due to swirling motion acts on the fuel jet as a cross flow, causing the GO_2/GCH_4 flame to lift. For the lifted flame, mixing between the propellants is promoted near the base of the flame to reduce the flame length. Thus, the lifting flame had favorable effects on the thruster performance due to the completeness of combustion in the chamber.

Figure 37 shows the intensities of the OH-radical along the axial distance from the injector exit for the three Sg values of GO_2/GH_2 flames. It was found that OH intensity for Sg= 0 was weakest for the three Sg values close to the injector and increased toward downstream. On the contrary, for Sg= 1.05, OH intensity was the strongest of the three Sg values at the location close to the injector and sharply decreased downstream. This indicates that, applying swirl to the oxygen jet increased the rate of turbulent mixing between the propellants, thus reducing the reaction time required to reach completion of combustion in the chamber.

Figure 38 shows the intensities of the OH-radical for the three flames at O/F = 2.9, 4.0, 5.0 against the axial distance from the injector exit for GO_2/GH_2 flames. At low O/F, the radical intensity upstream of the chamber was higher than that downstream. At high O/F, the reverse tendency was obtained. As O/F decreased, injection velocity of H_2 jet increased. It reduced the divergence angle of the inner oxygen jet, and improved the turbulent mixing between the propellants. This effect promoted rapid completion of combustion in the chamber.

Discussion of the Effect of Oxidizer Swirl on Combustion Characteristics of Coaxial Injectors

Based on the results shown in the previous paragraphs, the effect of oxygen-swirling on the combustion characteristics is discussed in this paragraph.

Coaxial Injectors without Swirl

For the case of gas-gas combustion, the atomization process is not included in combustion. Thus, the mixing process is a dominant factor in this combustion. For a coaxial injector without swirl, mixing between propellants is controlled by the shear force due to the velocity differences of both propellants. For the case of GO_2/GH_2 combustion, the injection velocity of hydrogen, Uf, was 1150 m/s and the injection velocity of oxygen, Uo, was 270 m/s at O/F = 4.0. An increase of O/F decreases the difference of Uf and Uo, and decreases the shear force by the velocity difference. An increase of O/F causes mixing performance and combustion efficiency to deteriorate as shown in Fig. 34 and 35.

For the case of liquid propellants, an atomization process is involved part in combustion. For LO_2/GH_2 combustion, typical injection velocities were Uf = 268 m/s and Uo = 4.6 m/s at Pc = 3.5 MPa and O/F = 5. And for the case of LO_2/LH_2 combustion, Uf = 43 m/s and Uo = 7.9 m/s at Pc = 3.5 MPa and O/F = 5. An increase of O/F deteriorates not only mixing but also atomization efficiency, and shifts the site where combustion actively take place actively downward. Thus, an increase of O/F deteriorated ηc^*, especially when a short chamber was used (Fig. 16, 17 and 18).

In the case of shear-coaxial injectors, a rim stabilized attached flame was always observed in GO_2/GH_2,[9] GO_2/GCH_4[8] and LO_2/GH_2[19] combustion tests.

Coaxial Injectors with Oxygen-Swirl

When swirling is applied to the oxygen jet, the oxygen jet spreads conically. The structure of the flame is drastically changed from a cylindrical sheath shape to a hollow cone shape with a recirculation zone along the center axis. As the swirling flow of oxygen acts as a cross flow to the surrounding fuel flow, a high intensity of swirling can cause the flame to lift (Fig. 36).

The effects of fuel injection velocity was observed through a change of fuel annulus area and a change of O/F. First, let us consider the effect caused by a change of fuel injection area with a constant O/F. A decrease of fuel annulus area (i.e. an increase of fuel injection velocity) enhances atomization, turbulent mixing and combustion near the injector exit. Thus, L50, where combustion take place actively, decreased with a decrease of fuel annulus area at a constant O/F (Fig. 27 and 28). The heat flux near the injector face also increased with a decrease of fuel annulus area (Fig. 29).

Second, let us consider the effect of a change of O/F at a constant fuel area. Figures 27 and 28 indicate that the L50 increases with a decrease of O/F. This means an increase of fuel injection velocity retards the combustion, which appears to contradict the above explanation. However, it can be considered to be explained as follows: A decrease of O/F introduces an increase of fuel jet and a decrease the angular momentum of oxygen jet. Thus, the fuel stream the surrounding oxygen jet acts to compress the diverging angle of the oxygen jet and reduces the size of a recirculation zone. Thus, the increase of fuel injection velocity results in deterioration of the global combustion rate near the injector face. For the case of gas-gas combustion, the observed flame intensity near the injector exit increased with a decrease of O/F (Fig. 38). This again appeared to contradict the above explanation. However, it can be explained as follows: The flame

intensity was observed by a small bore scope which might cover only a part of flame.[9] As mentioned above, an increase of fuel injection velocity reduces the size of a recirculation zone. Thus an increase of fuel injection velocity concentrates the combustion at the center of the axis. Thus, it retard the global rate of combustion, but the flame intensity near the center of axis observed by a small bore scope can increase.

Finally, let us consider the ηc^* on coaxial injector with oxygen-swirl. An increase of fuel injection velocity resulting from a decrease of fuel injection area at a constant O/F increased ηc^* with the uni-element thruster (Fig. 19), but decreased ηc^* for the case of the 9-element thruster (Fig. 20). This contradiction can be explained as follows: An increase of fuel injection velocity enhances turbulent mixing and atomization near the injector exit, but compresses the diverging angle of oxygen jet as mentioned before. This effect can reduce mutual mixing between elements for a multi-element injector and can decrease ηc^* for a multi-element thruster. For the case of a uni-element thruster, the enhancement of atomization and mixing near the injector exit still can improve ηc^*. When fuel injection velocity was increased by decreasing O/F, ηc^* was decreased for both the uni-element thrusters and the multi-element thrusters. This means an increase of fuel injection velocity enhances atomization and mixing near the injector exit, however, a large diverging angle of oxygen jet is more effective to improve ηc^*, that is, the smaller the fuel injection velocity, the larger size of recirculation region, and the higher the ηc^*.

SUMMARY OF COMBUSTION CHARACTERISTICS

Effects of oxidizer swirling on combustion characteristics of coaxial injector were investigated. with LO_2/GH_2, LO_2/LH_2, GO_2/GH_2 and GO_2/GCH_4 propellants. The progress of combustion was estimated by measuring the chamber pressure distribution and heat flux distribution for the LO_2/GH_2 and LO_2/LH_2 studies. The flame structure and the flame intensity distribution in the combustion chamber were observed for the gas-gas propellant studies.

It was found that applying swirl to the oxygen jet greatly enhances the combustion near the injector exit. Applying swirl to the oxygen jet greatly enhances the combustion near the injector exit and thus reduces the required chamber length to complete combustion. The stronger the swirl intensity with a smaller fuel annulus area, the nearer the site where combustion take place actively. With gas-gas propellants, stable diffusion flame attached to the oxygen post rim was observed as long as the ratio of the angular momentum of the oxygen jet to the linear momentum of fuel jet was weak. When the relative angular momentum of oxygen jet was strong, a lifted flame was observed with gas-gas propellants. An introduction of oxygen-swirling was not always improve ηc^*. The significant improvement was observed with a shorter chamber. ηc^*s of uni-element oxygen-swirl injectors are improved with a small fuel area. However, ηc^*s of multi-element oxygen-swirl injectors, on the contrary, are tend to be improved with a large fuel area.

References

[1] Hulka, J. and J.A. Schneider, "A Single Element Injector Cold Flow Testing For STME Swirl Nonlinear Model of Combustion Instability in Liquid Coaxial Injector Element Design," AIAA Paper No. 93-2161, 1993.

[2] Doumas, M. and R. Laster, "Liquid-Film Properties for Centrifugal Spray Nozzles," Chemical Engineering Progress, Vol. 49, No. 10, pp. 518-526, Oct. 1953.

[3] Dombrowski, N. and D. Hasson, "The Flow Characteristics of Swirl (Centrifugal) Spray Pressure Nozzles with Low Viscosity Liquids," CAIChE Journal, Vol. 15, No. 4, pp. 604-611, July, 1969.

[4] Dexter, C. E., "ALS LOX/H2 Subscale Coaxial Injector Testing," AIAA 91-1871, 1991.

[5] Elam, S. K., "Subscale LOX/Hydrogen Testing with a Modular Chamber and a Swirl Coaxial Injector," AIAA 91-1874, 1991.

[6] Sasaki, M. et al., "Comparative Study of Recessed and Nonrecessed Swirl Coaxial Injectors," AIAA 97-2907, 1997.

[7] Tamura, H. et al., "LOX/LH2 Subscale Swirl Coaxial Injector Testing," AIAA 97-2906, 1997.

[8] Kato, H., Ikezaki, T. and Yuasa, S., "Effects of Flame Behavior on a Gaseous Methane/Oxygen Small Thruster Performance," Challenges in Propellants and Combustion, Edited by K. K. Kuo, begall house inc. new york, pp.743-752, 1997.

[9] Yuasa, S., Kubota, S. and Fujita, M., "Combustion Characteristics in a Gaseous Hydrogen/Oxygen Small Thruster," Challenges in Propellants and Combustion, Edited by K. K. Kuo, begall house inc. new york, pp. 753-761, 1997.

[10] Hulka, J. and D. Makel, "Liquid Oxygen/Hydrogen Testing of a Single Swirl Coaxial Injector Element in a Windowed Combustion Chamber," AIAA Paper No. 93-1544, 1993.

[11] Rahman, S. A. et al., "Swirl Coaxial Atomization: Cold-Flow and Hot-Fire Experiments," AIAA Paper No. 95-0381, 1995.

[12] Anatony, V. et al., "Auto vibration of Coax Injector Elements of O2/H2 Staged Combustion Liquid Rocket Engines," AIAA 95-2837, 1995.

[13] Bazarov, V. and V. Yang, "Liquid-Propellant Rocket Engine Injector Dynamics" J. of Propulsion and Power, Vol. 14, No. 5, pp.797-806, 1998.

[14] Hulka, J. and J. Hutt, "Instability Phenomena in Liquid Oxygen/Hydrogen Propellant Rocket Engine," Liquid Rocket Engine Combustion Instability, Vol 169, Progress in Astronautics and Aeronautics, Edited by V. Yang and W.E. Anderson

[15] Tokuoka, N., Nagaosa, S., Hora, S., and Sato, G. T., "Study on the Disintegration of a Liquid Film by Air Impingement," Atomization and Spray Technology, Vol.1, pp.103-123, 1985.

[16] Ishigai, K., Nakanishi, S., Mizuno, M., and Imamura, T., "Heat Transfer by Impingement of Round Water Jet," Trans. JSME (Ser.2), Vol.42, No.357, pp.1502-1510, 1976 (in Japanese).

[17] Tanasawa, Y., and Kobayashi, K., "Design Method of Swirl Atomizer by Potential Theory" Trans. JSME (Ser.2), Vol.17, No.58, pp.107-111, 1951 (in Japanese).

[18] F. V. Bracco, "The Direct Method as Applied to Liquid Rocket Engine Combustion and

Explosion Problems, Ph.D. Thesis, Princeton University Dept. of Aerospace and Mechanical Science Rept. No. 902, June, 1970.

[19] W. Mayer and H. Tamura, "Propellant Injection in a Liquid Oxygen/Gaseous Hydrogen Rocke Engine," J. of Propulsion and Power, Vol. 12, No. 6, pp.1137-1147, 1996.

Table 1 Experimental conditions

Liquid Mass Flow Rate, M1, (g/s)	10 - 48
Liquid Injection Pressure, P1, (MPa)	0.033 - 0.7
Gas Mass Flow Rate, Mg, (g/s)	2.5 - 6.0
Gas Injection Pressure, Pg, (MPa)	0.13 - 0.25
Length of Center Post Tube, L, (mm)	50, 70, 100

Table 2 Configuratons of injectors and combustion chambers and nominal chamber condition for LO_2/GH_2

Propellants	LO_2/GH_2	LO_2/GH_2
Chamber	Short	Long
Fuel annulus dia. (mm)	9.0, 9.0, 10.0, 11.5	12.0, 12.0 14.0 16.0 17.0
Fuel slit width (mm)	1.0, 1.0, 1.5, 2.0	2.5, 2.5 3.5 4.5 5.0
Fuel annulus area , (mm2)	25.1, 25.1, 40.1, 65.4	74.6 74.6 115. 163. 189
Af/Ao	1.28, 1.28, 2.04, 3.33	3.8, 3.8 5.88 8.28 9.60
Oxygen inj. dia. (mm)	5.0	5.0
Rim thickness (mm)	1.0	1.0
Oxygen inj. area., (mm2)	19.63	19.63
Swirl Charcteristic number K	--- 0.240	--- 0.540
Cavity coefficient k	--- 0.774	--- 0.644
Chamber diameter (mm)	23.0	23.0
Chamber length (mm)	180	287
Throat diameter (mm)	10	16
Contraction ratio	5.29	2.07
Chamber pressure, Pc (MPa)	3.5	2.6
Fuel mass flow rate, mF (kg/s	0.020	0.037
O2 mass flow rate, mO2 (kg/s	0.100	0.185
Stoichiometric O/F: (O/F) stoic	8.0	8.0
Nominal mixture ratio (O/F)	5.0	5.0

Table 3 Configuratons of injectors and combustion chambers and nominal chamber condition for LO_2/LH_2

Propellants	LH_2/LO_2
Fuel annulus dia. (mm)	6.7, 6.7 6.9 7.1 7.4 8.0
Fuel slit width (mm)	0.2, 0.2 0.30 0.40 0.55 0.85
Fuel annulus area , (mm2)	25.1, 25.1, 40.1 65.4 74.6 116
Af/Ao	1.14, 1.14, 1.82 2.96 3.38 5.24
Oxygen inj. dia. (mm)	5.3
Rim thickness (mm)	0.5
Oxygen inj. area., (mm2)	22.06
Swirl Charcteristic number K	0.408
Cavity coefficient k	0.693
Chamber diameter (mm)	64
Chamber length (mm)	307
Throat diameter (mm)	42
Contraction ratio	2.32
Chamber pressure, Pc (MPa)	3.5
Fuel mass flow rate, mF (kg/s)	0.039
O2 mass flow rate, mO2 (kg/s)	0.195
Stoichiometric O/F: (O/F) stoich	8.0
Nominal mixture ratio (O/F)	5.0

Table 4 Configuratons of injectors and combustion chambers and nominal chamber condition for $GO_2/GH_2/GCH_4$

Propellants	GO_2/GCH_4	GO_2/GCH_4	GO_2/GH_2
Injector type	A	B	C
Fuel annulus dia. (mm)	12.0	12.5	12.0
Fuel slit width (mm)	1.0	0.75	1.0
Fuel annulus area , (mm2)	34.6	27.7	34.6
Af/Ao	0.898	0.55	0.898
Oxygen inj. dia. (mm)	7.0	8.0	7.0
Rim thickness (mm)	1.5	1.5	1.5
Oxygen inj. area., (mm2)	38.5	50.3	38.5
Swirl number Sg	0, 0.78, 1.4	0, 0.68	0, 0.67, 1.05
Chamber diameter (mm)	50.0	50.0	50.0
Chamber length (mm)	173	173	173
Throat diameter (mm)	20	20	20
Contraction ratio	6.25	6.25	6.25
Chamber pressure, Pc (MPa)	0.39	0.39	0.39
Fuel mass flow rate, mF (kg/s)	0.021	0.021	0.010
O2 mass flow rate, mO2 (kg/s)	0.051	0.051	0.040
Stoichiometric O/F: (O/F) stoich	4.0	4.0	8.0
Nominal mixture ratio (O/F)	2.5	2.5	4.0

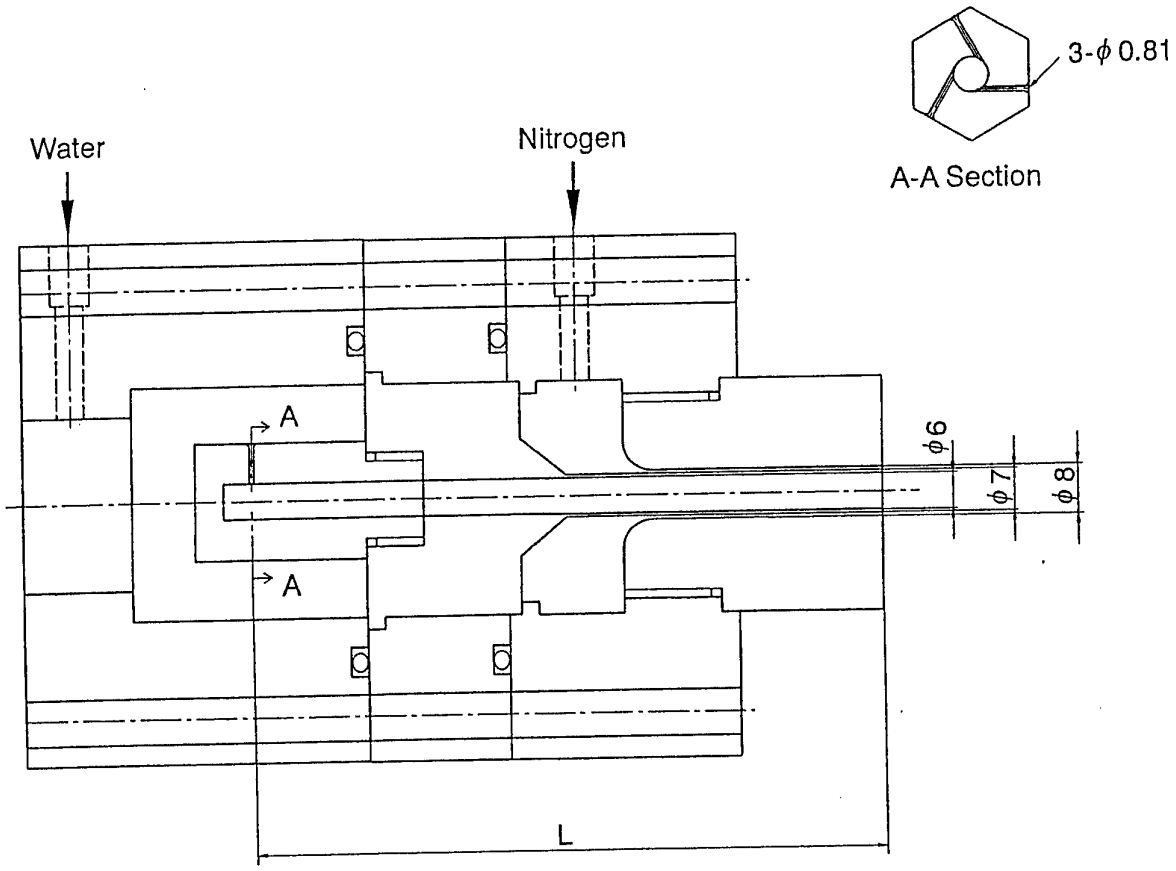


Fig. 1 Swirl coaxial injector

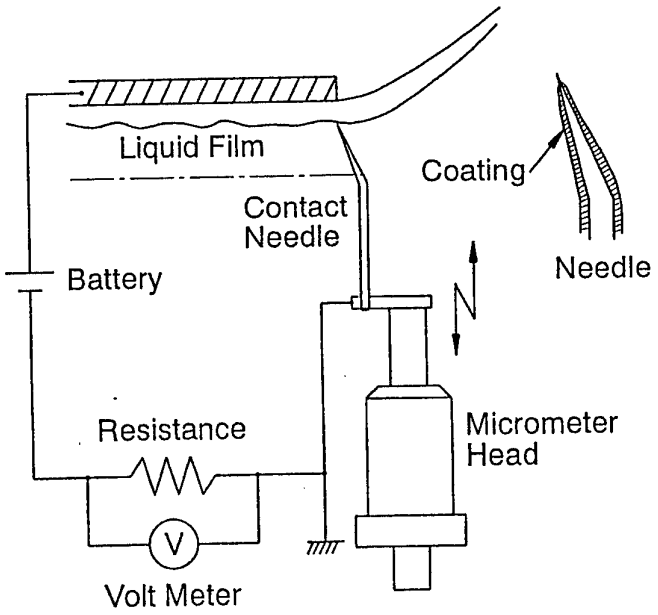


Fig.2 Contact needle method

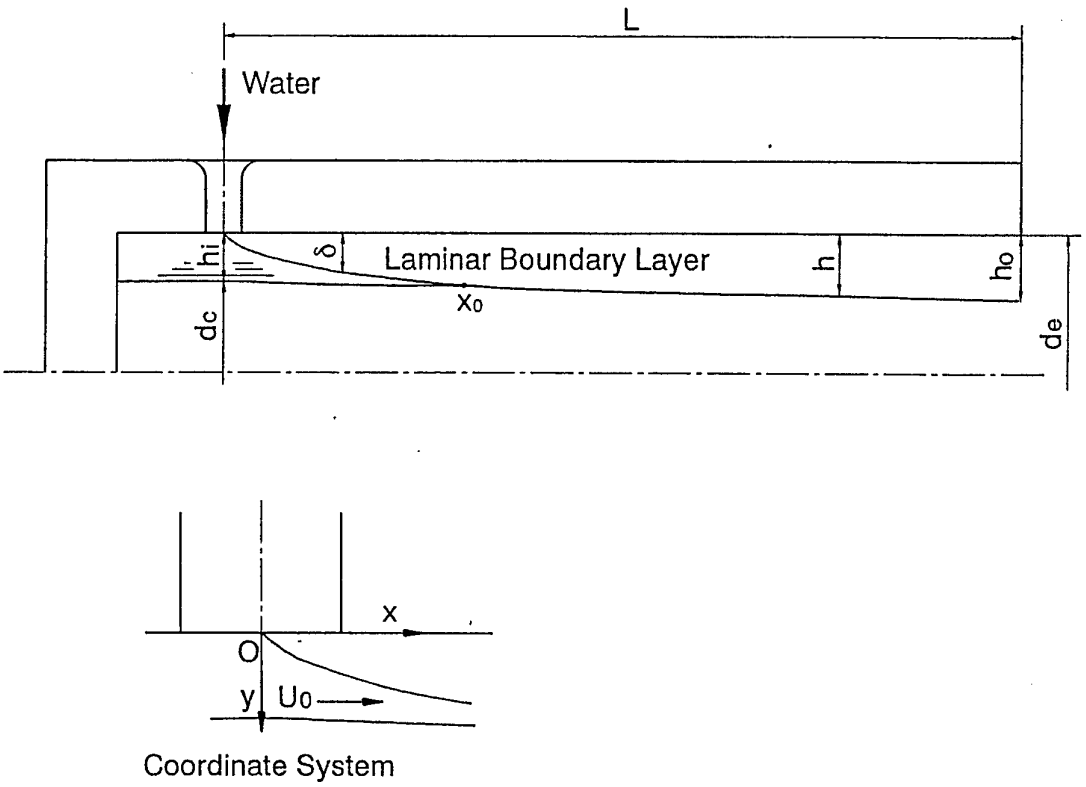
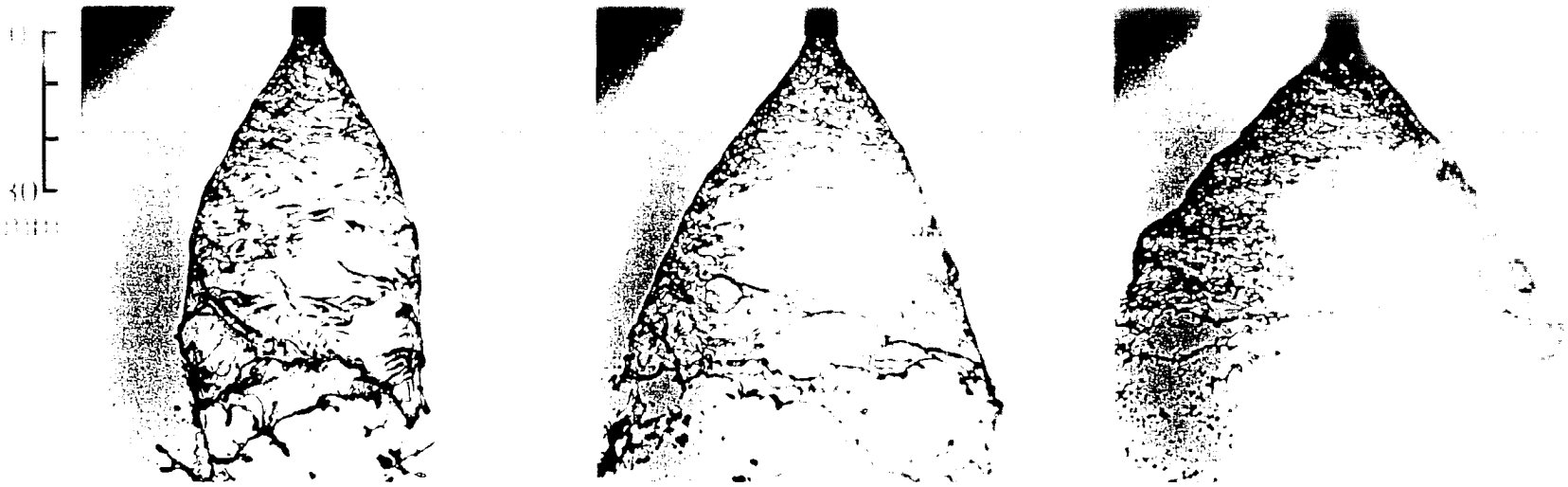


Fig.3 Coordinate system and variables



(1) MI=26.1g/s (2) MI=32.5g/s (3) MI=48.6g/s

Fig.4 Disintegration phenomena of hollow cone sheet (L/de=11.67)

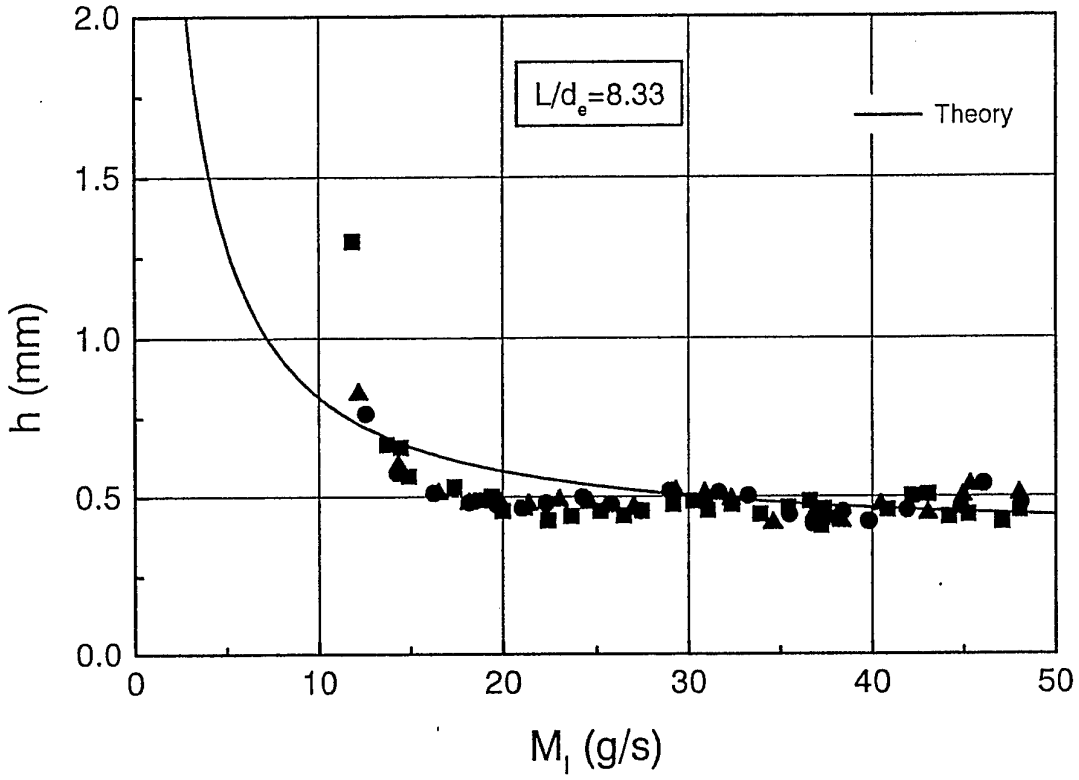


Fig.5 Comparison of measured and theoretically predicted film thickness

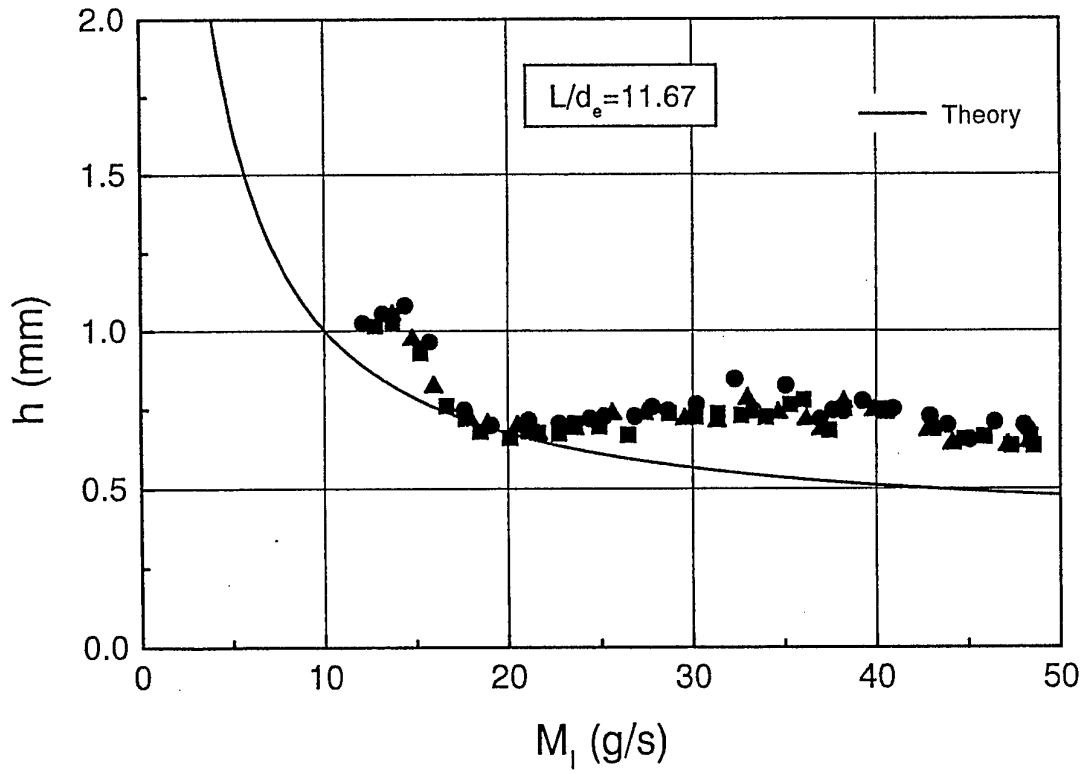


Fig.6 Comparison of measured and theoretically predicted film thickness

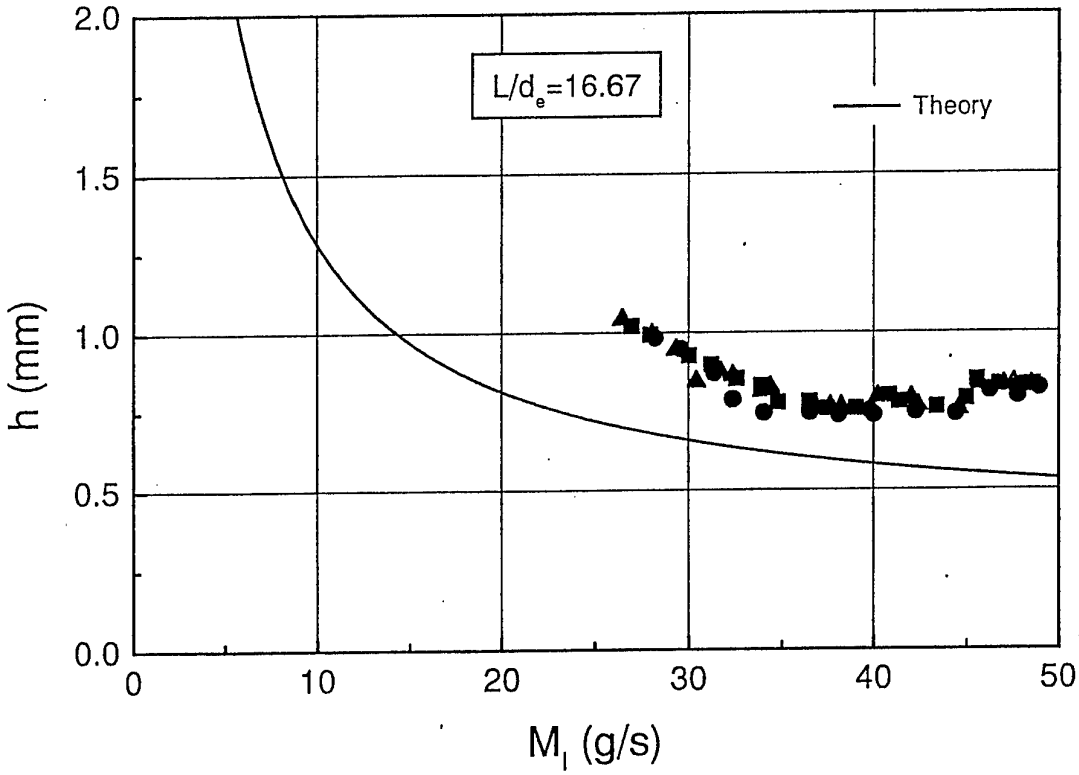


Fig.7 Comparison of measured and theoretically predicted film thickness

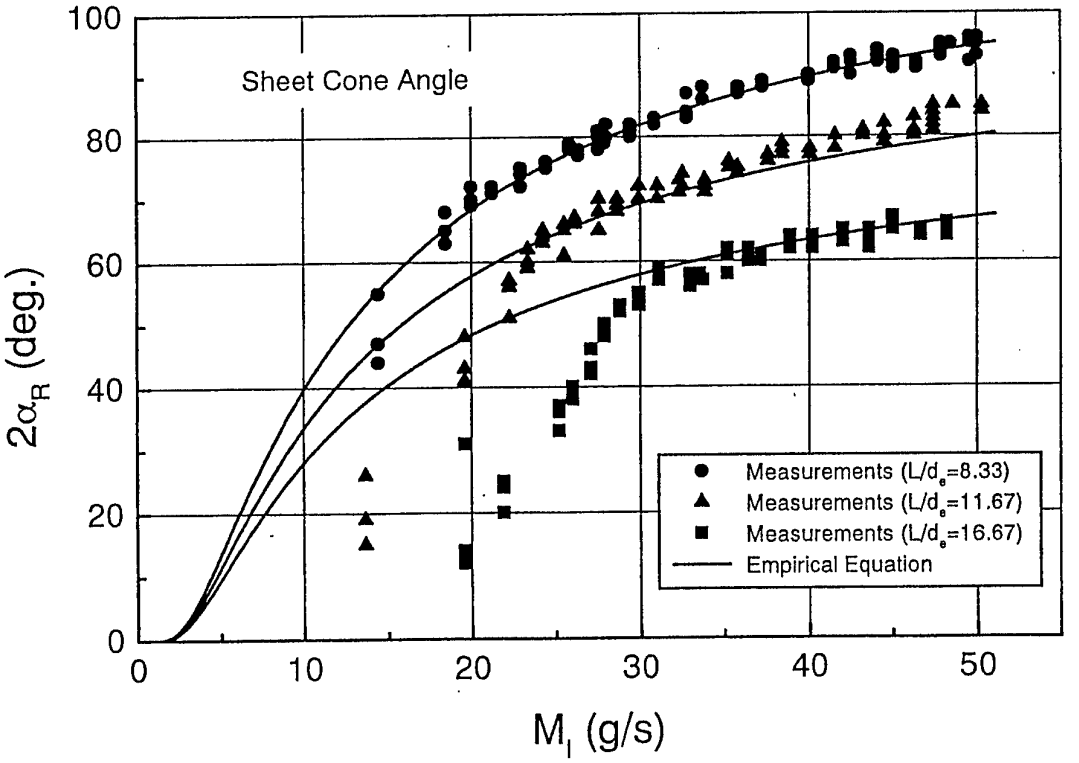


Fig.8 Comparison of measured sheet cone angle and empirical equation

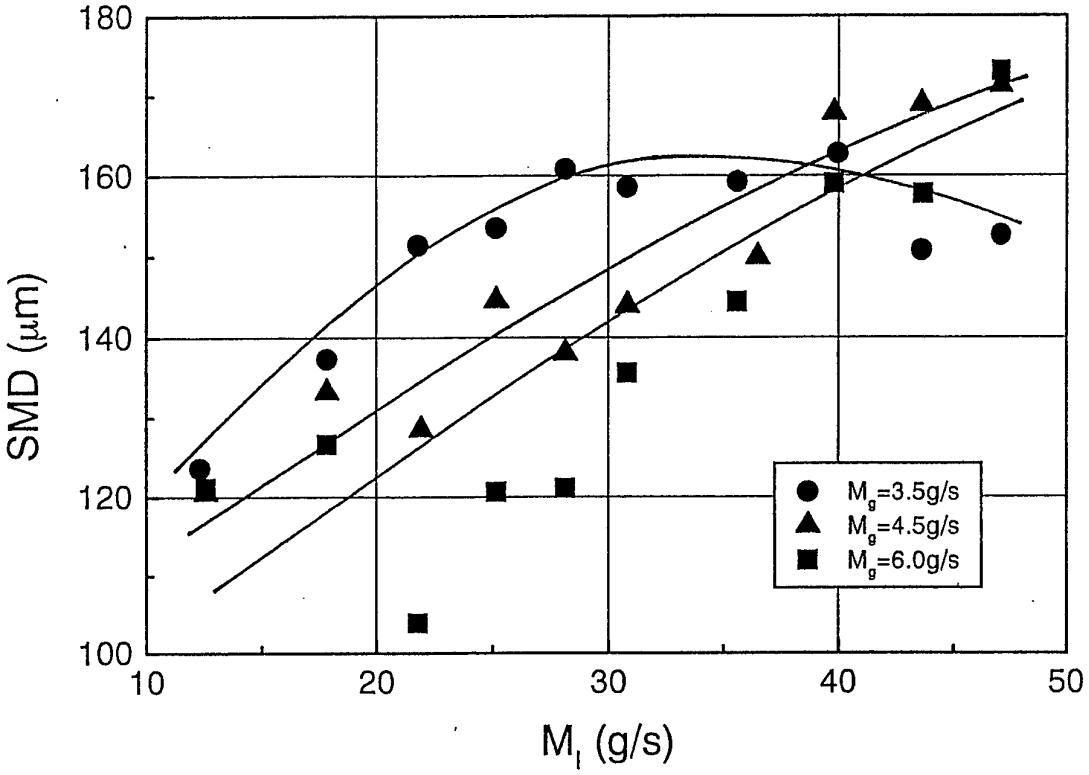


Fig.9 Local Sauter mean diameter versus liquid flow rate

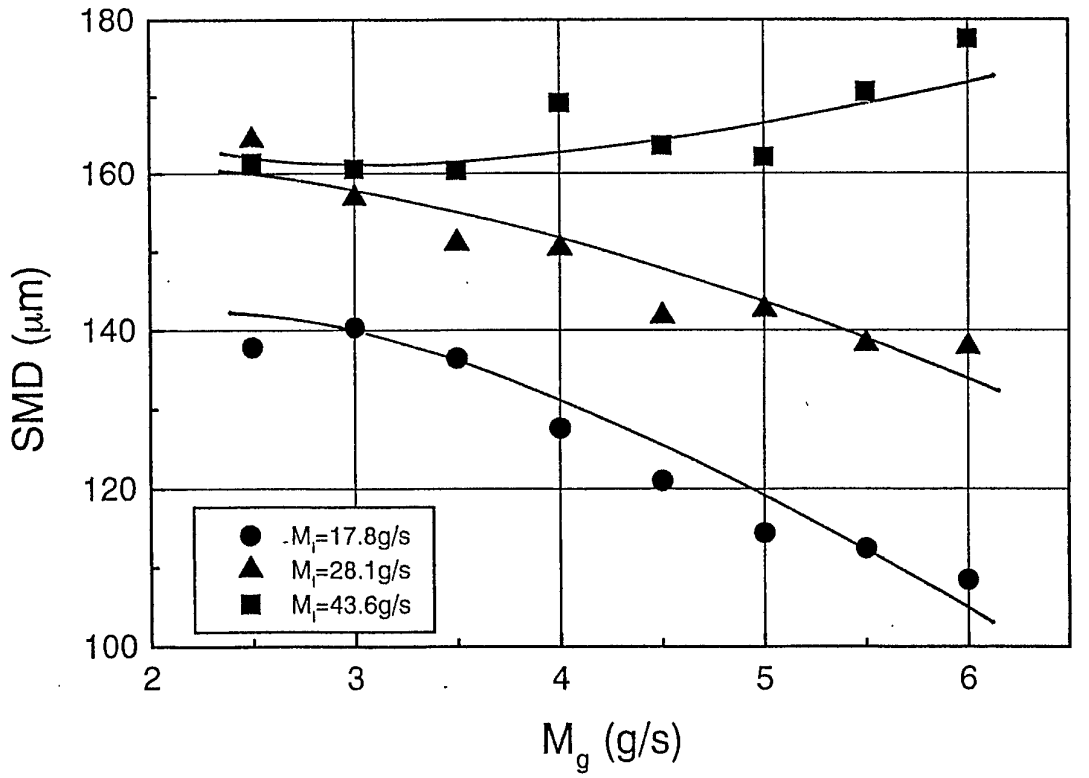


Fig.10 Local Sauter mean diameter versus gas flow rate

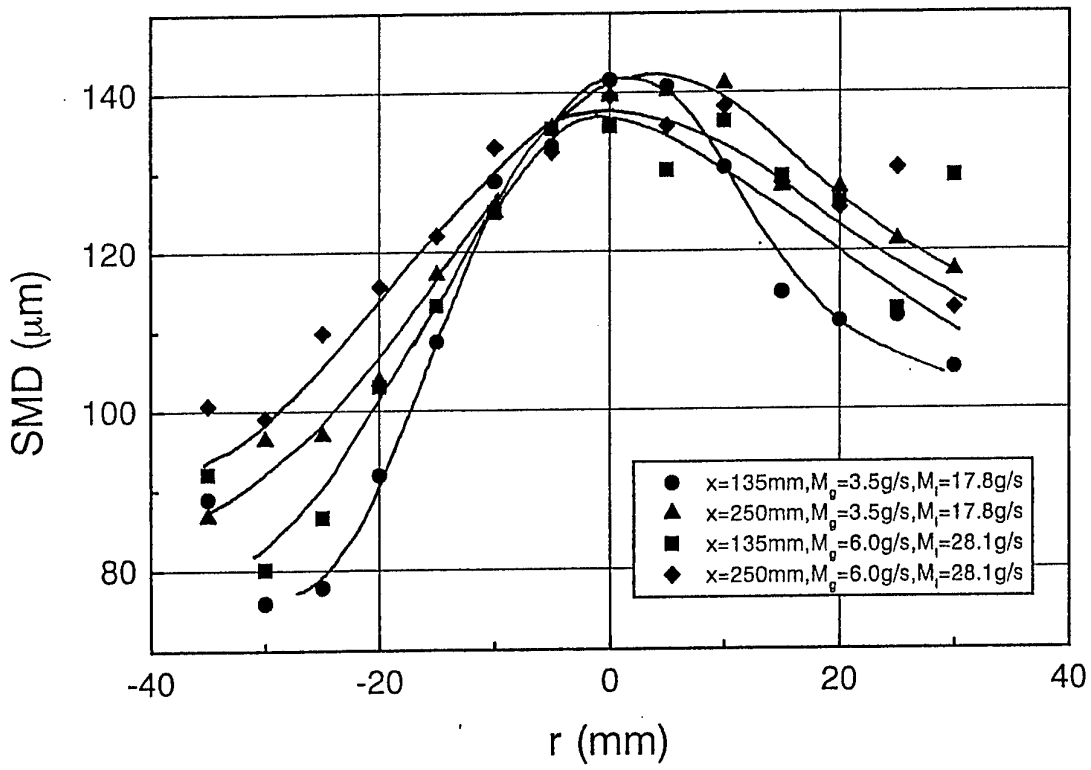


Fig.11 Radial profile of Sauter mean diameter

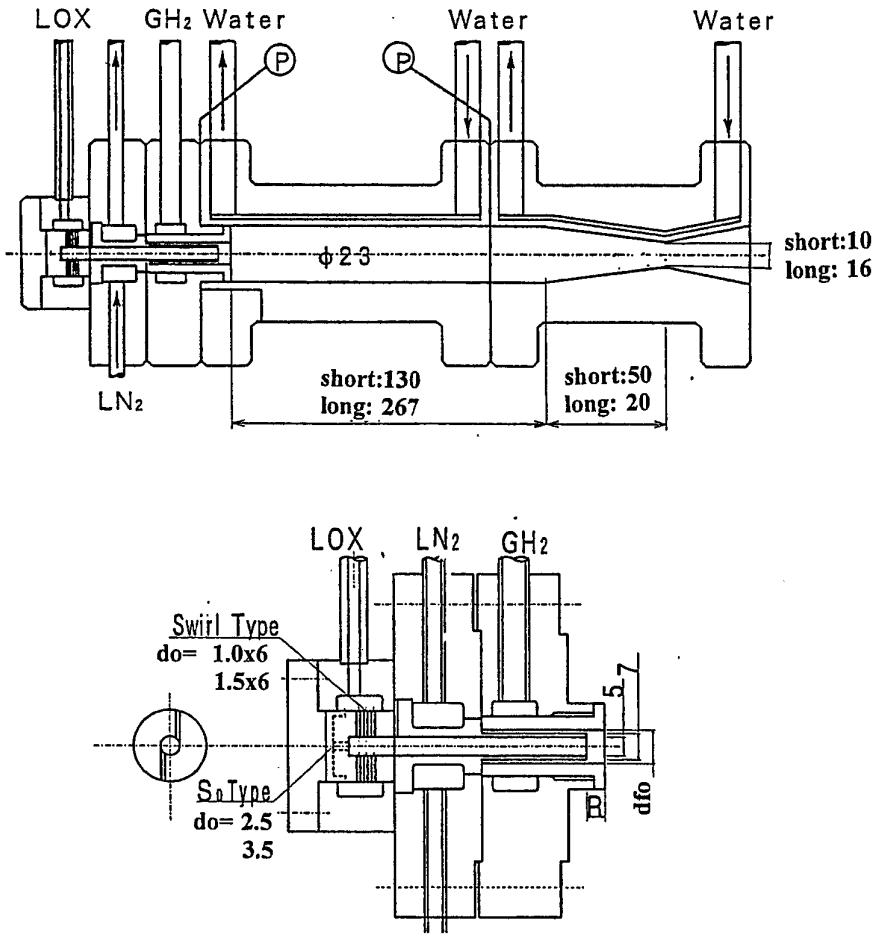


Fig. 12. Schematics of water cooled thruster and uni-element injector for LO_2/GH_2 propellant.

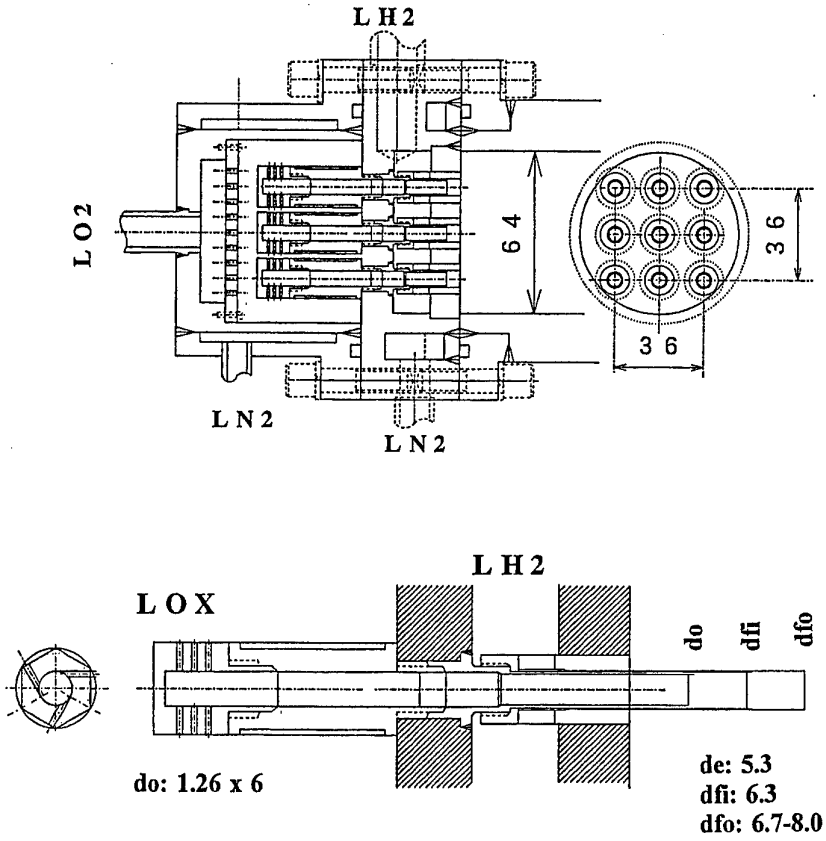


Fig. 13. Schematics of heat sink thruster and 9-element injector for LO_2/LH_2 propellant.

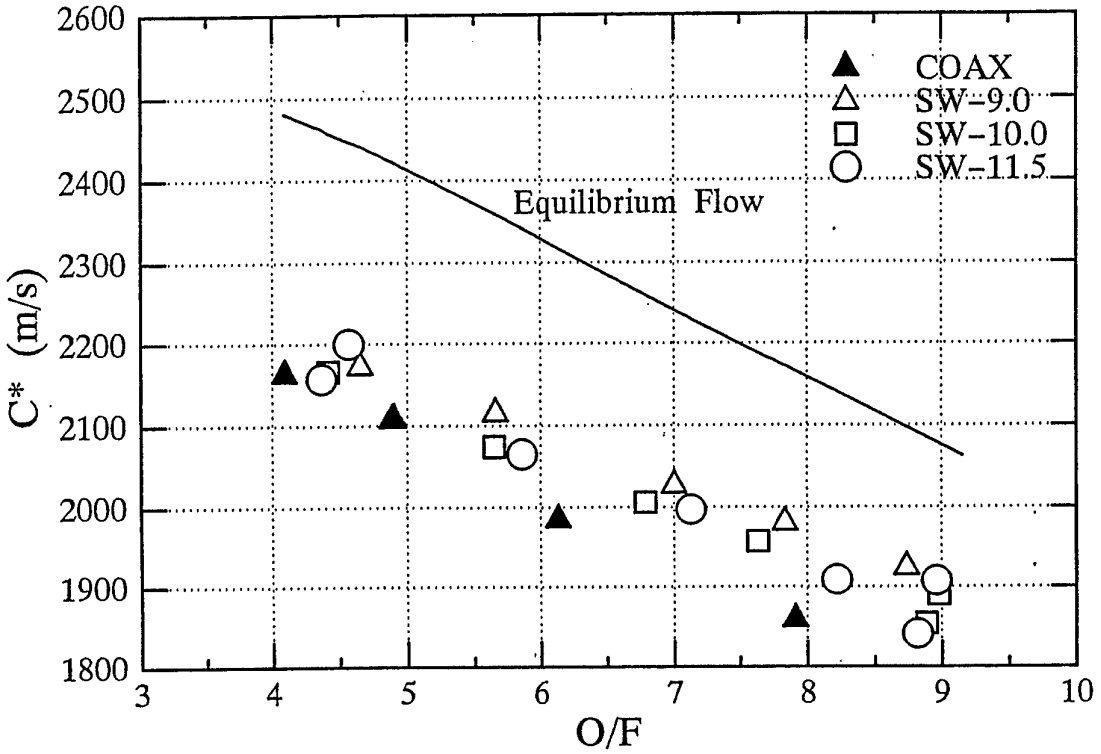


Fig. 14. Variation of c*s as a function of O/F with the uni-element short chamber (180 mm)

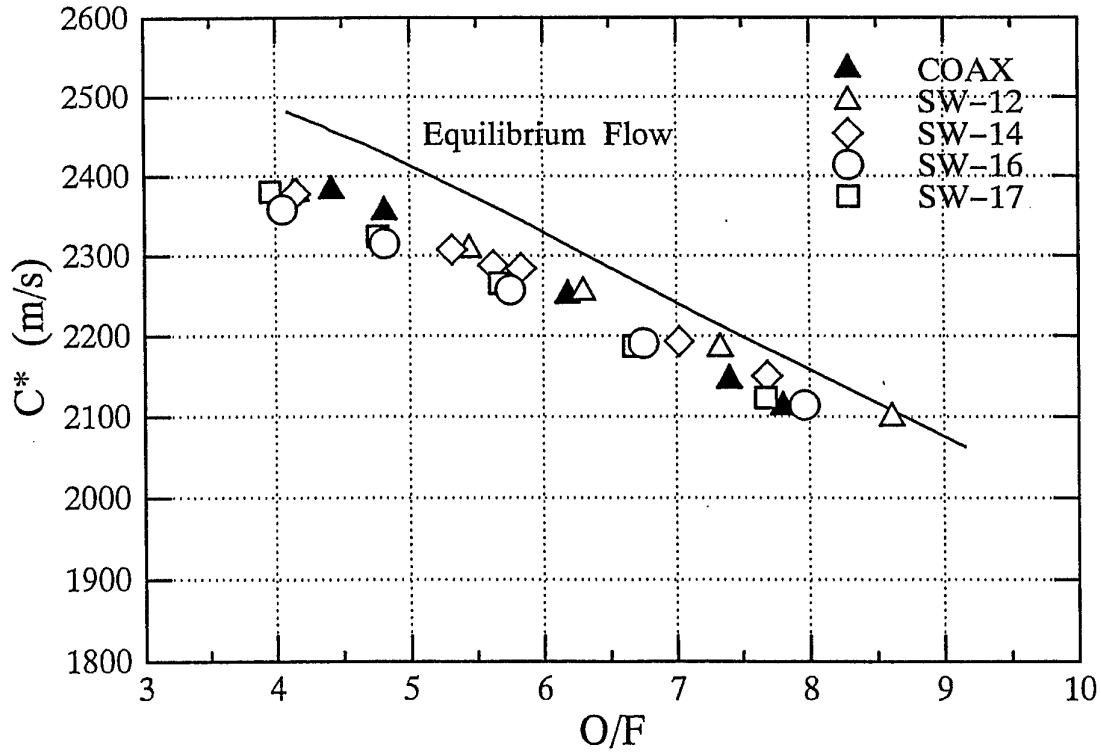


Fig. 15. Variation of c*s as a function of O/F with the uni-element long chamber (287 mm)

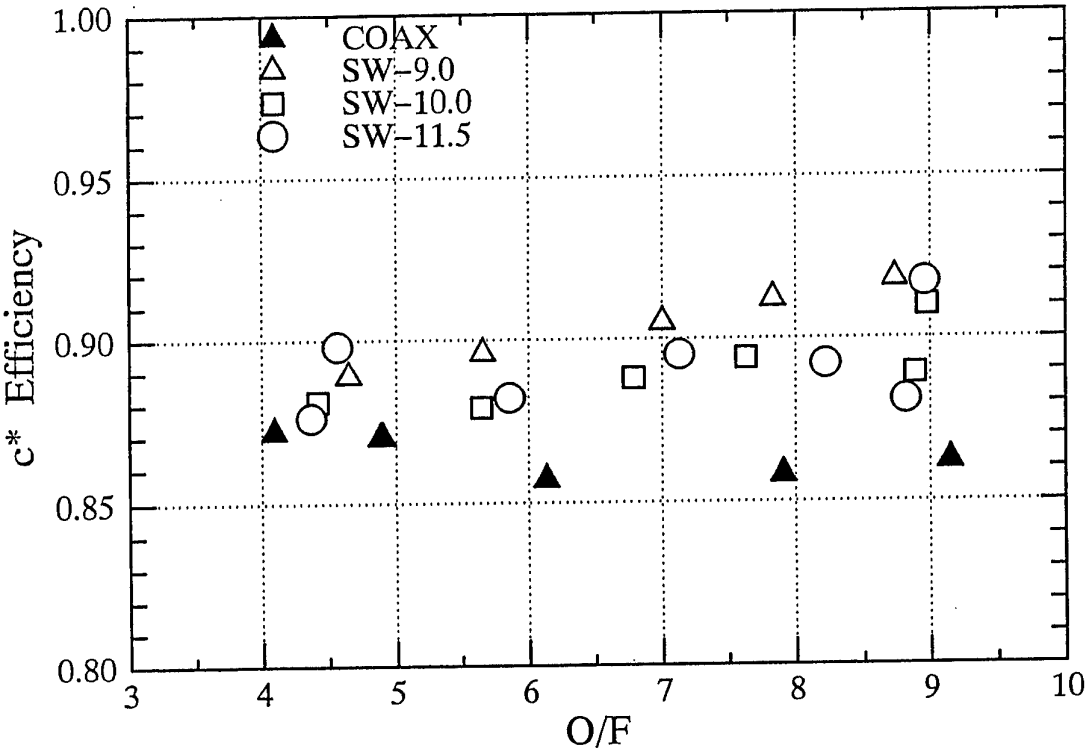


Fig. 16. Variation of ηc*s as a function of O/F with the uni-element short chamber (180 mm)

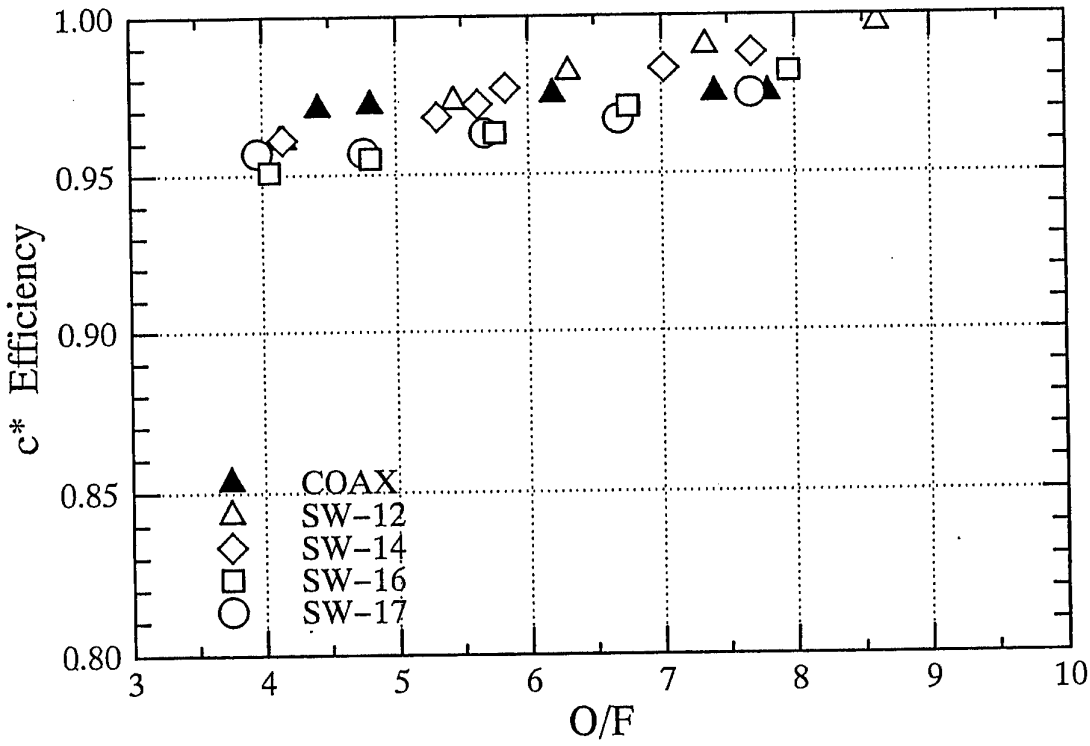


Fig. 17. Variation of ηc*s as a function of O/F with the uni-element long chamber (287 mm)

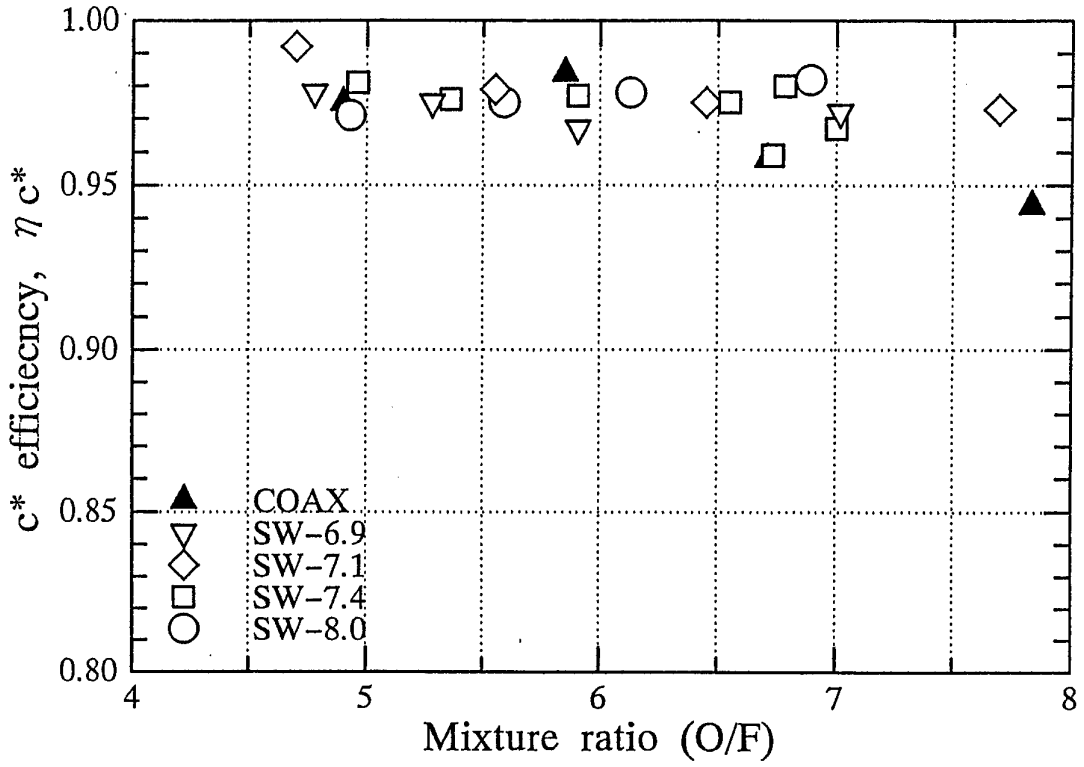


Fig. 18. Variation of ηc*s as a function of O/F with the 9-element chamber

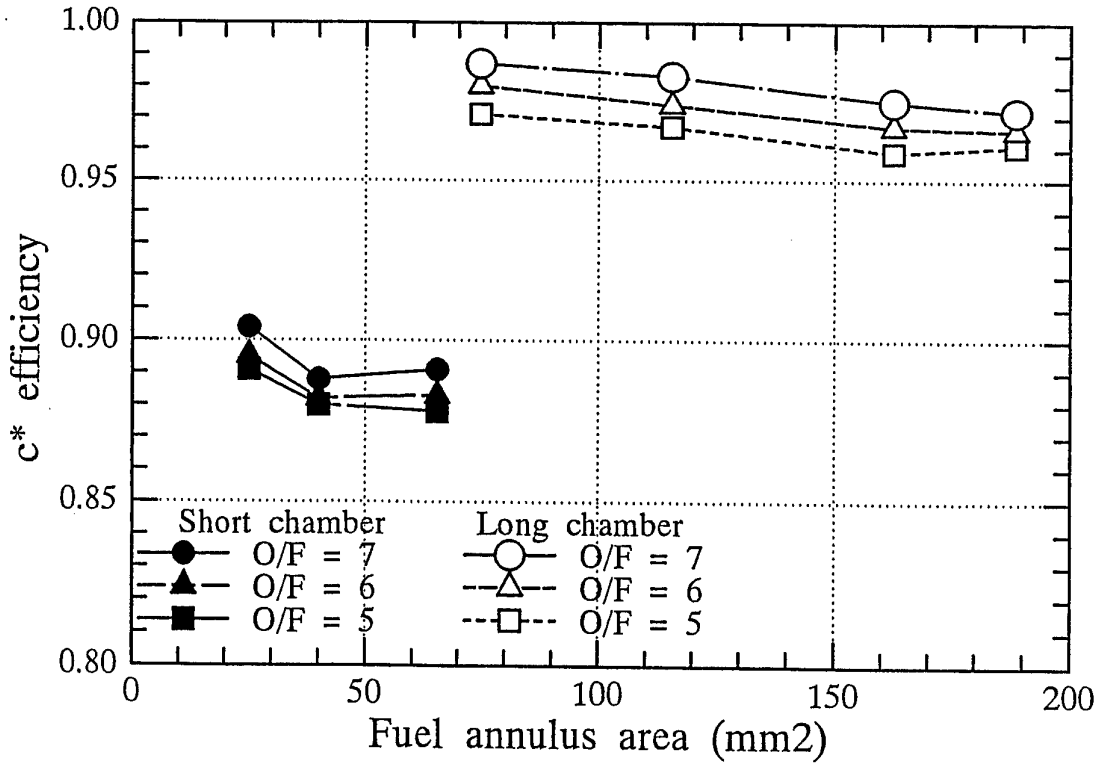


Fig. 19. Estimated variation of ηc* as a function of fuel annulus area for the uni-element long chamber (287 mm)

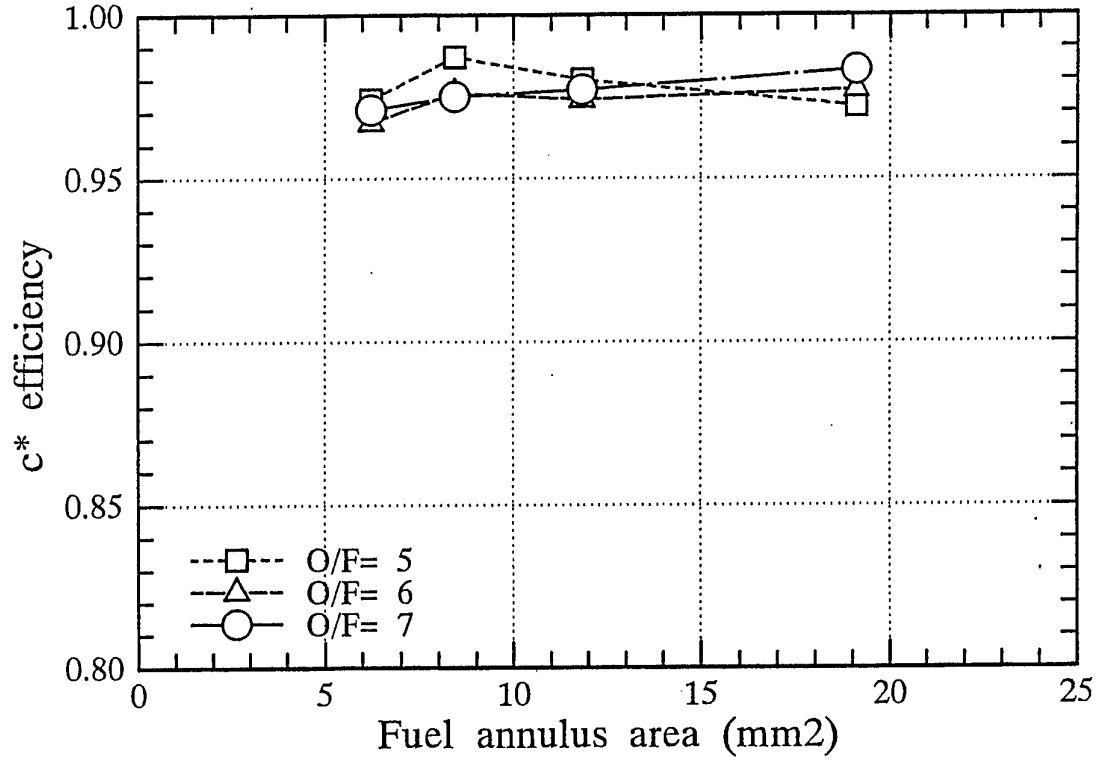


Fig. 20. Estimated variation of ηc* as a function of fuel annulus area for the 9-element chamber.

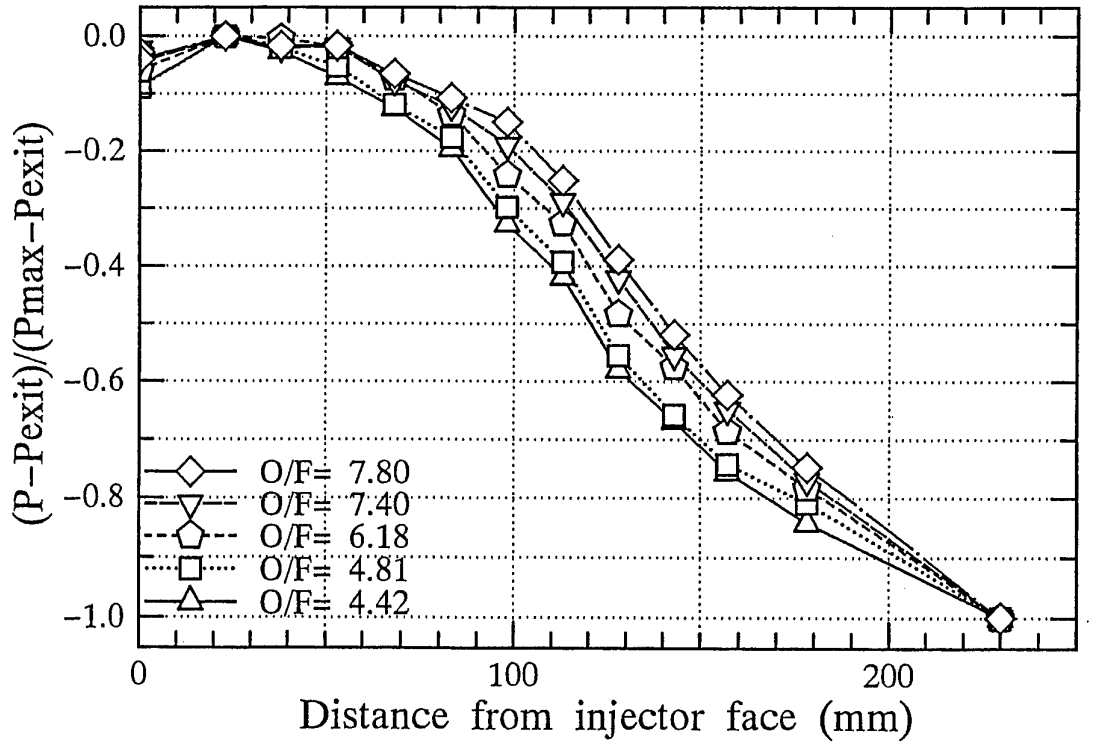


Fig. 21. Pc distribution along the x-axis for the shear-coaxial injector for the uni-element chamber. (Effect of mixture ratio)

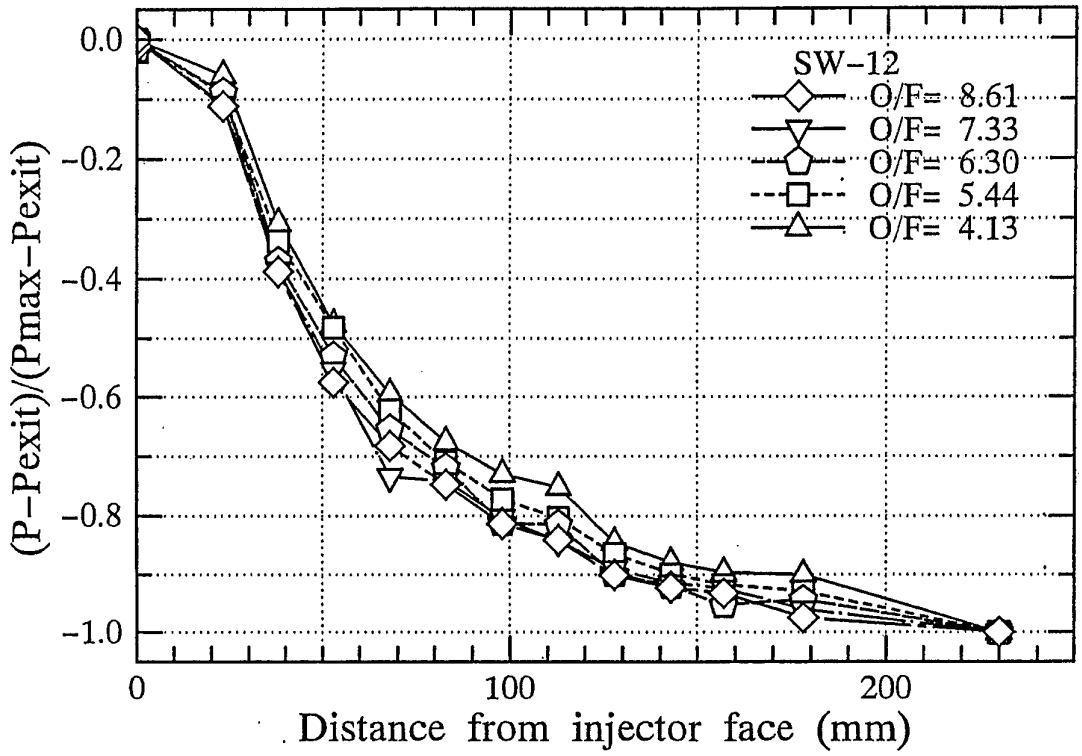


Fig. 22. Pc distribution along the x-axis for the oxygen-swirl injectors for the uni-element chamber. (Effect of mixture ratio)

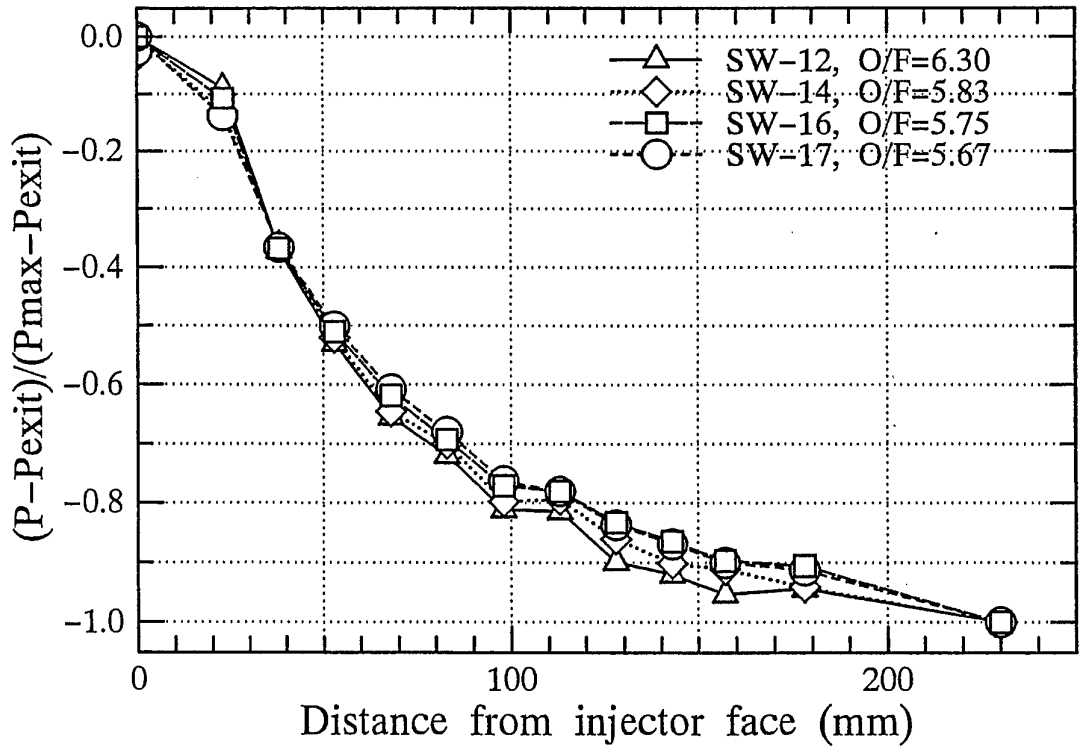


Fig. 23. Pc distribution along x-axis for oxygen-swirl injectors for the uni-element chamber. (Effect of fuel injection area)

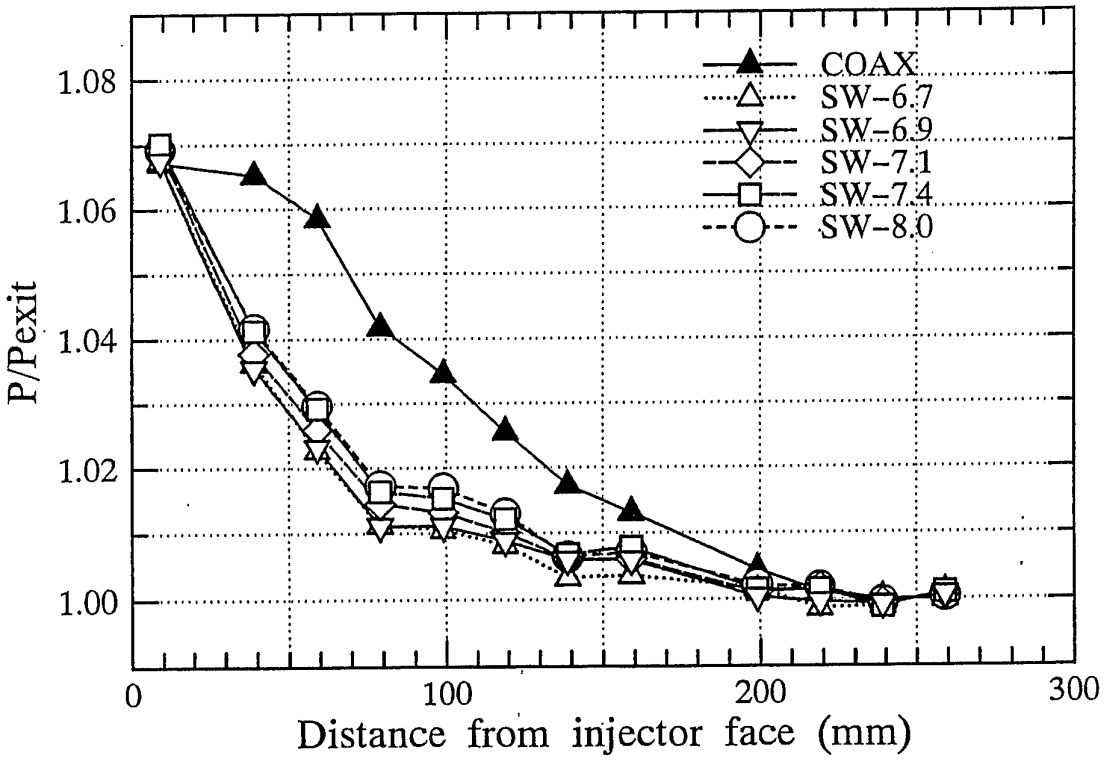


Fig. 24. Pc distribution along x-axis for the 9-element chamber.
(Effect of type of injector)

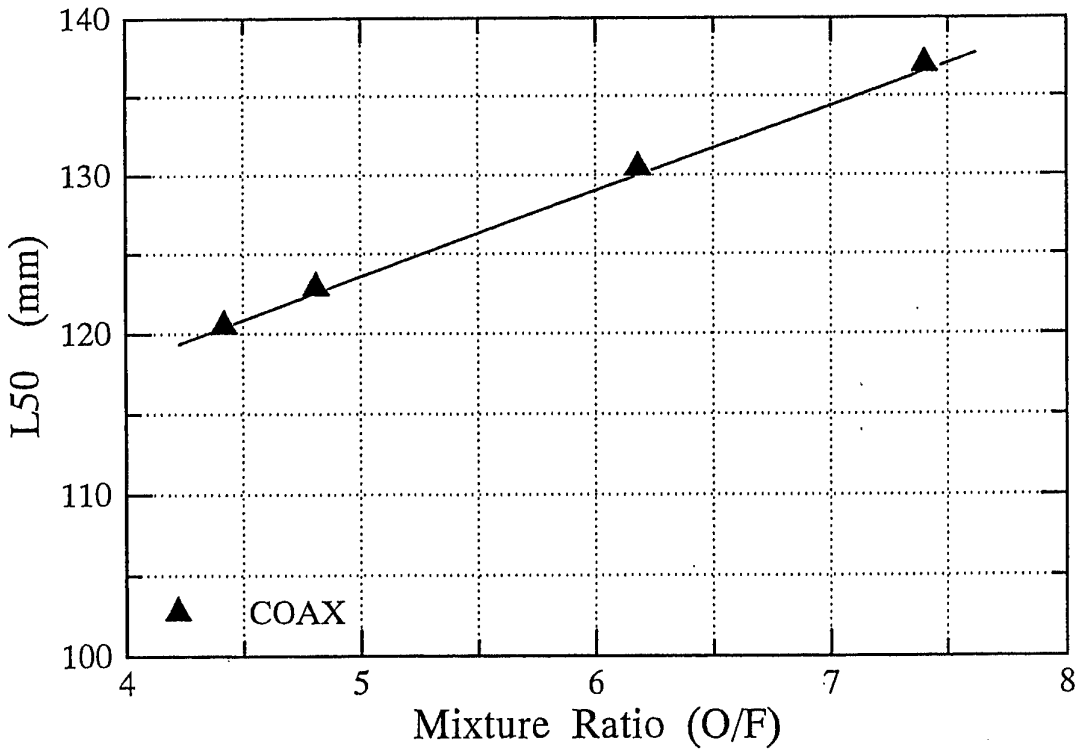


Fig. 25. Variation of L50 as a function of O/F for the shear-coaxial injector with the uni-element chamber.

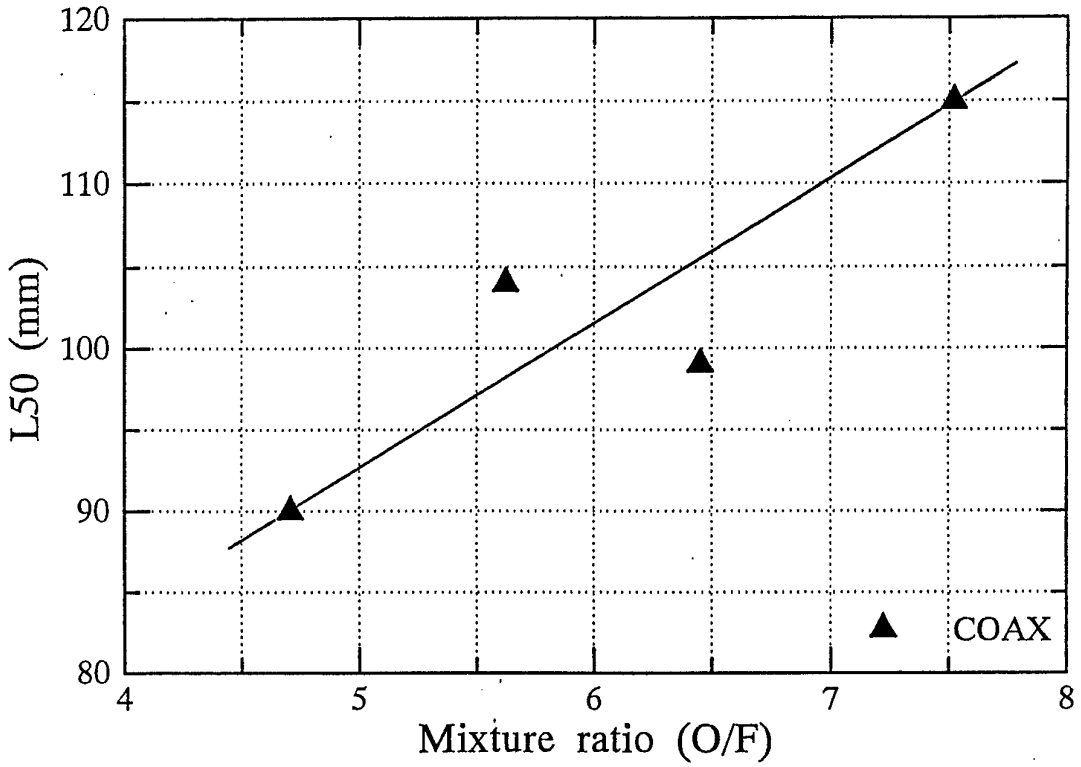


Fig. 26. Variation of L50 as a function of O/F for the shear-coaxial injector with the 9-element chamber.

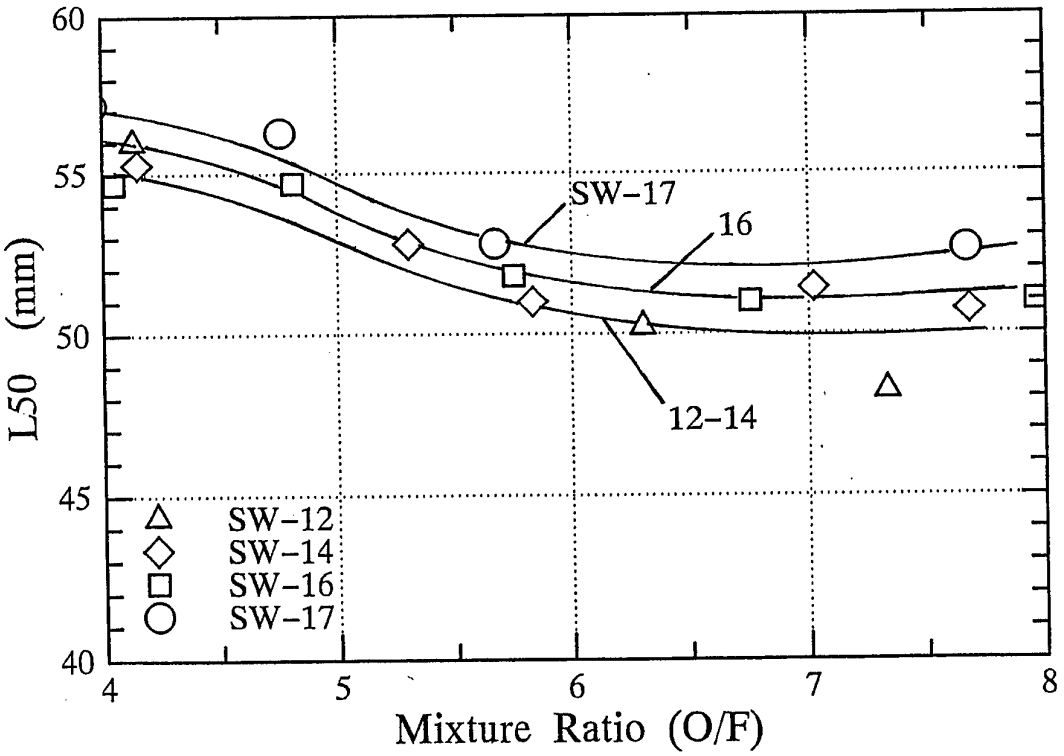


Fig. 27. Variation of L50 as a function of O/F for the oxygen-swirl injectors with the uni-element chambers.

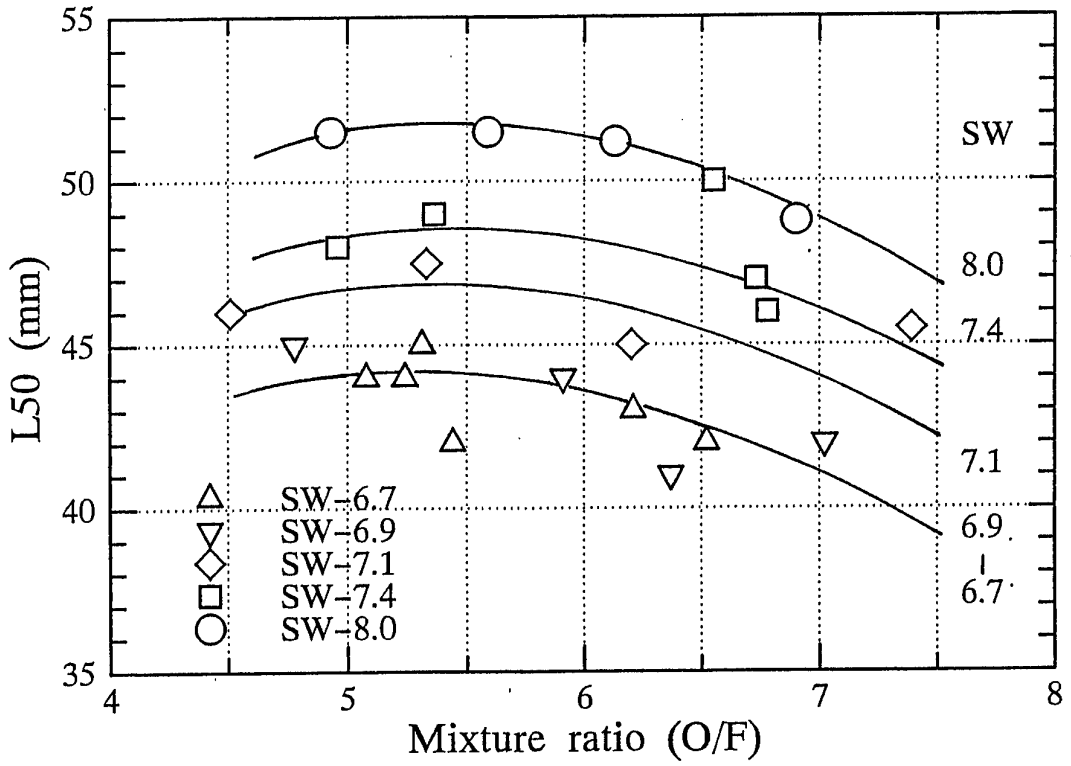


Fig. 28. Variation of L50 as a function of O/F for the oxygen-swirl injectors with the 9-element thrusters.

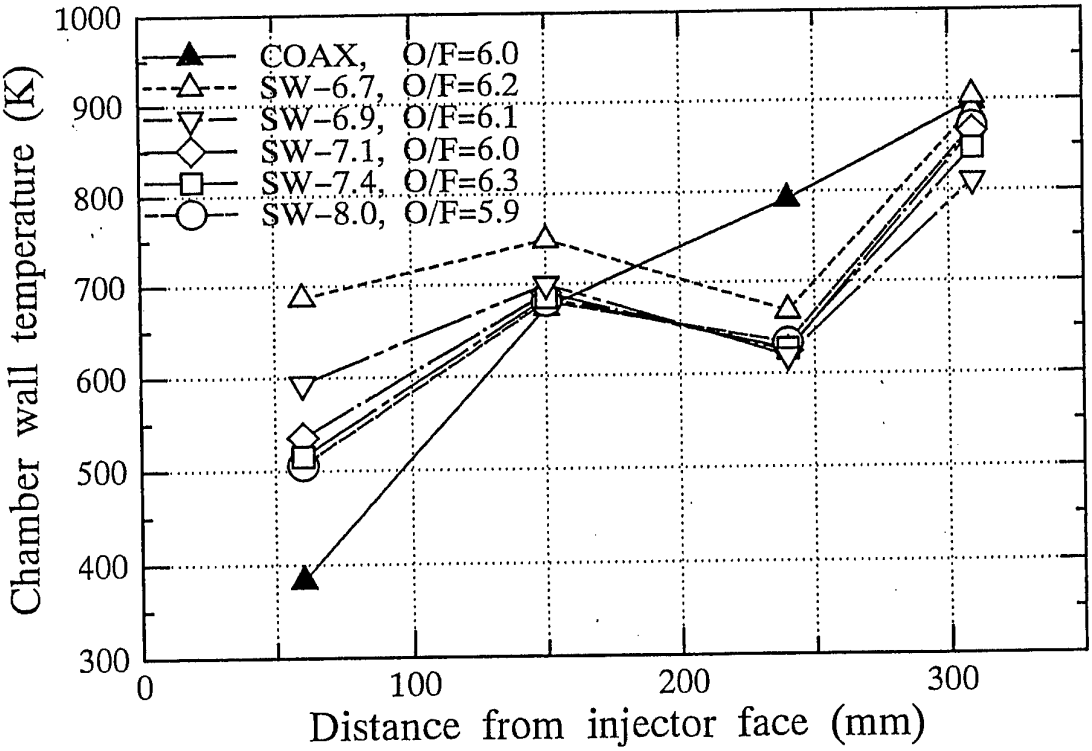


Fig. 29. Temperature distributions along the x-axis at 1.5 seconds after combustion with the 9-element thruster, O/F is about 6.

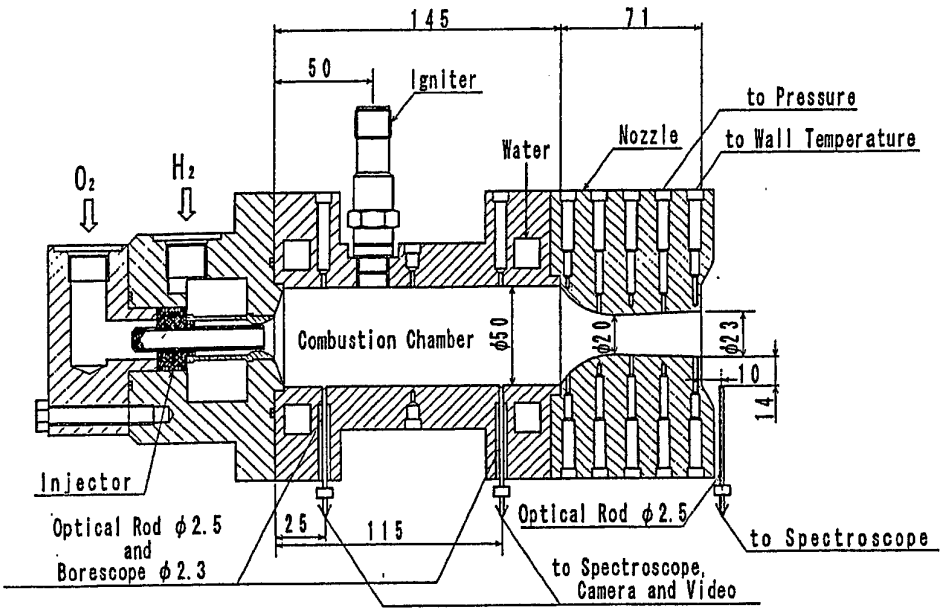


Figure 30. Schematic of water-cooled thruster used in gas-gas combustion study. Dimensions are in mm.

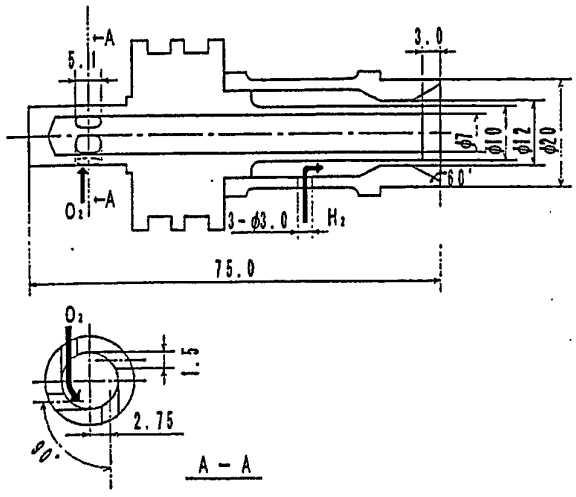


Figure 31. Schematic of the swirl-coaxial injector for gas-gas combustion study.

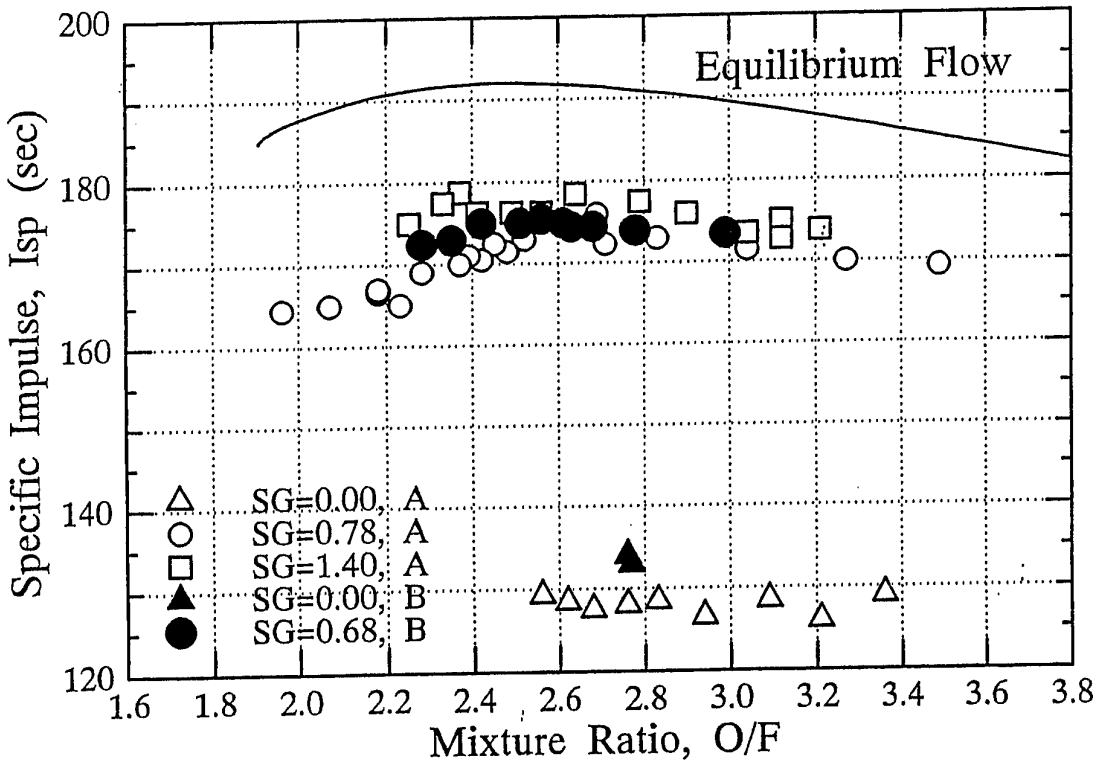


Figure 32. Variation of specific impulse, Isp as a function of O/F for GO_2/GCH_4.

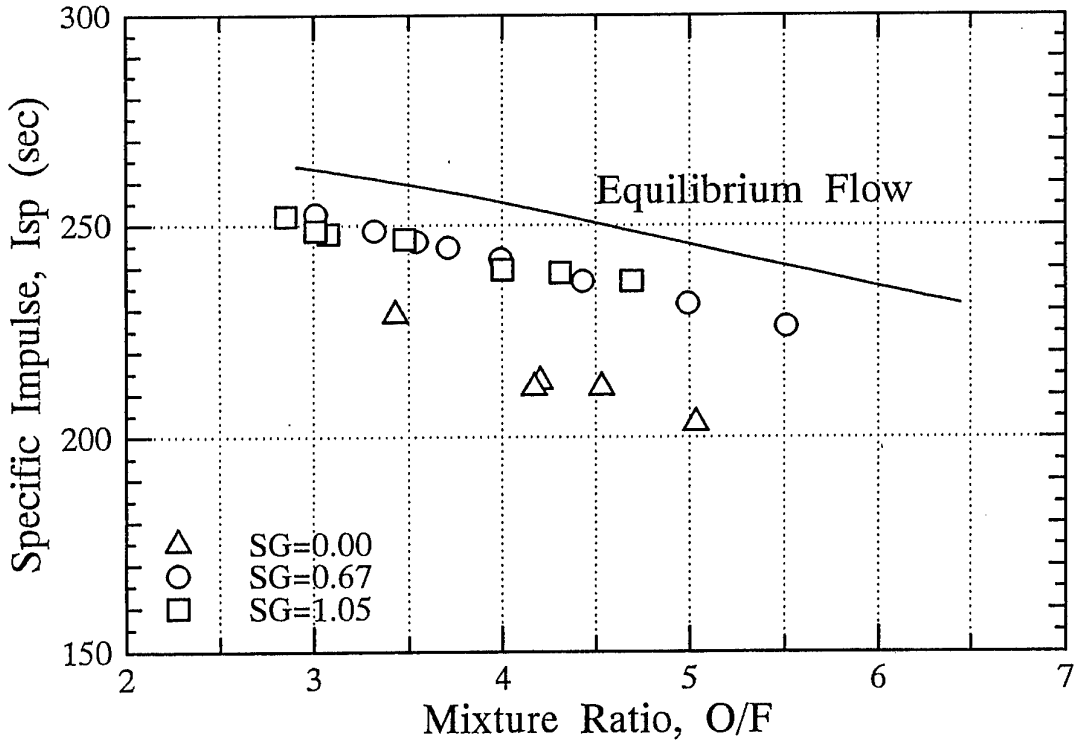


Figure 33. Variation of specific impulse, Isp as a function of O/F for GO_2/GH_2.

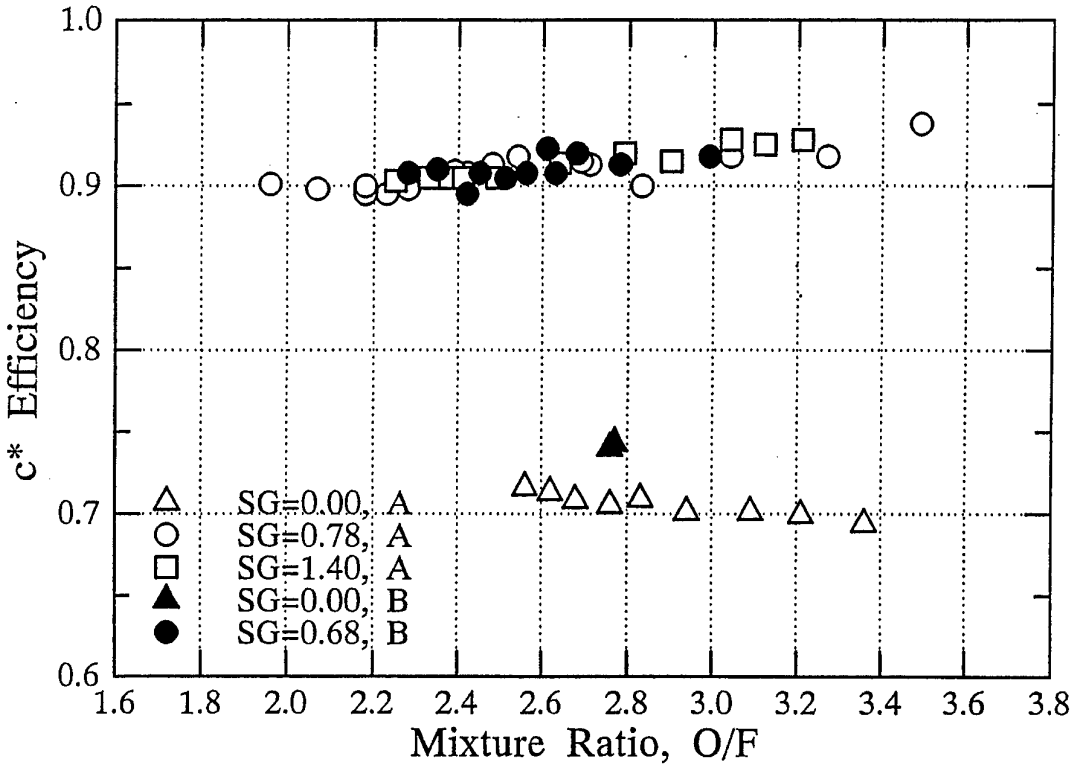


Figure 34. Variation of c* efficiency ηc* as a function of O/F for GO_2/GCH_4.

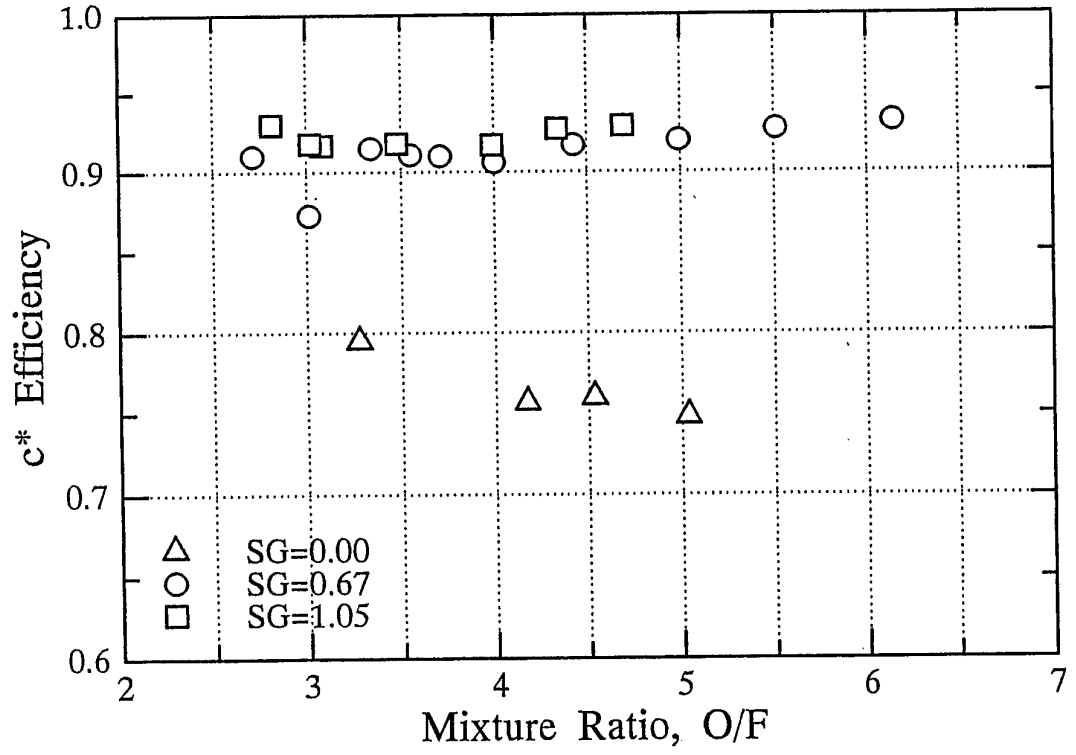


Figure 35. Variation of c* efficiency ηc* as a function of O/F for GO_2/GH_2.

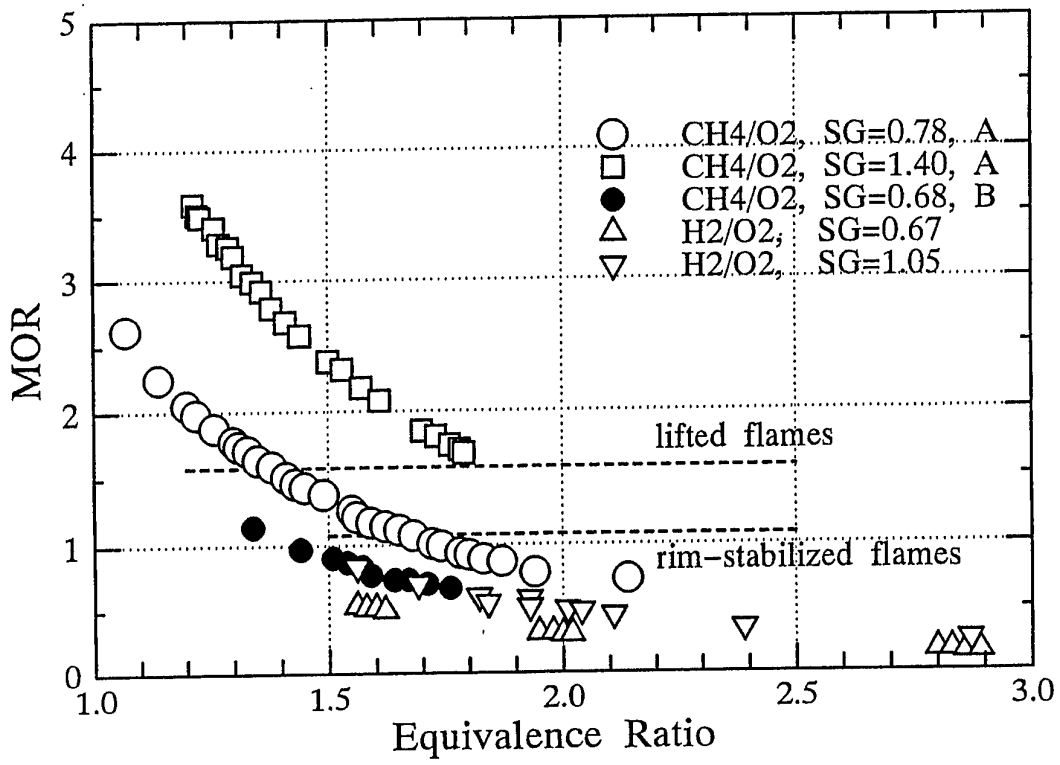


Figure 36 Boundaries of an attached flame and a lifted flame for the swirl-coaxial injector with gas-gas combustion

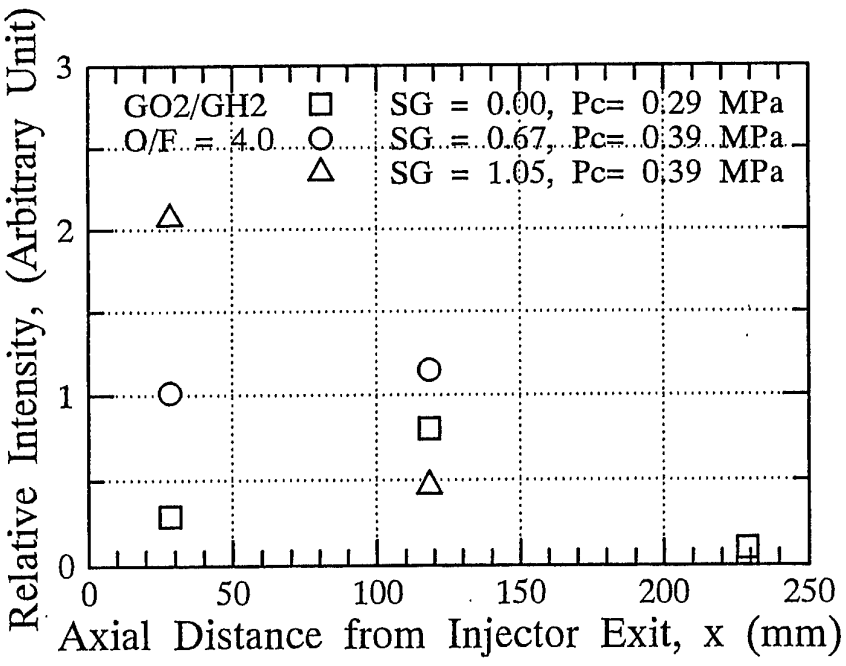


Figure 37 OH-radical intensity comparisons along the axial distance for the three Sg values of GO_2/GH_2 flames.

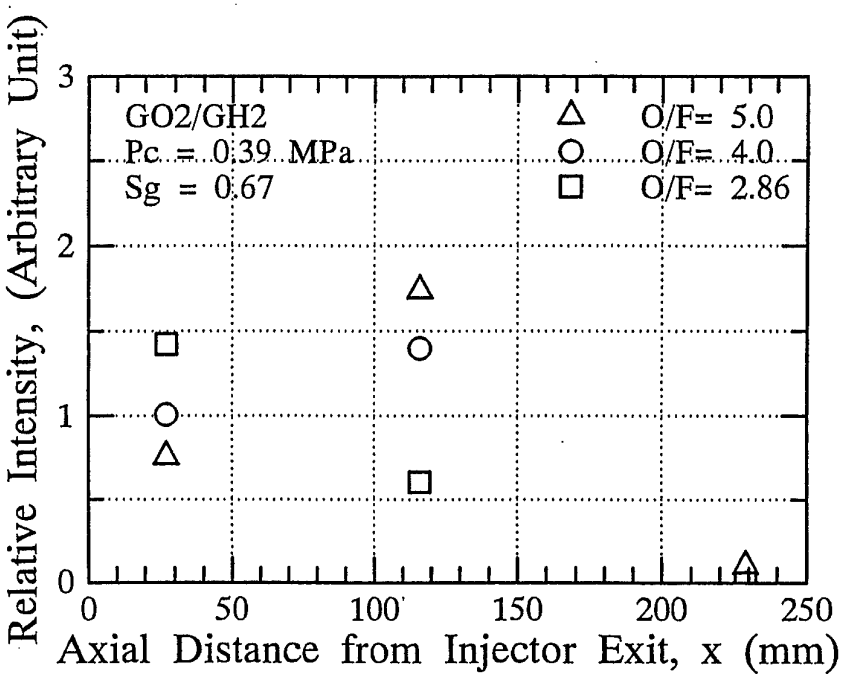
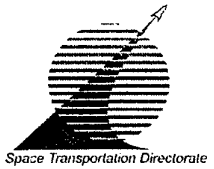


Figure 38 OH-radical intensity comparisons for the three flames at O/F = 2.9, 4.0, 5.0 along the axial distance for GO_2/GH_2 flames.



A Global Optimization Methodology for GO_2/GH_2 Single Element Injector Design

P. K. Tucker
NASA
Marshall Space Flight Center

W. Shyy & R. Vaidyanathan
Department of Aerospace Engr.,
Mechanics & Engr. Science
University of Florida

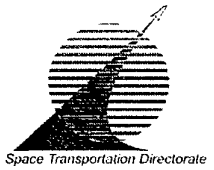
Fourth International Symposium on Liquid Space Propulsion

Lampoldshausen, Germany

March 13-15, 2000

OVERVIEW

- **Introduction**
- ***Method i* Application**
- Injector Design
  - Injector Design Models
  - Design Data Generated
  - Response Surfaces
- ***Method i* Optimization Results**
  - Original Constraints & Equal Weights
  - Original Constraints & Unequal Weights
  - Element Trend Comparison
- **Summary**



INTRODUCTION-Motivation

- **New launch vehicle/propulsion system development programs have-**
  - ambitious goals
  - relatively low budgets
  - aggressive schedules
- **These budgets/schedules are not conducive to large-scale hot-fire programs**
- **Injector/combustor design will be key in meeting program goals**
  - determines performance and stability
  - governs heat flux/combustor compatibility issues
- **New injector designs should be robust**
  - design space considered must be enlarged
  - more variables must be included earlier in the design process

INTRODUCTION-*Method i*

- ***method i* (Methodology for Optimizing Design of Injectors) addresses above issues via:**
  - Response Generation-generation of appropriate design data (responses) by physical or numerical experiments
  - Optimization-guides designer to an optimum design subject to his constraints
- **Scope**
  - *method i* is not restricted to any propellant combination or element type
  - Any relevant design information can be used
- **Useful during any stage of design**
  - Breadth allows use during early design phases
  - Depth allows use for element/injector optimization
- **Responses can be generated from any relevant source**
  - Takes advantage of existing experimental data and empirical design information
  - State-of-the-art experimental data (e.g., LDV and Raman spectroscopy), CFD analyses & other sources
- **Optimization**
  - Allows a larger design space to be evaluated
  - Allows objective evaluation of large amounts of inter-related information



INTRODUCTION--*Method i* Status

- **Work to Date**
  - Simple shear coaxial element optimized with Response Surface Methodology (RSM) in terms of Energy Release Efficiency, *ERE* and Wall Heat Flux, Q_w
  - RSM used to optimize an impinging element in terms of *ERE*, Q_w, Injector Heat Flux, Q_{inj}, Relative Weight, W_{rel} and Relative Cost, C_{rel}
  - RSM used to optimize a swirl coaxial element in terms of *ERE*, Q_w, Q_{inj}, W_{rel} and C_{rel}
  - Neural Networks (both back propagation & radial basis) trained and used to augment existing (but, sometimes scarce) design data to construct more accurate response surfaces

- **Future Work**
  - Continued work on neural networks to extract the maximum information from small quantities of data
  - Introduce CFD analysis to generate new design data to augment empirical data
  - Demonstrate capability as element selection and preliminary design tool
  - Demonstration on multi-element injector



INTRODUCTION--Use of GO_2/GH_2 Propellant System

- **Rationale for Use of GO_2/GH_2 Propellant System**

  GO_2/GH_2 propellant system provides an ideal framework for development and evaluation of injector optimization techniques

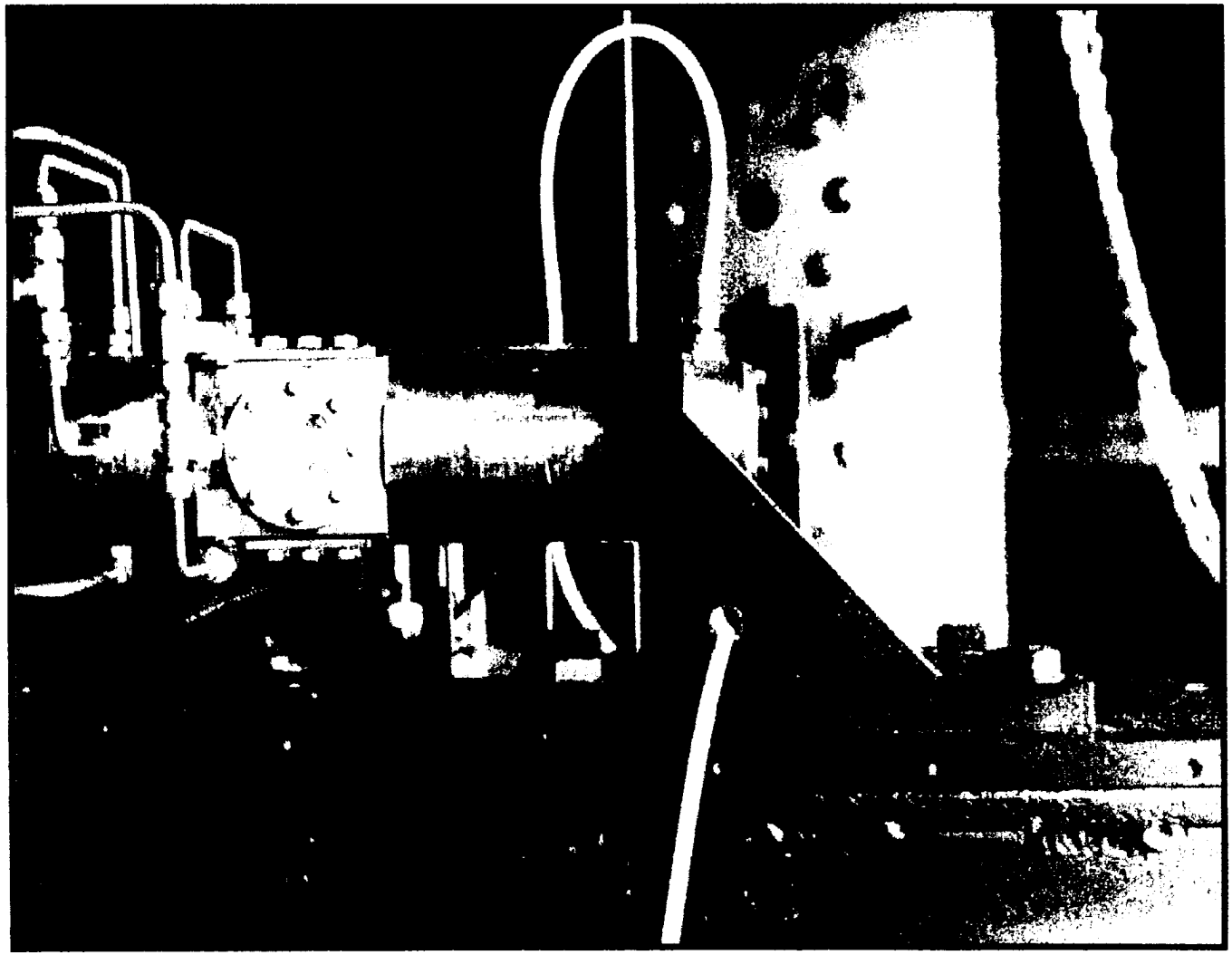
  - A fairly broad empirical design methodology exists
  - Physics of the system are relatively simple (no atomization or vaporization)
  - Amenable to use of both--
    - Modern laser-based diagnostic techniques
    - CFD analyses

- **Link to Other Propellant Systems**

  - Techniques developed for GO_2/GH_2 injector optimization are generic and will be applicable to other propellant combinations
  - Overall methodology and framework developed for GO_2/GH_2 injector optimization will also be applicable to other propellant combinations
  - Affordable and more reliable CFD solutions for other propellant combinations are within reach due to emergence of enabling technologies for parallel computing

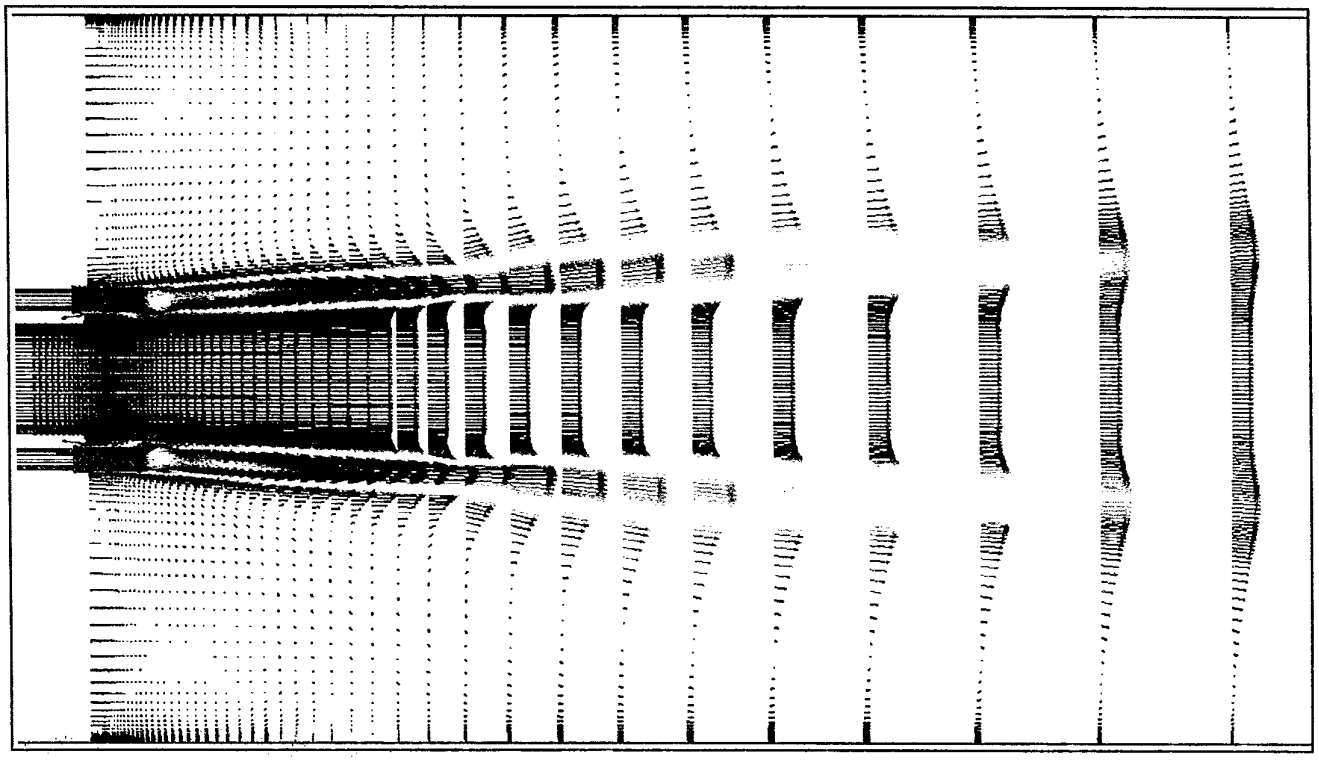
INTRODUCTION--Use of GO_2/GH_2 Propellant System

Injector Element Firing at Penn State Cryogenic Combustion Lab



INTRODUCTION--Use of GO_2/GH_2 Propellant System

Shear Coaxial Element Near-Injector Solution from FDNS

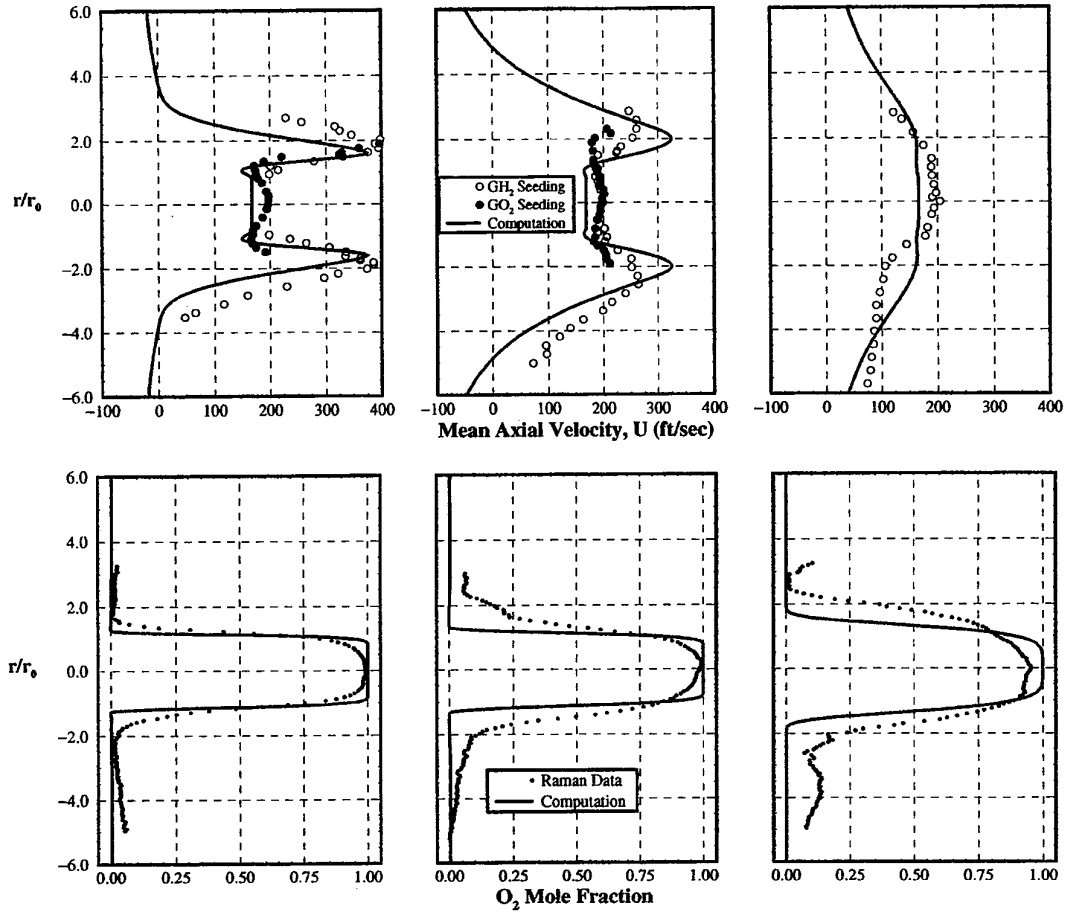


Space Transportation Directorate

INTRODUCTION--Use of GO_2/GH_2 Propellant System

CFD Results Compared to Data for GO_2/GH_2 Shear Coaxial Injector

- Velocity and Species Data from Penn State Cryogenic Combustion Lab
- Comparisons from MSFC CFD model using the FDNS Code



Method i APPLICATION

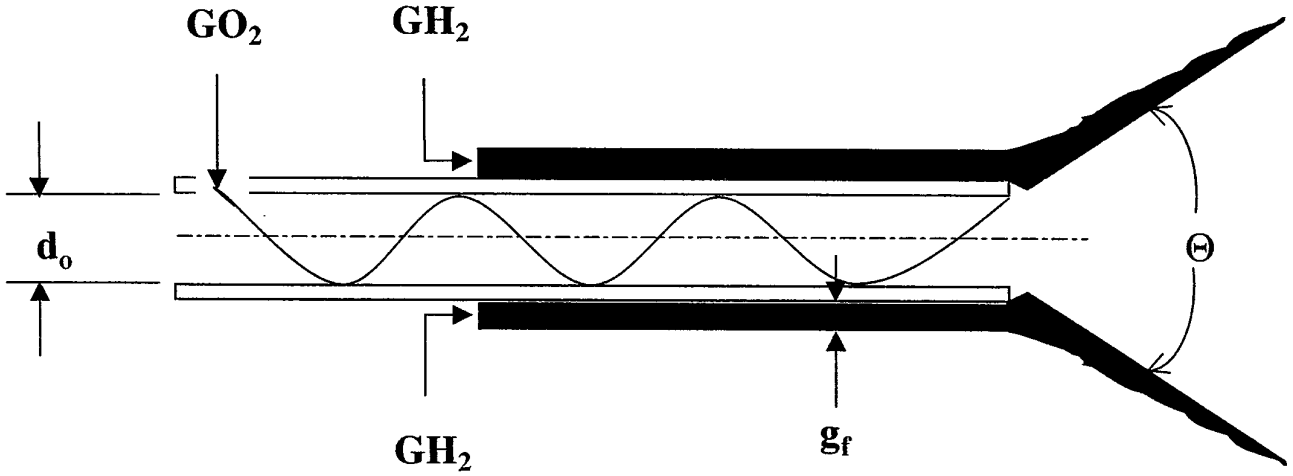
Method i is used to optimize a swirl coaxial GO_2/GH_2 injector element

Independent (Design) Variables & Ranges

- Oxidizer pressure drop, ΔP_o (10-20% of P_c)
- Fuel pressure drop, ΔP_f (2-20% of P_c)
- Full cone swirl angle, Θ (30-90°)
- Combustor Length, L_{comb} (2-8 inches)

Dependent Variables

- Energy Release Efficiency, *ERE* (maximize)
- Wall Heat Flux, Q_w (minimize)
- Injector Heat Flux, Q_{inj} (minimize)
- Relative Combustor Weight, W_{rel} (minimize)
- Relative Injector Cost, C_{rel} (minimize)



GO_2/GH_2 Swirl Coaxial Element

Method i APPROACH--Injector Design Model

- **Chamber & Flow Conditions**
  - P_c = 1000 psi
  - MR = 6
  - GO_2 flowrate/element = 0.25 lb_m/sec
  - GH_2 flowrate/element = 0.042 lb_m/sec
- ***ERE* & Q_w**
  - Design information generated from empirical design methodology (Doumas and Laster, 1953 & Calhoon, Ito and Kors; Aerojet, 1973)
  - $ERE = f(\Delta P_o, \Delta P_f, \Theta, L_{comb})$
  - $Q_w = f(\Delta P_o, \Delta P_f, \Theta)$
- **Other Design variables**
  - $Q_{inj} = f(\Delta P_o, \Delta P_f, \Theta)$
  - $W_{rel} = f(L_{comb})$
  - $C_{rel} = f(\Delta P_o, \Delta P_f, \Theta)$

Method i APPROACH--Design Data Generated

Matrix of ΔP_o & ΔP_f Values Considered

	ΔP_o						
ΔP_f	100	120	140	150	160	180	200
20	X (25)			X (35)			X (45)
50							
80							
110	X			X			X
140							
170							
200	X			X			X

APPROACH--Design Data Generated

Sample Design Results from Empirical Design Methodology

ΔP_o	ΔP_f	L_{comb}	Θ	ERE	Q_w	Q_{inj}	W_{rel}	C_{rel}
100	200	2	30	93.0	0.624	8.89	0.923	0.87
100	200	2	45	94.2	0.628	14.00	0.923	0.95
100	200	2	60	94.6	0.635	20.00	0.923	1.05
100	200	2	75	94.6	0.641	27.33	0.923	1.20
100	200	2	90	94.7	0.647	36.59	0.923	1.42
100	200	4	30	95.3	0.624	8.89	1.000	0.87
100	200	4	45	96.2	0.628	14.00	1.000	0.95
100	200	4	60	96.5	0.635	20.00	1.000	1.05
100	200	4	75	96.5	0.641	27.33	1.000	1.20
100	200	4	90	96.7	0.647	36.59	1.000	1.42
100	200	6	30	96.2	0.624	8.89	1.077	0.87
100	200	6	45	97.0	0.628	14.00	1.077	0.95
100	200	6	60	97.3	0.635	20.00	1.077	1.05
100	200	6	75	97.3	0.641	27.33	1.077	1.20
100	200	6	90	97.5	0.647	36.59	1.077	1.42
100	200	8	30	96.8	0.624	8.89	1.154	0.87
100	200	8	45	97.5	0.628	14.00	1.154	0.95
100	200	8	60	97.7	0.635	20.00	1.154	1.05
100	200	8	75	97.8	0.641	27.33	1.154	1.20
100	200	8	90	97.9	0.647	36.59	1.154	1.42

Space Transportation Directorate

Method i APPROACH--Joint Response Surface

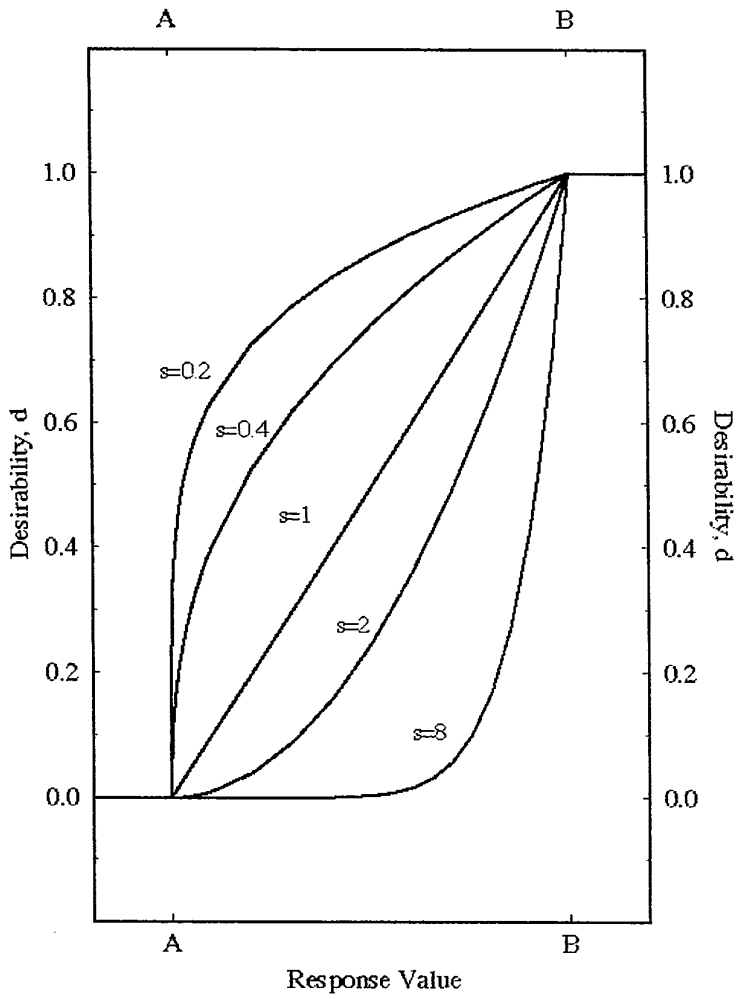
Joint ERE/Q_w Response Surface

- Objective is to maximize *ERE* & minimize Q_w
- Individual response surfaces linked through desirability function
- To maximize *ERE*, $d_1 = \left(\frac{ERE - A}{B - A}\right)^s$
- To minimize Q_w, $d_2 = \left(\frac{Q - E}{C - E}\right)^t$
- The general composite response, D, is given by

$$D = (d_1 \bullet d_2 \bullet d_3 \ldots\ldots d_m)^{1/m}$$

- Here

$$D = (d_1 \bullet d_2)^{1/2}$$





RESULTS--Original Constraints & Equal Weights

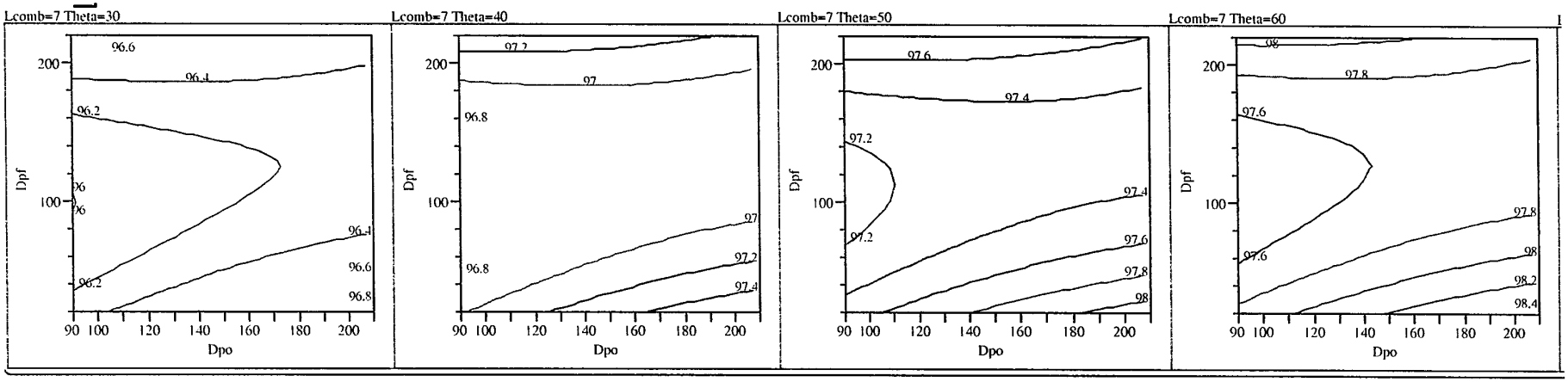
Stepwise Optimization for Swirl Coaxial Element

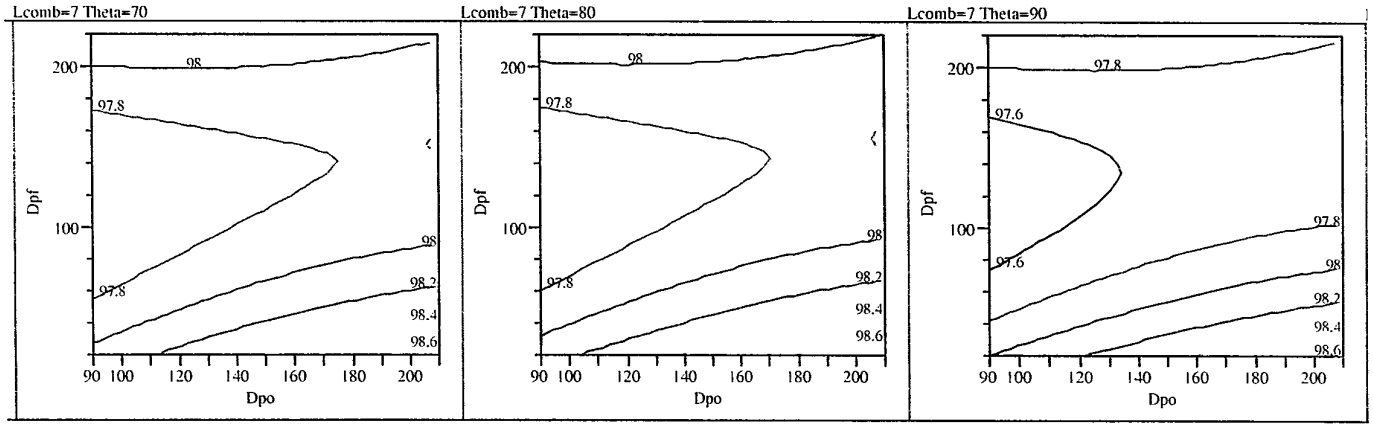
Independent Variable	Constraints	Results 1	Results 2	Results 3	Results 4	Results 5
ΔP_o	100-200	200	200	200	200	104
ΔP_f	20-200	41	41	42	47	20
L_{comb}	2-8	7.2	7.2	7.6	3.2	3.4
Θ	30-90	81.0	81.0	37.0	47.0	44.0
Dependent Variable	**Desirability Limits**	**ERE**	**ERE, Q_w**	**ERE, Q_w, Q_{inj}**	**ERE, Q_w, Q_{inj}, W_{rel}**	**ERE, Q_w, Q_{inj}, W_{rel}, C_{rel}**
ERE	92.3-99.0	98.5	98.5	97.2	96.0	95.7
Q_w	0.60-0.65	0.60	0.60	0.60	0.60	0.60
Q_{inj}	7.0-37.0	26.8	26.8	9.1	12	10.5
W_{rel}	0.90-1.15	1.13	1.13	1.14	0.97	0.98
C_{rel}	0.73-1.42	0.98	0.98	0.81	0.84	0.76

Space Transportation Directorate

RESULTS--Contours

ERE for Θ=30-90° and L_{comb}=7 in.

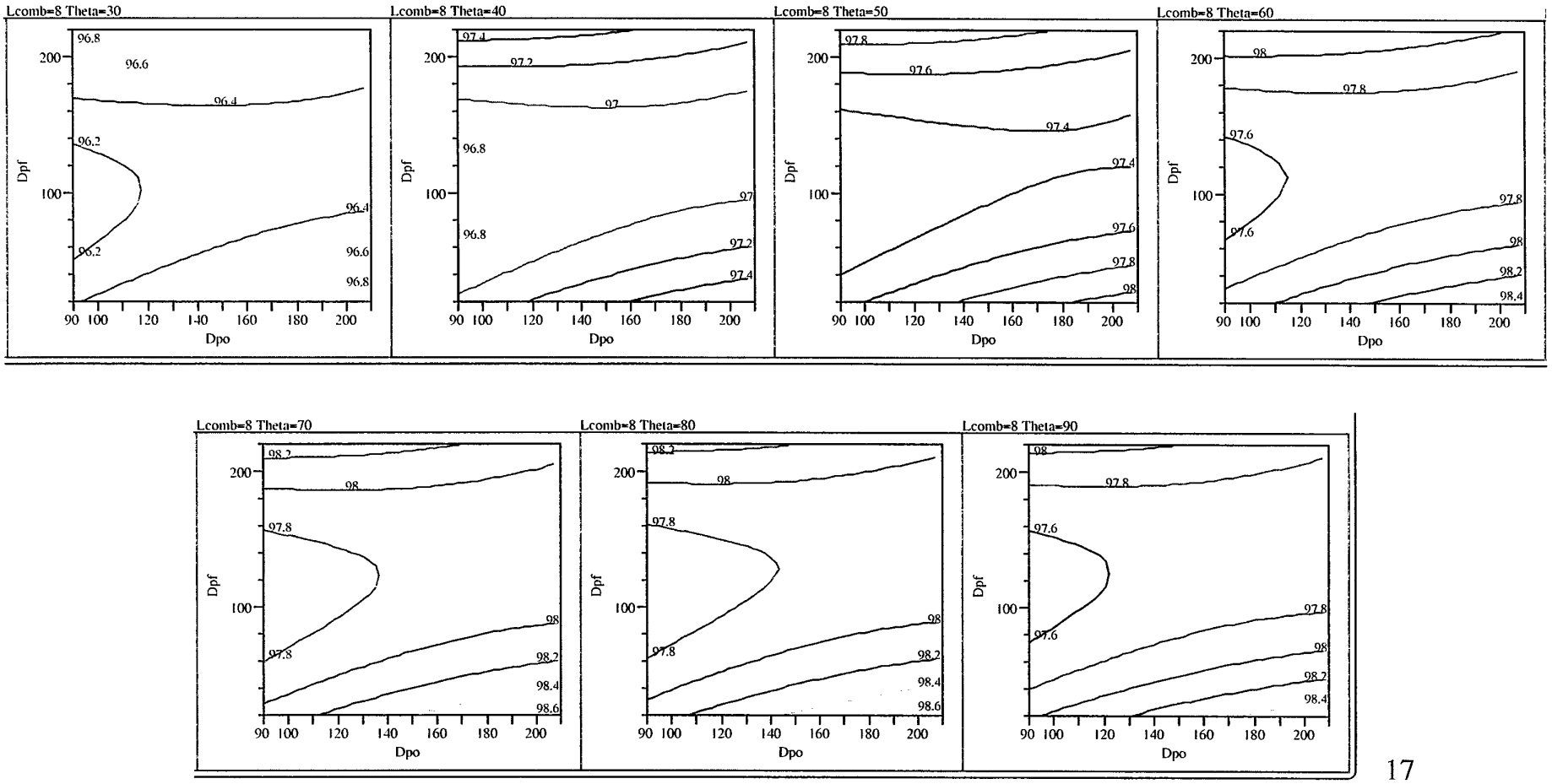




Space Transportation Directorate

RESULTS--Contours

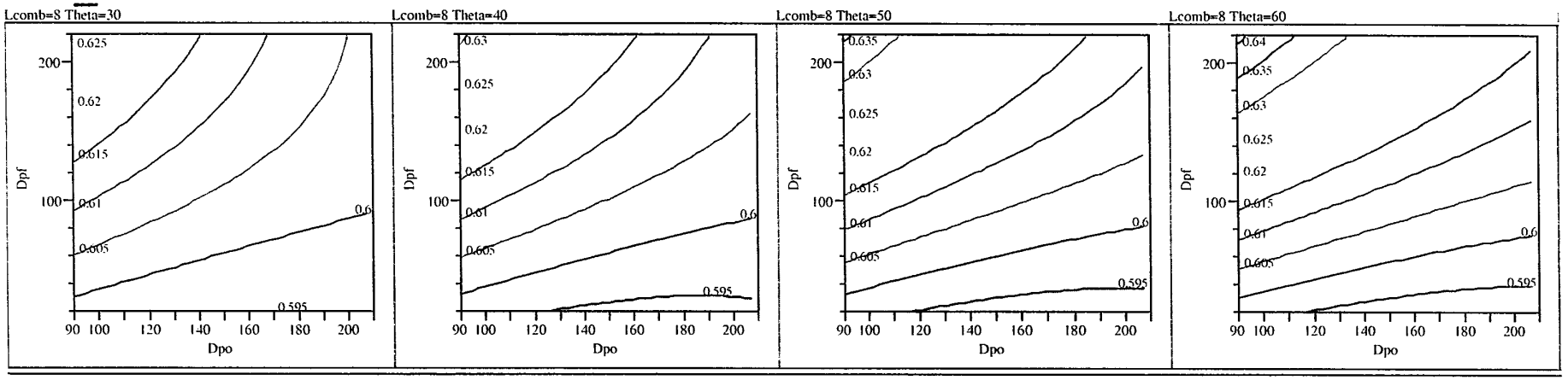
ERE for Θ=30-90° and L_{comb}=8 in.

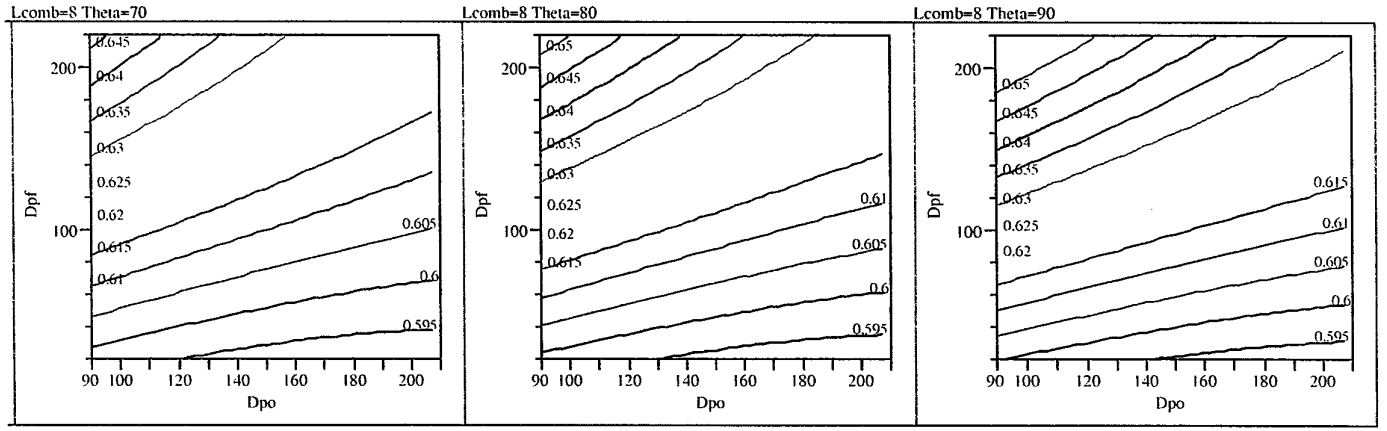


Space Transportation Directorate

RESULTS--Contours

Q_w for Θ=30-90° and L_{comb}=8 in.

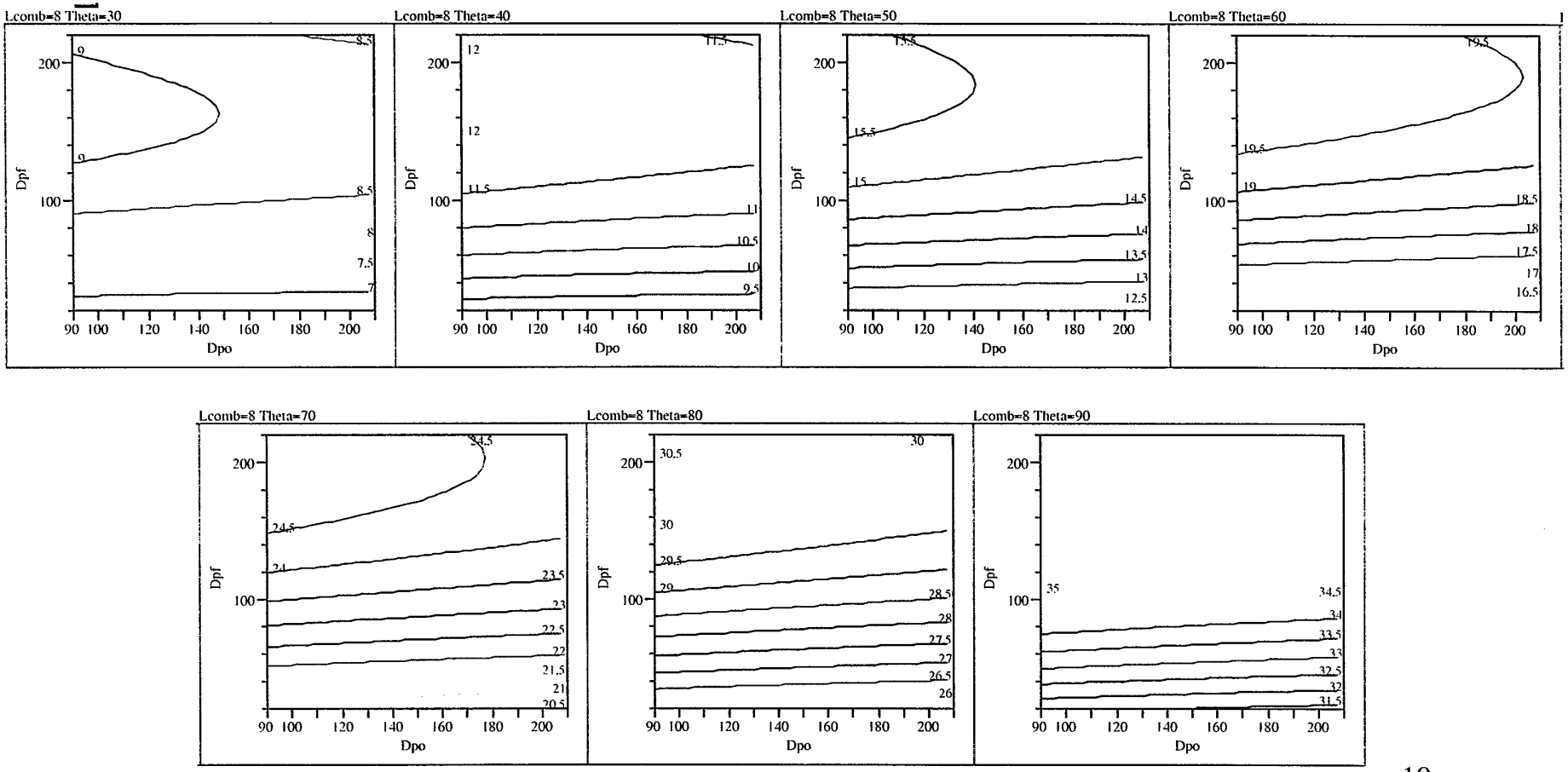




Space Transportation Directorate

RESULTS--Contours

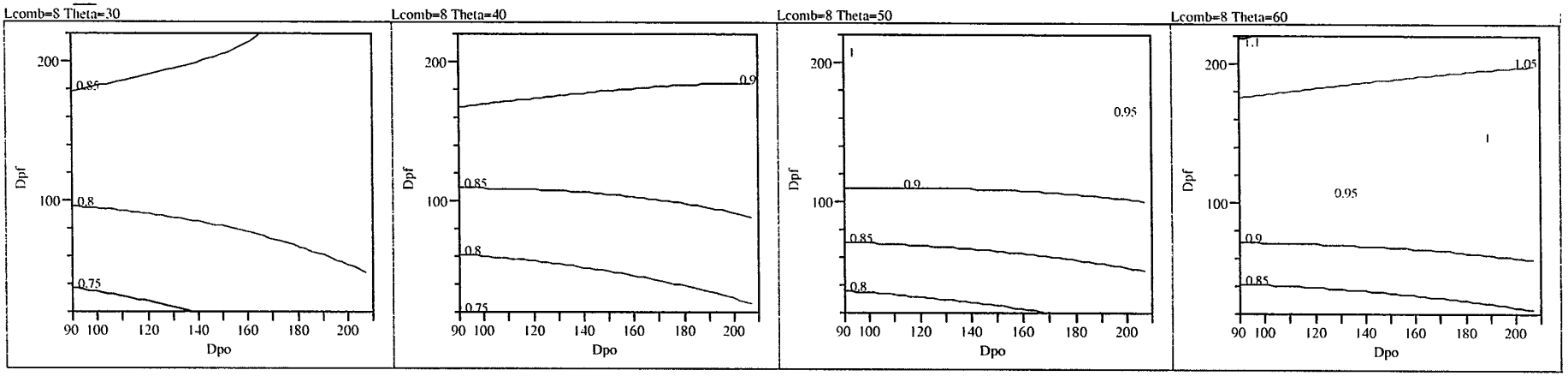
Q_{inj} for Θ=30-90° and L_{comb}=8 in.

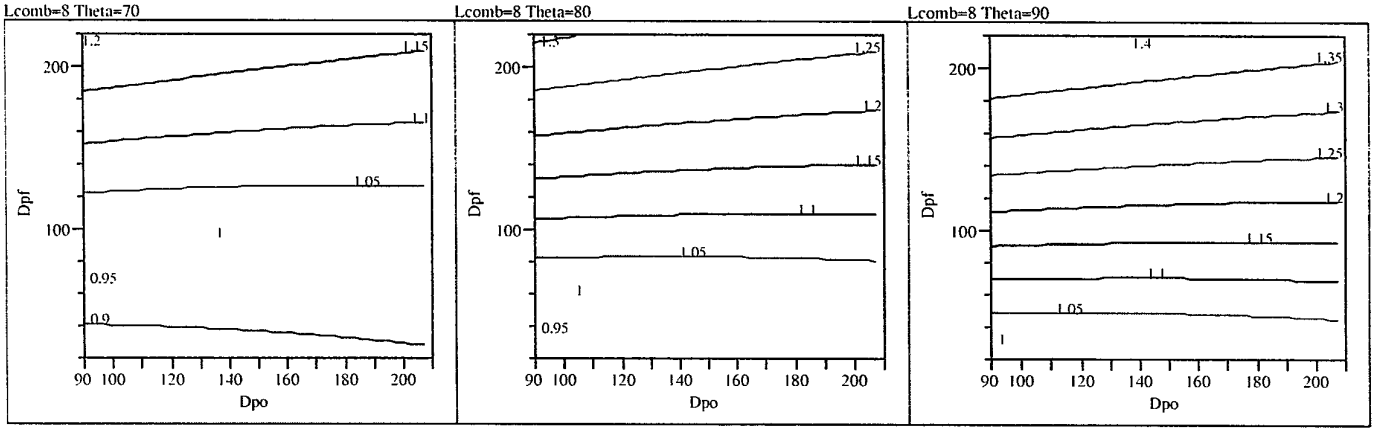


Space Transportation Directorate

RESULTS--Contours

C_{rel} for Θ=30-90° and L_{comb}=8 in.





RESULTS--Original Constraints & Variable Weights

Modified Variable Weights for Swirl Coaxial Element

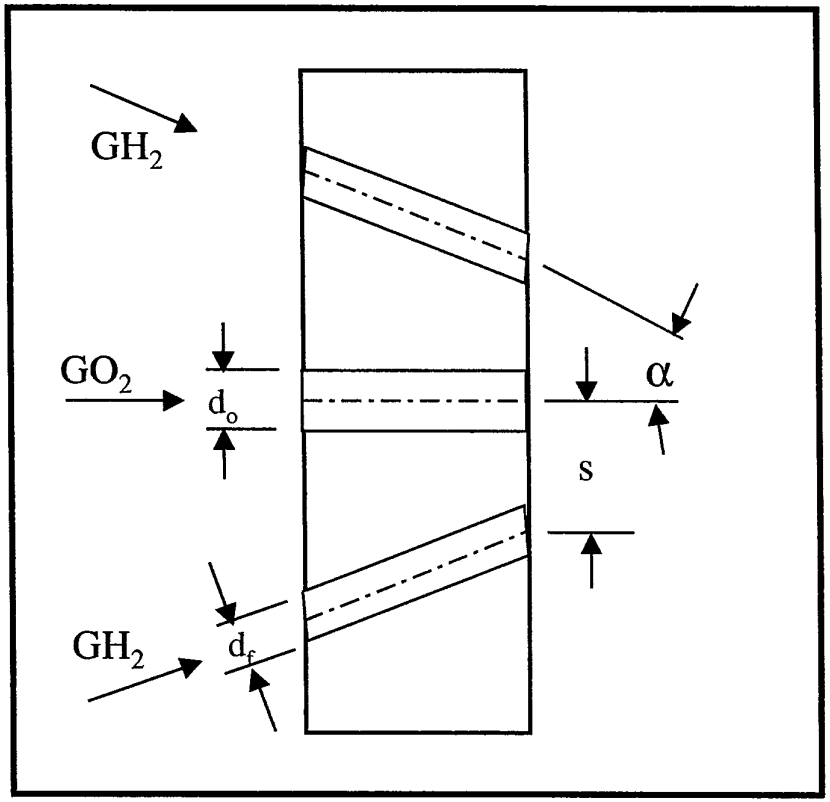
Independent Variable	Constraints	Results Baseline	Constraints	Results Case 1	Constraints	Results Case 2
ΔP_o	100-200	104	100-200	200	100-200	200
ΔP_f	20-200	20	20-200	32	20-200	44
L_{comb}	2-8	3.4	2-8	3.6	2-8	2.9
Θ	30-90	44.0	30-90	30.0	30-90	72.0
Dependent Variable	***Baseline*** **Variable Weight**		***Life*** **Variable Weight**		***Thrust/Weight*** **Variable Weight**	
ERE	1	95.7	1	95.3	10	96.7
Q_w	1	0.60	5	0.60	1	0.60
Q_{inj}	1	10.50	10	6.9	1	22.6
W_{rel}	1	0.98	1	0.99	2	0.96
C_{rel}	1	0.76	1	0.79	1	0.94

Space Transportation Directorate

RESULTS--F-O-F Impinging Element

***Method i* is used to optimize an unlike impinging GO_2/GH_2 injector element**

- **Design Variables and Ranges**
  - Oxidizer pressure drop, ΔP_o (10-20% of P_c)
  - Fuel pressure drop, ΔP_f (10-20% of P_c)
  - Impingement half-angle, α (15-50°)
  - Combustor Length, L_{comb} (2-8 inches)
- **Dependent Variables**
  - Energry Release Efficiency, *ERE* (maximize)
  - Wall Heat Flux, Q_w (minimize)
  - Injector Heat Flux, Q_i (minimize)
  - Relative Combustor Weight, W_{rel} (minimize)
  - Relative Injector Cost, C_{rel} (minimize)



GO_2/GH_2 F-O-F Impinging Element

RESULTS--F-O-F Original Constraints & Variable Weights

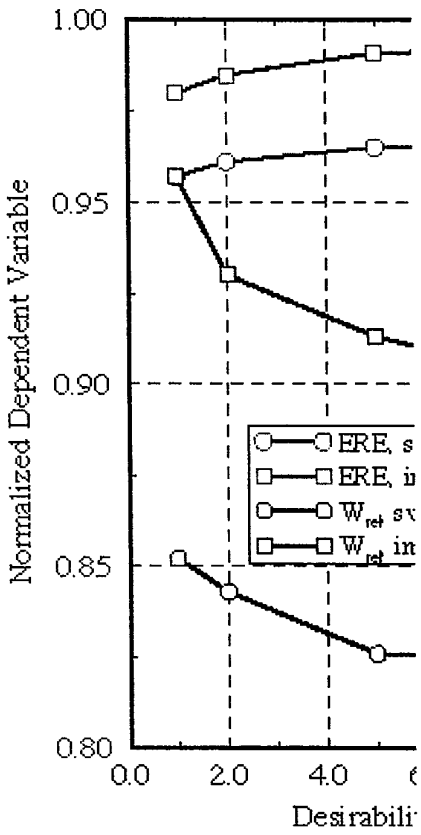
Modified Variable Weights for F-O-F Impinging Element

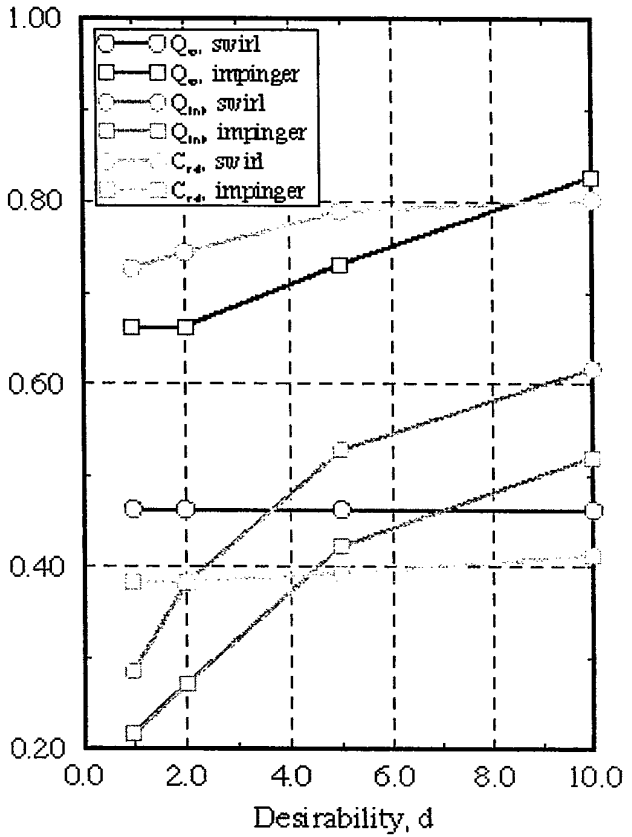
Independent Variable	Constraints	Results Baseline	Constraints	Results Case 1	Constraints	Results Case 2
ΔP_o	100-200	100	100-200	158	100-200	100
ΔP_f	100-200	100	100-200	100	100-200	137
L_{comb}	2-8	6.5	2-8	7.7	2-8	5.2
α	15-50	24.0	15-50	15.0	15-50	36.0
Dependent Variable	***Baseline*** **Variable Weight**		***Life*** **Variable Weight**		***Thrust/Weight*** **Variable Weight**	
ERE	1	98.0	1	96.7	5	99.1
Q_w	1	0.86	5	0.75	1	0.95
Q_{inj}	1	7.9	5	5.3	1	15.6
W_{rel}	1	1.10	1	1.14	5	1.05
C_{rel}	1	0.93	1	0.97	1	0.95

Space Transportation Directorate

RESULTS--Trend Comparisons

Thrust to Weight Trends for Swirl and Impinging Elements

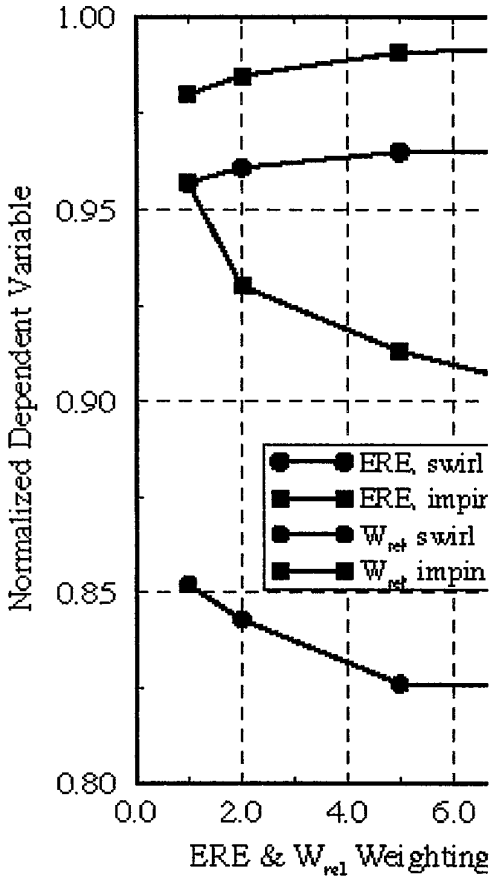


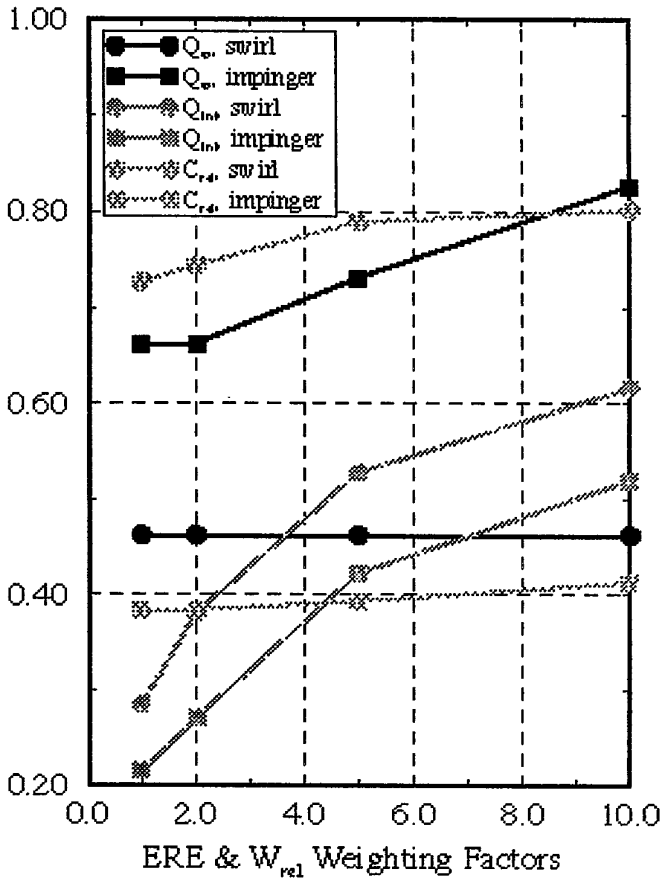


Space Transportation Directorate

RESULTS--Trend Comparisons

Thrust to Weight Trends for Swirl and Impinging Elements





SUMMARY

- **Responses generated for 3 GO_2/GH_2 element types:**
  - Shear Coaxial
  - Swirl Coaxial
  - F-O-F Impinging
- **Dependent variable response surfaces for each element linked for optimization**
- **Optimization methodology facilitates maximum use of available data**
  - Use with original weights and constraints
    - Effects of individual design variables on design are shown
    - Impact of weight & cost on design is illustrated
  - Capability to modify independent variable constraints & dependent variable weights
    - Allows flexibility
    - Allows designer to use his experience/intuition via
      - Evaluation of specific area of the design space
      - Emphasis on certain aspects of the design